Methods in Cell Biology • Volume 89

Biophysical Tools for Biologists, Volume 2

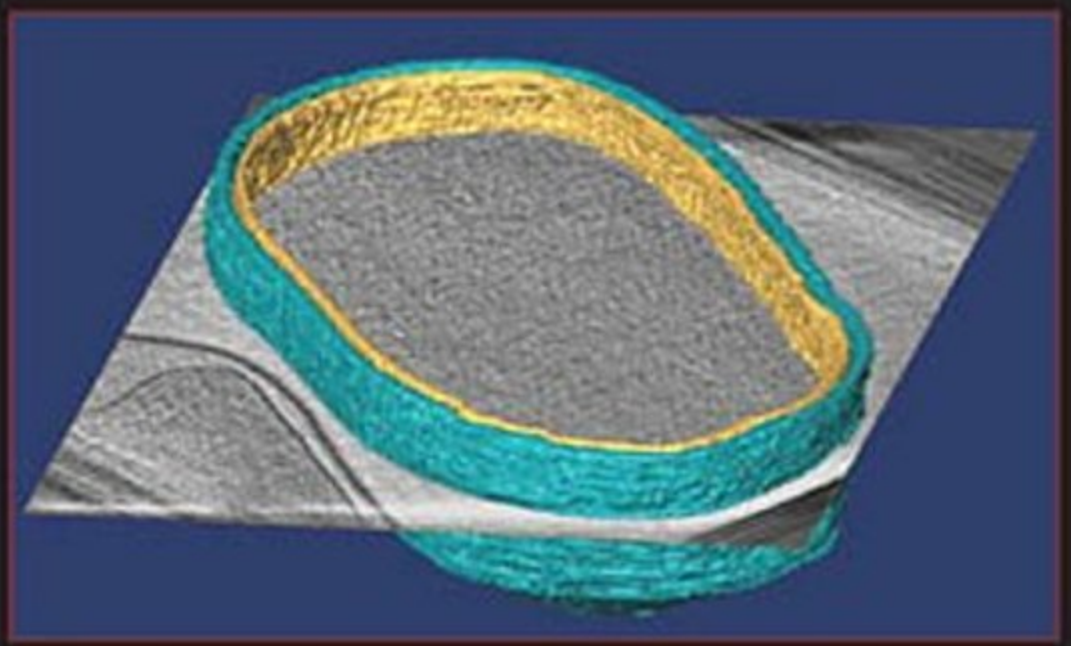

Edited by

John J. Correia • William Detrich

AP

Series Editors

Leslie Wilson
Department of Molecular, Cellular and Developmental Biology
University of California
Santa Barbara, California

Paul Matsudaira
Whitehead Institute for Biomedical Research
Department of Biology
Division of Biological Engineering
Massachusetts Institute of Technology
Cambridge, Massachusetts

Academic Press is an imprint of Elsevier
30 Corporate Drive, Suite 400, Burlington, MA 01803, USA
525 B Street, Suite 1900, San Diego, CA 92101-4495, USA

First edition 2008

ISBN: 978-0-12-372521-9
ISSN: 0091-679X

For information on all Academic Press publications visit our website at elsevierdirect.com

Printed and bound in USA

08 09 10 11 12 10 9 8 7 6 5 4 3 2 1

CONTRIBUTORS

Numbers in parentheses indicate the pages on which the authors' contributions begin.

Bharath Ananthanarayanan (37), Department of Pharmacology and Molecular Sciences, The Johns Hopkins University School of Medicine, Baltimore, Maryland 21205

Erdinc Atilgan (601), Department of Anatomy and Structural Biology, Albert Einstein College of Medicine and Yeshiva University, Bronx, New York 10461

Daniel Axelrod (169), Departments of Physics and Biophysics, University of Michigan, Ann Arbor, Michigan 48109

Margarida Barroso (569), Albany Medical College, Center for Cardiovascular Sciences, Albany, New York 12208

Benjamin Bird (275), Department of Chemistry and Chemical Biology, Northeastern University, Boston, Massachusetts 02115

Clifford P. Brangwynne (487), School of Engineering and Applied Sciences, Harvard University, Cambridge, Massachusetts 02143

Damian Brunner (521), European Molecular Biology Laboratory, Meyerhofstrasse 1, 69117 Heidelberg, Germany

Huimin Chen (3), School of Applied and Engineering Physics, Cornell University, Ithaca, New York 14853-2501

Ye Chen (569), University of Virginia, W. M. Keck Center for Cellular Imaging, Department of Biology, Charlottesville, Virginia 22904

Tatyana Chernenko (275), Department of Chemistry and Chemical Biology, Northeastern University, Boston, Massachusetts 02115

Edward C. Cox (223), Department of Molecular Biology, Princeton University, Princeton, New Jersey 08544

Jeremy Cribb (433), Department of Biomedical Engineering, University of North Carolina, Chapel Hill, North Carolina 27599

Max Diem (275), Department of Chemistry and Chemical Biology, Northeastern University, Boston, Massachusetts 02115

Terrence M. Dobrowsky (411), Department of Chemical and Biomolecular Engineering, The Johns Hopkins University, Baltimore, Maryland 21218, and Howard Hughes Medical Institute Graduate Training Program and Johns Hopkins Institute for NanoBioTechnology, The Johns Hopkins University, Baltimore, Maryland 21218

Marileen Dogterom (521), FOM Institute for Atomic and Molecular Physics (AMOLF), Kruislaan 407, 1098 SJ Amsterdam, The Netherlands

Elaine R. Farkas (3), School of Applied and Engineering Physics, Cornell University, Ithaca, New York 14853-2501

Margaret L. Gardel (487), Department of Physics and Institute for Biophysical Dynamics, University of Chicago, Illinois 60637

Lila M. Gierasch (59), Department of Biochemistry and Molecular Biology, and Department of Chemistry, University of Massachusetts, Amherst, Amherst, Massachusetts 01003

Ido Golding (223), Department of Physics, University of Illinois at Urbana-Champaign, Urbana, Illinois 61801

Travis J. Gould (329), Department of Physics and Astronomy and Institute for Molecular Biophysics, University of Maine, Orono, Maine 04469

Samuel T. Hess (329), Department of Physics and Astronomy and Institute for Molecular Biophysics, University of Maine, Orono, Maine 04469

Zoya Ignatova (59), Department of Biochemistry, Institute of Biology and Biochemistry, University of Potsdam, 14476 Potsdam-Golm, Germany

Jorge V. José (623), Physics Department and Department of Physiology and Biophysics, State University of New York Buffalo, New York 14260-1611

Petr Kalab (541), Department of Cell Biology, University of California, Berkeley, California 94720

Karen E. Kasza (487), School of Engineering and Applied Sciences, Harvard University, Cambridge, Massachusetts 02143

Konstantinos Konstantopoulos (411), Department of Chemical and Biomolecular Engineering, and Howard Hughes Medical Institute Graduate Training Program and Johns Hopkins Institute for NanoBioTechnology, The Johns Hopkins University, Baltimore, Maryland 21218

Ganhui Lan (601), Department of Mechanical Engineering and Biomedical Engineering, Johns Hopkins University, Baltimore, Maryland 21218

Jeff W. Lichtman (309), Department of Molecular and Cellular Biology and the Center for Brain Science, Harvard University, Cambridge, Massachusetts 02138

Jiayu Liu (487), Department of Physics, Harvard University, Cambridge, Massachusetts 02143

Carmen Mannella (129), Department of Health, Resource for Visualization of Biological Complexity, Wadsworth Center, New York, Albany, New York 12201-0509

Michael Marko (129), Department of Health, Resource for Visualization of Biological Complexity, Wadsworth Center, New York, Albany, New York 12201-0509

David Marshburn (433), Department of Computer Science, University of North Carolina, Chapel Hill, North Carolina 27599

Paul Matsudaira (391), Whitehead Institute, Massachusetts Institute of Technology, Cambridge, Massachusetts 02139

Christian Matthäus (275), Department of Chemistry and Chemical Biology, Northeastern University, Boston, Massachusetts 02115

Chad D. McCormick (253), Department of Molecular Biophysics and Biochemistry, Yale University, New Haven, Connecticut 06520

Bruce F. McEwen (129), Department of Health, Resource for Visualization of Biological Complexity, Wadsworth Center, New York, Albany, New York 12201-0509

Miloš Miljković (275), Department of Chemistry and Chemical Biology, Northeastern University, Boston, Massachusetts 02115

Eric B. Monroe (361), Department of Chemistry and the Beckman Institute, University of Illinois, Urbana, Illinois 61801

Qiang Ni (37), Department of Pharmacology and Molecular Sciences, The Johns Hopkins University School of Medicine, Baltimore, Maryland 21205

E. Tim O'Brien (433), Department of Physics and Astronomy, University of North Carolina, Chapel Hill, North Carolina 27599

Don O'Malley (95), Department of Biology, Northeastern University, Boston, Massachusetts 02115

Porntula Panorchan (411), Department of Chemical and Biomolecular Engineering, The Johns Hopkins University, Baltimore, Maryland 21218

Ammasi Periasamy (569), University of Virginia, W. M. Keck Center for Cellular Imaging, Department of Biology, Charlottesville, Virginia 22904

David W. Piston (71), Department of Molecular Physiology and Biophysics, Vanderbilt University Medical Center, Nashville, Tennessee 37232

Thomas D. Pollard (253), Department of Molecular Biophysics and Biochemistry, Yale University, New Haven, Connecticut 06520, and Department of Molecular, Cellular and Developmental Biology and Department of Cell Biology, Yale University, New Haven, Connecticut 06520

Arnd Pralle (541), Department of Cell Biology, University of California, Berkeley, California 94720, and Department of Physics and Department of Physiology and Biophysics, State University of New York, Buffalo, New York 14260

Drazen Raucher (451), Department of Biochemistry, University of Mississippi Medical Center, Jackson, Mississippi 39216

Christian Renken (129), Department of Health, Resource for Visualization of Biological Complexity, Wadsworth Center, New York, Albany, New York 12201-0509

Jonathan V. Rocheleau (71), Institute of Biomaterials and Biomedical Engineering, University of Toronto, Toronto, Ontario M5S 3G9, Canada

Stanislav S. Rubakhin (361), Department of Chemistry and the Beckman Institute, University of Illinois, Urbana, Illinois 61801

Melissa Romeo (275), Department of Chemistry and Chemical Biology, Northeastern University, Boston, Massachusetts 02115

Stuart C. Schaffner (623), Center for Interdisciplinary Research on Complex Systems and Physics Department, Northeastern University, Boston, Massachusetts 02115

Jonathan V. Sweedler (361), Department of Chemistry and the Beckman Institute, University of Illinois, Urbana, Illinois 61801

Sean X. Sun (601), Department of Mechanical Engineering and Biomedical Engineering, Johns Hopkins University, Baltimore, Maryland 21218

Richard Superfine (433), Department of Physics and Astronomy, University of North Carolina, Chapel Hill, North Carolina 27599

Russell M. Taylor II (433), Department of Computer Science, University of North Carolina, Chapel Hill, North Carolina 27599

Melissa S. Thompson (467), Department of Chemical and Biomolecular Engineering, Johns Hopkins University, Baltimore, Maryland 21218

Winston Timp (391), Whitehead Institute, Massachusetts Institute of Technology, Cambridge, Massachusetts 02139

Christian Tischer (521), FOM Institute for Atomic and Molecular Physics (AMOLF), Kruislaan 407, 1098 SJ Amsterdam, The Netherlands

Kevin R. Tucker (361), Department of Chemistry and the Beckman Institute, University of Illinois, Urbana, Illinois 61801

Stephen G. Turney (309), Department of Molecular and Cellular Biology and the Center for Brain Science, Harvard University, Cambridge, Massachusetts 02138

Horst Wallrabe (569), University of Virginia, W. M. Keck Center for Cellular Imaging, Department of Biology, Charlottesville, Virginia 22904

Watt W. Webb (3), School of Applied and Engineering Physics, Cornell University, Ithaca, New York 14853-2501

David A. Weitz (487), School of Engineering and Applied Sciences, and Department of Physics, Harvard University, Cambridge, Massachusetts 02143

Denis Wirtz (411, 467), Department of Chemical and Biomolecular Engineering, and Howard Hughes Medical Institute Graduate Training Program and Johns Hopkins Institute for NanoBioTechnology, The Johns Hopkins University, Baltimore, Maryland 21218

Jian-Qiu Wu (253), Department of Molecular Genetics and Department of Molecular and Cellular Biochemistry, The Ohio State University, Columbus, Ohio 43210

Jin Zhang (37), The Solomon H. Snyder Department of Neuroscience and Department of Oncology, The Johns Hopkins University School of Medicine, Baltimore, Maryland 21205

Tyler A. Zimmerman (361), Department of Chemistry and the Beckman Institute, University of Illinois, Urbana, Illinois 61801

PREFACE

"To measure is to know." William Thomson, Lord Kelvin

We biologists live in remarkable times. Our understanding of the structure and function of cells and organisms is developing at a startling pace, particularly in the qualitative realm. Yet it is clear that to understand living systems, one must also make *measurements* of their components and interactions at all levels of biological organization. Although Lord Kelvin did not experience the revolution in biological knowledge, which has largely been the product of the last century, his assertion of the necessity to make *quantitative* assessments of natural processes clearly holds true for cells and organisms. Until recently such a goal has been difficult to achieve, but today we are witnessing the clever, and yet practical, application of biophysical methods to quantify biological phenomena *in living cells*.

In Volume 89 of *Methods in Cell Biology, Biophysical Tools for Biologists: Vol. 2. In Vivo Techniques*, we have sought to recruit contributions from investigators who are pioneering the application of biophysical methods to living systems. The volume provides in a single venue access to a broad range of novel and cutting-edge *in vivo* techniques in cellular biophysics. Chapters cover the theory and practice of (1) fluorescence methods [fluorescence correlation spectroscopy (FCS), fluorescence (Förster) resonance energy transfer (FRET), fluorescent reporter-based analysis of protein folding, etc.]; (2) microscopic methods [optical sectioning, electron tomography, total internal reflectance microscopy (TIRF), atomic force microscopy (AFM), quantitative fluorescence measurement with single-event resolution, protein counting by quantitative fluorescence, infrared microspectroscopy (IR-MSP), and Raman microspectroscopy (RA-MSP), fluorescence photoactivation localization microscopy (FPALM) for breaking the "diffraction barrier," etc.]; (3) methods at the *in vitro/in vivo* interface [mass spectrometry imaging (MSI) using multiple ionization techniques, environmental scanning electron microscopy (ESEM), and wet SEM]; (4) methods for diffusion, viscosity, force, and displacement measurements [single-molecule force microscopy, magnetic microbead manipulation for force measurements, driven microbead rheology (DMBR), laser optical tweezers for membrane-cytoskeleton adhesion studies, ballistic intracellular nanorheology (BIN), rheological analysis of cytoskeletal networks, automated spatial mapping of microtubule dynamics]; (5) techniques for protein activity and protein–protein interaction measurements [analysis of spatially distributed protein activity by fluorescence lifetime imaging microscopy (FLIM), confocal FRET for protein–protein interactions]; and (6) computational

modeling methods [stochastic modeling of intracellular phenomena, computational modeling of mitotic spindle assembly]. The chapters are methods oriented, often tutorial and practical in terms of how to do it. Many present a strong emphasis on data analysis and computational approaches, because fitting of data is typically the most difficult part of learning how to apply these methods.

This volume is directed toward the broad audience of cell biologists, biophysicists, pharmacologists, and molecular biologists who wish to use cutting-edge biophysical techniques to interrogate biological processes and to solve biological problems in living cells. We trust that this volume will serve the reader as a convenient, reliable compilation of biophysical methods *in vivo*, thereby complementing our previous volume on *in vitro* techniques (Vol. 84 of *Methods in Cell Biology*). Because the application of biophysical methods *in vivo* is a relatively new expansion of the discipline of biophysics, we can anticipate the future development of many more imaginative and informative physical strategies for analysis of cellular processes. We also hope that this work will stimulate increased collaboration between biophysicists, cell and molecular biologists in the years to come. We gratefully acknowledge our many contributors, who are advancing the application of biophysical methods to living systems; it is they who have made this volume possible.

John J. Correia
H. William Detrich, III

CHAPTER 1

In Vivo Applications of Fluorescence Correlation Spectroscopy

Huimin Chen, Elaine R. Farkas, and Watt W. Webb

School of Applied and Engineering Physics
Cornell University
Ithaca
New York 14853-2501

Abstract

Fluorescence correlation spectroscopy provides a sensitive optical probe of the molecular dynamics of life *in vivo* and *in vitro*. The kinetics of chemical binding, transport, and changes in molecular conformations are detected by measurement of fluctuations of fluorescence emission by sensitive marker fluorophores. The fluorophores within a defined volume are illuminated by laser light that excites

METHODS IN CELL BIOLOGY, VOL. 89

0091-679X/08 $35.00
DOI: 10.1016/S0091-679X(08)00601-8

their fluorescence. While conventional confocal illumination by short-wavelength laser light is sufficient for two-dimensional targets, multiphoton fluorescence excitation by simultaneous quantum absorption of two or more long-wavelength photons of ~100 fs laser pulses provides the more precise submicron three-dimensional spatial resolution required in cells and tissues. Chemical kinetics, molecular aggregation, molecular diffusion, fluid flows, photophysical interactions, conformational fluctuations, concentration fluctuations, and other dynamics of biological processes can be measured and monitored in volumes ~1 μm^3 at timescales from <1 μs and upward for many orders of magnitude. Theory, motivations, methods, *in vivo* applications, and future directions for improvement and new applications for fluorescence correlation spectroscopy are summarized in this chapter.

I. Introduction

Creation of fluorescence correlation spectroscopy (FCS) was originally motivated in the 1960s by a timely puzzle: the molecular mechanisms of separating the double helix of DNA to enable its transcription. FCS enabled measurements of the reaction of the DNA double helix with ethidium bromide, which was thought to interfere with transcription by intercalating in the double helix (Magde *et al.*, 1972). Intercalation distorts the ethidium bromide molecule and enhances its fluorescence, inducing fluorescence fluctuations as it reacts, thereby enabling FCS measurements of the chemical kinetics and diffusibility of these species. Douglas Magde, Elliot Elson, and Watt W. Webb created FCS for this purpose, and they found that it provided a powerful tool to measure chemical kinetics that is now widely used to measure similar kinetics and the dynamics of life processes. The experimental procedures for the technique were reported (Elson and Magde, 1974) then augmented by the theoretical details (Magde *et al.*, 1974).

This approach to chemical kinetics arose as a natural extension of quasi-elastic light scattering (QELS), which had been used by Webb and many others to analyze the molecular dynamics of continuous phase transitions around critical points in liquid solutions (Huang and Webb, 1969). While QELS is relatively insensitive to biomolecular reactions, molecular fluorescence can be altered dramatically by chemical reactions, allowing one to effectively access the statistical thermodynamics of chemically reactive systems, conformationally fluctuating molecules, distribution of diffusion coefficients, and so on by correlating the time-dependent fluorescence fluctuations. Summaries of early applications (Webb, 1976) and principles (Elson and Webb, 1975) suggested possible uses for the technique. Later theoretical and experimental research advanced FCS beyond chemical reactions (Elson, 1985), to measurements of flow rates (Magde *et al.*, 1978), photophysics (Haupts *et al.*, 1998; Koppel *et al.*, 1976; Widengren *et al.*, 1995), molecular aggregation (Palmer and Thompson, 1987), rotational and translation diffusion (Aragon and Pecora, 1976), etc.

However, the instrumentation and computational technology available in the 1970s and 1980s prevented widespread application of FCS. Lasers were unstable and inherently noisy, necessitating compensation for their fluctuations (Koppel, 1974). Correlation instruments were slow and inflexible, and photodetectors were insensitive. Confocal microscopic imaging was employed to circumvent some of these problems when measuring micelle formation reactions (Koppel *et al.*, 1976). Nevertheless, it was not until the 1990s that advances in laser technology, detector sensitivity, accessibility of efficient computation, and diverse fluorescent probes enabled researchers to realize the technique's capabilities to a much fuller extent (Eigen and Rigler, 1994; Rigler *et al.*, 1993). FCS requirements still push the technological limitations of optical technologies, data acquisition rates, and computational analysis.

Although early *in vivo* FCS experiments on cell surface diffusion had been successful (Elson *et al.*, 1976), only in the 1990s (Berland *et al.*, 1995) the technique was thought to be mature, tractable, and powerful for studying dynamics in living systems. Unlike other fluorescence techniques that required high concentrations of probe molecules, FCS incorporates single-molecule sensitivity and is therefore particularly suited for cellular studies where target molecules tend to be present in low concentrations (nanomolar to picomolar). FCS is noninvasive and allows for the study of dynamics under equilibrium conditions with minimal perturbations. Its high spatial (nanometer) and temporal (microsecond) resolution enable measurements of fast dynamics *in vivo* in localized regions within the cell. However, *in vivo* FCS can suffer from low signal-to-noise (S/N) ratios due to autofluorescence, photobleaching, phototoxicity, and light scattering. The major problems, – scattering, autofluorescence, and phototoxicity, – can be overcome by using two-photon (2PE) or multiphoton (MPE) excitation which gives better depth discrimination, deeper penetration into layers of cells, and results in less photobleaching (Denk *et al.*, 1990; Schwille *et al.*, 1999a). Another major complication of FCS experiments in living cells is the ubiquitous presence of fluid flows in the cytoplasm and membranes, which must be taken into account and measured (Magde *et al.*, 1978).

A. Theory

The theoretical background and experimental implementation of FCS can be found in greater detail in many excellent reviews (Boukari and Sackett, 2008; Hess *et al.*, 2002; Rigler and Elson, 2001; Webb, 2001a,b). FCS measures the spontaneous fluctuations of a system from its equilibrium as monitored by fluctuations in fluorescence intensity as shown in Fig. 1B, and it can provide insight into processes that give rise to these fluctuations. These processes can include diffusion of molecules in and out of the sampling volume and *in situ* chemical reactions that change the conformations and/or quantum yield of the fluorophore (Widengren and Schwille, 2000; Widengren *et al.*, 1995, 1999). In FCS, the sampling volume is determined by the spatial profile of the laser's focus, inside of which fluorescent molecules are excited and consequently emit photons, as shown in Fig. 1A. The

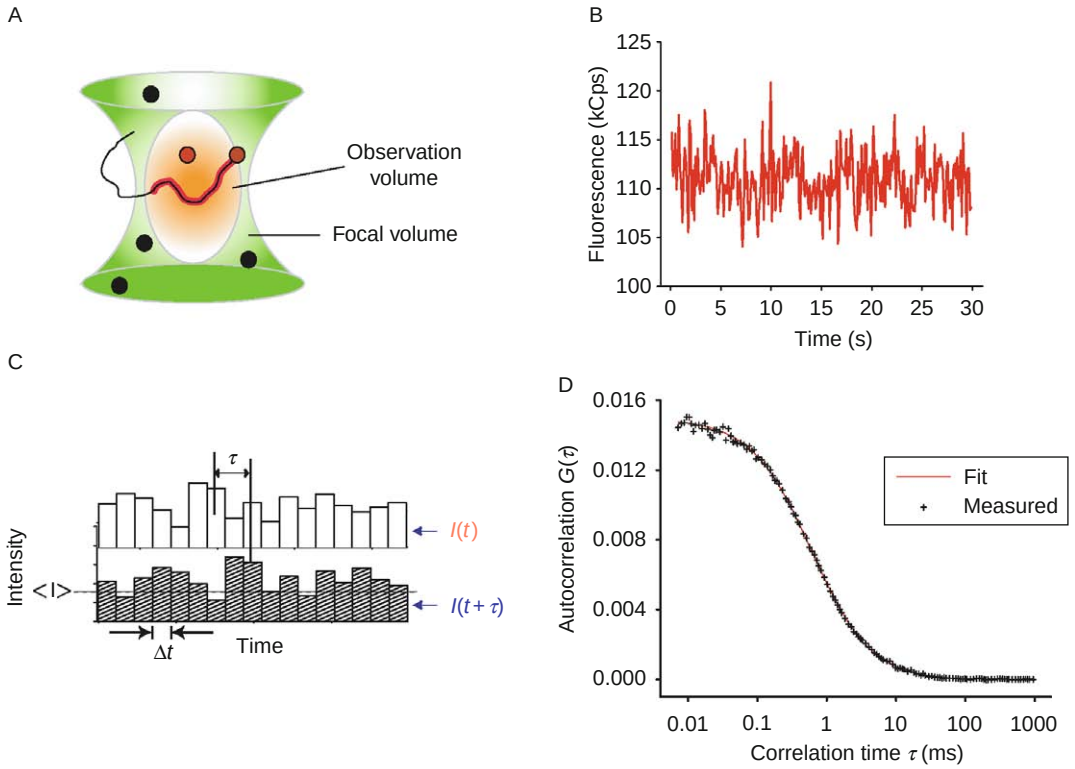

Fig. 1 Fluorescence fluctuations. (A) Fluorophores (black dots) diffuse through the focus (pale orange) of a laser beam (green) where they are excited (red) only in this region. Fluctuations in the detected fluorescence intensity are caused by diffusion of fluorophores in and out of the focal volume, and by additional fluctuations that might arise from fluorophore kinetics. (B) A typical trace of the detected intensity as a function of time. (C) The intensity trace is divided into discrete time bins (Δt). The fluctuation about the mean intensity $\langle I \rangle$ at time (t) is compared with that at a time delay τ later $(t + \tau)$ to calculate the autocorrelation function. (D) The correlation function is plotted against the logarithm of the delay time τ, because the measurement spans several decades in time (microsecond to second). Diffusion and thermodynamic parameters can be extracted by fitting various models to the measured data.

temporal measure of these changes in fluorescence intensity is given by the autocorrelation function (Fig. 1D),

$$G(\tau) = \frac{\langle \delta I(t) \delta I(t+\tau) \rangle}{\langle I(t) \rangle^2}. \tag{1}$$

Simply put, the similarity of the fluorescence intensity fluctuations $\delta I(t)$, given by $\delta I(t) = I(t) - \langle I(t) \rangle$, at one time t and by $\delta I(t + \tau)$ at a time delay τ later is analyzed and normalized by the mean time averaged fluorescence intensity $\langle I(t) \rangle$ (Fig. 1C). For a system at equilibrium, the autocorrelation function is independent of the time t when the mean intensity is measured, and depends only on the time lag τ.

For a single fluorescent species without chemical kinetics, undergoing three-dimensional Brownian diffusion within a homogenous fluid medium and illuminated with a typical prolate Gaussian ellipsoid excitation intensity profile, the autocorrelation function has the form

$$G_{\mathrm{D}}(\tau) = \frac{1}{\mathrm{N}} \frac{1}{(1+\tau/\tau_{\mathrm{D}})} \frac{1}{(1+\tau/\omega^2\tau_{\mathrm{D}})^{1/2}} \tag{2}$$

where N is the average number of molecules in the focal volume, τ_{D} is a characteristic diffusion time representing the most probable time which a molecule spends in the focal volume, and ω is the ratio of the axial to radial dimensions of the mean square excitation intensity of the focal volume. The zero time correlation $G(0)$ is the normalized variance of $I(t)$, and it can yield the concentration $\langle C \rangle$ of the species if the effective focal volume V is well defined by the illumination pattern:

$$G(0) = \frac{\langle I(t)^2 \rangle}{\langle I(t) \rangle^2} = \frac{1}{\langle N \rangle} = \frac{1}{\langle C \rangle V} \tag{3}$$

If the focal volume is well calibrated so that the $1/e^2$ radial beam waist r_0 is known, then the diffusion coefficient D of the species can also be calculated by

$$D = \frac{r_0^2}{4\tau_{\mathrm{D}}} \tag{4}$$

This calibration can be done by measuring the characteristic diffusion time τ_{D} of a solution of fluorophore with a known diffusion coefficient D. A more precise and independent measurement can also be obtained from the point-spread functions (PSFs) of the fluorescence intensities of subresolution fluorescent particles.

If the solution contains m multiple, noninteracting, diffusing species without chemical kinetics, the correlation function is a sum of the correlations of each individual species weighted by the square of its fluorescence intensity:

$$G_{\mathrm{D}}(\tau) = \frac{\sum_{i=1}^{m} I_i^2 G_{\mathrm{Di}}(\tau)}{\sum_{i=1}^{m} I_i^2} \tag{5}$$

However, simulations and experiments have shown that for FCS to resolve multiple species with the same fluorescence wavelength solely by their diffusion times, the τ_{D}s must differ by at least a factor of $\sim$1.6 (Meseth *et al.*, 1999). Thus, the masses must differ by a factor of $\sim(1.6)^3$, according to the Stokes-Einstein relation.

In 2PE, a fluorophore simultaneously absorbs two photons of approximately twice the one-photon excitation (1PE) wavelength; thus, each provides 1/2 the energy of the absorption band required for excitation. While conventional fluorescence intensity depends linearly on the excitation intensity, 2PE is a nonlinear process that depends on the mean squared intensity of the excitation light (assuming the excitation intensity is below that for the saturation level of the fluorophore). Since intensity is the flux of photons through a given area, for a laser beam with

uniform total power along its path, the intensity of the laser beam drops off very rapidly away from a tight focal point. In the context of 2PE-FCS, only a small prolate ellipsoid region around the focal plane is capable of being excited. The general principles underlying 2PE-FCS are the same as in conventional FCS, with the exception of the effective dimensions of the focal volume (ω_{xy} and ω_z), which can be closely approximated by the following equations (Zipfel *et al.*, 2003b):

$$\omega_{xy} = \begin{cases} \dfrac{0.320\lambda}{\sqrt{2}\mathrm{NA}} & \mathrm{NA} \leq 0.7 \\ \dfrac{0.325\lambda}{\sqrt{2}\mathrm{NA}^{0.91}} & \mathrm{NA} > 0.7 \end{cases} \tag{6}$$

$$\omega_z = \frac{0.532\lambda}{\sqrt{2}} \left[\frac{1}{n - \sqrt{n^2 - \mathrm{NA}^2}} \right] \tag{7}$$

where λ is the excitation wavelength, NA is the numerical aperture of the objective used, and n is the index of refraction of the sample.

B. Diffusion Models and Additional Photophysics

The wide variety of dynamic processes accessible to FCS merits a brief discussion of some of those more commonly encountered *in vivo* and their expected autocorrelation functions. As shown in Fig. 2, diffusion processes dominate the longer timescale, while kinetic processes that include fast intracellular biochemical reactions and photophysical processes occupy the shorter timescale. Photophysical processes like intersystem crossing (triplet conversion) and dye isomerization of cyanine dyes that change the quantum yield or excited states of the fluorophore can give rise to *nanosecond* to *microsecond* timescale fluctuations, while non-Brownian slow diffusion can be observed in the *microsecond* to *millisecond* regime.

For example, a photophysical problem which can interfere with *in vivo* applications of FCS may occur when a fluorophore absorbs a photon and is excited to the singlet excited state. It has a probability of undergoing an intersystem crossing, where it transitions to a triplet excited state which relaxes back to ground state via a nonfluorescent pathway. A fluorophore trapped in the triplet, or "dark," state must relax back to the ground state before it can once again be excited to a fluorescent state. Since the relaxation from a triplet state to a ground state is spin-forbidden, the lifetime of the triplet state is often much longer than that of the singlet state. At high illumination powers (consequently higher frequency of excitation), the probability of intersystem crossing is greatly enhanced. The autocorrelation function of the transition to a "dark" state may be described by (Widengren *et al.*, 1995):

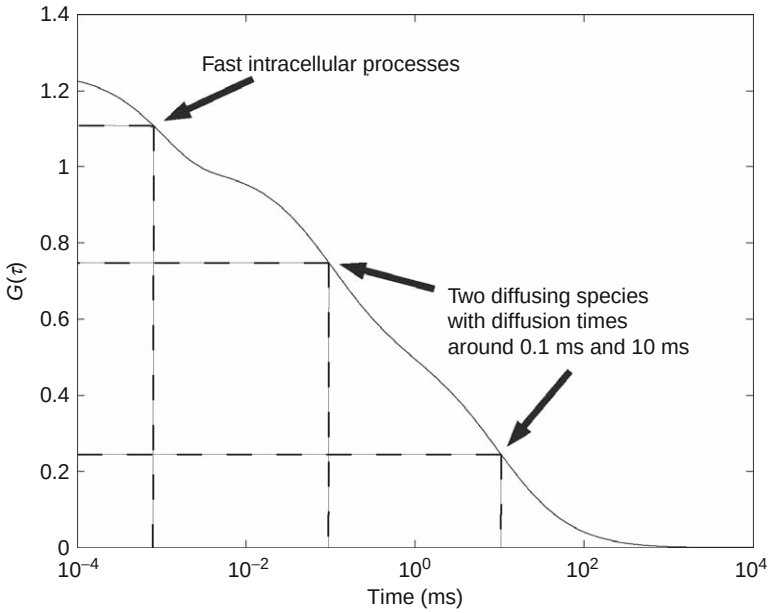

Fig. 2 The autocorrelation function, $G(\tau)$, displaying kinetics and diffusion accessible at different timescales. The fastest time regime (nanosecond to microsecond) is usually dominated by triplet state kinetics, rotational diffusion, and/or structural fluctuations such as dye isomerization. The intermediate (10–100 μs) and long (>100 μs) time regimes are usually dominated by diffusion of the fluorophores in and out of the focal volume. A longer diffusion time is associated with slow processes such as two-dimensional diffusion on membranes. Here, a species with two distinct diffusion times at 0.1 ms and 10 ms is depicted. These diffusion times are well separated and thus can be resolved in the correlation function.

$$G_{\text{kin}}(\tau) = \frac{1}{1-F}(1 - F + Fe^{-\tau/\tau_{\text{kin}}}) \tag{8}$$

where F is the fraction of the total fluorophore population in the triplet state and τ_{kin} is the lifetime of the triplet state. The full correlation function is thus a multiplication of the diffusive and triplet components given by

$$G(\tau) = G_{\text{D}}(\tau) \times G_{\text{kin}}(\tau) \tag{9}$$

These equations may also be generalized for any case where the fluorophore switches between a fluorescent and a nonfluorescent state, in which case τ_{kin} is the characteristic timescale of the switching. A photo-induced cis-trans isomerization that results in such a fluorescence "flicker" has been observed in cyanine dyes (Widengren and Schwille, 2000). This "flicker" can potentially be exploited for *in vivo* applications to give information about the environment of the fluorophore.

Examples of other "fast" processes that can couple with fluorophore diffusion in and out of the focal volume are rotational diffusion and directed transport, will be addressed in the context of *in vivo* measurements later in this chapter.

The middle range of the time spectrum (10–100 μs) is usually dominated by Brownian diffusion. Brownian diffusion is such that the probability distribution of the positions $r(t)$ of a collection of particles is Gaussian with respect to the position variables in the long time limit (Bouchaud and Georges, 1990; Einstein, 1906):

$$\text{Probability}\left\{u_1 \leq \frac{\left(r(t) - V_t t\right)}{2\sqrt{Dt}} \leq u_2\right\} \underset{t\to\infty}{\rightarrow} \frac{1}{\sqrt{\pi}} \int_{u_2}^{u_1} e^{-\xi^2} d\xi \tag{10}$$

where V_t is given by the mean step length l divided by the mean time per step τ, D is the time-independent diffusion coefficient which depends on the size and shape of the particle as well as the surroundings (i.e., viscosity), and u and ξ are dimensionless position variables. This is the behavior of so-called "random walkers"; that is, they do not interact with each other or their surroundings. The above equation applies only when the distance and time are related by

$$\langle r^2(t)\rangle = \langle l^2\rangle t/\tau = 4Dt \quad (2\text{D}) \tag{11}$$

$$\langle r^2(t)\rangle = \langle l^2\rangle t/\tau = 8Dt \quad (3\text{D}) \tag{12}$$

In the case of 3D Brownian diffusion, the autocorrelation function is given by Eq. (2).

When a particle's diffusion is obstructed, the above Eqs. (10–12) are no longer valid. Bouchaud and Georges described a general model for obstructed diffusion that is developed using the concept of energy barriers that impose different waiting times on the particles (versus a single finite mean time per step, τ, for all points in space in a Brownian model) (Bouchaud and Georges, 1990). In this model, the barriers fluctuate in both space and time and are uncorrelated such that a particular site is not associated with a particular dwell time in the long time limit. Depending on both the form of the distribution of dwell times and of the traps, a variety of behaviors may be observed. When the distributions are such that the mean dwell time, τ_a, approaches infinity in the long time limit, one observes subdiffusion. The mean square displacement is found to vary as follows:

$$\langle r^2(t)\rangle = \langle l_a^2\rangle (t/\tau_a)^{\alpha} = \Gamma t^{\alpha} 0 < \alpha < 1 \tag{13}$$

where Γ is the analog of the diffusion coefficient known as the transport coefficient, which may or may not be time-dependent, depending on the forms of l_a and τ_a. Note that if the mean dwell time, τ_a, is finite and constant, one recovers "normal" Brownian diffusion in the long time limit despite the presence of spatial and temporal fluctuations of the barrier heights. This means that to distinguish between anomalous diffusion and very slow Brownian diffusion, the timescale of

the experiment must span the dynamic range imposed by the distribution of the mean dwell times for processes considered "slow" (relative to the time resolution of the experimental apparatus).

With respect to FCS experiments, "slow" diffusion (100 μs to ms) is often associated with anomalous subdiffusion. It has been observed that molecules both on the membrane and in the cytosol undergo a much slower diffusion than particles in aqueous solution. On the membrane, diffusion is effectively two-dimensional and is described by the following correlation function:

$$G_{\mathrm{D}}(\tau) = \frac{1}{N}\frac{1}{(1+\tau/\tau_{\mathrm{D}})} \tag{14}$$

In the case of anomalous subdiffusion on a membrane, the correlation function is described as follows:

$$G_{\mathrm{D}}(\tau) = \frac{1}{N}\frac{1}{(1+\Gamma\tau^{\alpha}/r_0^2)} \quad (2\mathrm{D}) \tag{15}$$

$$G_{\mathrm{D}}(\tau) = \frac{1}{N}\frac{1}{(1+\Gamma\tau^{\alpha}/r_0^2)}\frac{1}{\left(1+\Gamma\tau^{\alpha}/(\omega^2 r_0^2)\right)^{1/2}} \quad (3\mathrm{D}) \tag{16}$$

where α and Γ are defined as in Eq. (13) (Bouchaud and Georges, 1990; Feder *et al.*, 1996; Schwille *et al.*, 1999b), ω is the ratio of the axial to radial dimensions of the mean square excitation intensity of the focal volume, and r_0 is the radial dimension of the focal volume.

Anomalous subdiffusion has also been observed in the cytoplasm (Arrio-Dupont *et al.*, 2000; Luby-Phelps *et al.*, 1986, 1987; Seksek *et al.*, 1997) and may be attributed to the fact that the cytosol is an extremely crowded environment. Whenever non-Brownian subdiffusion is encountered in the cell, there is a conundrum over the choice of models used to fit the data, since both anomalous subdiffusion Eqs. (15 and 16) and multiple diffusing species Eq. (5) models often fit the data well when slow diffusion is observed (Gennerich and Schild, 2000; Periasamy and Verkman, 1998); this sometimes complicates biological interpretation. Does the species of interest interact with other molecules in the cell, thus giving rise to multiple diffusion timescales? Or should one assume that the species undergoes anomalous subdiffusion with a single diffusion time, even if the cell contains a large concentration of barriers of various sizes? There have been many investigations using model systems (Fatin-Rouge *et al.*, 2004; Szymanski *et al.*, 2006), which suggest that for some species, anomalous subdiffusion with a single diffusion time is the more accurate model. In these experiments, the dependence of the fractional diffusion exponent α on the concentration or size of barriers demonstrated that obstructed diffusion, rather than multiple populations, provided the correct physical interpretation. *In vivo*, however, the choice of model can be highly dependent on the protein and the cell type.

II. FCS Technology

A. Experimental Setup: Confocal FCS

A typical confocal FCS setup is shown in Fig. 3, consisting of a laser beam that is directed into a high NA (>0.9) objective lens, which focuses the beam down to a diffraction-limited focal volume ($\sim 10^{-15}$ l) in the sample. The objective lenses commonly used are water-immersion lenses, because most studies, *in vitro* or *in vivo*, take place in aqueous solutions. The resulting fluorescence is collected back through the objective, separated from the excitation beam by a dichroic mirror and focused onto a confocal aperture that provides depth discrimination.

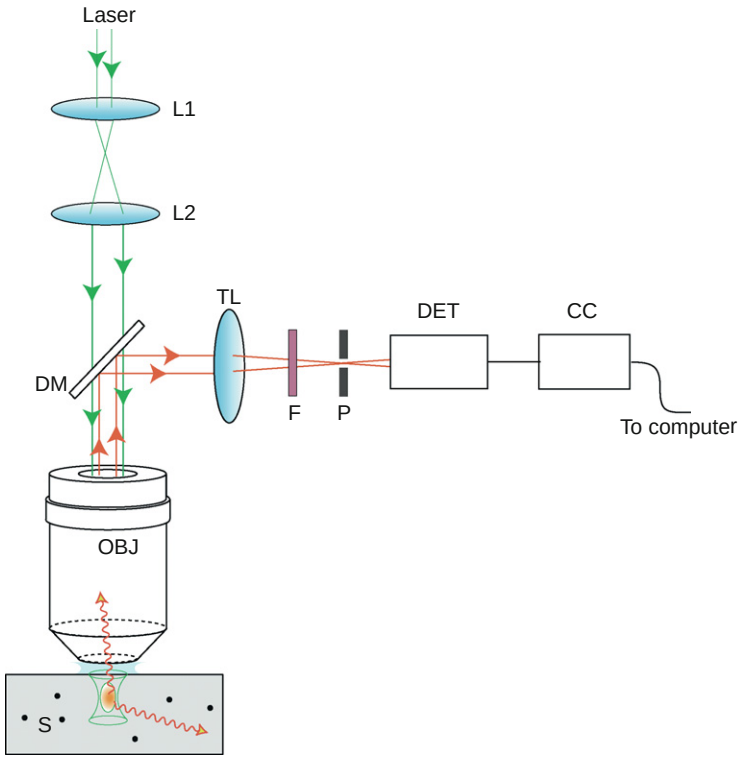

Fig. 3 A typical experimental fluorescence correlation spectroscopy (FCS) setup with confocal optics. Laser excitation light (green arrows) is expanded and collimated by two lenses (L1 and L2) before entering a high-NA objective. The objective focuses the excitation beam down to a well-defined focal volume in the sample (S). Emitted fluorescence (red arrows) is collected back through the same objective and separated from the incoming excitation beam by a dichroic mirror (DM). The fluorescence is focused down with a tube lens (Luby-Phelps *et al.*, 1987), attenuated by an emission filter (F), and passed through a pinhole (P) which serves to reject out-of-focus fluorescence and scattered light. The detector (DET), either a photomultiplier tube (PMT) or an avalanche photodiode (APD), records the fluorescence intensity, and the signal is sent to a hardware or software correlator card (CC) for analysis. For two-photon excitation (2PE) FCS, the P is omitted and F and DET are placed close to the DM.

The photons are then detected and counted by avalanche photodiodes (APDs) or photomultiplier tubes (PMTs), which convert the optical signal to an electrical one. A correlator card calculates the correlation function from this electrical signal. The correlation function can then be fitted to appropriate analytic functions using standard fitting software.

The quality of the correlation function is determined primarily by the S/N ratio of the fluorescence signal (Koppel, 1974); thus, it is advantageous to collect as much fluorescence signal as possible. However, good depth discrimination and a quasi-Gaussian focal volume profile are achieved in confocal optics by reducing the size of the confocal aperture, which in turn reduces the amount of signal collected. Therefore, a good correlation curve requires the careful selection of an aperture size that allows the trade-off to be made. *In vivo* studies especially require a small and well-characterized focal volume for good spatial resolution. This is often attempted by overfilling the back aperture of the objective lens, which results in a non-Gaussian excitation profile that must be corrected for by applying the appropriately sized aperture in the confocal image plane (Sandison and Webb, 1994; Sandison *et al.*, 1995). The assumed intensity profile for a 1PE focal volume is often a Gaussian function of the radial dimensions and a Lorentzian function of the axial dimension. Because the analytical correlation functions are most conveniently derived based on this prolate Gaussian ellipsoid focal volume, the fits of the data are susceptible to artifacts if the focal volume is nonideal, and care must be taken in adjusting the optics to establish the confocal pinhole size and the back aperture overfilling to approximate this set of ideal parameters (Hess and Webb, 2002).

B. Experimental Setup: Two-Photon and/or Multiphoton FCS

The use of MPE reduces many of the difficulties associated with defining the focal volume of the confocal setup. Because the intensity-squared dependence provides inherent depth discrimination, a confocal pinhole is not needed (Denk *et al.*, 1990). This feature is depicted in Fig. 4. The longer wavelengths used for 2PE [infrared (IR) to near-IR] do not yield a larger diffraction-limited effective focal volume since excitation is proportional to the square of the local illumination intensity. In practice, the resolution and diffraction-limited focal volume of a 2PE system are comparable to that of a confocal system. The longer wavelengths used in 2PE-FCS have further penetration into turbid samples, excite less autofluorescence in the cells, and are less phototoxic to the cells. These attributes make 2PE-FCS superior to conventional confocal FCS when working *in vivo*, although confocal FCS is still useful for membrane studies where penetration into the cell is not needed.

C. Limitations

1. Limitations of the Detection Apparatus

In theory, all processes that produce spontaneous fluctuations in the fluorescent signal can be autocorrelated and analyzed. The upper limit on the timescale of the processes that can be measured is determined by the photobleaching of the

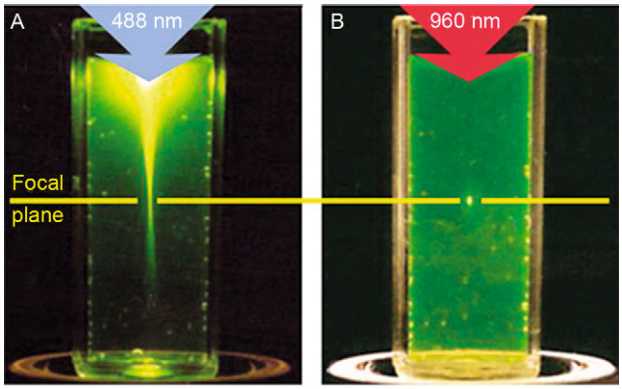

Fig. 4 One-photon (1PE) versus two-photon (2PE) excitation. (A) 1PE of fluorescein using 488 nm excites a large region above and below the focal plane. (B) Using the same objective, 2PE with 960 nm, 100 fs pulsed light excites only a localized region around the focal volume due to the nonlinear dependence of the excitation probability on the intensity of the excitation beam (Zipfel *et al.*, 2003b).

fluorophore and the residence time of the molecule in the focal volume. Fluorophores will become irreversibly damaged under extended exposure to excitation light, or if the excitation intensity is too high. This complicates the studies of slow dynamics, but techniques like scanning FCS (discussed in a later section) have been developed to overcome this problem. The lower limit is determined by the lifetime of the fluorescent state and thus the statistics of the emission process (on the order of *nanosecond* or faster). In practice, however, the lower limit is usually confined to the *nanosecond* deadtime of the detectors upon the detection of a photon, during which the detector is insensitive to further incoming signal. Another limitation arises from the inherent afterpulsing in the detectors, where each detected signal pulse has a probability of being followed by an afterpulse some time later. This effect produces a strong correlation signal on the timescale (*nanosecond* to *microsecond*) of the afterpulsing event. While the deadtime of the detectors remains a technical challenge, one can overcome the afterpulsing of the detectors by equally splitting the emission signal into two channels and detecting each one with a separate detector. Cross-correlation of the two signals will eliminate the afterpulse, although splitting the signals reduces the effective count rate and consequently the S/N is sacrificed in the process (Burstyn *et al.*, 1980).

2. Limitations of the Correlators (Computational)

There are two general ways to correlate the stream of intensity data. Hardware correlation uses a dedicated correlator card that electronically correlates the photon stream (depicted as *CC* between the detector and the host computer in Fig. 2), then transfers the correlated data to the host computer. On the contrary, software correlation imports the entire stream of photon arrival times (presumably after

passing through a counter), then uses software to correlate or analyze the data. A drawback of hardware correlation is that users can access only the resultant correlated signal, and not the original raw data of photon arrival times which is useful for other forms of analysis such as fluorescence lifetime studies and photon-counting histograms (PCH). Moreover, the algorithm used to produce the hardware correlation is determined by the electronics within the card and is generally inflexible to alterations that a user may desire for a particular experiment. Despite these drawbacks, hardware correlators are still prevalent and are essentially "plug and play." They are less demanding on the host computer's memory allocation and transfer architecture (Eid *et al.*, 2000). Software correlation may require specialized host computer architecture that allows high data transfer speeds and large memory allocation. Dedicated hardware correlators often operate in real time and are able to display a correlation curve as the data is taken, but software correlation can be limited by the speed of the computer to display "real time" data.

Hardware correlators have evolved to allow for a large dynamic range of lag times τ without requiring a significant increase in computation time and memory storage. Instead of a linear correlation scheme which integrates every single time bin, a multi-tau correlator employs different integration or gate times Δt for different lag times τ such that the ratio $\tau/\Delta t$ is constant. This reduces the number of computations required to produce the correlation function at each lag time. However, as discussed in some excellent reviews, multi-tau correlation may introduce significant error to the correlation function (compared to linear correlators) and requires longer overall measurement times (Kojro *et al.*, 1999; Saffarian and Elson, 2003).

Many efforts are underway, in our laboratory and others, to combine the versatility of software-based analysis with the speed of hardware correlators for a card that can both record the full digitized photon count trace and also correlate the trace. Recent developments include a data acquisition card able to switch between photon counting and photon arrival time detection modes (Eid *et al.*, 2000), and a card that allows simultaneous correlation and lifetime data collection (Felekyan *et al.*, 2005).

D. Fluorophore Selection

Because the quality of an autocorrelation curve depends only on the S/N ratio (Koppel, 1974), it is preferable to select a fluorophore with high quantum efficiency and a large absorption cross-section. Additionally, the fluorophore must be stable against photobleaching during its residence time in the focal volume. These stringent FCS criteria eliminate many commonly used fluorophores, such as fluorescein (FITC). Furthermore, when measuring *in vivo*, extra precaution should be taken to characterize the fluorophore to ensure that (1) it does not disrupt the native behavior of the system of interest and that (2) the heterogeneous environment of the cell does not affect the photophysics of the fluorophore. Note that good fluorophores for 1PE are not necessarily good for 2PE excitation.

The fluorophores used for *in vivo* studies can be loosely divided into two categories. In one category are fluorophores that are attached to the target molecule outside of

the cell, with the labeled product subsequently bound to or internalized by the cell either by applying it in solution or by microinjection. For example, antigen-mediated reactions on the cell can be observed using Alexa dyes (Molecular Probes) conjugated to the cell surface antibody under study (Larson *et al.*, 2005). These fluorophores can often be small enough to avoid disrupting the native biological processes. However, with extrinsic labels, specificity in labeling of the target with tight binding is required to minimize problems of background signal from unbound dye.

The second category consists of fluorescent proteins (or target peptide binding sites) that are genetically encoded into the cells so that labeling takes place *in vivo* after these proteins are expressed. Examples of such fluorophores are the green fluorescent protein (GFP) family of intrinsically fluorescent proteins such as enhanced green fluoroscent protein (EGFP) (Tsien, 1998). The GFP family has been modified (Heim *et al.*, 1995) to enhance photostability and to include a wide range of excitation and emission wavelengths. The sensitivity of GFP to pH (Haupts *et al.*, 1998; Heikal *et al.*, 2001; Hess *et al.*, 2004) can be exploited to gain information about pH-dependent cellular processes. A remarkably extensive spectrum of colors of fluorescent proteins has been created by Tsien and coworkers (Shaner *et al.*, 2004). Another example is the commercially available synaptosome-associated protein (SNAP)-tag system (Covalys), where the target protein is fused to the DNA repair enzyme O^6 alkylguanine-DNA alkyltransferase (AGT). This fusion product reacts specifically with an O^6 benzylguanine (BG) group contained on a derivatized fluorophore allowing its attachment (Keppler *et al.*, 2004). Genetically expressed labels offer greater specificity at lower concentrations, provided that the label can be expressed and attached to the target of interest. However, since such labels are themselves proteins, they can be bulky and have their own chemical properties. An example is the red fluorescent protein, dsRed, which tends to aggregate into tetramers (Heikal *et al.*, 2000). Thus, the new fusion target must be evaluated by independent methods to ensure that its native biochemistry is retained.

Recent developments in genetics have aimed at allowing small nonfluorescent molecules to become fluorescent when bound to a small genetically inserted amino acid sequence in the target protein of interest. An example is the biarsenical compound, FlAsH, which exhibits a 50-fold increase in quantum efficiency upon binding to an inserted CCPGCC motif on the peptide of interest (Adams *et al.*, 2002; Griffin *et al.*, 1998). Because FlAsH is not fluorescent before it binds the target sequence, there is no need to wash out unlabeled fluorophores, making it tractable for *in vivo* studies. Similar to the fusion targets, these labeled proteins should also be checked to ensure their native properties are retained.

III. Applications of *In Vivo* FCS

In the following section, we will describe *in vivo* applications of FCS that are of interest to cell biologists. *In vivo* FCS is complicated; not only does the heterogeneous environment of the cell change the properties of fluorophores, but different

modes of diffusion can occur at different locations in the cell. FCS can be used to characterize these diverse dynamics in various parts of the cell, for example, biomolecules undergoing directed transport, diffusion, or movement under flow conditions. Biomolecules undergo 3D diffusion in cellular spaces that can be altered by interactions with binding partners or constrained by crowding in the cytoplasm, whereas within membranes, they undergo 2D diffusion and can interact with membrane-associated receptors. In this section, we will treat *in viv*o FCS by showing examples of the various motions and dynamics accessible to the technique.

A. Diffusion on Membranes

The first successful *in vivo* applications of FCS were directed at measuring protein diffusion in the cell membrane (Elson *et al.*, 1976; Schlessinger *et al.*, 1976), as a natural extension of earlier measurements on model systems such as planar supported bilayers (Fahey *et al.*, 1977). Before the widespread use of FCS, most of the early studies of membrane protein diffusion relied on fluorescence recovery after photobleaching (FRAP) originally known as fluorescence photobleaching recovery (FPR) (Axelrod *et al.*, 1976a,b) and single particle tracking (SPT) (Barak and Webb, 1982). In FRAP, fluorescence in the area of interest is bleached out with an intense laser beam. The rate and extent of the return of fluorescence to the area depends on the diffusion coefficient of the fluorescent molecule. In these FRAP experiments (Elson *et al.*, 1976; Webb, 1981), fluorescently labeled proteins on cell membranes *in vivo* were found to diffuse orders of magnitude slower than predicted by the hydrodynamic Saffman–Delbruck theory (Saffman and Delbruck, 1975; Saffman, 1976), which was the predominant theory for model and reconstituted membranes at the time. However, as explained in the earlier theory section, it was not possible to distinguish between a protein hindered by an ''immobile'' fraction in the membrane and one that was undergoing slow anomalous subdiffusion, because this would require the measurement timescale to span at least 8 orders of magnitude, while a typical FRAP experiment could span only 6 at most (Brown *et al.*, 1999; Feder *et al.*, 1996). Results from many of the FRAP experiments were thus explained by a model that assumes anomalous subdiffusion invoking the theoretical description of a system with energy barriers that fluctuate in space and time as proposed by Bouchaud and coworkers (Bouchaud and Georges, 1990). Saxton has applied these theoretical models to biological systems and proposed physical explanations for the barriers of diffusion (Saxton, 1990, 1996). Reexaminations of single-phase model and cellular membranes in the 1990s using FCS corroborated the presence of anomalous subdiffusion on cell membranes, and confirmed that anomalous subdiffusion was not an artifact of the FRAP technique (Schwille *et al.*, 1999b).

The first model of the cell membrane posed by Singer and Nicolson (1972) depicted membrane proteins floating in a liquid-phase sea of lipids. However, the subsequent discovery of detergent-resistant lipid fractions colocalizing with certain

membrane proteins (Brown and London, 2000; Brown and Rose, 1992) led to the formulation of the lipid raft hypothesis. In this model, lateral concentration inhomogeneities of the lipid species, termed "rafts" in the membrane, result in a thermodynamically favorable colocalization of certain proteins with cholesterol and saturated-chain lipids such as ceramides and sphingomyelin. These small domains may correspond to the "liquid-ordered" phase based on the observations of such a phase in model binary and ternary lipid systems containing cholesterol (Dietrich *et al.*, 2001; Vist and Davis, 1990). It is still unclear whether the presence of proteins in cells nucleates and stabilizes rafts from an otherwise homogenous membrane, or whether the rafts exist independently of proteins (and cytoskeletal contacts) (Baumgart *et al.*, 2003, 2007). This recent paradigm shift about the lateral organization of membranes has renewed considerable interest in the mechanism of anomalous subdiffusion on the membrane.

Although the exact mechanism causing slow protein diffusion is still unknown, it had been attributed to cytoskeletal interactions (Barak and Webb, 1982; Kusumi *et al.*, 1993; Tank *et al.*, 1982b; Thomas *et al.*, 1992), protein crowding (Peters and Cherry, 1982; Tank *et al.*, 1982a), and/or lipid phase separation (Korlach *et al.*, 2005; Schwille *et al.*, 1999b). Recent models appropriately implicate the cytoskeleton (Lenne *et al.*, 2006; Ritchie *et al.*, 2005; Wawrezinieck *et al.*, 2005) as first experimentally demonstrated by Axelrod *et al.* on myotube membranes (Schlessinger *et al.*, 1976), while others suggest protein crowding and protein–protein interactions (Frick *et al.*, 2007; Kucik *et al.*, 1999; Ryan *et al.*, 1988). Studies on model membranes with varying cholesterol (Korlach *et al.*, 1999, 2005; Schwille *et al.*, 1999b) and lipid content (Bacia *et al.*, 2004; Hac *et al.*, 2005; Ratto and Longo, 2002) using FCS showed that lipid diffusion coefficients on the membrane depended on the lipid phase. In phase-separated model membranes, anomalous subdiffusion has also been observed but only as the membrane nears a phase transition or critical point (Korlach *et al.*, 1999; Schwille *et al.*, 1999b). Thus, a variety of factors could give rise to anomalous subdiffusion in cells, and it is not surprising that various sources of obstructed diffusion in cells are observed as different protein targets and cell types are studied. Nonetheless, FCS remains a powerful technique for diffusion studies on cellular membranes.

FCS on membranes is not without its difficulties. The geometry of the focal volume relative to the cell membrane is depicted in Fig. 5A. The thickness of the cell membrane and the focal volume are about 10 nm and 1 μm, respectively, implying that the focal volume will encompass some of the cytosol and the extracellular space. Thus, careful calibrations should be performed to measure the signal at, above, and below the membrane so that the positions of maximum signal are well characterized (Fig. 5B). Any extraneous labeled or autofluorescent species near the membrane should be subtracted so they do not contribute to the signal (Schwille *et al.*, 1999a). If the system is sufficiently stable, one can measure the diffusion time as a function of the distance Δz between the focal plane and the membrane to obtain the most accurate value of D (Benda *et al.*, 2003; Humpolickova *et al.*, 2006; Sorscher and Klein, 1980) via

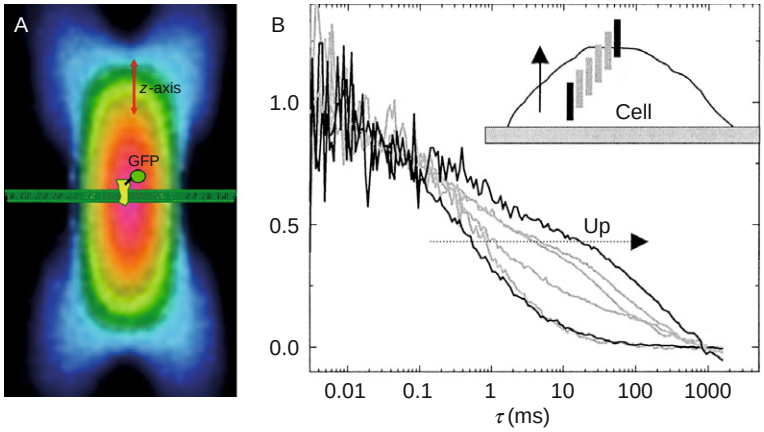

Fig. 5 Fluorescence correlation spectroscopy (FCS) on a cell membrane. (A) The typical cell membrane is about 10 nm in thickness, ~100 times smaller than the axial dimension of the focal volume (~1 μm). Thus, on the scale of the observation volume, a membrane is essentially a flat sheet and the observed diffusion is two-dimensional, provided the membrane is stationary with respect to the optical axis. The correlation function $G(\tau)$ is thus very sensitive to the position of the membrane relative to the focal volume. (B) As the position of the focal volume relative to the membrane is varied, the shape of the resultant correlation function is radically changed. Therefore, care must be taken to make sure that the membrane is positioned exactly in the middle of the focal volume (Schwille *et al.*, 1999a). Note that fluorophore is only present in the membrane. Fluorophores in the cytoplasm or extracellular space would not be spectrally separated and would thus contribute to the signal and resultant correlation function.

$$\tau_D = \left(\frac{r_0^2}{4D}\right)\left(\frac{1+\lambda_0^2\Delta z^2}{\pi^2 n^2 r_0^4}\right) \tag{17}$$

where r_0 is the beam waist radius at the focal plane, λ_0 is the wavelength of the excitation light, and n is the refractive index of the medium. τ_D (or D) varies parabolically with respect to Δz, with the extremum corresponding to the optimal value of τ_D (or D) when the membrane is located exactly at the focal plane ($\Delta z = 0$). This dependence is illustrated qualitatively by the correlation curves shown in Fig. 5B. Here, 2PE is especially useful due to the small focal volume and its inherent depth discrimination.

The dependence of τ_D on the beam waist radius r_0 in the above relationship has also been exploited to characterize the obstructed diffusion for a variety of protein and lipid labels on the membranes of COS-7 cells (Wawrezinieck *et al.*, 2005; Widengren *et al.*, 1999) based on models of proteins confined to specific zones. However, one should note that when the length scale of the confinement zone is on the order of the size of the beam radius, the autocorrelation functions given in Eqs. (14 and 15) may not be valid (Chen *et al.*, 1999; Gennerich and Schild, 2000). For example, when the lateral confinement zone of a planar system is less than

twice the beam radius, the resulting correlation function was shown to be dissimilar to that for standard or anomalous 2D diffusion (Gennerich and Schild, 2000).

The presence of anomalous subdiffusion poses two serious technical challenges for FCS measurements on membranes. Slowly diffusing species spend longer times in the focal volume, thus increasing the likelihood of the fluorophore photobleaching. This can lead to an overestimation of the number of molecules and an underestimation of diffusion times in the correlation curves obtained by FCS. Furthermore, slowly moving species require longer acquisition times, especially at the reduced illumination intensities necessary to avoid photobleaching. The effective 2D geometry of the sampled region makes the system more sensitive to the relative position of the sample in the focal volume. As mentioned above, care must be taken to position the cell membrane axially in the center of the focal volume (Fig. 5A), which is a problem since flaccid membranes undulate (Fradin *et al.*, 2003). Recent technological innovations have addressed such issues with the introduction of techniques like scanning FCS (Ries and Schwille, 2006; Ruan *et al.*, 2004) and multiple spot FCS, which will be discussed in the later sections.

B. Diffusion Within the Cell

Previous theoretical and experimental studies have demonstrated that as in membranes, molecules may exhibit anomalous subdiffusion in the cytoplasm (Arrio-Dupont *et al.*, 2000; Luby-Phelps *et al.*, 1986, 1987; Seksek *et al.*, 1997). This is not surprising, because the cytoplasm contains high concentrations of proteins, aggregates, and lipid vesicles traversing higher-order structures made up of cytoskeletal elements and organelles such as the Golgi apparatus and the endoplasmic reticulum (ER) (Alberts, 2002). The cell cytoplasm is a crowded environment with many species including RNAs, ribosomes, proteins, and other macromolecules diffusing through it and binding together or to structural elements. It was demonstrated using FCS that when the cytoskeleton was chemically disrupted, subdiffusion of dextran molecules persisted in the cytoplasm, indicating that anomalous subdiffusion is not caused solely by hindrance due to higher-order structures (Weiss *et al.*, 2004). Rather, computer simulations and experiments on fluorescently labeled proteins in a crowded *in vitro* environment also exhibit the same anomalous subdiffusion (Banks and Fradin, 2005). However, the reduced mobility of molecules in cells appears to depend on cell type (Verkman, 2002), location within the cell (Wachsmuth *et al.*, 2000), and size of the diffusing molecule (Arrio-Dupont *et al.*, 2000). All of these reflect the complicated and heterogeneous environment that makes up the cytoplasm, and indicates that it is misleading to assume that diffusion of molecules in the cell should be fitted to a model with just one diffusing component.

FCS was employed to measure the diffusion of fluorescein-labeled oligodeoxynucleotides in the nucleus of cultured rat myoblasts (Politz *et al.*, 1998). It was observed that a large fraction of the oligos moved rapidly at a rate similar to the diffusion rate observed in aqueous solution. There were also some fractions that

moved slowly, and these were thought to be hybridizing to endogenous RNA or macromolecular complexes.

FCS offers the potential for studying kinetic processes in and on cells at the molecular level, down to the single-molecule limit. When working *in vivo*, autofluorescence from other molecules present in the cytoplasm or membrane contributes to the constant background signal and even though it should not have any correlation, it will cause the concentration to be overestimated. A variety of molecules within the cell may be intrinsically fluorescent; two well-known and well-characterized examples are flavoproteins and nicotinamide adenine dinucleotide (NADH) (Vishwasrao *et al.*, 2005). Background signals are also produced by autofluorescence from many proteins, conspicuously elastin (Zipfel *et al.*, 2003a), and by second harmonic generation in collagen structures (Williams *et al.*, 2005). The amount of autofluorescence depends not only on the excitation wavelength (Schwille *et al.*, 1999a) but also on the location within the cell. For example, in HeLa cells, the cytoplasm shows a factor of two higher autofluorescence intensities than the nucleus at the same excitation wavelength. Within the cytoplasm, autofluorescence is brighter and heterogeneous, and the autofluorescence can fluctuate on the timescale of seconds (Chen *et al.*, 2002). Two-photon excitation-FCS is especially useful in this respect, because most of the autofluorescent molecules do not absorb at wavelengths higher than 900 nm.

C. Nondiffusive Dynamics

1. Interactions and Aggregation in the Cell

To understand the workings of a cell, it is important to identify the biomolecular constituents of the cell, but more so to elucidate the dynamics of interactions amongst these biomolecules. The high sensitivity of fluorescence measurements allows us to study these interactions on a molecular level. In particular, FCS provides a sensitive, noninvasive method of probing in real time the dynamics of molecules in their natural environment of the cell without perturbing cellular function.

When two molecules interact with each other, binding changes the mobility of the reactants, lending itself well to FCS measurements. For example, this has been exploited to study the binding of proinsulin C-peptide to specific G-coupled receptors on human cell membranes (Rigler *et al.*, 1999). In this case, one expects both a membrane-bound fraction undergoing lateral diffusion in 2D and also a cytosolic fraction undergoing diffusion in 3D. The correlation function must be changed accordingly:

$$G(\tau) = \frac{1}{N}\left[A\left(\frac{1}{1+\tau/\tau_{\mathrm{M}}}\right) + (1-A)\left(\frac{1}{1+\tau/\tau_{\mathrm{C}}}\right)\left(\frac{1}{1+\tau/\omega^2\tau_{\mathrm{C}}}\right)^{1/2}\right] \qquad (18)$$

where A is the fraction that is bound to the membrane, τ_{M} is the characteristic diffusion time of the membrane-bound species and τ_{C} is that of the cytosolic

fraction. As long as one can fluorescently label the ligand of interest, it seems that the variety of systems that can be studied with this technique is limitless (Pramanik *et al.*, 2001; Pramanik and Rigler, 2001), provided the system is fast enough to preclude photobleaching.

This method can also be used to study the binding or aggregation of molecules in the cytoplasm. However, unlike the case of a ligand binding to a membrane where the ligand's mobility is significantly retarded, the binding of two similarly sized molecules diffusing in the cytoplasm may not change the mobilities by more than the factor of 1.6 needed to resolve the bound and unbound states (Meseth *et al.*, 1999). It is also difficult to resolve the different diffusion times if one of the diffusing components exists in a very small fraction relative to the other, for example, if the binding constant is very low. Similarly, if the binding of the two reactants is transient such that they are bound together for times shorter than the residence time of the molecules in the focal volume, the diffusion of the molecule could be retarded such that it appears to be undergoing anomalous subdiffusion as described theoretically by Saxton (1996).

There have been a number of innovations used to overcome these issues, one of which is dual-color cross-correlation spectroscopy (Eigen and Rigler, 1994; Schwille *et al.*, 1997). In this scheme, the two interacting species are labeled individually with spectrally distinct fluorophores. The emission signals from each species are then separated by dichroic mirrors and cross-correlated with one another. A nonzero cross-correlation signal indicates similarity between the fluctuation changes of the two species, which arises from concomitant diffusion as a result of binding. The two fluorophores can be excited by two different colors, although great care must be taken to ensure that the two different focal volumes are of the same size and well-overlapped. Dual-color cross-correlation is most conveniently implemented using 2PE-FCS, because a single wavelength is often able to excite two fluorophores that have both overlapping 2PE spectra and well-separated emission spectra.

Dual-color cross-correlation spectroscopy was applied to study the complex binding stoichiometry of EGFP-labeled Ca^{2+}/CaM-dependent protein kinase II and up to 12 Alexa633-labeled CaM ligands (Kim *et al.*, 2005), interactions between a cytosolic protein, Lyn kinase, and a membrane-bound receptor in 2H3-RBL cells (Larson *et al.*, 2005), the endocytic pathway (Bacia *et al.*, 2002), as well as interactions between Gag proteins in the cytoplasm (Larson *et al.*, 2003). Since this technique involves two fluorophores that may be in close physical proximity, there is a possibility that Förster resonant energy transfer (FRET) may occur. This phenomenon will be explained in more detail in later sections, but undesired FRET will result in erroneous cross-correlation data. Furthermore, in circumstances allowing the very close proximity of fluorophores, quenching and/or excimer formation can also affect fluorescence fluctuations and quantum yields.

Another approach to distinguish different diffusing components uses software, rather than modifications to the experimental setup. Maximum entropy method (MEM) is a data-fitting algorithm first developed in astronomy (Skilling and

Bryan, 1984). This algorithm is capable of determining the distribution of diffusion times (and hence molecular size) in a heterogeneous sample (Sengupta *et al.*, 2003a). The aggregation of $A\beta_{1-40}$ implicated in the progression of Alzheimer's disease has been studied *in vitro* using this method (Sengupta *et al.*, 2003b), whereby the size distribution of the soluble oligomers was followed as a function of time. It is possible that this technique can be extended to *in vivo* research wherein the concentration of molecules is very heterogeneous. Two other approaches based on higher-order auto-correlations (Palmer and Thompson, 1987) and photon-counting histograms (Chen *et al.*, 1999) have also been used to distinguish between multiple species.

2. Directed Transport

For a cell to function, many biochemical processes take place that require substrates or metabolites to be transported between compartments. Newly synthesized molecules must be distributed to the cytosol and parts of the cell where they are needed. Relying solely on diffusion to achieve this transport is not always efficient, and mediated transport is often employed to traffic biomolecules against a gradient. FCS has also been used to distinguish between diffusion and flow modes of dynamics (Foquet *et al.*, 2004; Magde *et al.*, 1978). If molecular motion includes active transport with velocity v in a direction in the plane of the radial dimension of the focal volume on top of 3D diffusion, the correlation function is modified:

$$G(\tau) = G_{\mathrm{D}}(\tau) \times G_{\mathrm{Flow}}(\tau) \tag{19}$$

where $G_{\mathrm{D}}(\tau)$ is given by Eq. (2) and $\mathrm{G}_{\mathrm{Flow}}(\tau)$ is given below.

$$G_{\mathrm{Flow}}(\tau) = \exp - \left(-\left(\frac{\tau}{\tau_{\mathrm{Flow}}} \right)^2 \right) \tag{20}$$

Here, τ_{Flow} is the average residence time of the molecule in the focal volume for active transport only. If the dimensions of the focal volume are well-defined, then the velocity can be calculated as follows:

$$V = \frac{r_0}{\tau_{\mathrm{Flow}}} \tag{21}$$

Using FCS to distinguish between active transport and passive diffusion was first demonstrated in plant biology. It had previously been observed using FRAP that organelles in plant cells known as plastids have tubular projections that connect plastids, which were thought to be separate in an interdependent network through which molecules can be exchanged (Kohler *et al.*, 1997). Experiments on chloroplasts in plant cells using FCS later showed that the GFP expressed in the plastids of these transgenic cells moved through the cytosol by free diffusion but moved through the tubules by a combination of diffusion and active transport (Kohler *et al.*, 2000). Diffusion in the tubules was 50 and 100 times slower than in the cytosol and aqueous solution, respectively, but it was also observed that large GFP

units were being transported along the tubules with a velocity of about 0.12 μm/s. This research showed that active transport was a more efficient mechanism for long-distance transport of biomolecules, especially in the face of hindered diffusion in the very crowded and viscous environment of the plastid tubules.

3. Fast Intracellular Processes

While the timescales that can be measured are limited by the afterpulsing and deadtime of the detectors, fast processes that occur on the nanosecond to microsecond timescale, like orientational fluctuations due to Brownian rotational diffusion (of large molecules and organelles at least), can still in principle be resolved with modifications for polarization sensitivity of the conventional optics. The probability of absorption for 1PE is proportional to the cosine (parallel component) of the angle between the absorption dipole and the polarization vector of the incident light. Thus, molecules with their absorption dipole parallel to the polarization of the incoming light are preferentially excited. Similarly, the fluorescence that is emitted by these molecules at a fluorescence lifetime τ_L will later be polarized parallel to the emission dipoles of the molecules. If linearly polarized light is used for excitation, one can calculate the rotational diffusion of the molecule by analyzing the polarization dependence of the emitted fluorescence. However, traditional time-resolved fluorescence anisotropy methods can only measure rotational diffusion times that occur within the fluorescence lifetime of the fluorophore. FCS has the advantage of accessing this information even if the rotational diffusion time is slower than the fluorescence lifetime, although the theoretical description of the motion and the resultant correlation function can be extremely complicated. This makes FCS particularly suited for *in vivo* measurements where rotational diffusion times are expected to be much longer on membranes or in the viscous cellular environment.

For rotational diffusion of a spherically symmetric rotor with parallel absorption and emission dipoles that are slow compared to the fluorescent lifetime, the correlation function can be approximated as follows:

$$G_{\mathrm{Rot}}(\tau) = \frac{1}{N}\left[A\ \exp\left(-\left(\frac{\tau}{\tau_{\mathrm{Rot}}}\right)\right) + B\ \exp\left(-\left(\frac{3\tau}{10\tau_{\mathrm{Rot}}}\right)\right)\right] \tag{22}$$

where $\tau_{\mathrm{Rot}}=1/6D_{\mathrm{Rot}}$ is the rotational correlation time and A and B are amplitude factors that depend upon the geometry of the experiment (Aragon and Pecora, 1975). Rotational diffusion has been successfully characterized using FCS *in vitro* thus far for Texas Red-labeled porcine pancreatic lipase (Kask *et al.*, 1989), bovine carbonic anhydrase B (Kask *et al.*, 1987), and GFP (Widengren *et al.*, 1999). Although the optics and hardware required for accurate measurement of rotational diffusion using FCS may complicate the conventional time-resolved anisotropy measurement, FCS can simultaneously access rotational and translation diffusion. This can be useful when studying molecular dynamics *in vivo*, where simultaneous

characterization of multiple parameters may be essential to distinguish processes at the single-molecule level.

Intermolecular or intramolecular chemical reactions that cause fluctuations in fluorescence intensity are also accessible to FCS if these happen at a timescale faster than the residence time of the molecule in the focal volume. If the molecule under study fluctuates between two states with different fluorescence quantum yield, then the correlation function is modified as follows:

$$G(\tau) = G_D(\tau) \times G_{\text{Reaction}}(\tau) \tag{23}$$

where $G_{\text{D}}(\tau)$ is given by Eq. (2) and $G_{\text{Reaction}}(\tau)$ is given below.

$$G_{\text{Reaction}}(\tau) = \frac{1 - A + A\ \exp(-\tau/\tau_{\text{R}})}{(1 - A)} \tag{24}$$

Here, A is the fraction of molecules undergoing the fluctuations, and τ_{R} is the characteristic timescale at which the molecule is fluctuating between the two states. FCS has been used to measure fast chemical kinetics *in vitro*, such as triplet state kinetics (Widengren *et al.*, 1995), dye isomerization (Widengren and Schwille, 2000), and protein conformational changes that alter the chemical environment (and hence quantum yield) of the attached fluorophore (Chattopadhyay *et al.*, 2002, 2005; Chen *et al.*, 2007; Neuweiler *et al.*, 2003). Although these experiments were all carried out *in vitro*, the single-molecule sensitivity and the timescales accessible indicate the vast *in vivo* potential of this technique.

IV. Future Directions for *In Vivo* FCS

New technology and improvements in existing FCS instrumentation hold promise in broadening the applicability of the technique in cellular systems by overcoming problems associated with autofluorescence, photobleaching, cell motion, and phototoxicity. In addition to temporal information, it is often useful to have spatial information on the dynamics that are occurring *in vivo*. Many of the new developments in FCS aim to make the technique more powerful by providing both temporal and spatial correlations.

Scanning FCS was first introduced about 30 years ago and has been used infrequently to study slow dynamics via temporal autocorrelations (Weissman *et al.*, 1976) and a combination of both temporal and spatial autocorrelations (Koppel *et al.*, 1994; Petersen, 1986). Spatial correlations alone have also been used to study extremely slow dynamics via image correlation spectroscopy (ICS) (Digman *et al.*, 2005; Wiseman *et al.*, 2000), in which the intensity fluctuations at different pixels are autocorrelated. A series of images acquired at different times may thus be used to examine the temporal evolution of the system. However, this method is inherently insensitive at the single-molecule level and limited to 2D geometries. In the past 3 years, scanning FCS was reintroduced to study both the spatial and the temporal dynamics of a heterogeneous system like the cell

membrane. By scanning the laser beam over the membrane surface either in a circular orbit (Ruan *et al.*, 2004) or in a linear scan (Ries and Schwille, 2006), the dwell time of the focal spot on any region of the membrane surface is minimized, thus reducing the problem of photobleaching. Scanning FCS can simultaneously give information about the spatial evolution of slow (very large or aggregated) species by correlating the signals both in time and space, as long as the slow species diffuse much slower than the scan or orbit rate. Manipulation of the scanning can give access to different time regimes. The ability of linear and circular scanning methods to obtain a spatial correlation can be useful in determining the mechanism (s) responsible for non-Brownian diffusion in phase-separated model membranes and cell membranes. Scanning FCS can also be used to correct for motions of the cell membrane (Peters and Cherry, 1982) since the positional information contained in the data makes it easy to detect the position of the membrane with respect to the focal volume.

Similar to scanning FCS, multiple focal spot FCS has been implemented to gain spatial information from a sample. In such setups, multiple laser beams are employed or a single excitation beam is split up into multiple focal spots so that the time-dependent fluorescence fluctuations from multiple locations can be correlated to give spatial information. This can be done using stationary focal spots (Blom *et al.*, 2002; Brinkmeier *et al.*, 1999; Xia *et al.*, 1995) or with scanning (Ries and Schwille, 2006). Spatial sensitivity was first exploited to characterize flow and diffusion *in vitro* simultaneously (Blom *et al.*, 2002; Brinkmeier *et al.*, 1999; Xia *et al.*, 1995). Spatial information is especially important in the cell since molecules are constantly undergoing dynamic movements and interactions during the cell life cycle. It has been shown in HeLa cells, for example, that signal from GFP-labeled glucocorticoid receptors can be monitored simultaneously in the cytoplasm and in the nucleus to study the translocation of the receptor upon external stimulus (Takahashi *et al.*, 2005). Spatial correlations can also access very slow dynamics such as that of proteins in membranes (Ries and Schwille, 2006). New tools are being developed to increase the amount of spatial information that can be gained, like using electron multiplying charge coupled device (EMCCD) for wide-field detection instead of PMTs and APDs (Burkhardt and Schwille, 2006).

Another way of getting spatial information is by coupling FRET with FCS. FRET is conventionally employed to determine the proximity between molecules of two species. A fluorescent signal is generated when two fluorophores (a donor and an acceptor) are sufficiently close together that energy from the excited donor fluorophore is transferred nonradiatively to the acceptor fluorophore by long-range dipole-to-dipole interactions. The fluorescence emission intensity from the acceptor molecule depends not only on the distance between the two fluorophores but also on their relative orientations; maximum acceptor fluorescence is achieved when the emission dipole of the donor is parallel to the absorption dipole of the acceptor. FRET–FCS measurements of end-labeled DNA hairpins demonstrate submillisecond fluctuations in the proximity correlation (Bonnet *et al.*, 1998; Wallace *et al.*, 2000). While the DNA hairpin is closed, the donor and acceptor are in close contact

and energy transfer is at maximum. The same technique has been extended to study conformational fluctuations of RNA three-helix junctions (Kim *et al.*, 2002) and the fast wrapping and unwrapping of DNA around a histone (Li *et al.*, 2005).

Total Internal Reflection–FCS (TIR–FCS) aims to reduce the axial dimension of the focal volume by employing evanescent excitation (Axelrod, 2008). When light passes from a medium of higher refractive index to one that is lower, there is a critical angle of incidence beyond which the transmitted beam is reflected back into the medium of higher refractive index. A component of the transmitted beam travels parallel to the interface, resulting in an evanescent field whose amplitude decays exponentially in the axial direction. This limits the excitation to a small region near the surface of the coverglass. Higher axial spatial resolution is necessary in membrane protein studies to exclude artifacts in the correlation function that result from membrane motions and residual fluorophores freely diffusing in the cytosol and extracellular space. There are two main configurations used for TIR excitation. In the first scheme, the sample is mounted on a prism that internally reflects the incident light (Thompson *et al.*, 1981) and the emitted fluorescence is collected through a separate lens. In the second scheme, a high-NA objective is used to create the critical angle at the glass–sample interface required for TIR and the fluorescence is collected back through the same lens. In prism-based TIR, the weak evanescent excitation field and the optics required for implementation limit the efficiency of collection and thus its application to FCS. Lens-based TIR, however, can reduce the axial dimension of the focal volume by almost tenfold to ~200 nm (Lieto *et al.*, 2003; Starr and Thompson, 2002), though it does not decrease the lateral dimension of the illuminated area. In fact, the lateral dimension is often enlarged due to the underfilling of the back aperture of the lens needed to produce the annular pattern. Recently, however, Hassler *et al.* have demonstrated higher counts per molecule and smaller overall detection volumes *in vitro* using a confocal TIR setup which employs lens-based illumination and confocal fiber-based epi-detection (Hassler *et al.*, 2005a,b). This technique is very promising, especially for 2D studies on biological membranes.

Cells are crowded environments where biomolecules are sometimes found at micromolar concentrations. To work at these biologically relevant concentrations while maintaining single-molecule sensitivity, the focal volume would need to be three orders of magnitude smaller than conventionally achieved. Zero-mode waveguides use a similar decaying evanescent excitation field within a nanoscopic hole in a metal sheet to confine the axial dimension of the focal volume. These subwavelength holes in a thin metal film confine the focal volumes in the radial dimension to measure chemical kinetics of a single enzyme in action (Levene *et al.*, 2003). Arrays of these structures have also been useful for *in vitro* studies to study enzyme kinetics at the single-molecule level (Samiee *et al.*, 2005). They can also reduce membrane motional artifacts by spatially confining supported membranes (Samiee *et al.*, 2006). For *in vivo* studies, plasma membrane has been shown to invaginate into these nanostructures to reach the excitation volumes at the bottom as the cell grows above (Edel *et al.*, 2005; Jose *et al.*, 2007). This improves the possibility of studying

molecular interactions at the plasma membrane of living cells in real time with single-molecule sensitivity without perturbation by membrane flow.

V. Conclusions

Ever since it was established as a sensitive technique for studying molecular dynamics *in vivo*, FCS has steadily gained in popularity. It has the advantage of being noninvasive and sensitive down to the single-molecule limit. In this chapter, we have described some of the biologically significant applications of FCS, in terms of the different types of dynamics measured by the technique. These range from anomalous subdiffusion in the membrane and the cytoplasm, to directed transport, to intermolecular interactions, and to fast rotational and conformational fluctuations that affect the fluorescence of the species of interest. Although the technique holds immense promise for *in vivo* applications, it is not as widely used as it could be because the technology may not be as accessible for the cell biologist. Difficulties encountered in applying FCS will be overcome with improved technology and new advances in the technique. It is to be expected that the demands of future *in vivo* applications will always push the limits of the science and technologies underlying FCS.

Acknowledgments

We acknowledge the support of NIH-NIBIB Grant No. 9-P41-EB001976 and NIH-NIA Grant No. 1-R21-AG026650 for H.C., E.R.F. and W.W.W. E.R.F. is supported by NIH Training Grant No. 2-T32-GM007469. We also thank Mark Williams for help with proofreading and editing the text.

References

Adams, S. R., Campbell, R. E., Gross, L. A., Martin, B. R., Walkup, G. K., Yao, Y., Llopis, J., and Tsien, R. Y. (2002). New biarsenical ligands and tetracysteine motifs for protein labeling *in vitro* and *in vivo*: Synthesis and biological applications. *J. Am. Chem. Soc.* **124,** 6063–6076.

Alberts, B. (2002). "Molecular Biology of the Cell." Garland Science, New York.

Aragon, S. R., and Pecora, R. (1975). Fluorescence correlation spectroscopy and brownian rotational diffusion. *Biopolymers* **14,** 119–137.

Aragon, S. R., and Pecora, R. (1976). Fluorescence correlation spectroscopy as a probe of molecular-dynamics. *J. Chem. Phys.* **64,** 1791–1803.

Arrio-Dupont, M., Foucault, G., Vacher, M., Devaux, P. F., and Cribier, S. (2000). Translational diffusion of globular proteins in the cytoplasm of cultured muscle cells. *Biophys. J.* **78,** 901–907.

Axelrod, D. (2008). Total internal reflection fluorescence microscopy. *In* "Biophysical Tools for Biologists, Volume 2: Methods *In Vivo*" (J. J. Correia, and H. W. Detrich, Eds.), pp. 461–476. Academic Press, San Diego.

Axelrod, D., Koppel, D. E., Schlessinger, J., Elson, E., and Webb, W. W. (1976a). Mobility measurement by analysis of fluorescence photobleaching recovery kinetics. *Biophys. J.* **16,** 1055–1069.

Axelrod, D., Ravdin, P., Koppel, D. E., Schlessinger, J., Webb, W. W., Elson, E. L., and Podleski, T. R. (1976b). Lateral motion of fluorescently labeled acetylcholine receptors in membranes of developing muscle-fibers. *Proc. Natl. Acad. Sci. USA* **73,** 4594–4598.

Bacia, K., Majoul, I. V., and Schwille, P. (2002). Probing the endocytic pathway in live cells using dual-color fluorescence cross-correlation analysis. *Biophys. J.* **83,** 1184–1193.

Bacia, K., Scherfeld, D., Kahya, N., and Schwille, P. (2004). Fluorescence correlation spectroscopy relates rafts in model and native membranes. *Biophys. J.* **87,** 1034–1043.

Banks, D. S., and Fradin, C. (2005). Anomalous diffusion of proteins due to molecular crowding. *Biophys. J.* **89,** 2960–2971.

Barak, L. S., and Webb, W. W. (1982). Diffusion of low density lipoprotein-receptor complex on human fibroblasts. *J. Cell Biol.* **95,** 846–852.

Baumgart, T., Hammond, A. T., Sengupta, P., Hess, S. T., Holowka, D. A., Baird, B. A., and Webb, W. W. (2007). Large-scale fluid/fluid phase separation of proteins and lipids in giant plasma membrane vesicles. *Proc. Natl. Acad. Sci. USA* **104,** 3165–3170.

Baumgart, T., Hess, S. T., and Webb, W. W. (2003). Imaging coexisting fluid domains in biomembrane models coupling curvature and line tension. *Nature* **425,** 821–824.

Benda, A., Benes, M., Marecek, V., Lhotsky, A., Hermens, W. T., and Hof, M. (2003). How to determine diffusion coefficients in planar phospholipid systems by confocal fluorescence correlation spectroscopy. *Langmuir.* **19,** 4120–4126.

Berland, K. M., So, P. T., and Gratton, E. (1995). Two-photon fluorescence correlation spectroscopy: Method and application to the intracellular environment. *Biophys. J.* **68,** 694–701.

Blom, H., Johansson, M., Gosch, M., Sigmundsson, T., Holm, J., Hard, S., and Rigler, R. (2002). Parallel flow measurements in microstructures by use of a multifocal 4×1 diffractive optical fan-out element. *Appl. Optics* **41,** 6614–6620.

Bonnet, G., Krichevsky, O., and Libchaber, A. (1998). Kinetics of conformational fluctuations in DNA hairpin-loops. *Proc. Natl. Acad. Sci. USA* **95,** 8602–8606.

Bouchaud, J. P., and Georges, A. (1990). Anomalous diffusion in disordered media—Statistical mechanisms, models and physical applications. *Phys. Rep.* **195,** 127–293.

Boukari, H., and Sackett, D. L. (2007). Fluorescence correlation spectroscopy and its application to the characterization of molecular properties and interactions. *In* ''Biophysical Tools for Biologists: Vol. 1 *in Vitro* Techniques'' Vol. 84, pp. 659–678, Elsevier, printed by Academic Press.

Brinkmeier, M., Dorre, K., Stephan, J., and Eigen, M. (1999). Two beam cross correlation: A method to characterize transport phenomena in micrometer-sized structures. *Anal. Chem.* **71,** 609–616.

Brown, D. A., and London, E. (2000). Structure and function of sphingolipid- and cholesterol-rich membrane rafts. *J. Biol. Chem.* **275,** 17221–17224.

Brown, D. A., and Rose, J. K. (1992). Sorting of GPI-anchored proteins to glycolipid-enriched membrane subdomains during transport to the apical cell surface. *Cell* **68,** 533–544.

Brown, E. B., Wu, E. S., Zipfel, W., and Webb, W. W. (1999). Measurement of molecular diffusion in solution by multiphoton fluorescence photobleaching recovery. *Biophys. J.* **77,** 2837–2849.

Burkhardt, M., and Schwille, P. (2006). Electron multiplying CCD based detection for spatially resolved fluorescence correlation spectroscopy. *Opt. Express* **14,** 5013–5020.

Burstyn, H. C., Chang, R. F., and Sengers, J. V. (1980). Non-exponential decay of critical concentration fluctuations in a binary-liquid. *Phys. Rev. Lett.* **44,** 410–413.

Chattopadhyay, K., Saffarian, S., Elson, E. L., and Frieden, C. (2002). Measurement of microsecond dynamic motion in the intestinal fatty acid binding protein by using fluorescence correlation spectroscopy. *Proc. Natl. Acad. Sci. USA* **99,** 14171–14176.

Chattopadhyay, K., Saffarian, S., Elson, E. L., and Frieden, C. (2005). Measuring unfolding of proteins in the presence of denaturant using fluorescence correlation spectroscopy. *Biophys. J.* **88,** 1413–1422.

Chen, H. M., Rhoades, E., Butler, J. S., Loh, S. N., and Webb, W. W. (2007). Dynamics of equilibrium structural fluctuations of apomyoglobin measured by fluorescence correlation spectroscopy. *Proc. Natl. Acad. Sci. USA* **104,** 10459–10464.

Chen, Y., Muller, J. D., Ruan, Q. Q., and Gratton, E. (2002). Molecular brightness characterization of EGFP in vivo by fluorescence fluctuation spectroscopy. *Biophys. J.* **82,** 133–144.

Chen, Y., Muller, J. D., So, P. T., and Gratton, E. (1999). The photon counting histogram in fluorescence fluctuation spectroscopy. *Biophys. J.* **77,** 553–567.

Denk, W., Strickler, J. H., and Webb, W. W. (1990). 2-photon laser scanning fluorescence microscopy. *Science* **248,** 73–76.

Dietrich, C., Bagatolli, L. A., Volovyk, Z. N., Thompson, N. L., Levi, M., Jacobson, K., and Gratton, E. (2001). Lipid rafts reconstituted in model membranes. *Biophys. J.* **80,** 1417–1428.

Digman, M. A., Sengupta, P., Wiseman, P. W., Brown, C. M., Horwitz, A. R., and Gratton, E. (2005). Fluctuation correlation spectroscopy with a laser-scanning microscope: Exploiting the hidden time structure. *Biophys. J.* **88,** L33–L36.

Edel, J. B., Wu, M., Baird, B., and Craighead, H. G. (2005). High spatial resolution observation of single-molecule dynamics in living cell membranes. *Biophys. J.* **88,** L43–45.

Eid, J. S., Muller, J. D., and Gratton, E. (2000). Data acquisition card for fluctuation correlation spectroscopy allowing full access to the detected photon sequence. *Rev. Sci. Instrum.* **71,** 361–368.

Eigen, M., and Rigler, R. (1994). Sorting single molecules—Application to diagnostics and evolutionary biotechnology. *Proc. Natl. Acad. Sci. USA* **91,** 5740–5747.

Einstein, A. (1906). The theory of the Brownian motion. *Annalen Der Physik* **19,** 371–381.

Elson, E. L. (1985). Fluorescence correlation spectroscopy and photobleaching recovery. *Ann. Rev. Phys. Chem.* **36,** 379–406.

Elson, E. L., and Magde, D. (1974). Fluorescence correlation spectroscopy. 1. Conceptual basis and theory. *Biopolymers* **13,** 1–27.

Elson, E. L., Schlessinger, J., Koppel, D. E., Axelrod, D., and Webb, W. W. (1976). Measurement of lateral transport on cell surfaces. *Prog. Clin. Biol. Res.* **9,** 137–147.

Elson, E. L., and Webb, W. W. (1975). Concentration correlation spectroscopy—New biophysical probe based on occupation number fluctuations. *Annu. Rev. Biophys. Bioeng.* **4,** 311–334.

Fahey, P. F., Koppel, D. E., Barak, L. S., Wolf, D. E., Elson, E. L., and Webb, W. W. (1977). Lateral diffusion in planar lipid bilayers. *Science* **195,** 305–306.

Fatin-Rouge, N., Starchev, K., and Buffle, J. (2004). Size effects on diffusion processes within agarose gels. *Biophys. J.* **86,** 2710–2719.

Feder, T. J., Brust-Mascher, I., Slattery, J. P., Baird, B., and Webb, W. W. (1996). Constrained diffusion or immobile fraction on cell surfaces: A new interpretation. *Biophys. J.* **70,** 2767–2773.

Felekyan, S., Kuhnemuth, R., Kudryavtsev, V., Sandhagen, C., Becker, W., and Seidel, C. A. M. (2005). Full correlation from picoseconds to seconds by time-resolved and time-correlated single photon detection. *Rev. Sci. Instrum.* **76,** 083104–083114.

Foquet, M., Korlach, J., Zipfel, W. R., Webb, W. W., and Craighead, H. G. (2004). Focal volume confinement by submicrometer-sized fluidic channels. *Anal. Chem.* **76,** 1618–1626.

Fradin, C., Abu-Arish, A., Granek, R., and Elbaum, M. (2003). Fluorescence correlation spectroscopy close to a fluctuating membrane. *Biophys. J.* **84,** 2005–2020.

Frick, M., Schmidt, K., and Nichols, B. J. (2007). Modulation of lateral diffusion in the plasma membrane by protein density. *Curr. Biol.* **17,** 462–467.

Gennerich, A., and Schild, D. (2000). Fluorescence correlation spectroscopy in small cytosolic compartments depends critically on the diffusion model used. *Biophys. J.* **79,** 3294–3306.

Griffin, B. A., Adams, S. R., and Tsien, R. Y. (1998). Specific covalent labeling of recombinant protein molecules inside live cells. *Science* **281,** 269–272.

Hac, A. E., Seeger, H. M., Fidorra, M., and Heimburg, T. (2005). Diffusion in two-component lipid membranes—A fluorescence correlation spectroscopy and Monte Carlo simulation study. *Biophys. J.* **88,** 317–333.

Hassler, K., Anhut, T., Rigler, R., Gosch, M., and Lasser, T. (2005). High count rates with total internal reflection fluorescence correlation spectroscopy. *Biophys. J.* **88,** L1–L3.

Hassler, K., Leutenegger, M., Rigler, P., Rao, R., Rigler, R., Gosch, M., and Lasser, T. (2005). Total internal reflection fluorescence correlation spectroscopy (TIR-FCS) with low background and high count-rate per molecule. *Opt. Express* **13,** 7415–7423.

Haupts, U., Maiti, S., Schwille, P., and Webb, W. W. (1998). Dynamics of fluorescence fluctuations in green fluorescent protein observed by fluorescence correlation spectroscopy. *Proc. Natl. Acad. Sci. USA* **95,** 13573–13578.

Heikal, A. A., Hess, S. T., Baird, G. S., Tsien, R. Y., and Webb, W. W. (2000). Molecular spectroscopy and dynamics of intrinsically fluorescent proteins: Coral red (dsRed) and yellow (Citrine). *Proc. Natl. Acad. Sci. USA* **97,** 11996–12001.

Heikal, A. A., Hess, S. T., and Webb, W. W. (2001). Multiphoton molecular spectroscopy and excited state dynamics of enhanced green fluorescent protein (EGFP): Acid-base specificity. *Chem. Phys.* **274,** 37–55.

Heim, R., Cubitt, A. B., and Tsien, R. Y. (1995). Improved green fluorescence. *Nature* **373,** 663–664.

Hess, S. T., Heikal, A. A., and Webb, W. W. (2004). Fluorescence photoconversion kinetics in novel green fluorescent protein pH sensors (pHluorins). *J. Phys. Chem. B* **108,** 10138–10148.

Hess, S. T., Huang, S. H., Heikal, A. A., and Webb, W. W. (2002). Biological and chemical applications of fluorescence correlation spectroscopy: A review. *Biochem.* **41,** 697–705.

Hess, S. T., and Webb, W. W. (2002). Focal volume optics and experimental artifacts in confocal fluorescence correlation spectroscopy. *Biophys. J.* **83,** 2300–2317.

Huang, J. S., and Webb, W. W. (1969). Viscous damping of thermal excitations on interface of critical fluid mixtures. *Phys. Rev. Lett.* **23,** 160–163.

Humpolickova, J., Gielen, E., Benda, A., Fagulova, V., Vercammen, J., Vandeven, M., Hof, M., Ameloot, M., and Engelborghs, Y. (2006). Probing diffusion laws within cellular membranes by Z-scan fluorescence correlation spectroscopy. *Biophys. J.* **91,** L23–L25.

Jose, M. M.-M., Alexis, J. T., Kevan, T. S., Barbara, A. B., and Harold, G. C. (2007). Cell investigation of nanostructures: Zero-mode waveguides for plasma membrane studies with single molecule resolution. *Nanotechnology* **18,** 195101.

Kask, P., Piksarv, P., Mets, U., Pooga, M., and Lippmaa, E. (1987). Fluorescence correlation spectroscopy in the nanosecond time range: Rotational diffusion of bovine carbonic anhydrase B. *Eur. Biophys. J.* **14,** 257–261.

Kask, P., Piksarv, P., Pooga, M., Mets, U., and Lippmaa, E. (1989). Separation of the rotational contribution in fluorescence correlation experiments. *Biophys. J.* **55,** 213–220.

Keppler, A., Pick, H., Arrivoli, C., Vogel, H., and Johnsson, K. (2004). Labeling of fusion proteins with synthetic fluorophores in live cells. *Proc. Natl. Acad. Sci. USA* **101,** 9955–9959.

Kim, H. D., Nienhaus, G. U., Ha, T., Orr, J. W., Williamson, J. R., and Chu, S. (2002). Mg2+-dependent conformational change of RNA studied by fluorescence correlation and FRET on immobilized single molecules. *Proc. Natl. Acad. Sci. USA* **99,** 4284–4289.

Kim, S. A., Heinze, K. G., Bacia, K., Waxham, M. N., and Schwille, P. (2005). Two-photon cross-correlation analysis of intracellular reactions with variable stoichiometry. *Biophys. J.* **88,** 4319–4336.

Kohler, R. H., Cao, J., Zipfel, W. R., Webb, W. W., and Hanson, M. R. (1997). Exchange of protein molecules through connections between higher plant plastids. *Science* **276,** 2039–2042.

Kohler, R. H., Schwille, P., Webb, W. W., and Hanson, M. R. (2000). Active protein transport through plastid tubules: Velocity quantified by fluorescence correlation spectroscopy. *J. Cell Sci.* **113**(Pt 22), 3921–3930.

Kojro, Z., Riede, A., Schubert, M., and Grill, W. (1999). Systematic and statistical errors in correlation estimators obtained from various digital correlators. *Rev. Sci. Instrum.* **70,** 4487–4496.

Koppel, D. E. (1974). Statistical accuracy in fluorescence correlation spectroscopy. *Phys. Rev. A* **10,** 1938–1945.

Koppel, D. E., Axelrod, D., Schlessinger, J., Elson, E. L., and Webb, W. W. (1976). Dynamics of fluorescence marker concentration as a probe of mobility. *Biophys. J.* **16,** 1315–1329.

Koppel, D. E., Morgan, F., Cowan, A. E., and Carson, J. H. (1994). Scanning concentration correlation spectroscopy using the confocal laser microscope. *Biophys. J.* **66,** 502–507.

Korlach, J., Baumgart, T., Webb, W. W., and Feigenson, G. W. (2005). Detection of motional heterogeneities in lipid bilayer membranes by dual probe fluorescence correlation spectroscopy. *Biochimica Et Biophysica Acta-Biomembranes* **1668,** 158–163.

Korlach, J., Schwille, P., Webb, W. W., and Feigenson, G. W. (1999). Characterization of lipid bilayer phases by confocal microscopy and fluorescence correlation spectroscopy. *Proc. Natl. Acad. Sci. USA* **96,** 8461–8466.

Kucik, D. F., Elson, E. L., and Sheetz, M. P. (1999). Weak dependence of mobility of membrane protein aggregates on aggregate size supports a viscous model of retardation of diffusion. *Biophys. J.* **76,** 314–322.

Kusumi, A., Sako, Y., and Yamamoto, M. (1993). Confined lateral diffusion of membrane-receptors as studied by single-particle tracking (Nanovid microscopy)–Effects of calcium-induced differentiation in cultured epithelial-cells. *Biophys. J.* **65,** 2021–2040.

Larson, D. R., Gosse, J. A., Holowka, D. A., Baird, B. A., and Webb, W. W. (2005). Temporally resolved interactions between antigen-stimulated IgE receptors and Lyn kinase on living cells. *J. Cell Biol.* **171,** 527–536.

Larson, D. R., Ma, Y. M., Vogt, V. M., and Webb, W. W. (2003). Direct measurement of Gag-Gag interaction during retrovirus assembly with FRET and fluorescence correlation spectroscopy. *J. Cell Biol.* **162,** 1233–1244.

Lenne, P. F., Wawrezinieck, L., Conchonaud, F., Wurtz, O., Boned, A., Guo, X. J., Rigneault, H., He, H. T., and Marguet, D. (2006). Dynamic molecular confinement in the plasma membrane by microdomains and the cytoskeleton meshwork. *EMBO J.* **25,** 3245–3256.

Levene, M. J., Korlach, J., Turner, S. W., Foquet, M., Craighead, H. G., and Webb, W. W. (2003). Zero-mode waveguides for single-molecule analysis at high concentrations. *Science* **299,** 682–686.

Li, G., Levitus, M., Bustamante, C., and Widom, J. (2005). Rapid spontaneous accessibility of nucleosomal DNA. *Nat. Struct. Mol. Biol.* **12,** 46–53.

Lieto, A. M., Cush, R. C., and Thompson, N. L. (2003). Ligand-receptor kinetics measured by total internal reflection with fluorescence correlation spectroscopy. *Biophys. J.* **85,** 3294–3302.

Luby-Phelps, K., Castle, P. E., Taylor, D. L., and Lanni, F. (1987). Hindered diffusion of inert tracer particles in the cytoplasm of mouse 3T3 cells. *Proc. Natl. Acad. Sci. USA* **84,** 4910–4913.

Luby-Phelps, K., Taylor, D. L., and Lanni, F. (1986). Probing the structure of cytoplasm. *J. Cell Biol.* **102,** 2015–2022.

Magde, D., Elson, E. L., and Webb, W. W. (1974). Fluorescence correlation spectroscopy.2. Experimental realization. *Biopolymers* **13,** 29–61.

Magde, D., Webb, W. W., and Elson, E. (1972). Thermodynamic fluctuations in a reacting system—Measurement by fluorescence correlation spectroscopy. *Phys. Rev. Lett.* **29,** 705–708.

Magde, D., Webb, W. W., and Elson, E. L. (1978). Fluorescence correlation spectroscopy. III. Uniform translation and laminar flow. *Biopolymers* **17,** 361–376.

Meseth, U., Wohland, T., Rigler, R., and Vogel, H. (1999). Resolution of fluorescence correlation measurements. *Biophys. J.* **76,** 1619–1631.

Neuweiler, H., Schulz, A., Bohmer, M., Enderlein, J., and Sauer, M. (2003). Measurement of submicrosecond intramolecular contact formation in peptides at the single-molecule level. *J. Am. Chem. Soc.* **125,** 5324–5330.

Palmer, A. G., and Thompson, N. L. (1987). Molecular aggregation characterized by high-order autocorrelation in fluorescence correlation spectroscopy. *Biophys. J.* **52,** 257–270.

Periasamy, N., and Verkman, A. S. (1998). Analysis of fluorophore diffusion by continuous distributions of diffusion coefficients: Application to photobleaching measurements of multicomponent and anomalous diffusion. *Biophys. J.* **75,** 557–567.

Peters, R., and Cherry, R. J. (1982). Lateral and rotational diffusion of bacteriorhodopsin in lipid bilayers—Experimental test of the Saffman-Delbruck equations. *Proc. Natl. Acad. Sci. USA-Biol. Sci.* **79,** 4317–4321.

Petersen, N. O. (1986). Scanning fluorescence correlation spectroscopy.1. Theory and simulation of aggregation measurements. *Biophys. J.* **49,** 809–815.

Politz, J. C., Browne, E. S., Wolf, D. E., and Pederson, T. (1998). Intranuclear diffusion and hybridization state of oligonucleotides measured by fluorescence correlation spectroscopy in living cells. *Proc. Natl. Acad. Sci. USA* **95,** 6043–6048.

Pramanik, A., Olsson, M., Langel, U., Bartfai, T., and Rigler, R. (2001). Fluorescence correlation spectroscopy detects galanin receptor diversity on insulinoma cells. *Biochem.* **40,** 10839–10845.

Pramanik, A., and Rigler, R. (2001). Ligand-receptor interactions in the membrane of cultured cells monitored by fluorescence correlation spectroscopy. *Biol. Chem.* **382,** 371–378.

Ratto, T. V., and Longo, M. L. (2002). Obstructed diffusion in phase-separated supported lipid bilayers: A combined atomic force microscopy and fluorescence recovery after photobleaching approach. *Biophys. J.* **83,** 3380–3392.

Ries, J., and Schwille, P. (2006). Studying slow membrane dynamics with continuous wave scanning fluorescence correlation spectroscopy. *Biophys. J.* **91,** 1915–1924.

Rigler, R., and Elson, E. (2001). "Fluorescence Correlation Spectroscopy: Theory and Applications" Springer, Berlin; New York.

Rigler, R., Mets, U., Widengren, J., and Kask, P. (1993). Fluorescence correlation spectroscopy with high count rate and low-background—Analysis of translational diffusion. *Eur. Biophys. J. Biophys. Lett.* **22,** 169–175.

Rigler, R., Pramanik, A., Jonasson, P., Kratz, G., Jansson, O. T., Nygren, P., Stahl, S., Ekberg, K., Johansson, B., Uhlen, S., Uhlen, M., and Jornvall, H. (1999). Specific binding of proinsulin C-peptide to human cell membranes. *Proc. Natl. Acad. Sci. USA* **96,** 13318–13323.

Ritchie, K., Shan, X. Y., Kondo, J., Iwasawa, K., Fujiwara, T., and Kusumi, A. (2005). Detection of non-Brownian diffusion in the cell membrane in single molecule tracking. *Biophys. J.* **88,** 2266–2277.

Ruan, Q., Cheng, M. A., Levi, M., Gratton, E., and Mantulin, W. W. (2004). Spatial-temporal studies of membrane dynamics: Scanning fluorescence correlation spectroscopy (SFCS). *Biophys. J.* **87,** 1260–1267.

Ryan, T. A., Myers, J., Holowka, D., Baird, B., and Webb, W. W. (1988). Molecular crowding on the cell-surface. *Science* **239,** 61–64.

Saffarian, S., and Elson, E. L. (2003). Statistical analysis of fluorescence correlation spectroscopy: The standard deviation and bias. *Biophys. J.* **84,** 2030–2042.

Saffman, P. G. (1976). Brownian motion in thin sheets of viscous-fluid. *J. Fluid Mech.* **73,** 593–602.

Saffman, P. G., and Delbruck, M. (1975). Brownian motion in biological membranes. *Proc. Natl. Acad. Sci. USA* **72,** 3111–3113.

Samiee, K. T., Foquet, M., Guo, L., Cox, E. C., and Craighead, H. G. (2005). Lambda-repressor oligomerization kinetics at high concentrations using fluorescence correlation spectroscopy in zero-mode waveguides. *Biophys. J.* **88,** 2145–2153.

Samiee, K. T., Moran-Mirabal, J. M., Cheung, Y. K., and Craighead, H. G. (2006). Zero mode waveguides for single-molecule spectroscopy on lipid membranes. *Biophys. J.* **90,** 3288–3299.

Sandison, D. R., Piston, D. W., Williams, R. M., and Webb, W. W. (1995). Quantitative comparison of background rejection, signal-to-noise ratio, and resolution in confocal and full-field laser-scanning microscopes. *Appl. Optics* **34,** 3576–3588.

Sandison, D. R., and Webb, W. W. (1994). Background rejection and signal-to-noise optimization in confocal and alternative fluorescence microscopes. *Appl. Optics* **33,** 603–615.

Saxton, M. J. (1990). Lateral diffusion in a mixture of mobile and immobile particles—A Monte-Carlo study. *Biophys. J.* **58,** 1303–1306.

Saxton, M. J. (1996). Anomalous diffusion due to binding: A Monte Carlo study. *Biophys. J.* **70,** 1250–1262.

Schlessinger, J., Koppel, D. E., Axelrod, D., Jacobson, K., Webb, W. W., and Elson, E. L. (1976). Lateral transport on cell-membranes—Mobility of concanavalin a receptors on myoblasts. *Proc. Natl. Acad. Sci. USA* **73,** 2409–2413.

Schwille, P., Haupts, U., Maiti, S., and Webb, W. W. (1999a). Molecular dynamics in living cells observed by fluorescence correlation spectroscopy with one- and two-photon excitation. *Biophys. J.* **77,** 2251–2265.

Schwille, P., Korlach, J., and Webb, W. W. (1999b). Fluorescence correlation spectroscopy with single-molecule sensitivity on cell and model membranes. *Cytometry* **36,** 176–182.

Schwille, P., Meyer-Almes, F. J., and Rigler, R. (1997). Dual-color fluorescence cross-correlation spectroscopy for multicomponent diffusional analysis in solution. *Biophys. J.* **72,** 1878–1886.

Seksek, O., Biwersi, J., and Verkman, A. S. (1997). Translational diffusion of macromolecule-sized solutes in cytoplasm and nucleus. *J. Cell Biol.* **138,** 131–142.

Sengupta, P., Garai, K., Balaji, J., Periasamy, N., and Maiti, S. (2003a). Measuring size distribution in highly heterogeneous systems with fluorescence correlation spectroscopy. *Biophys. J.* **84,** 1977–1984.

Sengupta, P., Garai, K., Sahoo, B., Shi, Y., Callaway, D. J., and Maiti, S. (2003b). The amyloid beta peptide (Abeta(1–40)) is thermodynamically soluble at physiological concentrations. *Biochemistry* **42,** 10506–10513.

Shaner, N. C., Campbell, R. E., Steinbach, P. A., Giepmans, B. N. G., Palmer, A. E., and Tsien, R. Y. (2004). Improved monomeric red, orange and yellow fluorescent proteins derived from Discosoma sp. red fluorescent protein. *Nat. Biotechnol.* **22,** 1567–1572.

Singer, S. J., and Nicolson, G. L. (1972). The fluid mosaic model of the structure of cell membranes. *Science* **175,** 720–731.

Skilling, J., and Bryan, R. K. (1984). Maximum-entropy image-reconstruction—General algorithm. *Mon. Not. R. Astrono. Soc.* **211,** 111–124.

Sorscher, S. M., and Klein, M. P. (1980). Profile of a focused collimated laser-beam near the focal minimum characterized by fluorescence correlation spectroscopy. *Rev. Sci. Instrum.* **51,** 98–102.

Starr, T. E., and Thompson, N. L. (2002). Local diffusion and concentration of IgG near planar membranes: Measurement by total internal reflection with fluorescence correlation spectroscopy. *J. Phys. Chem. B* **106,** 2365–2371.

Szymanski, J., Patkowski, A., Wilk, A., Garstecki, P., and Holyst, R. (2006). Diffusion and viscosity in a crowded environment: From nano- to macroscale. *J. Phys. Chem. B* **110,** 25593–25597.

Takahashi, Y., Sawada, R., Ishibashi, K., Mikuni, S., and Kinjo, M. (2005). Analysis of cellular functions by multipoint fluorescence correlation spectroscopy. *Curr. Pharm. Biotechnol.* **6,** 159–165.

Tank, D. W., Wu, E. S., Meers, P. R., and Webb, W. W. (1982a). Lateral diffusion of gramicidin C in phospholipid multibilayers. Effects of cholesterol and high gramicidin concentration. *Biophys. J.* **40,** 129–135.

Tank, D. W., Wu, E. S., and Webb, W. W. (1982b). Enhanced molecular diffusibility in muscle membrane blebs: Release of lateral constraints. *J. Cell Biol.* **92,** 207–212.

Thomas, J. L., Feder, T. J., and Webb, W. W. (1992). Effects of protein concentration on IgE receptor mobility in rat basophilic leukemia cell plasma membranes. *Biophys. J.* **61,** 1402–1412.

Thompson, N. L., Burghardt, T. P., and Axelrod, D. (1981). Measuring surface dynamics of biomolecules by total internal-reflection fluorescence with photobleaching recovery or correlation spectroscopy. *Biophys. J.* **33,** 435–454.

Tsien, R. Y. (1998). The green fluorescent protein. *Annu. Rev. Biochem.* **67,** 509–544.

Verkman, A. S. (2002). Solute and macromolecule diffusion in cellular aqueous compartments. *Trends Biochem. Sci.* **27,** 27–33.

Vishwasrao, H. D., Heikal, A. A., Kasischke, K. A., and Webb, W. W. (2005). Conformational dependence of intracellular NADH on metabolic state revealed by associated fluorescence anisotropy. *J. Biol. Chem.* **280,** 25119–25126.

Vist, M. R., and Davis, J. H. (1990). Phase-equilibria of cholesterol dipalmitoylphosphatidylcholine mixtures—H-2 nuclear magnetic-resonance and differential scanning calorimetry. *Biochem.* **29,** 451–464.

Wachsmuth, M., Waldeck, W., and Langowski, J. (2000). Anomalous diffusion of fluorescent probes inside living cell nuclei investigated by spatially-resolved fluorescence correlation spectroscopy. *J. Mol. Biol.* **298,** 677–689.

Wallace, M. I., Ying, L. M., Balasubramanian, S., and Klenerman, D. (2000). FRET fluctuation spectroscopy: Exploring the conformational dynamics of a DNA hairpin loop. *J. Phys. Chem. B* **104,** 11551–11555.

Wawrezinieck, L., Rigneault, H., Marguet, D., and Lenne, P. F. (2005). Fluorescence correlation spectroscopy diffusion laws to probe the submicron cell membrane organization. *Biophys. J.* **89,** 4029–4042.

Webb, W. W. (1976). Applications of fluorescence correlation spectroscopy. *Q. Rev. Biophys.* **9,** 49–68.

Webb, W. W. (1981). Molecular mobility on the cell surface. *Biochem. Soc. Symp.* **46,** 191–205.

Webb, W. W. (2001a). Fluorescence correlation spectroscopy: Genesis, evolution, maturation and prognosis. *In* "Fluorescence Correlation Spectroscopy Theory and Applications" (R. Rigler, and E. S. Elson, Eds.), pp. 305–330. Springer-Verlag, Berlin.

Webb, W. W. (2001). Fluorescence correlation spectroscopy: Inception, biophysical experimentations, and prospectus. *Appl. Optics* **40,** 3969–3983.

Weiss, M., Elsner, M., Kartberg, F., and Nilsson, T. (2004). Anomalous subdiffusion is a measure for cytoplasmic crowding in living cells. *Biophys. J.* **87,** 3518–3524.

Weissman, M., Schindler, H., and Feher, G. (1976). Determination of molecular-weights by fluctuation spectroscopy—Application to DNA. *Proc. Natl. Acad. Sci. USA* **73,** 2776–2780.

Widengren, J., Mets, U., and Rigler, R. (1995). Fluorescence correlation spectroscopy of triplet-states in solution—A theoretical and experimental-study. *J. Phys. Chem.* **99,** 13368–13379.

Widengren, J., Mets, U., and Rigler, R. (1999). Photodynamic properties of green fluorescent proteins investigated by fluorescence correlation spectroscopy. *Chem. Phys.* **250,** 171–186.

Widengren, J., and Schwille, P. (2000). Characterization of photoinduced isomerization and back-isomerization of the cyanine dye Cy5 by fluorescence correlation spectroscopy. *J. Phys. Chem. A* **104,** 6416–6428.

Williams, R. M., Zipfel, W. R., and Webb, W. W. (2005). Interpreting second-harmonic generation images of collagen I fibrils. *Biophys. J.* **88,** 1377–1386.

Wiseman, P. W., Squier, J. A., Ellisman, M. H., and Wilson, K. R. (2000). Two-photon image correlation spectroscopy and image cross-correlation spectroscopy. *J. Microsc.* **200,** 14–25.

Xia, K. Q., Xin, Y. B., and Tong, P. (1995). Dual-beam incoherent cross-correlation spectroscopy. *J. Opt. Soc. Am. A* **12,** 1571–1578.

Zipfel, W. R., Williams, R. M., Christie, R., Nikitin, A. Y., Hyman, B. T., and Webb, W. W. (2003). Live tissue intrinsic emission microscopy using multiphoton-excited native fluorescence and second harmonic generation. *Proc. Natl. Acad. Sci. USA* **100,** 7075–7080.

Zipfel, W. R., Williams, R. M., and Webb, W. W. (2003). Nonlinear magic: Multiphoton microscopy in the biosciences. *Nat. Biotechnol.* **21,** 1368–1376.

CHAPTER 2

Molecular Sensors Based on Fluorescence Resonance Energy Transfer to Visualize Cellular Dynamics

Bharath Ananthanarayanan,[*] Qiang Ni,[*] and Jin Zhang[*,†]

[*]Department of Pharmacology and Molecular Sciences
The Johns Hopkins University School of Medicine
Baltimore, Maryland 21205

[†]The Solomon H. Snyder Department of Neuroscience and
Department of Oncology
The Johns Hopkins University School of Medicine
Baltimore, Maryland 21205

METHODS IN CELL BIOLOGY, VOL. 89

0091-679X/08 $35.00
DOI: 10.1016/S0091-679X(08)00602-X

Abstract

Visualizing a variety of signaling events in the native cellular environment is now possible with the advent of genetically encodable fluorescent labels like green fluorescent proteins made *de novo* by living cells themselves. The focus of this method chapter is on genetically encodable molecular sensors based on fluorescence resonance energy transfer (FRET) for visualization of cellular dynamics. This chapter discusses the process of developing a molecular sensor, from choosing donor–acceptor pairs to designing the protein modules that actually sense the signaling events. A few examples of biosensors are discussed to showcase the designs of such FRET-based sensors for live-cell imaging of signaling events. Subsequently, Section III covers the experimental procedure of DNA work, microscope instrumentation, data collection through imaging acquisition, data comprehension, and evaluation. Furthermore, a case study of the PI3K/Akt signaling pathway using a series of FRET sensors highlights the tremendous potential of the method in exploring relevant biological systems.

I. Introduction

The intracellular environment is a truly dynamic place, with signaling molecules constantly being synthesized and degraded, interacting and transforming. In order to maintain normal cellular functions, all these dynamic processes are spatially organized and temporally regulated by an elaborate cellular signaling network which is an integral part of a live cell. While the completion of the human genome project has generated a nearly complete list of the proteins that constitute this signaling network, the quest for a comprehensive understanding of the functional roles of these molecules in various cellular processes is just getting underway.

Our ability to understand cellular processes at the molecular level is directly impacted by the availability of methods and tools that allow visualization and quantification of specific signaling events with high spatial and temporal resolution in the cellular context. Therefore, there exists a tremendous need for such methods and tools. Now, molecular sensors based on fluorescent proteins and fluorescence resonance energy transfer (FRET) have provided windows that enable visualization of complex cellular processes such as enzyme activation/activity, protein–protein interactions, and second messenger dynamics in living cells. In this chapter, we focus mainly on the development and applications of such molecular sensors.

II. Basic Principles of FRET-Based Molecular Sensors

A. Basics of FRET Theory

The current form of FRET theory was proposed in the late 1940s by Prof. Theodor Förster. In simple terms, FRET is a nonradiative energy transfer process by which the transfer of energy from an excited donor to an acceptor in its close proximity

occurs. FRET efficiency (E) is inversely proportional to the sixth power of the distance between the donor and acceptor (r), as determined by the following equation.

$$E = 1/[1 + (r/R_0)^6] \quad (1)$$

where R_0 is the Förster distance, at which the FRET efficiency is 50%. Since this energy transfer occurs only when the donor and acceptor are in molecular proximity (i.e., <10 nm apart) and the efficiency of this process is highly sensitive to variations in the distance between the donor and the acceptor when they are within the Förster distance (inverse sixth power dependence) (Fig. 1), FRET has been commonly applied as a spectroscopic ruler for measuring distance between biomolecules in various biological systems (Stryer, 1978).

Although the Förster distance R_0 has a well-defined physical meaning, it is not a constant for a given FRET pair by definition. This is because the value of R_0 depends not only on the intrinsic fluorescence properties of a given FRET pair, namely, the spectral overlap between the donor emission and the acceptor absorption, and the quantum yield of the donor, but also on environmental factors, namely, the refractive index (n) of the medium and the relative orientation between the donor and acceptor, represented by the orientation factor k^2 (Clegg, 1992). It should be recognized that for calculation of R_0 values for different FRET pairs, these environmental factors are universally assigned constant values, typically $n = 1.33$ and $k^2 = 2/3$, assuming aqueous medium and complete random orientation between the donor and acceptor can be achieved during the donor excited-state lifetime. In reality, while the refractive index of the medium is usually a constant, the orientation factor k^2, which describes the alignment between the donor emission dipole moment and the acceptor absorption dipole moment

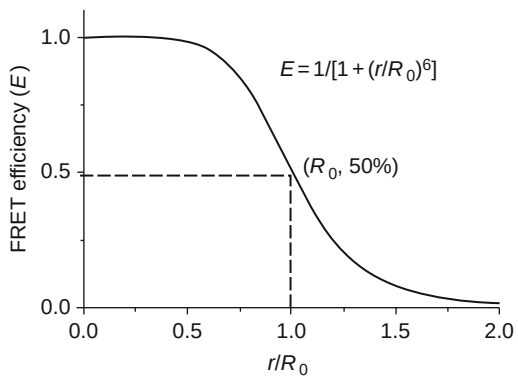

Fig. 1 Dependence of fluorescence resonance energy transfer (FRET) efficiency (E) on distance (r). R_0 is the Förster distance.

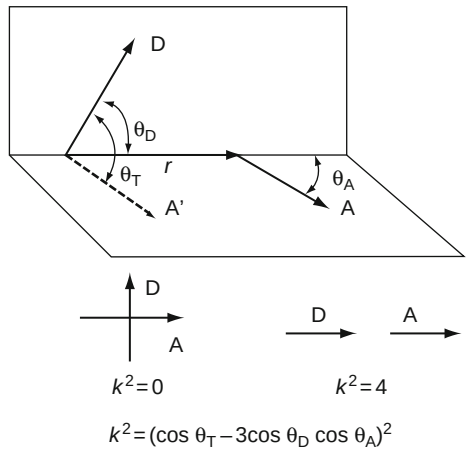

Fig. 2 Dependence of the orientation factor k^2 on the alignment between the donor emission dipole moment (D) and the acceptor absorption dipole moment (A).

(Fig. 2), ranges from 0 when the dipole moments are perpendicular to each other to 4 when the dipole moments are perfectly collinear and varies continuously when the orientation between the donor and acceptor is not locked in one of these two extreme states. Such uncertainty in k^2 has important implications for FRET applications (dos Remedios and Moens, 1995).

Donor–acceptor fluorophore pairs used for FRET (Shanker and Bane, 2008) are of diverse nature, ranging from small molecules to complex nanoparticles like quantum dots (Sapsford *et al.*, 2006). However, specific labeling of biomolecules with fluorophores in cellular environments was a major challenge until the successful cloning and expression of the jellyfish green fluorescent protein (GFP) and development of its color variants (Tsien, 1998).

B. Fluorescent Protein-Based FRET Pairs

Among fluorescent proteins found in various luminous coelenterates, the most widely used and well characterized is the GFP from the jellyfish *Aequorea victoria* (Prasher *et al.*, 1992; Shimomura *et al.*, 1962). Further protein engineering has resulted in expanding the color variety of fluorescent proteins from green to blue, cyan and yellow, hence enabling us to label multiple signaling components and visualize them with minimal interference from each other in living systems (Tsien, 1998). Importantly, these GFP color variants have made genetically encodable FRET pairs a reality (Heim and Tsien, 1996; Mitra *et al.*, 1996).

For FRET applications, the choice of fluorescent proteins as donor and acceptor is critical. First, for FRET to occur, the emission spectrum of the donor fluorescent protein should overlap with the excitation spectrum of the acceptor

fluorescent protein. Second, to allow independent excitation and separate emission measurements, both the excitation and emission spectra of the donor and of the acceptor should be well separated. In practice, however, these two requirements often run into conflict with each other, and as a result a compromise has to be made. Additional considerations for fluorescent proteins employed in FRET applications include brightness, photostability, reduced environmental sensitivity, and minimal tendency to dimerize or oligomerize. In early FRET experiments (Heim and Tsien, 1996; Mitra *et al*., 1996), blue fluorescent protein (BFP) was used as the donor and GFP as the acceptor, but due to the dimness and poor photostability of BFP, the BFP–GFP pair was soon replaced with the cyan fluorescent protein (CFP) and yellow fluorescent protein (YFP) FRET pair (Miyawaki *et al*., 1997).

Also as a general rule of thumb, use of monomeric fluorescent proteins in FRET applications is recommended because potential intersubunit interactions *within* multimeric fluorescent proteins could complicate the interpretation of the FRET signal observed. At the present time, the most commonly employed FRET pair is still CFP–YFP, with monomeric cerulean being the preferred CFP mutant and monomeric venus or citrine being the preferred YFP mutants. Recently, a cyan and yellow fluorescent pair named CyPet-YPet was coevolved to be a good FRET pair, providing a much improved signal change when used in a protease indicator (Nguyen and Daugherty, 2005). However, a recent study showed that most of the improved FRET signal was probably due to enhanced dimerization, thus limiting the usefulness of this particular FRET pair (Ohashi *et al*., 2007).

Notably, longer wavelength emission such as red is missing from the GFP color variants. In principle, red-shifted fluorescent proteins are valuable for a number of reasons. In addition to providing a wealth of new colors for multiple labeling, their imaging-friendly properties in living systems, such as better tissue penetration and better contrast due to less interference from cellular autofluorescence at longer wavelengths, make them suitable for imaging in tissues and even whole organisms. The first red fluorescent protein (RFP) named DsRed was isolated from coral of the *Dicosoma* genus (Matz *et al*., 1999) as an obligate tetramer (Baird *et al*., 2000). Subsequent engineering efforts have led to a whole range of orange to far red monomeric fluorescent proteins with improved properties (Campbell *et al*., 2002; Shaner *et al*., 2004). With this complete rainbow of fluorescent proteins, the choices of FRET pairs have now reached longer wavelengths in the spectrum. These include pairs that utilize a donor with large Stokes' shift, such as UV excitable T-sapphire (Zapata-Hommer and Griesbeck, 2003), paired with RFP or orange fluorescent protein (OFP), as well as pairs with both excitation and emission shifted to longer wavelengths, such as the GFP–RFP, YFP–RFP, and OFP–RFP FRET pairs (Goedhart *et al*., 2007). Furthermore, novel FRET pairs can be engineered using a strategy based on tunable FRET circuit (Allen and Zhang, 2008). With all these possible combinations, imaging using multiple FRET pairs has also been demonstrated, such as in the case of three-chromophore FRET (Galperin *et al*., 2004). Importantly, these red-shifted FRET pairs have R_0 values up to 6.4 nm (Goedhart *et al*., 2007), significantly larger than the commonly used

CFP–YFP pairs (Rizzo *et al.*, 2006). The β-barrel structure shared among all fluorescent proteins, with a diameter of 2.4 nm and height of 4.2 nm, imposes a minimal separation between the two fluorophores of the fluorescent proteins, often limiting the maximum FRET signal achievable. Therefore, this increased R_0 value is advantageous for fluorescent protein-based FRET applications because it enables higher FRET efficiency and therefore better signal at the same distance of separation.

In addition to an optimal FRET signal, there are additional properties of fluorescent proteins that should be taken into consideration for their application in living cells. First, both fluorescent proteins and the host proteins to which they are fused should fold efficiently, and the attachment of a fluorescent protein should not affect the function of the fusion protein. Second, the expression level in the system of interest should be high enough to manifest sufficient brightness and show negligible photobleaching over the time period of the experiment, but not so high as to cause significant cellular toxicity or other perturbations.

C. Modular Design of FRET-Based Molecular Sensors

Key to the design of a genetically encodable FRET sensor is the engineering of a protein-based molecular switch that can generate a signal-specific conformational change. Here, the existence of endogenous sensing modules for virtually any cellular signal offers plenty of opportunities for the design of such protein-based molecular switches.

In some cases, wild-type proteins themselves can be utilized as molecular switches in FRET-based sensors when they show signal-dependent conformational changes (Neininger *et al.*, 2001; Ramanoudjame *et al.*, 2006). For example, ICUE (indicator of cAMP using Epac) was created by sandwiching Epac (exchange protein directly activated by cAMP) between the CFP and YFP FRET pair (DiPilato *et al.*, 2004). Epac is a cAMP receptor protein which mediates cAMP signaling through its cAMP-dependent guanine nucleotide exchange activity toward a small guanosine triphosphatase, Rap1. ICUE not only serves as a reporter of Epac activation but also can monitor cAMP dynamics due to its cAMP-dependent, conformationally responsive elements (DiPilato *et al.*, 2004; Violin *et al.*, 2007). The general usefulness of this approach, however, is limited by the availability of wild-type proteins that can generate suitable conformational changes to alter a FRET signal in response to specific cellular signals.

For more generalizable designs of engineered molecular switches, the existing knowledge of endogenous protein domains and peptide sequences that are involved in particular signaling events has proven to be extremely valuable. For example, our knowledge about kinase substrate specificity as well as the phosphoamino acid binding domains has led to a generalizable design of kinase activity reporters (Ni *et al.*, 2006; Zhang and Allen, 2007). In this design, a molecular switch is formed by concatenation of a substrate peptide specific for the kinase of interest and a phosphoamino acid binding domain, such as the Src

homology 2 (SH2), 14-3-3, or forkhead-associated (FHA) modules. Upon phosphorylation, the phosphoamino acid binding domain binds intramolecularly to the phosphorylated substrate to generate a conformational change. Sensors for monitoring various tyrosine kinases as well as serine/threonine kinases have been developed by sandwiching such engineered molecular switches between a fluorescent protein FRET pair, including PKA (Allen and Zhang, 2006; Allen *et al*., 2006; Zhang *et al*., 2001, 2005), Src (Ting *et al*., 2001; Wang *et al*., 2005), PKC (Violin *et al*., 2003), PKB/Akt (Kunkel *et al*., 2005; Sasaki *et al*., 2003), PKD (Kunkel *et al*., 2007), and others (Johnson *et al*., 2007; Sato *et al*., 2002, 2007; Ting *et al*., 2001). The FRET signals of these sensors can often be reversed by dephosphorylation due to phosphatase activities, thus enabling monitoring the dynamic balance maintained by protein kinases and phosphatases in live cells.

Another example of an engineered molecular switch is InPAkt (indicator for phosphoinositides based on Akt) which reports membrane-restricted lipid molecules, more specifically phosphatidyl inositol (3,4,5) trisphosphate (PIP_3) and phosphatidyl inositol (3,4) bisphosphate ($PI(3,4)P_2$) (Ananthanarayanan *et al*., 2005). In this design, we exploited the specific binding property of Akt's pleckstrin homology (PH) domain for PIP_3 and $PI(3,4)P_2$. The crystal structure of this PH domain complexed to its ligand shows that the motif forms a bowl-like structure lined with basic residues into which the highly negatively charged PIP_3/$PI(3,4)P_2$ molecule is accommodated. In order to generate a conformational change upon phosphatidyl inositol (PI) binding, a ''pseudoligand'' peptide sequence was engineered to associate with the basic patch of amino acids responsible for PI binding (Fig. 3A). It consists of a series of acidic residues taken from nucelolin1, which has been shown to bind to the PH domain of insulin receptor substrate 1. In the absence of PIs, the pseudoligand interacts with the basic residues in the PH domain. As the natural ligand accumulates, it competes with the pseudoligand for binding to the PH pocket, thus generating a conformational change that alters the distance and/or orientation between the donor and acceptor fluorescent proteins at the N- and C-termini, respectively; the result is a change in FRET. This generalizable molecular switch design could be applied to other ligands with appropriate binding domains and custom-engineered psuedoligands.

FRET sensors created using these designs are known as unimolecular or intramolecular sensors since the donor and acceptor fluorophores are attached to the same protein. On the contrary, donor and acceptor fluorophores can be fused to two different proteins to create bimolecular FRET sensors for dynamic monitoring of cellular signaling. Bimolecular, or intermolecular, FRET sensors have proven to be particularly useful in studies of protein–protein interaction, ligand–protein association/dissociation, and protein dimerization/oligomerization, in real time and space. For instance, the well-known concept of $G\alpha$ and $G\beta\gamma$ subunit association (high FRET) and dissociation upon activation (loss of FRET) in G proteins has been demonstrated through dynamic visualization using CFP-tagged $G\alpha$ and YFP-tagged $G\beta\gamma$ (Azpiazu and Gautam, 2004; Janetopoulos *et al*., 2001).

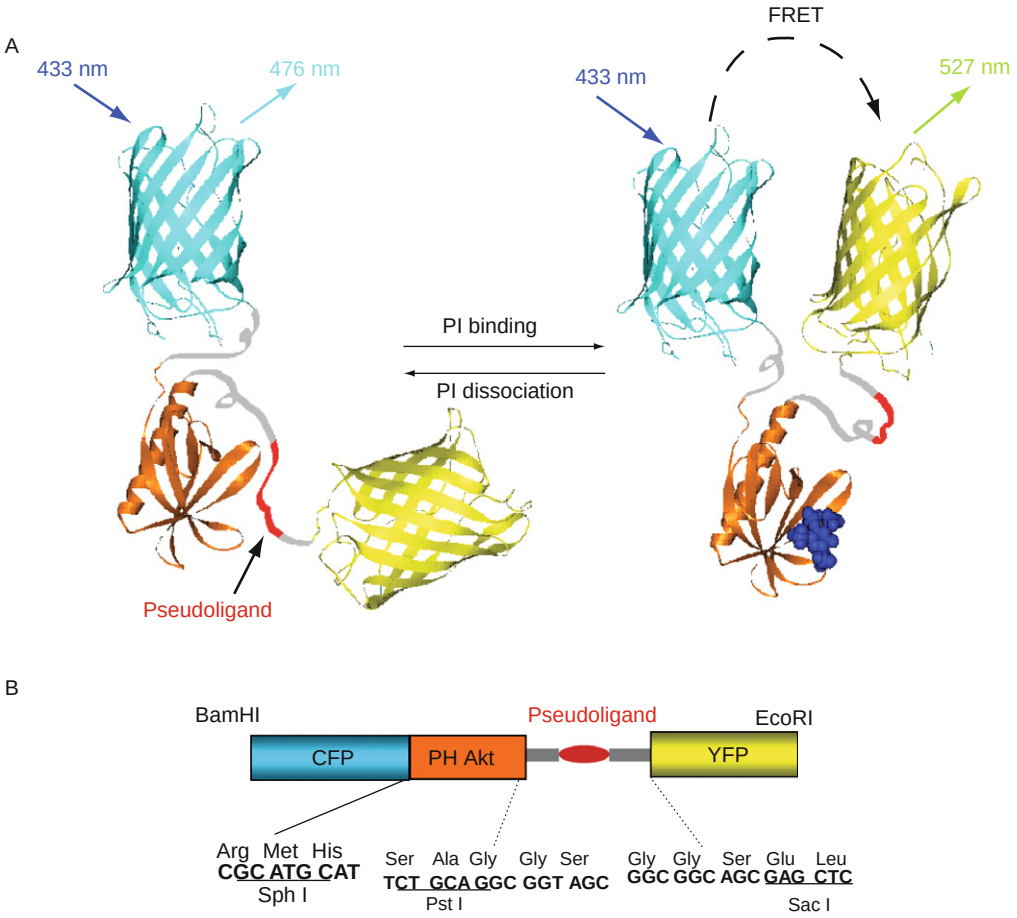

Fig. 3 Development of indicator for phosphoinositides based on Akt (InPAkt). (A) A cartoon depicting the design of InPAkt and illustrating the conformational change upon phosphatidyl inositol (3,4,5) trisphosphate (PIP_3) binding, which yields a fluorescence resonance energy transfer (FRET) response. (B) Domain structure of the construct showing the restriction sites linking individual components.

When designing an intermolecular FRET sensor, the goal is to ensure that the FRET readout reports exclusively on the interaction between the two proteins of interest. While conceptually straightforward, intermolecular FRET sensors are subject to several potential problems that the investigators should avoid. First, to study the potential interaction between two proteins, the two fluorescent protein tags must be able to approach within 6–8 nm of each other to yield a FRET signal. In some cases, the two proteins of interest may interact, but in such a way that the fluorescent proteins remain far apart and fail to detect the interaction, thus giving rise to

false negatives. Second, incorporation of the fluorescent protein tags may interfere with the binding surfaces of the proteins of interest, thereby perturbing their native structures. Therefore, when designing fusion constructs, the fluorescent proteins should be attached in such a way that they do not interfere with the interaction between the two protein partners. Third, measures to prevent dimerization/oligomerization of the fluorescent proteins are also crucial to minimize false-positive signals. Specifically, fluorescent proteins from *Aequorea* show a weak tendency to dimerize; therefore using nonoligomerizing variants containing a Ala206Lys mutation is strongly recommended (Zacharias *et al.*, 2002). Fourth, untagged endogenous protein partners can also compete with the fusion chimera, resulting in unproductive mixed complexes that reduce the anticipated FRET signal. Finally, when homodimerization of a protein of interest is to be detected, true dimers that contain donor–donor or acceptor–acceptor pairs will not contribute to the FRET signal.

In many cases, either unimolecular or bimolecular designs can be applied to track the same signaling event. Dynamic visualization of signaling molecules such as calcium and cAMP, for example, has been achieved with both bimolecular (Miyawaki *et al.*, 1997; Zaccolo *et al.*, 2000) and unimolecular (DiPilato *et al.*, 2004; Miyawaki *et al.*, 1997) FRET-based sensors. The choice between unimolecular and bimolecular designs is often dependent on the specific requirements of a particular application, and more detailed discussions about these two different designs can be found elsewhere (Miyawaki, 2003).

III. Methods

A. DNA Work

After choosing the individual modules of a FRET sensor as discussed in the above sections, their assembly to form a chimeric cDNA can be carried out by introducing restriction sites via the polymerase chain reaction (PCR). When we constructed InPAkt (Fig. 3B), the Akt/PKB PH domain (1–164) was first amplified by PCR using full-length Akt as the template, a forward primer incorporating an SphI restriction site at its 5′ end, and a reverse primer containing a 3′ PstI site. The SphI site at the 5′ end of PH domain was used to couple it to the C-terminus of enhanced cyan fluorescent protein (ECFP). The pseudoligand peptide sequence was created using primers incorporating PstI and SacI sites, permitting it to be inserted between the PH domain and YFP. Finally, the DNA for the entire sensor, including donor ECFP at the N-terminus and YFP at the C-terminus, was inserted into the bacterial expression vector pRSET B (Invitrogen) between the BamHI and EcoRI restriction sites of the vector polylinker. For mammalian cell expression, the construct was subcloned into modified pcDNA3 (Invitrogen) behind a Kozak sequence. In addition, nuclear or plasma membrane localization signals were incorporated at the N- or C-terminus of the construct to generate nuclear or plasma membrane targeted InPAkt (Ananthanarayanan *et al.*, 2005).

B. Instrumentation

1. Available Methods

Several FRET techniques exist based on wide-field, confocal, multiphoton/2-photon, and fluorescence lifetime imaging microscopy (FLIM)–FRET microscopy, each with its own distinct features. Among these, wide-field FRET microscopy is the simplest and currently most widely used technique. Its major disadvantage is that the emission signals from both above and below the focal plane contribute to out-of-focus signals, thereby reducing the contrast and quality of acquired images. Confocal FRET microscopy using a laser excitation source, overcomes the out-of-focus limitation of wide-field microscopy due to its ability to reject signals from outside the focal plane. However, the wavelengths available for excitation of different fluorophore pairs may be limited to standard lasers lines. Another major drawback of confocal microscopy is that the intense laser illumination can result in substantial photobleaching of the sensor and photodamage to the specimen. Fortunately, this limitation can be overcome by using multiphoton/2-photon microscopy. Finally, combination of fluorescence lifetime measurement and FRET (FLIM–FRET) provides the most rigorous method of measuring FRET efficiency but requires additional hardware and software. For more detailed descriptions of this method, please refer to chapters in this volume by Pralle *et al.* and Periasamy *et al.*

2. Wide-Field FRET Microscopy Setup

Wide-field FRET is the most widely used technique due to the simplicity of its instrumentation and the ease of data deconvolution. The instrumentation is built around a regular epifluorescence microscope with a shutter-controlled excitation light source, filter sets for the donor and acceptor, and a charge coupled device (CCD) camera that collects the output signal. First, the imaging system requires a stable excitation light source (Hg or Xe arc lamps) with neutral density filters to control the excitation light intensity. Second, an excitation filter is required for selecting proper wavelengths for exciting the donor fluorophore, and a dichroic mirror is required for separating emission from excitation. Third, at least two emission filters are required, one for the acceptor fluorophore emission upon donor excitation (FRET emission), and the other for the donor fluorophore. It is important to carefully select filter combinations that reduce the spectral bleed-through (SBT) to improve the signal-to-noise (S/N) ratio for the FRET calculation. A list of excitation and emission filters commonly used for many available fluorescent proteins can be found as a useful resource (Shaner *et al.*, 2005). Fourth, the hardware to change the filter configuration for appropriate signal acquisition is critical because the time lapse between image acquisition of the donor and FRET emissions should be minimal. To this end, separate filter cubes with automated turrets or simply an automated emission filter wheel can be used. In either configuration, images can be acquired with a delay as little as tens of milliseconds.

For experiments requiring shorter delay intervals, dual-view imaging setups are now available to acquire both FRET emission and donor emission simultaneously. More detailed descriptions of filters and their configurations can be found on the websites of various optical vendors. The last and final component of the setup is the detector. The most commonly used is a CCD camera from which the data are deconvoluted using an application software interface. Other components can be added to the setup for specific experimental needs. For example, a heating stage and a CO_2 chamber may be incorporated to maintain the cell viability for longer experimental periods.

One typical imaging setup that we use (Fig. 4) consists of a Zeiss Axiovert 200 M microscope with a 40×/1.3 NA (numerical aperture) oil-immersion objective lens, and a MicroMAX BFT512 cooled CCD camera (Roper Scientific) controlled by Metafluor software (Universal Imaging). Dual-emission ratio imaging for the CFP–YFP FRET pair requires a 420DF20 excitation filter, a 450DRLP dichroic mirror, and two emission filters (475DF40 for CFP and 535DF25 for YFP). The latter are switched by a Lambda 10-2 filter changer (Sutter Instruments).

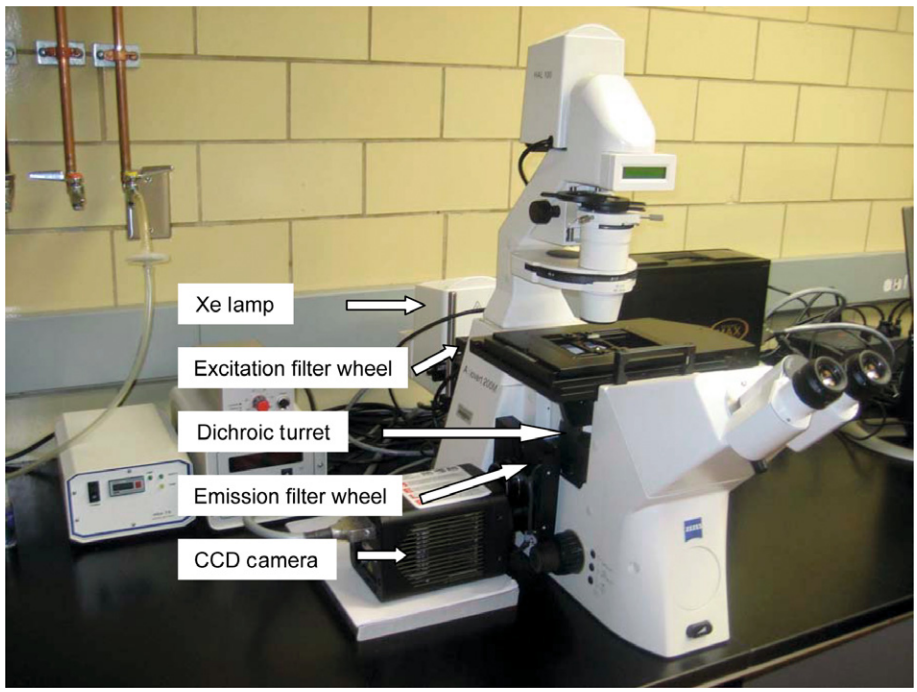

Fig. 4 Layout of a wide-field fluorescence resonance energy transfer (FRET) imaging setup.

C. Cellular Characterization

1. Cell Culture

Appropriate cell lines are chosen to characterize whether the sensor constructed is functional in living cells. For instance, a typical cell line used in our lab is HEK293. HEK293 cells are maintained in Dulbecco' modified Eagle's medium (DMEM) media supplemented with 10% fetal bovine serum at 37 °C with 5% CO_2. For imaging experiments, cells are plated onto sterilized glass coverslips in 35-mm dishes and allowed to grow to 30–90% confluency. Cells are then transfected with the sensor cDNA using FuGENE 6 (Roche) or Lipofectamine 2000 (Invitrogen). Depending on the cell line and the basal activity of the signaling event of interest, the cells may need to be serum starved for 24–36 h before imaging.

2. Imaging

For a typical imaging experiment, cells are washed twice with Hanks' balanced salt solution buffer and maintained in the dark at room temperature or maintained at 37 °C with a heating stage. Cells are treated with appropriate pharmacological drugs at recommended dosage levels to stimulate the desired signaling event. Cells are then exposed to appropriate excitation wavelengths for 50–500 ms, and images are taken every 15–30 s to monitor the change in FRET signal. For each time point, three image channels are acquired. In the case of the CFP–YFP FRET pair, the channels are (1) CFP direct (excitation of donor CFP and acquisition of CFP emission), (2) YFP FRET (excitation of donor CFP and measurement of acceptor YFP emission), and (3) an optional YFP direct (excitation of acceptor YFP and acquisition of YFP emission) as a control to check for photobleaching. Fluorescence images are then corrected for background by subtracting the autofluorescence intensities of untransfected cells (or an area of the imaging field without cells) from the emission intensities of cells expressing the FRET sensors.

When characterizing a FRET sensor in living cells, one crucial control is to verify the specificity of the sensor for reporting only the intended signaling event. To this end, application of specific pharmacological agents or other perturbations to inhibit the signal should abolish the FRET response. Another important negative control involves perturbation of other closely related signaling pathways; an absence of FRET signal indicates that the experimental signal is not due to off-pathway events.

D. Signal Comprehension and FRET Quantification

As discussed in the previous section, at least two overlapping images of CFP direct and YFP FRET are acquired for each time point, before and after perturbation (e.g., drug addition) to measure the FRET signal. For InPAkt, we employ NIH3T3 cells and use 50 ng/ml of platelet-derived growth factor (PDGF) to stimulate PIP_3 generation. Fig. 5A shows an InPAkt-expressing NIH3T3 cell in

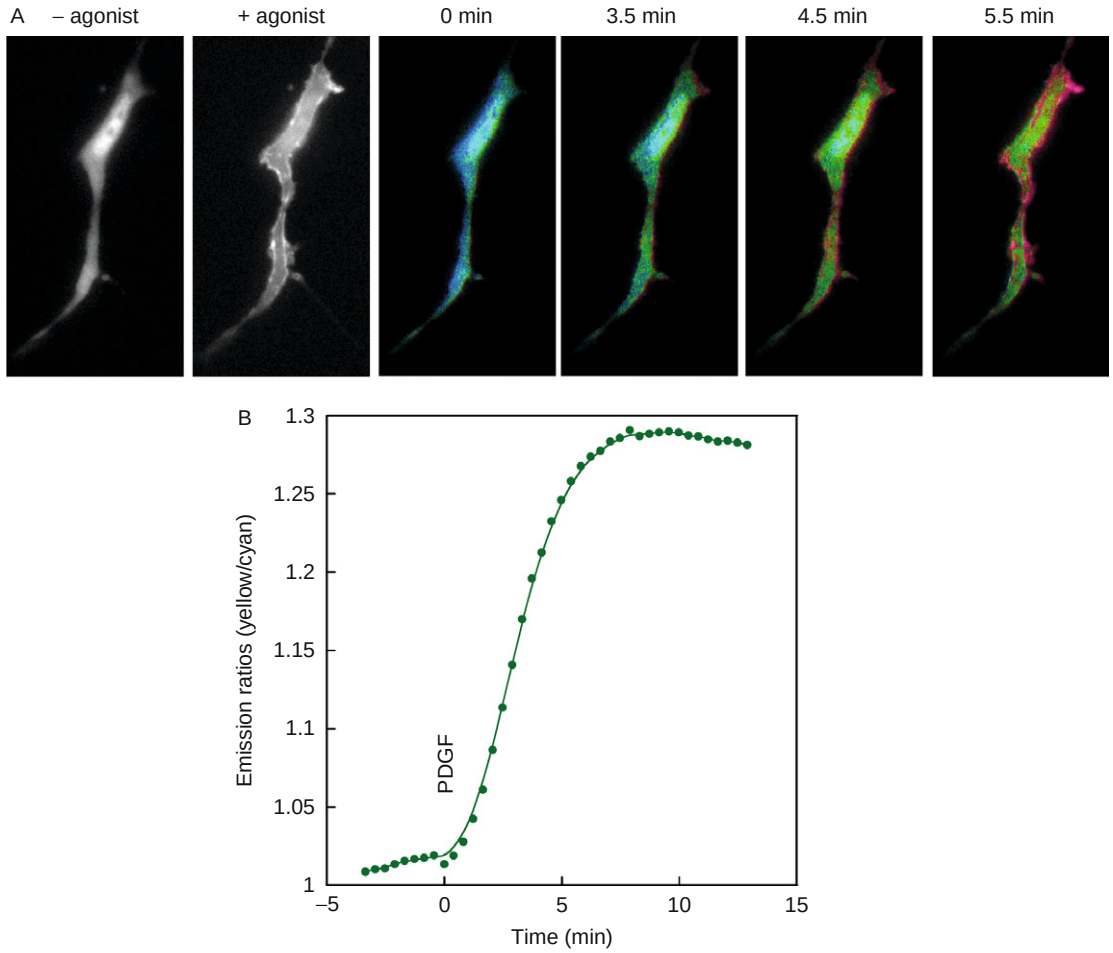

Fig. 5 (A) Fluorescence resonance energy transfer (FRET) response of indicator for phosphoinositides based on Akt (InPAkt) expressed in NIH3T3 cells. The first two images are yellow fluorescent protein (YFP)-only image before and after stimulation. The following pseudocolor images show the FRET response of the reporter at various time points. (B) Representative emission ratio time courses of InPAkt stimulated with 50 ng/ml platelet-derived growth factor (PDGF). InPAkt showed a response of $25.4 \pm 3.7\%$ (average $\pm$ standard dev.) ($n = 9$).

which fluorescence is observed throughout (first image). Stimulation of endogenous PDGF receptor (PDGFR) generates a FRET increase, resulting in a steady increase in cyan (donor) to yellow (acceptor) energy transfer shown by pseudocolor images where warmer colors represent high FRET and cooler colors low FRET (Fig. 5A). The FRET change occurs predominantly at the plasma membrane and is accompanied by translocation of the sensor to the plasma membrane (Fig. 5A, second image), confirming that PIP_3 is mainly produced at the plasma membrane.

After image acquisition, specific regions are selected within the image to tabulate the CFP direct and YFP FRET intensities at various time points for evaluation and quantification of FRET. FRET can either be quantified as the quenching of the donor emission or the enhancement of acceptor fluorescence upon donor excitation. Many software packages, such as Metafluor (Universal Imaging), FRET Macro (Zeiss), PFRET (CircuSoft), OpenLab FRET module (Improvision), have been developed for these measurements. Concise discussions of various methods for FRET quantification can be found elsewhere (Piston and Kremers, 2007). The two commonly used ones are discussed below.

1. Donor and Acceptor Emission Ratio

Since FRET is the transfer of energy from donor to acceptor, the fluorescence intensity of the donor decreases with a concomitant increase in the acceptor intensity. When both intensities are used together in a ratiometric relationship, the resulting FRET emission ratio becomes more sensitive to small changes.

$$\text{FRET emission ratio} = F_A/F_D \tag{2}$$

where F_A is the fluorescence intensity of acceptor emission upon donor excitation and F_D is the intensity of donor emission upon its direct excitation.

Because the stoichiometry between the donor and acceptor fluorescent proteins is fixed for a unimolecular sensor, the change in emission ratio can be directly correlated with FRET efficiency changes, making quantification of FRET signals more straightforward. In practice, this method also offers the best contrast (Rizzo *et al.*, 2006).

In the case of InPAkt, stimulation of endogenous PDGFR generates a FRET increase, resulting in an increase in the ratio of yellow-to-cyan emission (Fig. 5B). Notably, InPAkt is able to detect the changes in emission ratios within several seconds and reaches a plateau signal increase of $25.4 \pm 3.7\%$ [average $\pm$ standard dev.] ($n = 9$; n, number of individual cells imaged) within minutes ($t_{1/2} = 3.4 \pm 0.6$ min), consistent with existing literature data.

2. Donor Recovery After Acceptor Photobleaching

In this technique, the acceptor is exclusively destroyed by photobleaching, thus disrupting the transfer of energy from donor to acceptor. The loss of a functional acceptor fluorophore causes recovery of donor fluorescence intensity.

Hence, FRET efficiency (E) can be calculated with the relative fluorescence intensity of the donor, before (F_{DA}) and after (F_D) acceptor photobleaching using the following equation.

$$E = 1 - (F_{DA}/F_D) \quad (3)$$

Although this method is straightforward, it involves irreversible damage to the acceptor due to photobleaching. Therefore, this procedure is usually performed at the end of any time-lapse experiments.

E. Improving Sensor Signal

Sensor construction and characterization is usually just the first step in sensor development. The next important step is to improve the signal or dynamic range, which often turns out to be a limiting factor for sensor applications. Such improvement should enable applications of the sensor in diverse systems, from detection of subtle yet physiologically significant signals in subcellular microdomains, to high-throughput screening for discovery of novel signaling regulators, such as agonists and antagonists, to analysis of protein interactions in transgenic animals. To this end, there exist several effective strategies that can be applied to improve the signal of a given FRET sensor, and thanks to the modular design of such sensors, these manipulations do not have to sacrifice desirable properties such as the specificity and reversibility that have already been established. A representative example is the calcium sensor cameleon, which went through several generations of modifications since its first report in 1997 to reach a maximum of 600% signal change (Nagai *et al*., 2004).

As discussed above, sensors are constructed with different modules that have unique roles. Suitable linkers should be introduced between these individual modules to facilitate optimal conformational changes for maximal FRET signal. However, our ability to predict appropriate linker sequences based on the domain structures of a specific sensor is still quite limited. As a result, flexible linkers that contain small and polar amino acids, [e.g., $(GGSGG)_n$], are often used in the initial construction to permit independent movement of individual components of the sensor. However, linker length as well as composition can have a significant impact on sensor signal. During the development of the A-kinase activity reporter (AKAR), for example, linkers of 7, 14, and 19 amino acids were compared. The 14 amino acid linker (SAGKPGSGEGSTKG) gave the best dynamic range (Ni *et al*., 2006). Additionally, the optimized conformational change of the molecular switch in the sensor may require rigid linker regions with suitable secondary structures, like α-helix or β-turn.

The most commonly applied and successful strategy to improve the dynamic range of a sensor is by modifying the FRET fluorescent protein pair. Specifically, newer generations of fluorescent proteins with improved properties, especially improved brightness and spectral profiles, can be used to improve sensor signal. In such cases, new fluorescent proteins not only improve the signal to noise ratio

but more importantly increase the R_0 value of the FRET pair, therefore effectively improving the FRET efficiency. Another such modification takes advantage of circularly permuted variants of fluorescent proteins to alter the FRET efficiency by changing the relative orientation of the two chromophores' transition dipoles. In these proteins, the original N- and C-termini of the fluorescent protein are connected using a short spacer, and new N- and C-termini are created (Baird *et al.*, 1999). GFP has been successfully engineered by changing the protein termini through use of exposed loops outside of the protected chromophore barrel (Topell *et al.*, 1999). To date, many different FRET-based sensors have been improved using this particular strategy (Allen and Zhang, 2006; Allen *et al.*, 2006; Nagai *et al.*, 2004).

IV. A Case Study of PI3K/Akt Signaling Pathway

As emphasized throughout this chapter, FRET-based sensors are powerful tools for visualizing signaling molecules/events in real time and space. Here, we focus on the application of these molecular sensors to the study of an important signaling pathway, the PI3K/Akt pathway.

Activation of the PI3K/Akt pathway in response to a variety of extracellular signals impacts a number of cellular processes, including cell growth, survival, and proliferation. Briefly, ligand activated receptors in the plasma membrane lead to recruitment and activation of PI3K and subsequent production of PIP_3 and PI(3,4)P_2. Akt interacts with these newly formed phospholipids through its PH domain, resulting in translocation of the kinase to the plasma membrane. Following translocation, Akt is phosphorylated at positions T308 and S473 by PDK1 and PDK2, respectively, and becomes fully activated. The activated Akt then detaches from the plasma membrane and translocates to distinct subcellular compartments, including the nucleus, to regulate various downstream substrates, which include BCL-2-antagonst of cell death (Bad), glycogen synthase kinase (GSK), and members of the forkhead family of transcription factors. Phosphorylation of these substrates inhibits apoptosis and promotes cell growth. Not coincidentally, it has been shown that components of the PI3K/Akt signaling pathway are frequently altered in human cancers, making them attractive drug targets (Hennessy *et al.*, 2005).

To better understand the molecular mechanisms underlying the complex regulation of the PI3K/Akt pathway, a series of FRET-based molecular sensors have been developed (Ananthanarayanan *et al.*, 2005, 2007; Kunkel *et al.*, 2005). First, BKAR (Kunkel *et al.*, 2005), a B kinase activity reporter, was designed to monitor spatiotemporal dynamics of Akt signaling in live cells. BKAR consists of a monomeric CFP–YFP FRET pair, flanking an FHA2 phosphothreonine-binding domain and a consensus Akt phosphorylation substrate sequence, RKRDRLGTLGI, where the underlined T represents the phosphorylation site. Using BKAR in NIH3T3 cells revealed that Akt signaling in the cytosol was more rapid and transient compared with that in the nucleus, which suggests the

presence of differentially regulated phosphatase activities in these two compartments. Furthermore, targeting of BKAR to the plasma membrane, where Akt is activated, resulted in a more rapid and sustained response compared with that in the cytosol, indicating that release of Akt or its substrates from the membrane is required for desensitization of Akt signaling.

Since Akt is recruited to the plasma membrane by phospholipids produced by PI3K, InPAkt (Ananthanarayanan *et al.*, 2005) was employed to investigate the spatiotemporal correlation between phospholipids dynamics and Akt signaling. Simultaneous imaging of plasma membrane targeted InPAkt and nuclear targeted BKAR revealed a gradual and sustained Akt signaling in the nucleus and a rapid and transient production of PIP_3 and $PI(3,4)P_2$ at the plasma membrane in the same cell, consistent with the hypothesis that signal propagation from membrane messengers to nuclear effectors is regulated by kinases as well as lipid and protein phosphatases (Ananthanarayanan *et al.*, 2005).

Although the Akt activation mechanism has been studied in much detail, several important steps in this process, including the mechanism by which active Akt detaches from the plasma membrane, remain to be elucidated. Membrane dissociation of active Akt enables it to gain access to various substrates in different subcellular compartments. Interestingly, results from simultaneous imaging of plasma membrane-targeted InPAkt and nuclear-targeted BKAR showed that nuclear Akt activity starts to accumulate while there are still high levels of PIP_3 and $PI(3,4)P_2$ at the plasma membrane (Ananthanarayanan *et al.*, 2005), demonstrating that active Akt can dissociate from the plasma membrane despite the presence of PIP_3 and $PI(3,4)P_2$. Therefore, it is hypothesized that conformational changes in the Akt during its activation alter its association with membrane phospholipids. To test this hypothesis, ReAktion was created by sandwiching full-length Akt between a CFP and YFP FRET pair to monitor the conformational changes within Akt as well as membrane translocation (Ananthanarayanan *et al.*, 2007). Furthermore, constructs with mutations in the two critical phosphorylation sites, namely T308 and S473, as well as plasma membrane-targeted constructs were also generated to help dissect the conformational changes and translocation events during the Akt activation process. In live cells, ReAktion reveals a conformational change in Akt that depends critically on the existence of a phosphorylatable T308 in the activation loop, as mutations of the Thr to either Asp or Ala abolished the change. Furthermore, the T308D mutant, a phosphorylation mimetic, showed diminished membrane association, which suggests that T308 phosphorylation is important in promoting the dissociation of active Akt from the plasma membrane. In addition, the PH domain of Akt was found to associate with the catalytic domain of Akt upon T308 phosphorylation, indicating that interdomain interactions mediated by phosphorylation affect membrane association.

Taken together, these studies demonstrate that FRET-based molecular sensors are useful not only in revealing spatiotemporal information of signaling events but also in uncovering the molecular mechanisms underlying signaling pathways in their native context.

V. Discussion and Conclusion

The genetically encoded molecular sensors for signaling dynamics discussed in this chapter offer precise molecular targeting, versatile construction, as well as unmatched spatiotemporal resolution in live cells. In addition to single cells, the very same advantages can be extended to more complex living systems such as tissues (Dunn *et al.*, 2006; Gervasi *et al.*, 2007) and even whole organisms.

On the other hand, the modular designs utilized in these molecular sensors can be readily extended to many other signaling molecules and events, making the development of new sensors relatively simple. These sensors also offer a unique opportunity to dissect the complex molecular mechanisms underlying the dynamic interplay and cross talk between various signaling molecules and pathways in their native context at the single cell level. Toward this goal, sensors with orthogonal fluorimetric properties or compatible alternative readouts (Zhang *et al.*, 2007) are extremely useful for simultaneous imaging of multiple signaling events in the same cellular context. Furthermore, these molecular sensors can provide robust ratiometric readout in high-throughput assays (Allen *et al.*, 2006) and should find increasing application in live-cell-based pharmacological profiling and high-throughput screening. In conclusion, molecular sensors that are capable of providing spatiotemporal information of various cellular signaling events are invaluable tools for researchers in many fields of biological science, and their ever expanding applications will undoubtedly help advance our understanding of the highly dynamic signal transduction network underlying the complex phenomenon of cellular life.

Acknowledgments

Work of the authors was supported by the National Institutes of Health (DK073368 and CA122673 to J. Z.), a Scientist Development Award from the American Heart Association (to J. Z.), a Young Clinical Scientist Award from Flight Attendant Medical Institute (to J. Z.), 3M (to J. Z.), and the W.M. Keck Center (to J. Z. and B. A.).

References

Allen, M. D., DiPilato, L. M., Rahdar, M., Ren, Y. R., Chong, C., Liu, J. O., and Zhang, J. (2006). Reading dynamic kinase activity in living cells for high-throughput screening. *ACS Chem. Biol.* **1,** 371–376.

Allen, M. D., and Zhang, J. (2006). Subcellular dynamics of protein kinase A activity visualized by FRET-based reporters. *Biochem. Biophys. Res. Commun.* **348,** 716–721.

Allen, M. D., and Zhang, J. (2008). A tunable FRET circuit for engineering fluorescent biosensors. *Angew. Chem. Int. Ed Engl.* **47,** 500–502.

Ananthanarayanan, B., Fosbrink, M., Rahdar, M., and Zhang, J. (2007). Live-cell molecular analysis of Akt activation reveals roles for activation loop phosphorylation. *J. Biol. Chem.* **282,** 36634–36641.

Ananthanarayanan, B., Ni, Q., and Zhang, J. (2005). Signal propagation from membrane messengers to nuclear effectors revealed by reporters of phosphoinositide dynamics and Akt activity. *Proc. Natl. Acad. Sci. USA* **102,** 15081–15086.

Azpiazu, I., and Gautam, N. (2004). A fluorescence resonance energy transfer-based sensor indicates that receptor access to a G protein is unrestricted in a living mammalian cell. *J. Biol. Chem.* **279,** 27709–27718.

Baird, G. S., Zacharias, D. A., and Tsien, R. Y. (1999). Circular permutation and receptor insertion within green fluorescent proteins. *Proc. Natl. Acad. Sci. USA* **96,** 11241–11246.

Baird, G. S., Zacharias, D. A., and Tsien, R. Y. (2000). Biochemistry, mutagenesis, and oligomerization of dsRed, a red fluorescent protein from coral. *Proc. Natl. Acad. Sci. USA* **97,** 11984–11989.

Campbell, R. E., Tour, O., Palmer, A. E., Steinbach, P. A., Baird, G. S., Zacharias, D. A., and Tsien, R. Y. (2002). A monomeric red fluorescent protein. *Proc. Natl. Acad. Sci. USA* **99,** 7877–7882.

Clegg, R. M. (1992). Fluorescence resonance energy transfer and nucleic acids. *Methods Enzymol.* **211,** 353–388.

DiPilato, L. M., Cheng, X., and Zhang, J. (2004). Fluorescent indicators of cAMP and Epac activation reveal differential dynamics of cAMP signaling within discrete subcellular compartments. *Proc. Natl. Acad. Sci. USA* **101,** 16513–16518.

dos Remedios, C. G., and Moens, P. D. (1995). Fluorescence resonance energy transfer spectroscopy is a reliable "ruler" for measuring structural changes in proteins. Dispelling the problem of the unknown orientation factor. *J. Struct. Biol.* **115,** 175–185.

Dunn, T. A., Wang, C. T., Colicos, M. A., Zaccolo, M., DiPilato, L. M., Zhang, J., Tsien, R. Y., and Feller, M. B. (2006). Imaging of cAMP levels and protein kinase A activity reveals that retinal waves drive oscillations in second-messenger cascades. *J. Neurosci.* **26,** 12807–12815.

Galperin, E., Verkhusha, V. V., and Sorkin, A. (2004). Three-chromophore FRET microscopy to analyze multiprotein interactions in living cells. *Nat. Methods* **1,** 209–217.

Gervasi, N., Hepp, R., Tricoire, L., Zhang, J., Lambolez, B., Paupardin-Tritsch, D., and Vincent, P. (2007). Dynamics of protein kinase A signaling at the membrane, in the cytosol, and in the nucleus of neurons in mouse brain slices. *J. Neurosci.* **27,** 2744–2750.

Goedhart, J., Vermeer, J. E., Adjobo-Hermans, M. J., van Weeren, L., and Gadella, T. W. (2007). Sensitive detection of p65 homodimers using red-shifted and fluorescent protein-based FRET couples. *PLoS ONE* **2,** e1011.

Heim, R., and Tsien, R. Y. (1996). Engineering green fluorescent protein for improved brightness, longer wavelengths and fluorescence energy transfer. *Curr. Biol.* **6,** 178–182.

Hennessy, B. T., Smith, D. L., Ram, P. T., Lu, Y., and Mills, G. B. (2005). Exploiting the PI3K/AKT pathway for cancer drug discovery. *Nat. Rev. Drug Discov.* **4,** 988–1004.

Janetopoulos, C., Jin, T., and Devreotes, P. (2001). Receptor-mediated activation of heterotrimeric G proteins in living cells. *Science* **291,** 2408–2411.

Johnson, S. A., You, Z., and Hunter, T. (2007). Monitoring ATM kinase activity in living cells. *DNA Repair (Amst)* **6,** 1277–1284.

Kunkel, M. T., Ni, Q., Tsien, R. Y., Zhang, J., and Newton, A. C. (2005). Spatio-temporal dynamics of protein kinase B/Akt signaling revealed by a genetically encoded fluorescent reporter. *J. Biol. Chem.* **280,** 5581–5587.

Kunkel, M. T., Toker, A., Tsien, R. Y., and Newton, A. C. (2007). Calcium-dependent regulation of protein kinase D revealed by a genetically encoded kinase activity reporter. *J. Biol. Chem.* **282,** 6733–6742.

Matz, M. V., Fradkov, A. F., Labas, Y. A., Savitsky, A. P., Zaraisky, A. G., Markelov, M. L., and Lukyanov, S. A. (1999). Fluorescent proteins from nonbioluminescent *Anthozoa* species. *Nat. Biotechnol.* **17,** 969–973.

Mitra, R. D., Silva, C. M., and Youvan, D. C. (1996). Fluorescence resonance energy transfer between blue-emitting and red-shifted excitation derivatives of the green fluorescent protein. *Gene* **173,** 13–17.

Miyawaki, A. (2003). Visualization of the spatial and temporal dynamics of intracellular signaling. *Dev. Cell* **4,** 295–305.

Miyawaki, A., Llopis, J., Heim, R., McCaffery, J. M., Adams, J. A., Ikura, M., and Tsien, R. Y. (1997). Fluorescent indicators for Ca^{2+} based on green fluorescent proteins and calmodulin. *Nature* **388,** 882–887.

Nagai, T., Yamada, S., Tominaga, T., Ichikawa, M., and Miyawaki, A. (2004). Expanded dynamic range of fluorescent indicators for Ca(2+) by circularly permuted yellow fluorescent proteins. *Proc. Natl. Acad. Sci. USA* **101,** 10554–10559.

Neininger, A., Thielemann, H., and Gaestel, M. (2001). FRET-based detection of different conformations of MK2. *EMBO Rep.* **2,** 703–708.

Nguyen, A. W., and Daugherty, P. S. (2005). Evolutionary optimization of fluorescent proteins for intracellular FRET. *Nat. Biotechnol.* **23,** 355–360.

Ni, Q., Titov, D. V., and Zhang, J. (2006). Analyzing protein kinase dynamics in living cells with FRET reporters. *Methods* **40,** 279–286.

Ohashi, T., Galiacy, S. D., Briscoe, G., and Erickson, H. P. (2007). An experimental study of GFP-based FRET, with application to intrinsically unstructured proteins. *Protein Sci.* **16,** 1429–1438.

Piston, D. W., and Kremers, G. J. (2007). Fluorescent protein FRET: The good, the bad and the ugly. *Trends Biochem. Sci.* **32,** 407–414.

Prasher, D. C., Eckenrode, V. K., Ward, W. W., Prendergast, F. G., and Cormier, M. J. (1992). Primary structure of the *Aequorea victoria* green-fluorescent protein. *Gene* **111,** 229–233.

Ramanoudjame, G., Du, M., Mankiewicz, K. A., and Jayaraman, V. (2006). Allosteric mechanism in AMPA receptors: A FRET-based investigation of conformational changes. *Proc. Natl. Acad. Sci. USA* **103,** 10473–10478.

Rizzo, M. A., Springer, G., Segawa, K., Zipfel, W. R., and Piston, D. W. (2006). Optimization of pairings and detection conditions for measurement of FRET between cyan and yellow fluorescent proteins. *Microsc. Microanal.* **12,** 238–254.

Sapsford, K. E., Berti, L., and Medintz, I. L. (2006). Materials for fluorescence resonance energy transfer analysis: Beyond traditional donor-acceptor combinations. *Angew. Chem. Int. Ed Engl.* **45,** 4562–4589.

Sasaki, K., Sato, M., and Umezawa, Y. (2003). Fluorescent indicators for Akt/protein kinase B and dynamics of Akt activity visualized in living cells. *J. Biol. Chem.* **278,** 30945–30951.

Sato, M., Kawai, Y., and Umezawa, Y. (2007). Genetically encoded fluorescent indicators to visualize protein phosphorylation by extracellular signal-regulated kinase in single living cells. *Anal. Chem.* **79,** 2570–2575.

Sato, M., Ozawa, T., Inukai, K., Asano, T., and Umezawa, Y. (2002). Fluorescent indicators for imaging protein phosphorylation in single living cells. *Nat. Biotechnol.* **20,** 287–294.

Shaner, N. C., Campbell, R. E., Steinbach, P. A., Giepmans, B. N., Palmer, A. E., and Tsien, R. Y. (2004). Improved monomeric red, orange and yellow fluorescent proteins derived from Discosoma sp. red fluorescent protein. *Nat. Biotechnol.* **22,** 1567–1572.

Shaner, N. C., Steinbach, P. A., and Tsien, R. Y. (2005). A guide to choosing fluorescent proteins. *Nat. Methods* **2,** 905–909.

Shanker, N., and Bane, S. L. (2008). Basic aspects of absorption and fluorescence spectroscopy and resonance energy transfer methods. *Methods Cell Biol.* **84,** 213–242.

Shimomura, O., Johnson, F. H., and Saiga, Y. (1962). Extraction, purification and properties of aequorin, a bioluminescent protein from the luminous hydromedusan, *Aequorea*. *J. Cell. Comp. Physiol.* **59,** 223–239.

Stryer, L. (1978). Fluorescence energy transfer as a spectroscopic ruler. *Annu. Rev. Biochem.* **47,** 819–846.

Ting, A. Y., Kain, K. H., Klemke, R. L., and Tsien, R. Y. (2001). Genetically encoded fluorescent reporters of protein tyrosine kinase activities in living cells. *Proc. Natl. Acad. Sci. USA* **98,** 15003–15008.

Topell, S., Hennecke, J., and Glockshuber, R. (1999). Circularly permuted variants of the green fluorescent protein. *FEBS Lett.* **457,** 283–289.

Tsien, R. Y. (1998). The green fluorescent protein. *Annu. Rev. Biochem.* **67,** 509–544.

Violin, J. D., DiPilato, L. M., Elston, T. C., Yildrim, N., Zhang, J., and Lefkowitz, R. J. (2008). β2-Adrenergic Receptor Signaling and Desensitization Elucidated by Quantitative Modeling of Real-Time cAMP Dynamics. *J. Biol. Chem.* **283,** 2949–2961.

Violin, J. D., Zhang, J., Tsien, R. Y., and Newton, A. C. (2003). A genetically encoded fluorescent reporter reveals oscillatory phosphorylation by protein kinase C. *J. Cell Biol.* **161,** 899–909.

Wang, Y., Botvinick, E. L., Zhao, Y., Berns, M. W., Usami, S., Tsien, R. Y., and Chien, S. (2005). Visualizing the mechanical activation of Src. *Nature* **434,** 1040–1045.

Zaccolo, M., De Giorgi, F., Cho, C. Y., Feng, L., Knapp, T., Negulescu, P. A., Taylor, S. S., Tsien, R. Y., and Pozzan, T. (2000). A genetically encoded, fluorescent indicator for cyclic AMP in living cells. *Nat. Cell Biol.* **2,** 25–29.

Zacharias, D. A., Violin, J. D., Newton, A. C., and Tsien, R. Y. (2002). Partitioning of lipid-modified monomeric GFPs into membrane microdomains of live cells. *Science* **296,** 913–916.

Zapata-Hommer, O., and Griesbeck, O. (2003). Efficiently folding and circularly permuted variants of the Sapphire mutant of GFP. *BMC Biotechnol.* **3,** 5.

Zhang, J., and Allen, M. D. (2007). FRET-based biosensors for protein kinases: Illuminating the kinome. *Mol. Biosyst*. **3,** 759–765.

Zhang, J., Hupfeld, C. J., Taylor, S. S., Olefsky, J. M., and Tsien, R. Y. (2005). Insulin disrupts beta-adrenergic signalling to protein kinase A in adipocytes. *Nature* **437,** 569–573.

Zhang, J., Ma, Y., Taylor, S. S., and Tsien, R. Y. (2001). Genetically encoded reporters of protein kinase A activity reveal impact of substrate tethering. *Proc. Natl. Acad. Sci. USA* **98,** 14997–15002.

Zhang, L., Lee, K. C., Bhojani, M. S., Khan, A. P., Shilman, A., Holland, E. C., Ross, B. D., and Rehemtulla, A. (2007). Molecular imaging of Akt kinase activity. *Nat. Med.* **13,** 1114–1119.

CHAPTER 3

A Fluorescent Window Into Protein Folding and Aggregation in Cells

Zoya Ignatova[⋆] and Lila M. Gierasch[†,‡]

[⋆]Department of Biochemistry
Institute of Biology and Biochemistry
University of Potsdam
14476 Potsdam-Golm, Germany

[†]Department of Biochemistry and Molecular Biology
University of Massachusetts, Amherst
Amherst, Massachusetts 01003

[‡]Department of Chemistry
University of Massachusetts, Amherst
Amherst, Massachusetts 01003

Abstract

Evolutionary selective pressures have tuned the efficiency of the protein-folding reaction in the crowded complex environment in the cell. Nevertheless, the fidelity of folding is imperfect, leading to off-pathway intermolecular interactions that compete with proper folding and to consequent formation of thermodynamically stable aggregates. Such aggregates constitute the histopathological hallmarks of many neurodegenerative pathologies. Yet, most of the approaches to characterize

METHODS IN CELL BIOLOGY, VOL. 89

0091-679X/08 $35.00
DOI: 10.1016/S0091-679X(08)00603-1

protein folding and/or misfolding are limited to *in vitro* conditions. Here, we describe a strategy to directly monitor the behavior of a protein in prokaryotic and eukaryotic cells. The method is based on incorporation of structurally non-perturbing, specific binding motifs for a *bis*-arsenical fluoroscein dye, FlAsH, in sites that result in distinct dye fluorescence signals for the folded and unfolded states of the protein under study. Our approach has been developed using as a case study the predominantly β-sheet intracellular lipid-binding protein, cellular retinoic acid-binding protein, alone or as a chimera fused to the exon 1-encoded fragment of huntingtin, which harbors a polyglutamine repeat tract. We have designed protocols to label this protein *in vivo* and to monitor the resulting fluorescence signal, which reports on any misfolding transition and formation of aggregates, yielding quantitatively interpretable data.

I. Introduction

Protein-folding pathways are remarkably complex, and the fidelity of the folding process has been optimized in the highly heterogeneous and crowded cellular environment. Intramolecular factors (e.g., mutations) and/or environmental stresses present additional challenges to the folding landscape and can drastically alter the fidelity of folding. As a result, alternative nonnative, partially folded states can be populated, leading to off-pathway intermolecular interactions. Despite the evolutionarily optimized mechanisms to avoid enrichment of misfolded species, some fraction of misfolded proteins can escape the cellular quality control mechanisms and form thermodynamically stable aggregates. Notably, failure in protein folding and the consequent deposition of metabolically stable aggregates constitute histopathological hallmarks of several neurodegenerative pathologies, including Alzheimer's, Huntington's, and Parkinson's diseases. Cellular protein misfolding also has implications in the research laboratory and biotechnology industry: Off-pathway aggregation limits the yield of recombinant proteins.

Technical challenges make the goal of monitoring protein folding and misfolding in cells extremely difficult; the protein of interest has to be specifically highlighted to allow observation at physiological concentrations in the background of all other cellular constituents. Ideally the approach should provide information on structure formation, and the signal should report on conformational states visited by the target protein. Few groups have interrogated the conformational states a protein can sample *in vivo*. Thomas and coworkers (Wigley *et al.*, 2001) devised a structural complementation assay with a direct read-out to monitor the formation of the soluble native structure. Similar approaches using structural complementation of a reporter protein provide an easily detectable phenotypic selection for mutants with improved folding efficiency *in vivo* (Maxwell *et al.*, 1999; Philipps *et al.*, 2003). However, these approaches are restricted to monitoring the end stage of the folding process and cannot readily be used to track various conformational explorations of a protein *in vivo*.

II. Rationale

Here we describe a fluorescence-based approach that we have recently developed to determine protein stability *in vivo* (in *Escherichia coli* cells) and *in vitro* (Ignatova and Gierasch, 2004) and that may be used to monitor *in vivo* folding propensities and aggregation kinetics in real time and in a noninvasive manner. The protein of interest is visualized in the context of all cellular macromolecules using the membrane-permeable *bis*-arsenical fluorescein-based dye "FlAsH" (named originally as a "fluorescein arsenical helix" binder), which specifically ligates to a genetically engineered, highly uncommon tetracysteine motif (Cys-Cys-Xxx-Yyy-Cys-Cys) (Griffin *et al.*, 2000). In addition to its utility in measuring the bulk fluorescence of a population of cells for overall folding data and real-time aggregation assays, the FlAsH-labeling strategy has been very useful for fluorescence microscopy imaging of the state of the expressed protein and in-cell aggregates. We have combined this approach with isolation and electron microscopy of aggregates to garner information about the nature of the aggregates (Ignatova and Gierasch, 2005) and the mechanism of aggregation (Ignatova *et al.*, 2007b). We have also extended our published work using *E. coli* cells and have developed methods to observe protein aggregation in eukaryotic cells. We describe these protocols here as well.

III. Methods

A. Design of the Tetra-Cys Protein Fluorescence Reporter System

We integrated the tetracysteine sequence (here Cys-Cys-Gly-Pro-Cys-Cys, incorporating the native Gly-Pro present in this loop) into an internal Ω-loop of the 136-amino acid cellular retinoic acid-binding protein I (referred to here as CRABP) (Ignatova and Gierasch, 2004). The Ω-loop shows the lowest sequence conservation among the intracellular lipid-binding protein family (Gunasekaran *et al.*, 2004) and tolerates sequence expansions and deletions (Ignatova and Gierasch, 2004). By this intramolecular insertion of the FlAsH-binding motif, we found that the FlAsH-fluorescence emission signal reports on the conformational state of the protein, with misfolded, denatured, and aggregated states hyperfluorescent compared to the native state (Ignatova and Gierasch, 2004). This system allowed us to measure *in vivo* stability using a urea titration (Ignatova and Gierasch, 2004; Ignatova *et al.*, 2007a). Mutation of the helix-terminating residue Pro39 to Ala is known to slow down the folding and unfolding of CRABP (Eyles and Gierasch, 2000), and P39A tetra-Cys CRABP shows a high tendency to form inclusion bodies *in vivo* (Ignatova and Gierasch, 2004) and aggregates *in vitro* (Ignatova and Gierasch, 2005). The structural integrity and alterations in the native structure of the host protein after the insertion of the tetra-Cys motif must be verified by different methods, for example, circular dichroism spectroscopy (CD), fluorescence, or activity. In their native states, both tetra-Cys CRABP

and the aggregation-prone P39A tetra-Cys CRABP variants are indistinguishable in structure and function from their native counterparts, whether FlAsH-labeled or unlabeled, based on far-UV CD or on ligand-binding (here, retinoic acid-binding) activity (Ignatova and Gierasch, 2004).

The FlAsH-labeled tetra-Cys CRABP protein was also useful as a reporter in chimeras in order to assess the impact of other domains, for example the exon 1-encoded fragment of huntingtin (Htt) (Ignatova and Gierasch, 2006), the protein that aggregates in Huntington's disease (Ross and Poirier, 2004). This chimera yielded insight into the aggregation mechanism of Htt domains and their flanking regions (Ignatova *et al.*, 2007b).

1. FlAsH Labeling in *E. coli* Cells

Step 1: The FlAsH-binding motif is engineered in the soluble pseudo-wild-type CRABP [carrying an N-terminal His-tag and harboring a stabilizing Arg→Gln mutation at position 131 (Zhang *et al.*, 1992)] and in the slow-folding and aggregation-prone P39A CRABP mutant in three successive mutational steps using the oligonucleotide-directed QuikChange mutagenesis protocol (Stratagene) (Ignatova and Gierasch, 2004). cDNAs encoding tetra-Cys CRABP and P39A tetra-Cys CRABP are cloned in a multi-copy pET16b (Amp^R) plasmid; transcription is under the control of the T7 promoter. *E. coli* BL21(DE3) cells, carrying the DE3 lysogen for high level expression of T7 polymerase, were used as a host. The Htt constructs (tetra-Cys CRABP Htt20, tetra-Cys CRABP Htt40, and tetra-Cys Htt53) are constructed by C-terminal in-frame fusion of the full-length exon 1 of Huntingtin, encoding polyQ tracts of 20, 40, or 53 residues, to the tetra-Cys CRABP. The genetic manipulations led to insertion of two new amino acids (Leu-Glu) at the junction between the C-terminus of tetra-Cys CRABP and the beginning of the exon 1-encoded fragment of Htt (Ignatova and Gierasch, 2006).

Step 2: A single colony from freshly transformed cells is inoculated in LB medium containing 100 μg/ml ampicillin and grown overnight at 30 °C by constant shaking at 200 rpm. The cultured cells are sterile-harvested (2060 × *g*, 15 min, 4 °C) and brought up to 25× the original volume in fresh LB medium containing 100 μg/ml ampicillin. The cultures are grown at 37 °C until the $OD_{600} = 0.5$ and then treated with lysozyme (50 ng/ml) for 10 min on ice. This gentle lysozyme pretreatment enhances the permeability of the outer membrane of the bacterial host cell for FlAsH (Fig. 1A) and enables preloading with FlAsH at a rate and concentration sufficient to saturate newly expressed tetra-Cys protein (Ignatova and Gierasch, 2004).

Step 3: The lysozyme-containing medium is removed by centrifugation (2060 × *g*, 15 min, 4 °C), and the cell pellet is resuspended in the same amount of fresh sterile LB medium containing 100 μg/ml ampicillin. Aliquots of 1 ml are labeled with 0.2 μM FlAsH–EDT_2 (marketed by Invitrogen under the name Lumio Green™) and 1 μM ethanedithiol (EDT). FlAsH and EDT remain in the

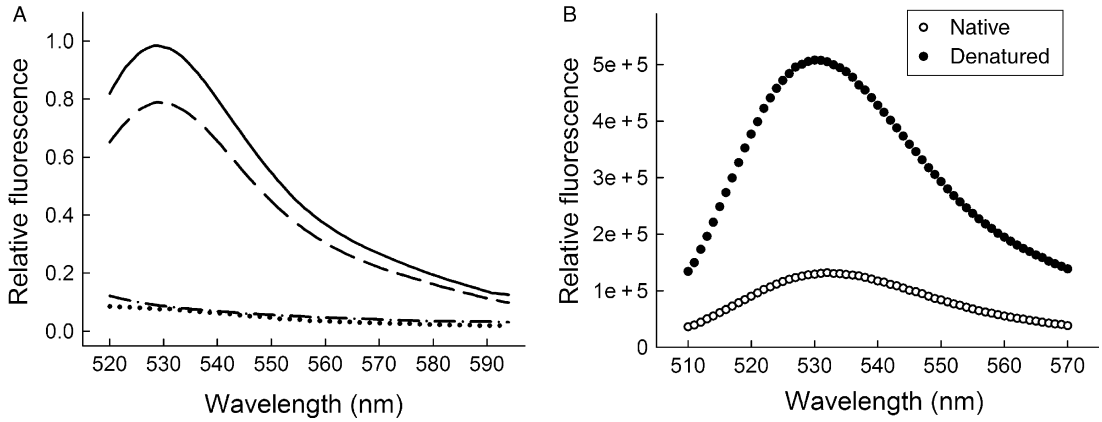

Fig. 1 FlAsH labeling in *E. coli* cells and *in vitro*. (A) FlAsH labeling of *E. coli* cells expressing tetra-Cys CRABP (dashed line) and P39A tetra-Cys CRABP (solid line). Note that cells expressing wild-type CRABP without the tetra-Cys motif do not fluoresce (dotted line). For comparison, the intrinsic fluorescence of non-labeled cells expressing tetra-Cys CRABP is shown (dash–dot lines). (B) Fluorescence of FlAsH-labeled purified tetra-Cys CRABP in its native and denatured states. Reproduced from Ignatova and Gierasch (2004).

medium during the entire time of culture growth. An excess of EDT suppresses the labeling of endogenous cysteines on other proteins (Griffin *et al.*, 2000).

Usually the dye is preloaded one generation before the induction of protein synthesis with IPTG to circumvent limitations from slow dye entry into the cells and to ensure that ample dye is available upon induction. In addition, excess dye is also present in the nutrient medium throughout the induction period and continues to enter the cells. Dye preloading is a prerequisite to application of labeling to kinetic experiments or to monitor folding and misfolding/aggregation reactions. For some studies of equilibrium processes in the cell (e.g., localization), lysozyme pretreatment and FlAsH preloading before the induction of biosynthesis are not necessary. FlAsH enters *E. coli* cells, albeit more slowly without the pretreatment, and the dye accumulated in the cells throughout the expression cycle will be sufficient to quantitatively label the entire amount of the expressed protein.

Step 4: Cells are further cultured in the dark by constant shaking at 200 rpm. After one generation at 37 °C, at $OD_{600} = 1.0$, protein synthesis is induced by adding 0.4 mM IPTG.

2. Monitoring Protein Aggregation: Bulk Cell Fluorescence

Over the time course of aggregation, 150-μl aliquots are withdrawn from the growing culture and subjected to fluorescence measurements in bulk at 530 nm (excitation 500 nm; excitation bandwidth 2 nm, emission bandwidth 3 nm). Fluorescence of cells transformed with a plasmid bearing the wild-type CRABP without the tetra-Cys motif and labeled with FlAsH is used as a blank, and the value is

subtracted from each point. The temperature of the cuvette holder is maintained at 37 °C with a water bath.

The intensity of fluorescence from the FlAsH-labeled P39A tetra-Cys CRABP cells is higher than that of tetra-Cys CRABP-expressing cells (Fig. 1A), and this higher quantum yield is due to the partial deposition of P39A tetra-Cys CRABP into hyperfluorescent inclusion bodies (Ignatova and Gierasch, 2004, 2005). The quantum yield and spectral properties of the aggregates are reminiscent of the hyperfluorescent denatured state of purified FlAsH-labeled tetra-Cys CRABP protein (Fig. 1B). The time course of bulk fluorescence of FlAsH-labeled P39A tetra-Cys CRABP in cells differs from that of cells expressing soluble tetra-Cys CRABP (Fig. 2A). The steady-state increase in the FlAsH fluorescence of tetra-Cys CRABP reports the synthesis of this protein and plateaus when *de novo* synthesis ceases and the cells enter stationary phase. The fluorescence curve of the aggregation-prone P39A tetra-Cys CRABP is a cumulative signal of both synthesis and aggregate formation, and the sharp rise in the fluorescent signal between 120 and 150 min reports the enrichment of misfolded and aggregated species.

The use of tetra-Cys CRABP as a reporter in chimeras to assess their aggregation propensity is illustrated by fusions of tetra-Cys CRABP with Htt exon

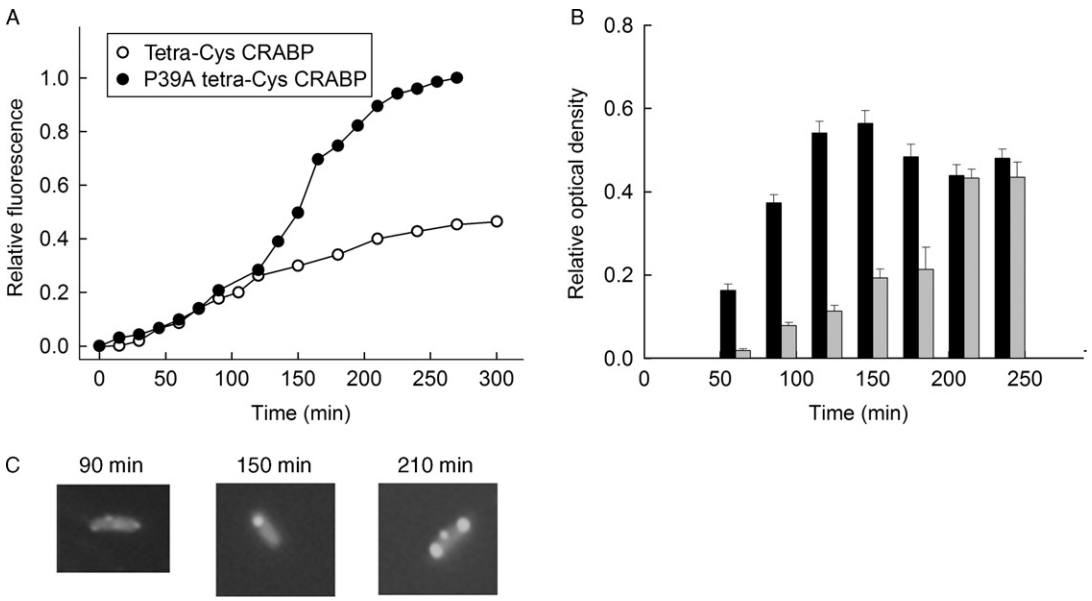

Fig. 2 Soluble and aggregation-prone variants of CRABP show different patterns of bulk FlAsH fluorescence. (A) Time evolution of the expression and aggregation of P39A tetra-Cys CRABP (filled symbols) and the expression of tetra-Cys CRABP (open symbols), monitored by fluorescence at 530 nm (excitation 500 nm). (B) Partitioning of P39A tetra-Cys CRABP protein between soluble (black bars) and insoluble (light gray bars) cytoplasmic fractions. (C) Examples of fluorescence microscopic images of the P39A tetra-Cys CRABP-expressing cells, taken at the indicated times after induction of protein synthesis with IPTG. Parts of the figure are reproduced from Ignatova and Gierasch (2004).

1-encoded domains containing polyQ repeats of varying length (Ignatova and Gierasch, 2006; Ignatova *et al.*, 2007b). Those with shorter polyQ repeats ($Q = 20$) (i.e., in the non-pathological range) show a fluorescence pattern (Fig. 3A) superimposable on that of tetra-Cys CRABP (Fig. 2A). Increasing the polyQ length beyond the threshold length of 35 consecutive glutamines characteristic of polyQ diseases (Ross and Poirier, 2004; Zoghbi and Orr, 2000) causes an increase in the bulk-fluorescence signal, and reduces the time for onset of the rise in fluorescence. Furthermore, the plateau fluorescence increases in proportion to length of the polyQ tract (Fig. 3A). The sharp increase in the FlAsH fluorescence of the bulk cell suspension expressing the tetra-Cys CRABP Htt53 chimera suggests that the aggregation is favored as soon as expression of protein commences.

3. Monitoring Protein Aggregation: Fractionation of *E. coli* Cells

Step 1:E. coli BL21(DE3) cells are transformed with either tetra-Cys CRABP or P39A tetra-Cys CRABP, and their expression is induced by adding 0.4 mM IPTG. Ten-milliliter aliquots are withdrawn at different time points after induction, and bacteria are harvested by centrifugation at $2060 \times g$ for 15 min at 4 °C.

Step 2: The cell pellet is resuspended in 1.5 ml of 50 mM phosphate buffer (pH 8) containing 300 mM NaCl. Cells are treated with lysozyme (at a final concentration of 500 μg/ml for 30 min) and DNAse (at a final concentration of 50 μg/ml for 15 min) followed by sonication with 20-s bursts for 3 min (30% duty cycle), all steps on ice. Cell lysates are fractionated into soluble and insoluble fractions by centrifugation at $27000 \times g$ at 5 °C in a tabletop centrifuge for 30 min.

Step 3: The insoluble pellet fraction is resuspended in 1.5 ml of 10 mM Tris–HCl buffer (pH 8) containing 8 M urea. In the case of tetra-Cys Htt chimeras, the insoluble fraction is resuspended in 1.5 ml of 50 mM phosphate buffer (pH 8) containing 8 M urea and 2% SDS and then centrifuged again at $15294 \times g$ at 5 °C in a tabletop centrifuge for 30 min. The detergent-insoluble fraction is solubilized in 100% formic acid for 3 h at 37 °C (Hazeki *et al.*, 2000). Twenty-microliter aliquots of each fraction, mixed with 10 μl 3× SDS-loading buffer and preheated for 3 min at 95 °C, are loaded onto an SDS-PAGE gel (12%), and the tetra-Cys CRABP content in each fraction is quantified by optical densitometry of the Coomassie-stained SDS gel, on which known amounts of purified tetra-Cys CRABP are electrophoresed for comparison.

Fractionation of the cell lysates of P39A tetra-Cys CRABP-expressing cells into soluble and insoluble components confirms that the increase in bulk fluorescence reports on the enrichment of insoluble protein in the cells (Fig. 2B). At t 120 min, both tetra-Cys CRABP and P39A tetra-Cys CRABP are expressed as native proteins in comparable quantity. Subsequently, the slow-folding P39A tetra-Cys CRABP shows a rapidly increasing fluorescence intensity, which corresponds to a growing quantity of partially folded states. When the population of the partially folded intermediates reaches a critical threshold, formation of inclusion bodies ensues (Fig. 2C).

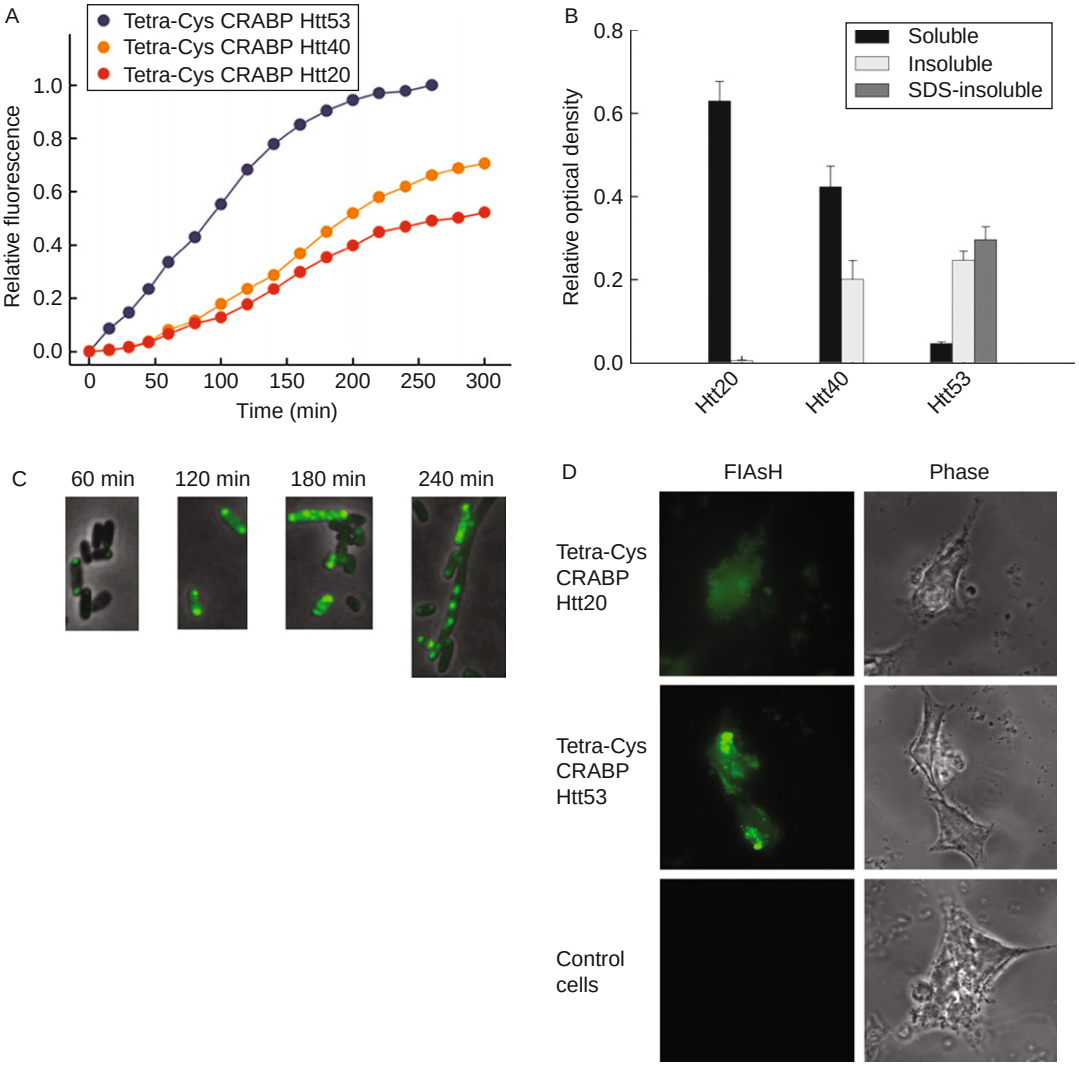

Fig. 3 Chimeras of tetra-Cys CRABP and the exon 1-encoded portion of Htt show polyQ-length-dependent aggregation. (A) Time course of bulk fluorescence (at 530 nm; excitation 500 nm) of FlAsH-labeled *E. coli* cells expressing tetra-Cys CRABP Htt20 (red), Htt40 (orange), and Htt53 (blue). (B) Partitioning of the chimeras between the soluble (black bars), detergent-labile insoluble (light gray bars), and SDS-resistant insoluble (dark gray bars) cytoplasmic fractions at the conclusion of the experiment shown in Fig. 2A (260 min after induction of the protein synthesis). (C) Tetra-Cys CRABP Htt53 chimera forms hyperfluorescent aggregates in the *E. coli* host, and the appearance of the SDS-resistant species coincides with the appearance of the filamentous phenotype of the *E. coli* cells. (D) Fluorescence microscopic images of FlAsH-labeled eukaryotic HEK293T cells transiently transfected with tetra-Cys CRABP Htt chimeras. Tetra-Cys CRABP Htt20 is soluble and yields uniformly distributed FlAsH fluorescence, whereas tetra-Cys CRABP Htt53 generates hyperfluorescent loci. Cells transfected with empty pcDNA3.1 vector serve as control. The localization of the tetra-Cys CRABP Htt chimeras is visualized as indicated (by FlAsH fluorescence or phase contrast). Parts of this figure are reproduced from Ignatova and Gierasch (2006).

In the set of the polyQ chimeras, the FlAsH-fluorescence intensity correlates with the partitioning of the chimeras between the soluble and insoluble fractions (Fig. 3A and B). The Q40 fusion protein is found equally distributed between the soluble and insoluble fractions, whereas the Q53 protein is almost entirely present in the insoluble fraction with near equal partitioning between the detergent-labile and SDS-resistant fractions. The Htt20 chimera remains soluble over the entire expression period (Fig. 3B).

4. Monitoring Protein Aggregation: Fluorescence Microscopy

During the time course of growth of the labeled cells expressing different proteins, 20-μl aliquots of cell suspension are withdrawn at intervals and concentrated twice by centrifugation [2655 $\times$ *g* for 3 min, resuspension in 10 μl of 50 mM Hepes buffer (pH 7.5)]. Two microliters of this concentrated suspension is immobilized in 1% agarose in LB, and the cells are imaged with a fluorescent microscope (Nikon Eclipse E600) with excitation at 485 nm and a 510-nm emission cutoff filter. The images are processed with the Openlabs software (Improvision, Lexington, MA).

The fluorescence microscopic images of individual *E. coli* cells (Figs. 2C and 3C) recapitulate the observations made by the FlAsH-fluorescence measurements in bulk and by the centrifugal fractionation studies. In the case of cells containing FlAsH-labeled P39A tetra-Cys CRABP, the fluorescence is initially diffuse throughout the cell, indicative of a soluble protein at early times post-induction. Subsequently, hyperfluorescent aggregates form at the poles of the cell (Fig. 2C), and their appearance coincides with the sharp increase in FlAsH fluorescence (Fig. 2A). The extremely high aggregation propensity of the tetra-Cys CRABP Htt53 chimera is confirmed by fluorescence microscopy; hyperfluorescent polarly localized loci appear at the earliest time points (Fig. 3C). At later time points (>180 min after induction) a fraction of the cells change their morphology into a filamentous phenotype, and this transition parallels the appearance of the detergent-resistant aggregates in the cytoplasm (Fig. 3C).

B. Aggregation Propensity in Eukaryotic Cells

1. Expression and FlAsH Labeling in Eukaryotic Cells

Step 1: For expression in mammalian cells, tetra-Cys CRABP Htt20 and tetra-Cys Htt53 fusions were sub-cloned into the pcDNA3.1 vector (Invitrogen). For transient transfections, 70% confluent human embryonic kidney (HEK) 293T cells are transfected with 20-μg plasmid DNA by electroporation. Transiently transfected cells are grown in 35-mm, 6-well plates for 24 h in 1-ml Dulbecco's modified Eagle's medium (Gibco/Invitrogen) supplemented with 10% fetal bovine serum and 100 U/ml penicillin at 37 °C in an atmosphere of 5% CO_2. Each well is supplied with a sterile polylysine precoated cover slip.

Step 2: The FlAsH labeling is performed as described (Gaietta *et al.*, 2002). Confluent cells, 24 h after transfection, are washed twice with phenol red-free and bovine-serum-free Dulbecco's modified Eagle's medium (D-MEM/F-12, Gibco/Invitrogen) and then incubated in D-MEM/F-12 supplemented with 1 μM FlAsH–EDT_2 and 10 μM EDT for 1 h at 37°C.

Step 3: Cells are fixed on cover slips with 4% formaldehyde (from paraformaldehyde) in phosphate-buffered saline for 30 min at room temperature. The coverslips are washed once for 5 min with relatively high concentrations of EDT (250 μM in PBS pH 7.2, Gibco/Invitrogen) to remove the nonspecifically bound FlAsH dye and twice with phosphate-buffered saline. Fixed samples are mounted in antifading solution (Invitrogen) and examined using a Leica inverted microscope equipped with a 63× oil objective. HEK 293T cells transfected with empty pcDNA3.1 vector, otherwise labeled and treated identically, serve as a negative control.

2. Monitoring Protein Aggregation in Eukaryotic Cells

The tetra-Cys CRABP Htt chimeras transiently expressed in HEK 293T cells (Fig. 3D) show the same phenotypes as observed in the *E. coli* expression system. The tetra-Cys CRABP Htt20 is diffusely distributed in the cytosol, indicative of soluble expression, and tetra-Cys CRABP Htt53 is localized in small hyperfluorescent aggregates that progressively fuse into one large inclusion body.

IV. Summary

We have exploited the specific labeling strategy introduced by Adams and Tsien and coworkers based on a *bis*-arsenical fluoroscein derivative "FlAsH" (Adams *et al.*, 2002; Gaietta *et al.*, 2002; Griffin *et al.*, 2000) to observe the folding and aggregation of a protein of interest in cells. By suitable incorporation of the FlAsH-binding tetra-Cys motif into an internal loop of a β-barrel intracellular lipid-binding protein, CRABP, we have been able to determine equilibrium stability in cells and to follow the time-course of aggregate formation by a slow-folding mutant and by a chimera containing a portion of Htt, including the polyglutamine-rich tract. The sensitivity of FlAsH fluorescence to conformational changes in the host CRABP protein converts it into an attractive reporter system to monitor misfolding and aggregation. The FlAsH-fluorescence time course measured in a bulk cell suspension upon induction of protein synthesis differs for soluble and aggregation-prone protein, and FlAsH intensity can be used as a read-out to monitor protein aggregation *in vivo* and *in vitro*. This general approach is amenable, as reported earlier, to quantitative determination of the size of the nucleus of an aggregating system *in vitro* (Ignatova and Gierasch, 2005) or to direct in-cell exploration of the impact of highly aggregation-prone sequences on the behavior of an otherwise stably folded protein when chimeras of the two are created

(Ignatova and Gierasch, 2006; Ignatova *et al.*, 2007b). This approach has equipped us with a tool to follow fundamental events of major biomedical importance for protein misfolding diseases directly in cells.

Our method may be applied more generally if appropriate care is taken in the design of the FlAsH-labeling site. The sensitivity of the FlAsH quantum yield to the conformational state of the protein of interest is the requisite precondition for the application of this approach to measure *in vivo* protein folding, stability, and aggregation propensity. We have carried out extensive studies of the relationship of the geometry of the tetra-Cys-binding sites to the FlAsH fluorescence (B. Krishnan and L. M. Gierasch, submitted). To apply this approach to other proteins, a careful structure-based design should be performed with consideration of all sequence-specific and structural constraints so that the incorporated tetra-Cys sequence would be tolerated within the protein of interest and the FlAsH quantum yield would be sensitive to the conformational states of the protein host.

Acknowledgments

The authors acknowledge support from the National Institutes of Health (grants GM027616 and a 2006 NIH Director's Pioneer Award to LMG), and DFG-project IG73/4-1 and the Heisenberg award IG73 1-1 (to ZI).

References

Adams, S. R., Campbell, R. E., Gross, L. A., Martin, B. R., Walkup, G. K., Yao, Y., Llopis, J., and Tsien, R. Y. (2002). New biarsenical ligands and tetracysteine motifs for protein labeling *in vitro* and *in vivo*: Synthesis and biological applications. *J. Am. Chem. Soc.* **124,** 6063–6076.

Eyles, S. J., and Gierasch, L. M. (2000). Multiple roles of prolyl residues in structure and folding. *J. Mol. Biol.* **301,** 737–747.

Gaietta, G., Deerinck, T. J., Adams, S. R., Bouwer, J., Tour, O., Laird, D. W., Sosinsky, G. E., Tsien, R. Y., and Ellisman, M. H. (2002). Multicolor and electron microscopic imaging of connexin trafficking. *Science* **296,** 503–507.

Griffin, B. A., Adams, S. R., Jones, J., and Tsien, R. Y. (2000). Fluorescent labeling of recombinant proteins in living cells with FlAsH. *Methods Enzymol.* **327,** 565–578.

Gunasekaran, K., Hagler, A. T., and Gierasch, L. M. (2004). Sequence and structural analysis of cellular retinoic acid-binding proteins reveals a network of conserved hydrophobic interactions. *Proteins* **54,** 179–194.

Hazeki, N., Tukamoto, T., Goto, J., and Kanazawa, I. (2000). Formic acid dissolves aggregates of an N-terminal huntingtin fragment containing an expanded polyglutamine tract: Applying to quantification of protein components of the aggregates. *Biochem. Biophys. Res. Commun.* **277,** 386–393.

Ignatova, Z., and Gierasch, L. M. (2004). Monitoring protein stability and aggregation *in vivo* by real-time fluorescent labeling. *Proc. Natl. Acad. Sci. USA* **101,** 523–528.

Ignatova, Z., and Gierasch, L. M. (2005). Aggregation of a slow-folding mutant of a β-clam protein proceeds through a monomeric nucleus. *Biochemistry* **44,** 7266–7274.

Ignatova, Z., and Gierasch, L. M. (2006). Extended polyglutamine tracts cause aggregation and structural perturbation of an adjacent beta barrel protein. *J. Biol. Chem.* **281,** 12959–12967.

Ignatova, Z., Krishnan, B., Bombardier, J. P., Marcelino, A. M., Hong, J., and Gierasch, L. M. (2007a). From the test tube to the cell: Exploring the folding and aggregation of a β-clam protein. *Biopolymers* **88,** 157–163.

Ignatova, Z., Thakur, A. K., Wetzel, R., and Gierasch, L. M. (2007b). In-cell aggregation of a polyglutamine-containing chimera is a multi-step process initiated by the flanking sequence. *J. Biol. Chem.* **282,** 36736–36743.

Maxwell, K. L., Mittermaier, A. K., Forman-Kay, J. D., and Davidson, A. R. (1999). A simple *in vivo* assay for increased protein solubility. *Protein Sci.* **8,** 1908–1911.

Philipps, B., Hennecke, J., and Glockshuber, R. (2003). FRET-based *in vivo* screening for protein folding and increased protein stability. *J. Mol. Biol.* **327,** 239–249.

Ross, C. A., and Poirier, M. A. (2004). Protein aggregation and neurodegenerative disease. *Nat. Med.* **10** (Suppl.), S10–S17.

Wigley, W. C., Stidham, R. D., Smith, N. M., Hunt, J. F., and Thomas, P. J. (2001). Protein solubility and folding monitored *in vivo* by structural complementation of a genetic marker protein. *Nat. Biotechnol.* **19,** 131–136.

Zhang, J., Liu, Z. P., Jones, T. A., Gierasch, L. M., and Sambrook, J. F. (1992). Mutating the charged residues in the binding pocket of cellular retinoic acid-binding protein simultaneously reduces its binding affinity to retinoic acid and increases its thermostability. *Proteins* **13,** 87–99.

Zoghbi, H. Y., and Orr, H. T. (2000). Glutamine repeats and neurodegeneration. *Annu. Rev. Neurosci.* **23,** 217–247.

CHAPTER 4

Combining Microfluidics and Quantitative Fluorescence Microscopy to Examine Pancreatic Islet Molecular Physiology

Jonathan V. Rocheleau* **and David W. Piston†**

*Institute of Biomaterials and Biomedical Engineering
University of Toronto
Toronto, Ontario M5S 3G9, Canada

†Department of Molecular Physiology and Biophysics
Vanderbilt University Medical Center
Nashville, Tennessee 37232

Abstract

Pancreatic islets are functional micro-organs involved in maintaining normoglycemia through regulated secretion of insulin and other hormones. Extracellular glucose stimulates insulin secretion from islet β-cells through an increase in metabolic state, which can be measured using two-photon

METHODS IN CELL BIOLOGY, VOL. 89

0091-679X/08 $35.00
DOI: 10.1016/S0091-679X(08)00604-3

NAD(P)H imaging. Extracellular glucose concentrations of >7 mM generate synchronous β-cell calcium (Ca^{2+}) oscillations leading to pulsatile insulin secretion. Our studies have focused on the coupling of cells within the islet using quantitative fluorescence imaging of metabolic (NAD(P)H) and electrical (Ca^{2+}) responses. This imaging requires immobilization of the tissue to achieve subcellular spatial and subsecond temporal resolutions. We have developed microfluidic devices to stimulate islets while holding them stationary against a glass coverslip. One device is a dual-channel microfluidic that allows heterogeneous islet stimulation by introducing a standing gradient in glucose concentration across the islet. The second device is a single channel microfluidic with the general utility to hold islets static. This chapter will describe the fabrication and use of these devices, with specific reference to their demonstrated utility for quantitative and dynamic imaging of living pancreatic islets. We will also highlight the general utility of these devices as a paradigm transferable to the study of other tissues.

I. Introduction

Pancreatic β-cells respond to rises in blood glucose levels by secreting insulin in a dose-dependent fashion. These cells sense changes in extracellular glucose through metabolic coupling, which can be assayed by measuring NAD(P)H autofluorescence intensity (Bennett *et al.*, 1996; Piston and Knobel, 1999a; Rocheleau *et al.*, 2002, 2004a). A rise in extracellular glucose increases the cellular [ATP]:[ADP] ratio, which closes the ATP-sensitive K^+ channels (K_{ATP}) and results in plasma membrane depolarization (Newgard and McGarry, 1995). Membrane depolarization induces Ca^{2+} influx through voltage-gated membrane channels and a concomitant release of insulin.

β-cells are found within the pancreatic islet. Pancreatic islets are 100–200 μm in diameter and comprise 1000–10,000 cells (~85% of which are β-cells; Unger, 1981). Consistent with significant coupling of cells within this tissue, islets exposed to >7 mM glucose show synchronous β-cell Ca^{2+} oscillations resulting in pulsatile insulin secretion (Atwater *et al.*, 1984; Bergsten, 1998). This chapter provides detailed methodological information on approaches to examine this coupling using microfluidics in combination with two-photon excitation of NAD(P)H and confocal imaging of Ca^{2+} using acetoxymethyl (AM)-loaded Fluo-4. We have taken advantage of these approaches to show that electrical activity does not traverse into regions of the islet with even a small number of open K_{ATP} channels (Rocheleau *et al.*, 2004b, 2006). Coupling of the K_{ATP} channel activity through gap junctions results in clamping of hyperexcitable β-cells at low glucose, which is critical to maintaining a normal glucose-dependent response. It is this clamping at low glucose that limits insulin secretion in this variably excitable medium.

II. Rationale

Our work examines the electrical coupling between β-cells within living pancreatic islets using quantitative fluorescence microscopy. To make these measurements, we needed to overcome several obstacles that had hampered previous work. First, we had to develop a method to expose islets to graded glucose concentrations. Techniques such as laminar flow of two streams over the islet or localized exposure to a higher concentration of glucose through a pipette proved too difficult to control in a reproducible way. It was also necessary to obtain a flat field of AM-dye-loaded cells, but this was originally not achievable; these dyes only penetrate the cells at the periphery of round islets. When observed with a confocal microscope, this loading pattern reveals only a donut of cells around the periphery of the islet complicating the measurement of cell–cell coupling across the whole islet. Most Ca^{2+} imaging in islets has been done using widefield fluorescence microscopes (Fura-2) to provide whole tissue responses that do not require the cells in the tissue to remain stationary throughout the experiment. This Ca^{2+} activity is easily observed in the widefield setting due to the synchrony of the oscillations across the whole tissue; however, this setup does not allow the observation of Ca^{2+} waves traversing across the tissue, nor does it permit measurements of Ca^{2+} activity changes in individual cells. It should be noted that an uncoupled (asynchronous) islet will not show oscillations and will have an apparent blunted Ca^{2+} response while imaging with Fura-2 in a widefield microscope when in fact each individual cell response may be normal.

To accurately measure Ca^{2+} waves and achieve subcellular resolution, islets must be held stationary during their imaging. To address this issue, our lab has previously used sticky substances coated on the coverslip such as CelTak (Piston and Knobel, 1999a, 1999b; Piston *et al.*, 1999; Wu *et al.*, 2004). While this method has utility, it does not provide a flat field of dye-loaded cells, which complicates prohibitively the measurement of Ca^{2+} waves. Our lab has also cultured islets for a period of time (weeks) on extracellular matrix (ECM) (Patterson *et al.*, 2000; Rocheleau *et al.*, 2002, 2004a). Such culturing maintains electrical coupling and metabolic responses, but it is unclear what underlying changes occur in the tissue during such long-term culture. Furthermore, single cell depth is rarely achieved and usually only at the outer edge of the attached tissue. Therefore, a method to hold freshly isolated islets stationary against a glass coverslip to provide a flat field of view is of great utility.

Some information concerning cell–cell electrical coupling in islets can be gathered by observing the velocity of Ca^{2+} waves across the tissue (Aslanidi *et al.*, 2001, 2002). We developed an alternative method of heterogenous islet stimulation (Rocheleau *et al.*, 2004b). Our goal was to expose the islet to a glucose gradient that resulted in stimulation of one region with >7 mM glucose, then to measure whether electrical activity was transmitted into regions experiencing less. To make these measurements, we designed a microfluidic device to stimulate

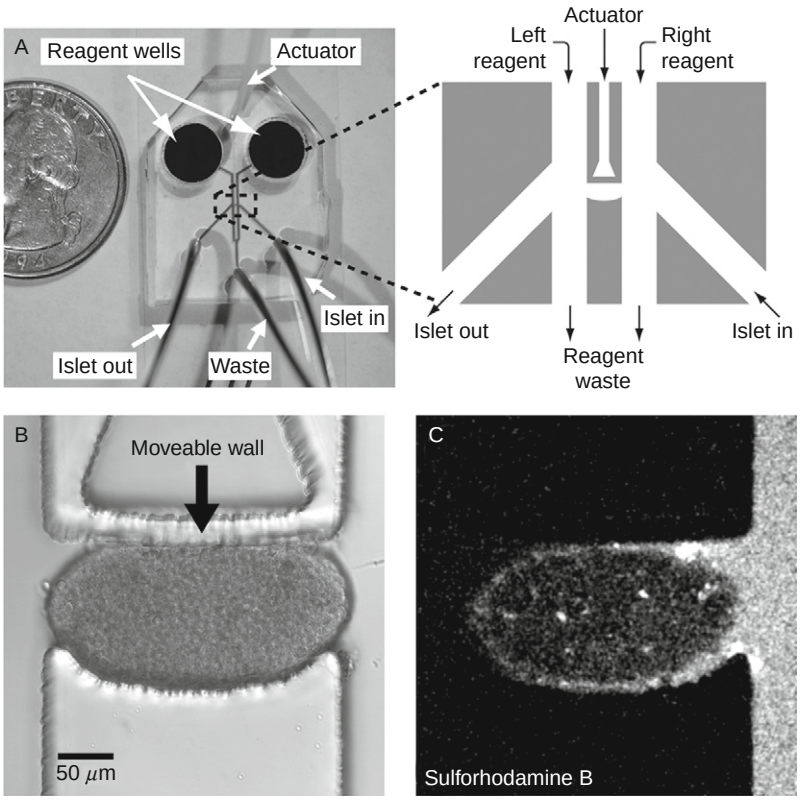

Fig. 1 Two-channel microfluidic device used to treat islets with independent fluid streams. (A) Microfluidic device composed of PDMS with 100-μm tall channels molded and fused to a glass coverslip. The channels are filled with dye for presentation. Left: Shown are the positions for the on-chip reservoirs (Reagent wells), access holes and tubing (Islet-in, Islet-out, and Waste), and the actuator access hole (Actuator). Right: An expanded schematic of the islet-holding area with its channels (Islet-in, Islet-out, Waste) and reagent conduits labeled. The channels are 600-μm wide and 100-μm tall. The islet is loaded by plugging the waste tubing and inducing gravity flow from the islet-in to Islet-out tubing. (B) A differential interference contrast image of an islet held in observation area. The PDMS moveable wall, which can be controlled by pressurizing the actuator tubing, is also indicated. (C) The same islet shown in (B) with 0.1 μM sulforhodamine B in the right reagent well. The right side of the islet remains fluorescent whereas the left is unlabeled, consistent with the establishment of a seal that prevents leakage around the islet to the other fluid stream. Thus, the two fluid streams are independent of one another. If a leak is observed, the actuator is pressurized to seal the islet in the holding area.

heterogeneously individual islets with glucose. Figure 1 shows a dye-filled device (A, top left), a schematic of the islet-holding area (A, top right), and a differential interference contrast (DIC) image of an islet trapped in the holding area of the device (B). Once loaded into the device (as described in Section III), the islet is immobilized in a central-holding area with a rounded wall. The device is composed of 100-μm tall channels micro-molded in polydimethylsiloxane (PDMS) that is bonded to a glass coverslip. Two large wells are used to deliver reagents to the

appropriate microchannel, and smaller channels with access tubing allow the loading of islets and release of waste. The islet-holding area is 100-μm tall (coverslip to PDMS ceiling), 300-μm wide, and 150-μm high. The device has a flat top with an actuator or moveable wall. Pressurizing the actuator moves the wall slightly to fit the islets securely. A plugged-holding area allows the solutions on either side of the islet to be independent (Fig. 1, sulforhodamine B).

We examined the glucose-stimulated metabolic response of islets to 11 mM glucose on both sides (11|11) or on either side (11|2 and 2|11) (Fig. 2). By placing

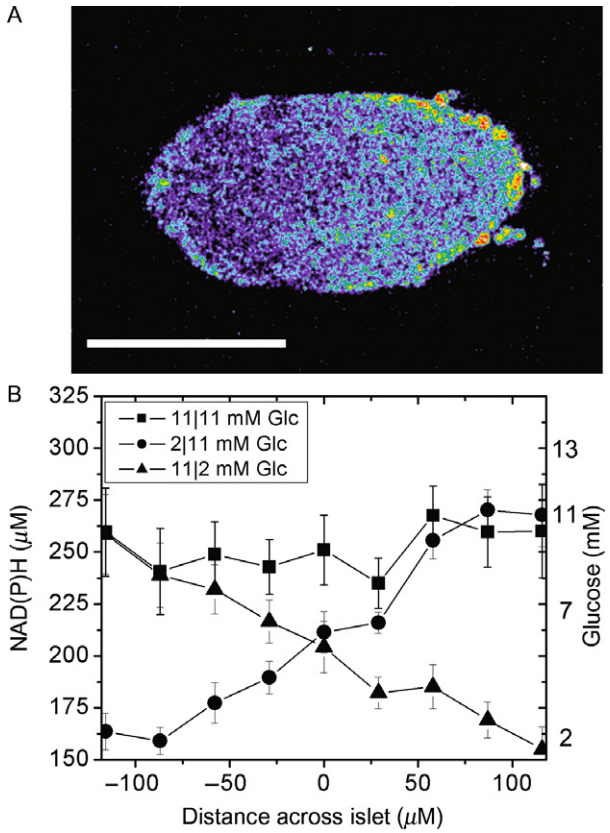

Fig. 2 Response of pancreatic islets in the two-channel microfluidic to treatment with NAD(P)H. (A) An islet subjected to a glucose gradient by placing 2 and 11 mM glucose solutions in the left and right fluid streams, respectively, for 10 min. This treatment produces an NAD(P)H gradient across the islet. (B) The NAD(P)H response of islets with 11 mM glucose in both streams (11|11 mM Glc) and with 2 and 11 mM in opposite fluid streams (2|11 and 11|2 mM Glc) (N=11 islets). These responses are consistent with the NAD(P)H responses of islets outside of the device. Local glucose concentrations (estimated on the y-axis), were determined either from comparison to an NAD(P)H glucose-dose response generated using islets not trapped in a device or fitting the linear response (assuming 2 and 11 mM responses on the edges of the islet).

2 and 11 mM glucose in opposite fluid streams, we create a glucose gradient across the tissue that results in a graded metabolic response, measured as NAD(P)H autofluorescence. These responses are similar to those of islets outside of the device, which indicates the device is not perturbing the response (Bennett *et al.*, 1996; Piston and Knobel, 1999a; Rocheleau *et al.*, 2002). Furthermore, this graded response is directly proportional to the local glucose stimulation across the islet as confirmed by comparison to the NAD(P)H responses of uniformly stimulated islets and the diffusion of the fluorescent glucose analogue NBD-glucose (Rocheleau *et al.*, 2004b) The right side axis illustrates that the edges of the islet experiences NAD(P)H responses consistent with 11 and 2 mM glucose stimulation, and that the NAD(P)H responses in between are proportional to the local glucose concentration. We also monitored the Ca^{2+} response from these islets by using Fluo-4 imaging (Fig. 3). Note that Fluo-4 is visible all across the islets in Fig. 3,

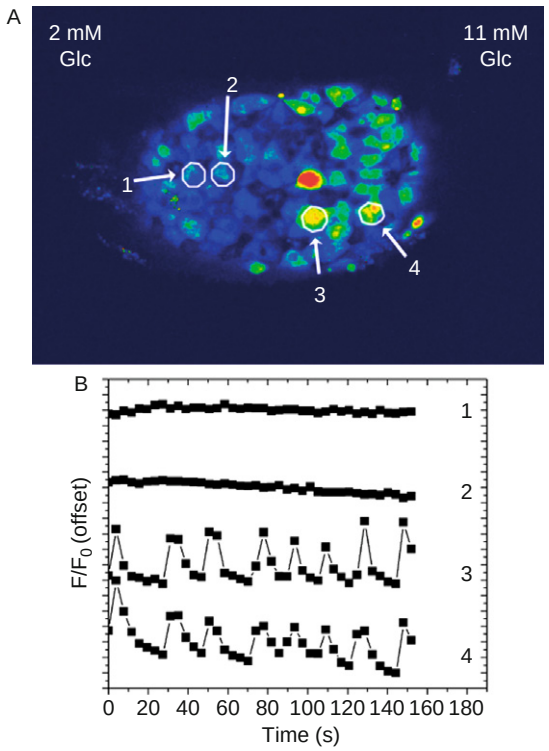

Fig. 3 The Ca^{2+} response in a glucose-gradient treated islet. (A) A Fluo-4, AM-loaded islet treated with 2 and 11 mM glucose in the left and right fluid streams, respectively, of the two-channel device. Four cells are indicated. (B) The relative Ca^{2+}-responses of the four cells indicated in (A). Cells 1 and 2 do not show any Ca^{2+} oscillations, whereas cells 3 and 4 show synchronous oscillations consistent with activated β-cells. Cells 1 and 2 responded with Ca^{2+} oscillations when the islet was treated with the 11|11 mM or 11|2 mM glucose regimes described in Fig. 2 (data not shown).

because they were lightly pressed into the 100-μm tall channels so that more of the peripheral cells were in the focal plane of the confocal microscope. Figure 3 (bottom) shows the relative calcium intensities as a function of time for four representative cells (1–4). This islet was treated with 2 and 11 mM glucose in the left and right streams, respectively. Oscillations in Ca^{2+} were only observed in cells 3 and 4 (see supplemental movies of Rocheleau *et al.*, 2004b). When the stimulation was switched (11|2 mM glucose in left|right streams), oscillations were observed in cells 1 and 2. Stimulatory glucose (11 mM) in both streams caused synchronous Ca^{2+} oscillations between cells in every sample (16 of 16 islet halves) with an average frequency of 2.7 ± 0.1 min^{-1}. This frequency is similar to that documented for isolated islets [$\sim 2.5\,min^{-1}$ (Bergsten *et al.*, 2002; Nadal *et al.*, 1999)], which again indicates that the microfluidic device does not significantly perturb the tissue. Synchronous oscillations were observed up to 129 ± 8 μm from the 11-mM glucose edge ($N = 8$). The NAD(P)H concentration at this distance was 210 ± 21 μM, corresponding to a local glucose concentration of 6.6 ± 0.7 mM. We extended the movement of Ca^{2+} oscillations further into the islet tissue by placing a K_{ATP} channel antagonist (tolbutamide) in the low glucose stream. Therefore, initiation of the Ca^{2+} response depends strongly on K_{ATP} channel activity. Overall, this work showed that Ca^{2+} oscillations were not initiated in regions of the islet experiencing less than $\sim$7 mM glucose and that the threshold of the β-cell response is strongly dependent on K_{ATP} channel control of membrane potential.

In the course of designing and using the two-channel microfluidic device, we recognized that a flat stationary field of cells was generated by trapping and holding the islet against the glass coverslip. To create a simpler method and still take advantage of the flat field of view created in these devices, we then designed and built a single-channel microfluidic device (Rocheleau *et al.*, 2006). The dye-loaded microfluidic device shown in Fig. 4 is labeled to show the Reagent well, Islet In/Out port, Wall trap area, and Waste port. This device relies on gravity flow from either the ''Reagent well'' or ''Islet In/Out'' port to the ''Waste'' port. Islets are brought into the device through the In/Out port, and travel through the main channel of the device until they come in contact with ''Wall'' area. The islet shown is in the main channel (height $\sim$100 μm and width $\sim$600 μm) touching the wall trap (bottom of image), with fluid flowing by gravity from the top to bottom of the image. Islets trapped in a microfluidic device channel of $\sim$100-μm height are pressed against the coverslip surface, thus producing a flat field of cells that is optimal for microscopic imaging. The islet is held stationary by the coverslip, ceiling and wall trap. Multiple image planes with sulforhodamine B (0.2 μM) in solution show the height of the drop wall with dye solution absent at the wall trap area. In this region of the device, the height of the channel drops from $\sim$100 to $\sim$15 μm. This channel height allows fluid to flow while blocking islet movement. Once islets are trapped in the device, the In/Out port is plugged and gravity flow started from the ''Reagent well'' to the waste tubing. The kinetics of fluid exchange, monitored by replacing the ''Reagent well'' fluid with the same containing sulforhodamine B (0.2 μM), resulted in complete change of solution in $\sim$1 min. Half-maximal

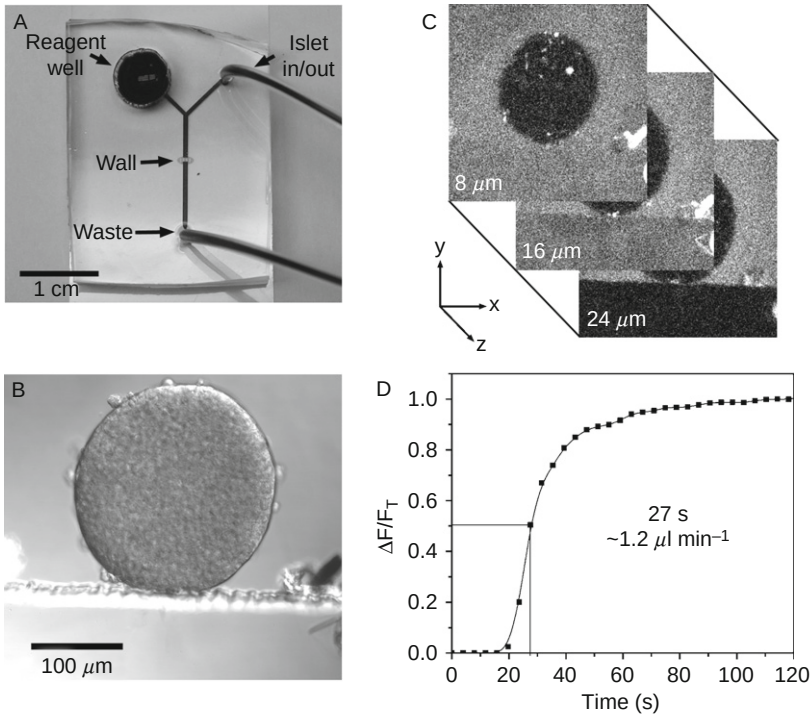

Fig. 4 The single-channel microfluidic device used to hold islets against the glass coverslip during reagent flow. (A) The microfluidic device composed of PDMS with 100-μm tall channels micro-molded and fused to a glass coverslip. The channels are filled with dye for presentation. Shown are the positions for the on-chip reservoir (Reagent well), access hole and tubing (Islet-in/out, and Waste), and the drop wall area (Wall). The main channel is 600-μm wide and 100-μm tall (glass coverslip to top of PDMS), and the drop wall area is ~15-μm tall. The islet is loaded by flowing solution from the islet in/out tubing to the waste tubing by gravity induced flow. (B) A differential interference contrast image of an islet in the main channel that is trapped against the drop wall. Solution flows past the islet from the top of the image and under the drop wall (bottom). (C) Sulforhodamine B in solution (0.1 μM) imaged at ~8, 16, and 24 μm from the glass coverslip. The islet (dark circle) excludes the dye and is non-fluorescent. The islet is touching the drop wall, shown as a dark region appearing between 16 and 24 μm. (D) Sulforhodamine B (0.1 μM) was added to the reagent well at $t = 0$ with the waste-tubing end held at a typical height (~−5 cm) below the on-chip reservoir. The images were collected at the drop wall area. The arrival of the dye at the wall area is plotted ($\Delta F/F$) versus time. Half-maximal fluorescence intensity was observed at ~27 s, which corresponds to a flow rate of ~1.2 μl min^{-1}.

exchange occurred in 27 s, which corresponds to a realized flow rate of ~1.2 μl min^{-1}, below the calculated maximal velocity (~3 μl min^{-1}) but slightly faster than the flow rate calculated from the device resistance and reservoir-to-outlet tubing height (~0.7 μl min^{-1}, calculation clearly described in Walker *et al.*, 2002). We did not observe warping of the islet at the experimental flow rate, which is consistent with low sheer across the tissue. Furthermore, the islets remained

stationary after long periods of flow (minutes to hours) and during reagent solution changes. The ability to hold the islet in a stationary position for long intervals facilitates time-lapse imaging and the observation of similar regions after many different treatments.

The flat fields of cells produced by these devices enable the measurement of electrical waves across the tissue. The devices also permit rapid solution exchange in the absence of significant movement, require small amounts of reagent, and facilitate control of islet stimulation (by, for example, glucose gradients). The combination of microfluidics and quantitative fluorescence microscopy reduces the complexity of some experiments and allows one to conduct experiments that were once impossible such as the islet glucose-gradient experiments described in this chapter. Many other microfluidic devices have been designed to probe biological processes, and new ones are continually in development (Beebe *et al.*, 2002; Melin and Quake, 2007; Sia and Whitesides, 2003; Walker *et al.*, 2004). This chapter describes our methods to create and use two such devices and can be used as a starting point for engineering novel devices to address very different biological questions.

III. Methods and Materials

A. Islet Isolation

Islets are isolated from mice pancreas using collagenase digestion as previously described (Scharp *et al.*, 1973; Stefan *et al.*, 1987) and maintained in complete RPMI medium 1640 containing 10% fetal bovine serum and 11 mM glucose at 37 °C under 5% humidified CO_2 for 24–72 h in non-gamma irradiated polystyrene culture dishes. Non-gamma irradiated dishes are used throughout this work to reduce the sticking of islets to the dish.

B. Loading Pancreatic Islets with Ca^{2+}-Sensitive Dye

Islets are labeled with 4 μM Fluo-4, AM (Invitrogen) at room temperature for 1–2 h in imaging buffer (125 mM NaCl, 5.7 mM KCl, 2.5 mM $CaCl_2$, 1.2 mM $MgCl_2$, 10 mM HEPES, 2 mM glucose, and 0.1% bovine serum albumin, pH 7.4). Bovine serum albumin is present to reduce sticking of the tissue to the microfluidic channel walls. The dye is prepared as a stock solution in DMSO (91 μl DMSO to 50 μg of Fluo-4, AM followed by vortexing). Add 8 μl of the DMSO stock to 1 ml of imaging buffer and mix thoroughly by a combination of vortexing and sonication (1–2×). While sonicating the DMSO/Fluo-4 AM/imaging buffer solution, pick three to five islets from the culture media using a 10-μl pipette and place them as a bead on the bottom of a 35-mm non-treated polystyrene dish. Pour the labeling solution onto the islets in the dish, cover with aluminum foil, and place on a rocker for 1–2 h. Rocking ensures even labeling of the islet's peripheral cells. Islets are then picked from this

dish using a 10-μl pipette (5–8 μl volume is typical) and placed directly into a ~300-μl bead of imaging media for loading into the microfluidic device (see below).

C. Device Fabrication

The basic steps of our fabrication method (mask design, master fabrication, and polydimethylsiloxane micromolding and bonding) have been described in detail elsewhere (McDonald *et al.*, 2000). These techniques require a clean room facility, which should be secured prior to attempting the microfabrication process. Since techniques are continually evolving, it is likely that future methods will lessen or eliminate the need for a clean room, thus permitting fabrication in any lab.

1. Mask Design

Masks are designed using programs that can save in encapsulated postscript (EPS) file format, the most common being Adobe Illustrator and Corel Draw. The masks are drawn to scale in black and white (Fig. 5). We start by drawing 3-in. black circles corresponding to the size of silicon (Si) wafers. The channels themselves are then drawn on each circle as white lines in millimeter units. As can be seen on the mask design in Fig. 5A, tubing-access channels are marked by a slightly larger diameter circle than the channels. The channels in this mask are 600 μm wide, large enough for islets to flow down them. Creating channels with varying heights, as we have done in the single-channel device requires the generation of two masks that can be overlapped (Fig. 5A and B). A typical mask file, containing one to six 3-in. circles on an 8.5 × 11 in. sheet, is sent to a print shop that will print to film at or above 3556 dots per inch resolution. The 3-in. circles are cut from the film prior to master fabrication.

2. Master Fabrication

The master is fabricated on a 3-in. silicon wafer using SU-8 negative-photoresist and following protocols recommended by the manufacturer (MicroChem, www.microchem.com). The protocol involves spin-coating the liquid photoresist onto the wafer to achieve a defined thickness as a function of the spin speed and viscosity (~3000 rpm for 30 s). The coated wafer is then soft baked (65 °C, 60 s to 95 °C for 2.5 h) to remove solvent prior to exposure of the coated wafer to UV light as defined by the film mask. The regions of photoresist under clear film (the channels) are stimulated to polymerize during UV illumination, and this polymerization is completed by hard baking the wafer (65 °C, 60 s to 95 °C for 1 h). Finally, excess un-polymerized photoresist is dissolved away during the developing process, leaving a finished master with polymerized SU-8 of a defined height and geometry. To achieve a multiple-height device as shown in Fig. 4, this process is first carried out using the short channel mask with SU-8 2015 (Fig. 5B) followed by the tall channel mask with SU-8 2100 (Fig. 5A). The crosshatches in each mask are used to properly overlap the two masks. Each of these steps will depend on the equipment

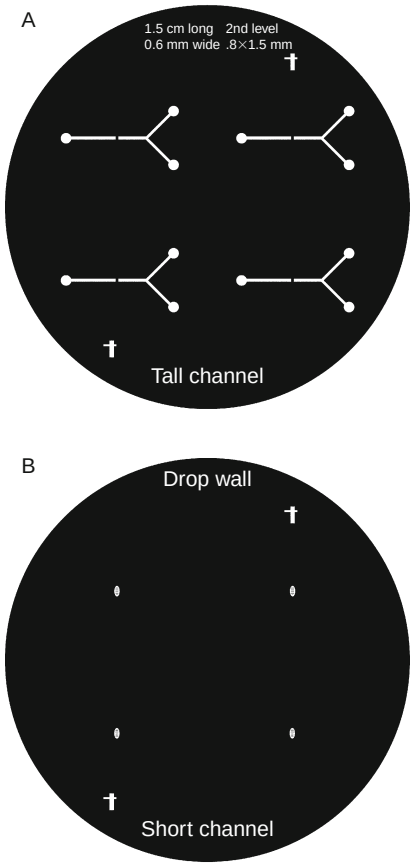

Fig. 5 Mask design for a two-layer microfluidic device. (A) The tall channel mask comprises a Y-shape with 600-μm wide channels. These channels will be ~100-μm tall due to fabrication with SU-8 2100 photoresist. Regions for the drop wall area are blocked (dark) in this mask. (B) The short channel mask comprises the drop wall area. This area is oval shaped with dark (un-polymerized) regions to provide stability to this shallow structure (~15 μm after fabrication). The hatches shown in each mask are used for alignment of the two masks so that the tall channel meets precisely the drop wall area.

available in your institutional clean room, so it is important to first discuss the fabrication project in detail with the manager of your facility. We use SU-8 2015 and 2100 to achieve channel heights of ~15 and ~100 μm, respectively.

3. PDMS Micromolding

After production of your working master, continue the fabrication process under normal laboratory conditions; necessary equipment includes a top-loading balance and a plasma-cleaner with vacuum pump (Harrick PDC-32G Plasma Cleaner). Pour ~15 g of pre-polymerized PDMS (Sylgard 184, Dow Corning)

per 3-in. wafer into a 100 × 20 mm non-treated polystyrene culture dish (Corning cat # 430591). Re-tare the balance, then add 1/10 the mass of curing agent (~1.5 g). Mix the polymer and curing agent for 5 min, either by hand using a plastic fork or by using an electric mixer. Do not be concerned about introducing bubbles; they actually indicate that the emulsion is well stirred. Place the mixed polymer in a vacuum desiccator under in-house vacuum until the bubbles disappear. Periodic venting and reapplication of vacuum accelerates removal of the bubbles.

In a separate 100 × 20 mm dish, place the master face-up and pour the degassed emulsion over it, taking care not to introduce new bubbles. Place the dish and its contents under vacuum to remove bubbles inadvertently introduced. Do not over-aspirate because retention of the large air bubble beneath the wafer will facilitate its removal post-polymerization. Cure the polymer by heating to 80 °C for 2.5 h on a hot plate or in an oven.

The cured polymer can be removed using a thin weighing spatula. Care must be taken during this process to avoid breaking the relatively inflexible master. We recommended that you practice this step with a waste silicon wafer prior to using a valuable master. Press the spatula between the dish and the cured PDMS resin with the majority of pressure exerted against the wall of the plastic dish. Move the spatula around the circumference of the dish; should the spatula slip out, go back to a loose edge, reinsert the spatula, and continue until the spatula has been run around the entire dish. As the cured resin becomes less attached to the dish, you may begin to slip the spatula underneath. Continue edging and peeling the PDMS out of the dish. Once removed, cut away excess PDMS found under the master and then peel the remainder away from the silicon wafer. Place the PDMS cast, channel-side up, onto the top of a 100-mm non-treated dish. From this point onward, handle the PDMS with gloves to limit the deposition of skin oils. A scalpel is then used to cut out individual devices (we often have five devices per silicon wafer).

Two types of access holes are bored into the PDMS: on-chip reservoirs and tubing-access ports. On-chip reservoirs are cut with a #3 cork borer. To minimize tearing of the resin, use a cork borer with an inner beveled edge. The smaller tubing-access holes are cut using a tool fashioned from an 18-gauge needle (violet top) sawed at mid-level. To introduce an inner bevel and reduce its abrasiveness, we repeatedly hone the inner diameter of the bore with a thin wire. (The wire is also used to remove plugs while boring the PDMS tubing-access holes.) The introduction of cracks in the resin during the boring of tubing-access holes indicates that the needle has become dull. Therefore, re-sharpen the inner surface regularly as the tool ages. Molds with cracked tubing-access holes cannot be used because they will leak.

4. PDMS Bonding

The PDMS mold with bored access holes is bonded to a 24 × 50 mm No 1 1/2 glass coverslip to seal the channels and provide an optical window for fluorescence microscopy imaging. Thicker coverslips are more robust, but are suboptimal for fluorescence imaging.

Just prior to mounting, the coverslips are cleaned with methanol and acetone by placing them onto Kim-wipes and repeatedly pooling solvent onto the glass followed by rubbing dry with a BetaWipe (ITW Texwipe Cat #TX2009). Put the coverslips into the plasma cleaner. Next, place the PDMS, channel-side up, on a piece of clean glass that fits into the plasma cleaner. The PDMS mould is cleaned of dust and fragments of PDMS by pressing scotch tape against the channel-side surface and then pulling it away. This step also seats the top of the PDMS mould on the glass surface, which reduces plasma access and unintentional bonding. The coverslips and PDMS are cleaned under plasma for 30–60 s (the time required will vary with the power of your plasma cleaner and must be determined by trial).

Remove the PDMS mold and place it, channel-side down, onto a plasma-treated coverslip. The PDMS should almost immediately stick to the glass. Some bubbles between the PDMS and coverslip may be present, but will disappear with time. A strong seal is indicated by the inability to pull the PDMS from the glass even at its edges. Failure to form a strong seal occurs when the coverslips are not sufficiently cleaned by methanol/acetone treatment or when the time of plasma exposure is inappropriate. The devices are stacked between aluminum foil to prevent them from bonding irreversibly to each other.

D. Filling the Devices with Fluid

We generally treat our microfluidic chambers as disposable and use them for 3 days at most. To prepare the device, insert $\sim$30 cm (12 in.) of Tygon tubing (0.02 in. inner diameter, 0.06 in. outer diameter; Cole Parmer Instrument Company Cat # 06418–02) into the smaller access holes using forceps. We attempt to seat the tubing snugly to half the depth of the holes. The device is then flushed with distilled water by coupling a 5-cc syringe to the islet-in tubing with a blunt-end needle (Howard Electronic Instruments Inc. El Dorado, KS Cat # JG25-0.5). To prevent over-flow, place a glass coverslip over the large on-chip reservoir holes prior to flushing, and unplug the remaining tubes. The solution will fill the channels and tubing in the order of least resistance to flow. Bubbles are often introduced into the PDMS channels during filling, in particular at the edges of access holes and at channel corners. To limit the formation of bubbles in the device, degas all solutions prior to use by heating in a water bath (37 $^{\circ}$C for $>$30 min). To remove any bubbles present after filling the device with solution, uncap one of the outlet tubes and press forcibly on the syringe plunger to generate a rapid flow of water while observing the bubbles release with a dissecting microscope. If bubbles still remain after this treatment, cap all outlets, exert downward pressure on the coverslip and syringe. In the absence of an outlet, pressure increases in the device. This pressure shrinks the bubbles due to the gas-permeability of PDMS. Repeat this process as necessary as the bubbles shrink progressively and attempt to press until the bubble nuclei are eliminated. One can also remove bubbles by this method after the chamber has been mounted

on the confocal microscope. However, do not attempt to remove bubbles after an islet has been placed in the device because damage to the tissue is likely.

E. Loading and Imaging Islets in Microfluidic Devices

1. The Stage Setup

Transport the water-filled microfluidic device to the microscope with all tubes plugged. The device is mounted on a temperature-controlled stage (Zeiss), and the tubes are unplugged briefly so that they may be threaded through access holes on the microscope stage. Place tape over the circular opening at the bottom of the stage heater to reduce heat loss, which is a source of focal-plane instability.

2. Gravity and Flow Rates

We generally control flow-rate via gravity and manipulation of solution heights (tubing in, out, and on-chip reservoir). Figure 6 shows a schematic (side-view) of a microfluidic device on a microscope stage. The heights outlined in this schematic are shown to assist the reader in the general use of the devices. As described below, the flow rates in the device are manipulated by changing the heights of

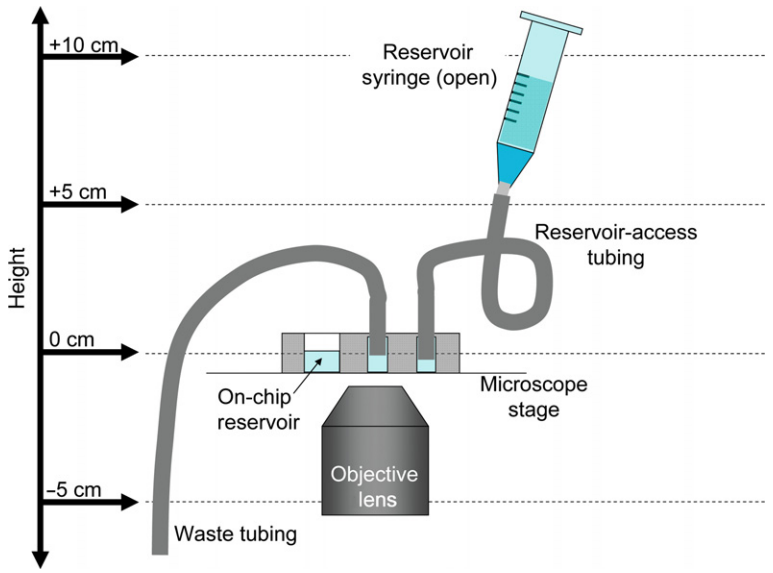

Fig. 6 A schematic showing typical tubing heights for the single-channel microfluidic. The schematic shows the chip on the microscope stage above the objective lens. Also shown in the schematic are the on-chip reservoir where reagents are quickly exchanged, the two access holes with tubing inserted (Waste and Reservoir-access tubing), and the open 5-cc syringe filled with reservoir solution. Heights typically used with the device are shown relative to the level of the on-chip reservoir (not to scale in schematic).

the inlet- and outlet-tubing relative to the chip- or imaging plane. These parameters are given as approximations that should be modified based on the user's developing experience.

To replace the water in the chamber, remove the blunt-end needle and attach a syringe containing the imaging buffer. Lower the inlet tubing below the on-chip reservoir level (0 to −5 cm) so that air does not enter the tubing while it is uncapped. Once the syringe is attached, adjust its height so that the top of the imaging buffer in the syringe is a few centimeters above the chip plane (0 to +5 cm), but *not* so high as to cause the on-chip reservoirs to overflow. Lower the waste tubing to a position 5–15 cm below the chip plane. At this time, turn on the heated stage (both air and stage heating). Warming the chamber from room temperature to 37 °C can cause the release of gas from the solution if it is not sufficiently degassed beforehand. This configuration during the warming of the chamber will maintain a slow flow from the syringe to the outlet tubing. The on-chip reservoir should be monitored closely since it will overflow if the syringe is kept too high, and it will empty if kept too low.

3. Gravity Loading Islets into the Devices

Place a ~300-μl bead of imaging buffer on the bottom of a 35-mm dish. After loading islets with AM (see Fluo-4, AM loading), transfer them via a 10-μl pipette to the ~300 μl bead of imaging buffer. Place a coverslip over the on-chip reservoirs of the microfluidic to resist the flow of imaging solution into these wells. Remove the inlet tubing from the syringe needle (syringe placed 0 to −5 cm with respect to the plane of the chamber) and place the end into the islet-containing drop. Elevate the dish and the tubing above the stage (+5 to +15 cm), taking care to prevent the end of the tubing from leaving the drop. Unplug the outlet tubing so that solution flows to the waste as the islet is drawn into the chamber. The islet can be observed by eye as it enters the tubing, which can be further aided by placing a dark background beneath the dish and behind the inlet tubing. Stop liquid flow after the islet is several centimeters down the tubing by lowering the tube and dish to the height of the stage or just below (0 to −2 cm); this prevents backflow of the islet. Replace the reservoir syringe and raise it above stage level (+5 to +10 cm) to resume flow.

Maintain flow until the islet arrives just above the device (~0.5 cm). Lower the syringe and tilt it so that the top of the solution column is 1–3 cm above stage level. The islet will continue to move slowly into the device due to residual flow and gravity. Meanwhile, move the stage so that the objective is beneath the access hole and watch the islet enter the device. As the islet enters the device, it will stop in the area just below the tubing. To flow the islet into the channel of the device, raise the loading syringe (+5 to +10 cm) to increase the flow rate. The islet will slow and stop at the channel opening as it presses against the PDMS and glass coverslip, then slowly slide into the 100-μm tall channel. Flick the tip of the loading syringe to assist islet entry into the channel and adjust the pressure head as necessary

(+5 to +15 cm for syringe, −5 to −20 cm for the waste outlet). Use caution in adjusting the flow rate as too fast a rate will cause the islet to quickly and uncontrollably pass into the on-chip reservoir, which is the path of least resistance. At a slow-controlled flow rate, the islet will often stick to the channel walls. If this occurs, flick the waste tubing to jostle the islet back into motion.

4. The One-Channel Microfluidic Device

When an islet approaches the Y in the single-channel device, lower the reservoir height to prevent it from flowing directly into the on-chip reservoir. The islet is coaxed past the Y by laying the syringe on its side (+1 to +3 cm relative to the stage level) and lowering the waste port (−10 to −20 cm) while flicking the end of the tubing. This will promote flow from both the loading syringe and the on-chip reservoir to the islet-holding area. Once the islet is past the Y in the device, the reservoir syringe can again be raised (+5 to +10 cm), although flow rate past the islet at this position in the device is determined largely by the height of the waste outlet. Slow the flow as the islet approaches the drop wall in the holding area to prevent shear-induced damage to the tissue. Damaged areas will show anomalous Ca^{2+} oscillations, and the islet will need to be discarded. Once the islet is in the larger channel and up against the drop-wall, slowly remove the inlet tubing from the syringe so that the induced negative pressure is sufficiently small to prevent the islet backing away from the drop wall, and plug the tubing. In this configuration, flow is maintained by filling the on-chip reservoir and keeping the waste tubing below the chip plane (0–5 cm).

5. The Two-Channel Microfluidic Device

To position an islet in the holding area of the two-channel microfluidic (Fig. 1), the islet is introduced into the device following the procedures described above. The islet is brought into the device by raising and lowering the islet-in and islet-out tubes, respectively, with the waste tubing plugged. With the waste tubing plugged and a coverslip placed over the on-chip reservoirs, the majority of flow will be directed from the islet-in tubing through the islet-holding area and to the islet-out tubing. Only large islets will be retained by the holding area of the two-channel device. Islets can be brought into the holding area by keeping the islet-in reservoir syringe slightly above the chip (0 to +5 cm) and holding the end of the islet-out tubing below the stage (−5 to −10 cm) while flicking the end of the tube. Once in the holding area, the islet-in and islet-out tubes are gently plugged.

6. Changing Solutions

Once the islet is held in the proper area of either device and the appropriate tubes are plugged, the coverslip over the on-chip reservoir is removed and the region around the reservoir is cleaned of any fluid overflow. Remove solution that entered

the on-chip reservoirs with a 200-μl pipette and replace with warm imaging buffer. Flow can then be monitored by observing the level of the solution in the on-chip reservoir. With the waste tubing held ~ -5 cm below the reservoir, we typically replenish the reservoir every 5–10 min. If flow is significantly reduced by the presence of a bubble or debris, one may need to discard the trapped islet, clean the device, and repeat the loading procedure.

7. Removing the Islet

Islets are removed from the device by placing a syringe onto the end of the waste or islet-out tubing and then raising the syringe above the chip. Some pressure may be necessary to achieve a useful flow rate. The islet will flow directly into the on-chip reservoir, and can be removed by repeated changes of the imaging buffer in the reservoir. The microfluidic is then examined for bubbles and prepared for reuse.

F. Imaging Parameters for Fluo-4 and NAD(P)H

One- and two-photon microscopy is performed on an LSM 510 microscope (or equivalent) with a 20 $\times$ Fluar objective (0.75 NA) (Carl Zeiss, Thornwood, NY). The device is held on the microscope in a humidified temperature-controlled stage (Carl Zeiss, Thornwood, NY) for imaging at 37 °C. Fluo-4 (Molecular Probes, Eugene, OR) fluorescence is observed in single-photon mode using an excitation wavelength of 488 nm and a long-pass 505-nm emission filter. NAD(P)H is imaged by two-photon microscopy using a 710-nm, mode-locked Ti:Saph laser ($\sim$3.5 mW at the sample), and fluorescence is collected through a non-descanned detector with a custom 380–550-nm band-pass filter (Chroma Inc., Rockingham, VT; Bennett *et al.*, 1996).

The power of the laser-light sources must be carefully attenuated to maintain islet health during repetitive imaging (Bennett *et al.*, 1996). The 710-nm laser is used at <5 mW excitation power to maintain a robust glucose-stimulated NAD(P)H response. Similarly, empirically high 488-nm laser power inhibits any observable glucose-induced Ca^{2+}-oscillations in islets. We therefore use the lowest excitation power that is consistent with imaging, and set the detector gain at or near the highest level. Although this strategy yields noisy images, it provides excellent measurements of intensity changes at cellular resolution. Note that NAD(P)H imaging can be performed on AM-loaded islets by focusing deeper into the tissue beyond the AM-dye-loaded cell layer.

The frequency of frame capture for Fluo-4 imaging is $\sim 0.5\ s^{-1}$, with frame duration <1 s. These settings permit the imaging of the "fast" Ca^{2+} oscillations of pancreatic islets. We collect a pair of 2-min time recordings for each islet and treatment, with a third collected if significant focal drift is observed in either of the first two recordings. To prevent focal drift, pre-warm all treatment solutions to 37 °C solution, and allow 3–5 min for the chamber temperature to equilibrate prior to imaging.

IV. Discussion

Our chapter has focused on the utility and use of two microfluidic devices. The two-channel device illustrates the power of microfluidics for the study of islet biology. We are able to produce a glucose gradient across individual islets using this device and to record simultaneously its metabolic and electrical responses. This device can also be used to partially treat the islet with agents other than glucose, such as tolbutamide (Rocheleau *et al.*, 2004b). Alternatively, new devices could be developed to create steps in glucose concentration across the tissue rather than the gradient generated in the present device. The single-channel device was developed to simplify the capture and stationary positioning of islets for imaging. It is simpler to load, allows rapid solution exchange, and provides a broad, flat field of cells. As currently designed, the fabrication and use of these chambers require that a new user develop an ''artful'' dexterity. We and others will continue to refine these devices facilitate their use and extend their utility to other biological samples.

An important concern for the novice user is the complexity of fabrication of the microfluidic chambers. Some may be daunted by the requirement for clean room fabrication facilities. We urge our colleagues to embrace these methods as currently available; most universities have the necessary facilities and expertise available in physics or engineering departments. Moreover, many labs are working to develop fabrication procedures that are faster, simpler, and suitable for use in non-clean room settings.

Novel devices can be generated by adapting the methods described in this chapter through iterative engineering. For example, we are developing microfluidic devices to examine the secretion of islets in concert with their metabolic and electrical responses. Simultaneous study of these proximal and distal processes should enhance our understanding of the hormone-stimulated secretory mechanism. On-chip capillary electrophoresis has previously been used to quantitatively measure insulin secretion from individual islets (Roche *et al.*, 1998; Roper *et al.*, 2003; Schultz *et al.*, 1995). Our strategy to monitor insulin output will entail fluorescent detection of Zn^{2+}, which is bound to insulin in β-cell secretory granules and co-secreted with the hormone (Blundell *et al.*, 1972; Emdin *et al.*, 1980; Foster *et al.*, 1993; Gold and Grodsky, 1984). To date, measurement of Zn^{2+} release from pancreatic β-cells via fluorescent indicators has been used to examine the spatial organization of the secretion response (Gee *et al.*, 2002; Michael *et al.*, 2006; Qian and Kennedy, 2001; Qian *et al.*, 2003), but these studies were limited to observing a halo of fluorescence around the secreting cells. Because diffusion and turbulence disturb the observation volume, this solution-based technique is only semi-quantitative. We propose to adapt this method to the microfluidic environment, in which we have precise control of the solution volume. Using chambers similar to the ones described here, we will control the rate of solution flow past an islet, which is contained in a microchannel of well-defined volume. The effluent solution will then be mixed with a fluorescent indicator for zinc. From previous studies, we

estimate that a flow rate of 0.002–0.008 μl min^{-1} past the islet will yield a concentration of ~150 nM Zn^{2+} in the downstream volume (Bergsten, 1995; Bergsten 1998; Bergsten and Hellman, 1993; Bergsten *et al.*, 1994; Longo *et al.*, 1991). There are several choices for fluorescent indicators of Zn^{2+}: for example, FluoZin-3 (Gee *et al.*, 2002) and ZynPyr-4 (Burdette *et al.*, 2003) have dissociation constants well below the anticipated output concentration of Zn^{2+}. With mixing and observation of the fluorescent response performed on chip, our method should yield immediate quantitative analysis of insulin (Zn^{2+}) secretion from individual pancreatic islets.

The role of the ECM in modulation of β-cell proliferation in pancreatic islets can also be investigated using microfluidic devices to manipulate the islet microenvironment. Although not normally considered proliferative, β-cells are stimulated to grow and divide to compensate for insulin resistance or changes in body mass. One striking example is the compensatory increase of β-cell mass observed in the mother during a normal pregnancy. Pancreatic islets are vascularized *in vivo* such that each β-cell is associated with a vascular endothelial cell (Cabrera *et al.*, 2006) that deposits ECM (Nikolova *et al.*, 2006). Specific interaction of human β-cells with the ECM is mediated by the integrins, including $\alpha_V\beta_5$, $\alpha_V\beta_1$, and $\alpha_1\beta_1$ (Kaido *et al.*, 2004). The importance of these interactions has been shown *ex vivo* by the capacity of laminin-rich matrices to down-regulate β-cell fibroblast growth factor receptor-1 activity (Kilkenny and Rocheleau, 2008), facilitate islet formation (Bonner-Weir *et al.*, 2000), maintain insulin secretion (Kaido *et al.*, 2006; Parnaud *et al.*, 2006), and amplify insulin secretion in response to secretagogues (Bosco *et al.*, 2000). Conversely, the culture of human β-cells on Collagen IV (Col IV) suppresses insulin production (Kaido *et al.*, 2006). Therefore, laminin appears to provide a permissive environmental signal for β-cell differentiation, whereas Col IV initiates dedifferentiation and/or proliferation. We plan to adapt our microfluidic chambers to pattern the deposition of various ECM molecules around islets (Chang and Hoying, 2006) and to measure their physiological responses to these manipulations.

Ackowledgments

J.V.R. was supported by an NIH career development award (DK68206). This work was also supported by an NIH grant (DK53434) to D.W.P. Confocal and widefield imaging was performed in part through the use of the VUMC Cell Imaging Shared Resource (supported by NIH grants CA68485, DK58404, HD15052, DK59637, and EY08126).

References

Aslanidi, O. V., Mornev, O. A., Skyggebjerg, O., Arkhammar, P., Thastrup, O., Sorensen, M. P., Christiansen, P. L., Conradsen, K., and Scott, A. C. (2001). Excitation wave propagation as a possible mechanism for signal transmission in pancreatic islets of Langerhans. *Biophys. J.* **80,** 1195–1209.

Aslanidi, O. V., Mornev, O. A., Vesterager, M., Sorensen, M. P., and Christiansen, P. L. (2002). A model for glucose-induced wave propagation in pancreatic islets of Langerhans. *J. Theor. Biol.* **215,** 273–286.

Atwater, I., Goncalves, A., Herchuelz, A., Lebrun, P., Malaisse, W. J., Rojas, E., and Scott, A. (1984). Cooling dissociates glucose-induced insulin release from electrical activity and cation fluxes in rodent pancreatic islets. *J. Physiol.* **348,** 615–627.

Beebe, D. J., Mensing, G. A., and Walker, G. M. (2002). Physics and applications of microfluidics in biology. *Annu. Rev. Biomed. Eng.* **4,** 261–286.

Bennett, B. D., Jetton, T. L., Ying, G., Magnuson, M. A., and Piston, D. W. (1996). Quantitative subcellular imaging of glucose metabolism within intact pancreatic islets. *J. Biol. Chem.* **271,** 3647–3651.

Bergsten, P. (1995). Slow and fast oscillations of cytoplasmic Ca^{2+} in pancreatic islets correspond to pulsatile insulin release. *Am. J. Physiol.* **268,** E282–E287.

Bergsten, P. (1998). Glucose-induced pulsatile insulin release from single islets at stable and oscillatory cytoplasmic Ca^{2+}. *Am. J. Physiol.* **274,** E796–E800.

Bergsten, P., and Hellman, B. (1993). Glucose-induced amplitude regulation of pulsatile insulin secretion from individual pancreatic islets. *Diabetes* **42,** 670–674.

Bergsten, P., Grapengiesser, E., Gylfe, E., Tengholm, A., and Hellman, B. (1994). Synchronous oscillations of cytoplasmic Ca^{2+} and insulin release in glucose-stimulated pancreatic islets. *J. Biol. Chem.* **269,** 8749–8753.

Bergsten, P., Westerlund, J., Liss, P., and Carlsson, P. O. (2002). Primary *in vivo* oscillations of metabolism in the pancreas. *Diabetes* **51,** 699–703.

Blundell, T. L., Cutfield, J. F., Cutfield, S. M., Dodson, E. J., Dodson, G. G., Hodgkin, D. C., and Mercola, D. A. (1972). Three-dimensional atomic structure of insulin and its relationship to activity. *Diabetes* **21,** 492–505.

Bonner-Weir, S., Taneja, M., Weir, G. C., Tatarkiewicz, K., Song, K. H., Sharma, A., and O'Neil, J. J. (2000). *In vitro* cultivation of human islets from expanded ductal tissue. *Proc. Natl. Acad. Sci. USA* **97,** 7999–8004.

Bosco, D., Meda, P., Halban, P. A., and Rouiller, D. G. (2000). Importance of cell-matrix interactions in rat islet beta-cell secretion *in vitro*: Role of alpha6beta1 integrin. *Diabetes* **49,** 233–243.

Burdette, S. C., Frederickson, C. J., Bu, W., and Lippard, S. J. (2003). ZP4, an improved neuronal Zn^{2+} sensor of the Zinpyr family. *J. Am. Chem. Soc.* **125,** 1778–1787.

Cabrera, O., Berman, D. M., Kenyon, N. S., Ricordi, C., Berggren, P. O., and Caicedo, A. (2006). The unique cytoarchitecture of human pancreatic islets has implications for islet cell function. *Proc. Natl. Acad. Sci. USA* **103,** 2334–2339.

Chang, C. C., and Hoying, J. B. (2006). Directed three-dimensional growth of microvascular cells and isolated microvessel fragments. *Cell Transplant* **15,** 533–540.

Emdin, S. O., Dodson, G. G., Cutfield, J. M., and Cutfield, S. M. (1980). Role of zinc in insulin biosynthesis. Some possible zinc-insulin interactions in the pancreatic B-cell. *Diabetologia* **19,** 174–182.

Foster, M. C., Leapman, R. D., Li, M. X., and Atwater, I. (1993). Elemental composition of secretory granules in pancreatic islets of Langerhans. *Biophys. J.* **64,** 525–532.

Gee, K. R., Zhou, Z. L., Qian, W. J., and Kennedy, R. (2002). Detection and imaging of zinc secretion from pancreatic beta-cells using a new fluorescent zinc indicator. *J. Am. Chem. Soc.* **124,** 776–778.

Gold, G., and Grodsky, G. M. (1984). Kinetic aspects of compartmental storage and secretion of insulin and zinc. *Experientia* **40,** 1105–1114.

Kaido, T., Yebra, M., Cirulli, V., and Montgomery, A. M. (2004). Regulation of human beta-cell adhesion, motility, and insulin secretion by collagen IV and its receptor alpha1beta1. *J. Biol. Chem.* **279,** 53762–53769.

Kaido, T., Yebra, M., Cirulli, V., Rhodes, C., Diaferia, G., and Montgomery, A. M. (2006). Impact of defined matrix interactions on insulin production by cultured human beta-cells: Effect on insulin content, secretion, and gene transcription. *Diabetes* **55,** 2723–2729.

Kilkenny, D. M., and Rocheleau, J. V. (2008). Fibroblast growth factor receptor-1 signaling in pancreatic islet β-cells is modulated by the extracellular matrix. *Mol. Endocrinol.* **22,** 196–205.

Longo, E. A., Tornheim, K., Deeney, J. T., Varnum, B. A., Tillotson, D., Prentki, M., and Corkey, B. E. (1991). Oscillations in cytosolic free Ca^{2+}, oxygen consumption, and insulin secretion in glucose-stimulated rat pancreatic islets. *J. Biol. Chem.* **266,** 9314–9319.

McDonald, J. C., Duffy, D. C., Anderson, J. R., Chiu, D. T., Wu, H., Schueller, O. J., and Whitesides, G. M. (2000). Fabrication of microfluidic systems in poly(dimethylsiloxane). *Electrophoresis* **21,** 27–40.

Melin, J., and Quake, S. R. (2007). Microfluidic large-scale integration: The evolution of design rules for biological automation. *Annu. Rev. Biophys. Biomol. Struct.* **36,** 213–231.

Michael, D. J., Ritzel, R. A., Haataja, L., and Chow, R. H. (2006). Pancreatic beta-cells secrete insulin in fast- and slow-release forms. *Diabetes* **55,** 600–607.

Nadal, A., Quesada, I., and Soria, B. (1999). Homologous and heterologous asynchronicity between identified alpha-, beta- and delta-cells within intact islets of Langerhans in the mouse. *J. Physiol.* **517** (Pt 1), 85–93.

Newgard, C. B., and McGarry, J. D. (1995). Metabolic coupling factors in pancreatic beta-cell signal transduction. *Annu. Rev. Biochem.* **64,** 689–719.

Nikolova, G., Jabs, N., Konstantinova, I., Domogatskaya, A., Tryggvason, K., Sorokin, L., Fassler, R., Gu, G., Gerber, H. P., Ferrara, N., Melton, D. A., and Lammert, E. (2006). The vascular basement membrane: A niche for insulin gene expression and Beta cell proliferation. *Dev. Cell* **10,** 397–405.

Parnaud, G., Hammar, E., Rouiller, D. G., Armanet, M., Halban, P. A., and Bosco, D. (2006). Blockade of beta1 integrin-laminin-5 interaction affects spreading and insulin secretion of rat beta-cells attached on extracellular matrix. *Diabetes* **55,** 1413–1420.

Patterson, G. H., Knobel, S. M., Arkhammar, P., Thastrup, O., and Piston, D. W. (2000). Separation of the glucose-stimulated cytoplasmic and mitochondrial NAD(P)H responses in pancreatic islet beta cells. *Proc. Natl. Acad. Sci. USA* **97,** 5203–5207.

Piston, D. W., and Knobel, S. M. (1999a). Quantitative imaging of metabolism by two-photon excitation microscopy. *Meth. Enzymol.* **307,** 351–368.

Piston, D. W., and Knobel, S. M. (1999b). Real-time analysis of glucose metabolism by microscopy. *Trends Endocrinol. Metab.* **10,** 413–417.

Piston, D. W., Knobel, S. M., Postic, C., Shelton, K. D., and Magnuson, M. A. (1999). Adenovirus-mediated knockout of a conditional glucokinase gene in isolated pancreatic islets reveals an essential role for proximal metabolic coupling events in glucose-stimulated insulin secretion. *J. Biol. Chem.* **274,** 1000–1004.

Qian, W. J., and Kennedy, R. T. (2001). Spatial organization of Ca(2+) entry and exocytosis in mouse pancreatic beta-cells. *Biochem. Biophys. Res. Commun.* **286,** 315–321.

Qian, W. J., Gee, K. R., and Kennedy, R. T. (2003). Imaging of Zn^{2+} release from pancreatic beta-cells at the level of single exocytotic events. *Anal. Chem.* **75,** 3468–3475.

Roche, M. E., Anderson, M. A., Oda, R. P., Riggs, B. L., Strausbauch, M. A., Okazaki, R., Wettstein, P. J., and Landers, J. P. (1998). Capillary electrophoresis of insulin-like growth factors: Enhanced ultraviolet detection using dynamically coated capillaries and on-line solid-phase extraction. *Anal. Biochem.* **258,** 87–95.

Rocheleau, J. V., Head, W. S., Nicholson, W. E., Powers, A. C., and Piston, D. W. (2002). Pancreatic islet beta-cells transiently metabolize pyruvate. *J. Biol. Chem.* **277,** 30914–30920.

Rocheleau, J. V., Head, W. S., and Piston, D. W. (2004a). Quantitative NAD(P)H/flavoprotein autofluorescence imaging reveals metabolic mechanisms of pancreatic islet pyruvate response. *J. Biol. Chem.* **279,** 31780–31787.

Rocheleau, J. V., Walker, G. M., Head, W. S., McGuinness, O. P., and Piston, D. W. (2004b). Microfluidic glucose stimulation reveals limited coordination of intracellular Ca^{2+} activity oscillations in pancreatic islets. *Proc. Natl. Acad. Sci. USA* **101,** 12899–12903.

Rocheleau, J. V., Remedi, M. S., Granada, B., Head, W. S., Koster, J. C., Nichols, C. G., and Piston, D. W. (2006). Critical role of gap junction coupled KATP channel activity for regulated insulin secretion. *PLOS Biol.* **4,** e26.

Roper, M. G., Shackman, J. G., Dahlgren, G. M., and Kennedy, R. T. (2003). Microfluidic chip for continuous monitoring of hormone secretion from live cells using an electrophoresis-based immunoassay. *Anal. Chem.* **75,** 4711–4717.

Scharp, D. W., Kemp, C. B., Knight, M. J., Ballinger, W. F., and Lacy, P. E. (1973). The use of ficoll in the preparation of viable islets of Langerhans from the rat pancreas. *Transplantation* **16,** 686–689.

Schultz, N. M., Huang, L., and Kennedy, R. T. (1995). Capillary electrophoresis-based immunoassay to determine insulin content and insulin secretion from single islets of Langerhans. *Anal. Chem.* **67,** 924–929.

Sia, S. K., and Whitesides, G. M. (2003). Microfluidic devices fabricated in poly(dimethylsiloxane) for biological studies. *Electrophoresis* **24,** 3563–3576.

Stefan, Y., Meda, P., Neufeld, M., and Orci, L. (1987). Stimulation of insulin secretion reveals heterogeneity of pancreatic B cells *in vivo*. *J. Clin. Invest.* **80,** 175–183.

Unger, R. H. (1981). The milieu interieur and the islets of Langerhans. *Diabetologia* **20,** 1–11.

Walker, G. M., Mensing, G. A., and Beebe, D. J. (2002). Physics and applications of microfluidics in Biology. *Ann. Rev. Biomed. Eng.* **4,** 261–286.

Walker, G. M., Zeringue, H. C., and Beebe, D. J. (2004). Microenvironment design considerations for cellular scale studies. *Lab Chip* **4,** 91–97.

Wu, L., Nicholson, W., Knobel, S. M., Steffner, R. J., May, J. M., Piston, D. W., and Powers, A. C. (2004). Oxidative stress is a mediator of glucose toxicity in insulin-secreting pancreatic islet cell lines. *J. Biol. Chem.* **279,** 12126–12134.

CHAPTER 5

Imaging in Depth: Controversies and Opportunities

Don O'Malley

Department of Biology
Northeastern University
Boston, Massachusetts 02115

METHODS IN CELL BIOLOGY, VOL. 89

0091-679X/08 $35.00
DOI: 10.1016/S0091-679X(08)00605-5

Abstract

One enduring challenge of biological imaging is achieving *depth of penetration*—into cells, tissues, and animals. How deeply can we probe and with what resolution and efficacy? These are critical issues as microscopists seek to push ever deeper, while resolving structural details and observing specific molecular events. In this guide to depth-appropriate modalities, standard optical platforms such as confocal and two-photon microscopes are considered along with complementary imaging modalities that range in depth of penetration. After an introduction to basic techniques, the trade-offs and limitations that distinguish competing technologies are considered, with emphasis on the visualization of subcellular structures and dynamic events. Not surprisingly, there are differences of opinion regarding imaging technologies, as highlighted in a section on point-scanning and Nipkow-disk style confocal microscopes. Confocal microscopy is then contrasted with deconvolution and multi-photon imaging modalities. It is also important to consider the detectors used by current instruments (such as PMTs and CCD cameras). Ultimately specimen properties, in conjunction with instrumentation, determine the depth at which subcellular operations and larger-scale biological processes can be visualized. Relative advantages are mentioned in the context of experiment planning and instrument-purchase decisions. Given the rate at which new optical techniques are being invented, this report should be viewed as a snapshot of current capabilities, with the goal of providing a framework for thinking about new developments.

I. Introduction

Biological imaging spans the scale from atomic-level, cryoEM reconstructions to whole-animal imaging (not counting satellite imaging of ecosystems!). Ultimately, the goal is to look deeply, dynamically, and with molecular specificity. While this "holy grail" remains elusive, the nexus of new tools and probes is producing remarkable gains. With the advent of genetic tools for the manipulation and imaging of cells, tissues, and animals (Bhaumik and Gambhir, 2002; Cubitt *et al*., 1995; Higashijima *et al*., 2000; Nasevicius and Ekker, 2000; Perkins *et al*., 2002), light microscopy has been delving into myriad new frontiers. Biologists are able to image living specimens more deeply and with greater resolution by employing an increasingly powerful range of tools and technologies (Beis and Stainier, 2006; Cox *et al*., 2000; Denk and Svoboda, 1997; Gahtan and Baier, 2004; Göbel *et al*., 2007; Holtmaat *et al*., 2005; Iyer *et al*., 2006; Jontes *et al*., 2000; Kerr *et al*., 2005; Kuo *et al*., 2007; Livet *et al*., 2007; O'Malley *et al*., 2003; Orger *et al*., 2008; Shcherbo *et al*., 2007). Which technique should be chosen, however, and which specific instrument should be employed, depend critically upon the experimental question being asked. This guide mentions a broad range of important techniques,

but the focus is on a smaller set of imaging modalities and their defining features, including instrumentation particulars and the underlying optical physics. Techniques are emphasized that provide details at the molecular, subcellular, and cellular levels, often within the context of larger cell assemblies inside living animals. By such imaging methods and optical manipulations, structures and processes previously occult to biologists can now be grasped. These technologies are ordered along the dimension of depth of penetration. Experimental results that illuminate key capabilities of these different imaging options are emphasized. While there are many powerful imaging modalities, this guide will focus mainly on three: confocal, two-photon, and deconvolution microscopy. But before getting into the depths of biological imaging, some mention of the visualization techniques used at the finest scales of biological structure is in order.

A. Imaging at the Atomic Level

At the nanometer scale, molecules and even individual atoms can be imaged and often resolved using atomic force microscopy (AFM) and/or electron microscopy (EM). AFM is one of a number of "near-field" imaging techniques where a mechanical imaging probe comes into contact with a sample (Ando *et al*., 2007; Frankel *et al*., 2006; Hansma and Hoh, 1994; Kellermayer *et al*., 2006). X-ray diffraction and cryoEM techniques provide atomic-scale views into the structure of macromolecules (see, e.g., Frangakis and Förster, 2004; Jiang and Ludtke, 2005; Koster and Klumperman, 2003; Wu *et al*., 2000), but they also pose significant demands in terms of sample purification and preparation, and are generally not suitable for live specimen imaging (but see Ackerley *et al*., 2006). While the near-field techniques examine surface structures via different means of probe–sample interaction, they are depth-limited, in general terms, to the surface of the sample—often the plasma membrane of a cell. In particular, AFM provides high-resolution views of biological surfaces such as the upper membrane of cells cultured in monolayers. A complementary technique, total internal reflectance fluorescence microscopy (TIRF), produces a detailed "bottom view" in that the specimen is typically resting on a coverslip and viewed from below. TIRF examines a region that extends for 100 nm or so into the tissue adjacent to the coverslip (Axelrod, 2003). Collectively these techniques provide fine molecular-level and/or topographic details of biological structures, which are necessary for piecing together the higher-level functioning of cells. Tissues and organisms, however, are thicker conglomerates of molecular devices and cell assemblies. To understand the organization and physiology of these structures one needs to image in greater depth and with resolution sufficient to characterize the biological processes of interest. In this guide, consideration is given to the range of optical tools and imaging approaches that can be employed across the scale of "depths" at which one would like to probe biological structures.

II. Basic Imaging Methodologies

A. Light and Fluorescence Microscopy

Light microscopy has myriad applications across the realms of biology, biotechnology, and medicine. Staining techniques are the staple of clinical histology labs (Bancroft and Gamble, 2001), illustrating the ageless value of the workhorse of biological imaging, the compound light microscope. Past innovations in light microscopy included phase contrast and differential interference contrast (DIC), both of which allow unstained (including living) specimens to be seen in far better detail due to enhanced contrast (Cox, 2007; Sluder and Wolf, 2007). With fluorescence techniques, one has the ability to visualize structures with molecular specificity using both traditional fluorophores (Taylor and Salmon, 1989) and genetically encoded fluorophores (Cubitt *et al*., 1995; Lippincott-Schwartz and Patterson, 2003; Shcherbo *et al*., 2007). The conjunction of fluorescent probe advances and newer imaging modalities (such as confocal and two-photon) is at the heart of the biological imaging revolution of the past 20 years. Adding to this imaging frenzy are higher-resolution light-microscopic techniques that improve spatial resolution well beyond the Abbé diffraction limit (Egner *et al*., 2002a; Hell, 2007). One technique called STORM relies on the photoswitching of fluorophores to achieve nanometer scale resolution (Rust *et al*., 2006). Perhaps the most advanced of these techniques is stimulated emission-depletion (STED) (Hell and Wichmann, 1994), which enables the resolution of nanometer scale structures within fluorescently labeled cells (also see article by S. Hess, this volume). STED has been effectively employed in double-labeling experiments (Donnert *et al*., 2007a), and has also revealed the dynamics of syntaxin protein clusters in living cells (Sieber *et al*., 2007; Willig *et al*., 2006). This was accomplished using a custom stage-scanning microscope, but if this approach becomes more widely available, it offers perhaps the highest resolution for imaging structures throughout the three-dimensional (3D) thickness of living cells. At present, the extent to which such "super-resolution" techniques can be pushed deeper into living tissues and intact animals is unclear.

B. TIRF Microscopy

Of the optical imaging techniques, TIRF is at the bottom of the depth-of-penetration list, both figuratively and literally. TIRF depends upon acute angular illumination of (usually) the bottom of a coverslip such that (1) all of the incident illumination is reflected off the interface and (2) the only illumination of the sample is due to the penetration of an evanescent wave through the coverslip and into the sample (reviewed by Axelrod, 2003; also see Axelrod, this volume). This limits TIRF illumination to a depth of roughly 100 nm, that is to just a small fraction of the thickness of a eukaryotic cell. What TIRF gains in return is the ability to better visualize near-surface structures and attachments to the substrate, which are of

interest in multiple areas of biomedical research (see, e.g., Bos and Kleijn, 1995; Ferko *et al.*, 2007; Lassen and Malmsten, 1996; Partridge and Marcantonio, 2006; Reichert and Truskey, 1990). While AFM and TIRF are wholly unrelated techniques, they both provide perimembrane views of the cell (from the top and bottom surfaces, respectively). AFM's mechanical approach is in some fashion "rougher" than the gentler touch of TIRF's photons, but more important is their complementary nature: TIRF, like other fluorescence modalities, offers potentially tremendous molecular specificity (determined by the specificity of the fluorescent probe), whereas AFM provides general structural context. In addition, TIRF can visualize dynamic events occurring just under the membrane such as the docking and fusion of secretory granules (Ohara-Imaizumi *et al.*, 2004). Because TIRF penetrates so shallowly into the cell, this gives it a very thin optical section—perhaps the thinnest of any optical technique.

C. DIC Microscopy

In contrast to TIRF and AFM, DIC imaging offers the ability to look through cells and groups of cells, and depending on size and opacity, through whole living organisms. Working with unstained specimens, it generates contrast that can be greatly enhanced via analog and/or digital signal processing (Salmon and Tran, 1998; Sluder and Wolf, 2007). DIC also produces better resolution than the more commonly available *phase contrast* imaging modality because of the higher numerical aperture of DIC illumination; see Cox (2007) for a succinct explanation of these imaging modalities. In regards to DIC's depth of penetration, it is similarly susceptible to influences that hinder conventional bright field and fluorescence microscopy, variously: opacity, turbidity, or light scattering. Nonetheless, DIC is useful for a variety of specimens including unstained cells, tissue sections, and living animals (Dahm *et al.*, 2007). One modification that improved the useful depth of DIC imaging was the use of infrared (IR) illumination (Dodt and Zieglgansberger, 1990). The greater penetration of IR light into biological tissues has led to its widespread use in electrophysiological experiments on brain slices (Bagnall *et al.*, 2007; Jagger and Housley, 2003; Stuart *et al.*, 1993; Wang *et al.*, 2003).

The ultimate depths attained with DIC vary based upon both specimen characteristics and the specific details of the DIC implementation. While suitable imaging details were initially reported for depths of 50–100 μm in rat brain slices (Stuart *et al.*, 1993), cell bodies may be visualized with IR-DIC up to 200 μm deep. Attention to such details as (1) perfusion of the animal with ice-cold saline prior to dissection, (2) choice of camera (e.g., Dage IR-1000), and (3) viewing method, for example via direct connection of the camera to a black and white TV monitor, can make a big difference in the ultimate performance of IR-DIC (Peter Saggau, personal communication). While such depths attained by DIC rival or even surpass those attainable with confocal microscopy, this would be situation dependent. A very bright GFP-labeled cell may be detected (in slices of rat brainstem), even with conventional fluorescence optics, at depths deeper than those where DIC is

able to reveal the structural details necessary for visually guided patch clamping (C-J. Yu and J. Gnadt, personal communication). Under favorable conditions, DIC does produce the finest optical sectioning capability of any "whole-cell" imaging approach, with an optical section thickness as narrow as 0.3 μm. The only method that produces superior whole-cell, z-axis image resolution is the physical cutting of very thin sections, which can then be stained and viewed by various imaging modalities, including light and electron microscopy.

Earlier we related AFM to TIRF as conveying structural details versus molecular specificity in regards to the specimen's surface. A similar relationship exists between confocal microscopy (discussed below) and DIC wherein both are able to look through cells (and deeper into tissues) while providing complementary details: structural for DIC, molecular for confocal fluorescence images. DIC is often the method of choice for unstained specimens (see, e.g., Concha and Adams, 1998; Dahm *et al.*, 2007) and it is often possible to record the same microscopic field of view with both DIC and confocal. As such, DIC can provide structural context within which to interpret fluorescent objects. But there can be issues if one wishes to acquire both DIC and fluorescence images without switching microscope objectives. While Nomarski-style DIC objectives are preferable in this respect, there is still significant loss of the fluorescence signal. One may encounter further complications with fiber-coupled confocal microscopes due to the varying ellipticity of polarization of laser light (Amos *et al.*, 2003). In instances where the DIC and confocal images cannot be suitably obtained with a single microscope objective, it then becomes necessary to rotate the microscope's objective turret. Because high-resolution imaging is often done with immersion objectives (e.g., oil or water), it is not trivial to swap objectives while maintaining a precisely registered field of view, so one should ascertain that both imaging modalities can be acquired together if image registration is important.

There are other developments in this area (Cody *et al.*, 2005). One promising approach is differential phase contrast (DPC) microscopy, which is more compatible with confocal imaging and requires less illumination than DIC, but DPC has not achieved much attention, perhaps because the specimen cannot be directly viewed as it can with DIC (Amos *et al.*, 2003). While the different nuances discussed above may seem esoteric, they can critically shape the options available to investigators. Such issues are especially important when it comes to the purchase of expensive instruments by individual researchers or by core facilities. In proceeding through the next set of imaging modalities, such nuances are highlighted while addressing some of the opportunities, trade-offs, and controversies that swirl in the winds of the biological imaging frontier.

III. Forays Deeper into Depth

To understand how confocal imaging (described in the next section) and other techniques have extended our view deeper into biological structures, we should first provide some important context. For starters, depth of penetration is entirely

contingent upon the optical properties of the specimen—how transparent, scattering, or opaque it is (Oheim *et al*., 2001). With basic light microscopy, one might see entirely through tissues and even whole animals—depending on transparency (or translucency). In the case of zebrafish, one can see entirely through an embryo or larva with basic light and fluorescence microscopy. This transparency was a major factor in the organism's skyrocketing popularity over the past 15 years leading to its current entrenchment as a model organism in developmental genetics, neuroscience, and other areas (Detrich *et al*., 2004). Conversely, the skull of mammals is so opaque that one can resolve little or no cellular detail within the cerebral cortex without first drilling holes. The opacity of brain tissue is itself variable depending both upon species (Cinelli, 2000) and upon age (Oheim *et al*., 2001). Embryonic and neonatal rat thalamic slices, for example, are more easily peered into (with confocal) than are slices from adult rats (Zhou *et al*., 1997). In the case of larval zebrafish, confocal imaging reveals synaptic-level details throughout the brain and spinal cord (Fetcho and O'Malley, 1995; Gahtan and O'Malley, 2003). This variability seems related to myelination and perhaps explains our ability to resolve fine neural structures throughout the 300 μm thickness of the larval zebrafish brain—while seeing little cellular detail 80 μm deep into an adult rat brain slice, even with confocal. Why brain translucency is so variable is not well defined, but even in the case of zebrafish, transparency is relative: Mutant lines have been made such as *nacre*, in which the larvae are almost glass-like in appearance (Lister *et al*., 1999; O'Malley *et al*., 2004).

So does one need a confocal microscope to look through the CNS of larval zebrafish? Not surprisingly, it depends on what one wishes to see. In a transgenic zebrafish line where the rod photopigment rhodopsin has been fused with green fluorescent protein, the now fluorescent photoreceptors are easily visualized in anesthetized larvae using a fluorescence dissecting microscope (Fig. 1A and B). The individual photoreceptors are not easily resolved (or counted) with the dissecting microscope, but with confocal (Fig. 1C–F), individual photoreceptors and subcellular details are resolved including the banding pattern of the GFP-rhodopsin protein in the outer segments (arrows in Fig. 1F). The instrumentation required thus depends upon the specific experimental needs: Fluorescence dissecting microscopes are becoming increasingly popular in the zebrafish community for screening embryos and larvae for fluorescence labeling (during genetic screens) and for taking low-resolution (but often deep-tissue) pictures. Conventional wide-field fluorescence microscopy can also be used for imaging neurons in larval zebrafish, but confocal microscopy becomes necessary for resolving the fine anatomical details needed to identify individual neurons in the larval spinal cord (Fetcho and O'Malley, 1995; Fetcho *et al*., 1998; Hale *et al*., 2001) and brainstem (Gahtan *et al*., 2002; O'Malley *et al*., 1996, 2003).

When it comes to mammalian brains, and many other animal tissues, the imaging conditions become less clear. The two-photon (or multi-photon) imaging technique (discussed below) often becomes necessary and David Piston speaks of a "6-fold rule" meaning that one can obtain comparable structural detail sixfold

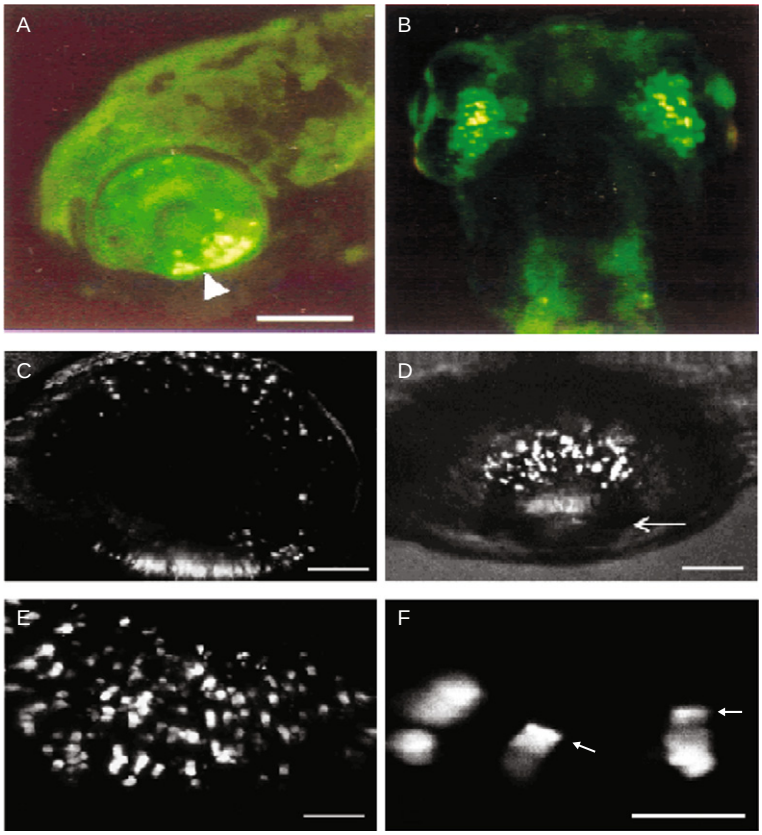

Fig. 1 Photoreceptors in anesthetized zebrafish. Images are from transgenic larvae expressing GFP-rhodopsin fusion protein. (A, B) Fluorescent rod photoreceptors in ventral retina (arrowhead) are easily viewed using a fluorescence dissecting microscope. Confocal maximum projection images (C–F) show photoreceptors at higher resolution, revealing banding patterns in rod outer segments (arrows in F). Arrow in (D) shows location of lens. Scale bars = 150 μm (A, B); 50 μm (C, D); 25 μm (E); and 10 μm in (F). Reprinted with permission from *Visual Neuroscience* (from Perkins *et al.*, 2002).

deeper with two-photon microscopes than with confocal microscopy; this is nicely illustrated using comparison confocal and two-photon images from shark choroid plexus (Piston, 2005). While an assortment of macroscopic imaging modalities enable peering through the entire bodies of animals (both small and large), two-photon represents the method of choice for resolving microscopic details *in vivo*. But two-photon is also the most expensive microscopic imaging modality and is often not available, so it is important to consider what one can do with the more widely available confocal methods, as well as with deconvolution methods that are available to anyone with a digital fluorescence microscope and an internet connection (Majewska *et al.*, 2000).

A. Confocal Microscopy: Basics

Confocal microscopy is (most commonly) a variant of fluorescence microscopy in which a simple optical trick is used to collect light from a narrow slice or ''optical section'' through a sample such as a cultured cell or intact animal. By selecting for photons that originate from a given focal plane, it provides superior resolution at tissue depths where wide-field fluorescence images become quite blurry. Confocal microscopic imaging was invented by Marvin Minsky in 1955 in his efforts to see more clearly the organization of the brain (Minsky, 1988). In trying to understand how to better resolve details of neural circuits from within brain tissue, Minsky reasoned that if one illuminated just a small point in a sample using a first pinhole in the illumination path (this is done more effectively today with lasers) and then collected light only from that point, using a second pinhole aperture in the image transmission path, then one could extract an optical section from a biological specimen. This ''double-focusing'' mechanism is described more familiarly today as the use of pinhole apertures in CONjugate FOCAL planes, wherein the term ''confocal'' actually derives (Sheppard and Choudhury, 1977). This is indeed the key element that defines the operation of the confocal microscope. Previously pinhole apertures had been used in spectroscopic studies (Naora, 1955), but Minsky was able to build a working (albeit crude) confocal microscope, in part by using a military surplus long-persistence radar scope.

The confocal technique enables acquisition of much narrower optical sections or optical slices through a specimen than is possible with wide-field (conventional) fluorescence microscopy. This allows one to peer deeper into tissues (within limits) and to pull detailed structures out of a fluorescent blur. The realization of commercially successful confocal imaging systems, however, would not occur until well into the 1980's. The Olympus Corporation web site (www.olympusfluoview.com) has put it thus: ''Fortuitously, shortly after Minsky's patent had expired, practical laser-scanning confocal microscope designs were translated into working instruments by several investigators.'' While the fortuitousness of this timing is perhaps subjective, the widespread commercialization of confocal technology depended upon the availability of computing systems both to control the instruments and to efficiently collect and utilize the large amounts of data generated. A far more detailed explanation of confocal microscopy is provided by the highly regarded Handbook of Biological Confocal Microscopy (Pawley, 2006); the historical realization of this instrument is described by Amos and White (2003).

B. Confocal Microscopy: Competing Designs

In Minsky's original design, the specimen was scanned under the light source; this was also done in some of the earliest confocal images of biological specimens (Brakenhoff, 1979; Brakenhoff *et al*., 1985; Valkenburg *et al*., 1985), but the most common confocal instrument is referred to variously as a point-scanning, line-scanning or laser-scanning confocal microscope. Here, a diffraction-limited spot

from a laser beam is raster scanned across the specimen, building up an image point by point as the signal is detected by a photomultiplier tube (PMT). Even with rapid scanning mirrors, this process takes sufficient time as to pose trade-offs. This is indeed the most crucial difference between point-scanning confocals and their biggest competitor, the spinning-disk confocal which scans many points simultaneously and records data in parallel onto a CCD camera. While either variant works well for many applications, each has distinctive features that become magnified in the context of purchasing decisions. A third model is the "slit scanning" confocal which rapidly acquires images that are "confocal" along one dimension within the *xy* plane (Bembenek *et al*., 2007; Gasparini *et al*., 2007). A further variant is reflectance confocal which uses reflected rather than fluorescence light to perform confocal sectioning. Reflectance confocal is frequently used in clinical and preclinical applications (see, e.g., Collier *et al*., 2007; Dwyer *et al*., 2006; González and Tannous, 2002). More recently, spectral scanning has been employed to enable finer spectral resolution of signals emanating from the sample (reviewed in Dickinson *et al*., 2001; Zimmermann *et al*., 2003). Despite the many options available, point scanning and spinning disk are the confocal platforms most commonly used. They also provide a convenient framework within which to consider the performance limits of confocal microscopy.

Spinning-disk confocals (also known as Nipkow-disk or disk-scanning confocals) scan many points at once in a spiral pattern and can thus obtain 2D images of large areas considerably faster than point-scanning instruments. An ensuing and quite practical feature is that one can directly view the specimen when using such spinning-disk confocals. In contrast, on point-scanning confocals, the specimen is viewed on a TV or computer monitor. Spinning-disk models, however, have a significant drawback in that they lack a continuously adjustable aperture at the emission pinhole. Since the earliest commercial confocals (such as the BioRad MRC500), point-scanning confocals have often had this feature, since there is only one pinhole to adjust. This facilitates the imaging of live specimens because the degree of optical sectioning can be traded away, to an arbitrary extent, in exchange for often dramatically increased signal. This option to adjust or "open" the pinhole aperture has often aided the visualization of dynamic physiological processes (see, e.g., O'Malley *et al*., 1996, 2003; O'Malley, 1994; Yu *et al*., 1994; Zhou *et al*., 1997). Because the greater signal passing through the open aperture may allow for a substantial reduction in the illumination intensity, this can reduce two of the most serious limiting factors in fluorescence microscopy—photodamage and photobleaching (Donnert *et al*., 2007b). With point scanners, once the physiological data are acquired, the aperture can be narrowed, and the laser intensity increased, to record finer anatomical details. In principle, the Nipkow-disk design might circumvent this limitation by providing a set of interchangeable disks with a good range of aperture settings. While there are efforts in this direction, the utility of such an approach remains to be documented.

The differences in confocal design come into play in a variety of confocal applications. For example, point-scanning instruments are easily employed in

diverse experiments where photo-manipulation is applied to precise locations on a biological specimen. Experiments in the area of FRAP (fluorescence recovery after photobleach; Braeckmans *et al.*, 2007; Klein *et al.*, 2003), photoactivation (Chudakov *et al.*, 2006), laser-ablation (Gahtan *et al.*, 2005; Liu and Fetcho, 1999), photoliberation (Korkotian *et al.*, 2004; Park *et al.*, 2001), and the optical control of neural activity (Wang *et al.*, 2007); all take advantage of the ability to direct the laser beam to specific regions or even a single point on the specimen. In the case of spinning-disk confocals, such applications are less common or may not be feasible. Point scanners also have an optical-zoom capability, where the specimen is sampled at higher magnification by scanning a smaller region of the sample. This is also useful in, for example, laser-ablation experiments where the full laser power can be directed into a small spot at the center of a target neuron (Liu and Fetcho, 1999; O'Malley *et al.*, 2003). Ultimately, the signal generated at a point on the specimen comes down to issues of pixel-dwell time, illumination intensity and emission-collection efficiency. In effect, both instrument types are doing the same thing, but with the spinning disk many points are scanned in parallel. The key issue, for many applications, is whether or not the benefits of parallel data-collection offset the lack of an easily adjustable pinhole aperture.

C. Dynamic Imaging with Confocal Microscopes

Researchers have used confocal microscopy to image calcium dynamics, other second messengers, protein diffusion, cell and organelle motility, cell division, and the growth of cellular processes such as neuronal axons and dendrites. Here, the speed of disk scanners is an apparent advantage, but given the fixed pinhole, photodamage, and photobleaching may become limiting because higher intensities may be needed to generate the signal necessary for dynamic tracking experiments. Conversely, when opening the pinhole aperture of point scanners, more signal is obtained (for a given intensity of illumination), but the accompanying loss of *z*-resolution may degrade the ability to follow the objects or structures of interest. While point scanners are slower to acquire full frame images, they collect smaller 2D images at physiologically relevant speeds and acquire 1D (line-scan) images very rapidly, as in some of the earliest confocal calcium imaging experiments where line-scans provided 2-ms temporal resolution and excellent 1D spatial resolution of nuclear and cytoplasmic calcium signals (Hernandez-Cruz *et al.*, 1990). This combined spatial–temporal resolution, in dynamic units of milliseconds×microns-squared (discussed in O'Malley *et al.*, 2003), may not be easily attainable with spinning-disk confocals. The utility of the line-scanning approach, however, depends on being able to obtain the desired experimental result with a spatially 1D image—an outcome that is frequently achieved (see examples below).

Ultimately, the basic interaction between light and sample is the same for point-scanning and spinning-disk instruments: The laser beam dwells on a pixel for some set amount of time, photons are absorbed, and signal photons are emitted. Faster acquisition with either line-scans or spinning-disk confocals does not alter this

fundamental interaction, nor does it minimize the intrinsically damaging nature of light. If the sample is not light sensitive, the faster 2D acquisition of pixels via spinning disks is clearly advantageous. But what is generally important is the "photodose cost" per unit signal obtained, and this is a direct function of pinhole aperture. The wider the confocal aperture, the lower the photodose (illumination) needed to deliver a given quantity of signal photons to the detector. Because scanning disk pinholes are usually set to optimize optical sectioning, they reject many photons that are collected during point-scanning experiments where the pinhole aperture has been opened to some extent. Such issues notwithstanding, spinning-disk confocals have been used to image many dynamic processes such as secretory granule movements and exocytosis (Varadi *et al*., 2002), neuronal cell death (Sun *et al*., 2001), phagocytotic infections (Chua and Deretic, 2004), lipid signal transduction (Blazer-Yost *et al*., 2004), cytoplasmic streaming (Serbus *et al*., 2005), and photoreceptor calcium dynamics (Cadetti *et al*., 2006). As documented in these varied examples, spinning-disk microscopy is useful in 3D and 4D (3D+time) applications, yet much of the fastest (millisecond resolution) cellular imaging has been accomplished via point scanning. We focus in the next section on calcium sparks—highly localized calcium responses that evolve on a millisecond time scale. These calcium sparks serve as a benchmark test of dynamic imaging performance.

Calcium sparks have been repeatedly visualized using point-scanning instruments, often in line-scan mode (see, e.g., Cheng *et al*., 1993; Hui *et al*., 2001; Lopez-Lopez *et al*., 1994; Parker *et al*., 1996; Wang *et al*., 2001). Spinning-disk confocals have been less frequently employed, but Lothar Blatter's group has used both a Yokogawa spinning-disk instrument and a Zeiss point-scanning instrument to visualize calcium sparks (Fig. 2; from Kockskamper *et al*., 2001). The 2D scanning disk images were collected at 17-ms intervals and were used to localize calcium release sites (Fig. 2A and B). Point-scanning confocal was then used to measure calcium events at multiple sites at 2 ms or better temporal acquisition speeds (Fig. 2C). This shows the complementary nature of these competing imaging modes. The rapid 2D imaging proved useful in visualizing the 2D distribution of calcium hot spots—which appear as a perimembrane ring. Recording of 1D line-scans, parallel to the cell's long edge, then yielded the best resolution of the hot-spots' temporal dynamics. Line-scans should be used with caution. For example, an apparent "variable amplitude" of calcium sparks can result from the scan line being offset slightly from the precise center of the calcium spark location (Pratusevich and Balke, 1996).

It should be noted that point scanners can do reasonably fast 2D imaging, as had been done earlier to visualize calcium influx rings in cultured neurons, with subsequent line-scanning used to precisely measure the flux of calcium ions across the nuclear envelope (O'Malley, 1994). The 2D images in most cases provide sufficient information to pick an appropriate location to conduct 1D line-scans (see Fig. 3 in O'Malley *et al*., 2003). Given their longer commercial availability, point-scanning instruments have (not surprisingly) a rich history of physiological

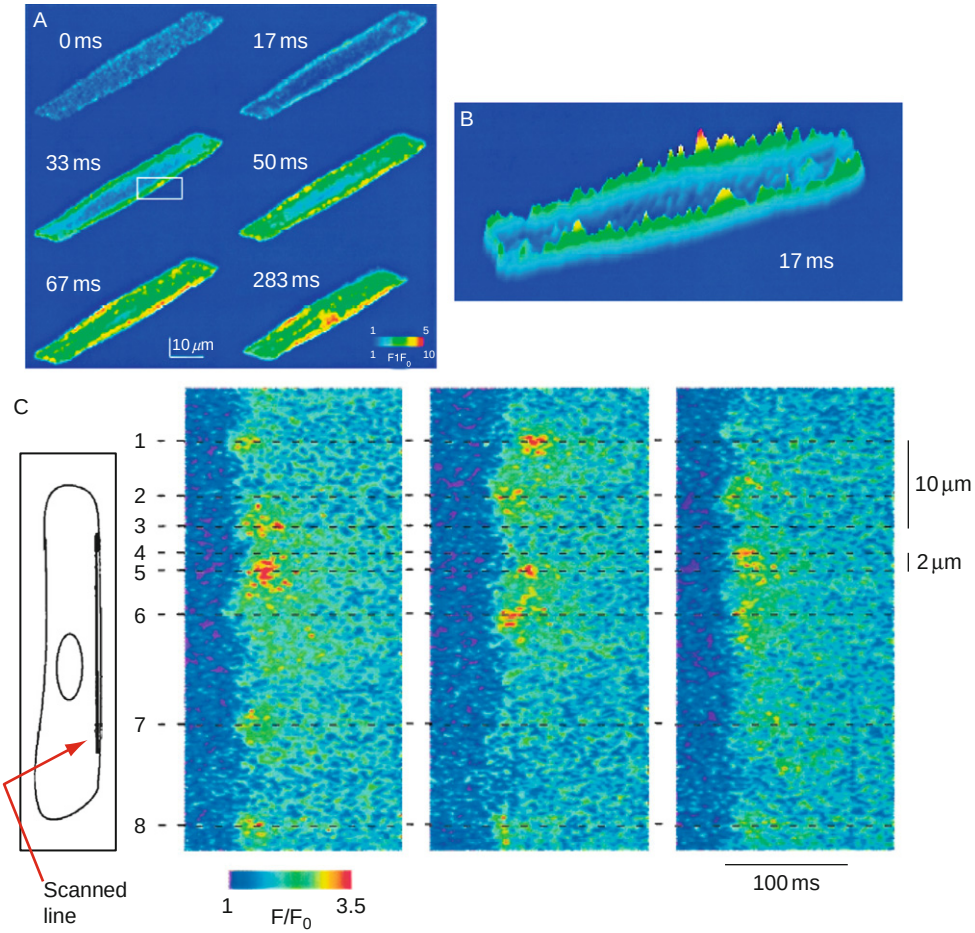

Fig. 2 *Spinning-Disk* and *Point-Scanning* confocal images of calcium sparks in atrial myocytes. (A) Spinning-disk images acquired at 60 frames/s show a ring of calcium influx at an early moment of an atrial action potential. (B) A surface plot of the calcium image at 17 ms shows calcium peaks in the sub-sarcolemmal space. (C) Line-scans oriented along the sub-sarcolemmal space provide a more detailed record of the temporal dynamics of the calcium sparks occurring at different locations. Reprinted with permission from the *Biophysical Journal* (from Kockskamper *et al.*, 2001).

imaging results (see, e.g., Cheng *et al.*, 1993; Denk *et al.*, 1995; Fetcho and O'Malley, 1995; Fetcho *et al.*, 1998; Lipp *et al.*, 1996; Lumpkin and Hudspeth, 1995; Svoboda *et al.*, 1996, 1997; Williams *et al.*, 1994; Zhou *et al.*, 1997). But even in recent years, much of the highest temporal-resolution imaging continues to be done with point-scanning confocal and two-photon instruments (Augustine *et al.*, 2003; Gahtan *et al.*, 2002; O'Malley *et al.*, 2003, 2004; Photowala *et al.*, 2005; Scheuss *et al.*, 2006; Yasuda *et al.*, 2004). Further developments in the field include

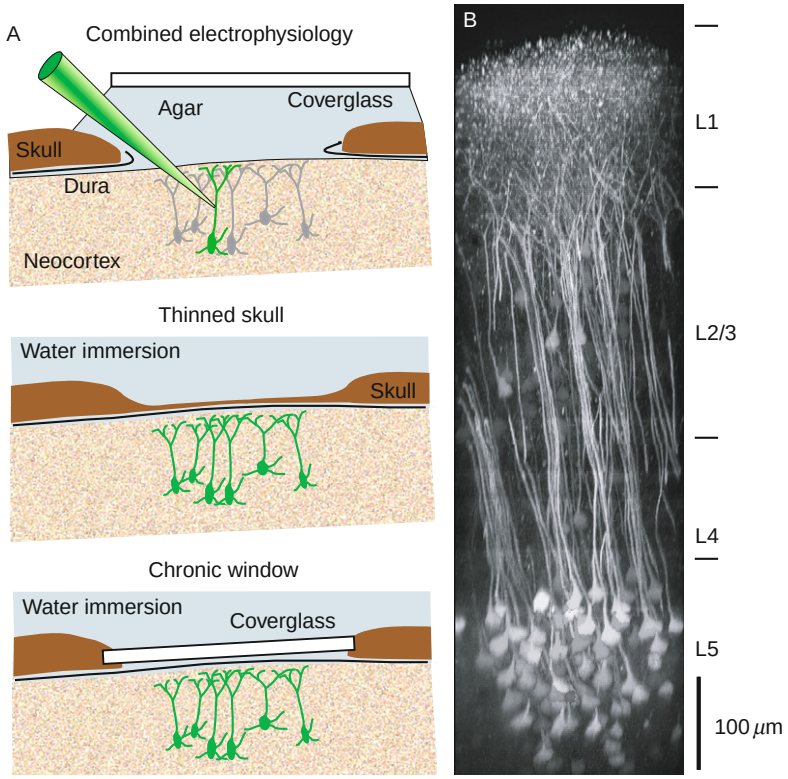

Fig. 3 Deep tissue imaging with two-photon microscopy. Mouse neocortex is visualized with the three different methods shown in (A). Shown in (B) is a side (*xz*) view of two-photon image stack. In a transgenic mouse expressing the genetically encoded chloride indicator Clomeleon, layer 5 (L5) pyramidal cells can be visualized as much as 700 μm deep into cortex. Reprinted with permission from *Nature Methods* (from Helmchen and Denk, 2005).

"resonance scanners" that scan points more rapidly than older model point scanners (Eisenstein, 2006), and newer slit-scanning models that can sample small regions at high frequencies (Bembenek *et al.*, 2007; Gasparini *et al.*, 2007). It is not yet clear whether or not these new approaches will match or outperform traditional point- and disk-scanning confocals.

All of these confocal imaging approaches can be successful across diverse imaging applications. In regards to pushing the envelope of dynamic imaging, a prudent approach would be to critically assess the combined spatial–temporal resolution of competing instruments in published dynamic recordings. One development to track is the increasing sensitivity of electron-multiplying or EMCCD cameras (Chong *et al.*, 2004; Guntupalli *et al.*, 2005; Smith *et al.*, 2004), which may allow Nipkow-disk machines to operate at lower light intensities. Another issue is

whether or not phototoxicity and photobleaching are related in a nonlinear fashion to light dosage within some critical time window. In such a case, Nipkow disks, by briefly crossing pixels but using a high repetition rate of, for example, 250 times/s, effectively spread out the photodose over separated time epochs. Whether or not a "greater continuous dose" that might occur with line-scans would increase phototoxicity or photodamage has not been rigorously determined (see discussion in Donnert *et al*., 2007b), but opening the pinhole aperture would offset this to some degree. The ultimate future of this technological competition remains uncertain, but there are several clear differences: Point scanning enables tailored laser-scan patterns, subcellular targeting, aperture-related signal increases, and optical zoom, while the scanning-disk confocal allows direct viewing of the sample and rapid acquisition of 2D, 3D, and 4D datasets.

Regarding the increasing popularity of disk scanners, this may be due in part to the perceived utility of "seeing" the specimen in confocal mode, but one also wonders whether purchasing decisions have been influenced by frequent claims of superior live-cell imaging capabilities, such as: "Traditional confocal microscopes can be too slow to study the most rapid cell processes, and the intensity of laser light can damage living cells," (Chapman, 2003) or "Spinning disk instruments are also optimized for live-cell imaging (and)...provide the technology for rapidly collecting images while minimizing cell damage," (Borg *et al*., 2005). Certainly spinning-disk instruments can kill cells (Knight *et al*., 2003), while point-scan-based imaging has been used to acquire intermittent calcium responses from a single nerve cell over a period of more than 24 h (Fetcho *et al*., 1998). But the truth is that lasers used in any fashion can be used to kill cells, and as shown quantitatively by Knight *et al*. (2003), reducing laser power is the best way to minimize phototoxicity in confocal imaging. Whether or not the option of opening a pinhole aperture will benefit a given experiment depends upon the specifics of that experiment. Both style confocals offer great research opportunities, that are amplified by the ongoing revolution in genetic imaging tools, but ultimately, as it turns out, both instruments pale in comparison to a newer and even more revolutionary imaging modality: two-photon (or multi-photon) imaging.

D. Two-Photon Imaging: Basics

At some combination of specimen thickness and specimen scattering/turbidity, all confocal imaging techniques ultimately fail. While some animals, such as zebrafish, can be made more transparent by mutagenesis or by treatment with a pigment-inhibiting compound (Elsalini and Rohr, 2003; Karlsson *et al*., 2001; Lister *et al*., 1999), most animals/tissues are more scattering or opaque and thus pose great obstacles if one wishes to obtain microscopic details at any significant depth. Fortunately as one shifts to longer wavelengths, in the IR range, and by using very intense pulses of light, one can take advantage of nonlinear photon absorption processes to effect a new kind of imaging: two-photon (or multi-photon) fluorescence microscopy (Denk and Svoboda, 1997; Denk *et al*., 1990;

Piston, 2005). Using pulsed lasers, extremely high-photon fluxes can be created in a small-focal volume [with roughly the dimensions of the point-spread function (PSF) of a point object]. The result of such intense photon fluxes is that some fluorophores will be struck by two photons with sufficient simultaneity that the two photons appear, energetically, to be one higher-energy (shorter-wavelength) photon. In other words, a fluorophore that would normally absorb a single 400 nm photon can absorb two 800 nm photons—but only under extreme photon flux conditions. This seemingly esoteric phenomenon, when implemented with IR lasers, has three key consequences that make two-photon microscopy a technique of extraordinary power.

First, IR light penetrates biological tissues much more effectively than do short wavelengths (as can be seen by holding a green vs a red laser pointer against one's finger), which means that fluorophores can be effectively excited much deeper inside tissues or animals. This feature (which is complemented by the next two features), effectively opens up a new realm within which high-resolution microscopy can be performed. Secondly, and crucially, two-photon absorption occurs almost entirely within a small-focal volume, because the probability of two photons striking a fluorophore simultaneously falls off dramatically outside this volume. This means that two-photon *excitation* provides intrinsic optical sectioning. The resulting images can be similar to confocal images in circumstances suitable for confocal, but in many tissues, confocal fails with depth because one-photon absorption processes are occurring above and below the focal plane, leading to reduced contrast. This, in conjunction with scattering of both the exciting light and the return emission, can lead to total loss of contrast, despite the use of confocal pinhole apertures. The scattering of the illuminating light is less problematic for two-photon imaging, as long as the photon flux at the focal volume remains high-enough to generate two-photon excitation events. This brings us to the third consequence of this imaging modality, namely that the scatter of the *emitted* light does not significantly degrade the optical signal or image quality. Because the vast majority of emitted photons are originating from the 2P-focal volume (providing intrinsic *xy*- and *z*-resolution), it does not matter how many times photons are scattered so long as they exit the sample to reach a detector (Helmchen and Denk, 2005). For this reason, two-photon instruments are designed to collect every possible photon that leaves the sample, which improves the signal-to-noise ratio. These attributes of two-photon imaging, along with other benefits, such as the lack of photobleaching or photodamage outside the plane of focus, have led to tremendous proliferation and usage of two-photon microscopes.

When this technology first appeared, confocal microscopes were adapted to two-photon mode by switching to pulsed lasers (typically titanium-sapphire) and using the confocal laser-scanning optics to scan the pulsed-laser beam (as a diffraction-limited spot of light) across the sample. The emission was then (preferably) routed to an external detector, to avoid light losses along the confocal light path to an internal detector. One feature of two-photon is that if one takes a molecule's normal (1P) absorption spectrum and multiplies it by 2 (as a first approximation),

the spectrum becomes broader and so any given fluorophore can be excited by a broad range of wavelengths (Xu *et al*., 1996). A corollary of this broad excitation spectrum (referred to as a two-photon "cross section") is that one can often use a single long-wavelength source to excite multiple, different wavelength fluorophores in double- or triple-labeling experiments. Moreover, since the excitation wavelength is in the IR domain, one can, in effect, use most of the visible spectrum for collecting signal, without need for multiple barrier filters to block multiple visible excitation wavelengths. Nonlinear excitation can be extended further to three-photon excitation processes, exciting molecules in the ultraviolet bands (Xu *et al*., 1996). For this reason, one often sees the term "multi-photon" used instead of "two-photon," but these terms refer to the same imaging systems.

E. Two-Photon Imaging: Applications

Two-photon (point scanning) microscopes are now used in many diverse applications but are especially prevalent in neuroscience where researchers visualize morphological plasticity (Holtmaat *et al*., 2005; Knott *et al*., 2006), synaptic circuits in brain slices (Cox *et al*., 2000; Nägerl *et al*., 2004), and neuronal population activity *in vivo* (Heim *et al*., 2007; Kerr *et al*., 2005). Indeed, it is possible to resolve subcellular features down to the deepest layers of living mouse neocortex (Fig. 3; from Helmchen and Denk, 2005). In Figure 3, deep pyramidal neurons have been labeled with the genetically encoded chloride indicator clomeleon. The axons of layer 5 pyramidal cells can be seen coming off the somata as deep as 700 μm into cortex. As with confocal, two-photon is often used in line-scanning mode to maximize combined spatial–temporal resolution. It is also possible to combine two-photon absorption with Nipkow-disk scanning instruments, and this can produce better results than obtained by confocal disk scanning (Egner *et al*., 2002b). One potential drawback of disk scanning two-photon is that the laser light is distributed over many points, possibly making it less suitable for deep tissue imaging than point-scanning two-photon. While this issue does not yet seem to have been experimentally addressed, the depth of useful imaging is clearly related to the amount of laser power that can be transmitted (and focused) to the desired imaging depth (Helmchen and Denk, 2005).

In terms of imaging trade-offs between confocal and two-photon imaging, it seems that two-photon systems either "tie" or "win" across the board in such terms as signal-to-noise, resolution, decreased photobleaching, depth of penetration, and localization of optical manipulation (as in laser-ablation, photoactivation, or optical control of membrane potential). In theory, confocal should have a spatial-resolution advantage because of its shorter-wavelength of illumination. But in practice, it seems that this starting advantage is rapidly lost, presumably because of out-of-plane absorption and scattering of both the exciting and emitted light. This does not mean that one should not try confocal. Figures 4 and 5 show, respectively, confocal and two-photon images (maximum projections) of the zebrafish brainstem (from two different zebrafish larvae) in which large numbers of

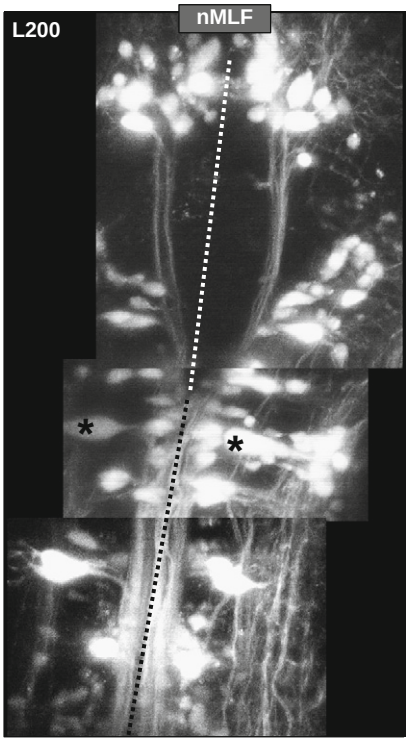

Fig. 4 Confocal montage (of maximum projections) of reticulospinal neurons in the brainstem of a restrained larval zebrafish. Neurons were labeled using the labeled-lesion technique in which large numbers of neurons are simultaneously labeled with fluorescent dextrans and disconnected from their spinal targets (Gahtan and O'Malley, 2001). Such lesions result in novel and highly abnormal bending patterns due to deconstraint of the spinal neural circuits (Day *et al*., 2005). Image courtesy of Leslie Day, Department of Biology, Northeastern University.

reticulospinal neurons were retrogradely labeled by injecting a fluorescent tracer into spinal cord. Both images show many details of neuronal cell bodies, axons, and dendrites that would not be evident if using wide-field fluorescence microscopy, even if deconvolution techniques were employed (see below). This is not a rigorous comparison because the specimen is not stable enough for perfectly equivalent image acquisition on two remote platforms, but our impression from looking at many such confocal image stacks is that finer structural details (at depths 200 μm or deeper into the larval brain) are evident in the two-photon image.

With two-photon, one can readily perform all of the techniques associated with point-scanning confocal including laser-ablation, FRAP, and photo-uncaging. In conjunction with a rapid 2D acoustical-optical device, single-point, two-photon imaging is able to rapidly image neural activity at sparsely distributed sites (Iyer *et al*., 2006). The most serious drawback to two-photon is its cost, which is equal to the cost of a high-quality confocal system plus an additional $100,000 or

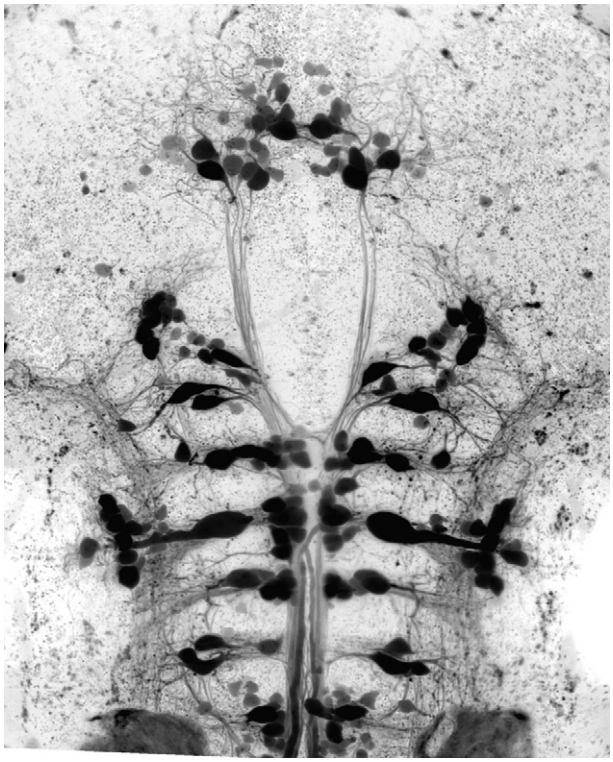

Fig. 5 Two-photon projection of reticulospinal neurons in the brainstem of a restrained larval zebrafish. Neurons were labeled with Texas-red dextran (10,000 MW) and slow-scan imaged with a 20X, 0.95 NA objective to produce maximum resolution deep inside this living animal. Contrast has been reversed (the darkest cells are the most fluorescent). Fine anatomical details (of e.g., axons and dendrites) are evident that are difficult to resolve in confocal images of similarly labeled fish. Image courtesy of Michael Orger, Adam Kampff, J. H. Bollmann and Florian Engert, Department of Molecular Cellular Biology, Harvard University.

so for the pulsed laser (although a number of enterprising labs have built such systems on their own; Majewska *et al*., 2000). Two-photon systems are also trickier to maintain and operate, but commercial vendors are working to make these systems more turnkey and user friendly. This does not mean that everyone needs to or should buy a two-photon system: If the less expensive microscopes described here achieve your experimental goals, the money saved can be spent elsewhere.

F. Deconvolution

Deconvolution represents yet another dimension of biological imaging, within the ''image analysis'' domain. The term ''deconvolution'' refers to a variety of image improvement techniques that mathematically ''deblur'' or otherwise ''restore''

microscopic images acquired by various imaging modalities. There are a number of detailed reviews of the different variations of these methods (see, e.g., McNally *et al*., 1999; Sarder and Nehorai, 2006; Wallace *et al*., 2001). In contrast to confocal and two-photon, which use optical tricks to optimize the resolution of objects (by minimizing the size of the diffracted, microscopically recorded image), deconvolution uses algorithms to undo this diffraction, that is to undo the optical PSF of the object. In principle, deconvolution is agnostic with regard to the imaging modality used to acquire an image, but ultimately, as with the imaging modalities themselves, its performance is dependent upon signal-to-noise issues. Deconvolution can be applied to 2D images (see, e.g., Donnert *et al*., 2007a), but is more commonly applied to 3D data sets, including those acquired by conventional fluorescence microscopes with a motorized objective. Some proponents have argued that deconvolution offers a cheaper and potentially superior alternative to confocal microscopy, to the point of one manufacturer labeling a deconvolution control on a wide-field fluorescence microscope as "confocal." In order to deblur this encroachment between optical and mathematical techniques, we will consider several applications of deconvolution including its use with confocal and two-photon microscopes.

3D-deconvolution seeks, in effect, to maximally undo the physical, *z*-axis spread of light from an optical point source. This diffraction-based spread of emitted light normally makes *z*-axis resolution about threefold worse than *xy*-plane resolution and so one goal of deconvolution is to whittle this diffracted image down to a representation more closely resembling its true 3D physical size. Figure 6A and B (from Schrader *et al*., 1996) show the effect of deconvolving already fine confocal point-spread functions (namely images of 50 nm gold beads mounted in immersion oil). The remarkable degree of "resolution" obtained for both the confocal and deconvolved images are discussed in more detail in Section IV, but the principle result from this example, using a maximum-likelihood estimation deconvolution algorithm (that is well suited for the restoration of photon-limited images), is a reduction in the *xy*-plane's PSF from 80 nm down to 40 nm, and a reduction in the *z*-plane's PSF from 460 nm down to 145 nm. This impressive result was obtained under stringent conditions (described below) and as such provides an upper bound on the degree of resolution that might be achieved under optimal circumstances. This particular result is unlikely to be achieved with most experimental preparations, or with wide-field fluorescence microscopy, but deconvolution can, under favorable circumstances, improve many biological images and yield data that is more readily interpreted.

So what can deconvolution really do? This approach works best with relatively non-scattering samples and is degraded with increasing depth into scattering samples. Once one ventures deeper into living specimens, the waters often become murky. There are clear instances where deconvolution results in better image quality, and this can be true in both wide-field (conventional) fluorescence microscopy (Falk and Lauf, 2001; Ferko *et al*., 2006; Jang and Ye, 2007; Manz *et al*., 2000) and with confocal image stacks (Difato *et al*., 2004; Strohmaier *et al*., 2000). Yet there are other reports indicating that deconvolution adds minimally to

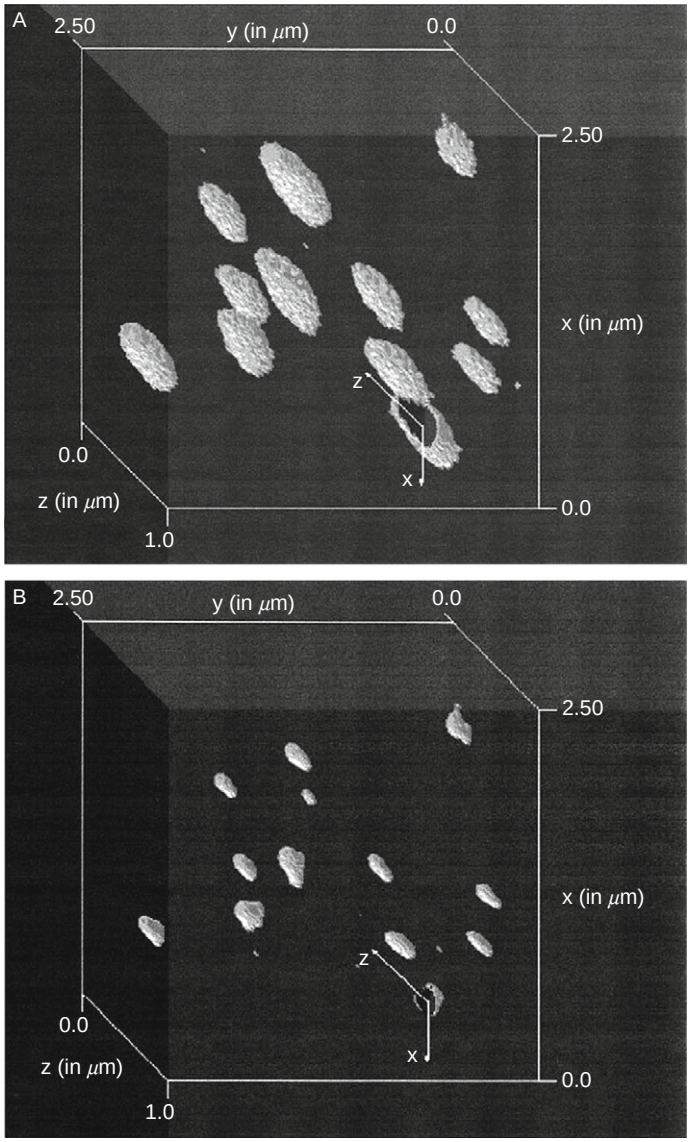

Fig. 6 Deconvolution of confocal image stack. Gold beads (50 nm) were dispersed in immersion oil and imaged using a 3D-piezoelectric stage-scanning confocal microscope. 3D stacks consisted of 30 *xy* images that were 40 nm apart in the *z*-direction. The pixel size was 10 nm in the *xy* plane. (A) Shows a rendered plot of the bead images. The beads are less than one-seventh of the illumination wavelength and so their rendered confocal images represent, in effect, the optical point-spread function. (B) Use of a maximum-likelihood deconvolution algorithm restores the images to a more faithful representation of the actual object dimensions. Reprinted with permission from *Applied Physical Letters* (from Schrader *et al.*, 1996).

confocal imaging (Wako *et al*., 1998) and that it does not perform well with certain far-field image specimens (Verveer *et al*., 1999). In any case, it is straightforward to apply deconvolution algorithms to 3D datasets, and so it makes sense to try. Deblurring "freeware" is available from several sources (Majewska *et al*., 2000), including NIH Image (or ImageJ for PC computers), while a variety of more extensive packages are available from commercial vendors.

Note that any image stack can be subjected to 3D deconvolution algorithms, but for this to be meaningful there must be shared optical information between neighboring images in the *z*-stack (i.e., overlapping PSFs in the *z*-dimension). If the image planes are much further apart, 3D deconvolution will not achieve much. Assuming the datasets are suitable, the different deblurring and image reconstruction techniques should generally provide some image improvement, but there are a variety of artifacts that may frequently appear (Majewska *et al*., 2000; McNally *et al*., 1999), and so it is important to (1) optimize image acquisition parameters/conditions and (2) ensure that for any "structures" revealed in the deconvolution process, there is at least some evidence of those structures in the raw images.

The most controversial point encountered in this literature is whether or not deconvolution can replace or even exceed the performance of confocal imaging (see, e.g., Verveer *et al*., 2007). Maierhofer *et al*. (2003) suggest that confocal has worse signal/noise than far-field deconvolution approaches and is more seriously affected by photobleaching, but no comparative confocal data are provided. Their report does provide elegant multicolor deconvoluted image stacks of clinical tissue samples, revealing details important for analyzing cytogenetic defects, but given that these are 30-μm thick, paraffin embedded, dehydrated specimens, this sample does not provide the optical challenge of many specimens, in terms of depth or light scattering. In certain instances, a combination of wide-field fluorescence imaging and deconvolution might be preferred over confocal. For example, in voltage-imaging studies in the relatively translucent olfactory bulb of the salamander, the voltage–dye signals are limited in quantity and durability and any photons lost by confocal optical sectioning would adversely affect signal-to-noise ratios (Cinelli, 2000). In this case, deconvolution of wide-field images helps to assign voltage signals to the appropriate regions and layers of the olfactory bulb in which the neural activity is occurring. Indeed, the tissue is optically segmented into 20-μm sections and the deeper depth-of-field of conventional fluorescence optics delivers more signals, yielding images that can be subsequently improved by deconvolution. The nature of this strategy is analogous to opening the pinhole of point-scanning confocal microscopes: If it is useful to integrate signal from (for example) a whole nerve cell body, then an open aperture will collect more of the cell's emission, improving the signal-to-noise ratio.

Still, in many applications, confocal is able to extract signals that are simply lost in the blur of wide-field fluorescence imaging. A cell visualization chapter in a popular cell and molecular biology textbook has a particularly nice example of this, while providing related deconvolution results (Alberts *et al*., 2002). This is not to say that deconvolution is not valuable, but rather that one should acquire data

with the best tools available and then judiciously employ different deblurring and restoration algorithms to see if the data can be meaningfully enhanced. While the rank order of depth of penetration (with good resolution) is clearly two-photon > confocal > wide-field deconvolution, the rank order of availability/economy is clearly deconvolution > confocal > two-photon. This is another example of the trade-offs encountered in imaging, but this one concerns economics rather than biophysical constraints.

G. CCD Versus PMT

Another twist in considering competing technologies is the detector that is used in acquiring the image. While a variety of optical detectors are available, including film, your eyes, CMOS devices, vidicon cameras, and avalanche photodiodes (APDs), the most common detectors used in light-microscopic applications are CCDs (charge-coupled devices; see Aikens *et al*., 1989) and PMTs. The CCD (including its newer EMCCD or electron-multiplying version) is in widespread use in diverse applications including consumer digital cameras, and is now the most common detector for both basic fluorescence microscopes and spinning-disk confocals. In contrast, PMTs (and sometimes APDs) are used in point-scanning confocals and two-photon instruments. As with the different modes of imaging, each detection mode has its own specific strengths and limitations.

Typically, the first question will be "which detector is more sensitive?" Sensitivity is poorly defined and even more difficult to compare, given the problem of comparing identical, appropriate samples on different platforms in a fair and meaningful way. One is left with the claim that "CCDs are more sensitive than PMTs" because they have higher quantum efficiency (the efficiency with which each impinging photon is converted into a photoelectron). It is true that CCDs can have quantum efficiencies of 90% or higher, while PMTs have efficiencies less than 10%, which might make CCDs seem the obvious choice. But what this simplified comparison lacks is consideration of the signal that is ultimately delivered by the imaging device. Each pixel in the CCD is read out serially and when reading out small signals very quickly (which is necessary for dynamic imaging applications that require rapid pixel read-out rates), one encounters as much as 20 electrons worth of read-out noise (James Pawley, confocal listserv, 10/6/07, http://listserv.buffalo.edu)—which makes it difficult to use signals on the order of 10 or 15 photons per pixel (with each detected photon producing a single photoelectron). In contrast, the PMT amplifies each photon that it does convert into an electron by up to a millionfold (depending on amplifier gain). If the PMT receives 20 photons, it will detect only about 10% of these (one or two photons), but for each photon detected it will amplify the signal enormously, with minimal read-out noise.

Given the foregoing considerations, the true disparity in performance is not so great as to dictate which type of instrument (spinning disk, slit scanner, or point scanner) to choose: Each detector serves its host microscopes well. The newest

generation EMCCD (electron-multiplying CCD) detectors have greater sensitivity due to their incorporation of an amplification step prior to the read-out stage (Chong *et al*., 2004; Guntupalli *et al*., 2005; Smith *et al*., 2004), which may improve the dynamic imaging abilities of disk- and slit-scanning confocal microscopes. Signal-to-noise issues take on greater importance when one is seeking to obtain finer spectral information from each pixel (sometimes referred to as "hyperspectral" imaging), because the photoelectrons generated from a given location are subdivided into spectral bins. Current generation CCD cameras are indeed being used for such applications, but when imaging at high speed with live samples, one must consider the sample's sensitivity. To achieve high-enough emission fluxes to fill all of the "imaging wells" (the spectral split of signal from each pixel location) and produce signal in excess of the noise, one must consider, as James Pawley has put it that "phototoxicity is proportional to EXCITATIONS rather than to incident light, (and so) the emission of this much signal is likely to be unpleasant to the cell."

IV. Discussion: Terms of Resolution

A. What is NOT Resolution

Resolution means resolving discrete items. This could mean *xy* spatial resolution, which is diffraction limited on conventional optical microscopes. This also applies to *z*-resolution and temporal resolution and is mentioned because of liberties that have been taken with the word. In some papers, the selected size for the *z*-axis motor-step is (quite naively) stated to be the *z*-axis resolution. While one indeed needs to make fine motor steps to if one is to produce a detailed 3D reconstruction of a specimen, the *z*-axis PSF and the motor step size are wholly unrelated entities. More common are claims that the acquisition speed of a device is the temporal resolution, with for example claims that events 2-ms apart can be resolved by 2-ms line-scans. This is equally invalid because one may need to bin together multiple pixels in time if one is to resolve, that is distinguish, discrete events separated in time. Whether discussing calcium dynamics (as above), or other cellular events, temporal resolution (like spatial resolution) depends on BOTH the imaging system's performance (microscope, detector) AND the signal-to-noise ratio of the pixels being acquired. One can often improve temporal resolution by spatially binning together pixels (i.e., trading off spatial resolution) or conversely, bin pixels over time to better resolve the spatial aspects of dynamic events, but like Heisenberg's uncertainty principle, you cannot do both at the same time. In the case of calcium dynamics, there is asymmetric resolution in time: with 2-ms line-scans (and a little 1D spatial binning), it is possible to reliably detect step (2 ms) increases in fluorescence, but closely following subsequent events may not be easily resolved or even detected because of the slow recovery dynamics of calcium signals. In this instance, the resolution is not compromised by pixel noise, but rather by the dynamics of the biological events themselves.

B. What IS Resolution—Resolution from Hell

Stefan Hell and colleagues (Schrader *et al*., 1996) present optical limits that one can obtain with confocal microscopy, achieving Full Width Half Maximum (FWHM) values of 460 nm in the *z*-dimension and 145 nm in the *xy*-plane (Fig. 6A; sample was illuminated with a 543 nm helium–neon laser). With deconvolution (maximum-likelihood method), these FWHM values are reduced to 80 nm (*z*) and 40 nm (*xy*) (Fig. 6B). The FWHM value is not *resolution* per se, but two-point objects that are separated by the FWHM distance would be distinguishable as discrete objects, that is, resolved. How is such remarkable resolution obtained? This result depended upon a set of conditions namely: (1) use of high-contrast 50 nm gold beads as targets, (2) slow scanning to optimize the signal/noise ratio, (3) placing the beads in immersion oil to avoid refractive-index mismatch-induced spherical aberration, and (4) use of a 3D piezoelectric stage-scanning microscope. Few labs have this specialized type of microscope, although piezoelectric controlled stages are seeing increased use. Moreover, oil-immersed gold beads are not representative of many biological samples, nor is the 10-μm thickness of the sample terribly "deep" in the context of our current discussion. But this does illustrate, in dramatic fashion, the potential resolution that one can obtain inside an actual 3D structure, with conventional light-microscopic imaging, given certain necessary conditions (instrument-wise and sample-wise) and the application of image restoration techniques. Given the ongoing advances in both instrumentation and super-resolution techniques such as STED and STORM (Hell, 2007; Rust *et al*., 2006), our resolution of living biological structures and dynamic events may extend into entirely new domains.

C. Whole-Animal Imaging

At the largest spatial scale, one can look deep into the interior of animals using visible, positron, X-ray, and radiofrequency radiation, as well as using sound waves. In the "human brain mapping" genre, neural activation patterns are revealed using positron emission tomography (PET) or functional magnetic resonance imaging (fMRI), but these approaches cannot detect individual neurons or axons. Instead they provide a regional, aggregate signal based on neural activation of volumes of brain tissue that may consist of tens or hundreds of thousands of cells. A number of techniques are being used to try and bridge the gap between regional brain mapping techniques and cellular–subcellular level imaging approaches. Techniques involving novel labeling approaches, transgenic animals and *in vivo* two-photon imaging are all beginning to reveal circuit-level details (Feng *et al*., 2000; Fetcho and O'Malley, 1997; Gahtan and O'Malley, 2003; Gahtan *et al*., 2002; Göbel *et al*., 2007; Kerr *et al*., 2005; Orger *et al*., 2008; Stosiek *et al*., 2003). Other *in vivo* techniques, such as bioluminescent imaging, can reveal distribution patterns of cell populations in intact mice, and have been used, for example, to track tumor metastasis as well as the proliferation and movements of tumor killing cells (see, e.g., Dickson *et al*., 2007;

Edinger *et al.*, 2003; Jenkins *et al.*, 2005; Wetterwald *et al.*, 2002). While such techniques are not able to resolve individual tumor cells or other fine tumor structure (Bhaumik and Gambhir, 2002; Deroose *et al.*, 2007; Kuo *et al.*, 2007; Shcherbo *et al.*, 2007; Weissleder and Ntziachristos, 2003), they do provide a noninvasive means to track and quantify tumor burden and distribution and evaluate efficacy of therapeutic compounds in different animal models of cancer. What we still cannot do is perform cellular- and subcellular-resolution imaging and optical manipulation deep in the tissues of mammals to either investigate neural circuitry or study pathological processes like cancer. This will have to await future technological breakthroughs.

V. Summary

Biologists would like to visualize molecular-scale processes deep inside animals (including humans) and would like to do so with good specificity and spatial–temporal resolution. There are formidable barriers to this goal, but the diverse approaches reviewed, and the ingenuity with which increasingly powerful techniques are being created, suggest that the great advances of the past 20 years could be matched over the next 20 years. Such advances would become increasingly important for both the natural scientist and the clinician. To look deep into a diseased human body and record molecular events with great specificity, precision and context would provide a treasure trove of information. This would allow us to examine complex physiological and pathological processes from a Systems Biology perspective. But for the present we cannot—we immediately encounter trade-offs even in our more depth- and specimen-limited imaging efforts. Biological imaging today is about trade-offs: trading off spatial resolution for either depth of imaging or speed of acquisition, and trading off temporal resolution to see structures in finer detail. Judicious choosing of technologies, in conjunction with a great variety of new molecular probes, will best allow researchers to negotiate the pertinent trade-offs and work towards visualizing cells, tissues, and organisms in their full 3D splendor.

Acknowledgments

The author appreciates comments from Barry Burbach, as well as extensive and generous help from many members of the confocal newsgroup, whose public list archives can be accessed via http://listserv.buffalo.edu.

References

Ackerley, C. A., Nielsen, C., and Hawkins, C. E. (2006). Experiences with wet capsule imaging exploring the potential for live cell imaging. *Microsc. Microanal.* **12**(Supp 2), 428–429.

Aikens, R. S., Agard, D. A., and Sedat, J. W. (1989). Solid-state imagers for microscopy. *Methods Cell Biol.* **29,** 291–313.

Alberts, B., Johnson, A., Lewis, J., Raff, M., Roberts, K., and Walter, P. (2002). Visualizing cells. *In* Molecular Biology of the Cell. pp. 547–580. Garland Science, New York.

Amos, W. B., Reichelt, S., Cattermole, D. M., and Laufer, J. (2003). Re-evaluation of differential phase contrast (DPC) in a scanning laser microscope using a split detector as an alternative to differential interference contrast (DIC) optics. *J. Microsc.* **210,** 166–175.

Amos, W. B., and White, J. G. (2003). How the confocal laser scanning microscope entered biological research. *Biol. Cell* **95,** 335–342.

Ando, T., Uchihashi, T., Kodera, N., Yamamoto, D., Taniguchi, M., Miyagi, A., and Yamashita, H. (2007). High-speed atomic force microscopy for observing dynamic biomolecular processes. *J. Mol. Recognit.* **20,** 448–458.

Augustine, G. J., Santamaria, F., and Tanaka, K. (2003). Local calcium signaling in neurons. *Neuron* **40,** 331–346.

Axelrod, D. (2003). Total internal reflection fluorescence microscopy in cell biology. *Methods Enzymol.* **361,** 1–33.

Bagnall, M. W., Stevens, R. J., and du Lac, S. (2007). Transgenic mouse lines subdivide medial vestibular nucleus neurons into discrete, neurochemically distinct populations. *J. Neurosci.* **27,** 2318–2330.

Bancroft, J. D., and Gamble, M. (2001). Theory and Practice of Histological Techniques 5th edn. Churchill Livingston, NY.

Beis, D., and Stainier, D. Y. (2006). *In vivo* cell biology: Following the zebrafish trend. *Trends Cell Biol.* **16,** 105–112.

Bembenek, J. N., Richie, C. T., Squirrell, J. M., Campbell, J. M., Eliceiri, K. W., Poteryaev, D., Spang, A., Golden, A., and White, J. G. (2007). Cortical granule exocytosis in *C. elegans* is regulated by cell cycle components including separase. *Development* **134,** 3837–3848.

Bhaumik, S., and Gambhir, S. S. (2002). Optical imaging of *Renilla luciferase* reporter gene expression in living mice. *Proc. Natl. Acad. Sci. USA* **99,** 377–382.

Blazer-Yost, B. L., Vahle, J. C., Byars, J. M., and Bacallao, R. L. (2004). Real-time three-dimensional imaging of lipid signal transduction: Apical membrane insertion of epithelial Na(+) channels. *Am. J. Physiol. Cell. Physiol.* **287,** C1569–C1576.

Borg, T. K., Stewart, J. A., Jr., and Sutton, M. A. (2005). Imaging the cardiovascular system: Seeing is believing. *Microsc. Microanal.* **11,** 189–199.

Bos, M. A., and Kleijn, J. M. (1995). Determination of the orientation distribution of adsorbed fluorophores using TIRF. II. Measurements on porphyrin and cytochrome c. *Biophys. J.* **68,** 2573–2579.

Braeckmans, K., Remaut, K., Vandenbroucke, R. E., Lucas, B., De Smedt, S. C., and Demeester, J. (2007). Line FRAP with the confocal laser scanning microscope for diffusion measurements in small regions of 3-D samples. *Biophys. J.* **92,** 2172–2183.

Brakenhoff, G. J. (1979). Imaging modes in confocal scanning light microscopy. *J. Microsc.* **117,** 232–242.

Brakenhoff, G. J., van der Voort, H. T., van Spronsen, E. A., Linnemans, W. A., and Nanninga, N. (1985). Three-dimensional chromatin distribution in neuroblastoma nuclei shown by confocal scanning laser microscopy. *Nature* **317,** 748–749.

Cadetti, L., Bryson, E. J., Ciccone, C. A., Rabl, K., and Thoreson, W. B. (2006). Calcium-induced calcium release in rod photoreceptor terminals boosts synaptic transmission during maintained depolarization. *Eur. J. Neurosci.* **23,** 2983–2990.

Chapman, T. (2003). Seeing is believing (technology feature). *Nature* **425,** 867–873.

Cheng, H., Lederer, W. J., and Cannell, M. B. (1993). Calcium sparks: Elementary events underlying excitation contraction coupling in heart muscle. *Science* **262,** 740–744.

Chong, F. K., Coates, C. G., Denvir, D. J., McHale, N. G., Thornbury, K. D., and Hollywood, M. A. (2004). Optimization of spinning disk confocal microscopy: Synchronization with the ultra-sensitive EMCCD. *Proc. SPIE* **5324,** 65–76.

Chua, J., and Deretic, V. (2004). Mycobacterium tuberculosis reprograms waves of phosphatidylinositol 3-phosphate on phagosomal organelles. *J. Biol. Chem.* **279,** 36982–36992.

Chudakov, D. M., Chepurnykh, T. V., Belousov, V. V., Lukyanov, S., and Lukyanov, K. A. (2006). Fast and precise protein tracking using repeated reversible photoactivation. *Traffic* **7,** 1304–1310.

Cinelli, A. R. (2000). High-definition mapping of neural activity using voltage-sensitive dyes. *Methods* **21,** 349–372.

Cody, S. H., Xiang, S. D., Layton, M. J., Handman, E., Lam, M. H., Layton, J. E., Nice, E. C., and Heath, J. K. (2005). A simple method allowing DIC imaging in conjunction with confocal microscopy. *J. Microsc.* **217,** 265–274.

Collier, T., Guillaud, M., Follen, M., Malpica, A., and Richards-Kortum, R. (2007)).Real-time reflectance confocal microscopy: Comparison of two-dimensional images and three-dimensional image stacks for detection of cervical precancer. *J. Biomed. Opt.* **12:051901,** 1–10.

Concha, M. L., and Adams, R. J. (1998). Oriented cell divisions and cellular morphogenesis in the zebrafish gastrula and neurula: A time-lapse analysis. *Development* **125,** 983–994.

Cox, C. L., Denk, W., Tank, D. W., and Svoboda, K. (2000). Action potentials reliably invade axonal arbors of rat neocortical neurons. *Proc. Natl. Acad. Sci. USA* **97,** 9724–9728.

Cox, G. (2007). Optical Techniques in Cell Biology. Taylor & Francis Group, Boca Raton, FL.

Cubitt, A. B., Heim, R., Adams, S. R., Boyd, A. E., Gross, L. A., and Tsien, R. Y. (1995). Understanding, improving and using green fluorescent proteins. *Trends Biochem. Sci.* **20,** 448–455.

Dahm, R., Schonthaler, H. B., Soehn, A. S., van Marle, J., and Vrensen, G. F. (2007). Development and adult morphology of the eye lens in the zebrafish. *Exp. Eye Res.* **85,** 74–89.

Day, L. J., Knudsen, D. P., Dhanota, H., Severi, K., Jose, J. V., and O'Malley, D. M. (2005). Lesions of descending motor pathways deconstrain spinal activity patterns: Results from larval zebrafish. *Soc. Neurosci. Abs.* **31,** 751.11.

Denk, W., Holt, J. R., Shepherd, G. M., and Corey, D. P. (1995). Calcium imaging of single stereocilia in hair cells: Localization of transduction channels at both ends of tip links. *Neuron* **15,** 1311–1321.

Denk, W., Strickler, J. H., and Webb, W. W. (1990). Two-photon laser scanning fluorescence microscopy. *Science* **248,** 73–76.

Denk, W., and Svoboda, K. (1997). Photon upmanship: Why multiphoton imaging is more than a gimmick. *Neuron* **18,** 351–357.

Deroose, C. M., De, A., Loening, A. M., Chow, P. L., Ray, P., Chatziioannou, A. F., and Gambhir, S. S. (2007). Multimodality imaging of tumor xenografts and metastases in mice with combined small-animal PET, small-animal CT, and bioluminescence imaging. *J. Nucl. Med.* **48,** 295–303.

Detrich, H. W., III, Zon, L. I., and Westerfield, M. (2004). The zebrafish: Cellular and developmental biology. *Methods Cell Biol.* **76,** 1–656.

Dickinson, M. E., Bearman, G., Tille, S., Lansford, R., and Fraser, S. E. (2001). Multi-spectral imaging and linear unmixing add a whole new dimension to laser scanning fluorescence microscopy. *Biotechniques* **31,** 1274–1278.

Dickson, P. V., Hamner, B., Ng, C. Y., Hall, M. M., Zhou, J., Hargrove, P. W., McCarville, M. B., and Davidoff, A. M. (2007). *In vivo* bioluminescence imaging for early detection and monitoring of disease progression in a murine model of neuroblastoma. *J. Pediatr. Surg.* **42,** 1172–1179.

Difato, F., Mazzone, F., Scaglione, S., Fato, M., Beltrame, F., Kubínová, L., Janácek, J., Ramoino, P., Vicidomini, G., and Diaspro, A. (2004). Improvement in volume estimation from confocal sections after image deconvolution. *Microsc. Res. Tech.* **64,** 151–155.

Dodt, H. U., and Zieglgansberger, W. (1990). Visualizing unstained neurons in living brain slices by infrared DIC-videomicroscopy. *Brain Res.* **537,** 333–336.

Donnert, G., Eggeling, C., and Hell, S. W. (2007). Major signal increase in fluorescence microscopy through dark-state relaxation. *Nat. Methods* **4,** 81–86.

Donnert, G., Keller, J., Wurm, C. A., Rizzoli, S. O., Westphal, V., Schonle, A., Jahn, R., Jakobs, S., Eggeling, C., and Hell, S. W. (2007a). Two-color far-field fluorescence nanoscopy. *Biophys. J.* **92,** L67–L69.

Dwyer, P. J., DiMarzio, C. A., Zavislan, J. M., Fox, W. J., and Rajadhyaksha, M. (2006). Confocal reflectance theta line scanning microscope for imaging human skin *in vivo*. *Opt. Lett.* **31,** 942–944.

Edinger, M., Cao, Y. A., Verneris, M. R., Bachmann, M. H., Contag, C. H., and Negrin, R. S. (2003). Revealing lymphoma growth and the efficacy of immune cell therapies using in vivo bioluminescence imaging. *Blood* **101,** 640–648.

Eisenstein, M. (2006). Something to see (technology feature). *Nature* **443,** 1017–1023.

Elsalini, O. A., and Rohr, K. B. (2003). Phenylthiourea disrupts thyroid function in developing zebrafish. *Dev. Genes Evol.* **212,** 593–598.

Egner, A., Andresen, V., and Hell, S. W. (2002b). Comparison of the axial resolution of practical Nipkow-disk confocal fluorescence microscopy with that of multifocal multiphoton microscopy: Theory and experiment. *J. Microsc.* **206,** 24–32.

Egner, A., Jakobs, S., and Hell, S. W. (2002a). Fast 100-nm resolution three-dimensional microscope reveals structural plasticity of mitochondria in live yeast. *Proc. Natl. Acad. Sci. USA* **99,** 3370–3375.

Falk, M. M., and Lauf, U. (2001). High resolution, fluorescence deconvolution microscopy and tagging with the autofluorescent tracers CFP, GFP, and YFP to study the structural composition of gap junctions in living cells. *Microsc. Res. Tech.* **52,** 251–262.

Feng, G., Mellor, R. H., Bernstein, M., Keller-Peck, C., Nguyen, Q. T., Wallace, M., Nerbonne, J. M., Lichtman, J. W., and Sanes, J. R. (2000). Imaging neuronal subsets in transgenic mice expressing multiple spectral variants of GFP. *Neuron* **28,** 41–51.

Ferko, M. C., Bhatnagar, A., Garcia, M. B., and Butler, P. J. (2007). Finite-element stress analysis of a multi-component model of sheared and focally-adhered endothelial cells. *Ann. Biomed. Eng.* **35,** 208–223.

Ferko, M. C., Patterson, B. W., and Butler, P. J. (2006). High-resolution solid modeling of biological samples imaged with 3D fluorescence microscopy. *Microsc. Res. Tech.* **69,** 648–655.

Fetcho, J. R., Cox, K., and O'Malley, D. M. (1998). Monitoring activity in neuronal populations with single-cell resolution in a behaving vertebrate. *Histochem. J.* **30,** 153–167.

Fetcho, J. R., and O'Malley, D. M. (1995). Visualization of active neural circuitry in the spinal cord of intact zebrafish. *J. Neurophysiol.* **73,** 399–406.

Fetcho, J. R., and O'Malley, D. M. (1997). Imaging neuronal networks in behaving animals. *Curr. Opin. Neurobiol.* **7,** 832–838.

Frangakis, A. S., and Förster, F. (2004). Computational exploration of structural information from cryo-electron tomograms. *Curr. Opin. Struct. Biol.* **14,** 325–331.

Frankel, D. J., Pfeiffer, J. R., Surviladze, Z., Johnson, A. E., Oliver, J. M., Wilson, B. S., and Burns, A. R. (2006). Revealing the topography of cellular membrane domains by combined atomic force microscopy/fluorescence imaging. *Biophys. J.* **90,** 2404–2413.

Gahtan, E., and Baier, H. (2004). Of lasers, mutants, and see-through brains: Functional neuroanatomy in zebrafish. *J. Neurobiol.* **59,** 147–161.

Gahtan, E., and O'Malley, D. M. (2001). Rapid lesioning of large numbers of identified vertebrate neurons: Applications in zebrafish. *J. Neurosci. Methods* **108,** 97–110.

Gahtan, E., and O'Malley, D. M. (2003). Visually-guided injection of identified reticulospinal neurons in zebra fish: A survey of spinal arborization patterns. *J. Comp. Neurol.* **459,** 186–200.

Gahtan, E., Sankrithi, N., Campos, J. B., and O'Malley, D. M. (2002). Evidence for a widespread brainstem escape network in larval zebrafish. *J. Neurophysiol.* **87,** 608–614.

Gahtan, E., Tanger, P., and Baier, H. (2005). Visual prey capture in larval zebrafish is controlled by identified reticulospinal neurons downstream of the tectum. *J. Neurosci.* **25,** 9294–9303.

Gasparini, S., Losonczy, A., Chen, X., Johnston, D., and Magee, J. C. (2007). Associative pairing enhances action potential back-propagation in radial oblique branches of CA1 pyramidal neurons. *J. Physiol.* **580,** 787–800.

Göbel, W., Kampa, B. M., and Helmchen, F. (2007). Imaging cellular network dynamics in three dimensions using fast 3D laser scanning. *Nat. Methods* **4,** 73–79.

González, S., and Tannous, Z. (2002). Real-time, *in vivo* confocal reflectance microscopy of basal cell carcinoma. *J. Am. Acad. Dermatol.* **47,** 869–874.

Guntupalli, R., Haganb, V., Cooper, A., and Simpson, R. (2005). New ultra-high speed CCD camera achieves sub-electron read noise using on-chip multiplication gain (EMCCD) technology. *Proc. SPIE* **5580,** 905–912.

Hale, M. E., Ritter, D. A., and Fetcho, J. R. (2001). A confocal study of spinal interneurons in living larval zebrafish. *J. Comp. Neurol.* **437,** 1–16.

Hansma, H. G., and Hoh, J. H. (1994). Biomolecular imaging with the atomic force microscope. *Annu. Rev. Biophys. Biomol. Struct.* **23,** 115–140.

Heim, N., Garaschuk, O., Friedrich, M. W., Mank, M., Milos, R. I., Kovalchuk, Y., Konnerth, A., and Griesbeck, O. (2007). Improved calcium imaging in transgenic mice expressing a troponin C-based biosensor. *Nat. Methods* **4,** 127–129.

Hell, S. H., and Wichmann, J. (1994). Breaking the diffraction resolution limit by stimulated emission: Stimulated-emission-depletion fluorescence microscopy. *Opt. Lett.* **19,** 780–782.

Hell, S. W. (2007). Far-field optical nanoscopy. *Science* **316,** 1153–1158.

Helmchen, F., and Denk, W. (2005). Deep tissue two-photon microscopy. *Nat. Methods* **2,** 932–940.

Hernandez-Cruz, A., Sala, F., and Adams, P. R. (1990). Subcellular calcium transients visualized by confocal microscopy in a voltage-clamped vertebrate neuron. *Science* **247,** 858–862.

Higashijima, S., Hotta, Y., and Okamoto, H. (2000). Visualization of cranial motor neurons in live transgenic zebrafish expressing green fluorescent protein under the control of the islet-1 promoter/enhancer. *J. Neurosci.* **20,** 206–218.

Holtmaat, A. J., Trachtenberg, J. T., Wilbrecht, L., Shepherd, G. M., Zhang, X., Knott, G. W., and Svoboda, K. (2005). Transient and persistent dendritic spines in the neocortex *in vivo*. *Neuron* **45,** 279–291.

Hui, C. S., Bidasee, K. R., and Besch, H. R., Jr. (2001). Effects of ryanodine on calcium sparks in cut twitch fibres of Rana temporaria. *J. Physiol.* **534,** 327–342.

Iyer, V., Hoogland, T. M., and Saggau, P. (2006). Fast functional imaging of single neurons using random-access multiphoton (RAMP) microscopy. *J. Neurophysiol.* **95,** 535–545.

Jagger, D. J., and Housley, G. D. (2003). Membrane properties of type II spiral ganglion neurones identified in a neonatal rat cochlear slice. *J. Physiol.* **552,** 525–533.

Jang, K. E., and Ye, J. C. (2007). Single channel blind image deconvolution from radially symmetric blur kernels. *Opt. Express* **15,** 3791–3803.

Jenkins, D. E., Hornig, Y. S., Oei, Y., Dusich, J., and Purchio, T. (2005). Bioluminescent human breast cancer cell lines that permit rapid and sensitive *in vivo* detection of mammary tumors and multiple metastases in immune deficient mice. *Breast Cancer Res.* **7,** R444–R454.

Jiang, W., and Ludtke, S. J. (2005). Electron cryomicroscopy of single particles at subnanometer resolution. *Curr. Opin. Struct. Biol.* **15,** 571–577.

Jontes, J. D., Buchanan, J., and Smith, S. J. (2000). Growth cone and dendrite dynamics in zebrafish embryos: Early events in synaptogenesis imaged *in vivo*. *Nat. Neurosci.* **3,** 231–237.

Karlsson, J., von Hofsten, J., and Olsson, P. E. (2001). Generating transparent zebrafish: A refined method to improve detection of gene expression during embryonic development. *Mar. Biotechnol.* **3,** 522–527.

Kellermayer, M. S., Karsai, A., Kengyel, A., Nagy, A., Bianco, P., Huber, T., Kulcsár, A., Niedetzky, C., Proksch, R., and Grama, L. (2006). Spatially and temporally synchronized atomic force and total internal reflection fluorescence microscopy for imaging and manipulating cells and biomolecules. *Biophys. J.* **91,** 2665–2677.

Kerr, J. N., Greenberg, D., and Helmchen, F. (2005). Imaging input and output of neocortical networks *in vivo*. *Proc. Natl. Acad. Sci. USA* **102,** 14063–14068.

Klein, C., Pillot, T., Chambaz, J., and Drouet, B. (2003). Determination of plasma membrane fluidity with a fluorescent analogue of sphingomyelin by FRAP measurement using a standard confocal microscope. *Brain Res. Brain Res. Protoc.* **11,** 46–51.

Knight, M. M., Roberts, S. R., Lee, D. A., and Bader, D. L. (2003). Live cell imaging using confocal microscopy induces intracellular calcium transients and cell death. *Am. J. Physiol. Cell Physiol.* **284,** C1083–C1089.

Knott, G. W., Holtmaat, A., Wilbrecht, L., Welker, E., and Svoboda, K. (2006). Spine growth precedes synapse formation in the adult neocortex *in vivo*. *Nat. Neurosci.* **9,** 1117–1124.

Kockskamper, J., Sheehan, K. A., Bare, D. J., Lipsius, S. L., Mignery, G. A., and Blatter, L. A. (2001). Activation and propagation of Ca(2+) release during excitation-contraction coupling in atrial myocytes. *Biophys. J.* **81,** 2590–2605.

Korkotian, E., Oron, D., Silberberg, Y., and Segal, M. (2004). Confocal microscopic imaging of fast UV-laser photolysis of caged compounds. *J. Neurosci. Methods* **133,** 153–159.

Koster, A. J., and Klumperman, J. (2003)).Electron microscopy in cell biology: Integrating structure and function*Nat. Rev. Mol. Cell Biol.* **4** (Suppl.), SS6–SS10.

Kuo, C., Coquoz, O., Troy, T. L., Xu, H., and Rice, B. W. (2007). Three-dimensional reconstruction of *in vivo* bioluminescent sources based on multispectral imaging. *J. Biomed. Opt.* **12,** 024007.

Lassen, B., and Malmsten, M. (1996). Competitive protein adsorption studied with TIRF and ellipsometry. *J. Colloid Interface Sci.* **179,** 470–477.

Lippincott-Schwartz, J., and Patterson, G. H. (2003). Development and use of fluorescent protein markers in living cells. *Science* **300,** 87–91.

Lipp, P., Lüscher, C., and Niggli, E. (1996). Photolysis of caged compounds characterized by ratiometric confocal microscopy: A new approach to homogeneously control and measure the calcium concentration in cardiac myocytes. *Cell Calcium* **19,** 255–266.

Lister, J. A., Robertson, C. P., Lepage, T., Johnson, S. L., and Raible, D. W. (1999). Nacre encodes a zebrafish microphthalmia related protein that regulates neural-crest-derived pigment cell fate. *Development* **126,** 3757–3767.

Liu, K. S., and Fetcho, J. R. (1999). Laser ablations reveal functional relationships of segmental hindbrain neurons in zebrafish. *Neuron* **23,** 325–335.

Livet, J., Weissman, T. A., Kang, H., Draft, R. W., Lu, J., Bennis, R. A., Sanes, J. R., and Lichtman, J. W. (2007). Transgenic strategies for combinatorial expression of fluorescent proteins in the nervous system. *Nature* **450,** 56–62.

Lopez-Lopez, J. R., Shacklock, P. S., Balke, C. W., and Wier, W. G. (1994). Local, stochastic release of Ca^{2+}in voltage-clamped rat heart cells: Visualization with confocal microscopy. *J. Physiol.* **480,** 21–29.

Lumpkin, E. A., and Hudspeth, A. J. (1995). Detection of Ca^{2+}entry through mechanosensitive channels localizes the site of mechanoelectrical transduction in hair cells. *Proc. Natl. Acad. Sci. USA* **92,** 10297–10301.

Maierhofer, C., Gangnus, R., Diebold, J., and Speicher, M. R. (2003). Multicolor deconvolution microscopy of thick biological specimens. *Am. J. Pathol.* **162,** 373–379.

Majewska, A., Yiu, G., and Yuste, R. (2000). A custom-made two-photon microscope and deconvolution system. *Pflugers Arch.* **441,** 398–408.

Manz, W., Arp, G., Schumann-Kindel, G., Szewzyk, U., and Reitner, J. (2000). Widefield deconvolution epifluorescence microscopy combined with fluorescence in situ hybridization reveals the spatial arrangement of bacteria in sponge tissue. *J. Microbiol. Methods* **40,** 125–134.

McNally, J. G., Karpova, T., Cooper, J., and Conchello, J. A. (1999). Three-dimensional imaging by deconvolution microscopy. *Methods* **19,** 373–385.

Minsky, M. (1988). Memoir on inventing the confocal scanning microscope. *Scanning* **10,** 128–138.

Nägerl, U. V., Eberhorn, N., Cambridge, S. B., and Bonhoeffer, T. (2004). Bidirectional activity-dependent morphological plasticity in hippocampal neurons. *Neuron* **44,** 759–767.

Naora, H. (1955). Microspectrophotometry of cell nucleus stained by Feulgen reaction I. Microspectrophotometric apparatus without Schwarzschild-Villiger effect. *Exp. Cell Res.* **8,** 259–278.

Nasevicius, A., and Ekker, S. C. (2000). Effective targeted gene 'knockdown' in zebrafish. *Nat. Genet.* **26,** 216–220.

Ohara-Imaizumi, M., Nishiwaki, C., Kikuta, T., Nagai, S., Nakamichi, Y., and Nagamatsu, S. (2004). TIRF imaging of docking and fusion of single insulin granule motion in primary rat pancreatic beta-cells: Different behaviour of granule motion between normal and Goto-Kakizaki diabetic rat beta-cells. *Biochem. J.* **381,** 13–18.

Oheim, M., Beaurepaire, E., Chaigneau, E., Mertz, J., and Charpak, S. (2001). Two-photon microscopy in brain tissue: Parameters influencing the imaging depth. *J. Neurosci. Methods* **111,** 29–37.

O'Malley, D. M. (1994). Calcium permeability of the neuronal nuclear envelope: Evaluation using confocal volumes and intracellular perfusion. *J. Neurosci.* **14,** 5741–5758.

O'Malley, D. M., Kao, Y.-H., and Fetcho, J. R. (1996). Imaging the functional organization of zebrafish hindbrain segments. *Neuron* **17,** 1145–1155.

O'Malley, D. M., Sankrithi, N. S., Borla, M. A., Parker, S., Banden, S., Gahtan, E., and Detrich, H. W. (2004). Optical physiology and locomotor behaviors of wild-type and nacre zebrafish. *In* The Zebrafish: Cellular and Molecular Biology, (H. W. Detrich, M. Westerfield, and L. I. Zon, eds.) Academic Press, San Diego, CA.

O'Malley, D. M., Zhou, Q., and Gahtan, E. (2003). Probing neural circuits in the zebrafish: A suite of optical techniques. *Methods* **30,** 49–63.

Orger, M. B., Kampff, A. R., Severi, K. E., Bollmann, J. H., and Engert, F. (2008). Control of visually guided behavior by distinct populations of spinal projection neurons. *Nat. Neurosci.* **11,** 327–333.

Parker, I., Zang, W. J., and Wier, W. G. (1996). Ca^{2+}sparks involving multiple Ca^{2+}release sites along Z-lines in rat heart cells. *J. Physiol.* **497,** 31–38.

Park, M. K., Lomax, R. B., Tepikin, A. V., and Petersen, O. H. (2001). Local uncaging of caged Ca(2+) reveals distribution of Ca(2+)-activated Cl(-) channels in pancreatic acinar cells. *Proc. Natl. Acad. Sci. USA* **98,** 10948–10953.

Partridge, M. A., and Marcantonio, E. E. (2006). Initiation of attachment and generation of mature focal adhesions by integrin-containing filopodia in cell spreading. *Mol. Biol. Cell* **17,** 4237–4248.

Pawley, J. B. (2006). Handbook of Confocal Microscopy 3rd edn. Springer, New York, NY.

Perkins, B. D., Kainz, P. M., O'Malley, D. M., and Dowling, J. E. (2002). Transgenic expression of a GFP-rhodopsin C-terminal fusion protein in zebrafish rod photoreceptors. *Vis. Neurosci.* **19,** 257–264.

Photowala, H., Freed, R., and Alford, S. (2005). Location and function of vesicle clusters, active zones and Ca^{2+}channels in the lamprey presynaptic terminal. *J. Physiol.* **569,** 119–135.

Piston, D. W. (2005). When two is better than one: Elements of intravital microscopy. *PLoS Biol.* **3,** e207.

Pratusevich, V. R., and Balke, C. W. (1996). Factors shaping the confocal image of the calcium spark in cardiac muscle cells. *Biophys. J.* **71,** 2942–2957.

Reichert, W. M., and Truskey, G. A. (1990). Total internal reflection fluorescence (TIRF) microscopy. I. Modelling cell contact region fluorescence. *J. Cell Sci.* **96,** 219–230.

Rust, M. J., Bates, M., and Zhuang, X. (2006). Sub-diffraction-limit imaging by stochastic optical reconstruction microscopy (STORM). *Nat. Methods* **3,** 793–795.

Salmon, E. D., and Tran, P. (1998). High-resolution video-enhanced differential interference contrast (VE-DIC) light microscopy. *Methods Cell Biol.* **56,** 153–184.

Sarder, P., and Nehorai, A. (2006). Deconvolution methods for 3-D fluorescence microscopy images. *Signal Process. Mag. IEEE* **23,** 32–45.

Scheuss, V., Yasuda, R., Sobczyk, A., and Svoboda, K. (2006). Nonlinear $[Ca^{2+}]$ signaling in dendrites and spines caused by activity-dependent depression of Ca^{2+}extrusion. *J. Neurosci.* **26,** 8183–8194.

Schrader, M., Hell, S. W., and van der Voort, H. T. M. (1996). Potential of confocal microscopes to resolve in the 50–100 nm range. *Appl. Phys. Lett.* **69,** 3644–3646.

Serbus, L. R., Cha, B. J., Theurkauf, W. E., and Saxton, W. M. (2005). Dynein and the actin cytoskeleton control kinesin-driven cytoplasmic streaming in Drosophila oocytes. *Development* **132,** 3743–3752.

Shcherbo, D., Merzlyak, E. M., Chepurnykh, T. V., Fradkov, A. F., Ermakova, G. V., Solovieva, E. A., Lukyanov, K. A., Bogdanova, E. A., Zaraisky, A. G., Lukyanov, S., and Chudakov, D. M. (2007). Bright far-red fluorescent protein for whole-body imaging. *Nat. Methods* **4,** 741–746.

Sheppard, C. J. R., and Choudhury, A. (1977). Image formation in the scanning microscope. *Opt. Acta* **24,** 1051–1073.

Sieber, J. J., Willig, K. I., Kutzner, C., Gerding-Reimers, C., Harke, B., Donnert, G., Rammner, B., Eggeling, C., Hell, S. W., Grubmuller, H., and Lang, T. (2007). Anatomy and dynamics of a supramolecular membrane protein cluster. *Science* **317,** 1072–1076.

Sluder, G., and Wolf, D. E. (2007). Digital Microscopy. *Methods Cell Biol.* **81,** 1–608.

Smith, N., Coates, C., Giltinan, A., Howard, J., O'Connor, A., O'Driscoll, S., Hauser, M., and Wagner, S. (2004). EMCCD technology and its impact on rapid low-light photometry. *Proc. SPIE* **5499,** 162–172.

Stosiek, C., Garaschuk, O., Holthoff, K., and Konnerth, A. (2003). *In vivo* two-photon calcium imaging of neuronal networks. *Proc. Natl. Acad. Sci. USA* **100,** 7319–7324.

Strohmaier, A. R., Porwol, T., Acker, H., and Spiess, E. (2000). Three-dimensional organization of microtubules in tumor cells studied by confocal laser scanning microscopy and computer-assisted deconvolution and image reconstruction. *Cells Tissues Organs* **167,** 1–8.

Stuart, G. J., Dodt, H. U., and Sakmann, B. (1993). Patch-clamp recordings from the soma and dendrites of neurons in brain slices using infrared video microscopy. *Pflugers Arch.* **423,** 511–518.

Sun, D. A., Sombati, S., and DeLorenzo, R. J. (2001). Glutamate injury-induced epileptogenesis in hippocampal neurons: An *in vitro* model of stroke-induced "epilepsy. *Stroke* **32,** 2344–2350.

Svoboda, K., Denk, W., Kleinfeld, D., and Tank, D. W. (1997). *In vivo* dendritic calcium dynamics in neocortical pyramidal neurons. *Nature* **385,** 161–165.

Svoboda, K., Tank, D. W., and Denk, W. (1996). Direct measurement of coupling between dendritic spines and shafts. *Science* **272,** 716–719.

Taylor, D. L., and Salmon, E. D. (1989). Basic fluorescence microscopy. *Methods Cell Biol.* **29,** 207–237.

Valkenburg, J. A., Woldringh, C. L., Brakenhoff, G. J., van der Voort, H. T., and Nanninga, N. (1985). Confocal scanning light microscopy of the Escherichia coli nucleoid: Comparison with phase-contrast and electron microscope images. *J. Bacteriol.* **161,** 478–483.

Varadi, A., Ainscow, E. K., Allan, V. J., and Rutter, G. A. (2002). Involvement of conventional kinesin in glucose-stimulated secretory granule movements and exocytosis in clonal pancreatic beta-cells. *J. Cell Sci.* **115,** 4177–4189.

Verveer, P. J., Gemkow, M. J., and Jovin, T. M. (1999). A comparison of image restoration approaches applied to three-dimensional confocal and wide-field fluorescence microscopy. *J. Microsc.* **193,** 50–61.

Verveer, P. J., Swoger, J., Pampaloni, F., Greger, K., Marcello, M., and Stelzer, E. H. (2007). High-resolution three-dimensional imaging of large specimens with light sheet-based microscopy. *Nat. Methods* **4,** 311–313.

Wako, T., Fukuda, M., Furushima-Shimogawara, R., Belyaev, N. D., Turner, B. M., and Fukui, K. (1998). Comparative analysis of topographic distribution of acetylated histone H4 by using confocal microscopy and a deconvolution system. *Anal. Chim. Acta* **365,** 9–17.

Wallace, W., Schaefer, L. H., and Swedlow, J. R. (2001). A workingperson's guide to deconvolution in light microscopy. *BioTechniques* **31,** 1076–1097.

Wang, H., Peca, J., Matsuzaki, M., Matsuzaki, K., Noguchi, J., Qiu, L., Wang, D., Zhang, F., Boyden, E., Deisseroth, K., Kasai, H., Hall, W. C., *et al.* (2007).High-speed mapping of synaptic connectivity using photostimulation in Channelrhodopsin-2 transgenic mice*Proc. Natl. Acad. Sci. USA* **104,** 8143–8148.

Wang, J., Wang, X., Irnaten, M., Venkatesan, P., Evans, C., Baxi, S., and Mendelowitz, D. (2003). Endogenous acetylcholine and nicotine activation enhances GABAergic and glycinergic inputs to cardiac vagal neurons. *J. Neurophysiol.* **89,** 2473–2481.

Wang, S. Q., Song, L. S., Lakatta, E. G., and Cheng, H. (2001). Ca^{2+}signalling between single L-type Ca^{2+}channels and ryanodine receptors in heart cells. *Nature* **410,** 592–596.

Weissleder, R., and Ntziachristos, V. (2003). Shedding light onto live molecular targets. *Nat. Med.* **9,** 123–128.

Wetterwald, A., van der Pluijm, G., Que, I., Sijmons, B., Buijs, J., Karperien, M., Löwik, C. W., Gautschi, E., Thalmann, G. N., and Cecchini, M. G. (2002). Optical imaging of cancer metastasis to bone marrow: A mouse model of minimal residual disease. *Am. J. Pathol.* **160,** 1143–1153.

Williams, R. M., Piston, D. W., and Webb, W. W. (1994). Two-photon molecular excitation provides intrinsic 3-dimensional resolution for laser-based microscopy and microphotochemistry. *FASEB J.* **8,** 804–813.

Willig, K. I., Rizzoli, S. O., Westphal, V., Jahn, R., and Hell, S. W. (2006). STED microscopy reveals that synaptotagmin remains clustered after synaptic vesicle exocytosis. *Nature* **440,** 935–939.

Wu, L., Lo, P., Yu, X., Stoops, J. K., Forghani, B., and Zhou, Z. H. (2000). Three-dimensional structure of the human herpesvirus 8 capsid. *J. Virol.* **74,** 9646–9654.

Xu, C., Zipfel, W., Shear, J. B., Williams, R. M., and Webb, W. W. (1996). Multiphoton fluorescence excitation: New spectral windows for biological nonlinear microscopy. *Proc. Natl. Acad. Sci. USA* **93,** 10763–10768.

Yasuda, R., Nimchinsky, E. A., Scheuss, V., Pologruto, T. A., Oertner, T. G., Sabatini, B. L., and Svoboda, K. (2004). Imaging calcium concentration dynamics in small neuronal compartments. *Sci. STKE* pl5.

Yu, S. P., O'Malley, D. M., and Adams, P. R. (1994). Regulation of M-Current by intracellular calcium in bullfrog sympathetic ganglion neurons. *J. Neurosci.* **14,** 3487–3499.

Zhou, Q., Godwin, D. W., O'Malley, D. M., and Adams, P. R. (1997). Visualization of calcium influx through channels that shape the *burst* and *tonic* firing modes of thalamic neurons. *J. Neurophys.* **77,** 2816–2825.

Zimmermann, T., Rietdorf, J., and Pepperkok, R. (2003). Spectral imaging and its applications in live cell microscopy. *FEBS Lett.* **546,** 87–92.

CHAPTER 6

Principles and Practice in Electron Tomography

Bruce F. McEwen, Christian Renken, Michael Marko, and Carmen Mannella

Department of Health
Albany, New York 12201-0509
Resource for Visualization of Biological Complexity
Wadsworth Center, New York

METHODS IN CELL BIOLOGY, VOL. 89

0091-679X/08 $35.00
DOI: 10.1016/S0091-679X(08)00606-7

I. Introduction

Electron tomography has emerged as an effective method to investigate cellular architecture in the nanometer range of resolution. In electron tomography, a three-dimensional (3D) image is reconstructed from 2D projection images, usually by back-projection methods (Fig. 1). The same back-projection approach is used in medical imaging methods such as computerized axial tomography (CAT) scanning, but electron tomography entails special considerations arising from the nature of the specimens examined and their interactions with the electron beam. Despite limitations imposed by specimen geometry and radiation dose, electron tomography is providing new and exciting insights into a wide range of biological processes.

A number of recent reviews have described the general approach of electron tomography and have provided surveys of biological applications (Koster and Barcena, 2006; Lucic *et al.*, 2005; McIntosh *et al.*, 2005). Protocols for carrying out electron tomography have also been published in recent volumes of *Methods in Cell Biology* and *Methods in Molecular Biology* (Hoog and Antony, 2007; Marko and Hsieh, 2007; O'Toole *et al.*, 2007). Here we describe the biophysical principles underlying the methodology, with particular emphasis on technical aspects that

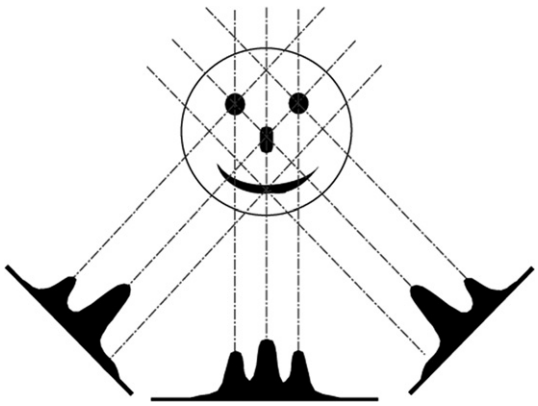

Fig. 1 The principle of back projection as illustrated by the reconstruction of a 2D image from 1D projections. The broken lines indicate selected projection rays. In transmission imaging, the projection rays also indicate the path taken by photons, electrons, etc. The graph along the solid line indicates the amount of specimen mass traversed by electrons that reach each point in the projection image (the actual number of electrons reaching the film is inversely proportional to the specimen mass traversed by the beam). Peaks of mass are recorded where the beam passes through the "eyes," "nose," and "mouth" of the face. Note that the shape of the projected mass plot changes with the direction of projection, that is, at the angle of the tilted projections, some rays traverse both an eye and the nose. For reconstruction via back projection, the mass recorded at each point in the projection image is smeared uniformly along projection rays, also represented by the broken lines. Such "back-projection rays," arising from areas of high recorded mass in different tilt views, intersect and reinforce one another at the locations of the main features in the image. In this way, the 2D image is "reconstructed" from a series of 1D projections. [Taken from McEwen and Marko (1999), with permission.]

have not been covered in previous reviews. We also attempt to convey an appreciation of the technical challenges of electron tomography, and the strategies that are being developed to surmount them.

II. Specimen Preparation

Specimen preparation is the most crucial step in electron microscopy (EM), with high-resolution studies having the most stringent requirement for optimal structural preservation. Consequently, almost all high-resolution EM methodologies, including single-particle analysis, electron crystallography, and helical reconstruction methods, use unstained plunge-frozen preparations. Striking results have been obtained from electron tomographic reconstructions of frozen-hydrated cells and tissue, but low throughput and technical hurdles restrict use of this method. Conventionally prepared and plastic-embedded specimens (Section II.A) are much easier to handle and image than frozen-hydrated specimens and thus offer the advantages of higher throughput, application to a much wider range of specimens, and the ability to carry out same-cell correlative light microscopy (LM) and EM (McEwen *et al.*, 2007; Rieder and Cassels, 1999). Although conventionally prepared specimens are adequate for some of the biological questions addressed by electron tomography, specimen preparation artifacts become glaringly apparent in the resultant 3D reconstructions (Maiato *et al.*, 2006; McEwen *et al.*, 2007). For many specimens, high-pressure freezing followed by freeze-substitution provides a good compromise between the optimal structural preservation of frozen-hydrated specimens and the relative technical efficiency of conventionally prepared specimens (Fig. 2).

A. Conventional Methods

1. Room Temperature Fixation and Dehydration

Methods for conventional room-temperature specimen preparation have been in use for nearly 50 years and are well documented (Glauert and Lewis, 1998; McEwen *et al.*, 2007). Most protocols start with 1–5% glutaraldehyde as the primary fixative, followed by osmium tetroxide postfixation and dehydration in a graded series of ethanol or acetone. Use of a graded solvent series minimizes the structural distortions that accompany rapid dehydration. Tannic acid and uranyl acetate are frequently used to improve structural preservation and provide *en bloc* staining. Modifications may be made to these protocols in order to preserve antigenicity in the case of immuno-EM, but such preparations are rarely studied by electron tomography because of poor structural preservation. After dehydration, specimens are transferred into a plastic resin and polymerized, usually at 60 °C. After polymerization, the plastic block is cut into serial sections, which for most electron tomography specimens should be in the thickness range of 100–500 nm. Thinner sections provide little depth information, whereas thicker sections are difficult to

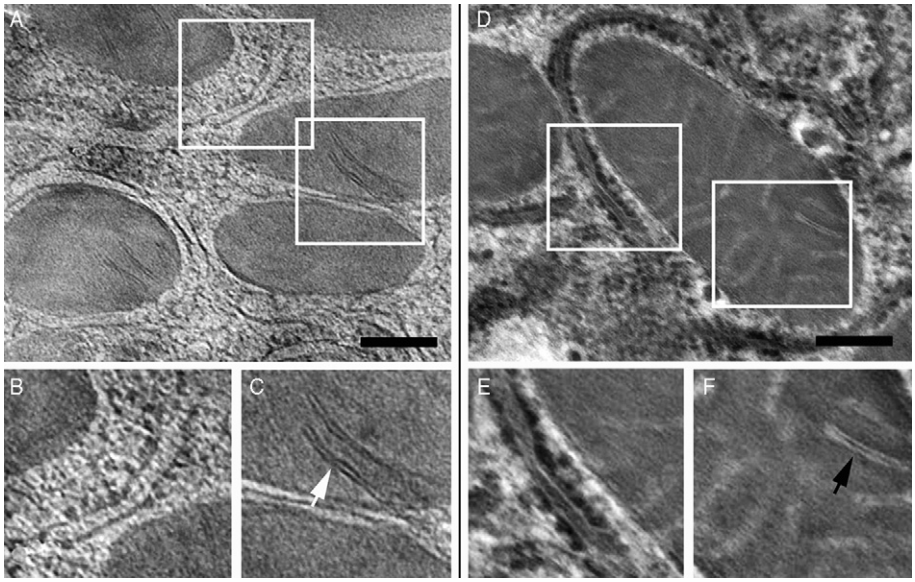

Fig. 2 Electron tomographic reconstructions of frozen-hydrated and freeze-substituted preparations of rat liver tissue. Comparison of 1.8-nm-thick slices from tomographic reconstructions of sections of frozen-hydrated (A–C) and freeze-substituted (D–F) specimens. Panels B and C show 1.5× magnifications of the areas boxed in A, whereas panels E and F show 1.5× magnifications of the areas boxed in D. Note that membranes (arrows in C and F) are unstained in freeze-substituted material, and ribosomes appear darker than those in the frozen-hydrated slices. The width of the endoplasmic reticulum is similar in the two preparations (B and E), as is the separation of the mitochondrial cristal membranes (arrows in C and F). Scale bar = 200 nm. [Adapted from Hsieh *et al.* (2006) with permission.]

image well, and require extremely fine angular sampling (Sections III.D and V.B). Selective stains are especially beneficial for thicker sections because structures of interest such as the Golgi apparatus and injected neurons can be contrasted against an unstained background (McEwen, 1992; Soto *et al.*, 1994; Wilson *et al.*, 1992).

2. Flat Embedment of Monolayer Cell Cultures

Monolayer cell cultures are widely used in cell biological research, due in part to their suitability for LM studies and because they enable same-cell correlative LM/EM studies (Muller-Reichert *et al.*, 2007; Rieder and Cassels, 1999). Examples of the latter include cells that have been followed by time-lapse video recording just prior to fixation, cells in a certain stage of the cell cycle, and cells expressing transfected proteins tagged with fluorescent reporters (Kapoor *et al.*, 2006; McEwen *et al.*, 1997; Muller-Reichert *et al.*, 2007; Sosinsky *et al.*, 2007). The prescreening capability afforded by LM analysis enables the investigator to apply

EM analysis to specific cells with known phenotypes and/or behaviors. LM prescreening of cell monolayers can be employed with conventional, freeze-substituted, or frozen-hydrated specimen preparations. For conventional fixation, cells are grown on glass coverslips, which are removed after resin embedding. Since the "flat-embedded" cells are embedded in a thin wafer of resin, cells of interest can be readily relocated postembedment using phase-contrast LM.

B. High-Pressure Freezing

Structural deterioration in conventionally prepared specimens is thought to occur because cellular components are mobile during chemical fixation and dehydration at room temperature (Dubochet, 2007; Dubochet *et al*., 1988; McDonald, 2007; Moor, 1987; Murk *et al*., 2003; Studer *et al*., 1989). Considerable distortion and extraction probably occur during the several seconds required for the primary fixative to fully penetrate the specimen and these effects continue during dehydration. The problem is exacerbated for tissue samples, and cells with dense permeability barriers, for example, yeast, plant cells, and the nematode *Caenorhabditis elegans*. Cryo-fixation methods avoid structural deterioration by freezing the specimen within a few milliseconds. This rapidly immobilizes cellular components in a vitreous (glass-like) state of water, without the formation of ice crystals that cause damage to cellular ultrastructure.

Suspensions of cellular components, and cells less than a micron in diameter, can be vitrified by plunge freezing (Section II.D.1). The penetration depth of good freezing can be extended to approximately10 μm by slam-freezing the specimen against a polished copper block cooled by liquid nitrogen or liquid helium (Heuser, 1986; Heuser *et al*., 1976). However, the most versatile and widely used method to freeze whole cells, tissue fragments, or other relatively large specimens is high-pressure freezing. This method has been reviewed elsewhere and will be only briefly described here (McDonald, 2007; McDonald *et al*., 2007). High pressure slows the rate of ice crystallization, thereby providing sufficient time for specimens to be well frozen to a depth of about 200 μm. A pressure of about 2000 bar is achieved in about 10–12 ms, after which liquid nitrogen is introduced. One potential drawback of high-pressure freezing is that exposure to a rapid pressure rise, even for a few milliseconds, might alter cellular ultrastructure. However, when done correctly, high-pressure freezing beautifully preserves even pressure-sensitive components such as microtubules (Hawes *et al*., 2007; McDonald, 2007; Murk *et al*., 2003; VandenBeldt *et al*., 2006).

Techniques for loading various specimens into the high-pressure freezer have recently been described in detail by McDonald (2007). However, little has been published on how to prepare monolayer cell cultures. One of us (BFM) routinely grows monolayer cell cultures for high-pressure freezing on 3-mm-diameter sapphire disks because sapphire has excellent optical and cooling properties (Hawes *et al*., 2007; Reipert *et al*., 2004). Cells can also be grown on gold EM grids with a Formvar support (Koning *et al*., 2008; Parsons, 1974). The sapphire disks or EM

grids are placed cells side up on the flat surface of half of a specimen carrier. [For a description of specimen carriers for the high-pressure freezer, see McDonald (2007)]. A half carrier with a 100-μm-deep well, or a circular slot grid followed by the flat surface of a half carrier, is placed on top of the specimen. This arrangement promotes optimal freezing by limiting the depth of medium above the specimen to 20–100 μm. A substance must be dissolved in the medium to retard the formation of extracellular ice crystals that might damage the specimen (Gilkey and Staehelin, 1986). For tissue and tissue-culture cells, polymers such as Ficoll, Dextran, and bovine serum albumin (BSA) protein are often used because they retard the formation of extracellular ice crystals without significantly changing the osmotic balance. Choice of the polymer used varies by specimen and by laboratory. For tissue-culture cells, Ficoll or BSA is used if freezing is to be followed by freeze-substitution (Hsieh *et al.*, 2006; McDonald, 2007; McEwen *et al.*, 1998). Many investigators prefer Dextran if freezing is to be followed by cyro-ultramicrotomy because Dextran solutions can be sectioned more easily. Regardless of which polymer is used, it is critical to completely fill the specimen carrier so as to prevent air pockets, which act as thermal insulators and shock-absorbers, and thereby interfere with both the rate of cooling and the pressure rise.

C. Freeze-Substitution

Specimens thick enough to require high-pressure freezing must be cut into sections sufficiently thin for transmission EM imaging. Freeze-substitution is currently the most commonly used method for specimen preparation for electron tomography because, compared with frozen-hydrated sections, stained plastic sections have higher contrast, greater tolerance to the electron beam, are more easily cut in long serial runs, and are generally easier to handle. However, freeze-substituted specimens are not in a hydrated state, and the contrast provided by heavy metal stains does not reflect the true mass-density distribution in the specimen. Nevertheless, numerous studies have shown that high-pressure freezing followed by freeze-substitution represents a significant improvement over conventional room-temperature chemical fixation, and often produces results that are comparable to results from frozen-hydrated specimens, especially for resolutions at or above 5 nm (Fig. 2; Al-Amoudi *et al.*, 2005; Dubochet, 2007; Hsieh *et al.*, 2006).

In freeze-substitution, the specimen is warmed from liquid nitrogen temperature to -90 °C so that acetone, which has a melting point of -95 °C, is able to slowly replace the water (Dubochet, 2007). The water remains in solid state throughout, changing from vitreous to microcrystalline ice as the temperature slowly rises above -135 °C, the devitrification temperature. Because diffusion coefficients of cellular molecules and macromolecules, including water, are near zero under these conditions, the ice crystals stay small and grow around the biological material without significantly displacing it. Hence, structural damage to the specimen is minimized.

The time required for full substitution of the solvent for frozen water depends on the size and nature of the specimen (McDonald, 2007). Times reported in the

literature range from 8 to 72 h. We generally keep tissue-culture specimens for 2 days at −90 °C, the first day in acetone with glutaraldehyde and tannic acid, and the second day in acetone with osmium and uranyl acetate (VandenBeldt *et al.*, 2006). The specimen is then allowed to reach room temperature over a 6- to 8-h period after which it is embedded in Epon (Section II.A.1). For postembedding immuno-EM, specimens are often embedded in a Lowicryl resin at −30 °C or −50 °C, and the resin is polymerized by UV light (Hawes *et al.*, 2007; Morphew, 2007).

D. Preparation of Frozen-Hydrated Specimens

1. Plunge Freezing

Plunge freezing at ambient pressure achieves vitrification with a very high success rate for thin specimens. There are no concerns about possible deleterious effects of high pressure on the specimen. Suitable specimens include isolated cell organelles and small cells not more than a few micrometers in diameter. The specimen is usually frozen suspended in a physiological medium or buffer. Good freezing of samples larger than 1 μm requires relatively low inherent water content (as in most bacteria, for example). However, for tomography, specimens should be less than 1 μm thick, even for 300–400 kV accelerating voltage (Sections III.A, III.C, and V.B).

The technique of plunge freezing has changed little from the original description (Dubochet *et al.*, 1988), except for the incorporation of automation for better reproducibility (e.g., Vitrobot, FEI Company, Hillsboro, OR). Specimens mounted on EM grids are simply plunged rapidly into liquid ethane or liquid propane cooled by a surrounding bath of liquid nitrogen (direct plunging into liquid nitrogen results in poor heat transfer due to cavitation). Excess medium is removed, just before plunging, by blotting with filter paper for 1–2 s. Excessive blotting causes distortion of soft specimens, with flattening due to surface tension effects, whereas insufficient blotting produces ice that is too thick. Optimal blotting parameters must be worked out in advance for new specimens by trial and error. Flattening can be detected by observing the specimen at different tilt angles.

Typically, specimens are mounted on 200-mesh grids having a thick (∼50 nm) carbon film that is perforated by regularly spaced 2–3.5 μm holes (e.g., C-flat grids, Protochips, Inc., Raleigh, NC, or Quantifoil grids, Quantifoil Micro Tools, Jena, Germany). Application of a thin (5–10 nm), continuous carbon film to the grid provides a flat surface that can accept fiducial markers (see below), and minimizes the accumulation of some specimens at the edges of the holes. Although copper grids are adequate in most cases, molybdenum grids are sometimes preferred because they are stiffer and have a coefficient of thermal expansion similar to that of carbon film, which prevents wrinkling of the support. If cells are to be grown on grids, gold grids are recommended to avoid the cytotoxic effects of other metals.

As will be explained in Section IV.A, tilt-series images of plunge-frozen specimens often can be aligned by cross-correlation methods, but better reliability is

achieved if colloidal gold particles are used as fiducial markers. The particles are provided by vendors in aqueous suspension. This is mixed 1:1 with double-strength medium, to avoid osmotic effects on the specimen when adding the gold solution to the cell suspension. The colloidal gold suspension can also be applied directly to the specimen grid, and dried down prior to specimen deposition. In this case, it is common to find that some of the markers have detached from the carbon film and appear in the frozen specimen layer.

2. Cryo-Ultramicrotomy

Large cells and tissue fragments prepared by high-pressure freezing are too thick for direct EM imaging, and so they must be thinned, usually by cryo-ultramicrotomy. A number of artifacts such as knife marks, chatter, crevasses, and compression can result. Their characteristics and possible causes have been described in detail (Al-Amoudi *et al.*, 2005; Dubochet *et al.*, 2007). Typical sections exhibit varying degrees of these artifacts. Crevasses may be caused by resistance to cutting due to residual microcrystalline ice and can be minimized by high-quality, high-pressure freezing (Hsieh *et al.*, 2006; Marko *et al.*, 2006a). Chatter and knife marks depend on the quality of the knife itself. At present, the only artifact that cannot be avoided by excellent technical practice is compression of the specimen in the cutting direction. Membranous structures such as vesicles and mitochondria are easily compressed, whereas more rigid structures, such as ribosomes, DNA crystals, and desmosomes, resist such forces (Dubochet and Sartori Blanc, 2001; Hsieh *et al.*, 2004; Leforestier *et al.*, 2001). Frozen-hydrated sections are best collected on C-flat or Quantifoil grids on which a thin carbon film and then colloidal gold particles have been previously applied.

Frozen-hydrated sections attach poorly to grids because of their wavy topology (Hsieh *et al.*, 2006; Marko *et al.*, 2006a). Poor section attachment can produce specimen drift or instability. Moreover, image alignment is degraded when the region of the specimen to be reconstructed is not in close apposition to the gold markers on the support film. Tilting of the specimen at low magnification will reveal the areas of good attachment that are most promising for tilt-series collection. The use of an electrostatic charge to aid attachment of the section to the grid is being investigated (P. Peters, personal communication). Recently, techniques have been developed to deposit markers directly on frozen-hydrated sections (Gruska *et al.*, 2008; Masich *et al.*, 2006).

3. Specimen Thinning Using a Focused Ion Beam

In focused ion beam (FIB) milling, a beam of (usually) Ga^+ ions is rastered across the specimen at a glancing angle. With each pass, the heavy ions sputter away the surface layer of the specimen to a depth of about 10 nm, resulting in rapid milling of the specimen in a direction that is nearly parallel to the ion beam. The method, which is widely used in material sciences, has recently been shown to work

for cells or large organelles that have been plunge-frozen on EM grids (Fig. 3). In this application, the EM grid is manually cut in half after freezing, and a region at the cut edge is then thinned with the FIB. The method does not introduce visible cutting artifacts, and it maintains the specimen in the vitreous state (Marko and Hsieh, 2007; Marko *et al*., 2006b). Methods for using the ion beam to thin bulk tissue are under development. Currently, FIB milling is the only way to thin frozen-hydrated specimens without compression. Also, because the ion beam, unlike a microtome knife, can cut crystalline ice smoothly, frozen-hydrated specimens containing a degree of microcrystallinity can be thinned successfully by FIB milling.

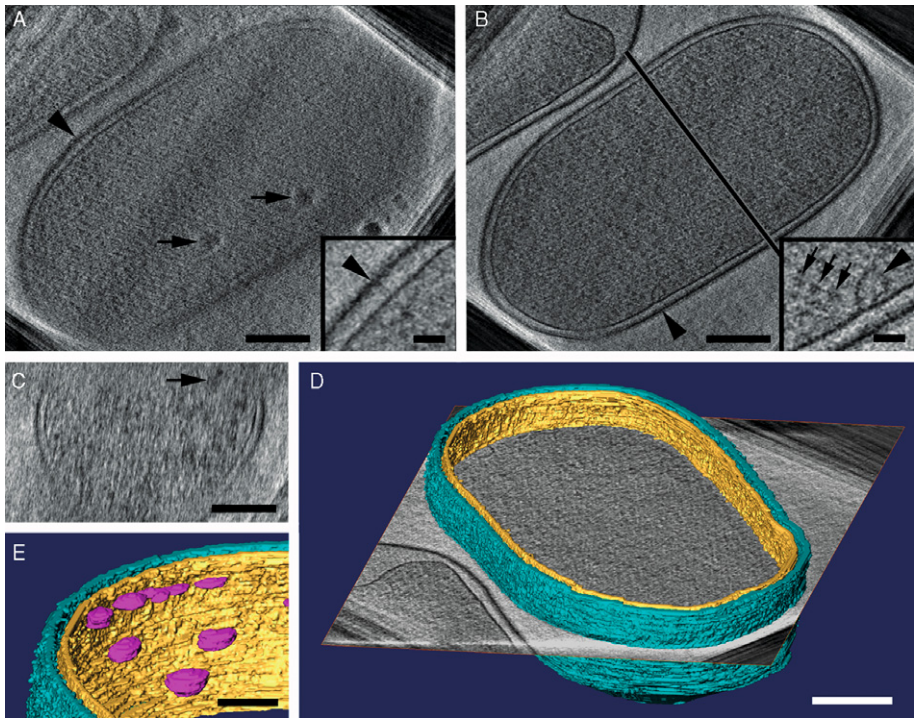

Fig. 3 Cryo-electron tomogram of an *Escherichia coli* cell that was prepared by cryo-FIB milling. A vitreously frozen cell was cut approximately in half with the FIB, and then transferred to the cryo-TEM for tilt-series acquisition. (A) A tomographic slice at cut surface showing frost particles (arrows) deposited after cutting. The arrowhead indicates the region that is enlarged in the inset showing a bridge between membranes. Clearly, fine structure is retained even at the cut surface. (B) Deeper tomographic slice: the arrowhead indicates the region that is enlarged in the inset showing a vesicle; the line indicates the plane of cross section in (C), in which the cut surface is uppermost, with a frost particle marked by an arrow. (D) Surface model showing membranes. (E) A portion of the surface model showing cluster of vesicles. Scale bars: 250 nm (A–D), 125 nm (E), 30 nm (insets in A and B). [Adapted with permission from Marko *et al*. (2007).]

III. Data Collection for Electron Tomography

A. Overall Strategy

Decisions about collection of the tilt-series images are guided by two fundamentals: (1) the biological questions being asked and (2) the capabilities and limitations of the available microscope. As will be described in detail in Section V, the simple formula $N = \pi D/d$ describes the relationship between the size of the specimen (D) and the number of projections (N) needed to reliably record features at a desired resolution (d) (Crowther *et al.*, 1970). Note that, strictly speaking, this relationship only holds in the direction normal to both the tilt axis and the electron beam. By convention, this is the x-axis, with the y-axis being along the tilt axis (for a single-tilt reconstruction), and the z-axis being in the direction of the electron beam (in the untilted image). Resolution in the z-direction is degraded by practical limitations to the tilting range as discussed in Sections IV.C and V.B.1. Thus, the first step in planning a reconstruction is to determine the specimen thickness needed to achieve the desired resolution (the thinner, the better); while retaining enough depth to contain the features of interest and their biological context (the thicker, the better), and keeping the number of images to be collected within a reasonable range. In general, a tomographic resolution of about 5 nm can be achieved with specimens that are several hundred nanometers thick, although data collection at these thicknesses requires the use of a transmission EM capable of accelerating voltages in the 300–400 kV range. Computer control of the microscope is also essential, in order to minimize the total electron dose accumulated by beam-sensitive specimens (Koster and Barcena, 2006; Koster *et al.*, 1997).

B. Tilt-Series Image Collection

Directional resolution loss can be minimized by collecting tilt series images of a specimen around two orthogonal axes (Sections IV.C, V.B, and V.C; Mastronarde, 1997; Penczek *et al.*, 1995). Tilt rotation or "flip-flop" stages facilitate dual-axis image collection on plastic sections and are necessary for dual-axis collection on frozen-hydrated specimens (Iancu *et al.*, 2005). Although it is generally preferable to collect dual-axis tilt series, in cases for which highest possible resolution is sought in a particular specimen direction, tilting about an axis normal to that direction would optimize the desired resolution. This strategy may be useful for some specimen geometries. Another reason for using single-axis tilting is that some specimen holders require that the specimen lie very close to the center of the specimen grid in order to achieve the full tilt range in two orthogonal directions. Thus, particularly when there is very little specimen available, single-axis tilting may be the only feasible approach.

In general, the tilt series should be collected over the greatest feasible tilt range. A single-axis tilt series with a maximum tilt angle of 75° will give approximately the same resolution in the worst direction (along the z-axis) as a dual-axis tilt series

with a maximum tilt angle of 60°. However, tilting beyond 60–70° is only useful for very thin specimens because image quality is degraded by the rapid increase of effective specimen thickness at the high tilt angles. Therefore, the most common approach is to collect a dual-axis tilt series with 60–70° maximum tilt.

Effective specimen thickness rapidly increases at high tilt angle because TEM specimens typically have slab geometry, that is, thin and planar (Barnard *et al.*, 1992). Consequently, there is an oversampling at low tilt angles and undersampling at high tilt angles, when a constant tilt interval (usually 1° or 2°) is used to collect the tomographic tilt series (Section V.B). Using a graduated tilt increment theoretically corrects this problem because of increased sampling at high tilt angles (Saxton *et al.*, 1984). However, in practice, little or no difference has been observed between using constant and graduated tilt increments. It is likely that the theoretical improvement expected from using graduated tilt increments is offset by the increased specimen thickness, which degrades the quality of high tilt images.

In principle, illumination of the specimen should remain constant during the tilt series, so that the 3D reconstruction will have a direct relationship between voxel intensity and specimen mass. (Voxel is a volume element in 3D images whereas pixel is a picture element in 2D images.) However, as most specimens have slab geometry, high-tilt images become quite noisy at constant illumination. The nearly universally adopted practice is to keep the mean image pixel value close to a set target value during tilt-series acquisition, by incrementally increasing the exposure time as the tilt angle increases (Grimm *et al.*, 1998a).

C. Considerations of Electron Dose

Plastic sections tend to thin under electron irradiation by 20–40% in the direction normal to the section plane (Luther, 2006; Luther *et al.*, 1988). This thinning has a biphasic correlation with electron dose: an initial thinning occurring in the range of 10^4 $e^-/Å^2$, followed by a more gradual rate of thinning. Because planar distortions are minimal, common practice is to preshrink plastic sections with a high electron dose (on the order of 10^5 $e^-/Å^2$) prior to collection of the images to be used for tomography.

Data collection strategy for beam-sensitive specimens, such as frozen-hydrated biological samples, is very different than for plastic sections. Here, it is critical that the total dose be kept below a threshold in order to prevent undesirable loss of specimen detail, or even gross distortions such as beam-induced bubbling. This beam sensitivity of frozen-hydrated specimens is the focus of the remainder of this section. In principle, the total electron dose that can be tolerated by a beam-sensitive specimen can be fractionated among as many images as necessary to achieve the desired tomographic resolution (Hegerl and Hoppe, 1976; McEwen *et al.*, 1995). However, as will be discussed, the minimum dose per image is limited in practice by the sensitivity (noise level) of the charge-coupled device (CCD) camera (Grimm *et al.*, 1998a; McEwen *et al.*, 2002).

1. Specimen Sensitivity

The minimum electron dose needed for a particular reconstruction is determined by the desired resolution, the specimen thickness, the accelerating voltage of the EM, and the noise level of the camera, while the maximum dose that can be tolerated by the specimen is determined by the nature of the specimen. Increased dose is required for higher resolution because (1) more tilt images are required to attain higher resolution for a given sample thickness, (2) the magnification must be higher, increasing the dose by the square of the magnification increase, and (3) higher resolutions require more electrons for a statistically significant signal-to-noise ratio (SNR). Together, the requirements for magnification increase and statistical significance leads to the prediction that the required number of electrons increases with the fourth power of the target resolution (McEwen *et al.*, 2002; Saxberg and Saxton, 1981).

Because the cross section of elastically scattered electrons in a material decreases with increasing energy, more electrons are required for the same SNR at higher accelerating voltage. However, this does not necessarily increase specimen damage because the cross section of inelastically scattered electrons also decreases with increasing accelerating voltage. Irradiation damage arises from energy lost by inelastically scattered electrons during their interaction with the specimen. Thus, in practice, although the incident dose is raised with the accelerating voltage, specimen damage is not increased.

Some frozen-hydrated specimens tolerate a higher cumulative electron dose than others. Pure vitreous ice tolerates a much higher electron dose than does an ice-embedded specimen; therefore, specimens with sparse structure are more resistant to overt types of specimen damage, such as ice radiolysis (“bubbling). For routine cryo-electron tomography, the maximum dose should not exceed 80–100 $e^{-}/Å^{2}$ at 200–400 kV. For example, studies on frozen-hydrated axonemes show that information from a 5-nm structure is reduced to 50% after 70 $e^{-}/Å^{2}$ at 400 kV (McEwen *et al.*, 2002).

2. Camera Sensitivity

Most CCD cameras intended for transmission EM use are capable of single-electron detection, but the yield of CCD counts per incident electron, and the noise level, varies considerably. For cryo-tomography, a minimum of 5 CCD counts per incident electron is recommended, unless the noise level is very low. At higher accelerating voltages, a thick phosphor scintillator may be needed to achieve adequate sensitivity, with the result that the point spread function can exceed the element size of the CCD pixel. In these cases, 2× binning of the CCD output is necessary, that is summing the signal from sets of 2×2 detector elements into a single output pixel, which of course reduces the effective detector array by a factor of 4. Ideally, this binning should be done after collection of the image, although it may be more convenient and faster to do it at the camera. Oversampling is a

common practice. For example, if a tomographic resolution of 4 nm is desired, a pixel size (after binning) of 1 nm is recommended. In this example, 2 nm corresponds to the minimum sampling needed for 4-nm resolution, and the additional oversampling is used to avoid alignment and interpolation errors, which can average 1 or 2 pixels, especially in the case of dual-axis tilt reconstructions (McEwen *et al.*, 1986).

It is necessary to calibrate the CCD camera with respect to the incident electron dose on the specimen. This is best done using a Faraday cage, which can be incorporated into a room-temperature specimen holder, or into the selected-area aperture holder. In the absence of a Faraday cage, the viewing-screen current can be used, although this use of the screen requires that it be properly calibrated when the EM was manufactured. Another alternative is to use photographic film of known sensitivity at the relevant accelerating voltage. It should be kept in mind that the incident dose is always measured with no specimen in the electron beam.

The practical performance of a camera system is measured by the minimum electron dose per image that can be used in the collection of a sequential series of images, without loss of information after the images are summed. Camera performance can be assessed with a specimen that yields spots or layer-lines in the power spectrum of the image. The layer-lines in the power spectrum give a quantitative measure of the intensity of features at a given resolution in an image created from a sum of low dose images, compared to the intensity in a single image recorded at the same total dose. For example, we found that for a 1-nm pixel size, images of axonemes can be recorded at a dose of 0.1 $e^{-}/Å^{2}$ at 400 kV, without loss of information (M. Marko, unpublished observation).

D. Optimization of Imaging Conditions

1. Accelerating Voltage and Inelastic Mean Free Path

Because frozen-hydrated biological specimens are composed of low-atomic-number elements, imaging must be done using phase contrast. For this reason, the specimen thickness should not greatly exceed one inelastic mean-free path. If the specimen is too thick, the SNR will be low because of a high background level created by inelastically scattered electrons, which are out of focus due to the chromatic aberration that arises from electrons that have lost energy. Thicker specimens will therefore require higher accelerating voltages, although energy filtering will help greatly (see below). Furthermore, it must be kept in mind that the effective specimen thickness doubles at 60° tilt and triples at 70° tilt.

If we take the inelastic mean-free path of vitreous ice at 120 kV to be about 200 nm (Grimm *et al.*, 1996; Sun *et al.*, 1993), then the value at 200 kV is 280 nm, the value at 300 kV is 350 nm, and the value at 400 kV is 398 nm [calculated according to Egerton (1996)]. These calculated values are consistent with a value of 380 nm for

frozen-hydrated biological specimens, as determined by correlation of electron energy loss spectroscopy with height measurements of cross sections from tomographic reconstructions (M. Marko, unpublished observation).

2. Energy Filtering

Zero-loss energy filtering is highly recommended for all but the thinnest specimens. In the thickness range of 0.5 to 1.5 inelastic mean-free paths, zero-loss filtering approximately doubles the SNR, for a given electron dose (Grimm *et al*., 1998b). Good phase-contrast images can be obtained with thicker specimens, but, as the fraction of elastically scattered electrons decreases, the electron dose must be increased to levels that are likely to damage the ultrastructure. However, tomographic reconstructions of bacteria as thick as 800 nm (twice the inelastic mean-free path) have been successfully recorded using zero-loss filtering at 400 kV accelerating voltage (Ting *et al*., 2007).

3. Defocus Imaging

In order to generate sufficient phase contrast in the image, the objective lens is normally set to a relatively high underfocus value. This results in a phase-contrast transfer function (CTF) that approximately follows a dampened sine curve (Fig. 4). Typically used defocus settings result in good transfer of only a narrow range of spatial frequencies. For optimization of resolution in the tomographic reconstruction, the underfocus should be set so that the band of information transfer extends to the highest resolution expected in the tomographic reconstruction (estimated according to Section III.A). It should be kept in mind that, because all spatial frequencies are not transferred with a uniform intensity, reconstructions made without correction of the CTF will lack a simple relationship between the voxel intensity and the mass at a corresponding location in the specimen.

4. Phase-Plate Imaging

Optimal phase-contrast imaging, without the variation in intensity transfer associated with underfocus, can be achieved by close-to-focus imaging with a phase plate in the back focal plane of the objective lens. The phase plate introduces a phase shift of $\pi/2$ between the unscattered electrons and the elastically scattered electrons. Consequently, with phase plate imaging, it is not necessary to use a high underfocus and CTF oscillation is largely avoided (Fig. 4). Phase plates (Fig. 5) consist of either a continuous film with a central hole or an electrostatic element suspended in the center of the objective aperture (Cambie *et al*., 2007; Danev and Nagayama, 2001; Majorovits *et al*., 2007). In the case of a continuous-film phase plate, spacings between 2 and 20 nm can be recorded with most conventional EMs. This range is adequate for cryo-tomography. The electrostatic elements currently in use are somewhat bulky, and a modified EM with a magnified back focal plane is

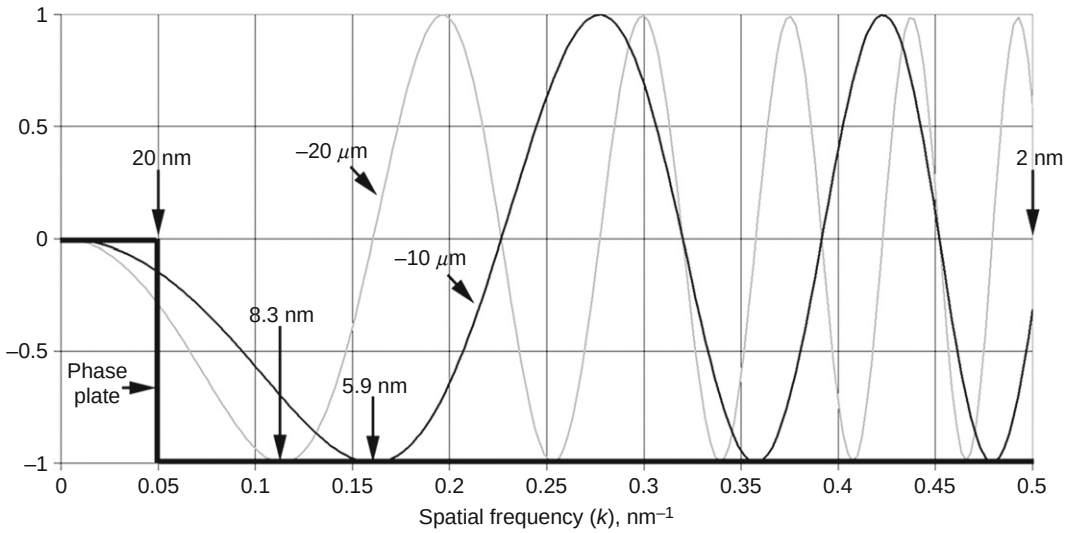

Fig. 4 Phase-contrast transfer function with and without a phase plate. The black and gray curves describe the phase-contrast transfer function obtained for 10- and 20-μm underfocus settings for a typical 300 kV TEM, whereas the heavy black step-function describes the phase-contrast transfer function obtained when using a phase plate and a close-to-focus setting. Note the narrow band of well-transferred spatial frequencies when either underfocus setting is used, contrasted with the wide band of good transfer when using the phase plate. The lowest spatial frequencies are cut off by the central element of the phase plate, which in this case has a diameter of 0.5 μm.

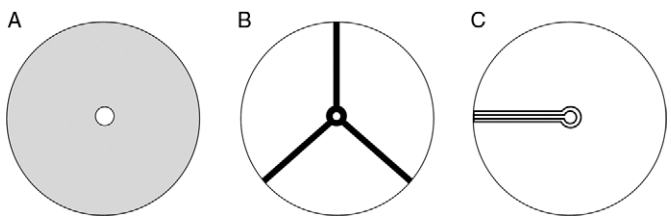

Fig. 5 Three types of phase plate. Only the central part is shown. Typically, the phase plate is built on an objective aperture 50 μm in diameter. (A) Zernike continuous-film type, as constructed by Danev and Nagayama (2001), in which a central hole allows passage of the unscattered beam, whereas electrons scattered by the specimen are phase-shifted by the inner potential of the thin film. (B) Boersch electrostatic type, as constructed by Majorovits *et al.* (2007), in which the unscattered beam is phase-shifted by an electrical potential applied to the ring element. (C) Alternative electrostatic type, as constructed by Cambie *et al.* (2007), in which the central element is a lightly biased drift tube that shifts the phase of the unscattered beam.

needed if important low spatial frequencies are to be retained. Unless the specimen is below one inelastic mean free path in thickness, energy filtering is needed for optimum use of a phase plate. Phase plates roughly double the overall image contrast, relative to defocused imaging, by eliminating the zones of poor contrast transfer. The lower range of spatial frequencies receives the greatest boost.

IV. Computation of an Electron Tomographic Reconstruction

A. Software for Electron Tomography

Electron tomography requires the use of specialized software for computation and subsequent analysis of 3D reconstructions. Tilt-series acquisition on modern microscopes is fully- or semiautomated and software-driven, in order to minimize specimen exposure and maximize throughput. Once the tilt series have been collected, another set of programs is used to compute the reconstruction. The reconstruction process described in this section includes algorithms for alignment, normalization, and computation of the 3D volume. Analysis and interpretation of the electron tomographic reconstruction, discussed in Section V, make use of both general 3D visualization software tools and specialized programs that have been developed for segmentation and rendering of the tomographic reconstruction. Most software packages, while including graphical user interfaces (GUIs) for ease of use, also have scripting options for more sophisticated user interaction. A list of software packages commonly used for electron tomography is provided in Table I. Additional information on EM software packages, including those dedicated to electron tomography, can be found in a special issue of the *Journal of Structural Biology* (Carragher *et al.*, 2007), and on the Wikipedia web site (http://en.wikipedia.org/wiki/Software_tools_for_molecular_microscopy). IMOD is a good choice for new users, especially those coming from the biological community. Other packages such as SPIDER and TOM offer additional features that are valuable for the specialist.

B. Tilt Series Alignment

For computation of a tomographic reconstruction, the tilt series images must first be aligned to a common coordinate system. Otherwise, density corresponding to a given feature in different 2D projections will not back-project to a consistent location in the 3D volume (Fig. 1). Tilt series alignment is achieved by algorithms that determine the rotation, translation, and magnification corrections that must be applied to the original tilt-series images. Although recent improvements in EM stage designs have made it much easier to automate tilt series collection with good initial alignment, a final computational alignment of the tilt-series remains essential.

Table I
Software Packages Commonly Used for Electron Tomography

Program	Tilt series collection	Reconstruction	Volume visualization	Contact
Bsoft/EM3DR2	No	FI	2D	bernard_heyman@nih.gov
EM3D	No	WBP	2D, 3D	contact@em3d.stanford.edu
IMOD/SerialEM	Yes	WBP	2D, 3D	mast@bio3d.colorado.edu
PROTOMO	No	WBP	External	info@electrontomography.org
SPIDER/WEB/SPIRE	No	WBP,FI, ART, SIRT	2D	spider@wadsworth.org
TomoJ/ImageJ	No	WBP, ART, SIRT	2D, 3D	tomoj@curie.u-psud.fr
TOM/MATLAB	Yes	WBP	2D	tom@biochem.mpg.de
UCSF EM Group	Yes	WBP, ART, SIRT	2D	ive@msg.ucsf.edu
Xplor3D/Inspect3D/Amira	Yes	WBP, ART, SIRT	2D, 3D	FEI Company Hilsboro, OR 97124

WBP, weighted back-projection; FI, Fourier interpolation; ART, algebraic reconstruction technique; SIRT, simultaneous iterative reconstruction technique; 2D, volume visualization via planar slices; 3D, volume visualization via volume rendering or surface rendering.

The most robust and universally applicable method of alignment utilizes colloidal gold fiducial markers deposited on the sample, or the support film, prior to data collection (Lawrence, 1992; Mastronarde, 1997; Penczek *et al.*, 1995). The gold particles should be large enough to be clearly visible in the tilt-series images, yet small enough that their centers can be accurately determined (ideally, diameters of 5–10 pixels in the digitized images). Colloidal gold particles 10–20 nm in diameter are typically used. Alignment begins by determination of the 2D coordinates for a set of the markers, on each projection image of the tilt series. These coordinates are used to calculate a 3D model of the marker locations. Projections of the 3D model are then computed to determine the consistency of marker locations between the model and the input images. Next the alignment algorithm computes the translation, rotation, and magnification corrections that must be applied to each input image, to optimize the fit between the marker locations in the images and the positions projected from the 3D model. After all corrections have been made, the 3D model is updated, and the process is iterated until the total difference between actual and projected marker positions stops decreasing. A minimum of 8–10 markers evenly distributed over the image area is recommended. While fewer markers can sometimes produce excellent results, the accuracy of alignment usually increases with the inclusion of more markers. Ideally, each marker will be tracked through the entire tilt series, but most alignment algorithms are able to accommodate some missing markers (Mastronarde, 2006).

A number of automatic marker-picking programs have been developed that alleviate the tedium and reduce the operator error associated with manual determination of the locations of 8+ markers on the 100+ tilt-series images used for a typical reconstruction (Mastronarde, 2006). These programs are included in most of the newer tomography software packages. The user can expect that a few of the calculated marker positions will need to be manually corrected, but such correction is much less laborious than a fully manual procedure. Newer automated fiducial marker-finding algorithms are being developed that use advanced statistical techniques to self-correct errors in assignment of fiducial markers (Amat *et al.*, 2007).

Because the deposition of gold particles is problematic for some types of specimens, attempts have been made to use structural features within the images as internal fiducial markers. Brandt *et al.* (2001, 2006) used image processing techniques to find "corners" in their data that were assigned as fiducial markers. Castano-Diez *et al.* (2007) used multiple cross-correlation windows to find features that could serve as fiducial markers. The success of each method depends on how well the statistical algorithms differentiate between good fiducial features and noise. As this differentiation becomes more difficult with increasing specimen thickness, these methods work best on relatively thin specimens. Furthermore, these "marker-free" alignment procedures perform poorly for the determination of rotation and magnification corrections. Cross correlation of successive tilt series images also has been used for alignment (McEwen and Frank, 1992; Winkler and Taylor, 2006) and is available on some packages provided by EM vendors. However, this procedure tends to produce systematic shifts in the direction normal to

the tilt axis in the absence of strong coplanar image features, especially for thicker specimens (C. Renken, unpublished observation).

In summary, alignments based upon colloidal gold markers should be employed whenever possible to generate accurate 3D reconstructions. Use of gold fiducial markers is especially important for very low dose imaging, in which the markers can be the only features that have sufficient signal for tracking during tilt-series collection.

C. Missing Information in Single- and Dual-Axis Tilt Series

The specimen geometry imposes important limitations on data collection in electron tomography. Most specimens are thin layers or sections with a thickness of 100–750 nm and lateral dimensions that extend hundreds of microns or even millimeters. As a result, when the specimen is tilted, the path length of the electron beam through the specimen increases inversely with the cosine of the tilt angle. Unless the specimen is very thin, the difficulty of imaging at high tilt angles sets a practical limit of 60–70° on the maximum tilt angle. Thus, tomographic reconstructions computed from single-axis tilt series generally are characterized by a wedge of missing data in the 3D Fourier transform (Fig. 6A) that gives rise to anisotropic resolution and a variety of artifacts (Sections V.B and V.C).

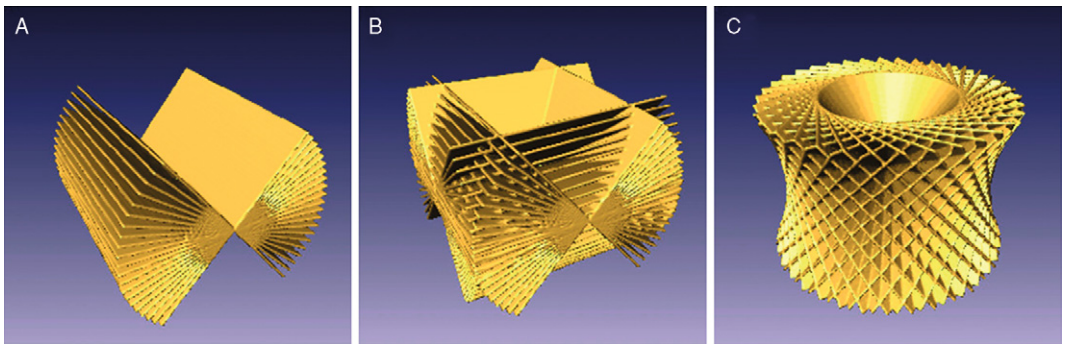

Fig. 6 Graphic depiction of missing Fourier information from a limited tilt angle range, for three data collection schemes. (A) A single-axis tilt series leaves a wedge of missing data in the 3D Fourier transform, which corresponds to a wedge of real space that is not covered during the tilt series collection. This results in anisotropic resolution, i.e., resolution that is different along each of the three coordinate axes. By convention, the *z*-axis is the direction of the electron beam in the untilted image, the *y*-axis is the direction of the tilt axis, and the *x*-axis is normal to both the electron beam and the tilt axis. (B) A dual-axis tilt series scheme leaves a missing pyramid, which results in nearly isotropic resolution in the *x*-*y* planes (planes normal to the direction of the electron beam). (C) A conical tilt series scheme leaves a missing cone, which also results in nearly isotropic resolution in the *x*-*y* planes. Thus, the increased Fourier space coverage for both dual-axis and conical tilting schemes, relative to single-axis tilting, produces isotropic resolution in *x*- and *y*-axis, but it does not reduce the resolution loss along the *z*-axis. [Reproduced with permission from Lanzavecchia (2006).]

Dual-axis tilting combines two tilt series, usually collected about perpendicular tilt axes, thereby reducing the missing wedge to a missing pyramid (Fig. 6B; Mastronarde, 1997; Penczek *et al.*, 1995). Resolution in the resultant reconstruction is nearly isotropic in 2D slices taken perpendicular to the direction of the electron beam, and artifacts (streaks) are less severe. For this reason, dual-axis data collection is usually employed for plastic-embedded specimens; it is also becoming increasingly common for frozen-hydrated specimens (Iancu *et al.*, 2005). Missing information in the 3D Fourier transform can be further reduced to a missing cone through the use of conical tilting (Fig. 6C; Frank and Radermacher, 1986; Zampighi *et al.*, 2006). Conical reconstruction is frequently employed in single-particle reconstructions for macromolecules that have a preferred orientation on the grid, but random azimuthal orientations (Radermacher *et al.*, 1987). However, conical tilting has not been widely used in electron tomography because, relative to dual-axis tilt-series collection, conical tilting requires a more complex tilt stage, produces only a modest gain in Fourier space coverage, and requires that all of the input images be collected at a high tilt angle where image quality is compromised by specimen thickness. Nevertheless, conical tilting has been used occasionally in electron tomography (Zampighi *et al.*, 2006).

The ideal solution to the missing-information problem is a cylindrical specimen geometry in which projections are recorded over the full 180° tilt range with a relatively uniform path length for the electron beam. An early attempt was successful in collecting a full 180° tilt series from a puffball spore mounted on a glass micropipette (Barnard *et al.*, 1992). However, most biological specimens are not amenable to being mounted on or in a micropipette, and imaging through the glass reduces contrast, even with high-voltage TEM. More recent attempts, with pillar-shaped specimens, have been reported, especially in materials sciences (Kaneko *et al.*, 2005), but formidable challenges remain, especially for frozen-hydrated biological specimens.

D. Reconstruction Algorithms

There are three basic types of reconstruction algorithms for electron tomography: (1) weighted back-projection (WBP), (2) direct Fourier methods (DFM), and (3) iterative methods such as the algebraic reconstruction technique (ART) and the simultaneous iterative reconstruction technique (SIRT). Of the three, the WBP algorithms are the least computationally intensive and, for most tomographic data, have yielded results that are equivalent to DFM, ART, and SIRT. For most users, the choice of reconstruction algorithm will be determined by the tomography software they use. Newer, graphically driven programs, such as IMOD, EM3D, and BSOFT, generally default to a single algorithm (WBP for IMOD and EM3D, and DFM for BSOFT). Users wishing to test multiple reconstruction methods must edit the script behind the GUI, or else use scripted software packages such as SPIDER and XMIPP that provide ready access to a broad range of algorithms.

The WBP and DFM reconstruction algorithms are based on the central section theorem, which states that the Fourier transform of a 2D projection through a 3D volume is equivalent to a central slice of the 3D Fourier transform (Figs. 6 and 7). Therefore, computation of a 3D volume from 2D projections in real space is equivalent to computation of the 3D Fourier transform from central slices in reciprocal space. The key problem that both techniques have to solve is that projections from tilted specimens describe the sampled volume in cylindrical or spherical coordinates that must be transformed to rectangular Cartesian coordinates (Fig. 7). When a rectilinear grid is superimposed on the central slices in reciprocal space, all of the central slices intersect at the center voxel ($R = 0$). Thus, the number of sampling points within that voxel is equal to the number of projections in the data set. Proceeding out from the center of the 3D transform, each voxel contains fewer sampling points. At the frequency determined by the resolution criterion of Crowther *et al.* (1970; see Section III.A), each voxel contains a single sampling point; beyond this frequency, the average number of sampling points per voxel is fractional.

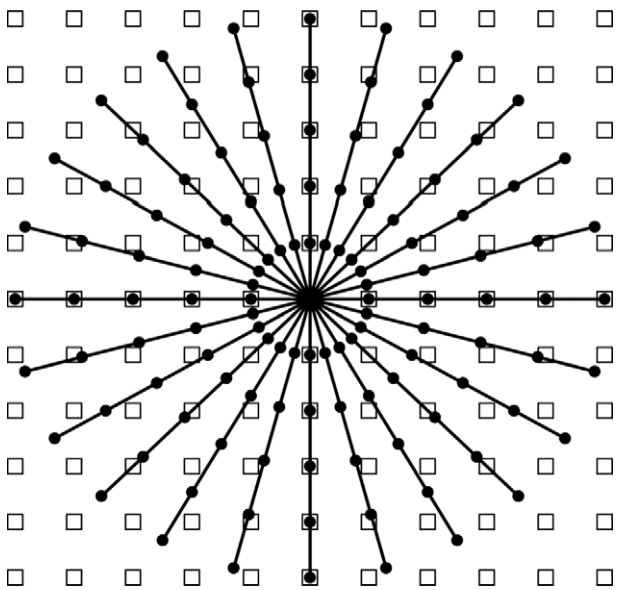

Fig. 7 Principle of unequal coverage of Fourier space in reconstruction from a tilt series. The diagram can be considered as a slice through a 3D Fourier transform of a volume reconstructed from 2D tilt projections that were collected as a single-axis tilt series. In Fourier space, the tilt series images form central slices, here represented by lines, of the reconstructed volume. There is a mismatch between the cylindrical geometry of the data points (circles) derived from the tilt series images (i.e., the set of central slices) and the rectilinear sampling grid (squares) imposed by digital imaging. Because the spacing between central slices increases with increasing Fourier radius, as illustrated by fewer circles per square, low-frequency components are overweighted relative to high-frequency components. [Taken with permission from Frank (1992).]

WBP algorithms simply sum the back-projected densities of all of the individual projections within a 3D voxel array in real space. This is equivalent to filling the 3D Fourier transform by summing of all of the central slices in reciprocal space. However, because the number of data points contributing to a given reciprocal-space voxel varies inversely with increasing R (distance from the tilt axis), direct summation of central slices overemphasizes the low spatial frequencies. The R-WBP method corrects this problem by multiplying each Fourier amplitude by the magnitude of its distance, R, from the tilt axis position in the 3D transform. R-weighting is exact only for single-axis data sets; for these, its application is compatible with computation of 3D reconstructions slice by slice along the tilt axis. Hence, parallel processing is readily applicable to WBP computation.

There are two different approaches for computing dual-axis reconstructions. The first is to reconstruct two separate volumes using the R-weighted algorithms, and then merge the two volumes in real space (Mastronarde, 1997, 2006). The second is to use a general weighting scheme that enables reconstruction from randomly oriented projections (Penczek *et al.*, 1995). The general weighting function is calculated at every voxel in reciprocal space, and is based on the number of sample values within that voxel. This weighting results in an exactly WBP, and for that reason, this approach is sometimes used for single-tilt reconstructions, even though it is more computationally intensive than R-weighting.

DFM was the first 3D reconstruction method used in EM (DeRosier and Klug, 1968). In this approach, the rectilinear Fourier transform of the volume is estimated through interpolation between the Fourier transforms of adjacent projections. The accuracy of the reconstruction depends on how far each voxel is from the sampled points from each of the projections. The method of interpolation differs from algorithm to algorithm, but all are numerical solutions to the Whittaker–Shannon theorem of interpolation (Crowther *et al.*, 1970; Hoppe, 1970; Lanzavecchia and Bellon, 1998; Lanzavecchia *et al.*, 1993; Radermacher, 1992). Implementation of the algorithms is generally done in 3D, but it can be broken down into a series of 2D problems (Crowther *et al.*, 1970) or even along individual 1D lattice lines (Taylor *et al.*, 1997). In the past, the computational requirements of Fourier interpolation made DFM much slower (and therefore less popular) than WBP. Recent developments (Penczek *et al.*, 2004) show promise in eventual production of Fourier algorithms that have the speed of WBP but with a higher reconstruction quality. Such programs have not yet been applied to tomographic data.

ART and SIRT are algebraic techniques that formulate the reconstruction as an optimization problem, in which the error between the data set and a set of projections through the reconstructed volume is minimized. The initial volume is usually generated by WBP, and an initial error function is calculated. During refinement, ART calculates the error function and adjusts each projection one at a time, while SIRT accumulates errors from all projections, and then adjusts the voxel intensities. The error is then minimized through adjustment of the voxel intensities within the volume. The algorithms are iterative, with adjustments followed by recalculation of the error function cycles, followed by readjustments. Our experience has

been that small improvements often occur within the first few iterations; however, the likelihood that the algorithm will settle at a false minimum requires that the process be supervised. In cases where tilt series data are sparse and/or entail missing images, use of an algebraic method can achieve significant improvement in the overall quality of the reconstruction. SIRT can also perform better than other algorithms in low SNR situations (Tong *et al.*, 2006). Overall, the advantages of the algebraic methods, relative to the less computationally intensive WBP methods, have yet to be settled.

V. Interpretation of Electron Tomographic Reconstructions

Electron tomographic reconstructions contain a wealth of information that, when properly extracted, has the potential to greatly add to our understanding of cell biology. However, interpretation of reconstruction volumes is complicated by the presence of artifacts arising from gaps in the 3D Fourier transform. Reconstructions of frozen-hydrated specimens are also limited by a low SNR. Typical steps in the analysis of tomographic reconstructions include contrast enhancement, resolution assessment, raw data visualization, noise filtering, segmentation and classification, and volume and surface rendering.

A. Contrast Enhancement

Electron tomographic reconstruction algorithms tend to use the full dynamic range for the output volume, which consequently will have few, if any, saturated voxels. Because a few outlier values are usually generated by fiducial gold and reconstruction artifacts, the bulk of the data is restricted to the gray levels near the mean density value. For this reason, it is important to stretch the histogram of the reconstruction so it spans a maximum of 3–4 standard deviations, before the grayscale resolution is reduced to 8 bits per voxel. Use of such a procedure ensures that the full grayscale resolution is maintained in the reconstruction.

B. Resolution Assessment

In contrast to LM, resolution in biological electron tomography is limited by a low SNR and directional gaps in the 3D Fourier transform (Section IV.C) rather than by diffraction. Therefore, in order to understand the nature of the limitations imposed by low SNR and limited angular sampling, biological electron tomography requires different resolution criteria than those used in LM. It is important to be aware of these differences when interpreting reconstruction volumes and developing approaches to improve the methodology.

1. Resolution Limits and Anisotropic Resolution in Electron Tomography

In EM, the SNR is dependent upon both specimen contrast and electron dose (McEwen *et al.*, 2002; Saxberg and Saxton, 1981). Hence, estimates of the maximum possible resolution in electron tomography depend on how the contrast is estimated. Nevertheless, the fourth-power dependence of resolution on electron dose, coupled with the extreme sensitivity of frozen-hydrated specimens to electron irradiation, predicts that resolution will not exceed 3–4 nm in the absence of single-particle averaging of structures from the tomographic reconstruction (Lucic *et al.*, 2005; McEwen *et al.*, 2002; Saxberg and Saxton, 1981). Theoretically, better resolution is possible for freeze-substituted material because plastic-embedded specimens tolerate a higher electron dose than frozen-hydrated specimens, and they have higher contrast due to the heavy metal staining. However, structural preservation is compromised by the solvent substitution, and the heavy metal stains enhance the contrast of some features while obscuring others. Hence, the limit to reliable resolution for freeze-substituted material is thought to be around 5 nm, although the actual value is specimen-dependent (Dubochet, 2007; Hsieh *et al.*, 2006).

Resolution in electron tomography is also a function of the interval between successive tilt images. At sufficiently large Fourier radii, the 3D transform is undersampled because of the missing information between neighboring central slices (Fig. 7). The Fourier radius at the point where the 3D Fourier transform becomes undersampled is the resolution limit specified by the criterion of Crowther *et al.* (1970) (see below). Resolution is further degraded in the direction of the missing information in the 3D Fourier transform that arises from a limited angular tilt range (Sections IV.C and V.C). Consequently, resolution is anisotropic in electron tomographic reconstructions (Mastronarde, 1997; Penczek *et al.*, 1995). For single-axis reconstructions, the resolution is least degraded in z-slices (2D slices along the z-axis, which is the direction of the electron beam in the zero-tilt image). Resolution is most degraded in y-slices (2D slices along the tilt axis). In dual-axis reconstructions, the resolution is nearly isotropic in the plane perpendicular to the direction of the electron beam. Hence, the resolutions of y- and x-slices are roughly equivalent.

2. Estimation of Resolution

The nature of the resolution limits in electron tomography makes it difficult to derive quantitative estimations of the overall resolution achieved. Nevertheless, reliable resolution estimates are needed to guide interpretation of tomographic reconstructions and to spur the development of new methodology.

A commonly used estimate of resolution is the frequency at which the 3D Fourier transform becomes undersampled (Crowther *et al.*, 1970):

$$R_{\max} = \frac{2N - 5}{4\pi a} \cong \frac{N}{2\pi a} \tag{1}$$

where $2a$ is the linear dimension of the projections, and N is the number of evenly spaced projections collected. This resolution criterion is more frequently used in its real space form:

$$d \cong \frac{\pi D}{N} \tag{2}$$

where d and D signify the resolution and the diameter of the volume, respectively.

Several problems arise when this formula is applied to electron tomography because this equation assumes full 180° angular coverage, as well as an idealized cylindrical specimen geometry with the tilt axis aligned along the cylinder axis. As discussed in Section IV.C, almost all EM specimens have slab geometry, making 180° angular coverage impractical, and the assignment of D problematic. Radermacher (1992) suggested that the thickness of the slab divided by the cosine of the maximum tilt angle be used for D, and that N be adjusted for partial angular coverage. In practice, however, D is simply replaced by thickness (see also McEwen and Marko (1999), suggesting that a 1° angular tilt interval ($N = 180$) is sufficient angular sampling to support 5-nm resolution for specimens less than 300 nm thick. Although in principle a tolerable electron dose can be fractionated into any number of tilt images, there is a practical lower limit to the dose that must be collected on each tilt image (Section III.C.2; Grimm *et al.*, 1998a; Hegerl and Hoppe, 1976; McEwen *et al.*, 1995, 2002). Hence, it will be difficult in practice to achieve adequate sampling to support 5-nm resolution for specimens thicker than 300–500 nm.

The above criterion only estimates the limits to resolution imposed by the available angular sampling. It does not take into account limits imposed by defocus effects, alignment errors, missing angular information, and the statistical significance at the maximum total electron dose the specimen can tolerate. Consequently, the tendency in the electron tomographic literature has been to estimate effective resolution in terms of the size of features detectable in the reconstructions. Two recent publications have presented the methods to quantify resolution based on consistency between the reconstruction and the input data. One approach is based on the "spectral signal-to-noise ratio" (SSNR), which is the SNR as a function of spatial frequency (Unser *et al.*, 1987, 2005). The SSNR measures, for each voxel in Fourier space, the variance in all of the contributions from the input projection images. Thus, the SSNR is sensitive to angular sampling, statistical significance, alignment errors, and defocus. Difficulties arising from undersampling in Fourier space can be avoided by applying SSNR to subvolumes of the tomographic reconstructions whose linear dimension (in voxels) is approximately equal to N (C. Renken, unpublished observations).

The second method for estimating the resolution available in a tomographic reconstruction is "noise-compensated leave one out" (NLOO) (Cardone *et al.*, 2005). NLOO builds on the theory of the Fourier shell correlation (FSC) criterion (Frank, 2006). However, instead of comparing two reconstructions computed

from half-sets of the data, a strategy that inevitably underestimates resolution, NLOO calculates a reconstruction from all input images minus one. A projection is then computed from the reconstruction along the direction of the missing input image, and the 2D Fourier ring correlation (FRC) is calculated between the computed projection and the missing input image. The procedure is repeated until all of the tilt series images have been left out once. A 3D FSC is then calculated as the average of the individual 2D FRCs and plotted as a function of spatial frequency. The resolution of the reconstruction is usually taken to be the spatial frequency at which the 3D FSC is equal to 0.5.

The SSNR and FRC are related (Penczek, 2002) by the equations:

$$\mathcal{S}\mathrm{SNR} = \frac{\mathrm{FRC}}{1 - \mathrm{FRC}} \tag{3}$$

$$\mathrm{FRC} = \frac{\mathcal{S}\mathrm{SNR}}{\mathcal{S}\mathrm{SNR} + 1} \tag{4}$$

A FSC of 0.5 is equal to an SNR of 1, which is generally (but not universally) accepted as the reliable resolution limit to 3D reconstructions in EM. There is still discussion in the EM community about the interpretation of FSC curves, with one report arguing that the acceptable FSC value should vary according to the number of voxels in the volume (van Heel and Schatz, 2005).

C. Recognition of Artifacts

Information theory predicts that *a priori* information lowers the SNR level at which known features can be resolved. Therefore, if an electron tomographic reconstruction contains well-characterized features, such as macromolecular assemblies of known structure, these features can be identified and localized despite limited resolution. However, the presence of directional artifacts must be taken into account during the interpretation of reconstructions, and care must be exercised in attempts to characterize features smaller than the estimated resolution limit.

One source of prominent artifacts is gaps in the 3D Fourier transform between neighboring central sections arising from the discrete nature of the angular sampling by the tilt series images and the missing wedge or pyramid in the 3D transform arising from the limited tilt range (Sections IV.C, IV.D, and V.B; and Figs. 6 and 7). In real space, the 3D reconstruction contains radial streaks in the directions that correspond to gaps between tilt series images and significant distortion in the direction that corresponds to the missing angular information (Fig. 8A–C). Consequently, high-resolution features detectable in 2D slices for the reconstruction are generally overlaid with streaks.

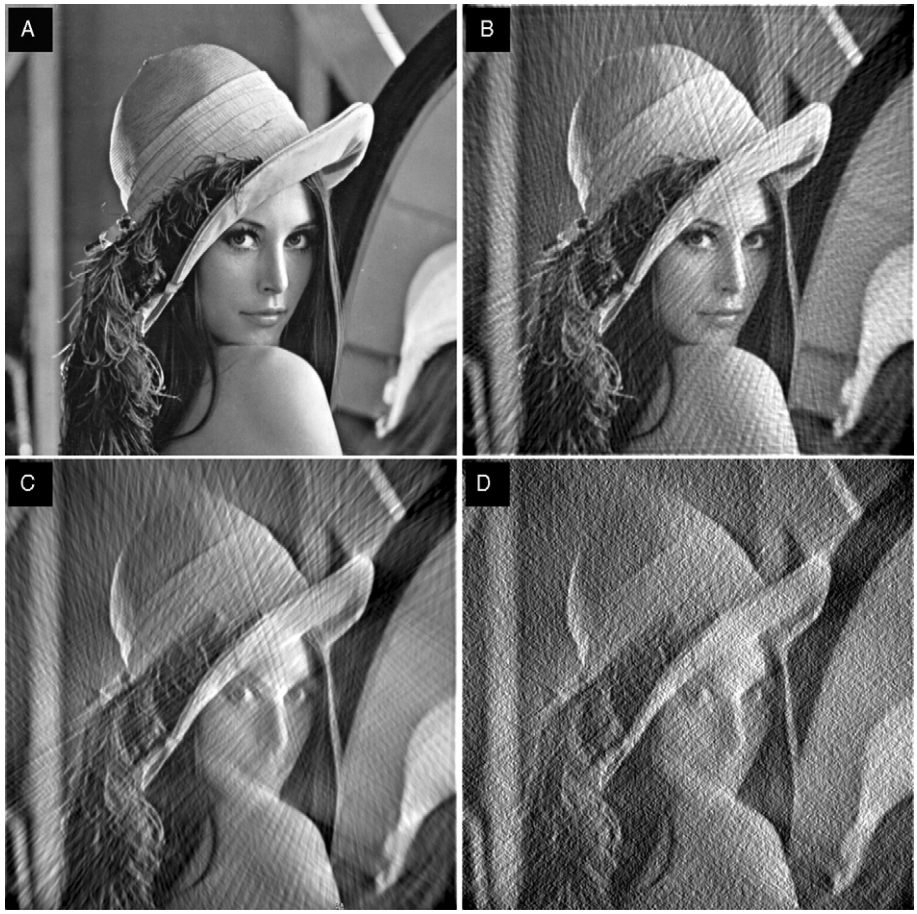

Fig. 8 Illustration of real-space artifacts arising from limited angular sampling and low SNR. (A) Original image of "Lena," a popular test image. (B) The 2D image reconstructed from 90 1D projections evenly distributed over a 180° tilt range. Note the numerous streaks that are produced by gaps between successive tilt images. (C) The 2D image reconstructed from 61 1D projections covering a 120° tilt range. Here, the missing wedge produces a smearing out of details in the vertical direction (e.g., the lips are nearly lost). (D) The 2D image reconstructed from 61 1D projections covering a 120° tilt range, with simulated shot noise added to each projection (SNR∼2) before calculation of the reconstruction. Note that high-resolution features, such as the feathers in Lena's hat, are present in (B) and (C) but overlaid with streaks. Fewer high-resolution features are present in (D) than in (C) because of the lower SNR, but the streak artifacts are also less prominent.

A generally underappreciated problem associated with the slab geometry is that projection images recorded at high tilt angles contain information that is absent from the low-tilt images of the specimen field (McEwen and Marko, 1999). The practical consequence is that artifacts due to strong features located outside the

subvolume of interest can enter into the reconstruction in the direction normal to the tilt axis. Therefore, while interpreting tomographic reconstructions, it is important to be aware of high-density features bordering the area of interest.

Low SNR generally is manifested as the inability to resolve known features in tomographic reconstructions, rather than in the generation of discrete artifacts (Fig. 8D). In fact, minor reconstruction artifacts can become less visible as the noise increases. Nevertheless, it is important to reduce noise for optimal interpretation of the 3D reconstructions. A number of strategies have been developed to reduce noise and other artifacts in the reconstructed volumes. Early in the development of electron tomography, it was recommended that images be low-pass filtered to the resolution limit defined by Eq. (2) (Frank *et al.*, 1987; McEwen *et al.*, 1986). Although such filtering eliminates most streak artifacts, it has the undesirable effect of indiscriminately blurring edges so that genuine high-resolution features are also lost.

This conundrum has led to efforts to develop more discriminating alternatives such as anisotropic diffusion and adaptive median filters (Fig. 9A and B) (Frangakis and Hegerl, 2001, 2006; van der Heide *et al.*, 2007). Anisotropic diffusion applies a smoothing function in directions in which the image gradient is small, but it recognizes edges and leaves them unaltered. Adaptive median filters replace a pixel with the median value of its neighbors, if that pixel diverges by more than a set number of standard deviations from the mean value. The critical factor in the application of these filters is to determine reasonable values for the threshold parameters.

Anisotropic diffusion and adaptive median filtering are used routinely for both frozen-hydrated and plastic-embedded specimens. Generally, a small test area is identified, and various combinations of filters, applied over a range of parameter settings, are tested to determine the optimal filtering. Additionally, the choice of filter type and the extent of filtering depend on the type of analysis that will follow. For simple viewing of the reconstruction, slight filtering is preferred to reduce the noise level without reducing the complexity of the reconstruction. In contrast, if the volume is to be autosegmented and surface-rendered, higher levels of filtration are needed in order to create smoothed and continuous boundaries between regions.

D. Analysis and Data Mining

1. Visualization

The first step in analyzing an electron tomographic reconstruction is usually viewing 2D slices from the z-direction, which have the best resolution (see Section V.B.1). Often, this is followed by viewing of 2D slices in orientations favorable for the visualization of particular features of interest. Most tomography software packages have this capability built-in.

While it is a good starting point, inspection of 2D slices does not provide a clear view of the 3D arrangement of complex features in the reconstruction, and can result in misinterpretation (Fig. 10). Hence, volume and surface-rendering

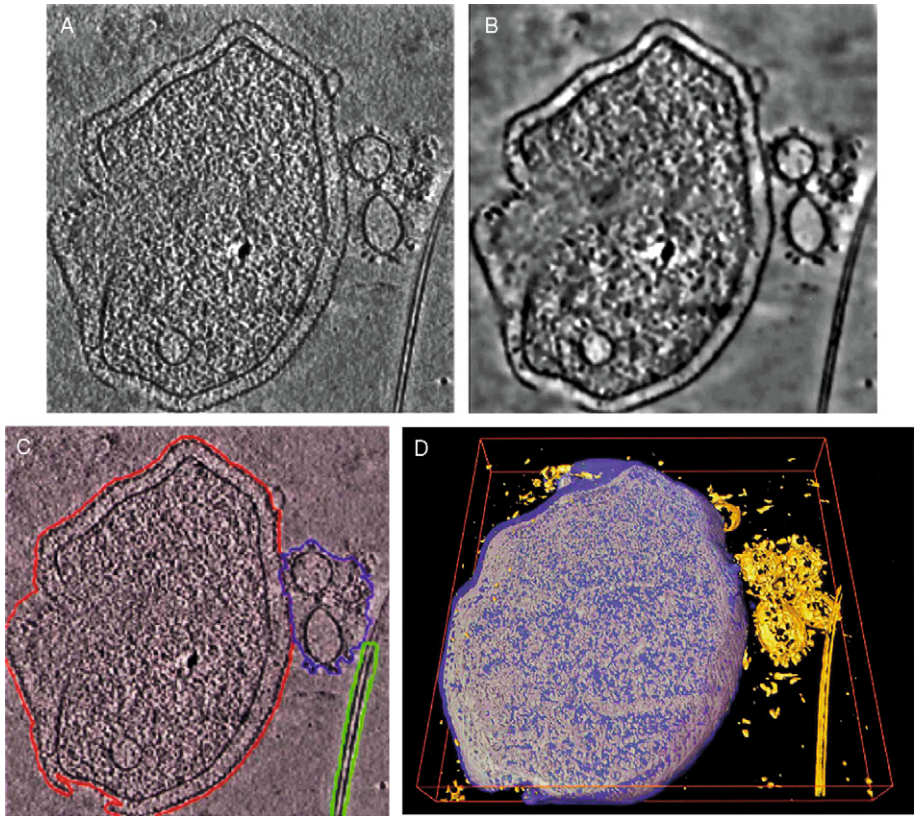

Fig. 9 Use of anisotropic filtering to denoise electron tomographic reconstructions prior to automated segmentation. (A) A slice from the tomographic reconstruction of a *Pyrodictium abyssi* cell. (B) Same slice as in panel A after application of the anisotropic diffusion noise filter. (C) Same slice as in panel A overlayed with segmentation boundaries that were calculated from the filtered image shown in B using an Eigenvector analysis of an affinity matrix. (D) Surface rendering of the complete 3D reconstruction of the *P. abyssi* cell after automated segmentation using noise reduction combined with eigenvector analysis as illustrated in panels B and C. [Adapted from Frangakis and Hegerl (2002) with permission.]

methods are essential (Fig. 11). Volume rendering converts voxel intensities to values of transparency and then calculates the transfer of illumination through the volume (Fig. 11B and E). The advantage of volume rendering is that it uses all of the data and avoids subjective segmentation. The disadvantage is that transparent objects are frequently difficult to analyze because of the overlap of features. In addition, volume rendering is computationally intensive and, until the introduction of modern graphics cards, could not be done in real time. Therefore, volume rendering is most effectively used on subvolumes of the reconstructions that are windowed from areas of interest.

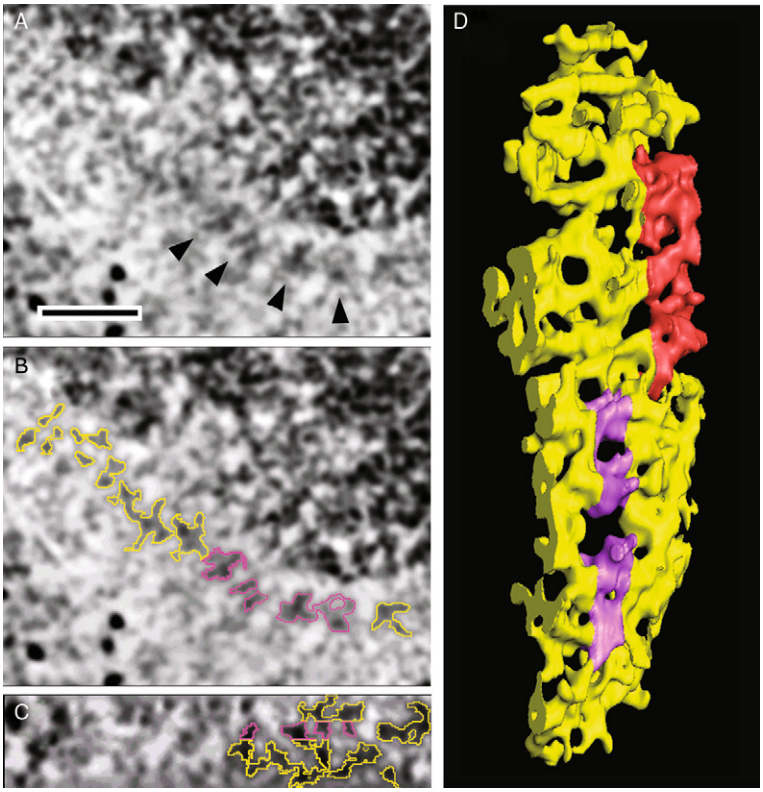

Fig. 10 Use of 3D rendering to understand the full context of structural features. (A) *Z*-slice through the tomographic reconstruction of a mammalian kinetochore from a PtK_1 cell. The cell has been treated with nocodazole to remove kinetochore-bound microtubules. The black arrowheads indicate features that appear to be distinct subunits of the kinetochore outer plate. (Dark material above the outer plate is the underlying heterochromatin.) (B) Semiautomated segmentation of the *z*-slice in panel A. The boundary selection tool in AMIRA finds boundaries of individual segments after the user sets a seed point. Contours through the features indicated in panel A are shown in purple. (C) *Y*-slice through the segmented region. Viewing from multiple directions facilitates editing selection made by the boundary selection tool. (D) Surface rendering of the full segmented outer plate in this reconstruction. Close examination of the surface-rendered model reveals that the subunit appearance (purple region) arises from large channels in a semiregular fibrous network. Red region gives a double-layered appearance to the outer plate in the corresponding 2D slices. The absence of a distinct subunit structure has important consequences for current models of how the kinetochore binds microtubules. Scale bar for A–C = 100 nm. [A,D from Dong *et al.*, 2007 with permission; B,C from Dong and McEwen, unpublished observations.]

Surface rendering is used more frequently than volume rendering because it mimics the physics of vision, in which light is reflected from surfaces (Fig. 11C and F). For surface rendering of a volume, boundaries between objects and the background are extracted and represented by meshes (Section V.D.2). These meshes are then

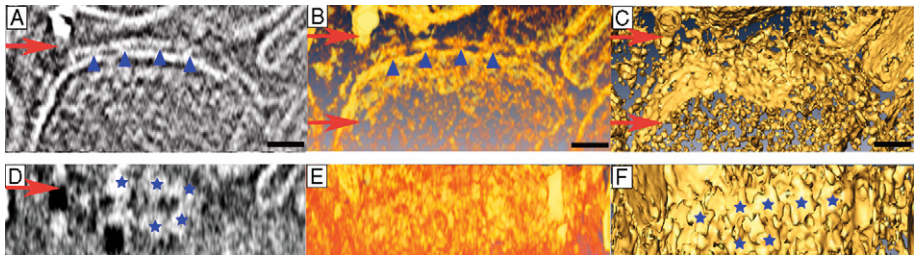

Fig. 11 Use of 2D slices, volume rendering, and surface rendering for visualizing components in an electron tomographic reconstruction. The specimen is an isolated triad junction vesicle from a plunge-frozen microsomal preparation. The triad junction contains ryanodine receptors (RyRs). (A) *Z*-slice with blue triangles indicating putative RyRs. The red arrow indicates the location of the *y*-slice shown in D. (B) Volume rendering viewed from the direction in which the *z*-slice is taken. RyRs are indicated by blue triangles. Red arrows indicate the boundaries of the subvolume rendered in panel E. (C) Surface rendering viewed from the same direction as in B. RyRs are difficult to discern. Red arrows indicate the boundaries of the subvolume used for surface rendering in F. (D) *Y*-slice containing the same RyRs (blue stars) indicated in A and others located at a different *z*-level. The red arrow indicates the location of the *z*-slice in A. (E) Volume rendering of the subvolume indicted by the red arrows in B does not produce a clear or informative view. (F) Surface rendering of the same subvolume clearly shows the RyRs projecting from the membrane (C. Renken, C. Mannella, and T. Wagenknecht, unpublished observation).

assigned properties of color, reflectivity, and transparency. Next, a virtual light source and camera are placed in the scene and the transmission of light is calculated from light source to camera. Once the mesh is calculated, rendering of the scene can be done in a low-resolution mode, in real time on most graphics cards, or in a publication-quality mode using ray-tracing algorithms. The latter method can be computationally intensive depending on the number of objects and the characteristics assigned to the surfaces.

2. Segmentation

Segmentation refers to identifying voxels or surfaces that belong to specified objects within the 3D reconstruction. It is one of the most critical, and time-consuming, steps in electron tomography. Segmentation is required to distinguish different features in a reconstructed volume and to remove background material before the application of rendering algorithms. The simplest approach is manual segmentation, which requires the user to draw contours that separate an object from the background. Manual segmentation programs aid the user in drawing contours, grouping contours into objects, and converting the contours into meshes and surfaces (Kremer *et al.*, 1996; Marko and Leith, 1996; McEwen and Marko, 1999). A model of the volume is then built, and surfaced objects are delineated from one another based on color. Alternatively, the contours can be used as a mask to select the voxels belonging to a particular structure, which can then be

volume-rendered. The fully segmented volume describes a scene that can be subsequently viewed from any direction, or as an animation of several views.

Clearly, hand-tracing of contours on individual slices of the volume is laborious and subjective. Therefore, a number of autosegmentation techniques have been proposed to free the user from this time-consuming task and provide greater objectivity in the surface determinations. However, the low SNR and the low contrast that results from a crowded cytoplasm filled with macromolecules and macromolecular complexes represent major challenges for automation (Jiang *et al.*, 2006c; Noske *et al.*, 2008; Salvi *et al.*, 2008; Sandberg, 2007). A thorough description of these challenges, and some of the methods being devised to overcome them, are provided by Sandberg (2007). Here, we give a brief summary of a few of these approaches, with particular focus on model-based and motif-search methods.

The simplest autosegmentation technique uses density thresholds to create closed isosurfaces that have equal pixel intensity at every point on their surface. Density thresholds work well when the objects of interest stand in clear contrast to the background. To aid in the delineation of objects of interest, edge-preserving noise reduction algorithms, such as anisotropic diffusion, can be used to enhance contrast (i.e., Fig. 9A and B; Section V.C). This approach enabled Frangakis and Hegerl (2002) to automatically segment a few well-defined boundaries in *Pyrodictium abyssi* cells using an eigenvector analysis of an affinity matrix (Fig. 9C and D). Nevertheless, the inherent complexity and low contrast of cellular environments generally require more than a single density threshold for feature extraction, even after noise reduction and contrast enhancement.

The difficulty in reliance on raw intensity and gradient information in the image is that these parameters tend to be poorly defined in electron tomographic reconstructions. A potentially powerful alternative strategy is to incorporate *a priori* knowledge into the segmentation process. Many cellular components have geometrically distinctive features such as linear fibers, small spherical vesicles, and membrane surfaces with a wide range of curvatures. Model-based methods attempt to use distinctive features to segment target components from the rest of the reconstruction volume (Jiang *et al.*, 2006c). It is important that size and shape constraints be flexible enough to take into account the innate biological variability. The most efficient and effective strategy is to proceed stepwise, from coarse down to fine features so as to reduce the search space for fine detail, and to minimize inclusion of irrelevant structures. This approach was used to segment kinetochore microtubules from tomographic reconstructions of metaphase PtK_1 cells (Jiang *et al.*, 2006a,b). First, microtubules were identified through sequential application of a specialized wavelet filter and a tubule enhancement filter. The precise microtubule boundaries were subsequently determined by edge-detection algorithms and extracted using active-shape modeling. Finally, microtubule plus-ends embedded in the kinetochore were extracted from 2D radial slices by means of a probabilistic tracing method.

Template matching is a special case of model-based segmentation that incorporates detailed prior knowledge of the target structure (Bohm *et al.*, 2000; Frangakis

and Rath, 2006). In this method, high-resolution structures of the target molecules, provided by preexisting X-ray crystallographic or single-particle EM reconstructions, are filtered to the resolution of the tomographic reconstructions and used as templates to probe the 3D volume. The search involves computation of a 6-D (i.e., the three coordinate axes, x, y, z, and the three Eulerian angles, φ, θ, ψ) cross-correlation function (CCF). Bohm *et al.* (2000) proposed the calculation of individual CCFs along the spatial axes (x,y,z) at discrete values of φ, θ, and ψ, and using spherical harmonic methods to calculate individual CCFs along the angular axes (φ, θ, ψ) at discrete values of x, y, and z (Cong *et al.*, 2003, 2005; Kovacs *et al.*, 2003). The choice of algorithm depends upon the size of the volume relative to the angular orientations that are to be sampled. False positives are a major challenge because the template will have significant but coincidental correlations with similar structures or even noise patterns within the tomographic volume. Frangakis *et al.* (2002) improved the CCF calculation by incorporating the missing wedge and a local variance measure, while Roseman (2003) derived a fast Fourier method that made computation of local variance feasible for moderately sized volumes. Computation time can be reduced by presegmentation of regions of the reconstruction known to contain the structures of interest (Bohm *et al.*, 2000). Postprocessing to remove false positives can be done either by segmentation or through the use of multivariate statistics (Frangakis and Rath, 2006; Ortiz *et al.*, 2006; Rath *et al.*, 2003). The latter approach reduces postprocessing to a classification problem that can be solved by one of several established schemes.

A number of autosegmentation techniques have been developed for medical imaging methods (MRI, X-ray computed tomography, positron emission tomography, etc.), but direct application to electron tomography has been limited by low contrast and low SNR. Nevertheless, medical segmentation methods continue to provide starting points for new approaches to image analysis, registration, and segmentation. An example is the *Insight ToolKit*, an extensive C/C++ library of medical segmentation and analysis algorithms (Ibanez *et al.*, 2005).

An intermediate approach of user-assisted autosegmentation is likely to be the most fruitful approach for current applications. For example, Dong *et al.* (2007) recently employed user editing to guide the "boundary selection" tool in the AMIRA software package (Fig. 10A–C). This interactive approach is less tedious and subjective than full manual tracing, and appears to be robust enough to handle crowded, high-noise cellular environments.

VI. Summary and Future Directions

Electron tomography is an invaluable tool for exploring cellular architecture with sufficient resolution to characterize extended structures and identify large macromolecular assemblies within a cell. Problems created by incomplete angular coverage of the input data can be minimized by using a fine angular sampling interval and by collecting a dual-axis tilt series over the greatest possible tilt range.

Cryo-electron tomography has made particularly impressive gains during the last 5 years, and its application to frozen-hydrated specimens will undoubtedly continue to grow in the near future, despite the low tolerance of frozen-hydrated specimens to electron exposure. In the meantime, important biological insights will continue to come from specimens that are high-pressure frozen, freeze-substituted, embedded in plastic, and stained with heavy metals.

The efficacy of electron tomography can be enhanced by prior knowledge of structural components located in the 3D reconstruction. In some cases, *a priori* knowledge is formally incorporated into motif searches or model-based segmentation, but more frequently it manifests as the observer's ability to discern familiar landmarks within the reconstruction.

Looking to the future, we expect technical advances in cryo-ultramicrotomy and FIB milling to extend cryo-electron tomographic applications to an ever-wider range of eukaryotic cell types. New detector systems could produce more sensitive cameras that significantly improve the SNR. This will be especially valuable for cryo-electron tomography. Fully automated segmentation algorithms face huge hurdles but steady progress is being made with semiautomated segmentation procedures and data-mining schemes such as motif search. Other technical developments appear distant but have the potential to revolutionize biological electron tomography. These include improved data collection geometries to eliminate the missing angular range and improved high density tags for labeling macromolecular complexes within frozen-hydrated or freeze-substituted cells.

Acknowledgments

The authors thank Adriana Verschoor for critical comments on the manuscript, and Dr. Yimin Dong for help in preparing Fig. 10. The authors acknowledge support from NIH grant RR41 01219 to CM for support of the Wadsworth Center's Resource for Visualization of Biological Complexity, and NIH grant R01 GM06627 to BFM. The authors are also grateful for technical support from the Wadsworth Center's Core Facility for Electron Microscopy.

References

Al-Amoudi, A., Studer, D., and Dubochet, J. (2005). Cutting artefacts and cutting process in vitreous sections for cryo-electron microscopy. *J. Struct. Biol.* **150,** 109–121.

Amat, F., Moussavi, F., Comolli, L. R., Elidan, G., Downing, K. H., and Horowitz, M. (2007). Markov random field based automatic image alignment for electron tomography. *J. Struct. Biol.* **161**(3), 260–275.

Barnard, D. P., Turner, J. N., Frank, J., and McEwen, B. F. (1992). A 360 degrees single-axis tilt stage for the high-voltage electron microscope. *J. Microsc.* **167,** 39–48.

Bohm, J., Frangakis, A. S., Hegerl, R., Nickell, S., Typke, D., and Baumeister, W. (2000). Toward detecting and identifying macromolecules in a cellular context: Template matching applied to electron tomograms. *Proc. Natl. Acad. Sci. USA* **97,** 14245–14250.

Brandt, S., Helkkonen, J., and Engelhardt, P. (2001). Automatic alignment of transmission electron microscope tilt series without fiducial markers. *J. Struct. Biol.* **136,** 201–213.

Brandt, S.S., and Ziese, U. (2006). Automatic TEM image alignment by trifocal geometry. *J. Microsc.* **222,** 1–14.

Cambie, R., Downing, K. H., Typke, D., Glaeser, R. M., and Jin, J. (2007). Design of a microfabricated, two-electrode phase-contrast element suitable for electron microscopy. *Ultramicroscopy* **107,** 329–339.

Cardone, G., Grunewald, K., and Steven, A. C. (2005). A resolution criterion for electron tomography based on cross-validation. *J. Struct. Biol.* **151,** 117–129.

Carragher, B., Potter, C. S., and Sigworth, F. J. (2007). Software tools for macromolecular microscopy. *J. Struct. Biol.* **157,** 1–2.

Castano-Diez, D., Al-Amoudi, A., Glynn, A. M., Seybert, A., and Frangakis, A. S. (2007). Fiducial-less alignment of cryo-sections. *J. Struct. Biol.* **159,** 413–423.

Cong, Y., Kovacs, J. A., and Wriggers, W. (2003). 2D fast rotational matching for image processing of biophysical data. *J. Struct. Biol.* **144,** 51–60.

Cong, Y., Jiang, W., Birmanns, S., Zhou, Z. H., Chiu, W., and Wriggers, W. (2005). Fast rotational matching of single-particle images. *J. Struct. Biol.* **152,** 104–112.

Crowther, R. A., Amos, L. A., Finch, J. T., De Rosier, D. J., and Klug, A. (1970). Three dimensional reconstructions of spherical viruses by fourier synthesis from electron micrographs. *Nature* **226,** 421–425.

Danev, R., and Nagayama, K. (2001). Transmission electron microscopy with Zernike phase plate. *Ultramicroscopy* **88,** 243–252.

DeRosier, D. J., and Klug, A. (1968). Reconstruction of three-dimensional structure from electron micrographs. *Nature* **217,** 130–134.

Dong, Y., Vanden Beldt, K. J., Meng, X., Khodjakov, A., and McEwen, B. F. (2007). The outer plate in vertebrate kinetochores is a flexible network with multiple microtubule interactions. *Nat. Cell Biol.* **9,** 516–522.

Dubochet, J. (2007). The physics of rapid cooling and its implications for cryoimmobilization of cells. *In* "Methods in Cell Biology" (J. R. McIntosh, ed.), **79,** pp. 7–21. Academic Press, New York.

Dubochet, J., Adrian, M., Chang, J. J., Homo, J. C., Lepault, J., McDowall, A. W., and Schultz, P. (1988). Cryo-electron microscopy of vitrified specimens. *Q. Rev. Biophys.* **21,** 129–228.

Dubochet, J., and Sartori Blanc, N. (2001). The cell in absence of aggregation artifacts. *Micron* **32,** 91–99.

Dubochet, J., Zuber, B., Eltsov, M., Bouchet-Marquis, C., Al-Amoudi, A., and Livolant, F. (2007). How to "read" a vitreous section. *In* "Methods in Cell Biology" (J. R. McIntosh, ed.), **79,** pp. 385–406. Academic Press, New York.

Egerton, R. F. (1996). Electron Energy-Loss Spectroscopy in the Electron Microscope Plenum, New York.

Frangakis, A. S., Bohm, J., Forster, F., Nickell, S., Nicastro, D., Typke, D., Hegerl, R., and Baumeister, W. (2002). Identification of macromolecular complexes in cryoelectron tomograms of phantom cells. *Proc. Natl. Acad. Sci. USA* **99,** 14153–14158.

Frangakis, A. S., and Hegerl, R. (2001). Noise reduction in electron tomographic reconstructions using nonlinear anisotropic diffusion. *J. Struct. Biol.* **135,** 239–250.

Frangakis, A. S., and Hegerl, R. (2002). Segmentation of two- and three-dimensional data from electron microscopy using eigenvector analysis. *J. Struct. Biol.* **138,** 105–113.

Frangakis, A. S., and Hegerl, R. (2006). Segmentation of three-dimensional electron tomographic images. *In* "Electron Tomography" (J. Frank, ed.), pp. 353–370. Springer, New York.

Frangakis, A. S., and Rath, B. K. (2006). Motif search in electron tomography. *In* "Electron Tomography" (J. Frank, ed.), pp. 401–416. Springer, New York.

Frank, J. (2006). Three-dimensional electron microscopy of macromolecular assemblies. pp. 250–251. Oxford University Press, Oxford.

Frank, J., McEwen, B. F., Radermacher, M., Turner, J. N., and Rieder, C. L. (1987). Three-dimensional tomographic reconstruction in high-voltage electron microscopy. *J. Electron Microsc. Tech.* **6,** 193–205.

Frank, J., and Radermacher, M. (1986). Three-dimensional reconstruction of non-periodic macromolecular assemblies from electron micrographs. *In* "Biological Electron Microscopy III" (J. K. Koehler, ed.), **3,** pp. 1–72. Springer-Verlag, Berlin.

Gilkey, J. C., and Staehelin, A. (1986). Advances in ultrarapid freezing for the preservation of cellular ultrastructure. *J. Electron Microsc. Tech.* **3,** 177–210.

Glauert, A. M., and Lewis, P. R. (1998). *In* "Biological Specimen Preparation," p. 326. Portland Press, London.

Grimm, R., Singh, H., Rachel, R., Typke, D., Zillig, W., and Baumeister, W. (1998). Electron tomography of ice-embedded prokaryotic cells. *Biophys. J.* **74,** 1031–1042.

Grimm, R., Typke, D., Barmann, M., and Baumeister, W. (1996). Determination of the inelastic mean free path in ice by examination of tilted vesicles and automated most probable loss imaging. *Ultramicroscopy* **63,** 169–179.

Grimm, R., Typke, D., and Baumeister, W. (1998a). Improving image quality by zero-loss energy filtering: Quantitative assessment by means of image cross-correlation. *J. Microsc.* **190,** 339–349.

Gruska, M., Medalia, O., Baumeister, W., and Leis, A. (2008b). Electron tomography of vitreous sections from cultured mammalian cells. *J. Struct. Biol.* **161,** 384–392.

Hawes, P., Netherton, C. L., Mueller, M., Wileman, T., and Monaghan, P. (2007). Rapid freeze-substitution preserves membranes in high-pressure frozen tissue culture cells. *J. Microsc.* **226,** 182–189.

Hegerl, R., and Hoppe, W. (1976). Influence of electronic noise on three-dimensional image reconstruction. *Z. Naturforsch.* **31a,** 1717–1721.

Heuser, J. E. (1986). Different structural states of a microtubule cross-linking molecule, captured by quick-freezing motile axostyles in protozoa. *J. Cell Biol.* **103,** 2209–2227.

Heuser, J. E., Reese, T. S., and Landis, D. M. (1976). Preservation of synaptic structure by rapid freezing. *Cold Spring Harb. Symp. Quant. Biol.* **40,** 17–24.

Hoog, J. L., and Antony, C. (2007). Whole-cell investigation of microtubule cytoskeleton architecture by electron tomography. *In* "Cellular Electron Microscopy" (J. R. McIntosh, ed.), **79,** pp. 145–167. Academic Press, New York.

Hoppe, W. (1970). Principles of electron structure research at atomic resolution using conventional electron microscopes for the measurements of amplitudes and phases. *Acta Crystallogr. A* **26,** 414–425.

Hsieh, C., He, W., Marko, M., and Stokes, D. L. (2004). 3D Tomographic map of desmosome from frozen-hydrated skin sections. *Microsc. Microanal.* **10**(S2), 1188CD.

Hsieh, C. E., Leith, A., Mannella, C. A., Frank, J., and Marko, M. (2006). Towards high-resolution three-dimensional imaging of native mammalian tissue: Electron tomography of frozen-hydrated rat liver sections. *J. Struct. Biol.* **153,** 1–13.

Iancu, C. V., Wright, E. R., Benjamin, J., Tivol, W. F., Dias, D. P., Murphy, G. E., Morrison, R. C., Heymann, J. B., and Jensen, G. J. (2005). A "flip-flop" rotation stage for routine dual-axis electron cryotomography. *J. Struct. Biol.* **151,** 288–297.

Ibanez, L., Schroeder, W., Ng, L., and Cates, J. (2005). The ITK Software Guide Insight Software Consortium, U.S. Nat'l Library Med., http://hdl.handle.net/1926/388.

Jiang, M., Ji, Q., and McEwen, B. F. (2006a). Automated extraction of fine-features of kinetochore microtubules and plous ends from electron tomography volume. *IEEE Trans. Image Process.* **15,** 2035–2048.

Jiang, M., Ji, Q., and McEwen, B. F. (2006b). Model-based extraction of microtubules from electron tomography volume. *IEEE Trans. Inf. Technol. Biomed.* **10,** 608–617.

Jiang, M., Ji, Q., Wang, X., and McEwen, B. F. (2006c). Segmentation of cell components using prior knowledge. *In* "Electron Tomography" (J. Frank, ed.), pp. 371–399. Springer, New York.

Kaneko, T., Nishioka, H., Nishi, T., and Jinnai, H. (2005). Reduction of anisotropic image resolution in transmission electron microtomography by use of a quadrangular prism-shaped section. *J. Electron Microsc.* **54,** 437–444.

Kapoor, T. M., Lampson, M. A., Hergert, P., Cameron, L., Cimini, D., Salmon, E. D., McEwen, B. F., and Khodjakov, A. (2006). Chromosomes can congress to the metaphase plate before biorientation. *Science* **311,** 388–391.

Koning, R. I., Zovko, S., Barcena, M., Oostergetel, G. T., Koerten, H. K., Galjart, N., Koster, A. J., and Mieke Mommaas, A. (2008). Cryo electron tomography of vitrified fibroblasts: Microtubule plus ends in situ. *J. Struct. Biol.* **161,** 459–468.

Koster, A. J., and Barcena, M. (2006). Cryotomography: Low dose tomography of frozen-hydrated specimens. *In* "Electron Tomography" (J. Frank, ed.), pp. 113–161. Springer, New York.

Koster, A. J., Grimm, R., Typke, D., Hegerl, R., Stoschek, A., Walz, J., and Baumeister, W. (1997). Perspectives of molecular and cellular electron tomography. *J. Struct. Biol.* **120,** 276–308.

Kovacs, J. A., Chacon, P., Cong, Y., Metwally, E., and Wriggers, W. (2003). Fast rotational matching of rigid bodies by fast Fourier transform acceleration of five degrees of freedom. *Acta Crystallogr. D Biol. Crystallogr.* **59,** 1371–1376.

Kremer, J. R., Mastronarde, D. N., and McIntosh, J. R. (1996). Computer visualization of three-dimensional image data using IMOD. *J. Struct. Biol.* **116,** 71–76.

Lanzavecchia, S., and Bellon, P. L. (1998). Fast computation of 3D Radon transform via a direct Fourier method. *Bioinformatics* **14,** 212–216.

Lanzavecchia, S., Bellon, P. L., and Tosoni, L. (1993). FT3D: Three-dimensional Fourier analysis on small Unix workstations for electron microscopy and tomographic studies. *Comput. Appl. Biosci.* **9,** 681–685.

Lawrence, M. C. (1992). Least-squares method of alignment using markers. *In* "Electron Tomography" (J. Frank, ed.), pp. 197–204. Plenum, New York.

Leforestier, A., Dubochet, J., and Livolant, F. (2001). Bilayers of nucleosome core particles. *Biophys. J.* **81,** 2414–2421.

Lucic, V., Forster, F., and Baumeister, W. (2005). Structural studies by electron tomography: From cells to molecules. *Annu. Rev. Biochem.* **74,** 833–865.

Luther, P. K. (2006). Sample shrinkage and radiation damage of plastic sections. *In* "Electron Tomography" (J. Frank, ed.), pp. 17–48. Springer, New York.

Luther, P. K., Lawrence, M. C., and Crowther, R. A. (1988). A method for monitoring the collapse of plastic sections as a function of electron dose. *Ultramicroscopy* **24,** 7–18.

Maiato, H., Hergert, P. J., Moutinho-Pereira, S., Dong, Y., Vandenbeldt, K. J., Rieder, C. L., and McEwen, B. F. (2006). The ultrastructure of the kinetochore and kinetochore fiber in *Drosophila* somatic cells. *Chromosoma* **115,** 469–480.

Majorovits, E., Barton, B., Schultheiss, K., Perez-Willard, F., Gerthsen, D., and Schroder, R. R. (2007). Optimizing phase contrast in transmission electron microscopy with an electrostatic (Boersch) phase plate. *Ultramicroscopy* **107,** 213–226.

Marko, M., and Hsieh, C. (2007). 3-D cryo-electron microscopy of cells and organelles. *In* "Electron Microscopy Methods and Protocols" (J. Kuo, ed.), **117,** pp. 407–429. Humana Press, Totowa, NJ.

Marko, M., Hsieh, C., and Mannella, C. (2006a). Electron tomography of frozen-hydrated sections of cells and tissues. *In* "Electron Tomography" (J. Frank, ed.), pp. 49–81. Springer, New York.

Marko, M., Hsieh, C., MoberlyChan, W., Mannella, C. A., and Frank, J. (2006b). Focused ion beam milling of vitreous water: Prospects for an alternative to cryo-ultramicrotomy of frozen-hydrated biological samples. *J. Microsc.* **222,** 42–47.

Marko, M., and Leith, A. (1996). Sterecon—three-dimensional reconstructions from stereoscopic contouring. *J. Struct. Biol.* **116,** 93–98.

Masich, S., Ostberg, T., Norlen, L., Shupliakov, O., and Daneholt, B. (2006). A procedure to deposit fiducial markers on vitreous cryo-sections for cellular tomography. *J. Struct. Biol.* **156,** 461–468.

Mastronarde, D. N. (1997). Dual-axis tomography: An approach with alignment methods that preserve resolution. *J. Struct. Biol.* **120,** 343–352.

Mastronarde, D. N. (2006). Fiducial marker and hybrid alignment methods for single- and double-axis tomography. *In* "Electron Tomography" (J. Frank, ed.), pp. 163–185. Springer, New York.

McDonald, K. (2007). Cryopreparation methods for electron microscopy of selected model systems. *In* "Methods in Cell Biology" (J. R. McIntosh, ed.), **79,** pp. 23–56. Academic Press, New York.

McDonald, K. L., Morphew, M., Verkade, P., and Muller-Reichert, T. (2007). Recent advances in high-pressure freezing: Equipment- and specimen-loading methods. *Methods Mol. Biol.* **369,** pp. 143–173. Humana Press, Totowa, NJ.

McEwen, B. F. (1992). Three-dimensional reconstructions of organelles and cellular processes. *In* "Electron Tomography" (J. Frank, ed.), pp. 281–311. Plenum, New York.

McEwen, B. F., Dong, Y., and VandenBeldt, K. J. (2007). Using electron microscopy to understand functional mechanisms of chromosome alignment on the mitotic spindle. *In* "Methods in Cell Biology" (J. R. McIntosh, ed.), **79,** pp. 259–293. Academic Press, New York.

McEwen, B. F., Downing, K. H., and Glaeser, R. M. (1995). The relevance of dose-fractionation in tomography of radiation-sensitive specimens. *Ultramicroscopy* **60,** 357–373.

McEwen, B. F., and Frank, J. (1992). Alignment by cross-correlation. *In* "Electron Tomography" (J. Frank, ed.), pp. 205–213. Plenum, New York.

McEwen, B. F., Heagle, A. B., Cassels, G. O., Buttle, K. F., and Rieder, C. L. (1997). Kinetochore fiber maturation in PtK1 cells and its implications for the mechanisms of chromosome congression and anaphase onset. *J. Cell Biol.* **137,** 1567–1580.

McEwen, B. F., Hsieh, C. E., Mattheyses, A. L., and Rieder, C. L. (1998). A new look at kinetochore structure in vertebrate somatic cells using high-pressure freezing and freeze substitution. *Chromosoma* **107,** 366–375.

McEwen, B. F., and Marko, M. (1999). Three-dimensional transmission electron microscopy and its application to mitosis research. *Methods Cell Biol.* **61,** 81–111.

McEwen, B. F., Marko, M., Hsieh, C. E., and Mannella, C. (2002). Use of frozen-hydrated axonemes to assess imaging parameters and resolution limits in cryoelectron tomography. *J. Struct. Biol.* **138,** 47–57.

McEwen, B. F., Radermacher, M., Rieder, C. L., and Frank, J. (1986). Tomographic three-dimensional reconstruction of cilia ultrastructure from thick sections. *Proc. Natl. Acad. Sci. USA* **83,** 9040–9044.

McIntosh, R., Nicastro, D., and Mastronarde, D. (2005). New views of cells in 3D: An introduction to electron tomography. *Trends Cell Biol.* **15,** 43–51.

Moor, H. (1987). Theory and practice of high pressure freezing. *In* "Cryotechniques in Biological Electron Microscopy" (R. A. Steinbrecht, and K. Zierold, eds.), pp. 175–191. Springer-Verlag, Berlin.

Morphew, M. K. (2007). 3D immunolocalization with plastic sections. *Methods Cell Biol.* **79,** 493–513.

Muller-Reichert, T., Srayko, M., Hyman, A., O'Toole, E. T., and McDonald, K. (2007). Correlative light and electron microscopy of early *Caenorhabditis elegans* embryos in mitosis. *In* "Methods in Cell Biology" (J. R. McIntosh, ed.), **79,** pp. 101–119. Academic Press, New York.

Murk, J. L., Posthuma, G., Koster, A. J., Geuze, H. J., Verkleij, A. J., Kleijmeer, M. J., and Humbel, B. M. (2003). Influence of aldehyde fixation on the morphology of endosomes and lysosomes: Quantitative analysis and electron tomography. *J. Microsc.* **212,** 81–90.

Noske, A. B., Costin, A. J., Morgan, G. P., and Marsh, B. J. (2008). Expedited approaches to whole cell electron tomography and organelle mark-up in situ in high-pressure frozen pancreatic islets. *J. Struct. Biol.* **161,** 298–313.

O'Toole, E. T., Giddings, T. H., Jr., and Dutcher, S. K. (2007). Understanding microtubule organizing centers by comparing mutant and wild-type structures with electron tomography. *Methods Cell Biol.* **79,** 125–143.

Ortiz, J. O., Forster, F., Kurner, J., Linaroudis, A. A., and Baumeister, W. (2006). Mapping 70S ribosomes in intact cells by cryoelectron tomography and pattern recognition. *J. Struct. Biol.* **156,** 334–341.

Parsons, D. F. (1974). Structure of wet specimens in electron microscopy. Improved environmental chambers make it possible to examine wet specimens easily. *Science* **186,** 407–414.

Penczek, P., Marko, M., Buttle, K., and Frank, J. (1995). Double-tilt electron tomography. *Ultramicroscopy* **60,** 393–410.

Penczek, P. A. (2002). Three-dimensional spectral signal-to-noise ratio for a class of reconstruction algorithms. *J. Struct. Biol.* **138,** 34–46.

Penczek, P. A., Renka, R., and Schomberg, H. (2004). Gridding-based direct Fourier inversion of the three-dimensional ray transform. *J. Opt. Soc. Am. A Opt. Image Sci. Vis.* **21,** 499–509.

Radermacher, M. (1992). Weighted back-projection methods. *In* "Electron Tomography" (J. Frank, ed.), pp. 91–115. Plenum, New York.

Radermacher, M., Wagenknecht, T., Verschoor, A., and Frank, J. (1987). Three-dimensional reconstruction from a single-exposure, random conical tilt series applied to the 50S ribosomal subunit of *Escherichia coli*. *J. Microsc.* **146,** 113–136.

Rath, B. K., Hegerl, R., Leith, A., Shaikh, T. R., Wagenknecht, T., and Frank, J. (2003). Fast 3D motif search of EM density maps using a locally normalized cross-correlation function. *J. Struct. Biol.* **144,** 95–103.

Reipert, S., Fischer, I., and Wiche, G. (2004). High-pressure freezing of epithelial cells on sapphire coverslips. *J. Microsc.* **213,** 81–85.

Rieder, C. L., and Cassels, G. (1999). Correlative light and electron microscopy of mitotic cells in monolayer cultures. *Methods Cell Biol.* **61,** 297–315.

Roseman, A. M. (2003). Particle finding in electron micrographs using a fast local correlation algorithm. *Ultramicroscopy* **94,** 225–236.

Salvi, E., Cantele, F., Zampighi, L., Fain, N., Pigino, G., Zampighi, G., and Lanzavecchia, S. (2008). JUST (Java User Segmentation Tool) for semi-automatic segmentation of tomographic maps. *J. Struct. Biol.* **161,** 287–297.

Sandberg, K. (2007). Methods for image segmentation in cellular tomography. *In* "Methods in Cell Biology" (J. R. McIntosh, ed.), **79,** pp. 769–798. Academic Press, New York.

Saxberg, B. E. H., and Saxton, W. O. (1981). Quantum noise in 2D projections and 3D reconstructions. *Ultramicroscopy* **6,** 85–90.

Saxton, W. O., Baumeister, W., and Hahn, M. (1984). Three-dimensional reconstruction of imperfect two-dimensional crystals. *Ultramicroscopy* **13,** 57–70.

Sosinsky, G. E., Giepmans, B. N., Deerinck, T. J., Gaietta, G. M., and Ellisman, M. H. (2007). Markers for correlated light and electron microscopy. *In* "Cellular Electron Microscopy" (J. R. McIntosh, ed.), **79,** pp. 575–591. Academic Press, New York.

Soto, G. E., Young, S. J., Martone, M. E., Deerinck, T. J., Lamont, S., Carragher, B. O., Hama, K., and Ellisman, M. (1994). Serial section electron tomography: A method for three-dimensional reconstruction of large structures. *Neuroimage* **1,** 230–243.

Studer, D., Michel, M., and Muller, M. (1989). High pressure freezing comes of age. *Scanning Microsc. Suppl.* **3,** 253–268.

Sun, S., Shi, S., and Leapman, R. (1993). Water distributions of hydrated biological specimens by valence electron energy loss spectroscopy. *Ultramicroscopy* **50,** 127–139.

Taylor, K. A., Tang, J., Cheng, Y., and Winkler, H. (1997). The use of electron tomography for structural analysis of disordered protein arrays. *J. Struct. Biol.* **120,** 372–386.

Ting, C. S., Hsieh, C., Sundararaman, S., Mannella, C., and Marko, M. (2007). Cryo-electron tomography reveals the comparative three-dimensional architecture of Prochlorococcus, a globally important marine cyanobacterium. *J. Bacteriol.* **189,** 4485–4493.

Tong, J., Arslan, I., and Midgley, P. (2006). A novel dual-axis iterative algorithm for electron tomography. *J. Struct. Biol.* **153,** 55–63.

Unser, M., Sorzano, C. O., Thevenaz, P., Jonic, S., El-Bez, C., De Carlo, S., Conway, J. F., and Trus, B. L. (2005). Spectral signal-to-noise ratio and resolution assessment of 3D reconstructions. *J. Struct. Biol.* **149,** 243–255.

Unser, M., Trus, B. L., and Steven, A. C. (1987). A new resolution criterion based on spectral signal-to-noise ratios. *Ultramicroscopy* **23,** 39–51.

van der Heide, P., Xu, X. P., Marsh, B. J., Hanein, D., and Volkmann, N. (2007). Efficient automatic noise reduction of electron tomographic reconstructions based on iterative median filtering. *J. Struct. Biol.* **158,** 196–204.

van Heel, M., and Schatz, M. (2005). Fourier shell correlation threshold criteria. *J. Struct. Biol.* **151,** 250–262.

VandenBeldt, K. J., Barnard, R. M., Hergert, P. J., Meng, X., Maiato, H., and McEwen, B. F. (2006). Kinetochores use a novel mechanism for coordinating the dynamics of individual microtubules. *Curr. Biol.* **16,** 1217–1223.

Wilson, C. J., Mastronarde, D., McEwen, B. F., and Frank, J. (1992). Measurement of neuronal surface area using high-voltage electron tomography. *Neuroimage* **1,** 11–22.

Winkler, H., and Taylor, K. A. (2006). Accurate marker-free alignment with simultaneous geometry determination and reconstruction of tilt series in electron tomography. *Ultramicroscopy* **106,** 240–254.

Zampighi, G. A., Zampighi, L. M., Fain, N., Lanzavecchia, S., Simon, S. A., and Wright, E. M. (2006). Conical electron tomography of a chemical synapse: Vesicles docked to the active zone are hemi-fused. *Biophys. J.* **91,** 2910–2918.

CHAPTER 7

Total Internal Reflection Fluorescence Microscopy

Daniel Axelrod

Departments of Physics and Biophysics
University of Michigan
Ann Arbor
Michigan 48109

METHODS IN CELL BIOLOGY, VOL. 89

0091-679X/08 $35.00
DOI: 10.1016/S0091-679X(08)00607-9

Abstract

Total internal reflection fluorescence microscopy (TIRFM), also known as evanescent wave microscopy, is used in a wide range of applications, particularly to view single molecules attached to planar surfaces and to study the position and dynamics of molecules and organelles in living culture cells near the contact regions with the glass coverslip. TIRFM selectively illuminates fluorophores only in a very thin (less than 100 nm deep) layer near the substrate, thereby avoiding excitation of fluorophores outside this subresolution optical section. This chapter reviews the history, current applications in cell biology and biochemistry, basic optical theory, combinations with numerous other optical and spectroscopic approaches, and a range of setup methods, both commercial and custom.

I. Introduction

Total internal reflection fluorescence (TIRF) provides a means to selectively excite fluorophores in an aqueous environment very near a solid surface (within $\leq$100 nm). When adapted to microscopy, TIRF produces wide-field images with very low background fluorescence from out-of-focus planes. The surface-selective illumination and the unique polarization features of TIRF, often in simultaneous combination with other fluorescence techniques, have enabled numerous

applications in chemistry, biochemistry, and cell biology. This chapter discusses the principles of TIRF microscopy and various methods (both commercial and homemade) to implement it for use in cell biological and biochemical research. For earlier reviews, see Axelrod (2003), Toomre and Axelrod (2005), Schneckenburger (2005), Axelrod and Omann (2006), and for a more mathematical treatment than here, see Hellen *et al.* (1988) and Axelrod (2007).

Although TIRF microscopy became widely used only in the 1990s and increasingly so thereafter, well after the introduction and popularity of confocal microscopy, it actually had much earlier origins in surface spectroscopy. Total internal reflection (TIR) in a nonmicroscopic nonfluorescent form had long been used for visible and infrared absorption spectroscopy (Harrick, 1967). Nonmicroscopic TIR combined with visible fluorescence spectroscopy at various kinds of interfaces also has a long history, beginning in the early 1960s (Carniglia *et al.*, 1972; Harrick and Loeb, 1973; Hirschfeld, 1965; Kronick and Little, 1975; Tweet *et al.*, 1964; Watkins and Robertson, 1977). The first application of TIR to microscopy was nonfluorescent, describing evanescent light scattering from cells (Ambrose, 1961). Only after all these advances, the three key elements of TIRF microscopy—TIR, fluorescence, and microscopy—were combined (Axelrod, 1981).

II. Rationale

TIRF microscopy has been used extensively in the last decade or so to study cellular organization and dynamics that occurs near the cell culture/glass substrate interface. Some examples are discussed below.

In all cases, it is important to bear in mind that cellular processes near an artificial surface may be altered from those in biologically native environments and even from those on the opposite side of the same cell.

A. Secretory Granule Tracking and Exocytosis

Secretory granules often reside through the whole depth of a cell. When viewed with standard epi-illumination, fluorescence-marked secretory granules are difficult to distinguish individually (Fig. 1A). When viewed with TIRF, the granules closest to the membrane appear very distinctly (Fig. 1B). The thin evanescent field allows small motions of individual fluorescence-marked secretory granules to manifest as small intensity changes arising from small motions in the direction normal to the substrate and plasma membrane (the "axial" or "*z*-" direction). The precision of such axial tracking can be as small as 2 nm, much smaller than the light microscope resolution limit. In some cases, dispersal of granule contents can be observed and interpreted as exocytosis and the steps immediately preceding exocytosis characterized (Bowser and Khakh, 2007; Fix *et al.*, 2004; Gonzalez and McGraw, 2006; Han *et al.*, 1999; Holz, 2006; Jaiswal and Simon, 2007; Jaiswal *et al.*, 2004; Johns *et al.*, 2001; Lang *et al.*, 1997; Loerke *et al.*, 2002; Nagamatsu,

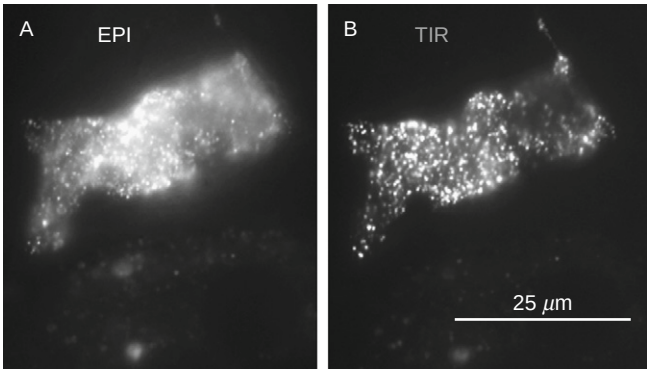

Fig. 1 EPI versus objective-based TIRF digital images, excited with an argon laser beam of wavelength 488 nm entering the side illumination port of an Olympus IX-70 microscope and viewed through an Olympus 1.45 NA 60× objective. This bovine chromaffin cell contains secretory granules marked with GFP-atrial natriururetic protein.

2006; Nofal *et al.*, 2007; Oheim, 2001; Oheim and Stuhmer, 2000a,b; Oheim *et al.*, 1998, 1999; Perrais *et al.*, 2004; Rohrbach, 2000; Scalettar, 2006; Scalettar *et al.*, 2002; Schmoranzer *et al.*, 2000, 2003; Serulle *et al.*, 2007; Silverman *et al.*, 2005; Steyer and Almers, 1999, 2001; Taraska and Almers, 2004; Toomre and Manstein, 2001; Toomre *et al.*, 2000; Toonen *et al.*, 2006; Tsuboi *et al.*, 2000, 2001, 2002). Because of the high contrast and low background, the position of the centers of granules can be measured with an accuracy down to about 10 nm and motions much smaller than the granule diameter can be followed before and after exocytosis-inducing chemical stimulation (Allersma *et al.*, 2004, 2006).

Most of these TIRF studies on the detailed mechanism of secretion have been on animal cells. However, the same techniques can be applied to plant cells, and in particular, have been applied to study secretion from pollen tubes (Wang *et al.*, 2006).

B. Clathrin, Coated Pits, and Endocytosis

TIRF has been used increasingly to observe the dynamics and specific proteins involved in endocytosis (Barr *et al.*, 2006; Kochubey *et al.*, 2006; Rappoport *et al.*, 2006; Zoncu *et al.*, 2007).

C. Cell–Substrate Contact Regions

TIRF can be used qualitatively to observe the position, extent, composition, and motion of contact regions even in samples in which fluorescence elsewhere would otherwise obscure the fluorescent pattern (Axelrod, 1981; Joos *et al.*, 2006; Weis *et al.*, 1982). The specific biochemistry of focal adhesions, using fluorescent proteins, has been studied with TIRF (Cohen *et al.*, 2006; Partridge and Marcantonio, 2006).

A variation of TIRF to identify cell–substrate contacts involves doping the solution surrounding the cells with a nonadsorbing and nonpermeable fluorescent volume marker; focal contacts then appear relatively dark (Gingell *et al.*, 1987; Todd *et al.*, 1988).

D. Submembrane Filament and Extracellular Matrix Structure and Assembly

Although TIRF cannot view deeply into thick cells, it can display with high contrast the fluorescence-marked submembrane filament structure at the substrate contact regions. Actin polymerization and its regulation, both *in vitro* and *in vivo*, have been studied by TIRF (Ada-Nguema *et al.*, 2006; Kim *et al.*, 2007; Kovar *et al.*, 2006; Kuhn and Pollard, 2005; Lang *et al.*, 2000; Mahaffey and Pollard, 2006; Manneville, 2006; Moseley *et al.*, 2006), as have microtubules (Shaw *et al.*, 2007) and microtubule-associated kinesin (Seitz and Surrey, 2006). The manner by which extracellular components such as fibronectin are organized through the membrane in concert with submembrane filaments can be investigated by TIRF (Yoneda *et al.*, 2007).

In combination with very low levels of specific filament labeling, which produces fluorescent speckles, TIRF illumination can visualize filament subunit turnover (Adams *et al.*, 2004).

E. Single-Molecule Fluorescence

Standard spectroscopies on bulk materials involve inherent ensemble averaging over all the molecules in the sample. The purpose of single-molecule detection (Dickson *et al.*, 1996, 1998; Graneli *et al.*, 2006; Ha *et al.*, 1999; Ichinose and Sako, 2004; Khan *et al.*, 2000; Knight and Molloy, 2000; Saito *et al.*, 1997; Sako *et al.*, 2000; Vale *et al.*, 1996; Wazawa and Ueda, 2005; Yokota *et al.*, 2004) is to avoid this averaging and instead to detect spectroscopic evidence of intermediate or transient states that otherwise are obscured. TIRF provides the very dark background needed to observe single fluorophores. Polarized TIRF illumination and detection can provide information about surface-bound single-molecule orientation and rotational dynamics (Forkey *et al.*, 2005; Osborne, 2005; Wang *et al.*, 2004). Combinations of other advanced spectroscopies with TIRF can be performed on single molecules: for example, observations of single actin molecules switching between conformational states that have different levels of fluorescence resonance energy transfer (FRET) (Kozuka *et al.*, 2006).

Related to single-molecule detection is the capability of seeing step-like fluorescence fluctuations as fluorescent molecules enter and leave the thin evanescent field region in the bulk (or as the fluorophores individually photobleach). These fluctuations (which are visually obvious in TIRF) can be quantitatively autocorrelated in a technique called fluorescence correlation spectroscopy (FCS) to obtain kinetic information about the molecular motion (Hassler *et al.*, 2005a,b; Starr and Thompson, 2001). FCS works best when the observation volume is very small so

it contains very few molecules. TIRF provides an observation volume with a very small depth; the effective length and width can be minimized by accessing data from individual CCD camera pixels or by a confocal-like aperture in an image plane (Borejdo *et al*., 2006a).

Seeing single molecules near a clean artificial surface is a significant technical achievement, but seeing them on living cells is even more remarkable due to the higher background due to cell autofluorescence. For a review of single-molecule studies on living cells, see Nenasheva and Mashanov (2006), and for an application to pleckstrin homology domains, see Mashanov and Malloy (2007). Single quantum dots can be easily located by TIRF (Seitz and Surrey, 2006) and their peculiar flickering behavior studied individually (Kobitski *et al*., 2004).

F. Cell-Surface Receptors at Biological and Artificial Membranes

TIR combined with fluorescence recovery after photobleaching (FRAP) or FCS can examine the specific or nonspecific binding kinetics of proteins to cellular or artificial membranes (Hellen and Axelrod, 1991; Hinterdorfer *et al*., 1994; Kalb *et al*., 1990; Lagerholm *et al*., 2000; McKiernan *et al*., 1997; Moran-Mirabal *et al*., 2005; Omann and Axelrod, 1996; Stout and Axelrod, 1994; Sund and Axelrod, 2000; Thompson and Axelrod, 1983). TIR/FRAP additionally can be used to measure lateral surface diffusion coefficients along with on/off kinetics of reversibly adsorbed fluorescent molecules (Burghardt and Axelrod, 1981; Fulbright and Axelrod, 1993; Gilmanshin *et al*., 1994; Thompson *et al*., 1981; Tilton *et al*., 1990). Interactions among channel or receptor proteins at surfaces can be studied by TIR/FRET (Khakh *et al*., 2005).

G. Micromorphological Structures and Dynamics on Living Cells

By utilizing the unique polarization properties of the evanescent field of TIR (to be discussed later), endocytotic or exocytotic sites, ruffles, and other submicroscopic irregularities can be highlighted (Hadjidemetriou *et al*., 2005; Sund *et al*., 1999).

H. Long-Term Fluorescence Movies of Cultured Cells

Since the cells are exposed to TIR excitation light only at their cell–substrate contact regions but not through their bulk, they tend to survive longer under observation, thereby enabling time-lapse recording of a week in duration. During this time, newly appearing cell-surface receptors can be immediately marked by fluorescent ligand that is continually present in the full cell culture medium. Because TIRF is utilized, background fluorescence from this bath of unbound fluorophore is minimized (Wang and Axelrod, 1994).

I. Membrane Ion Channels and Ions at Surfaces

TIRF can be used to visualize single Ca^{2+} channels with good spatial and temporal resolution (Demuro and Parker, 2004). TIRF is completely compatible with standard epifluorescence, bright field, dark field, or phase contrast illumination. These methods of illumination can be switched back and forth rapidly with TIRF by electro-optical devices to compare membrane-proximal ionic transients and deeper cytoplasmic transients (Omann and Axelrod, 1996). The spatiotemporal evolution of artificial induced pH gradients at surfaces has been studied by combining TIRF with scanning electrochemical microscopy (Boldt *et al.*, 2004).

J. *In Vitro* Detection and Behavior of Biomolecules at Surfaces

Many (perhaps most) biochemical processes in cells occur on surfaces. Although this chapter emphasizes living cell biology, the study of surface processes in artificial systems has both fundamental interest in biology and practical applications to medicine.

Biosensors in immunological assays are often surface-based and use TIRF because of its ability to detect binding to a surface molecule selectively while excluding background in the bulk. Biosensors incorporating TIRF have seen a variety of recent enhancements in sensitivity, simultaneous multidetection, selectivity, and rapidity of interaction (Hoshino *et al.*, 2005; Jennissen and Zumbrink, 2004; Matveeva *et al.*, 2004; Willard *et al.*, 2003).

Spectroscopy of molecules adsorbed at liquid hydrophobic/hydrophilic interfaces can be studied with TIRF (both microscopic and nonmicroscopic), provided there is an ample refractive index difference between the two liquids (Hashimoto *et al.*, 2003; Ishizaka *et al.*, 2004; Pant and Girault, 2005).

A nearby surface can affect the local freedom of motion of a solute for a variety of reasons, including local fields, local viscosity, tethering, steric hindrance, and spatial patterning on the surface. The motions can be studied by single molecule or FCS techniques (Banerjee and Kihm, 2005; Blumberg *et al.*, 2005; He *et al.*, 2005; Kihm *et al.*, 2004; McCain and Harris, 2003; McCain *et al.*, 2004; Mei *et al.*, 2005). Larger particles can be followed by observing the nonfluorescent light scattering of evanescent illumination (Bike, 2000).

III. Theoretical Principles

A. Basic TIR

When a light beam (see Fig. 2A) propagating through a transparent medium 3 of high index of refraction (e.g., glass) encounters a planar interface with medium 1 of lower index of refraction (e.g., water), it undergoes TIR for incidence angles θ (measured from the normal to the interface) greater than the "critical angle" θ_c given by:

$$\theta_c = \sin^{-1}\left(\frac{n_1}{n_3}\right) \tag{1}$$

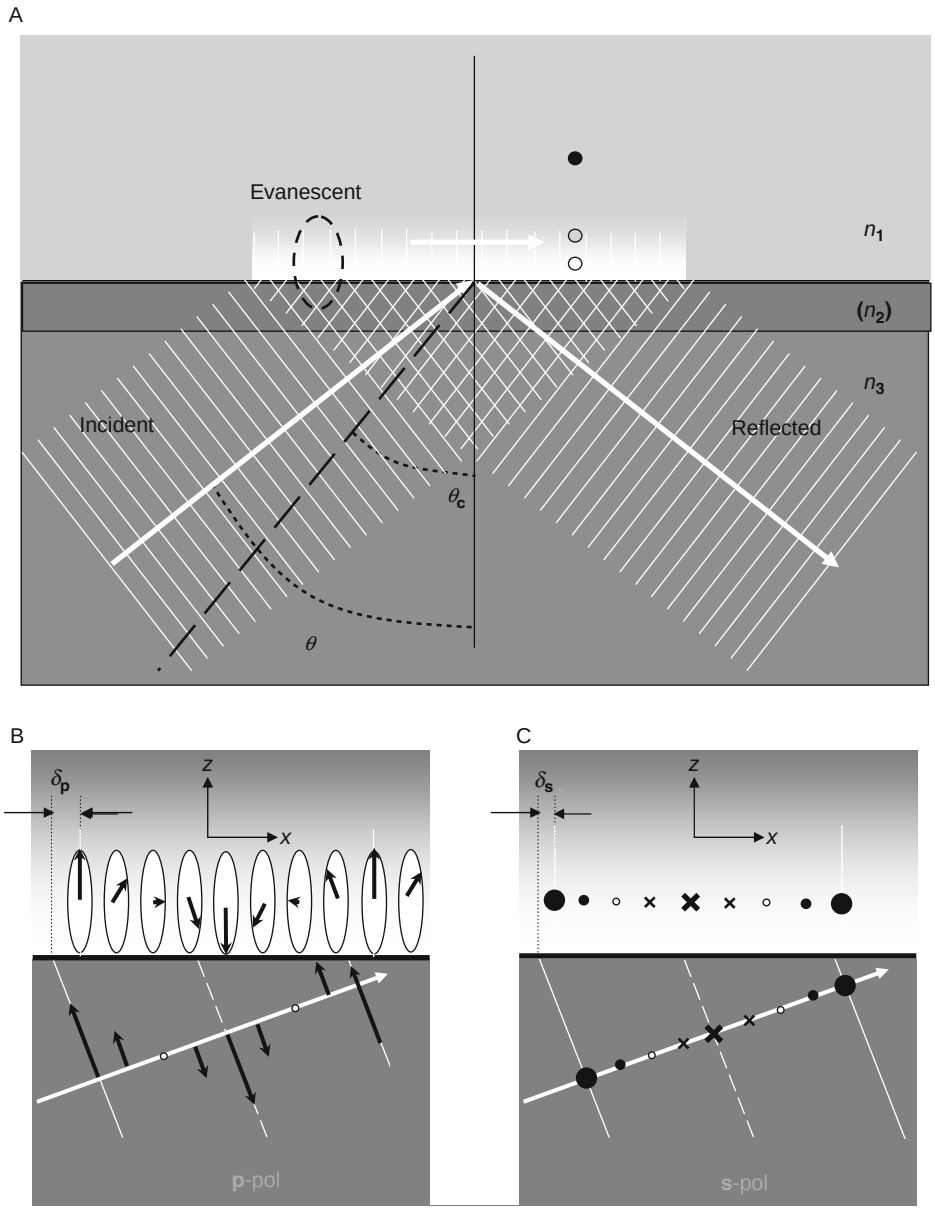

Fig. 2 (A) TIR illumination scheme. Refractive index n_3 must be greater than n_1. The intermediate layer (consisting of metal or a dielectric material of refractive index n_2) is not necessary for TIR to occur, but can introduce some useful optical properties as explained in the text. Most applications of TIRF do not use an intermediate layer. The incidence angle θ must be larger than the critical angle θ_c for TIR to occur. The exponentially decaying evanescent field in the n_1 material is used to excite fluorophores in TIRF. The wavelength of the incident and reflected beams in the n_3 medium is λ_o/n_3. The dashed oval

where n_1 and n_3 are the refractive indices of the liquid and the solid, respectively. Ratio n_1/n_3 must be less than unity for TIR to occur. (A refractive index n_2 will refer to an optional intermediate layer to be discussed below.) For "subcritical" incidence angles $\theta < \theta_c$, most of the light propagates through the interface into the lower index material with a refraction angle (also measured from the normal) given by Snell's Law. (Some of the incident light also internally reflects back into the solid.) But for "supercritical" incidence angles $\theta > \theta_c$, all of the light reflects back into the solid. Even in this case, some of the incident light energy penetrates through the interface and propagates parallel to the surface in the plane of incidence. The field in the liquid (sometimes called the "evanescent wave") is capable of exciting fluorescent molecules that might be present near the surface, as depicted schematically in Fig. 2A.

The intensity I of the evanescent field at any position (measured as perpendicular distance z from the TIR interface) exponentially decays with z:

$$I(z) = I(0)e^{-z/d} \tag{2}$$

where

$$d = \frac{\lambda_0}{4\pi}(n_3^2 \sin^2 - \theta - n_1^2)^{-1/2} = \frac{\lambda_0}{4\pi n_3}(\sin^2\theta - \sin^2\theta_c)^{-1/2} \tag{3}$$

Parameter λ_o is the wavelength of the incident light in vacuum. Depth d is independent of the polarization of the incident light and decreases with increasing θ. Except for supercritical $\theta \to \theta_c$ (where $d \to \infty$), d is generally in the order of λ_o or smaller.

Although the emission from a fluorophore excited by an evanescent field as viewed by a microscopic objective might be expected to follow an exponential decay with z according to Eq. (2), this is not precisely true. Fluorescence emission near a dielectric interface is rather anisotropic and the degree of anisotropy is itself z-dependent (Hellen and Axelrod, 1987; Mertz, 2000). One cause of the anisotropy of emission is simply partial reflection from the interface and consequent optical interference between the direct and reflected emission beams. But another more subtle cause is the interaction of the fluorophore's "near field" with the interface and its consequent conversion into light propagating at high angles into the higher index n_3 material (the solid substrate). In general, the closer a fluorophore is to the

region toward the left is magnified in panels (B) and (C) to depict the details of the evanescent polarization within approximately one wavelength of distance. (B) P-pol incident field, giving rise to a p-pol evanescent field, with phase lag δ_p and coordinate system convention indicated. The p-pol evanescent field is elliptically polarized in the x-z plane as shown (primarily polarized in the z-direction with a weaker x-component at a relative phase of $\pi/2$). (C) s-pol incident field, giving rise to s-pol evanescent field, with phase lag δ_s indicated. The phase lags $\delta_{p,s}$ as given by Eqs. (6) and (7) are actually phase angles but they are shown schematically as distances here.

surface, the larger the proportion of its emitted light will enter the substrate. If a sufficiently high-aperture objective is used to gather the near-field emission through the substrate, then the effective thickness of the surface detection zone is reduced beyond surface selectivity generated by the evanescent field excitation of TIR. Low-aperture objectives will not produce this enhanced effect because they miss capturing the near-field light. On its own, the near-field emission capture effect can be the basis of surface-selective fluorescence detection and imaging (Axelrod, 2001).

B. Evanescent Field Polarization and Intensity

The polarization (i.e., the vector direction of the electric field **E**) of the evanescent wave depends on the incident light polarization, which can be either "p-pol" (polarized in the plane of incidence formed by the incident and reflected rays, denoted here as the x-z plane) or "s-pol" (polarized normal to the plane of incidence, here the y-direction). In both polarizations, the evanescent wave fronts travel parallel to the surface in the x-direction.

For p-pol incident light (see Fig. 2B), the evanescent electric field vector direction remains in the plane of incidence, but it "cartwheels" along the surface with a nonzero longitudinal component:

$$\begin{aligned} \boldsymbol{E}_p(z) = {} & 2\cos\theta(\sin^4\theta_c\cos^2\theta + \sin^2\theta - \sin^2\theta_c)^{-1/2} e^{-i\delta_p} e^{-z/2d} \\ & [-i(\sin^2\theta - \sin^2\theta_c)^{1/2}\hat{\mathbf{x}} + \sin\theta\hat{\mathbf{z}}] \end{aligned} \tag{4}$$

The p-pol evanescent field is a mix of transverse (z) and longitudinal (x) components; this distinguishes the p-pol evanescent field from freely propagating subcritical refracted light, which has no component longitudinal to the direction of travel. The longitudinal $\hat{\mathbf{x}}$ component of the p-pol evanescent field diminishes to zero amplitude as the incidence angle is reduced from the supercritical range back toward the critical angle.

For s-pol incident light (see Fig. 2C), the evanescent electric field vector direction remains purely normal to the plane of incidence (the y-direction).

$$\boldsymbol{E}_s(z) = 2\frac{\cos\theta}{\cos\theta_c} e^{-i\delta}, e^{-z/2d}\,\hat{\mathbf{y}} \tag{5}$$

In Eqs. (4) and (5), the incident electric field amplitude in the substrate is normalized to unity for each polarization, and the phase lags relative to the incident light are

$$\delta_p = \tan^{-1}\left[\frac{(\sin^2\theta - \sin^2\theta_c)^{1/2}}{\sin^2\theta_c\cos\theta}\right] \tag{6}$$

$$\delta_s = \tan^{-1}\left[\frac{(\sin^2\theta - \sin^2\theta_c)^{1/2}}{\cos\theta}\right] \tag{7}$$

The evanescent intensities (which are proportional to the scalar product $\mathbf{E}^*\cdot\mathbf{E}$) for both the s- and p-polarizations (assuming incident intensities normalized to unity) are plotted versus θ in Fig. 3. The evanescent intensity approaches zero as $\theta \to 90^\circ$. On the other hand, for supercritical angles within 10° of θ_c, the evanescent intensity is as great or greater than the incident light intensity. The plots can be extended without breaks to the subcritical angle range, where the intensity is that of the freely propagating refracted light in medium 1.[1]

Regardless of polarization, the spatial period of the evanescent electric field is $\lambda_o/(n_3 \sin\theta)$ as it propagates along the surface. Unlike the case of freely propagating light, the evanescent spatial period is not at all affected by the medium 1 in which it resides. It is determined only by the spacing of the incident light wave fronts in medium 3 as they intersect the interface. This spacing can be important experimentally because it

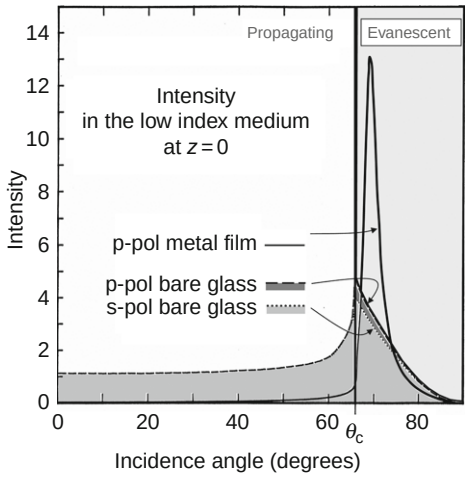

Fig. 3 Evanescent intensities $I_{p,s}$ at z = 0 versus θ, assuming the incident intensities in the glass are set equal to unity. At angles $\theta > \theta_c$, the transmitted light is evanescent; at angles $\theta < \theta_c$, it is propagating. Both s- and p-polarizations are shown. Refractive indices $n_3 = 1.46$ (fused silica) and $n_1 = 1.33$ are assumed here, corresponding to $\theta_c = 65.7^\circ$. Also shown is the evanescent intensity that would be obtained with a thin (20 nm) aluminum film coating, as discussed in the text.

[1]One might at first expect the subcritical intensity to be slightly less than the incident intensity (accounting for some reflection at the interface) but certainly not more as shown. The discrepancy arises because the intensity in Fig. 3 refers to the squared amplitude of the electric field (EE*) alone rather than to the actual energy flux of the light, which involves a product of EE* with the refractive index of the medium in which the light propagates.

determines the spacing of interference fringes produced when two coherent TIR beams illuminate the same region of the surface from different directions.

C. Emission of Light near a Surface

Clearly, the effective excitation intensity in TIRF for a particular fluorophore dipole is strongly dependent on its z-distance from the surface and on polarization. But the effective efficiency of emission collection—regardless of the mode of excitation—also turns out to be a function (albeit less strongly) of z, dipole orientation, emission polarization, and observation angle (and hence, microscopic objective aperture). Scalar electromagnetic diffraction theory describes the emission pattern (Hellen and Axelrod, 1987 and numerous references therein). But the key points can be stated qualitatively. When an excited fluorophore is located near a dielectic (e.g., glass) surface (as generally occurs in TIRF illumination), its nonpropagating electromagnetic "near field" interacts with the surface. Some of the energy in the near field is drawn into the glass and propagates at a high angle (relative to the normal) into the glass. This increases the fraction of energy propagating into the glass and reduces the fraction propagating into the water. (Partially countervailing this effect is reflection of far-field light off the glass surface and back into the water.) Note that the light-collecting advantage of very high-aperture objectives (>1.33) resides purely in their ability to capture *near*-field light from a sample at a glass/water interface. The "extra" numerical aperture above 1.33 does not help in gathering *far*-field emission light because none of it propagates in the glass at the high angles uniquely observed by high apertures.

The capture of the fluorophore near-field and its conversion into light propagating into the substrate causes deviations from the expected exponential decay of the TIR evanescent field implied by Eq. (3). It is true that the *excitation* rate follows the exponential decay in z, but the *emission* pattern depends on the distance the fluorophore resides from the surface in a complicated manner. Therefore, as every objective gathers only part of this emission pattern, the dependence of gathered emission upon z will be nonexponential and will depend upon the numerical aperture of the objective (as well as upon the orientational distribution of the fluorophore dipoles, the refractive indices bordering the interface, and the polarization of the excitation). For objectives of moderate aperture (NA < 1.33) through which no near-field light is gathered, the deviation from the simple exponentiality is generally only 10–20%. For very high-aperture objectives that do gather some near-field emission, the deviation is larger and generally leads to a steeper z-dependence. This corrected z-dependence can be approximated as an exponential with a shorter decay distance, but the exact shape is not truly exponential.

Proximity of a fluorophore to a surface can also slightly affect its emission spectrum and excited state lifetime, due to local surface fields that might affect the position of molecular energy level or the conformation of the fluorophore and its environs.

D. Measurement of Distances from a Surface

In principal, the distance z of a fluorophore from the surface can be calculated from the fluorescence intensity $F(z)$ that as an approximation might be considered to be proportional to the evanescent intensity $I(z)$ as given by Eq. (2). In practice, the situation is more complicated for several reasons.

- The proportionality factor between F and I depends on efficiencies of absorption, emission, and detection, all of which can be (at least slightly) z-dependent, as explained above.
- $F(0)$ may not be known if a fluorophore positioned exactly at $z = 0$ (the substrate surface) cannot be identified. In this circumstance, Eq. (3) can be used only to calculate relative distances. That is, if a fluorophore moves from some (unknown) distance z_1 with observed intensity I_1 to another distance z_2 with intensity I_2, then assuming (as an approximation) an exponentially decaying $F(z)$,

$$\Delta z = z_1 - z_2 = d\ln\left(\frac{F_2}{F_1}\right) \tag{8}$$

This relationship is (approximately) valid even if the fluorescent structure consists of multiple fluorophores and is large or irregularly shaped (e.g., a secretory granule). Again assuming an exponentially decaying $I(z)$, a motion of $\triangle z$ for the whole structure causes each fluorophore in the structure to change its fluorescence by the same multiplicative factor, and the whole structure therefore changes its fluorescence by that same factor.

For small frame-to-frame changes in I, Eq. (8) can deduce very small motions of subcellular organelles, as small as 2 nm. But this deduction should be interpreted cautiously. Shot noise and CCD camera dark noise and readout noise can cause apparent fluctuations in I where none exist. A theoretical method of separating out the actual Δz due to organelle motion from the artifactually overestimated Δz that includes the effect of instrumental noise has been published (Allersma *et al.*, 2006).

- The z-dependence of the emission pattern (because of near-field capture by the substrate as discussed above) causes $F(z)$ to deviate from exponential decay behavior, as discussed above. Since the deviation depends on numerical aperture in a theoretically predictable manner, comparison of the emission intensity gathered by moderate and very high-aperture objectives on the same sample should allow calculation of absolute z distances.
- For TIRF studies on biological cells, the distance of a fluorophore or organelle from the plasma membrane is likely to be of more interest than its distance from the substrate surface. The absolute distance between the plasma membrane and the substrate can be deduced by adding a membrane impermeant fluorescent dye to the medium of the cell culture under TIRF illumination. (For viewing labeled organelles at the same time as this impermeant dye, fluorophores of distinctly different spectra should be selected.) In off-cell regions, the fluorescence F_{offcell} will appear uniformly bright, arising from the full depth of the evanescent

field. In cell–substrate contacts, the dye will be confined to a layer thinner than the evanescent field. The fluorescence F in contact regions will be darker by a factor that can be converted to separation distance h between the substrate and the plasma membrane gap according to:

$$h = -d \ln\left[1 - \frac{F}{F_{offcell}}\right] \tag{9}$$

This formula is an approximation because it assumes an exponential decay of gathered fluorescence intensity versus z and thereby neglects the near-field effects discussed earlier.

E. Variable Incidence Angle TIR: Concentration Profiles

It may be of interest to deduce what is the concentration profile $C(z)$ of fluorophores within the evanescent field, to a resolution much shorter than the evanescent field depth. As can be seen from Eq. (3) and Fig. (3), the exponential decay depth d and intensity I (at $z = 0$) of the evanescent field both vary with polar incidence angle θ of the excitation light. The observed fluorescence $F(\theta)$ is

$$F(\theta) \int_{z=0}^{\infty} \beta(z) I_{z=0}(\theta) C(z) e^{-z/d(\theta)} \mathrm{d}z \tag{10}$$

where $\beta(z)$ combines all the previously discussed effects of z-dependent emission collection efficiency through the chosen numerical aperture objective. In principle, it should be possible to measure F at several different values of θ and use Eq. (10) to rule in or rule out various hypothesized forms for $C(z)$. This approach has been employed in practice to measure cell surface-to-substrate separation distances (Loerke *et al.*, 2000; Stock *et al.*, 2003) and the z-position of subcellular organelles (Loerke *et al.*, 2002).

F. Intermediate Dielectric Layers

In actual experiments in biophysics, chemistry, or cell biology, the interface may not be a simple interface between two media, but rather a stratified multilayer system. One example is the case of a biological membrane or lipid bilayer interposed between glass and an aqueous medium. Another example is a thin metal film coating, which can be used to quench fluorescence within the first ~10 nm of the surface. We discuss here the TIR evanescent wave in a three-layer system in which incident light travels from medium 3 (refractive index n_3) through the intermediate layer (n_2) toward medium 1 (n_1). Qualitatively, several features can be noted:

- Insertion of an intermediate layer never thwarts TIR, regardless of the intermediate layer's refractive index n_2. The only question is whether TIR takes place at the n_3:n_2 interface or the n_2:n_1 interface. Since the intermediate layer is likely to be

very thin (no deeper than several tens of nanometers) in many applications, precisely which interface supports TIR is not important for qualitative studies.

- Regardless of n_2 and the thickness of the intermediate layer, the evanescent wave's profile in medium 1 will be exponentially decaying with a characteristic decay distance given by Eq. (3). However, the intermediate layer affects intensity at the interface with medium 1 and the overall distance of penetration of the field as measured from the surface of medium 3.
- Irregularities in the intermediate layer can cause scattering of incident light that then propagates in all directions in medium 1. Experimentally, scattering appears not be a problem on samples even as inhomogeneous as biological cells. Direct viewing of incident light scattered by a cell surface lying between the glass substrate and an aqueous medium confirms that scattering is many orders of magnitude dimmer than the incident or evanescent intensity, and will thereby excite a correspondingly dim contribution to the fluorescence.

G. Intermediate Metal Layer: Quenching and Surface Plasmons

A particular interesting kind of intermediate layer is a metal film. Classical electromagnetic theory (Hellen and Axelrod, 1987) shows that such a film will reduce the s-polarized evanescent intensity to nearly zero at all incidence angles. But the p-polarized behavior is quite different. At a certain sharply defined angle of incidence θ_p (''the surface plasmon (SP) angle''), the p-polarized evanescent intensity becomes an order of magnitude brighter than the incident light at the peak (see Fig. 3).

This strongly peaked effect is due to a resonant excitation of electron oscillations at the metal/water interface. Qualitatively, the SP effect arises because the mutual interaction of free electrons in the metal, coupled with their effective inertial mass, gives the system of electrons a ''natural frequency'' of oscillation. If an external driving force (such as an imposed electromagnetic field) is exactly matched to this natural frequency, the electron distribution will be driven into a large resonance. In the case of a metal film between water and glass, this resonance of oscillating electrons emits radiation in the form of an evanescent field in the water or propagating light into the glass substrate.

For an aluminum, gold, or silver film at a glass/water interface, θ_p is greater than the critical angle θ_c for TIR. The intensity enhancement is rather remarkable since a 20-nm-thick metal film is almost opaque to the eye.

There are some potentially useful experimental consequences of TIR excitation through a thin metal film coated on glass:

- The metal film will almost totally quench fluorescence within the first 10 nm of the surface, and the quenching effect is virtually gone at a distance of 100 nm. Therefore, TIR with a metal film-coated glass can be used to selectively excite

fluorophores in the 10–200 nm distance range (Burghardt *et al.*, 2006; Fulbright and Axelrod, 1993).

- A light beam incident upon a 20 nm aluminum film from the glass side at a glass/aluminum film/water interface evidently does not have to be collimated to produce TIR. Those rays that are incident at the SP angle will create a strong evanescent wave, and those rays that are too low or high in incidence angle will create a negligible field in the water. This phenomenon may ease the practical requirement for a collimated incident beam in TIR and make it easier to set up TIR with a conventional arc light source.
- The metal film leads to a highly polarized evanescent wave, regardless of the purity of the incident polarization.
- The SP angle is strongly sensitive to the index of refraction on the low-density side of the interface. This effect can be used as the basis of ''surface plasmon microscopy (SPM)'' (Zhang *et al.*, 2006).

In SPM, the sample (such as a cell culture) adheres to a thin metal film coating on a standard glass substrate. SPM takes two distinct forms: excitation and emission.

Excitation SPM involves the propagation of excitation light toward the surface through the glass and the creation of an evanescent field, much as in TIR. However, since the surface is coated with a thin metal film, the intensity of the evanescent field is generally very weak, except for a sharp and intense maximum at a very particular incidence angle (Axelrod, 2003). This angle is very sensitive to small changes in the local refractive index in the sample, and thereby creates an image contrast mechanism on both fluorescent and nonfluorescent samples.

Emission SPM has the possibility of providing high sensitivity coupled with a low photobleaching rate. Emission SPM involves the emission (rather than excitation) light field within a fraction of a wavelength from the fluorophore (known as the emission near-field). The emission near-field stimulates an SP resonance in the metal, which then reemits propagating light into the glass (Lakowicz, 2005). A remarkable feature of this light is that it emerges into the glass substrate only in a very thin hollow-cone distribution (see Fig. 4A). The cone's half angle depends on the emission wavelength and particular type of metal. In many practical situations, this hollow cone can be completely captured by a sufficiently high-aperture objective (Mattheyses and Axelrod, 2005a), as experimentally shown in Fig. 4B. Even on bare glass, a hollow cone is produced (Burghardt and Thompson, 1984; Hellen and Axelrod, 1987) with a slightly smaller cone angle, but it is not nearly as sharply distinct as the metal-coating-associated SP cone.

The efficiency by which the emitted light is channeled into the SP hollow cone is sensitively dependent on the distance between a fluorophore and the metal, with the highest efficiency at distances of 20–200 nm. Fluorophores closer than 10 nm suffer almost complete quenching of their emission into any direction. Even with the presence of this hollow cone, most of the emitted light actually propagates into the water because of reflection from the metal film. A fluorophore that is

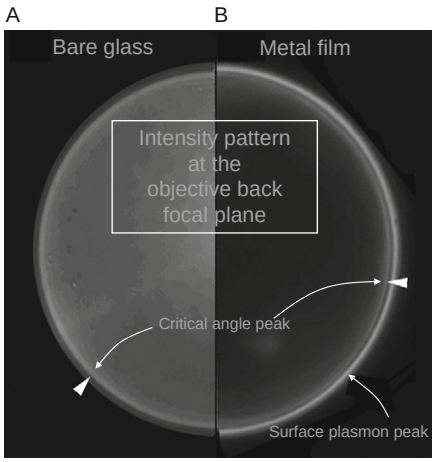

Fig. 4 Back focal plane (BFP) intensity distributions produced by a fluorescent sample and actually recorded by a digital camera. (The BFP is the plane at which all rays emerging from the sample at the same particular angle converge to a unique point, regardless of the location of the source of those parallel rays in the sample plane.) The view is split down the middle between (A) bare glass coverslip and (B) coverslip coated with 20 nm of aluminum. These are views of the BFP, *not* of the sample plane. The sample was a silica bead (refractive index 1.42), surface coated with carbocyanine dye in an index-matched glycerol–water medium, although the nature of the sample is not detectable from the BFP intensity pattern shown here. Angles of emission map into radii at the BFP. On bare glass, the intensity peaks at the critical angle for the emission wavelength; an arrowhead indicates this intensity peak. On metal film-coated glass, this critical intensity peak still appears at the same radius, again shown with an arrowhead. But a new strong peak also appears at a larger radius (and thereby larger emission angle) due to the surface plasmon (SP) emission light. The objective was a 63× 1.4 NA.

positioned within 100 nm of the metal film transfers energy into the metal so rapidly that the average time a fluorophore resides in the excited state near the metal is significantly reduced. The short excited state lifetime effectively increases the number of excitations that can be experienced by a fluorophore before it photobleaches away. The transfer rate is also dependent on the emitting fluorophore's dipole orientation. The SP hollow cone is produced almost entirely by fluorophore dipoles that are oriented perpendicularly to the interface.

H. Image Deconvolution

Deconvolution of an image with the actual imaging point spread function (or blind deconvolution that does not require an input of the point spread function is a form of filtering, used frequently to sharpen images. With standard epi-illumination, a stack of images stepped through z must be obtained because features in any one z-plane appear out of focus in adjacent planes. The deconvolution procedure must then be iterative, involving at least neighboring planes. This

procedure is fairly computer-intensive and time-consuming. In the case of TIR, deconvolution is extremely fast because no iteration is necessary: adjacent out-of-focus planes make no contribution to the image.

IV. Combinations of TIRF with Other Techniques

TIRF by itself is useful for qualitative viewing or for quantitative measurement of positions of sample features with improved contrast and resolution. But in combination with other techniques and spectroscopic effects—polarization, energy transfer, single molecule, fluctuation analysis, local quenching, time-resolved excited state lifetime, local photobleaching, optical trapping, multiphoton excitation, atomic force microscopy, and interference reflection—TIRF can provide a wide variety of data on molecular-scale and organelle-scale dynamics in living cells.

A. Polarization and TIRF

The unique polarization properties of the TIR evanescent field discussed earlier can be utilized to detect orientational features of fluorescent molecules and the cellular structures (such as membranes) that contain them. Several types of polarized TIRF experiments can be utilized.

1. Polarized Excitation TIRF

In polarized excitation TIRF, the emission path need not contain any polarizing elements at all. But the evanescent field used for excitation must be polarized either in the p- or in the s-orientation. In objective-based TIRF, this is most easily done with a polarized laser source impinging upon the sample from one distinct azimuthal angle (as opposed to the broad range of azimuthal angles typical of arc source TIRF). At some position "upbeam" from the microscope's filter cube/dichroic mirror, the laser beam polarization should be alternately changeable between completely horizontal and completely vertical; the resulting polarization of the evanescent field in each case depends on the choice of azimuthal angle and consequently the plane of incidence. For prism-based TIRF, the incident laser beam should be directly switchable between s- and p-polarizations.

For heavily labeled samples, polarized excitation TIR requires all of the fluorophore molecules to be somewhat oriented relative to each other, thereby providing a well-defined excitation polarization preference. For example, a membrane label might be chosen because its excitation dipole is always parallel to the membrane surface. One such fluorophore employed frequently in cell biology is 3,3′-dioctadecylindocarbocyanine (diI; Molecular Probes, Eugene OR) (Axelrod, 1979). By using excitation light that is polarized in the direction perpendicular to the surface, only those regions of the plasma membrane that are not parallel to the substrate will be excited (Fig. 5). For this purpose, a "p-pol" excitation beam with

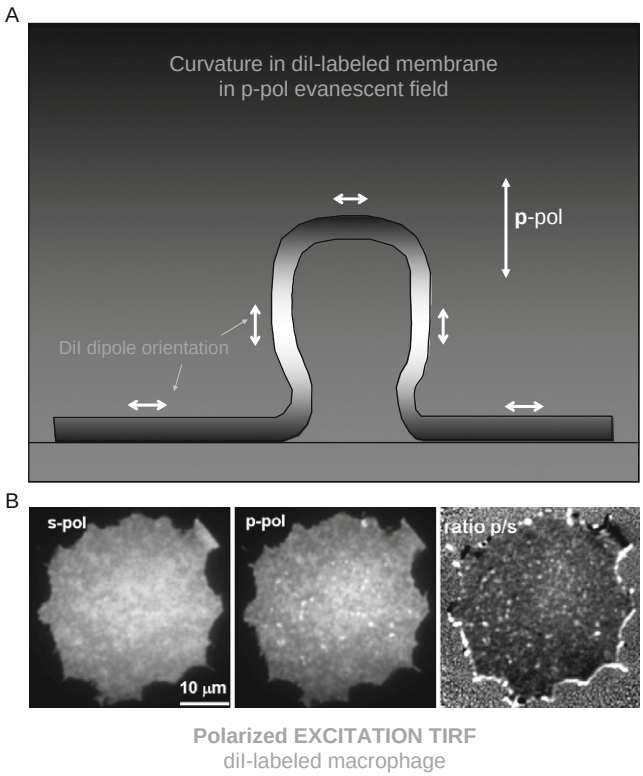

Fig. 5 Polarized excitation TIRF. (A) Schematic drawing of the excitation probability of oriented carbocyanine fluorophores embedded in a membrane in a *z*-polarized evanescent field (the dominant direction of a p-pol evanescent field). The membrane is depicted in cross section with a curved region corresponding to a bleb or an invagination. The direction of absorption dipole of the fluorophores is shown with bidirectional arrows. Higher excitation probability is depicted by lighter shades. The *z*-component of the electric field selectively excites the regions of oblique membrane orientation. (B) Mouse macrophage labeled with plasma membrane marker diI. Fluorescence is excited by s-pol (left photo) and p-pol (middle photo) incident light. The right image is a ratio (p-pol/s-pol, abbreviated p/s) of these images; it distinctly shows regions of nonparallelism of the membrane with respect to the substrate as bright spots.

a highly oblique incidence angle (such as used for TIR) is required. To normalize against spatial intensity variations that arise from actual place-to-place fluorophore-concentration differences, an "s-pol" TIR beam is also used to acquire an alternate image of each scene. The ratio of images taken with sequential p- and s-pol excitation is then calculated; the "p/s" result reports only orientational effects and not local concentration effects. Actual p-pol, s-pol, and p-pol/s-pol (p/s) ratio images of diI-labeled macrophages can be seen in Fig. 5B. Polarized TIR has also been used to quantify the amount of order of a phospholipid-like probe in an artificial phospholipid bilayer (Thompson *et al.*, 1984).

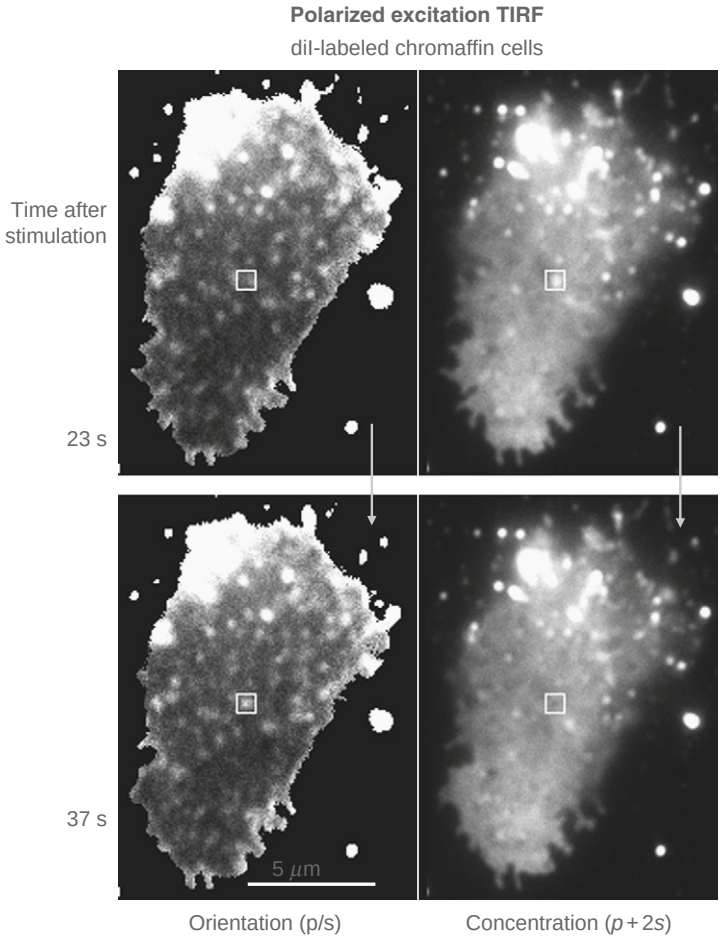

Fig. 6 Polarized excitation TIRF on diI-labeled chromaffin cells. The left panels are two time points (23 and 37 s after chemical stimulation) for p/s image ratios (which show membrane orientation); the right panels are the corresponding $p + 2s$ linear combinations (which show total concentration of diI or distance of diI from the substrate, rather than membrane orientation). The small white boxes highlight a region where the plasma membrane orientational dynamics clearly differ from the concentration and distance dynamics. The relative darkness inside the box in the lower $p + 2s$ image could result from either lower total diI concentration there, or a lifting of the membrane from the substrate there, or both.

What combination of p and s images will report only concentrations and distances but *not* orientations? This question is of broad interest because intensities in TIRF images in general will report a convolved mix of orientations with concentrations and distances, and we want to know how the concentrations and distances vary over the image without getting orientational effects mixed in. It can be shown that the

correct answer depends on the numerical aperture of the objective because high-aperture objectives can "see around" the optical axis. This permits them to detect emission from dipoles oriented along the optical axis (i.e., perpendicular to a membrane parallel to the substrate), emission that otherwise would not be well detected by low-aperture objectives. For very high-aperture objectives (NA $\geq$ 1.4), the efficiency of gathering light from a dipole is about as high from an excited dipole normal to the membrane as a dipole parallel to the membrane. For such objectives, it turns out that the combination "p + 2s" (i.e., the image taken with p-pol TIRF excitation added to twice the image taken with s-pol TIRF excitation) reports local concentration without significant orientational artifacts.

Shows a sequence of dil-labeled chromaffin cells that were treated with an exocytosis stimulant. An orientation-dependent time sequence (p/s) is compared with a contemporaneous concentration-dependent time sequence (p+2s). An interesting feature illustrating the utility of following both combinations is that transient changes in micromorphology and in local concentration do not always occur together. An obvious next step would be to examine changes in dil-labeled plasma membrane micromorphology by polarized excitation TIRF simultaneously with viewing the 3D location of secretory granules labeled by a fluorescent protein in a contrasting color.

2. Polarized Emission TIRF

In polarized emission TIRF, the emitted image is viewed separately through two orthogonal polarizers but excitation light can be completely unpolarized. This is in contrast to standard fluorescence polarization with EPI (i.e., non-TIR) excitation, which does require polarized excitation. But note that, in general, "unpolarized" propagating light is not really unpolarized: it does not have electric field strength pointing in *all* directions. The electric field is always zero in the direction of light propagation. "Unpolarized" propagating light that totally reflects at an interface sets up an evanescent field that has only a very weak electric field in the direction of wave front traveling along the surface (called the x-direction here: see Fig. 2). The two other directions—the direction normal to the substrate (called "z") and the direction parallel to the substrate and perpendicular to the plane of incidence) (called "y")—both have substantial evanescent electric field strengths.

For perfect temporal simultaneity in observing the two emission polarizations, the emission path can be broken down into two images by a commercial image splitter, each with an orthogonal polarizer placed in it. The split emission images are arranged with their polarizers oriented in the x and the y directions. This emission path configuration is similar to any standard fluorescence polarization observation: view the sample in two orthogonal polarizations, either simultaneously (with an image splitter) or sequentially (with alternating polarizers). Denote the fluorescence detected from corresponding pixels in the two split images as F_x and F_y.

With this optical scheme, polarized emission TIRF can distinguish among different fluorophore orientational distributions. Consider, for example, diI which is either in a flat membrane parallel to the substrate (a "2D" distribution) or in a small membrane invagination that is roughly spherical (a "3D" distribution). If the evanescent field is purely s-pol (y-pol in our coordinate system), then $F_y > F_x$ because the y-polarized excitation tends to produce y-polarized emission, and the x-polarized excitation is very weak. In fact, $F_x/F_y = 1/3$ for *both* 2D or 3D orientational distributions, so we cannot distinguish between 2D and 3D orientational distributions based on the ratio observed from s-pol excitation. If the evanescent field is purely p-pol (largely z-pol with a very minor amount of x-pol), then in general, $F_x = F_y$ by symmetry; that is, $F_x/F_y = 1$. Again, this is true for either 2D or 3D orientational distributions. For 3D, both F_x and F_y are equal and substantial. For 2D orientations, F_x and F_y are (still) equal but very close to zero because z-pol light will not excite fluorophore dipoles lying in the x-y plane. So the magnitude of F_x and F_y can distinguish the two orientational distributions. However, we cannot distinguish between a low magnitude due to a 2D orientational distribution and a low magnitude due to a low local fluorophore concentration.

We need a method to normalize out concentration effects. For this purpose, we use an unpolarized *mix* of y- and z-pols, In 2D, the mix will produce $F_x/F_y = 1/3$ because that is what the y-pol part of the mix produces, and the z-pol part of the mix will not produce any fluorescence at all. But in 3D, F_x/F_y will be distinctly different from 1/3, somewhere between 1/3 and 1, depending on the relative amount of y- and z-pol excitation. The fact that we are taking a ratio F_x/F_y rather than analyzing absolute intensities will normalize out fluorophore concentration effects. Figure 7 shows polarized emission TIRF on artificial and biological samples with interesting local orientational variations across the field of view.

3. Single-Molecule Polarization

If one views single molecules that have been labeled with single fluorophores, the requirement for orientational order among fluorophores becomes irrelevant. Polarized TIR can successfully determine the orientation of single molecules, as was done recently for sparsely labeled F-actin (Forkey *et al.*, 2005). The ability to follow the orientational changes of single molecules as they proceed through their functional states is a real advantage over ensemble polarization readings, which report only an average orientation and thereby blur over what might be key distinctions between conformational and orientational states.

An unusual kind of single-molecule polarized emission TIR has been demonstrated that depends on optical aberrations. Molecules with emission dipoles oriented orthogonally to the substrate emit very little of their light along the dipole axis. Most of their light is emitted at more skimming angles to the substrate surface; this light is captured by the periphery of high-aperture objectives. If a source of aberration is deliberately introduced into the detection system (e.g., a layer of water), those extreme rays will not focus well into a spot but

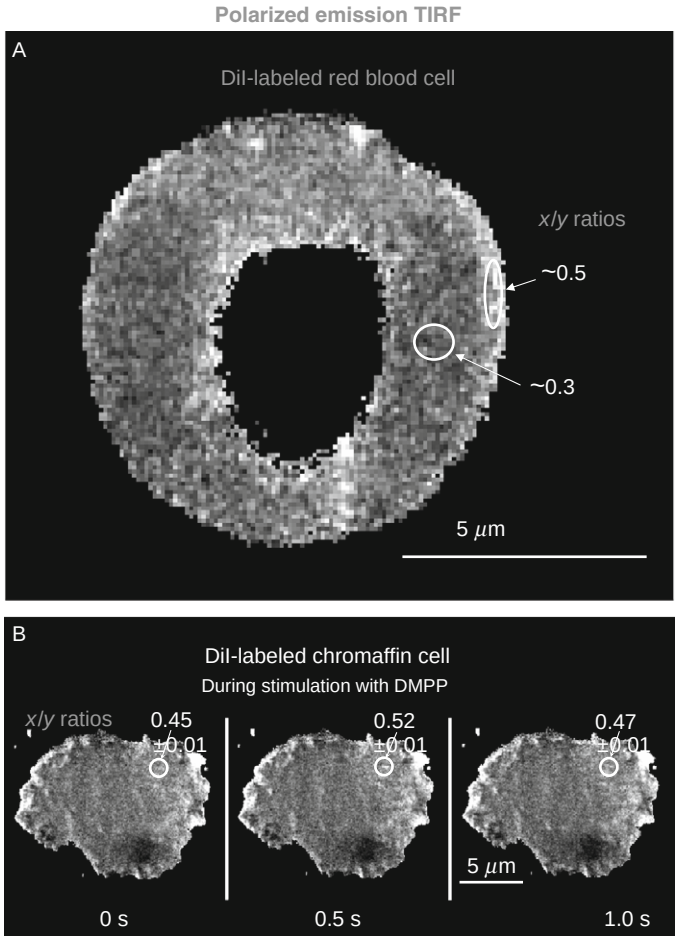

Fig. 7 Polarized emission TIRF. These are "x/y" ratios of images viewed through an x-oriented emission polarizer versus a y-oriented polarizer, with unpolarized excitation. (A) A human erythrocyte. The x/y ratio clearly varies from region to region, reporting changes in the orientation of the membrane relative to the coverslip substrate. (B) diI-labeled bovine chromaffin cell. The x/y ratio varies not only spatially but also temporally, as can be seen in the selected location indicated by white circles.

instead form a small doughnut of illumination at the image plane. This doughnut can be readily distinguished from a dipole oriented parallel to the substrate, which focuses well to a spot (Dickson *et al.*, 1998).

The asymmetry of the emission from oriented dipoles can manifest itself as an anisotropy of intensity at the back focal plane (BFP) of the objective, since the BFP essentially forms a spatial map of the angular distribution of rays emanating from the sample molecule. This technique has been demonstrated on single molecules

illuminated with standard epioptics (Lieb *et al.*, 2004), but it should also work well with TIR illumination.

It may sometimes be desirable to suppress the effect of molecular orientation or rotation on the observed fluorescence, which might otherwise be mistaken for fluctuations in the local concentration or chemical environment. Two orthogonally directed TIR beams with appropriate polarizations can be made to produce isotropic excitation in two or three dimensions (Wakelin and Bagshaw, 2003).

B. FRET and TIRF

TIR-FRET provides an opportunity to observe real-time changes in the conformation of single molecules attached to the substrate due to the much reduced background provided by TIR. This combination has been applied to studying transitions in actin conformation that are correlated with the presence of myosin (Kozuka *et al.*, 2006).

C. Time-Resolved Lifetime and TIRF

TIR-fluorescence lifetime measurements should give somewhat different results than results of the same fluorophores in solution. Proximity to the surface may directly perturb the molecular state structure, thereby affecting lifetimes. In addition, the near-field capture effect generally increases the rate of transfer of energy out of the fluorophore and thereby decreases lifetimes. The rotational mobility of surface-proximal molecules can be studied by TIR combined with fluorescence polarization anisotropy decay (Czeslik *et al.*, 2003; Schneckenburger *et al.*, 2003).

D. FRAP and TIRF

In TIR-FRAP, a bright flash of the evanescent field bleaches the surface-proximal fluorophores, and the subsequent rate of recovery of fluorescence excited by dimmer evanescent illumination provides a quantitative measure of the desorption kinetic rate k_{off} (Burghardt and Axelrod, 1981; Fulbright and Axelrod, 1993; Hellen and Axelrod, 1991; Pisarchick *et al.*, 1992; Thompson *et al.*, 1981), which is simply the reciprocal of a typical time that a molecule resides at the surface. Such measurements can be done even on living cells at the cell–substrate contact regions in the evanescent field. As applied to whole images (Chang *et al.*, 2005), the postbleach recovery is observed at each pixel. Figure 8 shows a TIR-FRAP spatial map of fluorescent chemoattractant dissociation rates from the cell-surface receptors of the human neutrophil (Axelrod and Omann, 2006). The surprising result is the great variability of recovery rates from place to place on the same cell.

A concentration jump in the bulk, rather than a bleaching flash, provides a different kind of perturbation and leads to a relaxation rate in the surface-proximal concentration that depends on a linear combination of both k_{off} and the adsorption kinetic rate k_{on}. Therefore, by combining concentration jump experiments with

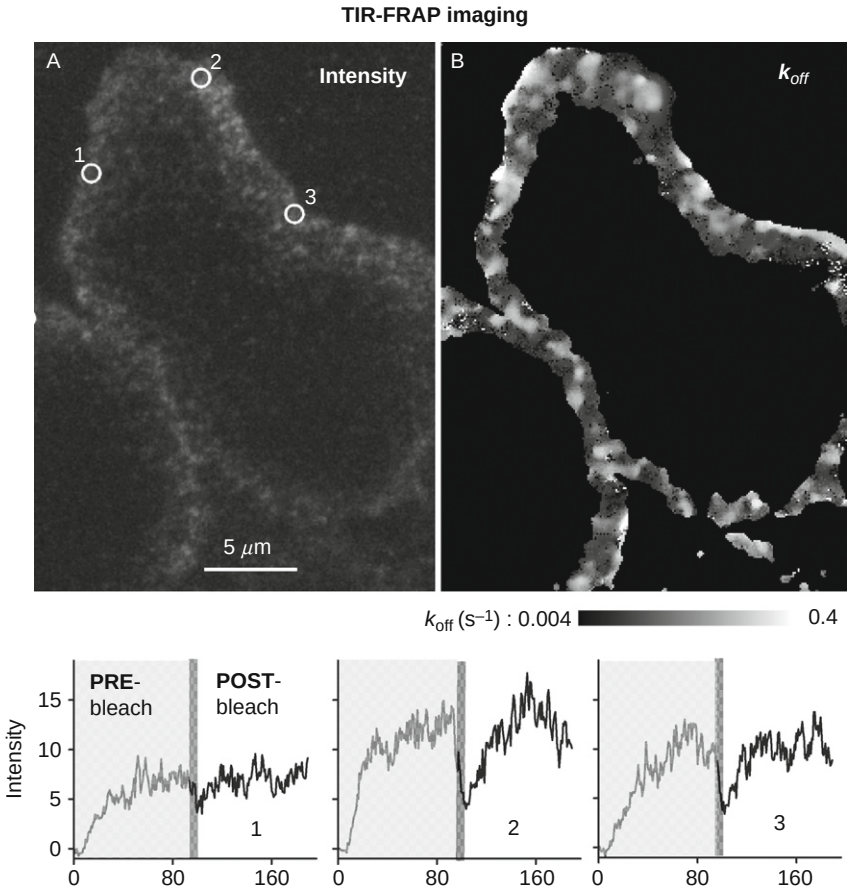

Fig. 8 TIR–FRAP on human neutrophils. The neutrophils were bathed in a 10 nM solution of chemoattractant *N*-formyl-methionyl-leucyl-phenylalanyl-lysine labeled with AlexaFluor532. (A) TIR illumination excites fluorescence only from ligand-bound receptors at cell–substrate contact regions around the periphery of each cell. At $t = 0$ s, fluorescent ligand was added to the solution. Beginning at $t = 90$ s, a bright photobleaching flash was administered. (B) The postbleach recovery rates observed at every location in the image are plotted with a logarithmic gray scale color ranging from 0.004 to 0.4/s. Locations with intensities falling below a threshold were not analyzed, accounting for the black regions everywhere outside the cell–substrate contact regions. (C) Actual fluorescence intensity versus time plots at three numbered locations indicated in panel (A), showing place-to-place variations in fluorescence intensity versus time. The bleaching flash event is indicated here by the vertical gray stripes. See Axelrod and Omann (2006) for more experimental details.

FRAP experiments on the same TIR-illuminated sample, both k_{off} and k_{on} can be deduced separately (Chang *et al.*, 2005).

The TIR bleaching pattern can be made to be spatially nonuniform, by weak focusing or by interference effects into ellipses, lines, or stripes (Abney *et al.*, 1992;

Burghardt and Axelrod, 1981; Fulbright and Axelrod, 1993; Schapper *et al*., 2003). Upon bleaching, spatial nonuniformity produces some areas that are more or less bleached than adjacent areas. Subsequent surface diffusion will relax those differences; this can be observed as a fluorescence recovery into more heavily bleached regions.

By bleaching with a polarized flash of light, dipoles oriented in the direction of polarization will be bleached preferentially, leading to an immediate postbleach orientational anisotropy of the remaining unbleached dipoles. Subsequent rotational relaxation toward isotopicity will lead to a fluorescence recovery as seen through a polarizing filter and a single channel photodetector (Selvin *et al*., 1990; Velez and Axelrod, 1988; Yoshida and Barisas, 1986; Yuan and Axelrod, 1995). The recovery can take place in as short as microseconds, so adapting this technique to imaging will challenge the frame rate of CCD detectors. Combining this capability with TIRF should allow measurement of local viscosities in tiny subvolumes of cells, such as the interior of secretory granules.

E. FCS and TIRF

In TIR-FCS, the thin evanescent field is combined with an image plane diaphragm that passes light only from a small (typically submicron) lateral region. This defines an extremely small observation volume ($\sim$0.02 μm^3) in the sample. Random fluctuations in the number of fluorophores in this small volume are relatively large and their rate provides information about the diffusive rate in the bulk solution near the surface, the kinetic desorption rate, and the absolute concentration of surface-proximal fluorophores (Hassler *et al*., 2005a,b; Starr and Thompson, 2001; Thompson *et al*., 1981).

In a manner similar to TIR-FRAP, polarization can be added to the mix of TIR and FCS to detect rates of orientational change of molecules in a very small volume. This approach was applied to fluorescence-labeled myosin in active contracting striated muscle (Borejdo *et al*., 2006b), where it is believed that the myosin head goes through an orientational change as a part of its cycle in contacting and releasing actin. TIRF allowed observation of only a few myosin heads in a very small volume, thereby leading to observably large fluctuations. Analysis of the power spectrum of the observed temporal fluctuations in polarized TIRF showed that the rate of orientational cycling was about equal to the rate of ATP hydrolysis, consistent with the theory that one hydrolysis occurs per action association/dissociation cycle.

F. Multiphoton Excitation and TIRF

In multiphoton TIRF, excitation by an intense flash of evanescent infrared light excites a fluorescent response that is proportional to the square (or higher order) of the incident light intensity (Chon and Gu, 2004; Oheim and Schapper, 2005; Schapper *et al*., 2003). This might seem at first to have some advantages for further

decreasing the effective evanescent wave depth d. Although d for two-photon TIR excitation should be half of that of the single-photon case described by Eq. (3), note that the infrared wavelength is double what would have been used in "single photon" TIRF, so the effect on the depth d would be minimal (apart from chromatic dispersion effects in the substrate and water). On the other hand, scattering of the evanescent field by inhomogeneities in the sample would likely not be bright enough to excite much multiphoton fluorescence, so multiphoton TIRF may produce a cleaner image, less affected by scattering artifacts.

One theoretical study proposes a three-way combination of TIR with two-photon excitation and with stripe-pattern FRAP. The advantage is a higher-contrast imprinted bleach pattern (Huang and Thompson, 1993) to improve lateral diffusion measurements.

G. Optical Trapping and TIRF

Nishikawa *et al.* (2006) used both optical trapping ("laser tweezers") and TIRF separately to examine the motion of myosin-IX on actin. It may be possible, however, to use the evanescent field of TIRF itself as the optical trap (Nieto-Vesperinas *et al.*, 2004) since the gradient of the evanescent intensity can be made comparable to the gradient of intensity in standard focused spot optical traps. The evanescent optical gradient force will always be directed toward the interface. The analogue of a "photon pressure" force may be directed parallel to the substrate in the plane of incidence; it might be canceled out by the use of oppositely directed TIR beams.

H. AFM with TIRF

By combining TIRF with simultaneous AFM (i.e., scanning with a cantilever mechanical probe), micromechanical properties can be directly measured on cellular and molecular samples (Kellermayer *et al.*, 2006; Mathur *et al.*, 2000; Shaw *et al.*, 2006; Trache and Meininger, 2005). Labeled molecules affixed to an AFM probe can be illuminated by TIRF (Yamada *et al.*, 2004).

I. Interference Reflection and TIR

Specific ligand binding to receptors immobilized on a surface can be viewed simultaneously with nonspecific mass adsorption by combining TIRF with reflectance interferometry, thus far in nonmicroscopic mode (Gavutis *et al.*, 2005). By combining TIRF with interference reflection contrast (IRC), Ca^{2+} microdomains can be viewed simultaneously with exocytosis events in synapses (Beaumont *et al.*, 2005). Both TIR and IRC were used on the same sample to study the approach of neuronal growth cones to the substrate (Tatsumi *et al.*, 1999).

V. Optical Configurations and Setup

Many alternative optical arrangements for TIRF are available. Some configurations use a high numerical aperture (NA > 1.4) microscope objective for both TIR illumination and emission observation, and others use a prism to direct the light toward the TIR interface with a separate objective for emission observation. The evanescent illumination is not "pure" with objective-based TIRF: a small fraction of the illumination of the sample results from excitation light scattered within the objective (discussed in more detail later), and a small fraction of the observed fluorescence arises from luminescence of the objective's internal elements. Prism-based TIRF avoids these problems but geometrical constraints leave it most workable only for low- and medium-power objectives.

This section gives examples of these arrangements. We assume for explanatory convenience that the sample consists of fluorescence-labeled cells in culture adhered to a glass coverslip.

A. High-Aperture Objective-Based TIR: General Scheme

By using an objective with a sufficiently high NA, supercritical angle incident light can be cast upon the sample by illumination through the objective (Axelrod, 2001; Stout and Axelrod, 1989). Although an arc lamp can be used as the light source, the general features are best explained with reference to a laser source.

The laser beam used for excitation is focused (by an external focusing lens) to a point at the BFP of the objective so that the light emerges from the objective in a collimated form (i.e., the "rays" are parallel to each other). This ensures that all the rays are incident upon the sample at the same angle θ with respect to the optical axis.

The point of focus in the BFP is adjusted to be off-axis. There is a one-to-one correspondence between the off-axis radial distance ρ and the angle θ. At a sufficiently high ρ, the critical angle for TIR can be exceeded. Further increases in ρ serve to reduce the characteristic evanescent field depth d in a smooth and reproducible manner.

The beam can emerge into the immersion oil (refractive index n_{oil}) at a maximum possible angle θ_m measured from the optical axis) given by:

$$NA = n_{oil}\sin\theta_m \tag{11}$$

Since $n \sin\theta$ is conserved (by Snell's Law) as the beam traverses through planar interfaces from one material to the next, the right side of Eq. (11) is equal to $n_3 \sin\theta_3$ (where subscript 3 refers to the coverslip substrate upon which the cells grow), therefore

$$NA = n_3\sin\theta_3 \tag{12}$$

For TIR to occur at the interface with an aqueous medium of refractive index n_1, θ_3 must be greater than the critical angle θ_c as calculated from

$$n_1 = n_3\sin\theta_c \tag{13}$$

From Eqs. (12) and (13), it is evident that the NA must be greater than n_1, preferably by a substantial margin. This is no problem for an interface with water with $n_1 = 1.33$ and an NA = 1.4 objective. But for viewing the inside of a cell at $n_1 = 1.38$, an NA = 1.4 objective will produce TIR at just barely above the critical angle. The evanescent field in this case will be quite deep, and dense heterogeneities in the sample (such as cellular organelles) will convert some of the evanescent field into scattered propagating light.

Fortunately, objectives are now available with NA > 1.4. The highest aperture available is an Olympus 100× 1.65NA; this works very well for objective-based TIRF on living cells. However, that objective requires the use of expensive 1.78 refractive index coverslips made of either LAFN21 glass (available from Olympus) or SF11 glass (custom cut by VA Optical Co, San Anselmo, CA). SF11 glass is the less expensive of the two but it has a chromatic dispersion not perfectly suited to the objective, thereby requiring slight refocusing for different fluorophores. The 1.65 objective also requires special $n = 1.78$ oil (Cargille), which is volatile and leaves a crystalline residue. Several other objectives that are now available circumvent these problems: Olympus 60× 1.45NA, Olympus 60× 1.49NA, Zeiss 100× 1.45NA, and four Nikon objectives: Nikon 60× 1.45NA w/correction collar, Nikon 100× 1.45NA, Nikon 60× 1.49NA w/correction collar, and Nikon 100× 1.49NA w/correction collar. The 1.45–1.49 objectives all use standard glass (1.52 refractive index) coverslips and standard immersion oil and yet still have an aperture adequate for TIRF on cells. The 1.49NA objectives are probably the method of choice for TIR except for cells that have particularly dense organelles. Dense organelles tend to scatter the evanescent field, and this effect is less prominent with the higher angles of incidence accessible through higher aperture objectives.

The angle of convergence/divergence of the laser beam cone at the BFP is proportional to the diameter of the illuminated region, subsequently created at the sample plane. Large angles (and consequent large illumination regions) can be produced by use of a beam expander placed just upbeam from the focusing lens.

The orientation of the central axis of the laser beam cone at the BFP determines whether the TIR-illuminated portion of the field of view is centered on the microscope objective's optical axis.

A microscope can be configured in several variations for objective-based TIRF excited by a laser beam by use of either commercial accessories or fairly simple custom-built add-on modifications (Fig. 9A–C). An arc lamp illumination system, rather than a laser, can also be configured for TIRF illumination by use of an opaque disk of the correct diameter, inserted in a plane equivalent (but upbeam) from the objective BFP (Fig. 9D). This allows only rays at significantly off-axis radii in the BFP to propagate through the TIR sample plane, upon which they are incident at supercritical angles. By placing or removing the opaque disk as shown, illumination can be switched easily between EPI and TIR. Arc illumination has the advantages of easy selection of excitation colors with filters and freedom from coherent light interference fringes, but it is somewhat dimmer because much of the arc lamp power directed toward the sample at subcritical angles is necessarily

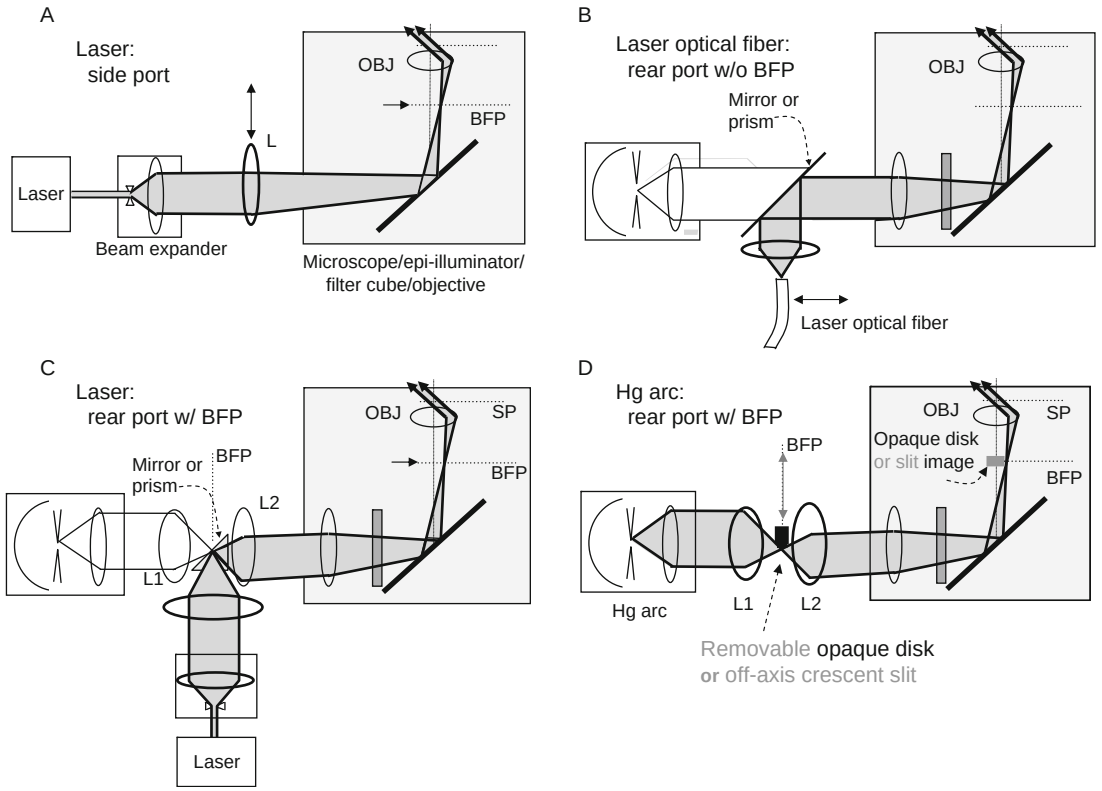

Fig. 9 Four arrangements for objective-based TIRF in an inverted microscope. In all of these configuration, OBJ refers to the objective, SP refers to sample plane, and BFP refers to the objective's back focal plane or its equivalent planes (also called "aperture planes"). Components drawn with heavier lines need to be installed; components in lighter lines are possibly preexisting in the standard microscope. (A) Laser illumination through a side port (requires a special dichroic mirror cube facing the side). The beam is focused at the back focal plane at a radial position sufficient to lead to supercritical angle propagation into the coverslip. Moving the focusing lens L transversely changes the angle of incidence at the sample and allows switching between subcritical (EPI) and supercritical (TIR) illumination. This is how Fig. 1 was produced. (B) Laser illumination introduced by an optical fiber through the rear port normally used by the arc lamp. This scheme is employed by commercial TIRF systems. (C) Laser illumination in microscope systems containing an equivalent BFP in the rear path normally used by an arc lamp. The laser beam is focused at the BFP where the arc lamp would normally be imaged. Some microscopes provide this BFP, marked as an "aperture plane." If an aperture plane does not exist in the indicated position, it can be created with the pair of lens L1 and L2. (D) Arc lamp TIR illumination with no laser at all. The goal is to produce a sharp-edged shadow image of an opaque circular disk at the objective back focal plane such that only supercritical light passes through the objective. The actual physical opaque disk (ideally made of aluminized coating on glass) must be positioned at an equivalent upbeam BFP that, in Kohler illumination, also contains a real image of the arc. The illumination at the back focal plane is a circular annulus; it is shown as a point on one side of the optical axis for pictorial clarity only. The through-the-lens arc lamp TIRF configuration D can be switched easily to laser TIRF configuration C by insertion of the reflecting prism in the arc lamp light path. As for panel C, lenses L1 and L2 may be necessary to create an equivalent BFP between them.

blocked. Somewhat more of the incident light can be utilized rather than wasted by employing a conical prism in the arc lamp light path (Stout and Axelrod, 1989). This kind of prism converts the illumination profile, normally brightest in the center, into a dark-centered ring.

Commercial arc lamp TIRF systems use a curved slit cutout at an equivalent BFP. The slit is positioned off-axis to transmit only a thin curved band of light at a radius that will produce supercritical angles. To optimize the throughput, the brightest part of the mercury arc is focused off-axis right upon the curved slit cutout, with a focusing aberration that curves the arc image to match well with the curved slit.

B. High-Aperture Objective-Based TIR: Step-by-Step Custom Setup

Commercial objective-based TIRF systems are available with both laser/optical fiber sources (often multiple ones for quick color switching) and arc lamp sources. They work well but are somewhat expensive. A less-expensive practical protocol follows for setting up "homemade" objective-based TIRF with free laser beam illumination through an inverted microscope, and verifying that the setup works correctly. Such a homemade setup is also more open and amenable to special modification. (However, an unshielded nonsafety-interlocked homemade system demands great caution from all users because of the potential for eye injury.) The description is most relevant to the setup in Fig. 9A, but modifications to the other Fig. 9 panels (in which the microscope already has lenses installed in the illumination beam path) are straightforward.

1. Prepare a test sample consisting of a film of fluorescent material adsorbed to a coverslip of the appropriate type of glass ($n = 1.52$ for NA = 1.45 or 1.49 objectives; $n = 1.78$ for NA = 1.65 objectives). A convenient and durable uniform film is made from diI. Dissolve the diI at about 0.5 mg/ml in ethanol, and place a single droplet of the solution on a glass coverslip. Then, before it dries, rinse off the coverslip with distilled water. A monolayer of diI fluorophore will remain adhered to the glass. When excited by laser light at 488 nm and observed through the filter set appropriate for fluorescein, the diI adsorbed to the surface will appear orange. Above the diI-coated surface, place an aqueous solution of fluorescein (just high enough concentration to appear slightly colored), the fluorescence of which will appear green in the same spectral system. Use enough aqueous fluid so that its upper surface is flat rather than a curved blob. As an alternative to the diI/fluorescein test sample, a dilute suspension of fluorescent microbeads in water can be used (just high enough concentration to create a slight turbidity). Some of the beads will adhere to the surface. Although the same color as the suspended beads, the surface-adhered beads will be immobile whereas the bulk suspended beads will jitter with Brownian motion. Place the sample on the microscope stage and raise the objective with the focusing knob to make optical contact through the appropriate immersion oil.

2. Remove all obstructions between the test sample and the ceiling. Allow a collimated laser beam (the "raw" beam) to enter the side or rear epi-illumination port along the optical axis. If the microscope has removable lenses in the path between the point of entry and the dichroic mirror (usually part of the optical system for arc illumination), it is best to remove them. A large area of laser illumination will be seen on the ceiling, roughly straight up.

3. Place a straight edge opaque obstruction (such as an index card) part way in the beam before it enters the microscope. A fuzzy shadow of the card edge will be seen on the ceiling illumination. By moving the card longitudinally in the right direction, the shadow will become fuzzier. After moving it beyond some point of complete fuzziness, it will again become sharper, but now as a shadow on the opposite side of the ceiling illumination. The longitudinal position of maximum fuzziness is a "field diaphragm plane" (FDP), complimentary to the sample plane. Once the location of the FDP is determined, remove the obstruction.

4. Place a simple focusing lens (plano- or double-convex) at that FDP, mounted on a 3D translator. The illuminated region on the ceiling will now be a different size, probably smaller. The goal is to choose a focal length for the focusing lens that almost minimizes the spot size on the ceiling. A focusing lens with close to the proper focal length will require only minor longitudinal position tweaking (i.e., along the axis of the laser beam) to absolutely minimize the illuminated region on the ceiling. At this lens position, the beam focuses at the objective's BFP and emerges from the objective in a nearly collimated form. This procedure also ensures that the focusing lens is also close to the FDP. Therefore, moving the focusing lens laterally will change the radial position of focus at the BFP (and hence the angle of incidence at the sample plane) but the motion will not affect the centering of the region of illumination in the sample plane.

Focusing the laser beam at the actual BFP is the goal, but the actual BFP is inside the objective housing itself. Additional optical elements found in the commercial microscope usually (but not necessarily) create an "equivalent" BFP (EBFP) farther upbeam, and the goal then becomes to focus at the EBFP. It may be difficult to find the location of an EBFP or to focus a laser beam there. If that is the case, try reinstalling (or leaving in place) the optics designed for an arc source, that will reposition the location of the EBFP (as well as the FDP). If the microscope contains a slot marked "A" at an accessible location in the excitation path, an EBFP (also called "aperture plane") is located there. By watching how well the custom-installed focusing lens creates a focused point of light (rather than a blur) at that plane, the correct focal length of the focusing lens can be chosen judiciously.

5. Fine tune the lateral position of the focusing lens so that the beam spot on the ceiling moves down a wall to the right or left. The inclined path of the beam through the fluorescent aqueous medium in the sample will be obvious to the eye. Continue to adjust the focusing lens lateral position until the beam traverses almost horizontally through the fluorescent medium and then farther, past where it just disappears. The beam is now totally reflecting at the substrate/aqueous interface.

6. View the sample through the microscope eyepieces. The diI/fluorescein sample should appear orange, not green, since only the surface is being excited; the microbead sample should show only immobilized dots. Back off the focusing lens to where the beam reappears in the sample (i.e., subcritical incidence). When viewed through the eyepieces, the diI/fluorescein sample should now appear very bright green and the microbead sample very bright with most beads jittering laterally and longitudinally in and out of focus.

7. If the illuminated region in the field of view is not centered, adjust the lateral position of the "raw" laser beam before it enters the focusing lens.

8. If the illuminated region is too small, increase the width of the beam before it enters the focusing lens with a beam expander or long focal length diverging lens.

9. Replace the test sample with the sample of interest and focus the microscope. As the lateral position of the external focusing lens is adjusted through the critical angle position, the onset of TIRF should be obvious as a sudden darkening of the background and a flat two-dimensional look to the features near the surface such that the entire field of view has only one plane of focus.

10. If interference fringe/stripe illumination TIR is desirable, use a beam splitter and arrange the second beam to enter the focusing lens off-center, parallel to the optic axis, but at a different azimuthal angle around it. A relative azimuthal angle of 180° will give the closest spaced fringes. Be sure that any difference in path length of the two beams from the beam splitter to the focusing lens is less than the coherence length of the laser (a few millimeter or centimeter); otherwise, no interference will occur.

11. In some applications (such as studies of multilabeled samples), the ability to switch among different excitation colors is important. However, the simple focusing lens placed near the FDP discussed earlier is not necessarily corrected for chromatic dispersion: the same lens will have a shorter focal length for shorter wavelengths. Therefore, use a multielement lens that is corrected for chromatic dispersion. Alternatively, prepare each colored beam in its own distinct beam path, but each with a slightly different divergence, possibly created by a long focal length concave lens in one or more of the paths. The beam paths are then superimposed into a single path by a dichroic mirror before hitting the simple focusing lens. The various divergences can be adjusted so that all colors will still focus in the same plane (the actual BFP or the EBFP).

C. Prism-Based TIRF: General Scheme

Although a prism may restrict sample accessibility or choice of objectives in some cases, prism-based TIR is very inexpensive to set up and produces a "cleaner" evanescent-excited fluorescence (i.e., less excitation light scattering in the optics) than objective-based TIR. Figure 10A–F shows several schematic drawings for setting up laser/prism-based TIR in inverted and upright microscopes.

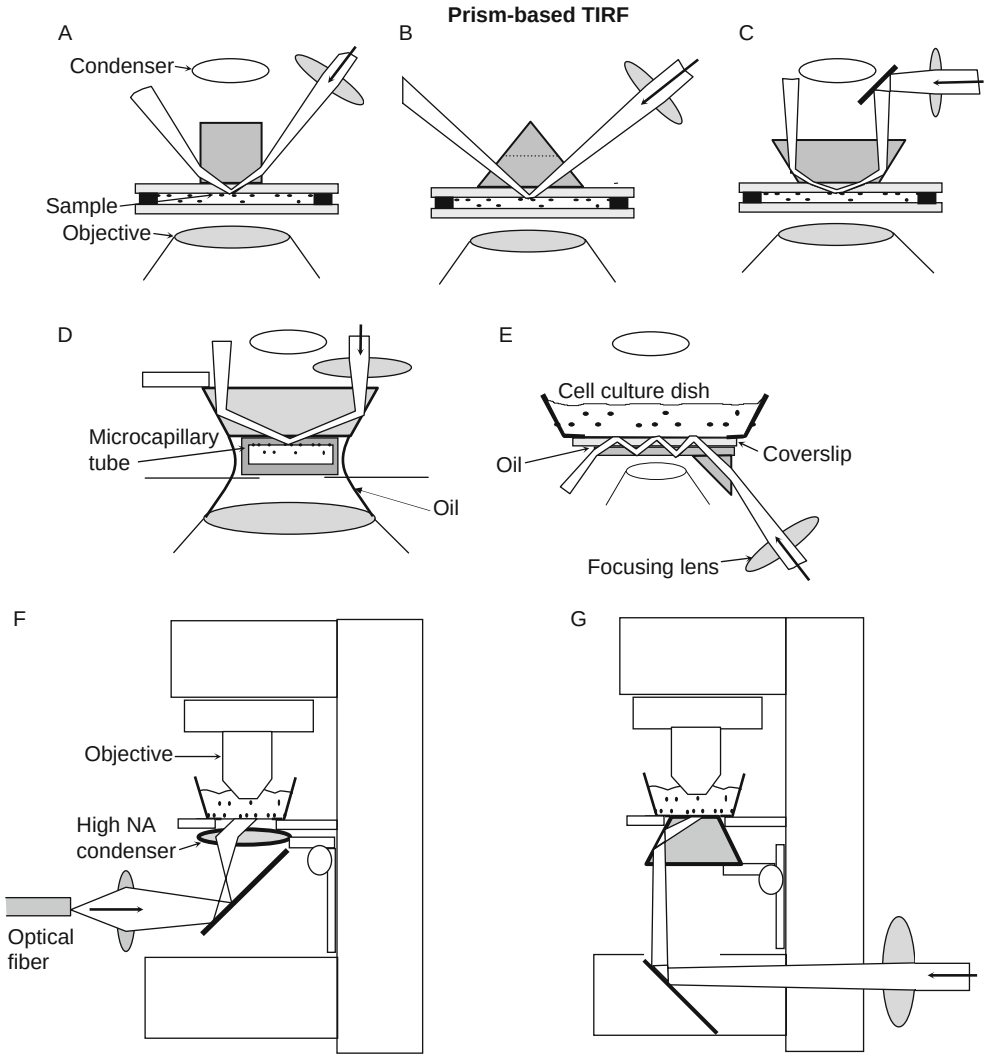

Fig. 10 Schematic drawings for prism-based TIR in inverted and upright microscope configurations, all using a laser as a light source. The vertical distances are exaggerated for clarity. The first four configurations (A)–(D) use a TIR prism above the sample. In configurations (A)–(C), the buffer-filled sample chamber sandwich consists of a lower bare glass coverslip, a spacer ring (made of 60-μm-thick Teflon or double-stick cellophane tape), and the cell coverslip inverted so the cells face down. The upper surface of the cell coverslip is put in optical contact with the prism lowered from above by a layer of immersion oil or glycerol. The lateral position of the prism is fixed but the sample can be translated while still maintaining optical contact. The lower coverslip can be oversized and the spacer can be cut with gaps so that solutions can be changed by capillary action with entrance and exit ports. Configuration (D) shows a rectangular cross-section microcapillary tube (Wilmad Glass Co., Buena, NJ) instead of a coverslip sandwich. With the ends of the microcapillary tube immersed in droplet-sized buffer baths delimited by silicon grease rings drawn on a support (one for supply and one for draining by absorption

In particular, Fig. 10G shows an exceptionally convenient (and low-cost) prism-based TIRF setup for an upright microscope. The laser beam is introduced in the same port in the microscope base as intended for the transmitted light illuminator (which should be removed), thereby utilizing the microscope's own in-base optics to direct the beam vertically upward. The prism, in the shape of a trapezoid, is mounted on the microscope's condenser mount, in optical contact (through a layer of immersion oil) with the underside of the glass coverslip sample plane. An extra lens just upbeam from the microscope base allows adjustment of the incident beam to totally reflect one of the sloping sides of the prism, from which the beam continues up at an angle toward the sample plane where it is weakly focused. This system gives particularly high-quality images if a water immersion objective is employed and submerged directly into the buffer solution in an uncovered cell chamber. Sample with cells adhering directly on the bottom of tissue culture plastic dishes rather than on coverslips can also be used; the plastic/cell interface is then the site of TIR. If the objective has a long enough working distance, reasonable accessibility to micropipettes is possible.

In this configuration with the trapezoidal prism, flexibility in incidence angle (to obtain a range of evanescent field depths) is sacrificed in exchange for convenience. However, a set of various-angled trapezoids will allow one to employ various discrete incidence angles. The most inexpensive approach is to start with a commercially available equilateral triangle prism (say $1'' \times 1'' \times 1''$ sides, and $1''$ length), cleave off and polish one of the vertices to form a trapezoid, and slice the length of the prism to make several copies. Note, however, that this prism will provide an incidence angle of only 60° at the top surface of the prism. If the prism is made from ordinary $n = 1.52$ glass, that angle is insufficient to achieve TIR at an interface with water. [Recall that we need (n sin 60°) to exceed 1.33, the refractive index of water.] However, equilateral prisms made from flint glass ($n = 1.648$) are commercially available (Rolyn Optics, Covina, CA) and these will provide a sufficiently high (n sin 60°) value for TIR to occur at the aqueous interface. In an alternative approach for varying incidence angles over a continuous range, a hemispherical or hemicylindrical prism can be substituted for the trapezoidal

into a filter paper tab), very rapid and low volume solution changes during TIRF observation can be accomplished. If an oil immersion objective is used here, the entire region outside the microcapillary tube between the objective and the prism can be filled with immersion oil. Configuration (E) places a small triangular prism below the sample off to the side and depends on multiple internal reflections in the substrate to bring the illumination into the field of view. This configuration thereby allows complete access to the sample from above for solutions changing and/or electrophysiology studies. However, only air or water immersion objectives may be used because oil at the substrate's lower surface will thwart the internal reflections. Configurations (F) and (G) are for an upright microscope. In (F), a high-aperture condenser plays the role of an external prism, used in conjunction with a fiber optic bundle. This system is commercially available. Configuration (G) utilizes the integral optics in the microscope base and a trapezoidal prism on the vertically movable condenser mount. The position of the beam is adjustable by moving the external lens.

prism (Loerke *et al.*, 2000, 2002). The incident laser beam is directed along a radius line at an angle set by external optical elements.

A commercially available variation of prism-based TIR uses a high-aperture condenser fed with laser light from an optical fiber tip instead of a custom-installed prism fed by a free laser beam (Fig. 10F). This system has the advantage of ready-made convenience and easy variation of both polar and azimuthal incidence angle adjustment, but is limited in maximum incidence angle.

Choice of optical materials for the prism-based methods is somewhat flexible, as follows.

- The prism used to couple the light into the system and the (usually disposable) slide or coverslip in which TIR takes place need not be matched exactly in refractive index.
- The prism and slide may be optically coupled with glycerol, cyclohexanol, or microscope immersion oil, among other liquids. Immersion oil has a higher refractive index (thereby avoiding possible TIR at the prism/coupling liquid interface at low incidence angles) but it tends to be more autofluorescent (even the "extremely low" fluorescence types).
- The prism and slide can both be made of ordinary optical glass for many applications unless shorter penetration depths arising from higher refractive indices are desired. Optical glass does not transmit light below about 310 nm and also has a dim autoluminescence with a long (several hundred microseconds) decay time, which can be a problem in some FRAP experiments. The autoluminescence of high-quality fused silica (often called "quartz") is much lower. Tissue culture plastic dish (particularly convenient as a substrate in the upright microscope setup) is also suitable, but tends to have a significant autofluorescence compared with ordinary glass. More exotic high n_3 materials such as sapphire, titanium dioxide, and strontium titanate (with n as high as 2.4) can yield exponential decay depths d as low as $\lambda_o/20$, as can be calculated from Eq. (3).

In all the prism-based methods, the TIRF spot should be focused to a width no larger than the field of view; the larger the spot, the more that spurious scattering and out-of-focus fluorescence from the immersion oil layer between the prism and coverslip will increase the generally very low fluorescence background attainable by TIRF. Also, the incidence angle should exceed the critical angle by at least a couple of degrees. At incidence angles very near the critical angle, the cells cast a noticeable "shadow" along the surface.

D. Prism-Based TIRF: Step-by-Step Custom Setup

Here is a practical protocol for setting up "homemade" prism-based TIRF, by far the least expensive approach to TIR. As always, be cautious to avoid eye injury from stray laser beams.

1. Mount the prism on the condenser mount carrier if possible.

2. Depending on the configuration, a system of mirrors with adjustable angle mounts fixed to the table must be used to direct the beam toward the prism. One of these mirrors (or a system of shutters) should be movable and placed near the microscope, so that switching between standard epi-illumination and TIR is possible without interrupting viewing.

3. Place a test sample (e.g., a diI-coated coverslip, see the description in the objective-based TIR section) in the same kind of sample holder as to be used for cell experiments. An aqueous medium, possibly containing some fluorescein, can be used to fill the sample chamber. Alternatively, a test sample of fluorescent microbeads can be used as previously described.

4. With the test sample on the stage, focus on the fluorescent surface with transmitted (usually tungsten) illumination. Usually, dust and defects can be seen well enough to assay the focus. Fluorescent epi-illumination can also be used to find the focus because laser interference fringes are seen sharply only at the focal position.

5. Place a small droplet of immersion oil on the non-diI surface of the sample coverslip or directly on the prism (depending on which one faces upward in the chosen configuration) and carefully translate the prism vertically so it touches and spreads the oil but does not squeeze it so tightly that lateral sliding motion is inhibited. Too much oil will bead up around the edges of the prism and possibly interfere with the illumination path.

6. Without any focusing lens in place, adjust the unfocused (''raw'') collimated laser beam position with the mirrors so that TIR occurs directly in line with the objective's optical axis. This can usually be seen by observing the scattering of the laser light as it traverses through the prism, oil, and TIR surface.

7. Insert the focusing lens so that the focus is roughly at the TIR area under observation. Adjust its lateral position with translators on the focusing lens so that the TIR region occurs directly in line with the objective. To guide this adjustment, look for three closely aligned spots of scattered light, corresponding to where the focused beam first crosses the immersion oil layer, where it totally reflects off the sample surface, and where it exits by recrossing the oil.

8. The TIR region should now be positioned well enough to appear in view in the microscope when viewed as test sample fluorescence with the standard filters in place. In general, the TIR region will appear as a yellow-orange ellipse or streak with a diI test sample and a region of discrete tiny bright dots with a microbead test sample. Make final adjustments with the focusing lens to center this area. The TIR area can be distinguished from two out-of-focus blurs past either end of the ellipse or streak (arising from autofluorescence of the immersion oil) because the TIR spot contains sharply focused images of defects in the diI coating or sharp dots of adsorbed microbeads. The focusing lens can be moved forward or backward along the laser optical path to achieve the desired size of the TIR area. If fluorescein

solution was used to fill the sample chamber, the characteristic green color of fluorescein should *not* be seen with successful TIR. If the alignment is not correct and propagating light reaches the solution, then a bright featureless blur of green will be seen.

9. With the optics now correctly aligned for TIR, translate the prism vertically to remove the diI sample and replace it with the actual cell sample. Relower the prism to make optical contact. Although the TIR region will not be exactly in the same spot (because of irreproducibility in the prism height), it will be close enough to make final adjustments with the focusing lens while observing fluorescence from the cell sample.

E. TIR from Multiple Directions

Configurations involving a single laser beam that produces TIR from one incidence direction (i.e., from one azimuthal angle around the optical axis) are the simplest ones to set up, but configurations involving multiple or a continuous range of azimuthal angles incident on the sample plane have some unique advantages. A single illumination direction tends to produce shadows on the "downstream" side of cells because of evanescent field scattering by the cells; these shadows are less apparent at higher incidence angles even with a single beam. However, a hollow cone of illumination over all the azimuthal angles around the optical axis virtually eliminates this shadow artifact. The objective-based TIR configuration that uses an arc lamp for illumination system automatically provides such a hollow cone. A hollow cone can also be produced from a laser beam by positioning a conical lens in the incident beam path exactly concentric with the laser beam, in a similar fashion as already described for arc illumination (Stout and Axelrod, 1989).

Illumination by two mutually coherent TIR laser beams produces a striped interference fringe pattern in the evanescent field intensity in the sample plane. For a relative azimuthal angle of φ between the two beams, both with an incidence angle of θ, the node-to-node spacing s of the fringes is given by:

$$s = \frac{\lambda_0}{2n_3 \sin\theta \sin(\varphi/2)} \tag{14}$$

The spacing s is not dependent on the refractive index n_1 of the medium (or cell). For beams coming from opposite azimuthal directions ($\varphi = \pi$), $s = \lambda_o/2$ at the critical angle of incidence and $s = \lambda_o/2n_3$ at glancing incidence ($\theta = \pi/2$). For a typical glass substrate with $n_3 = 1.5$, this latter spacing is smaller than the Raleigh resolution limit of the microscope and can barely be discerned by the imaging system although the fringes do exist physically at full contrast.

These interference stripes can be used in combination with TIR-FRAP (see above) to bleach antinode regions but not node regions. The subsequent

fluorescence recovery will then provide information about surface diffusion of fluorophores.

The spatial phase of the node/antinode intensity stripe pattern can be controlled easily by retarding the phase of one of the interfering beams with an extra glass plate inserted into its light path. By illuminating with four discrete coherent TIR beams at relative azimuthal angles of $\varphi = 0$, $\pi/2$, π, and $3\pi/2$, a checkerboard evanescent pattern in both the x and y lateral directions (i.e., the sample plane) can be produced. Then by imaging a sample at lateral node/antinode spatial phase steps of 0°, 120°, and 240°, images with super-resolution well below the Raleigh resolution limit in the sample plane can be computed. Such "structured illumination" by stripes or checkerboard can be produced in standard epi-illumination with a grid at the FDP. But with interfering-beam TIRF, the spacing of the stripes can be made smaller and thereby produce unprecedented lateral resolution, down to about 0.13 μm for 514 nm wavelength illumination (Cragg and So, 2000; Gustafsson, 2005; Gustafsson *et al*., 2000; Lagerholm *et al*., 2003; Neil *et al*., 1997).

In general, incident light approaching the interface from a single angle cannot produce a small illumination region. For this goal, converging illumination from a large range of angles is needed. However, the angular range must not include subcritical polar angles in order to preserve TIR. A system called "confocal TIR" utilizes a range of polar incidence angles (Ruckstuhl and Seeger, 2003, 2004). To ensure that these polar angles are confined to the supercritical range, an opaque disk installed into a custom-made parabolic glass reflection objective blocks subcritical rays. In that system, only high polar angle emitted light can pass that opaque disk, but the fluorescence rays that do so are focused onto a small pinhole, behind which resides a nonimaging detector (as in standard confocal systems). An image is constructed by scanning the sample. The advantage of this system is that only a very small volume is illuminated at one time, and the effective lateral resolution appears at least as good as standard epi-imaging. It is likely that this sort of ring illumination could also be produced through a commercially available high-aperture objective by placing the opaque disk farther "upstream" at an aperture plane and thereby avoid blocking any emitted rays.

F. Rapid Chopping Between TIR and EPI

Regardless of the method chosen to produce TIR in a microscope, it is often desirable to switch rapidly between illumination of the surface (by TIR) and deeper illumination of the bulk (by standard epifluorescence). For example, a transient process may involve simultaneous but somewhat different fluorescence changes in both the submembrane and the cytoplasm, and both must be followed on the same cell in response to some stimulus (Omann and Axelrod, 1996). For spatially resolved images, beam switching itself can be done rapidly by acousto-optic modulators; the overall switching rate in practice is often limited by the readout speed of the digital camera or by photon shot noise. Single channel integrated

intensity readings over a region defined by an image plane diaphragm can be performed much more rapidly.

VI. General Experimental Considerations

A. Laser Source

A laser with a total visible output in the 100 mW or greater range is more than adequate for most TIRF applications. Air-cooled argon or diode lasers in the 10–100 mW (the types generally provided in commercial TIRF systems) are also usually adequate, but possibly marginal for dim samples or for samples where a weaker laser line (e.g., the 457 nm line of argon) may be desired to excite a shorter wavelength fluorescent marker (such as cyan fluorescent protein).

B. Laser Interference Fringes

Laser illumination can produce annoying interference fringes because optical imperfections in the beam path can shift the local phase of coherent light. For critical applications, several approaches can alleviate the problem. One approach employs an optical fiber bundle in which individual fiber-to-fiber length differences exceed the laser light's coherence length. This produces an extended source at the output tip with point-to-point relative phases that are temporally randomized and defocused on the sample (Inoue *et al*., 2001). This elegant system, with no moving parts, produces a speckle pattern that changes so rapidly that it appears uniform down to the nanosecond timescale. Commercially available mode scramblers and rapid flexing of optical fibers may also reduce some fringing.

Another set of methods uses a free laser beam rather than fibers. For example, a finely frosted glass surface or a plastic plate (such as tissue culture dish bottom), spinning laterally to the laser beam, temporally randomizes the phase and produces a fringe pattern that fluctuates and can be averaged over the duration of a camera exposure (Kuhn and Pollard, 2005).

Interference fringes can be effectively suppressed by spinning the azimuthal angle of TIR incidence with electro-optical or mechano-optical devices such that the incident beam traces a circle where it focuses at the objective's BFP. Since only one azimuthal direction illuminates the sample at any instant but the spinning period is much shorter than the camera's exposure time or retinal image retention time, the interference fringes are superimposed in their intensities (rather than in their electric fields), giving the illusion of a much more uniform illumination field (Mattheyses *et al*., 2006). An example of the fringe suppression effect is shown in Fig. 11.

An alternative nonoptical approach to suppressing fringes computes a normalization of sample digital images against a control digital image of a uniform concentration of fluorophores. This works well only if the fringes were not induced by the sample itself.

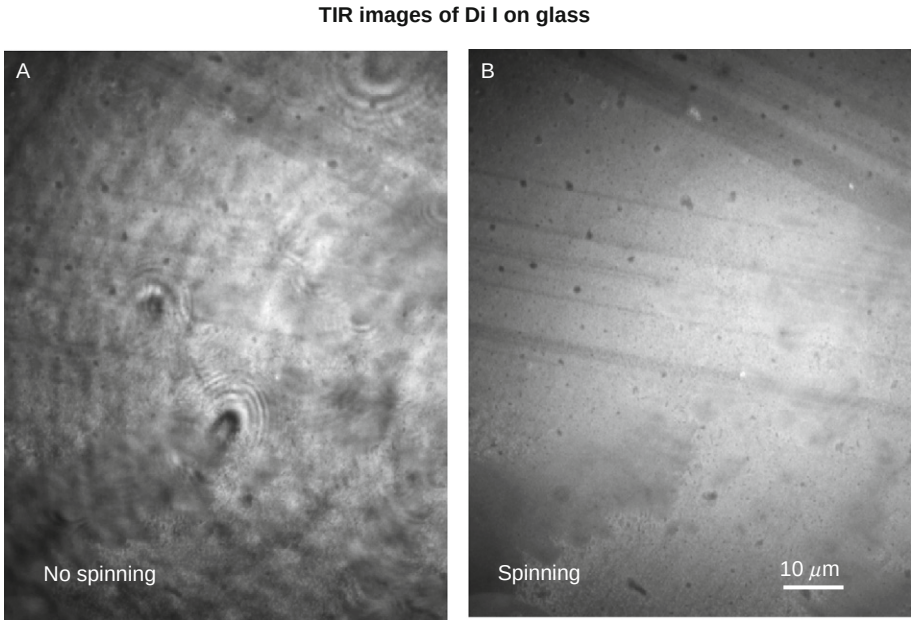

Fig. 11 Effect of azimuthal spinning on TIRF images of diI adsorbed to a glass coverslip. The spinning effect was produced by a rapidly rotating optical wedge in the laser beam. (A) Sample illuminated with a single azimuthal incidence angle, that is, wedge not spinning. Interference fringes are very evident. (B) Same field of view with wedge spinning. The laser interference fringes are no longer visible. The remaining nonuniformities are due to features of the sample and also the fading of illumination intensity toward the corners.

C. Functionalized Substrates

TIRF experiments often involve specially coated substrates. A glass surface can be chemically derivatized to yield special physi- or chemiabsorptive properties. Covalent attachment of certain specific chemicals is particularly useful in cell biology and biophysics, including poly-L-lysine for enhanced adherence of cells; hydrocarbon chains for hydrophobicizing the surface in preparation for lipid monolayer adsorption; and antibodies, antigens, or lectins for producing specific reactivities. Derivatization generally involves pretreatment of the glass by an organosilane (Fulbright and Axelrod, 1993). Aluminum coating (for surface fluorescence quenching) can be accomplished in a standard vacuum evaporator; the amount of deposition can be made reproducible by completely evaporating a premeasured constant amount of aluminum. After deposition, the upper surface of the aluminum film spontaneously oxidizes in air very rapidly. This aluminum oxide layer appears to have some similar chemical properties to the silicon dioxide of a glass surface; it can be derivatized by organosilanes in much the same manner.

A planar phospholipid coating (possibly with incorporated proteins) on glass can be used as a model of a biological membrane. Methods for preparing such model membranes on planar surfaces suitable for TIR have been reviewed by Thompson *et al.* (1993).

D. Photochemistry at the Surface

Illumination of surface-adsorbed proteins can lead to apparent photochemically induced cross-linking. This effect is observed as a slow, continual, illumination-dependent increase in the observed fluorescence. It can be inhibited by deoxygenation (aided by the use of an O_2-consuming enzyme/substrate system such as protocatachuic deoxygenase/protocatachuic acid or a glucose/glucose oxidase system) or by 0.05 M cysteamine (Fulbright and Axelrod, 1993).

E. Actual Evanescent Field Depth and Profile

The evanescent field characteristic depth in an actual sample may deviate from that predicted by Eq. (4), even if the incidence angle θ is well measured, for several reasons. Depth d depends on the refractive index of the liquid sample above the TIR surface, and this is not well known for samples such as cell cytoplasm. So far, no good way of accurately measuring the local evanescent field depth and profile in an actual heterogeneous sample has been proposed.

Measurements of evanescent depth in a homogeneous artificial sample with a refractive index that approximated the average in a heterogeneous sample can be done. In such a sample, the characteristic time for diffusion of fluorescent beads through the evanescent field (possibly by TIR/FRAP or TIR/FCS) can be measured and converted to a corresponding characteristic distance (given a known diffusion coefficient). However, this method gives only a single number for effective depth but does not provide unambiguous information about the possibly nonexponential intensity profile as a function of z.

In samples with heterogeneous refractive index, regions with higher index may not support TIR, whereas lower index regions do. Clearly, it is best to illuminate with as high an incidence angle as possible to be sure that all regions support TIR. Even if the incidence angle is sufficiently high to support TIR everywhere, irregularities and heterogeneities in the sample give rise to scattering of the evanescent field. This scattered light can excite fluorescence as it penetrates much more deeply into the liquid than does the evanescent light. Figure 12 shows an example of this effect, with glass beads in an aqueous fluorescein solution, under TIR illumination. The beads capture evanescent light and focus it into bright propagating light "comets" on the downbeam side of the beads' equatorial planes, as can be visualized by the higher fluorescence in those regions. The effect is much less pronounced for higher TIR incidence angles.

The TIR optics themselves, particularly the high-aperture objectives used in objective-based illumination, can produce scattered light. Actual intensity profiles

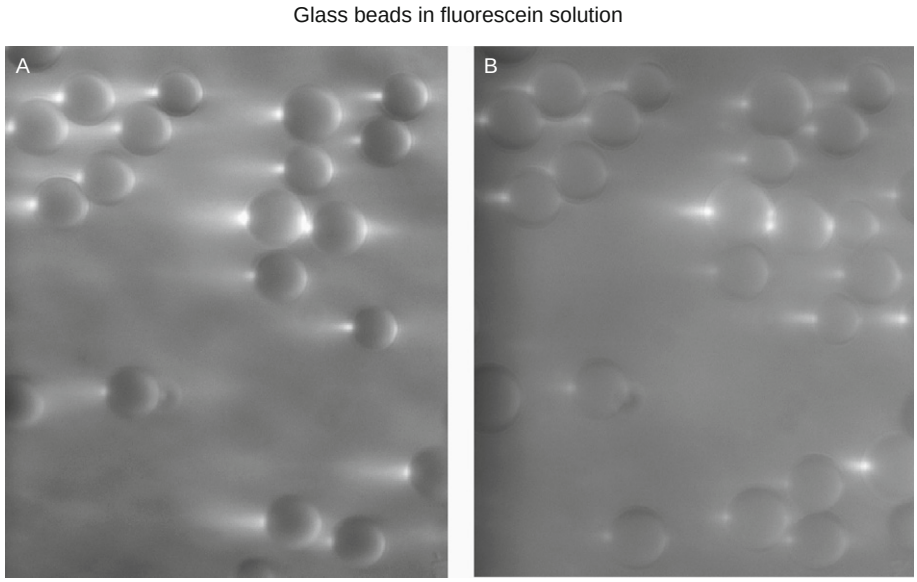

Fig. 12 Effect of increasing incidence angle on evanescent field scattering. High n (=1.5) beads of 10 μm diameter are settled onto the TIR surface in an aqueous medium containing fluorescein. (A) The incidence angle is about 1° greater than the critical angle. The beads clearly convert some of the local evanescent field into propagating light, creating beacons and shadows immediately "downstream." (B) These effects are reduced with a thinner evanescent field created by an incidence angles several degrees higher. In both images, the microscopic focus is at the bead equatorial plane, not at the TIR surface.

arising from objective-based TIR can be obtained by at least a couple of methods. In one method, a quantum dot can be attached to the tip of an AFM cantilever probe mounted onto a z-translator. In this way, intensity can be measured directly as a function of the quantum dot z-position (Sarkar *et al.*, 2004). One problem with this approach (aside from the necessity of using AFM equipment) is that the probe and quantum dot themselves can disrupt the evanescent field and produce scattering.

Another approach is to observe a large (~8 μm diameter) spherical bead with a refractive index matched to the surrounding liquid to avoid disruption and scattering. The bead can be fluorescence-labeled on its surface. At the image of the point of contact between the bead and the TIR substrate, the fluorescence is the brightest. It becomes dimmer with increasing distance in the TIR plane from the contact point. Simple geometry then allows calculation of the fluorescence versus z. In an actual test of this method in 1.45NA and 1.65NA objective-based TIRF (Mattheyses and Axelrod, 2005b), the evanescent field was found to account for about 90% of the intensity at $z = 0$, and the exponential decay depth agreed well with expectations based on angle and refractive indices. However, a much slower

decaying component, presumably from scattering within the objective, was also evident, and this component became dominant in the distant $z > 2d$ zone.

Apart from this dim scattering component, bright collimated shafts of scattered light, emanating from the edge of the top lens of the objective, can be seen in objective-based TIR. Fortunately, however, these shafts do not cross the field of view so they do not excite spurious fluorescence in the image.

VII. Summary: TIRF Versus Other Optical Section Microscopies

TIRF is only one of several optical sectioning techniques enjoying wide use in microscopy including confocal, multiphoton, and interference reflection contract microscopies. Each has particular distinct advantages and drawbacks.

Confocal microscopy achieves axial selectivity by exclusion of out-of-focus emitted light with a set of image plane pinholes. Confocal microscopy has the clear advantage in versatility; its method of optical sectioning works at any plane of the sample, not just at an interface between dissimilar refractive indices. However, other differences exist that, in some special applications, can favor the use of TIRF.

- The depth of the optical section in TIRF is typically ≤ 0.1 μm whereas in confocal microscopy, it is a relatively thick ~ 0.6 μm.
- In some applications (e.g., FRAP, FCS, or on cells whose viability is damaged by light), illumination and not just detected emission is best restricted to a thin section; this is not possible with standard confocal.
- Since TIRF can be adapted to and made interchangeable with existing standard microscope optics, even with "homemade" components, it is much less expensive than confocal microscopy. Laser-based and arc-based TIRF microscopy kits are now available from most of the major microscope manufacturers and third-party suppliers.
- Unlike confocal microscopy, TIRF is suitable not only for microscopic samples but also for macroscopic applications; in fact, those were the first TIRF studies. An older review covers much of that early work (Axelrod *et al.*, 1992).

Two-photon (or more generally, multiphoton) microcopy has many desirable features, including true optical sectioning, whereby the plane of interest is the only one that is actually excited, as in TIRF. Multiphoton microscopy is not restricted to the proximity of an interface, but its optical section depth is still several times thicker than that of TIRF. The setup expense of multiphoton microscopy for an infrared laser with sufficient pulse peak intensity can also be a consideration. Both multiphoton and confocal microscopies are necessarily scanning techniques; TIRF microscopy is a "wide-field" technique and is thereby not limited in speed by the scanning system hardware or image reconstruction software.

Cell–substrate contacts can be located by a nonfluorescence technique completely distinct from TIRF, known as IRC microscopy. Using conventional illumination sources, IRM visualizes cell–substrate contacts as dark regions. Internal reflection microscopy has the advantage that it does not require the cells to be labeled, but the disadvantages that it contains no information of biochemical specificities in the contact regions and that it is less sensitive to changes in contact distance (relative to TIRF) within the critical first 100 nm of the surface.

Acknowledgments

This work was supported by NIH grant 5 R01 NS38129. The author wishes to thank Drs. Ron Holz and Edwin Levitan for the chromaffin cells and the GFP construct, respectively, depicted in Fig. 1, and Dr. Geneva Omann for reviewing a draft of this chapter. The author also thanks all the coworkers who have contributed to aspects of the TIRF work described here: Ron Holz, Thomas Burghardt, Nancy Thompson, Edward Hellen, Ariane Mc Kiernan, Andrea Stout, Michelle Dong Wang, Robert Fulbright, Laura Johns, Susan Sund, Miriam Allersma, Mary Bittner, Alexa Mattheyses, Keith Shaw, and Geneva Omann.

References

Abney, J. R., Scalettar, B. A., and Thompson, N. L. (1992). Evanescent interference patterns for fluorescence microscopy. *Biophys. J.* **61,** 542–552.

Ada-Nguema, A. S., Xenias, H., Sheetz, M. P., and Keely, P. J. (2006). The small GTPase R-Ras regulates organization of actin and drives membrane protusions through the activity of PLC epsilon. *J. Cell Sci.* **119,** 1307–1319.

Adams, M. C., Matov, A., Yarar, D., Gupton, S. L., Danuser, G., and Waterman-Storer, C. M. (2004). Signal analysis of total internal reflection fluorescent speckle microscopy (TIR-FSM) and wide-field epi-fluorescence FSM of the actin cytoskeleton and focal adhesions in living cells. *J. Microsc.* **216,** 138–152.

Allersma, M. W., Bittner, M. A., Axelrod, D., and Holz, R. W. (2006). Motion matters: Secretory granule motion adjacent to the plasma membrane and exocytosis. *Mol. Biol. Cell* **17,** 2424–2438.

Allersma, M. W., Wang, L., Axelrod, D., and Holz, R. W. (2004). Visualization of regulated exocytosis with a granule-membrane probe using total internal reflection microscopy. *Mol. Biol. Cell* **15,** 4658–4668.

Ambrose, E. J. (1961). The movement of fibrocytes. *Exp. Cell Res.* **8**(Suppl. 1), 54–73.

Axelrod, D. (1979). Carbocyanine dye orientation in red cell membrane studied by microscopic fluorescence polarization. *Biophys. J.* **26,** 557–574.

Axelrod, D. (1981). Cell surface contacts illuminated by total internal reflection fluorescence. *J. Cell Biol.* **89,** 141–145.

Axelrod, D. (2001). Selective imaging of surface fluorescence with very high aperture microscope objectives. *J. Biomed. Opt.* **6,** 6–13.

Axelrod, D. (2003). Total internal reflection fluorescence microscopy in cell biology. "Biophotonics, Part B," *Methods Enzymol.* **361,** 1–33.

Axelrod, D. (2007). Total internal reflection fluorescence microscopy. *In* "Optical Imaging and Microscopy: Techniques and Advanced Systems, Springer Series in Optical Sciences" (P. Török, and F.-J. Kao, eds.), 2nd edn. pp. 195–236. Springer-Verlag, Berlin, Heidelberg.

Axelrod, D., and Omann, G. M. (2006). Combinatorial microscopy. *Nat. Rev. Mol. Cell Biol.* **7,** 944–952.

Banerjee, A., and Kihm, K. D. (2005). Experimental verification of near-wall hindered diffusion for the Brownian motion of nanoparticles using evanescent wave microscopy. *Phys. E Rev*. **72,** 042101.

Barr, V. A., Balagopalan, L., Barda-Saas, M., Polishuk, R., Boukari, H., Bunnell, S. C., Bernot, K. M., Toda, Y., Nossal, R., and Samelson, L. E. (2006). T-cell antigen receptor-induced signaling complexes: Internalization via a cholesterol-dependent endocytic pathway. *Traffi* **7,** 1143–1162.

Beaumont, V., Llobet, A., and Lagnado, L. (2005). Expansion of calcium microdomains regulates fast exocytosis at a ribbon synapse. *Proc. Natl. Acad. Sci. USA* **102,** 10700–10705.

Bike, S. G. (2000). Measuring colloidal forces using evanescent wave scattering. *Curr. Opin. Colloid Interface Sci.* **5,** 144–150.

Blumberg, S., Gajraj, A., Pennington, M. W., and Meiners, J. C. (2005). Three-dimensional characterization of tethered microspheres by total internal reflection fluorescence microscopy. *Biophys. J.* **89,** 1272–1281.

Boldt, F. M., Heinze, J., Diez, M., Petersen, J., and Borsch, M. (2004). Real-time pH microscopy down to the molecular level by combined scanning electrochemical microscopy/single-molecule fluorescence spectroscopy. *Anal. Chem.* **76,** 3473–3481.

Borejdo, J., Talent, J., and Akopova, I. (2006). Measuring rotations of a few cross-bridges in skeletal muscle. *Exp. Biol. Med.* **231,** 23–38.

Borejdo, J., Talent, J., Akopova, I., and Burghardt, T. P. (2006). Rotations of a few cross bridges in muscle by confocal total internal reflection microscopy. *Biochim. Biophys. Acta Mol. Cell Res.* **1763,** 137–140.

Bowser, D. N., and Khakh, B. S. (2007). Two forms of single-vesicle astrocyte exocytosis imaged with total internal reflection fluorescence microscopy. *Proc. Natl. Acad. Sci. USA* **104,** 4212–4217.

Burghardt, T. P., and Axelrod, D. (1981). Total internal reflection/fluorescence photobleaching recovery study of serum albumin adsorption dynamics. *Biophys. J.* **33,** 455–468.

Burghardt, T. P., Charlesworth, J. E., Halstead, M. F., Tarara, J. E., and Ajtai, K. (2006). *In situ* fluorescent protein imaging with metal film-enhanced total internal reflection microscopy. *Biophys. J.* **90,** 4662–4671.

Burghardt, T. P., and Thompson, N. L. (1984). Effect of planar dielectric interfaces on fluorescence emission and detection. Evanescent excitation with high-aperture collection. *Biophys. J.* **46,** 729–737.

Carniglia, C. K., Mandel, L., and Drexhage, K. H. (1972). Absorption and emission of evanescent photons. *J. Opt. Soc. Am.* **62,** 479–486.

Chang, P. S., Axelrod, D., Omann, G. M., and Linderman, J. J. (2005). G-protein threshold behavior in the human neutrophil oxidant response: Measurement of G-proteins available for signaling in responding and non-responding subpopulations. *Cell. Signal.* **17,** 605–614.

Chon, J. W. M., and Gu, M. (2004). Scanning total internal reflection fluorescence microscopy under one-photon and two-photon excitation: Image formation. *Appl. Optics* **43,** 1063–1071.

Cohen, M., Kam, Z., Addadi, L., and Geiger, B. (2006). Dynamic study of the transition from hyaluronan- to integrin-mediated adhesion in chondrocytes. *EMBO J*. **25,** 302–311.

Cragg, G. E., and So, P. T. C. (2000). Lateral resolution enhancement with standing evanescent waves. *Opt. Lett*. **25,** 46–48.

Czeslik, C., Royer, C., Hazlett, T., and Mantulin, W. (2003). Reorientational dynamics of enzymes adsorbed on quartz: A temperature-dependent time-resolved TIRF anisotropy study. *Biophys. J.* **84,** 2533–2541.

Demuro, A., and Parker, I. (2004). Imaging the activity and localization of single voltage-gated Ca2+ channels by total internal reflection fluorescence microscopy. *Biophys. J.* **86,** 3250–3259.

Dickson, R. M., Norris, D. J., and Moerner, W. E. (1998). Simultaneous imaging of individual molecules aligned both parallel and perpendicular to the optic axis. *Phys. Rev. Lett.* **81,** 5322–5325.

Dickson, R. M., Norris, D. J., Tzeng, Y.-L., and Moerner, W. E. (1996). Three-dimensional imaging of single molecules solvated in pores of poly(acrylamide) gels. *Science* **274,** 966–969.

Fix, M., Melia, T. J., Jaiswal, J. K., Rappoport, J. Z., You, D. Q., Sollner, T. H., Rothman, J. E., and Simon, S. M. (2004). Imaging single membrane fusion events mediated by SNARE proteins. *Proc. Natl. Acad. Sci. USA* **101,** 7311–7316.

Forkey, J. N., Quinlan, M. E., and Goldman, Y. E. (2005). Measurement of single macromolecule orientation by total internal reflection fluorescence polarization microscopy. *Biophys. J.* **89,** 1261–1271.

Fulbright, R. M., and Axelrod, D. (1993). Dynamics of nonspecific adsorption of insulin to erythrocyte membrane. *J. Fluoresc.* **3,** 1–16.

Gavutis, M., Lata, S., Lamken, P., Muller, P., and Piehler, J. (2005). Lateral ligand-receptor interactions on membranes probed by simultaneous fluorescence-interference detection. *Biophys. J.* **88,** 4289–4302.

Gilmanshin, R., Creutz, C. E., and Tamm, L. K. (1994). Annexin IV reduces the rate of lateral lipid diffusion and changes the fluid phase structure of the lipid bilayer when it binds to negatively charged membranes in the presence of calcium. *Biochemistry* **33,** 8225–8832.

Gingell, D., Heavens, O. S., and Mellor, J. S. (1987). General electromagnetic theory of internal reflection fluorescence: The quantitative basis for mapping cell-substratum topography. *J. Cell Sci.* **87,** 677–693.

Gonzalez, E., and McGraw, T. E. (2006). Insulin signalling diverges into Akt-dependent and -independent signals to regulate the recruitment/docking and the fusion of GLUT4 vesicles to the plasma membrane. *Mol. Biol. Cell* **17,** 4484–4493.

Graneli, A., Yeykal, C. C., Prasad, T. K., and Greene, E. C. (2006). Organized arrays of individual DIVA molecules tethered to supported lipid bilayers. *Langmuir* **22,** 292–299.

Gustafsson, M. G. L., Agard, D. A., and Sedat, J. W. (2000). Doubling the lateral resolution of wide-field fluorescence microscopy using structured illumination. *In* ''Three-Dimensional and Multidimensional Microscopy: Image Acquisition Processing VII''. (J.-A. Jose-Angel Conchello, C. J. Cogswell, and T. Wilson, eds.), Proc SPIE **3919** pp. 141–150.

Gustafsson, M. G. L. (2005). Nonlinear structured-illumination microscopy: Wide-field fluorescence imaging with theoretically unlimited resolution. *Proc. Natl. Acad. Sci. USA* **102,** 13081–13086.

Ha, T. J., Ting, A. Y., Liang, J., Caldwell, W. B., Deniz, A. A., Chemla, D. S., Schultz, P. G., and Weiss, S. (1999). Single-molecule fluorescence spectroscopy of enzyme conformational dynamics and cleavage mechanism. *Proc. Natl. Acad. Sci. USA* **96,** 893–898.

Hadjidemetriou, S., Toomre, D., and Duncan, J. S. (2005). Segmentation and 3D reconstruction of microtubules in total internal reflection fluorescence microscopy (TIRFM). *Medical Image Computing and Computer-Assisted Intervention, Lecture Notes in Computer Science* **3749,** 761–769.

Han, W., Ng, Y.-K., Axelrod, D., and Levitan, E. S. (1999). Neuropeptide release by efficient recruitment of diffusing cytoplasmic secretory vesicles. *Proc. Natl. Acad. Sci. USA* **96,** 14577–14582.

Harrick, N. J. (1967). ''Internal Reflection Spectroscopy''. Wiley Interscience, New York.

Harrick, N. J., and Loeb, G. I. (1973). Multiple internal reflection fluorescence spectroscopy. *Anal. Chem.* **45,** 687–691.

Hashimoto, F., Tsukahara, S., and Watarai, H. (2003). Lateral diffusion dynamics for single molecules of fluorescent cyanine dye at the free and surfactant-modifted dodecane-water interface. *Langmuir* **19,** 4197–4204.

Hassler, K., Anhut, T., Rigler, R., Gosch, M., and Lasser, T. (2005a). High count rates with total internal reflection fluorescence correlation spectroscopy. *Biophys. J.* **88,** L1–L3.

Hassler, K., Leutenegger, M., Rigler, P., Rao, R., Rigler, R., Gosch, M., and Lasser, T. (2005b). Total internal reflection fluorescence correlation spectroscopy (TIR-FCS) with low background and high count-rate per molecule. *Opt. Express* **13,** 7415–7423.

He, Y., Li, H. W., and Yeung, E. S. (2005). Motion of single DNA molecules at a liquid-solid interface as revealed by variable-angle evanescent-field microscopy. *J. Phys. Chem. B* **109,** 8820–8832.

Hellen, E. H., and Axelrod, D. (1987). Fluorescence emission at dielectric and metal-film interfaces. *J. Opt. Soc. Am. B* **4,** 337–350.

Hellen, E. H., and Axelrod, D. (1991). Kinetics of epidermal growth factor/receptor binding on cells measured by total internal reflection/fluorescence recovery after photobleaching. *J. Fluoresc.* **1,** 113–128.

Hellen, E. H., Fulbright, R. M., and Axelrod, D. (1988). Total internal reflection fluorescence: Theory and applications at biosurfaces. *In* "Spectroscopic Membrane Probes" (L. Loew, ed.), pp. 47–79. CRC Press, Boca Raton.

Hinterdorfer, P., Baber, G., and Tamm, L. K. (1994). Reconstitution of membrane fusion sites. A total internal reflection fluorescence microscopy study of influenza hemagglutinin-mediated membrane fusion. *J. Biol. Chem.* **269,** 20360–20368.

Hirschfeld, T. (1965). Total reflection fluorescence (TRF). *Can. Spectrosc.* **10,** 128.

Holz, R. W. (2006). Analysis of the late steps of exocytosis: Biochemical and total internal reflection fluorescence microscopy (TIRFM) studies. *Cell. Mol. Neurobiol.* **26,** 439–447.

Hoshino, A., Fujioka, K., Manabe, N., Yamaya, S., Goto, Y., Yasuhara, M., and Yamamoto, K. (2005). Simultaneous multicolor detection system of the single-molecular microbial antigen with total internal reflection fluorescence microscopy. *Microbiol. Immunol.* **49,** 461–470.

Huang, Z. P., and Thompson, N. L. (1993). Theory for 2-photon excitation in pattern photobleaching with evanescent illumination. *Biophys. Chem.* **47,** 241–249.

Ichinose, J., and Sako, Y. (2004). Single-molecule measurement in living cells. *Trends Anal. Chem.* **23,** 587–594.

Inoue, S., Knudson, R. A., Goda, M., Suzuki, K., Nagano, C., Okada, N., Takahashi, H., Ichie, K., Iida, M., and Yamanak, K. (2001). Centrifuge polarizing microscope. I. Rationale, design and instrument performance. *J. Microsc.* **201,** 341–356.

Ishizaka, S., Ueda, Y., and Kitamura, N. (2004). Time-resolved total internal reflection fluorescence study on hybridization of complementary single-stranded DNAs at a water/oil interface. *Anal. Chem.* **76,** 5075–5079.

Jaiswal, J. K., Chakrabarti, S., Andrews, N. W., and Simon, S. M. (2004). Synaptotagmin VII restricts fusion pore expansion during lysosomal exocytosis. *PLOS Biol.* **2,** 1224–1232.

Jaiswal, J. K., and Simon, S. M. (2007). Imaging single events at the cell membrane. *Nat. Chem. Biol.* **3,** 92–98.

Jennissen, H. P., and Zumbrink, T. (2004). A novel nanolayer biosensor principle. *Biosens. Biolectron.* **19,** 987–997.

Johns, L. M., Levitan, E. S., Shelden, E. A., Holz, R. W., and Axelrod, D. (2001). Restriction of secretory granule motion near the plasma membrane of chromaffin cells. *J. Cell Biol.* **153,** 177–190.

Joos, U., Biskup, T., Ernst, O., Westphal, I., Gherasim, C., Schmidt, R., Edinger, K., Pilarczyk, G., and Duschl, C. (2006). Investigation of cell adhesion to structured surfaces using total internal reflection fluorescence and confocal laser scanning microscopy. *Eur. J. Cell Biol.* **85,** 225–228.

Kalb, E., Engel, J., and Tamm, L. K. (1990). Binding of proteins to specific target sites in membranes measured by total internal reflection fluorescence microscopy. *Biochemistry* **29,** 1607–1613.

Kellermayer, M. S. Z., Karsai, A., Kengyel, A., Nagy, A., Bianco, P., Huber, T., Kulcsar, A., Niedetzky, C., Proksch, R., and Grama, L. (2006). Spatially and temporally synchronized atomic force and total internal reflection fluorescence microscopy for imaging and manipulating cells and biomolecules. *Biophys. J.* **91,** 2665–2677.

Kihm, K. D., Banerjee, A., Choi, C. K., and Takagi, T. (2004). Near-wall hindered Brownian diffusion of nanoparticles examined by three-dimensional ratiometric total internal reflection fluorescence microscopy (3-D R-TIRFM). *Exp. Fluids* **37,** 811–824.

Kim, K., McCully, M. E., Bhattacharya, N., Butler, B., Sept, D., and Cooper, J. A. (2007). Structure/function analysis of the interaction of phosphatidylinositol 4,5-bisphosphate with actibn-capping protein—implications for how capping protein binds the actin filament. *J. Biol. Chem.* **282,** 5871–5879.

Knight, A. E., and Molloy, J. E. (2000). Muscle, myosin and single molecules. *In* "Molecular Motors, Essays in Biochemistry" (S. J. Higgins, and G. Banting, eds.), Vol. 35, p. 200. Portland Press, London.

Khakh, B. S., Fisher, J. A., Nashmi, R., Bowser, D. N., and Lester, H. A. (2005). An angstrom scale interaction between plasma membrane ATP-gated P2X(2) and alpha(4)beta(2) nicotinic channels

measured with fluorescence resonance energy transfer and total internal reflection fluorescence microscopy. *J. Neurosci.* **25,** 6911–6920.

Khan, S., Pierce, D., and Vale, R. D. (2000). Interactions of the chemotaxis signal protein CheY with bacterial flagellar motors visualized by evanescent wave microscopy. *Curr. Biol.* **10,** 927–930.

Kobitski, A. Y., Heyes, C. D., and Nienhaus, G. U. (2004). Total internal reflection fluorescence microscopy—a powerful tool to study single quantum dots. *Appl. Surf. Sci.* **234,** 86–92.

Kochubey, O., Majumdar, A., and Klingauf, J. (2006). Imaging clathrin dynamics in *Drosophila melanogaster* hemocytes reveals a role for actin in vesicle fusion. *Traffic* **7,** 1614–1627.

Kovar, D. R., Harris, E. S., Mahaffy, R., Higgs, H. N., and Pollard, T. D. (2006). Control of the assembly of ATP- and ADP-actin by formins and profilin. *Cell* **124,** 423–435.

Kozuka, J., Yokota, H., Arai, Y., Ishii, Y., and Yanagida, T. (2006). Dynamic polymorphism of single actin molecules in the actin filament. *Nat. Chem. Biol.* **2,** 83–86.

Kronick, M. N., and Little, W. A. (1975). A new immunoassay based on fluorescence excitation by internal reflection spectroscopy. *J. Immunol. Methods* **8,** 235–240.

Kuhn, J. R., and Pollard, T. D. (2005). Real-time measurements of actin filament polymerization by total internal reflection fluorescence microscopy. *Biophys. J.* **88,** 1387–1402.

Lagerholm, B. C., Starr, T. E., Volovyk, Z. N., and Thompson, N.L (2000). Rebinding of IgE Fabs at haptenated planar membranes: Measurement by total internal reflection with fluorescence photobleaching recovery. *Biochemistry* **39,** 2042–2051.

Lagerholm, B. C., Vanni, S., Taylor, D. L., and Lanni, F. (2003). Cytomechanics applications of optical sectioning microscopy. *Methods Enzymol.* **361,** 175–197.

Lakowicz, J. R. (2005). Radiative decay engineering 5: Metal-enhanced fluorescence and plasmon emission. *Anal. Biochem.* **337,** 171–194.

Lang, T., Bruns, D., Wenzel, D., Riedel, D., Holroyd, P., Thiel, C., and Jahn, R. (2001). SNAREs are concentrated in cholesterol-dependent clusters that define docking and fusion sites for exocytosis. *EMBO J.* **20,** 2202–2213.

Lang, T., Wacker, I., Steyer, J., Kaether, C., Wunderlich, I., Soldati, T., Gerdes, H.-H., and Almers, W. (1997). Ca2+-triggered peptide secretion neurotechnique in single cells imaged with green fluorescent protein and evanescent-wave microscopy. *Neuron* **18,** 857–863.

Lang, T., Wacker, I., Wunderlich, I., Rohrbach, A., Giese, G., Soldati, T., and Almers, W. (2000). Role of actin cortex in the subplasmalemmal transport of secretory granules in PC-12 cells. *Biophys. J.* **78,** 2863–2877.

Lieb, M. A., Zavislan, J. M., and Novotny, L. (2004). Single-molecule orientations determined by direct emission pattern imaging. *J. Opt. Soc. Am. B* **21,** 1210–1215.

Loerke, D., Preitz, B., Stuhmer, W., Oheim, M., and Biomed, J. (2000). Super-resolution measurements with evanescent-wave fluorescence excitation using variable beam incidence. *Optics* **5,** 23–30.

Loerke, D., Stuhmer, W., and Oheim, M. (2002). Quantifying axial secretory-granule motion with variable-angle evanescent-field excitation. *J. Neurosci. Methods* **119,** 65–73.

Mahaffey, R. E., and Pollard, T. D. (2006). Kinetics of the formation and dissociation of actin filament branches mediated by Arp2/3 complex. *Biophys. J.* **91,** 3519–3528.

Manneville, J. B. (2006). Use of TIRF microscopy to visualize actin and microtubules in migrating cells. *Methods Enzymol.* **406,** 520–532.

Mashanov, G. I., and Malloy, J. E. (2007). Automatic detection of single fluorophores in live cells. *Biophys. J.* **92,** 2199–2211.

Mathur, A. B., Truskey, G. A., and Reichert, W. M. (2000). Atomic force and total internal reflection fluorescence microscopy for the study of force transmission in endothelial cells. *Biophys. J.* **78,** 1725–1735.

Mattheyses, A. L., and Axelrod, D. (2005a). Fluorescence emission patterns near glass and metal-coated surfaces investigated with back focal plane imaging. *J. Biomed. Opt.* **10,** 054007/1–6.

Mattheyses, A. L., and Axelrod, D. (2005b). Direct measurement of evanescent field profile and depth in TIRF microscopy. *J. Biomed. Opt.* **11,** 014006/1–7.

Mattheyses, A. L., Shaw, K. D., and Axelrod, D. (2006). Effective elimination of laser interference fringing in fluorescence microscopy by spinning azimuthal incidence angle. *Microsc. Res. Tech.* **69,** 642–647.

Matveeva, E., Gryczynski, Z., Malicka, J., Gryczynski, I., and Lakowicz, J. R. (2004). Metal-enhanced fluorescence immunoassays using total internal reflection and silver island-coated surfaces. *Anal. Biochem.* **334,** 303–311.

McCain, K. S., and Harris, J. M. (2003). Total internal reflection fluorescence-correlation spectroscopy study of molecular transport in thin sol-gel films. *Anal. Chem.* **75,** 3616–3624.

McCain, K. S., Schluesche, P., and Harris, J. M. (2004). Modifying the adsorption behavior of polyamidoamine dendrimers at silica surfaces investigated by total internal reflection fluorescence correlation spectroscopy. *Anal. Chem.* **76,** 930–938.

McKiernan, A. M., MacDonald, R. C., MacDonald, R. I., and Axelrod, D. (1997). Cytoskeletal protein binding kinetics at planar phospholipid membranes. *Biophys. J.* **73,** 1987–1998.

Mei, E., Sharonov, A. J., Ferris, H., and Hochstrasser, R. M. (2005). Direct visualization of nanopatterns by single-molecule imaging. *Appl. Phys. Lett.* **86,** 043102.

Mertz, J. (2000). Radiative absorption, fluorescence, and scattering of a classical dipole near a lossless interface: A unified description. *J. Opt. Soc. Am. B* **17,** 1906–1913.

Moran-Mirabal, J. M., Edel, J. B., Meyer, G. D., Throckmorton, D., Singh, A. K., and Craighead, H. G. (2005). Micrometer-sized supported lipid bilayer arrays for bacterial toxin binding studies through total internal reflection fluorescence microscopy. *Biophys. J.* **89,** 296–305.

Moseley, J. B., Okada, K., Balcer, H. I., Kovar, D. R., Pollard, T. D., and Goode, B. L. (2006). Twinfilin is an actin-filament-severing protein and promotes rapid turnover of actin structures *in vivo*. *J. Cell Sci.* **119,** 1547–1557.

Nagamatsu, S. (2006). TIRF microscopy analysis of the mechanism of insulin exocytosis. *Endocr. J.* **53,** 433–440.

Neil, M. A. A., Juskaitis, R., and Wilson, T. (1997). Method of obtaining optical sectioning by using structured light in a conventional microscope. *Opt. Lett.* **22,** 1905–1907.

Nenasheva, T. A., and Mashanov, G. L. (2006). Visualizing single fluorophores in live cells. *Biofizika* **51,** 454–465.

Nieto-Vesperinas, M., Chaumet, P. C., and Rahmani, A. (2004). Near-field photonic forces. *Philos. Trans. R. Soc. London A-Math. Phys. Eng. Sci.* **362,** 719–737.

Nishikawa, M., Nishikawa, S., Inoue, A., Iwane, A. H., Yanagida, T., and Ikebe, M. (2006). A unique mechanism for the processive movement of single-headed myosin-IX. *Biochem. Biophys. Res. Commun.* **343,** 1159–1164.

Nofal, S., Becherer, U., Hof, D., Matti, U., and Rettig, J. (2007). Primed vesicles can be distinguished from docked vesicles by analyzing their mobility. *J. Neurosci.* **27,** 1386–1395.

Oheim, M. (2001). Imaging transmitter release. II. A practical guide to evanescent-wave imaging. *Lasers Med. Sci.* **16,** 159–170.

Oheim, M., Loerke, D., Stuhmer, W., and Chow, R. H. (1998). The last few milliseconds in the life of a secretory granule: Docking, dynamics and fusion visualized by total internal reflection fluorescence microscopy (TIRFM). *Eur. Biophys. J.* **27,** 83–98.

Oheim, M., Loerke, D., Stuhmer, W., and Chow, R. H. (1999). Multiple stimulation dependent processes regulate the size of the releasable pool of vesicles. *Eur. Biophys. J.* **28,** 91–101.

Oheim, M., and Schapper, F. (2005). Non-linear evanescent-field imaging. *J. Phys. D-Appl. Phys.* **38,** R185–R197.

Oheim, M., and Stuhmer, W. (2000a). Tracking chromaffin granules on their way through the actin cortex. *Eur. Biophys. J.* **29,** 67–89.

Oheim, M., and Stuhmer, W. (2000b). Interaction of secretory organelles with the membrane. *J. Membr. Biol.* **178,** 163–173.

Omann, G. M., and Axelrod, D. (1996). Membrane proximal calcium transients in stimulated neutrophils seen by total internal reflection fluorescence. *Biophys. J.* **71,** 2885–2891.

Osborne, M. A. (2005). Real-time dipole orientational imaging as a probe of ligand-protein interactions. *J. Phys. Chem. B* **109,** 18153–18161.

Pant, D., and Girault, H. H. (2005). Time-resolved total internal reflection fluorescence spectroscopy—Part I. Photophysics of Coumarin 343 at liquid/liquid interface. *Phys. Chem. Chem. Phys.* **7,** 3457–3463.

Partridge, M. A., and Marcantonio, E. E. (2006). Initiation of attachment and generation of mature focal adhesions by integrin-containing filopodia in cell spreading. *Mol. Biol. Cell* **17,** 4237–4248.

Perrais, D., Kleppe, I. C., Taraska, J. W., and Almers, W. (2004). Recapture after exocytosis causes differential retention of protein in granules of bovine chromaffin cells. *J. Physiol.* **560,** 413–428.

Pisarchick, M. L., Gesty, D., and Thompson, N. L. (1992). Binding kinetics of an anti-dinitrophenyl monoclonal Fab on supported phospholipid monolayers measured by total internal reflection with fluorescence photobleaching recovery. *Biophys. J.* **63,** 215–223.

Rappoport, J. Z., Kemal, S., Benmerah, A., and Simon, S. M. (2006). Dynamics of clathrin and adaptor proteins during endocytosis. *Am. J. Physiol. Cell Physiol.* **291,** C1072–C1081.

Rohrbach, A. (2000). Observing secretory granules with a multiangle evanescent wave microscope. *Biophys. J.* **78,** 2641–2654.

Ruckstuhl, T., and Seeger, S. (2003). Confocal total-internal-reflection fluorescence microscopy with a high-aperture parabolic mirror lens. *Appl. Opt.* **42,** 3277–3283.

Ruckstuhl, T., and Seeger, S. (2004). Attoliter detection volumes by confocal total-internal-reflection fluorescence microscopy. *Opt. Lett.* **29,** 569–571.

Saito, K., Tokunaga, M., Iwane, A. H., and Yanagida, T. (1997). Dual-colour microscopy of single fluorophores bound to myosin interacting with fluorescently labelled actin using anti-Stokes fluorescence. *J. Microsc. Oxf.* **188,** 255–263.

Sako, Y., Miniguchi, S., and Yanagida, T. (2000). Single-molecule imaging of EGFR signalling on the surface of living cells. *Nat. Cell Biol.* **2,** 168–172.

Sarkar, A., Robertson, R. B., and Fernandez, J. M. (2004). Simultaneous atomic force microscope and fluorescence measurements of protein unfolding using a calibrated evanescent wave. *Proc. Natl. Acad. Sci. USA* **101,** 12882–12886.

Scalettar, B. A. (2006). How neurosecretory vesicles release their cargo. *Neuroscientist* **12,** 164–176.

Scalettar, B. A., Rosa, P., Taverna, E., Francolini, M., Tsuboi, T., Terekawa, S., Koizumi, S., Roder, J., and Jeromin, A. (2002). Neuronal calcium sensor-1 binds to regulated secretory organelles and functions in basal and stimulated exocytosis in PC12 cells. *J. Cell Sci.* **115,** 2399–2412.

Schapper, F., Goncalves, J. T., and Oheim, M. (2003). Fluorescence imaging with two-photon evanescent wave excitation. *Eur. Biophys. J.* **32,** 635–643.

Schmoranzer, J., Goulian, M., Axelrod, D., and Simon, S. M. (2000). Imaging constitutive exocytosis with total internal reflection microscopy. *J. Cell Biol.* **149,** 23–31.

Schmoranzer, J., Kreitzer, G., and Simon, S. M. (2003). Migrating fibroblasts perform polarized, microtubule-dependent exocytosis towards the leading edge. *J. Cell Sci.* **116,** 4513–4519.

Schneckenburger, H. (2005). Total internal reflection fluorescence microscopy: Technical innovations and novel applications. *Curr. Opin. Biotechnol.* **16,** 13–18.

Schneckenburger, H., Stock, K., Strauss, W. S. L., Eickholz, J., and Sailer, R. (2003). Time-gated total internal reflection fluorescence spectroscopy (TG-TIRFS): Application to the membrane marker laurdan. *J. Microsc. Oxf.* **211,** 30–36.

Seitz, A., and Surrey, T. (2006). Progressive movement of single kinesins on crowded microtubules visualized using quantum dots. *EMBO J.* **25,** 267–277.

Selvin, P., Scalettar, B., Axelrod, D., Langmore, J. P., Hearst, J., and Klein, M. P. (1990). Rotational diffusion of DNA in intact nuclei. *J. Mol. Biol.* **214,** 911–922.

Serulle, Y., Sugimori, M., and Linas, R. R. (2007). Imaging synaptosomal calcium concentration microdomains and vesicle fusion by using total internal reflection fluorescent microscopy. *Proc. Natl. Acad. Sci. USA* **104,** 1697–1702.

Shaw, J. E., Oreopoulos, J., Wong, D., Hsu, J. C. Y., and Yip, C. M. (2006). Coupling evanescent-wave fluorescence imaging and spectroscopy with scanning probe microscopy: Challenges and insights from TIRF-AFM. *Surf. Interface Anal.* **38,** 1459–1471.

Shaw, R. M., Fay, A. J., Puthenveedu, M. A., von Zastrow, M., Jan, Y. N., and Jan, L. Y. (2007). Microtubule plus-end-tracking proteins target gap junctions directly from the cell interior to adherens junctions. *Cell* **128,** 547–560.

Silverman, M. A., Johnson, S., Gurkins, D., Farmer, M., Lochner, J. E., Rosa, P., and Scalettar, B. A. (2005). Mechanisms of transport and exocytosis of dense-core-granules containing tissue plasminogen activator in developing hippocampal neurons. *J. Neurosci.* **25,** 3095–3106.

Starr, T. E., and Thompson, N. L. (2001). Total internal reflection with fluorescence correlation spectroscopy: Combined surface reaction and solution diffusion. *Biophys. J.* **80,** 1575–1584.

Steyer, J. A., and Almers, W. (1999). Tracking single secretory granules in live chromaffin cells by evanescent-field fluorescence microscopy. *Biophys. J.* **76,** 2262–2271.

Steyer, J. A., and Almers, W. (2001). A real-time view of life within 100 nm of the plasma membrane. *Nat. Rev. Mol. Cell Biol.* **2,** 268–275.

Stock, K., Sailer, R., Strauss, W. S. L., Lyttek, M., Steiner, R., and Schneckenburger, H. (2003). Variable-angle total internal reflection fluorescence microscopy (VA-TIRFM): Realization and application of a compact illumination device. *J. Microsc. Oxf.* **211,** 19–29.

Stout, A. L., and Axelrod, D. (1989). Evanescent field excitation of fluorescence by epi-illumination microscopy. *Appl. Opt.* **28,** 5237–5242.

Stout, A. L., and Axelrod, D. (1994). Reversible binding kinetics of a cytoskeletal protein at the erythrocyte submembrane. *Biophys. J.* **67,** 1324–1334.

Sund, S. E., and Axelrod, D. (2000). Actin dynamics at the living cell submembrane imaged by total internal reflection fluorescence photobleaching. *Biophys. J.* **79,** 1655–1669.

Sund, S. E., Swanson, J. A., and Axelrod, D. (1999). Cell membrane orientation visualized by polarized total internal reflection fluorescence. *Biophys. J.* **77,** 2266–2283.

Taraska, J. W., and Almers, W. (2004). Bilayers merge even when exocytosis is transient. *Proc. Natl. Acad. Sci. USA* **101,** 8780–8785.

Tatsumi, H., Katayama, Y., and Sokabe, M. (1999). Attachment of growth cones on substrate observed by multi-mode light microscopy. *Neurosci. Res.* **35,** 197–206.

Thompson, N. L., and Axelrod, D. (1983). Immunoglobulin surface binding kinetics studied by total internal reflection with fluorescence correlation spectroscopy. *Biophys. J.* **43,** 103–114.

Thompson, N. L., Burghardt, T. P., and Axelrod, D. (1981). Measuring surface dynamics of biomolecules by total internal reflection with photobleaching recovery or correlation spectroscopy. *Biophys. J.* **33,** 435–454.

Thompson, N. L., McConnell, H. M., and Burghardt, T. P. (1984). Order in supported phospholipid monolayers detected by the dichroism of fluorescence excited by polarized evanescent illumination. *Biophys. J.* **46,** 739–747.

Thompson, N. L., Pearce, K. H., and Hsieh, H. V. (1993). Total internal reflection fluorescence microscopy—application to substrate-supported planar membranes. *Eur. Biophys. J.* **22,** 367–378.

Tilton, R. D., Gast, A. P., and Robertson, C. R. (1990). Surface diffusion of interacting proteins. Effect of concentration on the lateral mobility of adsorbed bovine serum albumin. *Biophys. J.* **58,** 1321–1326.

Todd, I., Mellor, J. S., and Gingell, D. (1988). Mapping of cell-glass contacts of *Dictyostelium amoebae* by total internal reflection aqueous fluorescence overcomes a basic ambiguity of interference reflection microscopy. *J. Cell Sci.* **89,** 107–114.

Toomre, D., and Axelrod, D. (2005). Total internal reflection fluorescent microscopy. *In* ''Cell Biology: A Laboratory Handbook'' (J. E. Celis, ed.), Vol. 3, Chapter 2. Elsevier Science, Elsevier Academic Press, New York.

Toomre, D., and Manstein, D. J. (2001). Lighting up the cell surface with evanescent wave microscopy. *Trends Cell Biol.* **11,** 298–303.

Toomre, D., Steyer, J. A., Keller, P., Almers, W., and Simons, K. (2000). Fusion of constitutive membrane traffic with the cell surface observed by evanescent wave microscopy. *J. Cell Biol.* **149,** 33–40.

Toonen, R. F., Kochubey, O., de Wit, H., Gulyas-Kovacs, A., Konijnenburg, B., Sorensen, J. B., Klingauf, J., and Verhage, M. (2006). Dissecting docking and tethering of secretory vesicles at the target membrane. *EMBO J.* **25,** 3725–3737.

Trache, A., and Meininger, G. A. (2005). Atomic force-multi-optical imaging integrated microscope for monitoring molecular dynamics in live cells. *J. Biomed. Opt.* **10,** 064023.

Tsuboi, T., Kikuta, T., Warashina, A., and Terakawa, S. (2001). Protein kinase C-dependent supply of secretory granules to the plasma membrane. *Biochem. Biophys. Res. Commun.* **282,** 621–628.

Tsuboi, T., Terakawa, S., Scalettar, B. A., Fantus, C., Roder, J., and Jeromin, A. (2002). Sweeping model of dynamin activity—Visualization of coupling between exocytosis and endocytosis under an evanescent wave microscope with green fluorescent proteins. *J. Biol. Chem.* **277,** 15957–15961.

Tsuboi, T., Zhao, C., Terakawa, S., and Rutter, G. A. (2000). Simultaneous evanescent wave imaging of insulin vesicle membrane and cargo during a single exocytotic event. *Curr. Biol.* **10,** 1307–1310.

Tweet, A. G., Gaines, G. L., and Bellamy, W. D. (1964). Fluorescence of chlorophyll alpha in monolayers. *J. Chem. Phys.* **40,** 2596–2600.

Vale, R. D., Funatsu, T., Pierce, D. W., Romberg, L., Harada, Y., and Yanagida, T. (1996). Direct observation of single kinesin molecules moving along microtubules. *Nature* **380,** 451–453.

Velez, M., and Axelrod, D. (1988). Polarized fluorescence photobleaching recovery for measuring rotational diffusion in solutions and membranes. *Biophys. J.* **53,** 575–591.

Wakelin, S., and Bagshaw, C. R. (2003). A prism combination for near isotropic fluorescence excitation by total internal reflection. *J. Microsc. Oxf.* **209,** 143–148.

Wang, C., Liu, L., Wang, G. Y., and Xu, Z. Z. (2004). A new method for determining dipole moment orientation of single molecules. *Chinese Phys. Lett.* **21,** 843–845.

Wang, M. D., and Axelrod, D. (1994). Time-lapse total internal reflection fluorescence video of acetylcholine receptor cluster formation on myotubes. *Dev. Dyn.* **201,** 29–40.

Wang, X. H., Teng, Y., Wang, Q. L., Li, X. J., Sheng, X. Y., Zheng, M. Z., Samaj, J., Baluska, F., and Lin, J. X. (2006). Imaging of dynamic secretory vesicles in living pollen tubes of *Picea meyeri* using evanescent wave microscopy. *Plant Physiol.* **141,** 1591–1603.

Watkins, R. W., and Robertson, C. R. (1977). Total internal reflection fluorescence technique for the study of protein adsorption. *J. Biomed. Mater. Res.* **11,** 915–938.

Wazawa, T., and Ueda, M. (2005). Total internal reflection fluorescence microscopy in single molecule nanobioscience. *Adv. Biochem. Eng. Biotechnol.* **95,** 77–106.

Weis, R. M., Balakrishnan, K., Smith, B., and McConnell, H. M. (1982). Stimulation of fluorescence in a small contact region between rat basophile leukemia cells and planar lipid membrane targets by coherent evanescent radiation. *J. Biol. Chem.* **257,** 6440–6445.

Willard, D., Proll, G., Reder, S., and Gauglitz, G. (2003). New and versatile optical-immunoassay instrumentation for water monitoring. *Environ. Sci. Pollut. Res.* **10,** 188–191.

Yamada, T., Afrin, R., Arakawa, H., and Ikai, A. (2004). High sensitivity detection of protein molecules picked up on a probe of atomic force microscope based on the fluorescence detection by a total internal reflection fluorescence microscope. *FEBS Lett.* **569,** 59–64.

Yokota, H., Kaseda, K., Matsuura, H., Arai, Y., Iwane, A., Ishii, Y., Kodama, T., and Yanagida, T. (2004). Single-molecule imaging of the dynamic interactions between macromolecules. *J. Nanosci. Nanotechnol.* **4,** 616–621.

Yoneda, A., Ushakov, D., Multhaupt, H. A. B., and Couchman, J. R. (2007). Fibronectin matrix assembly requires distinct contributions from rho kinases I and II. *Mol. Biol. Cell* **18,** 66–75.

Yoshida, T. M., and Barisas, B. G. (1986). Protein rotational motion in solution measured by polarized fluorescence depletion. *Biophys. J.* **50,** 41–53.

Yuan, Y., and Axelrod, D. (1995). Subnanosecond polarized fluorescence photobleaching: Rotational diffusion of acetylcholine receptors on developing muscle cells. *Biophys. J.* **69,** 690–700.

Zhang, J., Pitter, M. C., Liu, S. G., See, C., and Somekh, M. G. (2006). Surface-plasmon microscopy with a two-piece solid immersion lens: Bright and dark fields. *Appl. Opt.* **45,** 7977–7986.

Zoncu, R., Perera, R. M., Sebastian, R., Nakatsu, F., Chen, H., Balla, T., Ayala, G., Toomre, D., and DeCamille, P. V. (2007). Loss of endocytic clathrin-coated pits upon acute depletion of phosphtidylinositol 4,5 bisphosphate. *Proc. Natl. Acad. Sci. USA* **104,** 3793–3798.

CHAPTER 8

Spatiotemporal Dynamics in Bacterial Cells: Real-Time Studies with Single-Event Resolution

Ido Golding[*] and Edward C. Cox[†]

[*]Department of Physics
University of Illinois at Urbana-Champaign
Urbana, Illinois 61801

[†]Department of Molecular Biology
Princeton University
Princeton, New Jersey 08544

METHODS IN CELL BIOLOGY, VOL. 89

0091-679X/08 $35.00
DOI: 10.1016/S0091-679X(08)00608-0

Abstract

To produce a quantitative picture of cellular life, one has to study the processes comprising it in individual living cells, quantifying intracellular dynamics with sufficient resolution to describe individual events in space and time. To perform such studies, we have recently developed a novel measurement approach, based on quantitative fluorescence microscopy, and applied it to the study of transcription in *Escherichia coli* and of the spatiotemporal dynamics of individual mRNA molecules in the cell (Golding and Cox, 2004, 2006a; Golding *et al.*, 2005). The ability to detect individual events in real time depends on the engineering of an endogenous cellular process for amplifying the biological signal, in a way which allows signal detection to be independent of slow and highly stochastic cellular processes (Golding and Cox, 2006a). In this chapter, we describe the ingredients of our system and the way data is acquired and analyzed. We attempt to give general lessons for researchers who wish to implement a similar approach for the study of transcription in other organisms and, more generally, for the study of cellular processes with single-event resolution.

I. Introduction

Most physiological mechanisms studied in molecular biology were first discovered and characterized in the bacterium *Escherichia coli.* This organism still serves as the basic paradigm for many cellular processes and features, ranging in scale from the molecular to the organismic level. Such processes include the multiple steps of gene expression and regulation (Pardee *et al.*, 1958); epigenetic stability and switching (Benzer, 1953; Novick and Weiner, 1957); viral infection and reproduction (Ellis and Delbruck, 1939); DNA replication (Lehman *et al.*, 1958); cellular response to DNA damage (Witkin, 1976); genetic recombination (Clark and Margulies, 1965); and more (Neidhardt, 1996). Questions asked in *E. coli* often yield insights relevant to eukaryotic systems, with regard to both mechanism and system properties (Golding and Cox, 2006a; Ptashne, 1992; Stillman, 1994).

A vast body of genetic and biochemical knowledge has accumulated over the last five decades, enabling the formation of an elegant and seemingly complete narrative for much of the observed phenomenology in terms of the microscopic interactions in the cell (Neidhardt, 1996; Ptashne, 1992). In the eyes of system biologists, the system thus appears ripe for the natural next step: forming a quantitative narrative, in the form of a mathematical model, which connects the microscopic components in the cell to the system-level properties (Di Ventura *et al.*, 2006). One often finds, however, that the resulting mathematical models offer little or no predictive power, and are therefore treated with much suspicion by the broader community of experimental biologists. The main reason for the inadequacy of theoretical models is that the biophysical parameters characterizing

the microscopic processes are rarely known. Their numerical values are often chosen so as to reproduce the observed kinetics (Arkin *et al.*, 1998). Where numerical estimates do exist, they come from two types of assays: (1) *in vivo* measurements made on whole populations, which average out much of the relevant dynamics in both space and time; and (2) *in vitro* measurements, far removed from actual physiological conditions and thus of uncertain relevance (Ellis, 2001). The bottom line is that a wide quantitative gap still exists between the genetic and biochemical knowledge on the one hand, and the observed population phenotype on the other.

To bridge this gap and "assign numbers to the arrows" (Ronen *et al.*, 2002), we need to study cellular life in real time, and in individual living cells, all the while quantifying intracellular dynamics with sufficient resolution to describe individual events. Using this approach, parameters characterizing the microscopic kinetics can be extracted. These kinetics are usually obscured not only by the cell-to-cell averaging involved in traditional assays, but also by within-cell averaging characteristic of contemporary single-cell fluorescent assays (Friedman *et al.*, 2005; Ronen *et al.*, 2002; Rosenfeld *et al.*, 2005). Another aspect of cell physiology which can only be unraveled by this approach is the unique spatiotemporal features of cellular dynamics, beyond the picture of a well-mixed environment where reactions are governed by diffusion kinetics.

The *E. coli* system is a natural choice for trying to implement such a strategy of real-time, high-resolution examination of cell dynamics because of our deep genetic and biochemical knowledge and the (relative) simplicity of this organism. In this chapter, we describe the novel approaches we have recently developed and applied to the study of transcription in *E. coli* (Golding and Cox, 2004; Golding *et al.*, 2005), and of the spatiotemporal dynamics of individual mRNA molecules in the cell (Golding and Cox, 2006b).

II. Studying Cellular Dynamics with Single-Event Resolution

The genetic components of the mRNA measurement system we have used are shown in Fig. 1. The ability to detect individual events in real time depends on several key features (Golding and Cox, 2006a): First is the use of an endogenous cellular process for amplifying the biological signal. In the case of transcription, this amplification is achieved by fusing, to each mRNA molecule from the gene of interest, 96 copies of the recognition sequence of phage MS2 coat protein (Peabody, 1989). The MS2 protein itself, which in the current application is fused to a green fluorescent protein (GFP), recognizes and binds to its RNA target with high specificity and affinity (Johansson *et al.*, 1998). The result is that each mRNA molecule becomes decorated by a large number of fluorescent proteins, with well-defined stoichiometry (Bertrand *et al.*, 1998; Forrest and Gavis, 2003; Golding and Cox, 2004; Le *et al.*, 2005).

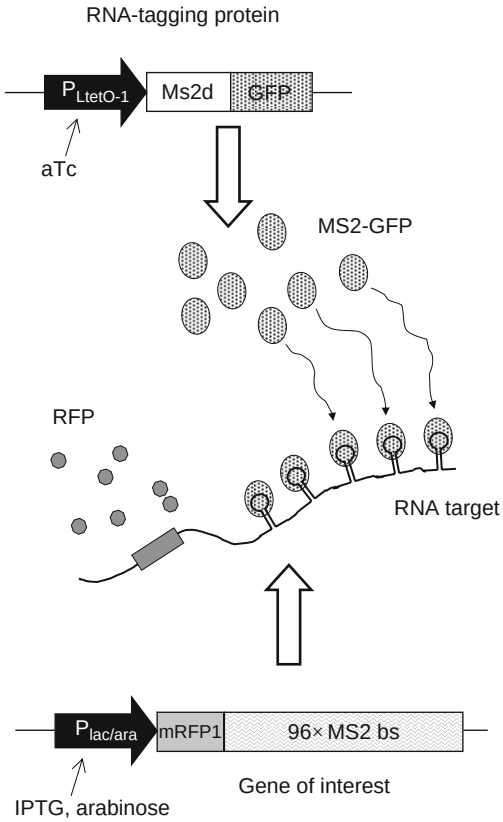

Fig. 1 Genetic components for tagging mRNA in live cells. The tagging protein (top) consists of a fused-dimer version of MS2 coat protein, fused to GFP. Protein production is regulated by the P_{LtetO} promoter (Lutz and Bujard, 1997), and inducible by anhydrotetracycline (aTc). This construct is on a high-copy plasmid. The RNA target (bottom) consists of the coding region for mRFP1, a monomeric red fluorescence protein (Campbell *et al.*, 2002), followed by a tandem array of 96 MS2 binding sites. This message is under the control of a $P_{lac/ara}$ promoter (Lutz and Bujard, 1997), which is repressed by LacI and activated by AraC, therefore inducible by isopropylthio-β-D-galactoside (IPTG) and arabinose. This construct is on an F plasmid, with a single copy per bacterial chromosome. Both plasmids were cotransformed into *Escherichia coli* DH5α-PRO, a constitutive producer of LacR and TetR repressors.

A second key feature, which enables the system to work in real time, is its independence from slow and highly stochastic cellular processes: The appearance of mRNA is detected by the rapid binding of MS2-GFP molecules which already preexist in the cell in large excess. Detection is not delayed by the kinetic bottlenecks of protein production and chromophore maturation which are typical of standard GFP-based reporter systems (Friedman *et al.*, 2005; Kalir *et al.*, 2001; Rosenfeld *et al.*, 2005; Zaslaver *et al.*, 2006). Thus, we can characterize events on

the temporal scale of approximately seconds, as opposed to >10 min in the aforementioned studies.

Last, and the feature that allows our approach to be turned into a real measurement system, is the use of fluorescent imaging as a quantitative tool (Wu and Pollard, 2005). Using the appropriate calibration, optics and camera, discrete numbers of mRNA molecules can be accurately estimated by measuring the intensity of localized fluorescence (number of target-bound MS2-GFP) above the cell background (number of free MS2-GFP) (Golding *et al.*, 2005). The measurements are followed by quantitative analysis of the data using the standard tools used in the studies of stochastic processes, dynamical systems, and pattern formation. During the entire endeavor, data acquisition is also coupled to mathematical modeling of the underlying dynamics. The modeling serves to interpret the observations as well as to design new experiments.

III. Methods

A. General

We have described above the principles underlying our approach for following intracellular kinetics in real time, with single-event resolution. We now give more details of the system and how it was constructed, tested, and calibrated (Golding and Cox, 2004, 2006b; Golding *et al.*, 2005). We will emphasize general lessons relating to the quantitative study of individual events. These lessons will be relevant to the detection of other cellular players and their dynamics. Standard techniques will be mentioned only briefly.

B. Construction of Genetic Components for Quantitative Measurements

A few points require special attention when constructing genetic components to be used for quantitative measurements, in addition to the standard considerations characteristic of molecular genetics. First, because we wish to characterize the true population heterogeneity with regard to our measured variables, our components themselves have to exhibit a high level of uniformity—between cells in the population and over time in individual cells. In addition, some features—such as mRNA and protein expression levels—have to be controlled by the user in an accurate and reproducible manner. In the case of the mRNA measurement system, significant modifications were made to convert it from the original pioneering scheme used to tag RNA in various eukaryotic systems (Bertrand *et al.*, 1998; Forrest and Gavis, 2003; Fusco *et al.*, 2003) into a system which enables us to reliably count the number of mRNA molecules in individual bacteria, as well as to track the individual mRNA molecules as they move inside the $\sim 2\ \mu$m bacterial cell (Golding and Cox, 2004, 2006a; Golding *et al.*, 2005).

C. The Target RNA

To detect single RNA molecules, a significant number of GFP molecules have to be localized in space, and hence a tandem array of binding sites must be constructed. In the lacO/lacI-GFP system devised by Belmont and coworkers for tagging DNA in live cells (Belmont and Straight, 1998; Robinett *et al.*, 1996), ~250 copies of the lac operator sites were used. This number proved to be sufficient for tracking the location of chromosome and plasmid DNA sites in *E. coli* as well (Gordon *et al.*, 1997, 2004). Singer and coworkers described the detection of single mRNA molecules in mammalian cells using 24 tandem MS2 binding sites (Fusco *et al.*, 2003). This allows the binding of 48 monomeric MS2-GFP proteins. In this case, however, it was not known what fraction of the target RNA molecules was successfully detected because 24 tandem copies are close to the detection limits.

Long tandem DNA repeats are known to be unstable in *E. coli* (Albertini *et al.*, 1982; Bzymek and Lovett, 2001). The problem is made worse in the MS2 system because each binding site contains a palindromic repeat. To increase the stability of the construct, we followed the strategy devised by Sherratt and coworkers (Lau *et al.*, 2003) of inserting random sequences between successive MS2 binding sites in the target RNA, thereby shortening the runs of perfect homology that serve as targets for recombinational instability. For construction of a 96 binding site (bs) tandem array, an ensemble of oligonucleotides containing 3 MS2 binding sites (19 bases each), separated by random sequences (of length 17 bases), was synthesized. This oligonucleotide mixture was then converted into double-stranded DNA and amplified by PCR. The product was cut and inserted into a high-copy plasmid (pBLUESCRIPT-SK, Stratagene), and sequential doublings of the array were carried out by repeated restriction and ligation (see Fig. 2). A 96 bs array was then inserted into an F-based plasmid (pTRUEBLUE-BAC2, Genomics One International). This very low copy vector was chosen because it was predicted to increase the stability of the inserts, and it would enable us to induce a low number of RNA molecules. In addition, the F-plasmid replication system has been well characterized and the plasmid's physical location in the cell in known (Gordon *et al.*, 1997).

Upstream of the 96 bs array we placed a $P_{lac/ara}$ promoter (Lutz and Bujard, 1997). This is a synthetic promoter whose behavior is well characterized, one that offers a high level of control over expression levels. The coding region for a red fluorescence protein, mRFP1 (including a ribosome binding site and a stop codon) was inserted between the promoter and the 96 bs array. The resulting vector is an F-based plasmid, with a $P_{lac/ara}$ promoter controlling the production of a message containing mRFP1 upstream of the 96 MS2 binding sites array. Additional constructs served as controls: one where the order of mRFP1 and 96 bs was reversed, as well as one which contains only the mRFP1 gene but not the bs array.

D. The MS2-GFP Protein

Previous studies used an aggregation-deficient mutant (MS2d1FG) of the MS2 coat protein (Peabody and Ely, 1992). Following initial unsatisfactory results with this mutant (no fluorescence signal), we fused a tandem dimer of the wild-type coat

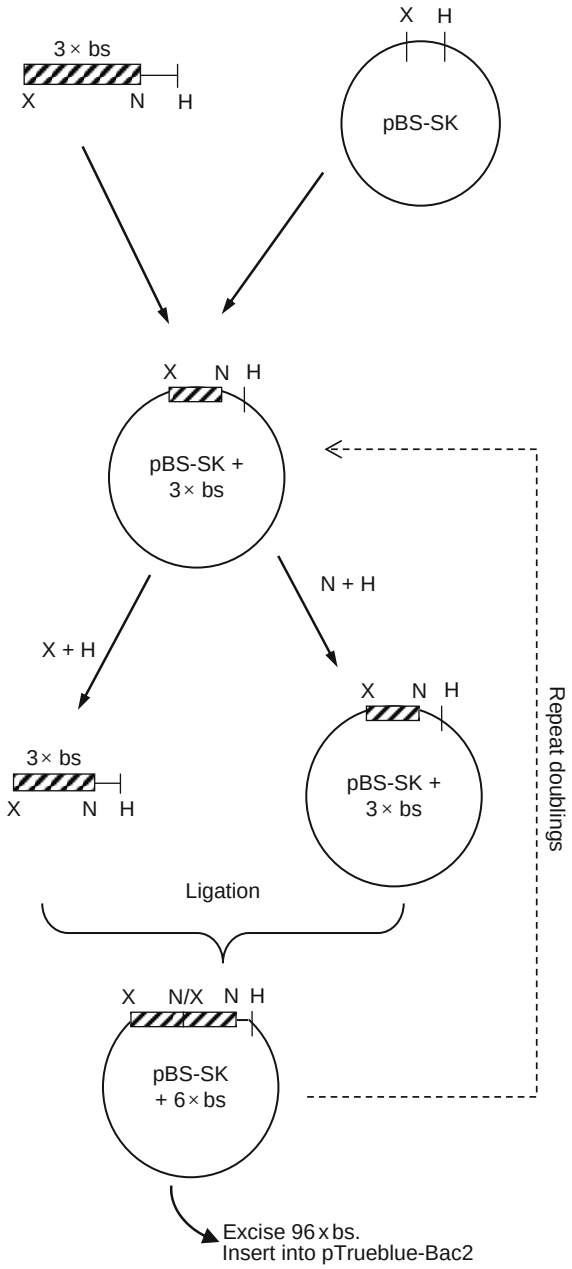

Fig. 2 Construction strategy for the MS2 bs array. The initial ensemble of 3 × bs array was inserted into pBS-SK and sequentially doubled by using the three restriction sites (X = *Xba*I, N = *Nhe*I, and H = *Hin*dIII). Use is made of the fact that *Xba*I and *Nhe*I have compatible sticky ends (a 5′ CTAG extension). The heterogeneity of the population was maintained at all stages by harvesting plasmids from the entire contents of transformant plates containing $\approx 10^5$ independent transformants. At several stages, the heterogeneity of the plasmid population was confirmed by sequencing.

protein with a version of GFP optimized for *E. coli*. The fused dinner, MS2d, is highly tolerant of structural perturbations, and retains its *in vivo* functionality following insertion at various locations (Peabody, 1997; Peabody and Lim, 1996). We fused MS2d to the N-terminus of a GFP, GFPmut3 (Cormack *et al.*, 1996), and placed the fusion on a high-copy number plasmid (K133, derived from the PROTET.E vector, Clontech), under the control of the tetracycline promoter $P_{LtetO-1}$ (Lutz and Bujard, 1997). After induction with anhydrotetracycline (aTc), cells become bright green, and protein of the correct molecular size is made, as judged by Western blotting using anti-GFP antibodies.

The RNA binding capacity of the protein was examined *in vitro* by an RNA gel-shift assay of purified protein using RNA probes consisting of six tandem repeats of the MS2 binding site. The MS2d-GFP bound at the predicted molarity. To test the activity of the protein *in vivo*, we used the blue/white β-galalcatosidase assay devised by Peabody (Peabody, 1990). In this test, a functional coat-protein represses the translation of an MS2-replicase/β-galactosidase fusion, thus yielding white (as opposed to otherwise blue) colonies. MS2d-GFP was active *in vivo* by this criterion.

E. The Optical System

For imaging intracellular dynamics inside *E. coli* cells, optical resolution has to be taken to the limit. At the same time, the small cell diameter means that confocal optics are not required, and ''wide field'' epifluorescence imaging is usually sufficient. Our microscopy is performed with a Nikon Eclipse (TE-2000-U, Nikon) inverted microscope equipped with a 60× (1.4 NA) objective and epifuorescence system with standard filter sets. For live fluorescent imaging, exposure times must be minimized to prevent phototoxicity and photobleaching. This issue becomes even more critical when trying to detect the emission from a small number of fluorophores. Thus, camera sensitivity is a central issue. In addition, since our fluorescent imaging is used for making quantitative measurements, a linear response and a wide dynamic range are equally important. We use the Roper Cascade 512B camera (Photometrics, Tuscon, AZ). This camera offers a quantum yield of close to 100% combined with 16 bit image depth. In our system, images are taken after an additional 4× magnification, where each camera pixel covers a square of size $\sim 67 \times 67\ nm^2$, thus oversampling the optical resolution limit (Airy radius ~200 nm).

F. Cell Growth

The two plasmids described above were cotransformed into an *E. coli* DH5α-PRO, a constitutive producer of LacR and TetR repressors (Lutz and Bujard, 1997). This phenotype guarantees the tight repression of both protein and target RNA production until the proper inducers are added to the medium. Cells were grown in LB (Miller, 1992), supplemented by antibiotics according to the specific

plasmids markers. For induction of protein and RNA, cells were grown overnight from a single colony, diluted 1:1000 into fresh medium and grown with aeration at 37 °C. To induce the production of the MS2-GFP tag, 100 ng/ml (215 nM) aTc was added. After ~45 min, a sufficient amount of protein is present for RNA detection. Detection is not sensitive to the exact MS2-GFP induction level. RNA target production was induced by various levels of arabinose (0–0.1%, 0–7 mM) and isopropyl-β-D-thiogalactopyranoside (IPTG) (0–1 mM). Unless stated otherwise, cells were preincubated with arabinose, to obtain full activation of the ara system before derepression of the lac component. mRNA levels were then tracked starting a few minutes after induction, and up to many hours afterward. To maintain exponential growth, cells were diluted into fresh prewarmed medium whenever the optical density approached $OD_{600} \sim 0.5$.

G. Imaging and Measurements

At each time point, a few microliter of culture was placed between a cover slip and a 1 mm slab of 0.8% agarose containing LB. Images were acquired using MetaView software (Universal Imaging) through the green (FITC filter) and red (Texas Red filter) channels of the epifluorescence system. Typical images of induced cells are shown in Fig. 3. Most cells contained green foci, each consisting of one or more tagged RNA molecules (see below). Cells also expressed mRFP1, leading to whole cell red fluorescence. Figure 4 shows typical kinetics for the green (foci) and red (whole cell) fluorescence levels, averaged over the cell population. RNA levels begin rising immediately after IPTG is added and approach a plateau after about 80 min. Protein levels rise more slowly, as expected: a stable protein should lag behind the mRNA, just as the mRNA lagged behind induction. The chromophore must also mature before fluorescence can be measured, adding at least a few minutes to the observed protein response (Campbell *et al.*, 2002).

In earlier work, we showed that at very low transcript levels, each mRNA molecule is detectable as a single focus occupied by 50–100 MS2-GFP molecules (Golding and Cox, 2004). This estimation is based, among other things, on comparing the photon flux from the fluorescent spots *in vivo* to that of individual MS2-GFP proteins imaged under similar optical conditions *in vitro*. At higher mRNA levels, however, simply counting the number of fluorescent spots is not a gauge of transcript number, since what appears as a single focus may consist of several transcripts. Our way of estimating the number of mRNA molecules in the cell is to *count the total number of bound MS2-GFP proteins*. We therefore measured the total photon flux of all green foci, above the cell background. This procedure was automated, so that data from many cells could be obtained. The automated extraction of quantitative data from "noisy" live images, taken at low photon intensities and close to the optical resolution limit, can be quite challenging and requires familiarity with the arsenal of digital image processing, especially so-called "morphological operations" (Gonzalez *et al.*, 2004). Image processing was performed with home made programs, using the Image Processing Toolbox of

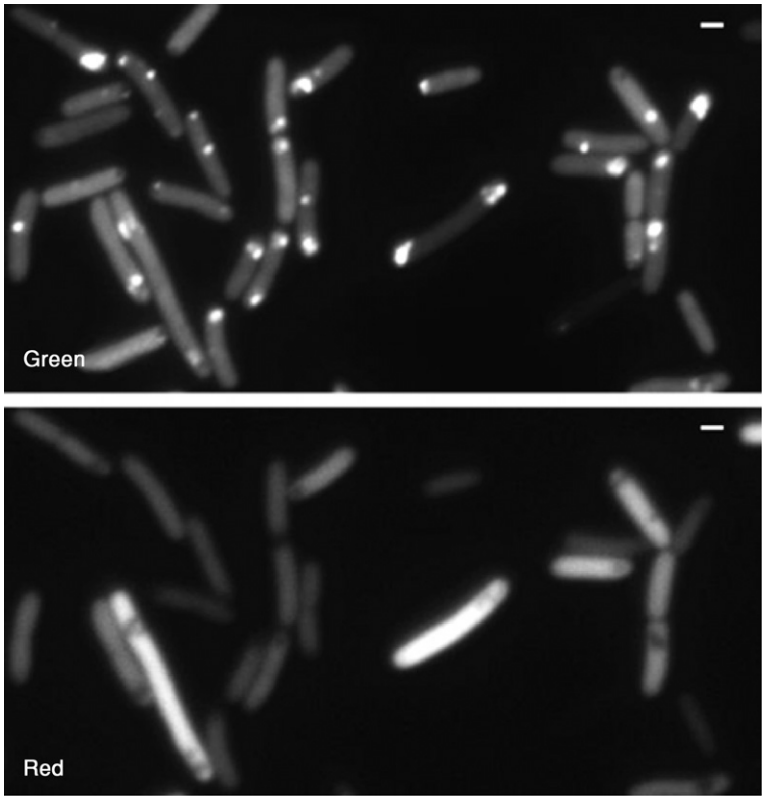

Fig. 3 Detection of mRNA and protein in living cells. Cells were grown and imaged as described in the text. Shown are the green (top) and red (bottom) channels. Scale bar, 1 μm. Target mRNAs appear as green foci, whereas the red fluorescent proteins produced from these transcripts appear as whole cell red fluorescence.

MATLAB (The Mathworks). For users who are less inclined to create their own programs we note that many of the required algorithms are available as modules in existing software packages, either freeware such as ImageJ (http://rsb.info.nih.gov/ij/) or commercial products such as MetaMorph (Molecular Devices Corporation).

Fluorescent images obtained through each filter were read into MATLAB in 16 bit TIFF format, and processed as described below. The specific sequence of operations to be used, as well as choice of parameters, needs to be chosen heuristically on a case by case base. Some useful insights regarding the proper choices are given in standard textbooks such as (Gonzalez *et al.*, 2004). In our case, each image was processed as follows:

- An *opening* morphological operation was performed to estimate the background level. This operation has the effect of removing objects that cannot completely contain a *structuring element* (e.g., a disk or a square) of a defined size. Thus,

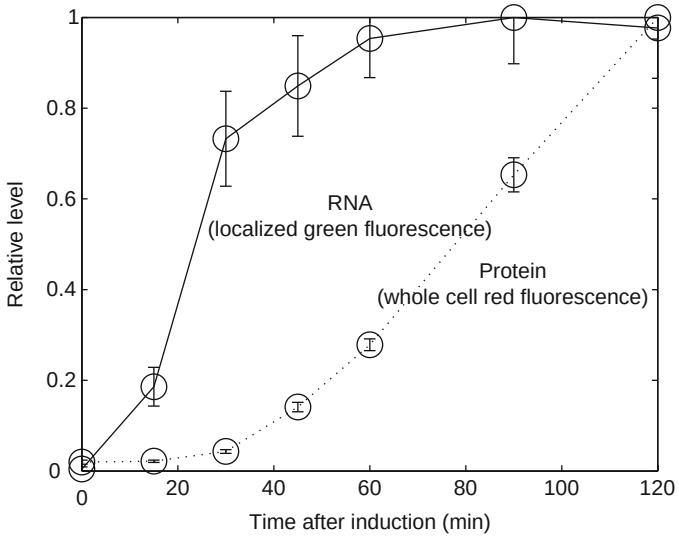

Fig. 4 Kinetics of mRNA (green) and protein (red) levels after addition of IPTG. Cells were grown and induced as described in the text. At different times after induction, 50–100 cells were imaged. The images were then automatically processed to identify individual cells, and within them the location of green particles. The average green signal ($\langle I_G \rangle$) is the average over all cells at one time point of the total photon flux from all green foci in the cell, from which the cell background green fluorescence was subtracted. The red signal ($\langle I_R \rangle$) is the average over all cells at one time point of total cell red fluorescence. Bars denote standard error of the sample over the population.

performing the opening with an element of the proper size removes all bacterial cells from the image and leaves the background only. The background image was then subtracted from the original image.

- The contrast of the image was adjusted. Adjustment is achieved by saturating a defined percentage (e.g., 1%) of the data at both low and high intensities of the image and by stretching the intensity values to fill the required dynamic range (e.g., 0–65535).
- A binary version of the image was created by using automatic thresholding. Typically, the threshold is chosen to minimize the intraclass variance of the black and white pixels.
- The resulting image was used to recognize individual bacteria in the picture, by labeling connected components in the binary image. Falsely recognized objects were automatically discarded based on criteria of size, axial ratio, and solidity.
- To identify fluorescent foci, a similar procedure was repeated within each bacterial cell, again using additional morphological parameters to decrease the number of false recognitions.
- Once the cells and foci were located, green fluorescent levels were measured on the original unprocessed TIFF image. For the measurement of protein levels (red fluorescence), only the cell recognition procedure was used.

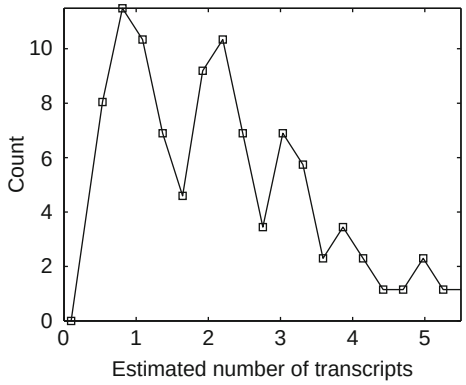

Fig. 5 Distribution of estimated mRNA copy numbers among different cells in a typical sample. The estimated copy number n is equal to green foci intensity (I_G) normalized by the intensity of a single-tagged mRNA molecule.

To obtain the values of green foci intensity (I_G) and red cell intensity (I_R), I_R was obtained by integrating the total photon flux per second of the red channel and subtracting the background level in the same image. I_G was obtained by integrating the total fluorescence of foci in the green channel and subtracting the background green level in the same cell. The number of tagged transcripts in the cell was estimated by normalizing I_G by the intensity of a single-tagged RNA molecule—equal to the first peak in the intensity histogram (Fig. 5). The normalized intensity histogram for the number of transcripts per cell consists of a series of discrete peaks, each corresponding to the integer-valued number of individual mRNA molecules in the cell. This result is central to our approach: When estimating an integer-valued distribution of numbers of molecules using a continuous quantity like fluorescence, such well-separated peaks are an indication of the measurement's fidelity.

H. Dynamic Range and Accuracy

We optimized the MS2-GFP induction level to enable robust mRNA detection and measurement. This means that we needed sufficient MS2-GFP to saturate all RNA targets, but not too much MS2-GFP, which would create too high a fluorescent background level in the cell. We have found that there exists a large "dynamic range" for MS2-GFP (obtained by inducing the Tet controlled system for 0.5–2 h at maximum induction), within which the above conditions are fulfilled. Based on fluorescence measurements, each cell contains $\sim 10^4$ MS2-GFP molecules (~ 10 μM) in this induction range. Of these molecules, typically only 3–4% are bound to RNA targets, with a maximum fraction of $\sim 10\%$ at the highest RNA levels (>10 transcripts per cell). These percentages are consistent with the fact that

the MS2-GFP gene is located on a ColE1 type plasmid, with a copy number >50 times higher than the plasmid carrying the RNA-coding target, and expressed from a stronger promoter (Lutz and Bujard, 1997). Because the dissociation constant between MS2 coat protein and our version of the binding site is in the approximately nanomolar range (Johansson *et al.*, 1998), all of the target RNAs are expected to be saturated by the MS2-GFP pool, that is, the occupancy of MS2 binding sites is expected to be close to 100%. In agreement with this view, population measurements show that cells with above-median RNA levels exhibit only a slightly lower (5–10% difference) level of unbound green fluorescence compared to cells with below-median RNA levels. At the single cell level, the appearance of a new mRNA is usually not accompanied by a detectable decrease in cell background fluorescence.

To check that the estimation of mRNA levels is consistent with other methods, we compared single cell measurements to three other indicators of gene expression: quantitative real-time PCR (QPCR), levels of the proteins encoded by the RNA transcripts, and luciferase levels measured from the same promoter as reported in the literature (Lutz and Bujard, 1997) (Fig. 6). Fluorescence measurements are in good agreement with the other indicators over most of the induction range. The agreement with QPCR further strengthens our belief that absolute levels of message copy number have been reliably estimated.

In addition to the integer-valued peaks in the photon-flux histograms and the comparisons with standard measures of gene activity (QPCR for RNA,

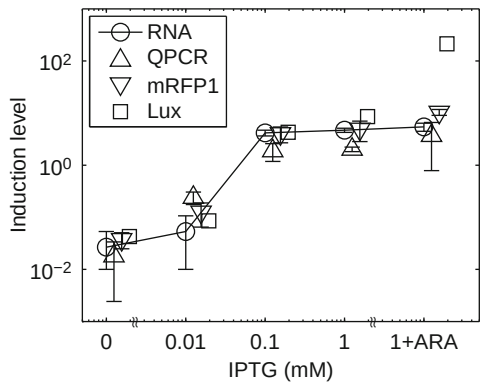

Fig. 6 Gene expression levels at various levels of induction, obtained by varying the levels of isopropyl-β-D-thiogalactopyranoside (IPTG) and arabinose. O = estimation of mRNA levels (molecules/cell) at steady state, using our fluorescence-based method. Bars are the standard error from two separate experiments (>300 cells in each), lines connect the averages. Δ = mRNA levels measured by quantitative real-time PCR (QPCR). Shown are the average and standard error of message levels in two separate experiments. Inverted triangle = red fluorescence levels of the induced cells in arbitrary units. Data are from the same experiments as the estimated mRNA levels. Δ = luciferase levels measured from the $P_{lac/ara}$ promoter [in arbitrary units; Data from Lutz and Bujard (1997)]. Data points are slightly offset horizontally to accommodate viewing.

fluorescence and luciferase for protein), a series of additional experimental controls (for details see Golding *et al.*, 2005) point to the fidelity of our measurements: (1) The observed statistics of RNA partitioning is approximately Binomial up to at least $n = 15$. A similar protein experiment (Rosenfeld *et al.*, 2005) used such statistics to estimate protein numbers, even without counting the number of molecules. (2) The adjustment to steady state follows a first-order model (see below). (3) We observe proportionality between RNA and protein levels over a broad range of induction.

Another possible concern is whether the long array of 96 MS2 binding sites (96 bs) hinders proper transcription and translation. To examine that, we measured expression levels (as indicated by red fluorescence of the individual cells) from two modified constructs, both having the same genetic background (pTRUEBLUE-BAC2 plasmid with $P_{lac/ara}$ promoter) as our mRFP1 +96 bs construct (1) A plasmid carrying the mRFP1 gene only, without the MS2 binding sites array. In this case, the protein levels obtained are almost indistinguishable from those of the original construct: [R]/[R+96 bs] = 0.82 ± 0.28 (2 experiments, 310 cells; where [] denotes mRFP1 fluorescence level). (2) A plasmid in which the mRFP1 gene is located downstream of the 96 bs array, instead of upstream, as in the original construct. In this case, there is measurable repression of the expression level (3.0- ± 0.3-fold; 3 experiments, 240 cells). Considering the length of the transcript on the 5′ side of the gene (~4 kb), this is a small polarity effect (Li and Altman, 2004).

These results are in agreement with additional data pointing to the normal behavior of the transcript: (1) We measured in two different ways the kinetics of mRNA chain elongation in the GFP-tagged (= MS2-bs array) portion of the transcript. This was done by measuring the increase in fluorescent signal and by measuring the physical elongation of the transcript (see below). Both methods reveal a very similar chain elongation rate, close to the rates estimated from *in vivo* population studies (Ryals *et al.*, 1982) and from *in vitro* single molecule studies (Shaevitz *et al.*, 2003). This result implies that the 96 bs array behaves as a normal transcript with regard to its transcription kinetics. (2) As described above, we also examined the "dose–response" of the two coding regions of our transcript: the mRFP1 gene (as measured by cell red fluorescence), and the 96 bs array (as measured by localized green fluorescence). As shown in Fig. 6, their behavior is very similar, again indicating that the 96-mer does not seriously perturb the dynamics of transcription.

I. Population Snapshots as a Window into Single Cell Kinetics

After assessing the fidelity of the measurement scheme, we next applied it to study the kinetics of transcription in our system. Our first means of examining single cell kinetics was by taking snapshots of mRNA levels in cell populations at different times after gene induction and under different levels of inducers.

The first observables obtained from these data relate to population averages. When mRNA number in the individual cells was averaged over the population, the

steady-state mRNA levels under different inducer levels were in agreement with population assays using quantitative PCR as well as with the known dose–response curve for the promoter (Fig. 6), thus fulfilling the obvious requirement that cell-by-cell data will "converge" to the known population value obtained by standard methods. When examining the average mRNA copy number over time after induction, the measured kinetics exhibited a constant production rate and a first-order elimination rate (Fig. 7). The zero-order production is a behavior consistent with older studies (Beckwith *et al.*, 1970), as well as with the traditional text book picture of mRNA synthesis as a simple Poisson process, with a constant probability per unit time of making a transcript. The first-order elimination is dominated by cell growth and division rather then by RNA degradation, due to the prolonged lifetime of our MS2-bound transcripts.

Beyond the reproduction of average values, potentially much richer information exists in the heterogeneity of the population (in mathematical terms, the higher statistical moment beyond the first moment, i.e., the mean). It is perhaps a common misconception that characterizing population heterogeneity only offers an estimation of the degree of "noisiness" in the system. More importantly, it offers a window into single cell kinetics, some features of which are masked by averaging over a population. The ability to examine many cells at once leads to high-quality data, whose analysis enables us to form hypotheses about the underlying dynamics. These hypotheses can then be directly examined by following single cell kinetics. However, as we discuss below, single cell kinetic data are often of a relatively lower quality (fluorescence signal-to-noise), resolution (sampling frequency), and quantity (numbers of cell examined), and thus often serve to confirm a model rather than to formulate one.

In the case of transcription from $P_{lac/ara}$, two features of population heterogeneity could be characterized: (1) the fraction of cells with no target RNA as a function of time after induction, $P_0(t)$ (Fig. 8A); and (2) the variance (σ^2) versus the mean ($\langle n \rangle$) of mRNA copy number at various steady state levels (Fig. 8B). Examining these data, we concluded that the naïve picture of transcription as a Poisson process does not hold. The fraction of cells with no RNA declines exponentially with time as expected under the Poisson scenario. However, counter to the Poisson case, the decline rate is not identical to the population-averaged transcription rate but is instead ~4 times lower. As for the variance in the number of mRNAs per cell, one finds that although σ^2 is proportional to $\langle n \rangle$, a discrepancy appears in the shape of the proportionality factor which is ~4 instead of 1, expected for a Poisson process. Both these features point to the fact that the underlying mechanism of mRNA production, although displaying some simple features, is not the simplest one imaginable. Rather, RNA creation has to involve two levels of stochasticity whose combined effect leads to the observed population statistics. We were thus led to the formulation of a "2-state" model for transcription. In this model, two independent events are needed to account for the appearance of transcripts in the cell. First, an induced gene can switch into an active state with constant probability as a function of time. Second, while in this state, it can at

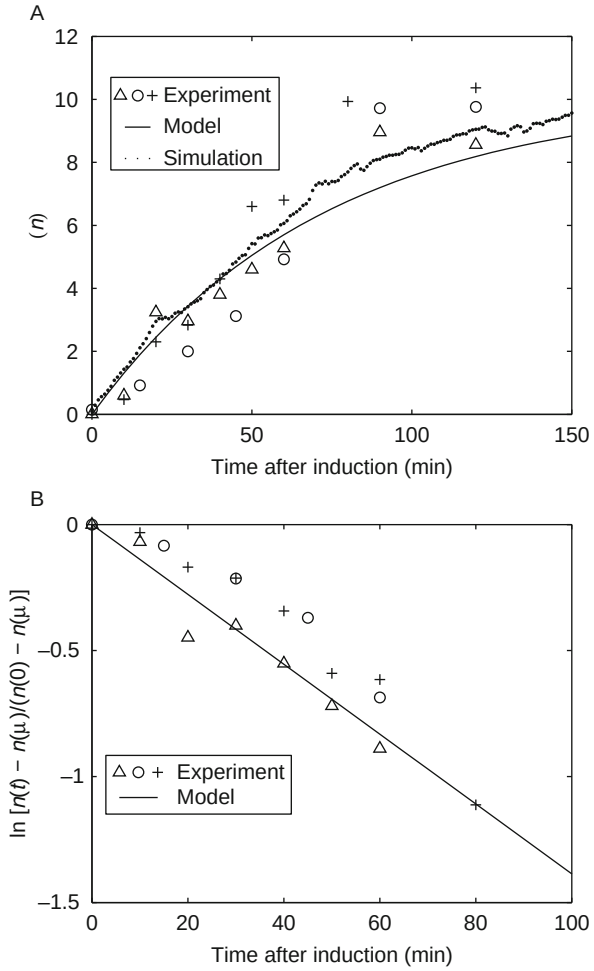

Fig. 7 Induction kinetics. (A) Estimated average number of transcripts per cell $\langle n \rangle$, as a function of time after induction t. 50–100 cells were imaged at each time point and the number of tagged mRNAs in each cell was estimated as described in the text. $\langle n \rangle$ is averaged over all cells at a given time. Symbols (+, o, Δ) are results of three different experiments. Solid line is the prediction of the first-order model, $\mathrm{d}/\mathrm{d}t\langle n \rangle = k_1 + k_2\langle n \rangle$, with parameters $k_1 = 0.14$ min^{-1} (synthesis rate) and $k_2 = \ln(2)/50$ min^{-1} (elimination rate constant, due to cell growth and division). The model can be solved to yield

$$\langle n(t) \rangle = \frac{k_1}{k_2}(1 - \mathrm{e}^{-k_2 t})$$

which is the curve plotted. Dotted line, the results of a stochastic simulation of the bursting model (see text). (B) Relative deviation from steady state, as a function of time after induction. Symbols are experimental data. Line is the prediction of the first-order model, which can be written as

$$\langle n(t) \rangle = \frac{k_1}{k_2}(1 - \mathrm{e}^{-k_2 t}) \Leftrightarrow \frac{\langle n(\infty) \rangle - \langle n(t) \rangle}{\langle n(\infty) \rangle - \langle n(0) \rangle} = \mathrm{e}^{-k_2 t}.$$

In agreement with the model, the relative deviation from steady state decreases exponentially and independently of k_1.

each moment produce an mRNA molecule with a constant probability, but it can also, with a constant probability, switch back to the inactive state (Kaern *et al.*, 2005; Paulsson, 2004). The resulting time series is characterized by periods of transcriptional inactivity, interspersed with limited time windows of transcriptional activity, in each of which a geometrically distributed number of mRNA molecules

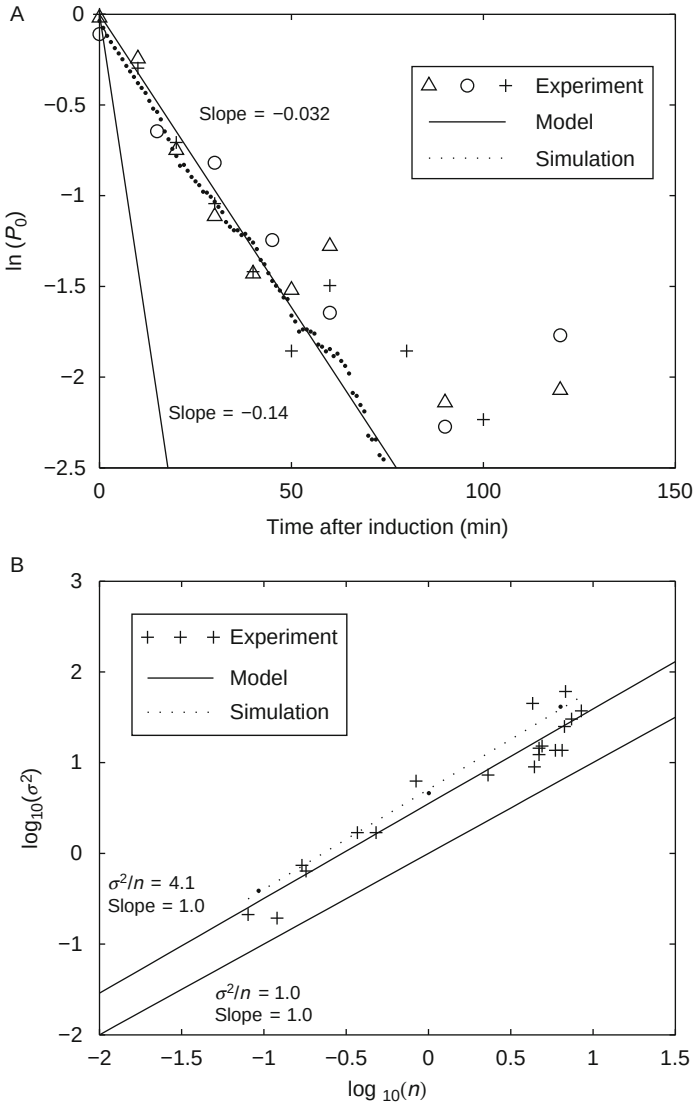

Fig. 8 (*continued*)

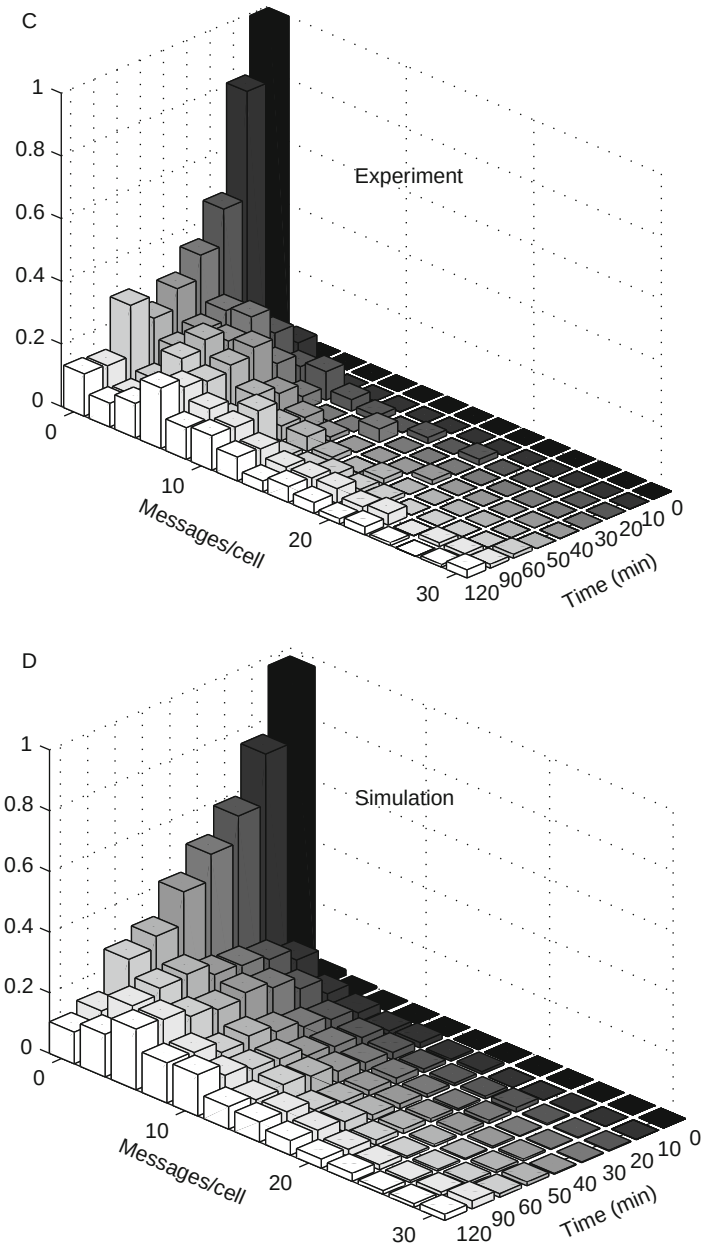

Fig. 8 Population statistics. (A) Fraction of cells having no tagged RNA (P_0) as a function of time after induction t. Data (+, o, Δ) are from the experiments in the previous figure. Also shown (rightmost solid line) is the theoretical prediction of the first-order transcription model $P_0(t) = e^{-k_1 t}$, with the same parameters used in the previous figure. The actual decline is about four times slower, with a rate of $\approx 0.032\ \text{min}^{-1}$ (leftmost solid line). Dotted line: a stochastic simulation of the bursting mRNA model.

is produced. In other words, RNA molecules are produced in "bursts" rather than one at a time. This model is simple enough that one can derive approximations for the expected behavior of σ^2 and of $P_0(t)$. The model reproduces the observed population statistics (Fig. 8A–B). In addition, to implement a fuller version of the model which includes cell growth and division, a stochastic Monte Carlo type simulation was implemented in Matlab and shown to reproduce the experimental results (Fig. 8A–D).

J. Following Transcription Events in Single Cells

To directly test the "2-state" model for transcription, we followed RNA kinetics in individual cells over time. The fluorescence imaging of live cells over long periods of time involves unique challenges in addition to the general issues of sensitivity and resolution discussed above. One problem is keeping the sample in focus for the duration of the experiment. The focus position can be corrected manually—which obviously becomes quite tedious for experiments lasting hours. Alternatively, in microscopy systems equipped with motorized Z axis control, an automated auto-focus routine can be implemented. Such routines typically scan a few horizontal planes and choose the one best focused based on maximization of image contrast. The main challenge of fluorescent imaging over long periods, however, is the limited amount of exciting light (total number of photons) which can be used before the fluoropores are photobleached or the live sample is photo-damaged. The requirement to minimize exposure is in direct conflict with the goal of sampling as many time points as possible, and of obtaining a high signal-to-noise ratio by prolonging exposure time in each sample. The amount of usable photons can be increased by working under anaerobic conditions and by using oxygen scavenging agents when the biological context allows for these features (Neuman *et al.*, 1999). Of course, high sensitivity optics and camera allow shorter exposure times. Nevertheless, a compromise has to be found in the shape of an optimal exposure program which keeps the cells healthy and fluorescent for the required period of time while offering data acquisition at a sufficient rate, with exposure times yielding images of high enough quality to be quantified. The resulting time series data is typically inferior to that obtained by population

(B) Variance (σ^2) versus average ($\langle n \rangle$) of mRNA copy number. The data (+) are from four different experiments at multiple induction levels. Lower solid line is the theoretical prediction based on a Poisson model, with $\sigma^2 = \langle n \rangle$. Upper solid line is a least-mean-square fit of the data to a first-order polynomial. This fit yields a slope of 1.0 (in log–log), implying proportionality of σ^2 to $\langle n \rangle$. The average of $\sigma^2/\langle n \rangle$ is 4.1. Also shown (individual dots and dotted line, least-mean-square fit) are the results of the mRNA-bursting simulation run at various bursting rates (the parameter k_1, corresponding to the experimental induction levels), using the same average burst of 4. (C) Histograms of mRNA copy numbers in the cell at various times after induction. Data is from one of the experiments in A. Starting from an almost uniform population, with most cells having no messages at $t = 0$, the average copy number increases with time, as does the width of the distribution. (D) Histogram resulting from simulation of the mRNA bursting model. Note the similarity with the experimental results.

snapshots. Analyzing it is usually preceded by smoothing with some type of filter (Friedman *et al.*, 2005). The extraction of parameters—for example, the timing and magnitude of discrete events—can be done by eye, or using automated algorithms. Such algorithms could be as simple as "threshold crossing," which counts an event whenever a predetermined signal level is crossed; or more sophisticated, such as so-called hidden Markov processes (McKinney *et al.*, 2006), where assumptions are made regarding the stochastic process underlying the data, and parameter values are determined iteratively based on the maximization of probability.

In the case of transcription, to demonstrate directly the occurrence of bursts and to measure the relevant physiological parameters, we followed transcription of individual messages over time and calculated the statistics of bursts and off-time intervals. Exponentially growing cells expressing MS2-GFP were placed between a cover slip and a 1-mm-nutrient agarose slab containing the required inducers (IPTG and aTc) at 22 °C where they grew and divided normally, with a generation time of ~2 h. We then followed RNA levels in individual cells as they increased during the cell cycle and abruptly dropped at cell division (Fig. 9). The cells exhibited a discrete distribution of measured RNA levels, corresponding to mRNA copy number. No increase in RNA levels was detected when cells were grown without IPTG. Under these conditions, we were also able to show that the rate of decrease in the intensity of individual foci was very low ($<1\ h^{-1}$), in accord with our previous observation that the tagged transcripts are stable.

Figure 9A shows that transcription is characterized by periods of inactivity Δt_{off}, followed by periods of activity Δt_{on}, each producing a random jump of size Δn in the RNA level. Figure 9B shows that the distribution of both Δt_{on} and Δt_{off} are accurately described by exponentials, as expected from the simplest models. The averages are $\langle \Delta t_{On} \rangle \approx 6$ min and $\langle \Delta t_{off} \rangle \approx 37$ min so transcription indeed seems to occur in intense periods, as can also be seen directly in the time series. Figure 9C shows the distribution of Δn from the same dataset, again very well approximated by the predicted geometric or exponential behavior. The statistics are consistent with a bursting model where $\Delta n > 1$ is the most likely event.

K. Spatiotemporal Dynamics of RNA Molecules in the Cell

The same experimental system which was used to measure mRNA numbers in the cell—genetic components, microscopy, image acquisition, and processing—allowed us to investigate the spatiotemporal dynamics of individual mRNA molecules in the cell. Some of the system parameters were modified for that purpose. First, low levels of gene induction were used, so that only ~1 molecule (or at most a few molecules) per cell were present. In addition, since the temporal resolution needed was typically higher than in the RNA counting experiments, image acquisition was performed at a higher frame rate, with the inevitable price of shorter experiments. In our system, the above limitations lead to coverage of the range ~1–1000 s. As for the tools used for data analysis, those came from the fields of nonequilibrium phenomena (e.g., Fourier analysis) and polymer physics (e.g., measurements of mean-squared-displacement).

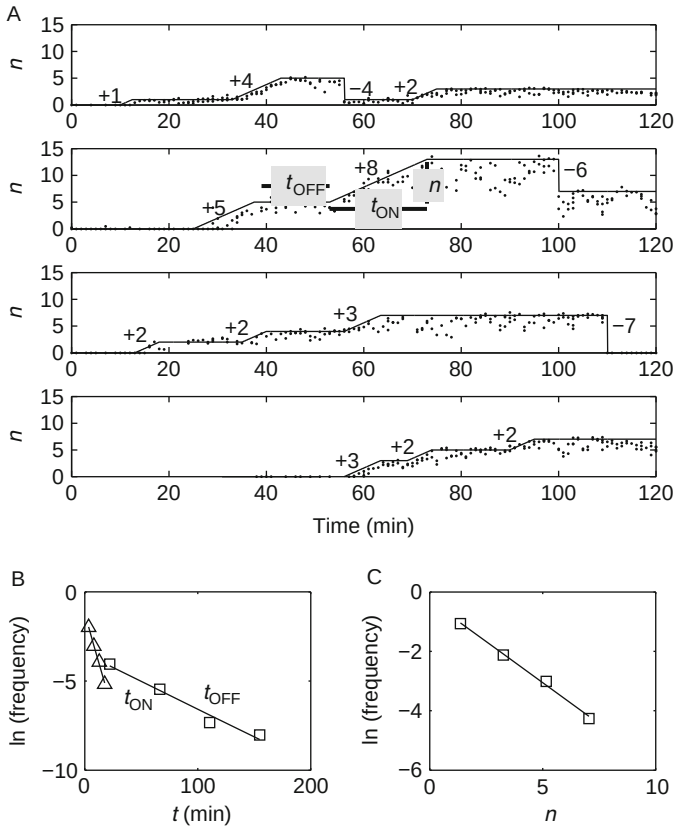

Fig. 9 Induction kinetics in individual cells. (A) Estimated number of transcripts per cell n, as a function of time t, in typical cells. Cells were grown as described in the text. Fluorescent images were taken for 2 h, at 2 frames/min. Dots, raw data. The data were smoothed by taking the maximum value in a 6-sample running window, and then fit by eye to a piecewise linear function (solid line). The fit describes periods of transcriptional inactivity (constant n), separated by transcriptional events, in which RNA is produced at a rate of 1 transcript per 2.5 min. This rate corresponds to a chain elongation rate of ~25 nucleotides/s, in close agreement with our earlier measurements (Golding and Cox, 2004) as well as with the known rate of chain elongation in *Escherichia coli* at 22 °C (Mathews *et al.*, 2000; Ryals *et al.*, 1982). Also marked in the figures are the measured jumps Δn in RNA level following transcription, as well as negative changes in n following cell division. (B) Distribution of inactivity periods (Δt_{OFF}, squares) and activity periods (Δt_{ON}, triangles). Data is from 20 cells and 77 transcription events. Line is a fit to an exponential distribution. Mean Δt_{OFF} is ≈37 min, Mean Δt_{ON} is ≈6 min. Note that Δt_{ON} is equal to Δn times the duration of transcribing 1 message, 2.5 min. (C) Distribution of RNA "jumps" (Δn). Squares are data, line is a fit to an exponential distribution. Same dataset as (B). The mean Δn is ≈2.2.

As before, theoretical modeling and numerical simulations were used in conjunction with experimental data acquisition.

In a typical experiment, ~1 μl from an induced culture was placed under a thin agar slice as before. Cells were imaged as described above. Time-lapse movies were

taken for up to 30 min at 1 frame/s, 200 ms exposure time. For analysis, movies were read into Matlab software. The fluorescent particles were automatically recognized and followed, to yield a time-series of particle coordinates $\mathbf{r}(t) = (x(t), y(t))$ for each RNA molecule.

Most fluorescent spots were found to be located near the center or the 1/4 points of the cell. Measurements of 100 spot positions gave 0.51 ± 0.05 cell length (15 spots) and 0.19 ± 0.07 (85 spots). These numbers correspond well to the location of F plasmids in the cell, as determined by others (Gordon *et al.*, 1997). In most cells, the motion of fluorescent particles was limited to a small area of the cell. Figure 10 is a typical example. Each spot appeared to move randomly but never left its restricted area. The distribution of displacements on the long axis of the cell is bell-shaped, with a half-width of ~50–200 nm. The most natural explanation for these observations is that we are looking at an RNA molecule tethered to DNA during transcription, and possibly afterward (Hamkalo and Miller, 1973). The observed variance is in agreement with the expectation from a simple model of the mRNA chain as a flexible polymer tethered to its DNA template (Golding and Cox, 2004).

In a few cells, we observed a fluorescent "chain" behaving like a typical polymer in solution, stretching and writhing along the axis of the cell (Golding and Cox, 2004). These chains were likely to be single RNA molecules, both because their contour length matched the transcript length and because the total integrated photon counts from the chain area were very close to that of the fluorescent particles observed in other cells. The contour length of the chain increased with time, with average elongation rate of ~15 nm/s (or ~25 nucleotides/s). This rate is in good agreement with the known rate of transcription in *E. coli* at 22 °C (Mathews *et al.*, 2000; Ryals *et al.*, 1982). Thus, the most straightforward explanation for the observed elongation is that we are watching RNA transcription.

The fact that a majority of the transcripts observed in our experiments were localized to the presumed location of transcription relates to the possible existence of "transcription factories" in bacteria. Based on the standard text book picture, one expects a nascent transcript to be released from its DNA template as soon as the terminator site is reached (Neidhardt *et al.*, 1990). However, we found that the number of transcripts which are localized in space—at the known position of their DNA template—is much higher than the value expected from the "immediate release" hypothesis above (data not shown, and see also Golding and Cox, 2004). This suggests the accumulation of mRNA molecules at their site of transcription, as observed previously in eukaryotes (Chuang and Belmont, 2005; Chubb *et al.*, 2006; Janicki *et al.*, 2004). Further studies are needed to better characterize this phenomenon.

We next focused on the motion of mRNA molecules released from their template DNA and free to move in the cytoplasm (Golding and Cox, 2006b). The tagged RNA moves randomly in the cell, spanning the complete cell length multiple times within a 30-min period (Fig. 11). We characterized the motion by measuring the mean squared displacement $\langle \delta^2(\tau) \rangle$, where $\delta = |\mathbf{r}(t+\tau) - \mathbf{r}(t)|$ is the particle

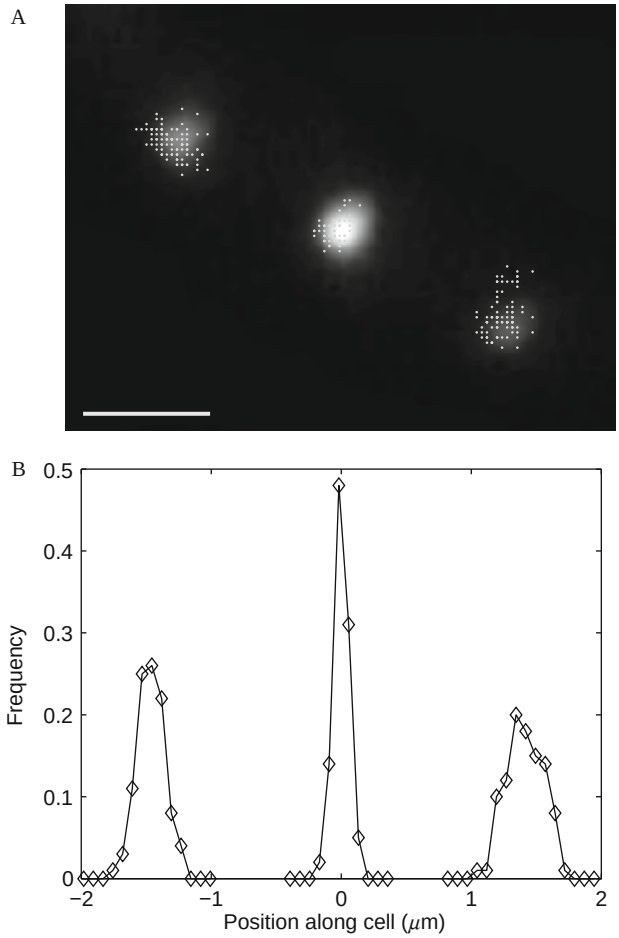

Fig. 10 Localized motion of multiple RNA particles in a cell. (A) The measured locations of three individual spots, superimposed on the epifluoresecne image of the cell. Scale bar, 1 μm. (B) Histogram of spots positions along the cell. Position along the cell was obtained by projecting the spot location (x, y) on the long axis of the cell (x_1): $x_1 = x \cos\theta + y \sin\theta$, where θ is the angle between the long axis of the cell and x axis. Each spot is localized in a small region of the cell, with a bell-shaped distribution of positions. Cells were grown and induced as described in the text. A single cell was tracked for 10 min (1 frame per 2 s, exposure time = 250 ms).

displacement between two time points, and δ^2 is averaged over all pairs of time points with difference τ between them. For Brownian motion, one expects the Einstein–Smoluchowski relation $\langle\delta^2(\tau)\rangle = 2dD\tau$, where d is the spatial dimension and D is the diffusion coefficient of the moving particle (Berg, 1993; Reif, 1965). Measuring $\langle\delta^2(\tau)\rangle$ for multiple RNA molecules, however, revealed very different behavior (Fig. 12): $\langle\delta^2(\tau)\rangle \sim \tau^\alpha$ with $\alpha = 0.70 \pm 0.07$ (21 trajectories). This

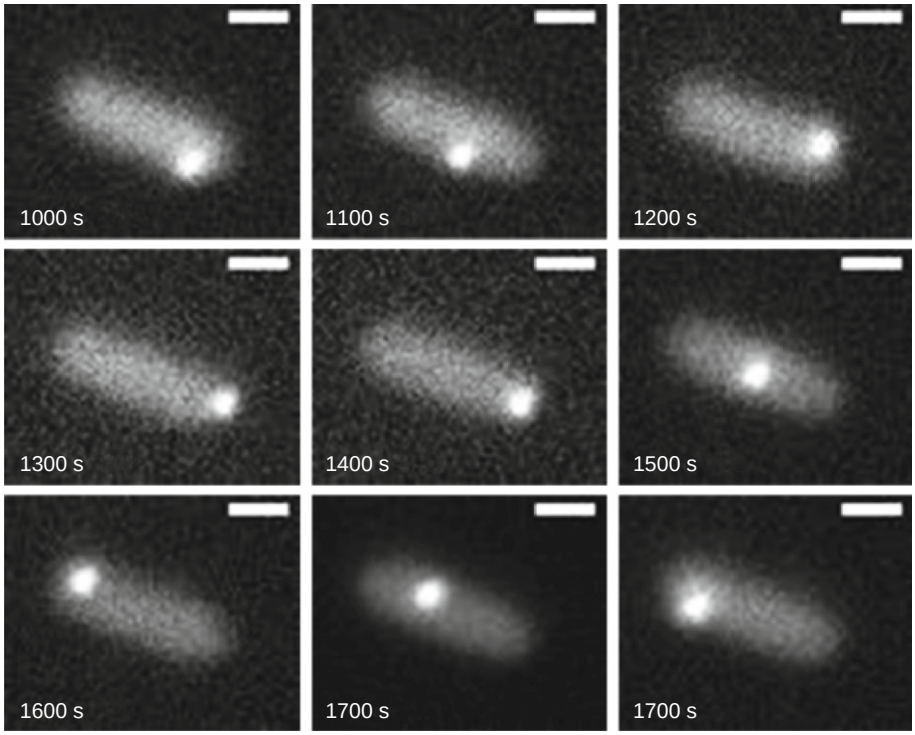

Fig. 11 Motion of a tagged RNA molecule inside an *Escherichia coli* cell. Time-lapse movies were taken for 30 min at 1 frame/s, 200 ms exposure time. Shown is a series of epifluorescent images of the cell. Images are 100 s apart (scale bar = 1 μm.)

subdiffusive behavior is well known in the physics of random systems. It arises when a particle interacts with the random medium in which it is moving. Whereas a particle moving in a uniform medium, whatever the viscosity, constantly makes small jumps due to thermal energy, some types of random media can "trap" the particle in one location for varying and widely distributed periods, allowing only infrequent "jumps" between locations and leading to the observed subdiffusion on the relevant time scale of particle–obstacle interactions (Bouchaud and Georges, 1990; Havlin and Ben-Avraham, 2002; Metzler and Klafter, 2000). This trapping can be geometrical—as in a percolation cluster, whose fractal geometry often causes the particle to get stuck in cul-de-sacs—or it can have a temporal origin, with the particle constantly binding to obstacles, with a broad distribution of binding times.

An additional way of characterizing subdiffusive motion is by measuring the power spectrum of the particle's motion: $P(f) = |X(f)|^2$ where $X(f)$ is the Fourier transform of the particle position $x(t)$ (and similarly for $y(t)$). The power spectrum is equal to the Fourier transform of the autocorrelation function, and thus characterizes the particle's "memory" of its previous positions. Under these

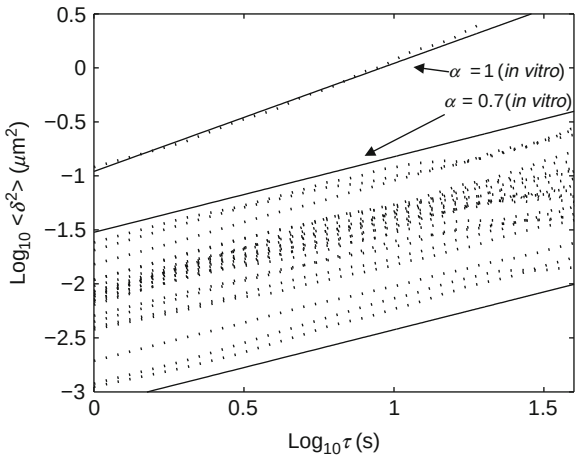

Fig. 12 Subdiffusive motion of RNA molecules in the cell. The vector $\mathrm{r}(t) = (x(t), y(t))$ was used to calculate the mean square displacement as a function of time interval: $\langle \delta^2(\tau) \rangle$, where $\delta = |r(t+\tau) - r(t)|$ and averaging is performed over all pairs of time points (t_1, t_2) obeying $|t_1 - t_2| = \tau$. The mean squared displacement $\langle \delta^2 \rangle$ of the molecule is plotted as a function of the time interval between measurements τ. Different trajectories (total of 23 trajectories from 3 different experiments) are shown as a dotted line. Solid lines = slope 0.7. Deviations from the 0.7 slope at longer times are due to the effect of limited cell size, and the averaging over a smaller number of position pairs. Also shown in the figure is a typical plot of $\langle \delta^2(\tau) \rangle$ for an RNA particle diffusing in 70% glycerol. In this case, the motion is normal diffusion ($\alpha = 1.04 \pm 0.03$, 4 trajectories) as demonstrated by the solid line with slope 1.

assumptions the power spectrum should obey a power-law: $P(f) \sim f^{-(1+\alpha)}$, where α is the subdiffusive exponent. This behavior is indeed observed, yielding an additional estimate of α in our system of 0.77 ± 0.03 (Fig. 13).

Next, we modified various physiological parameters and examined the effect on mRNA motion. This was done to obtain insight into the possible sources of the anomalous diffusion in the cytoplasm. The modifications include features of the tagged RNA molecules: presence or absence of ribosome-binding-site sequence and length of the tagged RNA molecule; growth conditions: growth rate and growth in the presence of tetracycline [inhibits protein synthesis by blocking ribosomal binding of aminoacyl tRNA (Sambrook and Russell, 2001)], Chloramphrenicol [inhibits translation by blocking peptidyl transferase (Sambrook and Russell, 2001)], and Nalidixic acid [inhibits DNA supercoiling by binding to DNA gyrase (Neidhardt *et al.*, 1990)]; and RNA movement in strains deficient in cytoskeletal elements: MreB, the prokaryotic actin-like protein, and FtsZ, the tubulin homologue. This variety of "control parameters" demonstrates again the strength of combining the tools of classical microbiology and genetics with quantitative measurements. The experiential findings led us to suggest a theoretical framework for understanding the random motion of mRNA and other macromolecules in the cell, in the general context of polymer motion in a crowded

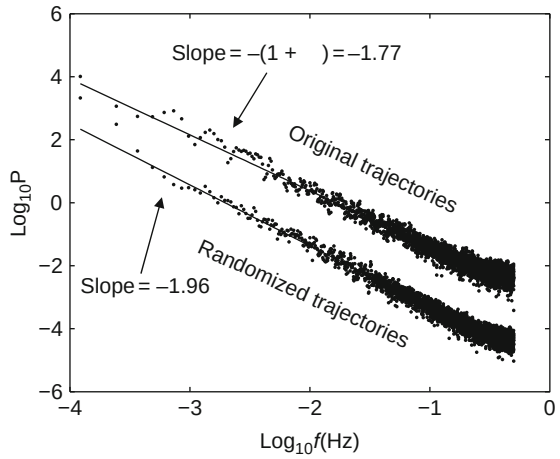

Fig. 13 Power spectrum $P(f)$ of RNA trajectories. The complete set of $x(t)$ and $y(t)$ trajectories were concatenated, and the power spectral density of the combined trajectory was calculated using the Welch method as implemented in Matlab. Dots = measured $P(f)$; solid line = linear fit yielding slope -1.77 ± 0.03. A calculation using only the $x(t)$ or $y(t)$ coordinates separately gave similar results (data not shown). As an additional test for the validity of the spectral density calculation, the trajectory steps ($\Delta x(t)$, $\Delta y(t)$) were randomly permutated and then reintegrated (Segev *et al.*, 2002). The resulting new trajectory should exhibit a random walk behavior, with $P(f) \sim f^{-2}$ (Mantegna *et al.*, 2000). The calculated spectral density (dots) is in agreement with this prediction, yielding a slope of -1.96 ± 0.04.

disordered medium (Banks and Fradin, 2005; Golding and Cox, 2006b). In addition, we explored theoretically the possible implications of cellular sub-diffusion on gene activity, in particular the kinetics of transcription factors finding their DNA targets (Golding and Cox, 2006b).

IV. Summary and General Lessons for Following Discrete Events

As can be gathered from the description above, the work discussed here employs a set of skills broader than those generally used within a single discipline. First, designing and implementing the genetic system requires the full arsenal of molecular biology and microbiology. Next comes the real-time imaging of live cells using high-resolution microscopy. Quantitative data are obtained from the images using programs written by the user, using the engineer's toolbox of image processing. Similarly, data analysis with signal-processing tools is performed using custom written applications. The use of "home made" programming serves to provide maximum flexibility while still allowing high-throughput data acquisition and analysis. The experimental effort is accompanied by theory, using the apparati of dynamical systems theory, stochastic processes, and nonequilibrium phenomena, with a constant feedback between the experimental and theoretical endeavors.

Acknowledgments

We thank J. Paulsson, R. Segev, R. Austin, J. Puchalla, and P. Wolanin for generous advice; D. Peabody, R. Tsien, P. Wolanin, K. Forrest, and R. Weisberg for stains and plasmids; L. Guo for technical assistance; and all members of the Cox laboratory.

This work was supported by the STC Program of The National Science Foundation under Agreement No. ECS-9876771 and in part by National Institute of Health grant HG 001506. I.G. was supported by The Lewis Thomas Fellowship from Princeton University.

References

Albertini, A. M., Hofer, M., Calos, M. P., and Miller, J. H. (1982). On the formation of spontaneous deletions: The importance of short sequence homologies in the generation of large deletions. *Cell* **29,** 319–328.

Arkin, A., Ross, J., and McAdams, H. H. (1998). Stochastic kinetic analysis of developmental pathway bifurcation in phage lambda-infected *Escherichia coli* cells. *Genetics* **149,** 1633–1648.

Banks, D. S., and Fradin, C. (2005). Anomalous diffusion of proteins due to molecular crowding. *Biophys. J.* **89,** 2960–2971.

Beckwith, J. R., and Zipser, D. (1970). Cold Spring Harbor Laboratory. The Lactose operon. Cold Spring Harbor Laboratory, Cold Spring Harbor, N.Y.

Belmont, A. S., and Straight, A. F. (1998). *In vivo* visualization of chromosomes using lac operator-repressor binding. *Trends Cell Biol.* **8,** 121–124.

Benzer, S. (1953). Induced Synthesis of Enzymes in Bacteria Analyzed at the Cellular Level. *Biochim. Biophys. Acta* **11,** 383–395.

Berg, H. C. (1993). Random walks in biology Princeton University Press, Princeton, N.J.

Bertrand, E., Chartrand, P., Schaefer, M., Shenoy, S. M., Singer, R. H., and Long, R. M. (1998). Localization of ASH1 mRNA particles in living yeast. *Mol. Cell.* **2,** 437–445.

Bouchaud, J. P., and Georges, A. (1990). Anomalous Diffusion in Disordered Media - Statistical Mechanisms, Models and Physical Applications. *Phys. Rep.-Rev. Sect. of Phys. Lett.* **195,** 127–293.

Bzymek, M., and Lovett, S. T. (2001). Instability of repetitive DNA sequences: The role of replication in multiple mechanisms. *Proc. Natl. Acad Sci. USA* **98,** 8319–8325.

Campbell, R. E., Tour, O., Palmer, A. E., Steinbach, P. A., Baird, G. S., Zacharias, D. A., and Tsien, R. Y. (2002). A monomeric red fluorescent protein. *Proc. Natl. Acad Sci. USA* **99,** 7877–7882.

Chuang, C. H., and Belmont, A. S. (2005). Close encounters between active genes in the nucleus. *Genome Biol.* **6,** 237.

Chubb, J. R., Trcek, T., Shenoy, S. M., and Singer, R. H. (2006). Transcriptional pulsing of a developmental gene. *Curr. Biol.* **16,** 1018–1025.

Clark, A. J., and Margulies, A. D. (1965). Isolation and Characterization of Recombination-Deficient Mutants of *Escherichia Coli* K12. *Proc. Natl. Acad Sci. USA* **53,** 451–459.

Cormack, B. P., Valdivia, R. H., and Falkow, S. (1996). FACS-optimized mutants of the green fluorescent protein (GFP). *Gene* **173,** 33–38.

Di Ventura, B., Lemerle, C., Michalodimitrakis, K., and Serrano, L. (2006). From *in vivo* to *in silico* biology and back. *Nature* **443,** 527–533.

Ellis, E. L., and Delbruck, M. (1939). The growth of bacteriophage. *J. Gen. Physiol.* **22,** 365–384.

Ellis, R. J. (2001). Macromolecular crowding: Obvious but underappreciated. *Trends Biochem. Sci.* **26,** 597–604.

Forrest, K. M., and Gavis, E. R. (2003). Live imaging of endogenous RNA reveals a diffusion and entrapment mechanism for nanos mRNA localization in Drosophila. *Curr. Biol.* **13,** 1159–1168.

Friedman, N., Vardi, S., Ronen, M., Alon, U., and Stavans, J. (2005). Precise temporal modulation in the response of the SOS DNA repair network in individual bacteria. *PLoS Biol.* **3,** e238.

Fusco, D., Accornero, N., Lavoie, B., Shenoy, S. M., Blanchard, J. M., Singer, R. H., and Bertrand, E. (2003). Single mRNA molecules demonstrate probabilistic movement in living mammalian cells. *Curr. Biol.* **13,** 161–167.

Golding, I., and Cox, E. C. (2004). RNA dynamics in live *Escherichia coli* cells. *Proc. Natl. Acad Sci. USA* **101,** 11310–11315.

Golding, I., and Cox, E. C. (2006). Eukaryotic transcription: What does it mean for a gene to be 'on'? *Curr. Biol.* **16,** R371–R373.

Golding, I., and Cox, E. C. (2006). Physical nature of bacterial cytoplasm. *Phys. Rev. Lett.* **96,** 098102.

Golding, I., Paulsson, J., Zawilski, S. M., and Cox, E. C. (2005). Real-time kinetics of gene activity in individual bacteria. *Cell* **123,** 1025–1036.

Gonzalez, R. C., Woods, R. E., and Eddins, S. L. (2004). Digital Image processing using MATLAB Pearson/Prentice Hall, Upper Saddle River, NJ.

Gordon, G. S., Sitnikov, D., Webb, C. D., Teleman, A., Straight, A., Losick, R., Murray, A. W., and Wright, A. (1997). Chromosome and low copy plasmid segregation in *E. coli*: Visual evidence for distinct mechanisms. *Cell* **90,** 1113–1121.

Gordon, S., Rech, J., Lane, D., and Wright, A. (2004). Kinetics of plasmid segregation in *Escherichia coli*. *Mol. Microbiol.* **51,** 461–469.

Hamkalo, B. A., and Miller, O. L., Jr. (1973). Electronmicroscopy of genetic activity. *Annu. Rev. Biochem.* **42,** 379–396.

Havlin, S., and Ben-Avraham, D. (2002). Diffusion in disordered media. *Adv. Phy.* **51,** 187–292.

Janicki, S. M., *et al*. (2004). From silencing to gene expression: Real-time analysis in single cells. *Cell* **116,** 683–698.

Johansson, H. E., Dertinger, D., LeCuyer, K. A., Behlen, L. S., Greef, C. H., and Uhlenbeck, O. C. (1998). A thermodynamic analysis of the sequence-specific binding of RNA by bacteriophage MS2 coat protein. *Proc. Natl. Acad Sci. USA* **95,** 9244–9249.

Kaern, M., Elston, T. C., Blake, W. J., and Collins, J. J. (2005). Stochasticity in gene expression: From theories to phenotypes. *Nat. Rev. Genet.* **6,** 451–464.

Kalir, S., McClure, J., Pabbaraju, K., Southward, C., Ronen, M., Leibler, S., Surette, M. G., and Alon, U. (2001). Ordering genes in a flagella pathway by analysis of expression kinetics from living bacteria. *Science* **292,** 2080–2083.

Lau, I. F., Filipe, S. R., Soballe, B., Okstad, O. A., Barre, F. X., and Sherratt, D. J. (2003). Spatial and temporal organization of replicating *Escherichia coli* chromosomes. *Mol. Microbiol.* **49,** 731–743.

Le, T. T., Harlepp, S., Guet, C. C., Dittmar, K., Emonet, T., Pan, T., and Cluzel, P. (2005). Real-time RNA profiling within a single bacterium. *Proc. Natl. Acad Sci. USA*.

Lehman, I. R., Bessman, M. J., Simms, E. S., and Kornberg, A. (1958). Enzymatic synthesis of deoxyribonucleic acid. I. Preparation of substrates and partial purification of an enzyme from *Escherichia coli*. *J. Biol. Chem.* **233,** 163–170.

Li, Y., and Altman, S. (2004). Polarity effects in the lactose operon of *Escherichia coli*. *J. Mol. Biol.* **339,** 31–39.

Lutz, R., and Bujard, H. (1997). Independent and tight regulation of transcriptional units in *Escherichia coli* via the LacR/O, the TetR/O and AraC/I1-I2 regulatory elements. *Nucleic Acids Res.* **25,** 1203–1210.

Mathews, C. K., Van Holde, K. E., and Ahern, K. G. (2000). "Biochemistry". Benjamin Cummings San Francisco, Calif.

McKinney, S. A., Joo, C., and Ha, T. (2006). Analysis of single-molecule FRET trajectories using hidden Markov modeling. *Biophys. J.* **91,** 1941–1951.

Metzler, R., and Klafter, J. (2000). The random walk's guide to anomalous diffusion: A fractional dynamics approach. *Phy. Rep.-Rev. Sect. of Phys. Lett.* **339,** 1–77.

Miller, J. H. (1992). "A Short Course in Bacterial Genetics: A Laboratory Manual and Handbook for *Escherichia coli* and Related Bacteria." Cold Spring Harbor Laboratory Press, Plainview, N.Y.

Neidhardt, F. C. (1996). "*Escherichia coli* and Salmonella: Cellular and Molecular Biology." ASM Press, Washington, D.C.

Neidhardt, F. C., Ingraham, J. L., and Schaechter, M. (1990). "Physiology of the Bacterial Cell: A Molecular Approach." Sinauer Associates, Sunderland, Mass.

Neuman, K. C., Chadd, E. H., Liou, G. F., Bergman, K., and Block, S. M. (1999). Characterization of photodamage to *Escherichia coli* in optical traps. *Biophys. J.* **77,** 2856–2863.

Novick, A., and Weiner, M. (1957). Enzyme Induction as an All-or-None Phenomenon. *Proc. Natl. Acad Sci. USA* **43,** 553–566.

Pardee, A. B., Jacob, F., and Monod, J. (1958). [The role of the inducible alleles and the consrtutive alleles in the synthesis of beta-galactosidase in zygotes of *Escherichia coli*.]. *C R Hebd Seances Acad Sci.* **246,** 3125–3128.

Paulsson, J. (2004). Summing up the noise in gene networks. *Nature* **427,** 415–418.

Peabody, D. S. (1989). Translational repression by bacteriophage MS2 coat protein does not require cysteine residues. *Nucleic Acids Res.* **17,** 6017–6027.

Peabody, D. S. (1990). Translational repression by bacteriophage MS2 coat protein expressed from a plasmid. A system for genetic analysis of a protein-RNA interaction. *J. Biol. Chem.* **265,** 5684–5689.

Peabody, D. S. (1997). Subunit fusion confers tolerance to peptide insertions in a virus coat protein. *Arch. Biochem. Biophys.* **347,** 85–92.

Peabody, D. S., and Ely, K. R. (1992). Control of translational repression by protein-protein interactions. *Nucleic Acids Res.* **20,** 1649–1655.

Peabody, D. S., and Lim, F. (1996). Complementation of RNA binding site mutations in MS2 coat protein heterodimers. *Nucleic Acids Res.* **24,** 2352–2359.

Ptashne, M. (1992). A Genetic Switch: Phage Lambda and Higher Organisms. Cell Press: Blackwell Scientific Publications, Cambridge, Mass.

Reif, F. (1965). "Fundamentals of Statistical and Thermal Physics." McGraw-Hill, New York.

Robinett, C. C., Straight, A., Li, G., Willhelm, C., Sudlow, G., Murray, A., and Belmont, A. S. (1996). *In vivo* localization of DNA sequences and visualization of large-scale chromatin organization using lac operator/repressor recognition. *J. Cell Biol.* **135,** 1685–1700.

Ronen, M., Rosenberg, R., Shraiman, B. I., and Alon, U. (2002). Assigning numbers to the arrows: Parameterizing a gene regulation network by using accurate expression kinetics. *Proc. Natl. Acad Sci. USA* **99,** 10555–10560.

Rosenfeld, N., Young, J. W., Alon, U., Swain, P. S., and Elowitz, M. B. (2005). Gene regulation at the single-cell level. *Science* **307,** 1962–1965.

Ryals, J., Little, R., and Bremer, H. (1982). Temperature dependence of RNA synthesis parameters in *Escherichia coli*. *J. Bacteriol.* **151,** 879–887.

Sambrook, J., and Russell, D. W. (2001). "Molecular Cloning: A Laboratory Manual." Cold Spring Harbor Laboratory Press, Cold Spring Harbor, N.Y.

Shaevitz, J. W., Abbondanzieri, E. A., Landick, R., and Block, S. M. (2003). Backtracking by single RNA polymerase molecules observed at near-base-pair resolution. *Nature* **426,** 684–687.

Stillman, B. (1994). Initiation of chromosomal DNA replication in eukaryotes. Lessons from lambda. *J. Biol. Chem.* **269,** 7047–7050.

Witkin, E. M. (1976). Ultraviolet mutagenesis and inducible DNA repair in *Escherichia coli*. *Bacteriol. Rev.* **40,** 869–907.

Wu, J. Q., and Pollard, T. D. (2005). Counting cytokinesis proteins globally and locally in fission yeast. *Science* **310,** 310–314.

Zaslaver, A., Bren, A., Ronen, M., Itzkovitz, S., Kikoin, I., Shavit, S., Liebermeister, W., Surette, M. G., and Alon, U. (2006). A comprehensive library of fluorescent transcriptional reporters for *Escherichia coli*. *Nat. Met.* **3,** 623–628.

CHAPTER 9

Counting Proteins in Living Cells by Quantitative Fluorescence Microscopy with Internal Standards

Jian-Qiu Wu,[*] Chad D. McCormick,[†] and Thomas D. Pollard[†,‡]

[*]Department of Molecular Genetics and Department of Molecular and Cellular Biochemistry
The Ohio State University
Columbus, Ohio 43210

[†]Department of Molecular Biophysics and Biochemistry
Yale University
New Haven, Connecticut 06520

[‡]Department of Molecular, Cellular and Developmental Biology and Department of Cell Biology
Yale University
New Haven, Connecticut 06520

METHODS IN CELL BIOLOGY, VOL. 89

0091-679X/08 $35.00
DOI: 10.1016/S0091-679X(08)00609-2

Abstract

This chapter describes how a confocal microscope can be treated as a spectrophotometer to measure the absolute number of fluorescent molecules in live cells (Wu and Pollard, 2005).[1] The method provides dynamic range of over three orders of magnitude for counting the number of molecules in a single cell. We present a step-by-step guide to measure concentrations *in vivo*, explaining many of the practical considerations for using this technique. This chapter is meant as a resource for cell biologists, biochemists, and biophysicists interested in quantifying macromolecules involved in their favorite molecular pathways in live cells.

I. Introduction

Understanding the molecular mechanisms of many complicated cellular processes requires quantifying the absolute amount of the relevant components in cells, but this information is rarely available. Concentrations are necessary to determine the various reaction rates during these cellular processes, to reveal the stoichiometries of protein complexes, and to formulate mathematical models for rigorous tests of mechanistic hypotheses. A specific antibody can be used to determine the total number of a particular protein in a sample of cells [e.g., see Higgs and Pollard (2000)]. Epitope tagging and immunoblotting can be used on a larger scale to estimate the abundance of proteins (Ghaemmaghami *et al.*, 2003). Methods like these are capable of measuring total protein concentrations (Table I). Here we describe a method to use quantitative immunoblotting to calibrate a confocal fluorescence microscope to measure both the global and the local concentrations of proteins tagged with fluorescent proteins and expressed at native levels. We used the method to quantitate 28 different cytoskeletal and signaling proteins that participate in cytokinesis in the fission yeast *Schizosaccharomyces pombe* (Wu and Pollard, 2005). This approach is applicable to a medium-scale analysis of numerous proteins participating in any cellular process.

[1] This chapter is based on the article by Wu and Pollard (2005).

Table I
Sample of Methods to Measure Cellular Protein Concentrations

References	Calibration method	Proteins measured	Measurement	Native level	Test for function	Advantage or main feature	Experimental error
Biochemical or biophysical methods							
Higgs and Pollard (2000); Kim *et al.*, (2004); many others	Quantitative immunoblots of whole cells with antibodies to native proteins with pure protein standards	WASp; actin, capping protein; many others	Molecules per gram of cells or global concentration	Yes	N/A	Simple and accurate for global concentration if antibodies are available	
Ghaemmaghami *et al.*, (2003)	Quantitative immunoblots of whole yeast cells expressing proteins with C-terminal TAP-tags from genome under the control of native promoters with pure protein standards	4250 proteins in budding yeast	Molecules per cell	Yes	No	High throughput	Median variation of two fold
Huang *et al.*, 2007	Count single molecules labeled with fluorescent antibody of cells lysed in a microfluidic device	β_2-adrenergic receptor and Phycobili protein	Molecules per cell	No	N/A	Good for low-copy proteins; requires antibody and specialized instrument	
Mutch *et al.*, 2007	Use single-molecule intensity distributions to deconvolve the number of molecules in a fluorescent puncta	Avidin–biocytin	Molecules per puncta	No	No	Single-molecule measurement on TIRF microscopy	
Imaging fluorescence intensity with external standards							
Hirschberg *et al.*, 1998, 2000	Fluorescence of external GFP standards, bulk samples, or solution in oil droplet	A transmembrane viral protein VSVG-GFP, in the secretory pathway of COS7 cells	Molecular flux from ER to Golgi apparatus to plasma membrane	N/A	N/A	Measures wide range of concentrations	
Patterson *et al.*, 1998; Piston *et al.*, 1999	Quantitative immunoblot and fluorescence imaging of purified GFP in deep-well slide or in PAGE gel on slide	GFP-TATA binding protein expressed on plasmids or at native level in budding yeast	Molecules per cell	Native and varied levels	Yes	Compared in vivo and in vitro methods	Molecules per cell from imaging is 10x less than immunoblots

(*continues*)

Table I *(continued)*

References	Calibration method	Proteins measured	Measurement	Native level	Test for function	Advantage or main feature	Experimental error
Chiu *et al.*, 2001; Khakh *et al.*, 2001	Imaging of 80–120 μm transparent beads with calibrated surface densities of His-GFP	GFP-P2X2 receptor in hippocampal neurons	Density of molecules	No	No	Measures wide range of concentrations	
Dundr *et al.*, 2002	External rotavirus-like particles with 120 GFP molecules	RNA polymerase I and II transiently expressed in CMT3 cells	Molecules per cell	No	No	Simple, rapid, noninvasive	SEM/mean: 30–70%; a factor of 2
Xu *et al.*, 2003	Imaging of fluorescence of a dilution series of PH-GFP on a microscope slide	PH-GFP in N1E-115 neuoblastoma cells	Concentrations	No	No	No immunoblotting is required	
Imaging fluorescence with internal standards							
Howell *et al.*, 2004	Low-level expression of GFP-fusion proteins, endogenous protein numbers measured by quantitative immunofluorescence	6 spindle checkpoint proteins in PtK2 cells	Molecules, concentrations and rate constants	No	No	Exchange rates measured by FRAP	Underestimation less than fivefold
Wu and Pollard, 2005	Molecules per cell measured by quantitative immunoblots with antibodies against YFP in fission yeast cells expressing YFP-fusion proteins from the genome under the control of native promoters; whole cell fluorescence measured by microscopy and flow cytometry	28 cytokinesis proteins	Total molecules and global[a] and local concentrations	Yes	Yes	Measures absolute numbers of proteins expressed at native levels globally and locally in live cells	Within a factor of 2
Ratio imaging							
Robinson *et al.*, 2002	Ratio of local to total fluorescence of GFP-tagged protein	Myosin II in Dictyostelium	Local concentration	No	Yes	Local concentration as fraction of total	
Joglekar *et al.*, 2006, 2008	Ratio of GFP fluorescence to internal standard GFP-Cse4p fluorescence in images	~30 kinetochore proteins	Molecules per kinetochore	Yes	Not reported	Requires known numbers of an internal GFP-marker	~7%

[a] Corrected for intracellular volumes occupied by organelles and ribosomes to obtain global cytoplasmic concentrations

II. Experimental Methods

A. Selection of Fluorescent Proteins

Several factors have to be considered in choosing the appropriate fluorophore for labeling proteins of interest *in vivo* (Shaner *et al.*, 2005). Monomeric forms of fluorescent proteins (e.g., YFP or GFP containing the A206K mutation) or tandem copies of these proteins should be used to limit aggregation of the fusion proteins in cells and ensure enough signal-to-noise ratio. Care must be taken to minimize interference of cellular autofluorescence with the emission of fluorescent proteins. The autofluorescence of wild-type *S. pombe* cells is much lower with excitation at 514-nm (the excitation wavelength of monomeric YFP, mYFP) than at 442-nm (for mCFP) or 488-nm (for mEGFP), which is critical for measuring weak signals. A careful balance between photostability and brightness of the fluorescent protein is crucial for maximizing signal-to-noise ratio. The mCFP signal is generally weaker than mEGFP, mYFP, and RFPs. The new RFP constructs mCherry and tdTomato are more photostable and brighter than mRFP1.

Fusion proteins should function normally in the cell (see Section II.C). However, we have found that proteins tagged with mCherry or tdTomato are less functional than their mEGFP and mYFP-fusion protein counterparts by inspecting the phenotypes and crossing these tagged strains with strains carrying mutations in other genes. Thus, we chose mYFP for our measurements.

B. Construction of Fluorescent Fusion Proteins

Fusion proteins can be expressed either from their chromosomal loci under the control of a native promoter in some cells including fission yeast or ectopically from a plasmid or after integration elsewhere in the genome. Making functional proteins through homologous recombination is preferred, as all of the targeted protein in the cell is labeled identically and competition with the wild-type protein is avoided. In fission yeast *S. pombe* (Bähler *et al.*, 1998) and budding yeast *S. cerevisiae* (Longtine *et al.*,1998), PCR-based gene targeting is very efficient and straightforward using primers with 40–80 bp identical to the target gene. Tagging at the C-terminus is usually attempted first via modular templates as it perturbs protein expression the least (Bähler *et al.*,1998; Longtine *et al.*, 1998). If a fusion protein is not functional, one may add to the targeting primers linkers between the GFP-variant and the protein of interest. Creation of some functional fusion proteins may require tagging the N-terminus under the control of a native promoter (Wu *et al.*,2003). Homologous recombination has been improved dramatically in other fungi by deletion of the protein KU70, which is crucial for nonhomologous end joining (Krappmann *et al.*, 2006; Meyer *et al.*, 2007; Nayak *et al.*, 2006; Ninomiya *et al.*, 2004; Takahashi *et al.*, 2006). This suggests that it may be possible to manipulate genetically other model organisms to increase the efficiency of homologous recombination for gene targeting and constructing fluorescent fusion proteins.

C. Verification That Fluorescent Fusion Proteins Are Functional

It is essential to use functional fusion proteins to measure protein concentrations accurately. We tested the functionality of fluorescent fusion proteins by screening for morphological defects and testing for synthetic genetic interactions in haploid strains with a fusion protein gene replacing the wild-type gene in the genome under the control of the native promoter. First, we tested all of the strains dependent on fusion proteins for their ability to form normal colonies and for wild-type morphology during growth on both minimal medium and rich medium at temperatures from 18 to 36 °C. Second, we crossed each strain dependent on a fluorescent fusion protein with mutant strains that are known to reveal a deleterious phenotype when combined with mutations in the gene for the tagged protein. The absence of such a "synthetic phenotype" is strong evidence that the fluorescent protein tag does not compromise the function of the protein of interest. Some proteins tagged with mYFP were not fully functional, so these constructs could not be used for *in vivo* protein quantification.

The effects of tagging on the protein expression level should be assessed. If an antibody against the native protein is available, the expression level can be measured on immunoblots (see Section II.F) of wild-type cells and cells expressing the fusion protein.

D. Culture Conditions for Fission Yeast Cells

We grew cells in rich liquid medium YE5S (for 1 liter: 980 ml dd H_2O, 5 g Difco **Y**east **E**xtract, 30 g dextrose, 225 mg each of the **5 S**upplements adenine, uracil, leucine, histidine, and lysine). Cells from −80 °C frozen stocks were streaked onto YE5S plates to grow colonies at 25 °C for 2–4 days. We then inoculated cells from these colonies into 5–15 ml of YE5S ($OD_{595} = \sim 0.1$) in a 50 ml baffled flask and incubated in the dark (shielded with aluminum foil) in an orbital water bath at a speed of 200 rpm at 25 °C at a density of $1–10 \times 10^6$ cells/ml for 36–48 h. We used cells from cultures of $OD_{595} = 0.1 – 0.5$ ($2 – 10 \times 10^6$ cells/ml) for microscopy and $OD_{595} = 0.30 – 0.45$ ($6 – 9 \times 10^6$ cells/ml) for immunoblotting.

E. Cloning and Purification of 6His-mYFP

We used purified mYFP to construct standard curves to calibrate quantitative immunoblots. These immunoblots were used to measure the number of molecules of fluorescent fusion proteins in the strains used to calibrate the fluorescence microscope. The coding sequence of mYFP in plasmid pFA6a-mYFP-kanMX6 (JQW86) was amplified by PCR using primers 5′-ACG GAT CCC CCG GGT TAA TTA ACA GTA AAG G-3′ (forward) and 5′-GTG GTC GAC CTA TTT GTA TAG TTC ATC CAT GC-3′ (reverse) and cloned into the plasmid vector pQE80 digested with *Bam* HI and *Sal* I to obtain the expression construct pQE80-6His-mYFP (JQW111). The 6His-mYFP was expressed in *Escherichia coli* BL21

(DE3) pLysS cells (Novagen) and purified by affinity chromatography (Piston *et al.*, 1999) on a TALON Metal Affinity column and ion exchange chromatography on a Mono-Q column as outlined below:

1. Grow cells transformed with the pQE80-6His-mYFP plasmid in Terrific Broth containing 100 μg/ml Ampicillin and 25 μg/ml Chloramphenicol. Dilute 3 ml of cells from a small culture into 300 ml of fresh medium and grow in a shaker at 37 °C for ~12 h. Dilute the cells tenfold and grow for ~3 h to $OD_{600} = 0.80$ at 25 °C in the dark.
2. Add 100 μl 1-M isopropylthio-β-D-galactopyranoside to a 1-liter culture to induce expression of 6His-mYFP while the cells are incubated with shaking in the dark at 25 °C for about 8 hours until they reach a final $OD_{600} = 3.0$.
3. Harvest the cells by centrifugation and store the pellet frozen at −80 °C.
4. Thaw frozen pellets and resuspend the cells in extraction buffer [50 mM Na_2HPO_4, 300 mM NaCl, 10 mM imidazole, 10 mM β-mercaptoethanol, 1 mM phenylmethylsulfonyl fluoride (PMSF), an EDTA-free protease inhibitor tablet (Roche Diagnostics, Indianapolis, IN)/50 ml, adjusted to pH 8.0 with NaOH].
5. Lyse the cells on ice by sonication using Branson S450 sonicator (Model S102) with maximum output and 50% duty. Centrifuge the lysate at 30,000×*g* for 20 min, followed by 50,000×*g* for 20 min at 4 °C.
6. Load the cleared cell extract onto a 5-ml (bed volume) TALON Metal Affinity column (BD Biosciences, Palo Alto, CA), wash with 100 ml of extraction buffer at 1.5 ml/min, and elute with ~15 ml of elution buffer (50 mM Na_2HPO_4, 300 mM NaCl, 200 mM imidazole, 10 mM β-mercaptoethanol, pH 8.0) at 0.5 ml per min.
7. Dialyze the eluted protein against 20 mM Tris, 25 mM NaCl, 1 mM dithiothreitol (DTT), 0.01% NaN_3, pH 8.1 and apply to a 1 ml Mono-Q column (Amersham Biosciences, Piscataway, NJ) equilibrated with the same buffer. Elute the protein from the column with a 75-ml linear gradient of 0.025–1 M NaCl in the sample buffer.
8. Dialyze the purified 6His-mYFP against 20 mM HEPES, 50 mM KCl, 1 mM EDTA, 1 mM DTT, and 0.01% NaN_3, pH 7.5 at 4 °C. Change the buffer every 4 days during storage. Alternatively, 6His-mYFP can be kept in small aliquots at −80 °C before using.
9. Determine the protein concentration by absorbance at 514 nm using an extinction coefficient of 79,000 M^{-1} cm^{-1} (Zacharias *et al.*, 2002).

F. Quantitative Immunoblots of *S. pombe* Cell Extracts

We used immunoblots with an antibody to YFP to quantitate the amount of mYFP-fusion protein in known number of cells (Fig. 1). The YFP provided an epitope tag for the protein of interest, which was expressed from its native promoter. The fusion protein was the only source of YFP in the cell. The protocol follows:

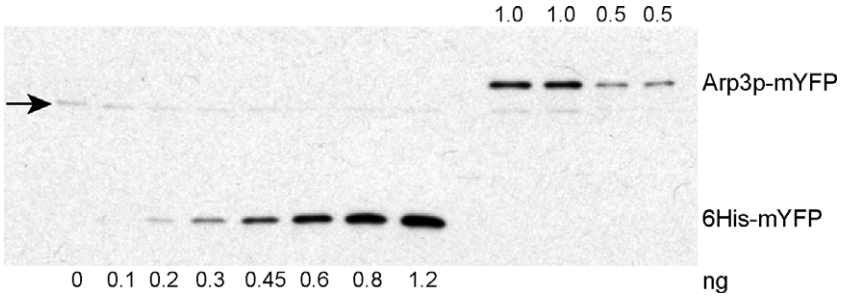

Fig. 1 Quantitation of Arp3p-mYFP in whole fission yeast cells by immunoblotting with a monoclonal antibody against YFP. Arp3p is a subunit of Arp2/3 complex. In lanes 1 to 8, 0–1.2 ng of purified 6His-mYFP was mixed with 1 μl of wild-type cell extract to generate a standard curve. Lanes 9 to 12 contained duplicate samples of 1.0 and 0.5 μl of cell extract from a strain-expressing Arp3-mYFP from its normal chromosomal locus under the control of its native promoter. The Arp3p-mYFP signals were within the linear range of the standard curve. The weak band (marked by an arrow) in all the lanes resulted from a nonspecific reaction between this batch of YFP antibody with a yeast protein in the extract. Because all Arp3p molecules in this strain were labeled with YFP and all YFP molecules are fused with Arp3p (no free YFP in lanes 9 to 12), the number of YFP molecules in the cell extract is equal to the number of Arp3p molecules.

1. Grow 15 ml cultures of *S. pombe* strains for 36–48 h to exponential phase with a final OD_{595}~0.40–0.50. Use the OD_{595} to calculate the total number of cells ($0.5\ OD_{595} = 1\times10^7$ cells/ml).

2. Harvest cells using a tabletop centrifuge. There is on average 30–50 mg wet cell pellet.

3. Resuspend cells in 100 μl of ice-cold lysis buffer [50 mM HEPES pH 7.5, 100 mM KCl, 3 mM $MgCl_2$, 1 mM EGTA, 0.1% Triton X-100, 1 mM DTT, 1 mM PMSF, 1 EDTA-free protease inhibitor tablet (Roche Diagnostics, Indianapolis, IN)/50 ml buffer]. Freeze and store at -80 °C to help lysis.

4. Thaw cells and add 1× lysis buffer to final volume 300 μl (1 mg wet cells ~1 μl).

5. Add 0.3 g of acid washed beads (Sigma G8772) and lyse cells at 4 °C in Bead Beater (Fast Prep FP120 Bio101 Savant) using six 30-s pulses with incubation on ice for 5 min between each pulse.

6. While lysing cells, heat 5× SDS sample buffer (250 mM Tris–HCl pH 6.8, 50% glycerol, 3.58 M β-mercaptoethanol, 15% SDS, 0.025% Bromophenol Blue) to 100 °C. When lysis is complete, add 150 μl of boiling sample buffer to the 300 μl sample, heat at 100 °C for 5 min and centrifuge at 14,000 rpm in a desktop centrifuge for 10 min at 23 °C. Divide the 300 μl supernatant into four aliquots and store at -80 °C.

7. Load 0.5–1 μl cell extract for abundant proteins or 2.5–5 μl for less abundant proteins (determined empirically) in duplicate on a 10–20% gradient SDS–PAGE gel. All volumes added should be the same, so dilute with SDS sample buffer

to 15 μl. Load a range of purified YFP standards along with the extract as in Fig. 1. Run gel at 170 V for 90 min.

8. Transfer the proteins to a PVDF membrane (Immobilon-P 0.45 μm membrane; Millipore #IPVH00010) using 23 V overnight at 4 °C using transfer buffer (25 mM Tris base, 192 mM glycine, 0.04% SDS, 20% methanol). The transfer efficiency may be monitored by staining the gel after transfer with Gel Code Blue (#24590, Pierce, Rockford, IL). Under these conditions, the transfer efficiency is routinely very high.

9. We found that probing with JL-8 primary antibody to YFP for 2 h (Biosciences #632380; diluted 1:1000 to 1 μg/ml) and a monoclonal secondary antibody, HRP-conjugated anti-mouse IgG for 1 h (SigmaA-4416; diluted 1:5000 to 0.2 μg/ml) at 23 °C yielded a robust dynamic range of detection, though other probes may be effective as well. The antibodies were diluted in TBS-Tween buffer (20 mM Tris–HCl pH 7.5, 150 mM NaCl, 0.1% Tween 20) with 0.5% nonfat dry milk. The blots were washed five times with the TBS-Tween buffer for durations of 5 min each.

10. Incubate the washed blot with 250 mM luminol, 90 mM p-coumaric acid, 100 mM Tris–HCl pH 8.5, 0.01% H_2O_2 for 1 min at 23 °C and then expose the blot to x-ray film for a range of exposure times to visualize bands containing YFP. Develop the x-ray film.

11. Scan the x-ray film with desktop scanner set to a minimum of 300 dpi. Use ImageJ software (http://rsb.info.nih.gov/ij/) to integrate the density of the bands. Compare the densities of the YFP standards with the densities of the YFP-fusion proteins to calculate the number of molecules per cell.

G. Observation Chambers

We observed cells sandwiched between a thin layer of gelatin in YE5S medium and a coverslip. Assemble growth chambers as follows:

1. Add 0.25 g gelatin (Sigma G-2500) to 0.9 ml YE5S liquid medium in a plastic microcentrifuge tube, mix by inverting three times, and incubate at 65 °C on a hot plate for ~20 min to dissolve the gelatin. The medium can be used right away or stored at room temperature.

2. Add 0.1 ml of 1.0 mM antioxidant *n*-propyl-gallate (Sigma P-3130) prepared in YE5S to one tube of melted gelatin medium to reduce phototoxicity and photobleaching during imaging. Mix the antioxidant by inverting the tube several times, and then incubate on a 65 °C hot plate until all the air bubbles disappear (~15 min).

3. Pipette 100 μl of gelatin medium onto the center of a 2.5 cm × 7.5 cm glass slide, cover with another slide immediately to flatten the medium, clamp the two slides together at the ends using two small binder clips (19 mm). The gelatin medium will solidify into a thin film about 2 cm in diameter and will be ready to use in ~10 min.

4. Add 0.1 ml of 1.0 mM *n*-propyl-gallate stock solution to 0.9 ml cells in YE5S. Pellet the cells by centrifugation for 5–10 s in a benchtop microcentrifuge at 4500 rpm.

5. Discard 900–950 μl of supernatant and resuspend the cells in the remaining medium.

6. Pry apart the two slides slowly by inserting a razor blade from one end. The gelatin medium pad usually sticks to one of the slides. Add 10 μl of cells to the center of the gelatin pad, cover with a cover slip, and seal with Valap (1:1:1 Paraffin:Vaseline:Lanolin).

H. Microscopy of Cells Expressing Fluorescent Proteins

We calibrated a spinning-disk confocal microscope (UltraView RS; Perkin Elmer Life and Analytical Sciences, Boston, MA) equipped with an argon ion laser set to an excitation wavelength of 514 nm for mYFP and operated at low power. The system is installed on an Olympus IX-71 inverted microscope equipped with a Plan-Apo 100X/1.4 NA objective. All images were acquired using a Hamamatsu ORCA-ER cooled CCD camera (Bridgewater, NJ). Pixels were binned 2×2 to increase the signal. The field size was 61.1×46.6 μm^2. Depending on specimen size and strength of fluorescent signal, other microscopy systems and cameras will also be well suited to measure protein concentrations with the appropriate calibration.

We calibrated the microscope by recording images of five to seven different cell types that express a 30-fold range of concentrations of fluorescent fusion proteins. The range of the standards allowed for imaging fluorescent proteins from a few hundred to hundreds of thousands of copies per cell. We recalibrated the microscope each time that we determined the concentration of a new protein of interest since the intensity of the laser varied slightly from day-to-day.

Before imaging cells in the growth chamber, all equipment for imaging was powered on and stabilized for at least 30 min. Laser power, settings of microscope, camera, image acquisition, and room temperature were kept constant during an experiment. The only variable was the exposure time. The fluorescent intensity recorded by the camera was directly proportional to the exposure time within the linear range of the camera (Fig. 2). The exposure time chosen for each strain was a compromise between the signal-to-noise ratio and photobleaching. Short exposure times for strong signals avoided saturation of the camera and resulted in minimal photobleaching, less than 8% during a Z series of 12 exposures (total 0.83 s). Weak signals required longer exposure times and resulted in substantial photobleaching, up to 25% during the collection of a single stack of 12 Z-sections.

We recorded stacks of 12 confocal Z-sections spaced 0.60 μm along the optical axis. We chose to sample specimens expressing YFP at intervals of 0.60 μm to limit bleaching. Stacks 7.2 μm thick extend beyond the upper and lower edges of the cells to gather all the fluorescent signals from cells (Fig. 3). To limit

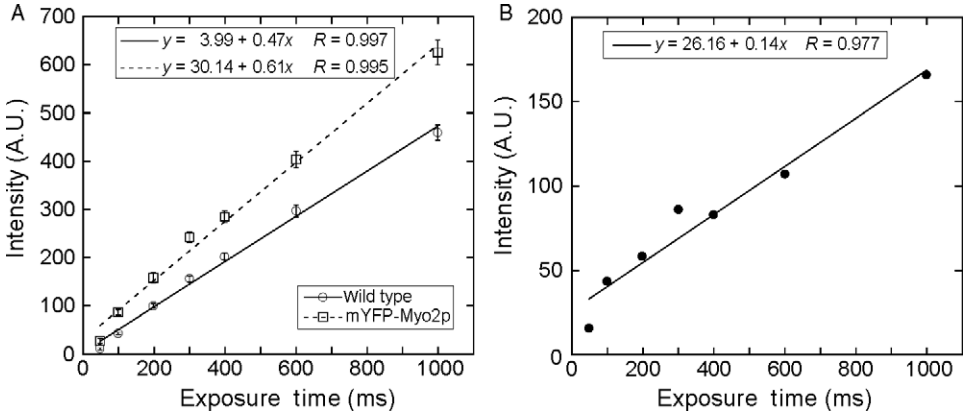

Fig. 2 Dependence of the fluorescence intensity recorded by the camera on the exposure time. Wild-type cells and cells expressing mYFP-Myo2p were imaged under the same conditions with exposure times from 48 ms to 1 s. The offset was subtracted from the sum of the Z-sections, and then corrected for uneven illumination. The mean fluorescence intensity of 5–20 cells at each exposure time for each strain was measured. (A) Mean fluorescent intensity (±1 standard deviation) of wild type (open circle) or cells expressing mYFP-Myo2p (open square) versus exposure time. This linear relationship was lost with the exposure times outside this range due to artifacts arising from noise and photobleaching. (B) Difference between the mean fluorescence intensity of cells expressing mYFP-Myo2p and wild-type cells as a function of exposure time. The fluorescence attributable to mYFP-Myo2p is a linear function of exposure time from 48 ms to 1 s.

photobleaching, we used wide field DIC observation to search for good fields and to focus on the cells before collecting a single Z-stack. A total of 3–10 different fields, with no more than 5 widely separated fields per slide, ~20–30 cells per fields, provided enough cells for quantitative analysis.

We used images of uniform films of fluorescent molecules to correct for uneven illumination across the field of view. The fluorescence intensity of a uniform sample is higher at the center than around the edge (Fig. 4). We made uniform films by mounting 20–50 μl of purified mYFP or fluorescein solution on the top of a gelatin pad in the absence of cells. Then we imaged a middle section of the solution since the solution near the surface was not always uniform. We used an average of at least five of these images to correct for uneven illumination (Fig. 4).

We corrected for system noise by acquiring images with a beam stop in place at every exposure time used for the experimental setup. We subtracted an average of five of these images from each image to correct for the noise inherent in the camera (offset).

In addition to imaging the standard curve, uneven illumination, camera offset, and fluorescent strain of interest, it is necessary to correct for the autofluorescence of wild-type cells. The fluorescence intensity of wild-type cells must be subtracted from the fluorescence of strains expressing a fusion protein to measure the global concentration. Figure 2A shows that autofluorescence is substantial and directly proportional

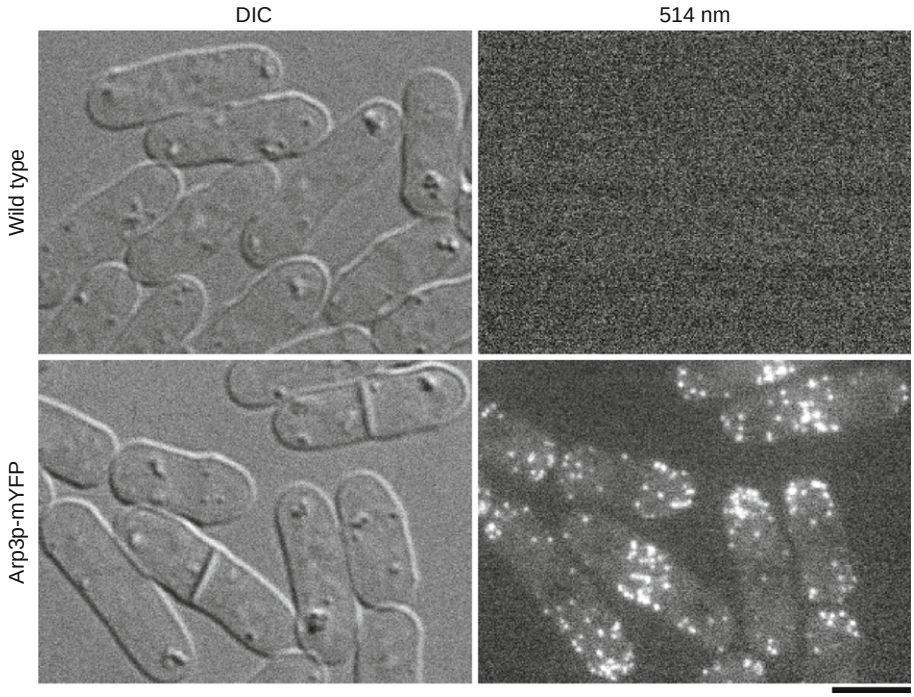

Fig. 3 Differential-interference contrast (DIC) and fluorescence micrographs (excitation at 514 nm) of wild-type cells and cells expressing Arp3p-mYFP at its endogenous level. We projected 12 Z-sections spaced at 0.6-μm intervals onto a 2D image using a sum intensity projection in ImageJ. Arp3p concentrates in actin patches at the cell ends or the cell-division site. Scale bar = 5 μm.

to exposure time. The fluorescence intensity of cells expressing a YFP-fusion protein is also proportional to exposure time. The difference gives the integrated fluorescence attributable to YFP. For the example given, mYFP-Myo2p with an average of 7300 molecules per cell, the signal was 1.5 times higher than the autofluorescence. For Cdc12p, the least abundant protein that we studied with 600 molecules per cell, the signal was barely detectable above the wild-type background. A triple YFP-tag increased the signal 3-fold to 1.13 times the background.

After these corrections for fluorescence attributable to other sources, the total fluorescence of strains expressing YFP-fusion proteins was directly proportional to the number of YFP molecules per cell (Fig. 5). Since all of the YFP was incorporated into the protein of interest, the fluorescence was proportional to the total number of protein molecules. The distribution of the fluorescent protein within cells had no detectable effect on the total fluorescence (Wu and Pollard, 2005). Thus, we did not detect any quenching due to concentrating a substantial fraction of any protein in actin patches, spindle pole bodies, or contractile rings. For example, mYFP-Myo2 is distributed uniformly through the cytoplasm during interphase, but about half of the

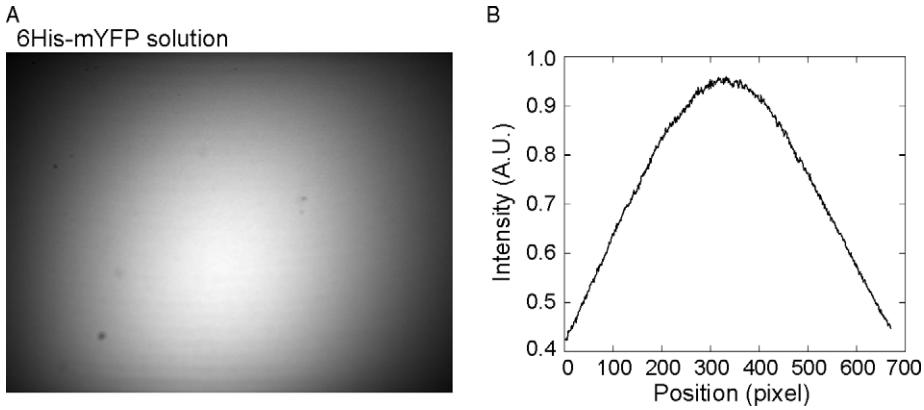

Fig. 4 Correction for uneven illumination. (A) Fluorescence micrograph of a thin film of purified 6His-mYFP solution mounted on top of a gelatin pad under conditions identical to imaging cells. The image, representing the whole field of view (672×512 pixels), was divided by its maximum pixel intensity. The images of cells were divided by this image to correct for the uneven illumination in the field. (B) Fluorescence intensity distribution along the long axis of the image in (A). The graph shows fluorescence intensity (in arbitrary units) along a horizontal line in the middle of the field.

molecules concentrate in the contractile ring during cytokinesis. Nevertheless, the mean fluorescence is the same across the cell cycle.

We used flow cytometry as a second method to measure the fluorescence intensity of all of our strains expressing fluorescent fusion proteins. Flow cytometry has the advantage of measuring a large number of cells quickly. For most of the 27 strains tested, the mean fluorescence intensities measured with the microscope were directly proportional to the mean fluorescence intensities determined by flow cytometry (Fig. S3 in Wu and Pollard, 2005).

I. Measurement of Cell Size

Fortunately, it is easy to calculate the cell volume of live fission yeast cells from DIC images, since they have a regular shape. To determine the cell borders, we took DIC images of 6.0-μm Focal Check Microspheres (Invitrogen, Eugene, OR; F14806) and compared their boundaries to cell borders. *S. pombe* is a rod-shaped cell with a constant diameter of 3.7 ± 0.2 μm including the cell wall. Assuming that *S. pombe* cells are cylinders with a diameter of 3.7 μm capped by hemispheres at both ends, the average volume of asynchronous cells is 92 μm^3. It is also possible to measure cell volumes from electron micrographs of thin sections, but shrinkage during fixation and embedding may present problems.

J. Estimation of Cytoplasmic Volume by Point Counting Stereology

The volume occupied by the molecule of interest is required to calculate the concentration. Most of our proteins of interest are found in the cytoplasm, so we needed to determine the fraction of the cell occupied by cytoplasm. Mary

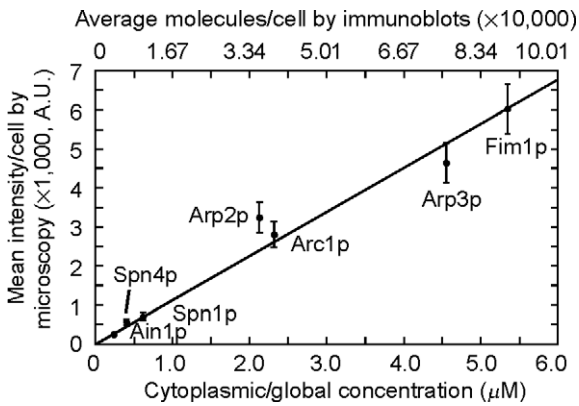

Fig. 5 Calibration curve showing the dependence of the mean fluorescence intensity (±1 standard deviation) per cell (corrected by cell size) measured by fluorescence microscopy on the mean YFP-tagged molecules per fission yeast cell measured by immunoblots. The fluorescence intensity per cell is directly proportional to the average molecules per cell for seven representative strains expressing mYFP-fusion proteins. The cytoplasmic or the global concentrations were calculated by dividing the average number of molecules per cell by Avogadro's number and the volume of cytoplasm.

Morphew and J. Richard McIntosh of the University of Colorado at Boulder generously provided electron micrographs of thin sections of quick-frozen, freeze-substituted *S. pombe* cells for this analysis. We used point-counting stereology to estimate the fractional volumes of the cells occupied by cell wall, nuclei, other organelles, ribosomes, and cytoplasm. A square grid of test points was positioned over each micrograph and each point was scored as hitting one of the compartments of interest. The technique is based on the principle that the ratio of the area of a compartment to that of the whole cell is proportional to the ratio of volume in random thin sections. We found that cytoplasm occupies 29% of cell volume, nucleus 12%, ribosomes 20%, cell wall 11%, and other organelles 28%. Thus, an average cell contains about 27 μm^3 of cytoplasm.

K. Measurements on Cells Expressing both a Native and a Tagged Protein

If an antibody to the protein of interest is available, our method for counting protein molecules globally and locally can be used even in model systems where homologous recombination is difficult or impossible (Wu and Pollard, 2005). Howell *et al.* (2004) used a similar approach to study spindle checkpoint proteins in animal cells. A tagged protein is expressed at a low level episomally from a plasmid in cells expressing the untagged protein at the native level. (High level episomal expression should be avoided to minimize possible adverse effects of over expression.) Quantitation of protein levels in cells expressing both the tagged and untagged proteins (via quantitative immunofluorescence or immunoblot) reveals the ratio of the tagged protein to the native protein. If the ratio of tagged to native

protein is the same globally and locally, one can convert the local fluorescence intensity from microscopy into local concentration.

We used this approach to study actin in *S. pombe* because actin tagged with YFP or GFP cannot replace native actin (Wu and Pollard, 2005). Tagged actin incorporates into filaments nucleated by Arp2/3 complex but not filaments nucleated by the formin Cdc12p. Therefore, quantitative fluorescence microscopy can be used to study some but not all aspects of actin assembly in fission yeast.

III. Data Analysis

A. Measurement of Global Fluorescent Intensity and Calculation of Global Concentrations

We used ImageJ software (http://rsb.info.nih.gov/ij/) to analyze images. The fluorescence stacks for the wild-type strain, strains with fusion proteins, and solutions of 6His-mYFP were projected into 2D images using a sum intensity projection. The offset pixel intensity (the pixel intensity without laser beam) at the same acquisition setting and exposure time was subtracted from the sum images. The sum image for 6His-mYFP solution divided by their maximal pixel intensity was used to correct images for uneven illumination (Fig. 4). The offset subtracted sum fluorescence images for all *S. pombe* strains were divided by the correction image. The resultant images were used to measure the intensity for each pixel.

To measure the global concentration of an unknown protein in cytoplasm, the inner boundaries of cells were marked on DIC images with the polygon selections tool in ImageJ to include all fluorescence from cell but little background fluorescence outside the cell. Then the marked area and mean pixel intensity from the fluorescent images within marked area were recorded and transferred to Microsoft Excel for analysis. We measured 42–302 cells for each strain (Wu and Pollard, 2005). From these cells, we calculated the minimum number of cells required to yield concentrations that are not significantly different from a large sampling (Fig. 6). If we choose a standard deviation threshold that is 1.5% of the cumulative average intensity, measuring 50 cells at random will give results similar to the published work (Wu and Pollard, 2005). The background intensity from wild-type cells at the same exposure was subtracted from the mean pixel intensity from cells expressing the fusion protein to obtain the mean fluorescence intensity from the mYFP-fusion protein. The subtracted intensity was normalized to that of 1 s exposure for mYFP [mYFP is 1.1× brighter than YFP (Zacharias *et al*., 2002)].

We calculate the mean number of a fusion protein per cell by dividing the mean fluorescence intensity attributable to the mYFP-fusion protein by the slope of the standard curve (Fig. 5). We calculate the mean concentration of a protein confined to the cytoplasm (global cytoplasmic concentration) by dividing the mean molecules per cell by the average volume of cytoplasm, 27 μm^3 (29% of whole cell volume).

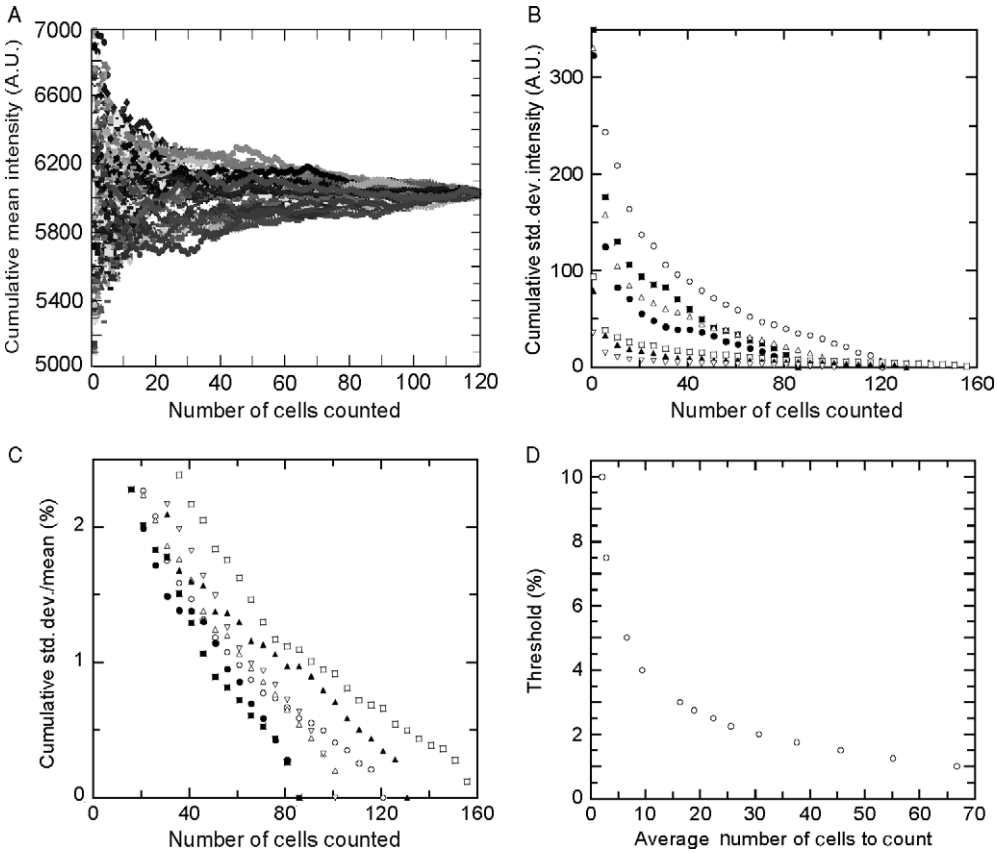

Fig. 6 Dependence of measurement error on the number of cells scored. (A) Dependence of the cumulative mean fluorescence of a sample of cells expressing the actin patch component, Fim1p-mYFP, on the number of cells counted for 100 trials where the cells in the same sample were counted in random orders. (B) Dependence of the standard deviation of the cumulative average intensity on the number of cells counted for the simulations of seven different cytokinesis proteins. Deviations are greater for more abundant proteins (i.e., Fim1p) than for less abundant proteins (i.e., Ain1p). (C) The standard deviations of the cumulative averages were normalized to their respective average intensities to determine the appropriate threshold to choose an adequate number of cells to analyze. (D) The percent cumulative standard deviation/mean is used as a threshold to determine how many cells to count. The number of cells counted over seven different strains was averaged and plotted against the normalized standard deviation threshold. We chose a standard deviation threshold that is 1.5% of the cumulative average intensity. As a rule of thumb, measuring 50 cells at random yields information content better than the 1.5% threshold, similar to published work (Wu and Pollard, 2005). For the extremes, Ain1p would deviate by only 54 molecules and Fim1p by only 1300 molecules, both of which are well within the reported cell-to-cell standard deviations. For (B) and (C), the ratio of the cumulative standard deviation/mean was calculated for every group of five cells to aid in clarity. For (B) and (C), Fim1p are open circles, Arp3p are closed squares, Arp2p are open triangles, Arpc1 are closed circles, Spn1p are open squares, Spn4p are closed triangles, and Ain1p are inverted open triangles.

B. Measurement of Local Fluorescent Intensity and Counting Molecules Locally

We used sum images corrected for offset and uneven illumination to measure local concentrations of YFP molecules in contractile rings, septin rings, and spindle pole bodies. We drew a small inner box or circle around the object of interest large enough to contain >95% fluorescence intensity from the target. At the division site, the rectangle width was typically 32 pixels (2.91 μm) for the broad band of nodes (precursors of the contractile ring) and 5–10 pixels for contractile or septin rings. The measuring circle was eight pixels (0.73 μm) in diameter for spindle pole bodies. To correct for background, we drew around each measuring area a concentric box or circle with 2.1 times the area of the inner box or circle within the cellular boundary.

The total fluorescence intensity within the small box (or circle) was calculated from its area and mean pixel intensity after background correction. We subtracted the total intensity in the inner box from the total intensity within the larger box to get the total intensity in the background region between the two boxes and then divided this intensity by the area between the two boxes to get background intensity per unit area (Hoffman *et al.*, 2001). This background intensity per unit area was subtracted from the mean pixel intensity of the small box. The standard curve (Fig. 5) was used to convert the normalized 1 s mYFP local intensity to molecules.

Correcting for background is an issue if the object of interest is not isolated from other fluorescent objects. For example, the fluorescence from actin patches, the sites of endocytosis, is often close to that from other actin patches. The fluorescence generally appears in three confocal sections with highest intensity in the middle section. To correct for background, Wu and Pollard (2005) used an inner circle of five pixels and an outer circle of seven pixels in diameter in each of the sections to avoid overlap between patches. The fluorescent intensity in three sections was measured, background corrected, and summed. Sirotkin *et al* (2008) used an alternative method to correct for the background within actin patches. They measured the intensity of an equivalent area of cytoplasm some distance from the patch and subtracted this background from the intensity of the actin patch. This method gave backgrounds about half of that in the area immediately surrounding the actin patch. Depending on the localization of the protein of interest, more complicated methods may be required to correct for background fluorescence.

IV. Conclusions

The fluorescence intensity at every point in a confocal section through a cell expressing a fluorescent fusion protein is directly proportional to the number of fusion proteins in the illuminated volume. If the microscope is calibrated by comparing the fluorescence of standard cells containing known numbers of fusion proteins measured by quantitative immunoblotting, one can measure the numbers of molecules in whole cells or at any point in the cell. This method not only

gives the relative fluorescence levels among fluorescent proteins in cells but also quantifies the absolute number of molecules in the cell (Fig. 7). Mass spectrometry has confirmed a subset of our measurements. Schmidt *et al.* (2007) used multidimensional prefractionation and tandem mass spectrometry to quantitate the relative protein abundance of 1465 fission yeast proteins. We had measured the absolute concentration of 10 of these proteins. The correlation of the relative abundance of these proteins with our measurements of absolute protein numbers is excellent ($r_p = 0.98$).

Other investigators have used quantitative fluorescence microscopy to count proteins in cells. These methods differ mainly in the approach to calibrate the microscope. Howell *et al.* (2004) used quantitative immunofluorescence to determine the levels of the proteins of interest in PtK1 cells. Howell *et al.* then expressed low levels of GFP-fusion proteins in addition to the untagged endogenous proteins and assumed that the fluorescence was attributable to a total concentration equal approximately to the total untagged protein. This simplifying assumption introduces error but was required because homologous recombination was not available to tag the proteins of interest in the genome.

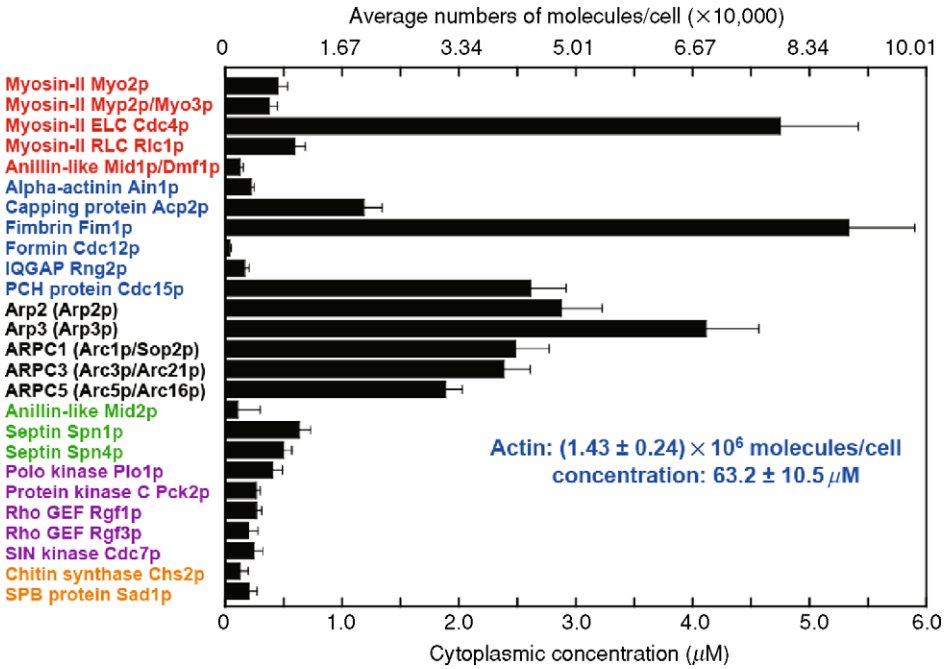

Fig. 7 Bar graph of the average number of molecules per fission yeast cell and global cytoplasmic concentrations of 28 proteins involved in cytokinesis. The data show the mean and one standard deviation obtained by immunoblotting and/or fluorescence microscopy. The proteins are grouped and color-coded by their functions and physical associations.

We (Wu and Pollard, 2005) used "internal standards" in the sense that we used quantitative immunoblots to determine fluorescent protein levels in cells. We added the YFP sequence to the coding sequence of each of our proteins of interest in the genome, so that all of the protein of interest was expressed as a fusion protein under the control of the native promoter. We used the YFP as an epitope tag in quantitative immunoblots to measure the total number of fusion proteins per cell for a sample of seven of our proteins. The linear dependence of the fluorescence on the number of fusion proteins allowed us to construct a standard curve for measuring many other YFP-fusion proteins. Knowing the total number of proteins, we could count their numbers locally anywhere in the cell. Our use of internal standards takes into account the effects of intracellular conditions on excitation and emission of fluorescent proteins. A further advantage of this approach is the ability to test the fusion proteins for biological function, an unknown in most studies with fluorescent fusion proteins.

Joglekar *et al.* (2006) used one well-characterized internal standard to study the accumulation of proteins at budding yeast kinetochores. They tagged all of the proteins of interest in the genome with GFP and calibrated their microscope knowing that each centromeric histone contains two molecules of Cse4p. The ratio of the fluorescence of GFP–Cse4p to other GFP-tagged proteins revealed that kinetochores contain 2–16 copies of other proteins.

Other groups have used external fluorescent standards to calibrate their microscopes (Table I). These standards include known numbers of GFP attached to beads (Chiu *et al.*, 2001; Khakh *et al.*, 2001) or viruses (Dundr *et al.*, 2002) and solutions of fluorescent proteins (Hirschberg *et al.*, 1998, 2000; Patterson *et al.*, 1998; Piston *et al.*, 1999; Xu *et al.*, 2003). This is simpler than internal standards but fails to account for any effects of intracellular conditions on excitation and emission of fluorescent proteins.

As imaging hardware and data analysis software improve, this medium-scale analysis can be scaled up to measure concentrations of all the relevant proteins in a molecular pathway in live cells. The local concentration measurements are a unique feature of this method. This novel *in vivo* technique will help elucidate additional pathways where cellular localization is related to biological function.

Counting of global and local concentrations of proteins has revealed novel insights on the molecular mechanisms of membrane traffic (Hirschberg *et al.*, 1998, 2000), mitosis (Howell *et al.*, 2004; Joglekar *et al.*, 2006, 2008), cytokinesis (Robinson *et al.*, 2002; Vavylonis *et al.*, 2008; Wu *et al.*, 2006), and endocytosis (Sirotkin *et al.*, 2008). Our studies in fission yeast revealed that all but one of the proteins we measured maintain relatively constant concentrations across the cell cycle, even though many of the proteins appear to function only in cytokinesis. We also found that large pools of these proteins exist in the cytoplasm to exchange with the molecules in the contractile ring (Pelham and Chang, 2002; Vavylonis *et al.*, 2008). The concentrations of the actin-binding proteins in the contractile ring remain constant as the ring constricts and decline in volume, whereas the concentration of myosin-II increases. Our measurement of

the stoichiometries of major cytokinesis proteins (Wu and Pollard, 2005) allowed us to propose a lateral contraction model for the assembly of the contractile ring (Wu *et al.*, 2006) and to simulate the ring formation mathematically (Vavylonis *et al.*, 2008). We are confident that similar measurements in other model systems will also provide insights about molecular mechanisms of complicated cellular processes.

Acknowledgments

We thank Vladimir Sirotkin for sharing unpublished results. This work is supported by The Ohio State University, a National Science Foundation Graduate Research Fellowship, and National Institutes of Health (NIH) research grants GM-26338 and GM-26132.

References

Bähler, J., Wu, J.-Q., Longtine, M. S., Shah, N. G., McKenzie, A., III, Steever, A. B., Wach, A., Philippsen, P., and Pringle, J. R. (1998). Heterologous modules for efficient and versatile PCR-based gene targeting in *Schizosaccharomyces pombe*. *Yeast* **14,** 943–951.

Chiu, C. S., Kartalov, E., Unger, M., Quake, S., and Lester, H. A. (2001). Single-molecule measurements calibrate green fluorescent protein surface densities on transparent beads for use with 'knock-in' animals and other expression systems. *J. Neurosci. Methods* **105,** 55–63.

Dundr, M., McNally, J. G., Cohen, J., and Misteli, T. (2002). Quantitation of GFP-fusion proteins in single living cells. *J. Struct. Biol.* **140,** 92–99.

Ghaemmaghami, S., Huh, W.-K., Bower, K., Howson, R. W., Belle, A., Dephoure, N., O'Shea, E. K., and Weissman, J. S. (2003). Global analysis of protein expression in yeast. *Nature* **425,** 737–741.

Higgs, H. N., and Pollard, T. D. (2000). Activation by Cdc42 and PIP(2) of Wiskott-Aldrich syndrome protein (WASp) stimulates actin nucleation by Arp2/3 complex. *J. Cell Biol.* **150,** 1311–1320.

Hirschberg, K., Miller, C. M., Ellenberg, J., Presley, J. F., Siggia, E. D., Phair, R. D., and Lippincott-Schwartz, J. (1998). Kinetic analysis of secretory protein traffic and characterization of golgi to plasma membrane transport intermediates in living cells. *J. Cell Biol.* **143,** 1485–1503.

Hirschberg, K., Phair, R. D., and Lippincott-Schwartz, J. (2000). Kinetic analysis of intracellular trafficking in single living cells with vesicular stomatitis virus protein G-green fluorescent protein hybrids. *Methods Enzymol.* **327,** 69–89.

Hoffman, D. B., Pearson, C. G., Yen, T. J., Howell, B. J., and Salmon, E. D. (2001). Microtubule-dependent changes in assembly of microtubule motor proteins and mitotic spindle checkpoint proteins at PtK1 kinetochores. *Mol. Biol. Cell* **12,** 1995–2009.

Howell, B. J., Moree, B., Farrar, E. M., Stewart, S., Fang, G., and Salmon, E. D. (2004). Spindle checkpoint protein dynamics at kinetochores in living cells. *Curr. Biol.* **14,** 953–964.

Huang, B., Wu, H., Bhaya, D., Grossman, A., Granier, S., Kobilka, B. K., and Zare, R. N. (2007). Counting low-copy number proteins in a single cell. *Science* **315,** 81–84.

Joglekar, A. P., Bouck, D. C., Molk, J. N., Bloom, K. S., and Salmon, E. D. (2006). Molecular architecture of a kinetochore-microtubule attachment site. *Nat. Cell Biol.* **8,** 581–585.

Joglekar, A. P., Bouck, D., Finley, K., Liu, X., Wan, Y., Berman, J., He, X., Salmon, E. D., and Bloom, K. S. (2008). Molecular architecture of a kinetochore-microtubule attachment site is conserved between point and regional centromeres. *J. Cell. Biol.* **181,** 587–594.

Khakh, B. S., Smith, W. B., Chiu, C. S., Ju, D., Davidson, N., and Lester, H. A. (2001). Activation-dependent changes in receptor distribution and dendritic morphology in hippocampal neurons expressing P2X2-green fluorescent protein receptors. *Proc. Natl. Acad. Sci. USA* **98,** 5288–5293.

Kim, K., Yamashita, A., Wear, M. A., Maeda, Y., and Cooper, J. A. (2004). Capping protein binding to actin in yeast: Biochemical mechanism and physiological relevance. *J. Cell Biol.* **164,** 567–580.

Krappmann, S., Sasse, C., and Braus, G. H. (2006). Gene targeting in *Aspergillus fumigatus* by homologous recombination is facilitated in a nonhomologous end-joining-deficient genetic background. *Eukaryot. Cell* **5,** 212–215.

Longtine, M. S., McKenzie, A., III, Demarini, D. J., Shah, N. G., Wach, A., Brachat, A., Philippsen, P., and Pringle, J. R. (1998). Additional modules for versatile and economical PCR-based gene deletion and modification in *Saccharomyces cerevisiae*. *Yeast* **14,** 953–961.

Meyer, V., Arentshorst, M., El-Ghezal, A., Drews, A. C., Kooistra, R., van den Hondel, C. A., and Ram, A. F. (2007). Highly efficient gene targeting in the *Aspergillus niger kusA* mutant. *J. Biotechnol.* **128,** 770–775.

Mutch, S. A., Fujimoto, B. S., Kuyper, C. L., Kuo, J. S., Bajjalieh, S. M., and Chiu, D. T. (2007). Deconvolving single-molecule intensity distributions for quantitative microscopy measurements. *Biophys. J.* **92,** 2926–2943.

Nayak, T., Szewczyk, E., Oakley, C. E., Osmani, A., Ukil, L., Murray, S. L., Hynes, M. J., Osmani, S. A., and Oakley, B. R. (2006). A versatile and efficient gene-targeting system for *Aspergillus nidulans*. *Genetics* **172,** 1557–1566.

Ninomiya, Y., Suzuki, K., Ishii, C., and Inoue, H. (2004). Highly efficient gene replacements in *Neurospora* strains deficient for nonhomologous end-joining. *Proc. Natl. Acad. Sci. USA* **101,** 12248–12253.

Patterson, G. H., Schroeder, S. C., Bai, Y., Weil, A., and Piston, D. W. (1998). Quantitative imaging of TATA-binding protein in living yeast cells. *Yeast* **14,** 813–825.

Pelham, R. J., and Chang, F. (2002). Actin dynamics in the contractile ring during cytokinesis in fission yeast. *Nature* **419,** 82–86.

Piston, D. W., Patterson, G. H., and Knobel, S. M. (1999). Quantitative imaging of the green fluorescent protein (GFP). *Methods Cell Biol.* **58,** 31–48.

Robinson, D. N., Cavet, G., Warrick, H. M., and Spudich, J. A. (2002). Quantitation of the distribution and flux of myosin-II during cytokinesis. *BMC Cell Biol.* **3,** 4.

Schmidt, M. W., Houseman, A., Ivanov, A. R., and Wolf, D. A. (2007). Comparative proteomic and transcriptomic profiling of the fission yeast *Schizosaccharomyces pombe*. *Mol. Syst. Biol.* **3,** 79.

Shaner, N. C., Steinbach, P. A., and Tsien, R. Y. (2005). A guide to choosing fluorescent proteins. *Nat. Methods* **2,** 905–909.

Sirotkin, V., Berro, J., Macmillan, K., Zhao, L., Yuan, S., and Pollard, T. D. (2008). Quantitative analysis of the assembly, movement, and disassembly of endocytic actin patches in fission yeast Submitted for publication.

Takahashi, T., Masuda, T., and Koyama, Y. (2006). Enhanced gene targeting frequency in ku70 and ku80 disruption mutants of *Aspergillus sojae* and *Aspergillus oryzae*. *Mol. Genet. Genomics* **275,** 460–470.

Vavylonis, D., Wu, J.-Q., Hao, S., O'Shaughnesy, B., and Pollard, T. D. (2008). Assembly mechanism of the contractile ring for cytokinesis by fission yeast. *Science* **319,** 97–100.

Wu, J.-Q., Kuhn, J. R., Kovar, D. R., and Pollard, T. D. (2003). Spatial and temporal pathway for assembly and constriction of the contractile ring in fission yeast cytokinesis. *Dev. Cell* **5,** 723–734.

Wu, J.-Q., and Pollard, T. D. (2005). Counting cytokinesis proteins globally and locally in fission yeast. *Science* **310,** 310–314.

Wu, J. Q., Sirotkin, V., Kovar, D. R., Lord, M., Beltzner, C. C., Kuhn, J. R., and Pollard, T. D. (2006). Assembly of the cytokinetic contractile ring from a broad band of nodes in fission yeast. *J. Cell Biol.* **174,** 391–402.

Xu, C., Watras, J., and Loew, L. M. (2003). Kinetic analysis of receptor-activated phosphoinositide turnover. *J. Cell Biol.* **161,** 779–791.

Zacharias, D. A., Violin, J. D., Newton, A. C., and Tsien, R. Y. (2002). Partitioning of lipid-modified monomeric GFPs into membrane microdomains of live cells. *Science* **296,** 913–916.

CHAPTER 10

Infrared and Raman Microscopy in Cell Biology

Christian Matthäus, Benjamin Bird, Miloš Miljković, Tatyana Chernenko, Melissa Romeo, and Max Diem

Department of Chemistry and Chemical Biology
Northeastern University
Boston, Massachusetts 02115

Abstract

This chapter presents novel microscopic methods to monitor cell biological processes of live or fixed cells without the use of any dye, stains, or other contrast agent. These methods are based on spectral techniques that detect inherent spectroscopic properties of biochemical constituents of cells, or parts thereof. Two

METHODS IN CELL BIOLOGY, VOL. 89

0091-679X/08 $35.00
DOI: 10.1016/S0091-679X(08)00610-9

different modalities have been developed for this task. One of them is infrared micro-spectroscopy, in which an average snapshot of a cell's biochemical composition is collected at a spatial resolution of typically 25 μm. This technique, which is extremely sensitive and can collect such a snapshot in fractions of a second, is particularly suited for studying gross biochemical changes. The other technique, Raman microscopy (also known as Raman micro-spectroscopy), is ideally suited to study variations of cellular composition on the scale of subcellular organelles, since its spatial resolution is as good as that of fluorescence microscopy. Both techniques exhibit the fingerprint sensitivity of vibrational spectroscopy toward biochemical composition, and can be used to follow a variety of cellular processes.

I. Introduction

Over the past decade, novel micro-spectroscopic methods have opened new avenues for imaging individual cells, or fractions thereof, using a number of spectroscopic techniques. Confocal (one- and two-photon) fluorescence microscopy (see Chapter 5 of this volume) (O'Malley, 2008) is the best known of these techniques and has revealed amazing details on the complex structures found inside cells. Although many of the components inside a cell will exhibit autofluorescence, this effect is quite weak and nonspecific, and is generally not used in confocal fluorescence microscopy. Rather, labels or dye molecules [such as green fluorescent protein (GFP), small molecule dyes, or nanoparticles] are used to visualize organelles or receptor sites in cells by binding highly specific ligands to the labels. The resulting images exhibit spatial resolution determined by the diffraction limit: for fluorescence excitation in the mid-visible spectral range, the diffraction limit will be of the order of a few hundred nanometers.

In all imaging techniques that require a dye or a label, the question arises whether or not this dye interferes with the viability of the cells to be studied, and whether the diffusion of a receptor or a ligand is affected by the presence of the label, in particularly a bulky label such as a nanosphere. Therefore, the possibility of using label-free imaging methods is of interest to the scientific community. Among the label-free methods, newly developed techniques of vibrational micro-spectroscopic imaging (Diem *et al.*, 2004) have gained acceptance in many fields such as nanoscience and semiconductor technology; however, their presence and acceptance in cell biology has been limited. The two most common techniques of vibrational micro-spectroscopy are infrared (IR) and Raman (RA) micro-spectroscopy (IR-MSP and RA-MSP). In both of these techniques, the inherent vibrational (IR or RA) spectra of the biochemical constituents of a cell are observed. Since every molecule exhibits its own distinct ("fingerprint") spectrum (Diem, 1993), external labels are not required in these techniques.

RA-MSP is an experiment, to be described in detail in Section II, that resembles fluorescence MSP in that monochromatic laser light is used to excite molecules in a sample. In fluorescence, the molecules are excited into a vibrationally excited state

of the electronically excited state, which decays nonradiatively to the vibrational ground state of the electronically excited state (see Fig. 1). From there, a photon of reduced energy (red shifted) is emitted to a vibrationally excited state of the electronic ground state. In Raman spectroscopy, the incident laser light momentarily promotes the system into a "virtual" state, from which a red-shifted photon is emitted when the system decays into the vibrationally excited state of the electronic ground state. Thus, both fluorescence and Raman spectroscopy are vibronic effects (i.e., they involve both electronic and vibrational states and wavefunctions); however, fluorescence probes more of the electronic states whereas

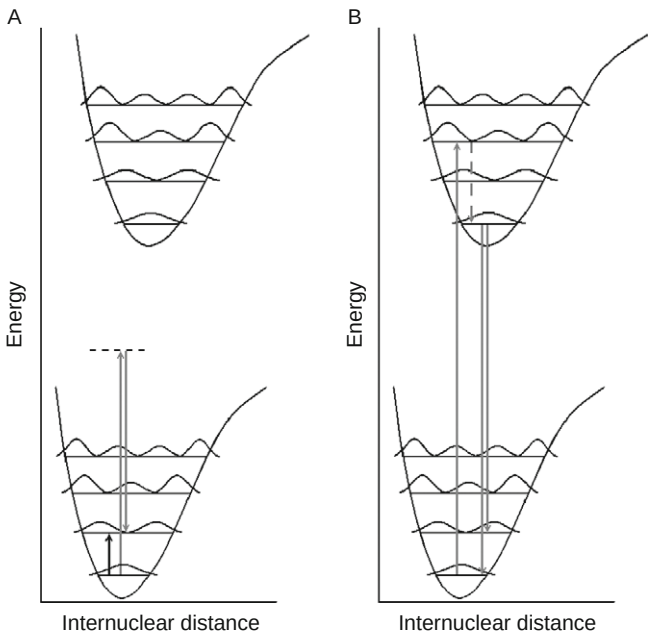

Fig. 1 (A) Energy level diagram for infrared, Raman, and fluorescence transitions. In both panels A and B, the lower diagram represents the ground electronic state with associated vibrational energy levels and associated (squared) wavefunctions. The upper diagram represents the electronically excited state with associated vibrational energy levels and associated wavefunctions. (A) An IR transition (short black up-arrow) is a dipole-mediated transition from a lower to a higher energy vibrational state. A Raman transition occurs when a photon (gray up-arrow) with energy much higher than required for a vibrational transition, but insufficient energy for an electronic transition, promotes the system into a virtual state (dashed line) from which a lower energy Raman photon is emitted (gray down-arrow). The emitted photon has lost the equivalent of the vibrational energy. (B). A fluorescence transition is initiated when a photon (gray up-arrow) promotes the system into an excited vibrational state of the electronically excited state. The vibrationally excited state depends on the overlap of the vibronic functions (Franck-Condon overlap). The system decays nonradiatively (dashed gray line) into the ground vibrational state of the electronically excited state. Red-shifted fluorescence (gray down-arrows) occurs from this state into various vibrationally excited states of the electronic ground state, depending on the maximal overlap of the wavefunctions involved.

Raman spectroscopy probes the vibrational states of a molecule. Since visible light is used for excitation in both cases, the spatial resolution (determined by the diffraction limit) is similar for both methods. However, Raman scattering is at least 6 orders of magnitude weaker than fluorescence, and consequently, could not be observed microscopically in cells until recently (Otto and Greve, 1998).

IR-MSP probes the same vibrational states that are sampled by Raman spectroscopy by inducing a direct transition from the vibrational ground to the first vibrationally excited state (see Fig. 1). The photon energies required for this lie in the infrared spectral range (2.5–25 μm wavelength). IR spectroscopy is a qualitative and a quantitative spectral method commonly used in chemical research and in quality control. It is a much stronger effect than Raman spectroscopy, with extinction coefficients of the order of 1000 [mol/l cm]. (A strong UV–vis absorption may have extinction coefficients up to 10^5 [mol/l cm].)

IR-MSP has two distinct disadvantages. First, due to the longer wavelengths of the light, the diffraction limit is much larger than that in the visible range (see Section II.F). Second, many materials composed of highly polar bonds, such as glass or water, have very strong infrared absorptions, and are therefore opaque in the infrared spectral regions. Thus, instruments using all reflective optics, or using refractive lenses constructed from transparent materials such as NaCl, KBr, or CaF_2 need to be designed. In spite of some experimental difficulties, both techniques are truly label-free in that the inherent vibrational signatures of the biochemical components of a cell are being observed.

The remainder of this chapter is organized as follows. First, instrumental methods and the mathematical procedures for data analysis will be presented. This discussion will be followed by IR-micro-spectral results collected for entire cells. These measurements monitor the composition averaged over the entire cell, and can detect variations of the composition as a gross observable. Very little spatial information of the compositional changes is available, due to the low spatial resolution of IR-MSP. On the other hand, the sensitivity to changes is very high, and IR-MSP can be used, for example, to determine the status of a cell during its progression through the cell cycle (Boydston-White *et al.*, 2006). RA-MSP, in contrast, monitors variations in cellular composition at a spatial resolution comparable to the size of subcellular organization. Therefore, biochemical processes such as motion of a mitochondrion, or uptake of drug carriers, can be detected.

II. Methods

A. Infrared Spectroscopy

IR spectroscopy is a method most chemists, biologists, and biochemists are vaguely familiar with, since the dreaded undergraduate organic chemistry laboratory usually includes a few experiments involving identification of compounds by IR spectroscopy. It is a well-understood spectroscopic method in which the $3N-6$

vibrational modes of a molecule consisting of N atoms are probed with IR light (2.5–25 μm wavelength). Each molecule, in principle, has its own distinct pattern of absorption peaks, which can be used as a fingerprint for molecular identification (Diem, 1993). Furthermore, the intensities of the absorption peaks are directly proportional to the concentration of components in a mixture; thus, IR spectroscopy serves both as a qualitative and a quantitative spectroscopic tool.

In typical undergraduate laboratory experiments, spectra from liquid samples (neat liquids or solutions) are collected from sample cells consisting of NaCl or KBr disks with spacers of appropriate thickness, which determine the sample path length. Solid samples are usually mixed with KBr and pressed into small pellets, or are ground up into a mull for data acquisition.

All commercial routine IR spectrometers employ interferometric techniques in which polychromatic IR radiation is intensity modulated by a Michelson-type interferometer (Diem, 1993). The resulting interferogram is Fourier-transformed to yield the familiar IR spectra displayed as percent transmission spectra, defined as $100\ I(\lambda)/I_0(\lambda)$, or absorption spectra, defined as $-\log[I(\lambda)/I_0(\lambda)]$, plotted against the inverse of the wavelength of the light. This inverse wavelength is known as the wavenumber $\bar{\nu}$ of the light (measured in inverse cm), where a wavelength λ=2.5 μm corresponds to $\bar{\nu} = 4000\ \text{cm}^{-1}$, and λ=25 μm corresponds to $\bar{\nu} = 400\ \text{cm}^{-1}$.

B. Infrared Micro-Spectroscopy (Infrared Microscopy)

In IR-MSP, infrared spectra are acquired through a special microscope (Humecki, 1995; Messerschmidt and Harthcock, 1988). We discuss here the instrument used for most of the studies reported in this chapter. This instrument is manufactured by Perkin Elmer, Inc. (Shelton, CT) and consists of a Spectrum One Fourier transform infrared (FT-IR) spectrometer bench coupled to a Spectrum Spotlight 300 IR microscope, henceforth referred to as the PE300. For single point (rather than imaging) application, a 100 μm × 100 μm HgCdTe (MCT) detector operating in photoconductive mode at liquid nitrogen temperature is used. The all-reflective objective provides an image magnification of 6×, and has a numerical aperture of 0.58. (Higher magnification could be achieved, but is irrelevant due to the long wavelength of the infrared light.) Visual image collection via a CCD camera is completely integrated with the microscope stage motion and IR spectra data acquisition. The visible images are collected under white light illumination, and are "quilted" together to give pictures of arbitrary size and aspect ratio. For single point measurements, individual cells are selected from the visually acquired sample image as seen on the screen. For each cell position on the sample substrate, the aperture is selected to straddle the cell, typically 30 μm × 30 μm. Cell position and apertures are stored for each cell. Data acquisition of all stored positions proceeds automatically. The microscope and the optical bench are continuously purged with purified, dry air to reduce water vapor absorptions in the observed spectra. In addition, the sample area in the focal plane of the microscope is enclosed in a purged sample chamber.

The output of IR-MSP experiments consist of thousands of spectra of individual cells, along with the coordinates of each cell on the microscope slide. These coordinates are particularly important since they allow cells to be reregistered between the imaging and spectral data acquisition, and after the staining steps for high quality image acquisition.

C. Raman Spectroscopy

Raman spectroscopy samples the same molecular vibrational states (Diem, 1993) as does IR spectroscopy discussed in Section II.A. However, Raman spectroscopy utilizes a scattering mechanism to excite the molecules into the vibrationally excited state, and visible wavelengths excitation is commonly used. Scattering phenomena are much less likely to occur than absorption processes; therefore, a laser which produces a large number of photons is needed for the excitation of Raman spectra. Despite the weak nature of the Raman effect, it offers several advantages over the more commonly used IR technique: since water has a very weak Raman scattering cross section (but a very strong IR absorption cross section), molecules and cells can be studied in aqueous environments. Furthermore, the use of visible excitation allows standard glass optics to be utilized, and the shorter wavelength light allows the detection of much smaller volume elements in RA-MSP than in IR-MSP. Aspects of the spatial resolution of both these techniques will be discussed later (Section II.F).

D. Raman Micro-Spectroscopy (Raman Microscopy)

In RA-MSP, Raman spectra are acquired from microscopic regions of a sample. For the studies reported here, RA-MSP Raman data were collected using a Confocal Raman Microscope, Model CRM 2000 (WITec, Inc., Ulm, Germany). Excitation (ca. 30 mW each at 488, 514.5, or 632.8 nm) is provided by an air-cooled Ar ion or HeNe laser (Melles Griot, Models 05-LHP-928 and 532, respectively). The exciting laser radiation is coupled into the Zeiss microscope through a single mode optical fiber, and reflected via a dichroic mirror through the microscope objective, which focuses the beam onto the sample. A Nikon Fluor (60×/1.00 NA, WD = 2.0 mm) water immersion or a Nikon Plan (100×/0.90 NA, WD = 0.26 mm) objective was used in the studies reported here (NA, numeric aperture; WD, working distance).

The sample is located on a piezo-electrically driven microscope scan stage with X–Y resolution of ca. 3 nm and a reproducibility of ±5 nm, and Z resolution of ca. 0.3 nm and ±2 nm repeatability. Raman backscattered radiation is collected for each data point through the same microscope objective, before being focused into a multimode optical fiber. The single mode input fiber (with a diameter of 50 μm) and the multimode output fiber (with a diameter of 50 μm as well) provide the optical apertures for the confocal measurement. The light emerging from the output optical

fiber is dispersed by a 30 cm focal length monochromator, fitted with a back-illuminated deep-depletion, 1024 × 128 pixel CCD camera operating at −82 °C.

The output of a typical mapping RA-MSP experiment is a hyperspectral data set (also referred to as a hyperspectral data cube), consisting typically of between 10,000 and 50,000 individual Raman spectra, along with the coordinates from which each spectrum was collected. Analysis of such a hypercube will be discussed in Section II.G.

E. Typical Infrared and Raman Spectra of Cellular Constituents

Raman and infrared spectra of a molecule are complimentary in the sense that the same vibrational states are accessed in both techniques. However, infrared spectra are composed of broader bands than Raman spectra; thus, IR and RA spectra are sometimes difficult to compare. In order to increase the apparent spectral resolution, IR absorption spectra may be converted numerically to second derivative spectra, $(d^2A/d\bar{\nu}^2)$, where A is the absorption spectrum. Second derivatives (2ndD) exhibit narrower and better-resolved peaks, and are more amenable to multivariate analysis (Section II.G). Bands strong in IR absorption often are weak in Raman scattering, and vice versa for reasons that are well understood.

Figure 2, panels A–G, shows reference IR (top traces), 2ndD-IR (middle traces), and Raman (bottom traces) spectra of a number of cellular components. All 2ndD spectra were multiplied by −1 to present the spectra with positive peaks. Panel A shows spectra for a mostly α-helical protein, albumin; panel B shows mostly β-sheet proteins (a mixture of various globulins), and panel C shows a model for many structural proteins, collagen, which exists in a triple helical structure. All protein infrared spectra are dominated by the amide A (N−H stretching mode, ca. 3300 cm^{-1}), the amide I (C=O stretching mode, ca. 1655 cm^{-1}), the amide II (C−N stretching mode, ca. 1550 cm^{-1}), and the amide III vibration (coupled N−H/C_α−H deformation mode). The complementary nature of RA and IR spectroscopy can be assessed by the fact that the amide II band is weak in the Raman spectra, but is strong in IR spectra. Similarly, the amide III mode is weak in IR, but strong in Raman spectra. Collagen exhibits a very characteristic spectrum in the amide III region, with a triplet of peaks at 1202, 1282, and 1336 cm^{-1} and another weak triplet between 1000 and 1100 cm^{-1}.

Amino acid side chains play minor roles in the spectra of proteins, and some of their spectral features are summarized in Table I. The strength of vibrational methods lies in their ability to distinguish protein secondary structures. A comparison of the 2ndD spectra of albumin and globulin shows distinct spectral differences in the amide I manifold of peaks: the helical protein exhibits a sharp peak at 1655 cm^{-1}, whereas the sheet protein exhibits two peaks at ca. 1635 and 1690 cm^{-1}. This comparison also demonstrates the usefulness of second derivative spectroscopy: the corresponding changes are harder to discern in the original IR spectra than in the 2ndD spectra.

The vibrational spectra of glycogen are shown in Fig. 2, panel D, as prototypical spectra of a carbohydrate. Glycogen spectral contributions are found prominently in the spectra of some epithelial cell types, and in tissues such as liver. Glycogen has a similar spectrum as its monomeric analogue glucose; however, glucose is metabolized rapidly and is normally not observed in cells or tissues. The major spectral bands of glycogen are the coupled C–O stretching and C–O–H deformation modes observed as a triplet of peaks at ca. 1025, 1080, and 1152 cm^{-1}.

Panels E and F show spectra of DNA and RNA, respectively. These molecules exhibit typical aliphatic and aromatic C−H stretching bands between 2850 and 3050 cm^{-1}, which are particularly pronounced in the Raman spectra, and C=N, C=C, and C=O double bond stretching frequencies of the planar bases between

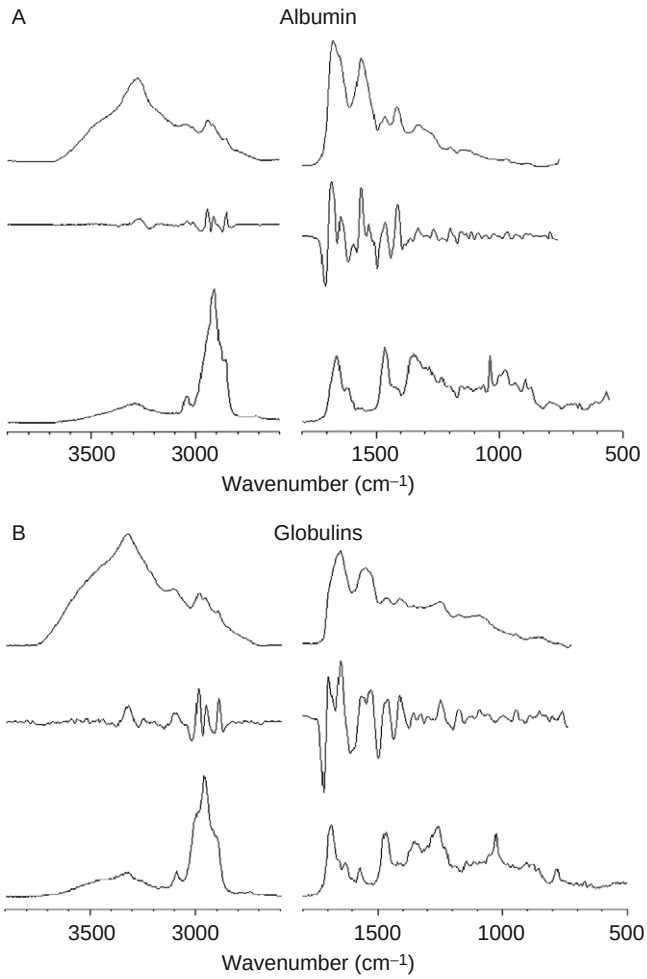

Fig. 2 *(continued)*

1600 and 1700 cm^{-1}. These spectra show distinct phosphate peaks at ca. 1235 and 1085 cm^{-1}. In the context of this discussion, the biochemical nomenclature is used, where "phosphate" refers to the phosphodiester linkage:

$$-O-PO_2^- -O-$$

The central phosphorus atom is tetrahedrally surrounded by four oxygen atoms and bears a negative charge that is countered in DNA by Na^+ ions. The central PO_2^- group also exhibits multiple bond character. The terms "symmetric" and "antisymmetric" phosphate stretching vibration refer to the vibrations of the

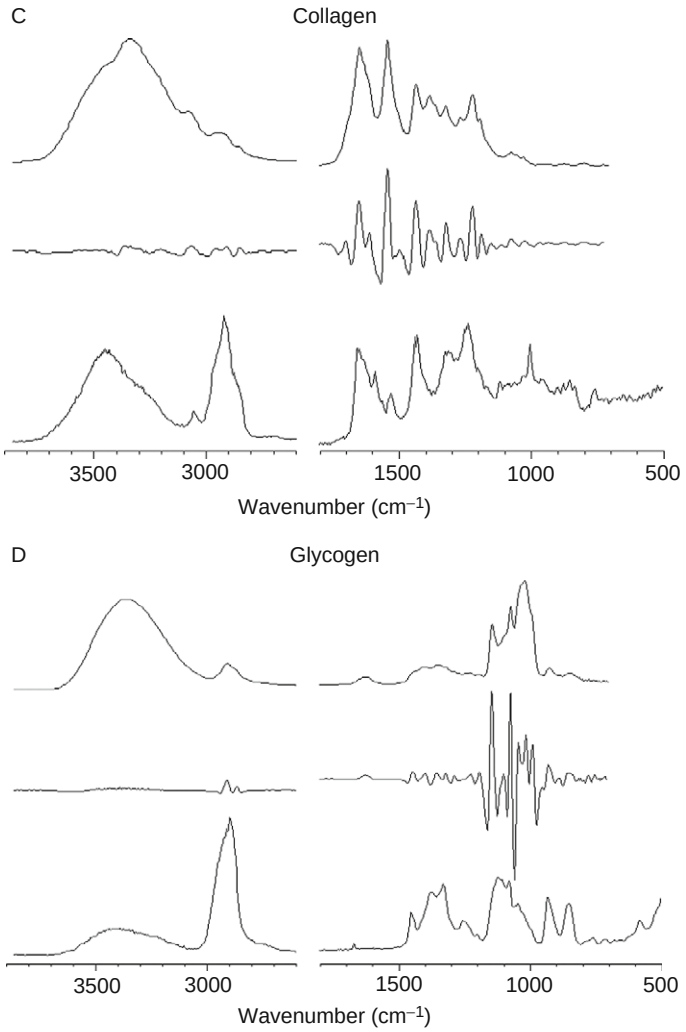

Fig. 2 *(continued)*

central PO_2^- group, and are normal modes observed at ca. 1085 and 1235 cm^{-1}, respectively. These vibrations are conserved between many species containing this group, that is, DNA, RNA, and phospholipids. The vibrations of the –O–P–O– moiety are referred to as the phosphodiester vibrations, which are less intense in the infrared. The vibrational modes of these molecules are summarized in Table I as well.

In phospholipids, the same phosphate group vibrations are found (see Fig. 2, panel G). In addition, these molecules exhibit strong C–H stretching vibrations, due to the long fatty acid side groups. The $–CH_2–$ vibrations of these groups

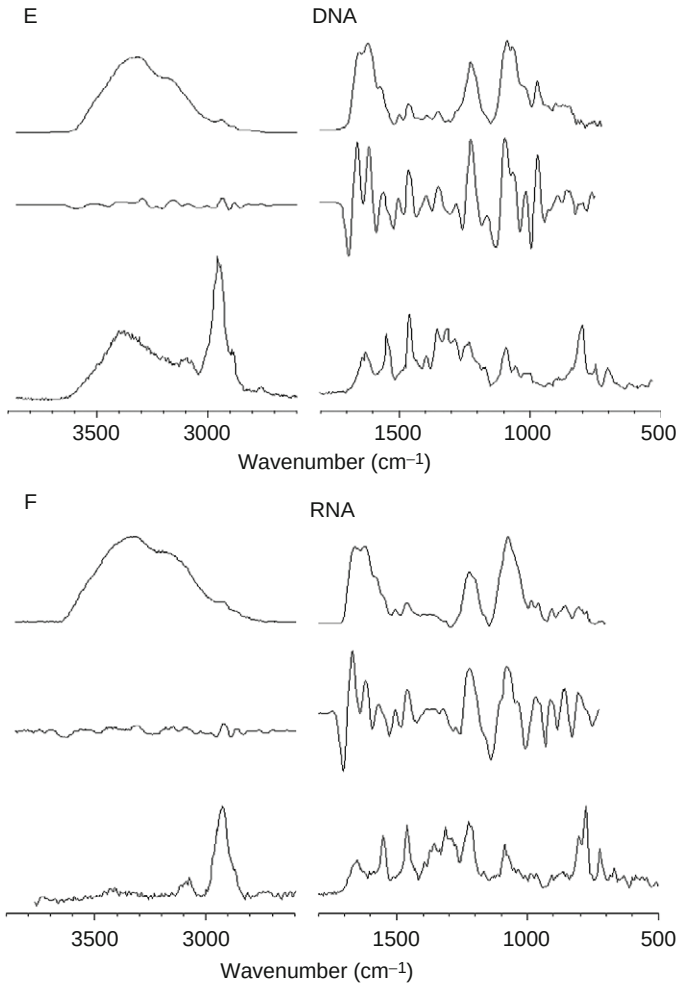

Fig. 2 *(continued)*

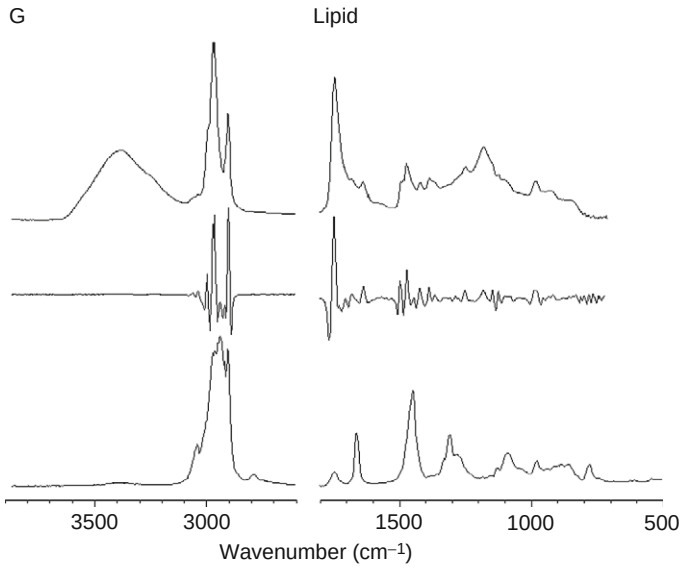

Fig. 2 Spectra of cellular components. In each panel, the top trace represents the infrared absorption spectrum (in arbitrary absorbance units), the middle trace represents the negative second derivative of the infrared spectrum, and the bottom trace represents the Raman spectra in arbitrary scattered intensity units. All spectra were acquired microscopically from thin films. (Panel A) Albumin (α-helical); (panel B) globulin mixture (β-sheet); (panel C) collagen (triple helical); (panel D) glycogen; (panel E) DNA; (panel F) RNA; and (panel G) lipid.

convey information on the local arrangement of the fatty acid chains. In addition, phospholipids exhibit a distinct vibration at ca. 1740 cm^{-1} due to the ester linkage.

F. Diffraction Limit and Spatial Resolution

RA-MSP data are acquired confocally; that is, using a two-pinhole arrangement that restricts the lateral size and depth of the sample volume element (voxel). In confocal microscopy, the lateral spatial resolution δ_{lat} of the acquired sampling area is determined by the diffraction limit, and is given by (Otto and Greve, 1998):

$$\delta_{lat} = \frac{0.62\lambda}{NA} \tag{1}$$

Depending on the laser wavelength (488, 514.5, or 632.8 nm for the RA-MSP unit described above) and objective used, a lateral resolution between ca. 300 and 435 nm can be achieved. The axial (depth) resolution is given by:

$$\delta_{ax} = \frac{2\lambda n}{(NA)^2} \tag{2}$$

Table I
Vibrational Frequencies (in cm^{-1}) and Assignments of Peaks Found in the Spectra of Cells

3300	Amide A (N–H stretching mode, peptide linkage)
2950	CH_3 antisymmetric stretching mode
2920	CH_2 antisymmetric stretching mode
2880	CH_3 symmetric stretching mode
2850	CH_2 symmetric stretching mode
1735	>C=O stretching mode, ester linkage
1690–1620	Amide I (>C=O stretching mode, peptide linkage)
1570–1530	Amide II (C–N stretching mode, peptide linkage)
1468–1455	CH_3/CH_2 antisymmetric bending mode
1397	$–COO^-$ symmetric stretching
1379	CH_3 symmetric bending mode
1340–1240	Amide III (coupled N–H/C–H deformations)
1237	O–P=O antisymmetric stretching mode (PO_2^-)
1150	C–O stretching, C–O–H bending modes (carbohydrates, mucin)
1083	O–P=O symmetric stretching mode (PO_2^-)
1063	–CO–O–C symmetric stretching mode
1050	C–O stretching mode (carbohydrates, mucin)
1004	Phenylalanine ring breathing mode
968	C–O–P phosphodiester residue (DNA)

resulting in a theoretical depth resolution for the water ($n = 1.33$) immersion objective (NA = 1) between ca. 1300 and 1700 nm, for 488 and 632.8 nm excitation, respectively.

The IR-MSP data reported here are not acquired confocally, although the microscope aperture (typically 30 μm) and the detector size somewhat restrict the confocal depth which is sampled. However, this depth is much larger than the sample thickness (<8 μm) that can be used before the absorption bands become too strong to be observed reliably. The lateral resolution predicted by the diffraction limit would be ~10 μm at a wavelength of 10 μm if the measurement was carried out confocally, but with an aperture of 10 μm, the light throughput would be compromised for the PE300 instrument. However, confocal IR-MSP measurements have been reported using synchrotron-based IR-MSP (Carr, 2001).

G. Multivariate Methods of Data Analysis

All multivariate methods of data analysis are based on the principle that there exist small, but reproducible changes in the spectra that can be associated with the variations in sample properties that are investigated. For cells during the cell cycle, for example, very slight shifts in the position of the amide I and II bands occur that are due to different protein compositions of cells at the different stages of the cell cycle. Although these changes may be masked by confounding factors, and may be hidden under uncorrelated (random) variations due to a large variance of the spectral data, multivariate methods will detect these changes and provide a

correlation with the stage in the cell cycle. For these methods to work properly, large data sets are required, and the analysis proceeds by calculation of a correlation matrix that expresses both random and correlated changes in the spectra.

1. Principal Component Analysis

The principal component analysis (PCA) is an ideal method to determine whether the variance in the spectral pattern of individual cells is correlated, or is due to random fluctuations (Adams, 2004). In PCA, an intensity point at a given wavenumber is correlated to other intensity point, and this correlation is summed over all spectra. A frequency correlation (covariance) matrix is obtained that consists of M^2 entries, where M is the number of intensity points in each spectrum. Subsequently, new spectra, known as the "principal components" (PCs), are computed to contain the maximum variance of the data set. Typically, the first few (5–8) PCs contain all the spectral information; higher PCs are mostly due to noise. Thus, each spectrum of the original data set can be expressed as a linear combination of a few PCs, with the expansion coefficients α expressing how much each PC contributes to a spectrum. Similar spectra will exhibit a set of similar values of α; thus, a plot of the contributions α_i for two PCs will yield a scatter plot, in which each dot represents a spectrum. Such a plot is known as a "scores plot." If these dots are found in distinctive clusters, the spectra in each cluster are closely related (similar) and distinct from spectra in a different cluster. If the dots in a scores plot are uniformly distributed around the origin, the variance in the data set is not correlated to any systematic changes.

2. Hierarchical Cluster Analysis

We use hierarchical cluster analysis (HCA) to construct spectral images from hyperspectral data cubes (see Section II.D) without human intervention. These spectral images are based solely on the similarity of the spectra in a hyperspectral data set. A detailed description of HCA has been published (Diem *et al.*, 2004; Lasch *et al.*, 2004; Wood *et al.*, 2004). For HCA, the pair-wise similarity coefficients of all spectra in a data set are collected as a matrix of correlation coefficients C, which contains N^2 entries, where N is the total number of spectra in a data set. Each correlation coefficient between two spectra can range from 1.0 for identical spectra to 0.0 for totally different spectra. The correlation matrix is then searched for the most similar spectra, which are merged into a new object employing an algorithm introduced by Ward (1963). The correlation matrix is recalculated and the merging process repeated until all spectra are combined into a small number of clusters. Each cluster is assigned a color, and these colors are displayed at the coordinates at which the spectra were collected creating a pseudo-color map based on the spectral similarity. Mean cluster spectra, obtained by averaging all spectra in a cluster, provide insight into the spectral differences between clusters, and offer a measure of the compositional variations of the cellular regions associated with

the clusters. The mean cluster spectra exhibit vastly improved signal-to-noise ratios over individual spectra. HCA, using Ward's algorithm as a merging method, was found to produce the best clusters as judged by the homogeneity of the spectra in each cluster (Helm *et al.*, 1991).

H. Sample Preparation

Because of the strong IR absorption of water, samples for IR-MSP are best prepared by drying the cells on a suitable sample substrate. Cells may be grown in culture directly on a substrate, or may be centrifuged or sedimented onto the substrate, and subsequently (formalin) fixed and dried. Suitable substrates are water-insoluble salt plates (CaF_2, BaF_2, and ZnSe) or Ag-coated glass slides (''low-e'' slides) used in reflectance measurements. It is difficult, yet possible, to observed cells in an aqueous environment (see Section III.B.5).

RA-MSP data can be acquired from aqueous environments due to the low Raman scattering cross section of water. To this end, cells centrifuged or otherwise attached to nonfluorescent, insoluble substrates (quartz or CaF_2) are immersed in water, buffer, or cell culture medium and studied through a water immersion objective. The aqueous environment also offers the advantage of dissipating the optical power of the laser beam ($\sim 5 \times 10^6$ W/cm^2 power density), thus preventing cell damage.

III. Results and Discussion

A. General Comments: Pros and Cons of IR-MSP and RA-MSP

IR-MSP and RA-MSP both monitor the total chemical composition contained in the sampling volume. Since a cell is composed of thousands of structural and metabolic proteins, nucleic acids, many different phospholipids, carbohydrates, and small molecules that may be involved in signaling pathways, the observed spectrum of a cell is a superposition of the spectra of thousands of cell constituents. The interior of a cell is not a homogeneous solution of the above-mentioned components, but rather a highly compartmentalized and organized structure. Only the largest of these organizations can be detected in IR-MSP (i.e., nucleus and cytoplasm), whereas organelles as small as 1 μm in diameter can be observed in RA-MSP. This is, of course, due to the diffraction limit, which is proportional to the wavelength and which determines the smallest object that can be resolved in microscopy. However, the average measurement performed in IR-MSP affords much higher spectral quality, as determined by the signal-to-noise (S/N) ratio of the data. Thus, small spectral shoulders, peak shifts, and intensity variations can be detected. In addition, IR-MSP measurements averaged over an entire cell can be carried out in a few seconds, whereas RA-MSP data acquisition will take 100 times longer, and usually samples only a small part of the cell. Thus, IR-MSP provides a

snapshot over the biochemical composition integrated for an individual cell, whereas RA-MSP provides a spatially resolved image of cellular compartments and structures, albeit at lower sensitivity and signal quality.

B. IR Results of Individual Cells

1. Monitoring Overall Cell Composition

We begin the discussion of observed cellular IR-MSP by presenting results collected from cultured human fibroblast cells (ATCC cell line CRL 7553). Figure 3 shows typical IR-MSP spectra for the nucleus and cytoplasm of such cells. These spectra

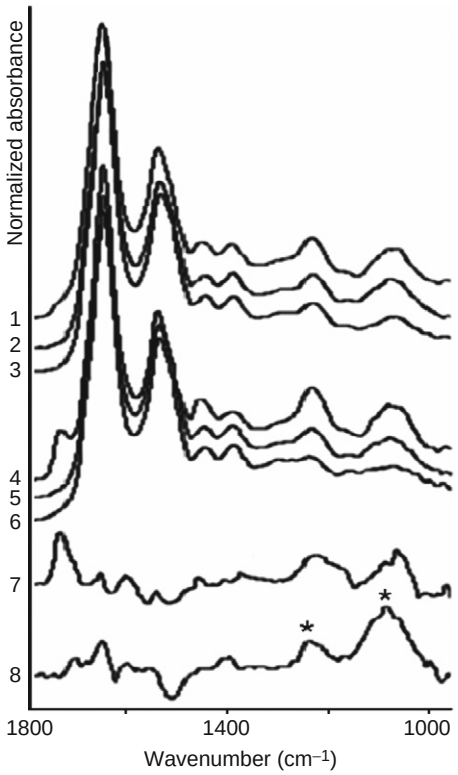

Fig. 3 IR-MSP spectra of cultured human fibroblast cells. Traces 1–6 represent average spectra from 15 individual cells, and were normalized for equal amplitudes at the amide I band (ca. 1650 cm^{-1}). Traces 1 and 4 are from the nuclei and cytoplasm of dried cells, respectively. Traces 2 and 5 are from the nuclei and cytoplasm, respectively, of cells after ethanol treatment to remove phospholipids. Traces 3 and 6 are from the nuclei and cytoplasm, respectively, after RNase digestion. Trace 7 shows the difference spectrum before and after ethanol treatment (trace 4–trace 5), amplified four times. Trace 8 (trace 2–trace 3) shows the effect of RNase digestion in the nucleus. The difference spectrum closely resembles that of pure RNA (see Fig. 2F).

represent average spectra from the nuclei of 15 individual cells (trace 1) and the cytoplasm of the same cells (trace 4). The spectra shown are typical for actively growing cultured cells, and are dominated by the protein spectra shown in Fig. 2A and B. In addition, peaks associated with phospholipids and nucleic acids can be observed. In order to identify the biochemical components in a cell, the cells were treated on the spectral substrate with ethanol, to partially dissolve phospholipids, and with RNase to remove nuclear and cytoplasmic RNA.

After each of the sample treatments (ethanol, RNase), the same 15 cells were reinvestigated. In addition to improving the *S*/*N* of the observed spectra, this averaging minimizes cell-to-cell variations in these data. The spectra shown in Fig. 3 were normalized for equal amplitudes at the amide I band (ca. 1650 cm^{-1}). In Fig. 3, traces 1, 2, and 3 represent spectra from nuclear, and traces 4, 5, and 6 from cytoplasmic regions, respectively. Traces 1 and 4 were collected from the untreated cells, traces 2 and 5 after ethanol extraction, and traces 3 and 6 after RNase digestion. These spectra reveal an enormous amount of information on the contributions to the observed spectra of the classes of biomolecules found in a cell. The spectra of nuclei and the cytoplasm differ mostly in the lipid band (at 1738 cm^{-1} due to $C{=}O_{ester}$, see traces 1 and 4).

Ethanol treatment was carried out by exposing cells on a substrate for 5 min to 96% ethanol (Fisher Scientific) to eliminate most phospholipids, the removal of which manifests itself by the disappearance of the $C{=}O_{ester}$ peak at 1738 cm^{-1} (Fig. 3, traces 2 and 5). The effect of ethanol treatment may also cause dehydration of proteins and nucleic acids, aggregation of proteins, and removal of phospholipids. However, the spectra of the treated cells showed minimal spectral changes aside from those expected due to the removal of the phospholipids.

After ethanol treatment, the intensity profiles of the symmetric and antisymmetric phosphate stretching bands at 1085 and 1235 cm^{-1}, respectively, display small differences between the nucleus and the cytoplasm, as shown in Fig. 3. These indicate that the concentration of the remaining $–PO_2^-–$ groups from DNA and RNA is higher in the nuclei than in the cytosol. A difference spectrum for the cytosol, before and after ethanol treatment (trace 4–trace 5), is shown in trace 7. This trace, amplified four times, represents the spectra of phospholipids reasonably well, and we may conclude that the spectral components removed from the cells were, indeed, phospholipids. The observed difference spectra were larger for the cytosol than for the nucleus.

RNase digestion of cells attached to substrates was accomplished by incubating them twice with a solution of RNase A (1 mg/ml, type III, from bakers yeast, Sigma-Aldrich Co.) for 15 min at 37 °C (Chiriboga *et al.*, 2000; Lasch *et al.*, 2002). Subsequently, the slides were rinsed twice with distilled water and allowed to air-dry. Normally, RNase treatment is preceded by washing with detergents to render the cell's interior accessible to the enzyme. Since the ethanol treatment removed most of the cell membrane, we found that RNase digestion works without the detergent treatment, reducing the cytoplasmic RNA concentration significantly.

Figure 3, traces 3 and 6, depicts the effect of RNase digestion. This step removes cytoplasmic and nuclear RNA, resulting in nearly complete removal of the RNA contribution to the spectra of cytosol. This demonstrates that the cytoplasmic RNA is detectable by IR-MSP. The cytoplasmic RNA is most likely in the form of ribosomes involved in protein synthesis. Nucleic acid features persist in the nuclear region, due to DNA and possibly undigested RNA in the nucleus. Further digestion with DNA removed nearly all nucleic acid contributions (data not shown, see Lasch *et al.*, 2002). The difference spectrum shown in trace 8 shows the effect of RNase digestion in the nucleus. The difference spectrum is that of pure RNA (Diem *et al.*, 1999), with the distinct structure of the 1080 cm^{-1} peak and an intensity ratio of nearly 2:1 for the 1080/1235 cm^{-1} vibrations (see Fig. 2F, bands marked by asterisks). The remaining spectra of the cytoplasm (trace 6 in panels A and B) are dominated by protein features, and resemble the spectra shown in Fig. 2A. The data reported here indicate that most of the observed phosphate signals in an active cell are due to RNA and phospholipids, which are found in high concentrations in the cytoplasm of active cells. One of the most fascinating aspects of the spatially resolved data is the detection of the sheer abundance of the phospholipids in the cytoplasm outside the nucleus. On the basis of the known thickness of the bilayer membrane surrounding a cell, an argument can be made that it is impossible to observe its contribution to the spectrum of a cell. Thus, we suggest that the phospholipid signal at 1738 cm^{-1} results mostly from membranes of subcellular organelles such as the endoplasmic reticulum and Golgi apparatus that contain large amounts of phospholipids. Recent confocal Raman data have confirmed this observation (see Section III.C). It is unlikely that the outer membrane can be observed in transmission micro-spectroscopy, since its thickness is insufficient for a detectable IR signal.

Another cellular compound that may be removed relatively easily is glycogen. Several tissue types, such as liver tissue, and many squamous cells (e.g., cells from the human ecto-cervix, esophagus, and distal urethra) accumulate glycogen in significant amounts. Since the signals of glycogen mask the low wavenumber region of cells and tissues, it is advantageous to remove glycogen by digestion with α-amylase. When squamous cells from the distal end of the urethra are treated with α-amylase following standard histological procedures, one finds that the glycogen signal is completely removed (see Fig. 4, glycogen region marked by an asterisk). However, the overall protein intensity is also reduced by nearly an order of magnitude. The reason for the reduction of the entire cell absorption intensity is not understood at this point. Possibly, the amylase digestion solubilizes glycoproteins on the cell surface, which are subsequently removed in the washing steps.

2. Infrared Spectral Heterogeneity of Exfoliated Cells and Distinction of Cell Types

We have used oral mucosa (buccal) cells as one of the most easily obtainable exfoliated cell types from volunteer donors. These cells were exfoliated by gently swiping the oral cavity with sterile polyester swabs, and washing the obtained cells

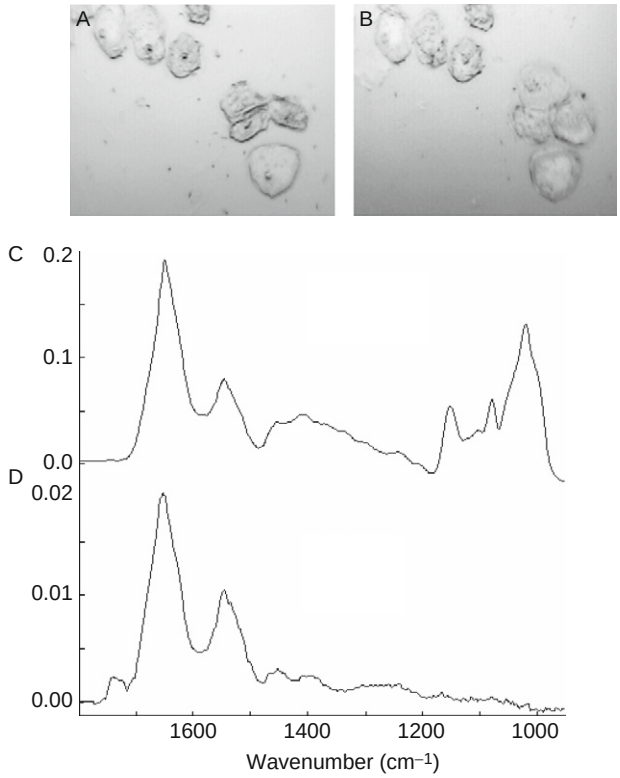

Fig. 4 Images and spectra of human superficial squamous cells before (A and C) and after (B and D) digestion of glycogen by α-amylase. Note the disappearance of the three glycogen peaks between 1000 and 1200 cm^{-1}, and the concomitant decrease in overall spectral amplitude.

repeatedly in buffered saline solution (BSS). In this section, spectra collected from entire individual cells are used to introduce the possibility of using infrared microspectral results to distinguish cell types and determine their state of health. We found that the spectra of harvested, mature human buccal cells show large heterogeneity, which is now well understood. This was discussed in detail before (Romeo *et al.*, 2006a). Similarly, the averaged spectra from several donors (data not shown, see Romeo *et al.*, 2006b) appeared quite different, and it was not clear at the onset of this work whether this heterogeneity would prevent application of IR-MSP as a diagnostic method.

Despite the apparent differences in the spectra shown in Fig. 5, we were able to interpret them via appropriate preprocessing and multivariate statistical methods. The preprocessing applied uniformly to all spectra includes computation of second derivatives of the absorption spectra with respect to wavenumber and subsequently normalization of the derivative spectra. This methodology was pioneered by the Naumann group at the Robert Koch Institut in Berlin, Germany, for the analysis

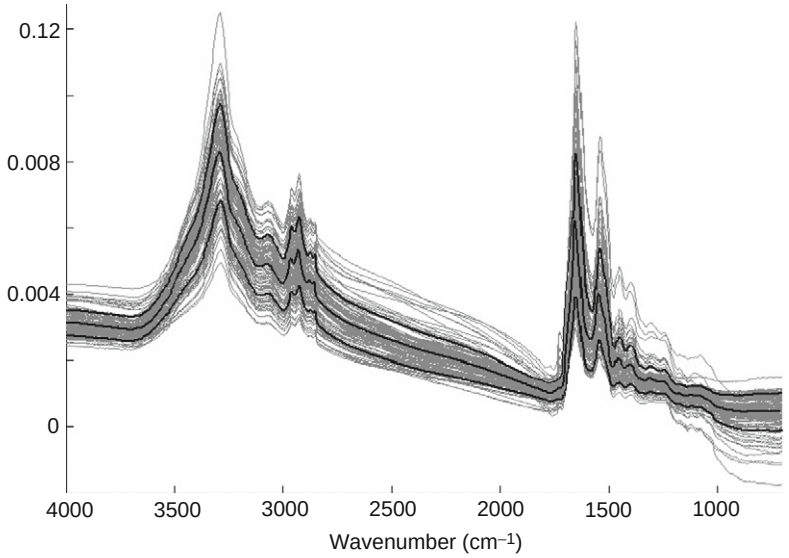

Fig. 5 (Panel A) Natural variance of IR spectra of exfoliated human oral mucosa (buccal) cells collected from one donor.

of spectral data of prokaryotic cell colonies (Naumann *et al.*, 1988). A PCA scores plot of these data, see (Romeo *et al.*, 2006a), collected from over 400 human cells, reveals a reasonably uniform distribution of the spectra, and indicates that there are only small variations between the cells from different donors.

Furthermore, the differences found between buccal cells are smaller than those observed when another cell type is added for comparison, for example, canine cervical cells. These cells were selected for a number of reasons. Morphologically, human oral mucosa cells and canine cervical cells are nearly identical, and both represent glycogen-free squamous epithelial cells. (Human cervical cells exhibit strong glycogen signals; therefore, their distinction from human buccal cells is trivial.) Furthermore, in terms of their biochemical composition, which ultimately determines the observed IR spectra, human buccal and canine cervical cells are expected to be very similar. Canine cervical cells can be obtained by gently scraping the excised cervix from spayed dogs with a miniature dental brush, and vortexing the cells from the brushes in BSS.

Thus, we thought it an important test of the spectral methodology to determine whether or not these cells could be distinguished. In total, seven sets of human oral mucosa cells (comprising 427 spectra), and five sets from animals (560 spectra) were combined into one data set and analyzed via PCA. The scores plots (PC2 vs PC3) of uniformly preprocessed data are shown in Fig. 6A, and the PC3 versus PC4 plot in Fig. 6B. The separation between canine cervical and human buccal cells is excellent in both plots.

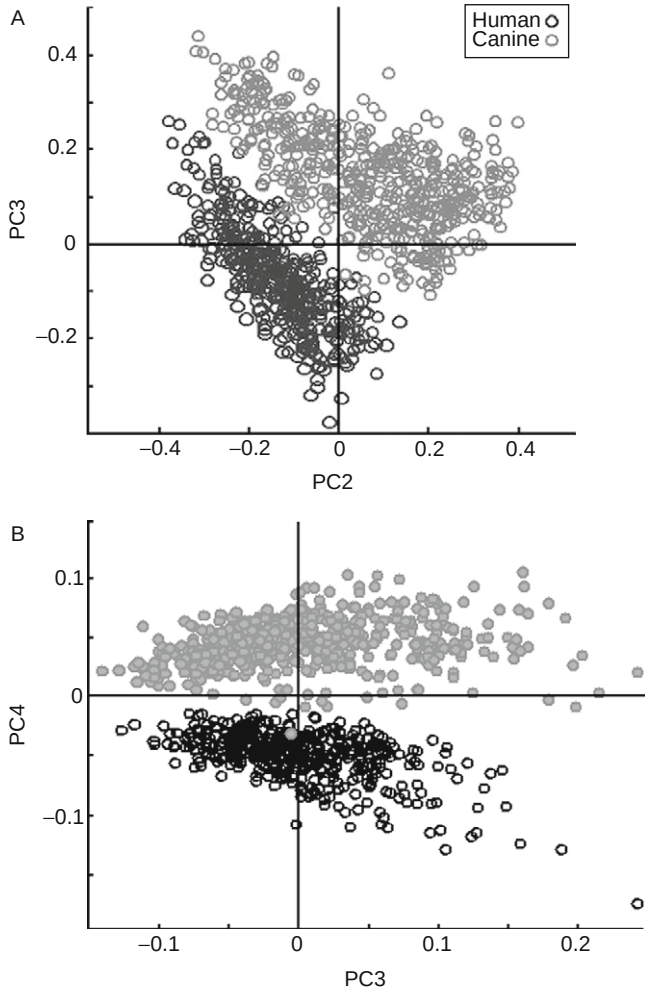

Fig. 6 (A) Scores plot (PC2 vs PC3) and (B) PC3 versus PC4 of human buccal and canine cervical data sets.

When the spectra of cells from dogs in estrus were incorporated into the PCA, they were found to fall exactly within the range of the human buccal cells, and were well separated from the spectra of cells of non-estrus dogs. The explanation of this spectral differentiation may be found in the level of maturity of the cells examined (Romeo *et al.*, 2006a). The human buccal cells, exfoliated from the oral mucosa, are mature squamous epithelial cells. These cells are typically between 50 and 60 μm on edge. For non-estrus dogs, the cervical cells are not completely mature, and are generally classified as intermediate squamous cells (Holst, 1985). These cells are

smaller, ~25–35 μm on edge. During estrous, hormonal changes cause maturation of the canine cervical cells from intermediate to superficial cells. In this process, the cells enlarge to about the same size as mature human cervical or human buccal cells. At the same time, the nucleus decreases in size and may even become pyknotic for completely mature cells. This fact is well known in cytology, and is used to differentiate between intermediate (immature) and superficial (mature) human cervical cells.

Thus, we have used the nucleus-to-cytoplasm ratio (N/C) of cells to explain the differentiation between human buccal and cervical cells from estrous dogs on one hand, and immature cervical cells on the other. Since the nucleus contributes much more strongly to the overall spectrum of the cell than the cytoplasm (Romeo *et al.*, 2006a), variations in the N/C ratio will greatly affect the observed spectra. Thus, we suggest that the discrimination between immature and mature cells is a direct consequence of the N/C ratio of these cells, as demonstrated for the (intermediate) canine cervical cells on one hand, and mature human buccal cells and mature canine cervical cells on the other.

3. Cell Cycle Dependence of Cellular Spectra

In order to explain the spectral heterogeneity of samples of cultured as well as exfoliated cells, we embarked on a study to investigate whether the stage in the cell's division cycle might influence their spectral characteristics. To this end, HeLa cells grown in culture were synchronized using "mitotic shake-off" and stained to identify the stage of the cell cycle.

Mitotic shake-off was carried out by first removing poorly adherent and dead cells by shaking the cell flasks on a laboratory vortex mixer and subsequently replacing the supernatant with 15 ml of fresh Dulbecco's Modified Eagle's Medium (DMEM, ATCC), supplemented with 10% fetal bovine serum (FBS, ATCC). After incubation for 1 h, the flasks were once again shaken on the vortex mixer to remove spherical cells presumed to be undergoing mitosis. The medium was immediately centrifuged for 6 min at $80\times g$ to collect the cells, which were resuspended in warm DMEM culture medium, seeded onto slides, and incubated at 37 °C and 5% CO_2. The appearance of two daughter cells was observed for most of the original cells.

At 1-h intervals, slides were removed from the incubator. All cells on a given slide should be in approximately the same stage of the cell cycle (or at the same "biological age"), since they all went through mitosis at the same time. To further determine the cells' biological age, we used common biochemical markers which indicate the presence of cell cycle-specific proteins (cyclin E for G1 phase, cyclin B1 for G2 phase) and 5-bromo-2′-deoxyuridine (BrdU) incorporation (Aten *et al.*, 1992) for S phase. BrdU incorporation needs to be carried out before infrared data acquisition, whereas the cyclin antibody stains could be added to the cells afterwards.

Following data collection, cells were subjected to immunohistochemical staining to determine their biochemical age in the cell cycle. Details of all procedures may be found in the literature (Boydston-White *et al.*, 2005). Figure 7A shows the typical staining pattern for each of the three populations (G1, S, and G2) of cells

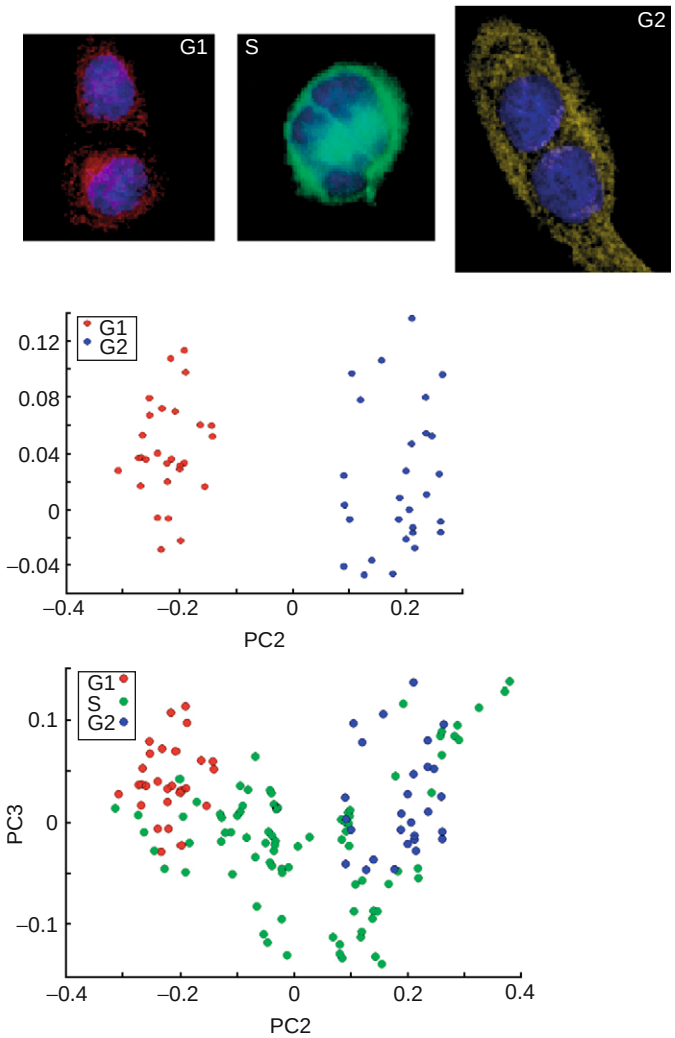

Fig. 7 (Panel A) Immunohistochemical staining to confirm the biological age of HeLa cells which were partially synchronized by mitotic shake-off. In addition to the immunohistochemical stains described in the text, the cells were DAPI-stained (blue) to visualize the nuclear DNA. (Panel B) PCA plot of cells which were determined to be in G1 and G2 stages via staining and synchronization procedures. (Panel C) PCA plot of cells which were determined to be in G1, S, and G2 stages via staining and synchronization procedures.

within the division cycle. Positive red staining for cyclin E indicates that the cells were in the G1 phase (Koff *et al.*, 1991) at the time of fixation. Since the thymidine analog BrdU is integrated into nuclear DNA only during DNA synthesis during the S phase, the green fluorescence staining for BrdU indicates that the cell was actively synthesizing DNA. Finally, a group of cells exhibited only positive yellow fluorescence staining for cyclin B1, and was assigned to the G2 phase.

In Fig. 7B, scores plots of cellular populations are presented. The separation between G1 and G2 stages is very good, indicating that there are systematic variations in the protein spectra between G1 and G2 stages. This result is not too surprising, considering that in G1 the proteins for DNA replication are synthesized, whereas in G2 proteins for mitosis are synthesized.

However, the S-phase spectra do not form a distinct cluster, but span the entire PC3/PC2 space, with much larger variance than the G1/G2 cells (Fig. 7C). Thus, we conclude that S-phase spectra cannot easily be separated from G1- and G2-phase spectra. Spectrally, some S-phase cells appear very similar to G1 cells, while others appear similar to G2-phase cells. Still other S-phase cells have quite different spectra from both G1- and G2-phase cells. The reasons for the spectral heterogeneity in the S phase are not clear at this point. The discrimination between G1 and G2 stages is based mostly on changes of the amide I and II bands. We observe a shift of 10 cm^{-1} in the amide I peak position, accompanied by a shift in an amide I shoulder, and a shift of the amide II peak, as the cells progress through the G1, S, and G2 phases, indicative of changes in protein structures (Boydston-White *et al.*, 2005).

4. Normal and Abnormal Cells

Although spectral differences between cancerous and normal tissues have been demonstrated by a number of research groups, and for a variety of tissue types, reliable results on the single cell level have been less frequent. This is, at least partially, due to the fact that large-scale single cell spectroscopy was not practical until about 2003, when more sophisticated and sensitive IR-MSP instruments became available. We have detailed spectral differences at the single cell level for cervical dysplasia, and more recently, between normal and malignant lymphocytes (see Fig. 8). Very similar results have been reported by Chan *et al.* (2006) using RA-MSP, followed by PCA analysis. A large-scale study of normal and cancerous urothelial cells is presently being carried out in the authors' laboratory.

5. Infrared Spectral Studies of Live Cells

Here, we wish to discuss briefly the observation of IR-MSP of individual human cervical cancer (HeLa) cells suspended in buffer or cell culture medium. IR spectroscopy of cells in an aqueous environment is difficult because of the very strong water vibrations that interfere with the protein amide I, II, and A vibrations. The strong absorption of water also necessitates the use of very short sample

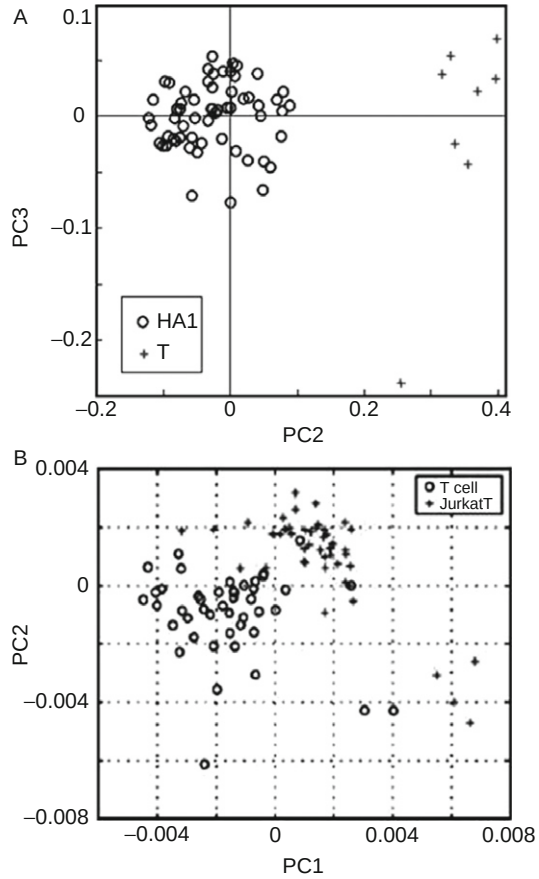

Fig. 8 (Panel A) PCA scores plot for infrared spectra of normal human T lymphocytes (crosses) and HA-1 T-cell lymphoma cells (circles). (Panel B) PCA scores plot for Raman spectral differentiation of normal human T-cells (circles) and Jurkat cells (crosses).

pathlength, typically between 8 and 10 μm. Such a short pathlength is suitable if cells grown on a substrate are investigated.

The sensitivity of modern IR micro-spectrometers is sufficiently high to permit observation of the cellular spectra even in the presence of the high water background signals. The results reported here might have far-reaching implication for the use of IR-MSP to monitor cell proliferation, drug response, and other cell biological parameters in live cells. In addition to the strong water absorption, another problem arises for spectroscopy of live cells. This problem is due to the fact that IR spectroscopy is always carried out as a ratio measurement of the background and the sample spectra. Since the cell contains less water signal than the background spectrum, which is collected from the aqueous layer around the

cell, the ratioed spectrum is overcompensated for the water contribution, which has to be corrected manually.

Nevertheless, good spectra could be obtained (Miljković *et al.*, 2004) for a live cell in growth medium. This spectrum agreed by and large with the spectra obtained from dried cells. However, the spectra of cells in growth medium show a sharp band in the symmetric phosphate stretching region (1085 cm^{-1}) with relatively large intensities throughout the nucleus and the cytoplasm. This band is not due to the growth medium itself, which has no spectral features in this region. The identity of this band is presently unknown, but its presence in both cytoplasm and nucleus suggests that it is due to a short-lived component containing phosphate groups, such as ATP, phosphorylated carbohydrates, or proteins that are particularly prevalent in metabolically active cells.

C. RA-MSP Maps of Individual Cells

The studies reported in this section are aimed at demonstrating the label-free advantages of RA-MSP imaging, which is able to reveal cellular compartmentalization and distribution of subcellular organelles. This research is still in its infancy and is being carried out only in a few laboratories worldwide. Therefore, the quality of the data is still somewhat limited; however, with rapid advances in technology, we expect RA-MSP to become a widely applicable technique for cellular biology.

1. High Resolution Raman Images of Cells

We present in Fig. 9 confocal Raman images of a hydrated exfoliated oral mucosa cell. Fig. 9B is constructed from HCA of 14,400 individual spectra collected using a 60× water immersion objective, and about 15 mW laser power at 514.5 nm excitation. The pixel size in this image is determined by the diffraction limit [see Eqs. (1) and (2)] and is given by about 320 nm laterally, and about 1400 nm axially. Figure 9C shows a X–Z section of the cell; this scan was taken along the direction of the black line in panel A. These images demonstrate the excellent image quality and biochemical information that is available from Raman spectral imaging, followed by multivariate data analysis methods. The red spots in panel B, for example, differ in chemical composition from the surrounding cytoplasm (blue trace in Fig. 9, panel D), and are mostly due to heterogeneously distributed phospholipids (red trace in panel D). From this image, the small size of the pyknotic nucleus in a terminally differentiated squamous cell can be estimated to be less than 10 μm in diameter.

Next, we discuss RA-MSP images of human cells at different stages of mitosis by following the spectral signatures of condensed chromatin, and other biochemical components, utilizing inherent protein and DNA spectral markers. In Section III.B.3, we discussed IR-MSP studies that have concentrated on the detection of variations of a cell's biomolecular composition during progression through the

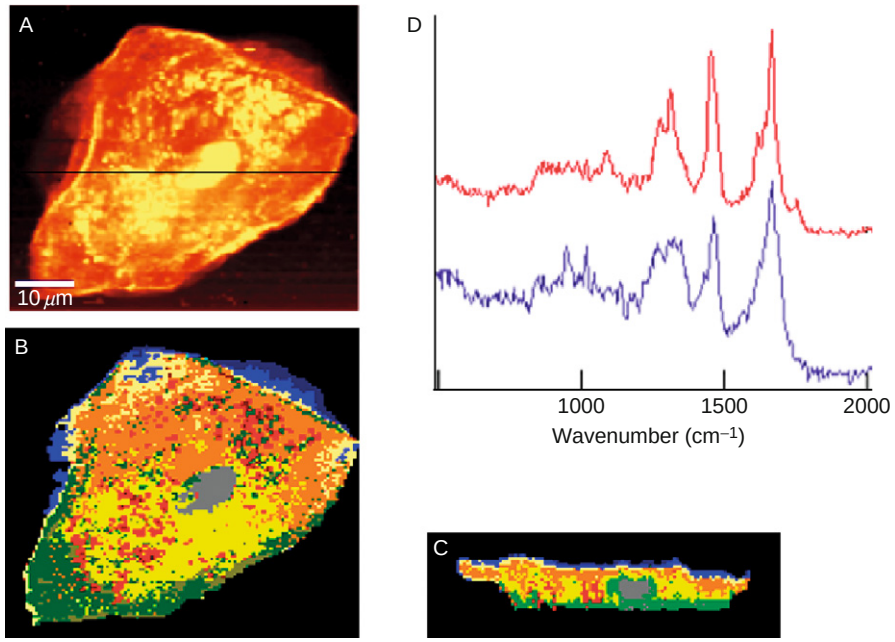

Fig. 9 Raman images of a human buccal cell. (A) Map of integrated C–H stretching intensities of an oral mucosa cell. (B) Pseudo-color X–Y map of the cell shown in (A), based on HCA of the Raman imaging data set. (C) Corresponding X–Z map, taken as a confocal section along the black line indicated in (A). (D) Normalized mean cluster Raman spectra of phospholipid-rich (top) and protein-rich (bottom) regions of the cytoplasm.

cell cycle, which precedes mitosis. Here, we present Raman spectral maps for the events that take place during mitosis. The exact sequence of events during mitosis is, of course, well understood from light and fluorescence microscopic studies. Spectral imaging methodology, however, affords the advantage of monitoring the distribution of biochemical components, using only their inherent vibrational fingerprints without employing any stains or other commonly used probes.

Mitotic cells were selected by microscopic inspection of fixed cells grown on a substrate in culture (Matthäus *et al.*, 2006). The spectral maps reported below for different stages of mitosis do not represent a time course of mitosis of one individual cell, but time points in mitosis of several different cells. Figure 10 shows HeLa cells undergoing the typical stages of mitosis: prophase, metaphase, anaphase, and telophase. The left column of images shows the cells as seen using an inverted phase contrast microscope. The second column shows maps of the nucleic acid Raman band intensity at 785 cm^{-1}, whereas the third column depicts the protein amide I intensity (1655 cm^{-1}). The protein intensity during mitosis is contributed largely by the micro-tubules and the dense histone-packed chromatin. The far right column shows, for comparison, the fluorescence images of the DAPI-stained

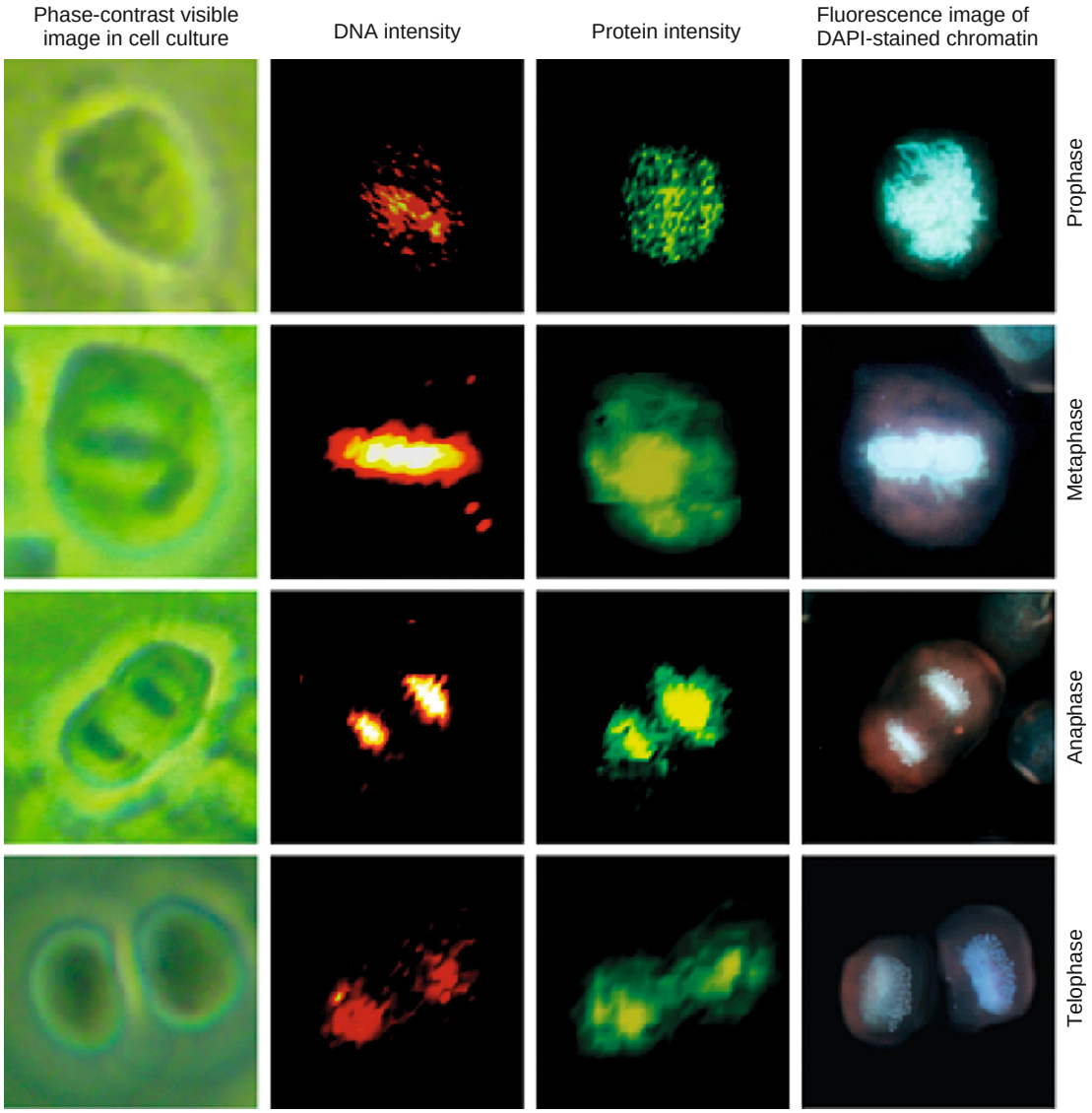

Fig. 10 Photomicrographs: Raman and fluorescence (DAPI stain) images of HeLa cells during various phases of mitosis. (Top row) Prophase, (2nd row) metaphase, (3rd row) anaphase, (bottom row) late telophase. All images are collected at 40× magnification. (Column 1) Phase-contrast images of cultured mitotic cells. (Column 2) Raman scattering intensity plots for the DNA scattering intensities. The colors range from black (low intensity) to red to white (high intensity). (Column 3) Raman scattering intensity plots for the protein scattering intensities. The colors range from black (low intensity) to green to yellow (high intensity). (Column 4) Fluorescence images of the DAPI-stained cells.

cells demonstrating the density and distribution of the condensed chromatin within the cell at each of the phases of mitosis.

The chromosomal condensation during metaphase and anaphase, shown in the second and third rows, respectively, is manifested by a large intensity increase of the DNA-related peaks (Matthäus *et al.*, 2006). The bottom row of images in Fig. 10 was taken for a cell in telophase. In contrast to the images of the cells in anaphase and metaphase, the DNA signal is reduced, since the DNA distribution has already become relatively diffuse during this stage of mitosis. However, the protein signals clearly indicate the presence of two newly formed nuclei.

The Raman chromatin intensities correlate very well with the DAPI fluorescence of chromatin. However, the Raman maps are constructed from the Raman scattering signals inherent in the cell, such as the protein/DNA distribution, rather than stains. The Raman images reproduce the chromatin distribution for the prophase, metaphase, and anaphase cells in exquisite detail. However, the chromatin exhibits low signals in the interphase and the late telophase cell since the protein–DNA chromatin complexes are packed much less densely, with a packing ratio of 40, as compared to a metaphase chromosome with a packing ratio of 10,000. Thus, the DNA or chromatin may be too diffuse to yield a detectable Raman signal in the volume probed in these experiments.

2. Label Free Imaging of Cellular Mitochondrial Distribution

This study was undertaken to demonstrate label-free detection of mitochondria in fixed cells. In principle, this methodology can be used in live cells to monitor mitochondrial movement and activity. Since the number of mitochondria in a human cell such as a HeLa cell is very large, detection of one individual mitochondrion is unlikely. However, this was achieved by RA-MSP methods for live yeast cells, which have only a few mitochondria (Huang *et al.*, 2005). Rather, we identified the mitochondria by comparison of Raman spectral clusters with regions exhibiting mitochondria-specific fluorescence emissions (Matthäus *et al.*, 2007). This was accomplished as follows.

HeLa cells were grown on CaF_2 substrates using standard cell culture procedures, and the cells adhering to the substrates were formalin-fixed. The cells were subsequently immersed in a drop of BSS solution, and Raman images were collected, as described before, using a water immersion objective, 488 nm excitation and 500 nm$\times$500 nm pixel size. The hyperspectral data sets were analyzed by unsupervised HCA (see Section II.G.2). Figure 11B shows a Raman map of a HeLa cell obtained from HCA of the data set. Although the bright-field image reveals low contrast (since it was taken of a cell in aqueous surrounding), the Raman image reveals the large nucleus typical for actively growing cells. Immediately after Raman data acquisition, a fluorescent stain specific for mitochondria (Mitotracker Green® FM, Invitrogen, Carlsbad, CA) was added to the sample without disturbing the optical settings of the instrument. Fluorescence images were collected ca. 20 min after the stain was added, using the confocal Raman setup

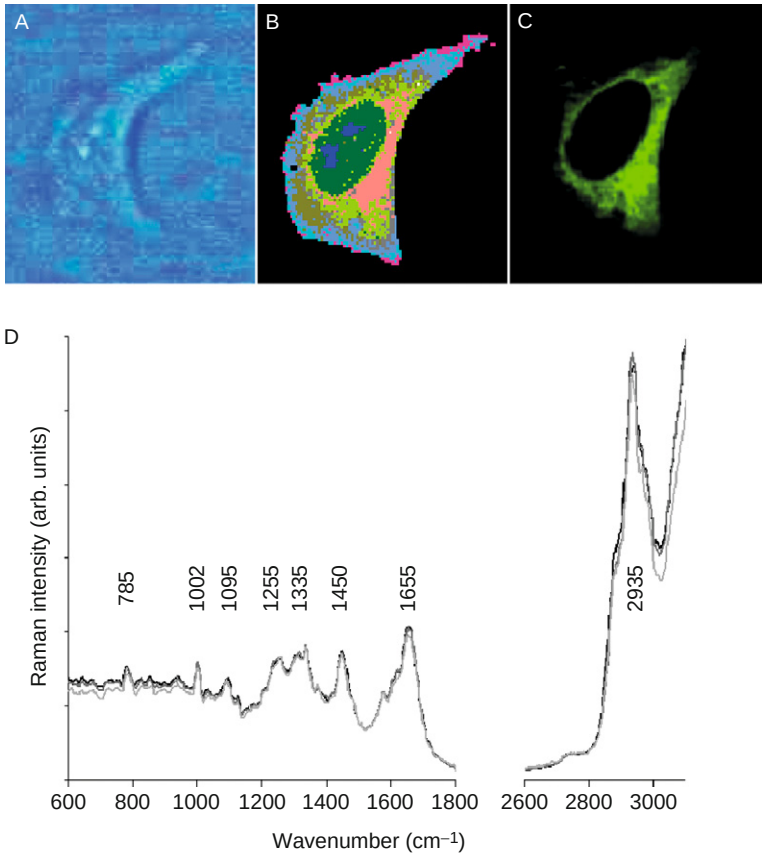

Fig. 11 Visualization of cellular mitochondrial distribution. (Panel A) Bright-field image of a HeLa cell in suspension in BSS, taken through a 60× water immersion objective. (Panel B) HCA-based pseudo-color map of cell shown in A. The color assignment is arbitrary and indicate similarities of spectral patterns. (Panel C) Fluorescence image collected after adding Mitotracker Green® FM stain to the buffer surrounding the cell. (Panel D) Mean Raman spectra, extracted from the nuclear regions of three cells used in this study.

described above and 488 nm excitation and significantly lower laser power (1 mW) and a dwell time of 0.2 s per data point.

Figure 11C shows the fluorescence image of the HeLa cell stained with Mitotracker® for mitochondrial distribution. Bright green areas correspond to high mitochondria content. The highest Mitotracker® fluorescence intensity was observed in the perinuclear region. A comparison of Fig. 11B and C reveals that the regions, from which significant fluorescence due to the Mitotracker® stain is observed, co-localizes very well with the Raman cluster shown in yellow and salmon hues in Fig. 11B. Since the number of spectra contributing to the mean cluster spectra is of the order of several hundred, the *S*/*N* ratio for the mean cluster

spectra is very good. Furthermore, we (Matthäus *et al.*, 2007) found that for a number of cells analyzed this way, the spectra are very reproducible. For example, the mean cluster spectra observed in the nuclei of three cells show excellent agreement, and even small details in the spectra are reproduced in all of them (Fig. 11D). Given that the Raman maps also can differentiate between nucleus and nucleolus in a cell, we analyzed the resulting means cluster spectra for changes that may be associated directly with the presence of mitochondria.

We found that the mean cluster spectra obtained between nuclear, cytoplasmic, and mitochondrial regions were too similar to interpret spectral changes reliably. All mean cluster spectra (nucleus, nucleolus, mitochondria-rich cytoplasm and remaining cytoplasm) are dominated by protein bands (the amide I vibration at 1655 cm^{-1}, the extended amide III region between 1270 and 1350 cm^{-1}, and the sharp phenylalanine ring stretching vibration at 1002 cm^{-1}), which is not surprising, given that the major component in all regions of the cell is protein. Nuclei and nucleoli exhibit a few, weak bands associated with nucleic acids (785, 1095, and 1575 cm^{-1}); although these bands are weak, they are sufficiently reproducible to be detected by HCA.

Apart from spectral features from proteins, lipid contributions may be observed in the spectra from within the cytoplasm. The alkane chains give rise to high C–H stretching intensities between 2850 and 2935 cm^{-1}. In addition, CH_2 deformations and the ester linkage C=O stretching are observed around 1735 cm^{-1}. We also observed a Raman band at 715 cm^{-1} in phospholipid-rich regions that is not present in the spectra from the nuclei. It is possible that this band originates from the symmetric stretching vibration of the N^+ $(CH_3)_3$ choline group of phosphocholine, which is vastly abundant in membranes.

Although the spectra from the mitochondria-rich regions differ from those of the nucleus and nucleolus, the mean spectra of the mitochondria-rich clusters are very similar to other phospholipid-containing regions of the cytoplasm. Thus, we were not able to reproduce the previous report that associated the spectra of mitochondria in yeast cells with spectral features from phospholipids (Huang *et al.*, 2005). Although we have frequently observed strong phospholipid spectra from small regions in the Raman maps of other cell types, we were not able to co-localize these with the position of mitochondria, and to reproduce these features for the HeLa cell model utilized here.

3. Liposome Uptake into Cells

Apart from imaging subcellular features, as discussed in the previous sections, Raman imaging may provide an opportunity to follow the uptake of molecules into cells. One way to distinguish incorporated molecules inside cells is to use deuterated compounds (van Manen *et al.*, 2005). C–D stretching vibrations are shifted away from those of C–H groups by a factor of about the square root of the masses of H and D, or about a factor of 1.4. Thus, C–D stretching vibrations occur around 2150 cm^{-1}, in a region devoid of any signals in the Raman spectra of cells

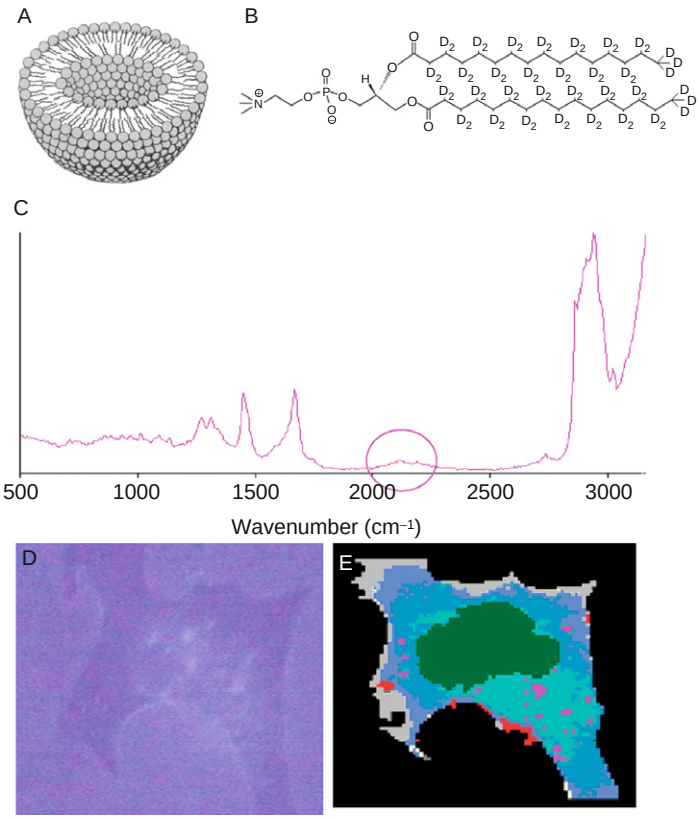

Fig. 12 Liposome uptake by cells. (Panel A) Schematic section through a liposome. (Panel B) Structure of DSPC-d_{70}. (Panel C) Raman spectrum obtained from a region of the cell containing deuterated liposomes. The C–D stretching region is shown by the circle. (Panel D) Bright-field image of breast adenocarcinoma (MCF-7) cells incubated for 3 h with TATp-LIP. (Panel E) HCA-based pseudo-color map of cell shown in panel D. Red areas correspond to the highest C–D stretching intensities (possibly due to condensed liposomes), whereas the purple spots inside the cytoplasm indicate small regions of deuterated lipids, possibly due to individual liposomes.

and cellular components (see Fig. 12, panel C). The deuterium "label" is invisible to the cell, since the isotopic species occupies nearly exactly the same volume, and acts chemically nearly identically, to hydrogen atoms.

We demonstrate the use of this technique (Matthäus *et al.*, 2008) to investigate the cellular uptake and intracellular fate of lipid-based nanoparticles known as liposomes (Fig. 12A). These are bilayer-based nanospheres with sizes ranging from ~50 to 300 nm. Currently, liposomes are widely used for drug delivery purposes (Gupta *et al.*, 2005), including intracellular drug and gene delivery (Rao and Gopal, 2006; Serpe *et al.*, 2006). Many aspects related to the detailed mechanisms of the liposome-to-cell interaction remain unresolved. This is especially true for the

case of liposomal nanocarriers modified by cell-penetrating peptides, such as the HIV-1 *trans*-activating transcriptional activator-derived TAT peptide (Gupta *et al.*, 2005). These carrier systems are currently considered a very promising way to bring various drugs, including protein and peptides, into cells (Wadia and Dowdy, 2005). Here we demonstrate the feasibility of Raman imaging to follow the uptake of TAT peptide-modified deuterated liposomes (TATp-LIP).

Deuterated liposomes were prepared according to literature procedures (Dipali *et al.*, 1996; Liang *et al.*, 2004) from a dried lipid film cast from a chloroform solution of DSPC-d_{70} (Avanti Polar Lipids, Inc., Alabaster, AL, Fig. 12B). This film was hydrated and vortexed with HEPES-buffered saline (HBS), pH 7.4, at a DSPC concentration of 1.6 mM. The resulting liposomes were sized through double stacked 200 nm pore size polycarbonate membranes (Nucleopore). The liposome size was analyzed by using a Coulter N4 MD Submicron Particle Size Analyzer (Coulter Electronics). TATp-liposomes were prepared as follows. Purified TATp was received from Tufts University Core Facility (Boston, MA). TATp peptide was coupled to TATp-PEG_{2000}-PE using published methods (Matthäus *et al.*, 2008). For preparing TATp-liposomes, TATp-PEG_{2000}-PE was added to the lipid film. Liposomes were subsequently sized as described above.

Human breast adenocarcinoma MCF-7 cells were incubated for different time intervals with deuterated LIP and TATp-LIP at a lipid concentration of 2 mg/ml. After the incubation, cells were fixed in a formalin-phosphate-buffered solution and subsequently washed and submerged in phosphate-buffered saline, to maintain the shape of the cells in their aqueous environment.

Figure 12D shows a microscopic image of an MCF-7 cell incubated with TATp-LIP for 6 h. Panel 12E is a pseudo-color map, constructed from the hyperspectral data set using HCA. The cluster analysis is based mainly on the detection of the C–D stretching vibrational signal, observed around 2150 cm^{-1}, and shown in trace 12C. Large amounts of the deuterated phospholipids were found in the cell periphery.

The most important result of this study is that RA-MSP clearly allows for the observation of lipid particle uptake by the cells. This uptake is enormously accelerated by TTAp, confirming previous experiments (Wadia and Dowdy, 2005). The uptake was clearly seen already after 3 h for TATp-LIP and only after 12 h for plain LIP. Although very small deuterated regions can be detected early in an uptake experiment, aggregation or incorporation of the deuterated phospholipids into other membrane structures occurs, resulting in contiguous regions of high deuterium content. To ascertain that the liposomes are observed within the cytoplasm and not just adsorbed on the cell surface, a depth profile in the *xz*-direction was collected (Matthäus *et al.*, 2008) which indicated that the deuterated liposomes penetrate the cell body. The spectral appearances of the C–D stretching region, with respect to band shapes and peak positions, did not change significantly upon uptake, indicating that the lipid side chains did not undergo substantial conformational changes.

IV. Conclusions

In this chapter, we have reviewed some of the most recent findings on Raman and infrared spectral studies of cells from our laboratory. Over the course of the past 4 years, we have collected spectra from in excess of 10,000 individual cells—both for high spatial resolution studies, in an effort to understand the spectral consequences of cell biological events, and for establishing data bases for eventual spectral diagnostic algorithms.

Acknowledgment

Partial support of this research from grants CA 81675 and CA 090346 from the National Institutes of Health is gratefully acknowledged.

References

Adams, M. J. (2004). "Chemometrics in Analytical Spectroscopy." Royal Society of Chemistry, Cambridge.

Aten, J. A., Bakker, P. J. M., Stap, J., Boschman, G. A., and Veenhof, C. H. N. (1992). DNA double labelling with IdUrd and CldUrd for spatial and temporal analysis of cell proliferation and DNA replication. *Histochem. J.* **24**(5), 251–259.

Boydston-White, S., Chernenko, T., Regina, A., Miljkovic, M., Matthaeus, C., and Diem, M. (2005). Microspectroscopy of single proliferating HeLa cells. *Vibrational Spectrosc.* **38**(1–2), 169–177.

Boydston-White, S., Romeo, M. J., Chernenko, T., Regina, A., Miljkovic, M., and Diem, M. (2006). Cell-cycle-dependent variations in FTIR micro-spectra of single proliferating HeLa cells: Principal component and artificial neural network analysis. *Biochim. Biophys. Acta* **1758**(7), 908–914.

Carr, G. L. (2001). Resolution limit for infrared microspectroscopy explored with synchrotron radiation. *Rev. Sci. Instrum.* **72**(3), 1613–1619.

Chan, J. W., Taylor, D. S., Zwerdling, T., Lane, S. M., and Ihara, K. (2006). "Micro-Raman Spectroscopy Detects Individual Neoplastic and Normal Hematopoietic Cells." *Biophys. J.* **90,** 648–656.

Chiriboga, L., Yee, H., and Diem, M. (2000). Infrared spectroscopy of human cells and tissue. Part VII: FT-IR microspectroscopy of DNase- and RNase-treated normal, cirrhotic, and neoplastic liver tissue. *Appl. Spectrosc.* **54**(4), 480–485.

Diem, M. (1993). "Introduction to Modern Vibrational Spectroscopy." Wiley-Interscience, New York.

Diem, M., Boydston-White, S., and Chiriboga, L. (1999). Infrared spectroscopy of cells and tissues: Shining light onto a novel subject. *Appl. Spectrosc.* **53**(4), 148A–161A.

Diem, M., Romeo, M., Boydston-White, S., Miljkovic, M., and Matthaeus, C. (2004). A decade of vibrational micro-spectroscopy of human cells and tissue (1994–2004). *Analyst* **129**(10), 880–885.

Dipali, S. R., Kulkarni, S. B., and Betageri, G. V. (1996). Comparative study of separation of non-encapsulated drugs from liposomes by different methods. *J. Pharm. Pharmacol.* **48**(11), 1112–1115.

Gupta, B., Levchenko, T., and Torchilin, V. P. (2005). Intracellular delivery of large molecules and small particles by cell penetrating proteins and peptides. *Adv. Drug Deliv. Rev.* **57,** 637–651.

Helm, D., Labischinski, H., Schallen, G., and Naumann, D. (1991). Classification and identification of bacteria by FT-IR spectroscopy. *J. Gen. Microbiol.* **137,** 69–79.

Holst, P. A. (1985). "Canine Reproduction: A Breeder's Guide." Alpine Publications, Loveland.

Huang, Y. S., Karashima, T., Yamamoto, M., and Hamaguchi, H. (2005). Molecular-level investigation of the structure, transformation, and bioactivity of single living fission yeast cells by time- and space-resolved Raman spectroscopy. *Biochemistry* **44,** 10009–10019.

Humecki, H. J. (1995). "Practical Guide to Infrared Microspectroscopy." Marcel Dekker, New York.
Koff, A., Cross, F., Fisher, A., Schumacher, J., Leguellec, K., Philippe, M., and Roberts, J. M. (1991). Human cyclin E, a new cyclin that interacts with two members of the CDC2 gene family. *Cell* **66**(6), 1217–1228.
Lasch, P., Pacifico, A., and Diem, M. (2002). Spatially resolved IR microspectroscopy of single cells. *Biopolymers* **67**(4–5), 335–338.
Lasch, P., Haensch, W., Naumann, D., and Diem, M. (2004). Imaging of colorectal adenocarcinoma using FT-IR microspectroscopy and cluster analysis. *Biochim. Biophys. Acta* **1688**(2), 176–186.
Liang, W., Levchenko, T. S., and Torchilin, V. P. (2004). Encapsulation of ATP into liposomes by different methods: Optimization of the procedure. *J. Microencapsul.* **21,** 151–161.
Matthäus, C., Boydston-White, S., Miljković, M., Romeo, M. J., and Diem, M. (2006). Raman and infrared microspectral imaging of mitotic cells. *Appl. Spectrosc.* **60**(1), 1–8.
Matthäus, C., Chernenko, T., Newmark, J. A., Warner, C. M., and Diem, M. (2007). Label-free detection of mitochondrial distribution in cells by nonresonant Raman Micro-Spectroscopy. *Biophys. J.* **93,** 668–673.
Matthäus, C., Chernenko, T., Kale, A., Torchilin, V. P., and Diem, M. (2008). "Raman-microspectroscopic Imaging of Liposomal Drug Delivery Systems Inside Individual Cells." *Mol. Pharm.* **5**(2), 287–293.
Messerschmidt, R. G., and Harthcock, M. A. (1988). "Infrared Microspectroscopy." Marcel Dekker, New York.
Miljković, M., Romeo, M. J., *et al.* (2004). Infrared microspectroscopy of individual human cervical cancer (HeLa) cells suspended in growth medium. *Biopolymers* **74**(1–2), 172–175.
Naumann, D., Fijala, V., Labischinski, H., and Giesbrecht, P. (1988). The rapid differentiation of pathogenic bacteria using Fourier transform infrared spectroscopic and multivariate statistical analysis. *J. Mol. Struct.* **174,** 165–170.
O'Malley, D. (2008). Confocal one and two photon fluorescence microscopy. *In* "Methods in Cell Biology, Vol. 2: Biophysical Techniques" (J. J. Correia and H. W. Detrich, eds.). Elsevier, Amsterdam.
Otto, C., and Greve, J. (1998). Progress in instrumentation for Raman micro-spectroscopy and Raman imaging for cellular biophysics. *Internet J. Vibrational Spectrosc.* **2**(3).
Rao, N. M., and Gopal, V. (2006). Cell biological and biophysical aspects of lipid-mediated gene delivery. *Biosci. Rep.* **26**(4), 301–324.
Romeo, M., Mohlenhoff, B., Jennings, M., and Diem, M. (2006a). Infrared micro-spectroscopic studies of epithelial cells. *Biochim. Biophys. Acta* **1758**(7), 915–922.
Romeo, M. J., Mohlenhoff, B., and Diem, M. (2006b). Infrared microspectroscopy of human cells: Causes for the spectral variance of oral mucosa (buccal) cells. *Vibrational Spectrosc.* **42,** 9–14.
Serpe, L., Guido, M., Canaparo, R., Muntoni, E., Cavalli, R., Panzanelli, P., Della Pepal, C., Bargoni, A., Mauro, A., Gasco, M. R., Eandi, M., and Zara, G. P. (2006). Intracellular accumulation and cytotoxicity of doxorubicin with different pharmaceutical formulations in human cancer cell lines. *J. Nanosci. Nanotechnol.* **6**(9–10), 3062–3069.
van Manen, H. J., Kraan, Y. M., *et al.* (2005). "Single-cell Raman and fluorescence microscopy reveal the association of lipid bodies with phagosomes in leukocytes.". *Proc. Natl. Acad. Sci. USA* **102**(29), 10159–10164.
Wadia, J. S., and Dowdy, S. F. (2005). Transmembrane delivery of protein and peptide drugs by TAT-mediated transduction in the treatment of cancer. *Adv. Drug Deliv. Rev.* **57**(4), 579–596.
Ward, J. H. (1963). Hierarchical grouping to optimize an objective function. *J. Am. Stat. Assoc.* **58**(301), 236–244.
Wood, B. R., Chiriboga, L., Yee, H., Quinn, M. A., McNaughton, D., and Diem, M. (2004). FTIR mapping of the cervical transformation zone, squamous and glandular epithelium. *Gynecol. Oncol.* **93**(4), 59–68.

CHAPTER 11

Imaging Fluorescent Mice *In Vivo* Using Confocal Microscopy

Stephen G. Turney and Jeff W. Lichtman

Department of Molecular and Cellular Biology and the Center for Brain Science
Harvard University
Cambridge, Massachusetts 02138

Abstract

In vivo imaging is the most direct way to uncover the dynamic events that occur during neural development. This approach is especially challenging in developing mammals where technical hurdles related to optical resolution, animal movement, phototoxicity, and postoperative complications need to be addressed. In our work

METHODS IN CELL BIOLOGY, VOL. 89

0091-679X/08 $35.00
DOI: 10.1016/S0091-679X(08)00611-0

concerning the process of naturally occurring synapse elimination at developing neuromuscular junctions, these technical issues are critical because we need to resolve multiple and very fine single axons that converge on the same synaptic site. In previous studies, we used wide-field microscopy with either intensified or high quantum efficiency cameras. We now have begun to use laser scanning confocal microscopy which improves contrast and resolution but comes with its own challenges. In this chapter, we describe the approaches we have taken to permit both rapid time-lapse (minutes to hours) and long-term time-lapse (days to months) to visualize the synaptic alterations associated with the development and maturation of the neuromuscular system.

I. Introduction

In this chapter, we will review the steps we take for routine live imaging of neuromuscular junctions in the sternomastoid muscle of mice. The mice we use for these studies are transgenic and express various colors of fluorescent proteins in axons (Feng *et al.*, 2000; Kasthuri and Lichtman, 2003; Walsh and Lichtman, 2003). Live animal imaging is beset with a number of technical issues. Some of these issues and their solutions have been discussed previously for imaging in adult mice (Balice-Gordon, 1997; van Mier and Lichtman, 1994) and earlier efforts to modify the approaches that work in adults for wide-field imaging of neonatal animals have also been described (Walsh and Lichtman, 2005). Here, we focus particularly on techniques that allow for the use of laser scanning microscopy for time-lapse fluorescence imaging. Although our main experience is with neuromuscular junction imaging, we believe these same techniques can guide biologists interested in imaging other cells and structures in developing mammals. In this chapter, we focus especially on issues that affect spatial and temporal resolution in live mammalian imaging studies, including optical access to tissue, anesthesia, animal movement during image acquisition, fluorescence labeling, and phototoxicity. We begin with a discussion of each of these issues. A detailed methods section can be found at the end of this chapter.

II. Rationale

The mechanisms underlying developmental processes such as synapse elimination can only be understood using techniques that follow cellular changes over time. If changes occur slowly over days to weeks, the ability to image in a live animal repeatedly is an advantage over determining stages of development from single time points each taken from a different animal. To illustrate the importance of repeatedly imaging the same cells, imagine trying to learn the rules of American football from pictures taken at different games (Lichtman and Fraser, 2001). In the single time point approach, we would take one picture per game, each staggered

according to the game clock—but no two from the same game. We would then arrange the photographs to analyze changes over time; however, because the plays unfold asynchronously with respect to the clock (except for the opening kickoff at the start of each half), the rules for advancing the ball, change of possession, and scoring could not be determined from pictures of unrelated plays. Instead the basic rules and their consequences would be deducible from time series data showing a progression of plays in the same game. Therefore, the ability to see the same cells repeatedly makes it possible to correlate changes with preceding or following events. The challenge of live imaging comes from factors that constrain repeated viewing of the same animal, as we will now discuss.

A. *In Vivo* Optical Access to Tissue

Because of the enormous scattering of light in living tissue, with visible light fluorescence microscopy, it is only possible to image at or near the tissue surface. We study the synaptic connections in the sternomastoid muscle mainly because of ease of access: the muscle is superficial in the ventrally exposed neck. Moreover, its neuromuscular junctions are relatively large and each has a unique morphology which makes it relatively straightforward to find the same junction for repeated imaging over days or months. The muscle fibers in the sternomastoid are unusual in that they each run the length of the muscle. Because there is a single band of neuromuscular junctions (the end plate band) that runs across the muscle nearer to the muscle origin on the sternum than its mastoid insertion, one need not search to find the synapses. This muscle is advantageous because in most mammalian muscles of comparable length, intramuscular tendons allow the fibers to be much shorter and typically there is more than one end plate band scattering the junctions throughout the muscle at low density. A diagram showing the position of the sternomastoid muscle in the neck is given in Fig. 1A. To expose the muscle, an incision is made along the midline of the neck in an anesthetized animal (see below). The large submandibular and smaller sublingual glands are retracted to one side, and the muscle is lifted on a thin metal support. Typically, little or no bleeding occurs with surgery as few blood vessels cross the midline. A coverslip may be placed on top of the muscle to lessen movement (Fig. 1B); however, it is advisable to use only those objectives that are coverslip-corrected since extra glass may cause some spherical aberration. By pressing the coverslip gently on the muscle surface, movement due to heartbeat is reduced and junctions on the muscle surface appear flat and in focus when imaged with high numerical aperture (NA) objectives. The muscle has a thin layer of connective tissue which can be removed with forceps. This connective tissue tends to increase with multiple viewing sessions. In general, only neuromuscular junctions at or near the surface of the muscle can be imaged at high resolution as those more than a few fibers deep are obscured as a result of index of refraction changes and scattering.

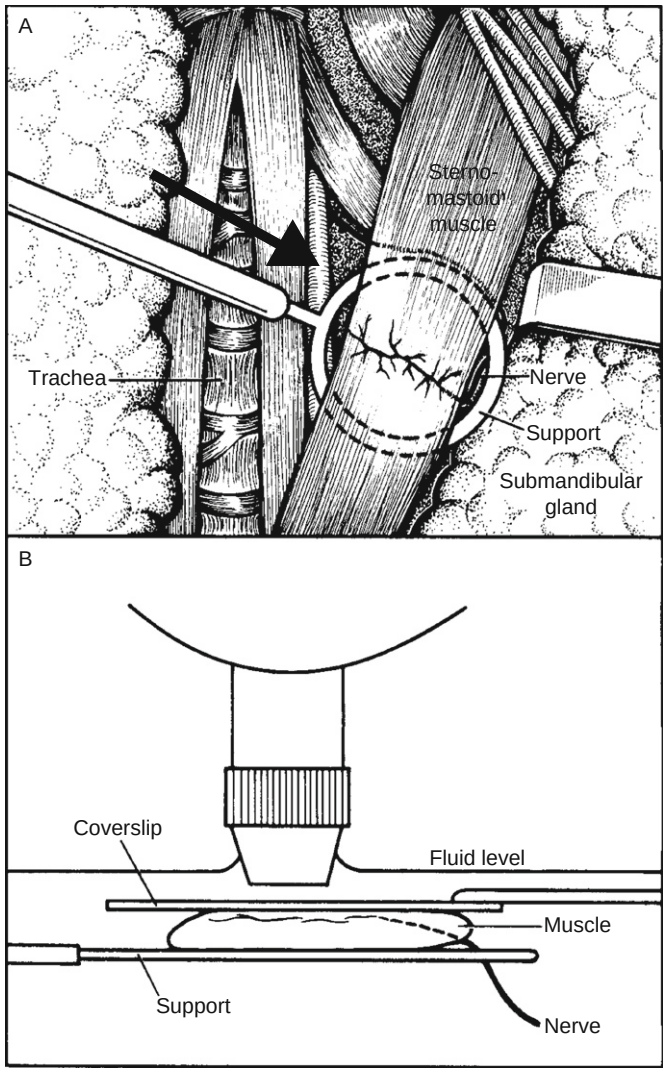

Fig. 1 Schematic showing the position of the sternomastoid muscle in the neck of a mouse (A). The muscle is exposed by retracting the submandibular and sublingual glands. A platform is inserted under the muscle at the position of the end plate band (roughly a third of the length of the muscle from its insertion at the sternum). The nerve bundle enters laterally, so the platform arm is brought across the mouse. To stabilize the muscle for imaging, the platform is raised and a glass coverslip may be pressed down gently on the ventral surface of the muscle (B). For imaging with a dipping cone objective, we do not use a coverslip to avoid spherical and chromatic aberrations. Reprinted with permission (J Neurosci., Apr 1987; 7:1215–1222).

B. Anesthesia

Obviously, work with living animals requires a judicious use of anesthesia. Animals that are too lightly anesthetized will move making high-resolution imaging difficult and it is inhumane for laboratory mammals to feel discomfort that is avoidable. Animals that are overanesthetized will have difficulty recovering from the imaging session which will prevent multiple time-lapse sessions. Because at developing neuromuscular junctions, changes in morphology occur gradually over days, it is necessary to do multiple sessions in one animal. For example, axonal inputs may gain and lose synaptic territory, or one input may withdraw from a junction completely over 2–5 days (Walsh and Lichtman, 2003). Over a period of hours, however, a junction appears largely unchanged. Ideally, we would prefer to image at frequent intervals (or even continuously) over days to capture the details of synaptic rearrangement. Practically, this has proven difficult because of the complications from prolonged anesthesia, which includes hypothermia, hypotension, and bradycardia. While rats can be anesthetized for periods up to 2 days (Jansen and Van Essen, 1975), our experience is that mice do not tolerate long duration general anesthesia. Typically, we image only once per day, anesthetizing with i.p. injectable agents for as short a period as possible (1–3 h). While adult mice can be returned to their cages immediately after surgery, pups are revived with a reversal agent (Antisedan; see Section III of this chapter) and allowed to right themselves fully before being returned to their mother. The pups need to recover fully before being reintroduced to the mother as cannibalization or biting of the wound site by the mother or another adult often ensues if the pup is not upright and awake. The entire imaging session, including surgery, imaging, and recovery, takes anywhere from 1 to 12 h. A 24-h interval between the start of surgeries is generally enough to allow repeated imaging day after day. If the interval is shorter, the animals do not fully recover from surgery, and morbidity and mortality are increased.

Once a mouse is anesthetized, the time that is available for imaging is limited by the time required for intubation and surgery. If everything goes smoothly the muscle can be exposed and ready for imaging in less than half an hour; however, complications frequently arise that delay imaging for an hour or more. For instance, inserting an endotracheal tube in a neonatal animal is not always straightforward. The tube must be thin and slightly curved to avoid esophageal placement. Repeated attempts can cause inflammation of the airway, delaying or preventing intubation. Another complication is that in subsequent imaging sessions, the previous surgical exposure invariably results in rapid overgrowth of connective tissue and infiltration by inflammatory cells. For repeated imaging, the muscle must first be cleaned of connective tissue that formed because of a previous surgery. Connective tissue is highly refractive and even a thin layer can degrade image quality. The layer often strongly adheres to muscle, making its removal difficult and time consuming if one is to avoid muscle fiber damage. Finally, if muscle twitching is observed at high magnification (i.e., on the microscope) the platform must be removed and repositioned under the muscle as the

twitching may be due to nerve or muscle fiber stretching. This repositioning involves moving the platform to a slightly different place along the length of the muscle and turning the muscle slightly by changing the angle of contact between the metal platform and the muscle. In general, any touching of the muscle must be done slowly and carefully in order not to damage muscle fibers or the innervating nerve bundle.

C. Movement

The ability to minimize animal movement is important for image quality. To obtain high-resolution images of neuromuscular junctions, we image surface muscle fibers using high NA immersion objectives. Junctions are relatively thin structures on a curved surface (i.e., the muscle fiber membrane) making them thicker than the depth of field of the high-NA objective. To visualize a whole junction, we acquire multiple images at different depths. For archiving, a final two-dimensional (2D) projection is obtained by using a standard maximum intensity projection algorithm of the image stack. If movement occurs during scanning, the individual image planes can be aligned and warped in software using programs such as ImageJ (plug-ins available from http://rsb.info.nih.gov/ij; ImageJ was developed by Wayne Rasband, National Institutes for Health, Bethesda, MD) or Autoquant (Media Cybernetics). Unfortunately, the movement during a scan may introduce some distortions that are not fully corrected by alignment (such as changes in focus during a single image scan); therefore, to achieve the highest possible resolution, the muscle must remain motionless during acquisition of the image stack.

The major sources of movement during imaging are breathing, heartbeat, and muscle twitching. Breathing-related movement is controlled by the mechanical ventilation of the intubated mouse. The respirator can be turned off for ~30–60 s before the anesthetized mouse attempts to breathe on its own. If the anesthesia is wearing off or if the mouse was inadequately anesthetized this interval will be shorter (<20 s). It is while the breathing is interrupted that an image stack is acquired.

Maximizing image quality on a confocal microscope system involves a trade-off between scan size, pixel rate, and step size in the Z axis. We typically acquire scans that are 512 × 512 pixels with a scan speed of 4 μs per pixel (1 s per scan) and a step size in the Z-axis of 1 μm (using a 20× 0.95NA dipping cone objective). A stack may comprise 20–25 planes. If the scan size is enlarged to 1024 × 1024 pixels, the scan time would increase 4 times. To keep the scan time constant, the pixel rate and/or step size must be increased, making images noisier and reducing resolution in the axial dimension.

To isolate the muscle from heartbeat movement, the sternomastoid muscle is raised on a thin metal support. Lifting the muscle isolates it from pulsing of the carotid artery (arrow in Fig. 1A) that lies beneath the sternomastoid muscle in the neck. Localized movement in the muscle can also occur because of pulsing of major blood vessels within the muscle. To minimize this localized movement, a coverslip may be pressed down gently on the muscle surface as mentioned above (Fig. 1B).

If the heartbeat-related movement continues, the platform must be removed and reinserted, perhaps changing the angle of the platform and rolling the muscle slightly while lifting to reorient the muscle. Overstretching the muscle can also exacerbate the pulsation.

In the past, we have also synchronized imaging to heartbeat and respiration. One approach was to use strobe light illumination. The duration of each flash was roughly 15 μs, effectively freezing movement. Triggering at the same point in the respiration cycle (and synchronized to the vertical blanking period of the camera) produced images that were very sharply focused, the disadvantage being the long time it took to integrate the signal from multiple flashes as each flash was dim compared to constant arc lamp illumination. While laser scanning microscope systems may accept an external trigger, the scan rate of a conventional galvanometer-based design is not fast enough to prevent distortion due to movement within a scan. External triggering may be possible with fast scanning systems such as the Zeiss LSM 5 Live (Carl Zeiss Microimaging, Inc.) or ones using a resonant galvanometer (Sanderson and Parker, 2003).

Muscle twitching may also occur if a mouse is inadequately anesthetized. In general, muscle twitching is not observed in mice that are deeply anesthetized. It is thus important to monitor the level of anesthesia. One way to determine whether a mouse is waking is to pinch its hindlimb or tail. If the mouse responds by moving, the anesthesia is wearing off. A decision must be made to reanesthetize by repeat injection of the anesthetic or to halt the imaging altogether. To minimize stress on the animal, especially if the mouse is going to be imaged repeatedly, we would typically end the imaging session. The incision is sutured closed, and the mouse is resuscitated including the use of a reversal agent and a postoperative analgesic (see Section III of this chapter for details).

D. Axon Labeling

Visualizing axons *in vivo* in a mammal requires use of epi-illumination optics as there is insufficient access and light throughput for transillumination approaches. The best epi-illumination strategy *in vivo* is fluorescence-based imaging. Moreover, to image and resolve multiple axons requires using multiple fluorescent colors. Multiple colors can be achieved by lipophilic dye labeling (Gan *et al.*, 2000) or transgenic expression of multiple fluorescent proteins. We have focused on transgenic approaches as they are ultimately easier (the animals are in essence "pre-labeled"). For our work in the peripheral nervous system (PNS), we take advantage of the bright labeling of axons in mice that express fluorescent protein under control of the Thy-1 regulatory element (Feng *et al.*, 2000). Crossing lines of mice that express different colors in different axons provide one strategy to get labeling that differentiates individual axons (see below). A new strategy in which single "Brainbow" transgenic animals express a multitude of colors may be useful as well (Livet *et al.*, 2007).

At birth, skeletal muscle fibers are contacted by multiple axonal inputs which appear intermingled at a junction. Over the next week, inputs are gradually lost

and the remaining inputs become segregated such that when a junction is innervated by only two inputs, each occupies a separate portion of the plaque-shaped neurotransmitter receptor-rich region of the muscle fiber (Gan and Lichtman, 1998). If one input gains territory, the other loses territory and no gap is observed between them. An input may be seen to gain synaptic territory at one time point only to lose territory at the next time point (Walsh and Lichtman, 2003). The timing of withdrawal relative to takeover and whether the inputs overlap where they interact is an active area of study for our laboratory. To visualize interactions between axonal inputs, we have time-lapse imaged transgenic mice that express different color fluorescent proteins in motor neurons.

In a previous time-lapse study, we imaged pups that expressed cyan fluorescent protein (CFP) in all motor neurons and yellow fluorescent protein (YFP) in a small subset of neurons or vice versa (Walsh and Lichtman, 2003). Because the number of YFP-positive neurons in the sternomastoid muscle was small (statistically less than 1 neuron per muscle at postnatal day 8), multiply innervated junctions had at most one YFP-positive input. Therefore, if a dually innervated junction had a YFP-positive input, the other input expressed only CFP, making it possible to distinguish the axonal inputs by color (Fig. 2).

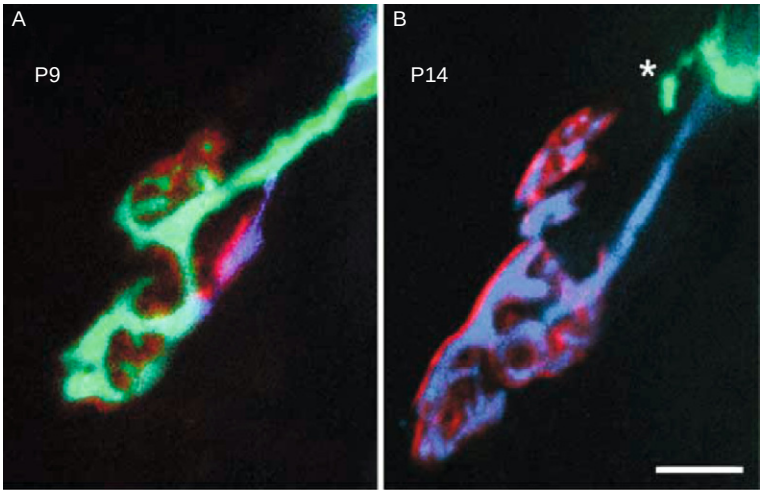

Fig. 2 Time-lapse imaging of a developing neuromuscular junction in a transgenic mouse pup that expressed yellow fluorescent protein (YFP) (green) in a small subset of motor neurons and cyan fluorescent protein (CFP) (blue) in all motor neurons. The acetylcholine receptors were labeled with alexa-594 conjugated α-bungarotoxin (red). The images were acquired on an epifluorescence microscope equipped with a cooled, back-illuminated, thinned charge coupled device (CCD) camera. CFP, YFP, and alexa-594 image stacks were acquired sequentially. The final two-dimensional images (above) were generated by manually selecting and recombining the in-focus portions of each image plane. This junction was 1 of 24 found after screening over 1000 pups (taken from Walsh and Lichtman, 2003). The YFP-only axon, which appeared to be the winning input at P9, was seen to retract 5 days later (asterisk). Scale bar is 10 μm. Adapted from Walsh and Lichtman (2003) with permission.

A disadvantage of the subset expression was the very small number of labeled axonal inputs on the limited number of muscle fibers that are optically accessible. In addition, at postnatal day 7 (the earliest we started imaging) the process of synapse elimination was partially complete, with half or less of the junctions still being multiply innervated. After screening over 1000 pups, we found only 24 junctions at the muscle surface that were innervated by two different color inputs (i.e., roughly 1 junction in every 40 mice).

For current imaging studies, we are using transgenic mice that express CFP and YFP (or other combinations of fluorescent proteins) in all motor neurons or large subsets of motor neurons. While subset expression has an advantage in terms of color separation (e.g., as above where only one of two inputs expresses a fluorophore), we have found that the color differences due to intrinsic variation in expression level of each fluorescent protein between neurons are sufficient to allow us to distinguish axons by color. The advantage of using mice that express fluorescent protein in large numbers of neurons is that the frequency of finding junctions that have different color inputs is much higher. Instead of screening multiple litters of mice to find one such junction at the muscle surface, we are now able to image multiple junctions in every animal (Fig. 3). This approach, using mice that express mixtures of fluorophores, is conceptually different from our previous studies (Kasthuri and Lichtman, 2003; Keller-Peck *et al.*, 2001; Walsh and Lichtman, 2003), all of which relied on the exclusiveness of subset expression to distinguish axons.

A challenge of imaging the multicolor neurons *in vivo* is achieving perfect color registration. In our previous multicolor time-lapse study (Walsh and Lichtman, 2003), the CFP and YFP channels were imaged sequentially using a cooled charge coupled device (CCD) camera on a standard epifluorescence microscope. An image stack was acquired for each channel. A composite image was created from each stack, selecting the in-focus portions of the image planes, and the composite images (one for each channel) were combined to form a final color image. To minimize movement, the muscle was immobilized between a metal platform underneath and a silicon O-ring on top of the muscle. Movement was not always completely eliminated, however, in which case there could be misalignment between channels that would affect color consistency.

E. Color Registration

In order to eliminate the effect of movement on color registration, we now acquire channels simultaneously. A key advantage of confocal microscopy is the ability to excite and detect multiple fluorophores at the same time and thus we have resorted to this imaging modality. While one could use multiple cameras and dichroic filters to pass different fluorescent colors to different detectors, this approach quickly becomes unwieldy if there are more than two channels being detected. Because two or even more confocal channels can easily be acquired in parallel, their alignment is unperturbed by movement of the specimen, enabling (with the use of apochromatic objectives) excellent color alignment. Simultaneous

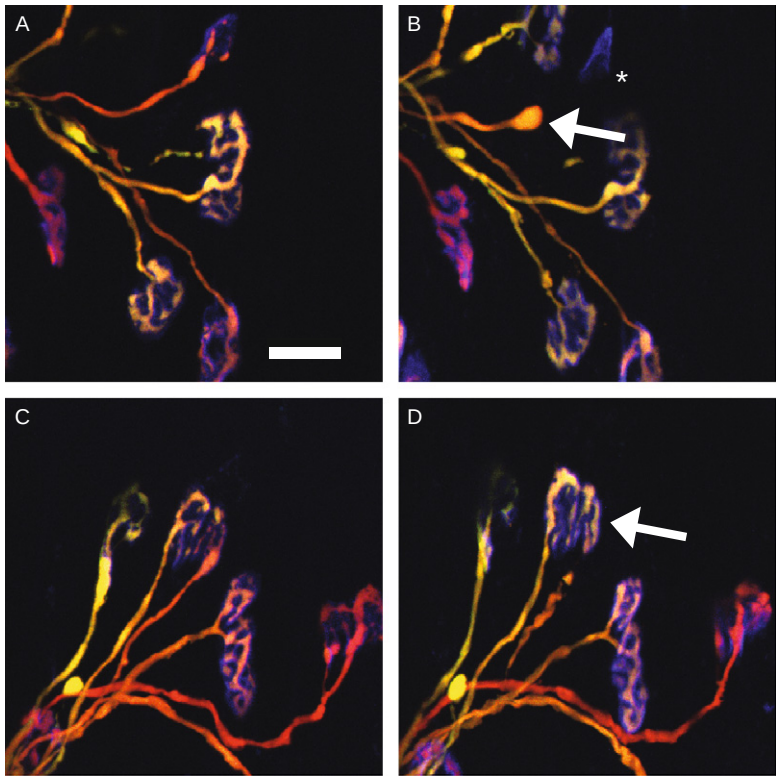

Fig. 3 Time-lapse imaging of developing neuromuscular junctions in sternomastoid muscle of a transgenic mouse pup expressing cytoplasmic cyan fluorescent protein (CFP) (green) and yellow fluorescent protein (YFP) (red) in all motor neurons. Color differences (i.e., different shades of yellow, orange, and red) are due to intrinsic variation between neurons in expression of CFP and YFP. Acetylcholine receptors were labeled with a light dose of alexa-647 conjugated α-bungarotoxin (blue). (A,C) Confocal image stacks were acquired of junctions at P9. The pup was resuscitated and returned to its mother. (B,D) The same junctions were reimaged a day later (P10). The channels were scanned simultaneously, exciting CFP, YFP, and alexa-647 with 440, 514 and 633 nm light, respectively. Image stacks were collapsed by taking a maximum intensity projection. There was minimal movement during image acquisition. The axon colors remain largely constant from day to day, allowing studies of changes in junctional innervation over time, for example, unambiguously determining the input (arrow) that innervated the now unoccupied receptor patch in B (asterisk), and visualizing takeover and withdrawal at the multiply innervated junction (arrow) in D. Scale bar is 20 μm.

acquisition is also an advantage in terms of minimizing total scan time. We typically acquire three channels per scan: CFP, YFP and alexa-647 α-bungarotoxin (a label to reveal the postsynaptic neurotransmitter acetylcholine receptor distribution). A single scan may take 1 s (512 × 512 pixels, 4 μs per pixel). The respirator can only be turned off briefly, so the ability to acquire more than one channel at the same time enables us to have a larger stack size (i.e., increased resolution in Z axis). By comparison, acquisition of a single image plane can be faster using a CCD

camera (~1/2 s per 512 × 512-pixel image), but the channels are imaged sequentially not simultaneously. Thus, the total acquisition time may actually be longer than for confocal imaging.

Confocal microscopy also rejects out of focus light, making 2D projections of image stacks much simpler than those obtained via wide-field imaging. While in the past, we painstakingly edited images to remove out-of-focus portions of image planes and recombined the in-focus portions to make a single 2D image, with confocal microscopy the individual image planes contain minimal out-of-focus information. An image stack may be collapsed into a single 2D image by taking a maximum intensity projection. If there is any misalignment between image planes due to movement, it is feasible to auto-align the image stack in software, for example, using the image alignment tool of AutoDeblur (Autoquant, Media Cybernetics). Alignment is determined for a selected channel (e.g., YFP) but must be applied to all channels (i.e., CFP, YFP, and alexa-647). If the channels are warped and aligned separately, the color registration of axons will be lost. Image warping is only an option if the scan distortions are small. In practice, we attempt to minimize movement to avoid need for image warping and alignment.

Another advantage of confocal microscopy is the ability to increase image magnification by electronic zoom. With a single high-NA dipping cone objective (20× 0.95NA, Olympus), we are able to survey the end plate band at low power (i.e., 1× scan zoom) and then image select junctions at higher power (e.g., 7× zoom is above the Nyquist limit for this objective with a full-field scan size of 512 × 512 pixels—see Section III of this chapter). The ability to change magnification without changing objectives allows us to quickly locate and image junctions using the same acquisition settings (i.e., laser intensity, PMT and amplifier gain, pinhole size) at both magnifications.

We have found that few dipping cone objectives are sufficiently bright (i.e., have high enough NA) to allow imaging of highly fluorescent neurons without rapid photobleaching. In most commercial confocal microscopes, unfortunately, the pupil of the 20× 0.95NA dipping cone objective is not fully filled, reducing its effective NA; nevertheless, because of its combination of low magnification and high NA, this objective is very bright and has been our objective of choice for live imaging. New low magnification high NA objectives are now available that better match the scanning optics of commercial microscope systems. High-NA oil-immersion objectives are also very bright and offer the highest possible spatial resolution, but they require a coverslip and have short working distances, typically less than 200 μm. In general, we wish to avoid touching the muscle with a coverslip, especially in mouse pups, making it difficult but not impossible to use these objectives.

We typically search for junctions in focus mode (scanning at 2× normal scan speed). The respirator is left on while adjusting acquisition and Z-stack settings. Image noise may be reduced by increasing the integration time (i.e., decreasing the pixel rate) or line averaging. Frame averaging is not used because of the possibility of movement between frames. Alternatively, the signal-to-noise ratio may be

increased without affecting scan speed by dropping the PMT and amplifier gain and exciting with more light or opening the pinhole (i.e., reducing confocality). Low excitation intensity may be necessary, however, to reduce the rate of photobleaching.

F. Photostability

Photobleaching is an inevitable part of fluorescence imaging in living animals. A concern for us is the cellular damage that may occur as a result. To avoid phototoxicity, we have excited with as little light as possible, and for this reason we have in the past been cautious about using confocal microscopy for live imaging. Certainly with *in vitro* experiments, the damaging effect of fluorescence excitation is well known. Cultured neurons expressing green fluorescent protein (GFP) are easily damaged by repeat viewing; typically only tens of images may be acquired before cells are killed. In addition, photobleaching can quickly reduce the sample brightness. Presumably, photobleaching contributes to photodamage through generation of free radicals. Attempts to protect living neuronal cells from photodamage using free-radical scavengers have met with limited success. On the contrary, there are a wide variety of slide mounting media that are quite effective at minimizing photobleaching.

In control experiments, we tested for phototoxicity *in vivo* by exciting CFP-, GFP-, or YFP-filled motor neurons with arc lamp illumination continuously for an hour (Walsh and Lichtman, 2003). The energy dose was one to two orders of magnitude higher than normally used for imaging yet not damaging to nerve terminals or axons. Exciting at a similar light level *in vitro* would cause damage in minutes, suggesting that while photobleaching is inevitable in live imaging of fluorescence, the consequences can be very different *in vivo* versus *in vitro*, perhaps due to better scavenging or glial cell protective mechanisms that are operative *in vivo*.

Typically, the excitation light dose required for imaging is higher with a laser scanning confocal system than with a wide-field imaging system and photobleaching is rapidly observed with confocal imaging of living specimens unless the laser intensity is very low (e.g., 1–2% of 0.8 mW at 514 nm). The ability to use low-intensity illumination with confocal depends on the efficiency of light detection and only recently have confocal systems achieved suitable sensitivity for robust live imaging. In addition, the fluorescent signal must be very strong. If it is weak, the signal can only be detected by increasing the laser intensity. At the higher laser intensities, we observe photobleaching of CFP, GFP, and YFP, as expected, but not photodamage, consistent with the controls performed using arc lamp illumination.

To determine the light level at which damage occurs in live imaging of motor axons, we increased the laser intensity, bleaching the fluorescence completely—either CFP alone (using 440 nm light) or YFP (using 514 nm light) or both CFP and YFP. Much to our surprise, while we were able to photobleach efficiently, we were unable to cause photodamage. We illuminated nerve terminals using 100% laser power at each wavelength for many minutes, causing fluorescence to

disappear, but without apparent phototoxicity. Nerve terminals and axons were not damaged in either adult mice or pups. We have not yet tested whether other neurons in the central nervous system (CNS) and PNS respond similarly, but our expectation is that they will also be highly resistant to photodamage. We also have not tested whether cells that express membrane-bound fluorescent proteins are similarly protected from photodamage. In our tests of multiphoton excitation, we observed damage which could be due to the inevitable three-photon (ultraviolet wavelength) absorption that accompanies two-photon (visible wavelength) absorption with fluorescence imaging. The damage was not observed during the first imaging session, but a day later when the mouse was re-imaged.

In CFP- and YFP-filled motor neurons, fluorescence recovery after photobleaching an axonal terminal occurs quickly (in minutes) due to the large amount of fluorescent protein in the cytoplasm of the axon. The rapid dynamics reflect continual movement of fluorescent protein molecules within the axon. There is a delay, however, before recovery is observed. In a motor neuron that expresses both CFP and YFP, either CFP or YFP can be bleached in an axonal input, temporarily changing the color of the input. Thus, photobleaching may be used as a tool to distinguish axonal branches (or cells) by color. For example, if two axonal inputs at a developing neuromuscular junction are the same color, that is, express the same mixtures of fluorophores, the color of one input may be changed by selectively bleaching one or the other fluorescent protein (Fig. 4). Therefore, the color of any cell expressing more than one fluorophore can be selectively altered temporarily by photobleaching, allowing it to be distinguished from neighboring cells. This approach may be useful for neuronal tracing and studies of cell–cell interactions.

III. Methods and Materials

A. Mice

We used transgenic mice that expressed cytoplasmic YFP and CFP under the neuron-specific Thy-1 promoter (Feng *et al*., 2000). Neonatal mice that expressed YFP and CFP in all motor neurons (cross of lines YFP-16 and either CFP-5 or CFP-23) were used for the live imaging experiments (protocol approved by Harvard University's IACUC).

We typically start imaging at postnatal day 7 (P7). Motor neurons are easily damaged before P7, perhaps due to lack of myelination. At P7, many junctions are still multiply innervated in the sternomastoid muscle, but a day later, only a few remain multiply innervated. Synapse elimination is complete by P14.

B. Anesthesia and Intubation

Neonatal mice are anesthetized by subcutaneous injection of a mixture of ketamine (Ketaset, Fort Dodge Animal Health) and medetomidine (Domitor, Pfizer Animal Health) (1.714 mg ketamine/ml + 0.023 mg medetomidine/ml in

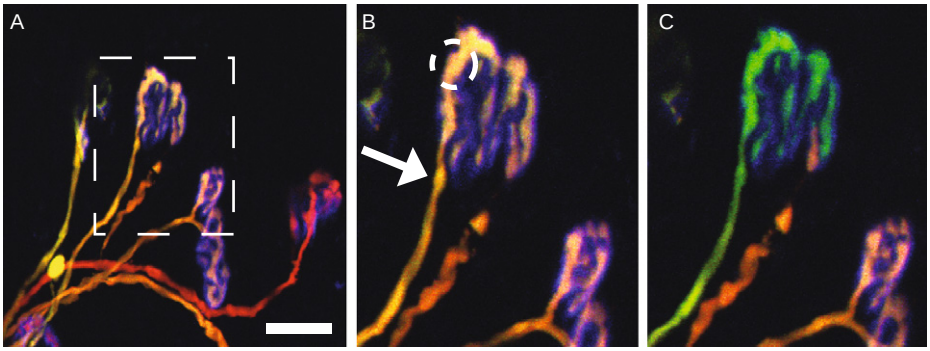

Fig. 4 Selective photobleaching to change the color of an axonal branch at a developing neuromuscular junction in a living animal. (A) Junctions in sternomastoid muscle of P10 transgenic mouse expressing cyan fluorescent protein (CFP) (green) and yellow fluorescent protein (YFP) (red) in all motor neurons (same field as in Fig. 3D). Acetylcholine receptors were labeled with alexa-647 conjugated α-bungarotoxin (blue). Variation in expression of CFP and YFP allow axons to be distinguished by color. A small color difference, however, makes it difficult to determine the territory occupied by each input at the dually innervated junction (boxed region). Scale bar is 20 μm. (B) Enlargement of boxed region in A. To increase the color difference, YFP of yellowish input (arrow) was selectively photobleached by scanning within the circled area using 514 nm excitation (100% laser power for 2–3 min). The respirator was left on while bleaching. (C) Immediately after bleaching, the colors can be clearly separated allowing the territory of each input to be more clearly defined. YFP fluorescence recovered quickly (in minutes) due to constant mixing of bleached and unbleached YFP, resulting in dilution of the bleached YFP in the axonal terminal. No photodamage was observed as a result of repeated photobleaching of YFP or CFP using high-intensity 514 and 440 nm excitation, respectively.

sterile saline; dose = 0.1 ml/5 g animal). Once a pup is anesthetized, it is placed in supine position on a steel magnetic plate with a gauze pad between the mouse and the plate. The pup is not warmed during an experiment.

The forelimbs are restrained using rubber bands attached to magnets. The rubber bands are pulled through a collar (cut from the tip of a disposable pipette) and cinched to the wrists. The forelimbs are pulled down (caudally) and to the side. A third rubber band is stretched across the roof of the mouth and held by magnets at each side of the head (Fig. 5). The body and head are positioned so that the ventral surface of the neck is straight and flat.

The skin on the ventral surface of the neck is then depilated and cleaned. At P7, there is very little body hair. By P9, pups have developed hair that can be removed using a commercial depilatory cream such as Nair (Church & Dwight Co., Inc.). The cream is applied with a cotton-tipped swab. After waiting a couple of minutes, the cream is removed using cotton-tipped swabs. The skin is cleaned with 70% ethanol, rinsed thoroughly with water, and dried.

A small longitudinal incision (~5 mm long) is made in the skin at the midline from the sternum to a point near the mandible. The salivary glands (left and right) are teased apart at the midline exposing the trachea and the area is flooded with phosphate buffered saline (PBS) (0.01 M) to keep the tissue hydrated.

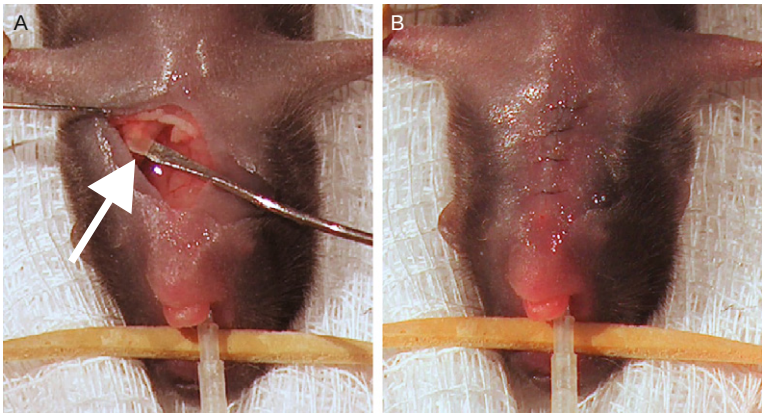

Fig. 5 Setup for *in vivo* imaging. (A) Close-up view of sternomastoid muscle lifted on thin metal platform in P7 mouse pup (arrow). Submandibular and sublingual gland and skin are retracted to one side using a hook. The neck cavity is filled with phosphate buffered saline (PBS) continuously to keep the muscle tissue hydrated. (B) Neck after closing with 9–0 sutures. See Section III for details.

The mouse is then intubated. The intubation tube is inserted into the trachea blind. The trachea is usually slightly slanted to the right. Once the lungs are seen to properly inflate (driven by the ventilator), the tube position is secured using magnets. The blind technique can be difficult to master, and as an alternative, the trachea can be located by indirect laryngoscopy, using the dissecting microscope and a fiber optic light source. The mouse is tilted under the dissecting microscope, setting the plate on an A-frame holder. A pair of blunt forceps is used to pull the tongue to one side. A second pair of blunt forceps is used to push down on the tongue. The first pair can then be released. The larynx is visible at the back of the throat. The trachea is on the ventral side, immediately behind the horseshoe-shaped hyoid bone. Pups are mechanically ventilated at ~80/min using a small animal ventilator (MiniVent Type 845, Harvard Apparatus, Holliston, MA). The stroke volume is typically 150–300 μl. This ventilator is small and does not vibrate, which allows it to be placed on the optical table next to the microscope. The pup must be intubated and ventilated quickly, since the anesthesia will cause its breathing to slow and eventually stop. The total time from anesthesia to intubation is ~15 min.

C. Exposing and Lifting Muscle

We typically only image the left sternomastoid muscle. Because we image starting at P7 and use mice that express CFP and YFP in all motor neurons, we are able to find labeled, multiply innervated junctions at or near the muscle surface in every mouse. If we start imaging later than P8 or use mice that express in subsets of

neurons, the chance of finding a junction suitable for imaging is very low, in which case we may look at both sternomastoid muscles in a mouse.

The salivary glands (white) and fat (yellowish) are retracted laterally, exposing the muscle (Fig. 5A). A thin layer of connective tissue covers the muscle. Sharp forceps are run along the medial side of the muscle to cut the connective tissue. The connective tissue is then grabbed and removed from the ventral surface of the muscle. If any connective tissue remains over the end plate band (at roughly a third of the length of the muscle from the sternum) the imaging quality will be negatively affected. After removing the connective tissue, PBS is again used to keep the tissue hydrated.

The muscle is then lifted on a thin metal platform similar in design to a spatula. The platform arm is raised and lowered via a swivel joint that is attached to a magnet. The innervating nerve bundle enters the muscle laterally. To avoid damaging the nerve bundle, the platform is brought across the animal and inserted under the muscle at or above (caudal to) the end plate band. The platform is moved under or just below the end plate band before the muscle is lifted.

Fluid is aspirated from the neck cavity. Acetylcholine receptors are then lightly labeled with a solution of alexa-647 conjugated α-bungarotoxin (5 μg/ml in PBS for 40 s; Invitrogen). The amount of α-bungarotoxin labeling is not enough to block muscle contractions. Unbound α-bungarotoxin is removed by rinsing thoroughly with PBS for 3–5 min.

D. Imaging

Axons innervating the central band of neuromuscular junctions are visualized using standard epifluorescence optics (YFP filter cube) at low magnification (XLUMPFL20XW 20× 0.95NA dipping cone objective, Olympus). Once a particular nerve terminal is selected, scans are acquired at high resolution (typically 7× electronic zoom, same 20× objective) using a confocal microscope system (FV1000-MPE on a BX61 upright stand, Olympus). To acquire images with the highest possible spatial resolution, the pixel size must be less than half the spatial resolution of the objective. For emission at 550 nm, the resolution of the 20× 0.95NA objective is ~350 nm (determined by the formula $0.61 \times \lambda/NA$). At 1× zoom, the pixel size in a 512 × 512-pixel scan is 1.242 μm. Therefore, the zoom must be at least 7× for sampling at or above the Nyquist frequency (i.e., twice the spatial resolution). YFP, CFP, and alexa-647 are excited using 514, 440, and 633 nm light, respectively. The respirator is turned off temporarily (30–60 s) to acquire an image stack. The fluorescence channels are acquired simultaneously. The scans are typically 512 × 512 pixels at 4 μs per pixel. We scan 15–25 planes per image stack, with a step size of 1–2 μm in the Z axis. The pinhole is adjusted to make images as confocal as possible, but without having to use high PMT and amplifier gain (because of image noise) or high laser intensity illumination (because of photobleaching). Movement artifacts are removed from stacks using special alignment software (Image alignment tool of AutoDeblur, Autoquant, Media

Cybernetics). A 2D image is obtained by taking a maximum intensity projection. The same junctions are imaged multiple times, usually at one-day intervals or longer.

E. Photobleaching

A region of interest (ROI) in the scanning confocal is defined to illuminate the terminal of a single axonal input. The ROI is scanned, allowing visualization of the decrease in fluorescence emission. CFP or YFP is bleached using 440 nm or 514 nm light, respectively, at 100% power for 2–5 min. The respirator is left on while bleaching. An image stack is acquired immediately after bleaching to capture the change in axon color. The fluorescence recovers quickly (in minutes) and can be photobleached repeatedly without any apparent phototoxic effects.

F. Recovery

After completing imaging, the incision is closed using thin sutures (9–0 Ethilon monofilament nylon, Ethicon, Inc., Somerville, NJ). The suturing is made as invisible as possible (Fig. 5B) so as not to attract the attention of the mother. The surgery should be completely bloodless. If there is any blood in the wound, the mother will likely chew open the neck, killing the pup.

The pup is resuscitated by subcutaneous injection of atipazemole (Antisedan, Orion; 0.25 mg/ml in sterile saline; dose = 0.05 ml/5 g animal) and an analgesic (Buprenex, Reckitt Benckiser, Inc.; 0.08 mg/ml in sterile saline; dose = 0.1 ml/25 g animal). Once the animal is moving well, the intubation tube is removed, and the pup is placed under a ceramic heat lamp (PT-2045 Exo Terra Heat Emitter – 60W, Rolf C Hagen, Inc.). The temperature should be 30–32 °C. If the temperature is allowed to rise above 34 °C, the pup will become overheated and quickly expire. Animals are monitored until fully awake. Pups must be able to right themselves before being returned to their mothers. If they are squirming vigorously but not upright, they are not fully recovered. The postoperative recovery time can take anywhere between 1 and 12 h depending on the stress of the operation and the dose of anesthetic that was used. Body weight and food intake are measured daily.

IV. Discussion and Summary

A number of basic criteria must be met for successful live imaging. First, the cells must be clearly visible against a background. In the work we describe here, this means imaging cells that are labeled with a fluorescent marker. Second, the cells must be brightly labeled and close to the surface. Structures that are deep may not be readily labeled with a fluorescent dye, and those that can be labeled may be difficult to image at high resolution due to index of refraction variations. To follow individual cells, it is also necessary to distinguish one cell from another. This may

be difficult to accomplish using fluorescent dyes except if the dyes are targeted to single cells by injection or ballistic techniques (Gan *et al*., 1999, 2000). Transgenic animals that express high levels of fluorescent protein in particular cell types offer another approach. In some cases, a subset of cells may express the fluorescent protein, making it possible to identify single cells (Feng *et al.*,2000; Kasthuri and Lichtman, 2003; Keller-Peck *et al*., 2001; Walsh and Lichtman, 2003). If more than one fluorescent protein is expressed, it is also possible to distinguish multiple cells by intrinsic color differences due to variations in expression levels. Third, in a living animal, movement due to heartbeat and respiration limits the time available for image acquisition. Structures are often distributed in three dimensions making it necessary to collect images at multiple focal planes. Rapid acquisition is also necessary to minimize photobleaching and potential photodamage. In our past studies, images were acquired using a microscope equipped with standard epifluorescence optics and a low-light camera such as a SIT (Silicon Intensified Target) video camera or a cooled CCD camera. The in-focus portions from the different focal planes were then pieced together to create a composite image. Because of advances in technology, we are now able to acquire images using a confocal microscope system. One advantage of the confocal for live imaging is the ability to reject of out-of-focus light, improving image sharpness. Image stacks are acquired by advancing the focus position automatically. Movement artifacts are minimized such that a final in-focus image can often be produced simply by taking a maximum intensity projection. Another advantage is the ability to acquire multiple channels simultaneously. This speeds up image acquisition and eliminates misalignment between channels. If the channels are acquired sequentially, there is inevitably misalignment due to movement. With perfect alignment between channels, irrespective of movement that might occur during a scan, we are able to use color differences to trace individual structures and follow developmental changes over time.

References

Balice-Gordon, R. (1997). *In vivo* approaches to neuromuscular structure and function. *Methods Cell Biol.* **52,** 323–348.

Feng, G., Mellor, R. H., Bernstein, M., Keller-Peck, C., Nguyen, Q. T., Wallace, M., Nerbonne, J. M., Lichtman, J. W., and Sanes, J. R. (2000). Imaging neuronal subsets in transgenic mice expressing multiple spectral variants of GFP. *Neuron* **28,** 41–51.

Gan, W. B., and Lichtman, J. W. (1998). Synaptic segregation at the developing neuromuscular junction. *Science* **282,** 1508–1511.

Gan, W. B., Bishop, D. L., Turney, S. G., and Lichtman, J. W. (1999). Vital imaging and ultrastructural analysis of individual axon terminals labeled by iontophoresis application of lipophilic dye. *J. Neurosci. Methods* **93,** 13–20.

Gan, W. B., Grutzendler, J., Wong, W. T., Wong, R. O., and Lichtman, J. W. (2000). Multicolor "DiOlistic" labeling of the nervous system using lipophilic dye combinations. *Neuron* **27,** 219–225.

Jansen, J. K., and Van Essen, D. C. (1975). Re-innervation of rat skeleton muscle in the presence of alpha-bungarotoxin. *J. Physiol.* **250,** 651–667.

Kasthuri, N., and Lichtman, J. W. (2003). The role of neuronal identity in synaptic competition. *Nature* **424,** 426–430.

Keller-Peck, C. R., Walsh, M. K., Gan, W. B., Feng, G., Sanes, J. R., and Lichtman, J. W. (2001). Asynchronous synapse elimination in neonatal motor units: Studies using GFP transgenic mice. *Neuron* **31,** 384–394.

Lichtman, J. W., and Fraser, S. E. (2001). The neuronal naturalist: Watching neurons in their native habitat. *Nat. Neurosci.* **4** (Suppl.), 1215–1220.

Livet, J., Weissman, T. A., Kang, H., Draft, R. W., Lu, J., Bennis, R. A., Sanes, J. R., and Lichtman, J. W. (2007). Transgenic strategies for combinatorial expression of fluorescent proteins in the nervous system. *Nature* **450,** 56–62.

Sanderson, M. J., and Parker, I. (2003). Video-rate confocal microscopy. *Methods Enzymol.* **360,** 447–481.

van Mier, P., and Lichtman, J. W. (1994). Regenerating muscle fibers induce directional sprouting from nearby nerve terminals: Studies in living mice. *J. Neurosci.* **14,** 5672–5686.

Walsh, M. K., and Lichtman, J. W. (2003). *In vivo* time-lapse imaging of synaptic takeover associated with naturally occurring synapse elimination. *Neuron* **37,** 67–73.

Walsh, M. K., and Lichtman, J. W. (2005). Imaging the development of the NMJ. *In* ''Imaging in Neuroscience and Development: A Laboratory Manual'' (R. Yuste, and A. Konnerth, eds.), pp. 215–223. Cold Spring Harbor Laboratory Press, Cold Spring Harbor, New York.

CHAPTER 12

Nanoscale Biological Fluorescence Imaging: Breaking the Diffraction Barrier

Travis J. Gould and Samuel T. Hess

Department of Physics and Astronomy and Institute for Molecular Biophysics
University of Maine
Orono, Maine 04469

METHODS IN CELL BIOLOGY, VOL. 89

0091-679X/08 $35.00
DOI: 10.1016/S0091-679X(08)00612-2

Abstract

Biological imaging has been limited by the finite resolution of light microscopy. Recent developments in ultra-high-resolution microscopy methods, many of which are based on fluorescence, are breaking the diffraction barrier; it is becoming possible to image intracellular protein distributions with resolution of tens of nanometers or better. Fluorescence photoactivation localization microscopy (FPALM) is an example of such an ultra-high-resolution method which can image living or fixed cells with demonstrated lateral resolution of better than 20 nm. A detailed description of the methods involved in FPALM imaging of biological samples is presented here, accompanied by comparison with existing methods from the literature.

I. Introduction

The image of a point source has finite size R_0, even if the source is infinitesimal. Therefore, distinguishing multiple point sources from one another is possible when those point sources are separated by more than R_0, but increasingly more difficult when sources are numerous and separated by less than R_0. In most biological samples, it is advantageous to image large numbers of molecules of interest, and in most cases these molecules are observed within a region containing even larger numbers of water molecules, ions, proteins, nucleic acids, and lipids. Simultaneous resolution of all of these molecules from one another becomes virtually impossible. Thus, resolution limits the size of structures that can be imaged using light microscopy to sizes of order R_0. In wide-field microscopy, the resolution has been quantified by the Rayleigh criterion (Born and Wolf, 1997):

$$R_0 = 0.61\lambda/\mathrm{NA} \tag{1}$$

where λ is the wavelength of the detected photons and NA is the numerical aperture of the lens system.

In laser-scanning microscopes, the resolution is directly related to the properties of the observation volume O(r), the region in which fluorescence is both excited and detected, defined as $O(r) = I(r) \cdot C(r)$, where I(r) is the illumination point-spread function, and C(r) is the detection profile. I(r) depends on the laser illumination wavelength, objective NA, the laser profile in the objective back aperture, objective aberrations, fluorescence saturation effects, and a number of other variables (Pawley, 1995; Sandison and Webb, 1994; Sandison *et al.*, 1995). Illumination

by high-NA lenses can produce a diffraction-limited illumination volume with full width at half maximum (FWHM) of $\sim 0.55\lambda/\mathrm{NA}$ (Pawley, 1995). In confocal microscopy, epifluorescence detection using the same high-NA lens as for illumination and a detector aperture placed in the image plane result in significant improvement in the resolution, but the detector aperture also reduces the fraction of light collected. For an infinitesimal detector aperture, the collection point spread function approaches that of the diffraction-limited illumination profile in the case of an overfilled back aperture (i.e., the $1/e^2$ radius of the laser beam is larger than the radius of the back aperture of the objective lens) and incoherent (uncorrelated) emission (Hess and Webb, 2002; Sandison and Webb, 1994; Sandison *et al*., 1995) and the resolution can be improved by as much as a factor of $\sqrt{2}$, neglecting the Stokes' shift of the fluorescence relative to the excitation wavelength, distortion of the illumination profile by polarization effects, and lens aberrations. However, the resolution is still limited to some fraction of a wavelength.

Two-photon microscopy provides numerous advantages for imaging biological samples, including reduced out-of-plane photobleaching, excitation of multiple fluorescent probes using the same illumination wavelength, and excellent signal-to-background ratio (Denk *et al*., 1990; Xu *et al*., 1996). However, because of the longer wavelengths used to excite fluorescence, and despite the intensity-squared dependence of the excitation rate, in practice the resolution is similar to that of a confocal microscope with detector aperture size optimized for maximum signal-to-noise ratio. Thus, a number of standard far-field methods are limited in resolution to approximately $\lambda/2n$, where n is the refractive index of the medium (Hell, 2007).

One method for resolution enhancement is to extract information about the structure of the object using the ''near-field'' electromagnetic waves found at distances less than λ from the object. Near-field optics often use an aperture or optical fiber with diameter significantly smaller than λ to create an excitation volume which has a width much less than λ near the aperture. Because coupling the emitted light back through the tiny aperture or fiber tip is often inefficient, a standard objective lens is often used to collect fluorescence excited from single molecules in such applications. The tip can be scanned to image an area with resolution of at least 12 nm under visible illumination (Betzig and Trautman, 1992; Betzig *et al*., 1991), or better than $\lambda/40$. Near-field interactions between a sharp probe and sample can be used to image at even higher ($\sim$12 nm) resolution (Betzig and Trautman, 1992). However, the requirement for proximity between the probe tip and the sample does pose a significant limitation for many biological applications (Hell, 2007).

Electron microscopy offers tremendous (near-atomic) resolution and has been used extensively to image a variety of biological samples. Unfortunately, requirements for sample fixation, freezing, or other preparation methods, the addition of heavy metals to improve contrast, and the reduced ambient pressure or vacuum for electron beam propagation have limited successful imaging of living biological specimens. Since understanding dynamics is crucial to the understanding of

biological processes, improved noninvasive methods based on far-field visible-light optics promise to reveal a great deal about biological function.

Development of "super-resolution" methods, namely, techniques that break the diffraction barrier and image samples at length scales much less than a wavelength, is currently of great interest. These methods can be grouped into several categories and compared to highlight advantages and disadvantages.

A. Observation Volume Confinement

The diffraction barrier has been broken using stimulated emission depletion (STED) fluorescence microscopy (Hell and Wichmann, 1994; Klar *et al*., 2000). STED causes molecules excited at the edges of a normal diffraction-limited volume to be driven to the ground state without fluorescence by illuminating them with an annular beam at a frequency that causes stimulated emission from the excited state. Only those molecules at the null (center) of the donut-shaped STED beam remain in the excited state long enough to fluoresce, resulting in emission from a highly confined volume. Focal plane resolution of 15–20 nm has been achieved in fixed biological samples using STED with nonlinear deconvolution (Donnert *et al*., 2006). The concept of STED has been generalized to other reversible saturable optical fluorescence transition (RESOLFT) (Hell *et al*., 2003) techniques, which exploit optically driven transitions between states with drastically different emission properties, such as photoswitching of fluorescent proteins (Hofmann *et al*., 2005) to achieve subdiffraction-limited resolution.

B. Modulated Illumination

4Pi microscopy (Schrader and Hell, 1996) and I^5M (Gustafsson *et al*., 1999) both use two opposing objective lenses to illuminate a sample and collect fluorescence with improved axial resolution. Structured illumination (Gustafsson *et al*., 1999) and saturated structured illumination microscopy (SSIM) use a spatially modulated sample illumination profile to, upon deconvolution, extract information at higher spatial frequencies and thereby improve resolution. SSIM resolution is in principle limited only by signal-to-noise ratio and the photobleaching properties of the probes, with demonstrated resolution of better than 50 nm (Gustafsson, 2005).

C. Hyperlens Imaging

A recent example of hyperlens imaging uses a multilayered anisotropic material with hyperbolic dispersion to convert scattered nonpropagating evanescent electromagnetic waves containing high spatial frequency information about a sample smaller than λ, into propagating far-field electromagnetic waves that were imaged using a high-NA objective (Liu *et al*., 2007). However, such methods have not yet been demonstrated on biological samples.

D. Single-Molecule Localization and Reconstruction

Single-molecule localization and image reconstruction is the basis for several super-resolution methods. Localization, namely determination of the position of an object using its image, has been achieved with precision as high as 1.5 nm (Yildiz *et al.*, 2003) for the diffraction-limited image of a single fluorescent molecule. Single-molecule detection methods provide additional information about absolute numbers of molecules, motion, and brightness of individual molecules, which can reveal population heterogeneities inaccessible to methods that image an ensemble of molecules. Ultrahigh-resolution colocalization (UHRC) (Lacoste *et al.*, 2000) is a scanning confocal microscopy technique capable of localizing multiple fluorophores that are excitable with a single laser source and of differing emission properties. While UHRC allows for simultaneous imaging of multiple probes, it is still difficult to use to resolve identical probe molecules separated by less than R_0. Fluorescence intermittency has been used to localize single-molecules and single-quantum dots with a precision on the order of tens of nanometers (Lagerholm *et al.*, 2006; Lidke *et al.*, 2005), as well as quantify velocities of individual biomolecules and protein assemblies by fluorescent speckle microscopy (Ponti *et al.*, 2005; Salmon *et al.*, 2002; Waterman-Storer *et al.*, 1998). Single-particle localization in three dimensions has been achieved with ~20 nm resolution and ~30 ms time resolution (Levi *et al.*, 2005a, b). Other methods have exploited the photobleaching characteristics of fluorophores to localize single molecules. Single-molecule high-resolution imaging with photobleaching (SHRImP) (Gordon *et al.*, 2004) and nanometer-localized multiple single-molecule (NALMS) fluorescent microscopy (Qu *et al.*, 2004) both take advantage of the stepwise photobleaching of single molecules to localize their positions with precision on the order of a few nanometers. So far, such photobleaching methods have required that relatively few fluorophores reside within a cross-sectional area of radius R_0. The points accumulation for imaging in nanoscale topography (PAINT) (Sharonov and Hochstrasser, 2006) method localizes single molecules that fluoresce as they bind to a target object of interest and then photobleach. While the methods described above provide a means of subdiffraction localization-based resolution, control over the density of fluorescent molecules in the field of view requires adjustment of the concentration of fluorophores.

Techniques such as fluorescence photoactivation localization microscopy (FPALM) (Hess *et al.*, 2006), and photoactivated localization microscopy (PALM) (Betzig *et al.*, 2006), which use photoactivatable fluorescent proteins (PA-FPs) or other photoactivatable fluorophores, allow for direct *optical* control over the number of fluorescent molecules by adjusting the rates of photoactivation and photobleaching (Fig. 1). In a similar manner, stochastic optical reconstruction microscopy (STORM) (Rust *et al.*, 2006) uses photoswitchable combinations of organic fluorophores to control the number of molecules fluorescing at a given time. Images are then reconstructed from the coordinates and intensities of localized molecules.

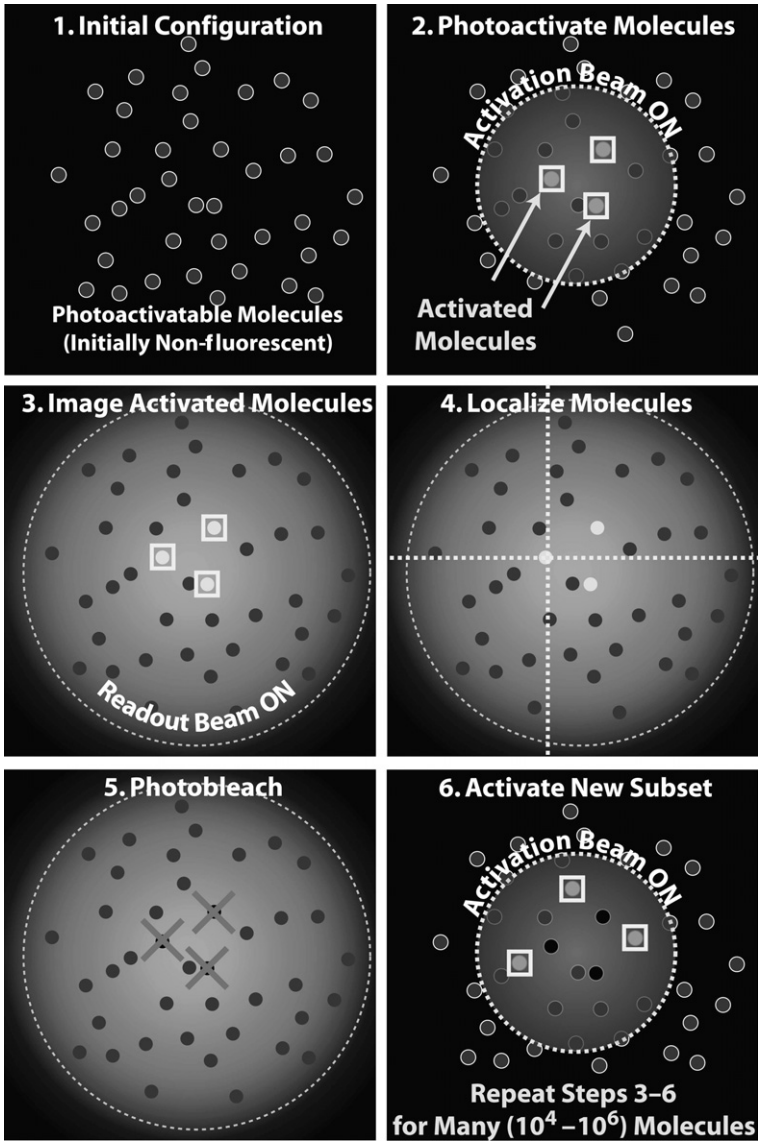

Fig. 1 Principle of fluorescence photoactivation localization microscopy (FPALM). (1) Initially, all molecules in the sample are inactive (dark circles), namely, in a nonfluorescent state, and virtually no fluorescence is emitted from the sample. Two lasers are used to control the number of active (potentially fluorescent) molecules. (2) A high-energy visible (typically ~400 nm) laser, called the activation laser (smaller dashed circle), is used to activate a small number of molecules in the sample (boxes). This number is kept small by making the activation laser intensity sufficiently weak in the focal plane of the sample. Activation of molecules occurs randomly: the probability of activation of a given molecule is proportional to the intensity of the activation laser at the location of that molecule, but typically very small. (3) The activation laser is turned off and molecules that were activated are read out, using

Compared to confined and modulated illumination methods, FPALM can be used in a standard wide-field microscope, does not require ultra-fast pulsed lasers or image deconvolution, and does not rely on nonlinear excitation. Compared to other single-molecule localization techniques, FPALM, PALM, and STORM also have the advantage that they rely on photophysical properties to control the number of fluorescent molecules in the field of view. The flexibility of using genetically encoded fluorescent markers such as green fluorescent proteins (GFPs) is both powerful and efficient, allowing existing GFP-constructs to be converted into PA versions using standard molecular biology procedures.

II. Theory and Rationale

The basis of FPALM (Fig. 1) is the localization of large numbers of single fluorescent molecules, imaged in small numbers at a time. Localization is defined as determination of the two- or three-dimensional position of the emitting object. In contrast, resolution is defined as determination that two emitting objects are distinct from one another. In FPALM, large numbers of molecules are ultimately localized within an observation area, but for those molecules to be resolvable from one another, a small number must be fluorescent at a given time. Thus, control over the number of fluorescent molecules visible at a given time is crucial. This control is achieved by the use of probes which can be optically switched from an inactive (nonfluorescent) state (I) into an active (potentially fluorescent) state (A). Irreversible or reversible activation can be used as long as the number of fluorescent molecules can be controlled within the observation area. The transition between inactive and active states is typically achieved by an activation laser, but a lamp or light-emitting diode (LED) could in principle be used as long as sufficient intensity is obtained at the sample. The activation laser is typically a different (higher) frequency than the readout laser used to image and photobleach the active molecules. The activation laser is used to stochastically activate a small number of inactive molecules, which are then imaged under excitation by the readout laser until they stochastically photobleach (or become deactivated in the case of reversible activation). The number of active molecules must be kept small enough

a second, typically lower energy laser, called the readout laser. Readout means detection of fluorescence from activated molecules (gray circles) within the illuminated area. During the time that the readout laser is on (and typically during the entire process), a high-sensitivity charge coupled device (CCD) camera is recording a movie of the same field of view being illuminated. (4) The movie frames are analyzed to identify and localize activated molecules (dashed lines delineate coordinates of an active molecule) for as long as they remain fluorescent. (5) Molecules spontaneously photobleach (crosses) under the high-intensity illumination of the readout beam, eventually reducing the number of visible molecules significantly. (6) A new set of molecules is activated by again briefly turning on the activation beam (equivalent to step 2). Steps 3–6 are repeated many times, either until enough molecules have been activated and imaged to obtain the desired image quality, or until all photoactivatable (PA) molecules within the sample have been exhausted.

(by adjusting the intensity of the activation laser) that virtually all molecules are optically distinguishable. Quantitatively, this requires that the average separation between molecules $L_0 \gg R_0$ (typically $L_0 > 4R_0$), where R_0 is the diffraction-limited resolution given by Eq. (1). Molecules closer than this minimum can be excluded from analysis because of the difficulties in determining their positions accurately, or more sophisticated analysis methods can be used. The process of activation, imaging, and photobleaching is repeated until the molecules in the sample are exhausted, or until sufficient numbers of molecules have been imaged for the particular application. Figure 2 shows examples of the actual readout and activation laser beam profiles, images of single molecules identified by the algorithm, and plotted positions of molecules without and with intensity weighting.

In practice, the sample is placed on the stage of a microscope, near the focus of a high-NA objective lens (Fig. 3). Only molecules within the focal plane can be successfully imaged and localized. During acquisition, the sample sits under

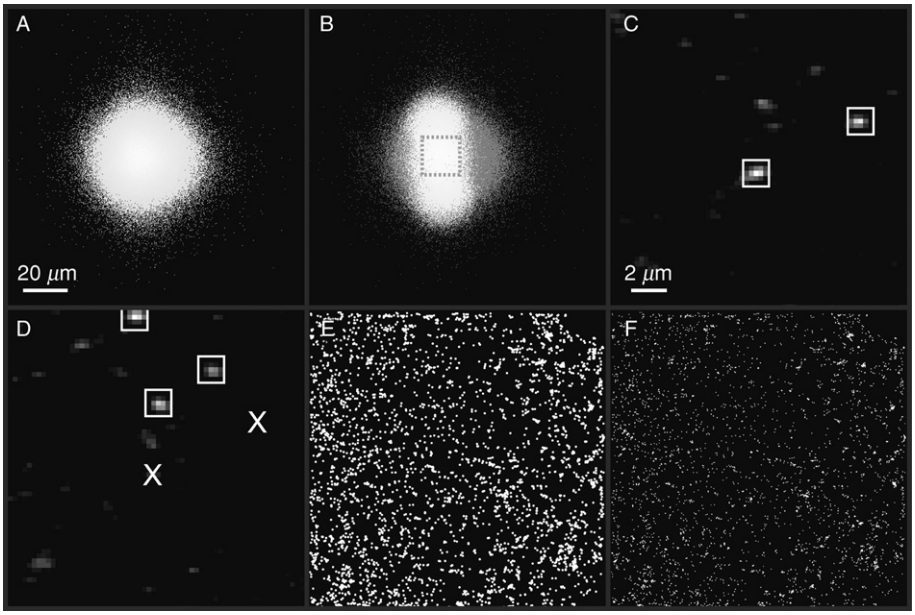

Fig. 2 Fluorescence photoactivation localization microscopy (FPALM) method illustrated using experimental results. (A) Profile of readout beam (488 nm). (B) Merged profiles of readout and (noncircular) activation (405 nm) beams. Dark gray indicates regions illuminated by the readout beam, while white indicates regions illuminated by *both* the readout and activation beams. (C–F) Examples of molecules imaged within the boxed region in (B). (C–D) Two successive frames from a time series acquisition of caged-fluorescein imaged on a coverslip. White boxes indicate localized single molecules in the given frame. An "*X*" in (D) indicates locations of molecules that were identified in the previous frame (C) but presumably photobleached during or before the acquisition of the frame shown in (D). (E) Rendering of positions of all 3,850 molecules localized over the entire acquisition (all molecules shown with same intensity and size). (F) Rendering of positions of all localized molecules, plotted with intensity proportional to the number of detected photons.

continuous illumination by the readout beam and continuous imaging using a high-sensitivity charge coupled device (CCD) camera which is sensitive enough to detect single fluorescent molecules. Pulses of the activation laser are applied whenever necessary to increase the number of active molecules in the observation area, or continuous low intensity illumination by the activation laser can be used, with intensity increasing over time as the pool of inactive molecules is depleted.

Once molecules have been activated, imaged, and photobleached, analysis of the images is performed to determine the positions of the molecules by localization. The precision with which a fluorescent object can be localized in two dimensions is given by σ_{xy}, where

$$\sigma_{xy}^2 = \frac{R_0^2 + q^2/12}{N} + \frac{8\pi R_0^4 b^2}{q^2 N^2} \tag{2}$$

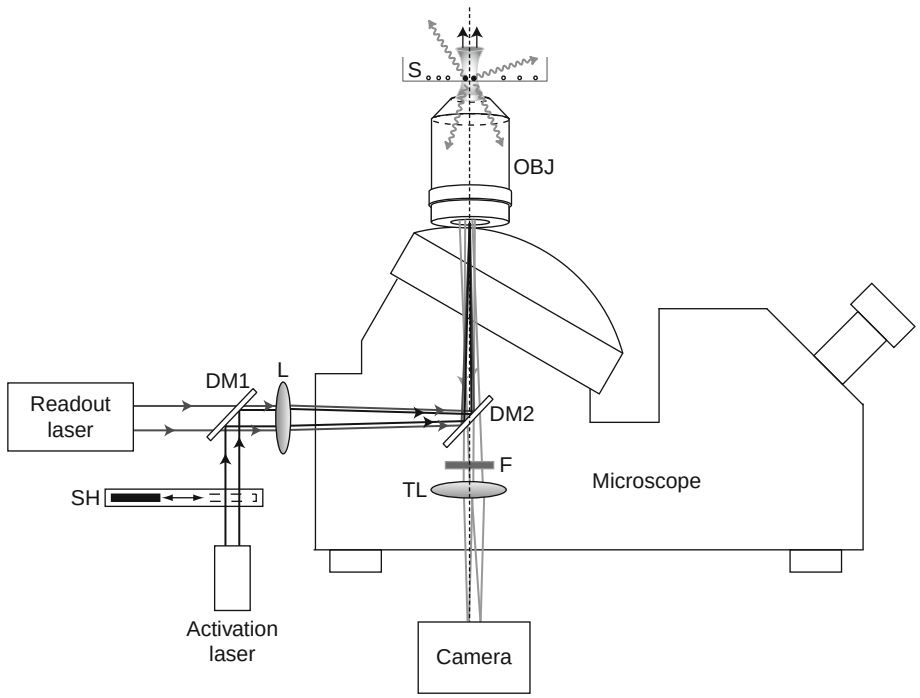

Fig. 3 The experimental geometry of fluorescence photoactivation localization microscopy (FPALM) is based on a wide-field fluorescence microscope with a high-sensitivity camera for single-molecule imaging. The activation laser beam is reflected by a dichroic mirror (DM1) and becomes collinear with the readout laser beam (passed by DM1). Both beams are focused by a lens (L) and reflected by a second DM2 to form a focus in the back aperture of a high numerical aperture objective (OBJ), which causes a large area of the sample (S) to be illuminated. Some emitted fluorescence photons (gray wavy arrows) are collected by the same OBJ, pass through DM2 and an emission filter (F), and are focused by the microscope tube lens (TL) to form an image on the camera. A shutter (SH) controls the activation laser beam for intermittent illumination. For simplicity, various mirrors for steering the laser beams, neutral density filters for attenuating the lasers, and the microscope stage and condenser are not shown. Drawing is not to scale.

where R_0 is the standard deviation of the point spread function, N is the total number of photons collected (not photons per pixel), q is the size of an image pixel, and b is the background *noise* per pixel (not background intensity). From Eq. (2), it is clearly possible to localize single fluorescent molecules with significantly better precision than $\pm R_0$. Thus, if a large number of molecules can be individually localized, their positions and intensities can be used to produce a map (image) of the distribution of molecules with localization-based resolution given by Eq. (2). In addition, the number of localized molecules must be large enough to represent the various regions within the observation area; a single molecule localized to ± 1 nm does not constitute an ''image'' of the sample at 1-nm resolution.

The localization precision σ_{xy} can be improved by increasing the number of detected photons. Probes which emit large numbers of photons before photobleaching are therefore advantageous. Many intrinsically fluorescent proteins (including GFP and dsRed) have (irreversible) photobleaching quantum yields Φ_B between 10^{-4} and 10^{-6} (Dickson *et al.*, 1997; Heikal *et al.*, 2000; Hess *et al.*, 2004; W. E. Moerner *et al.*, 2002), where the value of Φ_B is the probability per excitation that the fluorophore is converted into a (permanently) non-fluorescent form. The ratio Φ_{Fl}/Φ_B gives a measure of the average number of photons emitted by a fluorophore before photobleaching, where Φ_{Fl} is the fluorescence emission quantum yield, and should be maximized by choice of fluorophore whenever possible. Including the detection efficiency Φ_{det}, the number of detected photons $N_{det} = \Phi_{Fl}.\Phi_{det}/\Phi_B$ yields a localization precision

$$\sigma_{xy}^2 = \frac{R_0^2 + q^2/12}{N_{det}} + \frac{8\pi R_0^4 b^2}{q^2 N_{det}^2} = \frac{\Phi_B(R_0^2+q^2/12)}{\Phi_{det}\Phi_{Fl}} + \frac{8\pi R_0^4 b^2 \Phi_B^2}{q^2 \Phi_{det}^2 \Phi_{Fl}^2} \quad (3)$$

III. Methods

A. Choice of Probe

The choice of an appropriate probe is dependent on its photophysical properties. Probes with high photoactivation yields and low rates of spontaneous activation (relative to light-induced activation) are desirable for controlling the number of active molecules. Unfortunately, there is currently very little data available on activation yields. For a recent review of PA and photoswitchable proteins see Lukyanov *et al.*, 2005. Probes should also have large contrast ratios; that is to say that the fluorescence from the inactive state must be weak in comparison to the active state since fluorescence from the inactive state contributes to the background noise (Hess *et al.*, 2006).

Maximizing localization-based resolution demands maximizing the number of collected photons, which implies that probes with high fluorescence emission rates and large numbers of photons emitted before photobleaching are attractive candidates for FPALM applications. While a large photobleaching quantum yield

ultimately results in fewer total emitted photons, a finite photobleaching yield is necessary to prevent the accumulation of too many active molecules,which would eventually make localization impossible. More specifically, to control the number of active molecules requires that under imaging conditions the photobleaching rate (plus the deactivation rate in the case of reversible activation) must be greater than or equal to the activation rate (Hess *et al*., 2006). If multiple probes are to be used, consideration must be taken to ensure that the emission of each probe will be spectrally separable using appropriate filter combinations.

B. Choice of Filters

The choice of appropriate filters is determined by the probes and the lasers being used to excite those probes. A suitable dichroic mirror must be chosen that can sufficiently reflect both the readout and activation beams while maximizing transmission of the desired fluorescence. Emission filters should be chosen to further reduce scattered laser light and other background while selectively transmitting as much of the probes emission spectra as reasonable. The use of multiple probe's will require additional dichroic mirrors and emission filters to separate the emission and minimize cross talk between channels.

C. Alignment and Characterization of the Illumination Area

FPALM requires the collinear alignment of a readout laser beam and a (typically shorter wavelength) activation laser beam. These beams are then focused to a small spot at the center of the back aperture of the microscope objective lens to produce an illumination area at the sample which is large enough to encompass the desired region of interest (ROI), such as an entire cell. If a long-pass (only wavelengths greater than a certain cutoff wavelength are transmitted) dichroic mirror is used to merge the two beams, alignment is most efficiently achieved by first aligning the straight-in (parallel) beam (typically the readout laser) into the center of the field of view, without the lens in place. The lens, typically mounted near or just inside one of the input ports of the microscope, should then be aligned to focus the readout beam at the center of the objective back aperture. The profile of the expanded beam area can then be viewed via the display of a CCD camera by focusing into a dilute solution of an appropriate fluorophore. This solution should be dilute enough so as not to saturate the camera, and the emission range of the fluorophore should be chosen to be compatible with the filter sets being used. Collinear alignment of the activation laser beam is now easily accomplished by adjusting the dichroic mirror while monitoring the camera view. Alignment of the centers of both beams is recommended. However, while the beam centers should be aligned as closely as reasonably achievable, as long as the two profiles are overlapping it will be possible to control the number of active molecules within the area

illuminated by both the activation and readout beams. Images of the profile of both beams should now be obtained for later reference. Example beam profiles are shown in Fig. 2. The activation beam area may be somewhat smaller than the readout beam to maximize activation intensity. The readout beam may be spread over an area larger than the desired ROI to yield a nearly uniform illumination intensity within the ROI.

Generally, illumination by the activation source will be intermittent, as is required to maintain a small number of (from ten to a few hundred) visible molecules within the ROI. Activation pulse duration is ideally regulated electronically (e.g., by computer) to allow a well-defined timing protocol or synchronization with various events such as camera frames, but it is also possible to manually control activation. It is also convenient to have shutter control over the readout source. In cases where having an expanded illumination area results in insufficient activation intensity (due to spreading the laser power over too large an area), it may be necessary to rotate the lens near the back port of the microscope out of the beam path in coordination with the activation pulse (e.g., by having the lens mounted in a motorized filter wheel) to produce a more intense (although smaller) activation area.

In some cases, a PA probe will be inefficiently activated by the readout beam. For some fluorophores, this readout-induced activation rate will be so low under normal readout laser intensities that it is negligible compared to the rate induced by the activation beam. For other fluorophores, the readout-induced rate will be so large that it prohibits FPALM because the activation cannot be efficiently controlled, and too many molecules become visible in the illuminated area. However, if the readout-induced rate of activation is comparable to the rate of activation induced by the activation beam itself, the activation beam is essentially redundant and can be omitted from the setup. In fact, for PA-GFP activated at 405 nm and imaged (readout) at 496 nm, the readout-induced activation rate is high enough to allow readout of thousands of molecules without illuminating the sample at 405 nm. For PA-GFP, the relative rates of readout-induced and normal activation can be adjusted to make the activation by a 1-s exposure of 405 nm light with ~0.1 mW at the sample comparable to the activation during ~10 s of continuous illumination at 496 nm with ~10 mW at the sample (M. Gunewardene, *unpublished results*). Such an FPALM setup is even simpler to align and requires only that the readout beam be turned on as image acquisition with the camera begins. One limitation to this version of the method is that fluorophores with an advantageous readout-induced activation rate must be used. Furthermore, if the number of molecules in the sample is too high initially, the activation during readout illumination will lead to too many molecules becoming active in the early stages of the acquisition, preventing their positions from being determined. In such a case, one must wait until after significant photobleaching occurs to reduce the total number of molecules available to be localized, to allow the individual molecules to be separated clearly.

D. Choice of Sample Region

Transmitted light from a microscope lamp can be used to locate cells or other sample features for imaging. To reduce unintentional activation of the sample before imaging, lamp light should be long-pass filtered to remove as much intensity as possible from within the range of activation wavelengths (e.g., $\lambda <$ 500 nm in the case of PA-GFP). For imaging, the sample should be positioned within the region of overlap between readout and activation beams. Manually marking the boundaries of both beam profiles on the display can be helpful. Sample regions should be selected for imaging when single molecules can be observed by eye or with the camera (usually with stepwise blinking and/or bleaching) during illumination with the readout source. Numerous fluorescent molecules may be present during initial illumination due to any molecules activated before the start of the acquisition (e.g., by inadvertent exposure to room light or ultraviolet sterilization lamps inside the cell incubator). When too many molecules are emitting at once, single molecules will not be distinguishable by eye and it will be necessary to allow some of these molecules to photobleach before beginning an acquisition. To efficiently localize activated molecules, it is desirable to have active molecules separated by $\sim 4R_0$ on average (Hess *et al.*, 2006). For PA-GFP imaged by a 1.2 NA objective ($R_0 \sim 260$ nm), the optimal density would be ~1-10 activated molecules per 10 μm^2 area. Once any inadvertently activated molecules have sufficiently photobleached, the density of activated (fluorescent) molecules can be controlled with intermittent pulses of the activation beam and a suitable continuous intensity of the readout beam. In short, an acquisition generally consists of continuous illumination by the readout beam and short pulses (~1 s) of the activation beam administered whenever the number of visible molecules is fewer than $\sim 0.1/\mu m^2$.

During sample region selection (before beginning the acquisition), it is also necessary to determine the location of the focal plane within the sample. Viewing with transmitted light may be of assistance in locating features on a surface, but this method is only sensitive to gross movements ($>>1$ μm) in the axial direction. For applications involving three-dimensional samples such as cells, a priori knowledge of the features or labeling with a secondary fluorescent marker (of distinguishable emission) may be necessary to identify the focal plane. For example, when imaging membrane-bound proteins in a cell, the coverslip-proximal membrane can be located by focusing below the coverslip and then moving the focus upwards through the sample until fluorescent molecules first come into focus. If imaging structures within the cell, the use of a secondary marker with emission distinct from the FPALM probe can serve as a reference.

Frame acquisition (exposure) times and overall acquisition length (total number of frames) vary based on the photophysical properties of the fluorophore used and the required resolution. The lower limit on frame acquisition time is determined by the detected photon rate per molecule such that a sufficient number of photons are detected per frame to obtain the desired resolution. In samples with immobile

molecules (e.g., fixed cells or molecules immobilized on a surface), the average photobleaching time should also be adjusted via the intensity of the readout laser to be approximately equal to the frame acquisition time. Times in the range of 100–150 ms are generally sufficient to yield a demonstrated resolution of ~30 nm using PA-GFP in cells illuminated at ~100–200 W/cm^2. In live cells where labeled molecules may undergo diffusion, the acquisition time should be short enough such that the image of a single molecule does not experience additional blurring due to diffusion. Motions of molecules can be quantified if the photobleaching time is greater than the frame acquisition time (see also section I on live cell applications).

E. Position Stability

Because localization of molecules can be achieved with nanometer precision, position stability of the sample relative to the imaging system is crucial. A nonmotorized microscope mounted on a vibration isolation table in a basement room provides reasonable position stability over timescales of minutes. Microscope lateral stability can be characterized by time-lapse transmitted light imaging of 1-μm diameter polystyrene spheres. Spheres are dried on a coverslip at low density, and imaged at ~8 frames per second under lamp illumination for 20.6 min. Images of the spheres are then analyzed to determine the X-Y (lateral) coordinates of the sphere as a function of time. A histogram of the positions (after subtraction of the mean position) of a single sphere is shown in Fig. 4 along with corresponding fits using a Gaussian. Twice the standard deviation of the Gaussian yielded $2\sigma_X =$ 7.1 nm and $2\sigma_Y = 5.9$ nm after 20.6 min. Thus, for acquisitions of roughly 20 min or less, localization precision, not drift, will dominate the resolution of images obtained if localization precision is >7 nm, as is typical in live cells and many other applications.

Longer acquisitions may be desirable and will require further attention to sample drift. In addition to the necessary characterization of microscope stage drift, positions of molecules may also be corrected by the use of fiduciary marks, such as quantum dots which are bright and photobleaching-resistant, or fluorescent microspheres which carry large numbers of fluorophores (Betzig *et al.*, 2006). While for shorter acquisitions, the necessary maintenance of the position of the focal plane can be achieved manually, longer acquisitions may benefit from automatic focus correction. Axial motion of much less than the depth of field ($<< \pm 1$ μm) over the experimental timescale may be acceptable if a two-dimensional sample image is desired, and the sample is approximately planar. However, samples which have significant three-dimensional extent may be difficult to image if fluorescent molecules are present in many focal planes, as activation can occur above and below the focal plane, and may eventually make identification of the original (desired) focal plane difficult.

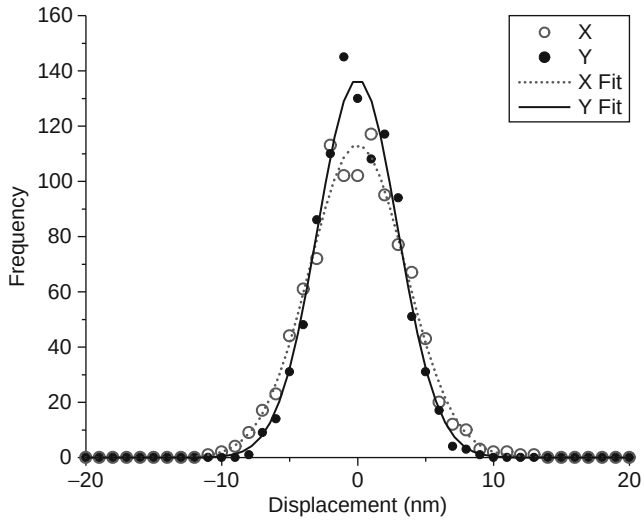

Fig. 4 Quantification of microscope stability by repeated imaging of a single immobilized bead. Polystyrene spheres with 1-μm diameter were imaged repeatedly under transmitted light illumination, and then their positions were quantified as a function of time for 20.6 min. Twice the standard deviation in the lateral positions $2\sigma_X = 7.1$ nm and $2\sigma_Y = 5.9$ nm provides a measure of lateral position stability over relevant experimental acquisition timescales. The measured distribution of positions was fitted with a Gaussian in X and Y (curves labeled X Fit and Y Fit, respectively).

F. Fluorescence Background

Before acquiring data, experimental considerations should always be taken to minimize background light from reaching the camera(s). Using lens tubes to shield the image beam path from the microscope to the camera is useful in eliminating background signal generated from external sources. Common internal sources of background include fluorescence from inactive molecules, out-of-focus active molecules, the immersion liquid, a dirty or dye-contaminated objective lens, the coverslip (fused quartz is sometimes better than glass), and scattered laser light. Cell imaging inevitably results in additional sources of background including autofluorescence, and fluorescence from the media (including ingredients such as phenol red and serum) and residual transfection reagents. The appropriate choice of filters will also help reduce background signal.

Before the position of a single molecule can be determined, a background subtraction is typically performed (background counts do not in general help to determine the position of an object, and add artificially to the apparent brightness of molecules and required threshold levels). First, the zero level (the counts measured with the camera on but no light striking its surface) should be subtracted from all images before any analysis is performed. Background subtraction methods include (a) constant baseline (uniform) or (b) position-dependent (nonuniform).

In the uniform method, a single (potentially time-dependent) value is subtracted from all pixels within the image. Typically, this value is chosen as the average pixel value from a region in the image where there is no fluorescence, or is chosen from analysis of the image intensity histogram.

For cell imaging, due to background fluorescence from inactive or out-of-focus active molecules, a nonuniform background subtraction is sometimes more appropriate. A typical method for nonuniform background subtraction is to generate a time-averaged wide-field image from all frames in the acquisition. From each individual frame to be analyzed, the average wide-field image is subtracted, weighted by (typically 95% of) the average intensity of that given frame. Such a subtraction requires the illumination profile within the ROI to be as uniform as possible, so that photobleaching occurs at a similar rate across the area. Alternatively, the rolling-ball algorithm (Sternberg, 1983) can be used as a time-dependent non-uniform background subtraction method where each frame is independent of the others.

G. Adjustment of Thresholds

The analysis of single-molecule localization begins with sequential analysis of each frame in the time series to identify and determine the position of individual molecules. In practice, custom or prepackaged software is used to select an ROI from a background subtracted image. After background subtraction, each pixel of the ROI is scanned to identify objects with intensity above an identification (ID) threshold usually on the order of a few hundred photons. Each identified object is surrounded by and centered within a square (typically 5×5 pixel) box that must meet additional criteria to ultimately be analyzed as a single molecule. Within this box, a minimum number of (typically 3–5) pixels must exceed a second threshold (typically 50–80% of the ID threshold, depending on the size of the image of the single molecule relative to one pixel) and no more than a certain maximum number of (typically 8–15) pixel values may exceed a third threshold (typically between 50% and 100% of the ID threshold) or this object will be rejected as too dim or too large, respectively, to be a single molecule.

H. Rendering the Results

FPALM images can be rendered by either of two methods: (A) unweighted, point-like plots of the positions of localized molecules, or (B) weighted plots of the positions of localized molecules, plotted as a spot with a Gaussian profile, an intensity proportional to the number of photons detected from each molecule, and a radius equal to the calculated or experimentally determined localization-based resolution. Because the weighted plots take into account the intensity and position uncertainty of each molecule, the resulting image is in some ways a more realistic representation of a fluorescence image with ultra-high resolution. Examples of both are shown in Fig. 2E–F. Typically, all molecules localized within a

particular area are rendered simultaneously, but in live cells or other time-dependent samples, time-dependent images may be rendered using subsets of molecules localized during various time periods. A threshold which includes only molecules within a particular range of intensities, or above a minimum intensity, can also be applied.

I. Biological Applications in Live Cells

Use of FPALM in live cells requires particular diligence for several reasons. In live-cell experiments, the molecules of interest may be themselves moving, and therefore their images will be further blurred compared to the ideal diffraction-limited point spread function. For this reason, the acquisition rate should be fast enough that the displacement of single molecules being localized is much less than the width of the point spread function. If the molecules are diffusing, this implies that $D\tau << R_0^2$ where τ is the frame acquisition time, and D is the diffusion coefficient. For example, hemagglutinin (HA) from influenza is a transmembrane protein with particularly slow diffusion; for the Japan variant of HA, using fluorescence photobleaching recovery, the diffusion coefficient is $D_{HA} = 0.069$ $\mu m^2/s$ (Shvartsman *et al.*, 2003). Within $\tau = 0.1$ s, each HA will on average move within an area of 0.0069 μm^2, which is approximately equal to $\sim 83 \times 83$ nm. For an emission wavelength of 520 nm, and a 1.2 NA objective, $R_0 = 264$ nm, and so diffusion of HA molecules will only modestly blur the image during the frame time. In contrast, for a faster-moving protein such as KRas with $D \sim 1.1 \pm 0.3$ $\mu m^2/s$ (Kenworthy *et al.*, 2004) and $\tau = 1$ s, the motion covers an area $D\tau = 1.1$ μm^2 which is significantly larger than R_0^2 and the image would be expected to be drastically blurred, making such an acquisition very difficult to analyze unless faster imaging frame rates are used. Furthermore, proteins which diffuse in three dimensions may move into or out of the focal plane, causing additional difficulty in analysis of results. Slowly moving plasma membrane-bound proteins are therefore good candidates for FPALM in live cells. Figures 5 and 6 show examples of FPALM images of PA-GFP-tagged influenza HA in fixed fibroblasts. High acquisition frame rates can reduce the motion of molecules within one frame.

IV. Materials

Cells are grown in chambers with a #1.5 coverslip bottom (e.g., Nunc Lab-Tek II growth chambers, #12-565-8 from Fisher Healthcare, Houston, TX) and fixed when necessary. Cells expressing a PA-GFP-tagged protein of interest or other PA-FP are illuminated by 6–10 mW of continuous-wave readout laser power (typically an Argon ion laser at 496 nm for excitation of PA-GFP), spread over an area of $\sim$100 to 1000 μm^2 to yield $\sim$600–10000 W/cm^2. For activation, 0.05–1.5 mW of power at 405 nm is used (e.g., the BCL-405 laser from Crystalaser, Reno, NV) which is spread over $\sim$125–250 μm^2 to yield 20–1200 W/cm^2. As described

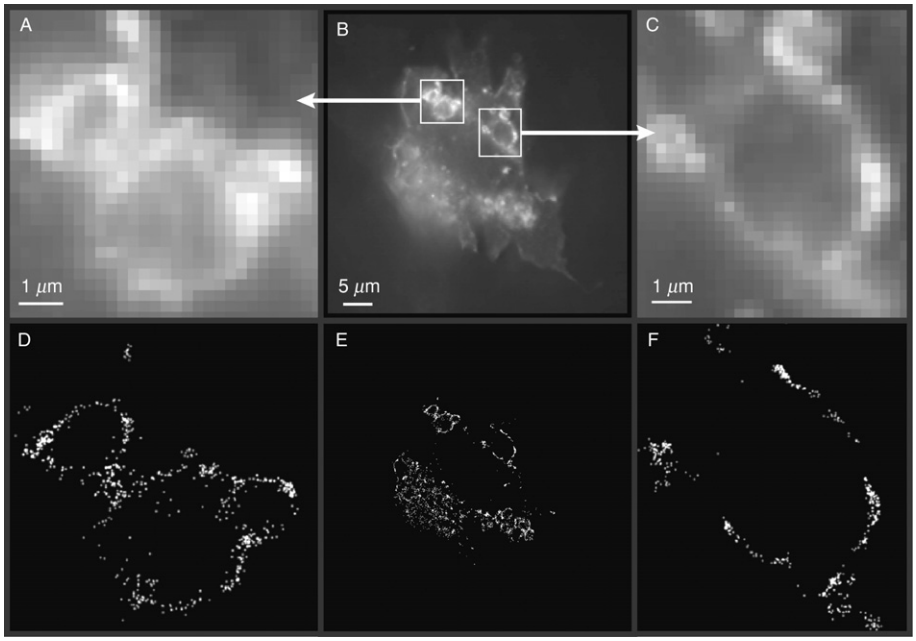

Fig. 5 Wide-field fluorescence (B) and fluorescence photoactivation localization microscopy (FPALM) images (E) of the protein hemagglutinin tagged with photoactivatable-green fluorescent protein (PA-GFP) in a fixed HAb2 fibroblast. (A, C, D, F) Zoom-in of selected regions to show agreement with wide-field fluorescence (A, C) and illustrate improvement in resolution by FPALM (D, F). Note that contrast was adjusted in (E) for visualization. The pairs of images (A and D), (B and E), and (C and F) have the same scale.

above (see also Figs. 2 and 3), the activation beam is aligned to illuminate the same (central) region of the field as the readout beam. The readout beam continuously illuminates the sample during data acquisition, while the activation beam is pulsed as needed (or is on continuously) for ~1–10 s to photoactivate PA-GFP molecules whenever the density of visible molecules within the sample declines to fewer than $\sim 0.1/\mu m^2$. Photoactivated molecules are visualized by imaging the fluorescence onto a CCD camera (e.g. Quantifire; Optronics, Goleta, CA) or an electron-multiplication CCD (e.g. Cascade 512B; Photometrics, Tucson, AZ, or iXon; Andor Technology, South Windsor, CT). Camera settings include (A) Quantifire: 2×2 binning, 0.1–0.2 s acquisition time, and gain 6–8, and (B) Cascade 512: 1×1 binning, 0.15 s acquisition time, on-chip multiplication gain 1500–2000, and conversion gain 6 e^-/ADU.

Estimated prices for components include inverted fluorescence microscope: $15–25k, high-NA objective lens: $7k, electron-multiplying CCD camera: $25–40k, 405 nm laser for activation: $5–10k, 488 nm laser for readout: $5–15k, miscellaneous optics, mounts, dichroic mirrors, and filters: $8k, computer and Matlab software: $2–3k, computer-controlled shutter: ~$1k.

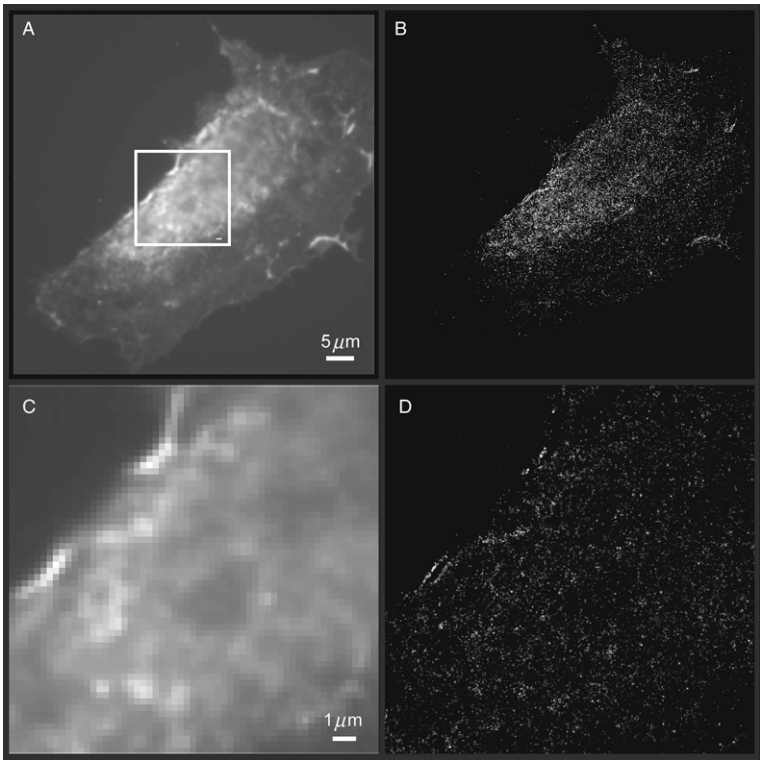

Fig. 6 Wide-field fluorescence (A) and fluorescence photoactivation localization microscopy (FPALM) images (B) of hemagglutinin tagged with photoactivatable-green fluorescent protein (PA-GFP) in a fixed HAb2 fibroblast. Here, a large number of molecules with high brightness have been localized ($n \sim 40{,}000$) in a large cell ($\sim$60 μm in width), so that the molecular coordinates obtained contain information on a wide (more than three orders of magnitude) range of length scales. (C–D) Zoom-in of boxed region showing the improved resolution of FPALM. Note that the contrast was adjusted linearly in (B, D) for visualization.

V. Discussion

Before interpreting FPALM images, it is highly recommended that users image a sample with known geometry to calibrate the microscope and method. While there is no particular sample that serves all purposes, one example of a calibration sample is the annealed R-cut sapphire surface shown in Fig. 7. The surface of this sample, which was described in detail previously (Hess *et al.*, 2006) is made up of terraces with straight edges and nanometer-scale step sizes. The sample was coated with a drop of PA-GFP in solution, allowed to dry, and imaged using FPALM. The resulting image was compared with atomic force microscope (AFM) images of different regions on the same sample. The width of and spacing between the terraces were found to agree by both methods, confirming that FPALM could

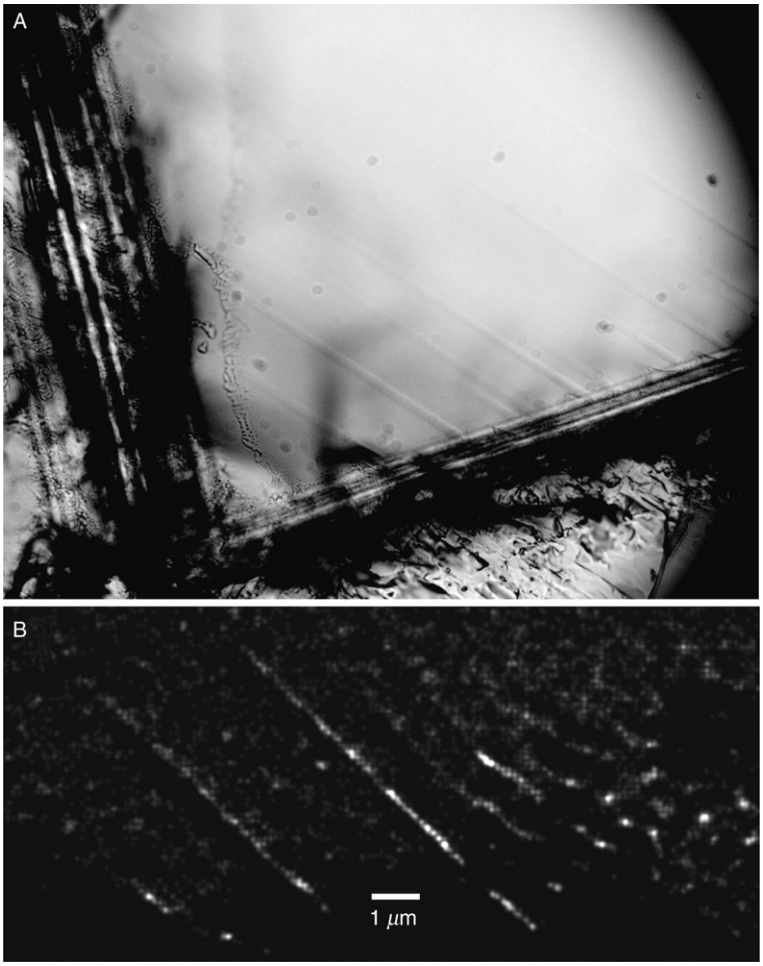

Fig. 7 Fluorescence photoactivation localization microscopy (FPALM) images of atomic terraces on an annealed sapphire surface reveal structures below the diffraction limit of light. A wafer of single-crystal sapphire within 0.05° of R-cut was annealed at 1700 °C in air for ten hours, cooled, cleaned, coated with a thin layer of photoactivatable-green fluorescent protein (PA-GFP), and imaged by wide-field transmitted light (A) and by FPALM (B). The surface contains terraces which appear as straight lines in (A) and (B). The sharp, corner-like edges of the terraces were imaged by atomic force microscopy to have a width of ~70 nm (Hess *et al.* 2006). FPALM results yielded a step width of 73 ± 3 nm defined by the $1/e^2$ width of the image of a single step, or 86 ± 4 nm defined by the full width at half maximum of the same step. These results demonstrate an independent confirmation of the FPALM results and prove that the method can image structures smaller than the diffraction-limited resolution of light, which in this case was ~264 nm. The FPALM image was generated by plotting the positions of all molecules weighted by their intensities and convolving the image of those plotted positions with a Gaussian filter with $1/e^2$ width of 73 nm (a conservative estimate of the resolution). Approximately 6,665 molecules are shown in panel (B).

successfully image a sample of known geometry with ~86 ± 4 nm resolution or better, more than threefold better than the diffraction-limited resolution of 264 nm for the same setup. Figure 8 shows a coverslip scored with a crisscross pattern of scratches, labeled with PA-GFP, and imaged by FPALM. Small features which

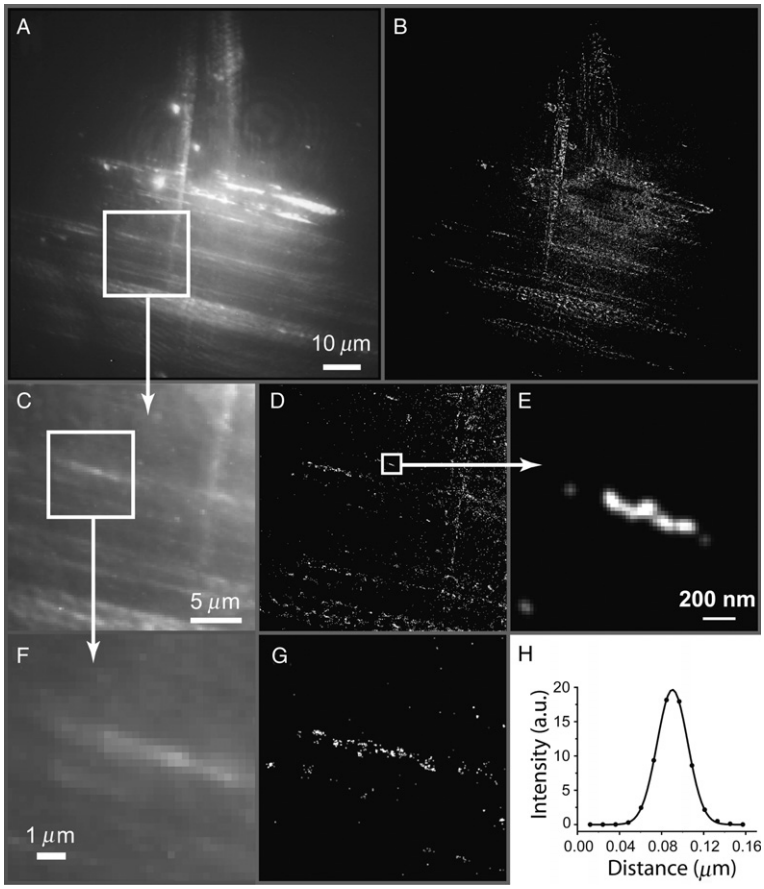

Fig. 8 (A) Wide-field fluorescence and (B) fluorescence photoactivation localization microscopy (FPALM) images of photoactivatable-green fluorescent protein (PA-GFP) in solution dried on a scratched coverslip. Two sets of approximately perpendicular scratches were formed by dragging a razor blade twice across the surface. (C–D) Zoom-in of boxed region in (A) showing (C) wide-field fluorescence and (D) FPALM images. Zoom-in of boxed region in (C) showing (F) wide-field fluorescence and (G) FPALM images. Note the significant improvement in resolution using FPALM. (E) Zoom-in of boxed region in (D) demonstrating the subdiffraction resolution of FPALM. Note that the contrast was adjusted linearly in (B, D, G) for visualization. (H) The cross-section of a linear structure within the same image was fitted with a Gaussian, yielding a full width at half maximum of ~34 nm and a $1/e^2$ radius of ~29 nm, demonstrating nearly eightfold improvement in the resolution compared to wide-field fluorescence microscopy.

collected the PA-GFP are visible with dimensions as small as ~34 nm in full width at half maximum, nearly eightfold smaller than the diffraction-limited resolution.

A. Density of Localized Molecules

If the goal is to reliably image structures at a resolution below the diffraction limit, the density of molecules within the structure of interest is arguably as important as the precision with which those molecules are localized. Too low a density of molecules (too high a sparseness) within a structure leads to large uncertainties in the concentration of molecules; for molecules distributed at a given density within a small region, following Poisson statistics the uncertainty σ_N in the number of molecules N, will be equal to $N^{1/2}$. Thus, even if the molecules are localized with phenomenal precision (e.g., $<<1$ nm), the resulting image will have an uncertainty in the density which is quite large if the number of molecules within a given area is small (e.g., <10). The effect of having a low number of molecules on FPALM images obtained with satisfactory localization precision is illustrated in Fig. 9. Even a sharp edge can be difficult to discern if the density of molecules is too small (Fig. 9A). In practice, localized molecules will have a distribution of intensities; those with the highest intensities will in general be fewer than the majority with average intensity. Thus, there will be a trade-off between generating an image with very many molecules (reduced sparseness) and an image which includes the molecules with the most precisely defined positions (those with the highest intensities).

B. Factors Which Can Bias the Measured Distribution of Molecules

To obtain an FPALM image which accurately reflects the real distribution of molecules in the sample, one must consider the same factors which can bias the image in a normal fluorescence microscope: nonuniform illumination, background and out-of-focus fluorescence, time dependence of the sample, optical aberrations, vibrations, and other motions of the sample relative to the microscope during acquisition. However, several additional effects can bias the measured distribution of molecules in an FPALM microscope. Because FPALM relies on identification and localization of single molecules, if the density of fluorescent molecules gets so high that individual molecules cannot be distinguished from one another, analysis of that region cannot be performed, and the molecules in that region will not be included in the image. In principle, this should not happen since the density of *fluorescent* molecules is controlled by the relative rates of photoactivation and photobleaching, but in situations where full control over the density of fluorescent molecules is not achieved, regions with densities per unit area of active molecules above some maximum level will appear in the image to have fewer molecules than they actually have. This maximum density $D_{\max}$ *within any given acquisition frame* (the density in the final image will be much higher) can be estimated as $D_{\max} = 1/R^2$, which requires the density $D = N/A$ to be $D << D_{\max}$, where N is

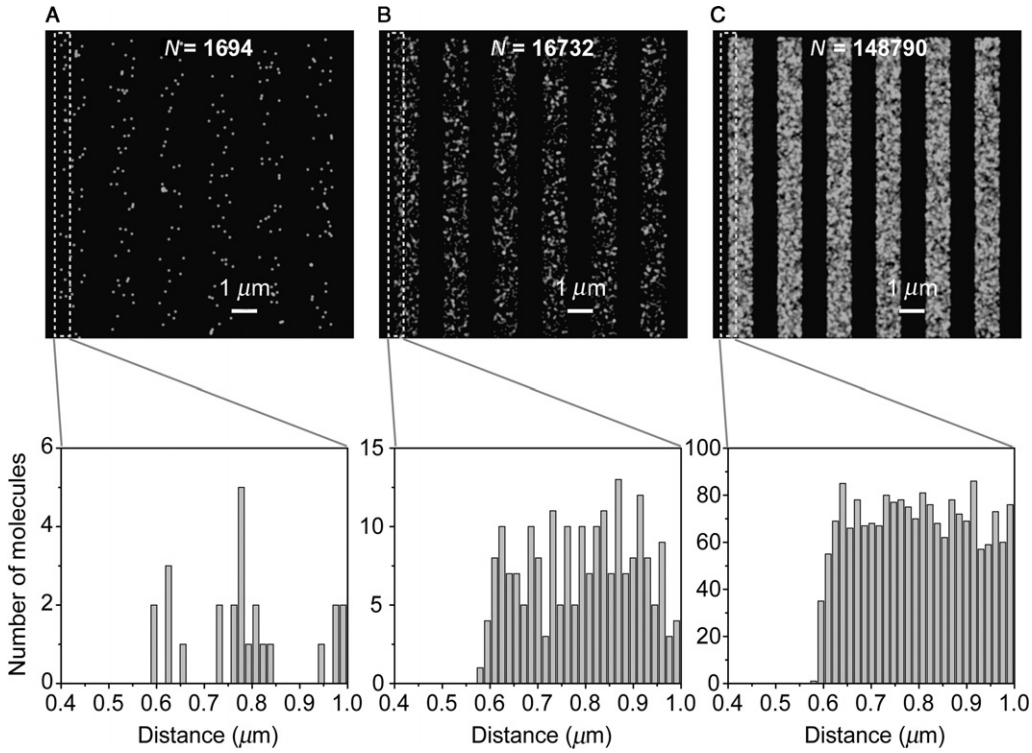

Fig. 9 Imaging of nanoscale structures requires a high density of localized molecules in addition to nanometer localization precision. The effect of the number of localized molecules on the fluorescence photoactivation localization microscopy (FPALM) image of a simulated patterned structure with ~1-μm wide strips in which all molecules reside is shown by zooming in on the edge of the strip. (upper row) Simulated FPALM images of (A) 1694 molecules, (B) 16732 molecules, and (C) 148790 molecules localized in a background-free area of ~12 × 12 μm. Molecular positions are plotted additively, weighted by the brightness of each individual molecule, the image of which was simulated to contain ~400 photons emitted at 520 nm and detected by a 1.2 NA (numerical aperture) lens with diffraction-limited resolution of 264 nm. (lower row) Histograms of the number of molecules localized within evenly spaced bins 15-nm wide show the lateral profile of the edge clearly for large numbers of molecules (right), but a limited number of molecules (left) limits the ability to discern the step, even though the localization precision was the same for all three cases (A–C).

the number of molecules within a region of area A, and R is the radius of the point spread function. If the illumination is nonuniform, activation rates will be increased in areas with higher activation laser intensity, leading to higher densities of fluorescent molecules, while in regions with lower readout laser intensity, molecules will be less likely to emit enough photons to be classified as above threshold. Thus, for quantitative characterization of molecular distributions, sample regions with a nearly uniform readout illumination profile are desirable. Nonuniform activation profile is less problematic as long as the density of molecules stays below $D_{\max}$, and as long as the acquisition lasts long enough to activate

molecules within regions illuminated at lower readout intensity. Thus, one advantage of spreading the readout beam to a larger radius than the activation beam is to achieve a small but nearly uniformly illuminated central area within the field of view.

C. Failed Localization: Pixelization Artifacts

If molecules are imaged in samples with high background levels or if insufficient numbers of emitted photons are collected, the algorithm which fits a Gaussian to the image of the molecule may not reliably find the center of the molecule. In such cases, small changes in the initial coordinates for the fitting routine may produce large changes in the final coordinates obtained, or the coordinates obtained may end up at the edges of the allowed regions. FPALM images suffering from such a problem will show significant numbers of molecules falling on the edges of image pixels. This "pixelization artifact" can be remedied by checking whether initial coordinates for the fitting algorithm have a strong effect on final apparent molecular coordinates, by increasing thresholds to include only the brighter molecules, or in some cases by using a nonuniform background subtraction.

The technical factors which limit the rate of imaging are the readout and activation laser intensities, and the camera frame rate and noise properties. Fundamentally, the photoactivation quantum yield, photobleaching quantum yield, and the maximum fluorophore emission rate per molecule (e.g., at saturation) also limit acquisition rate because localization-based resolution depends on controlling the number of active molecules, on detecting as many photons as possible in the shortest time possible, and on photobleaching. However, once the utility of a method has been established, technological advances are often motivated, and new tools, such as improved PA markers, can be developed. The FPALM acquisition rate can in principle be increased significantly, given that camera frame rates can be increased without inducing prohibitively large readout noise, and given that sufficient numbers of photons can be detected from each molecule to provide a useful improvement in resolution. Based on estimated saturating intensities for enhanced green fluorescent protein (EGFP) and other GFPs, and given current intensities used for cellular FPALM imaging, improvements in FPALM frame rate of at least tenfold are likely possible with current technology and PA-FPs. When active molecules remain fluorescent for several frames, Betzig *et al*. combine data from each frame to improve the number of detected photons per molecule (Betzig *et al*., 2006), which is feasible in fixed samples where molecules are not moving during the acquisition.

D. Light Exposure

Exposure of living cells to laser radiation typically causes damage and alters biological function, especially at high intensities. In FPALM, the readout laser intensities used so far are of order $\sim$1000 W/cm^2. In confocal microscopy, from a

few μW up to $\sim$1 mW of power may illuminate the sample in a diffraction-limited focal area of $\sim$0.2 μm^2, yielding intensities as high as 5×10^5 W/cm^2 during the brief ($\sim$1 μs) dwell time within a given region. While the illumination in FPALM is continuous, and in the confocal illumination in a given region occurs once per scan (of order 1 μs per second), the dose received by the cells in these two methods is arguably similar for the following reason: in practice, during imaging by confocal microscopy, a small but significant fraction of fluorophores will photobleach during the time it takes to find a suitable sample, optimize microscope parameters, and acquire several images. Each photobleached fluorophore has a certain probability of generating reactive oxidative species, which can lead to cell damage. If N_B, the number of bleached fluorescent molecules in the focal plane of a confocal microscopy experiment is at least a few percent (here use 10%) of N_I, the initial number of molecules, and a probe concentration of $\sim$5 μM is present initially, one can estimate N_I if the focal plane is 0.6-μm thick and 200 μm $\times$ 200 μm in lateral extent with 20% coverage of regions by the probe. Using $N_I = C \cdot V_{illum}$ where C is the concentration of dye and V_{illum} is the volume illuminated during the scan, we find $N_I \sim 1.4 \times 10^7$ molecules, and $N_B \sim 1.4 \times 10^6$ molecules. In FPALM, the number of molecules bleached is similar to or greater than the number localized, neglecting a modest fraction of activated molecules which are not localized due to thresholds and a small number of pairs of molecules not localized because they are too close together. The number of localized molecules is typically 10^4–10^6 (Betzig *et al.*, 2006; Hess *et al.*, 2006), which is in the same range as or lower than the number of bleached molecules in the above estimate for one type of confocal experiment. Thus, it is expected that photodamage in FPALM experiments could be similar to that received during acquisition of a single frame-averaged confocal microscope image. However, only rigorous testing of effects on specific cell lines and specific biological processes will definitively answer this question.

E. Additional Single-Molecule Information Extracted by FPALM

In addition to the position map (image) which is obtained, FPALM also measures the number and brightness of individual molecules, information which is not available to standard imaging techniques. The distribution of fluorescence intensities can be a useful measure of probe performance, and can reveal population heterogeneities inaccessible to bulk measurements. Figure 10 shows fluorescence intensity histograms for PA-GFP, Dendra2-actin (Gurskaya *et al.*, 2006), and Dronpa (Ando *et al.*, 2004) expressed in fibroblast cells and imaged by FPALM, demonstrating information that would not be easily obtained in normal fluorescence microscopes unless the concentration of the probes were known. Please note that these data were not corrected for relative differences in excitation rate or detection efficiency, and should therefore not be considered a quantitative comparison among the three species. Furthermore, environmental variables such as probe dipole moment orientation, pH, membrane potential, ion concentration,

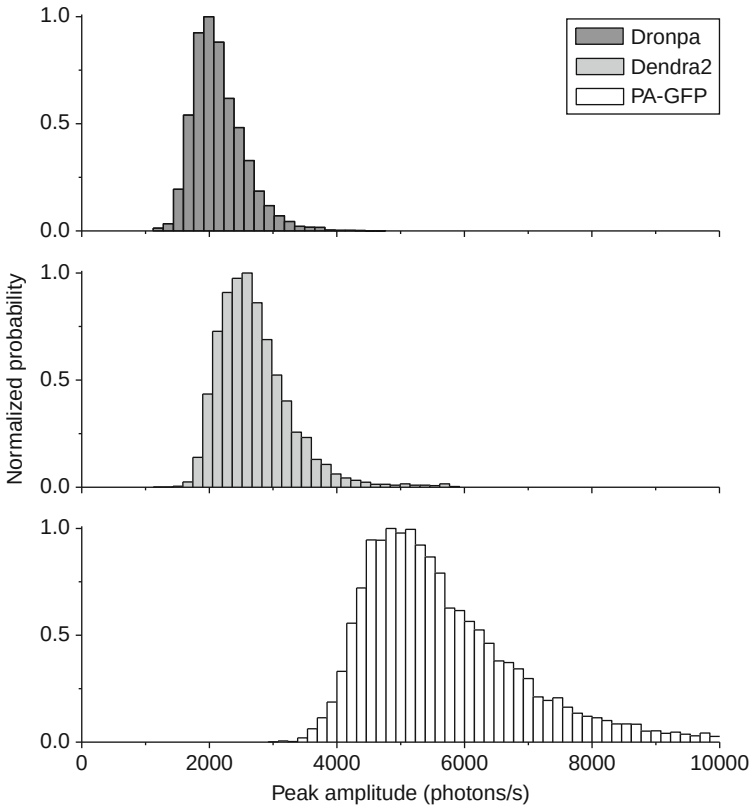

Fig. 10 Intensity distributions of many localized single molecules of the photoactivatable (PA) proteins Dronpa, Dendra2, and PA-GFP (green fluorescent protein) in fixed fibroblasts imaged by fluorescence photoactivation localization microscopy (FPALM). Since the results for each protein were obtained on different days, under differing excitation (readout) intensities, and have not been corrected for filter transmission, they do not provide a reliable comparison of relative brightness between different proteins, but they do demonstrate the ability to quantify the brightness of a variety of molecular species in cells using FPALM image data. Constructs and purified protein provided courtesy of Uli Nienhaus and Joerg Wiedenmann (Ulm), George Patterson (NIH), and Vladislav Verkhusha (Albert Einstein).

and local viscosity can change the spectral and photophysical characteristics of many fluorescent probes.

F. Future Directions

While a PA version of any protein with known sequence can in principle be produced, currently there are a limited number of PA-FPs (Gurskaya *et al.*, 2006; Lukyanov *et al.*, 2005). Those available are not easy to combine with other PA-FPs

because of spectral overlap. In particular, many of the red fluorescent PA-FPs are fluorescent in their preactivated state, and therefore prohibit use of that portion of the spectrum for another probe. For multicolor applications, PA-FPs which emit in the blue or far red portions of the spectrum and are nonfluorescent before activation are in demand.

Of considerable interest are values for the photoactivation quantum yields (Φ_{PA}) of existing probes. The value of Φ_{PA} is the probability that a molecule will be converted from its inactive (preactivation) form into its active form, given that it absorbed a photon. Furthermore, the total conversion yield, the fraction of a given population of PA-FPs that can ultimately be activated, is not known for any PA-FP. Such numbers are crucial for biological applications where it is desirable to image potentially rare molecular species, and for making quantitative comparisons between PA probes. For two-color imaging with a single activation laser, in the case of an inactive probe whose emission overlaps with the emission of the active form of a second probe, the relative magnitudes of Φ_{PA} will determine whether both probes can feasibly be used together.

Of course, since FPALM resolution ultimately depends on density of molecules and localization precision, probes are desired which emit as many photons as possible before photobleaching. Another consideration is the rate at which those photons are emitted, which should be as high as possible to minimize frame acquisition times for live-cell applications and improve contrast of molecules against background. Probe molecules must also have a finite photobleaching yield or a finite conversion yield back into the inactive state to allow control over the number of fluorescent molecules. Without such control, the number of fluorescent molecules will eventually grow so large that individual molecules cannot be distinguished.

Multicolor FPALM is of considerable interest for a variety of biological applications. The ability to colocalize two molecular species at the nanometer length scale in a living cell has been long coveted. Two-species single-particle tracking experiments have already led to significant biological insights (Douglass and Vale, 2005). Two-color STED imaging has been demonstrated recently with <30 nm and $\sim$65-nm resolution for each probe, respectively (Donnert *et al.*, 2007). Unfortunately, for FPALM the available PA-FPs are so far difficult to use in concert, particularly because of spectral overlap between their (as many as four) emission spectra, and the increased number of excitation and activation wavelengths needed (as many as four in total). One potentially ideal combination would be two PA-FPs which emit only in their active forms, activate with the same wavelength, and read out with the same wavelength, but have nonoverlapping emission spectra. A bright red fluorescent PA-FP with high contrast ratio, $\sim$500-nm excitation, and $\sim$400-nm activation would be ideal. Perhaps slight modification of an existing red-emitting PA-FP would yield a good pair with PA-GFP or Dronpa. Alternatively, probes which emit at the same wavelength but have completely separable activation spectra are also feasible options. Two-color PALM using a combination of Dronpa and Eos was recently reported (Shroff *et al.*, 2007).

VI. Summary

FPALM can image living or fixed biological samples with localization-based resolution well below the diffraction limit. Initially, nonfluorescent PA molecules are (1) activated in small numbers at a time, (2) imaged, and (3) photobleached or converted back to the inactive state. Steps 1–3 are then repeated to read out as many molecules as possible or as are desired. An image is then reconstructed by plotting the positions of each localized molecule. Structures in living cells can be imaged with 20–40 nm localization-based resolution, depending on a number of factors, including photon emission rate per fluorophore, fluorescence background noise, diffusion coefficient of the labeled species, and acquisition time, which can be as fast as a few seconds.

Acknowledgments

The authors thank George Bernhardt, Scott Collins, and Patrick Spinney for the sapphire calibration sample, Joshua Zimmerberg and Paul Blank for the argon laser and CCD camera, Vladislav Verkhusha for the Dendra2 construct, Joerg Wiedenmann and Uli Nienhaus for EosFP constructs and purified protein, George Patterson for the PA-GFP construct and purified protein, Sarah Maas and Kevin Mills for the PA-GFP-HA construct, Thomas Tripp for machining, Manasa Gudheti for assistance with cell culture, and Dean Astumian, Joerg Bewersdorf, and Sharon Ashworth for useful discussions. This work was supported by National Institutes of Health grant K25AI65459, National Science Foundation Grant CHE-0722759, and funds from the University of Maine Office of the Vice President for Research. T.G. benefited from a University of Maine Summer Research Fellow Award.

References

Ando, R., Mizuno, H., and Miyawaki, A. (2004). Regulated fast nucleocytoplasmic shuttling observed by reversible protein highlighting. *Science* **306,** 1370–1373.

Betzig, E., and Trautman, J. K. (1992). Near-field optics—Microscopy, spectroscopy, and surface modification beyond the diffraction limit. *Science* **257,** 189–195.

Betzig, E., Patterson, G. H., Sougrat, R., Lindwasser, O. W., Olenych, S., Bonifacino, J. S., Davidson, M. W., Lippincott-Schwartz, J., and Hess, H. F. (2006). Imaging intracellular fluorescent proteins at nanometer resolution. *Science* **313,** 1642–1645.

Betzig, E., Trautman, J. K., Harris, T. D., Weiner, J. S., and Kostelak, R. S. (1991). Beating the diffraction barrier: Optical microscopy on a nanometer scale. *Science* **251,** 1468–1470.

Born, M., and Wolf, E. (1997). (''Principles of Optics: Electromagnetic Theory of Propagation, Interference and Diffraction of Light.'') Cambridge University Press, Cambridge, UK; New York.

Denk, W., Strickler, J. H., and Webb, W. W. (1990). 2-Photon laser scanning fluorescence microscopy. *Science* **248,** 73–76.

Dickson, R. M., Cubitt, A. B., Tsien, R. Y., and Moerner, W. E. (1997). On/off blinking and switching behaviour of single molecules of green fluorescent protein. *Nature* **388,** 355–358.

Donnert, G., Keller, J., Medda, R., Andrei, M. A., Rizzoli, S. O., Luhrmann, R., Jahn, R., Eggeling, C., and Hell, S. W. (2006). Macromolecular-scale resolution in biological fluorescence microscopy. *Proc. Natl. Acad. Sci. USA* **103,** 11440–11445.

Donnert, G., Keller, J., Wurm, C. A., Rizzoli, S. O., Westphal, V., Schonle, A., Jahn, R., Jakobs, S., Eggeling, C., and Hell, S. W. (2007). Two-color far-field fluorescence nanoscopy. *Biophys. J.* **92,** L67–L69.

Douglass, A. D., and Vale, R. D. (2005). Single-molecule microscopy reveals plasma membrane microdomains created by protein-protein networks that exclude or trap signaling molecules in T cells. *Cell* **121,** 937–950.

Gordon, M. P., Ha, T., and Selvin, P. R. (2004). Single-molecule high-resolution imaging with photobleaching. *Proc. Natl. Acad. Sci. USA* **101,** 6462–6465.

Gurskaya, N. G., Verkhusha, V. V., Shcheglov, A. S., Staroverov, D. B., Chepurnykh, T. V., Fradkov, A. F., Lukyanov, S., and Lukyanov, K. A. (2006). Engineering of a monomeric green-to-red photoactivatable fluorescent protein induced by blue light. *Nat. Biotechnol.* **24,** 461–465.

Gustafsson, M. G. (2005). Nonlinear structured-illumination microscopy: Wide-field fluorescence imaging with theoretically unlimited resolution. *Proc. Natl. Acad. Sci. USA* **102,** 13081–13086.

Gustafsson, M. G. L., Agard, D. A., and Sedat, J. W. (1999). I^5M: 3D widefield light microscopy with better than 100 nm axial resolution. *J. Microsc.* **195,** 10–16.

Heikal, A. A., Hess, S. T., Baird, G. S., Tsien, R. Y., and Webb, W. W. (2000). Molecular spectroscopy and dynamics of intrinsically fluorescent proteins: Coral red (dsRed) and yellow (Citrine). *Proc. Natl. Acad. Sci. USA* **97,** 11996–12001.

Hell, S. W. (2007). Far-field optical nanoscopy. *Science* **316,** 1153–1158.

Hell, S. W., Jakobs, S., and Kastrup, L. (2003). Imaging and writing at the nanoscale with focused visible light through saturable optical transitions. *Appl. Phys. A* **77,** 859–860.

Hell, S. W., and Wichmann, J. (1994). Breaking the diffraction resolution limit by stimulated emission: Stimulated-emission-depletion fluorescence microscopy. *Opt. Lett.* **19,** 780–782.

Hess, S. T., Girirajan, T. P., and Mason, M. D. (2006). Ultra-high resolution imaging by fluorescence photoactivation localization microscopy. *Biophys. J.* **91,** 4258–4272.

Hess, S. T., Heikal, A. A., and Webb, W. W. (2004). Fluorescence photoconversion kinetics in novel green fluorescent protein pH sensors. *J. Phys. Chem. B* **108,** 10138–10148.

Hess, S. T., and Webb, W. W. (2002). Focal volume optics and experimental artifacts in confocal fluorescence correlation spectroscopy. *Biophys. J.* **83,** 2300–2317.

Hofmann, M., Eggeling, C., Jakobs, S., and Hell, S. W. (2005). Breaking the diffraction barrier in fluorescence microscopy at low light intensities by using reversibly photoswitchable proteins. *Proc. Natl. Acad. Sci. USA* **102,** 17565–17569.

Kenworthy, A. K., Nichols, B. J., Remmert, C. L., Hendrix, G. M., Kumar, M., Zimmerberg, J., and Lippincott-Schwartz, J. (2004). Dynamics of putative raft-associated proteins at the cell surface. *J. Cell Biol.* **165,** 735–746.

Klar, T. A., Jakobs, S., Dyba, M., Egner, A., and Hell, S. W. (2000). Fluorescence microscopy with diffraction resolution barrier broken by stimulated emission. *Proc. Natl. Acad. Sci. USA* **97,** 8206–8210.

Lacoste, T. D., Michalet, X., Pinaud, F., Chemla, D. S., Alivisatos, A. P., and Weiss, S. (2000). Ultrahigh-resolution multicolor colocalization of single fluorescent probes. *Proc. Natl. Acad. Sci. USA* **97,** 9461–9466.

Lagerholm, B. C., Averett, L., Weinreb, G. E., Jacobson, K., and Thompson, N. L. (2006). Analysis method for measuring submicroscopic distances with blinking quantum dots. *Biophys. J.* **91,** 3050–3060.

Levi, V., Ruan, Q., and Gratton, E. (2005a). 3-D particle tracking in a two-photon microscope: Application to the study of molecular dynamics in cells. *Biophys. J.* **88,** 2919–2928.

Levi, V., Ruan, Q., Plutz, M., Belmont, A. S., and Gratton, E. (2005b). Chromatin dynamics in interphase cells revealed by tracking in a two-photon excitation microscope. *Biophys. J.* **89,** 4275–4285.

Lidke, K. A., Rieger, B., Jovin, T. M., and Heintzmann, R. (2005). Superresolution by localization of quantum dots using blinking statistics. *Opt. Express* **13,** 7052–7062.

Liu, Z., Lee, H., Xiong, Y., Sun, C., and Zhang, X. (2007). Far-field optical hyperlens magnifying sub-diffraction-limited objects. *Science* **315,** 1686.

Lukyanov, K. A., Chudakov, D. M., Lukyanov, S., and Verkhusha, V. V. (2005). Photoactivatable fluorescent proteins. *Nat. Rev. Mol. Cell Biol.* **6,** 885–891.

Moerner, W. E. (2002). "Single-molecule optical spectroscopy of autofluorescent proteins." *J. Chem. Phys.* **117,** 10925–10937.

Pawley, J. B. (1995). ("Handbook of Biological Confocal Microscopy.") Plenum Press, New York.

Ponti, A., Matov, A., Adams, M., Gupton, S., Waterman-Storer, C. M., and Danuser, G. (2005). Periodic patterns of actin turnover in lamellipodia and lamellae of migrating epithelial cells analyzed by quantitative fluorescent speckle microscopy. *Biophys. J.* **89,** 3456–3469.

Qu, X. H., Wu, D., Mets, L., and Scherer, N. F. (2004). Nanometer-localized multiple single-molecule fluorescence microscopy. *Proc. Natl. Acad. Sci. USA* **101,** 11298–11303.

Rust, M. J., Bates, M., and Zhuang, X. (2006). Sub-diffraction-limit imaging by stochastic optical reconstruction microscopy (STORM). *Nat. Methods* **3,** 793–796.

Salmon, W. C., Adams, M. C., and Waterman-Storer, C. M. (2002). Dual-wavelength fluorescent speckle microscopy reveals coupling of microtubule and actin movements in migrating cells. *J. Cell Biol.* **158,** 31–37.

Sandison, D. R., Piston, D. W., Williams, R. M., and Webb, W. W. (1995). Quantitative comparison of background rejection, signal-to-noise ratio, and resolution in confocal and full-field laser-scanning microscopes. *Appl. Opt.* **34,** 3576–3588.

Sandison, D. R., and Webb, W. W. (1994). Background rejection and signal-to-noise optimization in confocal and alternative fluorescence microscopes. *Appl. Opt.* **33,** 603–615.

Schrader, M., and Hell, S. W. (1996). 4PI-confocal images with axial superresolution. *J. Microsc.* **183,** 189–193.

Sharonov, A., and Hochstrasser, R. M. (2006). Wide-field subdiffraction imaging by accumulated binding of diffusing probes. *Proc. Natl. Acad. Sci. USA* **103,** 18911–18916.

Shroff, H., Galbraith, C. G., Galbraith, J. A., White, H., Gillette, J., Olenych, S., Davidson, M. W., and Betzig, E. (2007). "Dual-color superresolution imaging of genetically expresssed probes within individual adhesion complexes. *Proc. Natl. Acad. Sci. USA* **104,** 20308–20313.

Shvartsman, D. E., Kotler, M., Tall, R. D., Roth, M. G., and Henis, Y. I. (2003). Differently anchored influenza hemagglutinin mutants display distinct interaction dynamics with mutual rafts. *J. Cell Biol.* **163,** 879–999.

Sternberg, S. R. (1983). Biomedical image processing. *IEEE Computer* **16,** 22–34.

Waterman-Storer, C. M., Desai, A., Bulinski, J. C., and Salmon, E. D. (1998). Fluorescent speckle microscopy, a method to visualize the dynamics of protein assemblies in living cells. *Curr. Biol.* **8,** 1227–1230.

Xu, C., Zipfel, W., Shear, J. B., Williams, R. M., and Webb, W. W. (1996). Multiphoton fluorescence excitation: New spectral windows for biological nonlinear microscopy. *Proc. Natl. Acad. Sci. USA* **93,** 10763–10768.

Yildiz, A., Forkey, J. N., McKinney, S. A., Ha, T., Goldman, Y. E., and Selvin, P. R. (2003). Myosin V walks hand-over-hand: Single fluorophore imaging with 1.5-nm localization. *Science* **300,** 2061–2065.

CHAPTER 13

Imaging of Cells and Tissues with Mass Spectrometry: Adding Chemical Information to Imaging

Tyler A. Zimmerman, Eric B. Monroe, Kevin R. Tucker, Stanislav S. Rubakhin, and Jonathan V. Sweedler

Department of Chemistry and the Beckman Institute
University of Illinois
Urbana, Illinois 61801

METHODS IN CELL BIOLOGY, VOL. 89

0091-679X/08 $35.00
DOI: 10.1016/S0091-679X(08)00613-4

Abstract

Techniques that map the distribution of compounds in biological tissues can be invaluable in addressing a number of critical questions in biology and medicine. One of the newer methods, mass spectrometric imaging, has enabled investigation of spatial localization for a variety of compounds ranging from atomics to proteins. The ability of mass spectrometry to detect and differentiate a large number of unlabeled compounds makes the approach amenable to the study of complex biological tissues. This chapter focuses on recent advances in the instrumentation and sample preparation protocols that make mass spectrometric imaging of biological samples possible, including strategies for both tissue and single-cell imaging using the following mass spectrometric ionization methods: matrix-assisted laser desorption/ionization, secondary ion, electrospray, and desorption electrospray.

I. Introduction

The intrinsic chemical and structural complexities of biological tissues and cells present significant analytical measurement challenges. Microscopy has long been one of the most powerful techniques to study the distribution of biologically relevant compounds in tissues. Chemical images of analyte distributions in biological specimens have been made possible via affinity labeling with antibodies or other chemical labels/stains in combination with optical microscopy. In fact, these imaging approaches have a several centuries-long history.

More recently, the last century has witnessed the development of the exceptionally effective chemical characterization approach known as mass spectrometry (MS). Using modern MS techniques, a small volume sample can be assayed and information on literally thousands of compounds observed. Can these two approaches—imaging and MS—be successfully combined to achieve even greater information content? As documented throughout this chapter, this combined imaging approach is now being used to examine a wide range of tissues and biological processes.

In general, MS imaging (MSI) techniques include a spatially resolved ionization method to collect mass spectra from an array of positions across a sample. Following data acquisition, the intensities of selected signals from the mass spectra are each plotted to create a pixel array and hence, an ion image or distribution map for the individual signal/compound (Fig. 1). The high level of spatial and chemical information afforded by MSI enables the distribution of many compounds to be imaged in a single experiment without the need for prior knowledge of the identity of the analyte(s) of interest.

At present, research efforts are actively directed toward furthering the development and application of MSI to study a broad range of compounds in tissues. Just as there are a number of optical techniques from which to choose for a particular

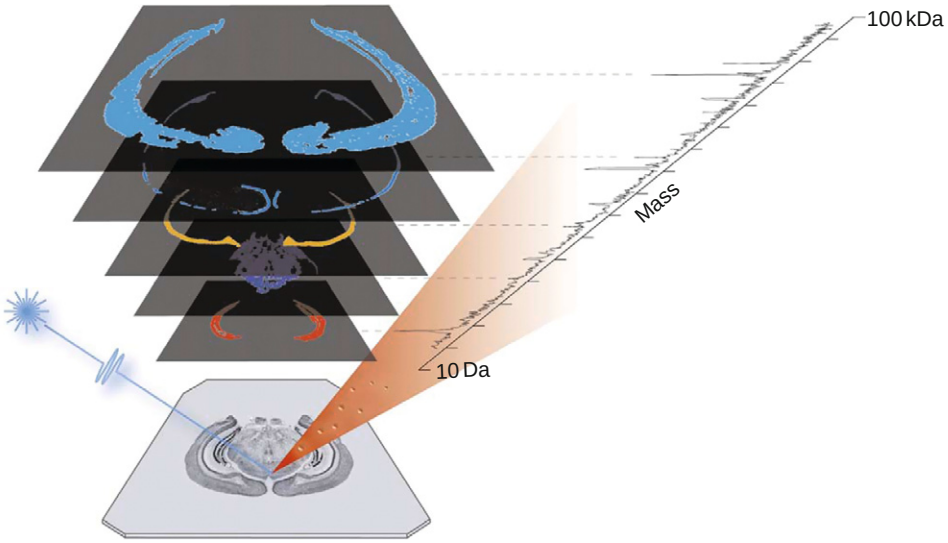

Fig. 1 Overview of mass spectrometry imaging (MSI). A series of complete mass spectra are taken in an ordered array across the sample. The intensity of the signal for selected compounds of interest is then plotted following data acquisition to create a series of ion images. Reprinted with permission from Rohner *et al.* (2005).

application, different MS approaches are available for characterizing the varying types of analytes, with many of these methods adaptable to MSI. For example, secondary ion mass spectrometry (SIMS) imaging is often used to study the distribution of atoms and small molecules in tissues and even single cells at spatial resolutions below a micron. Matrix-assisted laser desorption/ionization (MALDI) MSI has become a popular imaging method for examining small molecules, peptides, and proteins from a variety of tissue sections at a wide range of spatial resolutions and scales, including whole animal preparations (Khatib-Shahidi *et al.*, 2006). Recently, imaging techniques using electrospray ionization (ESI) and desorption electrospray ionization (DESI) have been developed as alternate methods for the direct analysis of tissues at atmospheric pressure (Takats *et al.*, 2004b).

Beyond higher resolution imaging, low-resolution spatial profiling of tissues is also useful for understanding the localization of compounds in a tissue sample, particularly via MALDI MS. In all cases of MSI, the chemical information content is high, but the data are at a lower spatial resolution than what is commonly afforded by optical microscopy. This chapter focuses on experimental strategies aimed at creating visual distribution maps of an analyte across a sample rather than profiling the sample at discrete points.

MSI relies on the desorption and the ionization of biologically relevant compounds from structurally and biochemically heterogeneous samples. Many of the fixation approaches developed for optical and electron microscopy are not

compatible with MSI and so new MS-specific protocols have been designed. As will be discussed in more detail later, care must be taken to ensure that analytes retain their native form and distribution within the samples. Mass spectra are obtained directly from the tissue surface (or in the case of MALDI MS, a thin coat of matrix on the tissue) such that the distribution of analytes resembles their *in vivo* state and the observed result is biologically relevant. The imaging approaches outlined in this chapter largely involve the *in situ* analyses of compounds from biological samples using the high vacuum instrumentation inherent to MS, although progress toward *in vivo* analyses has been made using the DESI scheme (Takats *et al.*, 2004b).

In addition to MS-compatible preparation protocols, an overview of each of the various ionization techniques (MALDI, SIMS, ESI, and DESI) is presented, with further details available elsewhere (Gross and Caprioli, 2007). While it seems obvious that selecting the ideal MS ionization methodology is important, it is the significance of choosing the appropriate sample preparation protocol that is consistently cited as being the key to experimental success. The optimal protocol depends, to some extent, on the nature of the tissue sample (Schwartz *et al.*, 2003). In the following sections, we highlight the instruments and sample preparation processes associated with MSI experiments, and briefly discuss the strategies used to analyze and visualize the large datasets that are associated with these investigations.

II. Instrumentation

Although spatial analysis of biological tissues with MSI employs a vast range of mass spectrometers and associated instrumentation, each mass spectrometer is conceptually similar in that it contains an ionization source, a mass analyzer, and a detector. Here, we describe the available mass spectrometer configurations and provide guidance in selecting the most appropriate setup for a particular MSI experiment.

A. Matrix-Assisted Laser Desorption/Ionization Mass Spectrometry

Laser-desorption MS has been used to profile tissues since the 1970s. However, the largest molecules that could be ionized were typically less than 1000 Da. The refined method of MALDI MS, introduced by Karas and Hillenkamp (1988) and Tanaka (Tanaka *et al.*, 1988) in the latter portion of the 1980s, can ionize higher molecular weight biomolecules, owing to the minimal analyte fragmentation induced during the desorption and ionization processes.

In this methodology, the sample is prepared by mixing it with a matrix. Although most MALDI applications use a solid organic matrix, a variety of liquid and solid matrices have been introduced, including glycerol and derivatives of benzoic and cinnamic acids. During the measurement process, the matrix absorbs

nanoseconds-long ultraviolet (UV) or infrared (IR) laser pulses that resonantly excite the matrix, causing rapid localized heating and subsequent ejection of neutral and charged analyte molecules, atoms, matrix molecules, and analyte–matrix clusters. UV lasers are commonly used in MSI applications (Rohner *et al.*, 2005) although IR lasers have been applied (Li *et al.*, 2007; Luxembourg *et al.*, 2005; Taban *et al.*, 2007). Analyte ionization occurs after laser irradiation or in the expanding plume. Primarily, the result is singly charged ions, either positive $[M+H]^+$ or negative $[M-H]^-$. The sample stage, laser, and mass analyzer are the key components in the MALDI imaging instrument.

1. Sample Stage

In MALDI MSI, images are acquired by moving, or rastering, the sample in a controlled manner under a fixed-position laser beam. The sample movement (on the stage) must be both precise and accurate at small length scales. This is not often an issue as modern translation stages can move in submicron steps with high reproducibility. However, many imaging experiments are performed on MALDI instruments not designed for imaging and so their stage movements may not be as accurate or precise as desired. Often, ion images must be overlaid on an optical image of the sample to assist in matching chemical information to morphological features, which may exacerbate any discrepancies in stage motion. The introduction of an ion microscope, where specialized optics are used to create ion images of the whole sample at once, eliminates the need for sample movement (Luxembourg *et al.*, 2004).

2. Laser

Selecting a laser and its operating parameters is important to the success of a MALDI MSI experiment. The laser beam diameter can limit the maximal spatial resolution of images to the beam spot size. Both UV and IR lasers have been used for imaging with remarkable results. Whereas UV irradiation is certainly more common and provides a smaller beam diameter, IR lasers offer some additional advantages, one of which is the ability to use a different family of matrices that includes water/ice.

The two most common UV lasers for MALDI MSI include the nitrogen (337 nm) and the frequency-tripled Nd:YAG (neodymium-doped yttrium aluminum garnet) lasers (355 nm). Both lasers can be focused to spot sizes considerably below 50 μm. Although the range of 50–100 μm is the common spot size, the use of additional focusing elements can further reduce the size of the probed area (Garrett *et al.*, 2007). To increase the spatial resolution of an imaging experiment, an alternative approach uses only a portion of the beam profile to ionize a sample by oversampling the raster pattern (Jurchen *et al.*, 2005). Briefly, this method involves completely ablating the MALDI matrix coat at each sample position before moving the sample to the next position. If the movement is smaller than the diameter of the laser beam, signals only originate from the portion of the laser

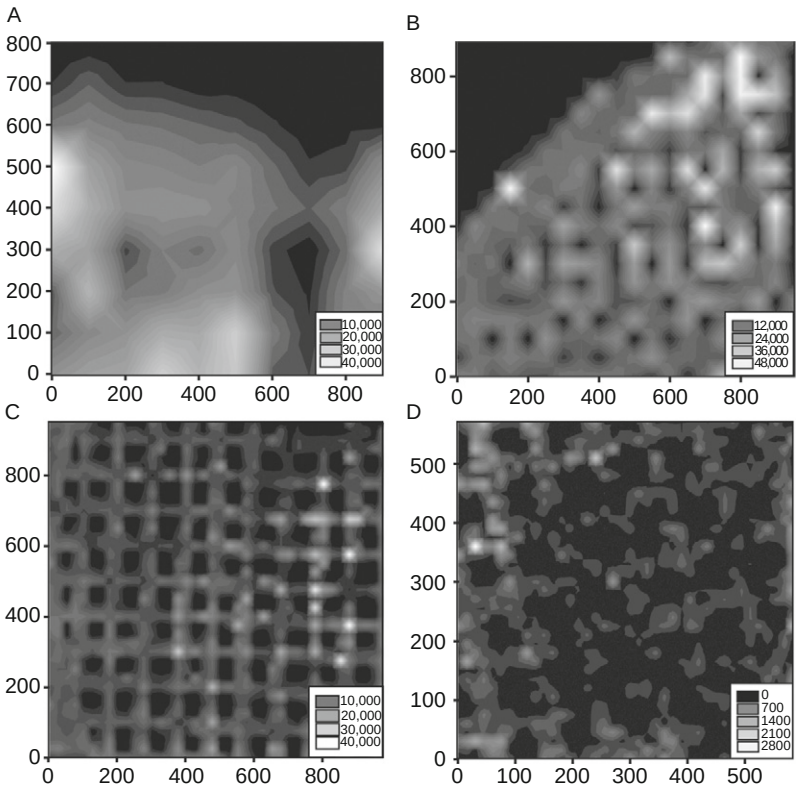

Fig. 2 Matrix-assisted laser desorption/ionization-mass spectrometry images of the peptide angiotensin I (*m/z* 1297) on electron microscopy calibration grids (100 μm hole-to-hole spacing), obtained using an oversampling technique at raster sizes of (A) 100 μm, (B) 50 μm, (C) 25 μm, and (D) 15 μm, illustrate the utility of oversampling to resolve small features in the sample. Reprinted with permission from Jurchen *et al.* (2005).

beam profile that overlaps with the nonablated portion of the sample surface. Using this method, images have been obtained at a spatial resolution of 15 μm with a 100 $\times$ 200 μm laser beam, as shown in Fig. 2 (Jurchen *et al.*, 2005).

Nitrogen lasers have been commonly used for MALDI MSI due, in part, to their relatively low cost and ability in providing high-quality mass spectra. In addition, significant research and development regarding sample preparation strategies have been performed with MS instruments equipped with a nitrogen laser. The low pulse rate (3–20 Hz) of the older N_2 lasers is a significant time constraint when tens to hundreds of thousands of laser shots are necessary to produce an image. Newer nitrogen lasers are able to operate faster, approaching the >200 Hz repetition rates of solid-state lasers. The frequency-tripled Nd:YAG, a diode-pumped solid-state laser, is attractive for high-throughput applications, such as proteomics or imaging, for both its robustness ($>10^9$ shot lifetime) and high repetition rate.

Overall, the Nd:YAG laser's performance has been favorable; however, it produces results inferior to nitrogen lasers in some applications. For instance, with the MALDI matrix sinapinic acid, the results have not been as good as with a comparable nitrogen laser, but similar results are obtained from both lasers when using α-cyano-4-hydroxycinnamic acid (CHCA) as the matrix. Lower laser powers and slightly defocused beams can reduce one negative aspect of the highly efficient Nd:YAG laser—fast sample consumption. Improvements in the performance of solid-state lasers for MALDI to the levels obtained from a nitrogen laser have focused on structuring and modulating the Nd:YAG beam, with great success (Holle *et al*., 2006).

While the use of UV lasers is nearly ubiquitous in MALDI MSI, other lasers have unique benefits and are worthy of consideration. For example, IR lasers such as Er:YAG (erbium-doped yttrium aluminum garnet) (2.94 μm) enable the use of matrices such as native frozen water (Berkenkamp *et al*., 1996) and frozen tissue, as well as glycerol (Leisner *et al*., 2004; Menzel *et al*., 2002), which is often employed as a preservative/stabilization compound during sample dissection and storage (Rubakhin *et al*., 2003). IR-MALDI also produces a low degree of metastable ion fragmentation and an analytical mass range similar to that of UV-MALDI; however, the long wavelength and difficulty in focusing the laser to a small spot size present challenges for higher spatial resolution MSI experiments using traditional scanning microprobe analyses. Fiber optics (Garrett *et al*., 2007), near-field operation (Spengler and Hubert, 2002), and the mass microscope (Luxembourg *et al*., 2004) help to alleviate these challenges and enable tissue imaging without the addition of acidic matrices that alter the physiological conditions of the sample.

3. Mass Analyzer

A large variety of mass analyzers are available for MS. Because of the pulsed nature of laser ionization, its high repetition rate, and the large mass range provided, MALDI MSI requirements well match the analytical figures of merit of time-of-flight (ToF) instruments. MALDI MSI has also been adapted to several other mass analyzers including the ion trap, hybrid quadrupole ToF, and Fourier transform (FT) (Taban *et al*., 2007). As we discuss each mass analyzer, special focus on their application to MSI experiments is included.

In ToF mass measurements, ions are accelerated to a constant kinetic energy and move into a field-free region. The ions separate while traveling along the flight tube because smaller ions have a higher velocity than larger molecules. What limits the resolution obtainable? During formation, ions have a range of kinetic energies causing a spread of flight times. This effect is often reduced and a higher resolution spectrum results when a reflectron is used in the instrument. Briefly, a reflectron, usually located at an end of the flight tube, uses electric fields to reflect ions back to the other end of the flight tube to an ion detector. The interaction of analyte ions with the reflectron's electric fields corrects for small differences in the ions initial kinetic energy such that ions of the same m/z reach the detector at the same time.

Thus, the mass resolution of a reflectron instrument is higher. ToF instruments are commonly used in MSI because of their high sensitivity, mass range, and duty cycle.

The addition of fragmentation capabilities to a ToF instrument not only enhances the confidence of analyte identification but also enables the identification of unknown signals via *de novo* or database-guided sequencing of peptides or proteins. Sequential ToFs (sometimes known as ToF/ToFs), like other tandem methods, are becoming more common. Using fragment signals acquired from a sample in MSI can also assist in distinguishing compounds of similar mass. This is particularly beneficial for the study of small molecules such as drugs and their metabolites in specific tissues (Hsieh *et al.*, 2006) and in the whole animal (Khatib-Shahidi *et al.*, 2006).

Another mass analyzer used with MALDI is the ion trap, which confines ions to a specific region by applying a radio frequency potential to a series of trapping electrodes. To detect the ions, the radio frequency potential is ramped or a supplemental voltage is applied to the endcap electrodes to sequentially eject the ions from the trap. Ion traps are well suited for analyzing small-to-moderate molecular weight molecules with MALDI, but the reduced mass-to-charge ratio (m/z) range prevents the investigation of large, singly charged proteins. In addition, the lower duty cycle of ion traps increases image acquisition time, an important consideration when an image consists of tens of thousands of individual mass spectra. However, unlike ToF instruments, ion traps enable multiple levels of analyte fragmentation (MS^n) to increase the amount of information available when identifying unknowns (Cha and Yeung, 2007; Drexler *et al.*, 2007). Further, ion traps tend to be less expensive than other mass analyzers. These characteristics make them attractive for MSI experiments of compounds with masses below several kilodaltons.

Hybrid ion trap or quadrupole ToF mass spectrometers place a quadrupole mass filter or ion trap between the ion source and the flight tube. In this case, the ion trap is used to filter and store ions before sending them into the ToF portion of the analyzer for mass separation and analysis. These instruments tend to have higher mass accuracy than ToF-only instruments and have the added benefit of MS^n capabilities; multiple fragmentation cycles may occur in the ion trap with the resulting fragments being sent to the ToF for analysis.

The FT mass spectrometer is the highest performance mass analyzer discussed here. FT mass spectrometers separate and detect ions in an ion cyclotron in the presence of a large magnetic field. The motion of the ions in the cyclotron induces a periodic signal from the detection plates. Because this ion motion is a function of the m/z, the frequency of the induced signals may be deconvolved by applying a Fourier transform to produce a mass spectrum. The advantages of this approach include the high mass accuracy and precision obtainable. Why are not most imaging experiments performed using FT MS? FT mass spectrometers require a large superconducting magnet, resulting in higher instrument cost. In addition, the limited mass range for singly charged analytes and the longer spectral acquisition time for ion accumulation/detection are considerations when using FT MS for imaging. Of course, the high mass resolution enables compounds with similar mass to be differentiated and imaged (Taban *et al.*, 2007).

Although the ToF has been the predominant mass analyzer used in MALDI MSI, the adaptation of multiple mass analyzers to imaging has expanded the range of applications amenable to MSI. Commercial MALDI mass spectrometers now commonly have imaging capabilities, and several instruments originally designed for other applications may be fitted with commercial MALDI sources. Each analyzer has specific benefits and shortcomings when applied to imaging applications; thus, instrument selection is based on the needs of the experiment.

Mass analyzers are often used in conjunction with other off-line, nonimaging strategies. For instance, serial sections adjacent to an imaged tissue section can be collected, homogenized, and analyzed with liquid chromatography (LC)–MS to increase the quantity of analyte available for identification via MS/MS studies (Han and Schey, 2006).

B. Secondary Ion Mass Spectrometry

Among all of the ionization techniques used in MSI, SIMS may be the original approach, having been documented as early as 1910, with imaging of tissues reported in the 1960s (Honig, 1985). In SIMS, the impact of a primary ion beam penetrates several nanometers into a sample, thereby causing the ejection, or sputtering, of material that may include atoms, clusters of atoms, and molecular fragments. The penetration depth and amount of ejected matter is determined largely by selection of the specific primary ion source (Szakal *et al.*, 2006), and will be discussed further in this section. Unlike MALDI MS, this ionization mechanism tends to be rather harsh and has, until recently, somewhat limited SIMS imaging to the analysis of atoms and smaller molecular ions. However, recent advances in both sample preparation and instrumentation (notably improved primary ion sources) have greatly expanded the mass range and sensitivity of SIMS measurements.

1. Primary Ion Source

Just as in MALDI MS, the first stage of the experiment is the generation of ions. Because the characteristics of the primary ion beam often determine overall performance, selecting the appropriate source is important. A wide variety of primary ion sources have been developed over the years including Ar^+, Xe^+, O_2^+, Cs^+, In^+, Au^+, Ga^+, He_3^+, SF_6^+, CO_2^+, $C_2F_6^+$, Au_x^+, and Bi_x^+ cluster ions and C_{60}^+ (buckminsterfullerene). Of these sources, Ga^+, Au_x^+, Bi_x^+, and C_{60}^+ are most commonly used for biological studies. Recent developments and the availability of several of these cluster ion sources (e.g., Au_x^+, Bi_x^+, C_{60}^+) have greatly expanded the mass range and sensitivity of SIMS imaging experiments, making the imaging of molecular (e.g., M^+) and pseudomolecular ions (e.g., $[M+H]^+$) from tissues and even isolated cells attractive. Nonetheless, the other ion sources still provide valuable tools to study the distribution of atomics or isotopically labeled compounds.

Besides the identity of the primary ion sources, the size of the beam and the primary ion flux, which are typically interdependent, influence the spatial resolution and duration of an imaging experiment. Unlike the laser pulses used in MALDI MSI, the primary ion beam is readily focused to well below a micrometer in diameter for most sources, and is rastered across the sample rather than moving the sample under an ionizing beam. This both speeds up analyses and reduces the impact of irregularities in sample stage movement, allowing high spatial resolution images to be obtained. Most imaging experiments are performed below the "static limit" such that the primary ion dosage is less than 10^{13} primary ion impacts/cm^2. This limit aims to prevent the gross sputtering of the sample by impacting only ~1% of the sample surface. Beyond the static limit, the surface of the sample begins to erode, which enables depth profiling of the sample. Although depth profiling is useful for hard materials, biological tissue depth profiling has been complicated by several issues including molecular fragmentation (Debois *et al.*, 2007). Even so, several examples have been reported, such as depth profiling of *Xenopus* oocytes with the C_{60} source (Fletcher *et al.*, 2007). As can be expected, approaching the static limit greatly benefits the sensitivity of analyses as it more completely samples the surface.

2. Mass Analyzers

Owing to the high repetition rates typically used for SIMS, only a few mass analyzers are appropriate for these imaging experiments. ToF mass spectrometers are most commonly used for molecular imaging, although dynamic SIMS instruments often include a sector mass analyzer, which employs an electric or magnetic field to filter ions on their flight toward a detector or array of detectors. The deflection magnitude depends on *m/z*, with lighter, faster moving ions being deflected more. If a single detector is used, the electric/magnetic field may be ramped or scanned to sequentially detect analytes. When investigating an individual analyte, the field is kept constant to continuously detect the analyte. Alternatively, in a selective-ion monitoring mode, a series of detectors may be used to monitor several ions at once. Sector mass spectrometers, often used for atomic analyses, have been applied to imaging human hair (Gillen *et al.*, 1999), the distribution of boron neutron capture therapy drugs (Lorey *et al.*, 2001), and human brain sections (Candy *et al.*, 1992).

The ToF instruments applied in SIMS imaging experiments operate on the same principles as discussed previously, with several utilizing a standard ToF arrangement for mass analysis. Alternatively, the TRIFT line of SIMS mass spectrometers from Physical Electronics employs a series of three electrostatic analyzers (ESAs) along the ion flight path to account for kinetic energy differences among the ions. To compensate for the small velocity differences in individual ions, three 90° turns in the ion path function much like the reflectron described earlier by causing ions of different kinetic energy, but with the same nominal *m/z*, to travel slightly longer or shorter paths before reaching the detector (Schueler *et al.*, 1990; Szakal *et al.*, 2006).

ESAs also enable stigmatic imaging experiments. Unlike the microprobe methodology of chemical imaging, the stigmatic imaging capabilities enable TRIFT spectrometers to serve as chemical microscopes. This is accomplished by desorbing ions from a relatively large region of a sample all at once, thus retaining the spatial distribution of the ions during mass separation, before their detection with a position-sensitive detector (Luxembourg *et al.*, 2004). Recently adapted to MALDI MSI, this approach enables an entire sample to be imaged for each laser or ion pulse. Although the summation of multiple laser shots greatly increases the fidelity of images, this method is currently limited to the imaging of a single analyte signal rather than the collection of a complete mass spectrum (Altelaar *et al.*, 2006, 2007; McDonnell *et al.*, 2005).

3. Other Instrumentation Considerations

Recognizing that the mass analyzer and primary ion source are the two most important instrument components, charge-compensating devices and temperature controls also may be beneficial for individual imaging experiments. A low-energy electron flood-gun is often used to reduce sample charging that may occur during the experiment, which can greatly degrade mass resolution and secondary ion yield (Delcorte *et al.*, 2003; Wittig *et al.*, 2005). In addition, several sample preparation strategies have been developed to limit sample charging, and will be discussed later. The ability to control the temperature of the sample surface itself can also be of significant benefit. Cooled sample stages enable the use of frozen-hydrated samples and *in situ* freeze-fractured samples, both of which have shown great value in imaging experiments (Roddy *et al.*, 2002a). The frozen water acts as a matrix to enhance secondary ion yields while freeze-fracturing protocols facilitate imaging of internal structures that may not otherwise be available for study, particularly in single-cell analyses.

C. Desorption Electrospray Ionization and Electrospray Ionization

DESI and ESI ion sources are a relatively recent development for MSI, and are currently undergoing rapid advancement. Both DESI and ESI produce a constant flow of ions for analysis, with the ion trap mass analyzer being most commonly used for these MSI studies.

In DESI, perhaps the newest ionization approach applied to imaging, pneumatically assisted electrosprayed droplets of solvent are directed onto a sample surface that is analyzed at atmospheric conditions. The method requires minimal adaptation to existing mass spectrometers and unlike the previously discussed ionization methods, the DESI source is relatively simple and may be readily constructed in house (Takats *et al.*, 2004b). The basic setup comprises a pneumatically assisted microelectrospray source, a positioning device, and often a sample holder/translation assembly for imaging purposes (Takats *et al.*, 2005). The ion source consists of a stainless steel T-junction that enables a high-pressure sheath gas to exit the source

supersonically and coaxially, along with the electrosprayed solvent, via several fused silica capillaries, delivering both gas and solvent to the sample surface (Takats *et al.*, 2003, 2004a). The sprayer should be mounted on a solid stage that enables its positioning in three dimensions and adjustment of the angle from the ion source to the surface. By placing the sample on its own translation stage, a continuous movement or raster/pixelation strategy may be used for MSI experiments. The various translational aspects facilitate the optimization of sprayer-to-mass spectrometer, sprayer-to-sample, and sample-to-mass spectrometer distances, as well as the angle from the sprayer-to-sample and sample-to-mass spectrometer, while also enabling compensation for surface height or profile variations. Commercialized ion sources (Prosolia, Indianapolis, IN) also use several charge coupled device (CCD) cameras for angle and sample visualization (Takats *et al.*, 2005).

Traditional ESI techniques have not been commonly used as ionization methodologies for MSI experiments, in part due to analyte collection concerns when using a liquid interface in a spatially distinct manner. Two methods have, however, been developed to accomplish these tasks. In one strategy, developed by Smith and coworkers (Petyuk *et al.*, 2007), a brain slice was divided into an ordered array of samples that were individually digested in separate vials and analyzed. Because sample preparation is very important in this methodology, it will be discussed in further detail in the following sample preparation section.

In the other strategy, a sampling probe is used to apply small amounts of a liquid to a sample surface, then the liquid is pulled back through a central channel to an electrospray tip (Ford and Van Berkel, 2004). The probe consists of nested capillaries whereby the eluting solvent is applied through the larger, exterior capillary and then drawn from the tissue surface in a continuous manner via the central capillary. The application of a solvent (such as 1:1 methanol:water) dissolves the analyte from the surface in the area directly under the probe. By scanning the surface in two dimensions via a series of line scans, the probe selectively scans the sample in a manner that enables the creation of ion images (Ford *et al.*, 2005). In practice, the solvent is pushed through a 330-μm inner diameter capillary at 10–15 μL/min with a standard syringe pump and is collected back through a 127-μm inner diameter capillary (254-μm outer diameter). The analytes are then transferred toward an electrospray tip held at a high potential to induce electrospray. The probe is kept 20–50 μm above the sample surface. For imaging experiments, the sample may be moved under the probe at $\sim$100 μm/s to produce $\sim$600 μm spatial resolution ion images (as defined by the sampling width of the probe) (Ford *et al.*, 2005).

III. Sample Preparation for MSI

A. Sample Collection and Isolation

Traditionally, imaging experiments have focused on the analysis of thin tissue sections. In order to preserve tissue morphology as well as native distribution of analytes, tissues must be rapidly dissected following animal sacrifice and

flash-frozen to inhibit enzymatic degradation and analyte redistribution. Immediately following dissection, the tissue is often briefly (30–60 s) submerged in a cryogenic liquid such as liquid nitrogen. Liquid nitrogen slushed–liquid propane is often used for its enhanced thermal conductivity and higher boiling point because it reduces freezing time. Alternatively, dry ice and ethanol may be used to freeze smaller tissues. The goal of these freezing protocols is to prevent enzymatic degradation as well as ice crystal formation. Sample cracking may be prevented by gently submerging the tissue and loosely wrapping it in aluminum foil to prevent it from adhering to the walls of a Dewar. Once frozen, tissues have been stored at −80 °C for more than a year with successful MSI after storage (Schwartz *et al*., 2003).

Once sample preparation is complete, the frozen tissues are then sectioned and transferred to a substrate suitable for MSI experiments. The intact tissue is first affixed to the cryostat stage using either a droplet of water or a small amount of optimal cutting temperature (OCT) embedding media. Tissues should not be embedded in the OCT as its presence on the tissue sections, which can occur during sectioning, has been found to reduce ion formation and the quality of the mass spectra (Schwartz *et al*., 2003). This effect may be eliminated by using only a small amount of OCT to affix the tissue to the stage, taking care to ensure that the OCT does not contact the cut tissue face or microtome blade during sectioning, as in Fig. 3. Note also that often a small film of oil is applied to separate individual microtome blades during packaging and should be removed by rinsing the blade

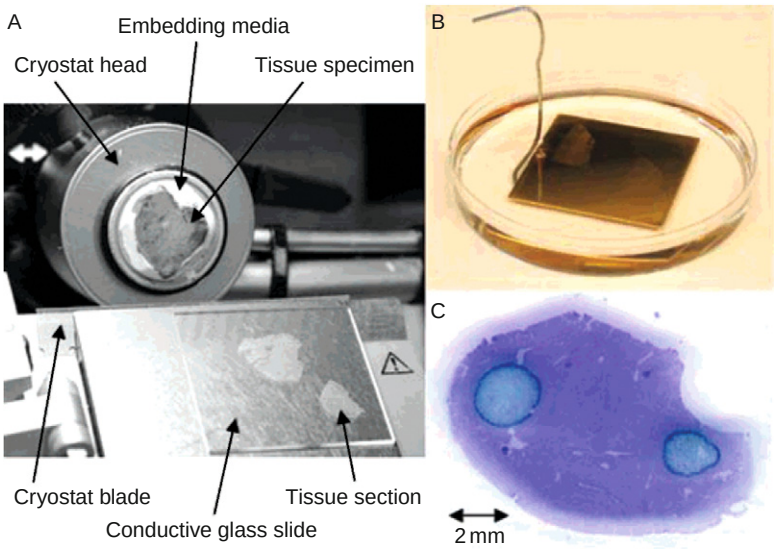

Fig. 3 Tissue processing. (A) Tissue oriented on a cryostat, before sectioning. (B) Sectioned tissues are then rinsed with ethanol and often (C) stained for histology (microphotograph of stained tissue is presented). Reprinted with permission from Chaurand *et al*. (2006).

with acetone or methanol to prevent any chemical contamination (Chaurand *et al.*, 2006). If the tissue must be embedded to facilitate sectioning, a thin layer of water may be used to coat the sample in a thin layer of ice while the tissue is held at cutting temperatures, or embedded in agar to help preserve tissue morphology without degrading the quality of the mass spectra (Borner *et al.*, 2007). The sections, 5–50-μm thick, are collected at -5 °C to -25 °C using a cryomicrotome. The exact temperature is tissue-dependant but typically is within this range of values. Although thicker sections are easier to collect and manipulate, thinner sections have been shown to provide higher quality mass spectra (Lemaire *et al.*, 2006b). During sectioning, tissue orientation should be considered to ensure the section contains the morphological features of interest.

After sectioning, tissues must be transferred to a suitable sample plate for MS analyses, using one of several available methodologies. Commonly, the tissue is transferred to a cold sample plate or conductive indium tin oxide (ITO)-coated glass slide using forceps for thicker sections or an artist's brush for thinner sections. Care should be taken during transfer as a thin tissue slice is easily deformed. The tissue section is then thaw-mounted to the cold sample plate by quickly warming them together. There are a number of ways to accomplish this. The easiest is by placing a finger or hand on the opposite side of the sample plate and using body heat to warm the sample and sample plate together. In another, the sample may be warmed in a desiccator, taking care to prevent condensation when moving from the cryotome to the desiccator. Finally, a sample plate that is at room temperature may be placed directly on a tissue section, which then thaws onto the plate. Although the transfer methods are similar in nature, the cold plate transfer produces superior mass spectra as the transfer is quantitative, whereas the warm plate transfer often leaves a small amount of ice on the cryostat cutting surface, which may retain analyte (Schwartz *et al.*, 2003). In the cold plate method, ice that contains water-soluble compounds is thawed on the sample plate so that these compounds remain with the tissue sample.

Although the majority of imaging experiments are performed using thin tissue sections, the sensitivity and resolution afforded by MSI experiments now enable the profiling and imaging of single, isolated or cultured cells. Isolation of single cells is useful when studying neural tissues, as individual cells often are chemically different from their immediate neighbors. As might be expected, the isolation of single cells from tissues is often nontrivial, but several protocols have been developed to assist with this process, including partial enzymatic digestion to remove connective tissue, glycerol stabilization, and freeze fracturing methodologies for cell cultures.

In the case of larger, more physically stable cells, such as those found in the nervous system of several invertebrate neurobiological models, cells may be isolated after partial enzymatic digestion of the ganglionic sheath in a physiological solution containing 1% protease for 1–2.5 h at 36 °C. Following sheath removal, cells are isolated using sharp needles or via suction from small glass or plastic pipettes and then transferred to a glass slide or other suitable mass

spectrometer target (Rubakhin *et al.*, 2003). Although samples for MALDI MSI may also be fixed in a 4% paraformaldehyde solution, cross-linking of the cellular membrane during the paraformaldehyde fixation may be detrimental to SIMS studies of the lipid membrane.

In contrast to invertebrate cells, the isolation of mammalian neurons is somewhat more involved as the cells are typically smaller than invertebrate neurons. To isolate single pituitary cells from rats, Rubakhin and coworkers (2006) used a physiological solution containing 30% glycerol to improve sample preparation and reduce the time required for isolation. A natural stabilizing agent, glycerol, allows extracellular physiological solution to be removed without lysing the cells or significantly altering the biochemical profile of neurons (Miao *et al.*, 2005). Following glycerol stabilization, cells may be mechanically separated with fine glass pipettes using micromanipulators under an inverted microscope.

In addition to isolating cells directly from tissues, cell culturing may also be of great value in MSI experiments. Glycerol stabilization may be applied to cultures in the same manner as the cell isolates. Cultures may also be flash-frozen and freeze-fractured or analyzed in a frozen-hydrated state (Ostrowski *et al.*, 2004). Although these freezing protocols require the sample to be maintained in a frozen state, frozen samples may also be freeze-dried. Alternatively, 50 mM trehalose may be added to the culture solution before freeze-drying to create a condition similar to a freeze-fracturing protocol, precluding the need for the sample to remain frozen over the course of preparation and analysis (Parry and Winograd, 2005).

B. Preparing the Sample for MSI

Each of the various MSI approaches (MALDI, SIMS, DESI, and ESI) has different ionization methods, and each works best with specific types of analytes. Thus, it should not be surprising that sample preparation methods are also distinct for each. In this section, the more common sample treatments are described for each of these ionization approaches.

1. Matrix-Assisted Laser Desorption/Ionization Mass Spectrometry Imaging

MALDI MS requires that analytes from a tissue be incorporated into a thin matrix layer. The extraction of analytes without fixation/cross-linking in the matrix often is accompanied by analyte migration. Thus, proper matrix application is one of the most important steps in the acquisition of high-quality MALDI MSI from tissue. Of course, heterogeneities in ion yield across the sample can introduce significant experimental artifacts into the produced ion images.

Can we address these concerns by optimizing protocol parameters? Matrix deposition conditions, including matrix composition, concentration, method of application, and thickness of matrix coat, are important factors in developing a matrix application protocol. Choosing the right matrix often depends on the mass range of interest and the laser wavelength. For UV lasers, sinapinic acid

(3,5-dimethoxy-4-hydroxycinnamic acid) performs well with higher mass analytes such as proteins, while CHCA performs well with compounds under ~3 kDa such as peptides. Because of a tendency to form large heterogeneous crystals, 2,5-dihydroxybenzoic acid (DHB) is less commonly used for imaging, with the exception of controlled spotting and crystallization in profiling experiments, which may be considered a low pixel count image (Lemaire *et al.*, 2006a). The selected matrix is often dissolved in 1:1 acetonitrile:water or ethanol:water solutions, which is useful for a variety of thin tissue measurements and analytes of different solubilities (Schwartz *et al.*, 2003). Matrix concentration and amount affects signal quality, crystal coverage, and crystal size. Often higher matrix:solvent ratios lead to larger crystals on the surface of the tissue section (Lemaire *et al.*, 2006a). Sinapinic acid matrix, for instance, has an optimal concentration of ~10–30 mg/mL; signal quality often increases with concentration, with a saturated solution of 30 mg/mL providing better results (Schwartz *et al.*, 2003). The other matrices tend to have an optimal concentration similar to that of the sinapinic acid.

Typically, other than ethanol washing, tissue processing is kept to a minimum. Washing increases the intensity of protein signal from three- to tenfold, depending on the specific sample. In ethanol washing, the target-affixed tissue is submerged in cold 70% high-performance liquid chromatography (HPLC) grade ethanol for 30 s, followed by drying under a nitrogen stream. The precipitation of proteins from the solution increases their signal intensity and decreases the amount of protein delocalization that otherwise occurs while the sample is exposed to a liquid phase, thus preserving spatial resolution (Chaurand *et al.*, 2006). To further increase signal quality, a second washing step in 90% ethanol, 9% glacial acetic acid, and 1% deionized water may also be used to help remove salts and phospholipids (Chaurand *et al.*, 2006). However, the ethanol washing procedure may potentially remove desirable ethanol-soluble compounds from the tissue. Variations in this ethanol rinsing procedure include employing 0.3–1% trifluoroacetic acid (an ion-pairing agent often added to MALDI matrix solutions) to further increase signal (Schwartz *et al.*, 2003), or applying a small amount of MALDI matrix to the ethanol wash to "seed" matrix crystallization on the tissue (Chaurand *et al.*, 2005).

The spatial resolution desired is an important factor in determining the method of matrix application. If relatively low-spatial resolution is acceptable, as when comparing diseased versus normal states, profiling experiments are often sufficient (Caldwell and Caprioli, 2005). In profiling, small discrete matrix droplets are manually deposited onto areas of the tissue, reducing spatial resolution to the size and spacing of the droplets. As a benefit, such matrix droplets often extract more analyte from the tissue and thus result in higher signal intensities compared to traditional imaging protocols. When a higher spatial resolution is required to examine the spatial structure of small morphological features, matrix can be applied in a thin homogenous layer across the tissue to enable imaging.

Several application strategies are used to apply MALDI matrix to tissue sections. A large drop may be dragged across the tissue or the sample may be immersed in an organic solvent solution that has been saturated with the selected

MALDI matrix. However, both of these methods increase the likelihood that some analyte redistribution will occur (Stoeckli *et al.*, 2001). Higher spatial resolution experiments may be achieved by the application of a homogenous layer of matrix or small, evenly distributed matrix droplets onto the tissue. Homogenous matrix application requires the use of a device to create a fine mist of matrix, sprayed in a series of even coats to the tissue. Typically, this consists of a glass spray nebulizer that is typically used to develop thin-layer chromatography (TLC) plates, an artist's airbrush, or a similar home-built sprayer. Applying the matrix in a series of thin coats prevents the matrix layer from becoming too thick (which may result in multiple crystal layers and reduced ion yields) or the tissue section becoming too wet (which may induce analyte redistribution). Roughly, ten passes, lasting 5–10 s each, with a drying period of 1–2 min between coats, limit the analyte migration that can occur when the tissue sample is wet and yield the most intense signals (Chaurand *et al.*, 2006). It is important to allow the tissue to nearly dry between coats but not become completely dry. This requires optimization of the protocol according to the tissue being studied and atmospheric conditions within the lab. Following matrix coating, samples may be coated with a thin layer of metal such as gold to increase ion yield from the tissue sections (Altelaar *et al.*, 2006); however, such treatment is often not necessary. Although samples may be stored at $-80\ ^{\circ}C$ until needed, it is preferable to analyze samples shortly following preparation.

An alternative to spray nebulizers is electrospray deposition, which applies high voltage to a liquid in a glass or metal capillary to create a matrix spray of small droplets (Kruse and Sweedler, 2003). By controlling the spray needle with an X-Y translation stage, this methodology offers a high level of homogeneity (Chaurand *et al.*, 2006).

Recently, an acoustic printer has been used to deposit high-density droplet patterns of matrix in an automated manner. Matrix is placed in a reservoir below the sample and an acoustic pulse ejects a small droplet of matrix onto the sample. The sample is mounted on a two-dimensional translation stage that enables the printing of spot arrays. Uniform droplets, ranging in size from 0.1 pL to 10 μL, may be applied by the acoustic ejection process at a spatial resolution of $\sim$200 μm (Aerni *et al.*, 2006). Unlike the homogenous coating methods where analyte redistribution is a problem, here such migration is limited to the diameter of the printed spot. Acoustic printing has recently been applied to the study of breast cancer (Cornett *et al.*, 2006), toxicity in rat kidney (Meistermann *et al.*, 2006), and pharmacokinetics (Khatib-Shahidi *et al.*, 2006).

Before the application of matrix as outlined above, tissues may be seeded with matrix to allow greater crystal homogeneity across the sample, as shown in Fig. 4. Matrix may be added to the ethanol washes, as mentioned previously, or to a solid matrix, such as sinapinic acid, which may be mechanically ground into a fine powder and then spread across the tissue section. The subsequent application of the dissolved matrix then forms smaller, more homogenous crystals to create a more stable, uniform signal across the entire tissue section. Smaller matrix crystals

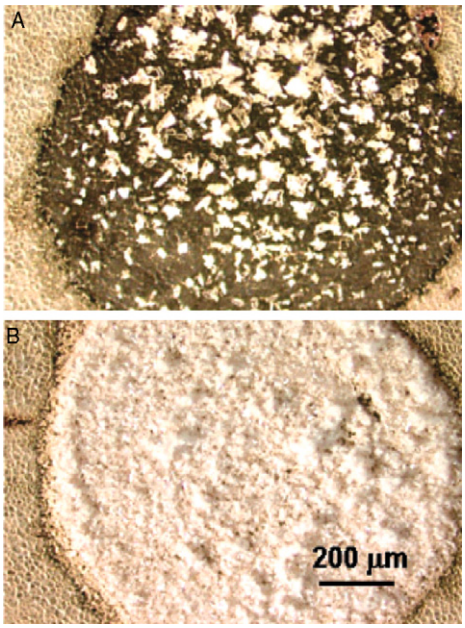

Fig. 4 Matrix-assisted laser desorption/ionization matrix applied to (A) unseeded rat liver tissue and (B) matrix-seeded tissue. Greater crystal homogeneity is observed in tissues that have been previously seeded with ground matrix. Reprinted with permission from Aerni *et al.* (2006).

also reduce the number of laser shots needed at each location, thus reducing the time needed to collect the mass spectra from the sample. Matrix seeding has only recently been applied to MALDI MSI of mouse brain tissue (Clerens *et al.*, 2006).

Another deposition method combines both matrix seeding and high-density microspotting to improve signal intensities for profiling/imaging experiments. In this two-step "spray-droplet" method, a sprayed low-concentration matrix seed layer is followed by microdroplet application via inkjet printing of a higher-concentration matrix solution (Sugiura *et al.*, 2006).

The previously outlined techniques have focused on analyzing intact, complete tissue sections. The Sweedler group (Monroe *et al.*, 2006) has developed a method, the "stretched sample" approach, to study tissue sections at approximately single-cell spatial resolution that allows maximal matrix-analyte incorporation while inhibiting analyte redistribution. Briefly, a substrate is prepared by affixing a monolayer of glass beads (~38-μm diameter from MoSci Corp., Rolla, MO) to a Parafilm M membrane using pressure and heat. A tissue section is then placed on the substrate and adheres strongly to the glass beads. The substrate is manually stretched to fragment the tissue as the beads separate. Fragmentation occurs because the mechanical stability of the tissue section is less than that of both the tissue-bead and bead-Parafilm M adhesion. As the substrate may be stretched to 4 times its original size, individual beads are separated by ~100 μm from one

another by the hydrophobic Parafilm M membrane, which inhibits analyte migration during matrix application. Additionally, water may be condensed onto the sample in small droplets to increase the time of analyte incorporation without fear of redistribution as long as the droplets do not form connections between adjacent beads. This slow extraction/crystal formation methodology has also been found to reduce the presence of alkali metal adducts by inducing mutually exclusive crystallization of the MALDI matrix and the salts from the tissue (Monroe *et al*., 2007).

2. SIMS Imaging

As mentioned previously, owing to a combination of decreased analyte redistribution and a smaller probe dimension, SIMS imaging provides higher spatial resolutions than MALDI MSI. This spatial resolution is routinely at the single micron to 100-nm range. Because SIMS uses primary ion impacts to desorb and ionize analytes from a sample, large molecules are ionized less effectively than in MALDI MS, in large part due to an increased level of fragmentation during the desorption/ionization process (McDonnell *et al*., 2005). This increased fragmentation has traditionally limited SIMS to the analysis of atomics and relatively small molecules. Nonetheless, developments in sample preparation techniques, including cryogenic treatment of tissue, surface metallization, and matrix enhancement, as well as the ''softer'' primary ion sources discussed previously, make the imaging of ever-larger biomolecules in tissues feasible. Sample preparation remains the principal challenge, particularly at high-spatial resolutions. Differences in ionization efficiency caused by variations in the chemical and topological properties across a sample surface can complicate analyses and sample preparation strategies (Delcorte, 2006). SIMS is a surface-sensitive ionization process, thus it is inherently attuned to the interaction of the ion beam with the surface. Fortunately, these surface effects can be largely controlled and/or overcome by choosing the appropriate sample preparation and data processing protocols.

Following isolation, samples for SIMS are often subject to cryogenic treatments such as flash freezing or freeze fracturing. Flash freezing fixes the sample by rapidly cooling it at a rate of ~5000 K/s in a coolant such as Freon 22 or liquid nitrogen-slushed propane (Chandra and Morrison, 1992). The rapid cooling rate quenches the movement of even atomic ions, such as sodium and potassium within a sample, which is indicative of the high level of preservation necessary for imaging at submicron spatial scales. Frozen samples may be transferred into the SIMS instrument using a cold transfer stage in a hydrated state (Roddy *et al*., 2002a) or freeze-dried to preserve the sample, keeping in mind that the drying process may allow some analyte redistribution to occur. The alternative cryogenic treatment, freeze-fracture, was originally developed for electron microscopy, and is used to access subcellular features within a sample (Roddy *et al*., 2002b). Often the sample is placed between two silicon shards before flash freezing. While under liquid nitrogen, the two pieces of silicon are then separated to fracture the frozen sample. This fracturing is beneficial for the study of single cells and may expose several different

regions of the cell; for example, the outer membrane surface or the intracellular components, which may be identified on the basis of the spatial and chemical patterns that arise from the SIMS analyses (Roddy *et al.*, 2002b). This fracturing enables the interior of isolated cells to be examined that would not otherwise be available due to the surface-profiling nature of static SIMS. To limit analyte migration, the freeze-fractured cells are freeze-dried at −90 °C or analyzed in a frozen-hydrated state in which the water ice helps to reduce analyte fragmentation (Roddy *et al.*, 2003). Phosphocholine was recently imaged in freeze-fractured cells from rat kidney tissue (Nygren *et al.*, 2005). An analogous fracture method was developed for SIMS imaging by using 50 mM trehalose at room temperature, instead of freezing, to stabilize cell cultures (Parry and Winograd, 2005).

In SIMS, when charged particles impact the sample surface, notable surface charging and analyte fragmentation can occur. One of the most promising means by which to address these issues is to apply a thin layer of metal to the sample surface. Sample metallization may be performed in either of two manners. In the imprint-imaging method, the sample is prepared and then pressed onto a silver surface, resulting in the transfer of a thin layer of sample to the metal; the metallized sample is then imaged. This technique has been shown to reduce the fragmentation of moderate-weight analytes and sub-kDa peptides and has been used to image phosphatidylcholine and cholesterol in human blood cells (Nygren *et al.*, 2003; Sjovall *et al.*, 2003). Higher secondary ion yields are obtained from the silver surface compared to the direct analysis of tissue, and this method may be applied easily to both tissue and isolated cells.

An alternative metallization technique completely covers the sample surface with a 1–5-nm thick layer of metal such as gold or silver applied with a conventional sputter coater. This methodology is consistent with strategies used for scanning electron microscopy preparations. The metal coating not only prevents charging but is also believed to help ''soften'' the initial impact of the primary ions by forming a protective shell over the sample surface. Surface metallization both increases sensitivity and greatly expands the mass range available for analyses (to ~5 kDa) while keeping the sample surface intact rather than transferring it to another surface. After using this silver coating technique, the cholesterol signal was found to be up to 600 times higher in rat kidney (Nygren *et al.*, 2004). Gold metallization has been used for ToF-SIMS imaging of cholesterol and other cell membrane components in rat brain (Altelaar *et al.*, 2006). Direct surface metallization has also been applied to detect large synthetic polymers such as polyalanine (Delcorte *et al.*, 2003), but not as yet to *in situ* large biomolecules. Although the sample is coated in this preparative strategy, analytes are not incorporated into the metal layer but rather are maintained in their native locations under the thin metallic coating.

Organic MALDI matrices are also being used for the analysis of tissues in SIMS. In matrix enhanced-SIMS (ME-SIMS), small-molecule organic matrices (typically traditional MALDI matrices such as CHCA) are used to coat tissues in a similar manner to those methods outlined for MALDI MSI. These approaches result in

the incorporation of analyte into the matrix layer. ME-SIMS has shown promise for extending the mass range to the level required for proteomics experiments, particularly when linked with surface metallization strategies (Delcorte *et al.*, 2003). In addition to improving the upper end of the mass range for SIMS, matrix enhancement also reduces the fragmentation of lower mass analytes, thus increasing sensitivity across the mass range (Delcorte, 2006). Although SIMS images can be collected at submicrometer spatial resolutions, matrix crystal size often limits the experimental spatial resolution to ~2–3 μm. Proteins as large as lysozyme, at 14 kDa (Wu and Odom, 1996), have been detected using the ME-SIMS approach, but thus far, compounds this large have not been directly detected from biological tissues. However, ME-SIMS has been used to create ion images of small peptides from a section of the cerebral ganglion of the pond snail, *Lymnaea stagnalis*, at 2.5 μm spatial resolution (McDonnell *et al.*, 2005).

3. Desorption Electrospray Ionization and Electrospray Ionization

Although used less frequently, DESI and ESI imaging methods have some advantages in that they require less sample preparation and do not have the vacuum requirements of SIMS and most MALDI MS instruments. Specifically, DESI relies on a supersonic electrosprayed solvent mixture to desorb analytes directly from a surface (Takats *et al.*, 2004b). Although the precise mechanism of this desorption is still under investigation, as little or no sample preparation is required, the desorption properties of DESI are rather well suited for the 2D imaging of biological samples. DESI MSI has been successfully used in detection, directly from the skin, of the antihistamine drug, loratadine, *in vivo* (Takats *et al.*, 2004b). Furthermore, DESI has shown promise for its ability to ionize small and nonpolar molecules (Van Berkel *et al.*, 2005), and provide images of tissue sections from rat brain for lipid analysis (Wiseman *et al.*, 2006), as well as images of the distribution of other small molecules. While the spatial resolution of such experiments is still low (~400 μm), DESI is useful in defining gross morphological features, as shown in Fig. 5 (Ifa *et al.*, 2007).

Efforts to apply traditional ESI to imaging are complicated by the fact that this method was not designed as a surface analysis technique. Several methodologies have, however, been developed that incorporate this approach. Smith and coworkers (Petyuk *et al.*, 2007) have developed a technique whereby a thick (1 mm) tissue section is dissected into 1 mm^3 cubes and individually digested and analyzed with LC coupled to FT MS. In this example, over 250 different protein distributions were imaged in a mouse brain by mapping the normalized intensity of a peptide resulting from the tryptic digest of the parent protein. Although the presented images were of low-spatial resolution (1 mm), improved sample handling procedures and increased throughput of sample analyses may increase both the resolution and speed of these experiments.

An alternative ESI methodology utilizes a surface probe to remove analyte from a sample with a suitable solvent and then delivers the eluent to the mass

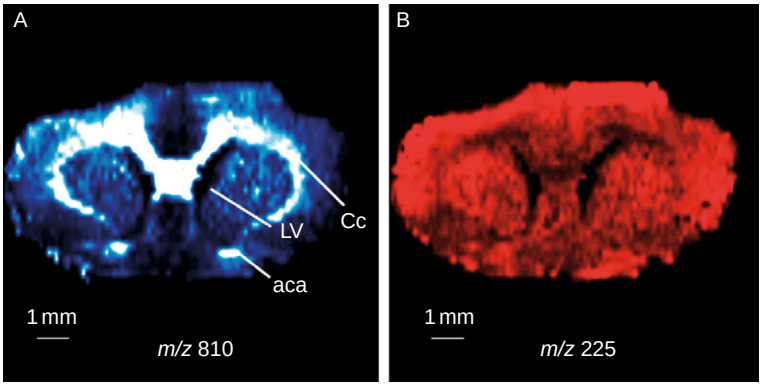

Fig. 5 Negative ion desorption electrospray ionization mass spectrometry images of (A) *m/z* 810 and (B) *m/z* 255 from a 4 μm coronal section of rat brain tissue illustrate the utility of the method to resolve morphological features in tissues. LV, lateral ventricle; Cc, corpus callosum; aca, anterior commissure anterior part. Reprinted with permission from Ifa *et al.* (2007).

spectrometer. This method has not yet been applied to the imaging of biological materials but is similar to online dialysates or push–pull perfusion probes. Furthermore, it would most likely require some desalting because the ESI process can be sensitive to the presence of high salt concentrations. Nonetheless, the spatial distribution of a dye mixture has been successfully examined from the surface of a thin-layer chromatography plate using the probe-ESI methodology (Ford and Van Berkel, 2004; Ford *et al.*, 2005).

IV. Image Acquisition and Data Analysis

Mass spectral images often contain 10^4 pixels and have been as large as 10^7 pixels (Amaya *et al.*, 2007), depending on the size of the sample and the spatial resolution. Since a mass spectrum is taken at each pixel location, dataset sizes can rapidly approach and even exceed several gigabytes. This presents challenges in both data acquisition and analysis. Software that interacts with the instrument to make acquisition of these large datasets more efficient is readily available for most MALDI mass spectrometers in either commercial (from instrument manufacturers) or freely available forms (www.maldi-msi.org). Although the specifics vary with each instrument, in general these programs create a list of positions on the sample target and gather mass spectra in an automated manner. Once collected, the mass spectra are processed into a form that is more easily analyzed. The freely available tools produce an Analyze 7.5 dataset that may be read by several software packages, such as BioMap or Matlab, to produce images (Clerens *et al.*, 2006; Stoeckli *et al.*, 2002). In general, commercially available software is tailored to the specific instrument and/or integrated into the instrument control and data analysis programs and results largely in proprietary formats. Unlike MALDI MS,

imaging is nearly inherent to static SIMS instruments as rastering of the primary ion beam is required to prevent the rapid ablation of the sample surface. Therefore, imaging is typically integrated directly into the instrument control and data analysis software.

The large number of mass spectra and surface variations across a sample may introduce some level of systematic error into an experiment but can often be compensated for in postprocessing. For example, an uneven sample surface topology may introduce mass errors or shifts in ToF-MS instruments, as the mass measurement depends on the flight distance and extraction efficiency. By measuring the shift in (the time of flight) of a particular *m/z* signal across the surface, a height map can be generated and used to correct the acquired mass spectra (McDonnell *et al*., 2005). Other widely used methods to correct for systematic errors include baseline subtraction, noise estimation, normalization, and spectral realignment (Chaurand *et al*., 2004, 2006). Localized charging may also introduce similar errors. However, this variation in ionization efficiency may be addressed by normalizing the ion image for a selected compound with the image of a ubiquitous compound (Monroe *et al*., 2005; Ostrowski *et al*., 2004).

Collecting a complete mass spectrum for each pixel in a high-density raster over a sample generates up to several gigabytes of raw data, and particularly in the case of MALDI MSI, consumes a fair amount of time (several hours). This process can result in a significant number of laser shots and extensive instrument usage. If the mass range of the compounds and specific tissue region of interest is known, the dataset may be vastly simplified. Often it is impractical to perform many MALDI MSI experiments and it is more advantageous to use profiling or low-density raster patterns before final, high-density imaging of a sample for optimization and reproducibility experiments. For example, serial sections of a tissue sample may be taken so that each has approximately the same chemical profile as one another. This enables parallel profiling and imaging experiments to be performed so that the profiling results may assist in driving the specifications of the imaging experiment.

Often experiments are designed to examine different physiological states to identify changes in protein expression patterns that may be correlated with a disease state or stimulus (pharmacological, conditioning, etc.). Comparisons between tissues of a different nature or physiological role are also of great interest. Uncovering such correlations from the entire raw dataset requires the use of statistical methods. Clustering methods, such as principal components analysis (PCA) combined with linear discriminants, have been used to identify pixels and spatial regions that are spectrally correlated in the MALDI MSI (McCombie *et al*., 2005) and SIMS data (Tyler *et al*., 2007). The analysis of mass spectra from 28 bacterial strains followed by PCA enabled the differentiation of gram-positive from gram-negative bacteria and, in some cases, individual species (Ingram *et al*., 2003). The analysis of cancer biopsies also resulted in the differentiation of the various stages of cancer, predicting patient mortality with an accuracy similar to traditional histological approaches (Chaurand *et al*., 2005; Cornett *et al*., 2006).

V. Specialized Methods

A. Combining MSI with Histological Staining

Histological staining may be used to associate mass spectral data to morphological structures in a tissue. This enables comparison of multiple tissue sections to each other, or to a tissue atlas. Combining optical microscopic and mass spectral images requires careful selection of stains. While cresyl violet and methylene blue have shown to be compatible with MALDI MSI experiments (Chaurand *et al.*, 2004), conventional hematoxylin and eosin dyes suppress mass spectral signals. Typically, following sectioning, the tissue is placed onto a conductive glass slide so that it may be examined by optical microscopy. Suitable slides should be optically transparent and conductive to prevent charging such as slides coated with indium-tin oxide. Several hundred microliters of a staining solution are then pipetted onto the tissue section. Any excess stain can be removed by submerging the tissue in ethanol, which as mentioned previously, also serves to fix proteins (Chaurand *et al.*, 2004). Combining MALDI MSI with histological examination has aided in the identification of several novel biomarkers in human brain tumors (Johnson *et al.*, 2006) and breast cancer samples (Chaurand *et al.*, 2006).

B. Three-Dimensional MSI

The ability to combine three-dimensional analyses with other imaging techniques such as magnetic resonance imaging (MRI) enables the highest information content available to be gleaned from a sample. In 3D MSI, serial sectioning is followed by the acquisition of 2D images of each section; then the individual sections are combined to create the 3D image. One issue when combining 3D imaging with MSI is the registration of adjacent serial tissue sections while creating the third dimension based on 2D morphologies. One way to address this issue is with histological staining, which assists in identifying landmark features in the tissue to aid in registration between sections. In addition, before sectioning, registration marks may be added to aid in image reconstruction. The efficacy of 3D image reconstruction has been demonstrated using a series of 20-μm thick sections from a mouse brain (Crecelius *et al.*, 2005). Three-dimensional images allow the study of detailed proteomic or pharmacodynamic information by enabling the chemical reconstruction of entire organs in a structural visualization scheme.

C. Tandem MSI

Although many analytes may be putatively identified on the basis of accurate mass match to a known compound, fragmentation data assist in the identification of novel signals or the verification of a signal's identity. In addition, imaging the distribution of a fragment ion across a sample separates signals from different

compounds with the same nominal molecular mass. Tandem MSI (MS/MS) has been used for the concurrent imaging and *de novo* sequencing of several insect neuropeptides (Verhaert *et al*., 2007). Imaging of the distribution of small organic molecules can be achieved by plotting the intensity of a selected fragment ion from a parent compound of interest. Khatib-Shahidi and coworkers (Khatib-Shahidi *et al*., 2006) have used the MS/MS transition from the parent to fragment ion to image the distribution of a drug and its metabolites in a complete sagittal section of a mouse following oral drug dosing. Similarly, a pharmaceutical study has mapped the location of an active drug in multiple types of rat tissues using tandem MSI (Drexler *et al*., 2007). Intermediate pressures (0.17 torr) with MALDI MS, along with an intermediate-pressure linear ion trap, reduce fragmentation of labile analytes, such as lipids, while also allowing tandem MSI experiments to resolve species of similar mass (Garrett *et al*., 2007). Tandem MSI has also been used to image the distribution of cerebroside lipids in nerve tissues (Cha and Yeung, 2007).

VI. Summary and Future Directions

The ability to map the distribution of a wide range of compounds directly from tissues and isolated cells will greatly aid researchers in many fields. A significant advantage of MS-based approaches is that analyte preselection or labeling is not typically required and little, if any, prior knowledge of the imaged compounds is needed. An additional benefit is that compounds may be directly sampled from a tissue (or following minimal preparation such as matrix coating) to enable the visualization of the native distribution of a wide range of both known and unknown compounds in a single experiment. Because of the reduced sample preparation steps, the amount of analyte required for characterization is often less than for separation/MS (e.g., LC–MS) approaches. Although the field of MSI is rapidly developing, sample preparation protocols still require optimization as most have not been fully standardized or validated. In fact, as discussed throughout this chapter, sampling protocols must be tailored not only to the various methodologies but also according to the type of tissue being analyzed.

The design of a successful MSI experiment requires consideration of several factors, including the mass range, spatial resolution, and sensitivity desired or required. Through careful selection of the right methodology and sample preparation strategy, high-quality mass spectra can be obtained at thousands of positions across a sample at a broad range of spatial resolutions, from submicron to hundreds of microns. As a result, tens to hundreds of compounds can be imaged in a single experiment. MS-based imaging has shown real promise in addressing several biological questions, but the full potential of the approach is just beginning to be realized. The recent and rapid application of MSI to drug development, disease prognosis, and fundamental biochemistry suggests that MSI will enable significant biological breakthroughs in the future.

Acknowledgments

The authors gratefully acknowledge the support of the National Institute on Drug Abuse under Award No. P30DA018310 to the UIUC Center on Neuroproteomics on Cell to Cell Signaling and Award No. PHS 5 R01DA17940. E.M. is also pleased to acknowledge fellowship support from Merck Research Laboratories and the ACS Division of Analytical Chemistry Graduate Fellowship sponsored by Proctor & Gamble.

References

Aerni, H. R., Cornett, D. S., and Caprioli, R. M. (2006). Automated acoustic matrix deposition for MALDI sample preparation. *Anal. Chem.* **78,** 827–834.

Altelaar, A. F., Klinkert, I., Jalink, K., de Lange, R. P., Adan, R. A., Heeren, R. M., and Piersma, S. R. (2006). Gold-enhanced biomolecular surface imaging of cells and tissue by SIMS and MALDI mass spectrometry. *Anal. Chem.* **78,** 734–742.

Altelaar, A. F. M., Taban, I. M., McDonnell, L. A., Verhaert, P. D. E. M., de Lange, R. P. J., Adan, R. A. H., Mooi, W. J., Heeren, R. M. A., and Piersma, S. R. (2007). High-resolution MALDI imaging mass spectrometry allows localization of peptide distributions at cellular length scales in pituitary tissue sections. *Int. J. Mass Spectrom.* **260,** 203–211.

Amaya, K. R., Monroe, E. B., Sweedler, J. V., and Clayton, D. F. (2007). Lipid imaging in the zebra finch brain with secondary ion mass spectrometry. *Int. J. Mass Spectrom.* **260,** 121–127.

Berkenkamp, S., Karas, M., and Hillenkamp, F. (1996). Ice as a matrix for IR-matrix-assisted laser desorption/ionization: Mass spectra from a protein single crystal. *Proc. Natl. Acad. Sci. USA* **93,** 7003–7007.

Borner, K., Malmberg, P., Mansson, J.-E., and Nygren, H. (2007). Molecular imaging of lipids in cells and tissues. *Int. J. Mass Spectrom.* **260,** 128–136.

Caldwell, R. L., and Caprioli, R. M. (2005). Tissue profiling by mass spectrometry: A review of methodology and applications. *Mol. Cell. Proteomics* **4,** 394–401.

Candy, J. M., Oakley, A. E., Mountfort, S. A., Taylor, G. A., Morris, C. M., Bishop, H. E., and Edwardson, J. A. (1992). The imaging and quantification of aluminium in the human brain using dynamic secondary ion mass spectrometry (SIMS). *Biol. Cell* **74,** 109–118.

Cha, S., and Yeung, E. S. (2007). Colloidal graphite-assisted laser desorption/ionization mass spectrometry and MS^n of small molecules. 1. Imaging of cerebrosides directly from rat brain tissue. *Anal. Chem.* **79,** 2373–2385.

Chandra, S., and Morrison, G. H. (1992). Sample preparation of animal tissues and cell cultures for secondary ion mass spectrometry (SIMS) microscopy. *Biol. Cell* **74,** 31–42.

Chaurand, P., Schwartz, S. A., Billheimer, D., Xu, B. J., Crecelius, A., and Caprioli, R. M. (2004). Integrating histology and imaging mass spectrometry. *Anal. Chem.* **76,** 1145–1155.

Chaurand, P., Schwartz, S. A., Reyzer, M. L., and Caprioli, R. M. (2005). Imaging mass spectrometry: Principles and potentials. *Toxicol. Pathol.* **33,** 92–101.

Chaurand, P., Norris, J. L., Cornett, D. S., Mobley, J. A., and Caprioli, R. M. (2006). New developments in profiling and imaging of proteins from tissue sections by MALDI mass spectrometry. *J. Proteome Res.* **5,** 2889–2900.

Clerens, S., Ceuppens, R., and Arckens, L. (2006). Createtarget and analyze this!: New software assisting imaging mass spectrometry on Bruker Reflex IV and Ultraflex II instruments. *Rapid Commun. Mass Spectrom.* **20,** 3061–3066.

Cornett, D. S., Mobley, J. A., Dias, E. C., Andersson, M., Arteaga, C. L., Sanders, M. E., and Caprioli, R. M. (2006). A novel histology-directed strategy for MALDI-MS tissue profiling that improves throughput and cellular specificity in human breast cancer. *Mol. Cell. Proteomics* **5,** 1975–1983.

Crecelius, A. C., Cornett, D. S., Caprioli, R. M., Williams, B., Dawant, B. M., and Bodenheimer, B. (2005). Three-dimensional visualization of protein expression in mouse brain structures using imaging mass spectrometry. *J. Am. Soc. Mass Spectrom.* **16,** 1093–1099.

Debois, D., Brunelle, A., and Laprevote, O. (2007). Attempts for molecular depth profiling directly on a rat brain tissue section using fullerene and bismuth cluster ion beams. *Int. J. Mass Spectrom.* **260,** 115–120.

Delcorte, A. (2006). Matrix-enhanced secondary ion mass spectrometry: The alchemist's solution? *Appl. Surf. Sci.* **252,** 6582–6587.

Delcorte, A., Bour, J., Aubriet, F., Muller, J. F., and Bertrand, P. (2003). Sample metallization for performance improvement in desorption/ionization of kilodalton molecules: Quantitative evaluation, imaging secondary ion MS, and laser ablation. *Anal. Chem.* **75,** 6875–6885.

Drexler, D. M., Garrett, T. J., Cantone, J. L., Diters, R. W., Mitroka, J. G., Prieto Conaway, M. C., Adams, S. P., Yost, R. A., and Sanders, M. (2007). Utility of imaging mass spectrometry (IMS) by matrix-assisted laser desorption ionization (MALDI) on an ion trap mass spectrometer in the analysis of drugs and metabolites in biological tissues. *J. Pharmacol. Toxicol. Methods* **55,** 279–288.

Fletcher, J. S., Lockyer, N. P., Vaidyanathan, S., and Vickerman, J. C. (2007). TOF-SIMS 3D biomolecular imaging of *Xenopus laevis* oocytes using buckminsterfullerene (C60) primary ions. *Anal. Chem.* **79,** 2199–2206.

Ford, M. J., and Van Berkel, G. J. (2004). An improved thin-layer chromatography/mass spectrometry coupling using a surface sampling probe electrospray ion trap system. *Rapid Commun. Mass Spectrom.* **18,** 1303–1309.

Ford, M. J., Kertesz, V., and Van Berkel, G. J. (2005). Thin-layer chromatography/electrospray ionization triple-quadrupole linear ion trap mass spectrometry system: Analysis of rhodamine dyes separated on reversed-phase C8 plates. *J. Mass Spectrom.* **40,** 866–875.

Garrett, T. J., Prieto-Conaway, M. C., Kovtoun, V., Bui, H., Izgarian, N., Stafford, G., and Yost, R. A. (2007). Imaging of small molecules in tissue sections with a new intermediate-pressure MALDI linear ion trap mass spectrometer. *Int. J. Mass Spectrom.* **260,** 166–176.

Gillen, G., Roberson, S., Ng, C., and Stranick, M. (1999). Elemental and molecular imaging of human hair using secondary ion mass spectrometry. *Scanning* **21,** 173–181.

Gross, M. L., and Caprioli, R. M. (eds.) (2007). "The Encyclopedia of Mass Spectrometry: Ionization Methods." Elsevier, Oxford; San Diego.

Han, J., and Schey, K. L. (2006). MALDI tissue imaging of ocular lens alpha-crystallin. *Invest. Ophthalmol. Vis. Sci.* **47,** 2990–2996.

Holle, A., Haase, A., Kayser, M., and Hohndorf, J. (2006). Optimizing UV laser focus profiles for improved MALDI performance. *J. Mass Spectrom.* **41,** 705–716.

Honig, R. E. (1985). The development of secondary ion mass spectrometry (SIMS): A retrospective. *Int. J. Mass Spectrom.* **66,** 31–54.

Hsieh, Y., Casale, R., Fukuda, E., Chen, J., Knemeyer, I., Wingate, J., Morrison, R., and Korfmacher, W. (2006). Matrix-assisted laser desorption/ionization imaging mass spectrometry for direct measurement of clozapine in rat brain tissue. *Rapid Commun. Mass Spectrom.* **20,** 965–972.

Ifa, D. R., Wiseman, J. M., Song, Q., and Cooks, R. G. (2007). Development of capabilities for imaging mass spectrometry under ambient conditions with desorption electrospray ionization (DESI). *Int. J. Mass Spectrom.* **259,** 8–15.

Ingram, J. C., Bauer, W. F., Lehman, R. M., O'Connell, S. P., and Shaw, A. D. (2003). Detection of fatty acids from intact microorganisms by molecular beam static secondary ion mass spectrometry. *J. Microbiol. Methods* **53,** 295–307.

Johnson, M. D., Floyd, J. L., and Caprioli, R. M. (2006). Proteomics in diagnostic neuropathology. *J. Neuropathol. Exp. Neurol.* **65,** 837–845.

Jurchen, J. C., Rubakhin, S. S., and Sweedler, J. V. (2005). MALDI-MS imaging of features smaller than the size of the laser beam. *J. Am. Soc. Mass Spectrom.* **16,** 1654–1659.

Karas, M., and Hillenkamp, F. (1988). Laser desorption ionization of proteins with molecular masses exceeding 10,000 daltons. *Anal. Chem.* **60,** 2299–2301.

Khatib-Shahidi, S., Andersson, M., Herman, J. L., Gillespie, T. A., and Caprioli, R. M. (2006). Direct molecular analysis of whole-body animal tissue sections by imaging MALDI mass spectrometry. *Anal. Chem.* **78,** 6448–6456.

Kruse, R., and Sweedler, J. V. (2003). Spatial profiling invertebrate ganglia using MALDI MS. *J. Am. Soc. Mass Spectrom.* **14,** 752–759.

Leisner, A., Rohlfing, A., Berkenkamp, S., Hillenkamp, F., and Dreisewerd, K. (2004). Infrared laser post-ionization of large biomolecules from an IR-MALD(I) plume. *J. Am. Soc. Mass Spectrom.* **15,** 934–941.

Lemaire, R., Tabet, J. C., Ducoroy, P., Hendra, J. B., Salzet, M., and Fournier, I. (2006a). Solid ionic matrixes for direct tissue analysis and MALDI imaging. *Anal. Chem.* **78,** 809–819.

Lemaire, R., Wisztorski, M., Desmons, A., Tabet, J. C., Day, R., Salzet, M., and Fournier, I. (2006b). MALDI-MS direct tissue analysis of proteins: Improving signal sensitivity using organic treatments. *Anal. Chem.* **78,** 7145–7153.

Li, Y., Shrestha, B., and Vertes, A. (2007). Atmospheric pressure molecular imaging by infrared MALDI mass spectrometry. *Anal. Chem.* **79,** 523–532.

Lorey, D. R., 2nd, Morrison, G. H., and Chandra, S. (2001). Dynamic secondary ion mass spectrometry analysis of boron from boron neutron capture therapy drugs in co-cultures: Single-cell imaging of two different cell types within the same ion microscopy field of imaging. *Anal. Chem.* **73,** 3947–3953.

Luxembourg, S. L., Mize, T. H., McDonnell, L. A., and Heeren, R. M. (2004). High-spatial resolution mass spectrometric imaging of peptide and protein distributions on a surface. *Anal. Chem.* **76,** 5339–5344.

Luxembourg, S. L., McDonnell, L. A., Mize, T. H., and Heeren, R. M. (2005). Infrared mass spectrometric imaging below the diffraction limit. *J. Proteome Res.* **4,** 671–673.

McCombie, G., Staab, D., Stoeckli, M., and Knochenmuss, R. (2005). Spatial and spectral correlations in MALDI mass spectrometry images by clustering and multivariate analysis. *Anal. Chem.* **77,** 6118–6124.

McDonnell, L. A., Piersma, S. R., MaartenAltelaar, A. F., Mize, T. H., Luxembourg, S. L., Verhaert, P. D., van Minnen, J., and Heeren, R. M. (2005). Subcellular imaging mass spectrometry of brain tissue. *J. Mass Spectrom.* **40,** 160–168.

Meistermann, H., Norris, J. L., Aerni, H. R., Cornett, D. S., Friedlein, A., Erskine, A. R., Augustin, A., De Vera Mudry, M. C., Ruepp, S., Suter, L., Langen, H., Caprioli, R. M., *et al.* (2006). Biomarker discovery by imaging mass spectrometry: Transthyretin is a biomarker for gentamicin-induced nephrotoxicity in rat. *Mol. Cell. Proteomics* **5,** 1876–1886.

Menzel, C., Dreisewerd, K., Berkenkamp, S., and Hillenkamp, F. (2002). The role of the laser pulse duration in infrared matrix-assisted laser desorption/ionization mass spectrometry. *J. Am. Soc. Mass Spectrom.* **13,** 975–984.

Miao, H., Rubakhin, S. S., and Sweedler, J. V. (2005). Subcellular analysis of D-aspartate. *Anal. Chem.* **77,** 7190–7194.

Monroe, E. B., Jurchen, J. C., Lee, J., Rubakhin, S. S., and Sweedler, J. V. (2005). Vitamin E imaging and localization in the neuronal membrane. *J. Am. Chem. Soc.* **127,** 12152–12153.

Monroe, E. B., Jurchen, J. C., Koszczuk, B. A., Losh, J. L., Rubakhin, S. S., and Sweedler, J. V. (2006). Massively parallel sample preparation for the MALDI MS analyses of tissues. *Anal. Chem.* **78,** 6826–6832.

Monroe, E. B., Koszczuk, B. A., Losh, J. L., Jurchen, J. C., and Sweedler, J. V. (2007). Measuring salty samples without adducts with MALDI MS. *Int. J. Mass Spectrom.* **260,** 237–242.

Nygren, H., Borner, K., Malmberg, P., Tallarek, E., and Hagenhoff, B. (2005). Imaging TOF-SIMS of rat kidney prepared by high-pressure freezing. *Microsc. Res. Tech.* **68,** 329–334.

Nygren, H., Eriksson, C., Malmberg, P., Sahlin, H., Carlsson, L., Lausmaa, J., and Sjovall, P. (2003). A cell preparation method allowing subcellular localization of cholesterol and phosphocholine with imaging TOF-SIMS. *Colloids Surf. B Biointerfaces* **30,** 87–92.

Nygren, H., Johansson, B. R., and Malmberg, P. (2004). Bioimaging TOF-SIMS of tissues by gold ion bombardment of a silver-coated thin section. *Microsc. Res. Tech.* **65,** 282–286.

Ostrowski, S. G., Van Bell, C. T., Winograd, N., and Ewing, A. G. (2004). Mass spectrometric imaging of highly curved membranes during *Tetrahymena* mating. *Science* **305,** 71–73.

Parry, S., and Winograd, N. (2005). High-resolution TOF-SIMS imaging of eukaryotic cells preserved in a trehalose matrix. *Anal. Chem.* **77,** 7950–7957.

Petyuk, V. A., Qian, W. J., Chin, M. H., Wang, H., Livesay, E. A., Monroe, M. E., Adkins, J. N., Jaitly, N., Anderson, D. J., Camp, D. G., 2nd, Smith, D. J., and Smith, R. D. (2007). Spatial mapping of protein abundances in the mouse brain by voxelation integrated with high-throughput liquid chromatography-mass spectrometry. *Genome Res.* **17,** 328–336.

Roddy, T. P., Cannon, D. M., Jr., Meserole, C. A., Winograd, N., and Ewing, A. G. (2002a). Imaging of freeze-fractured cells with *in situ* fluorescence and time-of-flight secondary ion mass spectrometry. *Anal. Chem.* **74,** 4011–4019.

Roddy, T. P., Cannon, D. M., Jr., Ostrowski, S. G., Winograd, N., and Ewing, A. G. (2002b). Identification of cellular sections with imaging mass spectrometry following freeze fracture. *Anal. Chem.* **74,** 4020–4026.

Roddy, T. P., Cannon, D. M., Jr., Ostrowski, S. G., Ewing, A. G., and Winograd, N. (2003). Proton transfer in time-of-flight secondary ion mass spectrometry studies of frozen-hydrated dipalmitoylphosphatidylcholine. *Anal. Chem.* **75,** 4087–4094.

Rohner, T. C., Staab, D., and Stoeckli, M. (2005). MALDI mass spectrometric imaging of biological tissue sections. *Mech. Ageing Dev.* **126,** 177–185.

Rubakhin, S. S., Churchill, J. D., Greenough, W. T., and Sweedler, J. V. (2006). Profiling signaling peptides in single mammalian cells using mass spectrometry. *Anal. Chem.* **78,** 7267–7272.

Rubakhin, S. S., Greenough, W. T., and Sweedler, J. V. (2003). Spatial profiling with MALDI MS: Distribution of neuropeptides within single neurons. *Anal. Chem.* **75,** 5374–5380.

Schueler, B., Sander, P., and Reed, D. A. (1990). A time-of-flight secondary ion microscope. *Vacuum* **41,** 1661–1664.

Schwartz, S. A., Reyzer, M. L., and Caprioli, R. M. (2003). Direct tissue analysis using matrix-assisted laser desorption/ionization mass spectrometry: Practical aspects of sample preparation. *J. Mass Spectrom.* **38,** 699–708.

Sjovall, P., Lausmaa, J., Nygren, H., Carlsson, L., and Malmberg, P. (2003). Imaging of membrane lipids in single cells by imprint-imaging time-of-flight secondary ion mass spectrometry. *Anal. Chem.* **75,** 3429–3434.

Spengler, B., and Hubert, M. (2002). Scanning microprobe matrix-assisted laser desorption ionization (SMALDI) mass spectrometry: Instrumentation for sub-micrometer resolved LDI and MALDI surface analysis. *J. Am. Soc. Mass Spectrom.* **13,** 735–748.

Stoeckli, M., Chaurand, P., Hallahan, D. E., and Caprioli, R. M. (2001). Imaging mass spectrometry: A new technology for the analysis of protein expression in mammalian tissues. *Nat. Med.* **7,** 493–496.

Stoeckli, M., Staab, D., Staufenbiel, M., Wiederhold, K. H., and Signor, L. (2002). Molecular imaging of amyloid beta peptides in mouse brain sections using mass spectrometry. *Anal. Biochem.* **311,** 33–39.

Sugiura, Y., Shimma, S., and Setou, M. (2006). Two-step matrix application technique to improve ionization efficiency for matrix-assisted laser desorption/ionization in imaging mass spectrometry. *Anal. Chem.* **78,** 8227–8235.

Szakal, C., Kozole, J., and Winograd, N. (2006). Fundamental studies of the cluster ion bombardment of water ice. *Appl. Surf. Sci.* **252,** 6526–6528.

Taban, I. M., Altelaar, A. F., van der Burgt, Y. E., McDonnell, L. A., Heeren, R. M., Fuchser, J., and Baykut, G. (2007). Imaging of peptides in the rat brain using MALDI-FTICR mass spectrometry. *J. Am. Soc. Mass Spectrom.* **18,** 145–151.

Takats, Z., Nanita, S. C., Cooks, R. G., Schlosser, G., and Vekey, K. (2003). Amino acid clusters formed by sonic spray ionization. *Anal. Chem.* **75,** 1514–1523.

Takats, Z., Wiseman, J. M., and Cooks, R. G. (2005). Ambient mass spectrometry using desorption electrospray ionization (DESI): Instrumentation, mechanisms and applications in forensics, chemistry, and biology. *J. Mass Spectrom.* **40,** 1261–1275.

Takats, Z., Wiseman, J. M., Gologan, B., and Cooks, R. G. (2004a). Electrosonic spray ionization. A gentle technique for generating folded proteins and protein complexes in the gas phase and for studying ion-molecule reactions at atmospheric pressure. *Anal. Chem.* **76,** 4050–4058.

Takats, Z., Wiseman, J. M., Gologan, B., and Cooks, R. G. (2004b). Mass spectrometry sampling under ambient conditions with desorption electrospray ionization. *Science* **306,** 471–473.

Tanaka, K., Waki, H., Ido, Y., Akita, S., Yoshida, Y., Yoshida, T., and Matsuo, T. (1988). Protein and polymer analyses up to m/z 100.000 by laser ionization time-of-flight mass spectrometry. *Rapid Commun. Mass Spectrom.* **2,** 151–153.

Tyler, B. J., Rayal, G., and Castner, D. G. (2007). Multivariate analysis strategies for processing ToF-SIMS images of biomaterials. *Biomaterials* **28,** 2412–2423.

Van Berkel, G. J., Ford, M. J., and Deibel, M. A. (2005). Thin-layer chromatography and mass spectrometry coupled using desorption electrospray ionization. *Anal. Chem.* **77,** 1207–1215.

Verhaert, P. D., Conaway, M. C. P., Pekar, T. M., and Miller, K. (2007). Neuropeptide imaging on an LTQ with vMALDI source: The complete 'all-in-one' peptidome analysis. *Int. J. Mass Spectrom.* **260,** 177–184.

Wiseman, J. M., Ifa, D. R., Song, Q., and Cooks, R. G. (2006). Tissue imaging at atmospheric pressure using desorption electrospray ionization (DESI) mass spectrometry. *Angew. Chem. Int. Ed. Engl.* **45,** 7188–7192.

Wittig, A., Wiemann, M., Fartmann, M., Kriegeskotte, C., Arlinghaus, H. F., Zierold, K., and Sauerwein, W. (2005). Preparation of cells cultured on silicon wafers for mass spectrometry analysis. *Microsc. Res. Tech.* **66,** 248–258.

Wu, K. J., and Odom, R. W. (1996). Matrix-enhanced secondary ion mass spectrometry: A method for molecular analysis of solid surfaces. *Anal. Chem.* **68,** 873–882.

CHAPTER 14

Electron Microscopy of Hydrated Samples

Winston Timp and Paul Matsudaira

Whitehead Institute
Massachusetts Institute of Technology
Cambridge, Massachusetts 02139

Abstract

Conventional electron microscopy offers a substantial resolution advantage over light microscopy, but requires difficult and often destructive preparation techniques. Recent advances in electron microscopy allow for imaging of hydrated samples, retaining the resolution advantage while removing the difficulty in preparation. Two new techniques, environmental scanning electron microscopy and wet electron microscopy offer this advantage, allowing for new possibilities in biological imaging.

METHODS IN CELL BIOLOGY, VOL. 89

0091-679X/08 $35.00
DOI: 10.1016/S0091-679X(08)00614-6

I. Introduction

When considering the utility of a microscopy technique for granting insight about biological systems, the key factors are contrast and resolution. Contrast is the difference in signal strength between various parts of the image, or the capability to differentiate cellular structures from one another and from the background. Resolution is the minimum separation distance required to identify objects as individual structures. For microscopy to be an effective investigative tool, the sample must have sufficient contrast and resolution.

When imaging using light microscopy, the natural contrast of the sample may be enhanced easily through the use of chromophores or fluorophores, allowing multicolor imaging through differential staining. However, the resolution of light microscopy is physically restricted by the Abbe limit. The Abbe limit dictates a minimum X–Y spatial resolution given by $\lambda/(2NA)$, where λ is the light wavelength and NA the numerical aperture of the objective lens (Pawley, 1995).

By comparison, electron microscopy (EM) has extremely fine spatial resolution. Using transmission electron microscopy (TEM), resolution on the order of 1 Å is possible, and scanning electron microscopy (SEM) provides resolution to ~100 Å (Hayat, 1978). However, obtaining *contrast* in EM is more difficult than in light microscopy. Complicated preparation techniques, including drying, coating, embedding, and sectioning, are required (Bozzola and Russell, 1999). Expensive equipment and extensive training are necessary, which creates a barrier which may prevent many researchers from using EM.

Preparative techniques for EM are not only time consuming but may also be detrimental to the experiment. Drying the sample, even in an *extremely* careful way, can still change critical sample dimensions. This is especially true when attempting to examine structures primarily composed of water, such as extracellular matrix or synthetic hydrogels. Unless drying is done carefully, even robust structures will be destroyed by surface tension, adding a further wrinkle to preparation.

New EM techniques provide a potential solution to this issue. Environmental SEM (ESEM) and Wet SEM are two such techniques, both of which allow the sample to be maintained in a more natural state. Here, we describe the operation of basic SEM for background, provide detail about the operation of ESEM and Wet SEM, and conclude by illustrating typical sample preparations and images.

II. Basic SEM

A. Mechanism of Operation

In SEM, a tightly focused electron beam is trained on a sample, and a signal is generated by collecting the resulting emitted electrons or photons (see Fig. 1). In order to scan the surface, the beam is rastered across the sample, with the signal from each point making up a single pixel of the image.

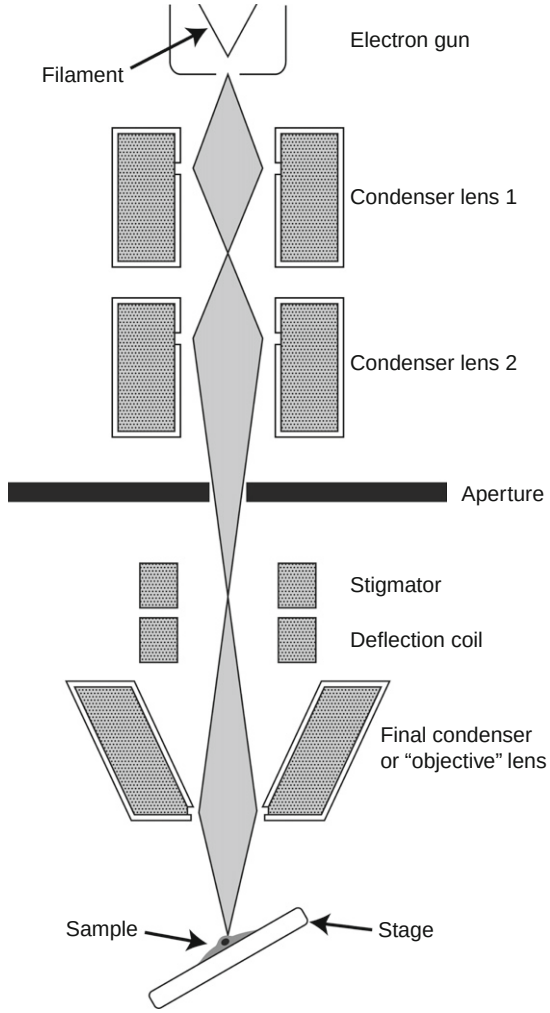

Fig. 1 Standard scanning electron microscopy (SEM) column, showing the major components.

To form a tightly focused beam, the SEM requires an electron source. This electron source, or gun, is usually in the form of a simple tungsten filament, which is heated to induce thermionic emission of electrons. The electrons are sent through a series of electromagnetic lenses, which gather and focus them into a beam. Electromagnetic lenses deflect the electron path using magnetic fields, whereas optical lenses bend light due to differences in the index of refraction of their elements.

To further improve the beam characteristics, apertures are placed in the electron beam path at a focal point to reject out-of-focus electrons, thus permitting only tightly focused electrons to pass. While this effectively shrinks the spot size, it does so at the cost of some resolution and beam power.

In SEM, the beam must be rastered across the surface of the sample to sequentially excite each point. This is accomplished with a deflection coil, which shifts the point of focus for the beam in the XY plane. The beam is then sent through the final condenser or "objective" lens, which focuses the beam to its ultimate spot size in the Z plane.

B. Signal Generation

When the beam electrons strike the sample, one of three detectable events occurs: elastic scattering, inelastic scattering, or photon emission. The first, elastic scattering, occurs when one of the electrons in the beam bounces off the electrostatic field produced by one of the nuclei in the sample. These electrons are detectable as *backscatter* if they exit the sample back along the beam path. Because the probability of backscattering is proportional to the square of the atomic number, contrast in backscattering detection is primarily generated from the elemental composition of the material. Untreated biological samples are usually composed of elements of low atomic number, which results in a low backscatter signal. Backscattered electrons, which are comparable in energy to the beam electrons, are recorded by use of a backscatter detector, usually consisting of an annular silicon diode, which is centered on the beam axis (see Fig. 2).

The second potential event is inelastic scattering of electrons by the sample. This occurs when the beam electrons interact with the atoms of the sample, which causes the ejection of some electrons from the outer valance shells of the sample's atoms. These *secondary* electrons are emitted at a relatively low energy (0–50 eV), so can only escape from the sample if within ~2 nm of the surface (Egerton, 2005). Secondary electrons may also be generated if either beam electrons or backscattered electrons strike parts of the microscope or chamber contaminants, which accounts for some of the noise in the signal.

Since secondary electrons are moving more slowly than backscattered electrons, it is possible to collect them through the application of an electric field. The most common design for a secondary electron collector is known as the Everhart-Thornley detector, which consists of a positively biased grid, a scintillator, and a photomultiplier. Electrons are attracted to and pass through the grid and are drawn rapidly toward the strongly positive scintillator. Upon reaching the scintillator, the electrons strike a phosphorescent material and generate a burst of light, which is then captured and measured by the photomultiplier tube, producing a detectable signal (see Fig. 2).

The third possible event is the emission of a photon through the interaction of the electron beam with a semiconductor. Essentially, the beam electron causes the promotion of a valence electron of the material to an excited state. When the excited electron relaxes back to its normal energy state, it emits a photon. This

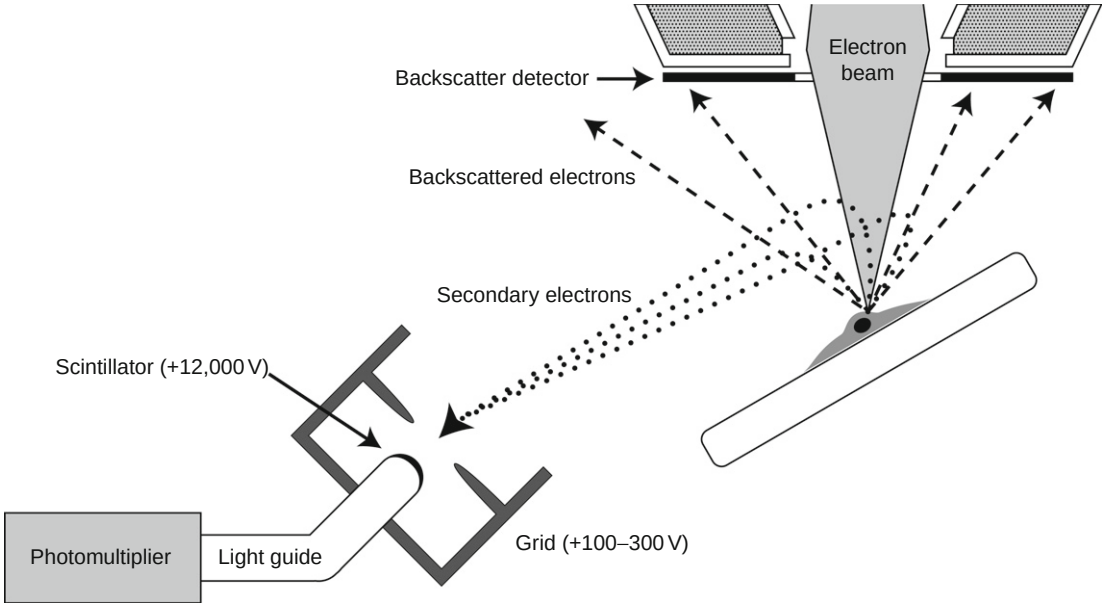

Fig. 2 Signal detection in conventional scanning electron microscopy (SEM): backscattered and secondary electrons.

phenomenon, known as cathodoluminescence, can then be detected through the use of a photomultiplier tube or other sensitive light detector connected to the sample chamber.

C. Problems/Limitations

The sample chamber for conventional SEM must be brought to a low pressure, around 10^{-6} Torr, to prevent diffraction of the electron beam. Low pressure is also required for some of the elements of the electron column, specifically the electron gun, which is subject to oxidation or arcing at higher pressures. This poses a major limitation with respect to the types of samples available for imaging. For most materials science, metallurgy, or semiconductor research samples, the requirement for a high vacuum is not an issue. However, biological samples consist primarily of water, and application of a high vacuum precludes keeping these samples in a hydrated state. Removing the water without perturbing the structure of the sample is a difficult problem.

There are several clever preparation techniques which have been developed to deal with this problem. Many require complicated or time-intensive processes which call for extensive training for proper performance. Moreover, these techniques can only be used on fixed samples, which prevent the acquisition of time-dependent data. The first step in standard biological sample preparation is fixation,

which preserves and protects the structure of sample against destruction by subsequent preparation or imaging techniques. In practice, fixation is done using a cross-linking agent, typically a weak (2–4%) glutaraldehyde solution which cross-links all free ε- and primary amino groups in the sample.

The next step involves dehydrating the sample, which is usually the most destructive step. The sample structure is often supported through its interactions with water, as in hydrogel samples, extracellular matrix, or many types of plant cells. Fixation is intended to ameliorate the effect of removing water but does not always succeed completely. The primary difficulty in drying the sample is motion at the air/water interface. Surface tension can create forces on the order of 2000 PSI (10^7 Pa) in the sample, which destroys most structures of interest to electron microscopists (Bozzola and Russell, 1999). To prevent this destruction, water is removed either by critical point drying or by freeze drying.

Critical point drying entails replacement of the water with ethanol, followed by a transitional fluid (usually freon or liquid CO_2), which is then vaporized at its critical point temperature. One problem with this technique is the possible extraction of sample material by the ethanol or transitional fluid. Another well-documented problem is an overall shrinkage of the sample due to the dehydration (Tingbeall *et al.*, 1995).

Freeze drying is accomplished by rapidly freezing water present in the sample, followed by sublimation of the ice under vacuum. To protect the sample from the formation of large ice crystals during this process, a cryoprotectant [e.g., sucrose, glucose, glycerol, ethanol, dimethyl sulfoxide (DMSO), or dextran] is added to reduce damage and crystal formation. Among these cryoprotectants, only ethanol is removed by sublimation. Other cryoprotectants will remain after processing, which can introduce artifacts and obscure the sample.

After dehydration, the sample is coated with a conductive layer, usually a thin, sputter-coated layer of Au or AuPd, for two purposes. First, the metal coating causes strong generation of secondary electrons from the sample due to the easily dislodged electrons in the conducting layer. Second, and of primary importance, the metal prevents charging of the sample. With beam electrons continuously striking the sample, and backscattered and secondary electrons being emitted, the sample can quickly acquire a charge. If the sample is coated with a metal that is in contact with the grounded mounting stub, any buildup of electrons is quickly dissipated, which prevents charging artifacts.

III. Environmental SEM

A. Mechanism of Operation

The operational parameters of ESEM are vastly different from those of normal SEM. The key operational difference is that the sample area is **not** subjected to high vacuum—instead, the pressure is maintained at 1–10 Torr using an appropriate gas

formulation. The higher pressure allows untreated samples to be imaged directly, without extensive dehydration and metal coating procedures. However, the increase in pressure requires large changes in the mechanism of signal detection and operation of the microscope.

As mentioned previously, certain elements of the electron optical column, specifically the electron gun, must be operated in a high vacuum, or they will degrade rapidly. Therefore, the pressure at the electron gun must be kept low, in the 10^{-6}–10^{-7} Torr range, while the sample pressure is maintained at 1–10 Torr. Differential pumping is applied to different parts of the microscope that are separated by pressure limiting apertures (PLAs). The apertures are small to minimize leakage yet large enough to pass the electron beam without restriction. Electron-transparent membranes were considered for use in the PLAs, but they were ultimately rejected because the gain in structural stability of the sample was more than offset by loss of beam intensity and focus (Danilatos, 1991).

At first glance, such a system would appear to allow hydrated samples to remain wet while scanning. However, during the pump-down process (760 → 10 Torr), some gases, such as water vapor, are often removed preferentially from the sample. If the partial pressure of water vapor drops too far, significant evaporation from the sample will occur. To prevent water loss, the vacuum is established in discrete stages; as each stage is completed the sample chamber is backfilled with an appropriate gas mixture (Cameron and Donald, 1994). Another option is to vent the sample chamber with a high humidity gas, which ensures that the initial concentration of water vapor in the sample chamber is sufficient to prevent evaporation during the pumping process.

B. Signal Generation

The gas in the sample chamber interacts with the electron beam, as well as with the backscattered and secondary electrons. In standard SEM, the beam encounters no impediments and strikes the sample with a minimum spot size. In ESEM, the beam travels through a low pressure gas, which causes the beam spot to change. Depending on the energy of the beam electron and the type and pressure of the gas, some of the electrons in the beam are deflected to form a "skirt" around the beam axis, which is distributed over a relatively large area and generates a nearly constant background signal. The remaining beam retains roughly the same spot size as in vacuum (Moncrieff *et al.*, 1979; Thiel and Toth, 2005). So, despite popular perception, the effect of gas in the imaging chamber on resolution is minimal.

Secondary electrons are detected very differently in ESEM than in conventional SEM. The standard Everhart-Thornley detector will not function under these conditions; the voltages produced by this detector to attract secondary electrons would cause arcing under the higher pressures used with ESEM. Instead, a gaseous secondary electron detector (GSED) is used, which functions by applying a small voltage (typically 300–600 V), between the sample surface and the detector (see Fig. 3).

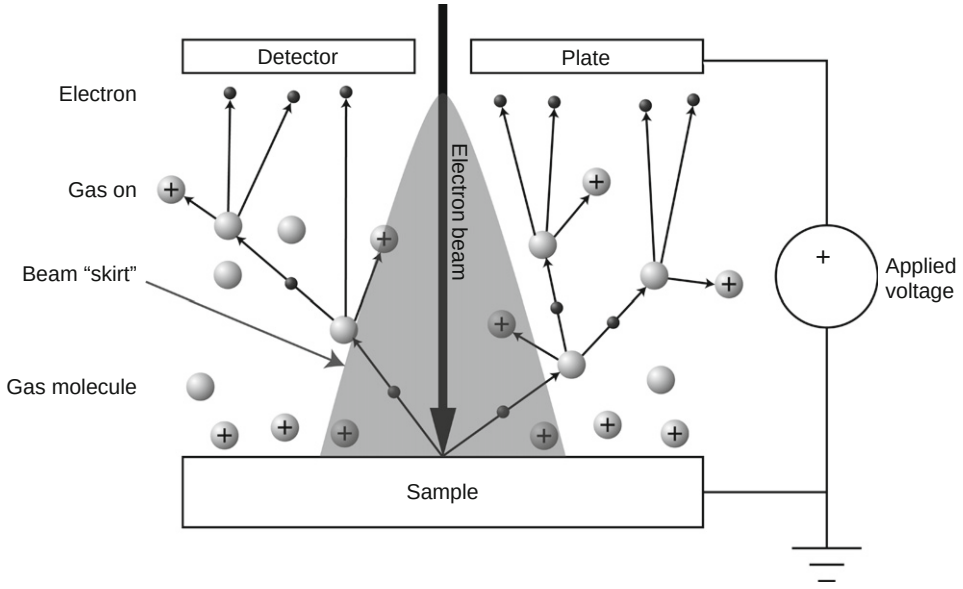

Fig. 3 Gaseous secondary electron detection.

When a low-energy secondary electron escapes the sample, it is accelerated by the electric field. The kinetic energy of the electron will increase as it accelerates toward the plate. As it travels toward the detector plate, the electron will invariably collide with a gas molecule, and, if its energy exceeds the ionization threshold of the gas, will strip an electron from the gas molecule. The result is two electrons and a positive gas ion. The two electrons are now accelerated—and the process repeats itself. This phenomenon is termed gas cascade amplification (Thiel and Toth, 2005). It is dependent on the type and partial pressure of the gas and the applied voltage.

The gas ions formed by gas cascade amplification actually play a beneficial role in imaging. Normally, the electron beam striking the sample causes charging, which will distort the resulting image. In conventional SEM, the conductive film on the sample surface keeps its potential tied to ground, eliminating such effects. In ESEM, the charge generated by the beam is largely compensated for by the gaseous ions. Although this is a simplistic view of complex behaviors occurring at the sample surface, the result is that insulating or semiconducting samples need **no** coating to be imaged using ESEM (Donald, 2003).

Backscattered electrons in ESEM behave and are detected similarly to those in conventional SEM. They are detected by a backscatter detector, which must be placed off the beam axis. In fact, the signal of the backscattered electrons is far less affected than that of the secondary electrons, due to the high energies and resulting lower ionization cross sections of the former (Fletcher *et al.*, 1997).

C. Samples/Examples

The performance of ESEM stands out in situations in which the sample is especially sensitive to water content. A good example is found in the hydrogels, which are drastically altered by dehydration. Cohen *et al.* (2003) used ESEM to investigate the hyaluronan (HA) pericellular coat, a polysaccharide-based hydrogel that is part of the normal extracellular matrix around certain cell types. RCJ-P rat chrondrocytes and A6 *Xenopus laevis* epithelial cells, cultured under standard conditions, were used for these experiments. Some of the cell samples were incubated with hyaluronidase to remove the pericellular coat from the cells. The cell samples were then fixed with 2% glutaraldehyde for 30 min. Samples for standard SEM were postfixed for 1 h with 1% osmium tetroxide, critical point dried with CO_2, and sputter coated with a ~10-nm film of AuPd. ESEM samples were either imaged directly after fixation or stained with 2% uranyl acetate at pH 3.5 for 45 min.

The results show the utility of ESEM quite elegantly. Figure 4A,B shows images of RCJ-P and A6 cells imaged in ESEM following a uranyl acetate stain. The cells clearly have a "halo," or surrounding coating of HA, whose thickness is cell dependent. After treatment with hyaluronidase, no such halo is visible, which confirms the nature of the coat (Fig. 4C,D). If the cells are imaged without the uranyl acetate stain, the halo is not visible, although the cells appear blurry (Fig. 4E,F). Finally, imaging these samples by conventional SEM shows no evidence of the HA coating (Fig. 4G,H). Indeed, the cells appear spiny with sharp protrusions, due to dehydration of the cell and removal of the surface-bound HA gel from the cell surface during preparation.

D. Problems/Limitations

ESEM has several quirks that should be resolved by future technical advances. First is the difficulty in the interpretation of the secondary electron signal. Cascade amplification of electrons and gaseous ions produces a signal that has added complexity. Uncoated samples can be imaged, but the interpretation of these images is nontrivial due to residual charging effects and sample stabilization by ions, which are poorly understood phenomena.

Maintaining the sample in a properly hydrated state is also a challenge. Both the sample temperature and the relative humidity of the surrounding gas must be carefully controlled. Currently, to image hydrated biological samples, the sample must be kept chilled between 2 °C and 8 °C range to minimize evaporation. If the relative humidity of the gas in the chamber is not carefully controlled, either condensation on, or evaporation from, the sample can result (Cameron and Donald, 1994). Because most biological samples have a high solute concentration, the calculation of the correct humidity level to achieve stable hydration is nontrivial.

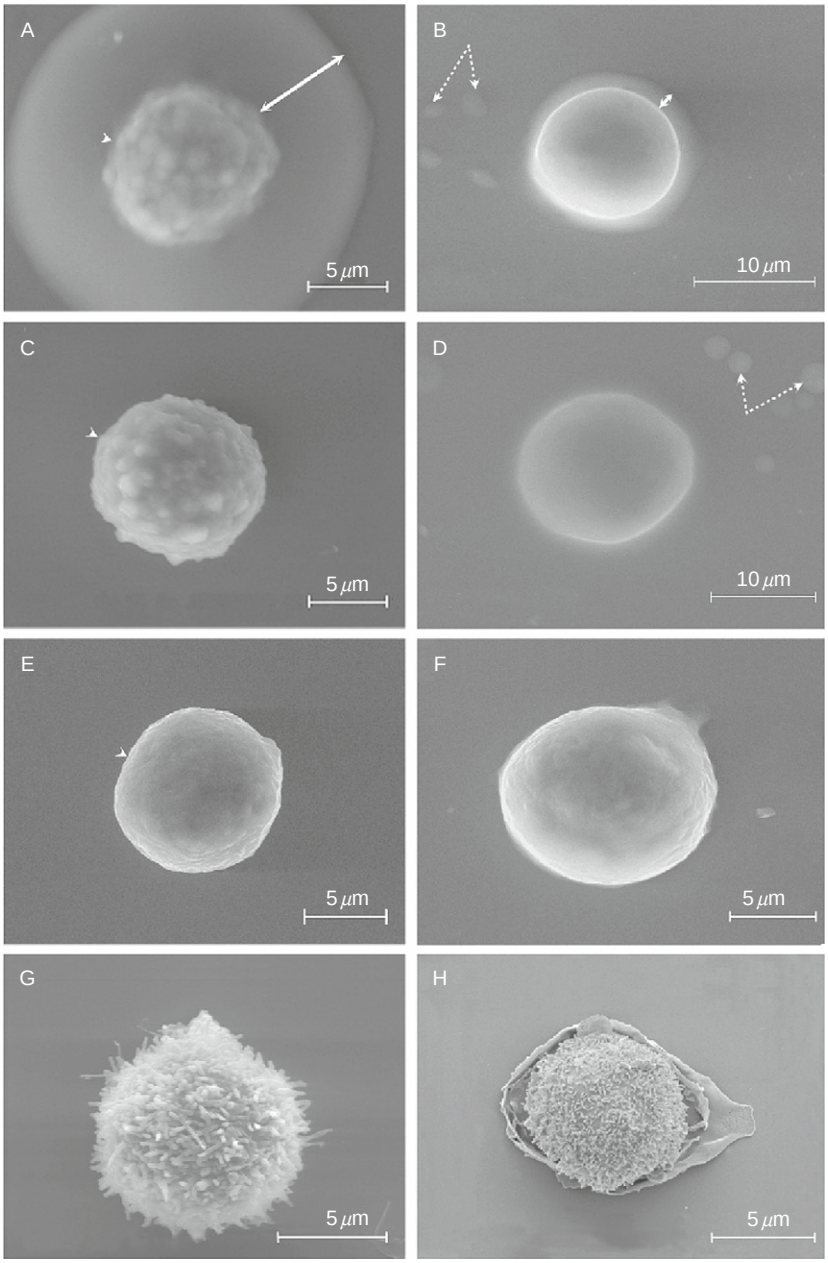

Fig. 4 Environmental scanning electron microscopy (ESEM) sample images, reproduced with permission from Cohen *et al.* (2003). Chrondocytes (A, C, E, G) and epithelial cells (B, D, F, H) were imaged: (A, B), untreated and labeled with uranyl acetate; (C, D), hyaluronidase-treated and labeled with uranyl acetate; (E, F), untreated without uranyl acetate; and (G, H), critical point dried.

IV. Wet SEM

A. Mechanism of Operation

A new technology available from Quantomix™ takes a different approach for hydrated EM (see Fig. 5). Their product consists of a sealable capsule with an electron-transparent membrane. An enclosed, fully hydrated sample is imaged through the membrane, which behaves as a coverslip does in light microscopy. The thin membrane is supported structurally against applied vacuum with a metal grid. This technique, dubbed "Wet SEM™," makes EM as easy to perform as light microscopy, while yielding a substantial resolution advantage over the latter (Thiberge *et al.*, 2004b).

Secondary electrons and accompanying topographic information about the sample are not accessible, as one normally expects from SEM. The electron-transparent membrane allows high-energy beam and backscattered electrons to pass but effectively blocks the transmission of the low-energy secondary electrons. Thus, imaging is limited to the backscattering mode, which yields information only on the composition of the sample. Backscattered contrast between dense areas of protein and nucleic acid and the surrounding liquid or cytoplasm can be achieved. If the sample is fixed and stained with heavy metals, such as uranyl acetate or

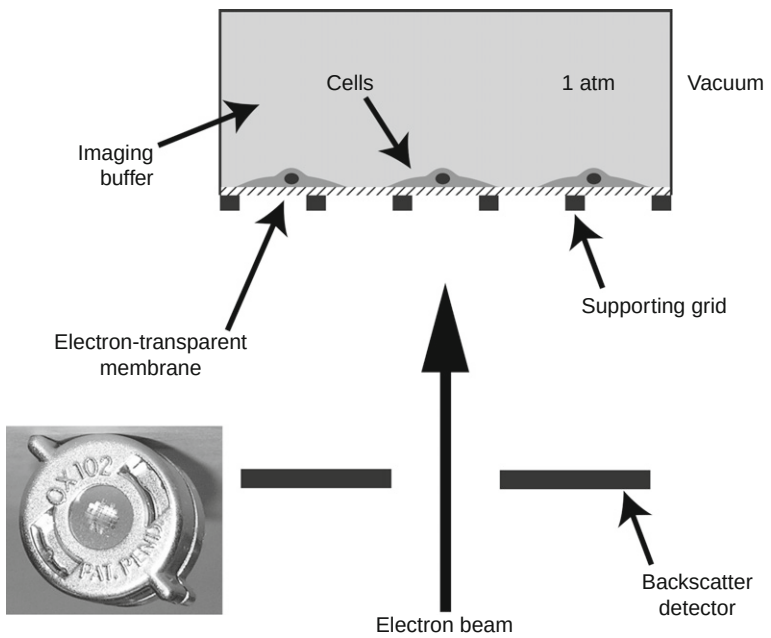

Fig. 5 Wet electron microscopy (EM) mechanism with Quantomix capsule pictured in bottom left.

osmium tetroxide, the low contrast of the biological sample itself is strongly enhanced. However, only backscattered electrons originating near the membrane surface retain enough energy to reach the detector, which therefore limits the effective focal depth to a few microns (Thiberge *et al.*, 2004b).

Because the membrane is transparent both to photons and to electrons, one may image the same cell by both electron and light microscopy. To provide contrast in both modes, an electron-dense fluorescent stain is needed. Two examples are colloidal gold bound to a fluorescent stain and quantum dots, which are composed of a CdSe/ZnS fluorescent material (Giepmans *et al.*, 2005; Michalet *et al.*, 2005; Timp *et al.*, 2006). It should also be possible to accomplish multicolor staining through cathodoluminscence with this platform. Quantum dots of different sizes fluoresce at different wavelengths. Thus, electron excitation of quantum dots that differ in size and distribution through the sample should reveal structure in multiple colors (Chan *et al.*, 2002; Khatsevich *et al.*, 2005). If this light is collected efficiently from the sample, it would provide multicolor imaging capability, albeit at the higher resolution provided by an electron beam.

B. Samples/Examples

The sensitivity of this technique is such that unstained cells may be imaged. Figure 6 shows an unstained Chinese hamster ovary (CHO) cell, in a normal culture environment, imaged with a JEOL 6400 SEM at high vacuum. The signal to noise is weak for this image, but several features stand out. First, the nucleus is brighter than the surrounding cytoplasm, as expected considering its greater density. Second, lipid droplets (Thiberge *et al.*, 2004a) are imaged as dark spherical objects. Lipids are notoriously difficult to image by EM because preparative

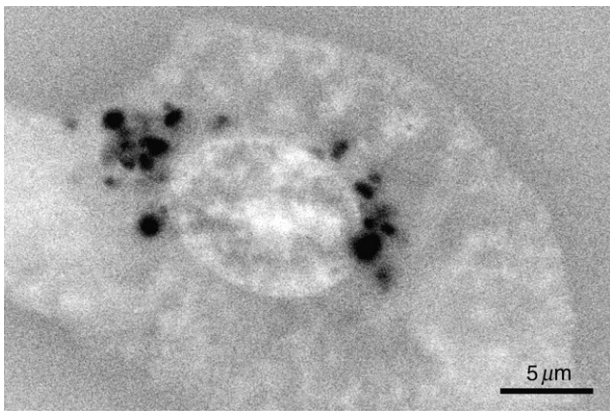

Fig. 6 Unstained Chinese hamster ovary (CHO) cell imaged using Wet electron microscopy (EM), images courtesy Quantomix.

methods usually damage or destroy them. Wet EM clearly provides a new modality for imaging lipid-based structures in cells, whether unstained or enhanced by staining with osmium tetroxide (Melo *et al.*, 2006).

Greater enhancement of protein/cellular structure is also possible with heavy metal stains. Figure 7A,B shows the cytoskeletal structure of C2C12, a mouse muscle cell line, after fixation with a 2% paraformaldehyde/1% gluteraldehyde (30 min) and staining with 2% phosphotungstic acid (PTA) (pH 1.5, 30 min) (Images

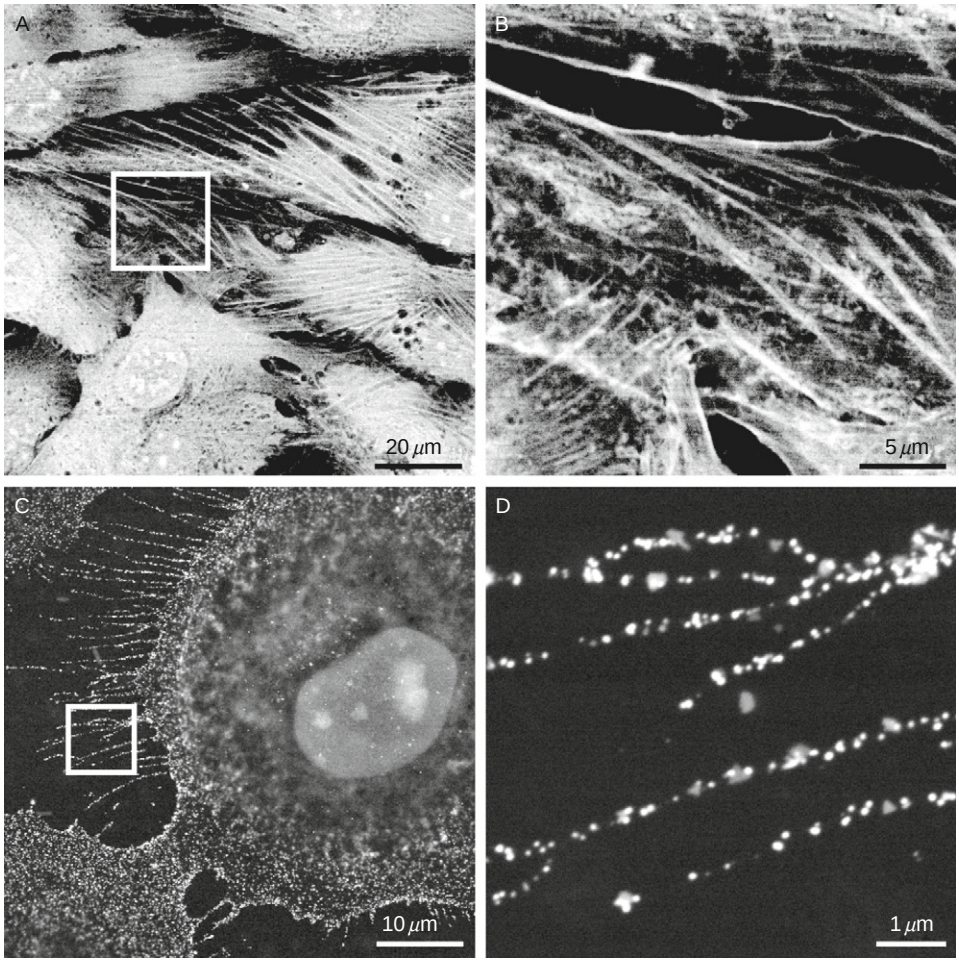

Fig. 7 Wet electron microscopy (EM) examples: (A, B), C2C12 cells stained with phosphotungstic acid (PTA); and (C, D), A431 cells stained with 2-nm gold particles conjugated to mouse-anti-epithelial growth factor (EGF) receptor, images courtesy Quantomix.

courtesy Quantomix). At this pH, the anionic PTA acts as a general protein and nucleic acid stain. The actin stress fibers are resolved with exquisite resolution.

Specific staining of proteins and their receptors can also be achieved using this technique in combination with immunolabeling. Figure 7C, D shows A431 cells which have been immunostained for the epithelial growth factor (EGF) receptor (Images courtesy Quantomix). These cells were fixed with 4% paraformaldeyde (10 min), then stained with 2-nm gold particles conjugated to a mouse-anti-EGF receptor antibody. After enhancement of the gold particles to improve their visibility, the EGF receptors are found to form dense foci along the cell's thin filopodia.

Figure 8 illustrates correlative light/EM of cells using the Wet EM modality (Timp *et al*., 2006). IC-21 cells, a mouse macrophage cell line, were fixed with 4% paraformaldehyde/0.1% Triton X-100 (15 min) on day one. The samples were blocked for 1 h with 2% bovine serum albumin (BSA), then incubated overnight with biotin-XX-phalloidin, which binds to F-actin. The next day, samples were blocked again with 1× Sigma Blocking Buffer (30 min), then incubated with streptavidin-conjugated quantum dots for 1 h. The sample was imaged by both electron and light microscopy. After accounting for rotation of and reflection by the image, one can align the electron and light microscopy images as shown in Fig. 8A,D. Using the Quantomix capsules, it is possible to do time-lapse fluorescence microscopy of living cells, then fix, stain, and examine the **same** cell at high resolution using EM. This type of correlative microscopy was previously very difficult due to the extensive searches required to relocate the same cell (Svitkina and Borisy, 1998).

C. Problems/Limitations

Despite the many advantages and potential applications of the Quantomix Wet EM system, there are significant limitations with this new technology. The practical resolution limit of Wet EM is on the order of 10 nm (Thiberge *et al*., 2004b). In most cases, resolution will be lower due to the poor signal-to-noise that arises from the backscattered electrons—the beam spot must be enlarged to achieve sufficient contrast to image the sample.

Quantomix capsules also prevent the measurement of any secondary electrons from the sample, which prevents the collection of topographic information. Therefore, Wet EM provides only compositional information about the interior of cells via backscattered electrons. Although samples may be imaged without stain, the contrast is weak. Samples may also be imaged live—but this is very difficult practically, as the electron beam is quite damaging to living cells.

V. Summary

ESEM provides the ability to image samples without complicated preparation techniques, and, perhaps more importantly, in a more realistic, hydrated environment. The decrement in resolution associated with ESEM is smaller than one

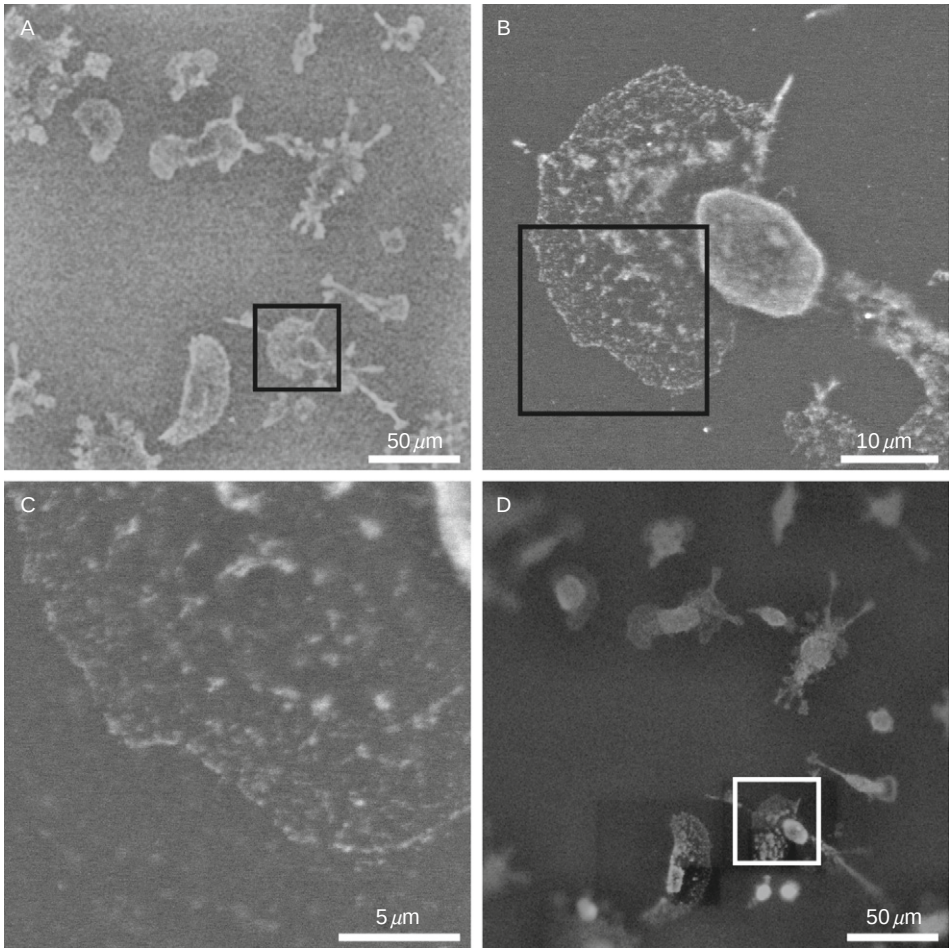

Fig. 8 IC-21 cells stained with quantum dots for electron/light microscopy (EM/LM) correlative microscopy: (A, B, C), images of cells by Wet EM; and (D), image of cells using fluorescence microscopy on the same cell.

might expect, such that this microscopic mode has a substantial advantage over light microscopy. Dynamic processes can also be observed, such as the reaction to changing water concentration.

Wet EM essentially creates a small space where the sample can remain in its natural state as it is being imaged by high-resolution EM. Contrast generation is a challenge, and resolution is limited by the sample chamber. However, Wet EM fills an empty niche in microscopy, that falling between the excellent resolution of TEM, and the relatively low resolution of light microscopy.

The technology underlying SEM is entering a new era and provides the capacity to image biological specimens in more realistic environments. Samples in a more natural state may now be imaged, with virtually the same resolution advantage over light microscopy that EM has always enjoyed.

References

Bozzola, J. J., and Russell, L. D. (1999). *Electron Microscopy: Principles and Techniques for Biologists* 2nd edn. Jones and Bartlett, Sudbury, Mass.

Cameron, R. E., and Donald, A. M. (1994). Minimizing sample evaporation in the environmental scanning electron microscope. *J. Microsc.* **173**(3), 227–237.

Chan, W. C. W., Maxwell, D. J., Gao, X. H., Bailey, R. E., Han, M. Y., and Nie, S. M. (2002). Luminescent quantum dots for multiplexed biological detection and imaging. *Curr. Opin. Biotechnol.* **13**(1), 40–46.

Cohen, M., Klein, E., Geiger, B., and Addadi, L. (2003). Organization and adhesive properties of the hyaluronan pericellular coat of chondrocytes and epithelial cells. *Biophys. J.* **85**(3), 1996–2005.

Danilatos, G. D. (1991). Review and outline of environmental SEM at present. *J. Microsc. Oxf.* **162,** 391–402.

Donald, A. M. (2003). The use of environmental scanning electron microscopy for imaging wet and insulating materials. *Nat. Mater.* **2**(8), 511–516.

Egerton, R. F. (2005). "*Physical Principles of Electron Microscopy: An Introduction to TEM, SEM, and AEM*." Springer Science, Inc, New York, NY.

Fletcher, A. L., Thiel, B. L., and Donald, A. M. (1997). Amplification measurements of alternative imaging gases in environmental SEM. *J. Phys. D Appl. Phys.* **30**(15), 2249–2257.

Giepmans, B. N. G., Deerinck, T. J., Smarr, B. L., Jones, Y. Z., and Ellisman, M. H. (2005). Correlated light and electron microscopic imaging of multiple endogenous proteins using quantum dots. *Nat. Methods* **2**(10), 743–749.

Hayat, M. A. (1978). "*Introduction to Biological Scanning Electron Microscopy*." University Park Press, Baltimore.

Khatsevich, S., Rich, D. H., Kim, E. T., and Madhukar, A. (2005). Cathodoluminescence imaging and spectroscopy of excited states in InAs self-assembled quantum dots. *J. Appl. Phys.* **97**(12), 123520.

Melo, R. C. N., Sabban, A., and Weller, P. F. (2006). Leukocyte lipid bodies: Inflammation-related organelles are rapidly detected by wet scanning electron microscopy. *J. Lipid Res.* **47**(11), 2589–2594.

Michalet, X., Pinaud, F. F., Bentolila, L. A., Tsay, J. M., Doose, S., Li, J. J., Sundaresan, G., Wu, A. M., Gambhir, S. S., and Weiss, S. (2005). Quantum dots for live cells, *in vivo* imaging, and diagnostics. *Science* **307**(5709), 538–544.

Moncrieff, D. A., Barker, P. R., and Robinson, V. N. E. (1979). Electron-scattering by gas in the scanning electron-microscope. *J. Phys. D Appl. Phys.* **12**(4), 481–488.

Pawley, J. B. (ed.) (1995). "*Handbook of Biological Confocal Microscopy*." 2nd Edn. Plenum Press, New York.

Svitkina, T. M., and Borisy, G. G. (1998). Correlative light and electron microscopy of the cytoskeleton of cultured cells. *Mol. Motors Cytoskeleton Pt B* **298,** 570–592.

Thiberge, S., Nechushtan, A., Sprinzak, D., Gileadi, O., Behar, V., Zik, O., Chowers, Y., Michaeli, S., Schlessinger, J., and Moses, E. (2004a). Scanning electron microscopy of cells and tissues under fully hydrated conditions. *Proc. Natl. Acad. Sci. USA* **101**(10), 3346–3351.

Thiberge, S., Zik, O., and Moses, E. (2004b). An apparatus for imaging liquids, cells, and other wet samples in the scanning electron microscopy. *Rev. Sci. Instrum.* **75**(7), 2280–2289.

Thiel, B. L., and Toth, M. (2005). Secondary electron contrast in low-vacuum/environmental scanning electron microscopy of dielectrics. *J. Appl. Phys.* **97**(5), 051101.01–051101.18.

Timp, W., Watson, N., Sabban, A., Zik, O., and Matsudaira, P. (2006). Wet electron microscopy with quantum dots. *Biotech.* **41**(3), 295–298.

Tingbeall, H. P., Zhelev, D. V., and Hochmuth, R. M. (1995). Comparison of different drying procedures for scanning electron-microscopy using human-leukocytes. *Microsc. Res. Tech.* **32**(4), 357–361.

CHAPTER 15

Live-Cell Single-Molecule Force Spectroscopy

Terrence M. Dobrowsky,[*,†] Porntula Panorchan,[*] Konstantinos Konstantopoulos,[*,†] and Denis Wirtz[*,†]

[*]Department of Chemical and Biomolecular Engineering
The Johns Hopkins University
Baltimore, Maryland 21218

[†]Howard Hughes Medical Institute Graduate Training Program and
Johns Hopkins Institute for NanoBioTechnology
The Johns Hopkins University
Baltimore, Maryland 21218

METHODS IN CELL BIOLOGY, VOL. 89

0091-679X/08 $35.00
DOI: 10.1016/S0091-679X(08)00615-8

Abstract

We describe a method to measure the kinetics and micromechanical properties of individual receptor–ligand bonds formed between two living cells. Using living cells rather than recombinant proteins ensures that the orientation, surface density, and posttranslational modifications of the probed receptors are physiological and that their regulated attachment to the cytoskeleton can occur. A cell is tethered to a flexible cantilever and brought into contact with cells adherent to a substratum before being pulled at a controlled retraction velocity. Measurements of bond rupture forces and associated bond loading rates over an extended range of retraction velocities allow us to compute precisely the tensile strength, reactive compliance, lifetime, and dissociation rate of individual intercellular receptor–ligand bonds. We also describe tests of specificity and Monte Carlo simulations, which ensure that measurements obtained by this method correspond to a single type of intercellular adhesion bond. We illustrate this live-cell single molecule force spectroscopy assay by characterizing homotypic bonds composed of vascular endothelial -cadherin pairs formed between living endothelial cells. This versatile assay could be used to establish the molecular principles that drive a wide range of important physiological processes involving receptor-mediated intercellular adhesion, such as the immunological synapse between a lymphocyte and an antigen-presenting cell and synaptic interactions between neuron cells, and pathological processes resulting in altered intercellular adhesion.

I. Introduction

A. Live-Cell Single-Molecule Force Spectroscopy

1. Distinguishing Single-Molecular Affinity from Multimolecular Avidity

It is fundamental to distinguish the *affinity* between an individual cell surface receptor on the surface of a cell and its ligand on the surface of an apposing cell from the global adhesion between these two cells, also called *avidity*. The avidity between two cells depends on a multitude of biochemical and biophysical parameters. Avidity may depend, in nontrivial ways, on the surface area of contact between apposing cells, the density of receptors on their plasma membrane, the local geometry and stiffness of the plasma membrane, the spatial arrangement and orientation of these molecules on the cell surface, the duration of contact between the cells, the rate of surface diffusion

of cell receptors, and of course the single-molecule affinity of the receptors for their ligands, to name a few.

The origin of an apparent change in total cell–cell avidity may be difficult to decipher. Indeed cell parameters that modulate avidity may change in uncontrolled ways when probing cell adhesion responses following, for instance, pharmacological treatment, or when testing mutants/gene silencing of adhesion molecules, or when comparing different members of the same family of adhesion molecules. The measurement of single-molecule level affinity is less ambiguous because it is much better controlled. It can directly monitor, for instance, the effect of (disease-causing) mutations in cell adhesion molecules or receptor activation following inside-out signaling on receptor–ligand affinity. Measurement of single-molecule level affinity can also detect the presence of subpopulations of receptors of different ligand binding capacity and can characterize the biophysical and biochemical properties of unknown ligands before their molecular identification (Hanley *et al.*, 2003).

Assays currently used to measure cell–cell interactions cannot directly distinguish single-molecular affinity between a receptor and its ligand from multimolecular avidity mediated by multiple receptor–ligand bonds between apposing cells. These assays, which include flow chamber assays (Alon *et al.*, 1995b; Niessen and Gumbiner, 2002), the dual micropipette assay (Chu *et al.*, 2004, 2005), and cell aggregation assays (Duguay *et al.*, 2003), are useful to quantify global cell–cell adhesion. However, these methods (linearly) extrapolate multiple-bond avidity to evaluate receptor–ligand affinity. Implicitly or explicitly, they assume that the total adhesion strength depends linearly on the number of receptor–ligand pairs. This is an oversimplification. In the simplest case, the total strength of adhesion depends exponentially on the number of adhesion molecules and the following assumptions: (1) receptors are uniformly distributed on the cell surfaces, (2) all have the same affinity, and (3) cell surfaces are flat and rigid. In the case where cell receptors form clusters and the cell plasma membrane is deformable, the dependence of avidity on the number of receptor–ligand pairs cannot be directly estimated. Multiple receptor–ligand bonds are generally necessary to effectively bind two apposing cells, therefore, there is a crucial need for an assay that can measure single-molecular affinity and can distinguish it from multimolecular avidity.

Here, we describe a method to measure the kinetics and micromechanical properties of individual receptor–ligand bonds formed between two living cells. This method relies on the molecular force probe (MFP), which measures adhesive forces with piconewton resolution as a function of cell–cell separation distance. Some of the key advantages of the live-cell single-molecule force spectroscopy assay described in detail in this chapter include: (1) the assay distinguishes single-molecule affinity between individual receptors on apposing cells from multiple-molecule avidity and measures the former, (2) it does not require protein labeling, (3) it probes single-bond dissociation rates in living cells (see later), (4) it tests interactions between cell receptors that display physiological orientation and posttranslational modifications, and (5) the assay can probe binding forces as a function of the rate of receptor disengagement.

2. Living Cells Versus Recombinant Proteins

Single-molecule force spectroscopy—using an atomic force microscope (Rief *et al.*, 1997, 1999), a biomembrane force probe (Evans *et al.*, 1995), microneedles (Rahman *et al.*, 2002), optical tweezers (Kuo and Sheetz, 1993; Wang *et al.*, 1997), or magnetic tweezers (Gosse and Croquette, 2002; Haber and Wirtz, 2000)—has been used extensively to probe single receptor–ligand interactions and single-molecule conformations using recombinant proteins. Our assay probes these interactions between living cells. Probing living cells rather than recombinant proteins (Baumgartner *et al.*, 2000, 2003; Perret *et al.*, 2004) ensures that the natural orientation of cell receptors on the cell surface and the posttranslational modifications of these receptors (e.g., glycosylation) are preserved. Moreover, using living cells rather than recombinant proteins ensures that transmembrane receptors (e.g., integrins, cadherins) can still interact with the cytoskeleton via interactions mediated by cytoplasmic proteins binding the cytoplasmic domain of the receptors, while recombinant proteins tethered to reconstituted phospholipid membranes cannot. Finally, the use of living cells ensures that cell signaling pathways, which may promote inside-out signaling and receptor activation mediated by a conformation change of the receptor, can occur.

B. The Molecular Force Probe

Our live-cell single-molecule force spectroscopy assay relies on the MFP (Asylum Research Inc., Santa Barbara, CA), an instrument that measures adhesion forces with piconewton resolution as a function of the cell–cell separation distance. The MFP has an architecture resembling that of the AFM. The MFP utilizes a flexible cantilever, which deflects in response to forces between the tip and the sample surface. Deflections are detected by a laser incident on the tip of the cantilever and, using the bending constant of the cantilever, transformed into time-dependent forces. The time-dependent deflection of the cantilever is determined by laser deflections on a photodetector (Fig. 1) at a rate of $\sim$2 kHz. The bending constant of each cantilever (nominal value, 10 pN/nm) is measured using the thermal oscillation method just before use (Hutter and Beccoeffer, 1993). Forces measured by the cantilever deflections are computed using Hooke's law, $f = k\Delta x$, where f is the force, k is the bending constant of the cantilever, and Δx is the deflection measured by the laser illumination. The cantilever bearing a few cells is positioned over target cells placed on a bottom cell culture dish, which is approached to establish contact of computer-controlled duration. Upon retraction of the cantilever, cell–cell interactions cause deflections of the cantilever, which are transformed into forces as a function of cell–cell separation.

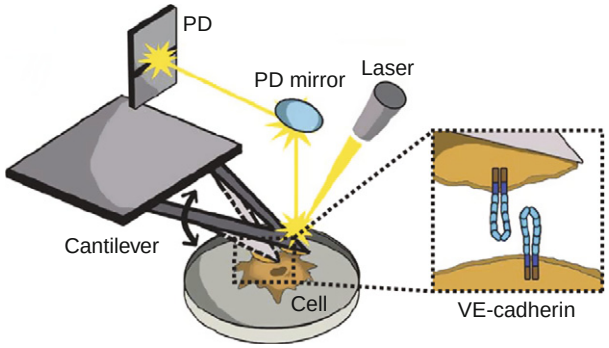

Fig. 1 Schematic of the molecular force probe-based assay used to measure vascular endothelial -cadherin-mediated intercellular interactions at single-molecule resolution and in living cells. *Inset*. vascular endothelial -cadherin pairs on apposing human umbilical endothelial cells are brought into contact, interact for a short time to form a bond, and are subjected to de-adhesion forces using a calibrated cantilever. Deviations of focused laser light incident on the cantilever detected by a photodetector measure the forces applied by the molecular force probe to the cadherin pair.

C. Probing Intercellular Adhesion at Single-Molecule Resolution—A Proof of Principle

1. Cadherin-Mediated Intercellular Adhesion

Here, we demonstrate the application of our live-cell single-molecule force spectroscopy assay by probing the kinetics and micromechanical properties of single homotypic bonds composed of two apposing vascular endothelial (VE)-cadherin pairs. The data presented here is taken from Panorchan *et al.* (2006a). VE-cadherin is the endothelial cell-specific cadherin which localizes to intercellular endothelial junctions (Allport *et al.*, 2000; Bibert *et al.*, 2002). Cadherins are single-pass transmembrane glycoproteins, which associate as cis-dimers on the cell surface and combine to form structures that promote intercellular adhesions (Corada *et al.*, 2001). Like other members of the cadherin family of cell-surface adhesion molecules, VE-cadherin mediates calcium-dependent, homophilic adhesion between cells and functions as a plasma membrane attachment site for the cytoskeleton through complex dynamic binding interactions of α-catenin and β-catenin to their cytoplasmic domain (Vincent *et al.*, 2004; Yamada *et al.*, 2005). We quantify the kinetics and the mechanical properties of VE-cadherin bonds at the single-molecule level and in living human umbilical vascular endothelial cells (HUVECs). These single-molecule force spectroscopy measurements reveal that VE-cadherins form bonds that are significantly stronger when subjected to low loading rates and have a significantly longer lifetime than those formed by classical type I cadherins E-cadherin pairs and N-cadherin pairs (Panorchan *et al.*, 2006b).

2. Resolving VE-Cadherin Pair Binding Interactions at Single-Molecule Resolution in Living Human Endothelial Cells

VE-cadherin/VE-cadherin pairwise binding interactions between apposing living HUVECs are measured at single-molecule resolution using the MFP (Fig. 1). Biotinylated HUVECs are placed using a streptavidin-coated microneedle on the surface of a strepavidin-coated cantilever. After overnight incubation, the cell on the cantilever is placed in contact with a cell on the bottom of the cell culture dish. The time of contact between the two cells is short, typically less than 1 ms, to allow for the formation of only a few adhesion bonds between cadherins on the surface of the two cells (see more later). To ensure that the biotinylation of adhesion molecules on cell surfaces does not alter their functionality, we compare the aggregation of biotinylated cells with the aggregation of nonbiotinylated cells using flow cytometry. We find that the extents of aggregation of biotinylated cells and nonbiotinylated cells are similar (data not shown).

The cantilever is retracted at a controlled retraction velocity (also called reproach velocity). The time-dependent adhesion force and time-dependent distance between the cells are recorded with high temporal ($<$1 ms), force ($<$3 pN), and distance ($<$1 nm) resolutions. Using a computer, approach and subsequent pulling experiments are conducted repeatedly, $\sim$30 times for a cell pair, before moving the cantilever to another cell on the bottom of the culture dish. Experiments are also repeated twice on three different days to test reproducibility. During the retraction of the cantilever, the rupture of adhesion bonds between the two cells cause distinct deflections of the cantilever, of amplitude larger than the background noise, which are recorded as abrupt drops in force in the force-distance curves.

During the approach of the cell on the cantilever toward the cell on the bottom dish, the force–distance curve is flat (noise $<$ 3 pN) (Fig. 2). A negative deflection of the cantilever occurs due to the deformation of the cell membrane by the impinging force. The force–distance curve increases during the retraction of the cantilever until the bonds between the cells, which are created during the approach of the cantilever, break (Fig. 2). For each retraction velocity, which ranges typically between 0.5 and 50 μm/s, hundreds of force–displacement curves are recorded and analyzed off line. Bond rupture forces, which correspond to the heights of the distinct force steps along the force–distance curve, and the loading rates applied to individual bonds are computed. The loading rate applied to the bond is computed by multiplying the computer-controlled retraction velocity of the cantilever (μm/s) and the measured slope of the force in the force–distance trace just before bond rupture (pN/μm). These adhesion forces and loading rates are subsequently used to calculate the kinetic and mechanical properties of individual VE-cadherin bonds between apposing HUVECs.

3. Control of Specificity

Calcium promotes the dimerization of cadherin molecules *in vitro* (Patel *et al.*, 2003), and cell-adhesion assays indicate that calcium is required for cadherin-mediated cell–cell adhesion (Gumbiner, 1996; Sivasankar *et al.*, 1999; Takeichi, 1991). To test

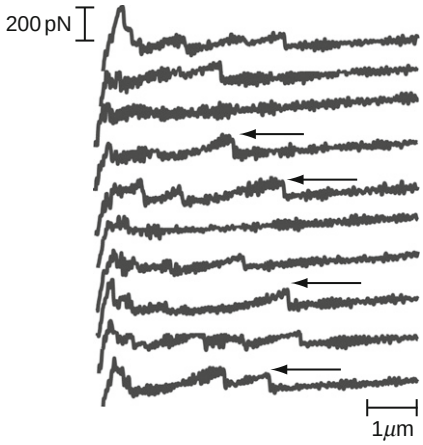

Fig. 2 Detection of the rupture of individual bonds between two apposing human umbilical vascular endothelial cells (HUVECs). Typical sequence of force-distance curves during the repeated de-adhesion of two apposing HUVECs at a constant cantilever retraction velocity of 25 μm/s. One HUVEC is attached to the cantilever; the other HUVEC is plated on a culture dish. These curves display either zero, one, or two bond-rupture events (marked by arrows).

the requirement of calcium for molecular interactions between individual VE-cadherin pairs on living cells, the chelating agent EDTA was added to the cell-culture medium. The addition of EDTA largely eliminates VE-cadherin/VE-cadherin binding; indeed the number of bond-rupture events was similar to background levels obtained without cells ($n = 300$).

Cell surface adhesion molecules different from VE-cadherins could interact during transient HUVEC–HUVEC adhesive contacts. Therefore, we test the specificity of VE-cadherin-mediated cell–cell adhesion probed by the MFP. Cells are pretreated with an anti-VE-cadherin function-blocking monoclonal antibody. The treatment of cells with VE-cadherin mAb significantly reduced the frequency of binding interactions between cells, from ~35% to less than 3%. This result indicates that the number of functional adhesive bonds between HUVECs diminished to background levels similar to those obtained with bare cantilevers without tethered cells and blocked with bovine serum albumine. In addition to VE-cadherins, HUVECs also express platelet endothelial cell adhesion molecules (PECAM), which can generate weak homotypic interactions. The application of PECAM mAb did not reduce the frequency of binding and yielded forces consistent with the absence of PECAM mAb. Therefore, the adhesive interactions between apposing HUVECs for short contact times involve only VE-cadherin-mediated binding interactions. The results from these three experiments indicate that measurements using the MFP are specific.

4. Single Versus Multiple Intercellular Bonds

Overall intercellular adhesion depends, among many parameters (see Section I.A), on the time of contact between the cells and the force applied by the top cell on the bottom cell during contact (Chu *et al.*, 2004). To limit the number of bonds

formed during cell–cell contacts, the time of interaction between cells and the impinging force can be reduced. Small impinging forces and short times of interaction between the two cells diminish the number of intercellular bonds. We promote single-bond engagement between apposing cells as opposed to multiple bonds by letting the cells interact for a short time of <1 ms to target a percentage of successful cell–cell binding interactions of 10–35%.

It can be shown that the probability of formation of bonds between two cells follows Poisson statistics (Chesla *et al.*, 1998). When only 30% of cell–cell contacts lead to bond rupture events on the force–distance curves, then >80% of the successful binding events involve only one bond, 15% involve two bonds, and <3% involve three bonds. This analysis applies to any ligand–receptor pair, including VE-cadherin pairs studied here (see also Hanley *et al.*, 2004; Konstantopoulos *et al.*, 2003; Dobrowsky *et al.*, 2008). To further reduce the number of bonds between probed cells, the contact force applied by the cantilever during approach is reduced to 200 pN. We also verify that the histogram of rupture forces obtained at each experimentally tested cantilever retraction velocity shows one well-defined peak, as opposed to multiple quantized peaks (Benoit *et al.*, 2000) (see also Monte Carlo simulations below). Therefore, cell adhesion measured with the present assay involves one type of adhesive bonds and nonspecific interactions between HUVECs are negligible.

5. Live-Cell Single-Molecule Force Spectroscopy Data Analysis

To characterize the binding interactions of individual VE-cadherin pairs between individual HUVECs, single-bond kinetics and micromechanical parameters are obtained using the Bell model. This kinetic model has been used extensively to characterize binding interactions between cell-surface adhesion molecules *in vitro* and in living cells (Alon *et al.*, 1995a; Chang *et al.*, 2005; Evans, 2001; Hanley *et al.*, 2003; Konstantopoulos *et al.*, 2003). The Bell model coupled with a probabilistic model of receptor–ligand bond dissociation predicts that the average adhesion force, $\langle f_m \rangle$, of a molecular bond depends on the natural logarithm of the loading rate, r_f, applied to the bond (Bell, 1978; Evans and Ritchie, 1997) as follows:

$$\langle f_m \rangle = \frac{k_B T}{x_\beta} \ln\left(\frac{x_\beta r_f}{k_{off}^0 k_B T}\right) \quad (1)$$

Here T is the absolute temperature, k_B is Boltzmann constant, k_{off}^0 is the unstressed bond dissociation rate, x_β is the bond reactive compliance. The reactive compliance approximately measures the distance along a reaction coordinate that describes the disengagement of the ligand from the receptor. The parameters k_{off}^0 and x_β are obtained by fitting the experimentally obtained mean rupture force—loading rate curve to Eq. (1).

As predicted by the Bell model, the force of adhesion of a single VE-cadherin/VE-cadherin bond increases logarithmically with the rate of mechanical loading

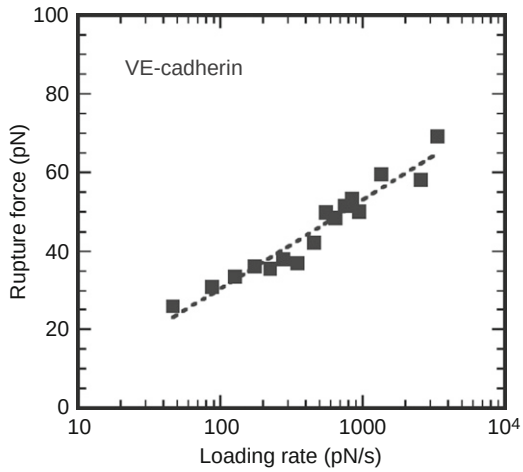

Fig. 3 Single-molecule analysis of vascular endothelial (VE)-cadherin mediated intercellular adhesion. Mean rupture force (adhesion force) of a single VE-cadherin/VE-cadherin bond as a function of loading rate applied to that bond in living human umbilical vascular endothelial cells. Curve fitting (dashed line) with Bell's model permits the computation of the unstressed dissociation rate, k_{off}^{0} and the reactive compliance x_{β}, of a bond.

on that bond (Fig. 3). This curve shows that VE-cadherin/VE-cadherin bonds can resist an average deadhesion force of 32 pN for a loading rate of 100 pN/s and 50 pN for a loading rate of 1000 pN/s (Fig. 3). Fitting the average rupture force to Eq. (1) yields an unstressed dissociation rate of 0.45 s^{-1} and a reactive compliance of 0.42 nm. The inverse of this dissociation rate corresponds to an equilibrium bond lifetime of 2.2 s. We note that this bond lifetime can be itself a function of the amplitude of the force applied to a bond, which is not measured here (Konstantopoulos *et al.*, 2003; Marshall *et al.*, 2003).

6. Monte Carlo Simulation of the Micromechanics of Individual Cadherin Bonds

To further verify that values for adhesion forces obtained by MFP correspond to the rupture of one type of adhesive bond characterized by one dissociation rate and one reactive compliance, Monte Carlo simulations of receptor–ligand bond rupture under constant loading rates are performed (Hanley *et al.*, 2004). Five thousands rupture forces, $f_{\text{rup}} = r_f\, n\Delta t$, were calculated. The probability of cadherin bond rupture, P_{rup}, is given by Bell Model's expression:

$$P_{\text{rup}} = 1 - \exp\left[-k_{\text{off}}^{0}\, \exp\left(\frac{x_{\beta} r_f n\Delta t}{k_{\text{B}}T}\right)\Delta t\right] \tag{2}$$

If P_{rup} is greater than a random number between 0 and 1, then receptor–ligand bond rupture occurs. In Eq. (2), Δt is the time interval and $n\Delta t$ is the time step; k_{off}^{0} and x_{β} are those obtained from Bell-model fits of the experimentally obtained

rupture forces. For VE-cadherins, simulated and experimentally obtained distributions of rupture forces are in good agreement. Since the computationally obtained distribution is obtained using one dissociation rate and one reactive compliance, this agreement indicates that only one type of adhesion molecules on the surface of HUVECs, VE-cadherins, are probed using the MFP. Disagreement between experimental and computed distributions could indicate that the measurements correspond to more than one type of bonds, characterized by more than one off-rate and reactive compliance.

II. Materials and Instrumentation

A. Cell Culture

HUVEC-C (Cat. No. CRL-1730), F-12K medium (Cat. No. 30-2004), and fetal bovine serum (10% v/v with culture medium, Cat. No. 30-2020) are obtained from American Type Tissue Culture. Cell culture medium is supplemented with 0.1 mg/ml heparin (Cat. No. H-3393; Sigma, St. Louis, MO), 0.05 mg/ml endothelial cell growth supplement (ECGS; Cat. No. E2759; Sigma), and 1:100 dilution of Pen-Strep solution (Cat. No. SV30010; Hyclone, Logan, UT). Hank's balanced salt solution (HBSS, Cat. No. 14170-112) and 0.25% trypsin—1 mM EDTA (Cat. No. 25200-056) are from Invitrogen. Cells were cultured on Poly-D-lysine coated 35 mm glass bottom dishes (Cat. No. P35GC-0-14-C; MatTek Corp., Ashland, MA). Cell cultures are maintained at 37 °C in a humidified, 5% CO_2 environment.

B. Preparation of Cantilevers

In all experiments, we use gold-coated, nonconductive silicon nitride cantilever probes (Mod. No. MLCT-AUHW; Veeco Probes, Camarillo, CA). Cantilevers are washed in 70% ethanol (Cat. No. 493546; Sigma) with 10% hydrochloric acid (Cat. No. H1758; Sigma), ultra pure filtered water, and 95% ethanol. They are then immersed in acetone (Cat. No. S70091; FisherSci, Pittsburgh, PA). Finally, the cantilevers are incubated in 0.5 mg/ml streptavidin (Cat. No. 21122; Pierce, Rockford, IL) overnight at 4 °C, and then washed with phosphate buffered saline (PBS) (Cat. No. 14190; Gibco, Carlsbad, CA).

C. Biotinylation of Cell Surface Receptors

For firm attachment to the cantilever, the surface of HUVEC cells is biotinylated. Cells are detached from tissue culture dishes using trypsin (Cat. No. 25200; Gibco). Cells are pelleted by centrifugation using a Centra bench top centrifuge (Mo. No. CL-2; from the International Equipment Company, Pittsburgh, PA). HUVECs are washed and suspended in PBS and sulfo-NHS-biotin (Cat. No. 21217; Pierce) is then added at a concentration of 1 mg/ml for 30 min.

D. Attachment of Cells to Cantilevers

Cell attachment to the cantilevers is performed on a Nikon TE300 inverted microscope equipped with a motorized InjectMan microinjection system (Cat. No. 6540.R094; Eppendorf, Westbury, NY). Borosilicate micropipettes (Cat. No. BF100-50-10; Sutter Instruments, Novato, CA), modified with streptavidin and mounted on the microinjector, are used to transport and attach biotinylated HUVECs to the cantilever. While placing biotinylated cells onto the cantilever, they are kept at 37 °C and manipulated in growth medium supplemented with 2% HEPES (Cat. No. 15630-080; Gibco). Cantilever-bound cells are maintained at 37 °C in a humidified, 5% CO_2 environment overnight.

E. Force Spectroscopy Data Acquisition and Analysis

Molecular force data are acquired using an MFP 1D Stand Alone AFM (Cat. No. 001.006.666; Asylum Research Inc). Analysis of rupture force data is performed using the technical graphing and data analysis software IGOR Pro, Version 4.09 (WaveMetrics, Lake Oswego, OR) integrated to the MFP analysis program (Asylum Research Inc.).

III. Procedures

A. Preparation of Cantilevers

Before use, cantilevers are chemically cleaned to remove nonspecific substances or particulate matter that may have adhered during manufacturing or storage. It should be noted that the surface tension of the wash solutions could potentially break the cantilever. To prevent this potential problem, cantilevers are moved in and out of solution on their side by breaking the surface with a probeless edge of the cantilever. Cantilevers are handled using fine tweezers, pinching the probeless edges of the cantilever. This is not a trivial process as the cantilevers are delicate and can (permanently) bend easily. One should practice moving cantilevers from one solution to another.

1. Cleaning of Silicon Nitride Cantilever Probes

a. **Steps**

i. Immerse cantilever probes successively in 70% ethanol/10% HCl, ultra pure water, and 95% ethanol solutions for 1 min each.

ii. Allow the cantilever probes to dry on clean glass surface. Probes should be moved at least once during the drying process to prevent their adhesion to the glass surface.

iii. Immerse the cantilever probes in 100% acetone solution for 5 min.
iv. Allow the cantilever probes to dry on a clean glass surface.

2. Treating Cantilevers with Streptavidin

a. **Materials**

i. 0.5 mg/ml streptavidin in PBS.

b. **Steps**

i. Place each cantilever into a ~100 μl droplet of the streptavidin solution. The cantilevers are deposited, back end first, into individual droplets. It helps to set droplets on a slightly hydrophobic surface to prevent them from spreading.
ii. Incubate cantilevers for 1 h at room temperature or, alternatively, overnight at 4 °C.

B. Preparation of Micropipettes

Glass micropipettes (Sutter Instruments) are drawn out above a flame and mounted on a motorized microinjection system used to pick up newly biotinylated cells in solution and place them on the cantilever probes.

a. **Materials**

i. Borosilicate micropipettes.
ii. 0.5 mg/ml streptavidin in PBS.

b. **Steps**

i. Hold a micropipette over a Bunsen burner with a clean blue flame. Quickly pull the ends of the micropipette apart to produce a thin glass needle. *Note:* This is a difficult step. If the needle is too thin, it may be too flexible to successfully navigate through a liquid medium. If the needle is too thick, the capillary action caused by its hollow center may make removing cells from the cantilever impossible. The general shape of the needle is also important. If the needle is too curved, moving it through the medium may be difficult. The orientation of the needle can also make the placement of a cell on the cantilever difficult.

ii. Plug the blunt end of the micropipette with epoxy (i.e., play-dough) to prevent unwanted capillary suction.

iii. Incubate the drawn microneedle end in 0.5 mg/ml streptavidin solution for 2 h at room temperature.

C. Biotinylation of Cell Surface Receptors

Cell surface adhesion proteins are biotinylated to adhere to the streptavidin treated micropipette and cantilever probes. This biotinylation process is per the manufacturer's instructions (Pierce).

a. **Materials**

i. HBSS
ii. Trypsin
iii. PBS (pH 8.0) chilled on ice
iv. Glycine
v. HUVEC growth medium
vi. HEPES
vii. 0.5 mg/ml Sulfo-NHS-LC-biotin in PBS, at room temperature

b. **Steps**

i. Wash cells using HBSS to remove cell debris.
ii. Remove cells from the tissue culture surface using trypsin. One milliliter is usually sufficient for a T-75 flask kept at 37 °C for 7 min.
iii. Dilute trypsinized cells with 5 ml of ice cold PBS and pellet by spinning the solution at 1200 rpm for 5 min in a typical desk top centrifuge. Wash cells twice more with ice cold PBS.
iv. Resuspend cells in 0.5 mg/ml Sulfo-NHS-LC-biotin in PBS for 30 min at room temperature.
v. Wash cells three times using PBS supplemented with 100 mM glycine to remove excess biotin reagents and quench the biotinylation reaction.
vi. Resuspend cells in HUVEC growth medium supplemented with 2% HEPES. For cells harvested from a T-75 flask, 6 ml of cell growth medium should suffice in a 35-mm tissue culture dish.

D. Attachment of Cells to Cantilevers

The previously prepared cantilever probes are placed in a solution of suspended cells over an inverted microscope equipped with a temperature-controlled chamber. Microneedles (see Section III.B) are mounted over this solution, immersed into it, and then used to transport cells that have settled to the bottom of the cell culture dish.

a. **Materials**

i. Solution of resuspended cells.
ii. Streptavidin-coated cantilever probes.
iii. Streptavidin-coated microneedles.

iv. Inverted microscope and phase contrast lens.

v. Temperature-controlled chamber for the microscope.

vi. Motorized microinjection system.

b. **Steps**

i. Bring the microscope chamber to 37 °C.

ii. Mount a streptavidin-coated microneedle in the motorized microinjection system attached to the inverted microscope.

iii. Place the streptavidin-coated cantilevers into the suspended cell solution.

iv. Position the cantilevers and cells under the microneedle. Almost immediately after cells are plated, they begin to settle to the bottom of the dish. It is possible that a cell will randomly settle on the cantilever surface after being plated. It is reasonable to wait and make sure this has not happened before attempting to manually place a cell. Move the microneedle into the cell solution. Avoid stabbing cells with the needle: once cells are punctured, they become difficult to remove. Pick up biotinylated cells using the (side) tip of the microneedle. Pressing the target cell gently for a short time will cause it to stick to the needle.

v. Gently raise the cell off the bottom of the cell culture dish and over the cantilever probe. The larger, more flexible cantilever probe will allow for detection of small rupture forces.

vi. Gently place the cell onto the tip of the cantilever. A ''wiping'' motion over the tip works best, but one must be careful not to press too hard and break the cantilever. Also, one has to be careful not to deform the cantilever too much or it will be useless later.

a. This is performed manually, with no automation. It is for this reason that the cantilevers must be treated with great care.

b. To initiate the wiping motion, slowly bring the cell/micropipette in contact with the cantilever in the z-direction. Once contact is made, move slowly in the x–y plane and attempt to ''roll'' the cell onto the cantilever. Axial motion should be used as needed to ensure cell-cantilever contact.

vii. Once one or more cells have been successfully attached to the cantilever tip, incubate the combination for at least 30 min within the microscope temperature chamber. After the cell has become more stably attached, keep the dish at 37 °C and 5% CO_2 overnight.

viii. Before experimentation, examine the cell bound to the cantilever under a microscope to ensure that the cell is still bound and displays a normal, well-spread morphology.

E. Force Spectroscopy Data Acquisition

An MFP is used to obtain rupture force data of cellular receptors on a piconewton force scale.

a. **Materials**

i. MFP.

ii. Previously prepared biotinylated cantilever probe with attached cell(s).

iii. Target cells seeded on a cell culture dish (<60% confluency).

iv. Data acquisition software (IGOR Pro 4.09 and Asylum Research Inc.).

b. **Steps**

i. Load the cells plated on a culture dish into the MFP.

ii. Withdraw a cell-mounted cantilever probe from serum-free medium solution.

iii. While holding the cantilever, remove excess medium by gently dabbing the end opposite the tip with a kimwipe. Excess liquid under the cantilever can lead to cantilever gliding from an original position during subsequent data acquisition. Also, if using a vacuum grease cantilever holder then excess liquid will make it difficult to mount the cantilever.

iv. Mount the cantilever into the MFP and carefully bring the cantilever close to the bottom dish.

v. Center the position-sensitive laser on the cantilever tip of interest. To make deflection detection as sensitive as possible, one should maximize the total sum of reflection intensity to detect most of the projected laser beam.

vi. Measure the bending rigidity of the cantilever using the thermal oscillation method (Hutter and Beccoeffer, 1993). With the cantilever away from the surface of the cell culture dish, obtain the cantilever spring constant using the thermal density application within IGOR Pro.

vii. Bring the cantilever close to the bottom of the dish in a clean, cell-free area. Deflect once against the plate bottom and obtain the inverse optical lever sensitivity (invOLS) constant per Asylum instructions. This is used to convert the voltage directly (mV) measured by the MFP into deflection distance (nm).

a. Use two data points on the linear portion of the force curve representing the cantilever deflection and the Calculate InvOLS command.

viii. Repeat steps vi and vii at least once to ensure consistency.

ix. Bring the cantilever above an area of confluent cells, flatly spread with no overgrowth.

x. Bring the cantilever slowly down to the cells on the bottom dish. Be careful not to apply too much pressure on the cells while finding an appropriate pulling distance. To avoid this, bring the cell down a little at a time, each time running a single pull over a short distance until contact is observed on a force versus extension curve. Once near cell–cell contact, begin altering the cantilever orientation and overall pulling distance to keep impingement forces below 200 pN so as not to rupture either cell.

a. If the cell on the tip or a cell near the tip is ruptured, binding becomes erratic and nonspecific.

xi. Perform some pulls on the cantilever-mounted cell to see if any binding occurs. If so, continue pulling while maintaining a cantilever distance that ensures an impingement force less than 200 pN. If no binding occurs, repeat steps ix and x.

a. At the initial cell-on-cell separation point, the retraction traces will likely produce a nonspecific adhesion profile that will differ from cell to cell. It is important to obtain clean retraction traces that have a small-initial-separation adhesion profile.

xii. Eventually, the cell experiences too much trauma and bursts. Every cell line will have a different rupture point, and it is important to determine a safe limit of number of pulls by repeating these experiments before acquiring data.

xiii. For a complete value system and to test reproducibility, each experimental condition should be composed of data from three different cell passages, with at least three different functionalized cantilevers.

F. Force Spectroscopy Data Analysis

The MFP data is stored in the form of force versus cantilever-pulling-distance curves for each individual pull of the cantilever. The curves used for calibration should be saved, but not used for analysis. Force versus distance curves with straight-and-even retraction traces are required for proper analysis of loading rates.

1. Initial Data Analysis and Acquisition of Raw Data from Retraction Traces

a. **Materials**

i. IGOR Pro 4.09 software.

ii. MFP analysis program.

b. **Steps**

i. Load all of the rupture force versus distance curves into the program.

ii. Create review graphs of the retraction traces.

iii. For each force–distance trace, record the index number, the number of bond rupture events along the trace, the spring constant of the cantilever, the approach velocity, and the retraction velocity.

iv. Magnify the force–distance trace at the rupture of interest.

a. On average, there should only be less than one rupture per trace. However, when more than one rupture trace is observed, record the rupture force of the final rupture.

b. Examples of successful ruptures are given in Fig. 2. They are composed of a gradual slope of increasing force, terminated by a dramatic decrease in force.

v. Record the change in force of the dramatic force drop that terminates the binding event on the force–distance curve.
   a. This is the rupture force required to break that bond.

vi. Using two points along the force–distance trace, one on the peak of the rupture and one at the base of the rupture where the level rupture curve and the deformation due to binding meet, measure both the change in force and the change in cantilever probe pulling distance to obtain a slope.

vii. Multiply the slope obtained in part vi with the retraction velocity of that particular force–distance trace.
   a. This is the loading rate applied to that ruptured bond.

viii. Repeat steps iv through vii for every rupture trace in the set.
   a. Loading rates should be able to be obtained for two logarithmic units to calculate kinetic data using the Bell model with sufficient precision.

2. Downstream Data Analysis and Computing Kinetic Parameters Using Bell Model Analysis

a. **Materials**

i. Statistical analysis program. *Posted on website http://www.jhu.edu/~cheme/wirtz/*

b. **Steps**

i. Bin the raw loading rate and rupture force data.
   a. Loading rates are binned in increments of 50 pN/s. In each bin average the loading rates and their respective rupture forces. This is done within the 100–1000 pN/s range on the log scale.
   b. For increasing rupture forces and exponentially increasing loading rates, the binning size should be increased accordingly above 1000 pN/s.
   c. This creates dataset Z, which is composed of N binned data points, $z_i = (x_i, y_i)$.

ii. Binned data should be fit to the Bell's model equation,

$$\langle f \rangle = \frac{k_B T}{x_\beta} \ln\left(\frac{x_\beta r_f}{k_{off}^0 k_B T}\right),$$

where $\langle f \rangle$ is the average rupture force that depends on the logarithm of the loading rate, r_f.

a. Fit the data using the reactive compliance of the bond, x_β, and the equilibrium dissociation rate of the bond, k_{off}^0, as the fit parameters.
b. Fitting is conducted using the method of nonlinear least squares coupled to the bootstrap method with replacement. This statistical approach fits the Bell model to the rupture force data, and uses random sampling to produce bootstrap datasets from which estimates of standard error of Bell model parameters are calculated.

3. Statistical Analysis of Kinetic Parameters and Monte Carlo Simulations

a. **Materials**

i. Statistical analysis program. *Posted on website http://www.jhu.edu/~cheme/wirtz/*

b. **Steps**

i. Calculate the probability of bond rupture, P_{rup}, using experimentally obtained k_{off}^0 and x_β.

a.

$$P_{rup} = 1 - \exp\left[k_{off}^0 \exp\left(\frac{-x_\beta r_f n\Delta t}{k_B T}\right)\Delta t\right],$$

where n is the iterative variable, Δt is the time interval, and $n\Delta t$ is the time step. A suitable Δt is 0.01 s. Begin with n equal to 1.

ii. Using a random number generator, produce a random probability of bond rupture, seP_{ran}.
iii. Compare P_{ran} and P_{rup}.
   a. If $P_{rup} > P_{ran}$, stop iterations. Use the value of n that produced P_{rup} to calculate the rupture force using $f_{rup} = r_f n\Delta t$.
   b. If $P_{rup} \leq P_{ran}$, iterate n and repeat steps i through iii.
iv. Perform these calculations thousands of times (typically 5000), then compare the experimental distributions of rupture forces with those produced computationally for each retraction velocity used in the experiments.

4. Error Analysis of Experimental Data and Nonrandom Sample Distribution

a. **Materials**

i. Statistical analysis program. *Posted on the website http://www.jhu.edu/~cheme/wirtz/.*

b. **Steps**

i. Create a bootstrap dataset, denoted Z^*, by randomly sampling N binned data points, $z_i = (x_i, y_i)$, with replacement.
   a. Bootstrap datasets are also of size N. Each data point with a bootstrap dataset has a probability of $1/N$ of appearing when sampling with replacement.

ii. Using the new bootstrap dataset, repeat step 2.b.ii, calculating the reactive compliance of the bond, denoted x_β^*, and the equilibrium dissociation rate of the bond, denoted k_{off}^0.

iii. Repeat steps i through ii.
   a. Bootstrap simulations are usually repeated between 50 and 200 times for estimation of standard error.
   b. The number of bootstrap simulations is denoted B.

iv. Using B number of bootstrap replicants, $x_\beta^*(b)$ and $k_{\text{off}}^0(b)$, corresponding to a respective bootstrap simulation b,

$$f^*(b) = x_\beta^*(b) \quad \text{or} \quad f^*(b) = k_{\text{off}}^0(b), \quad \text{with} \quad b = 1, 2, \ldots, B.$$

   a. Replicants are the Bell model parameters calculated from the randomly formed bootstrap datasets.

Calculate the standard error,

$$\widehat{\text{se}}_B = \left\{ \sum_{b=1}^{B} \frac{[f^*(b) - f^*(\bullet)]^2}{(B-1)} \right\}^{1/2}$$

where

$$f^*(\bullet) = \sum_{b=1}^{B} \frac{f^*(b)}{B}.$$

IV. Pearls and Pitfalls

Functionalizing force probe cantilevers requires skill that can only be learned with practice. In the beginning, cantilever tips will break easily; therefore practice is key. We strongly encourage potential users of our assay to practice moving cantilever probes in and out of solution, and then mount them on the MFP to see how much cleaning the cantilevers will bear before being deformed permanently or before altering the bending constant of the cantilever. Placing the cells onto the cantilever can be frustrating and, initially, could take a long time. We suggest that users of our assay make sure they have an undamaged cell-mounted cantilever before prepping for the rest of the experiment.

V. Concluding Remarks

We have described a new quantitative assay that can measure precisely the kinetics (dissociation rate and lifetime) and micromechanical properties (reactive compliance and tensile strength) of individual molecular bonds formed between two living cells brought in contact for a controlled duration and pulled apart at controlled retraction velocities. Unlike previous single-molecule force spectroscopy assays, this assay can probe adhesive bonds formed between living cells. This key advantage opens the way to testing important hypotheses in integrin/cadherin/selectin biology and inside-out signaling at the single-molecule level. Inside-out signaling through a transmembrane receptor would be caused by the regulated binding interaction of a cytoplasmic protein to the cytoplasmic domain of a single transmembrane receptor (or its phosphorylation) resulting in an allosteric conformation change, which in turn would change this receptor's affinity for its ligand. This assay can also be used to discover novel ligands. For instance, live-cell single-molecule force spectroscopy characterized completely the biophysical and biochemical properties of an unknown selectin ligand on colon carcinoma cells (Hanley *et al.*, 2003). This ligand was later discovered to be a variant isoform of CD44 (Hanley *et al.*, 2006; Napier *et al.*, 2006). This versatile assay can also be used to establish mechanistic principles that drive a wide range of important physiological processes involving receptor-mediated intercellular adhesion, such as the immunological synapse between a lymphocyte and an antigen-presenting cell (Dustin *et al.*, 2001), virus-mediated intercellular adhesive interactions (Piguet and Sattentau, 2004), synaptic interactions between neurons, and pathological processes that result in altered intercellular adhesion due to disease-causing mutations in adhesion molecules (Suriano *et al.*, 2003).

References

Allport, J. R., Muller, W. A., and Luscinskas, F. W. (2000). Monocytes induce reversible focal changes in vascular endothelial cadherin complex during transendothelial migration under flow. *J. Cell Biol.* **148,** 203–216.

Alon, R., Hammer, D. A., and Springer, T. A. (1995a). Lifetime of P-selectin-carbohydrate bond in response to tensile force in hydrodynamic flow. *Nature* **374,** 539–542.

Alon, R., Hammer, D. A., and Springer, T. A. (1995b). Lifetime of the P-selectin-carbohydrate bond and its response to tensile force in hydrodynamic flow. *Nature* **374,** 539–542.

Baumgartner, W., Hinterdorfer, P., Ness, W., Raab, A., Vestweber, D., Schindler, H., and Drenckhahn, D. (2000). Cadherin interaction probed by atomic force microscopy. *Proc. Natl. Acad. Sci. USA* **97,** 4005–4010.

Baumgartner, W., Schutz, G. J., Wiegand, J., Golenhofen, N., and Drenckhahn, D. (2003). Cadherin function probed by laser tweezer and single molecule fluorescence in vascular endothelial cells. *J. Cell. Sci.* **116,** 1001–1011.

Bell, G. I. (1978). Models for the specific adhesion of cells to cells. *Science* **200,** 618–627.

Benoit, M., Gabriel, D., Gerisch, G., and Gaub, H. E. (2000). Discrete interactions in cell adhesion measured by single-molecule force spectroscopy. *Nat. Cell Biol.* **2,** 313–317.

Bibert, S., Jaquinod, M., Concord, E., Ebel, C., Hewat, E., Vanbelle, C., Legrand, P., Weidenhaupt, M., Vernet, T., and Gulino-Debrac, D. (2002). Synergy between extracellular modules of vascular endothelial cadherin promotes homotypic hexameric interactions. *J. Biol. Chem.* **277,** 12790–12801.

Chang, M. I., Panorchan, P., Dobrowsky, T. M., Tseng, Y., and Wirtz, D. (2005). Single-molecule analysis of human immunodeficiency virus type 1 gp120-receptor interactions in living cells. *J. Virol.* **79,** 14748–14755.

Chesla, S. E., Selvaraj, P., and Zhu, C. (1998). Measuring two-dimensional receptor-ligand binding kinetics by micropipette. *Biophys. J.* **75,** 1553–1572.

Chu, Y. S., Eder, O., Thomas, W. A., Simcha, I., Pincet, F., Ben-Ze'ev, A., Perez, E., Thiery, J. P., and Dufour, S. (2005). Prototypical type-I E-cadherin and type-II cadherin-7 mediate very distinct adhesiveness through their extracellular domain. *J. Biol, Chem.* **281**(5), 2901–2910.

Chu, Y. S., Thomas, W. A., Eder, O., Pincet, F., Perez, E., Thiery, J. P., and Dufour, S. (2004). Force measurements in E-cadherin-mediated cell doublets reveal rapid adhesion strengthened by actin cytoskeleton remodeling through Rac and Cdc42. *J. Cell Biol.* **167,** 1183–1194.

Corada, M., Liao, F., Lindgren, M., Lampugnani, M. G., Breviario, F., Frank, R., Muller, W. A., Hicklin, D. J., Bohlen, P., and Dejana, E. (2001). Monoclonal antibodies directed to different regions of vascular endothelial cadherin extracellular domain affect adhesion and clustering of the protein and modulate endothelial permeability. *Blood* **97,** 1679–1684.

Dobrowsky, T. M., Zhou, Y., Sun, S. X., Siliciano, R. F., and Wirtz, D. (2008). Monitoring early fusion dynamics of human immunodeficiency virus type 1 at single molecule resolution. *J. Virol.* **82,** 7022–7033.

Duguay, D., Foty, R. A., and Steinberg, M. S. (2003). Cadherin-mediated cell adhesion and tissue segregation: Qualitative and quantitative determinants. *Dev. Biol.* **253,** 309–323.

Dustin, M. L., Allen, P. M., and Shaw, A. S. (2001). Environmental control of immunological synapse formation and duration. *Trends Immunol.* **22,** 192–194.

Evans, E. (2001). Probing the relation between force—lifetime—and chemistry in single molecular bonds. *Annu. Rev. Biophys. Biomol. Struct.* **30,** 105–128.

Evans, E., and Ritchie, K. (1997). Dynamic strength of molecular adhesion bonds. *Biophys. J.* **72,** 1541–1555.

Evans, E., Ritchie, K., and Merkel, R. (1995). Sensitive force technique to probe molecular adhesion and structural linkages at biological interfaces. *Biophys. J.* **68,** 2580–2587.

Gosse, C., and Croquette, V. (2002). Magnetic tweezers: Micromanipulation and force measurement at the molecular level. *Biophys. J.* **82,** 3314–3329.

Gumbiner, B. M. (1996). Cell adhesion: The molecular basis of tissue architecture and morphogenesis. *Cell* **84,** 345–357.

Haber, C., and Wirtz, D. (2000). Magnetic tweezers for DNA micromanipulation. *Rev. Sci. Instrum.* **71,** 4561–4570.

Hanley, W., McCarty, O., Jadhav, S., Tseng, Y., Wirtz, D., and Konstantopoulos, K. (2003). Single molecule characterization of P-selectin/ligand binding. *J. Biol. Chem.* **278,** 10556–10561.

Hanley, W. D., Napier, S. L., Burdick, M. M., Schnaar, R. L., Sackstein, R., and Konstantopoulos, K. (2006). Variant isoforms of CD44 are P- and L-selectin ligands on colon carcinoma cells. *FASEB. J.* **20,** 337–339.

Hanley, W. D., Wirtz, D., and Konstantopoulos, K. (2004). Distinct kinetic and mechanical properties govern selectin-leukocyte interactions. *J. Cell. Sci.* **117,** 2503–2511.

Hutter, J. L., and Beccoeffer, J. (1993). Calibration of atomic-force microscope tips. *Rev. Sci. Instr.* **64,** 1868–1873.

Konstantopoulos, K., Hanley, W. D., and Wirtz, D. (2003). Receptor-ligand binding: 'Catch' bonds finally caught. *Curr. Biol.* **13,** R611–R613.

Kuo, S., and Sheetz, N. P. (1993). Force of single kinesin molecules measured with optical tweezers. *Science* **260,** 232–234.

Marshall, B. T., Long, M., Piper, J. W., Yago, T., McEver, R. P., and Zhu, C. (2003). Direct observation of catch bonds involving cell-adhesion molecules. *Nature* **423,** 190–193.

Napier, S. L., Healy, Z. R., Schnaar, R. L., and Konstantopoulos, K. (2006). Selectin ligand expression regulates the initial vascular interactions of colon carcinoma cells: The roles of CD44V and alternate sialofucosylated selectin ligands. *J. Biol. Chem.* **282**(6), 3433–3441.

Niessen, C. M., and Gumbiner, B. M. (2002). Cadherin-mediated cell sorting not determined by binding or adhesion specificity. *J. Cell. Biol.* **156,** 389–399.

Panorchan, P., George, J. P., and Wirtz, D. (2006a). Probing intercellular interactions between vascular endothelial cadherin pairs at single-molecule resolution and in living cells. *J. Mol. Biol.* **358,** 665–674.

Panorchan, P., Thompson, M. S., Davis, K. J., Tseng, Y., Konstantopoulos, K., and Wirtz, D. (2006b). Single-molecule analysis of cadherin-mediated cell-cell adhesion. *J. Cell Sci.* **119,** 66–74.

Patel, S. D., Chen, C. P., Bahna, F., Honig, B., and Shapiro, L. (2003). Cadherin-mediated cell-cell adhesion: Sticking together as a family. *Curr. Opin. Struct. Biol.* **13,** 690–698.

Perret, E., Leung, A., Feracci, H., and Evans, E. (2004). Trans-bonded pairs of E-cadherin exhibit a remarkable hierarchy of mechanical strengths. *Proc. Natl. Acad. Sci. USA* **101,** 16472–16472.

Piguet, V., and Sattentau, Q. (2004). Dangerous liaisons at the virological synapse. *J. Clin. Invest.* **114,** 605–610.

Rahman, A., Tseng, Y., and Wirtz, D. (2002). Micromechanical coupling between cell surface receptors and RGD peptides. *Biochem. Biophys. Res. Commun.* **296,** 771–778.

Rief, M., Gautel, M., Oesterhelt, F., Fernandez, J. M., and Gaub, H. E. (1997). Reversible unfolding of individual titin immunoglobulin domains by AFM. *Science* **276,** 1109–1112.

Rief, M., Pascual, J., Saraste, M., and Gaub, H. E. (1999). Single molecule force spectroscopy of spectrin repeats: Low unfolding forces in helix bundles. *J. Mol. Biol.* **286,** 553–561.

Sivasankar, S., Brieher, W., Lavrik, N., Gumbiner, B., and Leckband, D. (1999). Direct molecular force measurements of multiple adhesive interactions between cadherin ectodomains. *Proc. Natl. Acad. Sci. USA* **96,** 11820–11824.

Suriano, G., Oliveira, C., Ferreira, P., Machado, J. C., Bordin, M. C., De Wever, O., Bruyneel, E. A., Moguilevsky, N., Grehan, N., Porter, T. R., Richards, F. M., Hruban, R. H., *et al.* (2003). Identification of CDH1 germline missense mutations associated with functional inactivation of the E-cadherin protein in young gastric cancer probands. *Hum. Mol. Genet.* **12,** 575–582.

Takeichi, M. (1991). Cadherin cell adhesion receptors as a morphogenetic regulator. *Science* **251,** 1451–1455.

Vincent, P. A., Xiao, K., Buckley, K. M., and Kowalczyk, A. P. (2004). VE-cadherin: Adhesion at arm's length. *Am. J. Physiol. Cell. Physiol.* **286,** C987–C997.

Wang, M. D., Yin, H., Landick, R., Gelles, J., and Block, S. M. (1997). Stretching DNA with optical tweezers. *Biophys. J.* **72,** 1335–1346.

Yamada, S., Pokutta, S., Drees, F., Weis, W. I., and Nelson, W. J. (2005). Deconstructing the cadherin-catenin-actin complex. *Cell* **123,** 889–901.

CHAPTER 16

Magnetic Manipulation for Force Measurements in Cell Biology

E. Tim O'Brien,[*] Jeremy Cribb,[†] David Marshburn,[‡] Russell M. Taylor II,[‡] and Richard Superfine[*]

[*]Department of Physics and Astronomy
University of North Carolina
Chapel Hill, North Carolina 27599

[†]Department of Biomedical Engineering
University of North Carolina
Chapel Hill, North Carolina 27599

[‡]Department of Computer Science
University of North Carolina
Chapel Hill, North Carolina 27599

METHODS IN CELL BIOLOGY, VOL. 89

0091-679X/08 $35.00
DOI: 10.1016/S0091-679X(08)00616-X

Abstract

Life is a mechanical process. Cells, tissues, and bodies must act within their environments to grow, divide, move, communicate, and defend themselves. The stiffness and viscosity of cells and biologic materials will vary depending upon a wide variety of variables including for example environmental conditions, activation of signaling pathways, stage of development, gene expression. By pushing and pulling cells or materials such as mucus or extracellular matrix, one can learn about their mechanical properties. By varying the conditions, signaling pathways or genetic background, one can also assess how the response of the cell or material is modulated by that pathway. Magnetic particles are available commercially in many useful sizes, magnetic contents, and surface chemistries. The variety of surface chemistries allow forces to be applied to a specimen through specific linkages such as receptors or particular proteins, allowing the biologist to ask fundamental questions about the role of those linkages in the transduction of force or motion. In this chapter, we discuss the use of a magnetic system designed to apply a wide range of forces and force patterns fully integrated into a high numerical aperture inverted fluorescence microscope. Fine, thin and flat magnetic poles allow the use of high magnification microscope objectives, and flexible software to control the direction and pattern of applied forces supports a variety of experimental situations. The system can be coupled with simple video acquisition for medium-bandwidth, two-dimensional particle tracking. Alternatively, the system can be coupled with a laser tracking and position feedback system for higher resolution, high bandwidth, three-dimensional tracking.

I. Introduction

Applying forces locally to biological materials or to living cells can help us understand the mechanical properties of that region, such as the stiffness or compliance of a lamellipodium or a collagen gel. Quantifying the mechanical properties of cells or biologic materials over time allows us to better understand the response of that system to the original stimulus or to other changes such as altered gene expression, activation of signaling cascades, or the addition of toxins or cytoskeletal agents. By assessing cellular responses against differing backgrounds of gene expression or the presence of pharmacologic agents, one can obtain clues about which

genes or signaling pathways are involved in that response. Probing the mechanical properties of the material generated by cells and tissues under different controlled conditions, can similarly generate information about which components of that material are responsible for which property we observe. In this chapter we discuss one approach to using the manipulation of magnetic particles to explore the mechanical responses of cells and biologic materials.

Magnetic force technologies bridge the gap between the range of forces available with the atomic force microscope (up to hundreds of nano Newtons), and the pN forces available with optical traps, but without the difficulty of an attached cantilever and with less local heating at high forces. Depending upon the size of particle used and the pole material, forces can be produced from sub-pN to 10 nN, with a frequency of up to 3000 cycles/s (Fisher *et al*., 2006b). Such forces can gently unwind a DNA strand, or lift a cell lamellipodium from the substrate. Magnetic probes also have the advantage of being able to apply force at a variety of size scales, from well under a micron to 10–20 μm. This is useful for understanding the heterogeneity of a material, and the effective "mesh size." The methods we describe employ a flexible electromagnetic system that, in its most general configuration, is capable of pulling or twisting in any direction with high forces and rapid on/off times. We generally use superparamagnetic beads, which do not rotate in a magnetic field and thus can pull in a specified direction. Ferromagnetic particles will orient in a magnetic field and thus could produce a twisting motion. Both twisting and displacement magnetic systems have proven to be very useful to the study of cell mechanics (Bausch *et al*., 1998, 1999, 2001; Fabry *et al*., 2001; Feneberg *et al*., 2004; Wang *et al*., 1993), and a recent chapter in this series has discussed the motivation for their use in detail (Lele *et al*., 2007).

Here we describe a flexible method for applying forces to cells and cellular materials that has been developed for use by cell biologists, is easily integrated into existing inverted microscopes, and can be used simply with video tracking or, for higher temporal and spatial resolution, with laser tracking (Desai *et al*., 2008; Fisher *et al*., 2006a,b). Combining laser tracking with a three-axis (XYZ) piezoelectric nanopositioning stage also enables experiments involving force or position feedback. Software has also been developed to control the magnetic system, to track beads in real time, and for analysis and visualization of generated data (Desai *et al*., 2008; Marshburn *et al*., 2005). Analysis of the application of force can take place simply by sub-pixel level video-based tracking of the targeted probe and affected structures at rates limited only by camera speed (usually 120–200 frames/s), or using laser-based tracking. Video tracking can approach 4 nm resolution in the XY plane, but is much less effective at tracking in Z (up or down from the plane of focus) than laser tracking. The laser-based tracking strategy, described in detail previously (Desai *et al*., 2008), allows updates of bead position in X, Y, and Z direction, with 2 nm accuracy, at sampling rates of 10,000 cycles/s. Thus laser tracking has greater potential for understanding subtle effects at very high time resolution, but requires a significantly higher degree of commitment from the experimenter.

II. Sample Preparation

The quality of data obtained from magnetic probe experiments is heavily dependent on sample preparation. While a large number of approaches exist to attach a magnetic bead to a particular protein or molecule of interest on a cell, in a gel, or on a coverslip, care must be taken to minimize non-specific binding and binding to multiple ligands, which could confound analysis. Each experiment is different, poses unique challenges, and, like all single molecule studies, requires a large sample size and multiple controls.

A. Preparation of Magnetic Particles

Magnetic particles are commercially available in a variety of sizes and magnetic content. Thus far, we find that the superparamagnetic beads smaller than about 1 μm are not reliably uniform. Dynal (Invitrogen, Corp) makes beads with the highest and most uniform magnetic content, in 1, 2.8, and 4.5 μm sizes. Other companies make many more sizes but with either less magnetic content or less uniformity. Still, many of those beads could be useful in certain situations. Beads are available with various surface chemistries such as streptavidin, carboxyl, amino or tosyl groups. It is simple to biotinylate antibodies to specific cell surface proteins of interest via commercial kits, and then to attach magnetic beads to those antibodies via streptavidin linkages. Care must be taken to limit the number of attachments sites, but titrations of the reactants can be used to achieve the desired linkages. Tosyl-activated beads can simply and easily link to amino groups on a membrane protein, in a mixture, or on a surface, and carboxy and amino-surfaced beads can be used with no modification or can be covalently linked to amino or carboxy groups on proteins using the carbodiimid (EDC or EDAC) reaction. The experimenter can determine whether high forces or a very fine graduation of forces is most desired for particular experiments. The former would favor large beads with high magnetic content like the Dynal 4.5 μm beads, while the latter would favor either small beads with high magnetic content like the Dynal MyOne beads, or a uniform bead with less magnetic content, like those offered by Spherotech (Libertyville, IL). In practice, we find that beads with carboxyl surface chemistries bind to most mammalian cells with strong affinity without any modification. However, when addressing specific questions, specific tethers become important. For rheology experiments, evaluating the visco-elastic properties of biologic fluids and materials, surface chemistry can be very important. Surface charge and functionality must be controlled for. Anti-adhesive molecules such as polyethylene glycol (PEG) have been used to good effect to reduce non-specific binding within a sample (Lai *et al.*, 2007) but again the PEGs and their actual effects must be carefully thought through for each experiment, and controls done to know the effects of all treatments.

B. Selection of Bead Size

Magnetic microspheres are chosen primarily by what forces are thought to be needed for a particular experiment. 4.5 μm beads can exert up to 10 nN of force, which is large enough to pull some cells from a coverglass. However, very large beads, with a large surface of contact with the cell or material may not be ideal for single molecule attachments. 2.8 μm beads can be pulled at up to 1–2 nN of force, are easily tracked, and have a smaller contact area. 1 μm beads can exert up to 1 nN under optimal conditions, but 100–200 pN is a useful range in practice. Due to practical limits on how close a pole tip can get to a cell without damaging it or surrounding cells, 1 μm beads are most often used exerting 0–50 pN, the 2.8 s in the 10–200 pN, and the 4.5 s up to 1 nN.

C. Preparation of Specimens for Magnetic Experiments

Our magnetic sample stages are designed to most easily use 24 $\times$ 50 mm coverslips, and it is most advantageous to apply the sample to the approximate center of the coverslip. Coverglasses can be cleaned using ultraviolet cleaners, plasma cleaners, or acid solutions. Thirty seconds of plasma cleaning is an excellent method to remove hydrocarbons from the glass surface. A ring of grease such as silicon vacuum grease can then be applied around the central 1 cm of the glass. Cells requiring special substrates such as collagen or fibronectin can have a solution containing those applied to the center sample area. Most adherent cells also attach and spread extremely well to clean glass. Cloning cylinders attached with grease work very well to contain cells and media over several days during attachment and growth, so any cell type that requires attachment can easily be used. Agar or extracellular matrix gels can also be applied and contained using cloning cylinders. An example of a sample on one of our stages, with a cloning cylinder still in place, is shown in Fig. 1A. Materials of rheologic interest, such as mucus from patients with cystic fibrosis, DNA samples, and fibrin gels, can also be applied and contained in this manner under specified conditions. For cell experiments, medium can be removed from the specimen just before the experiment and replaced with cell medium stabilized with 10 mM HEPES buffer to maintain pH during exposure to room air.

Figure 1A also shows two examples of magnetic lids on either side of our sample stage. Previous publications have shown the details of how our small coils transmit magnetic flux to thin magnetizable foil poles to generate strong magnetic gradients within our samples (Fisher *et al.*, 2006a,b). Our new sample stages and lids incorporate these coils into a circuit board that makes manufacture and assembly much simpler and more reproducible. The metal foils that comprise our poles are chosen to conduct high magnetic flux, but to resist being magnetized permanently. In practice the metals that transmit the highest flux density also retain their magnetization after the current is turned off, so that high force procedures must incorporate rapid de-magnetization (degaussing) procedures throughout force

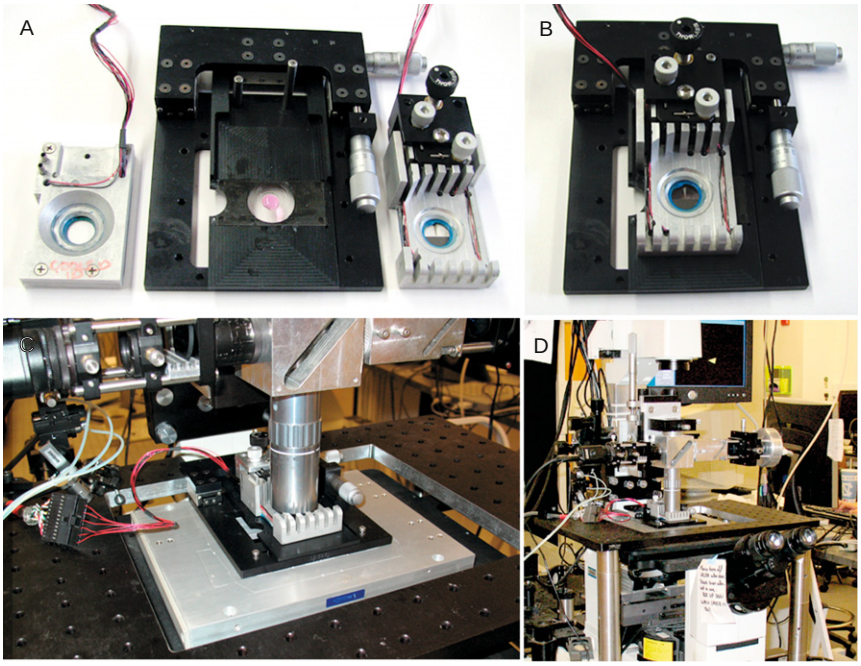

Fig. 1 Views of the sample stage and lid. (A) A cell culture specimen with cloning cylinder in position is in the specimen slot in the stage base (center). Two magnetics lids are shown on either side of the base. The left hand lid has a channel for cooling-heating fluid to circulate. The right lid has fins for passive cooling. The right-hand lid also is shown with a "pole-flat" pole configuration, and the 3-axis adjustment connector in place. (B) The fully assembled stage, ready to be placed onto the microscope. The cloning cylinder was removed before placing the lid. (C) The stage on top of a Nikon TE 2000 inverted microscope. A Mad City Labs 3-dimensional piezo stage is directly underneath the magnetics stage. The upper optics is needed for the laser tracking function, but is not needed for video. (D) A wider view of the microscope with stage in place.

application. This is accomplished in practice by driving the current to the magnetic coils in a decaying rapid oscillation of current (Fisher *et al.*, 2006b). User interface software allows the user to set degaussing parameters (discussed below), or one can drive the force server computer directly using scripts in programs such as Matlab (Mathworks.com). The magnetic poles, typically 0.004″ MuMetal are acid or laser etched to a fine point, and coated with parylene to slow oxidation of the metal during use. Biologic samples are often immersed in a saline solution or buffer, and this would otherwise rapidly degrade unprotected MuMetal. The poles are glued onto number 0 coverglasses and then affixed to the lids, positioned just under the magnetic cores of the lid. The lid on the left in the Fig. 1A does not have a pole plate attached, while the lid on the right does. The left-hand lid illustrates a temperature-controlled lid, which has incorporated channels for the flow of

water or other fluid to maintain a constant temperature during experiments. The lid on the right incorporates cooling fins to passively remove heat generated during the application of magnetic force. A new lid with electrical resistive heating is also being developed.

The sample stage, or base, has an improved ease of movement in the *XY* plane, with larger and simpler knobs, and the ability to easily remove or adjust lid height and angle during experiments compared with earlier versions (Fisher *et al*., 2006b). A channel in the base accommodates the coverslip. Figure 1B shows the sample stage and lid ready to be placed on a microscope, and 1C and D show the sample stage in the context of a Nikon TE2000 inverted microscope. Any inverted microscope would work for this stage, with the addition of two to four holes drilled to secure the base. The stage in Fig. 1 rests on a three dimensional piezoelectric nanopositioning stage (Mad City Labs, Madison, WI). This is required for the laser-based tracking system, but is not needed for a primarily video-based system.

III. Video and Laser-Based Magnetic Systems

Figure 2 shows block diagrams comparing video (A) with laser tracking (B) systems. For highest resolution in both time and space, laser tracking of single beads during magnetic pulls offers the best results. At 10,000 data points per second for position and 2 nm spatial resolution in the *XY* plane, extremely subtle and interesting phenomena can be assessed. Laser tracking also allows excellent tracking in the up-down ("*Z*") direction, which for some experiments may reveal critical insight into the biological issue being assessed. Sophisticated user interface programs allow the experimenter to watch a virtual representation of a bead's motion in three dimensions in real time, and a video of the experiment can put that motion into context (Marshburn *et al*., 2005). On the other end of the spectrum, relatively inexpensive high speed video can provide 120–200 positional data points per second, while cameras offering 1000–3000 frames/sec are available. The *XY* resolution using updated video tracking algorithms is comparable to laser tracking (CISMM). For some applications, simple video rate experiments would offer adequate sample rates for very little cost in cameras and interface boards. Recent progress with video tracking even provides some *Z* information and may soon allow active tracking. Advantages of video tracking are that the images of the experiment automatically provide the experimenter with the milieu under which data was taken, and that the response of many beads can be assessed at once. However, since each bead will feel a different force depending on the distance from the pole, careful calibration is necessary (discussed below). The other main advantage of video tracking of magnetic experiments is much lower cost. Laser tracking requires the laser, associated optics, special condenser, quadrant photodiode detector, *XYZ* piezo stage and a separate video camera and computer. In practice, we find that many experiments can take advantage of applying magnetic forces using a video system with 120 frames/s frame rate.

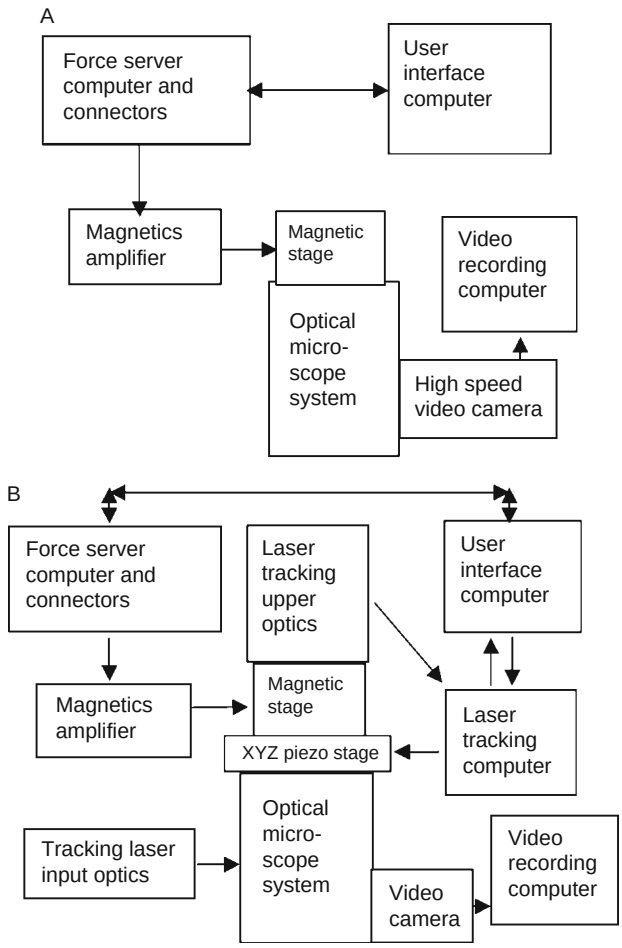

Fig. 2 Block diagram of the functional parts of (A) a video only system, or (B) a video and laser-tracking system. The laser-tracking system offers higher resolution, real-time tracking in three dimensions, and much higher data acquisition rates, but is not required for some experiments.

IV. Calibration of Pole Tips

The magnetic force supplied to a bead varies strongly with the distance from the center of the pole tip, the amount of magnetic material in each bead, and the current applied to the magnetic coils. While some experiments do not require the user to know the exact force applied to a system (or they incorporate internal calibrations), many situations do require such knowledge for a full interpretation of the result. As mentioned, we have found that Dynal (Invitrogen, Inc) 1, 2.8, and 4.5 μm beads have the most consistent loading of magnetic material, at a very high magnetic content per bead, and a very uniform size distribution. Variation in size

and magnetite content in the Dynal beads typically produce less than 10% of the variation we see in calibration experiments (Fisher *et al.*, 2006b). The uniformity of commercial beads allows calibration primarily in terms of distance to the pole within a sample.

In practice we calibrate our poles by applying specified currents to a pole and acquiring high speed video of the movement of all the beads in the area while the pole is on. Current is applied periodically and the poles are degaussed between trains of pulses. Any constant movement of the bead between pulses is calculated as remnant magnetization, which is then checked after the degauss procedure. A solution of known viscosity, normally 2–2.5M sucrose, is used for calibration. The velocity of each bead during each pulse is calculated using Video Spot Tracker (CISMM) of the beads. That velocity is used to calculate the force experienced by the bead during that pulse using Stoke's law, i.e. $F = 6\pi a\eta v$, where F is the force on the bead, η is the solution viscosity, a is the bead radius and v its velocity. Figure 3A shows a "merged time lapse projection" of a time sequence of images acquired at 120 frames per second. The greater velocity experienced by each bead as it approaches the pole tip can be observed as more distinctly separate bead images along each track. That information is used to construct graphs like the one in Fig. 3B for a series of 1 μm MyOne Dynal beads. Note the maximum force produced by these 1 μm beads approached 120 pN at maximum coil current and closest approach. In practice it is easiest to position the pole tip 20–30 μm away from beads attached to cells, preventing possible damage to the cells, and thus the most reliably usable forces are in the 20–40 pN maximum for this pole tip.

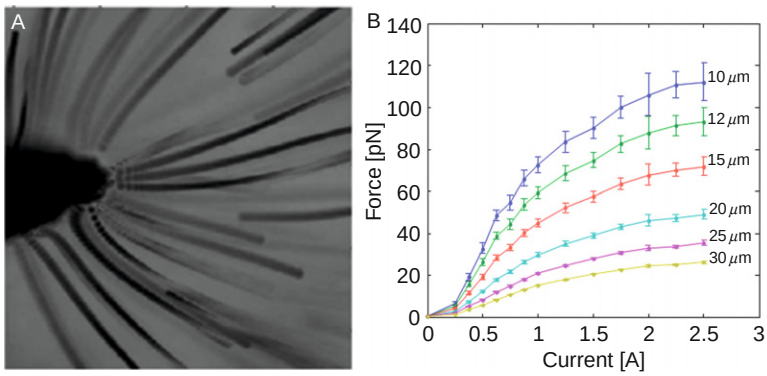

Fig. 3 Calibration of the poles. The force on a particular size bead will vary with the coil current and distance from the center of the pole tip. The forces around a pole are calculated from Stokes law by estimating the velocity of each bead during each pole activation. Video Spot Tracker software (CISMM) of movies made during pole activation in solutions of known viscosity provides position and time information for the calculation. (A) A "merged time lapse projection" of all the frames from the movie during a calibration run. Note the bead images are more distinct closer to the pole due to higher forces and higher velocities as they near the tip. (B) Graph of force vs applied current, calculated at the distances from the pole tip indicated.

V. Pole Configurations

The use of six poles, with three above and three below the specimen, could drive a bead in any direction the user needed. In practice, poles below the sample require very long working distance objectives, which decreases image magnification and/or resolution. We generally use either three poles or a "pole-flat" configuration with no poles below the sample. This allows high numerical aperture objectives close to the sample, which helps both brightfield and fluorescence microscopy during an experiment. In a three pole configuration, one pole of the user's choice is dominant, and the other two supply a return path. Since that choice can be rapidly modulated, the bead can be moved in all directions in the XY plane, with a slight upward, $+Z$ vector. In the pole-flat configuration, only the pole is dominant, and a bead can only be pulled toward that pole. The "flat" covers three opposite cores to supply the return path. The pole-flat is the configuration that, thus far, allows the most force to be generated on a bead, and is most used when high force and not fine position control is needed.

VI. Modes of Magnet Controls

Both the video-based and laser-tracked magnetic system can use the same magnetic controls. These are shown in Fig. 4, and are referred to by their labels (red lettering). These control modes offer a great variety of options for controlling the coil currents to each of six coils independently. The center top box shows the user interface (UI) representation of the current levels in each of the six poles driven by the software. This gives the user useful feedback as to the progress of the experiment.

A. Pole Control Mode

With this method, the current to each pole may be set independently. This is very close to a traditional "force clamp" experiment. However, since the force is dependent on bead position relative to pole tips, non-varying pole currents result in varying forces for moving beads. For immobile beads or beads moving in a very small area, this method of control closely approximates constant force. A three-dimensional input device, such as a Phantom from SensAble Technologies, can be used to specify pole currents via hand motion. In that case, the magnet control software updates the pole currents, in a real-time manner, based on bead position to maintain a constant force on a laser-tracked, moving bead.

B. Force Curve Control Mode

This method is most commonly used for simple experiments. A single pole is chosen as the "dominant" pole, and all other poles serve as a return path for magnetic flux. In this method of control, the current to the dominant pole is ramped from the initial amplitude to the final amplitude, held for a time, and then ramped back down to the initial amplitude. This pattern can be set to repeat indefinitely.

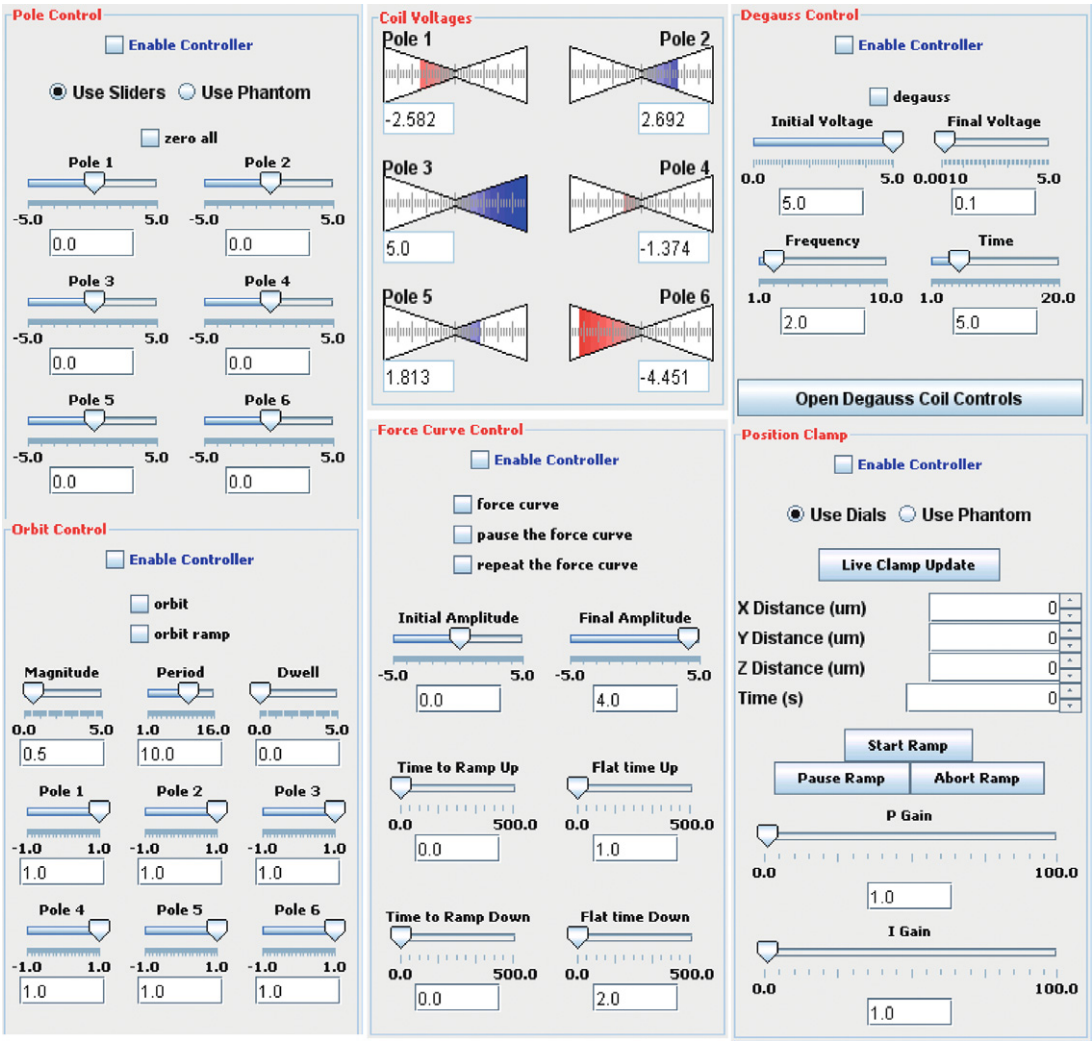

Fig. 4 Six panels from the Magnetics Control User Interface for the magnetics system. The uppermost labels (red) describe the main functionality of that panel. Each is discussed in detail in the main text.

C. Degauss Control Mode

This method of control is used to remove any remnant magnetization from the pole tips. An exponentially damped sinusoid of the given frequency is applied to all poles. For the damped sinusoid, users specify initial and final amplitudes, frequency, and the time over which the sinusoid decays from the initial to the final value. Individual poles can be excluded or have a sinusoid of opposite polarity.

D. Orbit Control Mode

This method of control allows users to pull a bead or magnetic rod in a small orbit with a controllable frequency. Each pole is activated in sequence. Each pole is independently addressable, so each leg of the orbit can be modified to a greater or lesser extent. In this manner, one can drive a very small "propeller" on the μm or sub-micron scale.

E. Position Clamp Control Mode

This method of control attempts to fix the position of a laser-tracked bead. In one mode, the present position of a bead is maintained via application of magnetic force. In another mode, the position of a bead is ramped to a given new position over a given time by magnetic force. A 3D-input device such as a Phantom, mentioned above, can be used to control the bead position with hand motion. All modes require that the bead be close to the magnetic center of a three- or six-pole magnet geometry. This method of control allows experimenters to ask questions such as: if I try to hold a bead attached to protein *X* in one place, what forces will act on it to move it, when do they start, how long do they last, and so on. The same questions can be asked of small motors within cells using this method of control.

VII. Cell Experiments with Magnetics

A. Video Tracked Cell Experiment

Experiments using the video-based magnetic system are straightforward to perform with cells or biological fluids. Figure 5A shows fibroblast cells with 2.8 carboxyl-magnetic beads attached. The displacement of the nearer bead is shown in panel B. The bead moves rapidly upon application of force, and then slowly continues to move until force is removed. The bead then returns with rapid and slow components of the curve toward its original position. The shape of both the active and return phases of these pulls provides information on the mechanical properties of the cell cytoplasm, the state of the cytoskeleton, anchors to the substrate, and other parameters that could be used to indicate reactions of the cell to local forces, or the response to drugs, or gene activity in response to knockouts or mutations.

B. Laser-Tracked Cell Experiment

An example of a laser-tracked experiment on live IMR90 cells is shown in Fig. 6. Figure 6A shows a brightfield image of the cells, pole tip and attached beads. Beads (1 μm Dynal MyOne) were attached to IMR90 cells via specific antibody linkages. In this case we attached the beads to biotinylated antibodies specific for either a ß1 integrin (CD 29) or a glycophosphotidal inositol (GPI)-linkage membrane protein (CD 73). Thus the ß1 should be anchored to the cytoskeleton, while the GPI

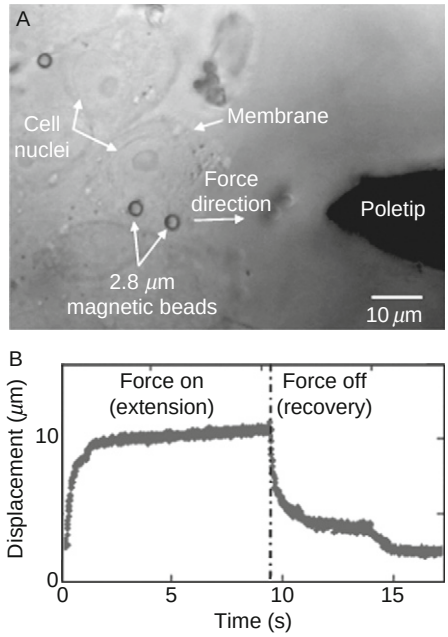

Fig. 5 An example of a video-based experiment used to text the viscoelastic properties of a cell body. (A) Human breast cancer cells were grown on a coverslip, and 2.8 μm carboxy magnetic beads (Dynal; Invitrogen, Inc) were added. (B) The displacement and recovery of the bead during and after a ~100 pN pull is shown.

anchor is expected to be coupled only to the outer leaflet of the cell membrane (Chen *et al.*, 2006). Since most of the movement was in the plane of the upper cell membrane (the X–Y plane), we display only displacements from the original position at zero time in the XY plane. We found that the GPI-anchored beads would often appear to be loosely tethered, and moved a great deal even without the application of force. In contrast, most of the beads treated with integrin antibodies appeared more tightly anchored, with less pre-force movement. Since we cannot know for certain that a bead is actually tethered as we expect, with only 1 or a few tethers, a large number of trials will be needed to establish these preliminary findings rigorously. However, the tracked bead data was often consistent with our impression during experiments, in that the pre-force movement of many GPI-anchored beads had a greater displacement, and the bead often moved farther with less force applied than did the bead attached via integrins. Panel B shows a typical response of a ß1-integrin tethered bead to a ~50 pN pull. The bead was displaced about 0.1 μm and returned slowly toward baseline after the force was turned off. The noise, or movement of the bead around its average position, stayed about the same during the pull as it was before and after. In contrast the GPI-anchored bead (Panel C) moved slight more but with only ~10 pN force application. It also showed a strong decrease in random movement during the pull, indicating a

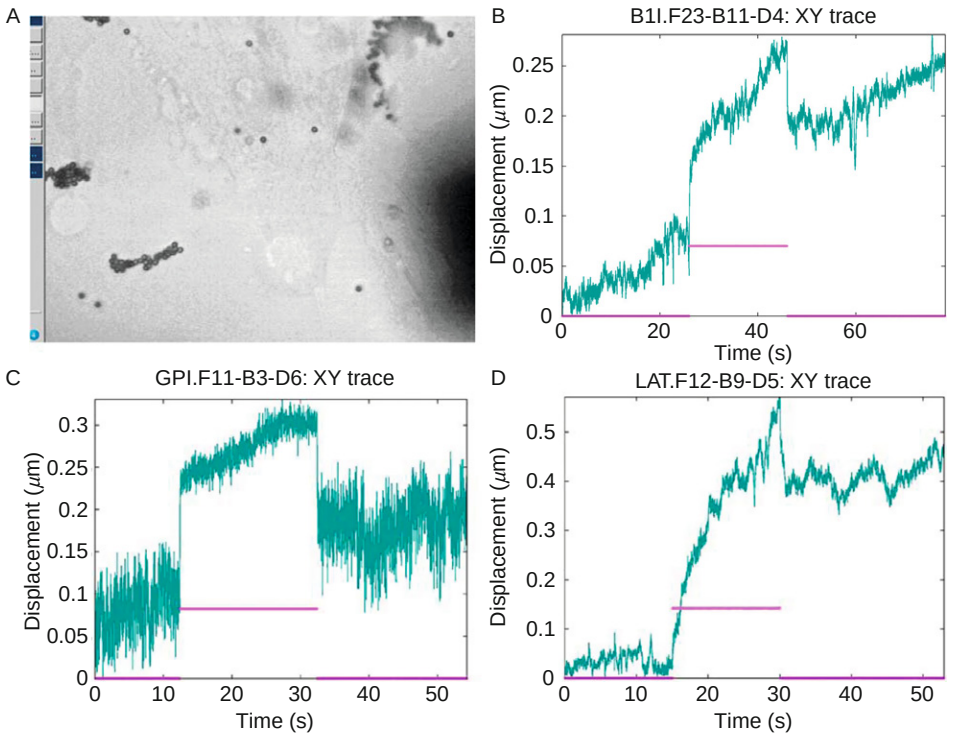

Fig. 6 Data from a laser-tracked experiment with 1 μm magnetic beads. The pole and IMR90 cells are shown in panel (A). Beads were attached via streptavidin-biotin linkages to antibodies to (B) CD29, an integrin, (C) CD73, an outer leaflet protein, or (D) CD29 but with an actin depolymerizing drug, latrunculin B (10 μM) present. 3D traces were generated, but only *XY* data is presented since most of the movement was in the plane of the upper cell membrane. The purple line shows when voltage was present at the coils.

non-linear response to forces (Desai *et al.*, 2008).The pre-pull level of noise immediately reappeared after the force returned to zero. Panel D shows a ß1-anchored bead after exposure of the cell to 1 μm latrunculin B for 10 min. The bead moves almost 400 nm, and does not return to its starting position, consistent with a breakdown of the actin cytoskeleton underneath the bead. These results are illustrative of the kinds of variables that can be explored using laser tracking with magnetics.

VIII. Driven Bead Rheology of Biologic Fluids

Driven microbead rheology (DMBR) is a rheological technique that has been used to study the viscoelastic response of cells and cell membranes (Bausch *et al.*, 1998, 1999) as well as to probe the semi-flexible regime of biopolymer networks

such as actin (Bausch *et al*., 2001). Measuring the material properties of soft solid biopolymers with DMBR offers several advantages over traditional techniques such as cone and plate (CAP). First, the sample sizes for driven-bead studies can be as small as 10 μL while CAP typically requires on the order of 1 mL. Microbeads offer the option of surface functionalization which provides a method for targeting specific components of a network or cell membrane (Fabry *et al*., 2001). Further, physiologically relevant length scales and time scales for biopolymer systems include those at the network and cellular level where macroscale measurements are insensitive. Examples include bacteria and cilia, which interact with mucus at length scales of 1 μm and 0.25 μm, far below CAP sensitivities but accessible to bead probes. Measurements at shorter time scales (higher frequencies) are possible with DMBR because inertia is minimized under low Reynolds number conditions. This provides a method for measuring spatial heterogeneities in a polymer system at length scales ranging from the size of the probe to the size of the specimen.

We present DMBR of two very different biopolymers: hyaluronic acid (HA) and sputum (Fig. 7). The first is expected to show a much higher uniformity in its properties, while sputum is very heterogeneous. HA is a viscoelastic biopolymer system that exhibits a thinning behavior where viscosity is diminished at high shear rates (Krause *et al*., 2001). Shown in Fig. 7A and B are creep measurements obtained using DMBR with 1 μm diameter beads embedded in a 10 mg/mL solution of HA. A creep experiment usually entails a constant force applied to a material for a finite period of time where the measured quantity is deformation, e.g. bead displacement. The material quantity derived from the experiment is the creep compliance, which is the inverse of stiffness. Materials that have high compliance deform easily when stressed. When measuring a linear material, although the displacement response of the bead will be faster at higher forces, the creep response is constant because force is normalized. The compliance curves in Fig. 7B all lie atop one another, denoting repeatability not only in the force-displacement measurement but the derived compliance measurement as well. The zero-shear viscosity is derived by computing the inverse-slope of steady-state compliance. Shown in Fig. 7B, inset, are macroscale measurements (line) shown where non-linear thinning is seen at high shear rates. Also plotted is the steady-state viscosity from the DMBR compliance curves. The viscosity measurements show correspondence between the two techniques, demonstrating that DMBR can be a reliable method for determining material rheological properties.

In contrast, sputum is a highly heterogenous material tested here with DMBR using 1 μm COOH-modified beads. The beads in sputum show widely varying velocities when given equal force impulses (Fig. 7C). Even in compliance space, these values vary widely (Panel 7D). Moreover, calculated viscosity of the sputum are seen to vary over two orders of magnitude (inset panel D). The lack of repeatability in the creep compliance indicates specimen heterogeneity at the length scale of the bead probe (Waigh, 2005). This heterogeneity may play an important role in bacterial motility through mucus layers (Matsui *et al*., 2006), and in particle transport for drug delivery (Dawson *et al*., 2003).

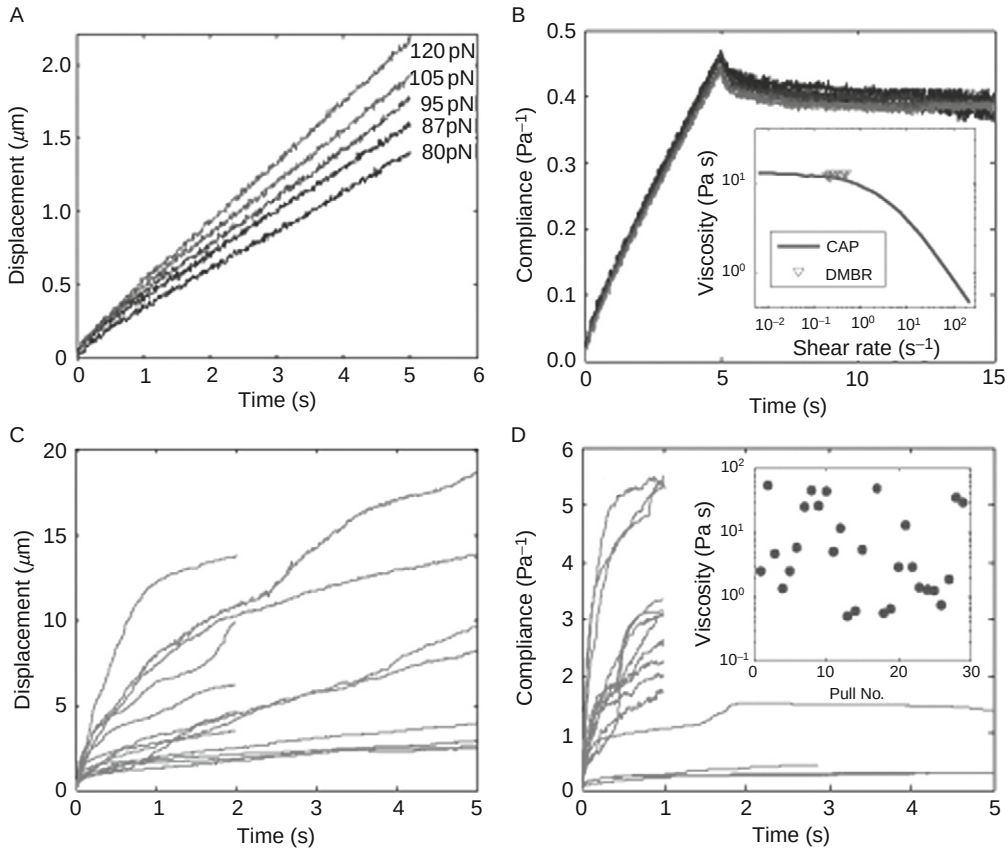

Fig. 7 Driven microbead rheology (DMBR) measurements of hyaluronic acid (HA) and human sputum using video analysis. Panel (A) shows displacement of 2.8 μm beads as they are pulled through a 10 mg/mL HA solution with forces that range from 80–120 pN. The curvature in the displacement at early time scales indicates elastic behavior, while the steady state velocity is related to the zero-shear viscosity. Panel (B) shows the reproducibility of the DMBR technique by plotting displacement that has been normalized by the step force, which results in a measure of ''creep'' compliance. Because this HA solution is a linear viscoelastic material at the probed shear rates, the disparate displacement curves in (A) collapse into a single curve when viewed in terms of compliance (B). Inverting the slope of the steady state compliance is equal to the long timescale (zero-shear) viscosity for HA. The inset shows a collection of these viscosities plotted with the cone and plate (CAP) flow profile for the same solution. This shows that the DMBR technique is internally reproducible and, under specific polymer system conditions, is consistent with CAP measurements. Panel (C) plots the displacements while Panel (D) plots compliance for 1 μm beads in human sputum. The displacement curves vary widely and show no tendency to collapse when viewed in terms of creep compliance, which implies that sputum could either be non-linear at the shear rates tested or that it is highly heterogeneous. Inconsistency in the curve shapes indicate spatial heterogeneity at length scales on the order of the bead's diameter. The inset shows that the range of computed viscosity felt by the beads in this sputum ranges widely across two orders of magnitude, from $\sim$1 Pa s up to $\sim$100 Pa s.

IX. Conclusions

Life is a mechanical process. Magnetic systems will be increasingly utilized to probe the mechanical properties of cells and tissues, and provide insight into the way those properties are controlled. The systems we describe are flexible, relatively easy to use, and can be tailored to a wide variety of experiments. They are easily combined with fluorescence microscopy, which will facilitate simultaneous readouts of effects of mechanical stimulation in the future. Magnetic manipulation can also be adapted to high throughput systems, which will allow more rapid exploration of complex signaling pathways related to force transduction via gene knockout or pharmacologic libraries.

Acknowledgements

We appreciate support from the National Institute of Biomedical Imaging and Bioengineering Resource grant for Computer Integrated Systems for Microscopy & Manipulation (CISMM) P41-EB002025–21A1, and NIH grant R01-EB000761 for 3D Force Microscopy. We also appreciate critical reading of the manuscript by Ben Evans and Vinay Swaminathan of UNC Chapel Hill.

References

Bausch, A. R., Hellerer, U., Essler, M., Aepfelbacher, M., and Sackmann, E. (2001). Rapid stiffening of integrin receptor-actin linkages in endothelial cells stimulated with thrombin: A magnetic bead microrheology study. *Biophys. J.* **80**(6), 2649–2657.

Bausch, A. R., Moller, W., and Sackmann, E. (1999). Measurement of local viscoelasticity and forces in living cells by magnetic tweezers. *Biophys. J.* **76**(1), 573–579.

Bausch, A. R., Ziemann, F., Boulbitch, A. A., Jacobson, K., and Sackmann, E. (1998). Local measurements of viscoelastic parameters of adherent cell surfaces by magnetic bead microrheometry. *Biophys. J.* **75**(4), 2038–2049.

Chen, Y., Thelin, W. R., Yang, B., Milgram, S. L., and Jacobson, K. (2006). Transient anchorage of cross-linked glycosyl-phosphatidylinositol-anchored proteins depends on cholesterol, Src family kinases, caveolin, and phosphoinositides. *J. Cell Biol.* **175**(1), 169–178.

CISMM. Computer integrated systems for microscopy and manipulation. Accessed from http://www.unc.edu/CISMM

Dawson, M., Wirtz, D., and Hanes, J. (2003). Enhanced viscoelasticity of human cystic fibrotic sputum correlates with increasing microheterogeneity in particle transport. *J. Biol. Chem.* **278**(50), 50393–50401.

Desai, K. V., Bishop, T. G., Vicci, L., O'Brien, E. T., Taylor, R. M., and Superfine, R. (2008). Agnostic particle tracking for three-dimensional motion of cellular granules and membrane-tethered bead dynamics. *Biophys. J.* **94**(6), 2374–2384.

Fabry, B., Maksym, G. N., Butler, J. P., Glogauer, M., Navajas, D., and Fredberg, J. J. (2001). Scaling the microrheology of living cells. *Phys. Rev. Lett.* **8714**(14), 148102(1–4).

Feneberg, W., Aepfelbacher, M., and Sackmann, E. (2004). Microviscoelasticity of the apical cell surface of human umbilical vein endothelial cells (HUVEC) within confluent monolayers. *Biophys. J.* **87**(2), 1338–1350.

Fisher, J. K., Cribb, J., Desai, K. V., Vicci, L., Wilde, B., Keller, K., Taylor, R. M., Haase, J., Bloom, K., O'Brien, E. T., and Superfine, R. (2006a). Thin-foil magnetic force system for high-numerical-aperture microscopy. *Rev. Sci. Instrum.* **77**(2), nihms8302: 1–8.

Fisher, J. K., Vicci, L., Cribb, J., O'Brien, E. T., Taylor, R. M., II, and Superfine, R. (2006b). Magnetic force micromanipulation systems for the biological sciences. *NANO Brief Rep. Rev.* **1**(3), 191–205.

Krause, W. E., Bellomo, E. G., and Colby, R. H. (2001). Rheology of sodium hyaluronate under physiological conditions. *Biomacromolecules* **2**(1), 65–69.

Lai, S. K., O'Hanlon, D. E., Harrold, S., Man, S. T., Wang, Y. Y., Cone, R., and Hanes, J. (2007). Rapid transport of large polymeric nanoparticles in fresh undiluted human mucus. *Proc. Natl. Acad. Sci. USA* **104**(5), 1482–1487.

Lele, T. P., Sero, J. E., Matthews, B. D., Kumar, S., Xia, S., Montoya-Zavala, M., Polte, T., Overby, D., Wang, N., and Ingber, D. E. (2007). Tools to study cell mechanics and mechanotransduction. *Methods Cell Biol.* **83,** 443–472.

Marshburn, D., Weigle, C., Wilde, B. G., Taylo, R. M., II, Desai, K. V., Fisher, J. K., Cribb, J., O'Brien, E. T., and Superfine, R. (2005). "The Software Interface to the 3D-Force Microscope." IEEE Visualization 2005, IEEE Computer Society, Minneapolis, MN.

Matsui, H., Wagner, V. E., Hill, D. B., Schwab, U. E., Rogers, T. D., Button, B., Taylor, R. M., II, Superfine, R., Rubinstein, M., Iglewski, B. H., and Boucher, R. C. (2006). A physical linkage between cystic fibrosis airway surface dehydration and *Pseudomonas aeruginosa* biofilms. *Proc. Natl. Acad. Sci. USA* **103**(48), 18131–18136.

Waigh, T. A. (2005). Microrheology of complex fluids. *Rep. Prog. Phys.* **68**(3), 685–742.

Wang, N., Butler, J. P., and Ingber, D. E. (1993). Mechanotransduction across the cell surface and through the cytoskeleton. *Science* **260**(5111), 1124–1127.

CHAPTER 17

Application of Laser Tweezers to Studies of Membrane–Cytoskeleton Adhesion

Drazen Raucher

Department of Biochemistry
University of Mississippi Medical Center
Jackson, Mississippi 39216

Abstract

Interaction between the plasma membrane and cytoskeleton is important in regulating cell functions such as lamellipodial extension, cell motility, and endocytosis. Here, we describe a method to determine plasma membrane-cytoskeleton adhesion by measuring tether force using laser optical tweezers. We show the basic components and instrumental setup of a laser optical tweezers system which is used

METHODS IN CELL BIOLOGY, VOL. 89

0091-679X/08 $35.00
DOI: 10.1016/S0091-679X(08)00617-1

to pull thin membrane tethers from the cell surface using one micron polystyrene beads coated with membrane binding ligands. We also show an application of tether force measurements in elucidating regulation of membrane-cytoskeleton adhesion. That phosphatidylinositol-4,5-biphosphate (PIP2) may play an important role in regulating membrane-cytoskeleton adhesion is suggested by correlating the plasma membrane concentration of PIP2 with membrane-cytoskeleton adhesion using tether force measurements. The assay described here enables us to investigate mechanochemical components of many important cellular processes, such as lamellipodial extension, cell motility, membrane resealing after cell wounding, and endocytosis. Furthermore, this method could be used to establish the link between biochemical function and physical properties of the plasma membrane which drives these dynamic cellular processes.

I. Introduction

A. Laser Tweezers Basic Principle

Optical tweezers, also known as optical traps, use a laser beam focused through a high-quality microscope objective to generate an "optical trap," which is able to constrain microscopic objects, such as small dielectric spheres.

The underlying principle of laser optical tweezers has been known for many years. At the beginning of the 19th century, microscopists learned that light of a high power density focused through a microscope could be used to manipulate biological objects. In 1970, Arthur Askhin found that small particles may be trapped by the radiation pressure of a laser beam. The first demonstration of optical tweezers with the basic three-dimensional single-beam trap configuration was reported in 1986 (Ashkin *et al*., 1986). Later in 1987, Ashkin and his group reported trapping viruses and *Escherichia coli* bacteria (Ashkin and Dziedzic, 1987; Ashkin *et al*., 1987). Recent technical innovations established optical tweezers as a biological tool for studying biological forces.

The principle of optical tweezers arises from the momentum of the light itself, which may be transferred to the refracting particle generating "radiation pressure." The momentum of the light is in the direction of propagation of the beam, and it is proportional to the propagation vector of the electromagnetic field. When the light passes through small objects made from a dielectric material (such as polystyrene beads) suspended in fluid media of lower refractive index, light rays will be bent by the refraction in the object and will change their direction. The change in the direction of light indicates a corresponding change in light momentum. The principle of conservation of momentum requires that there should be an opposite and equal momentum change on the object. As a result, force exerted by the light ("radiation pressure") is acting on the object, and that force is capable of pushing the object around. However, to use optical tweezers to trap and move dielectric particles and biological objects, it is necessary to hold them in all three dimensions.

This can be accomplished by a Gaussian profile laser beam focused through a high numerical aperture (NA) microscope objective. Because of Gaussian beam symmetry and the high NA of the objective, a sharp three-dimensional light-intensity gradient forms near the focal point of the lens. As a result, this gradient introduces a force directed toward the focal point that has the ability to optically trap small particles in both lateral and axial directions. Trapped particles can then be moved by translating the microscope stage or by adjusting the focal point of the laser beam.

B. Current Applications of the Laser Optical Tweezers

Because of its ability to trap and release objects ranging from tens of nanometers to many micrometers, optical tweezers may be used for many applications. For stable trapping, laser powers in the range of several milliwatts up to several watts are used, producing forces ranging from 0.1 to 200 pN. Optical tweezers may be used to apply forces on proteins, DNA, cell organelles, and living cells and therefore offers a unique advantage for studying biological forces. As a result, optical tweezers have been used as force transducers for force measurements in many biological applications. There are an extensive number of applications for optical tweezers at the molecular level. For example, optical tweezers have been used to pull DNA apart to investigate its resistance to stretching (Smith *et al.*, 1996) and to measure forces needed to unfold chromatin DNA from nucleosomes (Bennink *et al.*, 2001). Optical tweezers have also been used to examine the mechanical properties of actin filaments, titin molecules, and microtubules. Using tweezers, Tsuda *et al.* (1996) determined the torsional rigidity and breaking force of single actin filaments. Visco-elastic properties of titin, which is responsible for the elasticity of relaxed striated muscle, were investigated by several groups (Kellermayer *et al.*, 2000; Linke, 2000; Tskhovrebova *et al.*, 1997). Felgner *et al.* used optical forces of the laser trap to directly manipulate microtubules and measure the flexural rigidity of single microtubules (Felgner *et al.*, 1996, 1997).

Optical tweezers are widely used to measure the force of molecular motors, such as cytoplasmic dynein (Mallik *et al.*, 2004; Wang *et al.*, 1995), kinesin, and myosin. In one study, Mallik *et al.* (2004) used an optical trap to quantify motion of polystyrene beads driven along microtubules by single cytoplasmic dynein motors. They reported that dynein has a step size of 8 nm and produces force up to 1.1 pN when moving against load applied by an optical trap. Several groups have measured isometric forces and the force dependence of steps in the mechanochemical cycle of kinesin (Block *et al.*, 1990; Kuo and Sheetz, 1993; Svoboda *et al.*, 1993). From these studies, it has been confirmed that the step size of kinesin is distributed stochastically around multiples of 8 nm, and it may produce a maximum force of about 2 pN.

While optical tweezers are mostly used in reconstituted systems, there are also some limited studies of subcellular organelles in living cells. Askhin and Dziedzic used an infrared laser trap to apply forces inside living cells to study the mechanical

properties of the cytoplasm of plant cells (Ashkin and Dziedzic, 1989). Optical tweezers have also been used to characterize the mechanical properties of the cell membrane and of membrane–cytoskeleton adhesion. When carboxylated polystyrene microparticles coated with IgG, IgM, or concavalin A were held on the lipid vesicle or cell surface for ~4–5 s and then pulled by laser tweezers, a membrane tube of constant diameter (tether) is formed. In pure lipid vesicles, tether formation is strongly dependent on the membrane's mechanical characteristics, such as bending stiffness and in-plane tension of the lipid bilayer (Bo and Waugh, 1989; Waugh *et al.*, 1992). In biological systems, such as living cells, the situation is more complicated (Sheetz, 2001). The eukaryotic plasma membrane is coupled to the intracellular cortical cytoskeleton. Since the cytoskeleton does not move into the membrane upon tether formation (Raucher *et al.*, 2000), there is a separation between tether membrane components and their cytoskeletal binding sites. Therefore, membrane components in a tether have higher free energy than membrane in contact with cytoskeleton, and the tethered membrane will tend to retract back to the cell surface. As a result, there is osmotic pressure between the membrane in a tether and the plasma membrane in contact with the cytoskeleton which contributes to tether force. The contribution of in-plane tension and bending stiffness of the plasma membrane may be estimated by measuring tether force in membrane blebs, which do not contain any cytoskeletal structures (Keller and Eggli, 1998b). The measured tether force in membrane blebs was only 20% of the tether force formed on cytoskeleton-containing regions (Raucher *et al.*, 2000), indicating that membrane–cytoskeleton adhesion contributes the major portion of tether force. Thus, the measurement of tether force directly reflects membrane–cytoskeleton adhesion. The exact relationship between tether force and membrane–cytoskeleton adhesion is presented in Section II.

C. Significance of Membrane–Cytoskeleton Adhesion Energy

Membrane–cytoskeleton adhesion is of essential importance not only in defining a cell's shape but also in the regulation of a variety of cell functions. In mitotic cells, a marked rise in membrane–cytoskeleton adhesion is accompanied by a drop in endocytosis rate (Raucher and Sheetz, 1999). Addition of detergents, organic solvents, or other amphiphilic compounds stimulates endocytosis and results in decreased membrane–cytoskeleton adhesion, which suggests that membrane–cytoskeleton adhesion plays an important role in regulating the endocytosis rate.

Membrane–cytoskeleton adhesion is also involved in the regulation of cell spreading and lamellipodial extension (Raucher and Sheetz, 2000). Polymerization of actin filaments during lamellipodial extension must overcome resistance from tension within the plasma membrane. Addition of fluorescent lipids or amphiphilic compounds stimulates new lamellipodial extensions and causes a decrease in membrane–cytoskeleton adhesion. Furthermore, quantitative analysis shows that the lamellipodial extension rate is inversely correlated with membrane–cytoskeleton adhesion.

Membrane–cytoskeleton adhesion is also involved in many other cell processes, such as stimulation of secretion and membrane resealing after cell wounding (reviewed in Sheetz, 2001). This chapter will describe the basic laser optical tweezers setup, a simple relationship used to calculate membrane–cytoskeleton adhesion energy from tether force, and a basic method for membrane–cytoskeleton adhesion measurements. The role of the phosphatidylinositol-4,5-biphosphate (PIP2) in controlling membrane cytoskeleton adhesion will be also considered.

II. Materials and Methods

A. Cell Culture

Mouse fibroblast NIH-3T3 cells were grown as a monolayer in Dulbecco's Modified Eagle Medium (DMEM, GIBCO, Grand Island, NY) supplemented with 100 units/ml penicillin and 100 mg/ml streptomycin, 1 mM glutamine, 7.5 mM 4-(2-hydroxyethyl)-1-piperazineethanesulfonic acid (HEPES), and 10% fetal bovine serum (FBS) at 37 °C in 5% CO_2. Cells were removed from the T-75 tissue culture flask by brief treatment with 0.25% trypsin/ethylenediaminetetraacetic acid (EDTA) and plated into Petri dishes that contained 24 × 50 mm coverslips. Cells were used for experiments one day after plating. In experiments designed to investigate the role of PIP2 in membrane–cytoskeleton adhesion, cells were transiently transfected with an expression vector that encoded the pleckstrin homology (PH) domain of phospholipase C δ fused to the amino terminus of the green fluorescent protein (GFP) as previously described (Raucher *et al.*, 2000).

B. Bead Preparation

To form a membrane tether, polystyrene beads must tightly bind to the plasma membrane surface. To achieve this, beads are coated with different proteins such as lectins, immunoglobulins or extracellular matrix proteins. To prepare IgG-coated beads, 100 ml of 2.5% carboxylated polystyrene (1 μm) beads (Polysciences, Warrington, PA) were placed into an Eppendorf centrifuge tube. The beads were then mixed with 1 ml of 0.1 M carbonate buffer prepared by adding 0.1 M Na_2CO_3 to 0.1 M $NaHCO_3$ until the pH was 9.6. The beads were then pelleted by centrifugation at 2000 × g at 4 °C for 10 min, the supernatant was removed, and the beads were resuspended in fresh carbonate buffer and recentrifuged. The beads were washed twice in 0.02 M sodium phosphate buffer (prepared by adding 0.02 M Na_2HPO_4 to 0.02 M NaH_2PO_4 until the pH was adjusted to 4.5) using the same procedure. The pellet was then resuspended in 0.625 ml of 2% carbodiimide solution (1-(3-dimethylaminopropyl)-3-ethyl)) carbodiimide hydrochloride dissolved in phosphate buffer) and 0.625 ml of sodium phosphate buffer. The beads were then gently stirred for 3–4 h at room temperature using a rotary shaker. Beads were washed twice with phosphate solution, washed twice with Dulbecco's

phosphate-buffered saline (DPBS, GibcoBRL, Grand Island, NY), resuspended in 100 μl of PBS and incubated overnight at 4 °C with 20 μl of 1 mg/ml mouse IgG (Sigma, St. Louis, MO). Next, beads were pelleted by centrifugation and washed twice in PBS to remove unbound IgG. Unreacted sites on the polystyrene beads were then blocked by resuspending beads in 1 ml of 1 mg/ml bovine serum albumin–PBS. Finally, the beads were washed 3 times and diluted 30-fold for the experiment.

C. Instrumental Setup of Laser Tweezers

The basic laser optical tweezers experimental setup includes a laser, focusing lenses, and mirrors, which are added to a Zeiss Axiovert 200 inverted microscope (Zeiss, Oberkochen, Germany). The Zeiss Axiovert is one of the latest generations of high-quality, inverted optical microscopes designed to perform differential interference contrast (DIC) microscopy as well as fluorescence microscopy in live cells, but any good research quality microscope can have laser optical tweezers added to it. The main requirement is that the objective lens has a high NA (1.0 or greater) to focus the laser light at a sufficient gradient angle to create a powerful optical trap (Svoboda and Block, 1994).

In our studies, we used the argon ion laser-pumped continuous-wave titanium-sapphire laser (Verdi 5 watt Laser System and 890 Ti:S Broadband Laser, Coherent, Inc., Palo Alto, CA). With the use of a tunable Ti:Sapphire laser, it is possible to select a wavelength between 780 and 1100 nm, which is the region of minimum absorption of biological material (Svoboda and Block, 1994). Therefore, to minimize thermal effects and avoid damage of biological samples from the laser light, a wavelength of 798 nm was used in this work.

The trapping system is schematically presented in Fig. 1A. The main purpose of the optics between the laser and the microscope is to expand and steer the laser beam to the microscope objective. An electronic shutter, which is operated by a foot pedal, is used to keep laser beam off at all times when not trapping. The laser beam first passes through the beam expander, which is used to magnify the laser's beam diameter. Then, the laser light is diverted to the microscope's epi-fluorescence port with a laser beam steerer, which consists of two kinematic mirrors oriented orthogonally over one another and mounted on gimbals capable of fine angular adjustments. The laser beam then passes through a variable attenuator, which is a simple polarizer used to vary the intensity of the beam while trapping and to minimize the intensity of the laser beam during optics alignment. A focusing lens, which is mounted on a three-axis translation stage, focuses the laser beam to a dichroic mirror transparent to the image illumination, which reflects the laser beam into the objective. The laser beam passes through the microscope objective and may be focused anywhere on the sample slide forming a laser optical trap. All essential components of the laser trap system using the epifluorescence port are shown in Fig. 1B.

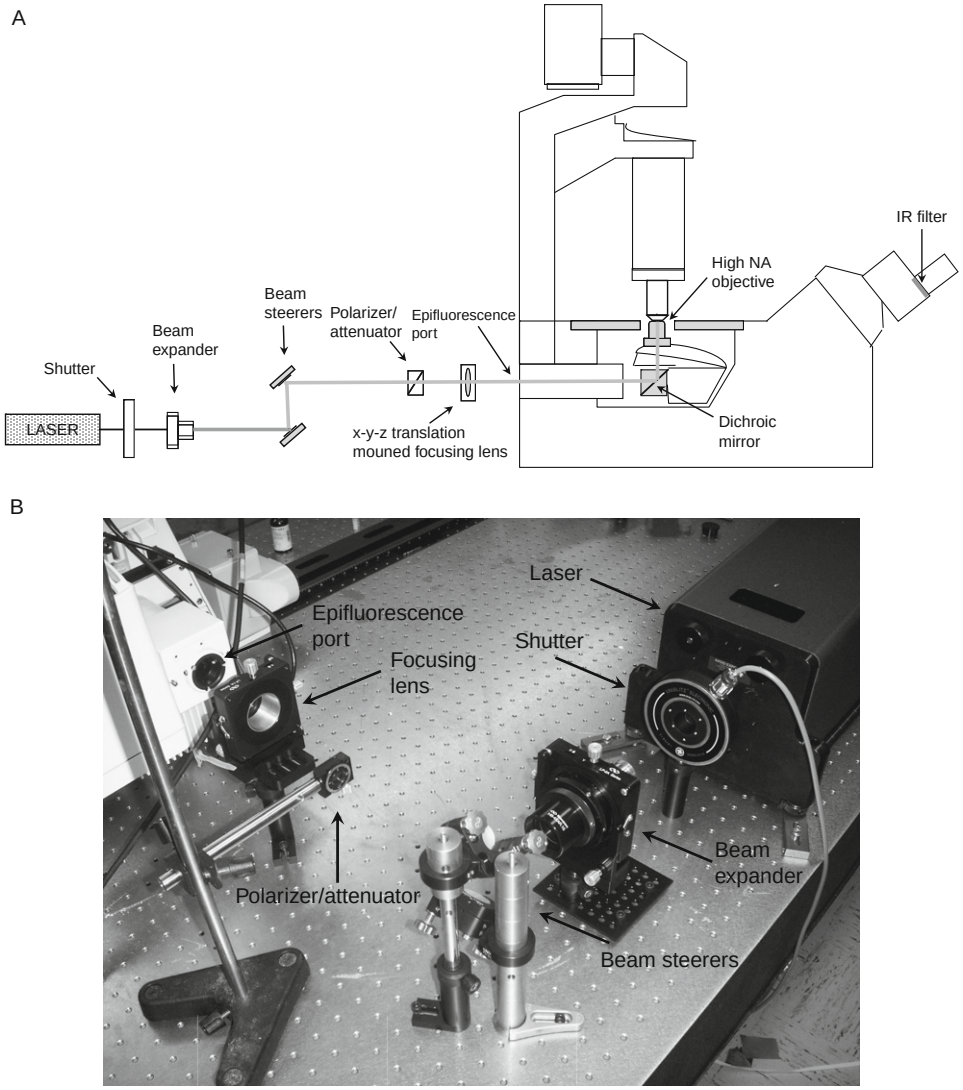

Fig. 1 Basic Laser Optical Tweezers System (A). Schematic presentation of a laser trapping system using the epifluorescence port with a beam expander, shutter, attenuator, and focusing lens. (B) Picture of laser optical tweezers system.

D. Data Acquisition and Analysis

To measure membrane–cellular adhesion, membrane tethers were formed as shown in Fig. 2A. Briefly, IgG-coated beads were trapped with laser tweezers, held on the cell surface for several seconds, and then pulled away from the cell surface, thus forming the thread-like membrane tethers. The beads were then held

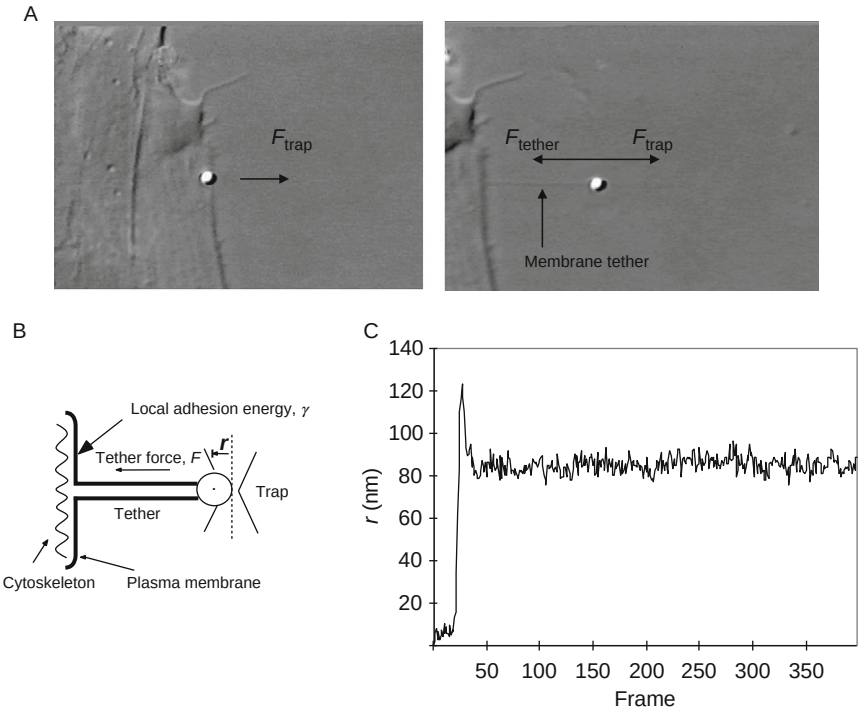

Fig. 2 Tether Force Measurement (A) Video-enhanced differential interference contrast (DIC) image of tether force measurement using laser optical tweezers. The bead was attached to the plasma membrane (left panel) and pulled away from the cell surface, thus forming a membrane tether. (B) Schematic presentation of optical tweezers tether force measurements. The force pulling the bead back to the cell (tether force) causes displacement of the bead from the center of the trap. (C) Displacement trace, showing that bead has moved from the center of the trap. Displacement is directly proportional to tether force.

at constant length (8–12 μm), and the tether force on the bead was measured by its displacement from the center of the laser trap (Fig. 2B). At a constant length, the force of the tether (F_{tether}) which is pulling the bead back to the cell surface is opposed by the force of the laser optical tweezers trap (F_{trap}). Displacement of the bead from the center of the trap (r) is directly proportional to the tether force. A typical displacement trace is shown in Fig. 2C. When the bead is attached to the plasma membrane, there is no displacement. The displacement increases during tether elongation and peaks during the initial tether extension due to the viscous flow of membrane into the tether. Finally, when the tether is held at a constant length, displacement from the center of the trap is constant and represents the static tether force. As further discussed below, the main contribution to tether force is the energy required to detach the plasma membrane from the cytoskeleton, called the membrane–cytoskeleton adhesion energy.

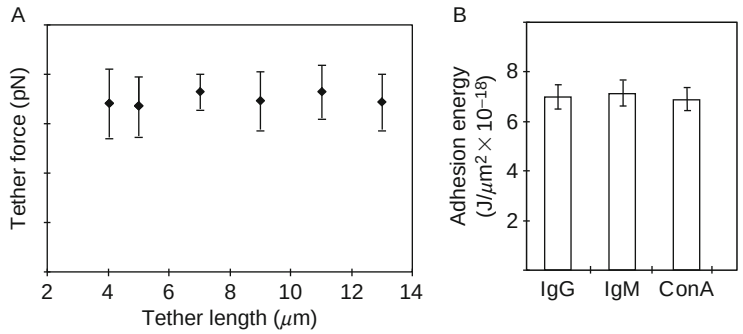

Fig. 3 Tether Force is Independent of Tether Length and Mechanism of Bead Attachment. (A) Single membrane tethers were pulled to different lengths, and the corresponding tether force was measured. (B) One micron polystyrene beads were coated with different membrane binding ligands. The measured adhesion energy is independent of the mechanism of bead attachment.

When tethers were pulled at different lengths, there was no detectable change in static tether force (Fig. 3A). Similarly, when the same bead was used to form membrane tethers varying in length from 3 to 14 μm, the static tether force did not change (data not shown) indicating that the static tether force is independent of tether length. While magnitude of tether force is dependent on the cell line, it is independent of tether length. To investigate whether tether force measurements are dependent on the mechanism of bead attachment, beads coated with different ligands were tested. Figure 3B shows that the tether force was independent of bead coating (IgG, IgM, or ConA). Similarly, fibroblasts plated on glass, laminin, or polylysine had the same plasma membrane to cytoskeleton adhesion energy (data not shown).

In order to correctly measure membrane–cytoskeleton adhesion forces, the optical tweezers have to be calibrated to accurately determine the tweezers force. Several methods have been developed to correlate the force in the trap to the measured displacement (Felgner *et al.*, 1996; Nambiar *et al.*, 2004; Svoboda and Block, 1994). One method is based on thermal fluctuations of a trapped particle. From parameters, such as particle temperature, thermal vibration amplitude, and frequency, one can calculate the force constant of the trap. In our studies, we have used a different method in which we compare trap stiffness with viscous drag generated by the oscillatory motion of the particle with respect to its liquid environment. The position of the bead is tracked, and displacement of the bead from the center of the trap is correlated with viscous force, which can be calculated from Stoke's friction law. The trap force is then calculated straightforwardly from this linear relationship between displacement of the bead and trap stiffness. Laser tweezers trap calibration is described in detail in Dai and Sheetz (1995). A Newvicon camera (model VE-1000; DAGE-MTI, Inc.) was used to acquire DIC images of the trapped beads, and sequences of tether pulling were digitally recorded and stored on a computer hard drive. Images were analyzed with a

commercial video tracking software package (ISee Imaging Systems, Raleigh, NC) using the nano-track cross-correlation routine. Displacement of the bead from the center of the trap has a tracking accuracy of 4–5 nm for the 1 μm particle (Galbraith *et al.*, 2002). A typical force pattern is shown in Fig. 2C.

III. Tether Force Measurements of the Adhesion Energy Between the Plasma Membrane and the Cortical Cytoskeleton

A. Relationship Between Tether Force and Membrane–Cytoskeleton Adhesion Energy

Tether force is the force needed to hold a plasma membrane tether at a constant length with laser tweezers. To assess membrane–cellular adhesion from tether force, it is necessary to consider all forces involved in tether formation. Tether formation requires changes in the shape of the underlying membrane and thus is dependent on the membrane's mechanical characteristics. Tethers formed from phospholipid vesicles may be accurately explained in terms of the curvature elastic modulus (bending stiffness) and membrane tension (Bo and Waugh, 1989; Waugh and Hochmuth, 1987), which is supported by an original theoretical analysis (Waugh and Hochmuth, 1987; Waugh *et al.*, 1992). However, the situation in living cells is much more complicated (Hochmuth and Marcus, 2002; Marcus and Hochmuth, 2002; Waugh and Bauserman, 1995). Cell membranes are intrinsically fluid in character and require stabilization by association with an underlying intracellular cortical cytoskeleton. In addition, the eukaryotic plasma membrane is highly heterogeneous, due to the presence of specialized membrane domains (lipid rafts) which are enriched in cholesterol, saturated phospholipids, and sphingolipids (Dopico and Tigyi, 2007; Foster and Chan, 2007).

Hochmuth *et al.* (1996) presented a basic energy analysis of the membrane tethers extracted at a constant velocity from neuronal growth cones using a force generated by a laser tweezer trap. The energy representation is clearer than the tension or force representation since the different terms that contribute to the tether force are additive. The measured tether force is the sum of the bending energy component, the energy component corresponding to tension in the membrane bilayer plane, and the energy of the membrane–cytoskeleton adhesion component (Fig. 4A) as described in the following equation:

$$\begin{aligned} E(R) = \pi BL/R(\text{bending energy}) + 2\pi RTL(\text{in} - \text{plane tension energy}) \\ + 2RL(\text{membrane} - \text{cytoskeleton adhesion energy}) \end{aligned} \quad (1)$$

where B is the bending modulus for a membrane bilayer, which depends on bilayer properties (e.g., fluidity or bending stiffness). The bending energy, therefore, is the work required to bend the membrane bilayer away from the cell surface. L is the length of the tether, R is the tether radius, T is the in-plane tension, and γ is the cytoskeleton to plasma membrane adhesion energy per unit area.

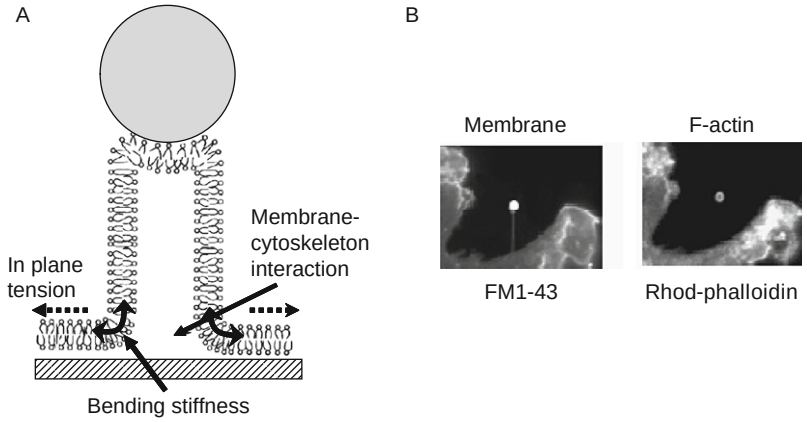

Fig. 4 Major Factors which Contribute to Tether Force (A) Schematic presentation of the major factors which contributes to the tether force: membrane–cytoskeleton adhesion energy, γ, tension in the bilayer plane, T_m, which resists deformation of the membrane, and membrane bending stiffness, *B*. (B) The membrane of a 3T3 mouse fibroblast cell was stained with FM1-43 (left panel), and the F-actin filaments of the same cell were co-stained with rhodamine phalloidin (right panel).

The cell plasma membrane normally conforms to the cytoskeleton, and the membrane in-plane tension term seems to be almost constant for the whole cell membrane surface. Nonspherical cells have a strong membrane–cytoskeletal interaction, and the in-plane tension term is small in comparison to the adhesion term and can therefore be omitted from Eq. (1):

$$E(R) = \pi BL/R + 2\pi R\gamma L \tag{2}$$

The energy Eq. (2) reaches its minimum for

$$dE/dR = 0 \; or \; R = [B/2\gamma]^{1/2} \tag{3}$$

Therefore, the relationship between the tether force (F) and the membrane adhesion energy (γ) is independent of R and L:

$$F = dE/dL = 2\pi[2\gamma B]^{1/2} \tag{4}$$

The final expression for membrane adhesion energy, γ, which is used to calculate adhesion energy from the measured tether force is

$$\gamma = F^2/[8\pi B] \tag{5}$$

The membrane bilayer bending modulus may be determined experimentally by measuring the tether force and tether diameter from the following equation (Waugh and Hochmuth, 1987):

$$B = FR/[2\pi] \tag{6}$$

Cell membranes are intrinsically fluid in character and require stabilization by association with an underlying cytoskeleton. Instability in the association between the membrane bilayer and the cytoskeleton results in membrane blebs. When tethers are pulled from membrane blebs, the measured tether force primarily reflects the bending energy. From a measured tether diameter of $\sim$0.34 μm and a force of 2.5 pN in blebs of NIH-3T3 fibroblasts, using the relationship derived in Eq. 6, the estimated bilayer bending modulus is $B = 6.8 \times 10^{-20}$ J. Therefore, using the relationship described in Eq. (6), the membrane–cytoskeleton adhesion energy (γ) may be estimated from the measured tether force (F).

The straightforward relationship between tether force and adhesion energy described in Eq. (6) is based on the findings that tethers lack cytoskeletal support. Ultrastructural evidence indicating that tethers do not contain membrane skeleton and that they are deficient in at least some integral membrane proteins was documented previously in red blood cells (Berk and Hochmuth, 1992; Waugh and Hochmuth, 1987). In order to confirm that tethers pulled from fibroblast do not have cytoskeletal structures, we tested the membrane tether for the presence of F-actin by comparing tethers co-stained with FM1-43, which fluoresces when bound to a membrane (Fig. 4B left), and with rhodamine phalloidin, which is a marker for actin filaments (Fig. 4B, right). As shown in Fig. 4, there were no F-actin filaments found in membrane tethers. That tethers have the same viscous properties as tethers pulled from lipid vesicles without cytoskeleton is also consistent with the observation that they retracted rapidly ($<$100 ms) when the trap was turned off (data not shown).

B. Molecular Basis of Plasma Membrane–Cytoskeleton Adhesion

It is well documented that membrane–cytoskeleton adhesion is of essential importance in the regulation of a variety of cell functions (reviewed in Sheetz, 2001). While cell–cell and cell–extracellular matrix adhesion have been the subjects of many studies and are fairly well understood, less is known about the molecular mechanism that regulates plasma membrane–cytoskeleton adhesion. Because of the rapid dynamics of the cell membrane in processes, such as endocytosis, lamellipodial extension, cell movement, and signaling, the interaction between membrane and cytoskeleton is better explained by many weak bonds between cytoskeleton and membrane lipids than by a few strong bonds between cytoskeletal and integral membrane proteins. One of the interesting candidates for such a weak and dynamic interaction between cytoskeleton and cell membrane is the plasma membrane phopholipid PIP2. This hypothesis is consistent with the observation that a decrease in membrane–cytoskeleton adhesion due to exposure to local anesthetics is accompanied by a decrease in PIP2 plasma membrane concentration (Raucher and Sheetz, 2001). Therefore, we investigated the link between membrane–cytoskeleton adhesion and PIP2 by manipulating the level of PIP2 in the plasma membrane and by measuring membrane–cytoskeleton adhesion using laser optical tweezers (Raucher *et al.*, 2000).

The pleckstrin homology (PH) domain from PLCδ has a very high affinity for plasma membrane PIP2. Therefore, to sequester PIP2 cytoskeletal binding sites in the plasma membrane, we expressed the PH domain from PLCδ tagged with green fluorescent protein (PH(PLCδ)-GFP) in NIH 3T3 fibroblasts. The exogenously expressed PH(PLCδ)-GFP showed plasma membrane localization, indicating binding to plasma membrane PIP2 (Fig. 5A). A control construct (PH*(PLCδ)-GFP) with mutations (Lys30Asn and Lys32Asn) that prevent binding of PIP2, showed no membrane localization (Fig. 5B). Expression of PH(PLCδ)-GFP was accompanied by a dramatic reduction in membrane–cytoskeleton adhesion (Fig. 5C). In control measurements, the adhesion energy was the same in cells expressing (PH*(PLCδ)-GFP) or a PH(Akt)-GFP construct which binds PI(3,4)P2 (Franke *et al.*, 1997).

In order to directly examine the connection between PIP2 concentration and adhesion energy, we selectively reduced the concentration of PIP2 in the plasma membrane by expressing PIP2-specific 5′ phosphatase (PM-5′-phosp-GFP) targeted

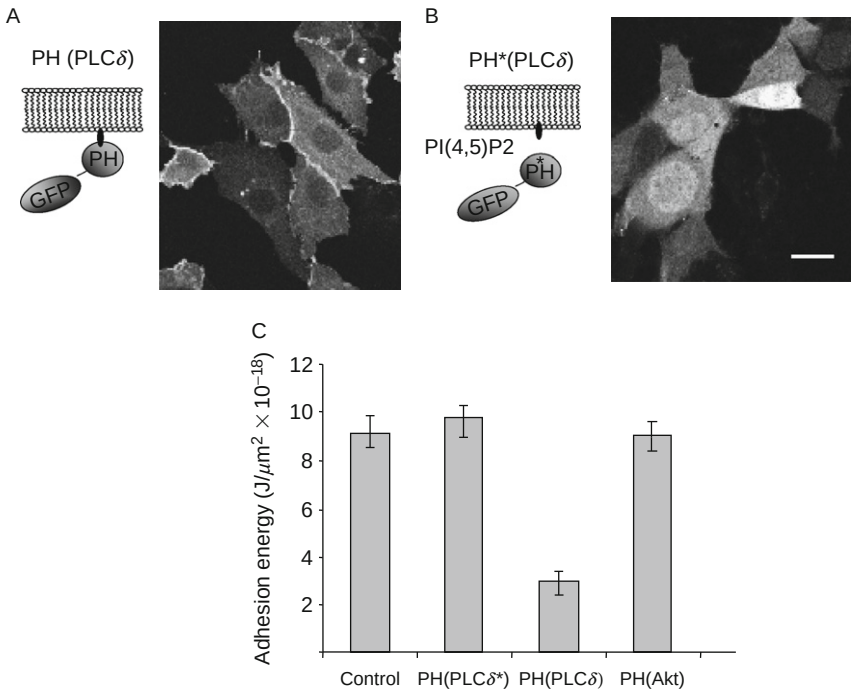

Fig. 5 Expression of pleckstrin homology (PH) domains that selectively bind to plasma membrane phosphatidylinositol-4,5-biphosphate (PIP2) significantly reduce membrane–cytoskeleton adhesion energy. (A) Schematic representation of the PH domain from PlCδ, PH-PLCδ-GFP, and its plasma membrane localization. (B) Schematic representation of the mutated control construct PH*-PLCδ-GFP, which does not bind to PIP2 and its cytosolic localization. (C) Bar diagram of membrane–cytoskeleton adhesion energy in control cells, in cells expressing PH-PLCδ-GFP, PH-PLCδ-GFP, or the PH domain from Akt that binds PI(4,3)P2.

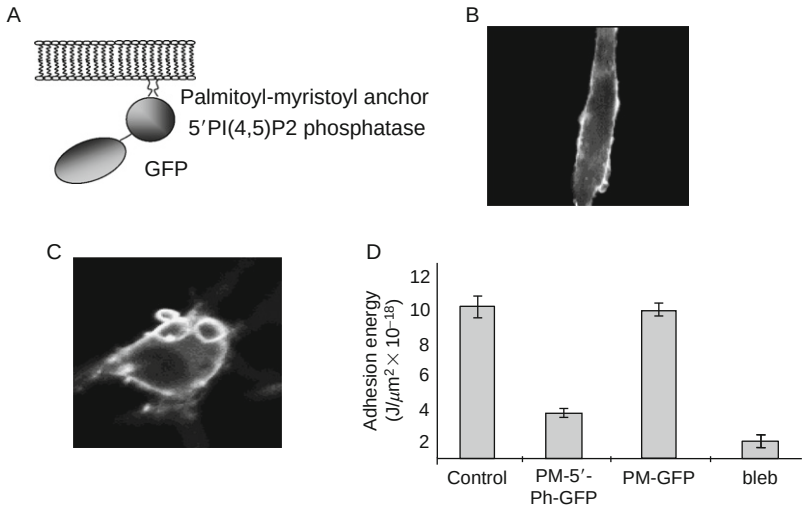

Fig. 6 Expression of plasma membrane targeted phosphatidylinositol-4,5-biphosphate (PIP2)-specific 5′ phosphatase selectively reduces PIP2 membrane concentration and membrane–cytoskeleton adhesion energy. (A) Schematic representation of the 5′ phosphatase fusion protein that is targeted to the plasma membrane with a mirystoylated/palmitoylated sequence. (B) Plasma membrane localization of PM-5′-phosphatase-GFP in NIH 3T3 cells. (C) Expression of PM-5′-phosphatase-GFP often induced cell rounding and appearance of membrane blebs. (D) Bar diagram of membrane–cytoskeleton adhesion energy in control cells, in cells expressing PM-5′-phosphatase-GFP or PM-GFP, and in blebs induced by expression of-5′-phosphatase-GFP.

to the plasma membrane (Fig. 6A). This construct localizes in the plasma membrane (Fig. 6B) and has a constitutively active 5′-phosphatase activity that hydrolyzes PIP2, thus reducing dramatically the level of PIP2 (Raucher *et al.*, 2000). Interestingly, longer expression (>10 h) of PM-5′-phosp-GFP induced membrane blebs and cell rounding (Fig. 6C), indicating complete loss of membrane–cytoskeleton adhesion. As shown in Fig. 6D, expression of PM-5′-phosp-GFP reduces the membrane–cytoskeletal adhesion energy. As a control, the adhesion energy was not affected by expression of GFP conjugated with a myristoyilation/palmitoylation sequence. We have also measured the tether force in membrane blebs. The tether force in blebs was small, which is consistent with the previously reported absence of cytoskeletal elements in membrane blebs (Keller and Eggli, 1998a).

IV. Concluding Remarks

Many cellular processes, such as lamellipodial extension, cell motility, membrane resealing after cell wounding, and endocytosis, are controlled not only biochemically through regulatory proteins but also by membrane–cytoskeleton adhesion (reviewed in Sheetz, 2001). To better understand these cellular processes,

it is important to have a means to measure membrane–cytoskeleton adhesion. Using laser optical tweezers, the membrane–cytoskeleton adhesion may be determined by measuring the tether force pulled from the cell surface by one micrometer polystyrene beads coated with different ligands. Here, we describe a basic laser optical tweezers setup and the simple relationship used to calculate membrane–cytoskeleton adhesion energy from tether force. We also show that plasma membrane PIP2 acts as a regulator of adhesion energy between the plasma membrane and cytoskeleton. In summary, cell membrane adhesion energy measurements by laser optical tweezers are a very powerful tool which enables us to examine and understand important mechanochemical components of basic cellular processes.

References

Ashkin, A., and Dziedzic, J. M. (1987). Optical trapping and manipulation of viruses and bacteria. *Science* **235,** 1517–1520.

Ashkin, A., and Dziedzic, J. M. (1989). Internal cell manipulation using infrared laser traps. *Proc. Natl. Acad. Sci. USA* **86,** 7914–7918.

Ashkin, A., Dziedzic, J. M., Bjorkholm, J. E., and Chu, S. (1986). Observation of a single-beam gradient force optical trap for dielectric particles. *Opt. Lett.* **11,** 288–290.

Ashkin, A., Dziedzic, J. M., and Yamane, T. (1987). Optical trapping and manipulation of single cells using infrared laser beams. *Nature* **330,** 769–771.

Bennink, M. L., Leuba, S. H., Leno, G. H., Zlatanova, J., de Grooth, B. G., and Greve, J. (2001). Unfolding individual nucleosomes by stretching single chromatin fibers with optical tweezers. *Nat. Struct. Biol.* **8,** 606–610.

Berk, D. A., and Hochmuth, R. M. (1992). Lateral mobility of integral proteins in red blood cell tethers. *Biophys. J.* **61,** 9–18.

Block, S. M., Goldstein, L. S., and Schnapp, B. J. (1990). Bead movement by single kinesin molecules studied with optical tweezers. *Nature* **348,** 348–352.

Bo, L., and Waugh, R. E. (1989). Determination of bilayer membrane bending stiffness by tether formation from giant, thin-walled vesicles. *Biophys. J.* **55,** 509–517.

Dai, J., and Sheetz, M. P. (1995). Mechanical properties of neuronal growth cone membranes studied by tether formation with laser optical tweezers. *Biophys. J.* **68,** 988–996.

Dopico, A. M., and Tigyi, G. J. (2007). A glance at the structural and functional diversity of membrane lipids. *Methods Mol. Biol.* **400,** 1–13.

Felgner, H., Frank, R., Biernat, J., Mandelkow, E. M., Mandelkow, E., Ludin, B., Matus, A., and Schliwa, M. (1997). Domains of neuronal microtubule-associated proteins and flexural rigidity of microtubules. *J. Cell Biol.* **138,** 1067–1075.

Felgner, H., Frank, R., and Schliwa, M. (1996). Flexural rigidity of microtubules measured with the use of optical tweezers. *J. Cell Sci.* **109**(Pt 2), 509–516.

Foster, L. J., and Chan, Q. W. (2007). Lipid raft proteomics: More than just detergent-resistant membranes. *Subcell. Biochem.* **43,** 35–47.

Franke, T. F., Kaplan, D. R., Cantley, L. C., and Toker, A. (1997). Direct regulation of the Akt proto-oncogene product by phosphatidylinositol-3,4-bisphosphate. *Science* **275,** 665–668.

Galbraith, C. G., Yamada, K. M., and Sheetz, M. P. (2002). The relationship between force and focal complex development. *J. Cell Biol.* **159,** 695–705.

Hochmuth, F. M., Shao, J. Y., Dai, J., and Sheetz, M. P. (1996). Deformation and flow of membrane into tethers extracted from neuronal growth cones. *Biophys. J.* **70,** 358–369.

Hochmuth, R. M., and Marcus, W. D. (2002). Membrane tethers formed from blood cells with available area and determination of their adhesion energy. *Biophys. J.* **82,** 2964–2969.

Keller, H., and Eggli, P. (1998a). Actin accumulation in pseudopods or in the tail of polarized walker carcinosarcoma cells quantitatively correlates with local folding of the cell surface membrane. *Cell Motil. Cytoskeleton* **40,** 342–353.

Keller, H., and Eggli, P. (1998b). Protrusive activity, cytoplasmic compartmentalization, and restriction rings in locomoting blebbing Walker carcinosarcoma cells are related to detachment of cortical actin from the plasma membrane. *Cell Motil. Cytoskeleton* **41,** 181–193.

Kellermayer, M. S., Smith, S., Bustamante, C., and Granzier, H. L. (2000). Mechanical manipulation of single titin molecules with laser tweezers. *Adv. Exp. Med. Biol.* **481,** 111–126.

Kuo, S. C., and Sheetz, M. P. (1993). Force of single kinesin molecules measured with optical tweezers. *Science* **260,** 232–234.

Linke, W. A. (2000). Stretching molecular springs: Elasticity of titin filaments in vertebrate striated muscle. *Histol. Histopathol.* **15,** 799–811.

Mallik, R., Carter, B. C., Lex, S. A., King, S. J., and Gross, S. P. (2004). Cytoplasmic dynein functions as a gear in response to load. *Nature* **427,** 649–652.

Marcus, W. D., and Hochmuth, R. M. (2002). Experimental studies of membrane tethers formed from human neutrophils. *Ann. Biomed. Eng.* **30,** 1273–1280.

Nambiar, R., Gajraj, A., and Meiners, J. C. (2004). All-optical constant-force laser tweezers. *Biophys. J.* **87,** 1972–1980.

Raucher, D., and Sheetz, M. P. (1999). Membrane expansion increases endocytosis rate during mitosis. *J. Cell Biol.* **144,** 497–506.

Raucher, D., and Sheetz, M. P. (2000). Cell spreading and lamellipodial extension rate is regulated by membrane tension. *J. Cell Biol.* **148,** 127–136.

Raucher, D., and Sheetz, M. P. (2001). Phospholipase C activation by anesthetics decreases membrane-cytoskeleton adhesion. *J. Cell Sci.* **114,** 3759–3766.

Raucher, D., Stauffer, T., Chen, W., Shen, K., Guo, S., York, J. D., Sheetz, M. P., and Meyer, T. (2000). Phosphatidylinositol 4,5-bisphosphate functions as a second messenger that regulates cytoskeleton-plasma membrane adhesion. *Cell* **100,** 221–228.

Sheetz, M. P. (2001). Cell control by membrane-cytoskeleton adhesion. *Nat. Rev. Mol. Cell Biol.* **2,** 392–396.

Smith, S. B., Cui, Y., and Bustamante, C. (1996). Overstretching B-DNA: The elastic response of individual double-stranded and single-stranded DNA molecules. *Science* **271,** 795–799.

Svoboda, K., and Block, S. M. (1994). Biological applications of optical forces. *Annu. Rev. Biophys. Biomol. Struct.* **23,** 247–285.

Svoboda, K., Schmidt, C. F., Schnapp, B. J., and Block, S. M. (1993). Direct observation of kinesin stepping by optical trapping interferometry. *Nature* **365,** 721–727.

Tskhovrebova, L., Trinick, J., Sleep, J. A., and Simmons, R. M. (1997). Elasticity and unfolding of single molecules of the giant muscle protein titin. *Nature* **387,** 308–312.

Tsuda, Y., Yasutake, H., Ishijima, A., and Yanagida, T. (1996). Torsional rigidity of single actin filaments and actin-actin bond breaking force under torsion measured directly by *in vitro* micromanipulation. *Proc. Natl. Acad. Sci. USA* **93,** 12937–12942.

Wang, Z., Khan, S., and Sheetz, M. P. (1995). Single cytoplasmic dynein molecule movements: Characterization and comparison with kinesin. *Biophys. J.* **69,** 2011–2023.

Waugh, R. E., and Bauserman, R. G. (1995). Physical measurements of bilayer-skeletal separation forces. *Ann. Biomed. Eng.* **23,** 308–321.

Waugh, R. E., and Hochmuth, R. M. (1987). Mechanical equilibrium of thick, hollow, liquid membrane cylinders. *Biophys. J.* **52,** 391–400.

Waugh, R. E., Song, J., Svetina, S., and Zeks, B. (1992). Local and nonlocal curvature elasticity in bilayer membranes by tether formation from lecithin vesicles. *Biophys. J.* **61,** 974–982.

CHAPTER 18

Sensing Cytoskeletal Mechanics by Ballistic Intracellular Nanorheology (BIN) Coupled with Cell Transfection

Melissa S. Thompson[*] and Denis Wirtz[*,†]

[*]Department of Chemical and Biomolecular Engineering
Johns Hopkins University
Baltimore, Maryland 21218

[†]Howard Hughes Medical Institute graduate training program and
Johns Hopkins Institute for NanoBioTechnology
Johns Hopkins University
Baltimore, Maryland 21218

METHODS IN CELL BIOLOGY, VOL. 89

0091-679X/08 $35.00
DOI: 10.1016/S0091-679X(08)00618-3

Abstract

Key processes in normal and diseased cells depend directly or indirectly on the viscoelastic properties of the cytoplasm. Particle-tracking microrheology is a highly versatile method that measures the viscoelastic properties of cytoplasm directly by tracking fluorescent nanoparticles embedded in the cytoskeleton with high spatial and temporal resolutions. Here we present a new method that combines cell transfection, ballistic injection, and particle-tracking microrheology to monitor changes in cytoplasmic micromechanics following controlled changes in protein expression. We demonstrate that cells transfected with GFP (green fluorescent protein) display viscoelastic properties identical to untransfected fibroblasts, that low levels of expression of GFP-α-actinin do not affect cell microrheology, and that the transient transfection with GFP-C3 transferase reduces the elasticity of the cytoplasm of fibroblasts to a similar extent as C3 transferase toxin, which deactivates the GTPase Rho. Combining cell transfection with particle-tracking microrheology opens the way to quantitative, single live-cell mechanical studies where stable cell lines cannot be easily established, but where commonly used transfections can be exploited to manipulate cytoskeletal organization.

I. Introduction

Key processes in normal and diseased cells depend directly or indirectly on the viscoelastic properties of the cytoplasm. For instance, cells migrating into a wound stiffen their leading edge to enable dendritic F-actin assemblies to produce net protruding forces (Kole *et al.*, 2005; Lee *et al.*, 2006; Pollard and Borisy, 2003). Cells adapt their intracellular physical properties to the physical properties of their extracellular milieu in order to grow, differentiate, and migrate (Pelham and Wang, 1997). The translocation of organelles (e.g., nucleus, mitochondria, ER) within the cytoplasm also depends on the local properties of the cytoplasm (Lee *et al.*, 2005; Tseng *et al.*, 2004b), which is stiffer (i.e., has a higher elasticity) in the cell periphery than in the perinuclear region of normal cells (Yamada *et al.*, 2000). Transformed cells collected from cancer patients or cells harvested from mouse models for progeria (premature aging) can display significantly softer (i.e., less elastic) cytoplasm, which affects their ability to adhere to substrata, to properly position their nuclei and centrosomes, to polarize under flow conditions, and to migrate at the edge of a wound (Lee *et al.*, 2007).

A. Nanorheology as a Quantitative Tool for Molecular Cell Mechanics

A major contributor to cytoplasmic stiffness is the cytoskeleton, which is composed of the filamentous proteins F-actin, microtubules, and intermediate filaments (Pollard and Borisy, 2003) and provides the cell's cytoplasm with its

structure and shape. In the cell, actin monomers assemble into semiflexible F-actin polymers that form highly entangled networks of filaments and bundles (Tseng and Wirtz, 2001; Tseng *et al*., 2004a), whose viscoelastic properties can be controlled by either altering the local density of assembled actin or the activity of F-actin crosslinking/bundling proteins such as α-actinin (Tseng *et al*., 2001, 2002a,c, 2005) or by subjecting these networks to external (Lee *et al*., 2006) or internal (Kole *et al*., 2004) mechanical stresses.

Current experimental approaches to cell mechanics can be categorized into those measuring global and local cell properties, those indirectly measuring cytoplasmic mechanics through a required physical contact of the probe with the plasma membrane, and those measuring cytoplasmic mechanics directly. For instance, micropipette suction (Tsai *et al*., 1993)—well suited to probing suspension cells (e.g., red blood cells)—measures the global stiffness of a cell, which may include contributions from the plasma membrane, the nucleus, and the cytoplasm. Methods that measure local properties include atomic force microscopy (AFM) (Hoh and Schoenenberger, 1994) and magneto-cytometry (Valberg and Albertini, 1985), the latter probing apparent cell mechanics by subjecting large ECM-coated beads tethered to cell receptors to rotational movements.

Because different techniques measure different (but often related) rheological quantities, intracellular mechanics is best characterized by multiple rheological parameters, including viscosity, elasticity, and creep compliance. Viscosity measures the propensity of cytoplasm to flow under mechanical forces. Elasticity (or elastic modulus) measures the stretchiness of a material, in this case, the pliability of the cytoplasm. A material that is more viscous than elastic is a viscoelastic liquid; a material that is more elastic than viscous is a viscoelastic solid. The cytoplasm of adherent cells is complex; it behaves as a viscoelastic liquid when sheared slowly, but as a viscoelastic solid when sheared rapidly (Kole *et al*., 2004; Tseng *et al*., 2002b). A similar behavior is observed in reconstituted actin filament networks in the presence of dynamic crosslinkers, such as filamin or α-actinin (Tseng *et al*., 2004a; Xu *et al*., 1998, 2000). When sheared more slowly than the lifetime of binding of the crosslinking protein to F-actin, the actin filament network flows and behaves largely as a liquid. When sheared at a rate faster than the inverse binding lifetime of the crosslinking protein, the actin filament network behaves as a stiff gel or solid. The creep compliance of the cytoplasm refers to its deformability. A high compliance indicates a low propensity to resist mechanical deformation following application of a shear stress; a low compliance indicates that a high propensity to resist such stress. In certain conditions, viscosity and elasticity can be directly computed from creep compliance measurements.

We have introduced the method of particle tracking microrheology (Tseng *et al*., 2002b), which measures the viscosity, elasticity, and creep compliance of the cytoplasm. In this approach, fluorescent nanoparticles are injected directly in the cytoplasm of live cells are tracked with high spatial and temporal resolutions. The size of these nanoparticles is chosen to be larger than the average mesh size of the cytoskeleton, typically 50 nm, measured by probing the diffusion of fluorescent

dextran using fluoresence recovery after photobleaching (Luby-Phelps *et al.*, 1986). These nanoparticles are also smaller than $\sim 1\ \mu m$; therefore these nanoparticles undergo Brownian motion and inertial (gravity) forces are negligible. The small random forces produced by the bombardment of water molecules and the movements of cytoplasmic structures induce their random displacements (Tseng *et al.*, 2002b). The amplitude of these Brownian displacements directly reflects the local viscoelastic properties of the cytoplasm in the vicinity of the nanoparticle (Gittes *et al.*, 1997; Mason *et al.*, 1997). Direct injection of the nanoparticles into the cytoplasm (Tseng *et al.*, 2002b), as opposed to passive transfer, circumvents the endocytic pathway and, therefore, the engulfment of the nanoparticles in endocytic vesicles tethered via motor proteins to cytoskeleton filaments (Suh *et al.*, 2003). The recent introduction of ballistic injection (Lee *et al.*, 2006; Panorchan *et al.*, 2006) has transformed the particle-tracking microrheology assay to high-throughput rather than using manual microinjection whereby thousands of cells are simultaneously injected with nanoparticles and, therefore, amenable to particle-tracking measurements (Fig. 1).

Manual microinjection, and to a lesser extent ballistic injection, can cause trauma to cells, which may subsequently undergo necrosis or apoptosis in large numbers. Therefore, cell microrheology has been used almost exclusively to compare the mechanical response of cells stably expressing a mutant protein to that of their wild-type counterpart or has been restricted to comparing untreated cells to cells subjected to drug treatments. Cell transfection with genes encoding dominant negative proteins or constitutively active proteins, or with small interfering RNAs (siRNAs), in combination with particle-tracking microrheology, has not been demonstrated. This may be due in part to the fact that a fraction of cells do not seem to survive the double trauma of nanoparticle injection and cell transfection.

Here we present a new method that allows one to combine cell transfection, ballistic injection, and particle-tracking microrheology. We demonstrate that cells transfected with GFP (green fluorescent protein) display viscoelastic properties identical to those of untransfected cells, that expression of GFP-α-actinin does not affect cell microrheology, and that the transient transfection with GFP-C3 transferase reduces the elasticity of the cytoplasm of fibroblasts to a similar extent as C3 transferase toxin. Combining cell transfection with particle-tracking microrheology opens the way to quantitative, single live-cell nano-mechanical studies for cell lines that cannot be stably transformed, but are amenable to transfections commonly used to manipulate cytoskeleton organization.

B. Transient Transfection to Induce Changes in the Cytoskeleton as Measured by Ballistic Intracellular Nanorheology (BIN)

BIN represents a unique *in vivo* tool to measure global and local viscoelastic properties of cells by high-throughput injection of many beads/cell, thereby increasing population size and increasing the probability of probing typical biological scenarios. Previous experiments employed manual microinjection of

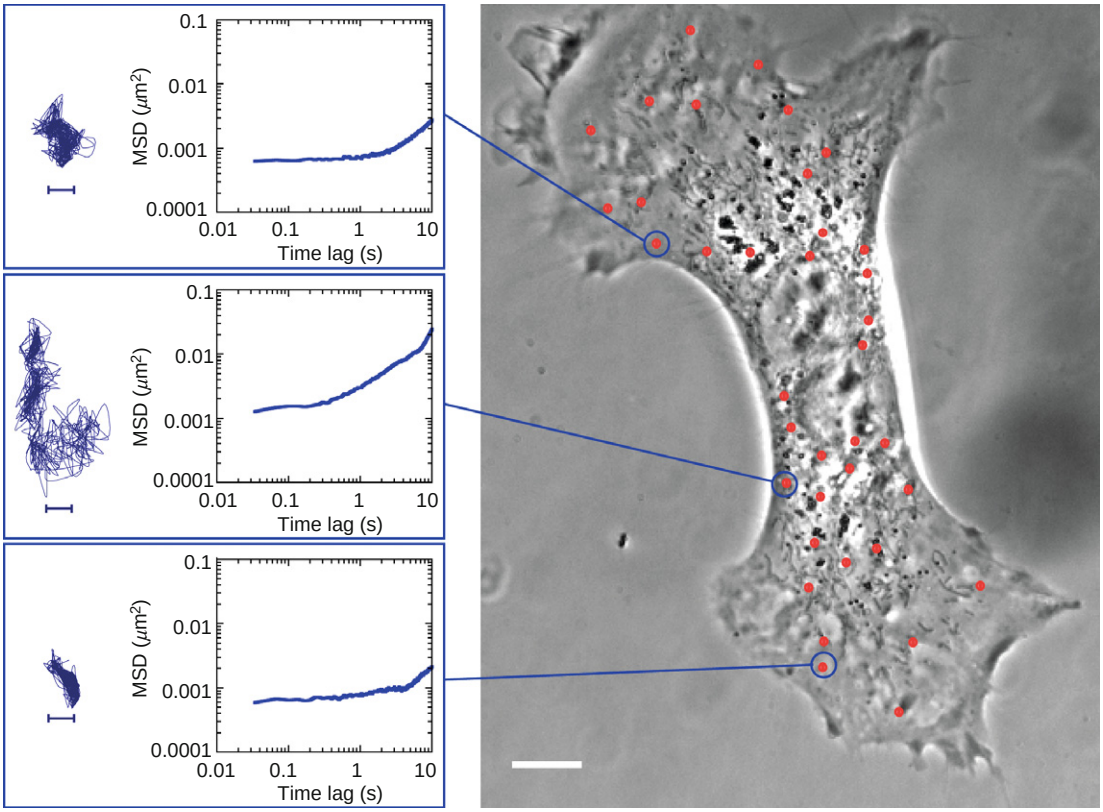

Fig. 1 Ballistic injection of 100-nm fluorescent carboxylated-polystyrene nanoparticles yields a range of 3–20 measurable nanoparticles per cell, which are distributed throughout the cell's cytoplasm. The diffraction-limited images of the nanoparticles are shown as red dots for ease of view. The displacements of the nanoparticles' centroids are recorded for 20 s at a rate of 30 frames per second. (Left panels). Trajectories of the centroids are plotted to ensure that each bead is undergoing random, Brownian motion. (Right panel) MSDs of the nanoparticles are calculated, from which rheological parameters describing the viscoelastic behavior of cytoplasm—including viscous and elastic moduli, creep compliance, and shear viscosity of cytoplasm—can be derived. Scale bar for phase contrast image of the cell is 10 μm. Scale bar for trajectories is 0.05 μm.

beads into cells (Daniels *et al*., 2006), which also permitted the microinjection of purified proteins in the cytoplasm, to induce and quantify cytoskeletal changes (Tseng *et al*., 2002b). However, protein microinjection is cumbersome, and injected proteins are often degraded with time. Moreover, microinjection can cause major mechanical trauma to cells. In contrast, the genetic manipulation of protein expression in live cells is often more benign, providing a longer lasting effect that is easier to implement. The use of transient transfection coupled with BIN provides a high-throughput means to probe the effects on cytoplasmic mechanics caused by controlled changes in protein expression.

Here we demonstrate how we use BIN to measure the rheological response of Swiss 3T3 cells to changes in protein expression. Swiss 3T3 fibroblasts exhibit strong stress fiber staining in serum (Fig. 2A). Numerous proteins regulate the formation and crosslinking/bundling of actin filaments into contractile stress fibers, including the small GTPase Rho and the F-actin-binding protein α-actinin, respectively.

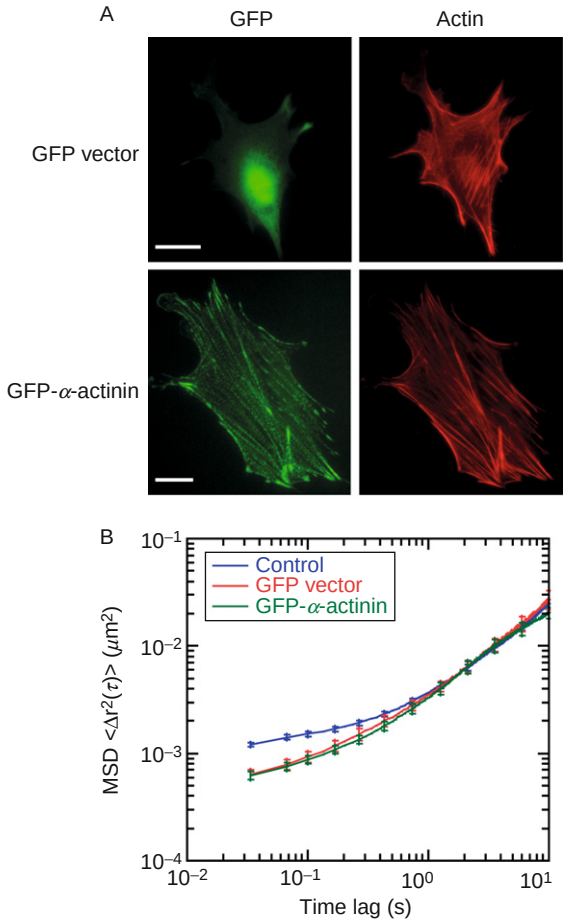

Fig. 2 Combined BIN and cell transfection: Control experiments. (A) Swiss 3T3 fibroblasts were both ballistically injected with 100-nm fluorescent nanoparticles and transiently transfected with either GFP only (top panels) or GFP-α-actinin (bottom panels) expression constructs. Post-experiments, fluorescence microscopy was used to visualize GFP (left panels) and F-actin structure by phalloidin staining (right panels). Scale bar, 10 μm. (B) Ensemble-averaged MSDs were calculated from the 2D trajectories of the nanoparticles in untreated control cells (blue curve), GFP-transfected cells (red curve), and GFP-α-actinin-transfected cells (green curve). The number of nanoparticles and cells used for each condition was: $n = 156$ and 27 for control cells; $n = 33$ and 20 for GFP-transfected cells; $n = 34$ and 20 for GFP-α-actinin cells. Error bars respresent standard error of the mean.

In previous reports, microinjection of purified α-actinin significantly increased the cytoplasmic viscoelasticity of Swiss 3T3 fibroblasts (Yamada *et al.*, 2000).

We combined the BIN assay with transient transfection to induce expression of GFP-tagged α-actinin. This was accomplished by plating the cells on a culture dish and ballistically injecting the cells with 100-nm fluorescent polystyrene nanoparticles. Following immediate and extensive washing, the cells were replated on poly-L-lysine-coated dishes, and, after a 4–6 h incubation, were transfected using a traditional lipophilic transfection method (Fugene HD Transfection Reagent, Roche). This process yields 30–40% of cells containing beads in a range of 3–20 beads per cell used for measurements (Fig. 1). After a 16-h incubation, measurements of the displacements of injected nanoparticles in large numbers of untransfected and transfected cells were collected following standard methods of multiple particle tracking (Kole *et al.*, 2004). Mean squared displacements (MSDs) of the nanoparticles were calculated, and rheological parameters that characterize the viscoelastic properties of the cytoplasm were computed, including creep compliance, viscoelastic moduli, and shear viscosities.

The control vector, which expresses GFP only, induced no significant changes in the viscoelastic properties of the cytoplasm compared to untransfected cells (Fig. 2), as shown by the absence of changes in the averaged MSD of the nanoparticles and associated rheological parameters. Similarly, transfection of cells with GFP-α-actinin induced no extensive change in the stiffness of the cytoplasm (Fig. 2). This is because the GFP-α-actinin fusion protein expressed in the cells comprised only 1% of the total α-actinin concentration in the cell (Varker *et al.*, 2003). Therefore, the additional crosslinking of F-actin induced by the expression of GFP-α-actinin was negligible and undetectable by our methods.

C3 transferase, a cell permeable toxin used extensively to study Rho GTPases (Aktories and Hall, 1989), abolishes RhoA, RhoB, and RhoC activity in cells and therefore prevents the formation of stress fibers (Hall, 1992). We found that the expression of GFP-C3 transferase yielded a similarly robust phenotype as the C3 toxin, in which the cells contained little to no actin structure and exhibited a distinctly different morphology than untreated cells (Fig. 3A–C). The altered cytoskeletal morphology leads to a more deformable cytoplasm than that of untreated cells, as measured by an increase in creep compliance, and softer cytoplasm, as shown by a reduced elasticity and viscosity (Fig. 3D–G). The measurements consisted of over a hundred MSD profiles, which were distributed similarly in the elastic regime but shifted significantly in the viscous regime (Fig. 4).

II. Materials and Instrumentation

A. Cell Culture

Swiss 3T3 cells (Cat. No. CRL-2658), Dulbecco's Modified Eagle's medium (Cat. No. 30-2002), and bovine calf serum (10% v/v with culture medium, Cat. No. 30-2030) are obtained from American Type Culture Collection (ATCC).

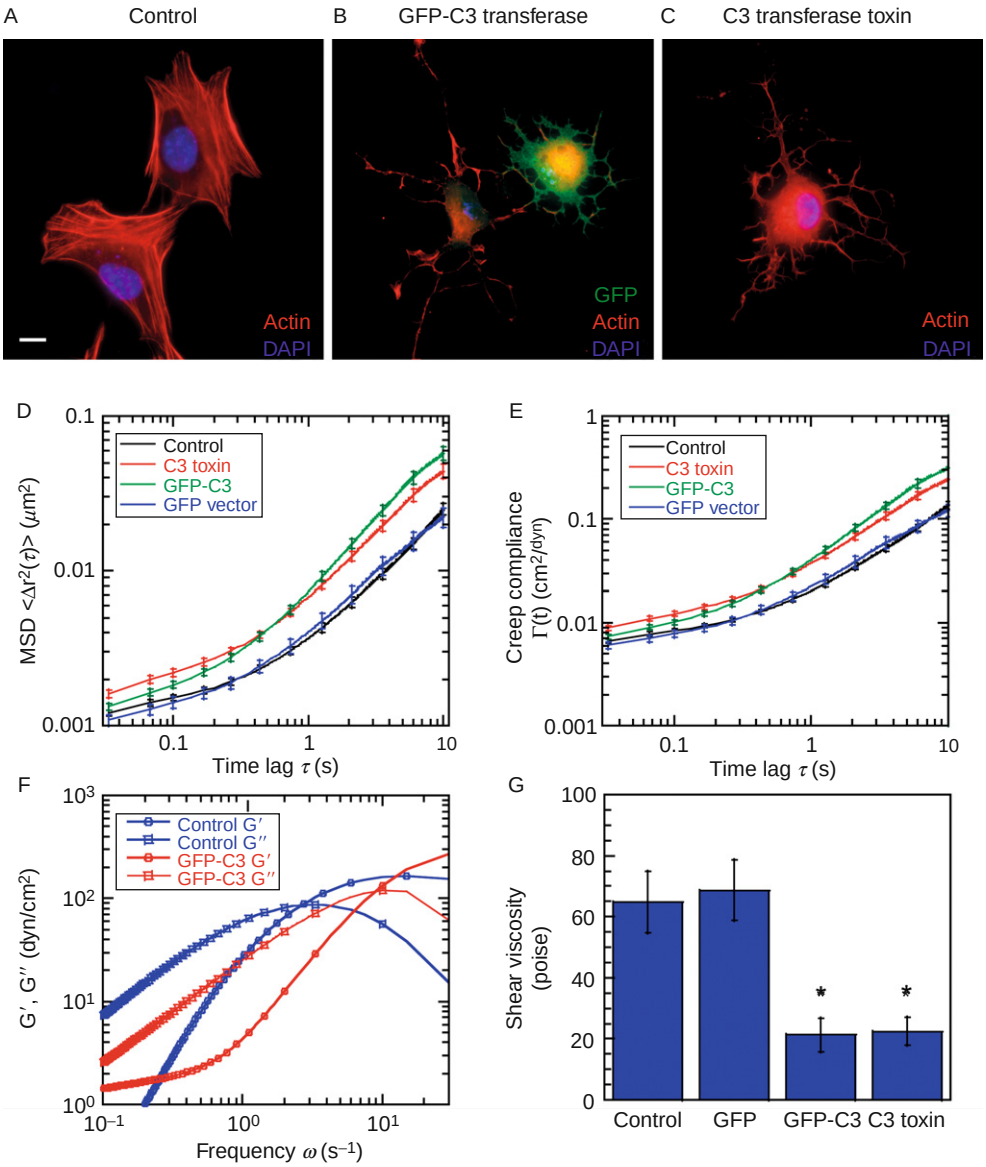

Fig. 3 Combined BIN and cell transfection: Monitoring cell-mechanical changes following C3-transferase transfection. Swiss 3T3 fibroblasts were grown in serum (control, A), transfected with the GFP-tagged C3 transferase construct (B), or treated with cell-permeable C3 transferase (C), then stained with phalloidin to visualize actin and DAPI to visualize the nucleus. Scale bar = 10 μm. For each condition, nanoparticles were ballistically injected, and their centroid displacements were monitored by high-resolution time-lapsed fluorescence microscopy. The number of nanoparticles and cells used for each condition was: $n = 156$ and 27 for control cells; $n = 55$ and 24 for GFP-transfected cells; $n = 117$ and 29 for GFP-C3-transfected cells; $n = 107$ and 29 for C3 Toxin-treated cells. (D) These displacements were

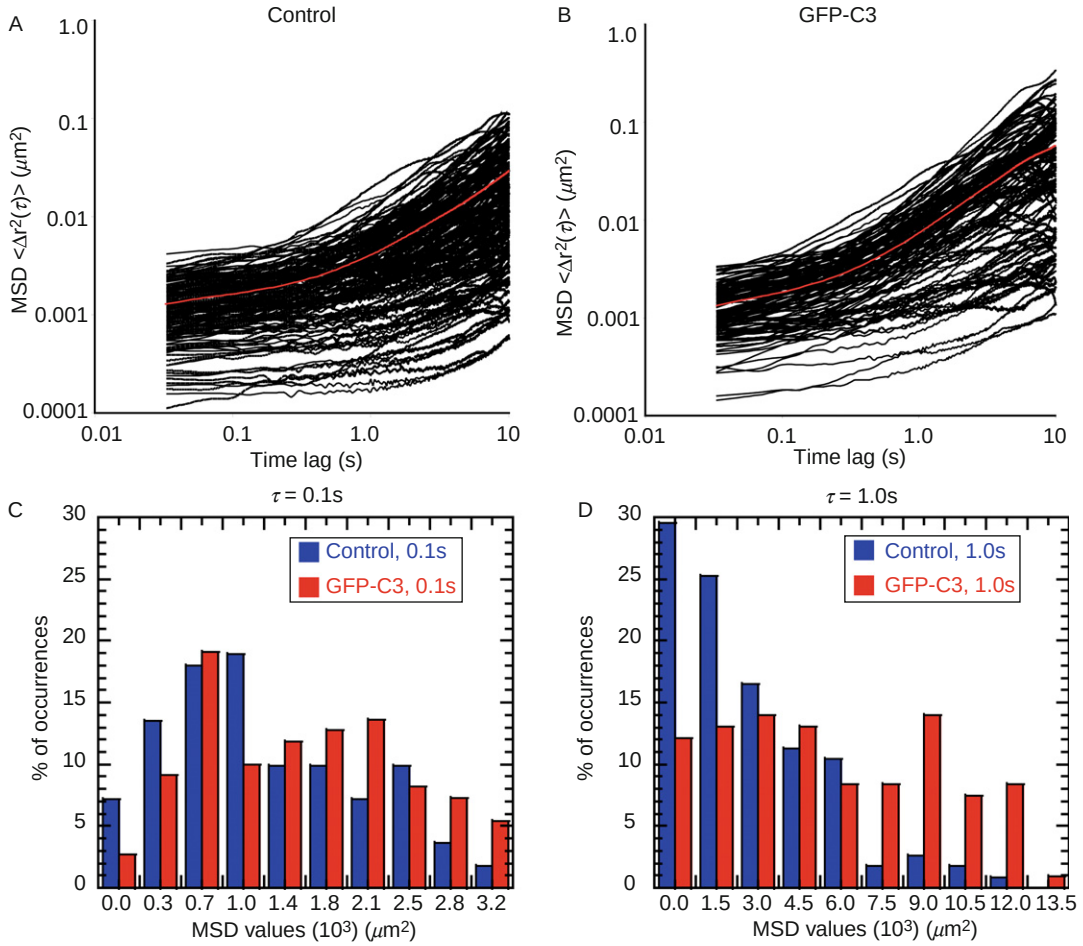

Fig. 4 Distributions of MSDs. (A and B) Over a hundred nanoparticles embedded in cytoplasm of Swiss 3T3 fibroblasts were tracked for each tested condition, cells transfected with GFP alone (A) or GFP-C3 transferase (B), which contributed to the ensemble-average MSDs (in red). (C and D) Distributions of MSD values for time lags of 0.1 s (C) and 1 s (D) are shown for control (blue) and GFP-C3-transfected cells (red).

averaged and converted to MSDs. (E) These averaged MSDs were converted to averaged creep compliances which measure the mean deformability of cytoplasm. (F) Mean frequency-dependent elastic modulus, $G'(\omega)$ (which measures the stretchiness of cytoplasm), and viscous modulus $G''(\omega)$ (which measures the propensity of cytoplasm to flow), were calculated from averaged MSDs, as well as (G) the mean shear viscosity. Error bars in each panel represent standard error of the mean. Significance was determined by student t-testing where * denotes statistical significance where $P<0.05$ compared with control. C3 Transferase, both in toxin and plasmid forms, reduces the elasticity of the cytoplasm.

Cell culture medium is supplemented with 1:100 dilution of Penicillin-Streptomycin solution (Cat. No. 15140-122, Invitrogen). Hank's balanced salt solution (HBSS, Cat. No. 21-021-CV) is from Mediatech, Inc. and 0.25% trypsin—1 mM EDTA (Cat. No. 25200-056) is from Invitrogen. Cells are cultured on 100-mm polystyrene dishes (Cat. No. 353003, Falcon) prior to bombardment. For post-ballistic injection, chambered coverslips (Cat. No. 155383, Labtek, Nalge Nunc,) are coated with 0.01% poly-L-lysine (PLL, Cat. No. P8920, Sigma) for 1 h, washed, and used for plating. Cell cultures are maintained at 37 °C in a humidified, 5% CO_2 environment.

B. Nanoparticles and Macrocarriers

In all experiments, we use 0.1 μm carboxylated-polystyrene fluorescent spherical nanoparticles (Cat. No. F8801, Invitrogen). Nanoparticles are dialyzed by immersing 3 ml of stock nanoparticle in 300,000 MWCO dialysis tubing (Cat. No. LAB-DIS001, Spectrum Labs) in 100% ethanol (Cat. No. 1110002000PL05, Warner Graham Co.). Dialysis is performed at 4 °C for 24 h with 1 change of ethanol. Nanoparticles are then stored in 500 μl aliquots at 4 °C, protected from light. Dialyzed nanoparticles are coated on macrocarriers (see also below; Cat. No. 165-2335, Bio-Rad).

C. Ballistic Injection

Ballistic injection of the nanoparticles is performed by the PDS-1000/He Hepta System (Cat. No. 165-2258, Bio-Rad) equipped with a hepta adaptor (Cat No. 165-2225) and a vacuum line produced by a pump (model 2560, Cat. No. 2560C-02, Welch Rietschle Thomas). The system is thoroughly cleaned with 70% ethanol prior to use, and an air canister is used to clean the hepta adaptor lines. System accessories used for injection include 1800 psi rupture discs (Cat. No. 165-2332), macrocarriers (Cat. No. 165-2335) and stopping screens (Cat. No 165-2336), all from Bio-Rad. Rupture discs require tweezers to pre-treat them with isopropanol (Cat. No I9516, Sigma).

D. Transfection and Drug Application

The plasmid expressing GFP-α-actinin is from AddGene (Cat. No. 11908, AddGene). The GFP vector was generated from the GFP-α-actinin by removing the α-actinin insert using restriction enzyme *Hind*III (Cat. No. R0104S, NEB Labs). The linear GFP-tagged DNA was ligated using T4 DNA Ligase (Cat. No. M0202S, NEB Labs), transformed into XL1-Blue competent cells (Cat. No. 200249, Stratagene) using Kanamycin plates (Cat. No. K0879, Sigma) and then midiprepped (Cat. No. A7640, Promega). The GFP-C3 transferase plasmid was kindly provided by Dr. Carol Williams, Medical College of Wisconsin. All plasmids were transfected into Swiss 3T3 cells using HD Transfection Reagent

(Cat. No. 04709705001, Roche) and Opti-MEM (Cat. No. 31985, Invitrogen). The cell permeable toxin C3 transferase was obtained from Cytoskeleton (Cat. No. CT04).

E. Nanoparticle Imaging, Acquisition, and Analysis

BIN experiments were imaged using a Nikon TE2000-E inverted microscope, which is equipped for epifluorescence and with a Nikon PlanFluor 60× oil immersion lens (N. A. 1.3). Movies were captured by a Cascade 1k camera (Roper Scientific). Data acquisition and analysis were executed by journal routines provided by the Metavue/Metamorph Imaging Series (MDS Analytical Technologies).

III. Procedures

A. Preparation of Nanoparticles and Macrocarriers

The nanoparticles obtained from Invitrogen are in a 2% w/v aqueous suspension. To coat the macrocarriers evenly with nanoparticles and to ensure that the solution remains sterile, the nanoparticle solution is dialyzed to replace the water with ethanol (Section II.B above).

Ballistic injection involves accelerating nanoparticle-coated macrocarriers to a high-speed towards a wire-mesh stopping screen in a vacuum chamber. The macrocarriers are stopped by the screen, while the nanoparticles continue through the mesh at a high speed and lodged in the cytoplasm of the cells below. Success of the injection depends on the quality of the thin-film created on the macrocarrier prior to injection.

a. **Materials**

i. Macrocarriers
ii. Nanoparticles in ethanol
iii. Large Petri dish, sterile
iv. 20 μl micropipette and tip
v. Ethanol

b. **Steps**

i. Inside a laminar flow hood, make 7 small dabs (<5 μl each) of ethanol on the petri dish where the macrocarriers will be placed. Transfer the macrocarriers on top of these dabs. This will ensure that the macrocarriers lay flat on the dish.

ii. Pipette 20 μl of nanoparticle solution to one macrocarrier and spread over the entire carrier with the micropipette tip. Continue to spread to keep beads from building at the edges of the layer as the ethanol dries. Stop spreading once solution layer becomes thin and continued spreading produces aggregation of the nanoparticles. Let dry.

iii. Pipette an additional 20 μl of nanoparticle solution onto the same macrocarrier. Spread the nanoparticles very carefully with the pipette tip, attempting to only touch the liquid and not the macrocarrier. The beads should be maximally spread in area. Avoid scratching the carrier with the pipette tip to reduce the formation of aggregates. Let dry.

iv. Repeat for each macrocarrier and let sit in laminar flow hood for at least 1 h or overnight for complete drying.

B. Ballistic Injection of Nanoparticles

The PDS-1000/He Hepta system ballistically injects cells by using pressurized helium to accelerate the macrocarriers against a wire mesh. The nanoparticle beads are carried by momentum through the mesh and into the cells in the dish below. This process requires removal of cell media from the dish. Therefore, this injection must be performed quickly to reduce cellular stress and apoptosis. In addition, cells are likely to engulf these beads through endocytosis. After injection, great care must be taken to thoroughly wash the cells to remove nanoparticles that may have lodged on the surface of the cell.

Following injection and subsequent wash, the cells are immediately incubated in cell culture media at 37 °C and 5% CO_2 to allow the holes in the membrane to close and reduce cell stress. The cells are then replated to an optimal confluency to remove any residual extracellular beads that may remain.

1. Preparation of PDS-1000/He Hepta System

a. **Materials**

i. 70% Ethanol
ii. Helium
iii. Isopropanol
iv. Rupture disc, 1800 psi
v. PDS-1000/He Hepta System and accessories including torque wrench and macrocarrier insertion tool
vi. Tweezers
vii. Vacuum pump
viii. Coated macrocarriers

b. **Steps**

i. Thoroughly spray the inside of the injection chamber, the target tray and the macrocarrier holder set with 70% ethanol and wipe with a kimwipe. Place target tray on the third level.

ii. Clean the wire mesh with 70% ethanol and a wire brush. Dry with a kimwipe.

iii. Clean hepta adaptor lines with air canister to remove any remaining bits of previously ruptured discs.

iv. Turn on system, helium tank, and vacuum pump.

v. With the chamber empty, load helium lines with helium by pulling vacuum on the chamber and fire the mechanism to pull helium through the lines.

vi. Using tweezers, transfer the macrocarriers to the holder.

vii. Secure the macrocarriers in the well with the macrocarrier insertion tool provided with the system. Ensure that they are firmly in place by inverting the holder. Assemble with wire mesh and holder.

viii. Immerse a single 1800-psi rupture disk in 100% isopropanol for 3 s. Dab on a kimwipe to remove excess isopropanol and place in the well inside the top part of the hepta adaptor. Screw onto flange inside the injection chamber. Tighten with the torque wrench tool as instructed.

ix. Slide macrocarrier holder into the second position.

x. Align pressure divider lines of the hepta adaptor with the holes in the macrocarrier holder.

2. Ballistic Injection

a. **Materials**

i. 100-mm dish of cells

ii. Aspirator

iii. Laminar Flow Hood

iv. Hank's Balanced Salt Solution (HBSS)

v. Cell media

b. **Steps**

i. Remove media from the 100-mm plate containing cells at approximately 80% confluency. Aspirate for an additional 30 s to remove residual fluid.

ii. Quickly place the cells on the target tray in the third position and close chamber door.

iii. Pull vacuum on the chamber until the vacuum gauge reaches 28 psi; press hold button on ballistic chamber.

iv. Fire the mechanism until a rupture is attained and release the pressure inside the chamber.

v. Immediately move the cells to the laminar flow hood and wash 2 times with 30 ml of HBSS by simultaneously adding media to one side of the dish and aspirating from the other side. Wash 2 times with 10 ml HBSS by applying directly

on the cells, forcefully enough to dislodge surface beads without detaching cells from the dish.

vi. Add 10 ml of pre-warmed media and let the cells incubate for 1 h in the cell culture incubator.

3. Replating Cells

After 1-h incubation, the cells are replated to PLL-coated chambered coverslips. Chambered coverslips were incubated with 0.01% PLL for 1 h, washed three times with PBS and then used for plating. In this step, it is important to centrifuge the cells once they have been detached from the cell culture dish. Centrifugation will remove any remaining nanoparticles that were in the dish, exocytosed by cells, or freely detached from the cell surface during the hour incubation period. Centrifugation speed and duration depend on cell line and centrifuge; however a gentle speed should be selected to pellet cells only. The nanoparticles will stay in solution since their momentum due to centrifugation will not overcome the drag force on the sphere, thereby separating extracellular beads from the cells. The supernatant is aspirated and the cells are plated according to desired cell density. In the case of Swiss 3T3 cells that undergo growth inhibition through cell-cell contact, the cells should be plated at about ~30% confluency.

C. Transfection

Transfection of the cells can be performed at the same time as plating or after cells have adhered to the dish, depending on what is being transfected and how it will affect the adhesive properties of the cells. In our case, we transfect cells after they had begun to adhere to the dish. Transfection is performed using the protocol provided with the HD Transfection reagent with DNA:HD ratio of 2:8. Transfection solution is added to cells after plating, and the cells are incubated overnight.

D. Multiple Particle Tracking Data Acquisition and Analysis

Data acquisition for the BIN analysis requires collection of movies that capture the movement of nanoparticles embedded in the cytoplasm. Tracking software within Metamorph Imaging Series is utilized to extract the movement of the centroid of the spherical nanoparticles into *x, y* coordinates from which individual MSDs are calculated via:

$$\langle \Delta r^2(\tau) \rangle = \langle [x(t+\tau) - x(t)]^2 + [y(t+\tau) - y(t)]^2 \rangle$$

where τ is time lag.

For each condition, approximately 10 cells are tracked, each containing a range of 3–20 measurable beads. Experiments are performed in triplicate. Microscopy of these ballistically injected cells is performed using a 60× objective on a Nikon

TE2000-E inverted microscope equipped with epifluorescence and a live cell incubator to maintain an 5% CO_2, 37 °C environment.

1. Sample Preparation prior to Microscopy

a. **Materials**

i. Cell culture media
ii. HBSS
iii. Drugs (C3 Toxin)
iv. Aspirator
v. Laminar flow hood

b. **Steps**

i. Remove cell culture media and wash cells gently with 1 volume of HBSS.

ii. Add pre-warmed cell culture media or treatment. In the case of C3 Toxin, add serum-free media with 2 μg/ml of C3 Toxin to the cells 2 h prior to data acquisition.

2. Initial Data Acquisition of Raw Data

a. **Materials**

i. Metavue Imaging Series
ii. TE-2000E equipped with epifluorescence, 60× objective
iii. Live Cell incubator

b. **Steps**

i. Turn on live cell incubator and allow carbon dioxide and temperature to equilibrate for 5 min.

ii. Scan sample for cells containing ballistically injected beads using a combination of fluorescence with phase contrast. For GFP transfection, the scan must be performed with the appropriate fluorescence filter set first and then the cells are checked for presence of nanoparticles.

iii. Center the cell of interest. Adjust the focus to bring the beads into the brightest, clearest view. This may have to be repeated since beads may reside in different focal planes within the cells. Acquire 20-s streams of video with a Cascade 1k camera at a frame rate of 30 frames per second. This frame rate is achieved by limiting the acquisition region to 500 × 300 pixels, with 3 × 3 binning.

iv. Repeat for beads residing in different focus planes within the cell.

v. Acquire phase contrast and fluorescent still images for overlay purposes.
vi. Save stack files and images files.
vii. Repeat for each cell within the data set.

3. Analysis of Movie Streams

a. **Materials**

i. Metamorph Imaging Series
ii. Microsoft Excel

b. **Steps**

i. Open stream file in Metamorph Imaging Series.
ii. Calibrate the image using the pixel to distance calibration file. This must be obtained in advance using a stage micrometer.
iii. Draw a square region around beads of interest. Zoom 400% and duplicate the entire stream with zoom.
iv. Using the "track objects" command within Metamorph, create inner and outer regions around each nanoparticle in the first frame of the stream. Aggregated spheres are omitted from analysis since they violate assumptions made in subsequent calculations, as are spheres moved by cellular organelles. The inner region is created to fit just outside the perimeter of the nanoparticles. The outer region is adjusted to encompass the nanoparticle in the remaining frames.
v. Duplicate this image with the regions and save.
vi. Open a log to Excel and track the nanoparticles using the regions created. Log the bead number and the time-dependent coordinates for each frame. Save this data spreadsheet.

4. Conversion of Aquired Data to MSDs, Creep Compliance, and Viscoelastic Moduli

a. **Materials**

i. Matlab

b. **Steps**

The MSDs resulting from the thermally induced fluctuations of the nanoparticles are calculated from the time-dependent coordinates $[x(t), y(t)]$ extracted from movie streams using the following equations:

$$\mathrm{MSD}_x(\tau) = \sum_{i=1}^{N} \frac{\left(x(t_i+\tau) - x(t_i)\right)^2}{(N+1)} \quad \mathrm{MSD}_y(\tau) = \sum_{i=1}^{N} \frac{\left(y(t_i+\tau) - y(t_i)\right)^2}{(N+1)} \quad (1)$$

The MSD of the nanoparticle, $\langle \Delta r^2(\tau) \rangle$, is the sum of the x and y components:

$$\mathrm{MSD}(\tau) = \mathrm{MSD}_x(\tau) + \mathrm{MSD}_y(\tau) \tag{2}$$

Trajectories are monitored as a function of time to ensure that all nanoparticles are undergoing random, Brownian motion. Nanoparticles with trajectories that exhibit directed motion due to being endocytosed, altered motion due to directed movement of other cytoplasmic bodies in the cell, or due to error by the tracking software (i.e., when beads change focal planes) are eliminated from analysis. As the nanoparticles are thermally excited and randomly fluctuate in the cytoplasm, force is exerted on the surrounding cytoplasm. The deformability of the surrounding cytoplasm due to these forces is described by the local creep compliance, $\Gamma(\tau)$. The creep compliance is therefore proportional to the MSD:

$$\Gamma(\tau) = \frac{3\pi a}{2k_B T} \langle \Delta r^2(\tau) \rangle \tag{3}$$

where k_B is Boltzmann's constant, T is the absolute temperature of the cell (in degrees Kelvin), and a is the radius of the nanoparticle. The creep compliance is the inverse of pressure or modulus and is expressed in units of cm^2/dyn. The method to obtain frequency-dependent viscoelastic moduli has been described in detail in (Kole *et al.*, 2004). Briefly, the complex viscoelastic modulus, $G^*(\omega)$, is obtained using the following equation:

$$G^*(\omega) = \frac{k_B T}{\pi a i \omega \ \Im_u\{\langle \Delta r^2(\tau) \rangle\}} \tag{4}$$

where $\omega = 1/\tau$ and $\Im_u\{\langle \Delta r^2(\tau) \rangle\}$ is the Fourier transform of $\langle \Delta r^2(\tau) \rangle$. The elastic modulus is the real part of Eq. (4) and the viscous modulus is the imaginary part of Eq. (4). While $G^*(\omega)$ may be calculated numerically, an analytical solution was obtained by (Mason *et al.*, 1997) by approximating the Fourier transformation of $\langle \Delta r^2(\tau) \rangle$ into the Fourier domain using a wedge assumption, which expanding $\langle \Delta r^2(\tau) \rangle$ locally around the frequency of interest ω using a power law, and retains the leading term (Mason *et al.*, 1997). The Fourier transform of $\langle \Delta r^2(\tau) \rangle$ then becomes:

$$i\omega \, \Im_u\{\langle \Delta r^2(\tau) \rangle\} \approx \langle \Delta r^2(1/\omega) \rangle \Gamma[1 + \alpha(\omega)] i^{-\alpha(\omega)} \tag{5}$$

where $\alpha(\omega) = d \ln \langle \Delta r^2(\tau) \rangle / d \ln \tau|_{\tau = 1/\omega}$ is the local logarithmic slope of $\langle \Delta r^2(\tau) \rangle$ at the frequency of interest $\omega = 1/\tau$ and Γ is the gamma function. The frequency-dependent elastic and viscous moduli, G' and G'', respectively, can then be calculated algebraically using the following relationships:

$$G'(\omega) = |G^*(\omega)| \cos\left(\pi\alpha(\omega)/2\right) \tag{6}$$

$$G''(\omega) = |G^*(\omega)| \sin\left(\pi\alpha(\omega)/2\right) \tag{7}$$

where

$$|G^*(\omega)| = \frac{2k_B T}{3\pi a \langle \Delta r^2(1/\omega)\rangle \Gamma\left(1+\alpha(\omega)\right)} \tag{8}$$

IV. Pearls and Pitfalls

The process of ballistic injection of cells with nanoparticles contains many steps which present possible obstacles for success and must be optimized for each procedure. For instance, the appropriate quantity of nanoparticles to coat on the macrocarriers for bombardment can vary among cell lines and must be optimized empirically. Too few particles will not yield enough intracellular beads for tracking and too many will lead to overwhelming cell death, leaving only the cells without beads for tracking. Furthermore, the process of coating is key to success in that one cannot allow the formation of aggregates as the ethanol-based bead solution dries. Spreading technique to reduce aggregate formation can only be perfected with practice and may require coating more macrocarriers that necessary to ensure even coating for a ballistic run.

The wash step immediately following injection is crucial to the success of the experiment. However, washing too harshly has the potential to wash away all the cells that remain after bombardment. Washing too lightly will leave beads that have nonspecifically bound to the cell surface, and can subsequently be endocytosed.

Ballistic injection and transfection have the potential to endanger cell health and lead to cell death. Measures must be taken in both cases to increase the chances of cell survival. For example, using pre-warmed media each time cells are incubated or replated and minimizing the time cells are kept out of the incubator environment increase cell survival. For transfection, the use of antibiotics is detrimental to the health of cells and must be absent from cell media upon incubation with transfection reagents. Waiting until cells have mostly adhered to the cell culture substrate to add the transfection reagent is beneficial to cell survival. Finally, as is typical with any lipophilic transfection, the ratio of DNA:reagent as well as the total amount of reagent to add to the cells must be optimized.

In general, enhancement of the percentage of cells that contain injected beads and of the percentage that exhibit protein expression will increase the probability of having cells with both beads and expression for experimental observations. Additionally, the use of cell culture dishes that are entirely glass-bottomed, as opposed to partially, increases the percentage of cells that can be tested and, therefore, the population size for each experiment.

Finally, during microscopic data acquisition, beads must be finely focused to yield clear centriods for data analysis. Overlays should be created to ensure that the beads lie in the cells of interest (control, with toxin, or with GFP). In addition, movies should

be monitored during data tracking to ensure that beads are undergoing random, Brownian motion and are tracked without error (i.e., changing focal planes).

V. Concluding Remarks

We have introduced a new method that combines the key advantages of the BIN assay with the convenience of transient transfections to correlate changes in cytoskeleton organization with changes in local mechanical properties of the cytoplasm. This method retains all the advantages of BIN and adds those of transfections using standard transfection reagents. This approach should greatly expand the applications of BIN in cell and molecular biology.

References

Aktories, K., and Hall, A. (1989). Botulinum ADP-ribosyltransferase C3: A new tool to study low molecular weight GTP-binding proteins. *Trends Pharmacol. Sci.* **10,** 415–418.

Daniels, B. R., Masi, B. C., and Wirtz, D. (2006). Probing single-cell micromechanics *in vivo*: The microrheology of *C. elegans* developing embryos. *Biophys. J.* **90,** 4712–4719.

Gittes, F., Schnurr, B., Olmsted, P. D., MacKintosh, F. C., and Schmidt, C. F. (1997). Microscopic viscoelasticity: Shear moduli of soft materials determined from thermal fluctuations. *Phys. Rev. Lett.* **79,** 3286–3289.

Hall, A. (1992). Ras-related GTPases and the cytoskeleton. *Mol. Biol. Cell* **3,** 475–479.

Hoh, J. H., and Schoenenberger, C. A. (1994). Surface morphology and mechanical properties of MDCK monolayers by atomic force microscopy. *J. Cell Sci.* **107**(Pt. 5), 1105–1114.

Kole, T. P., Tseng, Y., Huang, L., Katz, J. L., and Wirtz, D. (2004). Rho kinase regulates the intracellular micromechanical response of adherent cells to rho activation. *Mol. Biol. Cell* **15,** 3475–3484.

Kole, T. P., Tseng, Y., Jiang, I., Katz, J. L., and Wirtz, D. (2005). Intracellular mechanics of migrating fibroblasts. *Mol. Biol. Cell* **16,** 328–338.

Lee, J. S., Chang, M. I., Tseng, Y., and Wirtz, D. (2005). Cdc42 mediates nucleus movement and MTOC polarization in Swiss 3T3 fibroblasts under mechanical shear stress. *Mol. Biol. Cell* **16,** 871–880.

Lee, J. S., Panorchan, P., Hale, C. M., Khatau, S. B., Kole, T. P., Tseng, Y., and Wirtz, D. (2006). Ballistic intracellular nanorheology reveals ROCK-hard cytoplasmic stiffening response to fluid flow. *J. Cell Sci.* **119,** 1760–1768.

Lee, J. S., Hale, C. M., Panorchan, P., Khatau, S. B., George, J. P., Tseng, Y., Stewart, C. L., Hodzic, D., and Wirtz, D. (2007). Nuclear lamin A/C deficiency induces defects in cell mechanics, polarization, and migration. *Biophys. J.* **93,** 2542–2552.

Luby-Phelps, K., Taylor, D. L., and Lanni, F. (1986). Probing the structure of cytoplasm. *J. Cell Biol.* **102,** 2015–2022.

Mason, T. G., Ganesan, K., van Zanten, J. V., Wirtz, D., and Kuo, S. C. (1997). Particle-tracking microrheology of complex fluids. *Phys. Rev. Lett.* **79,** 3282–3285.

Panorchan, P., Lee, J. S., Kole, T. P., Tseng, Y., and Wirtz, D. (2006). Microrheology and ROCK signaling of human endothelial cells embedded in a 3D matrix. *Biophys. J.* **91,** 3499–3507.

Pelham, R. J., Jr., and Wang, Y. (1997). Cell locomotion and focal adhesions are regulated by substrate flexibility. *Proc. Natl. Acad. Sci. USA* **94,** 13661–13665.

Pollard, T. D., and Borisy, G. G. (2003). Cellular motility driven by assembly and disassembly of actin filaments. *Cell* **112,** 453–465.

Suh, J., Wirtz, D., and Hanes, J. (2003). Efficient active transport of gene nanocarriers to the cell nucleus. *Proc. Natl. Acad. Sci. USA* **100,** 3878–3882.

Tsai, M. A., Frank, R. S., and Waugh, R. E. (1993). Passive mechanical behavior of human neutrophils: Power-law fluid. *Biophys. J.* **65,** 2078–2088.

Tseng, Y., An, K. M., Esue, O., and Wirtz, D. (2004a). The bimodal role of filamin in controlling the architecture and mechanics of F-actin networks. *J. Biol. Chem.* **279,** 1819–1826.

Tseng, Y., An, K. M., and Wirtz, D. (2002a). Microheterogeneity controls the rate of gelation of actin filament networks. *J. Biol. Chem.* **277,** 18143–18150.

Tseng, Y., Fedorov, E., McCaffery, J. M., Almo, S. C., and Wirtz, D. (2001). Micromechanics and microstructure of actin filament networks in the presence of the actin-bundling protein human fascin: A comparison with α-actinin. *J. Mol. Biol.* **310,** 351–366.

Tseng, Y., Kole, T. P., and Wirtz, D. (2002b). Micromechanical mapping of live cells by multiple-particle-tracking microrheology. *Biophys. J.* **83,** 3162–3176.

Tseng, Y., Lee, J. S., Kole, T. P., Jiang, I., and Wirtz, D. (2004b). Micro-organization and visco-elasticity of the interphase nucleus revealed by particle nanotracking. *J. Cell Sci.* **117,** 2159–2167.

Tseng, Y., Schafer, B. W., Almo, S. C., and Wirtz, D. (2002c). Functional synergy of actin filament cross-linking proteins. *J. Biol. Chem.* **277,** 25609–25616.

Tseng, Y., and Wirtz, D. (2001). Mechanics and multiple-particle tracking microheterogeneity of alpha-actinin-cross-linked actin filament networks. *Biophys. J.* **81,** 1643–1656.

Tseng, Y., Kole, T. P., Lee, J. S., Fedorov, E., Almo, S. C., Schafer, B. W., and Wirtz, D. (2005). How actin crosslinking and bundling proteins cooperate to generate an enhanced cell mechanical response. *Biochem. Biophys. Res. Commun.* **334,** 183–192.

Valberg, P. A., and Albertini, D. F. (1985). Cytoplasmic motions, rheology, and structure probed by a novel magnetic particle method. *J. Cell Biol.* **101,** 130–140.

Varker, K., Phelps, S., King, M., and Williams, C. (2003). The small GTPase RhoA has greater expression in small cell lung carcinoma than in non-small cell lung carcinoma and contributes to their unique morphologies. *Int. J. Oncol.* **22,** 671–681.

Xu, J., Tseng, Y., and Wirtz, D. (2000). Strain hardening of actin filament networks: Regulation by the dynamic cross-linking protein a-actinin. *J. Biol. Chem.* **275,** 35886–35892.

Xu, J., Wirtz, D., and Pollard, T. D. (1998). Dynamic cross-linking by α-actinin determines the mechanical properties of actin filament networks. *J. Biol. Chem.* **273,** 9570–9576.

Yamada, S., Wirtz, D., and Kuo, S. C. (2000). Mechanics of living cells measured by laser tracking microrheology. *Biophys. J.* **78,** 1736–1747.

CHAPTER 19

Mechanical Response of Cytoskeletal Networks

Margaret L. Gardel,[*] Karen E. Kasza,[†] Clifford P. Brangwynne,[†] Jiayu Liu,[‡] and David A. Weitz[†,‡]

[*]Department of Physics and Institute for Biophysical Dynamics
University of Chicago, Illinois 60637

[†]School of Engineering and Applied Sciences
Harvard University
Cambridge, Massachusetts 02143

[‡]Department of Physics
Harvard University
Cambridge, Massachusetts 02143

METHODS IN CELL BIOLOGY, VOL. 89

0091-679X/08 $35.00
DOI: 10.1016/S0091-679X(08)00619-5

Abstract

The cellular cytoskeleton is a dynamic network of filamentous proteins, consisting of filamentous actin (F-actin), microtubules, and intermediate filaments. However, these networks are not simple linear, elastic solids; they can exhibit highly nonlinear elasticity and athermal dynamics driven by ATP-dependent processes. To build quantitative mechanical models describing complex cellular behaviors, it is necessary to understand the underlying physical principles that regulate force transmission and dynamics within these networks. In this chapter, we review our current understanding of the physics of networks of cytoskeletal proteins formed *in vitro*. We introduce rheology, the technique used to measure mechanical response. We discuss our current understanding of the mechanical response of F-actin networks, and how the biophysical properties of F-actin and actin cross-linking proteins can dramatically impact the network mechanical response. We discuss how incorporating dynamic and rigid microtubules into F-actin networks can affect the contours of growing microtubules and composite network rigidity. Finally, we discuss the mechanical behaviors of intermediate filaments.

I. Introduction

Many aspects of cellular physiology rely on the ability to control mechanical forces across the cell. For example, cells must be able to maintain their shape when subjected to external shear stresses, such as forces exerted by blood flow in the vasculature. During cell migration and division, forces generated within the cell are required to drive morphogenic changes with extremely high spatial and temporal precision. Moreover, adherent cells also generate force on their surrounding environment; cellular force generation is required in remodeling of extracellular matrix and tissue morphogenesis.

This varied mechanical behavior of cells is determined, to a large degree, by networks of filamentous proteins called the cytoskeleton. Although we have the tools to identify the proteins in these cytoskeletal networks and study their structure and their biochemical and biophysical properties, we still lack an understanding of the biophysical properties of dynamic, multiprotein assemblies. This knowledge of the biophysical properties of assemblies of cytoskeletal proteins is necessary to link our knowledge of single molecules to whole cell physiology. However, a complete understanding of the mechanical behavior of the dynamic cytoskeleton is far from complete.

One approach is to develop techniques to measure mechanical properties of the cytoskeleton in living cells (Bicek *et al.*, 2007; Brangwynne *et al.*, 2007a; Crocker and Hoffman, 2007; Kasza *et al.*, 2007; Panorchan *et al.*, 2007; Radmacher, 2007). Such techniques will be critical in delineating the role of cytoskeletal elasticity in dynamic cellular processes. However, because of the complexity of the living cytoskeleton, it would be impossible to elucidate the physical origins of this cytoskeletal elasticity from live cell measurements in isolation. Thus, a complementary

approach is to study the behaviors of reconstituted networks of cytoskeletal proteins *in vitro*. These measurements enable precise control over network parameters, which is critical to develop predictive physical models. Mechanical measurements of reconstituted cytoskeletal networks have revealed a rich and varied mechanical response and have required the development of qualitatively new experimental tools and physical models to describe physical behaviors of these protein networks. In this chapter, we review our current understanding of the biophysical properties of networks of cytoskeletal proteins formed *in vitro*. In Section II, we discuss rheology measurements and the importance of several parameters in interpretation of these results. In Section III, we discuss the rheology of F-actin networks, highlighting how small changes in network composition can qualitatively change the mechanical response. In Section IV, the effects of incorporating dynamic microtubules in composite F-actin networks will be discussed. Finally, in Section V, we will discuss the mechanics of intermediate filament (IF) networks.

II. Rheology

Rheology is the study of how materials deform and flow in response to externally applied force. In a simple elastic solid, such as a rubber band, applied forces are stored in material deformation, or strain. The constant of proportionality between the stress, force per unit area, and the strain, deformation per unit length, is called the elastic modulus. The geometry of the measurement defines the area and length scale used to determine stress and strain. Several different kinds of elastic moduli can be defined according to the direction of the applied force (Fig. 1). The tensile

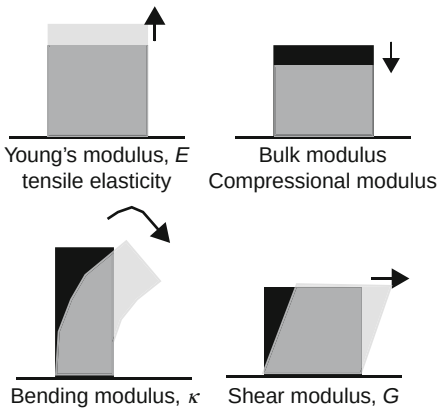

Fig. 1 Schematics showing the direction of the applied stress in several common measurements of mechanical properties; the light gray shape, indicating the sample after deformation, is overlaid onto the black shape, indicating the sample before deformation. The Young's modulus, or tensile elasticity, is the deformation in response to an applied tension whereas the bulk (compressional) modulus measures material response to compression. The bending modulus measures resistance to bending of a rod along its length and, finally, the shear modulus measures the response of a material to a shear deformation.

elasticity, or Young's modulus, is determined by the measurement of extension of a material under tension along a given axis. In contrast, the bulk modulus is a measure of the deformation under a certain compression. The bending modulus of a slender rod measures the object resistance to bending along its length. And, finally, the shear elastic modulus describes object deformation resulting from a shear, volume-preserving stress (Fig. 2). For a simple elastic solid, a steady shear

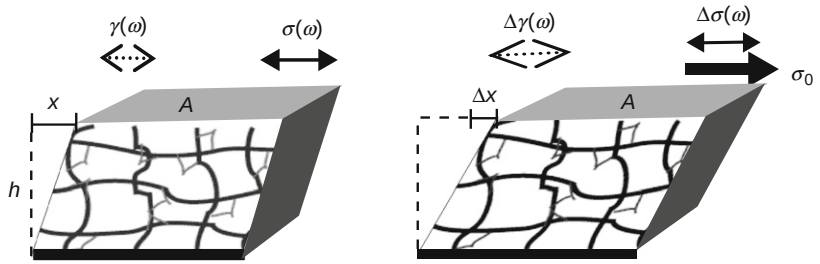

Term	Symbol	Units	Definition
Strain	γ	None	$\frac{x}{\text{Height } (h)}$; sample deformation
Stress	σ	Pascal (Pa)	$\frac{\text{Force}}{\text{Area } (A)}$
Frequency	ω	Time^{-1}	Frequency of applied + measured waveforms: $\gamma(\omega) = \gamma \sin(\omega t)$, $\sigma(\omega) = \sigma \sin(\omega t)$
Prestress	σ_0	Pascal (Pa)	Constant external stress applied to sample during measurement
Phase Shift	δ	Degrees	$\delta(\omega) = \tan^{-1}(G''(\omega)/G'(\omega))$ $\delta = 0°$, elastic solid; $\delta = 90°$, fluid
Shear moduli:			
$\sigma_0 = 0$			
Elastic (storage) modulus	G'	Pascal (Pa)	$G'(\omega) = \sigma(\omega)/\gamma(\omega) \cos(\delta(\omega))$
Viscous (loss) modulus	G''	Pascal (Pa)	$G''(\omega) = \sigma(\omega)/\gamma(\omega) \sin(\delta(\omega))$
$\sigma_0 > 0$			
Differential elastic modulus	K'	Pascal (Pa)	$K'(\omega) = \Delta\sigma(\omega)/\Delta\gamma(\omega) \cos(\Delta\delta(\omega))$
Differential loss modulus	K''	Pascal (Pa)	$K'(\omega) = \Delta\sigma(\omega)/\Delta\gamma(\omega) \cos(\Delta\delta(\omega))$

Fig. 2 This schematic defines many of the rheology terms used in this chapter. (Left) To measure the shear elastic modulus, $G'(\omega)$, and shear viscous modulus, $G''(\omega)$, an oscillatory shear stress, $\sigma(\omega)$, is applied to the material and the resultant oscillatory strain, $\gamma(\omega)$ is measured. The frequency, ω, is varied to probe mechanical response over a range of timescales. (Right) To measure how the stiffness varies as a function of external stress, a constant stress, σ_0, is applied and a small oscillatory stress, ($\Delta\sigma(\omega)$), is superposed to measure a differential elastic and viscous loss modulus.

stress results in a constant strain. In contrast, for a simple fluid, such as water, shear forces result in a constant flow or rate of change of strain. The constant of proportionality between the stress and strain rate, $\dot{\gamma}$, is called the viscosity, η.

To date, most rheological measurements of cytoskeletal networks have been that of the shear elastic and viscous modulus. Mechanical measurements of shear elastic and viscous response over a range of frequencies and strain amplitudes are possible with commercially available rheometers. Recent developments in rheometer technology now provide the capability of mechanical measurements with as little as 100 μl sample volume, a tenfold decrease in sample volume from previous generation instruments. Recently developed microrheological techniques now also provide measurement of compressional modulus (Chaudhuri *et al.*, 2007). Reviews of microrheological techniques can be found in Crocker and Hoffman (2007), Kasza *et al.* (2007), Panorchan *et al.* (2007), Radmacher (2007), and Weihs *et al.* (2006).

A. Frequency-Dependent Viscoelasticity

In general, the rheological behaviors of cytoskeletal polymer networks display characteristics of both elastic solids and viscous fluids and, thus, are viscoelastic. To characterize the linear viscoelastic response, small amplitude, oscillatory shear strain, $\gamma \sin(\omega t)$, is applied and the resultant oscillatory stress, $\sigma \sin(\omega t+\delta)$, is measured , where δ is the phase shift of the measured stress and is $0 < \delta < \pi/2$. (Figure 2 describes much of the terminology used in this chapter.) The in-phase component of the stress response determines the shear elastic modulus, $G'(\omega) = (\sigma/\gamma)\cos(\delta(\omega))$, and is a measure of how mechanical energy is stored in the material. The out-of-phase response measures the viscous loss modulus, $G''(\omega) = (\sigma/\gamma)\sin(\delta(\omega))$, and is a measure of how mechanical energy is dissipated in the material. In general, G' and G'' are frequency-dependent measurements. Thus, materials that behave solid-like at certain frequencies may behave liquid-like at different frequencies; measurements of the frequency-dependent moduli of solutions of flexible polymers (polyethylene oxide) and the biopolymer, filamentous actin (F-actin) are shown in Fig. 3A. The solution of flexible polymers (black symbols) is predominately viscous, and the viscous modulus (open symbols) dominates over the elastic modulus (filled symbols) over the entire frequency range. In contrast, the solution of F-actin filaments (gray symbols, Fig. 3A) is dominated by the viscous modulus at frequencies higher than 0.1 Hz but becomes dominated by the elastic modulus at lower frequencies. Thus, it is critical to make measurements over an extended frequency range to ascertain critical relaxation times in the sample. Moreover, frequency-dependent dynamics should be carefully considered in establishing mechanical models.

The measurements shown in Fig. 3A are measurements of *linear* elastic and viscous moduli. In the linear regime, the stress and the strain are linearly dependent and, since the moduli are the ratio between these quantities, the measured moduli are independent of the magnitude of applied stress or strain. For flexible polymers, the moduli can remain linear up to extremely high (>100%) strains. (Consider

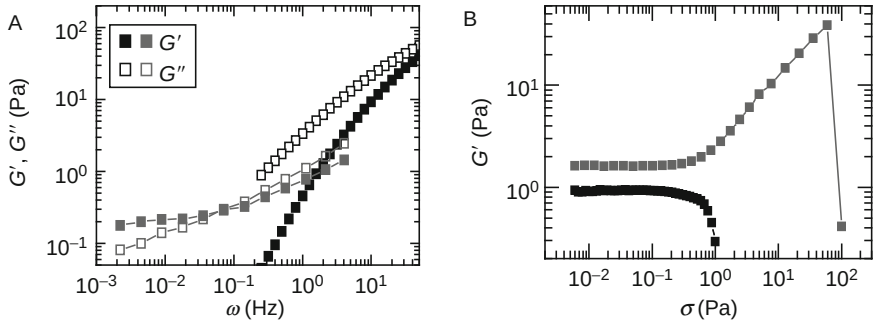

Fig. 3 (A) Frequency-dependent elastic (filled symbols) and viscous (open symbols) moduli of a network of F-actin (gray symbols) and solution of flexible polymers (black symbols) illustrating the frequency dependence of these parameters (B) Measurement of G' as a function of applied stress for a network that stress stiffens (top, gray squares) and stress weakens (bottom, black squares).

extending a rubber band; the force required to extend it a certain distance will remain linear up to several times its original length.) However, for many biopolymer networks, the linear elastic regime can be quite small (<10%). To confirm you are measuring linear elastic properties, it is recommended that you make measurements at two different levels of stress and confirm you measure identical frequency-dependent behaviors.

B. Stress-Dependent Elasticity

The mechanical response of cytoskeletal networks can be highly nonlinear such that the elastic properties are critically dependent on the stress that is applied to the network. When the elasticity increases with increasing applied stress or strain, materials are said to ''stress-stiffen'' or ''strain-stiffen'' (Fig. 3B). In contrast, if the elasticity decreases with increased stress, the material is said to ''stress-soften'' or, likewise, ''strain-soften'' (Fig. 3B).

Stress-stiffening behavior has been observed for many cytoskeletal networks, for example, F-actin networks cross-linked with a variety of actin-binding proteins (Gardel *et al.*, 2004a, 2006b; MacKintosh *et al.*, 1995; Storm *et al.*, 2005; Xu *et al.*, 2000) and intermediate filament networks (Storm *et al.*, 2005). In this nonlinear regime, F-actin networks compress in the direction normal to that of the shear and exert negative normal stress (Janmey *et al.*, 2007). The origins of stress-stiffening can occur in nonlinearities in elasticity of individual actin filaments or reorganization of the network under applied stress.

Not all reconstituted cytoskeletal networks exhibit stress stiffening under shear. Some show stress weakening: the modulus decreases as the applied stress increases. This is usually found in networks that are weakly connected. For example, pure F-actin solutions, weakly cross-linked actin networks (Gardel *et al.*, 2004a; Xu

et al., 1998), and pure microtubule networks (Lin *et al.*, 2007) all show stress-softening behavior. Under compression, branched, dendritic networks of F-actin are also shown to reversibly stress soften at high loads (Chaudhuri *et al.*, 2007).

In the nonlinear elastic regime, large amplitude oscillatory measurements are inaccurate, as the response waveforms are not sinusoidal (Xu *et al.*, 2000). To accurately measure the frequency-dependent nonlinear mechanical response, a static prestress can be applied to the network, and the linear, differential elastic modulus, K', and loss modulus, K'' are determined from the response to a small, superposed oscillatory stress (Gardel *et al.*, 2004a,b; Fig. 2, right). However, if a material remodels and the strain changes with time when imposed by a constant external stress alternative, nonoscillatory rheology measurements may be necessary.

C. Effect of Measurement Length Scale

Due to the inherent rigidity of cytoskeletal polymers, cytoskeletal networks formed *in vitro* are structured at micrometer length scales. The mechanical response of cytoskeletal networks can depend on the length scale at which the measurement is taken (Gardel *et al.*, 2003; Liu *et al.*, 2006). Conventional rheometers measure average mechanical response of a material at length scales $>100\ \mu$m. By contrast, microrheological techniques can be used to measure mechanical response at micrometer length scales; however, interpretations of these measurements are not usually straightforward for cytoskeletal networks structured at micrometer length scales (Gardel *et al.*, 2003; Valentine *et al.*, 2004; Wong *et al.*, 2004). Direct visualization of the deformations of filaments such as F-actin and microtubules (Bicek *et al.*, 2007; Brangwynne *et al.*, 2007a) can also be used to calculate local stresses (see Section IV).

III. Cross-Linked F-Actin Networks

A. Biophysical Properties of F-Actin and Actin Cross-linking Proteins

1. Actin Filaments

Actin is the most abundant protein found in eukaryotic cells. It comprises 10% of the total protein mass in muscle cells and up to 5% in nonmuscle cells (Lodish *et al.*, 1999). Globular actin (G-actin) polymerizes to form F-actin with a diameter, d, of 5 nm and contour lengths, L_c, up to 20 μm (Fig. 4). The extensional modulus, or Young's modulus, E, of F-actin is approximately 10^9 Pa, similar to that of plexiglass (Kojima *et al.*, 1994). However, due to the nanometer-scale filament diameter, the bending modulus, $\kappa_0 \sim Ed^4$, is quite soft. The ratio of κ_0 to thermal energy, k_BT, defines a length scale called the persistence length, $\ell_p \sim \kappa_0/k_BT$. This is the length over which vectors tangent to the filament contour become uncorrelated by the effects of thermally driven bending fluctuations. For F-actin, $\ell_p \approx 8 - 17\mu$m, (Gittes *et al.*,

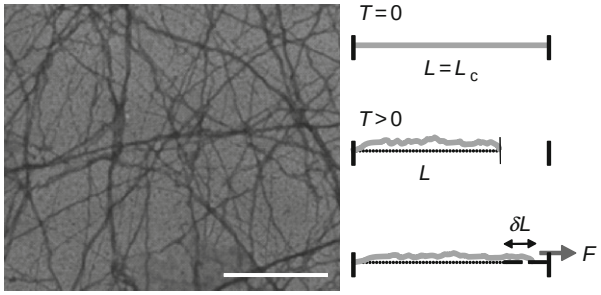

Fig. 4 (Left) Electron micrograph of F-actin. Scale bar is 1 μm. (Right) In the absence of thermal forces ($T = 0$), a semiflexible polymer appears as a rod, with the full polymer contour length, L_c, identical to the shortest distance between the ends of the polymer, L. However, thermally induced transverse bending fluctuations ($T > 0$) lead to contraction of L such that $L < L_c$. An applied tensile force, F, extends the filament by a length, δL, and, because L_c is constant, this reduces the amplitude of the thermally induced bending fluctuations, giving rise to a force-extension relation that is entropic in origin.

1993; Ott *et al.*, 1993) and, thus, is semiflexible at micrometer length scales with a persistence length intermediate to that of DNA, $\ell_p \approx 0.05$ μm, and microtubules, $\ell_p \approx 1000$ μm.

Transverse fluctuations driven by thermal energy ($T > 0$) also result in contraction of the end-to-end length of the polymer, L, such that $L < L_c$ (Fig. 4). In the linear regime, applied tensile force, τ, to the end of the filament results in extension, δL, of the filament such that: $\tau \sim [\kappa^2/(\kappa T L^4)] \times (\delta L)$ (MacKintosh *et al.*, 1995). This constant of proportionality, $\kappa^2/(\kappa T L^4)$, defines a spring constant that arises from purely thermal effects, which seek to maximize entropy by maximizing the number of available configurations of the polymer. The distribution and number of available configurations depends on the length, L, of the polymer such that the spring constant will decrease simply by increasing filament length. However, as $L \to L_c$, the entropic spring constant diverges such that the force-extension relationship is highly nonlinear (Bustamante *et al.*, 1994; Fixman and Kovac, 1973; Liu and Pollack, 2002). At high extension, the tensile force diverges nonlinearly with increasing extension such that: $\tau \sim 1/(L_c - L)^2$. Thus, the force-extension relationship depends sensitively on the magnitude of extension.

The elastic properties of actin filaments are also sensitive to binding proteins and molecules. For instance phalloidin and jasplakinolide, two small molecules that stabilize F-actin enhance F-actin stiffness (Isambert *et al.*, 1995; Visegrady *et al.*, 2004). It has been shown that a member of the formin family of actin-binding and nucleator proteins, mDia1, decreases the stiffness of actin filaments (Bugyi *et al.*, 2006).

2. Actin Cross-Linking Proteins

In the cytoskeleton, the local microstructure and connectivity of F-actin is controlled by actin-binding proteins (Kreis and Vale, 1999). These binding proteins control the organization of F-actin into mesh-like gels, branched dendritic

networks, or parallel bundles, and it is these large-scale cytoskeletal structures that determine force transmission at the cellular level. Some proteins, such as fimbrin and α-actinin, are small and tend to organize actin filaments into bundles, whereas others, like filamin and spectrin, tend to organize F-actin into more network-like structures.

The cross-linking proteins found inside most cells are quite different from simple rigid, permanent cross-links in two important ways. Most physiological cross-links are dynamic, with finite binding affinities to actin filaments that results in the disassociation of cross-links from F-actin over timescales relevant for cellular remodeling. Moreover, physiological cross-links have a compliance that depends on their detailed molecular structure and determines network mechanical response. Thus, not surprisingly, the kinetics and mechanics of F-actin-binding proteins can have a significant impact on the mechanical response of cytoskeletal networks.

Typical F-actin cross-linking proteins are dynamic; they have characteristic on and off rates that are on the order of seconds to tens of seconds. The cross-linking protein α-actinin, which is commonly found in contractile F-actin bundles, is a dumb-bell shaped dimer with F-actin-binding domains spaced approximately 30 nm apart. Typical dissociation constants for α-actinin are on the order of $K_d = 1\ \mu M$ and dissociation rates are on the order of $1\ s^{-1}$, but vary between different isoforms (Wachsstock *et al.*, 1993), with temperature (Tempel *et al.*, 1996) and the mechanical force exerted on the cross-link (Lieleg and Bausch, 2007).

Physiologically relevant cross-links cannot be thought of simply as completely rigid structural elements; they can, in fact, contribute significantly to network compliance. Filamin proteins found in humans are quite large dimers of two 280-kDa polypeptide chains, each consisting of 1 actin-binding domain, 24 β-sheet repeats forming 2 rod domains, and 2 unstructured "hinge" sequences (Stossel *et al.*, 2001). The contour length of the dimer is approximately 150 nm, making it one of the larger actin cross-links in the cell (Fig. 5A). Unlike many other

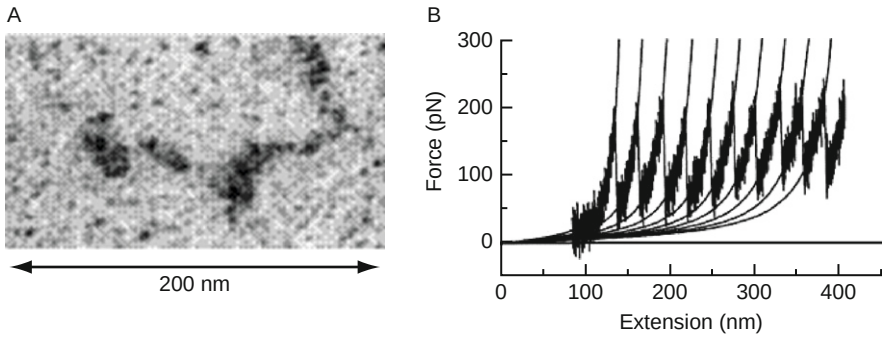

Fig. 5 (A) Electron micrographs of filamin A dimer (with permission, Stossel *et al.*, 2001). (B) Force-extension curve for a filamin A molecule measured by atomic force microscopy. The characteristic sawtooth pattern is associated with unfolding events of β-sheet domains in the molecule (with permission, Furuike *et al.*, 2001).

cross-linking proteins that dimerize parallel to each other in order to form a small rod, the filamin molecules dimerize such that they form a V-shape with actin-binding domains at the end of each arm. This geometry is thought to allow filamin molecules to preferentially cross-link actin filaments orthogonally and to form strong networks even at low concentrations.

The compliance of a single filamin molecule can be probed with atomic force microscopy force-extension measurements. Initial results suggest that for forces less than 50–100 pN, a single filamin A molecule can be modeled as a worm-like chain; for larger forces, reversible unfolding of β-sheet repeats occurs, leading to a large increase in cross-link contour length (Furuike *et al.*, 2001; Fig. 5B). It is important to note that forces reported for these types of unfolding measurements are rate dependent; the longer a force is applied to the molecule, the lower the threshold force required for the conformational change.

One additional class of binding proteins is molecular motors such as myosin. The conformation change of the molecule as it undergoes ATP hydrolysis can generate pico-Newton scale forces within the F-actin network or bundle. These forces can generate filament motion, such as observed in F-actin sliding within the contraction of a sarcomere. These actively generated forces can significantly change the mechanical properties and the structure of the cytoskeletal network in which they are embedded (Bendix *et al.*, 2008).

B. Rheology of Rigidly Cross-Linked F-Actin Networks

Although the importance of understanding mechanical response of cytoskeletal networks has been appreciated for several decades, predictive physical models to describe the full range of mechanical response observed in these networks have proven elusive. This has been, in part, due to the large sample volumes required by conventional rheology (1–2 ml per measurement) and the inability to purify sufficient quantities of protein with adequate purity to perform *in vitro* measurements. Improvement in the torque sensitivity of commercially available rheometers as well as the establishment of bacteria and insect cell expression systems for protein expression has overcome many of these difficulties.

In the last several years, much progress has been made in understanding the elastic response of F-actin filaments cross-linked into networks by very rigid, nondynamic linkers. This class of cross-linkers greatly simplifies the interpretations of the rheology in two distinct ways. When the cross-linkers are more rigid than F-actin filaments, then the mechanical response of the composite network is predominately determined by deformations of the softer F-actin filaments; in this case, the cross-linkers serve to determine the architecture of the network. When cross-linkers have a very high binding affinity and remain bound to F-actin over long times (>minutes), then we do not have to consider the additional timescales associated with cross-linking binding affinity, which can lead to network remodeling under external stress.

Two realizations of this are cross-linking through avidin–biotin cross-links (MacKintosh *et al.*, 1995) and the actin-binding protein, scruin (Gardel *et al.*, 2004a; Shin *et al.*, 2004). In these networks, network compliance is due to the semiflexibility of individual F-actin filaments. Such a network can be considered to have an average distance between actin filaments, or mesh size, $\xi \sim 1/\sqrt{c_A}$ with a distance between cross-links, ℓ_c where $\ell_c > \xi$ for homogeneous networks.

1. Network Elasticity and Microscopic Deformation

In order to establish an understanding of the elastic properties of a material, it is required to know how it will deform in response to an external shear stress. For semiflexible polymers, such as F-actin, strain energy can be stored either in filament bending or in stretching. These elastic constants depend on the length of filament segment that is being deformed, for instance, ℓ_c for a homogeneous cross-linked F-actin network. Recent theoretical work has shown that the deformation of F-actin networks under an external shear stress is dominated by stretching of filaments in the limit of high cross-link and F-actin concentration and long filament lengths (Head *et al.*, 2003a,b). Here, the deformations in the network are self-similar at all length scales, or affine (Fig. 6). In contrast, in the limit of low cross-link and F-actin concentration and short F-actin lengths, deformations imposed by the external shear stress result in filament bending and nonaffine deformation throughout the network (Das *et al.*, 2007;

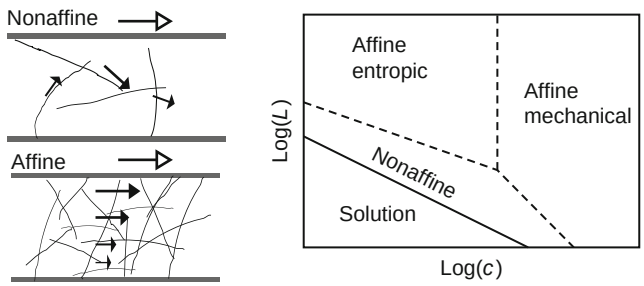

Fig. 6 (Left) Schematics indicating difference between affine and nonaffine deformations. A fibrous network is indicated by slender black rods that is confined between two parallel plates indicated by dark gray rods. The direction of shear at the macroscopic level is indicated by the arrow with the open arrowhead, whereas filled arrows indicate direction of microscopic deformations within the sample. In nonaffine deformations, the directions of deformation within the sample are not similar to each other or to the direction of macroscopic shear; this type of deformation is realized in very sparse networks. In affine deformation, the direction of macroscopic deformation is highly self-similar to the directions of microscopic deformation within the sample; this type of deformation is realized in highly concentrated polymer networks. (Right) A sketch of the various elastic regimes in terms of molecular weight L and polymer concentration c. The solid line represents where network rigidity first appears at the macroscopic level. For affine deformation, elastic response can arise both from the filament stretching of entropically derived bending fluctuations or from the Young's modulus of individual filaments.

Head *et al.*, 2003a,b; Fig. 6). These predictions have been confirmed in experiments by visualizing the deformations of F-actin networks during application of shear deformation using confocal microscopy (Liu *et al.*, 2007) where nonaffinity is calculated as the deviation of network deformations after shear from the assumed affine positions; these experiments confirmed that weakly cross-linked F-actin networks exhibited nonaffine deformations, whereas deformations of strongly cross-linked networks were more affine.

2. Entropic Elasticity of F–Actin Networks

In networks of F-actin cross-linked with incompliant cross-links where shear stress results in affine deformations, the elastic response is dominated by stretching of individual actin filaments. At the filament length scale, the strain, γ, is proportional to δ/ℓ_c where δ is the extension of individual filaments and ℓ_c is the distance between cross-links. The stress, σ, can be considered as F/ξ^2, where F is the force applied to individual filaments and ξ is the mesh size of the network. Thus, we can relate the force-extension of single filaments (Section III.A.1) to the network elasticity. For networks structured at micrometer length scales, the spring constant determined by entropic fluctuations determines the elastic response at small strains such that:

$$G' \sim \frac{\sigma}{\gamma} \sim \frac{\kappa^2}{k_B T \xi^2 \ell_c^3}$$

where the contour length is determined by the distance between cross-links and is proportional to the entanglement length. Because the entropic spring constant is highly sensitive to the contour length, this model predicts a sharp dependence of the elastic stiffness with both the F-actin concentration, c_A, and the ratio of cross-links to actin monomers, R, such that:

$$G' \sim c_A^{11/5} R^{(6x+15y)/5}$$

where the exponent x characterizes how efficiently the cross-linker bundles F-actin and y characterizes the cross-linking efficiency (Shin *et al.*, 2004). The variation of the elastic stiffness as a function of F-actin concentration has been observed experimentally (Gardel *et al.*, 2004a; MacKintosh *et al.*, 1995; Fig. 7). The pronounced dependence of the elastic stiffness observed as a function of polymer and cross-link density is in sharp contrast to the weak dependence observed in networks of flexible polymers.

Densely cross-linked F-actin networks exhibit nonlinear elasticity at large stresses and strains, where G' increases as a function of stress until a maximum stress,σ_{max}, and strain, γ_{max}, at which the network "breaks" (Fig. 2B). In this system, the breaking stress is linearly proportional to the density of F-actin filaments and suggests that individual F-actin ruptures (Gardel *et al.*, 2004b). The maximum strain is observed to vary such that $\gamma_{max} \sim \ell_c \sim c_A^{-2/5}$ and directly

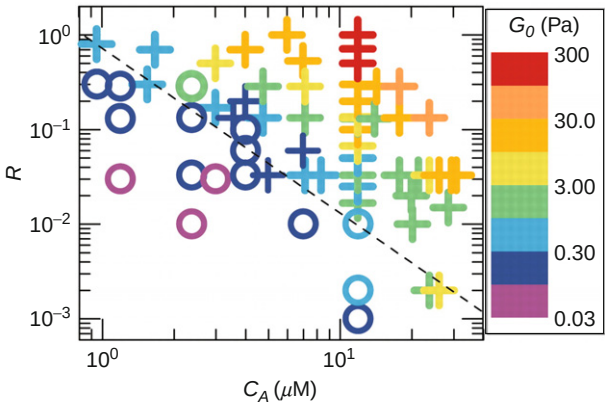

Fig. 7 State diagram of rigidly cross-linked F-actin networks over a range of R, the cross-link concentration, and c_A, F-actin concentration. The range in colors corresponds to the magnitude of the linear elastic modulus, G_0 (indicated by the heat scale) whereas the symbols denote networks that exhibit stress stiffening (+) or stress weakening (o) (with permission, Gardel *et al.*, 2004).

reflects the change in contour length resulting from varying F-actin concentration (Gardel *et al.*, 2004a). Moreover, the qualitative form of the nonlinearity in the stress–strain relationship at the network length scale is identical to divergence observed in the force–extension relationship for single semiflexible polymers as the extension approaches the polymer contour length (Gardel *et al.*, 2004a,b). Thus, the nonlinear strain-stiffening response of these F-actin networks at macroscopic length scales directly reflects the nonlinear stiffening of individual filaments.

3. Other Regimes of Elastic Response

As the concentration of cross-links or the filament persistence length increases, the entropic spring constant to stretch semiflexible filaments will increase sufficiently such that the deformation of filaments is dominated by the Young's modulus of the filament. Here, the elasticity is still due to stretching individual F-actin filaments, but thermal effects do not play a role and the elastic response of these networks is more similar to that of a dense network of macroscopic rods (e.g., imagine a dense network of cross-linked pencils or spaghetti). Here, no mechanism for significant stress stiffening at the scale of individual rods is established. However, reorganization of these networks under applied stress may lead to stress stiffening. Such a regime of elasticity may be observed in networks of highly bundled F-actin filaments; such networks have not been observed experimentally.

In contrast, as the density of cross-links or filament persistence length decreases, filaments will tend to bend (and buckle) under an external shear deformation. Bending deformations result in deformations that are not self-similar, or affine, within the network (Head *et al.*, 2003a,b). Experimental measurements have shown an increase

in nonaffine deformations at low cross-link concentrations (Liu *et al.*, 2007) as well as an abrogation of stress-stiffening response (Gardel *et al.*, 2004a). Instead, these networks soften under increasing strain and linear response is observed for strains as large as one. For these networks, the linear elastic modulus is less sensitive to variations in cross-link density and actin concentration. While a complete comparison with theory is still required, it appears that in this regime, network elasticity is dominated by filament bending, with nonlinear response due to buckling of single filaments (Gardel *et al.*, 2004a; Head *et al.*, 2003a,b; Liu *et al.*, 2007).

The rich variety of elastic response in even a model system of F-actin cross-linked by rigid, nondynamic cross-links demonstrates the complexity involved with building mechanical models of networks of cross-linked semiflexible polymers that can exhibit both entropic and enthalpic contributions to the mechanical response.

C. Physiologically Cross-Linked F-Actin Networks

F-actin networks formed with rigid, incompliant cross-links form a benchmark to understanding the elastic response of cytoskeletal F-actin networks. However, as discussed in Section III.A.2, physiological F-actin cross-linking proteins typically have a finite binding affinity to F-actin and significant compliance. The extent of F-actin-binding affinity of the cross-linker determines a timescale over which forces are efficiently transmitted through the F-actin/cross-link connection and dramatically affects how forces are transmitted and dissipated through the network. When the cross-link that has comparable stiffness to that of an F-actin filament, the network will elasticity will some superposition of the elastic response of each element individually. Thus, the changes in the kinetics and mechanics of individual cross-linking proteins can dramatically affect the mechanical response of the F-actin network.

1. Effects of Cross-Link Binding Kinetics: α-Actinin

The contribution of cross-link binding kinetics to network material properties has been studied most explicitly in the α-actinin and fascin systems. The dynamic nature of cytoskeletal cross-links means that networks formed with them are able to reorganize and remodel, or look ''fluid-like'' at long times (Sato *et al.*, 1987). In particular, temperature has been used to systematically alter the binding affinity of α-actinin to F-actin, and the mechanics of the resulting network probed with bulk rheology (Tempel *et al.*, 1996; Xu *et al.*, 1998). The key experimental observation is that as temperature is increased from 8 to 25 °C, the α-actinin cross-linked F-actin networks become softer and more fluid-like. At 8 °C, the networks are stiff, elastic networks that look similar to networks cross-linked with rigid, static cross-links. As the temperature is raised to 25 °C, the network stiffness decreases by nearly a factor of 10 and the network becomes more fluid-like.

There are a variety of effects that could contribute to this behavior, including changes to F-actin dynamics and the fraction of bound α-actinin cross-links. However, these experiments found that the dominant effect of increasing

temperature is to increase the rate of α-actinin unbinding from F-actin, implying that as cross-link dissociation rates increase, the network becomes a more dynamic structure that can relax stress. This suggests that if cells require cytoskeletal structures to reorganize and remodel, it is important to have dynamic cross-link proteins like α-actinin, not permanent ones like scruin. One interesting example where cross-link binding kinetics has a strong biological consequence is in an α-actinin-4 isoform having a point mutation that causes increased actin-binding affinity (Weins *et al.*, 2005; Yao *et al.*, 2004). This increased binding affinity is associated with cytoskeletal abnormalities in focal segmental glomerulosclerosis, a lesion found in kidney disease that results from a range of disorders including infection, diabetes, and hypertension.

Mechanical load can also have an effect on cross-link binding kinetics. When large shear stresses are applied to fascin cross-linked and bundled F-actin networks, network elasticity depends on the forced unbinding of cross-links in a manner that depends on the rate at which stress is applied (Lieleg and Bausch, 2007). Although temperature is unlikely to be an important control parameter *in vivo*, mechanical force on actin-binding proteins may regulate both mechanical response of the network and organization of signaling within the cytoplasm. However, it is unknown to what extent cross-link kinetics play a role in regulation of mechanical stresses within live cells to enable rapid and local cytoskeletal reorganization.

2. Effect of Cross-Link Compliance: Filamin A

Cross-link geometry and compliance can also contribute significantly to F-actin network elasticity. Rigidly cross-linked networks have a well-defined elastic plateau where the elastic modulus is orders of magnitude larger than the viscous modulus, and energy is stored elastically in the network. In contrast, networks formed from F-actin cross-linked with filamin A (FLNa) have an elastic modulus that is only two or three times the viscous modulus, and the elastic modulus decreases as a weak power law over timescales between a second and thousands of seconds (Gardel *et al.*, 2006a,b) (Fig. 8), similar to the timescale dependence of the elasticity of living cells (Fabry *et al.*, 2001). Moreover, in contrast to the F-actin–scruin networks where the linear elastic modulus can be tuned over several orders of magnitude by varying cross-link density, the linear elastic modulus for F-actin–FLNa networks is only weakly dependent on the FLNa concentration and is typically in the range of 0.1–1 Pa (Gardel *et al.*, 2006a), less than tenfold larger than for F-actin solutions formed without any cross-links.

Insight into how cross-link compliance can alter macroscopic mechanical response can be gained from a recent experiment in which the total length of the cross-link ddFLN, a filamin isoform from *Dictyostelium discoideum*, is systematically altered and the mechanics of the resulting network are probed using bulk rheology (Wagner *et al.*, 2006). In these networks, as the length of the cross-linker is systematically increased, the stress transmission in networks becomes

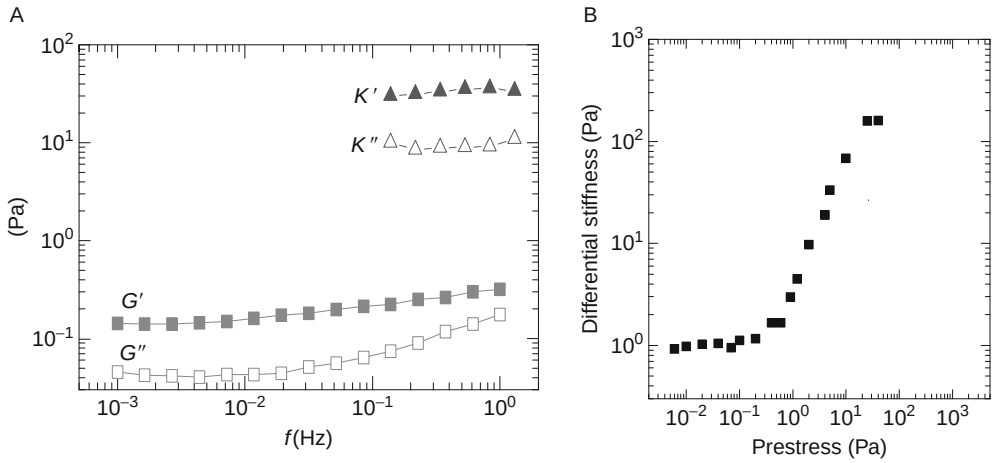

Fig. 8 (A) Frequency-dependent rheology of *in vitro* actin-filamin networks. In the linear regime, the network is a weak, viscoelastic solid with the elastic modulus, G' (closed gray squares), only a few time larger than the viscous modulus, G'' (open gray squares), over a broad range of frequencies. Upon application of a large steady shear stress ($\sigma_0 = 20$ Pa), the network stiffens dramatically; the differential shear moduli, K' (closed gray triangles) and K'' (open gray triangles), are two orders of magnitude larger than the linear moduli (with permission, Gardel *et al.*, 2006). (B) Differential shear elastic modulus of *in vitro* actin networks cross-linked with the physiologically relevant cross-linking protein filamin. Application of a prestress stiffens the networks by two orders of magnitude to the stiffness of typical living cells.

increasingly fluid-like: the magnitude of the elastic modulus decreases and becomes more sensitive to frequency.

Similar to rigidly cross-linked actin networks, FLNa cross-linked F-actin networks show strong nonlinear strain-stiffening behavior. At low stresses, the linear elastic modulus is approximately 1 Pa; at a critical stress of 0.5 Pa and critical strain of about 15%, the network can stiffen by over two orders of magnitude and support a maximum stress up to 100 Pa (Gardel *et al.*, 2006b). This remarkable nonlinear stiffening is a larger percentage over the linear elasticity than reported for any other cross-linked F-actin network. The network stiffness varies linearly as a function of applied stress to vary the differential stiffness from 1 Pa up to 1000 Pa (Fig. 8), stiffnesses that are characteristic of living cells. This system strongly suggests that nonlinear elastic effects may play an important role in determining the mechanical response of the cellular cytoskeleton.

Unlike in the F-actin–scruin system where network failure is consistent with F-actin filament rupture, the maximum stress that the F-actin–FLNa networks can withstand before breaking depends strongly on FLNa concentration, again highlighting the fact that FLNa contributes significantly to the overall network elasticity. The F-actin–FLNa networks allow very large strains, on the order of 100%, before network failure, whereas F-actin–scruin networks typically break at much smaller strains of around 30%. It is still unknown whether the F-actin–FLNa network

mechanical response arises merely from the large size, geometry, and compliance of the FLNa molecules or if, in fact, the stresses in the networks are large enough to unfold the β-sheet repeat sequences in the molecule so that the extensibility and flexibility of the FLNa molecule are further enhanced. In the ddFLN system, the maximum stress and strain supported by these networks increase with cross-link length (Wagner *et al.*, 2006), suggesting that the cross-link size itself is an important factor. Together, these results strongly suggest that the detailed microstructure of cross-linking proteins is critically important to the ability of the network to support large stresses and deformations without breaking.

Thus, it is not clear in networks of F-actin cross-linked with α-actinin or FLNa what the exact mechanism of network failure is. Actin filament rupture, cross-link rupture, F-actin-cross-link unbinding, and poor adhesion of the network to the site of applied force are all possibilities. Single-molecule experiments are starting to give good approximations for the rate-dependent breakage forces for both the F-actin and the cross-links (Furuike *et al.*, 2001). In all of these cases, the stress and strain at which the network fails can depend on the magnitude and duration of stress applied to the network and the details of how these stresses are felt by the individual network components at the microscopic scale. There is much interest in understanding the mechanical failure of cytoskeletal network for understanding biological phenomena ranging from cell shape and polarization to cell blebbing to symmetry breaking in model actin-based propulsion systems (Paluch *et al.*, 2006).

3. Effect of Myosin-II Motors

In the cellular cytoskeleton, F-actin is also cross-linked by minifilaments (8–13) of myosin-II motors to form contractile networks. In highly organized F-actin bundles, such as sarcomeres, conformational changes in the myosin-II motor proteins result in sliding of F-actin and shortening of bundle length. It has been observed that, at sufficiently high motor activity, the myosin–actin networks remain isotropic, but myosin-II-induced F-actin sliding accelerates mechanical relaxations within the network to fluidize the F-actin network (Humphrey *et al.*, 2002). However, as the percentage of active myosin-II motors decreases by ATP depletion, the tight, rigor binding of ADP-bound myosin-II to the F-actin serves to cross-link filaments. In this regime, the F-actin filaments *in vitro* condense into compact gels and self-organize into asters (Smith *et al.*, 2007). After full ATP depletion, these structures are stabilized and the elastic stiffness of these networks can be 100-fold enhanced over those F-actin solutions in the absence of myosin-II (Mizuno *et al.*, 2007). Moreover, the degree of stiffening observed in these networks is correlated to the concentration of active myosin-II; this suggests that nonlinear elastic stiffening due to motor proteins within the networks at the molecular scale is, to some degree, similar to that of external shear stresses imposed at the macroscopic level (Bendix *et al.*, 2008). These two competing roles of fluidization and stiffening of myosin-II at different levels of activity underscore the importance of the regulation of myosin-II activity in determining how forces

are transmitted through these networks in live cells. Further work is required to delineate the role of different cross-linking proteins and other mechanisms of myosin-II regulation in understanding force transmission through these contractile networks.

The nonlinear mechanics of *in vitro* cross-linked F-actin networks suggests a mechanism by which a cell can actively regulate its stiffness: embedded motor proteins apply stress to the actin cytoskeleton and push it into the nonlinear strain-stiffening regime. In this scheme, motor protein activity, not the exact concentration of cross-link, would set the local cell stiffness. This is consistent with known effects of internally generated myosin-II forces on cytoskeletal organization and mechanical response (Mizuno *et al.*, 2007). These behaviors suggest that the cellular cytoskeleton is composed of elements under tension, as described in tensegrity models (Ingber, 1997).

IV. Effects of Microtubules in Composite F-Actin Networks

In addition to F-actin, the cytoskeleton of eukaryotic cells is also composed of a network of microtubule filaments that plays a large number of important biological roles. Structurally, these filaments are hollow tubes and have remarkable features that are very different from those of F-actin. Within the composite cytoskeletal network, microtubules can give rise to complementary and, in some cases, synergistic mechanical properties. Microtubules are highly dynamic, exhibiting repeated cycles of growth and rapid depolymerization known as dynamic instability (Mitchison and Kirschner, 1984). This dynamic behavior allows microtubules to rapidly restructure into different functional network architectures; these include the highly specialized mitotic spindle within dividing cells, and the radial microtubule network that controls directional migration of polarized interphase cells. In addition to the capability for rapid restructuring, the microtubule network must also exhibit mechanical stability under load. For example, microtubules continually experience mechanical loads from motor proteins that drag their cargo through the cell along microtubule tracks. Actomyosin contractility is also known to mechanically load microtubules during cell migration (Waterman-Storer and Salmon, 1997) and during the periodic contractility of beating heart cells (Brangwynne *et al.*, 2006). Indeed, some models of cytoskeleton mechanics propose that the microtubule network functions as the compressive load-bearing component of the cytoskeleton, balancing tensile forces generated by actomyosin contractility (Ingber, 2003). Mechanical stability of the microtubule network is clearly necessary for its varied tasks within the cell.

Microtubules have a high bending rigidity that arises from their large diameter, $D \sim 25$ nm. The mechanical properties of the microtubule wall appear roughly similar to those of the actin backbone, $E \sim 1$ GPa, although the wall is not truly an isotropic continuum material, and its precise mechanical rigidity may depend on

the details of the applied stress (de Pablo *et al.*, 2003; Needleman *et al.*, 2004). However, as a first approximation, a continuum elastic picture holds remarkably well: since the bending rigidity scales as $\kappa \sim d^4$, microtubules should have a persistence length about $(25/7)^4 \sim 160$ times larger than actin filaments, in agreement with measurements showing $\ell_p^{MT} \sim 1$mm. Measurements of the mechanical properties of microtubules have been performed using a variety of techniques that actively apply a force and then determine the resulting bending, including optical tweezers (Felgner *et al.*, 1996; Kikumoto *et al.*, 2006), hydrodynamic flows (Kowalski and Williams, 1993; Venier *et al.*, 1994), osmotic pressure (Needleman *et al.*, 2004), and atomic force microscopy (de Pablo *et al.*, 2003). However, as with F-actin and other microscopic polymers, microtubules are subjected to randomly fluctuating thermal forces, and passive mechanical measurements utilizing these fluctuations are also frequently used for measuring microtubule bending rigidity (Brangwynne *et al.*, 2007a; Gittes *et al.*, 1993; Janson and Dogterom, 2004; Pampaloni *et al.*, 2006).

A. Thermal Fluctuation Approaches

Direct observation of conformational changes induced by thermal energy can be used as a powerful probe of the dynamic mechanical response of biopolymer filaments. The essential principle behind this technique arises from the equipartition theorem of statistical mechanics, whereby it can be shown that, on average, an independent (quadratic) mode of a system in thermal equilibrium has, on average, $k_B T$ of energy. Since the extent of bending that corresponds to this energy scale is determined by the rigidity of the filament, this rigidity can be determined by simply measuring the average magnitude of thermally induced bending fluctuations. The power of this simple idea can be fully exploited by tracing the entire contour of a freely fluctuating filament. At each time point, the contour is then subjected to Fourier analysis by decomposing its tangent angle as a function of arc length, $\theta(s)$, into a sum of cosine modes: $\theta(s) = \sqrt{2/L}\sum_{n=0}^{\infty} a_q \cos(qs)$ (Gittes *et al.*, 1993). Here, the Fourier amplitude, a_q, describes the amplitude of bending at wave vector, q, the inverse length scale over which bending takes place, $\lambda = 2\pi/q$, as shown schematically in Fig. 9. Bending fluctuations from one time to the next can be characterized by the mean-squared fluctuation in mode amplitude: $\langle \Delta a_q(\Delta t)^2 \rangle \equiv 1/2 \langle \left(a_q(t+\Delta t) - a_q(t) \right)^2 \rangle_\tau$, where Δt is the lag time. For thermally fluctuating filaments in aqueous buffer, the fluctuations are predicted to behave according to $\langle \Delta a_q(\Delta t)^2 \rangle \equiv (1 - e^{-\Delta t/\tau}) k_B T/\kappa q^2$ (Brangwynne *et al.*, 2007a; Gittes *et al.*, 1993), where τ is a relaxation time that determines the timescale over which successive shapes remain correlated. For $\Delta t \ll \tau$, the mode fluctuations grow linearly in time, whereas for $\Delta t \gg \tau$, the mode fluctuations will be saturated to the equilibrium values $\langle \Delta a_q^2 \rangle = k_B T/\kappa q^2$. Microtubules fluctuating in a quasi-2D chamber are well described by these equations, and one finds microtubule

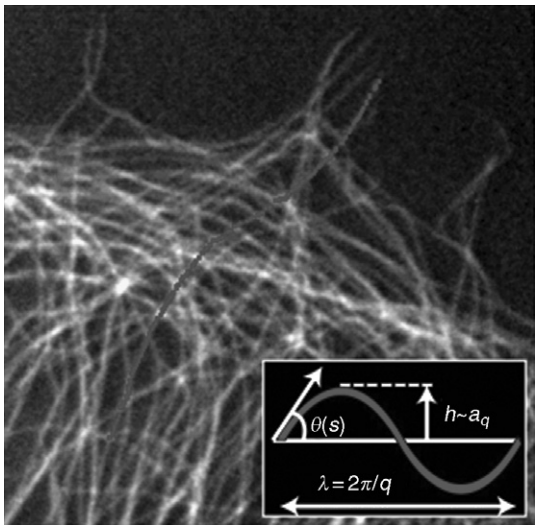

Fig. 9 Fluorescently labeled microtubules showing highly bent shapes, with a single microtubule highlighted. The inset defines the parameters used to extract the amplitude, a_q, and the wavelength, λ, of the Fourier modes describing the contour of the microtubule.

persistence lengths on the order of 1 mm. However, using such an approach, it has been suggested that a population of microtubules has heterogeneous bending behaviors that are more complex than that of actin filaments, arising from the fact that the wall of the tube is actually composed of an assembly of protofilaments (Brangwynne *et al.*, 2007a). Using a similar approach, it was shown that microtubules appear to have a bending rigidity that depends on their speed of polymerization (Janson and Dogterom, 2004). Moreover, another recent study suggests that the bending rigidities of microtubules may in fact depend on the length scale of the measurement (Pampaloni *et al.*, 2006); however, a similar finding was mistakenly reported for actin filaments (Kas *et al.*, 1993), and such behavior can arise from improper consideration of the experimental noise (Brangwynne *et al.*, 2007a). In addition to affecting the bending rigidity, the hierarchical microtubule structure may also contribute to an anomalous behavior of the bending timescales. Specifically, hydrodynamic drag is predicted to give rise to a relaxation time, $\tau \sim \eta/\kappa q^4$; actin filament fluctuations show good agreement with this predicted behavior (Brangwynne *et al.*, 2007a). In contrast, microtubules appear to exhibit a slight deviation from this hydrodynamic scaling at high wave vector (Janson and Dogterom, 2004), possibly due to the effects of internal dissipation mechanisms (Brangwynne *et al.*, 2007a; Poirier and Marko, 2002). These considerations suggest that the mechanical behavior of microtubules may actually be more variable and complex than previously believed; however, care must be taken in interpreting these experiments, since even in the absence of bending, the mode amplitudes will fluctuate due to noise (Brangwynne *et al.*, 2007a).

B. *In Vitro* MT Networks

There have been few studies of *in vitro* networks composed of purified microtubules. This is likely to change since the unique mechanical properties of these filaments will lead to interesting network properties different from those of actin filament networks. In particular, the mesh size of an *in vitro* microtubule network will be orders of magnitude smaller than the microtubule persistence length, and thus thermal fluctuations are likely to be negligible. This will give rise to very different behavior at high strain, as well as a high-frequency scaling unlike the $t^{3/4}$ scaling observed in actin networks (Koenderink *et al.*, 2006). Moreover, if the fluctuation timescales of microtubules are dominated by internal dissipation on short-length scales, the high-frequency rheological behaviors of microtubule networks may exhibit distinct and interesting scaling behaviors that have yet to be explored.

Microtubules in cells are typically embedded in the surrounding cytoskeletal network, and composite actin–microtubule networks are increasingly studied. A recent study focused on the fluctuation dynamics of individual filaments in a network of microtubules within an entangled actin network (Brangwynne *et al.*, 2007b). Because the network is not purely elastic, the Fourier spectrum of these fluctuating microtubules exhibits long-time saturating fluctuations that obey $\langle \Delta a_q^2 \rangle = k_B T/\kappa q^2$, with a corresponding persistence length approximately 1 mm, similar to the behavior of microtubules thermally fluctuating in aqueous buffer. Their relaxation dynamics are subdiffusive, reflecting fluctuations in a viscoelastic background medium; however, the long-time relaxation behavior is roughly consistent with the hydrodynamic prediction, $\tau \sim \eta_{\text{eff}}/\kappa q^4$, with an effective long-time viscosity, η_{eff}, about 1000 times that of water. If the actin network were cross-linked, behaving as a true elastic solid, the fluctuations of embedded microtubules would be restricted beyond a length scale, $\ell \sim (\kappa/G')^{1/4}$, where G' is the elastic modulus of the network; in this case, the saturating behavior $\langle \Delta a_q^2 \rangle = k_B T/\kappa q^2$ would not be observed.

This microscopic picture of the dynamics of microtubule fluctuations may begin to shed light on the bulk mechanical behavior of composite F-actin–microtubule networks. Recent work suggests that microtubules play a role in changing the internal deformation field of such networks in an important way. As described in Section III.B.1, at low cross-link density, an F-actin network will deform non-affinely under an applied stress, whereas at higher cross-link density, the network will transit into an affine entropic deformation regime associated with the important nonlinear strain-stiffening response. When microtubules are added to this network, this affine transition occurs at much lower cross-link density. The stiff microtubule rods appear to help homogenize the strain distribution in the actin network, and the local mechanical deformations reflect the bulk mechanical deformation, even at low cross-link density (Y.C. Lin, in preparation). This behavior suggests that the microtubule network could play an important role in controlling the nonlinear response of the prestressed cytoskeleton.

These findings also suggest that motor-driven composite F-actin–microtubule networks may be of particular interest. Indeed, microtubules may help facilitate the motor-induced nonlinear stiffening response of the network by ensuring that the deformation is locally affine. Moreover, it is conceivable that microtubules could help balance the internal prestress of "free-standing" cytoskeletal networks, enabling a nonlinear strain-stiffening response even in nonadherent cells or those only weakly coupled to the extracellular matrix (Ingber, 2003).

Although to our knowledge there are no published studies of the bulk mechanical response of motor-driven composite actin–microtubule networks, a recent study investigates the nonequilibrium dynamical behavior of microtubules in a composite network driven by myosin-II force generation (Brangwynne *et al.*, 2007b). Here, the bending dynamics of microtubules are used to determine the local force fluctuations within the network. In the absence of motors, a microtubule in an entangled actin network only undergoes small thermal fluctuations that evolve subdiffusively, as described above. However, in the presence of myosin motors, microtubules undergo large, highly localized bending fluctuations that exhibit rapid, step-like relaxation behavior. The localized bends are well-described by the function: $\gamma(x) = \gamma_0[\sin(|x|/\ell) + \cos(|x|/\ell)]e^{-|x|/\ell}$ that characterizes the bending of a rod embedded in an elastic material under the action of localized transverse forces. From the amplitude, γ_0, forces on the order of approximately 10 pN were determined, consistent with the action of a few myosin motors. As above, the decay length, $\ell \sim (\kappa/G')^{1/4}$, arises as a natural consequence of the competition between microtubule bending and deformation of the surrounding elastic network; the measured value, $\ell \sim 1 - 2$ μm, is consistent with the elastic modulus obtained from independent rheology measurements. Such localized fluctuations give rise to anomalously large Fourier bending amplitudes, particularly on short-length scales. Interestingly, the dynamics of these driven Fourier modes appear to be diffusive, consistent with step-like relaxations of force arising from binding and rapid unbinding of force-generating myosin. Because the microtubules are not cross-linked to the actin network, compressive forces cannot be maintained. Future work will focus on tuning the network interactions by cross-linking microtubules to the F-actin network, as well as using various F-actin cross-linking proteins to tune the properties of the F-actin network itself.

C. Mechanics of Microtubules in Cells

Upon considering the mechanical aspects of microtubule behavior in cells, the first thing one will notice is that the microtubule network in cells is typically highly bent (Fig. 9). This has been suggested as evidence that microtubules experience significant mechanical loads in cells. In particular, a long-held view maintains that microtubules function as compressive load-bearing elements within the cytoskeleton, and these bends reflect large compressive forces generated within cells (Ingber, 1997, 2003). However, this view is controversial, and others maintain that microtubules can only bear small compressive loads since they are so long. But, several

studies noted that microtubules often appear to compressively buckle into short-wavelength bends at the leading edge of cells, with wavelengths on the order of 3 μm; as seen in Fig. 11. At first glance, this is unexpected, since the lowest energy bends are those on the longest wavelengths (small curvature). Long-wavelength bending in response to compressive forces is known as Euler buckling, and can be readily observed if one compresses a flexible rod, such as a plastic ruler or a coffee stirrer, with length, L: upon reaching a critical force of order $f_{\text{compress}} \sim \kappa/L^2$, it will buckle into a single long arc. Isolated microtubules that are compressively loaded will undergo a similar buckling behavior, and the resulting shape can be quantitatively described by classic Euler buckling (Dogterom and Yurke, 1997).

While isolated microtubules buckle into long wavelengths, microtubules in cells are not isolated but rather are surrounded by other components of the composite cytoskeletal network. As described above for composite *in vitro* networks, the surrounding elastic network gives rise to a natural length scale of lowest-energy bending. As a result, microtubules will indeed buckle into short-wavelength shapes, with a wavelength given by $\lambda \sim (K/G)^{1/4}$. This physical behavior can be demonstrated in a simple model system consisting of a plastic rod embedded in elastic gelatin, as shown in Fig. 10. With appropriate prefactors, one can estimate that in cells, the buckling wavelength should be approximately 2 μm.

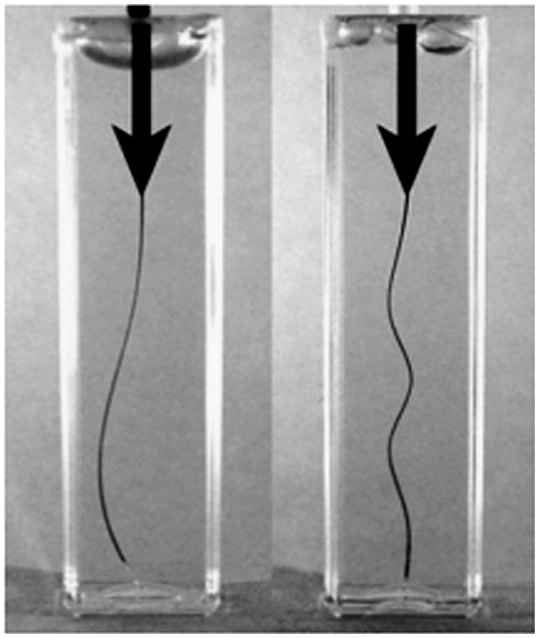

Fig. 10 The effect of compressive force on a plastic rod embedded in a purely viscous fluid (left) and a soft elastic gel, gelatin (right).

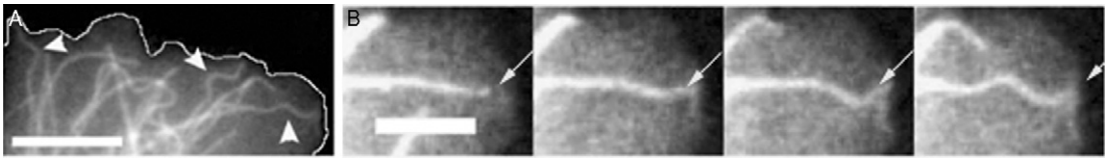

Fig. 11 (A) Fluorescently tagged microtubules in an adherent cell exhibit short-wavelength bends. Scale bar = 10 μm. (B) A magnified view of a microtubule from (A) buckling against the leading edge of the cell. Scale bar = 5 μm.

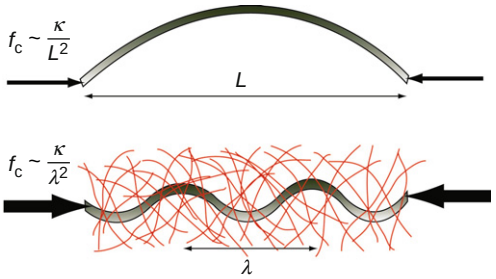

Fig. 12 Schematic showing the critical buckling force, f_c, in the absence (top) and presence (bottom) of a surrounding elastic matrix. In the presence of a surrounding elastic matrix, the characteristic bending wavelength is reduced, $\lambda < L$, such that f_c is substantially increased.

As described in a recent study, microtubules in cells indeed buckle on short wavelengths of approximately 3 μm in response to compressive loads generated by adherent epithelial cells, and in response to the periodic actomyosin contractility of beating heart cells (Brangwynne *et al.*, 2006). Moreover, initially straight microtubules can be made to buckle into this same short-wavelength shape by exogenous compressive forces applied with a microneedle. Unlike isolated rods undergoing simple Euler buckling, for this type of constrained short-wavelength buckling response, the critical buckling force is $f \sim \kappa/\lambda^2$. Microtubules in cells are typically tens of micrometers long. Thus, the buckling wavelength is on the order of ten times smaller than the total length, and the critical force is larger by a factor of approximately 100. This short-wavelength buckling response is thus indicative of a surrounding elastic network that effectively reinforces microtubules, allowing them to bear much larger compressive forces in cells, as shown schematically in Fig. 12.

In spite of the short-wavelength bending characteristic of composite microtubule networks, microtubules in cells also exhibit long-wavelength bends. The origin of this was addressed in a recent study, in which Fourier analysis of an ensemble of microtubule shapes in cells revealed bends on both short and long

wavelengths (Brangwynne *et al.*, 2007c). Moreover, this Fourier spectrum is remarkably thermal-like, with $\langle a_q^2 \rangle = (1/l_p^{\text{apparent}})(1/q^2)$. However, unlike microtubules in thermal equilibrium, the persistence length associated with this spectrum, l_p^{apparent}, is approximately 30 μm, about 100 times smaller than *in vitro* measurements. This is very surprising because even if some thermal-like agitation were the cause, there is no reason to expect a thermal-like spectrum, since, as discussed above, the surrounding network completely changes the energetics of microtubule bending.

By studying the time-dependent bending of individual microtubules, the bending fluctuations were found to be roughly diffusive, $\langle \Delta a_q(\Delta t)^2 \rangle \sim \Delta t$, similar to the behavior of thermally fluctuating microtubules in aqueous buffer. However, the cytoplasm is viscoelastic, and if thermal fluctuations were the cause, the bending fluctuations should be subdiffusive, as described above for microtubules thermally fluctuating in a composite actin–microtubule network. Moreover, these fluctuations are actually only significant on short-length scales. In contrast, the long-wavelength bends are effectively frozen-in; for an instantaneous bend with a wavelength of 10 μm, it would take approximately 1000 s to fully fluctuate to the ensemble-averaged values, which is longer than the lifetime of most microtubules (Schulze and Kirschner, 1986). Thus, unlike equilibrium materials, $\langle a_q^2 \rangle \neq \langle \Delta a_q^2 \rangle$, the cell exhibits behavior analogous to that of nonergodic materials far from thermal equilibrium. Indeed, while intracellular microtubule bending appears thermal-like, this behavior is actually completely analogous to microtubule dynamics in motor-driven composite actin networks (Brangwynne *et al.*, 2007b), suggesting that similar motor-driven, step-like stress relaxation dynamics also occur in cells.

This nonergodicity, or "frozen-ness", of long-wavelength microtubule bends suggests that microtubules may actually grow into these highly bent shapes. To test this, the trajectories of growing microtubule tips were tracked, using the microtubule tip-tracking protein Clip-170. This reveals that microtubules indeed grow into highly bent shapes; moreover, these trajectories exhibit a Fourier spectrum that closely resembles that of the ensemble spectrum of instantaneous shapes. This is consistent with a model in which the bending fluctuations of microtubules reorient the tips of growing microtubules, leading to a persistent random walk growth trajectory and a corresponding $\langle a_q^2 \rangle \sim 1/q^2$ mode spectrum; a simulation of this type of growth process, and the resulting thermal-like, but anomalously large Fourier spectrum, is shown in Fig. 13. Thus, the anomalous thermal-like instantaneous bending spectrum of intracellular microtubules appears to arise from the coupling of microtubule growth dynamics and non-thermal intracellular stress fluctuations within the composite cytoskeleton. The resulting small apparent persistence length, approximately 30 μm, has important implications for the ability of microtubules to rapidly restructure by dynamic instability, and their ability to stochastically locate cytoplasmic targets by the search and capture mechanism (Kirschner and Mitchison, 1986).

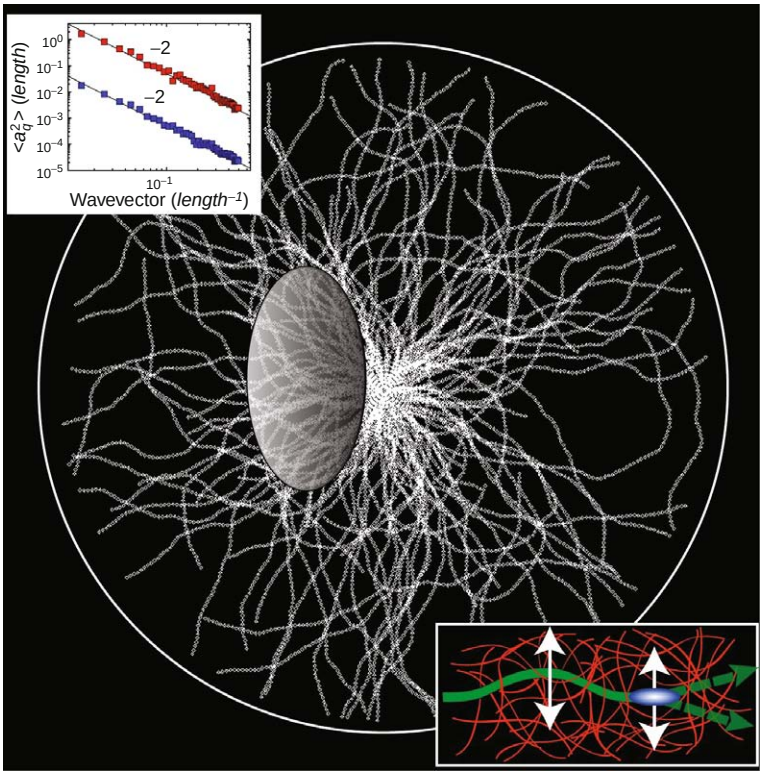

Fig. 13 Simulation to examine the contour of dynamic microtubules in the presence of nonthermal stress fluctuations. Top inset: The mode spectrum as a function of wave vector calculated for this simulation, using a small nonthermal (top) and large thermal (bottom) persistence length. Bottom inset: Schematic showing how lateral bending fluctuations will reorient the growing microtubule tip.

V. Intermediate Filament Networks

A. Introduction

A large family of proteins, collectively referred to as intermediate filaments (IFs), is the third and less well-studied class of biopolymers found in the cytoskeleton. Each IF protein, including keratins, vimentin, desmin, neurofilaments, and lamins, has a distinct chemical structure and function within the cell (Fig. 14). For example, vimentin localizes to the cytoplasm, often forms a composite network with both F-actin and microtubules, and is thought to be responsible for the cellular mechanical integrity. Lamins, on the other hand, maintain the shape and mechanical stability of the nucleus.

All IF proteins can assemble into approximately 10-nm-wide filaments. The particular architecture of IFs is important for understanding their unique

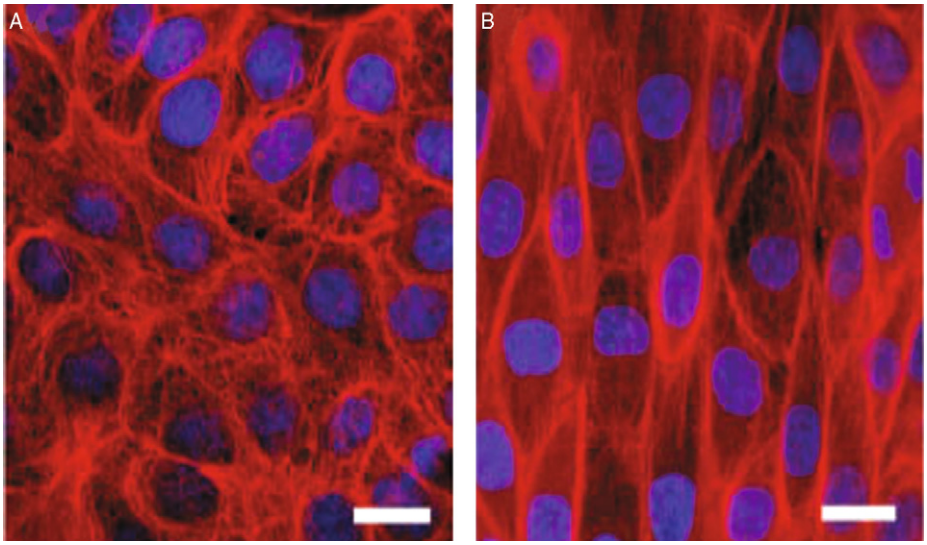

Fig. 14 Effect of stretch on intermediate filament networks in MDCK cells. Control cells (left). Cell after uniaxial stretch (right). Keratins (red) and nuclei (blue) (with permission, Kreplak and Fudge, 2007).

mechanical properties (Herrmann and Aebi, 2004; Kreplak and Fudge, 2007). The assembly of IFs is quite complex and distinct from the assembly process of F-actin or microtubules (Herrmann and Aebi, 1998; Herrmann *et al.*, 1999). The molecular building blocks of IFs are fibrous α-helical proteins that associate laterally and longitudinally to form a bundle of coiled-coils. The diameter of the filament depends on the specific protein, assembly conditions, and may also vary along the length of a single filament. Unlike F-actin or microtubules, these filaments are nonpolar. Moreover, the length of individual filaments and the details of connectivity between filaments in the cytoskeleton are poorly understood. IF assembly is tightly regulated by the cell and can be highly dynamic with turnover rates similar to those for F-actin or microtubules (Helfand *et al.*, 2004).

B. Mechanics of IFs

Recent measurements show that the structure of IFs leads to single filament mechanics that are different from both actin and microtubules (Guzman *et al.*, 2006; Kiss *et al.*, 2006; Kreplak and Fudge, 2007; Kreplak *et al.*, 2005). Imaging measurements suggest that the persistence length for vimentin filaments is on the order of 1 μm, one order of magnitude smaller than for F-actin and three orders of magnitude smaller than for microtubules (Mucke *et al.*, 2004).

Atomic force microscopy measurements of single IFs that are either adsorbed to a solid surface or lying across a small well give us estimates of the single filament extensibility and bending modulus, respectively. Measurements of both unstabilized and glutaraldehyde-stabilized vimentin filaments lying across small wells suggest a bending modulus of 300 MPa and Young's modulus of 900 MPa, but a shear modulus of only 2 MPa (Guzman *et al.*, 2006). This work implies that individual subunits in the filament may slide relative to each other, yielding a complicated bending modulus that actually depends on the type of deformation and the filament length.

Measurements of neurofilaments, desmin, and keratin adsorbed to a solid substrate show that the filaments can be stretched several times their original length before breaking (Kreplak *et al.*, 2005). Stretching of the filament is associated with a marked decrease in the filament diameter, perhaps associated with an irreversible structural transition. The full stress–strain curve for individual IFs is not yet known, but some insight can be drawn from large bundles of IFs that are found in the slime produced by hagfish (Fudge *et al.*, 2003). These IF bundles are highly extensible, like the single filaments, and can support very large stresses before breaking. This impressive extensibility places IFs in stark contrast to actin or microtubules, which break under small extensional strains. These unique mechanical properties suggest a role for IFs in providing mechanical stability to cells that are subjected to large deformations.

C. Mechanics of Networks

Compared to networks of cross-linked actin filaments, the mechanical properties of IF networks have been less widely studied. Here, we describe results from two IF systems. Vimentin networks have a concentration-dependent linear elastic modulus that ranges between 10 and 100 Pa (Janmey *et al.*, 1991). These networks strain stiffen and can withstand large stresses and strains before rupturing, possibly reflecting the extensibility of the individual filaments themselves. The mechanics of neurofilament networks in many ways look similar to the behavior of cross-linked actin networks, with effective cross-linking thought to be provided by interactions between the highly charged sidearms that protrude from the filaments (Rammensee *et al.*, 2007; Fig. 15). These networks show strain-stiffening behavior, but with a different dependence of the modulus on stress than is seen in rigidly cross-linked actin networks. This suggests that the underlying physical mechanism for stiffening in these networks may not be the same type as that discussed in Section II.C.2.

Understanding the physical principles that regulate the dynamics and stress transmission in these complex IF networks remains a current challenge. Furthermore, exploring the mechanical responses of composite networks of IFs with microtubules and F-actin will provide new clues about the complex mechanical response of live cells.

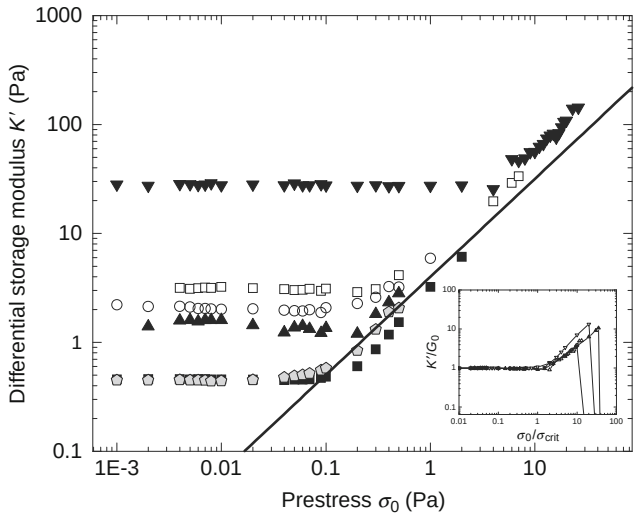

Fig. 15 Nonlinear rheology of neurofilament networks with increasing concentrations: 0.2 mg/ml (filled gray pentagon and filled black square), 0.5 mg/ml (filled up triangle), 0.8 mg/ml (open circle), 1 mg/ml (open square), 5.0 mg/ml (filled upside down triangle). Differential elastic modulus, K', as a function of applied shear prestress. In the nonlinear regime, K' increases nearly linearly with prestress. Inset: Curves from different concentrations can be scaled so that they fall on the same master curve (with permission, Rammensee *et al.*, 2007).

VI. Conclusions and Outlook

Although the importance of understanding cytoskeletal force transmission has been appreciated for some time, recent advances in biochemical and biophysical techniques now enable precise measurements of mechanical response of purified cytoskeletal protein networks over a large range of compositions and length scales. These measurements reveal a wide range of surprising behaviors that arise from the underlying biophysical properties of individual proteins and the nonthermal processes within these networks. In close collaboration with theory, it is now possible to build predictive physical models to describe these behaviors. This process often requires questioning many of the implicit assumptions made when building models of physical, "nonliving" materials and is an exciting area of modern materials science. In the context of the cell, it is clear that there is cross talk between all of these cytoskeletal systems. Future work is required to delineate the role of these dynamics and biophysical processes in complex cellular processes such as cell division and migration.

Acknowledgments

MLG would like to acknowledge support from a Career Award at the Scientific Interfaces from the Burroughs Wellcome Fund as well as a NIH Director's Pioneer Award.

References

Bendix, P. M., Koenderink, G. H., Cuvelier, D., Dogic, Z., Koeleman, B. N., Brieher, W. M., Field, C. M., Mahadevan, L., and Weitz, D. A. (2008). A quantitative analysis of contractility in active cytoskeletal protein networks. *Biophys. J.* **94**(8), 3126–3136.

Bicek, A. D., Tuzel, E., Kroll, D. M., and Odde, D. J. (2007). Analysis of microtubule curvature. *Methods Cell Biol.* **83,** 237–268.

Brangwynne, C. P., Koenderink, G. H., Barry, E., Dogic, Z., MacKintosh, F. C., and Weitz, D. A. (2007a). Bending dynamics of fluctuating biopolymers probed by automated high-resolution filament tracking. *Biophys. J.* **93**(1), 346–359.

Brangwynne, C. P., Koenderink, G. H., MacKintosh, F. C., and Weitz, D. A. (2007b). Non-equilibrium microtubule fluctuations in a model cytoskeleton. *Phys. Rev. Lett.* **100**(11), 118104.

Brangwynne, C. P., MacKintosh, F. C., Kumar, S., Geisse, N. A., Talbot, J., Mahadevan, L., Parker, K. K., Ingber, D. E., and Weitz, D. A. (2006). Microtubules can bear enhanced compressive loads in living cells because of lateral reinforcement. *J. Cell Biol.* **173**(5), 733–741.

Brangwynne, C. P., MacKintosh, F. C., and Weitz, D. A. (2007c). Force fluctuations and polymerization dynamics of intracellular microtubules. *Proc. Natl. Acad. Sci. USA* **104**(41), 16128–16133.

Bugyi, B., Papp, G., Hild, G., Lorinczy, D., Nevalainen, E. M., Lappalainen, P., Somogyi, B., and Nyitrai, M. (2006). Formins regulate actin filament flexibility through long range allosteric interactions. *J. Biol. Chem.* **281**(16), 10727–10736.

Bustamante, C., Marko, J. F., Siggia, E. D., and Smith, S. (1994). Entropic elasticity of lambda-phage DNA. *Science* **265**(5178), 1599–1600.

Chaudhuri, O., Parekh, S. H., and Fletcher, D. A. (2007). Reversible stress softening of actin networks. *Nature* **445**(7125), 295–298.

Crocker, J. C., and Hoffman, B. D. (2007). Multiple-particle tracking and two-point microrheology in cells. *Methods Cell Biol.* **83,** 141–178.

Das, M., MacKintosh, F. C., and Levine, A. J. (2007). Effective medium theory of semiflexible filamentous networks. *Phys. Rev. Lett.* **99**(3), 038101.

de Pablo, P., Schaap, I. A. T., MacKintosh, F. C., and Schmidt, C. F. (2003). Deformation and collapse of microtubules on the nanometer scale. *Phys. Rev. Lett.* **91**(9), 098101.

Dogterom, M., and Yurke, B. (1997). Measurement of the force-velocity relation for growing microtubules. *Science* **278,** 856–860.

Fabry, B., Maksym, G. N., Butler, J. P., Glogauer, M., Navajas, D., and Fredberg, J. J. (2001). Scaling the microrheology of living cells. *Phys. Rev. Lett.* **87**(14), 148102.

Felgner, H., Frank, R., and Schliwa, M. (1996). Flexural rigidity of microtubules measured with the use of optical tweezers. *J. Cell Sci.* **109**(Pt 2), 509–516.

Fixman, M., and Kovac, J. (1973). Polymer conformational statistics. III. Modified Gaussian models of stiff chains. *J. Chem. Phys.* **58,** 1564.

Fudge, D. S., Gardner, K. H., Forsyth, V. T., Riekel, C., and Gosline, J. M. (2003). The mechanical properties of hydrated intermediate filaments: Insights from hagfish slime threads. *Biophys. J.* **85**(3), 2015–2027.

Furuike, S., Ito, T., and Yamazaki, M. (2001). Mechanical unfolding of single filamin A (ABP-280) molecules detected by atomic force microscopy. *FEBS Lett.* **498**(1), 72–75.

Gardel, M. L., Nakamura, F., Hartwig, J. H., Crocker, J. C., Stossel, T. P., and Weitz, D. A. (2006a). Stress-dependent elasticity of composite actin networks as a model for cell behavior. *Phys. Rev. Lett.* **96**(8), 088102.

Gardel, M. L., Nakamura, F., Hartwig, J. H., Crocker, J. C., Stossel, T. P., and Weitz, D. A. (2006b). Prestressed F-actin networks cross-linked by hinged filamins replicate mechanical properties of cells. *Proc. Natl. Acad. Sci. USA* **103**(6), 1762–1767.

Gardel, M. L., Shin, J. H., MacKintosh, F. C., Mahadevan, L., Matsudaira, P. A., and Weitz, D. A. (2004a). Elastic behavior of cross-linked and bundled actin networks. *Science* **304**(5675), 1301–1305.

Gardel, M. L., Shin, J. H., MacKintosh, F. C., Mahadevan, L., Matsudaira, P. A., and Weitz, D. A. (2004b). Scaling of F-actin network rheology to probe single filament elasticity and dynamics. *Phys. Rev. Lett.* **93**(18), 188102.

Gardel, M. L., Valentine, M. T., Crocker, J. C., Bausch, A. R., and Weitz, D. A. (2003). Microrheology of entangled F-actin solutions. *Phys. Rev. Lett.* **91**(15), 158302.

Gittes, F., Mickey, B., Nettleton, J., and Howard, J. (1993). Flexural rigidity of microtubules and actin filaments measured from thermal fluctuations in shape. *J. Cell Biol.* **120**(4), 923–934.

Guzman, C., Jeney, S., Kreplak, L., Kasas, S., Kulik, A. J., Aebi, U., and Forro, L. (2006). Exploring the mechanical properties of single vimentin intermediate filaments by atomic force microscopy. *J. Mol. Biol.* **360**(3), 623–630.

Head, D. A., Levine, A. J., and MacKintosh, F. C. (2003a). Deformation of cross-linked semiflexible polymer networks. *Phys. Rev. Lett.* **91**(10), 108102.

Head, D. A., Levine, A. J., and MacKintosh, F. C. (2003b). Distinct regimes of elastic response and deformation modes of cross-linked cytoskeletal and semiflexible polymer networks. *Phys. Rev. E Stat. Nonlin. Soft. Matter Phys.* **68**(6 Pt 1), 061907.

Helfand, B. T., Chang, L., and Goldman, R. D. (2004). Intermediate filaments are dynamic and motile elements of cellular architecture. *J. Cell Sci.* **117**(Pt 2), 133–141.

Herrmann, H., and Aebi, U. (1998). Intermediate filament assembly: Fibrillogenesis is driven by decisive dimer-dimer interactions. *Curr. Opin. Struct. Biol.* **8**(2), 177–185.

Herrmann, H., and Aebi, U. (2004). Intermediate filaments: Molecular structure, assembly mechanism, and integration into functionally distinct intracellular Scaffolds. *Annu. Rev. Biochem.* **73,** 749–789.

Herrmann, H., Haner, M., Brettel, M., Ku, N. O., and Aebi, U. (1999). Characterization of distinct early assembly units of different intermediate filament proteins. *J. Mol. Biol.* **286**(5), 1403–1420.

Humphrey, D., Duggan, C., Saha, D., Smith, D., and Kas, J. (2002). Active fluidization of polymer networks through molecular motors. *Nature* **416**(6879), 413–416.

Ingber, D. E. (1997). Tensegrity: The architectural basis of cellular mechanotransduction. *Annu. Rev. Physiol.* **59,** 575–599.

Ingber, D. E. (2003). Tensegrity I. Cell structure and hierarchical systems biology. *J. Cell Sci.* **116**(7), 1157–1173.

Isambert, H., Venier, P., Maggs, A. C., Fattoum, A., Kassab, R., Pantaloni, D., and Carlier, M. F. (1995). Flexibility of actin filaments derived from thermal fluctuations. Effect of bound nucleotide, phalloidin, and muscle regulatory proteins. *J. Biol. Chem.* **270**(19), 11437–11444.

Janmey, P. A., Euteneuer, U., Traub, P., and Schliwa, M. (1991). Viscoelastic properties of vimentin compared with other filamentous biopolymer networks. *J. Cell Biol.* **113**(1), 155–160.

Janmey, P. A., McCormick, M. E., Rammensee, S., Leight, J. L., Georges, P. C., and MacKintosh, F. C. (2007). Negative normal stress in semiflexible biopolymer gels. *Nat. Mater.* **6**(1), 48–51.

Janson, M. E., and Dogterom, M. (2004). A bending mode analysis for growing microtubules: Evidence for a velocity-dependent rigidity. *Biophys. J.* **87,** 2723–2736.

Kas, J., Strey, H., and Sackmann, E. (1993). Direct measurement of the wave-vector-dependent bending stiffness of freely flickering actin filaments. *Europhys. Lett.* **21,** 865–870.

Kasza, K. E., Rowat, A. C., Liu, J., Angelini, T. E., Brangwynne, C. P., Koenderink, G. H., and Weitz, D. A. (2007). The cell as a material. *Curr. Opin. Cell Biol.* **19**(1), 101–107.

Kikumoto, M., Kurachi, M., Tosa, V., and Tashiro, H. (2006). Flexural rigidity of individual microtubules measured by a buckling force with optical traps. *Biophys. J.* **90,** 1687–1696.

Kirschner, M., and Mitchison, T. (1986). Beyond self-assembly: From microtubules to morphogenesis. *Cell* **45**(3), 329–342.

Kiss, B., Karsai, A., and Kellermayer, M. S. (2006). Nanomechanical properties of desmin intermediate filaments. *J. Struct. Biol.* **155**(2), 327–339.

Koenderink, G. H., Atakhorrami, M., MacKintosh, F. C., and Schmidt, C. F. (2006). High-frequency stress relaxation in semiflexible polymer solutions and networks. *Phys. Rev. lett.* **96,** 138307.

Kojima, H., Ishijima, A., and Yanagida, T. (1994). Direct measurement of stiffness of single actin filaments with and without tropomyosin by *in vitro* nanomanipulation. *Proc. Natl. Acad. Sci. USA* **91** (26), 12962–12966.

Kowalski, R. J., and Williams, R. C., Jr. (1993). Microtubule-associated protein 2 alters the dynamic properties of microtubule assembly and disassembly. *J. Biol. Chem.* **268**(13), 9847–9855.

Kreis, T., and Vale, R. (1999). ''Guidebook to the Cytoskeletal and Motor Proteins.'' Oxford University Press, New York.

Kreplak, L., Bar, H., Leterrier, J. F., Herrmann, H., and Aebi, U. (2005). Exploring the mechanical behavior of single intermediate filaments. *J. Mol. Biol.* **354**(3), 569–577.

Kreplak, L., and Fudge, D. (2007). Biomechanical properties of intermediate filaments: From tissues to single filaments and back. *Bioessays* **29**(1), 26–35.

Lieleg, O., and Bausch, A. R. (2007). Cross-linker unbinding and self-similarity in bundled cytoskeletal networks. *Phys. Rev. Lett.* **99,** 158105.

Lin, Y. C., Koenderink, G. H., MacKintosh, F. C., and Weitz, D. A. (2007). Viscoelastic properties of microtubule networks. *Macromolecules* **40,** 7714–7720.

Liu, J., Gardel, M. L., Kroy, K., Frey, E., Hoffman, B. D., Crocker, J. C., Bausch, A. R., and Weitz, D. A. (2006). Microrheology probes length scale dependent rheology. *Phys. Rev. Lett.* **96** (11), 118104.

Liu, J., Koenderink, G. H., Kasza, K. E., Mackintosh, F. C., and Weitz, D. A. (2007). Visualizing the strain field in semiflexible polymer networks: Strain fluctuations and nonlinear rheology of F-actin gels. *Phys. Rev. Lett.* **98**(19), 198304.

Liu, X., and Pollack, G. H. (2002). Mechanics of F-actin characterized with microfabricated cantilevers. *Biophys. J.* **83**(5), 2705–2715.

Lodish, H., Berk, A., Zipursky, S. L., Matsudaira, P., Baltimore, D., and Darnell, D. (1999). ''Molecular Cell Biology.'' W.H. Freeman Co., New York.

MacKintosh, F. C., Kas, J., and Janmey, P. A. (1995). Elasticity of semiflexible biopolymer networks. *Phys. Rev. Lett.* **75**(24), 4425–4428.

Mitchison, T., and Kirschner, M. (1984). Dynamic instability of microtubule growth. *Nature* **312**(15), 237–242.

Mizuno, D., Tardin, C., Schmidt, C. F., and Mackintosh, F. C. (2007). Nonequilibrium mechanics of active cytoskeletal networks. *Science* **315**(5810), 370–373.

Mucke, N., Kreplak, L., Kirmse, R., Wedig, T., Herrmann, H., Aebi, U., and Langowski, J. (2004). Assessing the flexibility of intermediate filaments by atomic force microscopy. *J. Mol. Biol.* **335**(5), 1241–1250.

Needleman, D. J., Ojeda-Lopez, M. A., Raviv, U., Ewert, K., Jones, J. B., Miller, H. P., Wilson, L., and Safinya, C. R. (2004). Synchrotron X-ray diffraction study of microtubules buckling and bundling under osmotic stress: A probe of interprotofilament interactions. *Phys. Rev. Lett.* **93**(19), 198104.

Ott, A., Magnasco, M., Simon, A., and Libchaber, A. (1993). Measurement of the persistence length of polymerized actin using fluorescence microscopy. *Phys. Rev. E Stat. Phys. Plasmas Fluids Relat. Interdiscip. Topics* **48**(3), R1642–R1645.

Paluch, E., van der Gucht, J., and Sykes, C. (2006). Cracking up: Symmetry breaking in cellular systems. *J. Cell Biol.* **175**(5), 687–692.

Pampaloni, F., Lattanzi, G., Jonas, A., Surrey, T., Frey, E., and Florin, E. L. (2006). Thermal fluctuations of grafted microtubules provide evidence of a length-dependent persistence length. *Proc. Natl. Acad. Sci. USA* **103**(27), 10248–10253.

Panorchan, P., Lee, J. S., Daniels, B. R., Kole, T. P., Tseng, Y., and Wirtz, D. (2007). Probing cellular mechanical responses to stimuli using ballistic intracellular nanorheology. *Methods Cell Biol.* **83,** 115–140.

Poirier, M. G., and Marko, J. F. (2002). Effect of internal friction on biofilament dynamics. *Phys. Rev. Lett.* **88**(22), 228103.

Radmacher, M. (2007). Studying the mechanics of cellular processes by atomic force microscopy. *Methods Cell Biol.* **83,** 347–372.

Rammensee, S., Janmey, P. A., and Bausch, A. R. (2007). Mechanical and structural properties of *in vitro* neurofilament hydrogels. *Eur. Biophys. J.* **36**(6), 661–668.

Sato, M., Schwarz, W. H., and Pollard, T. D. (1987). Dependence of the mechanical properties of actin/alpha-actinin gels on deformation rate. *Nature* **325**(6107), 828–830.

Schulze, E., and Kirschner, M. (1986). Microtubule dynamics in interphase cells. *J. Cell Biol.* **102**(3), 1020–1031.

Shin, J. H., Gardel, M. L., Mahadevan, L., Matsudaira, P., and Weitz, D. A. (2004). Relating microstructure to rheology of a bundled and cross-linked F-actin network *in vitro*. *Proc. Natl. Acad. Sci. USA* **101**(26), 9636–9641.

Smith, D. M., Ziebert, F., Humphrey, D., Duggan, C., Steinbeck, M., Zimmermann, W., and Kas, J. A. (2007). Molecular motor-induced instabilities and crosslinkers determine biopolymer organization. *Biophys. J.* **93**(12), 4445–4452.

Storm, C., Pastore, J. J., MacKintosh, F. C., Lubensky, T. C., and Janmey, P. A. (2005). Nonlinear elasticity in biological gels. *Nature* **435**(7039), 191–194.

Stossel, T. P., Condeelis, J., Cooley, L., Hartwig, J. H., Noegel, A., Schleicher, M., and Shapiro, S. S. (2001). Filamins as integrators of cell mechanics and signalling. *Nat. Rev. Mol. Cell Biol.* **2**(2), 138–145.

Tempel, M., Isenberg, G., and Sackmann, E. (1996). Temperature-induced sol-gel transition and microgel formation in alpha-actinin cross-linked actin networks: A rheological study. *Phys. Rev. E Stat. Phys. Plasmas Fluids Relat. Interdiscip. Topics* **54**(2), 1802–1810.

Valentine, M. T., Perlman, Z. E., Gardel, M. L., Shin, J. H., Matsudaira, P., Mitchison, T. J., and Weitz, D. A. (2004). Colloid surface chemistry critically affects multiple particle tracking measurements of biomaterials. *Biophys. J.* **86**(6), 4004–4014.

Venier, P., Maggs, A. C., Carlier, M. F., and Pantaloni, D. (1994). Analysis of microtubule rigidity using hydrodynamic flow and thermal fluctuations. *J. Biol. Chem.* **269**(18), 13353–13360.

Visegrady, B., Lorinczy, D., Hild, G., Somogyi, B., and Nyitrai, M. (2004). The effect of phalloidin and jasplakinolide on the flexibility and thermal stability of actin filaments. *FEBS Lett.* **565**(1–3), 163–166.

Wachsstock, D. H., Schwartz, W. H., and Pollard, T. D. (1993). Affinity of alpha-actinin for actin determines the structure and mechanical properties of actin filament gels. *Biophys. J.* **65**(1), 205–214.

Wagner, B., Tharmann, R., Haase, I., Fischer, M., and Bausch, A. R. (2006). Cytoskeletal polymer networks: The molecular structure of cross-linkers determines macroscopic properties. *Proc. Natl. Acad. Sci. USA* **103**(38), 13974–13978.

Waterman-Storer, C. M., and Salmon, E. D. (1997). Actomyosin-based retrograde flow of microtubules in the lamella of migrating epithelial cells influences microtubule dynamic instability and turnover and is associated with microtubule breakage and treadmilling. *J. Cell Biol.* **139**(2), 417–434.

Weihs, D., Mason, T. G., and Teitell, M. A. (2006). Bio-microrheology: A frontier in microrheology. *Biophys. J.* **91**(11), 4296–4305.

Weins, A., Kenlan, P., Herbert, S., Le, T. C., Villegas, I., Kaplan, B. S., Appel, G. B., and Pollak, M. R. (2005). Mutational and biological analysis of alpha-actinin-4 in focal segmental glomerulosclerosis. *J. Am. Soc. Nephrol.* **16**(12), 3694–3701.

Wong, I. Y., Gardel, M. L., Reichman, D. R., Weeks, E. R., Valentine, M. T., Bausch, A. R., and Weitz, D. A. (2004). Anomalous diffusion probes microstructure dynamics of entangled F-actin networks. *Phys. Rev. Lett.* **92**(17), 178101.

Xu, J., Tseng, Y., and Wirtz, D. (2000). Strain hardening of actin filament networks. Regulation by the dynamic cross-linking protein alpha-actinin. *J. Biol. Chem.* **275**(46), 35886–35892.

Xu, J., Wirtz, D., and Pollard, T. D. (1998). Dynamic cross-linking by alpha-actinin determines the mechanical properties of actin filament networks. *J. Biol. Chem.* **273**(16), 9570–9576.

Yao, J., Le, T. C., Kos, C. H., Henderson, J. M., Allen, P. G., Denker, B. M., and Pollak, M. R. (2004). Alpha-actinin-4-mediated FSGS: An inherited kidney disease caused by an aggregated and rapidly degraded cytoskeletal protein. *PLoS Biol.* **2**(6), e167.

CHAPTER 20

Automated Spatial Mapping of Microtubule Catastrophe Rates in Fission Yeast

Christian Tischer,[*] Damian Brunner,[†] and Marileen Dogterom[*]

[*]FOM Institute for Atomic and Molecular Physics (AMOLF)
Kruislaan 407, 1098 SJ Amsterdam,
The Netherlands

[†]European Molecular Biology Laboratory
Meyerhofstrasse 1, 69117 Heidelberg,
Germany

METHODS IN CELL BIOLOGY, VOL. 89

0091-679X/08 $35.00
DOI: 10.1016/S0091-679X(08)00620-1

Abstract

Microtubules (MTs) are cytoskeletal polymers whose spatial organization is dynamically regulated, depending on their biological function during different cell cycle stages. Growing MT ends are, for example, specifically targeted towards the cortex of motile or growing cells during interphase or towards chromosomal attachment sites during mitosis. An important parameter that cells use to control the average length of MTs, and thus the distance over which these targeting processes may operate, is the so-called catastrophe frequency f_{cat}: the rate at which MTs switch from a growing to a shrinking state. To understand how spatial targeting and the local control of f_{cat} are related, quantitative *in vivo* measurements are needed that allow for the measurement of f_{cat} in a spatially resolved way. Since catastrophes are intrinsically stochastic events, it is essential to acquire enough statistics to obtain the underlying rate constant f_{cat}. Here, we present automated image processing methodology, developed using GFP-tubulin expressing fission yeast cells, that makes it possible to measure f_{cat} both spatially resolved and with high statistical accuracy. Although certain aspects of the analysis are specific to the system under investigation the basic concepts of the methodology are applicable to any kind of movies of fluorescently labeled MTs.

I. Introduction

Microtubules (MTs) are long, stiff, and dynamic biopolymers that are part of the cytoskeleton of eukaryotic cells. MTs are crucially involved in a variety of processes, including the redistribution of chromosomes during cell division, the positioning of organelles such as the nucleus, and directing the polarized cell growth (Hayles and Nurse, 2001; Kirschner and Mitchison, 1986). An important phenomenon that enables MTs to fulfill these functions is ''dynamic instability'' (Desai and Mitchison, 1997; Mitchison and Kirschner, 1984). Dynamic instability is an intrinsic property of MTs that is characterized by repeated switching between a polymerizing (growing) and a depolymerizing (shrinking) state. Dynamic instability is usually described by four parameters: the growth and shrinkage rates and the rescue and catastrophe frequencies (Walker *et al.*, 1988). The f_{cat} is the average rate at which individual MTs undergo transitions from growth to shrinkage, whereas the rescue frequency describes the opposite process. *In vivo*, these parameters are regulated by numerous MT-associated proteins (MAPs) (Howard and Hyman, 2007). This allows cells for instance to adjust average MT length (Dogterom and Leibler, 1993; Verde *et al.*, 1992) or to adopt different spatial configurations of their MT networks during interphase and mitosis (Rusan *et al.*, 2001; Verde *et al.*, 1992).

While there is substantial information regarding global regulation of dynamic instability on a cellular level, local regulation within a cell is much less understood. This is however important for understanding how functional MT networks form

and how they target selected cellular structures such as chromosomes or the cell boundary. In fact, there is some evidence that f_{cat} is specifically enhanced at the boundary of different animal cells (Komarova *et al.*, 2002; Mimori-Kiyosue *et al.*, 2005). How such local control is achieved is however not well understood. It is not known, for example, whether f_{cat} changes slowly or whether there is sudden increase once MTs "hit" the cell membrane. Such information would help to distinguish gradual effects mediated by graded distributions of certain MAPs (Niethammer *et al.*, 2004) or by MT length dependent effects (Dogterom *et al.*, 1996) from sudden local effects mediated by the cell boundary, such as polymerization force induced catastrophes (Dogterom and Yurke, 1997; Janson *et al.*, 2003). One reason that such detailed measurements are lacking is the fact that statistics are a limiting factor in research on MT dynamics. The challenge is that the distribution of the time intervals that MTs grow before undergoing a catastrophe is very broad, both *in vivo* and *in vitro* (Howell *et al.*, 1997; Odde, 1995). This suggests that each catastrophe is a stochastic event that happens with at a certain probability, given by f_{cat}. This intrinsic stochasticity makes it necessary to record a large number of events before statistically significant differences in f_{cat} can be detected. To solve this problem, we developed a computer based analysis system that automatically extracts the positions of MT tips and of catastrophe events from movies of fluorescently labeled MTs. In addition to providing unprecedented statistics, the automated detection also avoids a generic problem of visual inspection, which is the viewer's bias to pick "nice-looking" events in a hardly reproducible manner. In this paper, we describe the methodology we developed, specifically focusing on the model system fission yeast. The biological results obtained by applying this methodology will be published elsewhere.

II. Methods

A. Spatial Catastrophe Frequency Mapping: General Considerations

The f_{cat} is the rate at which individual MTs undergo a transition from the growing to the shrinking state. f_{cat} is defined as $f_{cat}=n_{cat}/t_{tip}$, where n_{cat} is the number of catastrophes that one observes during the time $t_{tip,}$ which is the time during which one monitors growing MT tips (Walker *et al.*, 1988). In an experiment, one calculates t_{tip} by multiplying the number of observed growing tips n_{tip} with the time Δt between successive images, yielding $f_{cat}=n_{cat}/(n_{tip}\times\Delta t)$. Thus, there is always an inaccuracy in t_{tip}, which is given by Δt. There is also a general limitation with regard to measuring n_{cat}. One misses a catastrophe if an MT switches from growth to shrinkage (catastrophe) and back (rescue) during Δt (also discussed in Verde *et al.* (1992)). As a consequence, one measures an effective f_{cat} that comprises switches to shrinkage events that last long enough to be observed. The definition of f_{cat} above can be readily generalized to spatially resolved measurements:

$$f_{\mathrm{cat}}(X) = \frac{n_{\mathrm{cat}}(X)}{n_{\mathrm{tip}}(X) \cdot \Delta t} \quad (1)$$

This means that the measurement of n_{cat} and n_{tip} is restricted to a particular intracellular region X. In addition to the inaccuracies in n_{cat} and t_{tip} mentioned above, spatial accuracy of the measurement now becomes an issue as well. Apart from microscopy limitations, the spatial resolution is limited by the distance that a MT tip travels during successive observations. If v_{g} is the growth velocity of a MT, this distance is on average $\Delta t \times v_{\mathrm{g}}$. In our studies of the fission yeast system, Δt was 8 s and v_{g} was about 30 nm/s, limiting the spatial resolution to about 240 nm.

B. The Model System Fission Yeast

We chose to investigate the spatial regulation of MT catastrophes in interphase fission yeast cells (see Fig. 1A) (Hayles and Nurse, 2001). This has both biological and technical reasons. Technically, the regular cylindrical cell shape greatly facilitates assigning events to a specific intracellular position. Furthermore, fission yeast cells contain a limited number of well-organized MTs, which are relatively easy to track. Two to six MTs arrange in an anti-parallel manner into bundles that can be connected to the nucleus (Hagan, 1998; Hoog *et al.*, 2007). MT minus ends reside in the bundle center while the dynamic plus ends grow and shrink between the cell centre and the two cell poles (Drummond and Cross, 2000; Tran *et al.*, 2001). Most catastrophes are observed at the cell pole regions (Brunner and Nurse, 2000), from where MTs shrink back into the bundle overlap zone, indicating that rescue (regrowth) events only occur in the cell center (Bratman and Chang, 2007).

The biological functions of interphase MT bundles comprise delivery of marker proteins to cell poles and centering of the nucleus through MT polymerization forces (Mata and Nurse, 1997; Tolic-Norrelykke *et al.*, 2005; Tran *et al.*, 2001). Both functions require a tight regulation of f_{cat}. For instance, if f_{cat} is too high, MTs do not reach the cell pole and can thus neither generate pushing forces nor deliver cell pole markers. If f_{cat} is too low, MT growth does not stop at the cell ends. This results in MTs curling around the cell pole and growing backwards, which impairs functionality as well (Janson *et al.*, 2005; Sawin *et al.*, 2004). It is thus important to understand quantitatively how fission yeast cells regulate f_{cat}.

C. Sample Preparation and Data Acquisition

In order to monitor MT catastrophes we use a fission yeast strain expressing GFP-α_2-tubulin from a single, exogenously integrated locus under the control of the nmt1 promoter (*h90 leu1–32 ura4-d18 lys1+::nmt1-GFP-α2tub* (Yamamoto *et al.*, 1999)). Cells are grown using standard conditions (Moreno *et al.*, 1991) in

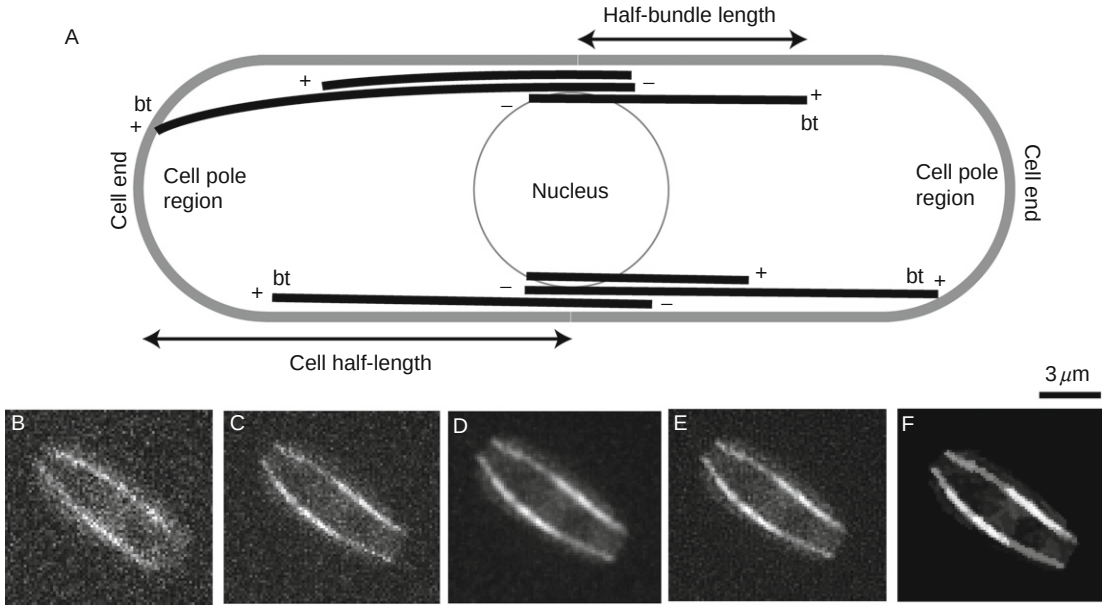

Fig. 1 Fission yeast scheme and image noise filtering. (A) Scheme of MT organization in fission yeast (bt=bundle tip). (B) Single image from a z-stack of images of a GFP-tubulin expressing cell. (C) Maximum projection of the stack. (D) Maximum projection after prior 3-D averaging, with (E) 2-D deconvolution, and with (F) modified Kuwahara filtering.

presence of 15 μM thiamine, which represses the expression of GFP-tubulin to minimal levels. Cells are mounted on agarose pads (Tran *et al.*, 2004) and imaged at 24–25 °C with a confocal spinning disc microscope, composed of a confocal scanner unit (CSU22, Yokogawa Electric Corp.) that is attached to an inverted microscope (DMIRB, Leica). The microscope is equipped with a 100×/1.3 NA oil immersion lens (PL FLUOTAR, Leica) and a built-in ×1.5 magnification changer lens. The sample is illuminated using a 488 nm laser (Sapphire 488–30, Coherent Inc.). Images are captured by an EM-CCD (C9100, Hamamatsu Photonics) controlled by software from VisiTech International.

Our catastrophe detection is based on the abrupt local changes in fluorescence intensity that are associated with the depolymerization of a GFP-stained MT. It is thus important to abolish other sources of intensity changes. To avoid MT intensity fluctuations due to growth in and out of the focal plane, we acquire 3-D stacks of whole cells where the distance between successive images in one stack is below the axial resolution of the microscope (axial=perpendicular to the coverslip).

Moreover, for automated analysis, the signal/noise ratio (SNR) within images is a crucial parameter (e.g. the SNR is low for dim signals due to photon counting noise). To avoid changes in the SNR one should first carefully identify good imaging parameters and then, if possible, keep them the same for all experiments.

For our system, the following parameters yield good results: time-lapse z-stacks are acquired with 8 s time delay between subsequent stacks. Each stack contains 20 images acquired at 125 ms exposure time and at 0.3 μm axial spacing (this covers an axial range of 6 μm, which readily contains the $\sim$3 μm wide fission yeast cells). We choose an 8 s time delay between the beginnings of stack acquisitions because it is appropriate for MT dynamics in fission yeast. MT growth speed is $\sim$30 nm/s and shrinkage speed is $\sim$180 nm/s. Thus, at 8 s time delay, a catastrophe is visible as a loss of intensity in about 8 s $\times$ 180 nm/s=1440 nm long region, which is readily detectable.

Notably, at these settings, single raw data images are very noisy (Fig. 1B). Nonetheless, we choose these settings to keep the rate of photo-bleaching low, such that we can acquire sufficiently long movies at the necessary temporal resolution (12 min at Δt=8 s). The noise in the images is reduced by a sequence of filtering steps, as described below.

D. 3-D to 2-D Conversion, Noise Reduction, and Illumination Correction

To minimize intensity fluctuations due to imaging noise we employ a sequence of filtering steps. Furthermore, to facilitate data analysis we project the three-dimensional (3-D) data into one plane. To this end we use a standard maximum projection procedure in which the final image is composed of the intensities of the brightest pixels along the axial direction at any given lateral position (lateral = parallel to coverslip). As the typical result of this procedure is relatively noisy (Fig. 1C), we in fact first average the 3-D data with a Gaussian filter (σ_{xy} = 160 nm, σ_z = 470 nm) and then perform the maximum projection, which now exhibits significantly less noise (Fig. 1D). To decrease the resulting blur, projected two-dimensional (2-D) images are deconvolved with the point spread function of the microscope (Fig. 1E).

A final noise reduction step is performed using an edge-preserving Kuwahara-type filter (Bakker *et al.*, 1999; Kuwahara *et al.*, 1976), which we specifically adapted to accommodate linear structures such as MTs. The filter efficiently reduces noise, preserves intensities, and introduces little blurring (Fig. 1F) (available from us as an ImageJ plugin).

Next, images are corrected for inhomogeneous sample illumination, which we measure by acquiring an image of a spatially homogeneous dye solution. We find an approximately Gaussian illumination profile by which we normalize all images (not shown). This measure decreases fluorescence intensity variations across the image, which is advantageous for later assignment of intensity threshold levels of cells and MTs (see below). (*Note*: one cannot avoid a gradient in the SNR across the image—cells at the periphery are less exposed and photon counting noise is thus higher; we therefore avoid analysis of cells that are close to the periphery of the field of view).

E. Sample Drift Correction

It is important to correct lateral sample drift, which can occur due to unstable *xy*-positioning mechanics of the microscope. Lateral drift during data acquisition causes the cell's positions to shift, thus hampering assignment of a proper intracellular coordinate system. In our setup, drift varied from non-detectable to about 1 μm in 10 min. To automatically correct this, the algorithm first identifies which pixels belong to cells. This is achieved by computing the histogram of the intensity values of all pixels in an image. As the field of view is relatively sparsely covered with cells, the histogram is dominated by background intensity values (Fig. 2B). We find that fitting these background intensities to a Gaussian and selecting pixels with intensities that are more than four standard deviations above the mean yield a sufficient separation of cells (Fig. 2C). The algorithm then corrects drift by shifting successive images such that the selected pixels overlap maximally, using a standard cross-correlation procedure (not shown).

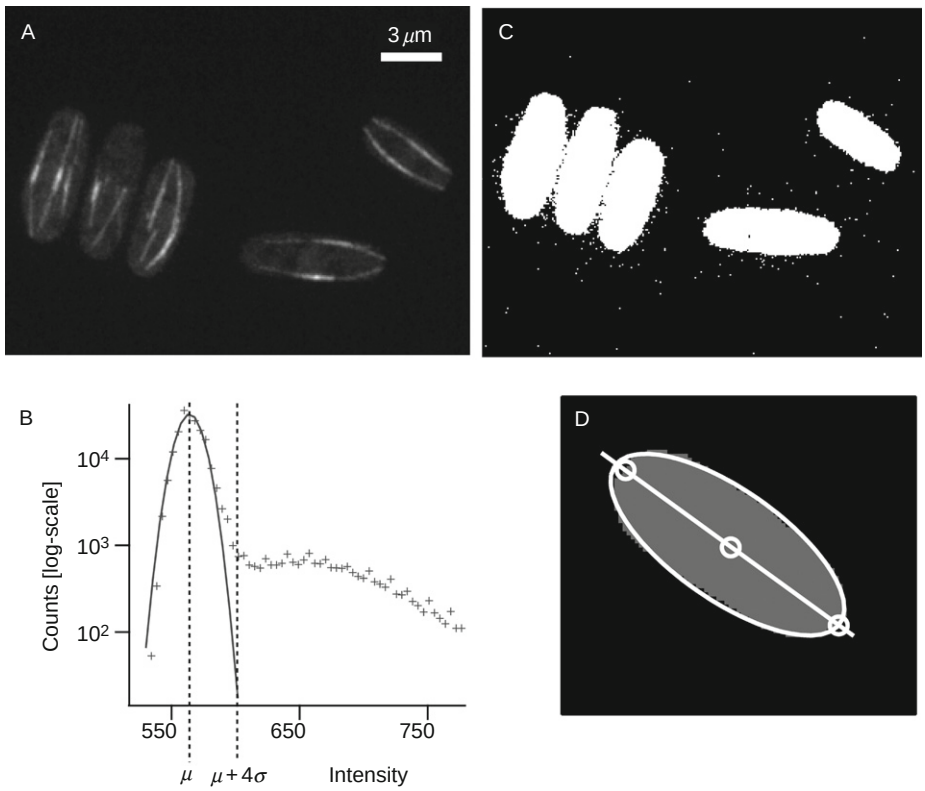

Fig. 2 Drift correction and intracellular coordinate system. (A) Maximum projection of a z-stack of GFP-tubulin expressing fission yeast cells. (B) Histogram of intensity values in the image in A with Gaussian fit (solid line). Dashed lines indicate position of the mean (μ) and of the mean plus 4 standard deviations (σ). (C) All pixels in the image in A that are brighter than $\mu+4\sigma$. (D) Mask of one cell with ellipsoidal fit, long axis (straight line), cell ends (small circles) and cell center (small circle).

F. Masking and Coordinate System Assignment

All the data processing steps described so far are fully automated and require no user input. The following step, which is the generation of cellular masks, is the only step that is performed manually. To generate masks, we manually adjust intensity threshold images such as shown in Fig. 2C, using simple drawing tools from ImageJ. During this process we delete cells that are mitotic, lying on top of each other, or are too close to the periphery of the field of view.

Once the masks are determined, the software automatically identifies the position of cell centers and cell ends. This is important, because catastrophes are sorted according to this coordinate system. To find the cell center the software performs a 2-D ellipsoidal fit to the mask of each cell (Fig. 2D). Cell ends are assigned where the long axis of the ellipsoid intersects with the boundary of the cellular mask. The cell center is assigned to the point at the long axis that lies in the middle between the two cell tips.

G. Microtubule Bundle Tip Detection

As described above, measuring f_{cat} requires both the detection of MT catastrophes and of MT tips. We describe the MT tip detection first. A special feature of MTs in fission yeast is that they are organized in bundles (Fig. 1A). For both technical and biological reasons, we restricted f_{cat} measurements to the leading MTs in each half bundle. Technically, we found it is quite difficult to write software that can distinguish catastrophes of non-leading MTs from MT sliding events that occur inside bundles during nucleation of new MTs along existing ones (Janson *et al.*, 2007). Moreover, the leading MTs may be functionally most active, because those are the ones making contact with the cell pole where they exert pushing forces to center the nucleus and where they deliver cell pole proteins (Hayles and Nurse, 2001; Tolic-Norrelykke *et al.*, 2005; Tran *et al.*, 2001). In the following, we call the tip of the leading (longest) MT in each half-bundle the ''bundle tip'' (BT) and the catastrophe of the longest MT in each half-bundle the ''bundle catastrophe'' (see also Fig. 1A). Simply speaking, we treat each bundle as one MT with two dynamic plus tips.

The detection of BTs is based on the computation of directional derivatives of the intensity images along bundle axes. Those derivatives are high at the BTs, because fluorescence abruptly drops from MT intensities to cellular background levels. This part of the algorithm is the most involved and comprises several steps: bundle thresholding, bundle axis determination, directional derivative computation, and BT thresholding (Fig. 3).

1. Bundle Thresholding

First, the computer needs to know which pixels in the image belong to MTs. The simplest way to separate MTs from background is to specify a threshold intensity value. We found that a reliable method to automatically find such a threshold

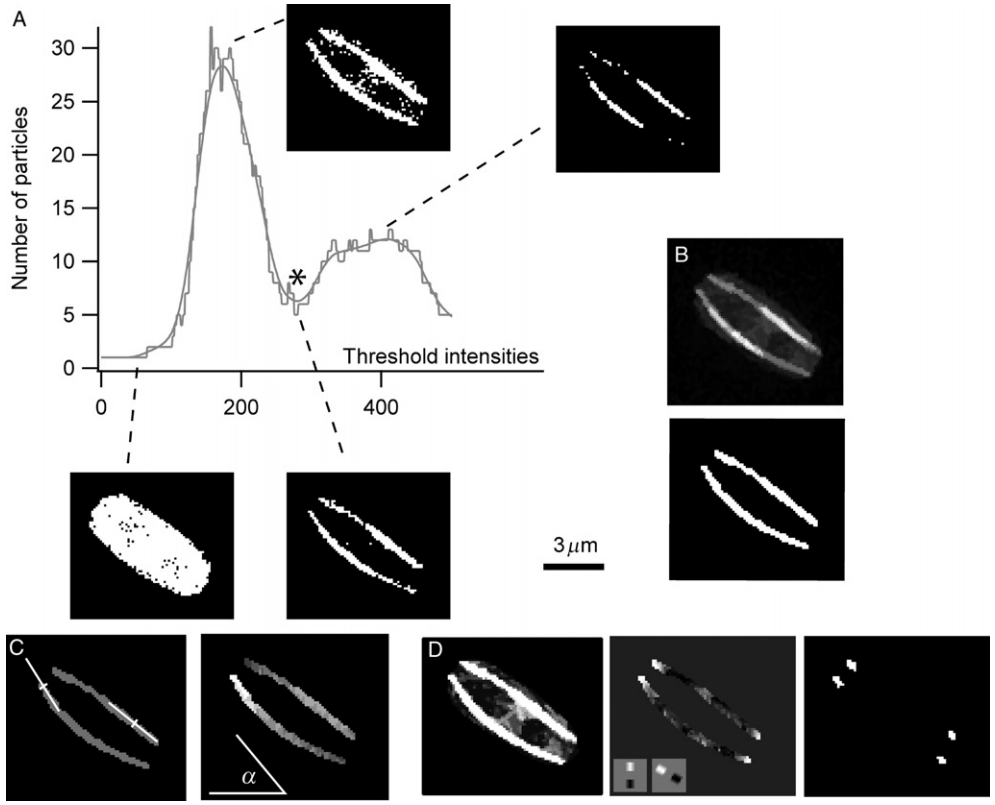

Fig. 3 Bundle tip detection. (A) MT thresholding on semi-processed ("noisy") images as shown in Fig. 1E. The graph shows the number of separated areas (particles) found in the images obtained at different thresholds (smooth solid line is an interpolation). Four examples of corresponding threshold images are shown. The first minimum in the particle/threshold graph is marked by a star. (B) Final thresholding as applied to a fully filtered image (as in Fig. 1F). Lower panel shows the resulting MT mask. (C) MT orientation determination. Left panel: lines (white) overlapping maximally with the MT mask (grey) as shown for two pixels (crosses). Right panel: MT orientations as determined from fits as shown in the left panel. The determined orientation of each pixel inside the MT mask is shown as a linear grey scale: alpha = 60 ° is white and alpha = 0 ° is black. (D) Bundle tip determination. Left panel: normalized intensity image. Middle panel: derivatives of the normalized intensity image along the MT orientations. Bright pixels correspond to high derivatives. The insets show two derivative kernels with different orientations. Right panel: threshold of the derivative image, corresponding to the final bundle tip assignment.

value is based on counting the "number of particles" (NoP) in images obtained at different thresholds. The idea is as follows (Fig. 3): at very low thresholds, there is only one large particle, because the whole cell is selected. At higher thresholds the NoP increases because different areas of the cell become disconnected. At some point, the NoP decreases again because small areas (noise) disappear. The NoP reaches a minimum when most of the noise is gone and MTs appear as connected particles.

Upon further threshold increase the NoP rises again because MTs "fall apart." Eventually, the NoP of course decreases to zero (not shown). Most importantly, we found that the first peak and the following minimum were remarkably reproducible. Moreover, the threshold values corresponding to the minimum yield a good selection of MTs. We thus implemented an automated detection of the minimum in graphs such as shown in Fig. 3A and used the corresponding threshold value for the generation of MT masks. In about 10% of all images the minimum could not be unambiguously found. We programmed the algorithm so that it does not assign a threshold value in such cases. This is not a serious problem, because missing threshold values can be readily interpolated from proceeding and following images in a movie.

A subtlety here is that the minimum was found more reliably in images that were not yet Kuwahara noise filtered (Fig. 1E). The "problem" is that Kuwahara noise reduction works so well that a large interval of threshold values yields the same NoPs, because there is no noise that would be removed by raising the threshold. Thus the shape of the NoP-threshold graphs lack detail and finding the minimum is more difficult. The software thus identifies the threshold in noisy images, and then applies it to the fully filtered images. Choosing the final threshold value for the noise-reduced images about 15% lower than the one identified in the noisy images yields good results (Fig. 3B).

2. Bundle Axes Determination

In order to compute directional derivatives the algorithm needs to determine the bundle orientation. This is achieved by fitting a line to the local bundle shape. For each pixel, the algorithm searches the maximal overlap of a line with the MT mask, as a function of line orientation (Fig. 3C). If the line is parallel to the bundle axis the overlap is maximal and the angle will be stored. The optimal length of the fitted line depends on average MT curvature. The longer the line, the more robust is the fitting. The shorter the line, the better the angular resolution. In our case a length of 2.8 μm yielded good results. In terms of improving our method we think it would be interesting to try fitting curved lines to the local MT shape. The directional derivatives (see below) would then have to be calculated along curved directions, too.

3. Directional Derivative Computation

The algorithm identifies a BT as an abrupt intensity drop along the bundle axis. In fission yeast, extra care is required because abrupt intensity changes not only occur at BTs, but also at trailing MTs tips inside bundles. We therefore divide intensity images by the MT threshold value and set all values in the resulting images that are above 1 to 1. In this way images are normalized and contrast inside the bundles is eliminated (Fig. 3D). Directional derivatives are then

computed by locally multiplying the normalized images with a step kernel that is oriented along the respective local bundle axes (Fig. 3D).

In principle, one may also perform the derivative computation in the MT mask images (as shown in Fig. 3B, lower panel) because these do not contain contrast inside bundles either. However, pixels that are just below the MT threshold are 0 in the masks, while they can take any values between 0 and 1 in the normalized images. Normalized images are thus locally smoother, which prevents artifactually high derivative values that could lead to false-positive BT assignments.

4. Bundle Tip Thresholding

Next, the algorithm must determine which pixels in the derivative images are BTs. The higher the derivative value the more likely the pixel belongs to a true BT. We choose to simply use one threshold value above which pixels are accepted as belonging to BTs. In addition, spurious noise is removed by keeping only areas with a minimum number of connected pixels (Fig. 3D shows the final result). Importantly, because derivative images are computed from normalized images, the same threshold value could be applied to all data sets, facilitating the fully automated analysis. Finally, due to close proximity of MTs it can sometimes occur that areas that are assigned as BTs contain more than one MT tip. In order to account for this, the software computes the size and fluorescence intensity of the identified areas and uses those values to determine the number of contributing tips.

5. Remark

Our bundle-tip detection method is rather involved. It may seem easier to employ a method where intensity images are directly convolved with a kernel that resembles the shape of a MT tip. In fission yeast however this method would also detect MT tips inside bundles. It seems thus necessary to first classify pixels as to whether they belong to a bundle or not, because this allows elimination of contrast inside bundles. A further benefit of our method is that one also obtains the bundle orientation which can be an interesting quantity by itself.

H. Catastrophe Detection

A catastrophe is the abrupt switch to disassembly of a MT. In movies of fluorescently labeled MTs, such an event shows up as an abrupt loss of fluorescence intensity in an extended region (Fig. 4A). The algorithm thus first identifies extended regions of significant intensity loss in difference images (DIs) (Fig. 4B). Analysis of DIs is a standard method for motion detection in movies, which has been previously used to aid visual detection of MT motions inside cells (Komarova *et al*., 2002). We, however, went one step further and implemented a fully automated detection of MT catastrophes.

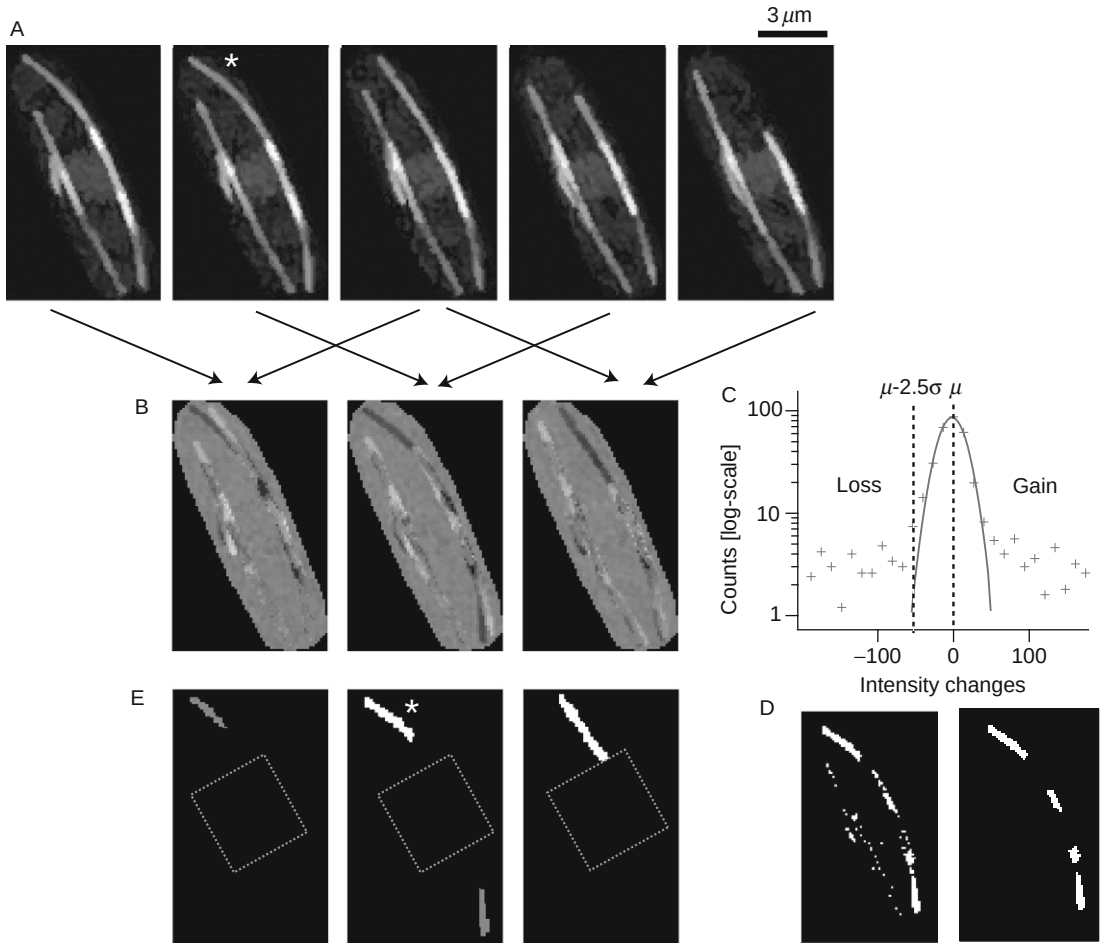

Fig. 4 Catastrophe detection. (A) Sequence of processed fluorescence intensity images. Time lag is 8 s. The MT marked with an asterisk undergoes a catastrophe. (B) Difference images computed from images in A as indicated by the arrows. Bright (dark) areas correspond to gain (loss) of fluorescence intensity. (C) Histogram of the values in the middle panel of B with Gaussian fit (solid line). Dashed lines indicate position of the mean (μ) and of the mean minus 2.5 standard deviations (σ). (D) Left panel: all pixels with values less than $\mu-2.5\sigma$ of middle panel in B, corresponding to values left of dashed line in C. Right panel: as left panel, but only areas with minimally 10 connected pixels are kept. (E) Motion label images; white (grey) areas denote automatically assigned shrinkage (translocation) events. The asterisk denotes a catastrophe. The dotted box encompasses the cell center region which was generally not analyzed because of high MT density.

To determine a significant intensity change, the algorithm first computes a histogram of the intensity changes that occurred in all pixels in a given cell (Fig. 4C). The majority of these values reflect background (BG) fluctuations, which are probably mainly due to photon counting noise and diffusion of

unpolymerized tubulin. Fitting a Gaussian to the histogram yields the standard variation and the mean of the BG fluctuations. In our case, intensity changes due to MT motions are well separated by selecting pixels with intensity changes more than 2.5 standard deviations above the mean BG fluctuations (Fig. 4D, left panel). Remaining noise was removed by retaining only connected areas of a minimal size (Fig. 4D, right panel). Importantly, there are also areas of significant intensity decrease that are not due to MT shrinkages but due to lateral MT translocation. The algorithm identifies these by scanning the neighborhood of an area of fluorescence loss for a matching area of fluorescence increase. The area is assigned as a shrinkage event only if *no* good match is found (Fig. 4E).

At our temporal resolution, depolymerization of a whole MT typically shows up as a sequence of shrinkage events in successive DIs. The actual time and position of the catastrophe is determined by the shrinkage onset. Thus, the "first" shrinkage event needs to be found. As can be seen in Fig. 4A and B, the algorithm operates on DIs calculated between every second image in a movie. Thus, shrinkage events in successive DIs contain overlapping information. This is useful because it facilitates testing whether a shrinkage event overlaps with a shrinkage event in the preceding DI. The algorithm takes the shrinking region in DI_n as a mask and checks whether there had been already shrinkages within this mask in DI_{n-1}. Only if this is *not* the case the shrinkage event is assigned as a catastrophe. Also secondary shrinkage events contain important information, because they are used to identify whether a detected BT belongs to a shrinking MT. If a BT area overlaps with a shrinkage area in the same image, it is not considered for f_{cat} calculation. Finally, only catastrophes are accepted for which a corresponding BT was found, too. In this way events inside bundles, which are difficult to interpret, are discarded. In addition, this measure is necessary for an accurate and robust calculation of f_{cat} (see next section).

I. Accuracy of the Algorithm

We tested the algorithm's accuracy by comparing its automated assignments of nonshrinking BTs and catastrophes with visual inspection in a random sample of 10 cells (corresponding to 2 h observation time). In this sample, the algorithm correctly found 4204 BTs (87%), missed 628 BTs (13%), and assigned 39 false BTs (1%). Thus, the algorithm misses more than 10% of all BTs. On the other hand, there are only 1% false-positives. We intentionally select for a rather conservative BT detection; the sensitivity can be readily adjusted in the BT thresholding step. The reason for choosing a conservative BT detection is that false-positive BTs lead to a systematic underestimation of f_{cat}, because there are no corresponding catastrophes. On the other hand, missed BTs are in principle no problem for measuring f_{cat} because the algorithm is programmed such that it only accepts catastrophes if the corresponding BT was detected, too. Comparably, if one observes MT dynamics by visual inspection one may also select MTs that are easier to follow.

The advantage of the automated analysis is that the selection criteria are well defined. In our case, MTs that stand out well from the cellular background will be analyzed preferentially. Regarding catastrophe detection, the algorithm correctly detected 279 catastrophes (95%), missed 14 (5%), and assigned 17 false-positives (6%). Thus, the error rates for false-positives and missed catastrophes are low and of similar magnitude.

In conclusion, in the best case scenario, all incorrect assignments are spatially random and the computed results are correct within their statistical errors bars. In the worst case scenario, all wrong catastrophe assignments are systematic to specific intracellular positions. For instance, if all missed catastrophes occurred at the cell pole and all false-positives were assigned to the cytoplasm, f_{cat} at the cell pole would be relatively about 10% too low. Thus, to be on the safer side, only spatial variations in f_{cat} above 10% should be considered trustworthy.

J. Implementation and Speed of the Algorithm

The full analysis, from raw data to labeled movies runs almost fully automated. Only masking of cells is performed manually. Excluding the time required for the manual cell masking and excluding the time for Kuwahara filtering in image, the processing of 1 movie, containing 100 image stacks of about 6 cells, takes about 35 min; the code being implement in Igor Pro 5 (WaveMetrics), running on a desktop computer equipped with 1 GB RAM and a 3.2 GHz CPU (Intel Pentium 4). Thus, the algorithm is fast enough to evaluate one set of experiments ($\sim$20 movies) over night ($\sim$8 h). Implementing the code in MatLab or C would probably further enhance the evaluation speed.

III. Results

A. Catastrophe Regulation at Fission Yeast Cell Poles

As an example for the kind of results that can be obtained using this methodology we show the spatial BT, catastrophe and f_{cat} distribution for MTs within the cell pole region of an interphase fission yeast cell (Fig. 5A). We find that the BT distribution strongly peaks at the very ends of the fission yeast cells (Fig. 5B). This could be due to mechanical constraints: the cell wall guides MT tips into the cell pole where they are trapped because they cannot easily bend and grow backwards because of their mechanical stiffness. Thus, MT tips spend a relatively long time at the cell pole. The distribution of catastrophes also peaks strongly at the cell pole (Fig. 5C). It is important to realize that this is in the first place mainly a consequence of the BT distribution: catastrophes occur where there are MT tips. Thus, Fig. 5C alone does *not* contain a lot of information regarding catastrophe regulation. To give a drastic example: there could be intracellular regions with very high f_{cat}, but without any observed catastrophes, just because no MTs grow there.

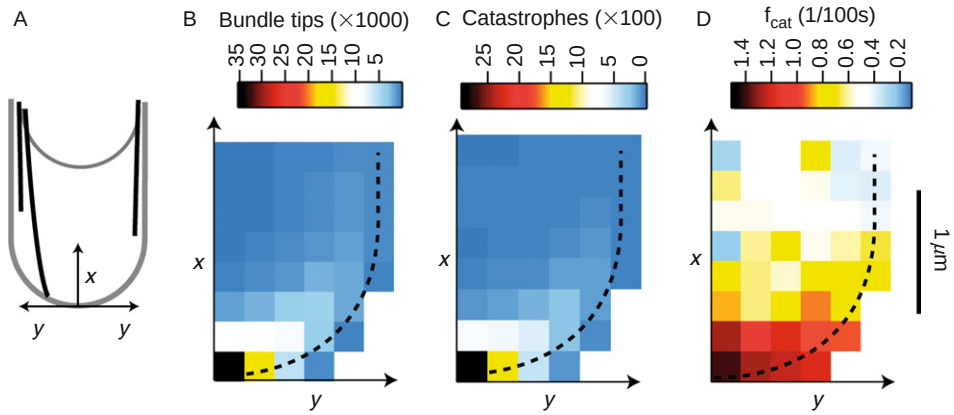

Fig. 5 Bundle tip, catastrophe and f_{cat} distributions. (A) Schematic of fission yeast cell, showing the coordinate system used in the following. (B) Bundle tip and (C) catastrophe distributions. (D) Map of f_{cat}. Numbers in B and C are total observations, obtained in 641 cells, where each cell was monitored for 12 min and an observation was made every 8 s. Numbers include a factor of 4 because observations from all four "corners" of each cell are projected into one. To eliminate areas with high statistical noise, panels B, C, and D only include areas with more than 400 detected bundle tips.

Thus, to investigate catastrophe regulation, one has to compute f_{cat} according to Eq. (1). Figure 5D shows that f_{cat} is highest at the very cell end (small fluctuations between neighboring areas are of statistical origin). Furthermore it seems that there may be a correlation between f_{cat} enhancement and cell wall curvature. This could be due to catastrophe promoting proteins that are deposited in a "cell wall curvature" or "cell end distance" dependent manner (Hayles and Nurse, 2001). Alternatively this could be due to MT growth opposing forces that increase the more perpendicular MTs hit against the cell wall (Dogterom and Yurke, 1997; Janson *et al.*, 2003). In fact, a more detailed analysis of our data supports a mechanism where growth opposing forces enhance f_{cat} (to be published elsewhere).

IV. Discussion

The algorithm presented was developed for measuring the spatial regulation of MT catastrophes in fission yeast. One has to be aware that it may be necessary to modify our algorithm when observing MTs in different cells. Important parameters are: signal to noise; spatial and temporal resolution of the microscopy images; MT growth, shrinkage, catastrophe and rescue rates; the extent to which MTs undergo lateral translocations and bending, and the overall spatial organization of MTs in the cell type of interest. Having made these qualifications, we think that many of the solutions that we present here are applicable to other cell types as well.

Finally, we would like to briefly compare our methodology with some other ways of measuring MT dynamics in a computerized manner. For many years

fluorescent speckle microscopy (FSM) data have been automatically analyzed, revealing intracellular dynamics of MTs and actin (Danuser and Waterman-Storer, 2006). In FSM, the fluorophore density is very low such that one observes fluorescent speckles on the MT and actin filaments. These speckles can be automatically tracked and it is thus possible to track filament translocations, even if they occur along the filament axis. Thus, FSM is very powerful for measuring phenomena like MT tread-milling (Grego *et al.*, 2001) and translocations such as "retrograde flow" (Waterman-Storer and Salmon, 1997). More closely related to our method is the fact that one may also obtain maps of polymer assembly and disassembly, because the appearance and disappearance of speckles reports polymer growth and shrinkage respectively. A difference with respect to our method is that FSM does not (yet) provide information about the position and time of catastrophes. In principle, this may be incorporated by tracing the sequential disappearance of speckles in time and space. However, we do not see an advantage in doing this with speckled MTs, as compared to our method that operates on fully labeled MTs.

Another way of automatically measuring catastrophe frequencies may be to use fluorescently labeled MT plus tip tracking proteins (Lansbergen and Akhmanova, 2006). To our knowledge this has not been published yet but we think it may have some advantages. First, one directly obtains the plus tip distribution, simply by detecting regions of high intensity in the cell. This should be easier than the bundle-tip detection algorithm presented by us. Second, a catastrophe event could be identified by the disappearance of the fluorescent spot that marks the plus tip. However, this approach also has its challenges. First of all, one has to find a suitable plus tip marker. In principle there are several candidates (Busch and Brunner, 2004; Komarova *et al.*, 2005), but the available data suggests that these proteins may disappear gradually from the MT end, before the actual catastrophe happens (Busch and Brunner, 2004). It may thus be challenging to detect and pinpoint the catastrophe event. Further, in order to distinguish the disappearance of plus tip markers (the catastrophes) from translocations one has to track them very reliably. If the density of MT tips is high this may be difficult. Here, our methodology seems advantageous because it does not require tracking of MT growth. In fission yeast, there is another complication of using plus tip markers for catastrophe detection: MTs in the bundle interior cannot be distinguished from the leading ones. This is a drawback because it is not clear whether both populations behave similarly. Despite these challenges, we think that automated plus-tip tracking may be an interesting alternative.

Acknowledgments

This work is part of the research program of the Stichting voor Fundamenteel Onderzoek der Materie (FOM), which is financially supported by the Nederlandse Organisatie voor Wetenschappelijk Onderzoek (NWO). We thank Pieter Rein ten Wolde for reading the manuscript. We gratefully acknowledge support from HSFP Research Grant RPG11/2005. C.T. was supported by a Marie Curie Fellowship.

References

Bakker, P., Van Vliet, L. J., and Verbeek, P. W. (1999). Edge preserving orientation adaptive filtering. IEEE Computer Society Conference on Computer Vision and Pattern Recognition, Vol. 1, 540pp.

Bratman, S. V., and Chang, F. (2007). Stabilization of overlapping microtubules by fission yeast CLASP. *Dev. Cell* **13**(6), 812–827.

Brunner, D., and Nurse, P. (2000). CLIP170-like tip1p spatially organizes microtubular dynamics in fission yeast. *Cell* **102,** 695–704.

Busch, K. E., and Brunner, D. (2004). The microtubule plus end-tracking proteins mal3p and tip1p cooperate for cell-end targeting of interphase microtubules. *Curr. Biol.* **14**(7), 548–559.

Danuser, G., and Waterman-Storer, C. M. (2006). Quantitative fluorescent speckle Microscopy of cytoskeleton dynamics. *Annu. Rev. Biophys. Biomol. Struct.* **35,** 361–387.

Desai, A., and Mitchison, T. J. (1997). Microtubule polymerization dynamics. *Annu. Rev. Cell Dev. Biol.* **13,** 83–117.

Dogterom, M., Felix, M.-A., Guet, C. C., and Leibler, S. (1996). Influence of M-phase chromatin on the anisotropy of microtubule asters. *J. Cell Biol.* **133**(1), 125–140.

Dogterom, M., and Leibler, S. (1993). Physical aspects of the growth and regulation of microtubule structures. *Phys. Rev. Lett.* **70**(9), 1347–1350.

Dogterom, M., and Yurke, B. (1997). Measurement of the force-velocity relation for growing microtubules. *Science* **278,** 856–860.

Drummond, D. R., and Cross, R. A. (2000). Dynamics of interphase microtubules in *Schizosaccharomyces pombe*. *Curr. Biol.* **10**(13), 766–775.

Grego, S., Cantillana, V., and Salmon, E. D. (2001). Microtubule treadmilling *in vitro* investigated by fluorescence speckle and confocal microscopy. *Biophys. J.* **81,** 66–78.

Hagan, I. M. (1998). The fission yeast microtubule cytoskeleton. *J. Cell Sci.* **111,** 1603–1612.

Hayles, J., and Nurse, P. (2001). A journey into space. *Nat. Rev. Mol. Cell Biol.* **2**(9), 647–656.

Hoog, J. L., Schwartz, C., Noon, A. T., O'Toole, E. T., Mastronarde, D. N., McIntosh, J. R., and Antony, C. (2007). Organization of interphase microtubules in fission yeast analyzed by electron tomography. *Dev. Cell* **12**(3), 349–361.

Howard, J., and Hyman, A. A. (2007). Microtubule polymerases and depolymerases. *Curr. Opin. Cell Biol.* **19**(1), 31–35.

Howell, B., Odde, D. J., and Cassimeris, L. (1997). Kinase and phosphatase inhibitors cause rapid alterations in microtubule dynamic instability in living cells. *Cell Motil. Cytoskeleton* **38**(2), 201–214.

Janson, M. E., Dood, M. E. D., and Dogterom, M. (2003). Dynamic instability of microtubules is regulated by force. *J. Cell Biol.* **161**(6), 1029–1034.

Janson, M. E., Loughlin, R., Loiodice, I., Fu, C. H., Brunner, D., Nedelec, F. J., and Tran, P. T. (2007). Crosslinkers and motors organize dynamic microtubules to form stable bipolar arrays in fission yeast. *Cell* **128**(2), 357–368.

Janson, M. E., Setty, T. G., Paoletti, A., and Tran, P. T. (2005). Efficient formation of bipolar microtubule bundles requires microtubule-bound {gamma}-tubulin complexes. *J. Cell Biol.* **169**(2), 297–308.

Kirschner, M., and Mitchison, T. (1986). Beyond self-assembly: From microtubules to morphogenesis. *Cell* **45,** 329–342.

Komarova, Y., Lansbergen, G., Galjart, N., Grosveld, F., Borisy, G. G., and Akhmanova, A. (2005). EB1 and EB3 control CLIP dissociation from the ends of growing microtubules. *Mol. Biol. Cell* **16** (11), 5334–5345.

Komarova, Y. A., Vorobjev, I. A., and Borisy, G. G. (2002). Life cycle of MTs: Persistent growth in the cell interior, asymmetric transition frequencies and effects of the cell boundary. *J. Cell Sci.* **115** (Pt. 17), 3527–3539.

Kuwahara, M., Hachimura, K., Eiho, S., and Kinoshita, M. (1976). "Digital Processing of Biomedical Images." pp. 187–203. Plenum Press, New York.

Lansbergen, G., and Akhmanova, A. (2006). Microtubule plus end: A hub of cellular activities. *Traffic* **7** (5), 499–507.

Mata, J., and Nurse, P. (1997). Tea1 and the microtubular cytoskeleton are important for generating global spatial order within the fission yeast cell. *Cell* **89,** 939–949.

Mimori-Kiyosue, Y., Grigoriev, I., Lansbergen, G., Sasaki, H., Matsui, C., Severin, F., Galjart, N., Grosveld, F., Vorobjev, I., Tsukita, S., and Akhmanova, A. (2005). CLASP1 and CLASP2 bind to EB1 and regulate microtubule plus-end dynamics at the cell cortex. *J. Cell Biol.* **168**(1), 141–153.

Mitchison, J., and Kirschner, M. (1984). Dynamic instbility of microtubule growth. *Nature* **312,** 237–242.

Moreno, S., Klar, A., and Nurse, P. (1991). Molecular genetic analysis of fission yeast *Schizosaccharomyces pombe*. *Methods Enzymol.* **194,** 795–823.

Niethammer, P., Bastiaens, P., and Karsenti, E. (2004). Stathmin-tubulin interaction gradients in motile and mitotic cells. *Science* **303**(5665), 1862–1866.

Odde, D. J. (1995). Kinetics of microtubule catastrophe assessed by probabilistic analysis. *Biophys. J.* **69,** 796–802.

Rusan, N. M., Fagerstrom, C. J., Yvon, A. M. C., and Wadsworth, P. (2001). Cell cycle-dependent changes in microtubule dynamics in living cells expressing green fluorescent protein-alpha tubulin. *Mol. Biol. Cell* **12**(4), 971–980.

Sawin, K. E., Lourenco, P. C. C., and Snaith, H. A. (2004). Microtubule nucleation at non-spindle pole body microtubule-organizing centers requires fission yeast centrosomin-related protein mod20p. *Curr. Biol.* **14**(9), 763–775.

Tolic-Norrelykke, I. M., Sacconi, L., Stringari, C., Raabe, I., and Pavone, F. S. (2005). Nuclear and division-plane positioning revealed by optical micromanipulation. *Curr. Biol.* **15**(13), 1212–1216.

Tran, P. T., Marsh, L., Doye, V., Inoue, S., and Chang, F. (2001). A mechanism for nuclear positioning in fission yeast based on microtubule pushing. *J. Cell Biol.* **153**(2), 397–411.

Tran, P. T., Paoletti, A., and Chang, F. (2004). Imaging green fluorescent protein fusions in living fission yeast cells. *Methods* **33**(3), 220–225.

Verde, F., Dogterom, M., Stelzer, E., Karsenti, E., and Leibler, S. (1992). Control of microtubule dynamics and length by cyclin A- and cyclin B-dependent kinases in xenopus egg extracts. *J. Cell Biol.* **118**(5), 1097–1108.

Walker, R. A., Obrien, E. T., Pryer, N. K., Soboeiro, M. F., Voter, W. A., Erickson, H. P., and Salmon, E. D. (1988). Dynamic instability of individual microtubules analyzed by video light-microscopy—Rate constants and transition frequencies. *J. Cell Biol.* **107**(4), 1437–1448.

Waterman-Storer, C. M., and Salmon, E. D. (1997). Actomyosin-based retrograde flow of microtubules in the lamella of migrating epithelial cells influences microtubule dynamic instability and turnover and is associated with microtubule breakage and treadmilling. *J. Cell Biol.* **139**(2), 417–434.

Yamamoto, A., West, R. R., McIntosh, J. R., and Hiraoka, Y. (1999). A cytoplasmic dynein heavy chain is required for oscillatory nuclear movement of meiotic prophase and efficient meiotic recombination in fission yeast. *J. Cell Biol.* **145**(6), 1233–1249.

CHAPTER 21

Quantitative Fluorescence Lifetime Imaging in Cells as a Tool to Design Computational Models of Ran-Regulated Reaction Networks

Petr Kalab* **and Arnd Pralle*,†**

*Department of Cell Biology
University of California
Berkeley, California 94720

†Department of Physics and Department of Physiology and Biophysics
State University of New York
Buffalo, New York 14260

METHODS IN CELL BIOLOGY, VOL. 89

0091-679X/08 $35.00
DOI: 10.1016/S0091-679X(08)00621-3

Abbreviations

FRET	Förster Resonance Energy Transfer
ET	Energy Transfer
FLIM	Fluorescence Lifetime Imaging Microscopy
EYFP	Enhanced Yellow Fluorescent Protein
FP	Fluorescent Protein, such as GFP (green), CFP (cyan), YFP (yellow), RFP (red), and others
TCSPC	Time-Correlated Single Photon Counting

Abstract

The understanding of cell function often requires that complex intracellular pathways are considered in quantitative terms. The access to precise measurement of activities in live cells is increasingly provided by the advances in fluorescence lifetime imaging microscopy (FLIM) of Förster (or fluorescence) resonance energy transfer (FRET)-based molecular biosensors. We discuss how quantitative *in vivo* imaging can be combined with *in vitro* biochemical characterization to develop computational systems models simulating the behavior of biochemical networks. We describe the application of such approach in computational modeling of the Ran GTPase function in mitotic spindle assembly. The RanGTP concentration gradient surrounding mitotic chromosomes induces the formation of a gradient of spindle assembly factors (SAFs) activated by RanGTP-induced release from inhibitory complexes of SAFs with importin β. To visualize the gradient of activated SAFs in live cells, we used FLIM to detect the signal of a FRET-based biosensor that reports its RanGTP-induced liberation from importin β. We review the technical aspects of FRET measurements by FLIM and discuss the step-wise design of systems models aided by quantitative imaging. As evidenced by the

example of mitotic Ran gradient studies, the computational simulations are a powerful tool to test new hypotheses on biological function.

I. Quantitative Imaging and Systems Modeling as a Tool in Cell Biology—The Rationale and Strategy

To understand a cell's response to a stimulus or perturbation, it is often insufficient to rely on qualitative picture of the regulatory networks involved in the response. The requirement to consider the biochemical interactions in live cells quantitatively is being met by advances in quantitative *in vivo* imaging with molecular biosensors. Combined with the accumulated knowledge acquired by more traditional *in vitro* biochemical techniques, many fields in cell biology now have access to large amount of data describing the behavior of biological networks. However, the complexity and dynamic nature which is characteristic of biological systems make the analysis of such data challenging and have spurred a development of novel methods, sometimes collectively referred to as *computational systems biology* (Kitano, 2002).

Computational systems biology offers two types of general approaches: identification of patterns from the often vast amounts of experimental data and a hypothesis-driven approach relying on the simulation of the biological systems behavior in mathematical models (Kitano, 2002). In particular, the latter parsimonious approach is appealing to cell biologists because it rigorously tests current hypotheses and does not require complete quantitative description of all biological system components. Instead, a minimal sufficient description of the biological process in question is used to develop the mathematical model for simulations, typically relying on already published data. However, the combination of both strategies is optimal and can be achieved in a step-wise process of simulation and implementation of new experimental data into the model.

In Fig. 1, we illustrate how the computational models based on biochemical *in vitro* measurements can be combined with quantitative *in vivo* imaging data to refine the computational model for simulations.

1. A computational model is built representing the biological system at equilibrium state (Alves *et al.*, 2006). The model includes a minimal defining set of biological system components, their regulatory connections, their concentrations, and kinetic parameters of their reactions obtained from published literature or measured (Fig. 1A). The parameters of not yet characterized system components are adjusted to produce a model matching the known parameters at equilibrium.

2. A molecular sensor is constructed to quantitatively report on the behavior of one of the components in the experimental system. For measurements in live cells, it is practical to design a sensor as a genetically encoded fluorescent protein (FP)-tagged Förster Resonance Energy Transfer (FRET) pair, either as two interacting proteins or a single Cameleon-like (Mitra *et al.*, 1996; Miyawaki *et al.*, 1999; Tsien *et al.*, 1993) molecule. The specificity of the sensor is evaluated in *in vitro*

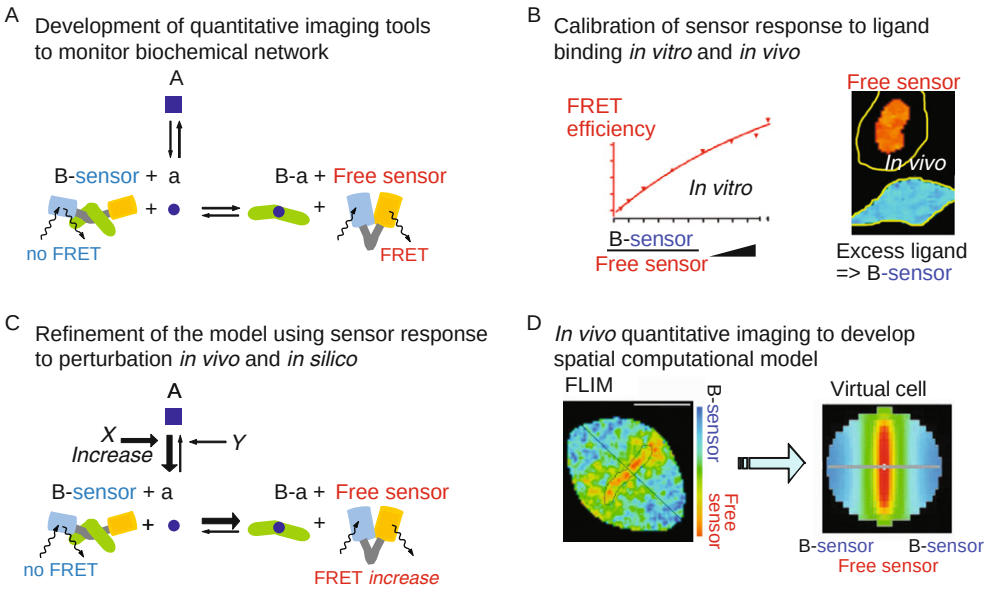

Fig. 1 Schematic diagram describing step-wise development of a computational Ran systems model guided by the application of a quantitative Förster (or fluorescence) resonance energy transfer (FRET) biosensor. A computational model was designed consisting of a minimal sufficient set of reactions controlling the guanine nucleotide exchange and GTP hydrolysis on Ran and the coupling of RanGTP production to the RanGTP-regulated binding of NTRs to their cargos. In the model, available published kinetic parameters and reactant concentrations were used and unknown parameters were fitted to obtain a model approximating the known behavior of the Ran system at equilibrium. (A) A FRET-based biosensor was developed to monitor the dynamics of RanGTP-regulated importin β cargo release quantitatively and in a nondestructive fashion in a variety of *in vitro* as well as *in vivo* conditions. In the diagram shown, "a" corresponds to RanGTP, A = RanGDP, B = Importin β, and the sensor is Rango. Provided that a FRET-based sensor mimicking the behavior of a system's component can be created, a similar approach is applicable in the design of computational models of other intracellular pathways. (B) The signal of the sensor (Rango) was calibrated *in vitro* by measuring the changes of its FRET efficiency to increasing concentrations of its ligand, recombinant purified importin β. Assuming the measured apparent dissociation constant of the Rango–importin β interaction ($K_d = 2$ nM), the fractional occupancy of Rango across the range of importin β concentrations was calculated and a dose–response calibration curve was fitted to the measurements. (C) To quantify the RanGTP-induced release of importin β cargos in the cytoplasm, increasing concentrations of GTP hydrolysis-deficient Ran mutant (RanQ69L) protein were added to functional mitotic *Xenopus laevis* egg extracts containing Rango. The corresponding increase of importin β dissociation was signaled by increase of Rango FRET. Conversely, the addition of importin β to the extracts increased the fraction of importin β-bound cargos, decreasing Rango FRET. The changes of free Rango fraction were calculated from FRET measurements in the cytoplasmic extracts, assuming the dose–response calibration curve obtained with purified proteins (above, C). In turn, such measured perturbation-induced changes of the cytoplasmic free Rango fraction were used as a guide to further refine the fitted parameters of the minimal computational Ran systems model. (D) Quantitative spatial imaging of the mitotic RanGTP-regulated gradient of importin β cargos in live cells guide the development of spatially resolved computational Ran systems models.

experiments with purified components. Next, the biochemically verified sensor–ligand binding is correlated with measurements of sensor's FRET signal by a variety of methods, including fluorescence lifetime imaging microscopy (FLIM). *In vitro* measurements with purified sensor and its ligand are used to determine the apparent dissociation constant of the sensor–ligand interaction (K_d). Also with purified proteins, the response of the sensor donor lifetime τ_{DA} to increasing concentration of the ligand is measured by FLIM. Assuming the measured K_d, a dose–response curve is then calculated that expresses how τ_{DA} changes depending on the proportion of the sensor molecules bound to the ligand (FRET efficiency/fractional occupancy calibration curve, Fig. 1B, left). Given the robustness of the FRET measurements by FLIM, such *in vitro* calibrations can be used to estimate the fractional occupancy of the sensor in live cells imaged by FLIM microscopy.

In case of a FRET sensor responding to its posttranslational modification rather than ligand binding, the calibration curve could be obtained by measuring samples containing known mixed proportions of fully modified and unmodified sensor. If the *in vitro* calibration is unavailable for technical reasons, the extreme physiological readings of the sensor may be obtained *in vivo* (in cells or extract) by treatments presumably fully activating or inhibiting the sensor (Fig. 1B, right).

3. The sensor is introduced into the otherwise unperturbed biological system (corresponding to the equilibrium state of the computational model) and its FRET signal is measured by FLIM. For example, the sensor is expressed in cells or added to the *Xenopus laevis* egg extracts. The dose–response data obtained *in vitro* (point 2 above) are then used to calculate the fractional occupancy of the sensor with its ligand in such *in vivo* system existing at its "equilibrium" state. Such estimates are then used to adjust the fitted parameters of the computed model simulating the presence of the sensor in the system. For example, the unknown concentrations of endogenous sensor ligands are changed in the model to match its measured fractional occupancy *in vivo*. Next, the signal of the sensor is measured by FLIM in response to experimental perturbations of the biological system. For example, live cells or functional extracts containing the sensor are treated with inhibitors or activators of the pathway in question, or with increasing concentrations of the ligand. The change of the fractional occupancy of the sensor measured by FLIM is then used to further refine the computed model (Fig. 1C).

4. The refined nondimensional computational model can be used to analyze quantitative imaging data obtained in cells. The combination of nondimensional modeling and cell imaging is then used to guide the construction of spatially resolved computational systems models. Such models encompassing the combined knowledge on the intracellular network provide rigorous tests of current hypotheses. In addition, these lead to otherwise unavailable insights into cellular function and aid the formulation of new functional hypotheses. Importantly, the computational systems models can be easily shared between different laboratories and evolved by implementing new data measured in live cells (Fig. 1D).

II. Quantitative Detection of Biochemical Interactions by FLIM

A. Introduction to FRET and FLIM

FRET is nonradiative transfer of energy from an excited donor fluorophore (D) to an acceptor (A). The efficiency of energy transfer (E) is inversely proportional to the sixth power of the distance between the fluorophores R (Förster, 1946, 1948):

$$E = \frac{R_0^6}{R_0^6 + R^6}$$

The Förster distance R_0 at which E is 50% is specific for each fluorophore pair. R_0 depends on the spectral overlap of donor and acceptor J, the orientation factor κ which is a function of the angles between the chromophore dipoles, the quantum yield of the donor Q_d, and the refractive index n of the medium (Clegg, 1966; Förster, 1946, 1948):

$$R_0 = 9.78 \times 10^3 \left(Q_d \kappa^2 n^{-4} J\right)^{1/6} \mathring{A}$$

E is commonly measured by exciting the donor and determining the intensity of the peak emissions from both fluorophores. The estimate of FRET efficiency is often calculated as the ratio of the intensity emitted at the acceptor wavelength to the total intensity emitted. However, E can also be directly derived from the measurements of the fluorescence lifetime of the donor τ_D (Gordon *et al.*, 1998), which is the principle of FLIM.

After absorbing the energy from a photon, the fluorophore remains in an excited state until it returns to the ground state by emitting a photon, releasing the energy difference in the form of heat or transferring the energy to another nearby molecule. Since the relaxation to the ground state is stochastic, the lifetimes of fluorophore molecules in the excited state are exponentially distributed (Lakowicz, 1999). The characteristic fluorescence lifetime τ of a fluorophore is the time after which e^{-1} molecules of the original populations remain in the excited state. If the excited fluorophore is located near a molecule that can accept its emission energy, the additional decay path out of the excited state shortens the lifetime. The FRET efficiency then corresponds to

$$E = 1 - \frac{\tau_{DA}}{\tau_D},$$

where τ_{DA} is the donor lifetime in the presence of acceptor and τ_D in its absence (Tsien, 2003). Because the fluorescence lifetime is an intrinsic molecular property of the fluorophore, it is independent of the fluorophore concentration and can be compared between instruments, laboratories, and samples. In practice, the τ_D can be considered as a constant (corresponding to, e.g., the lifetime of the recombinant donor molecule measured *in vitro* or an arbitrary number), and the only variable needed to be measured in live cell imaging with FLIM is the τ_{DA}. The advantage of FLIM is that the measurements of τ_{DA} are in principle not influenced by

concentration of the fluorophores, by the effects of donor on acceptor fluorescence, and by direct excitation of the acceptor, that is, the typical problems greatly complicating FRET detection by other methods. The presently available instrumentation, fluorophores, and analysis software make it possible that within a wide range of conditions typical for many cell biological samples, the detection of FRET by FLIM can deliver its promise also in experimental practice.

B. Other Modes of FRET Microscopy as Controls for FLIM

For the successful application of FLIM, it is important to realize that the detection of FRET in biological samples by any technique is influenced by many variables. These variables include the biochemical and photophysical properties of the FRET sensor, the spectral properties of the sample, the detection instrument, and the physics of the process used for the detection. Any of these factors can contribute to detection artifacts and erroneous conclusions. Although FLIM has distinct advantages over other FRET detection methods, it is by no means an exception to the requirement for rigorous controls. Arguably the most straightforward approach is to seek consistency of results across independent FRET detection methods to validate FLIM results. Likely, one or more such methods would be available in many FLIM-capable laboratories and should be combined with biochemical controls to verify the interactions of the biosensor presumably detected by FLIM. In the study of the RanGTP gradient in somatic cells, we combined spectral analysis of the Rango sensor in a spectrofluorimeter, epifluorescence intensity ratio imaging, donor fluorescence intensity change after acceptor bleach, and time-correlated FLIM with extensive biochemical characterization of the sensor (Kalab *et al.*, 2006).

Most epifluorescence microscopes can be adapted for the detection of FRET by wide-field *epifluorescence intensity ratios*. Typically either the increased emission of the donor and decreased emission of the acceptor are used (Erickson *et al.*, 2001), and normalized to the amount of protein by measuring the directly excited acceptor emission as well (Kalab *et al.*, 2002, 2006). The contemporary highly sensitive and fast CCD cameras can provide excellent speed of acquisition and sufficient resolution. However, out-of-focus artifacts typical to wide-field acquisition may greatly complicate FRET detection in structures with small vertical dimension. Any intensity ratio technique requires extreme care to account for varying background and autofluorescence in the samples, spectral overlaps between the donor and the acceptor, and for example, for flickering of Mercury lamps used for excitation. Although quantitative FRET measurement based on intensity ratios is challenging, it is potentially an excellent qualitative control to validate FLIM results.

The measurements of *donor fluorescence intensity change after acceptor bleach* performed with a laser scanning confocal microscope is a relatively robust and straightforward method of semi-quantitative FRET detection in cells. One of the disadvantages of the ''acceptor bleach'' method is that the motion of the imaged cell and structures within it during the bleaching period often causes shifts between

pre- and post-bleach images that cannot always be remedied by postimaging realignment. Temporal changes also cannot be measured because it is a photodestructive method. The optimal bleaching of YFP without bleaching CFP would require a 540-nm laser but the 514 nm line of the Argon laser is often the closest available. The optimal excitation wavelength for CFP (around 435 nm) is not provided by the spectrum of Argon/Krypton laser, whose closest line of 458 nm produces strong direct excitation of YFP. Thus, high-quality, CFP-selective emission filters are essential. Despite such drawbacks, in the study of the mitotic Ran gradient in HeLa, we found an excellent correlation between the relative E estimated by acceptor bleach method and FLIM results obtained in cells imaged under a variety of experimental treatments (Kalab *et al.*, 2006; and data not shown).

C. Design of FRET-Based Sensors for FLIM Applications

In addition to the currently prevalent use of FPs as a donor and acceptor, organic fluorescent molecules linked to proteins offer several potential advantages, such as better spectral properties, smaller size, and lower environmental sensitivity (Alves *et al.*, 2006). In some cases, functional donor and acceptor molecules can be created by relatively nonspecific covalent *in vitro* modification of recombinant proteins by commercially available dyes (Caudron *et al.*, 2005). There is also promising progress in specifically targeted labeling of proteins, for example, via a tag that is subsequently modified by small organic fluorescent molecule (Johnsson and Johnsson, 2007), and in the use of nonnatural fluorescent amino acids to produce a FRET sensor (Kajihara *et al.*, 2006).

However, at present, the FRET sensor design based on FPs is a more mature technology readily applicable for many *in vivo* applications and FLIM measurements. Genetically encoded FP-based FRET biosensors may be formed by two molecules labeled by donor and acceptor fluorophore. The interaction of the two labeled molecules will be detected by increased FRET between the donor and acceptor. In particular, if the concentration of the donor and acceptor can be accurately controlled, the bimolecular sensor design is well suitable for quantitative FLIM (Caudron *et al.*, 2005). Compared to intensity-based FRET detection methods, FLIM is an advantageous approach if the donor and acceptor concentrations locally vary within cells because the τ_{DA} measurement is insensitive to FP concentration. However, if the donor and acceptor concentrations are highly disproportionate, it is critical to ensure tight separation of the donor fluorescence emission by good choice of the FP pair and by the use of stringent emission filters.

In comparison, in the single-molecule FRET biosensor, the donor and acceptor molecules are present at equimolar concentrations throughout the cell, simplifying the FLIM acquisition and analysis. Such a sensor is constructed as a peptide chain containing a sensory domain flanked by donor and acceptor FPs at its N- and C-termini, respectively. The binding of a ligand induces a conformational change of the sensor peptide and a concomitant change in the distance and orientation of the FPs at its termini (Fig. 2). The resulting change of FRET between the FPs

provides readout of ligand binding to the sensor domain. Such a design principle was pioneered by the calmodulin domain-based calcium indicator Cameleon (Mitra *et al.*, 1996; Miyawaki *et al.*, 1999; Tsien *et al.*, 1993) and was subsequently applied to the design of FRET probes that detect many different ligands. While Cameleon closes upon calcium binding (Mitra *et al.*, 1996; Tsien *et al.*, 1993), ligand-induced extension of the sensory domain is equally effective (Kalab *et al.*, 2002) (Fig. 2). Cameleon-like sensors can also detect posttranslational sensor modifications such as induced by phosphorylation (Niethammer *et al.*, 2004).

Successful design of a Cameleon-like FRET probe requires that its sensory domain undergoes significant reversible conformational changes. Because of the size of GFP-derived FPs, the minimal separation of their fluorophores is ~3 nm. The distance at which the FRET is barely detectable corresponds usually to $1.5 \times R_0$, that is, 7–8 nm for the FPs (Lakowicz, 1999). Because E decreases with

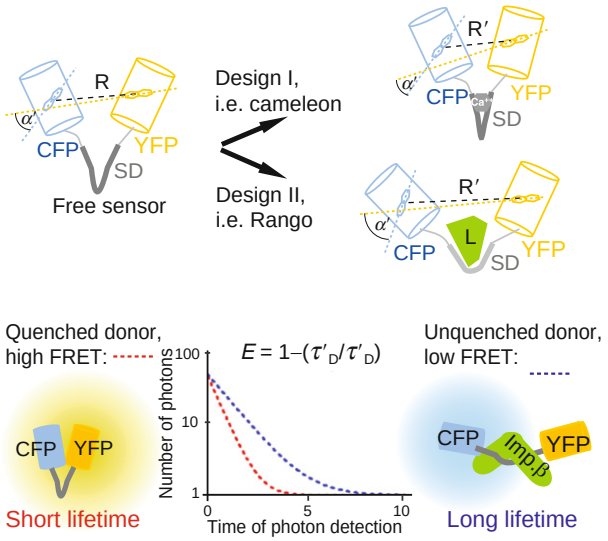

Fig. 2 (Top) Commonly used single-molecule Förster (or fluorescence) resonance energy transfer (FRET) sensors consist of donor–acceptor fluorescent protein (FP) pair (e.g., cyan FP as a donor and yellow FP as an acceptor) linked by a sensory domain (SD). The specific binding of a ligand to SD induces conformational change of the SD, inducing change of the distance (R) between the donor and acceptor FPs and/or of their fluorophore orientation (α–α'). As a result, the FRET efficiency changes upon ligand binding to the SD. In the Ca^{++} sensor Cameleon, the donor and acceptor become closer upon Ca^{++} binding to its SD (calmodulin), increasing FRET, while the binding of importin β to the SD in Rango [where the SD is importin β binding (IBB) domain of importin α] pushes the FPs apart, quenching FRET. (Bottom) In free Rango (left), FRET occurs with high efficiency E due to short distance between the donor and acceptor FPs, compared to Rango bound to importin β (right). The increased FRET efficiency in free Rango results in lower emission intensity from the donor FP, corresponding to the donor FP's shorter fluorescent lifetime τ'_D

the sixth power of the distance, increasing the amplitude of the donor–acceptor distance in the open versus closed conformation has lesser influence on improving the performance of the sensor, as compared to the effect of shortening the average distance between FPs. The minimal distance of FPs in the closed sensor conformation should not exceed the R_0 (~5 nm for many current FPs).

Often, published structural data can guide the FRET sensor design (Kalab *et al.*, 2002). The distance between FPs separated by an unstructured peptide can also be estimated based on its sequence and the model of a worm-like chain (Bustamante *et al.*, 1994; Ohashi *et al.*, 2007). The first choice after identification of a suitable sensory domain is to trim to a minimal functional domain. However, as the FPs may affect the sensor domain mobility and the access of its ligand (in particular if the ligand is a macromolecule), this should be considered carefully. It is a good precaution to create the connections of the sensory domain with FPs as short flexible peptides (such as GGSGGS; Evers *et al.*, 2006) to allow free mobility of the FPs. If the sensory domain is rigid and relatively large in the closed conformation, the addition of longer flexible linkers may increase FRET as the FPs may be allowed to move closer to each other. The distance between FPs in a FRET probe can be shortened by removing up to 5 N-terminal and 11 C-terminal amino acids from the FPs without loss of fluorescence (Shimozono *et al.*, 2006). To minimize potential nonspecific interactions, the open reading frame of the FRET probe should be kept as small as possible and devoid of unnecessary peptide sequence on its N- and C-terminal termini. Bulky protein tags added to FPs (such as protein A domain, GST) may interfere with the function of the sensory domain and decrease the probe's signal amplitude (P.K., unpublished data). Among smaller epitope tags, one should avoid 6His, which displays mild toxic effects when expressed in tissue culture cells (P.K., unpublished data).

After choosing the sensor design, the biggest gain in FRET probe performance comes from the selection of the donor–acceptor FP pair. In addition to the semirational improvements of genetically encoded fluorophores by point mutagenesis, molecular "breeding" by evolutionary selection performed in the laboratory (Rizzo *et al.*, 2004; Shu *et al.*, 2006; Tsien, 2006; Wang and Tsien, 2006; Zacharias and Tsien, 2006) resulted in a spectacular array of fluorophores available to contemporary cell biology (Giepmans *et al.*, 2006). We will only briefly point to the desirable characteristics of FPs for FLIM.

1. A donor with a *single exponential fluorescence lifetime* is preferred. A single exponential lifetime can be determined to better than 10% precision by counting less than 200 photons (Kollner and Wolfrum, 1992), while a similar precision in measurements of a biexponential lifetime requires at least 10–100 times more photons. Multiple fluorescence decay components are indicative of an undesirable biochemically nonhomogeneous donor protein population. If the donor displays more than one decay component but one is strongly dominant (such as Cerulean (Yasuda *et al.*, 2006), it is possible to approximate the donor lifetime as a single exponential decay (Kalab *et al.*, 2006).

2. The requirement for *large FRET signal changes* of the donor–acceptor pair is balanced with the requirement for dominant single exponential decay pattern of the donor. While the ECFP–EYFP pair displays larger FRET signal changes compared to Cerulean–EYFP as detected by intensity ratio measurements (Nguyen and Daugherty, 2005; P.K., unpublished data), the Cerulean–EYFP pair provides significantly more robust FLIM measurements *in vitro* and in live cells (Kalab *et al.*, 2006) and is therefore preferable.

3. Fast and complete maturation of both FPs, in particular the acceptor, is essential. If rapidly maturing donor molecules would be linked to slowly maturing acceptors, erroneously long fluorescence lifetimes would be recorded (low FRET). An excess of immature nonfluorescent donor molecules would decrease signal and complicate the fluorescence lifetime analysis as well.

4. Good photophysical properties, in particular slow bleaching rate, no blinking, and low sensitivity to local environmental parameters (e.g., pH) are desirable. Although such parameters have been published for some available FPs, controls for such variables should be run in any given experimental system. For example, FLIM measurements of a donor FP expressed by itself in a cell (i.e., without acceptor) should yield homogeneous fluorescence lifetime throughout the nucleus and cytoplasm, thus providing a basic assurance that the donor is not overtly environmentally sensitive.

It is important to consider that excitation of FP chromophores produces reactive oxygen species that can react with other molecules adjacent to FPs and thus potentially influence the behavior of the sensory domain in the FRET probe, the FP donor lifetime, and the physiology of the imaged cells (Remington, 2006). FPs can significantly differ in how much their fluorescence lifetimes are affected by photobleaching. Photobleaching of ECFP strongly shortens its fluorescence lifetime (2.59 vs. 1.59) compared to EGFP which is much less sensitive in that regard (2.64 vs. 2.56 ns) (Tramier *et al.*, 2006).

D. Donor–Acceptor FP Pairs Suitable for FLIM

Some of the most widely used FP pairs for FRET are derivatives of the CFP (a GFP with the mutations Y66W, N146I, M153T) and YFP (a GFP with the mutations S65G, V68L, Q69K, S72A, T203Y) (Tsien, 1998). The chromophore of the ECFP may exist in several conformations resulting in multiple fluorescent states and lifetimes (Rizzo *et al.*, 2004; Yasuda, 2006). An improved, —two to three times brighter ECFP variant called Cerulean was obtained by introducing mutations predicted to stabilize one preferred conformation (H148D) and to improve its maturation (S72A, Y145A) (Rizzo *et al.*, 2004). Cerulean still exhibited detectable two-exponential decay, in contrast with single-exponential decay of GFP and Venus (Tramier *et al.*, 2006; Yasuda *et al.*, 2006; A.P., unpublished data).

Improved donor–acceptor pairs were *in vitro* evolved that strongly outperformed the original CFP–YFP (Nguyen and Daugherty, 2005). The best pair called CyPet–YPet displayed a sevenfold increase in the FRET signal amplitude compared to CFP–YFP (Nguyen and Daugherty, 2005). Also the amplitude of the donor lifetime changes in the CyPet–YPet probe ($\tau_{no\ FRET}$ = 2.43 ns)/($\tau_{max\ FRET}$ = 0.53 ns) was markedly increased compared to CFP–YFP ($\tau_{no\ FRET}$ = 2.99 ns)/($\tau_{max\ FRET}$ = 1.87 ns) (Nguyen and Daugherty, 2005). The increase of ET in CyPet–YPet pair depends on increased intramolecular CyPet to YPet binding induced by the S208F mutation in YPet (Ohashi *et al.*, 2007). In sensors where the donor–acceptor dimerization would compete with high affinity ligand binding, such a relative drawback can be outweighed by significant gain in the signal amplitude.

The photophysical properties of enhanced GFP [mutation S65G] (Tsien, 1998) (single-exponential fluorescence lifetime decay, good photostability, and fast maturation) (Jung *et al.*, 2005; Yasuda *et al.*, 2006) make it one of the best available donor FPs. Excellent performance of EGFP as a donor in FLIM measurements was observed with various coral-derived red FPs as acceptors (Peter *et al.*, 2005; Yasuda *et al.*, 2006). The major limitation of the currently available RFPs as acceptors for EGFP remains relatively slow and/or incomplete maturation, estimated to represent 40–50% (Yasuda *et al.*, 2006) and the tendency of some to aggregate.

Attempts were made to generate ''dark'' acceptors, that is, fluorophores that are good acceptors of FRET but emit the transferred energy by thermal loss with minimal fluorescence. REACh (Resonance Energy-Accepting Chromo-protein) is a nonfluorescent YFP mutant (Ganesan *et al.*, 2006) with excellent spectral overlap with EGFP. As REACh is virtually nonfluorescent, in principle no spectral filtering is needed and photons can be collected in the entire spectral window of GFP emission increasing the detection sensitivity. Moreover, the elimination of acceptor fluorescence emission reduces the spectral bandwidth needed by the FRET sensor, and hence is a promising strategy for designing FRET pairs that can be used for simultaneous quantitative FLIM-based detection of multiple protein activities in single cells.

III. Technical Considerations for FLIM in Live Cells

The reported fluorescence lifetime τ_D of FPs ranges between 1 and 5 ns (Nguyen and Daugherty, 2005; Rizzo *et al.*, 2004; Yasuda *et al.*, 2006). However, in FRET-based sensors introduced to live cells, the entire physiologically relevant amplitude of the lifetime may only be a few hundred picoseconds (Kalab *et al.*, 2006). To detect spatially well-resolved intermediate fluorescence lifetime values in cells, the fluorescence lifetime therefore often needs to be measured with the precision of few tens of picoseconds.

A. Time- and Frequency-Domain FLIM

Two alternative approaches to fluorescence lifetime measurements are currently used: (1) in time-domain FLIM, a very short laser pulse excites the fluorophores in the sample and the time until the arrival of a fluorescent photon to a time-correlated detector is measured; or (2) in frequency-domain FLIM, the intensity of the excitation light is modulated and the detected lag of the fluorescence emission phase and decrease of its amplitude is used to calculate the donor lifetime (van Munster and Gadella, 2005) (Fig. 3). In both approaches, pixel-by-pixel fluorescence lifetime 2D ''image'' of the sample is calculated and displayed.

A variety of light sources such as LEDs, lasers, and lamps can be used for the donor fluorophore excitation in frequency-domain FLIM as long as the excitation light can be modulated. A reliable resolution of multiexponential decays requires that a wide range of excitation frequencies is used (van Munster and Gadella, 2005). However, the typically available fractionally modulated sinusoidal excitation extracts lifetime information out of only a small fraction of the photons (Philip and Carlsson, 2003). Hence, frequency-domain FLIM in practice requires relatively bright samples. On the other hand, the frequency-based FLIM can be significantly faster than time-domain measurements because the fluorescence emission can be recorded at all pixels simultaneously as in wide-field fluorescence microscopy. The commercially available instrumentation for frequency-domain FLIM (Lambert Instruments; http://www.lambert-instruments.com/, Jobin Yvon Horiba; http://www.jyinc.com/) can be installed on most epifluorescence microscopes and are significantly less expensive compared to typical time-domain FLIM setups.

In the most commonly used version of time-domain FLIM measurement, *t*ime-*c*orrelated *s*ingle *p*hoton *c*ounting (TCSPC), the sample is excited with a very short light pulse, and the arrival time of the first fluorescent photon to the detector is measured (Becker *et al.*, 2004; Suhling *et al.*, 2005). After registering the first photon, the detector is blind to following photons for a characteristic time period, the dead-time. Because only the first photon is registered, the excitation intensity, detector sensitivity, and detection time window must be matched so that at most one photon arrives to the detector during one detection time window. Otherwise, the measured photon distribution would be biased toward shorter lifetimes. Such measurement scheme works best for relatively weakly fluorescent samples with short lifetimes such as FPs. Time-domain FLIM builds an intensity versus time decay curve directly during the measurement. Visual inspection of this decay curve allows immediate judgment of the data quality and fitting of even complex multiexponential fluorescence lifetime decays is straightforward. Commercial providers of TCSPC FLIM equipment include Becker & Hickl (http://www.becker-hickl.de/), PicoQuant (http://www.picoquant.com), and Horiba Jobin Yvon (http://www.jyinc.com).

The nanosecond lifetime of FPs requires a pulsed excitation source with picosecond and shorter pulses. The mode-locked Ti:Sapphire laser system providing 150fs infra-red (IR) pulses are used to excite the FPs via two-photon (2p)

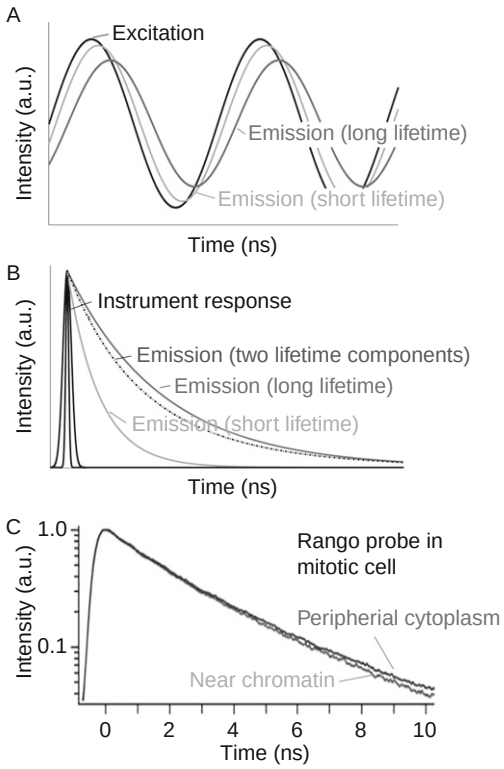

Fig. 3 Principles of (A) frequency-domain (FD) (B) and time-domain (TD) fluorescence lifetime imaging microscopy (FLIM): (A) In FD-FLIM, the sample is excited using light with modulated intensity. A larger phase lag of the fluorescence emission behind the intensity-modulated excitation indicates a longer lifetime. (B) In TD-FLIM, the sample is excited using a pulsed light source and the exponential decay of the fluorescence intensity is measured directly. A longer single exponential decay is easily distinguished from a short lifetime. With sufficient data, even small changes in lifetimes are measurable, and double exponential decays can be determined correctly. (C) Current FLIM instrumentation can measure and spatially resolve small differences in fluorescence lifetime of Förster (or fluorescence) resonance energy transfer (FRET) biosensors expressed in live cells. Shown is an example of Rango fluorescence lifetime decay profiles measured in a live mitotic HeLa cell near chromatin and at the periphery of the same cell.

absorption (Denk and Svoboda, 1997; Denk *et al.*, 1990; Helmchen and Denk, 2002). Alternatively, frequency doubling of the IR pulse may be used to create short pulses of visible light covering a wide range of excitation maxima typical for FPs. Compared to the 2p excitation, the available wider confocal sections in frequency doubled excitation are advantageous in samples containing low concentration of homogeneously distributed donor (Kalab *et al.*, 2006). Pulsed laser diodes offer an economical alternative excitation source to expensive Ti:Sapphire laser systems. However, the pulse duration of the diode lasers is significantly longer and output power dependent, averaging 40–50 ps per pulse at minimal power, increasing

to 100 ps with increased power. This pulse length may challenge the detection of small changes in fluorescence lifetime. In the future, broadband continuum lasers might provide a good pulsed excitation source for TCSPC (Owen *et al.*, 2007). For costs between a Ti:Sapphire laser system and single diode lasers, these lasers provide 2 ps pulses over the entire useful excitation spectrum.

B. The Limitations of TCSPC FLIM

TCSPC FLIM dataset is sequentially composed by scanning from pixel-to-pixel. The galvanometer-driven scan heads in commonly available confocal scanning microscopes provide enough accuracy and speed to match the detection capacity of high quality TCSPC FLIM equipment. At each pixel, individual photons are counted to build up the fluorescence lifetime decay curve. The scanning rate and the rate at which the photons are counted per pixel determine the time needed to acquire one complete FLIM dataset.

The need to determine precisely the time between the excitation pulse and the detection for each detected photon requires processing the photons one-by-one. The rate at which individual photons can be detected and counted is called count-rate and represents the bottle neck for speed for TCSPC FLIM. The maximal count-rate is limited by the instrumentation used and the sample:

1. A Ti:Sapphire laser provides excitation pulses with ~80 MHz repetition rate.
2. GFP's have fluorescent lifetimes between 2 and 5 ns which means that the tail of the fluorescent decays reaches past the 12.5 ns interval of the Ti:Sapphire pulses.
3. The detection electronics consisting of detector and counter may process photons at rates between 1 and 10 MHz depending on the model [according to datasheets from Becker & Hickl (http://www.becker-hickl.de/) and PicoQuant (http://www.picoquant.com/)].

The maximal rates possible with particular detection electronics therefore appear to limit the maximal count rate for TCSPC FLIM. However, absorption and emission of photons are stochastic processes so that it is impossible to generate always exactly one fluorescent photon to hit the detector at the maximal count rate. As the rate of emitted photons reaches the detection speed, it becomes likely that two photons arrive within the same detection interval. This would lead to an error in the lifetime estimate as only the first of the two would be counted. Hence, typical useful counting rates in TCSPC FLIM are an order of magnitude lower than the maximal detection rates.

For example, at a 500-kHz count rate, the 200 photons per pixel that are sufficient to determine a single exponential decay to better than 10% precision (Kollner and Wolfrum, 1992) under ideal conditions could be counted in 0.4 ms. However, *in vivo* measurements with a background typical for biological samples often require 10 times more counts (Philip and Carlsson, 2003). Hence acquiring an *in vivo* image of 128 × 128 pixels would require about 1min at 500 kHz count rate

and theoretically, a proportionally shorter time with faster TCSPC FLIM boards. As the counting capacity of the contemporary FLIM equipment increases, the number of FRET donor molecules that can be expressed and excited in the sample without perturbing the biological system is becoming a limiting factor.

C. The Use of Tissue Culture Cells for Quantitative FRET Detection by FLIM

The precise measurement of the donor fluorescence lifetime for quantitative FLIM FRET requires optimization of the signal to noise ratio in the spectral window of the donor emission. Unfortunately, the emission of the CFP-related donors overlaps with major sources of autofluorescence in cells such as flavins, NADH, and lipids (Monici, 2005). The very short fluorescence lifetime of NADH (emission peak 450–460 nm, $t = 0.4$ ns) (Lakowicz *et al.*, 1992) and flavins ($\sim$0.3 ns; Chorvat and Chorvatova, 2006) can in principle be separated from the CFP lifetime. Other autofluorescence sources, such as protein-bound NADH (emission 435 nm, $t = \sim$2 ns; Lakowicz *et al.*, 1992; Skala *et al.*, 2007) may be suppressed by using narrow emission filters. However, conditions that negatively influence cell vitality (confluence, ageing, oxidative stress, apoptosis, necrosis) typically induce strong autofluorescence that can change over a wide spectrum of emission wavelengths and fluorescence lifetimes. The autofluorescence detected in MCF10A breast cancer cells in tissue culture showed complex multiexponential pattern whose components and their proportions changed depending on the plating density (Bird *et al.*, 2005). While filtering out the background autofluorescence, either through its characteristic lifetime or spectrally may be possible in postacquisition analysis, completely relying on such approach is therefore not advisable.

In order to obtain reproducible and indeed meaningful FLIM measurements, the best practice is to limit the analysis to cell samples that are in a reproducible physiological state. In case of tissue culture cells, this would typically mean to only perform experiments analyzed by FLIM in healthy, nonconfluent cells that do not display strong autofluorescence.

The commonly used tissue cell cultures are composed of phenotypically diverse collection of cells differing in size, shape, growth rate, adherence, vitality, and so on. If individual cells are propagated in isolation, it is readily observable that such phenotypic differences can be maintained over a number of cell division. On the other hand, any change in culture conditions (stress, overgrowth, change of media type) can lead to significant selection drift and change of the cell sample used for analysis. In our experience, the effect of the cell-to-cell variation on quantitative analysis of intracellular pathways by FRET-based methods can be significantly suppressed by working with single cell-derived ''monoclonal'' cell cultures. At the same time, such an approach allows one to better evaluate the physiological significance of the variability detected between cells.

We recommend the following steps to maximize the reproducibility of FLIM/FRET detection in tissue culture cells:

1. Start with a verified cell stock from a reputable source, such as ATCC. Do not use any poorly documented cells or cells held for many passages in culture. Regularly inspect and test the cells for the presence of infection such as mycoplasma.

2. Establish a robust protocol that will reproducibly deliver cells in optimal health and confluency for the days of the FLIM experiment.

3. The cell-to-cell variability of the recorded data may represent phenotypic variability between cells in culture. The existence of such variability can be evaluated and controlled for in experiments with "monoclonal" cell cultures (see Section V).

IV. Analysis of the Mitotic RanGTP Gradient Function by FLIM and Computational Modeling

A. Ran-Nuclear Transport Receptor System

Ran is a conserved small nuclear GTPase related to Ras. The Ran-specific guanine nucleotide exchange factor RCC1 binds chromatin and is imported to the nucleus, while Ran GTPase activating protein RanGAP is cytoplasmic throughout the cell cycle. Because both RCC1 and RanGAP catalyze $\sim 10^5$-fold increase in the respective intrinsic activities of Ran, the nucleotide charge of Ran is dominantly influenced by the local concentration of both regulators. As a result, more RanGTP exists around chromosomes and more RanGTP is converted to RanGDP at the periphery of the cell, giving rise to a RanGTP gradient which marks the position of the chromatin throughout the cell cycle (Hetzer *et al.*, 2002).

The RanGTP gradient provides directionality to nucleocytoplasmic transport across nuclear envelope in interphase cells by regulating interactions between nuclear transport receptors (NTRs) of the importin β family and their cargos (Pemberton and Paschal, 2005; Weis, 2003). RanGTP concentrated in the nucleus dissociates complexes of importins with nuclear localization signal (NLS) containing cargos, resulting in nuclear accumulation of cargos. On the other hand, nuclear export receptors (exportins) bind stably to nuclear export signal (NES) containing cargos only in the presence of RanGTP. The heterotrimeric RanGTP–exportin–NES cargo complexes transit through nuclear pore complexes to the cytoplasm where their disassembly is induced by RanGAP-catalyzed hydrolysis of GTP on Ran.

The dynamic RanGTP-regulated NTR–cargo assembly/disassembly continues after nuclear envelope breakdown in vertebrate cells undergoing open mitosis, resulting in the formation of diffusion-limited intracellular gradients of RanGTP-regulated importin α/β-free cargos. Importantly, some importin α/β cargos are essential spindle assembly factors (SAFs) and their mitotic function is activated by RanGTP-induced release from the inhibitory complexes with importin α/β (Gruss and Vernos, 2004; Weis, 2003). As a result, the Ran-regulated gradients of liberated

importin α/β cargos are thought to correspond to gradients of activated SAFs that ensure the correct assembly and function of the mitotic spindle in the segregation of the genome to daughter cells (Bastiaens *et al.*, 2006; Weis, 2003).

B. Rango Sensor Design

To visualize the mitotic RanGTP and importin α/β-regulated cargo gradient in living cells, we developed a fluorescence resonance energy transfer (FRET) biosensor termed Rango (*Ran*-regulated importin β car*go*) (Fig. 2) (Kalab *et al.*, 2002, 2006).

Importin β binds to its NLS cargos either directly or via adaptor proteins such as importins α. The importin α/β cargos bind through their NLS to the C-terminus of importin α, where they compete with the very flexible N-terminal importin β binding domain (IBB) of importin α for access. Only when the IBB binds to importin β molecule, inserting deeply into its structure (Cingolani *et al.*, 1999), the NLS cargo can efficiently load on importin α. The high affinity RanGTP binding to importin β displaces the IBB and thus induces rapid disassembly of the importin α/β complex and consequently the IBB-promoted release of the NLS cargo from importin α.

The IBB is unstructured on its own and assumes an extended rod-like conformation in complex with importin β (Cingolani *et al.*, 1999). We exploited this large conformational change to design a sensor detecting the RanGTP-regulated importin α/β-cargo dissociation. The original version of this sensor, called YIC (YFP–IBB–CFP) is composed of IBB from human importin α_1 flanked by EYFP and ECFP at its N- and C-termini, respectively (Kalab *et al.*, 2002). In its free form (i.e., also in the presence of importin β and RanGTP), YIC emits strong FRET signal which is significantly quenched upon importin β binding. The interactions of YIC and importin β were shown to be highly specific (Kalab *et al.*, 2002), allowing the use of the sensor to detect RanGTP-regulated mitotic gradient of liberated importin β cargos around mitotic chromatin in live *Xenopus* egg extracts (Kalab *et al.*, 2002). To detect importin β cargo liberation by FLIM in live cells, we replaced ECFP with Cerulean, and used IBB from Snurportin 1 instead of importin α1, calling this FLIM-optimized sensor Rango. While the results obtained with the original YIC and Rango in cells were similar, Rango was better tolerated by transfected and microinjected mitotic cells. The use of Cerulean in Rango produced more robust and better spatially resolved FLIM detection compared to ECFP-based sensors (Kalab *et al.*, 2006; A.P.,P.K., unpublished data).

C. *In Vitro* and *In Vivo* Calibration of Rango

To quantify the *in vivo* measurement, the FLIM FRET response of the probe needs to be calibrated. Usually this requires that recombinant FRET sensor and its ligand are expressed and purified and then used to obtain full binding curve where the FRET signal of the sensor is used as a readout for the binding (Fig. 1B, left). Such *in vitro* titrations should be done in conditions similar to the *in vivo* FLIM

detection, namely the same temperature, similar pH, and viscosity. However, as it is essentially impossible to exactly mimic *in vitro* complex intracellular conditions, reference FRET data from cells are needed to see whether and how much the behavior of the sensor differs in comparison of the *in vitro* calibration and cell imaging. To obtain reference points, we microinjected HeLa cells with the Rango sensor together with dominant negative proteins expected to cause either full release (nonhydrolyzing RanGTP mutant) or full binding of Rango to importin β (RanGTP binding-deficient importin β mutant) (Fig. 1B, right).

D. Nondimensional Ran System Model

Several research groups are developing software packages to model spatially resolved reaction-diffusion networks and provide the software free to the academic community. The solutions vary in user interface, their way of handling space, and diffusion, and whether they deal with the molecules stochastically or as concentration (Alves *et al.*, 2006). We chose Virtual Cell (Slepchenko *et al.*, 2003) (http://www.nrcam.uchc.edu/) to construct a computation model simulating the GTP/GDP cycle on Ran coupled to a minimal set of NTRs and their cargos. The initial phases of model construction and testing were performed with Jarnac and a set of conditions used for simulation of Ran-regulated nuclear transport (Smith *et al.*, 2002).

Any model of a particular biological reaction network will represent only a subset of the entire network of intracellular reactions. Because of the redundancy and complexity of biological systems, several models might be possible corresponding to alternative physiologically relevant states of the network producing similar phenotypic outcome.

To identify the minimal and sufficient set of reactants and their parameters (such as concentrations and reaction kinetics of their interactions) representing faithfully the behavior of a given network, the response of the computed system to perturbations therefore needs to be examined (Figs. 1C and 4A). For example, the concentration of one of the regulatory components of the model is varied and the response of other system components is evaluated. The application of a well-biochemically characterized and calibrated FRET-based sensor allows that similar experiments can be performed with the biological sample and the sensor-reported response can then be used to refine the computed model. Even in the case of the highly organized Ran-NTR system, it is initially advantageous to use an experimental model system devoid of the spatial anisotropy such as the cytoplasmic *Xenopus* egg extracts and to apply corresponding nondimensional computational models for the simulations. The response of the Ran-regulated importin β cargo release in *Xenopus laevis* egg extracts to biochemical perturbation is compared with the response of the computational mitotic Ran system model by varying the amount of free RanGTP (Fig. 4A).

As expected, in initial computed simulations, we found that the concentrations of transport receptors and their cargos, respectively, have a dominant effect on the

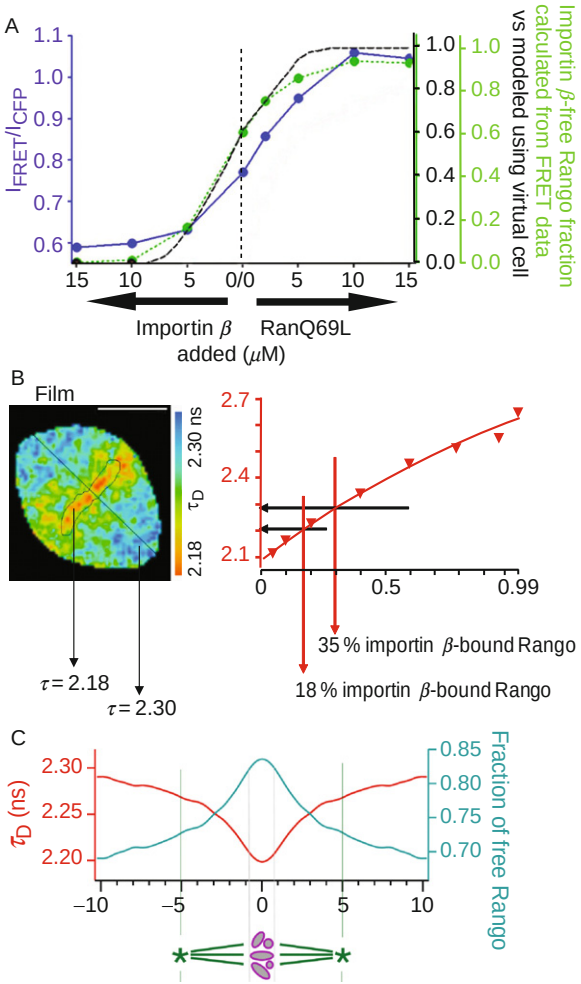

Fig. 4 (A) The response of the Ran-regulated importin β cargo release in *Xenopus laevis* egg extracts to biochemical perturbation, compared with the response of the computational mitotic Ran system model to simulated identical treatment. The amount of free RanGTP in the extracts was varied by adding increasing concentrations of RanQ69L or importin β. The Rango Förster (or fluorescence) resonance energy transfer (FRET) signal was measured as FRET intensity ratios (I_{FRET}/I_{CFP}, blue in color plate), and the corresponding fraction of importin β-free Rango calculated based on *in vitro* calibration (green in color plate). As the scales of the measured and calculated free Rango fraction nearly overlap, only the measured (green in color plate) scale is shown. Similarly, increasing concentrations of RanQ69L or importin β were added to a minimal computational mitotic Ran system containing Rango. The concentrations of the liberated Rango in the models were recorded upon reaching equilibrium (black). Note that the equilibrium conditions (0/0) in the extracts exhibit high sensitivity of importin β cargo liberation to small changes of RanGTP and importin β concentration. (B) The use of *in vitro* Rango fluorescence lifetime dose–response calibration to estimate the proportion of free versus importin β-bound Rango in live cells. The arrows indicate two points on the calibration curve corresponding to two selected areas in mitotic HeLa cell expressing Rango. (C) The average distribution

resulting Rango fractional occupancy at equilibrium. Next, we used Rango FRET measurements in mitotic *Xenopus* egg extracts to estimate the fraction of Rango bound to importin β at equilibrium. We used this measured fractional occupancy value (40% of Rango bound to importin β) to adjust the initial reactant concentrations in our computational model of Ran. After such adjustment (Table I), the response of our minimal computed Ran system model to simulated perturbations (addition of importin β and dominant RanGTP binding mutant, respectively) matched Rango occupancy values that were measured by FRET in the *Xenopus* egg extracts over a wide range of concentrations (Fig. 4). This liberation of Rango from importin β was quantitatively represented in our computer model. Importantly, the computed response of the minimal Ran-NTR system to RanGTP concentration validated the initially unexpected high concentration of free importin β cargos detected by FLIM in mitotic cells. Combined, the computational systems modeling and quantitative FLIM imaging in cells thus provided a fundamentally new important insight into the function of the mitotic RanGTP gradient. Instead of controlling SAFs as an on/off switch as previously hypothesized (Weis, 2003), the mitotic RanGTP gradient regulates spindle assembly by inducing local breaks in the symmetry between the cytoplasmic spindle assembly activators and inhibitors (Kalab and Heald, 2008; Kalab *et al.*, 2006).

E. Spatial Modeling and Protein Diffusion inside Cells

The refined nondimensional model validated by side-by-side *in vivo* and *in silico* perturbations is an excellent starting point for the construction of dimensional models. For example, in Virtual Cell, the model may be mapped on the actual 3D cellular geometry imported from microscopy images, including in the newest version reactions happening within the 2D cell membrane. Spatial symmetries in the model should be exploited to reduce the volume of computation. Often, 2D geometry can be found to sufficiently represent the 3D geometry.

In diffusion-limited reaction networks such as the mitotic Ran system, the particularly critical value influencing the outcome of the simulation is the diffusion rate of each model component. In the existing models of the Ran system, the diffusion of proteins inside cells was slowed down by an arbitrary factor relative to water to arrive at spatial dimensions of the measured Ran-regulated gradients (Caudron *et al.*, 2005). What are the factors defining diffusion of proteins in cells

---

of Rango fluorescence lifetime distribution measured in four mitotic HeLa cells (red line) was transformed to the corresponding distribution of the free Rango fraction (green line) calculated from the *in vitro* Rango calibration data [see (B) above]. This analysis revealed that ~68% cargos similar to Rango are importin β free at the cell periphery and ~86% importin β cargos are liberated at the peak of the RanGTP gradient at mitotic chromosomes, indicating that RanGTP gradient does not act as an of/off switch to regulate mitotic spindle assembly (Kalab and Heald 2008). The diameter of the free importin β cargo gradient is similar to the mitotic spindle size in HeLa cells (Kalab *et al.*, 2006)

Table I
Final Equilibrium Concentrations of the Components of the Minimal Computed Ran System

RanGTP	3 μM	RanBP	1.2 μM
RanGDP	3.6 μM	NTF2	0.6 μM
GDP	1.6 μM	Importin β	3 μM
GTP	470 μM	Importin β cargos	8 μM
RCC1	0.25 μM	Rango	2 μM
RanGAP	0.4 μM	Importin β-like transport receptors	5 μM

and how it is best described is a subject of intense research (Banks and Fradin, 2005; Petrasek and Schwille, 2007; Sanabria *et al.*, 2007; Verkman, 2002).

Detailed spatially resolved Ran systems models will require application of new developments in instrumentation, such as high speed FLIM imaging, such as spinning disk confocal FLIM (http://www.lambert-instruments.com/) and automated imaging in dividing cells (Pepperkok and Ellenberg, 2006) together with novel sensitive sensors for Ran function in cells.

V. Materials and Methods

A. Protein Expression and Purification

The plasmids for *E. coli* expression of Rango (pKW1648), IBB-Cerulean (pKW1648), EYFP-IBB (pKW1648), and ZZ-RanQ69L (pKW1234) were constructed in pRSET A (all with 6His tag) as described (Kalab *et al.*, 2006) and human importin β (pKW485) in pET30a (6His- S tag; Beresford *et al.*, 2001).

All proteins were expressed in BL21 DE3 *E. coli* cells. The cultures were inoculated with freshly transformed cells, grown until $OD_{600\ nm}$ 0.5–0.6 at 37 °C, transferred to room temperature shaker and induced with 0.3 mM IPTG. After 16-18 h, the cells were harvested by centrifugation, resuspended in ice-cold lysis buffer (PBS, 10 mM Imidazole, pH 7.4, 100 mM PMSF, 10μg/ml each of chymostatin, peptstatin, and leupeptin) and lysed by French pressure cell. The lysates were clarified (2 × 20 min, 15,000 rpm in Sorvall SS34), the 6His tagged proteins were batch bound to Ni-agarose beads (Qiagen or Sigma), and beads were washed on disposable plastic columns with the PBS, 10 mM Imidazol, pH 7.4. Proteins eluted with 0.2 M Imidazole, PBS were dialyzed overnight in XB (50 mM sucrose, 100 mM KCl, 0.1 mM $CaCl_2$, 1 mM $MgCl_2$, 10 mM HEPES, pH 7.7) and purified by gel filtration in XB buffer on FPLC on Separose 6 (Pharmacia). Absorbance at 435 and 512 nm was used to detect Cerulean and YFP and eliminate trailing fractions with partially inactivated fluorophores. Proteins were concentrated on Amicon 30 ultrafiltration colums (Millipore) to 100–200 μM, passed through 0.45 μm filter, snap-frozen in single use aliquots in liquid nitrogen and stored

at –80 °C. The protein concentration was measured with Bradford reagent (Pierce) using BSA as a standard and the purity of the proteins was assessed on SDS-PAGE with Coomassie Blue R250 staining. All fluorescent proteins expressed as soluble and typically we obtained ~10–20 mg of >95% pure protein/liter of culture.

B. Importin β-Rango Dissociation Constant

To obtain the apparent dissociation constant of Rango–importin β interaction, we monitored the importin β binding-induced loss of Rango I_{FRET}/I_{CFP} signal (Kalab *et al.*, 2006) in spectrofluorimeter. Aliquots of 40 nM Rango in PBS were diluted with increasing concentrations of importin β in PBS to achieve final concentration of 6 nM Rango and 0–40 nM importin β. The samples were placed in cuvettes, excited at 435 ± 2 nm and emission intensities at 474 nm (I_{CFP}) and 512 nm (I_{FRET}) was recorded. The I_{FRET}/I_{CFP} ratios were determined in two samples (2–3 scans each) from each dilution aliquot. The I_{FRET}/I_{CFP} values were plotted against the importin β concentration and data were fitted with a down to bottom curve, standard slope using GraphPad Prism version 4.00 for Windows (GraphPad Software, San Diego, CA). The Rango–importin β dissociation constant was determined using the importin β concentration at 50% amplitude of Rango I_{FRET}/I_{CFP} curve.

C. HeLa Cell Culture

Adherent HeLa cells were obtained from ATCC and maintained in 75 cm^2 flat bottom flasks at 37 °C, 5% CO_2. After the first two passages in DMEM (Gibco, Invitrogen) with 10% FBS, the cells were transferred to culture in Opti-MEM (Gibco, Invitrogen) with 4% FBS by increasing the proportion of the new media by 1/3 in each passage. New passages were initiated before reaching confluency (confluency: ~10 × 10^6cells/75 cm^2 flask). The cells were lifted with Trypsin-Versene (Gibco, Invitrogen), thoroughly resuspended, and 1/4–1/5 cells seeded into a new flask containing 11 ml media equilibrated in the incubator.

D. Monoclonal HeLa Cell Culture

To obtain single-cell derived cell cultures, dispersed ATCC HeLa cells were plated at ~200 cells per 9 cm diameter tissue culture dish and kept in culture for 4–5 weeks while regularly exchanging the media. Colonies displaying good growth were marked on the bottom of the dish. The medium from the plate was removed and few cells were picked from the marked colonies with plastic pipette tips and seeded into individual 24-well plates containing 0.1 ml Trypsine-Versene (Gibco-BRL)/well. The cells were dispersed by pipetting and 0.5 ml serum containing media was added. Well-growing colonies were identified and used for second round of single colony selection. Three selected cell lines were amplified in 75 cm^2 flasks and frozen in multiple aliquots from their first and second passages. Cells used for FLIM experiments underwent at most 15 passages.

E. Glass Cover Slides for Cell Culture

Round cover glass (25 mm diameter, Fisher Scientific) used for live cell imaging was cleaned using modified acid wash protocol (Salmon lab: www.bio.unc.edu/faculty/salmon/lab/). The slides were first soaked in 1 M HCl at 65 °C overnight. After a thorough rinse with distilled and deionized water (ddH_2O), slides placed in 100-ml screw cap covered bottles were sonicated on water bath for 30min. The sonication in ddH_2O was repeated two more times followed with 30-min sonication each in 50, 60, 70, 80, 90, and twice in 100% ethanol (Gold Shield, Rossville Alcohol). In order to remove any residues, the ethanol was burnt from the slides in a gas burner flame in sterile tissue culture hood just before the slides were used for seeding cells.

F. Preparation of Cells for Live Cell Imaging

Two to four days before the experiment, cells were seeded from sub-confluent cultures to 6-well plates containing 25 mm round glass slides/well, at two concentrations: 2×10^4 and at 5×10^4cells/well. Sixteen to 24h later, the cells were transfected with the FRET probes using Fugene 6 (Roche Pharmaceuticals) according to the protocol of the manufacturer. Cells plated at higher concentration were used for FLIM at least 20–24h following the transfection. The cells plated at the lower density were typically suitable for microscopy 4 days since the start of the culture.

We tested several media for imaging and found that high FBS concentration and Phenol Red induced short-lifetime background in FLIM in our conditions (absence of enclosed environmental chamber on the microscope stage). The best results were obtained with Dulbecco's PBS (Gibco, Invitrogen) supplemented with 1mM sodium pyruvate (Gibco, Invitrogen) (Kalab *et al.*, 2006) although also DMEM without Phenol Red (Cellgro), 4% FBS was acceptable. For live cell imaging experiments, cells were maintained at 30 °C in a temperature controlled imaging chamber (Warner instruments). The bottom of the imaging chamber was formed directly with the 25 mm round glass with cells taken from the culture just before imaging. The cells were gently rinsed once with the imaging media and the microscopy was performed within the next 60–90 min.

G. Spectrophotometry

Emission spectra were analyzed with a Fluorolog 2spectrofluorimeter controlled by Datamax 2.2 (Jobin Yvon Spex) and the Grams 3.04 II software package (Galactic Industries, Salem, NH).

H. Imaging Conditions Used in the Rango FLIM Study

The FLIM data in the Rango study (Kalab *et al.*, 2006) were acquired on an inverted Zeiss LSM510 Axiovert 200M microscope with a NeoFLUAR 40 × 1.3 NA oil-immersion objective lens, equipped with a TCSPC controller (Becker &

Hickl SPC-730 card). Samples were excited by 6 μW of 435 nm laser light generated by frequency-doubling (Pulse-Selector 3980, SpectraPhysics, USA) the 870 nm pulses from a mode-locked Ti:Sapphire laser (Tsunami, SpectraPhysics, 120–150 fs pulse width, 80 MHz repetition rate). The pulse length and shape of the Ti:Sapphire laser were adjusted to provide maximum conversion to blue light. The 435 nm pulses were filtered by a 435BP40 filter, merged with the light from a 532-nm laser used to excite Rhodamine-labeled tubulin, and coupled via a single-mode fiber (PointSource, UK) into the scanhead of the Zeiss LSM510. The emission light was filtered with a 480-nm bandpass filter (480BP40, Chroma) and detected by a PMC-100 photomultiplier (Becker & Hickl) coupled to the fiber-out port of the LSM510. Images of 64 $\times$ 64 pixels or 128 $\times$ 128 pixels were acquired over 1–4 min.

I. FLIM Image Analysis: Fitting TCSPC Data to Obtain a Lifetime

Each decay curve is fitted to obtain the lifetime(s) in that image point. The Rango FLIM date was analyzed off-line using pixel-based fitting software (SPCImage, Becker & Hickl), assuming single exponential incomplete decay during the 12.5 ns interval between laser pulses.

To obtain the correct fluorescence lifetime, the time that it takes for the light to travel from the laser to the sample and then from the sample to the detector has to be known. This instrument-specific variable is called *instrument response (IR) function* of the microscope and limits the shortest measurable lifetimes. Usually, the IR is either measured with a reflecting sample or may be fitted from the shape of lifetime data obtained from a fluorescent sample.

J. Statistical Analysis

Statistical analyses were performed with Excel (Microsoft) and with GraphPad Prism version 4.00 for Windows, GraphPad Software (www.graphpad.com).

K. Computational Modeling

The computational model of a minimal Ran system coupled to the minimal set of nuclear transport receptors, including importin β and Rango, was built using Virtual Cell (www.vcell.org/index.html). The kinetic parameters that we applied have been described previously (Gorlich *et al.*, 2003; Riddick and Macara, 2005).

References

Alves, R., Antunes, F., and Salvador, A. (2006). Tools for kinetic modeling of biochemical networks. *Nat. Biotechnol.* **24,** 667–672.

Banks, D., and Fradin, C. (2005). Anomalous diffusion of proteins due to molecular crowding. *Biophys. J.* **89,** 2960–2971.

Bastiaens, P., Caudron, M., Niethammer, P., and Karsenti, E. (2006). Gradients in the self-organization of the mitotic spindle. *Trends Cell Biol.* **16,** 125–134.

Becker, W., Bergmann, A., Hink, M. A., Konig, K., Benndorf, K., and Biskup, C. (2004). Fluorescence lifetime imaging by time-correlated single-photon counting. *Microsc. Res. Technol.* **63,** 58–66.

Beresford, P., Zhang, D., Oh, D., Fan, Z., Greer, E., Russo, M., Jaju, M., and Lieberman, J. (2001). Granzyme A activates an endoplasmic reticulum-associated caspase-independent nuclease to induce single-stranded DNA nicks. *J. Biol. Chem.* **276,** 43285–43293.

Bird, D. K., Yan, L., Vrotsos, K. M., Eliceiri, K. W., Vaughan, E. M., Keely, P. J., White, J. G., and Ramanujam, N. (2005). Metabolic mapping of MCF10A human breast cells via multiphoton fluorescence lifetime imaging of the coenzyme NADH. *Cancer Res.* **65,** 8766–8773.

Bustamante, C., Marko, J., Siggia, E., and Smith, S. (1994). Entropic elasticity of lambda-phage DNA. *Science* **265,** 1599–1600.

Caudron, M., Bunt, G., Bastiaens, P., and Karsenti, E. (2005). Spatial coordination of spindle assembly by chromosome-mediated signaling gradients. *Science* **309,** 1373–1376.

Chorvat, D., Jr., and Chorvatova, A. (2006). Spectrally resolved time-correlated single photon counting: A novel approach for characterization of endogenous fluorescence in isolated cardiac myocytes. *Eur. Biophys. J.* **36,** 73–83.

Cingolani, G., Petosa, C., Weis, K., and Muller, C. W. (1999). Structure of importin-beta bound to the IBB domain of importin-alpha. *Nature* **399,** 221–229.

Clegg, R. M. (1966). "Fluorescence Resonance Energy Transfer." Wiley, New York.

Denk, W., Strickler, J. H., and Webb, W. W. (1990). Two-photon laser scanning fluorescence microscopy. *Science* **248,** 73–76.

Denk, W., and Svoboda, K. (1997). Photon upmanship: Why multiphoton imaging is more than a gimmick. *Neuron* **18,** 351–357.

Erickson, M. G., Alseikhan, B. A., Peterson, B. Z., and Yue, D. T. (2001). Preassociation of calmodulin with voltage-gated Ca^{2+} channels revealed by FRET in single living cells. *Neuron* **31,** 973–985.

Evers, T. H., van Dongen, E. M., Faesen, A. C., Meijer, E. W., and Merkx, M. (2006). Quantitative understanding of the energy transfer between fluorescent proteins connected via flexible peptide linkers. *Biochemistry* **45,** 13183–13192.

Förster, T. (1946). Energiewanderung und Fluoreszenz. *Naturwissenschaften* **6,** 166–175.

Förster, T. (1948). Zwischenmoleculare Energiewanderung und Fluoreszenz (Inter-molecular energy migration and fluorescence). *Annalen der Physik* **2,** 55–75.

Ganesan, S., Ameer-Beg, S. M., Ng, T. T., Vojnovic, B., and Wouters, F. S. (2006). A dark yellow fluorescent protein (YFP)-based resonance energy-accepting chromoprotein (REACh) for Forster resonance energy transfer with GFP. *Proc. Natl. Acad. Sci. USA* **103,** 4089–4094.

Giepmans, B. N., Adams, S. R., Ellisman, M. H., and Tsien, R. Y. (2006). The fluorescent toolbox for assessing protein location and function. *Science* **312,** 217–224.

Gordon, G. W., Berry, G., Liang, X. H., Levine, B., and Herman, B. (1998). Quantitative fluorescence resonance energy transfer measurements using fluorescence microscopy. *Biophys. J.* **74,** 2702–2713.

Gorlich, D., Seewald, M. J., and Ribbeck, K. (2003). Characterization of Ran-driven cargo transport and the RanGTPase system by kinetic measurements and computer simulation. *EMBO J.* **22,** 1088–1100.

Gruss, O. J., and Vernos, I. (2004). The mechanism of spindle assembly: Functions of Ran and its target TPX2. *J. Cell Biol.* **166,** 949–955.

Helmchen, F., and Denk, W. (2002). New developments in multiphoton microscopy. *Curr. Opin. Neurobiol.* **12,** 593–601.

Hetzer, M., Gruss, O. J., and Mattaj, I. W. (2002). The Ran GTPase as a marker of chromosome position in spindle formation and nuclear envelope assembly. *Nat. Cell Biol.* **4,** E177–E184.

Johnsson, N., and Johnsson, K. (2007). Chemical tools for biomolecular imaging. *ACS Chem. Biol.* **2,** 31–38.

Jung, G., Wiehler, J., and Zumbusch, A. (2005). The photophysics of green fluorescent protein: Influence of the key amino acids at positions 65, 203, and 222. *Biophys. J.* **88,** 1932–1947.

Kajihara, D., Abe, R., Iijima, I., Komiyama, C., Sisido, M., and Hohsaka, T. (2006). FRET analysis of protein conformational change through position-specific incorporation of fluorescent amino acids. *Nat. Methods* **3,** 923–929.

Kalab, P., and Heald, R. (2008). The RanGTP gradient – A GPS for the mitotic spindle. *J. Cell Sci.* **121,** 1577–1586.

Kalab, P., Pralle, A., Isacoff, E. Y., Heald, R., and Weis, K. (2006). Analysis of a RanGTP-regulated gradient in mitotic somatic cells. *Nature* **440,** 697–701.

Kalab, P., Weis, K., and Heald, R. (2002). Visualization of a Ran-GTP gradient in interphase and mitotic *Xenopus* egg extracts. *Science* **295,** 2452–2456.

Kitano, H. (2002). Computational systems biology. *Nature* **420,** 206–210.

Kollner, M., and Wolfrum, J. (1992). How many photons are necessary for fluorescence-lifetime measurements. *Chem. Phys. Lett.* **200,** 199–204.

Lakowicz, J. R. (1999). ''Principles of Fluorescence Spectroscopy,'' 2nd edn. Plenum, New York.

Lakowicz, J. R., Szmacinski, H., Nowaczyk, K., and Johnson, M. L. (1992). Fluorescence lifetime imaging of free and protein-bound NADH. *Proc. Natl. Acad. Sci. USA* **89,** 1271–1275.

Mitra, R. D., Silva, C. M., and Youvan, D. C. (1996). Fluorescence resonance energy transfer between blue-emitting and red-shifted excitation derivatives of the green fluorescent protein. *Gene* **173,** 13–17.

Miyawaki, A., Griesbeck, O., Heim, R., and Tsien, R. Y. (1999). Dynamic and quantitative Ca^{2+} measurements using improved cameleons. *Proc. Natl. Acad. Sci. USA* **96,** 2135–2140.

Monici, M. (2005). Cell and tissue autofluorescence research and diagnostic applications. *Biotechnol. Annu. Rev.* **11,** 227–256.

Nguyen, A. W., and Daugherty, P. S. (2005). Evolutionary optimization of fluorescent proteins for intracellular FRET. *Nat. Biotechnol.* **23,** 355–360.

Niethammer, P., Bastiaens, P., and Karsenti, E. (2004). Stathmin-tubulin interaction gradients in motile and mitotic cells. *Science* **303,** 1862–1866.

Ohashi, T., Galiacy, S. D., Briscoe, G., and Erickson, H. P. (2007). An experimental study of GFP-based FRET, with application to intrinsically unstructured proteins. *Protein Sci.* **16,** 1429–1438.

Owen, D. M., Auksorius, E., Manning, H. B., Talbot, C. B., de Beule, P. A. A., Dunsby, C., Neil, M. A. A., and French, P. M. W. (2007). Excitation-resolved hyperspectral fluorescence lifetime imaging using a UV-extended super-continuum source. *Opt. Lett.* **32,** 3408–3410.

Pemberton, L. F., and Paschal, B. M. (2005). Mechanisms of receptor-mediated nuclear import and nuclear export. *Traffic* **6,** 187–198.

Peter, M., Ameer-Beg, S. M., Hughes, M. K., Keppler, M. D., Prag, S., Marsh, M., Vojnovic, B., and Ng, T. (2005). Multiphoton-FLIM quantification of the EGFP-mRFP1 FRET pair for localization of membrane receptor-kinase interactions. *Biophys. J.* **88,** 1224–1237.

Pepperkok, R., and Ellenberg, J. (2006). High-throughput fluorescence microscopy for systems biology. *Nat. Rev. Mol. Cell Biol.* **7,** 690–696.

Petrasek, Z., and Schwille, P. (2007). Precise measurement of diffusion coefficients using scanning fluorescence correlation spectroscopy. *Biophys. J.* **94,** 1437–1448.

Philip, J., and Carlsson, K. (2003). Theoretical investigation of the signal-to-noise ratio in fluorescence lifetime imaging. *J. Opt. Soc. Am. A Opt. Image Sci. Vis.* **20,** 368–379.

Remington, S. J. (2006). Fluorescent proteins: Maturation, photochemistry and photophysics. *Curr. Opin. Struct. Biol.* **16,** 714–721.

Riddick, G., and Macara, I. G. (2005). A systems analysis of importin-α-β mediated nuclear protein import. *J. Cell Biol.* **168,** 1027–1038.

Rizzo, M. A., Springer, G. H., Granada, B., and Piston, D. W. (2004). An improved cyan fluorescent protein variant useful for FRET. *Nat. Biotechnol.* **22,** 445–449.

Sanabria, H., Kubota, Y., and Waxham, M. (2007). Multiple diffusion mechanisms due to nanostructuring in crowded environments. *Biophys. J.* **92,** 313–322.

Shimozono, S., Hosoi, H., Mizuno, H., Fukano, T., Tahara, T., and Miyawaki, A. (2006). Concatenation of cyan and yellow fluorescent proteins for efficient resonance energy transfer. *Biochemistry* **45,** 6267–6271.

Shu, X., Shaner, N. C., Yarbrough, C. A., Tsien, R. Y., and Remington, S. J. (2006). Novel chromophores and buried charges control color in fruits. *Biochemistry* **45,** 9639–9647.

Slepchenko, B. M., Schaff, J. C., Macara, I., and Loew, L. M. (2003). Quantitative cell biology with the virtual cell. *Trends Cell Biol.* **13,** 570–576.

Skala, M. C., Riching, K. M., Bird, D. K., Gendron-Fitzpatrick, A., Eickhoff, J., Eliceiri, K. W., Keely, P. J., and Ramanujam, N. (2007). *In vivo* multiphoton fluorescence lifetime imaging of protein-bound and free nicotinamide adenine dinucleotide in normal and precancerous epithelia. *J. Biomed. Opt.* **12**, 024014.

Smith, A. E., Slepchenko, B. M., Schaff, J. C., Loew, L. M., and Macara, I. G. (2002). Systems analysis of Ran transport. *Science* **295,** 488–491.

Suhling, K., French, P. M., and Phillips, D. (2005). Time-resolved fluorescence microscopy. *Photochem. Photobiol. Sci.* **4,** 13–22.

Tramier, M., Zahid, M., Mevel, J. C., Masse, M. J., and Coppey-Moisan, M. (2006). Sensitivity of CFP/YFP and GFP/mCherry pairs to donor photobleaching on FRET determination by fluorescence lifetime imaging microscopy in living cells. *Microsc. Res. Tech.* **69,** 933–939.

Tsien, R. Y. (1998). The green fluorescent protein. *Annu. Rev. Biochem.* **67,** 509–544.

Tsien, R. Y. (2003). Breeding molecules to spy on cells. *Harvey Lect.* **99,** 77–93.

Tsien, R. Y. (2006). Breeding and building molecules to spy on cells and tumors. *Keio J. Med.* **55,** 127–140.

Tsien, R. Y., Backsai, B. J., and Adams, S. R. (1993). FRET for studying intracellular signalling. *Trends Cell Biol.* **3,** 242–245.

van Munster, E. B., and Gadella, T. W. (2005). Fluorescence lifetime imaging microscopy (FLIM). *Adv. Biochem. Eng. Biotechnol.* **95,** 143–175.

Verkman, A. (2002). Solute and macromolecule diffusion in cellular aqueous compartments. *Trends Biochem. Sci.* **27,** 27–33.

Wang, L., and Tsien, R. Y. (2006). Evolving proteins in mammalian cells using somatic hypermutation. *Nat. Protoc.* **1,** 1346–1350.

Weis, K. (2003). Regulating access to the genome: Nucleocytoplasmic transport throughout the cell cycle. *Cell* **112,** 441–451.

Yasuda, R. (2006). Imaging spatiotemporal dynamics of neuronal signaling using fluorescence resonance energy transfer and fluorescence lifetime imaging microscopy. *Curr. Opin. Neurobiol.* **16,** 551–561.

Yasuda, R., Harvey, C. D., Zhong, H., Sobczyk, A., van Aelst, L., and Svoboda, K. (2006). Supersensitive Ras activation in dendrites and spines revealed by two-photon fluorescence lifetime imaging. *Nat. Neurosci.* **9,** 283–291.

Zacharias, D. A., and Tsien, R. Y. (2006). Molecular biology and mutation of green fluorescent protein. *Methods Biochem. Anal.* **47,** 83–120.

CHAPTER 22

Quantitation of Protein–Protein Interactions: Confocal FRET Microscopy

Ammasi Periasamy,[*] Horst Wallrabe,[*] Ye Chen,[*] and Margarida Barroso[†]

[*]University of Virginia
W. M. Keck Center for Cellular Imaging, Department of Biology
Charlottesville, Virginia 22904

[†]Albany Medical College
Center for Cardiovascular Sciences
Albany, New York 12208

Abstract

Förster resonance energy transfer (FRET) is an effective and high resolution method to monitor protein–protein interactions in live or fixed specimens. FRET can be used to estimate the distance between interacting protein molecules *in vivo* or

0091-679X/08 $35.00
DOI: 10.1016/S0091-679X(08)00622-5

in vitro using laser-scanning confocal FRET microscopy. The spectral overlap of donor and acceptor—essential for FRET—also generates a contamination of the FRET signal, which should be removed in order to carry out quantitative data analysis with confidence. Quantitative FRET data analysis addresses the wealth of information contained in the data set, once optimized FRET imaging has been completed. In this chapter, we describe step-by-step what the issues are in quantitative FRET data analysis, using membrane receptor trafficking and organization as an example. The assays described are applicable to many other biological applications.

I. Introduction

Protein–protein interactions mediate the majority of cellular processes. Identification of a protein's interacting partners is critical in understanding its function, placing it in a biochemical pathway, and thereby establishing its relationship to important disease processes. Protein localization studies using microscopy techniques can indicate what proteins are expressed, where those proteins are expressed, and where they go over time. Tracking these parameters would allow us to gain a better understanding of these proteins' functions and determine for example, which are likely to be the best drug targets. Förster (or fluorescence) resonance energy transfer (FRET) is an excellent technique to monitor not only protein–protein interactions (Wallrabe and Periasamy, 2005) but also the organization of proteins at the nanometer level in intracellular membranes and other substrates (Wallrabe *et al.*, 2003a). The monitoring of protein–protein interactions *in vivo* or *in vitro* and the accuracy of FRET measurement using microscopy techniques has tremendously increased since 1997 after the introduction of various mutant forms of green fluorescent proteins (GFPs) (Dobbie *et al.*, 2008; Giepmans *et al.*, 2006; Tsien and Miyawaki, 1998). The development of novel fluorophores, with higher photo-stability and quantum yields, for conjugation to proteins and other cellular components has also kept pace with microscopy and GFP developments; a wide selection of fluorophores is now available. In addition, quantum dots have entered the stage and are likely to impact fluorescence imaging in the future.

Recent advances in fluorescence microscopy, including improved optics and high sensitivity cameras coupled with technological advances in computers and sophisticated imaging analysis software, now permit quantitative measurement and noninvasive acquisition of spectroscopic information from tissue to single molecule (Demarco *et al.*, 2006a,b; Patterson and Lippincott-Schwartz, 2002; Periasamy and Day, 1999; Wallrabe and Periasamy, 2005).

Each of the available FRET microscopy techniques has its own advantages and disadvantages (Periasamy and Day, 1999, 2005). For example, wide-field FRET (W-FRET) microscopy is the simplest and most widely used technique (Day *et al.*, 2003). In addition, the W-FRET system allows the use of any excitation wavelength using interference filters for various FRET pairs. It is used for quantitative comparisons of cellular compartments and time-lapse studies for cell motility,

intracellular mechanics, and molecular movement. Laser-scanning confocal and two-photon (2P) FRET microscopy provide the advantage of rejecting out-of-focus information (Chen and Periasamy, 2004; Chen *et al.*, 2003; Wallrabe and Periasamy, 2005; Wallrabe *et al.*, 2003b, 2006). They also allow associations occurring inside the cell to be localized in three dimensions. Confocal FRET (C-FRET) microscopy, however, is limited to standard laser lines of defined wavelengths. In general, two-photon (2P)-FRET microscopy is superior for deep tissue FRET imaging rather than for monolayer cells, particularly cells that express mutant forms of GFPs as they potentially are excited by one wavelength (Mills *et al.*, 2003). Spectral imaging, either by confocal or two-photon systems, is an intensity-based imaging technique which provides an excellent way to obtain a FRET signal (Chen *et al.*, 2007). However, each of these intensity-based FRET techniques requires post-image processing methods to remove the unwanted spectral bleed-through (SBT) components in the sensitized FRET signal. Fluorescence lifetime microscopy (FLIM) avoids some of these difficulties, but is technically challenging. Measuring the donor quenching or donor lifetime also provides a method for estimating energy transfer efficiency (E%) (Chen *et al.*, 2003).

Here, we describe the data acquisition and processing methodology involved in FRET imaging, using confocal microscopy techniques to determine the nature of protein organization during endocytic trafficking; we will also use quantitative FRET data analysis to differentiate between random versus clustered distributions of membrane-bound receptor–ligand complexes.

II. Rationale

Quantitative analysis of FRET takes advantage of the wealth of information contained in FRET signals to make powerful deductions about the nature and dynamics of cellular components and their interactions. While the data shown here was acquired with laser-scanning confocal FRET microscopy, the analysis is applicable to any other FRET modality. Once all the critical data correction steps have established that one has an unequivocal and reliable FRET signal (or absence of FRET), the question is whether the FRET signal originates from two proteins that are in 1–10 nm proximity due to specific-and-regulated or random encounters. Having taken great care and considerable time to optimize our experimental and imaging conditions, it seems logical to take the next step and examine our results that answer some important questions. Are we detecting random encounters of proteins diffusing freely in the cytosol or are the protein partners in FRET proximity because they have formed macromolecular complexes in the cytosol? Most importantly, if the protein partners are attached to a substrate, such as a membrane organelle, qualitative FRET data may not be sufficient as random encounters may occur frequently, since the ability of the proteins to

freely diffuse in all directions is greatly reduced. The core question is therefore—and it potentially applies to virtually all cellular investigations by FRET microscopy—whether the observed FRET signal is due to a "random" or "specifically regulated" event, that is whether the FRET signal is due to some cellular mechanism or process that causes specific cellular components to directly or indirectly aggregate, cluster, bind, or associate so that the two fluorophore-labeled target proteins can come together within 1–10 nm to undergo a FRET event. Many of these questions can be answered based on the relationship between the level of $E\%$ and the levels of donor and acceptor fluorescence and their ratio; here we will address important issues related to generate and analyze FRET quantitative data.

III. Material and Methods

A. FRET Theory and Analysis

1. Introduction to FRET

FRET has been described widely in the literature (Clegg, 1995; Forster, 1965; Jares-Erijman and Jovin, 2003; Lakowicz *et al.*, 1999; Vogel *et al.*, 2006; Wallrabe and Periasamy, 2005). FRET is a process involving the radiationless transfer of energy from a donor fluorophore to an appropriately positioned acceptor fluorophore: (i) FRET can occur when the emission spectrum of a donor fluorophore significantly overlaps (>25%) the absorption spectrum of an acceptor (Fig. 1; spectral overlap). If the spectra do not overlap, no FRET can occur. (ii) The emission dipole of the donor and the acceptor absorption dipole must be appropriately oriented to each other and it must not be oriented perpendicularly. A dipole is an electromagnetic field that exists in a molecule that has regions with oppositely charged areas, one of negative charge and the other of positive charge. If the spectra are overlapped, the donor's oscillating emission dipole will look for a partner from the absorption dipole of an acceptor to oscillate in synchrony. The magnitude of the relative orientation of the dipole–dipole coupling values should be 1–4 (Lakowicz, 1999). (iii) Because the efficiency of energy transfer varies inversely with the sixth power of the distance separating the donor and acceptor fluorophores, the distance over which FRET can occur is limited to between 1–10 nm. In practice, one can observe the FRET signal when the distance between protein molecules is about 2–8 nm and this varies depending on the sensitivity of the detector. When the spectral, dipole orientation, and distance criteria are satisfied, excitation of the donor fluorophore results in sensitized fluorescence emission of the acceptor, while quenching the donor simultaneously, indicating that the tagged proteins are separated by <10 nm. This FRET-based inferred proximity between two labeled cellular components considerably surpasses the resolution of general light microscopy, which at best can resolve distances of ~200nm.

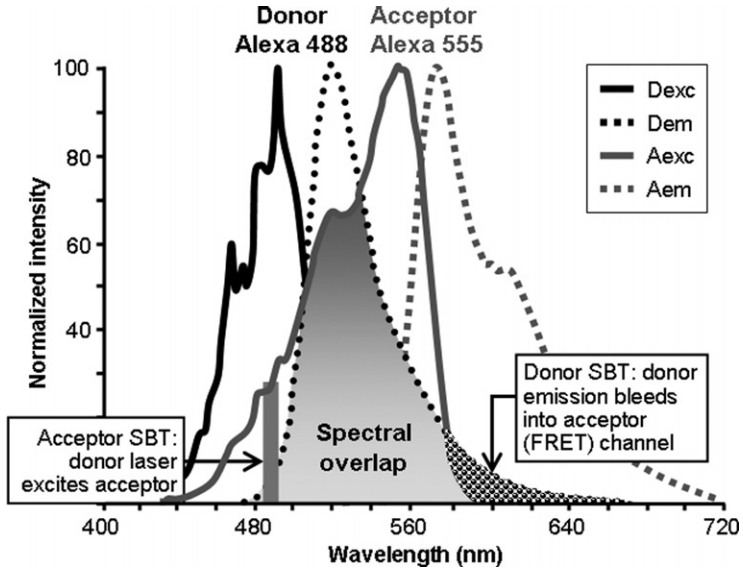

Fig. 1 Intensity-based FRET requires SBT correction: FRET's requirement for spectral overlap occurs at the expense of SBT. Significant spectral overlap (gray shaded area) between donor (Alexa Fluor 488) emission and acceptor (Alexa Fluor 555) excitation is essential for the occurrence of FRET. Acceptor SBT occurs when the donor excitation wavelength (488 nm) excites acceptor fluorophores leading to spillover contamination into the FRET signal in the acceptor channel (gray vertical bar at 488 nm). Donor SBT occurs when the donor emission contaminates the FRET signal in the acceptor channel (area of black/white circles). D_{ex} = Donor absorption wavelength spectrum; A_{ex} = Acceptor absorption wavelength spectrum; D_{em} = Donor emission wavelength spectrum; A_{em} = Acceptor emission wavelength spectrum.

The energy transfer (E), the rate of energy transfer (k_T), and the distance between donor and acceptor molecule (r) are calculated using the following equations (Lakowicz, 1999):

$$E = 1 - (\tau_{DA}/\tau_D) \tag{1}$$

$$k_T = (1/\tau_D)(R_0/r)^6 \tag{2}$$

$$r = R_0\{[1/E] - 1\}^{1/6} \tag{3}$$

$$R_0 = \left\{ \left[\frac{[9000(\ln 10)\kappa^2 Q_D}{128\pi^5 N n^4} \right] \int_0^\infty F_D(\lambda)\epsilon_A(\lambda)\lambda^4 d\lambda \right\}^{1/6} \tag{4}$$

$$R_0 = \left\{ \left[\frac{[9000(\ln 10)\kappa^2 Q_D}{128\pi^5 N n^4} \right] J(\lambda) \right\}^{1/6} \quad (5)$$

where τ_D and τ_{DA} is the donor (D) excited state lifetime in the absence and presence of the acceptor (A); R_0 is the Förster distance—that is, the distance between D and A at which half the excitation energy of the donor is transferred to the acceptor while the other half is dissipated by all other processes, including light emission; κ^2 is a factor describing the relative dipole orientation in space of the donor and acceptor (normally assumed to be 2/3, which is appropriate for dynamic random averaging of D and A); Q_D is the quantum yield of the donor in the absence of acceptor; N is the Avogadro's number; n is the refractive index ($n = 1.4$ for biomolecules in aqueous solution); $F_D(\lambda)$ is the corrected fluorescence intensity of the donor in the wavelength range λ to $\lambda + d\lambda$; $\varepsilon_A(\lambda)$ is the extinction coefficient of the acceptor at λ (M^{-1} cm^{-1}); $J(\lambda)$ is the overlap integral which expresses the degree of spectral overlap between the donor emission and the acceptor absorption (see Fig. 1).

2. FRET Measurements

One of the important conditions for FRET to occur is the overlap of the emission spectrum of the donor fluorophore with the absorption spectrum of the acceptor fluorophore. Because of spectral overlap, the FRET signal is contaminated by donor emission into the acceptor channel (Donor SBT) and by the excitation of acceptor molecules by the donor excitation wavelength (Acceptor SBT) (Fig. 1). In addition to SBT, other sources of noise contaminate the FRET signal, including spectral sensitivity variations in donor and acceptor channels, autofluorescence, and detector and optical noise. There are various methods to assess the SBT contamination in the FRET image. The donor SBT can be calculated and corrected using the percentage of the spectral area of the donor emission spill over into the acceptor emission spectrum (Fig. 1). But, it is difficult to determine the acceptor SBT because one does not know the percentage of the donor excitation wavelength that may excite the acceptor absorption spectrum. Moreover, this does not correct for variations in expression or concentration of fluorophore-labeled cells.

One method to measure FRET that overcomes some of the problems associated with SBT is acceptor photobleaching FRET. In this method, the difference between quenched donor (qD, donor fluorescence in the presence of acceptor) and unquenched donor (D, donor fluorescence after the acceptor has been bleached) is used to calculate E% levels (Bastiaens and Jovin, 1996; Day *et al.*, 2001; Kenworthy, 2001; Wouters *et al.*, 1998; Zal *et al.*, 2002). While this approach has the advantage of using only double-label specimens, there are some limitations: It cannot be used in live cells to examine highly mobile protein complexes (Day *et al.*, 2001). It has been shown that extended exposure of the cells to laser energy has significant ill-effects due to an increased production of reactive oxygen

species (Knight *et al.*, 2003; Wu *et al.*, 2007), which may introduce artifacts into the data analysis. The use of antioxidants during live-cell imaging results in the reduction of reactive oxygen species (Knight *et al.*, 2003). However, their use is not widespread due to potential secondary effects.

An alternative method is to use computer-based algorithms to measure, and then remove the SBT contaminating signals from the FRET image based on single-labeled reference samples. Depending on the level of sensitivity desired, some methods use two or three filter sets (wide-field microscopy configuration) and normalize the FRET signal for the donor and acceptor (Gordon *et al.*, 1998; Xia and Liu, 2001) SBT signal. There are other approaches that correct after image acquisition with single-label reference specimens (Chamberlain *et al.*, 2000). These methods assume a linear relationship between single- and double-labeled specimens imaged under the same conditions and use that for the correction of donor and acceptor SBT signal.

Our Processed FRET (PFRET) algorithm-based image acquisition and processing approach to correct SBT has several advantages over the other methods mentioned above. The PFRET algorithm is actually based on the average value of narrow fluorescence ranges, allowing the estimation of SBT correction for linear as well nonlinear intensity distributions. Moreover, this algorithm normalizes the expression-level variation in the cellular images (Chen *et al.*, 2005, 2007). Our method can be used for any intensity-based FRET-imaging techniques including wide-field, total internal reflection (TIRF), confocal, spectral imaging, and two-photon microscopy FRET data analysis.

B. FRET Assay

1. Cellular Uptake of TFR–Tfn Complexes

Confluent MDCK–PTR cells, Madin Darby canine kidney cells that express the stably transfected human transferrin receptor (TFR) at the plasma membrane (PM), are grown on membrane inserts for 3–4 days until they reach a polarized status (Barroso and Sztul, 1994; Wallrabe *et al.*, 2007). TFR behaves as a homodimeric type II transmembrane receptor; TFR's monomer contains a small cytoplasmic domain, a single-pass transmembrane region and a large extracellular domain, which binds a Tfn ligand bearing two iron molecules. Therefore, each TFR homodimer binds two molecules of Tfn, at the basolateral PM (Fig. 2A; Cheng *et al.*, 2004; Richardson, 2004). Alexa Fluor 488 (Donor)-labeled and Alexa Fluor 555 (Acceptor)-labeled Tfn ligands are used to follow the intracellular trafficking of TFR in polarized MDCK–PTR cells (Fig. 2A; Wallrabe *et al.*, 2006). Alexa Fluor 488- and/or Alexa Fluor 555-Tfn are co-internalized for 30 min at 37 °C into the basolateral surface of polarized MDCK–PTR cells with different internalization ranges (10–100 μg/ml) and donor/acceptor fluorophore ratios (e.g., 1:2, 1:1, 2:1). Cells are fixed with 4% paraformaldehyde, washed with PBS, imaged at room temperature and tracked spatially and temporally using confocal FRET microscopy (Wallrabe *et al.*, 2006, 2007).

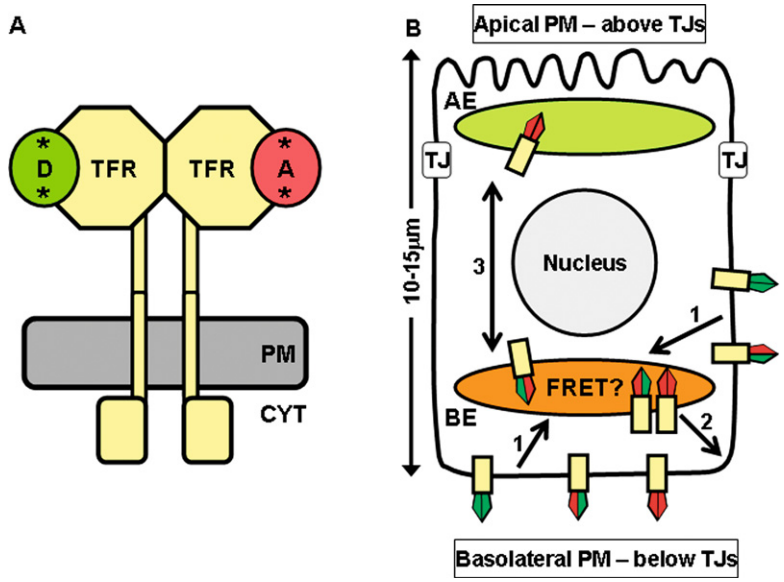

Fig. 2 Structure and polarized trafficking of TFR–Tfn complexes. (A) TFR dimer structure. Each apo-Tfn molecule binds two Fe^{3+} (asterisks) in the extracellular media. Two molecules of Tfn (iron-bound) bind each TFR dimer at the PM. In this particular example, one donor-labeled Tfn (green) and one acceptor-labeled (red) Tfn bind a TFR dimer (yellow). (B) Polarized endocytic trafficking of TFR–Tfn complexes. Tfn-Alexa Fluor 488 (green diamond) and Tfn-Alexa Fluor 555 (red diamond) were co-internalized for 30 min at 37 °C into the basolateral surface of polarized MDCK–PTR cells, and confocal FRET imaging (FRET?) was performed at the level of the basolateral endosome (BE). Step 1: Donor and acceptor-labeled Tfn molecules bind TFR at the basolateral PM. The three potential TFR–Tfn binding patterns are shown, that is one donor-labeled Tfn and one acceptor-labeled Tfn, two donor-labeled Tfn or two acceptor-labeled Tfn can bind one TFR dimer. Then TFR–Tfn complexes are endocytosed via a clathrin-dependent mechanism into the BE. Step 2: Iron is released from Tfn as Fe^{2+} in the BE, and the TFR–Tfn complexes are recycled back to the basolateral PM. Step 3: A minor fraction of TFR–Tfn complexes reaches the apical endosome (AE), from where it is delivered back to the BE (Wallrabe *et al.*, 2007).

2. Polylysine-coated Coverslips

As a positive control for random distribution (negative control for clustering) of substrate-bound proteins, Alexa Fluor 488-Tfn and Alexa Fluor 555-Tfn were incubated for 30 min at room temperature on polylysine-coated glass coverslips, fixed with 4% paraformaldehyde, washed in PBS, and imaged at room temperature using confocal FRET microscopy (Wallrabe *et al.*, 2007).

C. C-FRET Microscopy

1. Issues in the Acquisition of Confocal FRET Images

Any confocal microscope, either laser scanning or spinning disk, can be configured for FRET imaging (Wallrabe and Periasamy, 2005). Most confocal microscopes have two or three of the standard laser lines (405, 458, 488, 514, 543, 561, 594, 633 nm), and this limits the choice of compatible FRET pairs. In the case of the arc lamp-based spinning disc system, the appropriate filter wheels are usually available. Most systems allow the user to vary the power level, the photomultiplier-tube (PMT) settings (manufacturers usually recommend an optimum/maximum level that should not be exceeded to avoid excessive background noise), the zoom level, the size of the pinhole (iris), background control, size of the image (influences resolution), and various forms of processing (e.g., accumulating, averaging, binning). Moreover, in spite of effective SBT correction methodologies, it is wise to optimize emission filter configurations, which maximize the FRET signal and minimize SBT (Wallrabe *et al.*, 2003b).

Before embarking on a series of FRET experiments, a great deal of homework needs to be completed to achieve the following objectives: maximizing the FRET signal, minimizing SBT, avoiding wide-spread saturation, avoiding unintended photobleaching, and minimizing background noise. Unfortunately, there is no hard-and-fast rule of the best combination of these factors, since they are influenced by the particular system, specimens, and fluorophores. As practical first steps, any photobleaching and high levels of saturation need to be controlled by reduction of laser power at the specimen plane and adjustment of PMT settings. In summary, optimizing all of the conditions allows the researcher to have confidence in the results of a series of experiments conducted under the same conditions. This is particularly important when biological treatments are introduced that affect intracellular processes, such as membrane trafficking, cytoskeletal dynamics, and cell migration.

An important question concerns the imaging of fixed cells versus live cells. Obviously, for all the right reasons, live cells that exhibit physiologically relevant processes are to be preferred. However, as part of the optimization of an assay, there is great merit and utility in working with fixed cells first to fine-tune the imaging parameters. After that, following the first live-cell data collection, the specimen can be quickly fixed and imaged again and the data compared with previous fixed sample results. In our particular experimental system, cell fixation does not affect the final results and provides more flexibility for developing protocols for FRET assays (Wallrabe *et al.*, 2003a, 2006, 2007).

2. Acquisition of Confocal FRET Images

For data collection, we used a Biorad Radiance 2100 laser-scanning confocal microscope, equipped with a 60× water immersion lens (1.2 NA), Argon (Donor excitation: 488nm) and Green HeNe (Acceptor excitation: 543nm) lasers, and

band-pass emission filters: 515/30 nm (range = 500–545 nm) and 590/70 nm (range = 555–625 nm). The following conditions should be set up prior to data collection. First, three imaging channel tracks, that is A_{ex} and A_{em} (Acceptor), D_{ex} and D_{em} (Donor), D_{ex} and A_{em} (FRET) (Table I), should be established according to instrument specifications. Second, optimal laser power levels and PMT settings should be determined at the double-label specimen plane to avoid photobleaching and saturation in all imaging channels. Whereas laser power levels may be different for donor and acceptor laser excitations, PMT gain levels should be identical for all three imaging channels. After optimization, both laser power and PMT gain levels should be kept constant throughout image collection. Third, these settings should produce a detectable fluorescence signal using the FRET channel settings

Table I
FRET Confocal Microscopy Worksheet

Specimen	Excitation	Emission	Channel	Description	Comments
Single-label acceptor "*A*"	$A_{ex} = 543$ nm	$A_{em} = 590/70$ nm	Acceptor	Signal from acceptor only specimen using acceptor excitation and emission filter	Acceptor signal reference
	$D_{ex} = 488$ nm	$D_{em} = 515–30$ nm	Donor	Signal from acceptor only specimen using donor excitation and emission filter	Background signal
	$D_{ex} = 488$ nm	$A_{em} = 590/70$ nm	FRET	Signal from acceptor only specimen using donor excitation and acceptor emission filter	Acceptor SBT signal
Single-label donor "*D*"	$A_{ex} = 543$ nm	$A_{em} = 590/70$ nm	Acceptor	Signal from donor only specimen using acceptor excitation and emission filter	Background signal
	$D_{ex} = 488$ nm	$D_{em} = 515–30$ nm	Donor	Signal from donor only specimen using donor excitation and emission filter	Donor signal reference
	$D_{ex} = 488$ nm	$A_{em} = 590/70$ nm	FRET	Signal from donor only specimen using donor excitation and acceptor emission filter	Donor SBT signal
Double-label donor and acceptor "$D + A$"	$A_{ex} = 543$ nm	$A_{em} = 590/70$ nm	Acceptor	Signal from donor and acceptor specimen using acceptor excitation and emission filter	Acceptor signal
	$D_{ex} = 488$ nm	$D_{em} = 515–30$ nm	Donor	Signal from donor and acceptor specimen using donor excitation and emission filter	Quenched donor signal
	$D_{ex} = 488$ nm	$A_{em} = 590/70$ nm	FRET	Signal from donor and acceptor specimen using donor excitation and acceptor emission filter	Uncorrected FRET signal

(~60–100 gray-level units—for 8-bit imaging). Fourth, fluorescence background levels should be determined for later subtraction. This can be achieved by visualizing unlabeled cells in all three imaging channels or by using donor or acceptor single-label images collected using acceptor- or donor-imaging channels, respectively. Images were collected at room temperature at the basolateral level of double-label and single-label specimens (Fig. 2B; FRET?) under identical imaging conditions: 512 × 512 pixel resolution, no processing, 2 × zoom, 8-bit images. Photobleaching was undetectable during the short exposure to collect the final images. A custom proprietary macro is used to toggle between donor and acceptor excitation lasers and thus minimize switching delay.

As described in Table I, nine images are collected for background and SBT correction and subsequent FRET analysis from single-label donor samples, single-label acceptor samples, and double-label samples containing donor and acceptor fluorophores (Fig. 3; Table I). For background removal, measurements are performed on single-label acceptor reference images using donor-imaging channel (Panel *B*) and on single-label donor reference images using acceptor-imaging channel (Panel *D*) (Table I). For SBT correction using the PFRET algorithm, seven background-subtracted images are collected: two single-label donor reference images using donor- and FRET-imaging channels (Panels *A* and *C*); two single-label acceptor reference images using acceptor- and FRET-imaging channels (Panels *E* and *F*); and three double-label images, that is acceptor (Panel *G*), q*D* (Panel *H*), and uFRET (Panel *I*), using acceptor-, donor-, and FRET-imaging channels, respectively (Table I) (Wallrabe *et al.*, 2003a, 2006).

D. Post-Acquisition FRET Processing

1. Algorithm-based Method to Remove SBT—PFRET

The PFRET algorithm follows fluorescence levels pixel-by-pixel, establishes the level of SBT in the single-labeled cells, and applies these values as a correction factor to the appropriate matching pixels of the double-labeled cell. The software allows the user to set a level of correction sensitivity based on the average value of narrow fluorescence ranges, for more efficient running of the correction algorithm (Chen *et al.*, 2005; Elangovan *et al.*, 2003). We choose the average of 10 fluorescence units, that is, 0–9, 11–20, etc., continuing to the highest fluorescent units in the image. Using the average of even narrower ranges does not improve the sensitivity. PFRET then is

$$\mathrm{PFRET} = \mathrm{uFRET} - \mathrm{ASBT} - \mathrm{DSBT} \tag{6}$$

where uFRET is uncorrected FRET (uFRET), ASBT is the acceptor SBT signal, and DSBT is the donor SBT signal. The DSBT and ASBT are established using the corresponding single-labeled cells. The mathematical equations and detailed descriptions of the algorithm for ASBT and DSBT correction have been described in the literature (Chen *et al.*, 2005; Elangovan *et al.*, 2003).

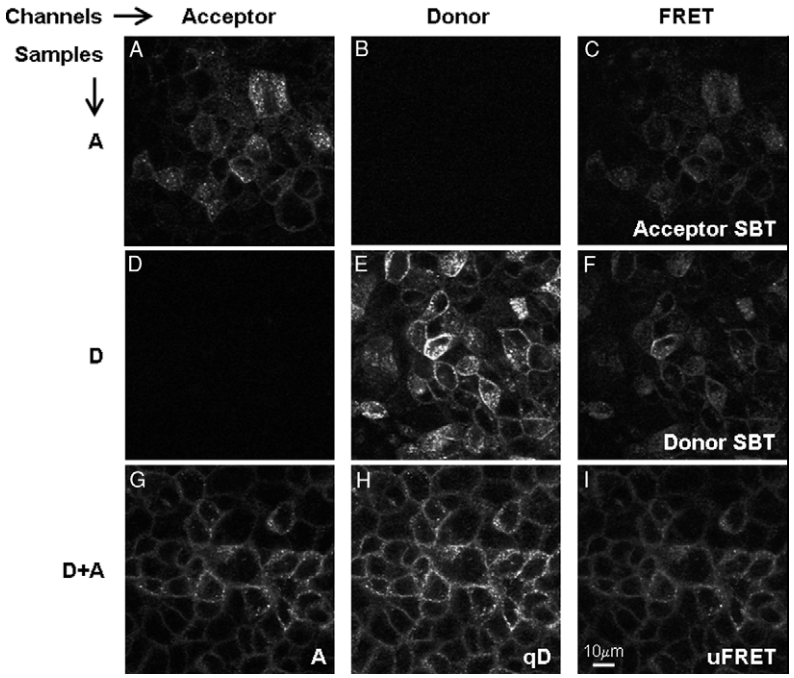

Fig. 3 Distribution of TFR–Tfn complexes in basolateral endocytic membranes using FRET confocal imaging. MDCK polarized cells containing basolaterally co-internalized Alexa 488- and/or Alexa 555-labeled TFR–Tfn complexes (30 min at 37 °C) were imaged by confocal microscopy at the basolateral endosome region. MDCK cells were co-internalized with both donor-labeled and acceptor-labeled Tfn (D + A; double-label cells), donor-only labeled Tfn (D; donor single-label cells) or acceptor-only labeled (A; acceptor single-label cells). (A, D and G) Acceptor channel shows acceptor fluorescence intensities. (B, E and H) Donor channel shows donor fluorescence intensities. (C) FRET channel shows the acceptor SBT in acceptor single-label cells. (F) FRET channel shows the donor SBT in donor single-label cells. (I) FRET channel shows the uncorrected FRET (uFRET) signal, which includes energy transfer levels plus the two SBT contaminants. FRET, acceptor, and donor-imaging channels are described in detail in Table I. (*A*) Acceptor fluorescence intensity levels. (q*D*) Quenched donor fluorescence intensity levels. These images were modified in Adobe Photoshop at the same rate to a higher level of contrast for better visualization. Check Tables I and II for detailed imaging channel characteristics and other FRET definitions.

2. *E*% Calculation

The measurements described here fall into the category of "apparent" *E*%, which is dependent on Förster-type energy transfer *E* (Lakowicz *et al.*, 1999; Wouters *et al.*, 1998), but is also influenced by the concentrations of those donor or acceptor molecules that are not involved in energy transfer; for brevity, we will use *E*%, instead of "apparent" *E*%. *E*% is an expression of the energy transfer as a percentage of the unquenched donor (*D*):

$$D = \mathrm{q}D + \mathrm{PFRET} \times \gamma \tag{7}$$

as described in the following equation:

$$E\% = 100 \times (1 - qD/D) \tag{8}$$

(Bonamy *et al.*, 2005; Elangovan *et al.*, 2003; Wallrabe and Barroso, 2005; Wallrabe *et al.*, 2003a, 2006). The γ factor, which is a function of the quantum yield of the fluorophores and the spectral sensitivity of the detection setup, plays a crucial role in recording precise $E\%$ and distances between fluorophores. Since the excitation efficiencies (ε), quantum yields of the fluorophore molecules, and the detection efficiencies (Q) remain constant throughout the experiments, the γ factor does not affect the answers that FRET quantitative analysis seeks. Therefore, for simplicity, we used $\gamma = 1$, as described previously (Elangovan *et al.*, 2003; Wallrabe *et al.*, 2003a,b, 2006, 2007). Nevertheless, different microscopes using different imaging collection instruments and settings will by definition have distinct γ factors. Therefore, the relative $E\%$ values differ for data collected using distinct microscopy systems.

However, when distance measurements are the research goal, the spectral sensitivity, quantum yield, and quantum efficiency factors need to be determined and applied to the PFRET and absolute energy transfer efficiency (E_n) calculation (Bonamy *et al.*, 2005; Chen *et al.*, 2005; Hoppe *et al.*, 2002). E_n is calculated by generating a new I_D (intensity of the single-label donor) image by including the detector spectral sensitivity of donor and acceptor channel and the donor/acceptor quantum yields Eqs. (9) or (10) (Chen *et al.*, 2005)

$$E_n = 1 - \left\{ \frac{I_{DA}}{[I_{DA} + \text{PFRET} \times (\psi_{dd}/\psi_{aa}) \times Q_d/Q_a]} \right\} \tag{9}$$

Or Eq. (9) can be rewritten as

$$E_n = \frac{\text{PFRET} \times SS \times QY}{[(\text{PFRET} \times SS \times QY) + I_{DA}]} \tag{10}$$

where

$$SS = (\psi_{dd}/\psi_{aa}) = [(\text{PMT gain of donor channel/PMT gain of acceptor channel}) \times (\text{spectral sensitivity of donor channel/spectral sensitivity of acceptor channel})] \tag{11}$$

And $QY = Q_d/Q_a$ (Q_d and Q_a are donor and acceptor quantum yields, respectively).

In Eq. (12), for estimating the distance between donor and acceptor, r, has changed to r_n. Förster's distance R_0 values have been calculated for various fluorophore pairs (Chen *et al.*, 2005):

$$r = R_0[(1/E) - 1]^{1/6} \tag{12}$$

$$r_n = R_0[(1/E_n) - 1]^{1/6} \tag{13}$$

3. Quantitative Data Analysis Software

An extension of the PFRET software includes a custom-written program to select pixels with values that range between 0 and a value below 255; such a value is calculated by subtracting the background value to 254 to exclude any saturated pixels; in actuality under our imaging conditions, there are very few saturated donor pixels. This final pixel selection becomes the template for all calculations. Then, we visually select appropriate regions of interest (ROIs) from the uFRET image and note their pixel coordinates. These pixel locations are applied to the other images and fluorescence values are extracted. A, qD, uFRET, and PFRET values are averaged over an ROI-based on the original pixel-by-pixel analysis and transferred to Excel spreadsheets for calculation of additional parameters such as E%, D, and actual D:A ratios (Tables II and III). Other parameters such as the level of SBT correction (%Corr), the percentage of saturated pixels removed (%pix rem), the number of pixels after removal of saturated pixels (fin pix), and the extent of SBT correction (ext corr) are obtained and reviewed as a safety check (Tables II and III). ROI coordinates and any ROI numbers are also included in the FRET data spreadsheet (Tables II and III). A detailed description is provided in Section IV of how the data, once generated, is further developed.

IV. Results and Discussion

Polarized epithelial MDCK–PTR cells are a well-recognized biological model system to investigate the intracellular trafficking of membrane-bound proteins. Moreover, TFR and its iron-loaded ligand, holo-tranferrin (Tfn), are well-studied, highly regulated, membrane-bound receptor–ligand complexes that are mainly internalized from the basolateral PM into clathrin-coated vesicles and basolateral endosomes (BE) (Fig. 2B, #1), where they undergo low pH-induced iron release (Maxfield

Table II
Definitions Used in Quantitative FRET Analysis

X-Y-W-H	Region of interest (ROI) coordinates
OrigPix	Original pixel No = pixels No per ROI before "bound"-application
FinPix	Final pixel No = pixels No per ROI after "bound"-application
% pix rem	% pixels removed = 100–(Fin Pix × 100/Orig Pix)
uFRET	Uncorrected FRET = D_{ex}/A_{em}
PFRET	uFRET-SBT = corrected FRET using PFRET software = Energy transfer
% Corr.	% SBT correction = uFRET-PFRET × 100/uFRET
Ext. Corr.	Extent of correction = uFRET–PFRET
qD	Quenched donor = D_{ex}/D_{em} [Eq. (7)]
D	Unquenched donor
D/A	D/A ratio
A	Acceptor = A_{ex}/A_{em}
E%	Energy transfer efficiency [Eq. (8)]

Table III
FRET Data Spreadsheet

ROIs No	X,Y;W,H	Orig pix	Fin Pix	% pix rem	uFRET	PFRET	%Corr	Ext. Corr	q*D*	*D*	*D*/*A*	*A*	*E*%
100	216, 316; 10, 10	100	83	17	23.2	8.2	64.6	15	33.7	41.9	1.54	27.2	19.6
155	453, 340; 10, 10	100	100	0	26.2	9.2	64.8	17	43.4	52.6	1.67	31.6	17.5
203	435, 420; 10, 10	100	94	6	33.0	11.0	66.5	22	56.1	67.1	1.68	39.9	16.4
131	378, 348; 10, 10	100	97	3	71.6	26.5	63.0	36.5	114.8	141.3	1.69	83.9	18.7
126	198, 324; 10, 10	100	99	1	29.6	10.3	65.1	19.3	50.05	60. 4	1.69	35.8	17.1
130	219, 328; 10, 10	100	99	1	27.4	8.9	67.5	18.5	44.0	2.9	1.7	31.2	16.9

FRET data for basolaterally co-internalized Tfn-Alexa 488/Tfn-Alexa 555, background subtracted (4 units; saturaton=251) and using bounds for q*D*, uFRET, and *A* levels between 0 and 250.

and McGraw, 2004). Then, the majority of TFR–Tfn complexes are transported via the basolateral recycling endocytic pathway back to the basolateral PM (Fig. 2B, #2); a minor fraction traffics to the apical endosome, where it is sorted out and delivered back to the basolateral endosome (Fig. 2B, #3) (Wallrabe *et al.*, 2007).

A. Quantitative FRET Analysis

A large field of biological investigation concerns the spatial and temporal association of different proteins and other cellular components—mostly highly regulated processes, such as dimerization, oligomerization of binding partners, and specific clustering or nonspecific aggregation of nonbinding partners, the latter being often in restricted, substrate-based environments. Many situations can benefit from quantitative FRET analysis, such as assaying intracellular processes involving lipid rafts and membrane microdomains formation (Kiskowski and Kenworthy, 2007; Rao and Mayor, 2005); activation of signal transduction molecules at specific intracellular locations (Ballestrem *et al.*, 2006; Nakamura *et al.*, 2006); subcellular localization analysis; and the clustering/oligomerization of several membrane proteins, ex. connexins, MHC components, and ER membrane proteins (Bonamy *et al.*, 2005; Di *et al.*, 2005; Herrick-Davis *et al.*, 2004; Pentcheva and Edidin, 2001; Spiliotis *et al.*, 2002; Vamosi *et al.*, 2004). The particular assay presented here showcases the capabilities of quantitative FRET analysis concerning the trafficking of membrane-associated receptor–ligand complexes. Recently, we have demonstrated the formation of clusters containing TFR–Tfn receptor–ligand complexes and other different receptor–ligand complexes, when they trafficking together via polarized endocytic pathways (Wallrabe *et al.*, 2007). Such behavior has important implications for the regulation of protein sorting throughout polarized endocytic pathways. As used here, TFR–Tfn complexes are a good positive control for a typical clustered distribution due to their homo-dimeric nature (see below); however, we cannot exclude the formation of higher-order clusters between TFR–Tfn receptor–ligand complexes (see below; Section IV.C.3).

B. Elements of Successful Quantitative FRET Data Analysis

Here, we are presenting data generated by following the organization of TFR–Tfn complexes in the basolateral endosomes at the cell periphery. As mentioned before, to carry out quantitative analysis with confidence, a number of steps are needed: background subtraction (BGs), SBT correction, ROI collection, selection of "bounds" (data ranges to be considered), outlier identification, and appropriate statistical parameter selection.

1. Removal of Background Contamination

There are two potential sources of background "noise": (a) nonspecific cellular background and (b) instrument-based background noise. This may vary from instrument to instrument and should be minimized at the optimization stage

with appropriate levels of PMT gain and power levels. The best way to obtain a combined cell (or specific cell component, such as the nucleus) and instrument background level is to image an unlabeled cell or layer of cells. These unlabeled specimens should be imaged at exactly the same conditions as the labeled specimens and data collected from different areas of the specimens, in both, acceptor and donor emission channels (Wallrabe *et al.*, 2006). Another way to measure instrument noise is to scan the acceptor single-label sample with the donor wavelength and establish the gray-level values in the donor channel (Fig. 3B; Table IV). Furthermore, excite the donor single-label specimen with the acceptor wavelength and collect data in the acceptor (Fig. 3D) and donor channels (Table IV). This does double duty, examining whether the acceptor excitation touches the donor fluorophore (back-SBT; Table IV)—it should rarely occur, if an optimal FRET pair was chosen. Initially, the data collected from unlabeled and single-label cells should be compared. When similar results are obtained within a few gray-level units as shown in Table IV, single-label samples may be used for background correction measurements, therefore reducing the number of cell samples necessary for FRET quantitative analysis (Fig. 3). If the background values are significantly different between donor and acceptor channels at the same PMT gain settings/instrument settings, the BG should to be tailored to each specific channel. Within a series of experiments under the same overall conditions, any major change of background levels should immediately raise concerns about instrument or specimen issue. In summary, for background removal, the images mentioned earlier in Fig. 3 and in Table IV, are routinely acquired and several ROIs (5–10) are collected across the image to determine the background value for each experiment. Previously, we have shown that background removal leads to an increased sensitivity of the quantitative FRET assay (Wallrabe *et al.*, 2006).

If the background is unusually high (>10–15 gray-scale units for 8-bit images), different remedies may have to be tried: check whether the background is constant/even across the image and whether it varies from experiment to experiment; this most likely points to a specimen-related inconsistency. The next step to try is by adjusting instrument parameters and reimage to see whether the problem is instrument- and imaging-settings related. Some BG can be performed using an automatic background-subtraction facility provided by the instrument. This should be used

Table IV
Background Values

Samples		Unlabeled		*A*		*D*		*D* + *A*	
Channels		Average	SD	Average	SD	Average	SD	Average	SD
D_{ex}/D_{em}	Donor	4.42	0.58	5.3	0.14	–	–	–	–
A_{ex}/A_{em}	Acceptor	3.28	0.1	–	–	3.05	0.07	–	–
A_{ex}/D_{em}	Back-SBT	–	–	3.9	0.14	3.3	0.14	3.15	0.64

with caution and this option should only be activated, after having compared the results with the more involved, but possibly more accurate methods described above.

2. SBT Correction

Briefly, the PFRET SBT correction algorithm has been designed to remove both the donor and acceptor SBT signals, associated with FRET imaging and to correct for variation in fluorophore expression level (Chen *et al.*, 2005; Elangovan *et al.*, 2003; Wallrabe *et al.*, 2003a). Implementation of the SBT correction allows for the estimation of levels of energy transfer from donor to acceptor fluorophores. Our approach works on the assumption that the double-label cells and single-label donor and acceptor cells, imaged under the same conditions, exhibit similar SBT dynamics. To overcome the problem of having three different type of cells (*D, A*, and $D + A$), where individual pixel locations cannot be compared, the algorithm compares pixels with matching fluorescence levels between single-label and double-label samples. The average value of narrow fluorescence ranges across the images is used to determine the level of SBT in the single-label cells. The SBT values are determined at different fluorescence intensity ranges of single-label cells by generating an intensity-dependent lookup table, which is then applied as a correction factor to the respective matching fluorescence ranges of the double-label cell.

As expected, there is a strong linear correlation between PFRET and uFRET values (r-value = 0.95) (Fig. 4A). A significant correlation (r-value = 0.98) is also detected between the extent of correction (Table 2–3) and the uFRET values, suggesting that there is a linear correlation between these two parameters (Fig. 4B). The % of SBT correction (%Corr; Table 2–3) shows a slight negative dependence on uFRET levels, suggesting an independent behavior from uFRET (Fig. 4C). As shown in Fig. 5, a significant level of SBT is removed from uFRET image upon PFRET algorithm implementation to generate PFRET images. In summary, the PFRET algorithm provides a tool to adequately remove SBT from uFRET, taking into consideration intracellular variability of fluorophore expression levels.

3. Choosing ROIs

Having completed BG and SBT correction, we now have a cleaned-up set of images, including a PFRET data set that is free from contaminations; we can now begin our data analysis with confidence. The more ROI data points we can collect, the greater will be the statistical weight for our conclusions. Choosing ROIs must be considered under several aspects: (a) The biological target (e.g., whole cell, cytosol, nucleus, membranes, or any part of the cell that can be visually isolated). We have choosen multiple ROIs manually by targeting a typical punctate endocytic structures (Fig. 6). (b) ROI selection may be performed either manually or using custom-written software programs for automated ROI selection. (c) The size of ROIs does matter, depending on the dimensions of the biological target itself.

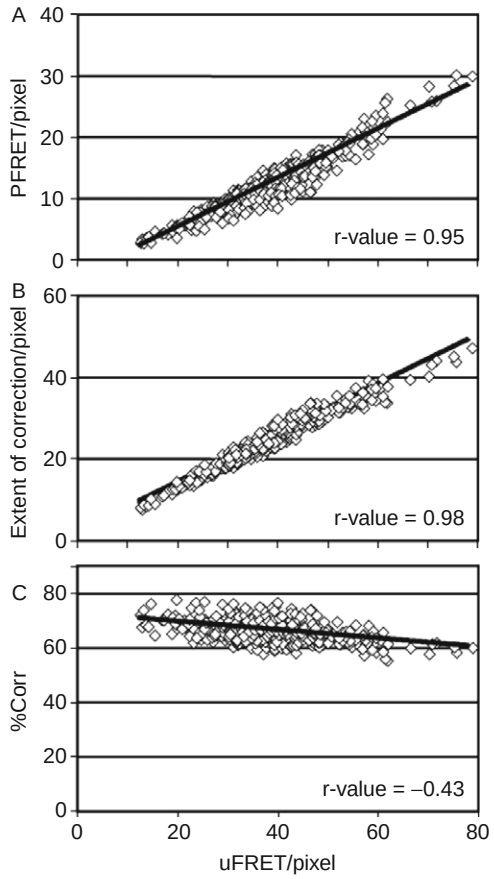

Fig. 4 Comparison of uFRET with PFRET levels after PFRET algorithm processing. These plots were obtained from ROI data collected from the images shown in Fig. 3. (A) PFRET versus uFRET signal. (B) The extent of correction versus *u*FRET signal. (C) The %Corr versus uFRET signal.

If the ROI is too small, its statistical power may be reduced as in all cases we deal with average values of ROIs/number of ROI pixels. If ROIs are too large, the data spread between ROIs may get very narrow and subtle differences may be missed. We have chosen ROIs containing 50–200 pixels (Fig. 6). (d) Different images may be chosen as the reference image for ROI selection, such as the uFRET and PFRET images. Contrast should be increased temporarily to allow an easier ROI selection. Other images such as q*D* and *A* should be reviewed in parallel to detect artifactual or atypical cellular features or noncellular artifactual fluorescence staining so that ROIs are not taken there. Alternatively, it may be useful to merge q*D* with *A* images to evaluate their overlap and base the ROI selection on the co-localization between the two fluorophore-labeled molecules.

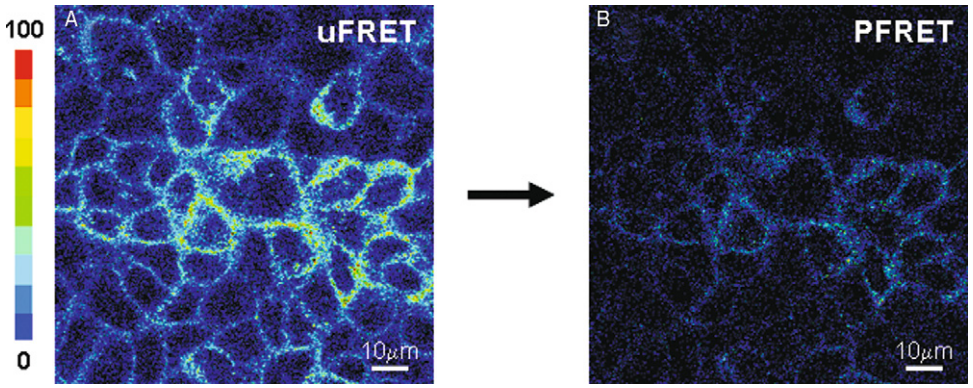

Fig. 5 SBT correction using the PFRET correction algorithm. uFRET images (A) are processed pixel-by-pixel by the PFRET correction algorithm to remove the donor and acceptor SBT and generate PFRET images (B) using single-labeled donor and acceptor images as reference, as shown in Fig. 3. The PFRET image represents the actual energy transfer levels (Tables II and III).

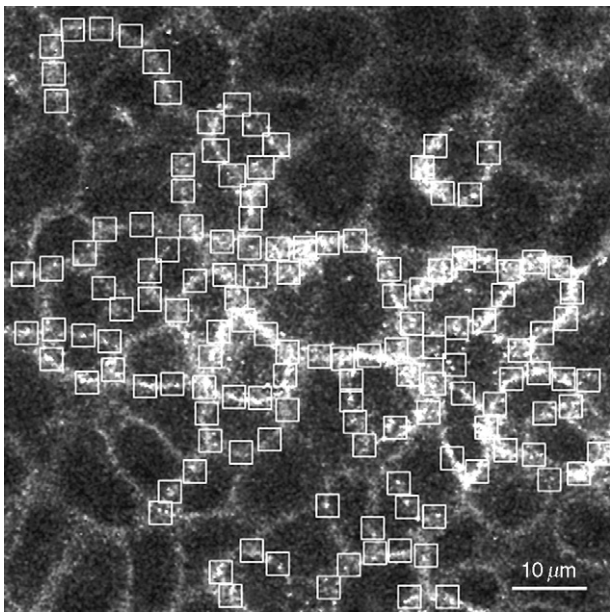

Fig. 6 ROI selection. ROIs (white boxes) of basolaterally internalized TFR–Tfn complexes were selected from an uFRET image with a typical basolateral endocytic staining. Contrast was temporarily increased for easier ROI detection and selection (~100 pixels).

4. Influence of Bound Selection

The bound range determines which pixels are to be included or excluded from the PFRET analysis. An 8-bit image has a range of 0–255 gray-level units. For example, after BG removal of 4 units, the saturated value moves to 251 and the upper bound should be 250 to exclude saturation values. Whether to include zeros or not is a judgment call; we do not, as the sensitivity of the data can potentially be lowered. When there are robust PFRET levels, eliminating lower level values can isolate the most meaningful populations. With good software, it is easy to run the analysis at different bounds and compare the results; attention should be given to percentage of pixel removed (%pix rem; Tables II and III), which should not be higher than 50% for ROIs of 100 pixels. Comparison of our data analysis at two different bounds (0 or 10 gray-levels below saturation levels) shows no difference with respect to the veracity of the assay (Wallrabe *et al.*, 2006).

C. Evaluating the Data and Statistics

1. Extracting Data from ROIs

Several proprietary as well as freely available programs, such as ImageJ plugins (http://rsb.info.nih.gov/ij/plugins/index.html), exist to analyze the selected ROIs. Independently of the tools used to extract data from ROIs, the following principles should be considered (Table III). First, for each ROI, the basic data of gray-level values for qD, A, uFRET, and PFRET need to be transferred to some data software, for example, Excel spreadsheets. Second, the ROI coordinates relating to each data set should be captured so that identification and visual inspection of that ROI can be revisited, should the data raise some questions at the analysis stage. Third, depending on the pixel selection criteria (''bounds''), certain pixels not meeting those criteria will have been eliminated from data analysis, such as pixels with zero fluorescence or with saturated fluorescence levels. The original and final pixel count should be known to make an assessment whether a particular ROI may need a closer look. Moreover, the percentage of saturated pixels removed by choice of bounds (%pix rem) will allow for the identification of unusually high pixel removal levels. Fourth, the basic FRET data on the spreadsheet is then used to calculate the level of SBT correction (%Corr) and extent of correction (Ext Corr) to provide for a safety check and to identify potential outliers. Fifth, the qD and PFRET values are then used to calculate D, D/A ratios and E% levels.

2. Dealing with "Outlier" Data

Potential outlier data may be identified at the spreadsheets, graphical or statistical evaluation stage. Irregardless, they must be investigated using the image sets upon which the data is based. We need to separate artifactual data (random fluorescence without any relation to cell structure elements) and data which may show unusually high or low values, but are visually part of the cellular structure. This may require

some empirical- and statistical-based approaches. The best insurance against the effects of outliers is a large database of >50–200 ROIs, in which the impact of a few outliers will be negligible. We have found [also confirmed in the literature (Berney and Danuser, 2003)] that it is advisable to exclude ROIs with high *D*:*A* ratios ($D/A > 6$) as well as ROIs with very high or very low *A* and/or *D* levels. As mentioned above, ROIs with high levels of % SBT correction or % pixels removed should also be considered as outliers and potentially removed. Typically, only a fraction of these are present, but a high proportion should give rise to concern and the images and data should be closely examined as this may compromise the FRET analysis. Something may be amiss with the specimen or instrument, particularly if the results are inconsistent with previous experiments.

3. Clustered Versus Random Distribution Analysis

To allow for a clear distinction between a random "molecular crowding" and a clustered distribution, well-established controls have been characterized using quantitative FRET-imaging analysis (Wallrabe *et al.*, 2007). As a clustered control, Tfn molecules labeled with Alexa Fluor 488 (Donor) or Alexa Fluor 555 (Acceptor) fluorophores were bound to TFR, a well-known homo-dimeric membrane-bound receptor, at the PM and TFR–Tfn complexes were internalized for 30 min at 37 °C (Fig. 7, Panel 1A). For a random distribution control, Tfn molecules labeled with Alexa Fluor 488 (Donor) or Alexa Fluor 555 (Acceptor) fluorophores were bound to a polylysine substrate (Fig. 7, Panel 1B) (Wallrabe *et al.*, 2007). These samples were then imaged using FRET-confocal microscopy (Fig. 7, Panels 2A and B) and the respective images were processed using PFRET algorithm (Fig. 7, Panel 3) and the resulting *E*%, *A*, and *D*/*A* ratios were analyzed for the *E*% versus *A* relationship under specific *D*/*A* ratios (Fig. 7, Panels 4A and B). To show whether *E*% is affected by increasing levels of *A* at specific *D*/*A* ranges as requested by FRET quantitative analysis to discriminate between random and clustered protein organizations, the data was arranged into several *D*/*A* and *A* ranges (Wallrabe *et al.*, 2003a, 2007). For *D*/*A* ranges, we used the following ranges: $D/A \approx 1$ ranged from *D*/*A* values of 0.7–1.4 (data not shown), whereas $D/A \approx 2$ ranged from values of 1.4–2.8 (Figs. 8 and 9).

4. Differentiating Between Random Versus Clustered Cellular Distribution of Membrane Proteins

The relationship of *E* % versus *A* and *D* intensity levels and the *D*/*A* ratio provides powerful evidence as to whether we are looking at a random, clustered, or mixed membrane protein distribution as described previously (Kenworthy and Edidin, 1998; Kenworthy *et al.*, 2000; Pentcheva *et al.*, 2002; Spiliotis *et al.*, 2002; Wallrabe *et al.*, 2003a, 2007). It is important to stress that FRET occurs in all of these situations. In a purely random distribution, *E* % rises with increasing acceptor fluorescence intensity levels, on the basis that there is more opportunity for a donor to make contact with an acceptor and transfer energy (Fig. 8A). In a purely

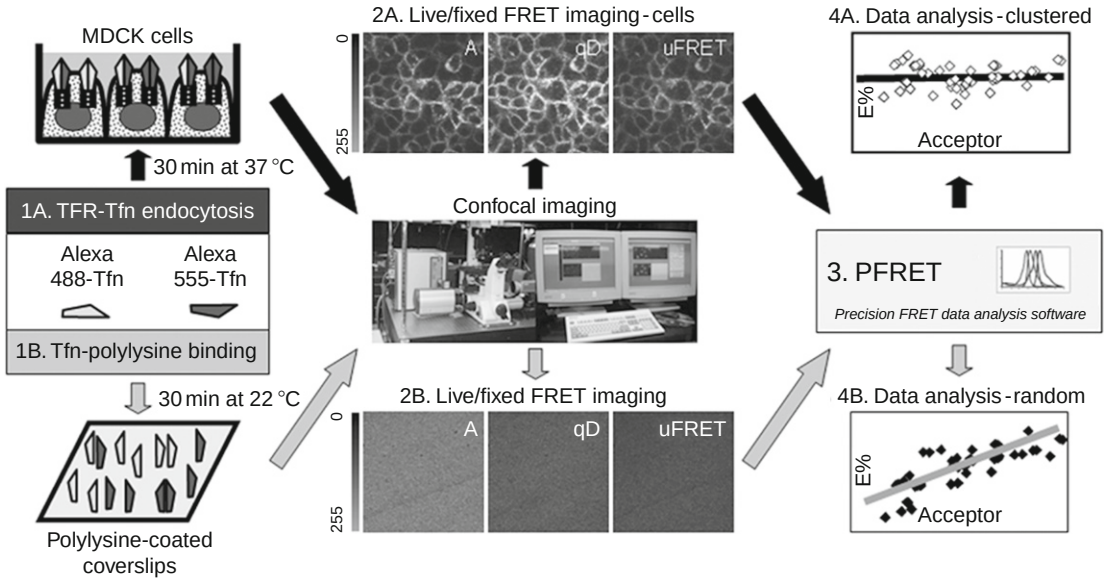

Fig. 7 Experimental flowchart of quantitative FRET analysis. (A) Endocytosis of TFR–Tfn complexes. (B) Tfn binding to polylysine-coated coverslips. Four important steps account for quantitative FRET analysis. (1) *In vivo* or *in vitro* binding, internalization or overexpression of fluorophore-labeled probes in cells, tissues or other substrates, such as polylysine-coated coverslips. (2) Live or fixed confocal FRET imaging using single- and double-labeled samples. Other imaging instruments such as wide-field microscopes can replace confocal microscopy in quantitative FRET assays. Acceptor, donor, and FRET-imaging channels, as described in Fig. 3, are used to collect acceptor (A), quenched donor (qD), and uncorrected FRET (uFRET) images. (3) Those images are then used for processing using PFRET algorithm SBT correction. (4) Data extracted from selected ROIs is then plotted in A versus $E\%$ charts to discriminate between clustered and random protein organizations.

clustered organization, where the components by definition are in proximity, $E\%$ is largely independent of acceptor levels and does not trend to zero upon decreasing acceptor levels, as a donor can only transfer energy to one acceptor at a time (Fig. 9A). Consideration must be given to the likelihood that with a surfeit of acceptors, there is a greater possibility that donor and acceptor are in a favorable dipole position for energy transfer to take place; the accepted probability contained in the original Förster equation is that this will happen 2/3 of the time. Furthermore, $E\%$ versus D/A is used to provide further insights into protein organization (Wallrabe *et al.*, 2003a, b, 2006). A cluster organization predicts a negative dependency between $E\%$ and D/A, whereas a random organization shows $E\%$ independent of D/A (data not shown). A mixed random/clustered organization, in which an assortment of clusters and randomly distributed proteins are found, shows a more complex relationship between $E\%$, A, and D/A (Bhatia *et al.*, 2005; Pentcheva and Edidin, 2001; Wallrabe *et al.*, 2007).

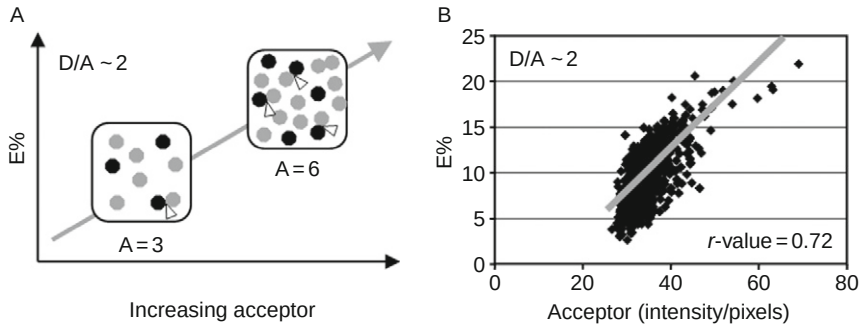

Fig. 8 Quantitative PFRET analysis to study the random organization of donor- and acceptor Tfn bound to polylysine-coated coverslips. (A) A random organization model, *E*% is dependent on acceptor levels. White arrowheads indicate FRET events. Gray circles: Donor molecules. Black circles: Acceptor molecules. (B) Alexa 488- and Alexa 555-Tfn are bound to polylysine-covered coverslips, imaged by confocal microscopy and processed for PFRET analysis. The *A, D*/*A*, and *E*% values were extracted for a wide variety of ROIs and plotted against *A* levels at $D/A \sim 2$ (diamonds). *E*% shows a clear dependency on *A* levels. Trendlines are shown as visual helpers.

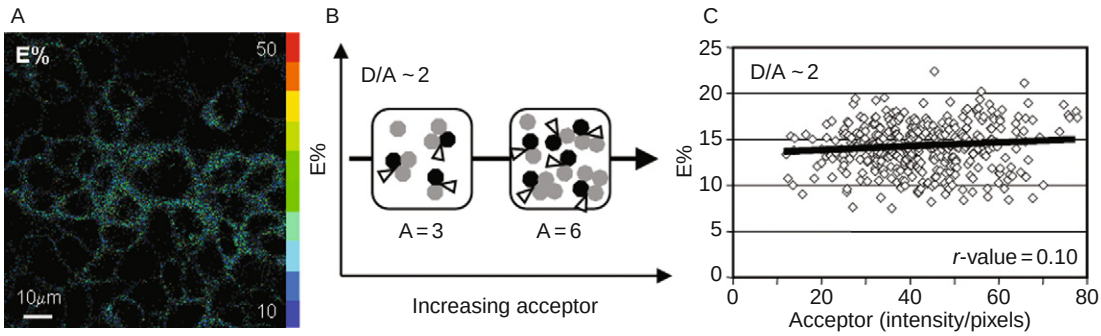

Fig. 9 Quantitative PFRET analysis to study the clustered organization of receptor–ligand (TFR–Tfn) complexes in basolateral endocytic membranes. (A) Pseudo-color image shows *E*% levels in a typical basolateral endocytic pattern. (B) In a clustered organization model, *E*% is independent of acceptor levels. White arrowheads indicate FRET events. Gray circles: Donor molecules. Black circles: Acceptor molecules. (C) Alexa 488- and Alexa 555-Tfn are bound to TFR at the basolateral PM and internalized for 30 min at 37 °C, imaged by confocal microscopy and processed for PFRET analysis. The *A, D*/*A*, and *E*% values were extracted for a wide variety of ROIs and plotted against *A* levels. *E*% is largely independent from *A* levels. Trendlines are shown as visual helpers.

5. Polylysine- Versus Cell-based FRET Controls

In the negative clustering control (random distribution), where Tfn are bound to polylysine-coated cover slips, *E*% is dependent on the *A* fluorescence levels. Without receptors and cellular regulation, one would expect the Tfn ligands (donors and acceptors) to attach randomly to the polylysine surface. As expected,

$E\%$ is clearly dependent on the A levels at the specific range of $D/A \sim 2$ (Fig. 8B). In contrast, TFR–Tfn complexes internalized into MDCK–PTR cells clearly show a clustered distribution pattern, with $E\%$ largely independent of the A levels at the specific range of $D/A \sim 2$ (Fig. 9B). The pseudocolor $E\%$ image highlights the endocytic morphology of a polarized cell layer at the basolateral focal plane near the nucleus, clearly showing different punctate structures with high and low levels of $E\%$ (Fig. 9C). In the cell-based data, a proportion of TFR homo-dimers will carry—based on probability of internalization concentrations—both donor and acceptor molecules leading to intra-dimer FRET (Fig. 10); a dimer must be considered a small cluster in this context. However, we cannot exclude the existence of inter-dimer FRET events between different TFR–Tfn complexes (higher-order clusters) during endocytic trafficking (Fig. 10). Several lines of evidence suggest that such higher-order clustering may actually be occurring:

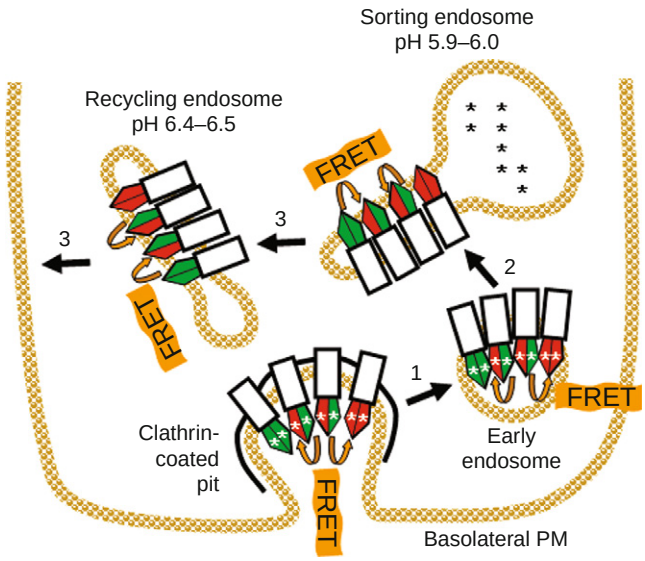

Fig. 10 FRET-based model for the organization of TFR–Tfn complexes in basolateral endocytic membranes. (1) TFR–Tfn complexes are bound to TFR at the basolateral PM and endocytosed via clathrin-coated pits. Different TFR–Tfn complexes can be formed depending on the presence of donor- and/or acceptor-labeled Tfn. TFR may be bound to: one donor-labeled and one acceptor-labeled Tfn molecules (red/green diamonds); two donor-labeled Tfn (green/green diamonds), or two acceptor-labeled Tfn (red/ red diamonds). (2) Clathrin-coated vesicles deliver TFR–Tfn complexes to the early endosomes and sorting endosomes, where in the presence of low pH, TFR–Tfn complexes release their iron content and apo complexes accumulate in the tubular region. (3) Tubular–vesicular structures deliver apo TFR–Tfn complexes from the sorting endosomes back to the basolateral PM via the recycling endosomes. In steps 1–3, FRET (yellow arrow) can occur between donor- and acceptor-labeled Tfn molecules bound to a TFR homodimer (intra-dimer FRET) as well as between donor- and acceptor-labeled Tfn molecules bound to different TFR dimers (inter-dimer FRET). Asterisks: iron molecule; white rectangle: TFR.

(1) The structure of the TFR–Tfn dimer indicates that the distance between the Tfn molecules should be ~80–100 nm (Cheng *et al.*, 2004; Lawrence *et al.*, 1999), at the lower $E\%$ threshold considering the R_0 of the Alexa Fluor 488–Alexa Fluor 555 FRET pair (Elangovan *et al.*, 2003; Wallrabe *et al.*, 2003a). (2) The Hardy–Weinberg probability calculation that projects the binding of donor- and acceptor-labeled Tfn molecules to TFR homo-dimers should also reduce the $E\%$ levels due to the formation of acceptor-labeled or donor-labeled TFR–Tfn complexes. (3) Furthermore, internalization of donor-labeled and acceptor-labeled TFR–Tfn complexes from opposite PM domains results in significant $E\%$ levels (data not shown); such behavior suggest that donor-labeled and acceptor-labeled TFR–Tfn complexes form higher-order clusters during endocytic trafficking, as suggested for other receptor–ligand complexes (Wallrabe *et al.*, 2003a, 2007).

6. Statistical Analysis

As with any data analysis, it is important to support charts and conclusions with rigorous statistical evaluations. Whether these are correlation coefficients, *t*-tests and *p*-values, ANOVA, etc., any additional mathematical modeling will depend on the objectives and the particular data set. Several statistical analysis parameters can be used to quantitate our ability to discriminate between random and clustered distribution using the $E\%$ versus A relationship (Wallrabe *et al.*, 2003b, 2006, 2007). One is the correlation coefficient (r-value); the closer the r-values are to 0 ($r < 0.5$), the less-dependent $E\%$ is on acceptor levels; the closer r-values are to 1 ($r \geq 0.5$), the more $E\%$ depends on acceptor levels. Therefore, when $r < 0.5$, the protein organization trends to the clustered distribution, and when $r \geq 0.5$, the random "molecular crowding" protein distribution should be predominant. The chart trendlines are helpful as visual markers but must not be the only indicator of differences, as ranges in x- and y-axis can visually distort the significance. Other parameters can be used such as the one-way ANOVA to establish whether $E\%$ cohorts at different acceptor levels were significantly different or not and the ANCOVA analysis using [R] to assess whether the treatment (alone) has an effect or not on the protein distribution. Statistical analysis allows powerful deductions to be made about the nature of membrane protein distribution. To measure the independence or otherwise of $E\%$ versus A and D:A, correlation coefficients are a reliable indicator. For example, in the polylysine data set, the correlation coefficient value is clearly above 0.5, with $r = 0.72$ (Fig. 8B), indicating that $E\%$ is dependent on A levels. On the other hand, in the cell-based TFR–Tfn data, correlation coefficient value is closer to 0, with $r = 0.1$ (Fig. 9B), indicating that $E\%$ is independent from A levels. In summary, this analysis confirms that Tfn bound to polylysine shows a random distribution, whereas Tfn bound to TFR in cells displays a clear clustered organization in endocytic membranes. These two systems can be used as parameters to distinguish between clustered versus random protein distributions, providing an important tool for the further investigation of the nature of the organization of different protein components in intracellular membranes.

V. Summary

The quantitative FRET assays presented here provide a versatile and powerful tool to analyze the organization of membrane proteins and it can be applied to many biological situations. Cooperation with other disciplines from statistics, mathematics, physics, and others leads to multiple levels of information about biological processes that qualitative investigation rarely provides. Here we present two FRET assays, the Tfn-bound to polylysine system or the TFR–Tfn cell-based system. Using extensive quantitative analysis and statistical evaluations, we have characterized these two systems as important examples to distinguish between random ''molecular crowding'' distribution (Tfn-bound polylysine data) and a typical clustered organization (TFR–Tfn cell-based data). These examples can be used to determine whether cellular components are forming clusters are randomly distributed with occasional encounters resulting in a FRET signal or possibly a mixture of the two. The latter is quite relevant in biological systems where a continuum between various stages of assembly may coexist.

For some time, FRET microscopy has been developing into a mainstream technique to investigate cellular and other processes that benefit from its unique ability to infer proximity between components in the 1–10 nm range. FRET measurements can be made with a wide range of microscopy systems and offers unique opportunities for quantitative analysis, as described in this book chapter. However, to draw conclusions with confidence from this quantitative approach, careful optimization of the specimen preparation and image collection is required. Dealing with SBT, background noise, collecting appropriate ROIs, evaluating ''outliers,'' and conducting statistical analyses are all part of this quantitative data collection. As mentioned, the basic assays presented here can be applied to many different experimental models in the life science areas.

References

Ballestrem, C., Erez, N., Kirchner, J., Kam, Z., Bershadsky, A., and Geiger, B. (2006). Molecular mapping of tyrosine-phosphorylated proteins in focal adhesions using fluorescence resonance energy transfer. *J. Cell Sci.* **119,** 866–875.

Barroso, M., and Sztul, E. S. (1994). Basolateral to apical transcytosis in polarized cells is indirect and involves BFA and trimeric G protein sensitive passage through the apical endosome. *J. Cell Biol.* **124,** 83–100.

Bastiaens, P. I., and Jovin, T. M. (1996). Microspectroscopic imaging tracks the intracellular processing of a signal transduction protein: Fluorescent-labeled protein kinase C beta I. *Proc. Natl. Acad. Sci. USA* **93,** 8407–8412.

Berney, C., and Danuser, G. (2003). FRET or no FRET: A quantitative comparison. *Biophys. J.* **84,** 3992–4010.

Bhatia, S., Edidin, M., Almo, S. C., and Nathenson, S. G. (2005). Different cell surface oligomeric states of B7–1 and B7–2: Implications for signaling. *Proc. Natl. Acad. Sci USA* **102,** 15569–15574.

Bonamy, G. M., Guiochon-Mantel, A., and Allison, L. A. (2005). Cancer promoted by the oncoprotein v-ErbA may be due to subcellular mislocalization of nuclear receptors. *Mol. Endocrinol.* **19,** 1213–1230.

Chamberlain, C. E., Kraynov, V. S., and Hahn, K. M. (2000). Imaging spatiotemporal dynamics of Rac activation *in vivo* with FLAIR. *Methods Enzymol.* **325,** 389–400.

Cheng, Y., Zak, O., Aisen, P., Harrison, S. C., and Walz, T. (2004). Structure of the human transferrin receptor-transferrin complex. *Cell* **116,** 565–576.

Chen, Y., Elangovan, M., and Periasamy, A. (2005). FRET dData aAnalysis: The aAlgorithm. *In* ''Molecular Imaging: FRET Microscopy and Spectroscopy'' (A. Periasamy, and R. N. Day, eds.), pp. 126–145. Oxford University Press, New York, 126–145.

Chen, Y., Mauldin, J. P., Day, R. N., and Periasamy, A. (2007). Characterization of spectral FRET imaging microscopy for monitoring the nuclear protein interactions. *J. Microscopy* **228**(2), 139–152.

Chen, Y., Mills, J. D., and Periasamy, A. (2003). Protein localization in living cells and tissues using FRET and FLIM. *Differentiation* **71,** 528–541.

Chen, Y., and Periasamy, A. (2004). Characterization of two-photon excitation fluorescence lifetime imaging microscopy for protein localization. *Microsc. Res. Tech.* **63,** 72–80.

Clegg, R. M. (1995). Fluorescence resonance energy transfer. *Curr. Opin. Biotechnol.* **6,** 103–110.

Day, R. N., Periasamy, A., and Schaufele, F. (2001). Fluorescence resonance energy transfer microscopy of localized protein interactions in the living cell nucleus. *Methods* **25,** 4–18.

Day, R. N., Voss, T. C., Enwright, J. F., III, Booker, C. F., Periasamy, A., and Schaufele, F. (2003). Imaging the localized protein interactions between Pit-1 and the CCAAT/enhancer binding protein alpha in the living pituitary cell nucleus. *Mol. Endocrinol.* **17,** 333–345.

Demarco, I. A., Periasamy, A., Booker, C. F., and Day, R. N. (2006a). Monitoring dynamic protein interactions with photoquenching FRET. *Nat. Methods* **3,** 519–524.

Demarco, I. A., Voss, T. C., Booker, C. F., and Day, R. N. (2006b). Dynamic interactions between Pit-1 and C/EBPalpha in the pituitary cell nucleus. *Mol. Cell Biol.* **26,** 8087–8098.

Di, W. L., Gu, Y., Common, J. E., Aasen, T., O'Toole, E. A., Kelsell, D. P., and Zicha, D. (2005). Connexin interaction patterns in keratinocytes revealed morphologically and by FRET analysis. *J. Cell Sci.* **118,** 1505–1514.

Dobbie, I. M., Lowndes, N. F., and Sullivan, K. F. (2008). Autofluorescent proteins. *Methods Cell Biol.* **85,** 1–22.

Elangovan, M., Wallrabe, H., Chen, Y., Day, R. N., Barroso, M., and Periasamy, A. (2003). Characterization of one- and two-photon excitation fluorescence resonance energy transfer microscopy. *Methods* **29,** 58–73.

Forster, T. (1965). Delocalized excitation and excitation transfer. *In* ''Modern Quantum Chemistry Part III: Action of Light and Organic Crystals'' (O. Sinanoglu, ed.), pp. 93–137. Academic Press, New York.

Giepmans, B. N., Adams, S. R., Ellisman, M. H., and Tsien, R. Y. (2006). The fluorescent toolbox for assessing protein location and function. *Science* **312,** 217–224.

Gordon, G. W., Berry, G., Liang, X. H., Levine, B., and Herman, B. (1998). Quantitative fluorescence resonance energy transfer measurements using fluorescence microscopy. *Biophys. J.* **74,** 2702–2713.

Herrick-Davis, K., Grinde, E., and Mazurkiewicz, J. E. (2004). Biochemical and biophysical characterization of serotonin 5-HT2C receptor homodimers on the plasma membrane of living cells. *Biochemistry* **43,** 13963–13971.

Hoppe, A., Christensen, K., and Swanson, J. A. (2002). Fluorescence resonance energy transfer-based stoichiometry in living cells. *Biophys. J.* **83,** 3652–3664.

Jares-Erijman, E. A., and Jovin, T. M. (2003). FRET imaging. *Nat. Biotechnol.* **21,** 1387–1395.

Kenworthy, A. K. (2001). Imaging protein-protein interactions using fluorescence resonance energy transfer microscopy. *Methods* **24,** 289–296.

Kenworthy, A. K., and Edidin, M. (1998). Distribution of a glycosylphosphatidylinositol-anchored protein at the apical surface of MDCK cells examined at a resolution of $<$100 A using imaging fluorescence resonance energy transfer. *J. Cell Biol.* **142,** 69–84.

Kenworthy, A. K., Petranova, N., and Edidin, M. (2000). High-resolution FRET microscopy of cholera toxin B-subunit and GPI-anchored proteins in cell plasma membranes. *Mol. Biol. Cell* **11,** 1645–1655.

Kiskowski, M. A., and Kenworthy, A. K. (2007). In silico characterization of resonance energy transfer for disk-shaped membrane domains. *Biophys. J.* **92,** 3040–3051.

Knight, M. M., Roberts, S. R., Lee, D. A., and Bader, D. L. (2003). Live cell imaging using confocal microscopy induces intracellular calcium transients and cell death. *Am. J. Physiol. Cell Physiol.* **284,** C1083–C1089.

Lakowicz, J. R. (1999). "Principles of Fluorescence Spectroscopy." 2nd edn., Kluwer Academic/Plenum Publishers, New York.

Lakowicz, J. R., Gryczynski, I., Gryczynski, Z., and Dattelbaum, J. D. (1999). Anisotropy-based sensing with reference fluorophores. *Anal. Biochem.* **267,** 397–405.

Lawrence, C. M., Ray, S., Babyonyshev, M., Galluser, R., Borhani, D. W., and Harrison, S. C. (1999). Crystal structure of the ectodomain of human transferrin receptor. *Science* **286,** 779–782.

Maxfield, F. R., and McGraw, T. E. (2004). Endocytic recycling. *Nat. Rev. Mol. Cell Biol.* **5,** 121–132.

Mills, J. D., Stone, J. R., Rubin, D. G., Melon, D. E., Okonkwo, D. O., Periasamy, A., and Helm, G. A. (2003). Illuminating protein interactions in tissue using confocal and two-photon excitation fluorescent resonance energy transfer microscopy. *J. Biomed. Opt.* **8,** 347–356.

Nakamura, T., Kurokawa, K., Kiyokawa, E., and Matsuda, M. (2006). Analysis of the spatiotemporal activation of rho GTPases using Raichu probes. *Methods Enzymol.* **406,** 315–332.

Patterson, G. H., and Lippincott-Schwartz, J. (2002). A photoactivatable GFP for selective photolabeling of proteins and cells. *Science* **297,** 1873–1877.

Pentcheva, T., and Edidin, M. (2001). Clustering of peptide-loaded MHC class I molecules for endoplasmic reticulum export imaged by fluorescence resonance energy transfer. *J. Immunol.* **166,** 6625–6632.

Pentcheva, T., Spiliotis, E. T., and Edidin, M. (2002). Cutting edge: Tapasin is retained in the endoplasmic reticulum by dynamic clustering and exclusion from endoplasmic reticulum exit sites. *J. Immunol.* **168,** 1538–1541.

Periasamy, A., and Day, R. N. (1999). Visualizing protein interactions in living cells using digitized GFP imaging and FRET microscopy. *Methods Cell Biol.* **58,** 293–314.

Periasamy, A., and Day, R. N. (2005). "Molecular Imaging: FRET Microscopy and Spectroscopy." Oxford University Press, NY.

Rao, M., and Mayor, S. (2005). Use of Forster's resonance energy transfer microscopy to study lipid rafts. *Biochim. Biophys. Acta* **1746,** 221–233.

Richardson, D. R. (2004). Mysteries of the transferrin–transferrin receptor 1 interaction uncovered. *Cell* **116,** 483–485.

Spiliotis, E. T., Pentcheva, T., and Edidin, M. (2002). Probing for membrane domains in the endoplasmic reticulum: Retention and degradation of unassembled MHC class I molecules. *Mol. Biol. Cell* **13,** 1566–1581.

Tsien, R. Y., and Miyawaki, A. (1998). Seeing the machinery of live cells. *Science* **280,** 1954–1955.

Vamosi, G., Bodnar, A., Vereb, G., Jenei, A., Goldman, C. K., Langowski, J., Toth, K., Matyus, L., Szollosi, J., Waldmann, T. A., and Damjanovich, S. (2004). IL-2 and IL-15 receptor alpha-subunits are coexpressed in a supramolecular receptor cluster in lipid rafts of T cells. *Proc. Natl. Acad. Sci. USA* **101,** 11082–11087.

Vogel, S. S., Thaler, C., and Koushik, S. V. (2006). Fanciful FRET. *Sci. STKE* **2006,** re2.

Wallrabe, H., and Barroso, M. (2005). Confocal FRET microscopy: Study of clustered distribution of receptor-ligand complexes in endocytic membranes. *In* "Molecular Imaging: FRET Microscopy and Spectroscopy" (A. Periasamy, and R. N. Day, eds.), pp. 95–111. Oxford University Press, New York.

Wallrabe, H., Bonamy, G., Periasamy, A., and Barroso, M. (2007). Receptor complexes cotransported via polarized endocytic pathways form clusters with distinct organizations. *Mol. Cell Biol.* **18,** 2226–2243.

Wallrabe, H., Chen, Y., Periasamy, A., and Barroso, M. (2006). Issues in confocal microscopy for quantitative FRET analysis. *Microsc. Res. Tech.* **69,** 196–206.

Wallrabe, H., Elangovan, M., Burchard, A., Periasamy, A., and Barroso, M. (2003a). Confocal FRET microscopy to measure clustering of ligand-receptor complexes in endocytic membranes. *Biophys. J.* **85,** 559–571.

Wallrabe, H., and Periasamy, A. (2005). Imaging protein molecules using FRET and FLIM microscopy. *Curr. Opin. Biotechnol.* **16,** 19–27.

Wallrabe, H., Stanley, M., Periasamy, A., and Barroso, M. (2003b). One- and two-photon fluorescence resonance energy transfer microscopy to establish a clustered distribution of receptor-ligand complexes in endocytic membranes. *J. Biomed. Opt.* **8,** 339–346.

Wouters, F. S., Bastiaens, P. I., Wirtz, K. W., and Jovin, T. M. (1998). FRET microscopy demonstrates molecular association of non-specific lipid transfer protein (nsL-TP) with fatty acid oxidation enzymes in peroxisomes. *EMBO J.* **17,** 7179–7189.

Wu, S., Xing, D., Wang, F., Chen, T., and Chen, W. R. (2007). Mechanistic study of apoptosis induced by high-fluence low-power laser irradiation using fluorescence imaging techniques. *J. Biomed. Opt.* **12,** 064015.

Xia, Z., and Liu, Y. (2001). Reliable and global measurement of fluorescence resonance energy transfer using fluorescence microscopes. *Biophys. J.* **81,** 2395–2402.

Zal, T., Zal, M. A., and Gascoigne, N. R. (2002). Inhibition of T cell receptor-coreceptor interactions by antagonist ligands visualized by live FRET imaging of the T-hybridoma immunological synapse. *Immunity* **16,** 521–534.

CHAPTER 23

Stochastic Modeling Methods in Cell Biology

Sean X. Sun,[*] Ganhui Lan,[*] and Erdinc Atilgan[†]

[*]Department of Mechanical Engineering and Biomedical Engineering
Johns Hopkins University
Baltimore, Maryland 21218

[†]Department of Anatomy and Structural Biology
Albert Einstein College of Medicine and Yeshiva University
Bronx, New York 10461

Abstract

Stochastic methods have been a staple for understanding complex systems in chemistry and physics. In the biological context, they are useful for understanding phenomena ranging from molecular-level fluctuations to cellular movement. We review the basic formalism behind stochastic methods and outline how they can be implemented for quantifying gene expression, movement of molecular motors, and the dynamics of cytoplasmic components. We show that stochastic methods are quantitative checks for proposed molecular mechanisms and can pose new

METHODS IN CELL BIOLOGY, VOL. 89

0091-679X/08 $35.00
DOI: 10.1016/S0091-679X(08)00623-7

questions for experiments. Structural information of cellular components can be incorporated into stochastic models to reveal new biological insights.

I. Introduction

As the name suggests, stochastic methods have an element of randomness that gives rise to probabilistic behavior. However, the justification of the method is firmly rooted in physics, and is an emerging principle in systems with many reacting/interacting components. The method is equally applicable to analyzing conformational transitions in a single molecule, or reaction dynamics in a cell with millions of proteins. The general argument starts from the microscopic equation of motion for atoms and molecules. Let us first consider a single protein in solution (Fig. 1). Typically, we are not interested in the motions of all the components (e.g., solvents), but are only interested in the motions of a selected set of degrees of freedom (e.g., the angle between two domains in Fig. 1). From the deterministic Newton's equation for all the atoms in the system, one can derive equations of motion for the select set (Hanggi *et al.*, 1990):

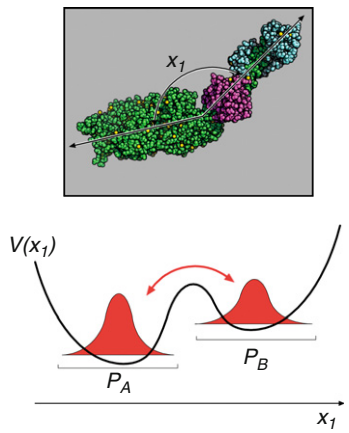

Fig. 1 In a complex system, only a few degrees of freedom are of specific interest. For example, this protein in solution undergoes a conformational change and the value of x_1 is the quantity of interest. The effective equation of motion for x_1 is given in Eq. (1). The free energy of the system as a function of x_1 typically shows several local minima (lower panel). The system fluctuates between these energetic basins (reactants and products), and these fluctuations are described by time dependent probability distributions (red distributions). Instead of considering continuous probability distributions, we can consider discrete probabilities, P_A and P_B, which are the integrals of the distributions over the basin regions. The dynamics of P_A and P_B are described by the Markov model in Eq. (2). Stochastic simulations of the model will give trajectories that jump between the basins.

$$\gamma \frac{\partial x_i}{\partial t} = -\frac{\partial V(x_1, x_2, \ldots)}{\partial x_i} + R(t) \quad (1)$$

where $V(x_1, x_2, \ldots)$ is the free energy as a function of the selected degrees of freedom while the other uninteresting degrees of freedom are in thermal equilibrium; γ is a friction constant related to energy loss to the uninteresting degrees of freedom; $R(t)$ is a random force representing the random bombardment of solvent molecules on x_i. When $V(x_1, x_2, \ldots)$ is zero or a constant, the familiar equation for the Brownian motion of a structureless particle results. However, $(x_1, x_2, \ldots)$ can be much more general. For example, they could represent the conformations of a protein or the coordinates of a substrate in an enzyme. The qualitative features of $V(x_1, x_2, \ldots)$ typically show several metastable minima, separated by barriers (Fig. 1). If there are many interesting degrees of freedom, then $V(x_1, x_2, \ldots)$ is a function of many variables too complex to be drawn here.

For typical biomolecular applications inside the cell, friction and random forces are dominant factors; trajectories from Eq. (1) show large fluctuations. The probability of observing a particular trajectory depends on the random force history. Therefore, it is more convenient to consider a time-dependent probability distribution, $P(x_1, x_2, \ldots, t)$, representing many trajectories averaged over the random forces. The evolution of $P(x_1, x_2, \ldots, t)$ on the energy landscape $V(x_1, x_2, \ldots)$ is described by the Fokker–Planck equation, which can be derived from Eq. (1) from first principles (Risken, 1989). Figure 1 shows a hypothetical energy landscape with two minima. If $P(x_1, x_2, \ldots, t)$ at $t = 0$ is concentrated at one of the minima, one will see an exponential increase of the probability in the other minima. The exponential time constant is related to a "rate constant" familiar from kinetic theories. A molecular theory of reaction rate can be derived from statistical mechanics and the fluctuation–dissipation theorem, and is discussed elsewhere (Chandler, 1987).

Behaviors of probability distributions separated by barriers are relatively independent of the detailed features of the energy landscape. The forward and reverse rate constants are most sensitive to the height of the barrier and the features of the barrier immediately surrounding the transition state (reaction bottleneck) (Hanggi *et al.*, 1990). If we integrate over regions of the probability distribution near the basins of stable states and re-label these regions as P_A, P_B, etc, where A and B now label these energetic basins, then the time-dependent behavior of $P_A(t)$ and $P_B(t)$ can be described by a generic set of dynamic equations, the so-called Master equation,

$$\frac{dP_A}{dt} = -k_1 P_A + k_2 P_B \quad \frac{dP_B}{dt} = k_1 P_A - k_2 P_B \quad (2)$$

These basins described by A and B are now recognized as chemical species, or reactants and products. Fluxes between these basins are related to forward and reverse rate constants k_1 and k_2, respectively. Note that this development simplifies the discussion of probability flow on the energy landscape; instead of considering a

continuous probability distribution, we are reduced to discrete probabilities of two states. The trade-off is the introduction of parameters k_1 and k_2, which typically must be measured from experiments; only very rarely can one compute the rate constants from first principles. Equation (2) is a simple 2-state *Markov chain* model and describes a *single* conversion process where one reactant is converted into one product. Analytic solutions to Eq. (2) are readily available.

The forward and reverse rate constants, k_1 and k_2, are related to the flux across the barrier. At steady-state, forward and reverse fluxes must be balanced to obtain a steady equilibrium probability distribution. The equilibrium probability distribution, in turn, depends on the relative energy difference between A and B. Thus, the condition of detailed balance requires that the ratio of the rate constants must be, $k_1/k_2 = e^{-(F_B - F_A)/k_B T}$, where $F_{A,B}$ are the free energies of A and B, respectively. k_B is the Boltzmann constant and T is the temperature. (At room temperature, $k_B T$ is roughly 0.6 kcal/mol.) This requirement ensures that Eq. (2) reproduces the correct equilibrium distribution at steady state. Suppose a force is applied along the x_1 direction in Fig. 1, then the energy landscape would be changed, and the relative energies of A and B would be changed. The forward and reverse rate constants then must be changed to reflect the energy change. A simple model to account for this is the Bell model (Bell, 1978; Hummer and Szabo, 2003). This issue is important whenever forces are present in biomolecular systems.

In more complex situations, there may be more than two basins in the energy landscape. Probabilities in these basins, P_A, P_B, P_C, etc., can flow among each other, resulting in a multi-state Markov model. Such models have been used to describe motions of molecular motors seen in single molecule experiments. Therefore, a multi-state Markov model is usually the basic starting point for stochastic simulation methods. Let us consider a simple multistate example. Let us take the example in Eq. (2), but for N reacting molecules shown in Fig. 2. The Master equation approach is still applicable, but we must redefine the definition of a Markov state: $s = (N_A, N_B)$ where N_A and N_B are the number of reactants and products, respectively. For example, if there are 10 molecules, then $N_A + N_B = 10$. The total number of states is 11, e.g., $s = (10,0)$ is a state, as well as $s = (9,1)$ and $s = (1,9)$, etc. Instead of 2 equations, we have 11 equations, one for each P_s. The rate constants k_1 and k_2 again describe conversions between states, e.g., $s = (10,0)$ can become $s = (9,1)$ with rate k_1, and $s = (9,1)$ can become $s = (10,0)$ with rate k_2. Not all of the states can directly convert to others; for example, $s = (5,5)$ cannot become $s = (2,8)$ with one reaction. However, $s = (5,5)$ can be converted to $s = (2,8)$ with three successive reactions, or jumps. Figure 2 shows one possible sequence of reactions in this system. The probability of observing the system in a particular state is obtained by solving a system of equations such as Eq. (2). Since there are now 11 states, Eq. (2) becomes a set of equations

$$\frac{dP_s}{dt} = -(k_1 + k_2)P_s + k_1 P_{s-1} + k_2 P_{s+1} \tag{3}$$

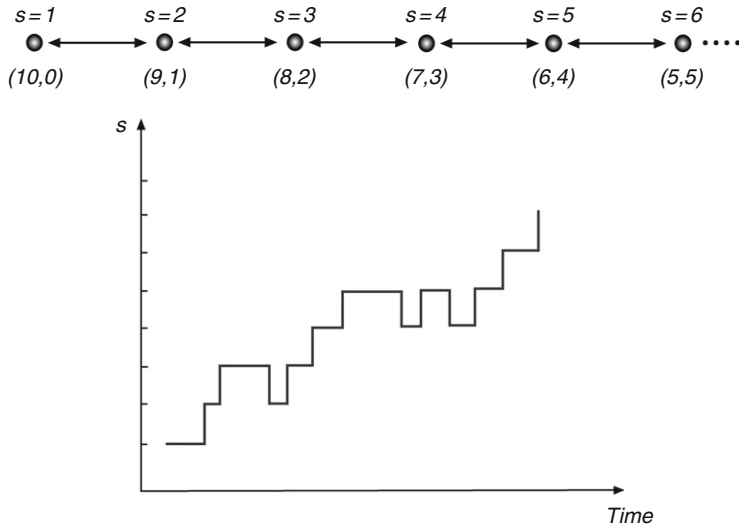

Fig. 2 A multistate Markov model where each state is characterized by the number of reactants and products, N_A and N_B, respectively. For example, $s = 1$ labels $N_A = 10$ and $N_B = 0$. The probability to be in a particular state is described by Eq. (3). A stochastic simulation will show jumps between states and stochastic changes in N_A and N_B.

where s denotes the index of the state. Note that this equation needs to be modified slightly for $s = 1$ and $s = 11$, since there are no $s - 1$ and $s + 1$ states, respectively. Solutions of Eq. (3) give the probability of observing a particular combination of reactants and products. It can be written in a matrix form and implemented using ordinary differential equation solvers in standard packages such as MATLAB.

So far, we have discussed a relatively general model of probability flow between energetic basins using the concept of Markov states. Indeed, the concept is not limited to reacting species because the definition of a Markov state can be much broader. A state can be generalized to regions of the energy surface even when there are no barriers separating them. For example, a diffusing particle can be modeled by a diffusion equation or by a Markov model where the particle hops on a lattice (Wang *et al.*, 2003). The rate of hopping is related to the diffusion constant. In this way, it is possible to model reactions and diffusions of a set of proteins and examine their spatial and temporal dynamics. Spatial hopping algorithms together with reactions have been applied to the MinCDE system in *Escherichia coli* to quantify the spatial–temporal oscillations of these proteins (Kerr *et al.*, 2006; Lutkenhaus, 2007).

When the number of reacting species is large, the number of Markov states increases. This leads to many equations of the form of Eq. (3), and can become prohibitively difficult to solve numerically. Therefore, instead of considering

reactions of individual molecules, we can examine the changes in species concentration. In the simple case of Eq. (2), the concentrations of A and B, C_A and C_B, are related to the probabilities P_A and P_B by a unit conversion. By considering the number of collisions between the reacting partners, familiar kinetic equations emerge. Therefore, the equations for C_A and C_B are the same as Eq. (2) and are the familiar kinetic equations for conversion between A and B. For more complicated situations involving many reacting species, kinetic equations can become nonlinear and exhibit complex and interesting dynamics. Kinetic models can be understood as a mean field approximation to the Master equation where instead of examining microscopic Markov states an equation for a set of averaged quantities is computed. This chapter will not discuss kinetic models, other than to point out that Markov Master equations models can be considered a detailed version of kinetic models. The reader can refer to many available textbooks on kinetic models (e.g., Murray, 1989; Reichl, 1998).

Solutions to equations such as Eq. (3) give the probability of observing a particular Markov state in time, $P_s(t)$. In an experiment, a sequence of states is usually measured. Only after averaging over many measurements, or an ensemble of the same event, does one obtain the probability of observing a particular state. Can we directly compare a single experiment with Eq. (3)? The answer is to use stochastic simulations. A method that is consistent with Eq. (3) was developed in the context of magnetic spin dynamics (Bortz *et al.*, 1975). The same stochastic simulation method applied to chemical reactions was developed by Gillespie (1977), and in this chapter, we shall refer to the algorithm as the Gillespie algorithm. We note that the Gillespie algorithm is a form of importance sampling, much like the Metropolis Monte Carlo algorithm in equilibrium simulations. The algorithm generates probable sequences of states and jump times (trajectories). The probability distribution sampled by the Gillespie algorithm is a time-dependent nonequilibrium distribution consistent with equations such as Eq. (3) (Sun, 2006). The procedure for generating Gillespie trajectories is described in Section V.

Since the algorithm generates stochastic trajectories according to their probability, we can compute observables by directly averaging over the trajectories. Suppose we are interested in measuring a particular quantity, $Z(t)$, which could be a function of time, we can directly evaluate:

$$Z(t) = \frac{1}{N}\sum_{i=1}^{N} Z_i(t) \tag{4}$$

where N is the number of trajectories and $Z_i(t)$ is the quantity of interest evaluated for the ith trajectory. The average would be more accurate if N is large. It is important to note that the algorithm is efficient when computing averages such as Eq. (4). However, just as in Metropolis Monte Carlo, the algorithm does not give the absolute probability of states, and therefore cannot compute $P_s(t)$ in Eq. (3). Nevertheless, we are often interested in average quantities and the Gillespie

algorithm is simple to implement. In the following sections, we discuss stochastic simulations based on the Gillespie algorithm in the context of several cell biological situations.

For some applications, Eq. (1) can be solved directly if the free energy surface is known. Algorithms for obtaining the trajectories can be found in textbooks (Frenkel and Smit, 1996). This type of simulation is often used in molecular dynamics and will not be discussed extensively here.

II. Stochastic Methods in Signaling and Genetic Networks

With improving experimental assays, it is possible to quantify many aspects of protein expression and signaling events in eukaryotic and prokaryotic cells. The number of copies of a particular gene, or a particular phosphorylated kinase can be quite small in a cell. The measured transcriptional activity sometimes shows quantitative differences from cell to cell. Variations in the transcriptional levels may be understood in terms of the stochastic model outlined above. Stochastic effects are especially relevant in bacteria where the regulatory control of gene systems is not rigorous. These issues have been discussed in other reviews and papers (McAdams and Arkin, 1997; Vilar *et al.*, 2003). Here, to illustrate this process, let us consider a simple hypothetical genetic switch shown in Fig. 3. This system is bistable and resembles several generic genetic switches (Kepler and Elston, 2001; Ptashne, 1992). The reaction network considered here is exceedingly simple: proteins A and B can both bind to an operator site which in turn controls the expression of A and B. Both A and B dimerize, and when A_2 is bound to the operator, B is not transcribed. When B_2 is bound to the operator, A is not transcribed. Thus A and B mutually inhibit each other.

To analyze this system stochastically, we can generalize the discussion in the introduction and consider a set of reactions. The system is characterized by the number of A proteins (N_A), the number of B proteins (N_B), and the number of A and B dimers (N_{A2} and N_{B2}). The operator is either empty or docked by A_2 or B_2. A and B can also be degraded. Changes in these variables are described by stochastic jumps with transition rates given in Fig. 3. For example, N_A can increase by one from the transcription process with rate $5k$. However, this increase only occurs when there is an A_2 bound to the operator. N_A can decrease by one from degradation, with rate $0.25k$. N_A can also decrease by two from the formation of an A_2 dimer with rate $5k$. A similar analysis can be done for N_B. A_2 and B_2 can also bind to the operator with rate $5k$. It is then a matter of applying the stochastic simulation procedure in Section V to obtain stochastic trajectories such as in Fig. 3.

The result from such a stochastic simulation is that the system will randomly switch between the configuration where there are many more A than B and the configuration where there are many more B than A. Most of the time, the system is dominated by either A or B (Fig. 3). Switching probability is determined by a number of factors, including the rate of A and B production and the difference

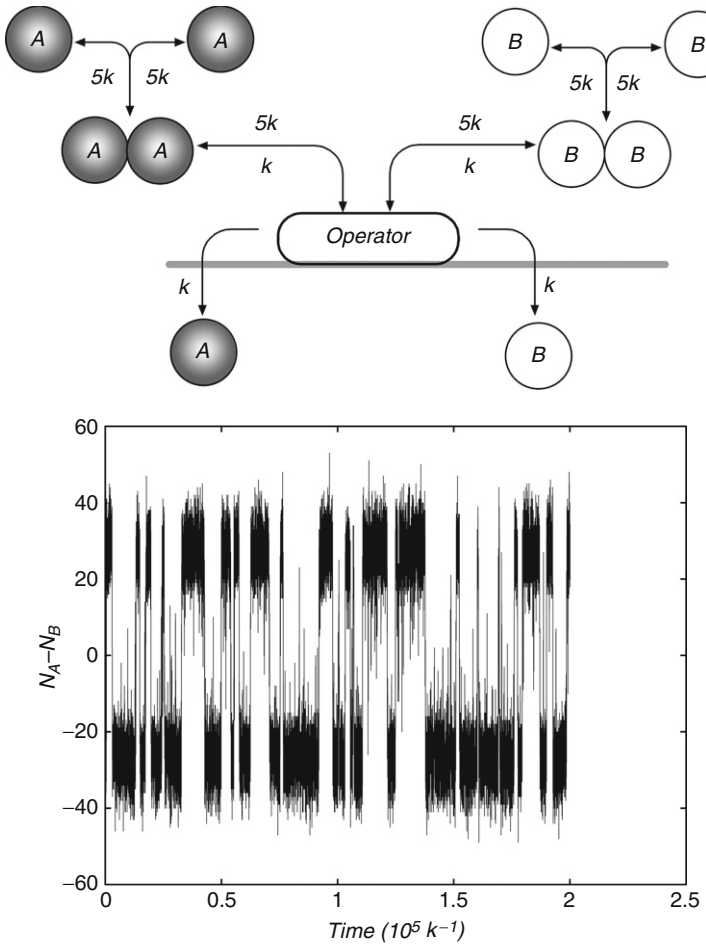

Fig. 3 A simple genetic switch. Here, A and B can form dimers. The dimers can bind to the operator to facilitate production of A or B. If the operator binds the dimer, only A is produced. If the operator binds the B dimer, only B is produced. The rate constants for these reactions are measured in units of k. The lower panel shows a typical stochastic simulation trajectory. The system switches mostly between A and B. The switch-like behavior would be absent if a kinetic model is used to describe the same system.

between N_A and N_B. Interestingly, if the same transcription cycle is analyzed using standard kinetic equations (namely a meanfield treatment), one will not observe the stochastic switching. This is because in the kinetic treatment, one computes the average probability of the operator being occupied by A_2 or B_2. This probability is roughly ½. This leads to simultaneous production of A and B with ½ of the rate, and the difference between N_A and N_B is zero at steady state. However, in the

stochastic model, the operator is either occupied by A_2 or B_2, leading to production of only one of the species. Therefore, the switch-like behavior of the operon only manifests itself when the stochastic model is considered. This is not a surprising result because we have noted that kinetic models are approximations to Markov models.

Beyond the simple genetic switch, any reaction system with any number of reacting partners can be analyzed using the stochastic approach. These are not limited to genetic switches, but include signaling, chemotactic, and developmental networks in bacteria and eukaryotic cells. However, there are a number of practical issues. Typically, the reaction rates *in vivo* are not known. In many cases, the reacting species and the relevant genes have not been identified. The discovery process of finding the important signaling pathways is usually the bottleneck. Cells also have redundant pathways, probably from evolutionary history in different environments. Stochastic models are useful in these problems to check the proposed mechanisms.

III. Molecular Motors and the Inclusion of Biomolecular Structure in Stochastic Models

Single molecule techniques can now measure conformational changes of biomolecules in real time. Conformational fluctuations are monitored using fluorescence resonance energy transfer (FRET), tethered optical traps, or direct fluorescent labeling of the protein (Bryant *et al.*, 2003; Myong *et al.*, 2005; Noji *et al.*, 1997; Visscher *et al.*, 1999; Yildiz *et al.*, 2003). For example, rotational motion of F_1-ATPase is first observed by attaching fluorescent F-actin to the rotating γ-subunit, and the observed motion is stochastic with occasional back rotation (Noji *et al.*, 1997). Stochastic stepping motions are observed in processive motors such as myosin-V (Mehta *et al.*, 1999), kinesin (Visscher *et al.*, 1999), and dynein (Mallik *et al.*, 2004) on F-actin and microtubules. All of these motors hydrolyze single ATP molecules as fuels. Interpretations of these experiments require stochastic models.

As we discussed above, stochastic models describe stochastic jumps between basins on an energy landscape. Therefore, the central question for molecular motors is: what is the energy landscape that explains the observed rotation or stepping behavior (Bustamante *et al.*, 2001)? How do we explain the observed step-size distributions and force–velocity curves? Since conformational fluctuations are measured in experiments, we need to consider a free energy surface as a function of the motor conformation. Since motors also bind and hydrolyze ATP, it is also necessary to consider the free energy surface as nucleotides are exchanged in the binding pocket. Thus, the general free energy surface is a function of two sets of variables, $V(q,\sigma)$, where q is the set of variables that describe the conformation of

the motor and σ is the set of variable that describe the nucleotide occupancy. In the case of F_1-ATPase, since the conformation is related to the rotation of the γ-subunit, q may be taken as θ, or the angle of the γ-subunit (Wang and Oster, 1998). (Note by taking this definition, we have assumed a tight-coupling between γ rotation and conformational changes in the α and β-subunits.) The nucleotide occupancy is determined by the occupancy states of the three catalytically active β-subunits; $\sigma = (s_1, s_2, s_3)$. Since each β-subunit can be either empty, ATP bound, ADP-Pi bound, and ADP bound, σ_i ranges from 1 to 4 and σ ranges from 1 to 64.

Free energy surfaces of biomolecules, in principle, can be computed from the known molecular structure. In practice, the computation for such large molecules is prohibitively costly. A coarse-grained approach is to consider the known conformational changes in the molecule and model them as simple mechanical elements. In F_1-ATPase, a hinge bending motion is seen in the β-subunit during the ATP hydrolysis cycle. The hinge motion is coupled to γ-subunit rotation through a linkage (Fig. 4A and 4B). Therefore, we can model the opening and closing of the β-subunit as a spring and map this motion to γ-subunit rotation (Fig. 4). The readers can refer to published articles for the details of $V(\theta,\sigma)$ (Sun *et al.*, 2004; Wang and Oster, 1998). This type of approach for specifying the energy surface does not include the atomic structure, but does incorporate the approximate large-scale structure of the protein. When possible, the mechanical constants may be computed from molecular dynamics simulations. Therefore, this approach potentially makes contact with several different kinds of data.

Note that in this formulation, the surface is continuous in the θ direction, but discontinuous or discrete in the σ direction. This is a simplification similar to going from Eq. (1) to (2). The energy surface, in reality, is continuous in all directions and there are barriers separating regions labeled by σ. The barriers are related to nucleotide binding and hydrolysis, and these atomic processes should depend on larger scale conformation of the protein. Instead of specifying the details of these energetic barriers in the σ direction, we describe the stochastic transitions between different σs by transition rates $k_{\sigma\to\sigma'}(\theta)$. The transition rate is determined by the barrier region of the energy landscape, which implies that the barriers are functions of protein conformation. Note that a connection to Bell's model of force-dependent reaction kinetics can be made here (Bell, 1978). Bell's model states that the reaction rate is modified exponentially in the presence of a mechanical force. This statement can be derived from a more detailed analysis using Kramer's rate theory (Hummer and Szabo, 2003). Here, in our context, if a force is applied to the motor protein, the protein will change its conformation, and the reaction rate changes. Reaction rates measured with purified proteins correspond to $k_{\sigma\to\sigma'}(\theta)$ for $\theta = \theta_0$, where θ_0 is the mechanical equilibrium conformation. Therefore, purified protein measurements can be used to estimate $k_{\sigma\to\sigma'}(\theta)$.

For processive molecular motors such as myosin-V, kinesin, and dynein, a similar analysis is also necessary to explain experimental measurements. Note that the situation is complicated by the fact that motors can bind and unbind from cytoskeletal tracks. The nucleotide occupancy variable, σ, needs to be

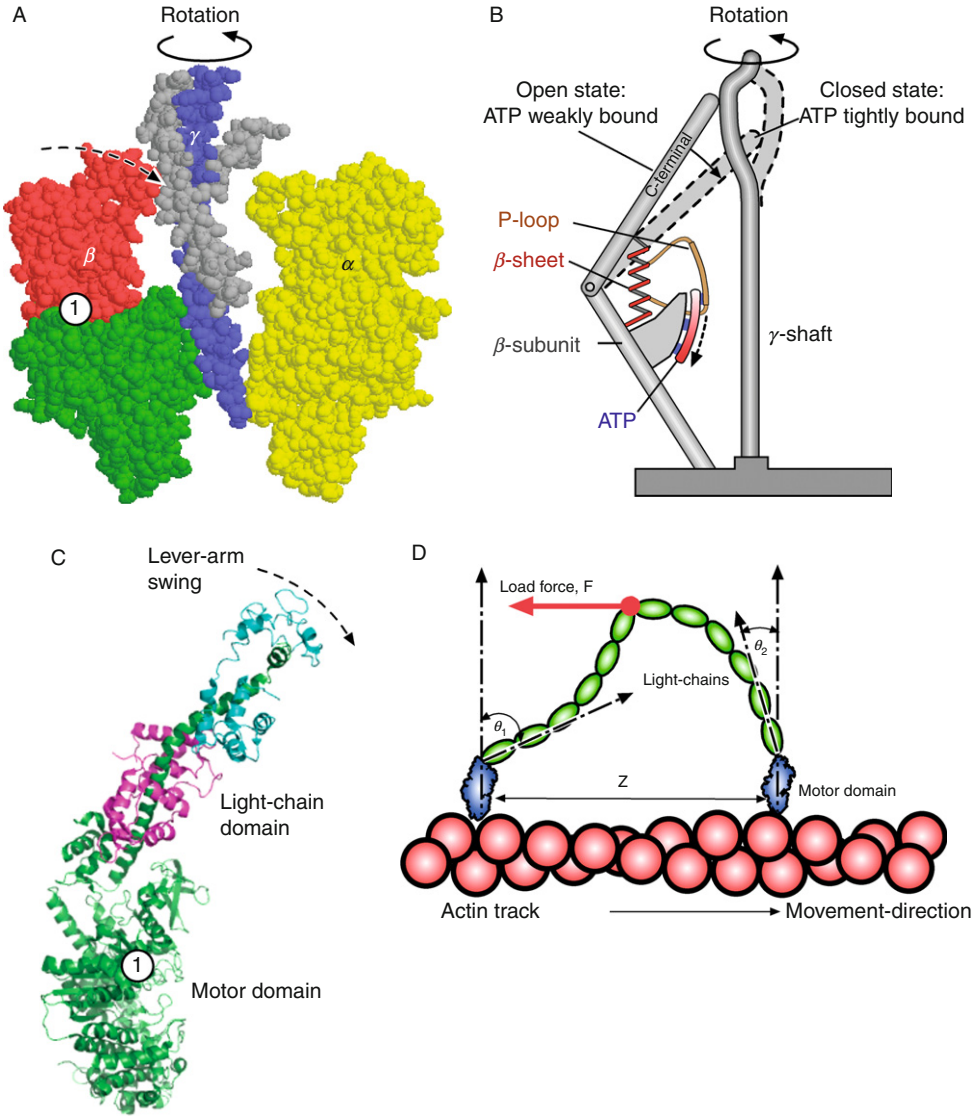

Fig. 4 Stochastic models of molecular motors incorporating the rough motor structure. (A) The γ-subunit of F_1-ATPase undergoes a rotation when the β-subunit is hydrolyzing ATP. A hinge bending motion in the β-subunit pushes the γ-subunit. The ATP binding site is labeled by 1. (B) To obtain an energy landscape description, we can consider the spring-like motion of the β-subunit and map it to the rotation of γ. (C) Myosin motors change conformation by changing the angle between the motor domain and the light-chain domain. (D) When two myosins are connected by the light-chain domain, the combined energy landscape can be written as Eq. (5). This energy depends on the conformations of the motor domains $(\theta_1, \phi_1, \theta_2, \phi_2)$, and the relative separations of the motor domains on F-actin, z. Any applied load force, F, also changes the motor conformation. Because actin binding sites are helical, binding to different sites changes the overall conformational energy. This leads to preferential binding to a few sites.

generalized to describe cytoskeleton binding of the motor domain. For the myosin-V motor, each motor domain can bind and hydrolyze ATP while attached or detached from F-actin. There are also two motor domains. Thus, $\sigma = (s_1, s_2)$ where $\sigma_{1,2}$ describes the nucleotide occupancy and F-actin binding activities of each motor. Also, unlike F_1-ATPase, conformational changes in the motor domains are not tightly coupled to the observed motor movement. Rather, the conformational changes of the motors change the conformation of the light-chain domain (also a coiled-coil motif) that links the motor domains. Examining the X-ray structures of the myosin motor domain shows that the conformational change is a rotation of the converter domain that reorients the light-chain domain (Fig. 4). The overall free energy surface can be written as (Lan and Sun, 2005, 2006).

$$V(\theta_1, \phi_1, \theta_2, \phi_2, z, \sigma_1, \sigma_2) = V_0(\theta_1, \phi_1, \sigma_1) + V_0(\theta_2, \phi_2, \sigma_2) + V_l(\theta_1, \phi_1, \theta_2, \phi_2, z) \quad (5)$$

where (θ_i, ϕ_i) is the 3-D orientation of the light-chain domain with respect to the motor (Fig. 4), z is the distance between the bound motor domains, and V_0 is the conformational energy of the monomer. And just as in the F_1-ATPase, V_0 depends on the occupancy of the nucleotide and F-actin binding activity. V_l is the conformation of the light-chain domain, and in addition to the conformational variables, it may also depend on any externally applied forces such as from an optical trap. Note that V_l is independent of (σ_1, σ_2), i.e., the light-chain domain does not have any catalytic activity. Again, simple mechanical elements can be used to model V_0 and V_l. We modeled V_0 as a mechanical spring and V_l as an elastic rod (Lan and Sun, 2005, 2006). This allows us to compute the energy surface with only a few parameters. It also allows us to compute the rough conformation of the molecule as it processes on F-actin.

The mechanical formulation outlined here predicts an asymmetrical structure when both motor domains are bound to F-actin and contain ADP. In this situation, the motor domains would like to have the same conformation. However, the light-chain domain connecting the motor domains resists such a conformation. If we compute the new mechanical equilibrium structure, the leading motor domain will have a different conformation than the trailing domain, and $(\theta_1, \phi_1) \neq (\theta_2, \phi_2)$. This suggests that ADP release rates from the bound motors will be different and the leading motor probably releases ADP slowly, resulting in preferential detachment of the trailing motor. This is a necessary outcome of the model to predict stepping behavior. Also, the free energy surface can be used to compute the energy difference between the situation where only one motor is bound and the other is free, and the situation where both motor domains are bound. This energy difference is a function of the relative distance between the bound motors, z. This energy difference also determines the relative binding rate of the free motor. The outcome determines the preferred binding site of the free motor. Since F-actin has a helical structure in its binding sites, the most favorable binding site occurs at $z = 36$ nm where the light-chain domain has the smallest deformation. These results are all consistent with experimental findings. Since the

approximate structures of the domains are included, it is possible to examine structural mutants. For example, truncating the light-chain domain leads to smaller steps, although the stepping behavior still persists (Lan and Sun, unpublished results). If the light-chain is made softer, such as in the myosin-VI isoform, the model can also predict the stepping behavior by changing the mechanical constants (Lan and Sun, 2006).

The same formalism outlined here is equally applicable for understanding other processive motors such as kinesin and dynein. The linkages between the motor domains in kinesin and dynein are structurally more complex and simple mechanical models are perhaps inadequate. Nevertheless, the overall energy of these motors can be decomposed in the same fashion as Eq. (5). If the structural changes associated with ATP hydrolysis and microtubule binding are known, kinesin and dynein can be understood using the framework outlined here.

We have shown that approximate biomolecular structure can be used to construct the free energy surface of molecular motors. Given the free energy surface, conformational motions of the motor can be computed using the stochastic equation of Eq. (1), or simplified schemes where only energetic basins and jumps between basins are considered in a Markovian stochastic model. The outcomes of these computations are essentially the same if the proper energy surface is considered first. Moreover, stochastic trajectories can be computed from these models and the results resemble many aspects of experimental data, and show features such as backward steps and substeps. Detailed structural explanations can be given for these features.

IV. Cytoskeleton and Cytoskeletal Network Structures

Stochastic models can be extended to consider the dynamic nature of the cytoskeletal network inside moving cells. The simplest situation is the growth of a single cytoskeleton filament such as F-actin. Here, the biochemistry of F-actin polymerization has been measured and quantified (Blanchoin, *et al.*, 2000; Marchand *et al.*, 1995; Mullins *et al.*, 1998; Pollard, 1986; Pollard and Borisy, 2003; Pollard *et al.*, 2000). Under typical cytoplasmic conditions, the barbed (plus) end of F-actin grows much faster than the pointed (minus) end. Thus, to simplify matters, let us neglect the pointed end and consider the growth dynamics at the barbed end. Let us also assume monomers are added in an alternating fashion, i.e., monomers are added to the left protofilament, then to the right, and so forth. These simplifications lead to the following equation for the probability of observing a filament with n-monomers:

$$\frac{\mathrm{d}P_n}{\mathrm{d}t} = k_+ P_{n-1} + k_- P_{n+1} - (k_+ + k_-) P_n \tag{6}$$

where $k_{\pm}$ are the monomer addition and subtraction rates. A filament of length n can occur by either adding a monomer from $n-1$, or losing a monomer from $n+1$. The monomer addition rate, k_+, will depend on the cytoplasmic monomer concentration. Equation (6) is similar to Eq. (3), and is also equivalent to a diffusion-convection equation for the probability of observing a filament with length l:

$$\frac{\partial P(l)}{\partial t} = D\frac{\partial^2 P}{\partial l^2} - v\frac{\partial P}{\partial l} \tag{7}$$

where $D = k_+\Delta^2$ is an effective diffusion constant and Δ the length increase with addition of one monomer, $v = (k_+ - k_-)\Delta$ is a "growth velocity." The diffusion–convection nature of Eq. (7) suggests that the length distribution will shift as well as spread in time. Equation (7) can be solved analytically, but a stochastic simulation algorithm can be implemented for Eq. (6), and the results will be equivalent. The stochastic simulation algorithm involves examining the current configuration (length n), and the two possible destination states (lengths $n + 1$ and $n - 1$), and carrying out the procedure in Section V.

Generalization to more than one filament is straightforward if the filaments are dynamically independent. The length distribution of a set of filaments is given by Eq. (7). Stochastic simulations of a set of filaments can be accomplished by recognizing that for any given configuration, there are many destination states because each filament can add or subtract monomers. If the filaments behave identically, then the rates of adding or subtracting monomers are identical. The only difference is that the number of accessible states is larger, i.e., $2N$ where N is the number of filaments.

In the cytoplasm, however, the growth of F-actin filaments is influenced by many factors (Pollard and Borisy, 2003), and different cell types exhibit a variety of behaviors. We will focus on the leading edge of motile cells such as the fish keratocyte which contains a dendritic network of actin filaments (Pollard and Borisy, 2003). A number of factors influence the network structure *in vivo*. First, actin monomer concentrations are not expected to be uniform throughout the cell; this influences the addition rate, k_+. Second, capping proteins and other actin-end proteins competes with monomer addition. Third, filaments physically interact with each other and can bundle and crosslink. Fourth, new filaments are initiated from mother filaments via the activated Arp2/3 complex, leading to a branched network structure. Final, filament severing proteins such as cofilin and profilin will disrupt networks and causes depolymerization. All of these factors contribute to the dynamic nature of the cellular leading edge. Biochemical evidences of these influences are summarized in excellent reviews (Pollard and Borisy, 2003). Additional questions regarding how extracellular signals are transmitted to growing filaments and the influences of the plasma membrane and membrane tethering proteins such as formin (Dickinson *et al.*, 2004; Kovar and Pollard, 2004) are still being debated.

Stochastic models of growing cytoskeletal networks can, in principle, incorporate all of the factors mentioned in the previous paragraph. However, the number of relevant Markov states would be enormous, and in many cases, the rate constants for modeling the stochastic jumps are still not known. Also, the mechanics and elastic properties of the cytoskeletal network also contribute to the dynamics of the leading edge. For these reasons, a full simulation of the cellular leading edge is presently unrealistic. However, simpler questions can be addressed using stochastic models. Simulations of growing networks have been used to examine the actin comet tail behind moving *Listeria monocytogenes*, and the actin networks behind rocketing beads (Alberts and Odell, 2004; Carlsson, 2001, 2003). Here, we will discuss the morphology of networks in the moving lamellipodium of fish keratocytes.

Electron microscopy studies of the lamellipodium in keratocytes show a dendritic branched structure for the F-actin network where the barbed ends of filaments are mostly pointed $\pm 35^\circ$ with respect to the leading edge (Maly and Borisy, 2001). From structural studies, it is known that the new daughter filament nucleated by the Arp2/3 complex forms 70° angle with the mother filament (Volkmann *et al.*, 2001). However, monomers in F-actin are arranged in a helical fashion and Arp2/3 can nucleate daughter filaments in all directions. When considering the 3-D nature of the network, it is unclear why the filaments are pointed in $\pm 35^\circ$ directions. Capping of F-actin ends are important in this situation because filaments away from the leading edge are probably quickly capped and do not grow further. The geometry of the network results from the competition between capping and branching. A stochastic simulation of this system, including branching, capping, and filament growth can examine the orientational distribution of filaments under different conditions. In this simulation, the geometry of new filaments is incorporated. The geometry of the plasma membrane is also included to examine the 3-D structure of the actin network (Atilgan *et al.*, 2005). The simulation shows that the filaments are pointed in $\pm 35^\circ$ directions only if the mother filament is pointed in a restricted set of directions (Fig. 5). Mathematically, this implies that the Arp2/3 branching rate is a function of the orientation of the mother filament (Atilgan *et al.*, 2005). This curious discovery can be explained if we consider an activated Arp2/3 complex that is attached to the plasma membrane, and the Arp2/3 is not freely diffusing in the cytoplasm (Fig. 5). New daughter filaments are generated only when the mother filament interacts with the attached Arp2/3 complex.

Several proteins are implicated in the activation of Arp2/3, and exactly how biochemical signals are translated to Arp2/3 is still being investigated. Additional questions can be posed about the localization of these signaling complexes and the effect of membrane curvature on signaling protein distribution (Atilgan and Sun, 2007; Atilgan *et al.*, 2005). Stochastic simulations studies, however, reveal that the geometry and the physical mechanism of filament growth are important in generating the observed network morphology. Further studies of F-actin dynamics *in vivo* can answer these questions.

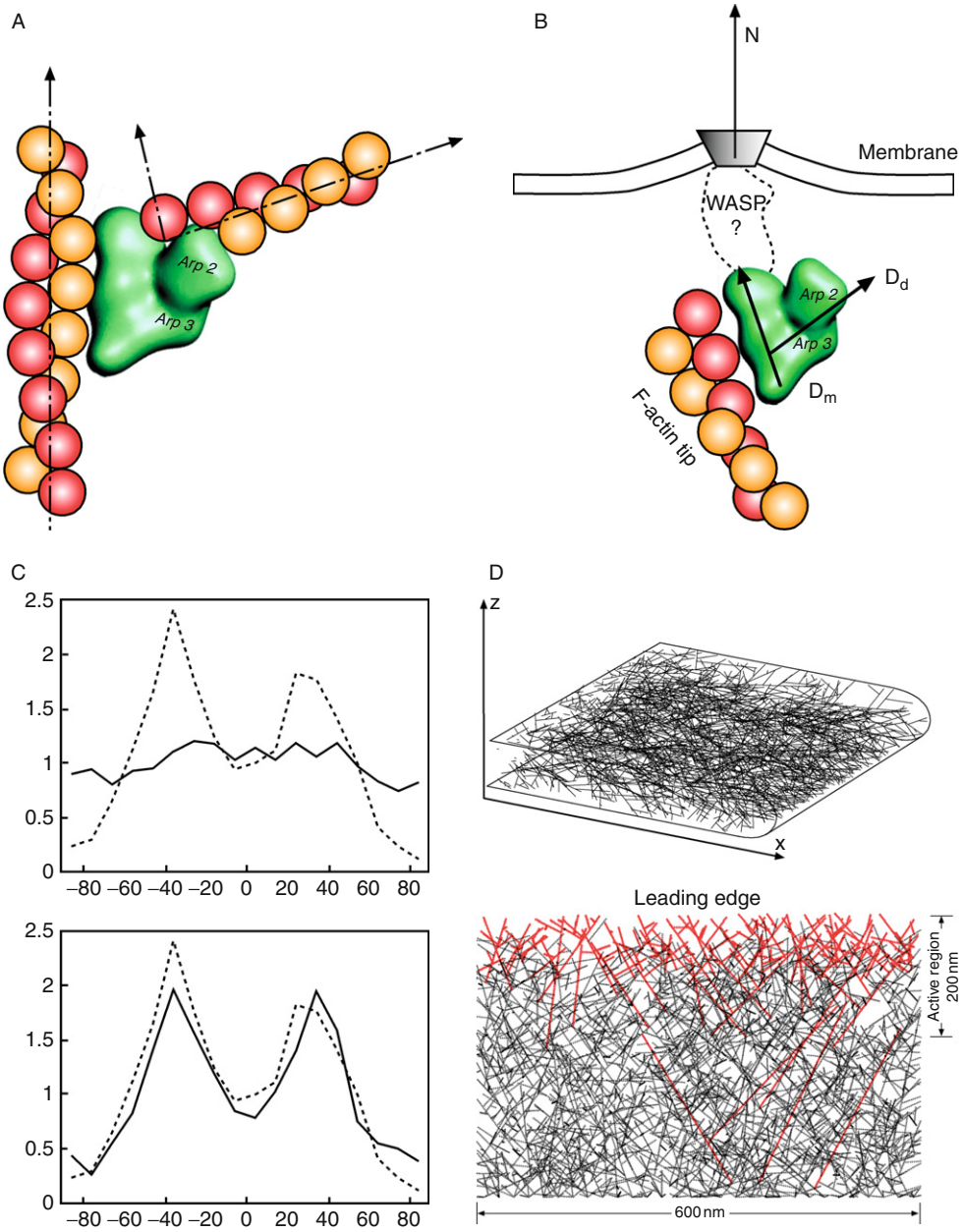

Fig. 5 Stochastic simulations can be used to analyze cytoskeletal network morphology in the lamellipodium. (A) New actin filaments are nucleated by Arp2/3. The structure of the filament junction is known, and is incorporated into the stochastic simulation. (B) If the Arp2/3 complex is still attached to the membrane during the nucleation of new filaments, then only filaments with the right orientation can generate new filaments. Here, $\mathbf{D}_m$ and $\mathbf{D}_d$ are the directional vectors of the mother and daughter

V. Procedures

In this section, the computational procedure for implementing Gillespie stochastic simulations is given. Before implementing the computer code, it is necessary to identify the variables that specify a particular Markov state. For example, when simulating a diffusing particle, a state would be specified by the spatial position of the particle on a grid. From any state, it is also necessary to identify all the possible states that are connected to it in one Markov jump. For a diffusing particle in 3-D, there are six neighboring states connected to any state. Finally, the transition rates to all the neighboring states, k_i, must be tabulated. The net escape rate is the sum of the transition rates to neighboring states: $K = \sum_{i=1}^{\text{neighbors}} k_i$. The simulation procedure can be listed as follows:

1. Establish an initial state of the system. This depends on the problem at hand. If we are modeling reactions, then an initial collection of reactants and products should constitute the initial state. If the system is in equilibrium, then the initial state can be randomly picked from the equilibrium distribution.
2. Compute the net escape rate from the current state, $K = \sum_{i=1}^{\text{neighbors}} k_i$.
3. Select a random number, $\triangle t$, according to the escape time distribution $e^{-K\Delta t}$. This is done by selecting a random number u distributed uniformly between 0 and 1, the escape time from the current state is $\Delta t = -(1/K) \ln u$.
4. Divide the interval from 0 to K into subintervals of length k_i, i.e., one subinterval for each transition rate to destination state i. Select another random number between 0 to K, v. Determine the subinterval j where v resides. This is the destination state of the transition event.
5. Update the current state to the destination state j, and record the jump time $\triangle t$. Obtain the current time by adding up the jump times.
6. Repeat step (2) for the new state.

This procedure generates a sequence of states and jump times, which we call a stochastic trajectory. From this sequence of states and times, it is possible to evaluate averages such as Eq. (4) by simply averaging over the trajectories. The most difficult step in this procedure is identifying all the possible neighboring states of any given state. For example, in the cytoskeleton simulation, all of the monomers in F-actin can potentially bind Arp2/3. Only a subset of these monomers can actually succeed in

filaments formed by the Arp2/3 junction, respectively. (C) The computed filament orientational distribution (solid lines) compared with the distribution from electron microscopy (dotted line). The upper panel shows the distribution when all filaments are allowed to generate new filaments. This corresponds to freely diffusing Arp2/3 in the cytoplasm. The lower panel shows the distribution when Arp2/3 is attached to the leading edge membrane. The lower panel results agree with experimental data. (D) Some representative F-actin network generated from stochastic simulations. Capping and branching events are included. The lower panel shows the projected network to the x–y plane. The red filaments are still growing, the black filaments have been capped.

binding. This is determined by the orientation of the mother filament. Therefore, during the simulation, the orientation of the mother filament is stored and the information is used to determine if an Arp2/3 can be added to the filament.

VI. Discussion and Concluding Remarks

In this review, we have examined the basic physics behind stochastic methods and applied the Gillespie method to several biological problems. The procedure to generate Gillespie stochastic trajectories is exceedingly simple and has wide applicability. We have discussed stochastic models for gene expression, stochastic movement of molecular motors, and the growth of cytoskeletal networks. We have shown that structural information can be incorporated into stochastic models to answer physical and morphological questions.

There are some technical issues when implementing stochastic simulations. We will comment on three of these issues. First of the issues has to do with rare events. The stochastic algorithm will generate the most probable stochastic trajectories, and the final state of the trajectory is usually a highly probable destination state. Suppose one is interested in a final state that is rarely visited by the trajectory. The algorithm does not offer a way to select for these rare trajectories. In order to obtain them, one has to simulate many trajectories, hoping for a few of them that reach the desired final state. Most of the computational effort is wasted in simulating undesirable but frequently occurring trajectories. To overcome this, one must develop an algorithm that generates trajectories with fixed end states. This is possible if one can compute the absolute probability of the stochastic trajectories explicitly. This problem has been analyzed and a possible solution is offered (Harland and Sun, 2007; Sun, 2006).

The second issue has to do with disparate time scales where some stochastic jumps occur at a much faster rate than others. During the simulation, most of the selected jumps will be fast jumps. In reaction–diffusion systems, this can be prevalent when the rate of diffusion is much faster than the rate of reaction. Most of the stochastic jumps will be diffusive steps. Of course, the simulation is reproducing the correct physics. But most of the computational time is wasted on generating trivial jumps. A possible solution to this is the τ-leap method (Gillespie, 2001). Instead of simulating these fast jumps explicitly, one can leap over a sequence of jumps to advance quickly.

The last issue has to do with system size. Stochastic simulations are computationally demanding when the number of Markov states is prohibitively large. In practice, the net escape rate from any state, K, is a large number so that the jump time, $\triangle t$, can be small. Many jumps are needed to simulate a long trajectory. Currently, there is a size limitation on how many reactions one can effectively simulate. Again, alternative algorithms may be devised for specialized problems or a completely new simulation algorithm may be devised to overcome the scaling problem.

Nevertheless, the ease of implementation makes stochastic models very attractive for examining complex systems ranging from single proteins to the cell. Simulations can be devised quickly to check the proposed mechanisms. Sometimes, simulations can raise additional questions and motivate new experiments. Thus, stochastic simulation methods should be a prominent tool for quantitative biologists working in both experimental and theoretical frontiers.

VII. Appendix Glossary of Terms

Several terms used in this chapter may be unfamiliar to the reader. A list of plain language definitions is given below.

Stochastic Models: A model that determines the configurations of a dynamical system probabilistically. This is in contrast with "dynamical models," which imply that given a configuration of system and laws governing the dynamics, future configurations are deterministic. Newtonian equation of motion is deterministic while the Langevin equation of Eq. (1) is stochastic.

Markov Models: A model based on a set of predefined states and a sequence of stochastic jumps between states. The stochastic jumps satisfy the Markov property which implies that the jumping probability only depends on the present state of the system, and does not depend on the history of states. Markov models are a subset of stochastic models.

Kinetic Models: A model to analyze changes in the average concentration of a set of reacting species. It usually assumes that the reactants are well-mixed and obey the law of mass action. Kinetic models are deterministic in the sense that given a set of initial concentrations and a reaction mechanism, all future concentrations are determined.

Importance Sampling (Metropolis Monte Carlo): A method to sample the most probable regions of a multi-dimensional probability distribution. A common application is in molecular dynamics where the Boltzmann distribution is a multi-dimensional probability distribution of atomic configurations. This method is usually applied for equilibrium simulations.

Gillespie Stochastic Simulation Method: A method to compute a sequence of stochastic states and jump times between states (or a stochastic trajectory). The method was discussed by Gillespie in the context of chemical reactions, although an equivalent method was mentioned by Bortz, Kalos, and Lebowitz (BLK) in the context of magnetic spin systems. Stochastic simulations of Markov models are usually based on this method. It can be shown that the Gillespie method is a form of importance sampling in trajectory space (see Sun *et al.*, 2004).

Mechanical Models: A model used to understand the dynamics of a system through the specification of forces between interacting components. The simplest mechanical model is an elastic spring which specifies the force, f, between two particles as proportional to the distance, x, between them: $f = -kx$. k is a spring constant or force constant.

Elastic Models: A subset of mechanical models which assumes that forces can be derived from a mechanical energy. The mechanical energy can be computed from atomistic models, or continuum theories with a few mechanical constants.

References

Alberts, J. B., and Odell, G. M. (2004). *In silico* reconstitution of *Listeria* propulsion exhibits nano-saltation. *PLoS Biol.* **2,** 2054–2066.

Atilgan, E., and Sun, S. X. (2007). Shape transitions in lipid membranes and protein mediated vesicle fusion and fission. *J. Chem. Phys.* **126,** 095102:1–10.

Atilgan, E., Wirtz, D., and Sun, S. X. (2005). Morphology of the lamellipodium and organization of actin filaments at the leading edge of crawling cells. *Biophys. J.* **89,** 3589–3602.

Bell, G. I. (1978). Models for the specific adhesion of cells to cells. *Science* **200,** 618–627.

Blanchoin, L., Pollard, T. D., and Mullins, R. D. (2000). Interactions of ADF/cofillin, Arp2/3 complex, capping protein and profilin in remodeling of branched actin filament networks. *Curr. Biol.* **10,** 1273–1282.

Bortz, A., Kalos, M., and Lebowitz, J. (1975). A new algorithm for Monte Carlo simulation of ising spin systems. *J. Comp. Phys.* **17,** 10–18.

Bryant, Z., Stone, M. D., Gore, J., Smith, S. B., Cozzarelli, N. R., and Bustamante, C. (2003). Structural transitions and elasticity from torque measurements on DNA. *Nature* **424,** 338–341.

Bustamante, C., Keller, D., and Oster, G. (2001). The physics of molecular motors. *Acc. Chem. Res.* **34,** 412–420.

Carlsson, A. E. (2001). Growth of branched actin networks against obstacles. *Biophys. J.* **81,** 1907–1923.

Carlsson, A. E. (2003). Growth velocities of branched actin networks. *Biophys. J.* **84,** 2907–2918.

Chandler, D. (1987). "Introduction to Modern Statistical Mechanics." Oxford University Press, Oxford.

Dickinson, R. B., Luzelena, C., and Purich, D. L. (2004). Force generation by cytoskeletal filament end-tracking proteins. *Biophys. J.* **87,** 2838–2854.

Frenkel, D., and Smit, B. (1996). "Understanding Molecular Simulations." Academic Press, New York.

Gillespie, D. T. (1977). Exact stochastic simulation of coupled chemical reactions. *J. Phys. Chem.* **81,** 2340–2361.

Gillespie, D. T. (2001). Approximate accelerated stochastic simulation of chemically reacting systems. *J. Chem. Phys.* **115,** 1716–1733.

Hanggi, P., Talkner, P., and Borkovec, M. (1990). Reaction-rate theory: Fifty years after Kramers. *Rev. Mod. Phys.* **62,** 251–341.

Harland, B., and Sun, S. X. (2007). Stochastic path sampling and the mean first passage time for Markovian dynamics. *J. Chem. Phys.* **127,** 104103.

Hummer, G., and Szabo, A. (2003). Kinetics from non-equilibrium single-molecule pulling experiments. *Biophys. J.* **85,** 5–15.

Kepler, T. B., and Elston, T. C. (2001). Stochasticity in transcriptional regulation: Origins, consequences and mathematical representations. *Biophys. J.* **81,** 3116–3136.

Kerr, R. A., Levine, H., Sejnowski, T. J., and Rappel, W. J. (2006). Division accuracy in a stochastic model of Min oscillations in *Escherichia coli*. *PNAS* **103,** 347–352.

Kovar, D. R., and Pollard, T. D. (2004). Insertional assembly of actin filament barbed ends in association with formins produces piconewton forces. *Proc. Natl. Acad. Sci. USA.* **101,** 14725–14730.

Lan, G., and Sun, S. X. (2005). Dynamics of myosin-V processivity. *Biophys. J.* **88,** 999–1008.

Lan, G., and Sun, S. X. (2006). Flexible light-chain and helical structure of F-actin explain the movement and step size of myosin-VI. *Biophys. J.* **91,** 4002–4013.

Lutkenhaus, J. (2007). Assembly dynamics of the bacterial minCDE system and spatial regulation of the Z ring. *Annu. Rev. Biochem.* **76,** 14.1–14.24.

Mallik, R., Carter, B. C., Lex, S. A., King, S. J., and Gross, S. P. (2004). Cytoplasmic dynein functions as a gear in response to load. *Nature* **427,** 649–652.

Maly, V. I., and Borisy, G. G. (2001). Self-organization of a propulsive actin network as an evolutionary process. *Proc. Natl. Acad. Sci. USA* **98,** 11324–11329.

Marchand, J.-B., Moreau, P., Paoletti, A., Cossart, P., Carlier, M.-F., and Pantoloni, D. (1995). Actin-based movement of Listeria monocytogenes: Actin assembly results from the local maintenance of the uncapped filament barbed ends at the bacterium surface. *J. Cell Biol.* **130,** 331–343.

McAdams, H. H., and Arkin, A. (1997). Stochastic mechanisms in gene expression. *PNAS* **94,** 814–819.

Mehta, A., Rock, R., Rief, M., Spudich, J., Mooseker, M., and Cheney, R. (1999). Myosin-V is a processive actin-based motor. *Nature* **400,** 590–593.

Mullins, R. D., Heuser, J. A., and Pollard, T. D. (1998). The interaction of Arp2/3 complex with actin: Nucleation, high-affinity pointed end and capping, and formation of branching networks of filaments. *Proc. Natl. Acad. Sci. USA* **95,** 8161–8186.

Murray, J. D. (1989). "Mathematical Biology." Springer-Verlag, Heidelberg.

Myong, S., Rasnik, I., Joo, C., Lohman, T. M., and Ha, T. (2005). Repetitive shuttling of a motor protein on DNA. *Nature* **437,** 1321–1325.

Noji, H., Yasuda, R. M., Yoshida, M., and Kinosita, K. (1997). Direct observation of the rotation of F1-atpase. *Nature* **386,** 299–302.

Pollard, T. D. (1986). Rate constants for the reaction of ATP- and ADP-actin with the ends of actin filaments. *J. Cell Biol.* **103,** 2747–2754.

Pollard, T. D., Blanchoin, L., and Mullins, R. D. (2000). Molecular mechanisms controlling actin-based filament dynamics in muscle cells. *Annu. Rev. Biophys. Biomol. Struct.* **29,** 545–576.

Pollard, T. D., and Borisy, G. G. (2003). Cellular motility driven by actin assembly and disassembly of actin filaments. *Cell* **112,** 453–465.

Ptashne, M. (1992). "A Genetic Switch: Gene Control and Phage λ." Blackwell, Oxford.

Reichl, L. E. (1998). "A Modern Course in Statistical Physics." Wiley, Chichester.

Risken, H. (1989). "The Fokker-Planck Equation." Springer-Verlag, Berlin.

Sun, S. X. (2006). Path summation formulation of the Master equation. *Phys. Rev. Lett.* **96,** 210602:1–4.

Sun, S. X., Wang, H., and Oster, G. (2004). Asymmetry in F1-atpase and its implications for the rotational cycle. *Biophys. J.* **86,** 1373–1384.

Vilar, J. M. G., Guet, C. C., and Leibler, S. (2003). Modeling network dynamics: The lac operon, a case study. *J. Cell Biol.* **161,** 471–476.

Visscher, K., Schnitzer, M. J., and Block, S. M. (1999). Single kinesin molecules studied with a molecular force clamp. *Nature* **400,** 184–189.

Volkmann, N., Amann, K. J., Stoilova-McPhie, S., Egile, C., Winter, D. C., Hazelwood, L., Heuser, J. E., Li, R., Pollard, T. D., and Hanein, D. (2001). Structure of Arp2/3 complex in its activated state and in actin filament branch junctions. *Science* **28,** 2456–2458.

Wang, H., and Oster, G. (1998). Energy transduction in F1 motor of ATP synthase. *Nature* **396,** 279–282.

Wang, H., Peskin, C. S., and Elston, T. C. (2003). A robust numerical algorithm for studying biomolecular transport processes. *J. Theor. Biol.* **221,** 491–511.

Yildiz, A., Forkey, J., McKinney, S. A., Ha, T., Goldman, Y. E., Selvin, P. R., and Myosin, V. (2003). Walks hand-over-hand: Single fluorophore imaging with 1.5 nm localization. *Science* **300,** 2061–2065.

CHAPTER 24

Computational Modeling of Self-Organized Spindle Formation

Stuart C. Schaffner[⋆] and Jorge V. José[†]

[⋆]Center for Interdisciplinary Research on Complex Systems and Physics Department
Northeastern University
Boston, Massachusetts 02115

[†]Physics Department and Department of Physiology and Biophysics
State University of New York Buffalo
New York 14260-1611

METHODS IN CELL BIOLOGY, VOL. 89

0091-679X/08 $35.00
DOI: 10.1016/S0091-679X(08)00624-9

Abstract

In this chapter, we provide a derivation and computational details of a biophysical model we introduced to describe the self-organized mitotic spindle formation properties in the chromosome dominated pathway studied in *Xenopus* meiotic extracts. The mitotic spindle is a biological structure composed of microtubules. This structure forms the scaffold on which mitosis and cytokinesis occurs. Despite the seeming mechanical simplicity of the spindle itself, its formation and the way in which it is used in mitosis and cytokinesis is complex and not fully understood. Biophysical modeling of a system as complex as mitosis requires contributions from biologists, biochemists, mathematicians, physicists, and software engineers. This chapter is written for biologists and biochemists who wish to understand how biophysical modeling can complement a program of biological experimentation. It is also written for a physicist, computer scientist, or mathematician unfamiliar with this class of biological physics model. We will describe how we built such a mathematical model and its numerical simulator to obtain results that agree with many of the results found experimentally. The components of this system are large enough to be described in terms of coarse-grained approximations. We will discuss how to properly model such systems and will suggest effective tradeoffs between reliability, simulation speed, and accuracy. At all times we have in mind the realistic biophysical properties of the system we are trying to model.

I. Introduction

Although biological systems can be complex, they can still be studied using the standard cycle of hypothesis and experiment. Experiments produce quantitative data on the behavior of a particular biological system. A hypothesis, or biological model, can be formed to explain this data. While acknowledging the complexity of a biological system, a successful model asserts that a smaller number of system elements largely determine certain important aspects of the system's behavior. The model can also be used to make predictions, and these predictions can (and should) be tested experimentally. In this chapter we review and elaborate on some of the technical details of our modeling studies of spindle formation patterns.

The mitotic spindle is a biological structure composed of microtubules. This structure forms the scaffold on which mitosis and cytokinesis occurs. Despite the seeming mechanical simplicity of the spindle itself, its formation and the way in which it is used in mitosis is complex and not completely understood. There are two known pathways for spindle formation: centrosome-directed and chromosome-directed (Karsenti and Vernos, 2001). We, and others, have used mathematical modeling and numerical simulation to help understand the self-organized spindle formation in both pathways.

Modeling of a system as complex as mitosis is by nature an interdisciplinary project. It requires that the research team have expertise in biology, biochemistry, mathematics, physics, and software engineering. This chapter is written for biologists and biochemists who wish to understand how biophysical modeling can complement a program of biological experimentation. It is also written for a physicist, computer scientist or mathematician unfamiliar with this class of biophysical models. We will describe how we have built such a model and a numerical simulator to obtain results from the mathematical expressions. The components of this system are large enough to be described in terms of coarse-grained elements like flexible beams in a viscous medium. However, these elements are also small enough that thermal motion plays an important role. These middle-scale or coarse-grained problems are common in biophysical modeling and pose challenges to the mathematical modeler. We will discuss how to correctly model such systems and will suggest effective tradeoffs between reliability, simulation speed, and accuracy.

II. Rationale

A. Two Pathways for Spindle Formation

The better-known centrosome-directed pathway for spindle formation is common in animal eukaryotic cells. It uses centrosomes and kinetochores (Heald, 2000b; Kapoor *et al*., 2006; Rieder *et al*., 2001), which directly force the pattern to form. There is an alternative, chromosome-directed, spindle pattern formation pathway in which spindle patterns self-assemble without the presence of centrosomes and kinetochores. The microtubules grow over the chromosomes and then extend outward to form spindle poles (Budde *et al*., 2001; Carazo-Salas *et al*., 1999; Hinchcliffe *et al*., 2001; Rieder *et al*., 2001). This pathway has attracted a significant amount of interest because it appears to form a spindle without the aid of specialized structures.

Heald and colleagues studied this pathway by using extracts of meiotic *Xenopus* eggs (Bastiaens *et al*., 2006; Budde *et al*., 2001; Gadde and Heald, 2004; Heald, 2000a,b, 2004; Heald *et al*., 1996, 1997; Kalab *et al*., 2006). The chromosomes were replaced by micron-sized chromatin-covered magnetic beads. Thus, these beads had no kinetochores. There were also no centrosomes. The extract medium extended isotropically and there was no cell cortex, so there were no external boundary-condition asymmetries to drive the pattern formation. Heald and colleagues hypothesized that three molecular motors are involved: A simple plus-directed kinesin motor is anchored to the chromatin surface on the beads. A complex of minus-directed dynein motors and a complex of plus-directed Eg5 motors both crosslink microtubules. When Eg5 is inactivated, the microtubules form a single cluster over the chromosomes, but do not form a bipolar spindle.

Heald and colleagues hypothesized a two-stage mechanism for spindle formation in their experiments. First, the microtubules grow over the cluster of chromosomes and the Eg5 motors arrange them into antiparallel bundles. Then, the kinesin motors attach the plus ends of the microtubules to the beads and the dynein motors gather the minus ends together into two poles.

Figure 1 shows a particular point in a simulation run of our biophysical model. The spindle pattern is evident even at this early point in the simulation.

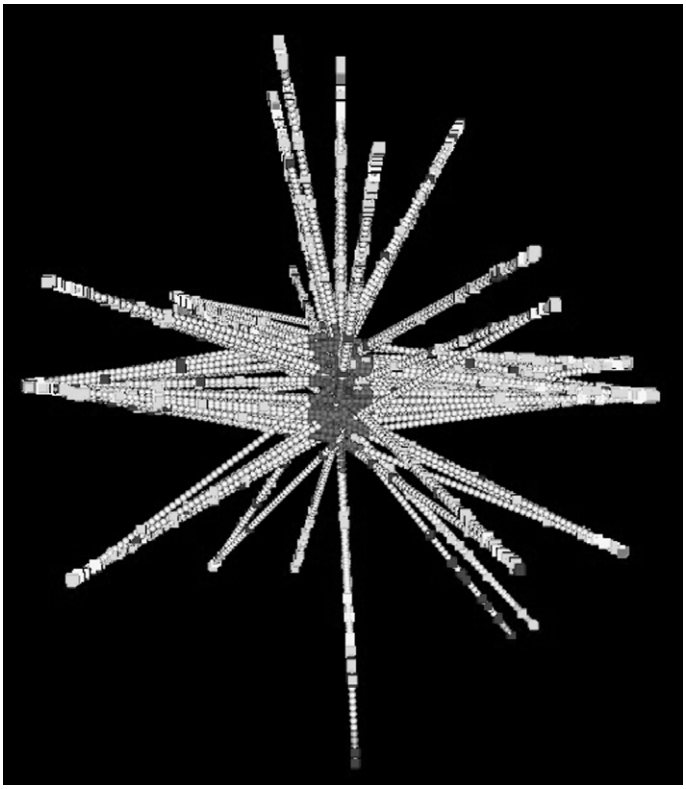

Fig. 1 Example of a simulation run result. This is a 3D grayscale visualization of the data from a simulation run for 200 microtubules, about 13 s of biological time after initialization. The pivot motors, on the chromatin surface, are arranged randomly throughout an oblate spheroid with radii 0.2, 2.0, and 2.0 μm. The plus ends of the microtubules are near the center of the image. The cubes arranged along the microtubule represent crosslinking minus-directed motors and microtubule–microtubule contacts. In this particular simulation run, the microtubules are all the same length and the crosslinking motors are processive. Two opposite poles are seen to be forming, but a substantial number of microtubules have not yet been captured. Note, however, that all microtubules are members of multi-microtubule bundles.

B. Basic Elements of Spindle Formation

Although the two pathways are distinct, both involve microtubules and molecular motors moving in a viscous medium, the cytoplasm. Microtubules are stiff orientable tubes with polymer walls. The polymers are formed from polar $\alpha\beta$-tubulin dimers, whose orientation is the same throughout the microtubule wall. A microtubule has a plus end and a minus end. Plus and minus are just a convenient pair of names; it is the lack of mirror symmetry in the microscopic electrical pattern that causes motors to move in particular directions on the microtubules. These small-scale patterns form oriented binding sites for motor domains and thereby determine the direction of motion of each kind of molecular motor (Bras *et al.*, 1998).

In addition to having mechanical stiffness and being composed of oriented subunits, a microtubule can also change length quickly in response to subtle changes in its chemical environment. This is called dynamic instability. It is usually important to include dynamic instability in some way in models involving microtubules (VanBuren *et al.*, 2005). However, it is difficult to correctly model because overall microtubule length is the result of a delicate balance between rates of growth and shrinkage. Although these rates can be measured experimentally in some cases, they would have to be measured for the specific experimental conditions being modeled. We will discuss this problem at length later in this chapter.

There are many different types of molecular motors. All contain substructures, called motor domains, which can attach to particular sites on the wall of a microtubule (or actin filament). A motor burns fuel, usually ATP, causing these domains to move to adjacent binding sites on the microtubule. The fuel is hydrolyzed; for example, ATP becomes ADP with a net release of energy. Motors are called plus-directed or minus-directed depending on their preferred direction of motion. As the fuel is burned, a motor domain will move from one stable binding site to another site. On a microtubule, adjacent binding sites are separated by a distance of approximately 8 nm, and motors can move a multiple of half this distance, or a multiple of about 4 nm. This distance is small relative to the length of a microtubule, on the order of 1–10 μm. It is often possible to model molecular motors as moving smoothly along a microtubule. Still, since each step is on the order of 1% of the length of a microtubule, there are cases where it is necessary to model the movement as individual steps. In our model of spindle formation, we are able to use the continuous-motion approximation. We will discuss this in more detail later in this chapter.

The binding sites for motor domains form potential wells with depths of several times $\frac{1}{2}k_{\mathrm{B}}T$, where k_{B} is the Boltzmann's constant and T is the ambient absolute temperature. This is the mean energy in a mechanical degree of freedom for a system in thermal equilibrium at temperature T. Thus, a motor domain in a binding site is unlikely to detach because of random thermal energy, although it can be torn off by a strong external force. However, while the motor domain is moving from one binding site to another it is more weakly bound and is subject to

random detachment. The likelihood of remaining attached is called processivity. It is generally defined as the probability p that an attached motor will remain attached to the microtubule during a single step. The processivity is defined for an entire motor rather than a single motor domain because other parts of a motor help to keep the motor aligned while any particular domain is moving between stable binding sites. For example, most highly processive motors are dimers and have closely spaced pairs of active domains. In each step, only one domain in the pair moves while the other remains tightly bound. This type of motion is often called walking; it produces slow but reliable motion. At the opposite extreme, a motor might have only one active domain. As a result, it will be nonprocessive by itself. However, if many such motors are attached to a single large load, at least a few will be attached at any one time. These stabilize the load, allowing individual motors to skip over several adjacent binding sites before becoming bound again. This is often called rowing; it produces faster motion, but it requires the cooperative action of many motors to prevent detachment.

The simplest kind of molecular motor, such as cytoplasmic dynein, is a protein rod on the order of 100 nm long, with one or two active motor domains on one end and a chemical binding site on the other. The end with the motor domains is called the head and the end with the binding site is called the foot or tail. This kind of motor attaches to a microtubule at one end and to a load at the other end. If both the load and the microtubule are suspended in a viscous medium, as in our system, the smaller object will have a lower coefficient of friction and will move the most. If the microtubule is attached to an immovable cortex or substratum, it will not move significantly. Conversely, if the load is an entire chromosome, or a chromatin-covered micrometer-sized bead as in (Heald *et al.*, 1996), then the microtubule will do most of the moving.

Motors can also have active motor domains at each end of the rod and can therefore crosslink microtubules. If the entire crosslinking motor is highly processive then there will be at least two active motor domains at each end. For example, Eg5 has two plus-directed kinesin motor domains at each end, forming a homotetramer.

The final basic model element is the medium in which the other modeled components are suspended. For mitosis, this is the cell cytoplasm. The mechanical properties of cytoplasm vary greatly. In most cellular processes the cytoplasm is a gel with cell size on the order of 5 μm. This gel structure could thus be expected to trap spindle microtubules that can grow to 10 or 20 μm in length. However, the cytoplasm surrounding the microtubules during prometaphase does not appear to have a gel structure, and can be modeled as a viscous fluid with about four times the viscosity of water (Phair and Misteli, 2000).

The cytoplasm not only supports the mitotic spindle and its mechanical elements, it also serves as a reservoir of basic building blocks. In particular, the cytoplasm supplies $\alpha\beta$-tubulin (to form microtubules), some of the motors, and the ATP to power the motor domains. These small elements diffuse quickly through the cytoplasm, compared to the rate of diffusion of much larger objects such as

entire microtubules. This allows us in some cases to ignore depletion effects and assign a single concentration parameter across the entire cytoplasm. In other cases, two elements can interact to produce biologically significant gradients. These usually require more complex treatment as a reaction–diffusion system (Kalab *et al.*, 2006).

Figure 2 shows some of the basic functional elements of our model and some of their interactions.

III. Methods

A. Basic Elements of Mathematical Modeling

This section describes how to model mitotic spindle formation through the chromosome-directed pathway. Our model tests the hypothesis that a collection of microtubules, two kinds of molecular motor, an asymmetrical distribution of

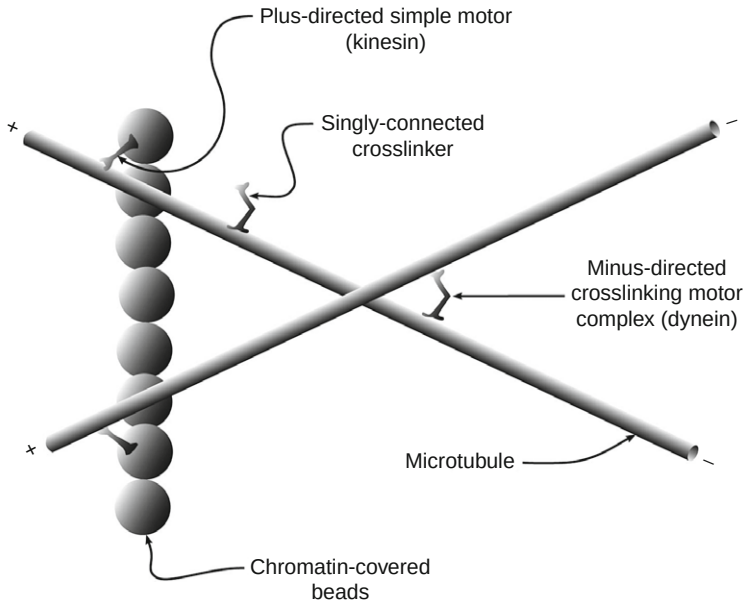

Fig. 2 Interactions between different model entities. Here, a column of chromatin-covered beads supplies anchor points for plus-directed kinesin-like motors. Two such motors are shown here, serving as pivot points for two microtubules. The plus-directed motion pushes the minus ends of the microtubules away from the chromatin surfaces. A minus-directed crosslinking motor, or dynein, complex attaches first to one microtubule and then moves toward its minus end. As it does so, it has a chance of connecting to a second microtubule, forming a crosslink. The crosslink moves toward the minus ends of both microtubules, helping to form poles.

motor binding sites (chromatin-covered beads), and a simple viscous medium is sufficient to create structures similar to a mitotic spindle.

Omitting extraneous detail from a model is often as important as selecting key functionality to include. For example, there is ample evidence that meiotic cytoplasm contains many more kinds of molecular motor than we included in our model. The simplified motors in our model can, in the real biological system, represent more than one kind of motor. We use experimental parameter values for, say, kinesin motors to ensure that our model motors represent at least one real motor.

Implementation of a numerical model-simulator depends on whether the model is driven by continuous processes or by discrete events. Mitotic spindle systems include both, making the modeling task more complex. In our model, the microtubules move continuously through the cytoplasm, in response to motor, thermal, and contact forces that change slowly. However, motor head attachments and detachments cause sudden changes to these forces. Our biophysical model includes a system that smoothly propagates the states in time but only between discrete events that cause discontinuous changes to the system.

Mitotic spindle formation, like most biological processes, happens at temperatures where random thermal fluctuations play an important role. Not only do motors attach and detach randomly, but also the mechanical motion of the microtubules is strongly affected by random thermal motion. This makes numerical simulation of the model more complex to implement and more computer-time intensive. Computationally, it would be convenient to separate the random and continuous motions. It is not in general mathematically correct to do this. However, we will discuss modeling techniques that allow some separation under some circumstances.

Even though a biophysical model is a simplification of a biological system, numerical simulation of that model can be quite complex to implement. Like a good laboratory instrument, the simulation program may be used and even modified by other researchers than the originator, often after the originator has left the project. The model must also be reliable. These three conditions, complexity, multiple users/implementers, and the need for reliability, place biophysical numerical simulations firmly in the class of computer programs that must be built with careful attention to basic software engineering principles.

B. First-Order Stochastic Equations

Our model can simulate several hundred microtubules, each on the order of 10 μm long. A few thousand molecular motors move along the microtubules. These motors generate forces, on the order of PicoNewtons, that move the microtubules. The surrounding medium is somewhat more viscous than water. For such a system, the Reynolds number is the ratio of inertial forces to viscous forces. Its precise definition depends on the specific system being studied, but it is proportional to the lengths and to the velocities of the objects in the system. It is also

inversely proportional to the viscosity. In this system, the length scale is on the order of tens of micrometers and the velocities are on the order of micrometers/minute. The Reynolds number is then on the order of 10^{-6}. This means that viscous forces dominate over momentum and that vortex flow in the medium is negligible. The relation between force and velocity in such an overdamped system is linear, allowing for a set of separate first-order differential equations, one for each mechanical degree of freedom. However, most of the degrees of freedom are subject to significant amounts of random thermal motion, and must be modeled by stochastic differential equations. The first-order nonequilibrium thermodynamic stochastic differential equations appropriate for this problem are known as Langevin equations, which have the form

$$\frac{\mathrm{d}}{\mathrm{d}t}x = \frac{1}{\zeta}F + \kappa\eta(t). \tag{1}$$

Here, x is an independent mechanical degree of freedom. The first term, called the *drift*, is easy to understand. F is the force in the direction of x and ζ is the friction coefficient for motion along x. Both of these are dependent on the nature of the local coordinate system. The second term, called the *diffusion*, represents thermal fluctuations. κ is a constant and $\eta(t)$ is a random Gaussian variable representing thermal fluctuations. The motion is assumed to be uncorrelated in time, so that

$$\begin{aligned} \langle\eta(t)\rangle &= 0 \\ \langle\eta(t)\eta(t+\alpha)\rangle &= \delta(\alpha), \end{aligned} \tag{2}$$

Informally, this means that the average of η over a time interval approaches zero as time interval approaches infinity. It also means that knowing the actual value of η for some particular time t_0 does not give you any extra information about the value at any other time $t_0 + \alpha$, as long as α is nonzero. Finally, very informally, it means that the mean-square signal is unity. The constant κ can be related to ζ via the Einstein relation (Doi and Edwards, 1986; Howard, 2001). The argument is based on the observations that the system satisfies the conditions for the fluctuation–dissipation theorem to hold (Pathria, 1996) and that the force can be represented as an energy potential gradient. Then

$$\dot{x} = D\beta F + \sqrt{2D}\eta(t), \tag{3}$$

where

$$\beta = \frac{1}{k_{\mathrm{B}}T}, \tag{4}$$

and

$$D = \frac{1}{\beta\zeta}. \tag{5}$$

The equations are separable in the sense that there is a one-to-one correspondence between the mechanical degrees of freedom and the Langevin equations. However, microtubule-microtubule contacts and crosslinking motors both make the force on one microtubule dependent on the positions of other microtubules. Depending on the choice of coordinates, the force along a particular degree of freedom for one microtubule can also depend on the values of the other degrees of freedom for the same microtubule. Thus, the system is highly coupled and the forces in the drift terms of the equations are potentially dependent on all degrees of freedom in the system.

One must be careful when assigning meaning to particular values of x at particular times t. The Langevin equation converts a precise value $x(t)$ to a probability distribution of values at later times. The integral form of the Langevin equation for variable $x^i(t)$ along the i-th direction shows this more clearly:

$$x^i(t+h) - x^i(t) = \frac{1}{\zeta_{ii}} \int_0^h \mathrm{d}\tau F_i\left(\vec{x}(t+\tau)\right) + \kappa^i \int_0^h \mathrm{d}\tau \eta(i; t+\tau). \tag{6}$$

The first integral is the mean force over the time interval h, multiplied by h itself. The second is an Ito integral (Kloeden and Platen, 1999). It converts one random variable with one probability distribution into another with another distribution. As a result, while $x(t)$ in this equation is a specific real number, $x(t+h)$ is a probability distribution. Given a particular state $x(t)$ at time t, we have generated a probability distribution of possible states at time $t+h$. The Monte-Carlo approach consists of picking a particular value for $x(t+h)$ fairly from that random distribution of possible values. By fairly, we mean that the choice is random, but that more-probable values are chosen more often than less-probable values. If $x(t)$ is a state value of the system at time t, $x(t+h)$ is then a representative state at time $t+h$. By repeating this for many such small time intervals, we calculate a "likely" history for the system. By repeating the entire calculation many times, we can develop a representative ensemble of likely histories.

The Monte-Carlo approach is not the only way to solve stochastic systems. Suppose that instead of calculating specific values for the system variables $x(t)$, we calculate the probability distributions of x at time t, $p_x(t)$. $p_x(t)$ satisfies the evolution equations known as Smoluchowski or Fokker–Planck. These equations are useful to do analytic approximate calculations while the Monte-Carlo approach is useful in computer evaluations. The Fokker–Planck approach is especially useful when the forces can be calculated directly from the probability distributions. It is difficult to use the Fokker–Planck approach in our problem since individual pairs of microtubules either contact each other or do not and are either connected by a crosslinking motor or are not connected. The force on any particular microtubule depends strongly on the precise positions of a small number

of other particular microtubules. This makes it difficult to calculate forces from probability distributions.

C. Dynamic Degrees of Freedom

An unconstrained microtubule in a three-dimensional (3D) model has six degrees of freedom: three for the position of a reference point, two for the orientation of the long axis about the reference point, and one for the degree of rotation about the long axis. If the microtubule is allowed to bend, the number of degrees of freedom can be higher. If the microtubule changes its length dynamically, the length becomes yet another degree of freedom. Our models have so far ignored rotation about the long axis; it is assumed that motors can move at will between adjacent protofilaments in a microtubule wall (lattice). If the microtubule motion is constrained in some way, there will be fewer degrees of freedom. For example, if each microtubule is anchored by a motor to a motionless chromosome or chromatin-covered magnetic bead, the three degrees of freedom for the reference point can be replaced by one, giving the signed distance of the pivot from the reference point. There are then three degrees of freedom (s, θ, ϕ) for each microtubule, where s is the length from the minus end of the microtubule to the pivot motor and (θ, ϕ) determines the direction of the plus end relative to the minus end. This approach reduces the dimensionality of the system, but prevents us from being able to model interactions between the microtubules and the chromatin surfaces. For instance, microtubules may float freely for awhile, or may move across a chromatin surface by breaking pivot motor bonds and remaking them to different motors in different locations. To model this requires five degrees of freedom (x, y, z, θ, ϕ). If each degree of freedom requires the same computer time to calculate, simulations would take 5/3, or 67% more computer time to run compared to the two-dimensional (2D) model where there are only three degrees of freedom for each microtubule.

Motors can attach to microtubules and exert forces on them, thereby causing the microtubules to move. The motors are so much smaller than the microtubules that we felt justified in neglecting frictional forces on the motors in our model. A crosslinking motor between two specific microtubules can be described by a pair (p_1, p_2) of real numbers, giving distances from the minus ends of the two microtubules to the binding points of the two ends of the motor. If the crosslinking motor is connected to only one microtubule, there is only one degree of freedom.

A system consisting of M microtubules and N connected crosslinking motor heads can then be modeled by $3M + N$ degrees of freedom. The system state can be propagated in time by using $3M$ Langevin equations, one for each of the three degrees of freedom for each of the M microtubules, and N first-order ordinary differential equations, one to model the attachment point of each of the N crosslinking motor heads. For a typical simulation with 200 microtubules and

2000 motors, this means 600 Langevin equations and 2000 ordinary differential equations.

Each time a microtubule is added or removed or a crosslinking motor head attaches or detaches from a microtubule, the dimensionality of the problem changes. Differential equations must be added or removed before continuous time propagation can proceed.

The degrees of freedom discussed so far are good ways to represent the system state, but may not involve the most effective coordinates for calculating changes in that state. In particular, (θ, ϕ) are polar coordinates and have singular points at the poles. This problem can be restated in a coordinate-independent way by using differential geometry. This is discussed in more detail in Appendix A.

D. Selecting Coordinate Patches for the State Propagation

One concept from differential geometry is important for an efficient implementation of the state propagator. The space of possible values of all of the system degrees of freedom is called a manifold. A manifold, even a connected manifold, does not have to be described by a single global coordinate system. Instead, it can be described by overlapping local coordinate systems called maps. Each map is a simple distortion of a Cartesian space and contains no singular points. By using many small maps, called patches, the distortions can be made arbitrarily small. Patches will greatly simplify the calculation of the coupled differential equation system by eliminating special points, such as the north and south poles of spherical polar coordinates.

Earlier, we showed that each single mechanical degree of freedom for a thermal object is controlled by a Langevin equation

$$\frac{\mathrm{d}}{\mathrm{d}t}x^i = \frac{1}{\zeta_{ii}}F_i(\vec{x}) + \kappa^i \eta(i;t). \tag{7}$$

Here the set index i represents several simultaneous degrees of freedom. The coupling between the separate degrees of freedom is contained in $F_i(\vec{x})$, where the force in the i-th direction is dependent on the current state of all coordinates, not just x^i. These equations are dependent on the local coordinate system, through the factors ζ_{ii} and κ^i. The local coordinate system must be orthogonal, or the factor ζ_{ii} will be a tensor ζ_{ij} instead of a single value. The term $1/\zeta_{ii}(F_i(\vec{x}))$ would then have to be replaced by $\Sigma_j 1/\zeta_{ij}(F_j(\vec{x}))$ in the Langevin equation, and the cross-terms where $i \neq j$ would introduce an unwanted coupling between the separate Langevin equations. The dependency on the local coordinate system arises because the values of x^i and F_i depend on the unit of length along the i-th coordinate. x^i is contravariant; it becomes smaller if the unit of length is greater. The force F_i is covariant; it becomes bigger if the unit of length is greater. This ensures that the work $F_i x^i$ created by a force between two points is independent of the unit of

distance used to measure the separation between those two points. This requires that the coefficient of friction ζ_{ii} be doubly covariant. If the unit of length is twice as long, ζ_{ii} must be four times larger. Similarly, since the random variable $\eta(i;t)$ is dimensionless, κ^i must be contravariant.

The friction coefficient ζ has units of Newton second/meter. We can use a metric tensor g_{ij} to express the effects of stretching and shrinking the local coordinate systems by using length units other than meters. If the coordinate system is orthogonal, the metric tensor will be diagonal. For coordinate patches, we will consider only orthogonal coordinate systems. The Langevin equation then becomes

$$\frac{\mathrm{d}}{\mathrm{d}t}x^i = \frac{1}{g_{ii}\zeta}F_i(\vec{x}) + \frac{1}{\sqrt{g_{ii}}}\kappa\eta(i;t) \tag{8}$$

where ζ and κ are defined in standard physical units. If ζ and κ are defined in units of meters, then for an orthogonal coordinate system also in units of meters $[g_{ij}] = \delta_{ij}$, with δ_{ij} the Kronecker unit matrix delta-function. For spherical coordinates (r, θ, ϕ), with r in meters and (θ, ϕ) in radians,

$$[g_{ij}] = \begin{bmatrix} 1 & 0 & 0 \\ 0 & r^2 & 0 \\ 0 & 0 & \sin^2(\theta)r^2 \end{bmatrix}.$$

The r^2 factor in each rotary term indicates that forces in rotary motions are torques rather than straight-line forces. The $\sin^2(\theta)$ factor is very close to 1 for $\theta \cong \pi/2$, corresponding to the equator, and it varies slowly with θ. However, it varies rapidly for $\theta \cong 0$ or $\theta \cong \pi$, corresponding to the north and south poles.

The Langevin equations considered here are first order and do not include derivatives of the metric. This reflects the physical fact that in the cytoplasm viscous forces dominate over inertial effects. This allows the differential equations to be treated separately. It also means that a slowly varying metric can be approximated as being constant over sufficiently small coordinate patches. A Langevin equation that uses this approximation will be wrong only by having a proportionally inaccurate coefficient of friction. This approximation introduces only a negligible error into our biophysical model results. Modelers using this technique on other models should ensure that this does not introduce spurious gradients that could generate false entropic forces.

The system of simultaneous Langevin equations controls the microtubule time evolution, and thereby the state of the system. The state trajectory of one microtubule is denoted by $(\vec{c}\,(t), \hat{a}(t))$, where $\vec{c}\,(t)$ is the position of the microtubule's center point and $\hat{a}(t)$ is the angular direction from the minus end to the plus end. This divides the state space for a single microtubule into two separate subspaces, corresponding to a 3D rectilinear space for $\vec{c}\,(t)$ and the 2D surface of a 3D sphere for $\hat{a}(t)$. In order to store the entire system state between time steps, we can choose

a single global rectilinear coordinate system $(\hat{x}, \hat{y}, \hat{z})$ for the microtubule center positions. For the angular positions, we choose a single global spherical coordinate system where $\hat{x} = \left(1, \frac{\pi}{2}, 0\right)$,$\hat{y} = \left(1, \frac{\pi}{2}, \frac{\pi}{2}\right)$, and $\hat{z} = (1, 0, 0)$. This global coordinate system is an efficient way of storing state information but it is not appropriate for calculating state changes over a time interval. For each microtubule, there are five Langevin equations: three for center point motion and two for angular motion. The metric for the center point motion is the unit diagonal matrix δ_{ij}, but the friction coefficient ζ is different for motion along the axis of the microtubule than it is for motion perpendicular to that axis. The metric for the two rotational degrees of freedom (θ, ϕ) is

$$g_{ij} = \begin{bmatrix} 1 & 0 \\ 0 & \sin^2(\theta) \end{bmatrix},$$

and the Langevin equation for motion in the φ direction is,

$$\frac{\mathrm{d}}{\mathrm{d}t}\phi = \frac{1}{\sin^2(\theta)\zeta_{\mathrm{rot}}} F_{\varphi}(\vec{x}) + \frac{1}{\sqrt{\sin^2(\theta)}} \kappa_{\mathrm{rot}} \eta(\phi; t) \tag{9}$$

will be highly sensitive to any motion in the θ direction if the microtubule happens to be aligned near the north or south poles. However, both problems can be solved by choosing a translated and rotated coordinate system such that the microtubule center point is at the origin and the microtubule is oriented along the $\hat{x}'$ axis. In the associated spherical coordinate system, $\theta' = \pi/2$. If a small-enough time interval h is chosen, the microtubule will not rotate far from this alignment, so the rotational metric will not change significantly over the interval h. Motion of the center point in the $\hat{x}'$ direction will be along the axis of the microtubule, while motion in the $\hat{y}'$ and $\hat{Z}'$ directions will be perpendicular to that axis. The five Langevin equations for this microtubule are then

$$\begin{aligned}
\frac{\mathrm{d}}{\mathrm{d}t}x' &= \frac{1}{\zeta_{\|}} F_{x'}(\vec{x'}) + \kappa_{\|}\eta(x'; t), \\
\frac{\mathrm{d}}{\mathrm{d}t}y' &= \frac{1}{\zeta_{\perp}} F_{x'}(\vec{x'}) + \kappa_{\perp}\eta(y'; t), \\
\frac{\mathrm{d}}{\mathrm{d}t}z' &= \frac{1}{\zeta_{\perp}} F_{z'}(\vec{x'}) + \kappa_{\perp}\eta(z'; t), \\
\frac{\mathrm{d}}{\mathrm{d}t}\theta &= \frac{1}{\zeta_{\mathrm{rot}}} T_{y'}(\vec{x}) + \kappa_{\mathrm{rot}}\eta(\theta; t), \\
\frac{\mathrm{d}}{\mathrm{d}t}\phi &= \frac{1}{\zeta_{\mathrm{rot}}} T_{z'}(\vec{x}) + \kappa_{\mathrm{rot}}\eta(\phi; t).
\end{aligned} \tag{10}$$

For clarity, the force terms in the last two equations have been replaced by the components of the total torque on the microtubule. Once these equations are integrated over the time interval h, the new position in the local coordinate system can be converted back to global coordinates.

Geometrically, this is equivalent to defining a local coordinate patch centered over the current system state. This coordinate patch was chosen so that, for states near the centers of the patches, the Langevin equations are separable and the coefficients of the terms in the equations can be approximated by constants, to an acceptable accuracy.

The coordinate transformations required for this are not computationally intensive. In particular, all forces and torques can be summed in global coordinates because forces and torques transform like vectors under this class of coordinate transformation.

E. Integrating the System of Langevin Equations

We now have a system of separate Langevin equations for the orientations of the microtubules, as well as a system of ordinary differential equations for the motor head positions. The ordinary differential equations (Boyce and DiPrima, 2004) are simple to calculate; we used a second-order Runge–Kutta scheme (Press *et al.*, 1992). For computer calculation, the Langevin equations must be converted into difference equations that, given a state at time t, will provide a sufficiently accurate approximation at a future time $t + h$. To minimize computer runtime, h should be as large as possible. This requires an expression for the error in the difference equation. The discrete integral form of the Langevin equations given in Eq. (11) provides the set of difference equations: The first integral is the mean force in the i-th direction over the time interval $(t, t + h)$. This makes the equations implicit because the forces over the interval depend on all of the values of $\vec{x}$ over the interval. $\eta(i; t)$ is a set of white-noise random variables, one for each distinct value of the arguments (i, t). In this particular problem the separate random variables are completely independent, that is,

$$\langle \eta(i; t)\eta(j; t + \tau)\rangle = \delta_{i,j}\delta(\tau).$$

These random variables are independent of time, as can be seen by the absence of t on the right-hand side of this equation. This will allow us to use time averages to calculate the mean values $\langle\cdot\rangle$. The term $\delta_{i,j}$ asserts that Brownian motions in different degrees of freedom are uncorrelated. This is true here, where we have set up the coordinate patches to ensure independence. Later we will discuss how to solve problems with coordinate systems where this is not true. The term $\delta(\tau)$ asserts that the Brownian motion is white, i.e. that thermal fluctuations occur equally at all time scales. This is an excellent approximation for this particular biological physics problem because frictional forces dominate over momentum at the time scale of this model.

The second integral in the difference equation is a linear combination of random variables, and is therefore itself a random variable.

$$\xi(i,t;v) = \int_0^v \mathrm{d}\tau \eta(i;t+\tau).$$

This is a random Gaussian variable. To see that this is reasonable, note that the integral is the limiting case of a summation of large numbers of well-behaved random variables and by the central limit theorem the resulting distribution of the sum will tend toward Gaussian.

The first integral, over the force, in the difference equation is implicit. This means that this term is also a Gaussian random variable. Finally, the difference $x^i(t+h) - x^i(t)$ is a Gaussian random variable because it is a linear combination of two Gaussian random variables. Finally, to get a representative system state for time $t+h$ we take a fair (random) sample from the final Gaussian distributions. This is the Monte-Carlo step.

An approximation would be to replace the average force over the interval $(t, t+h)$ by the force at time t. Then the difference equations would no longer be implicit:

$$x^i(t+h) - x^i(t) = \frac{h}{\zeta_{ii}} F_i\left(\vec{x}(t)\right) + \kappa^i \xi(i,t;h). \tag{11}$$

Unfortunately, this is too coarse an approximation for this particular problem. It assumes, among other things, that the Brownian motion of the microtubules over the time interval h has little effect on the forces on those microtubules. However, the microtubules are connected to each other by molecular motors, creating potential wells having length scales on the order of tens of nanometers. To ensure that Brownian motion was much less than this would require a very short time interval h and simulations would be prohibitively slow.

In Appendix B, we describe an approach that allows us to resolve this problem in an efficient way.

F. Bent Microtubules

We have used a straight-line-segment approximation for all of our spindle models so far. This greatly simplifies computer calculations, but it may not always be biophysically justified. A case can be made, however, that bending is not an important part of spindle formation in the chromosome-directed pathway. In this pathway, there are no centrosomes and kinetochores that influence dynamic instability by generating tension and compression forces on the microtubules. In contrast, the centrosome-directed pathway does involve these elements and

microtubule bending is believed to play a significant role in spindle formation. The latter pathway has been modeled by Nédélec and colleagues (Goshima *et al*., 2005; Karsenti *et al*., 2006; Nedelec, 2002; Nedelec and Surrey, 2001; Nedelec *et al*., 2001, 2003; Surrey *et al*., 2001). Their model calculations break each microtubule into some number L of straight-line segments. The number L varies over a simulation, but it is the same for all microtubules at any one time. This substantially expands the dimensionality of the state space. Suppose there are M microtubules, and if each microtubule is represented by a single line segment, then each has $p + a$ degrees of freedom, where p is the number of dimensions required to fix the position of a microtubule reference point and a is the number of dimensions required to express the microtubule orientation. For example, in our 2D model with fixed pivot points, $p = 1$ and $a = 1$. In a 3D model where the pivot points are not fixed, $p = 3$ and $a = 2$. If each microtubule is represented by L linked straight-line segments then a microtubule state can be fixed by giving the reference-point position of the first microtubule segment and the orientations of all of the segments. Thus, the state space for the microtubules has $M \times (p + L \times a)$ degrees of freedom. This assumes that the length of each segment is fixed. These lengths must be stored, but they will not change over the course of a simulation run.

These arguments show that microtubule dynamics, including curvature, require a $M \times (p + L \times a)$ dimensional state space. However, the particular state variables given above are unsuitable for dynamics calculations because they produce Langevin equations that are strongly coupled. For example, the position and orientation of the last segment of a microtubule depends on the position of the first segment as well as the orientations of all of the segments used to model each curved microtubule. In practice, this means that even the simplest calculations, such as determining the torque on a particular segment, involve large numbers of expensive geometrical function evaluations (see chapter by Gardel for further discussion, in this volume).

There is also a subtler difficulty in using an approximation with a large number of short segments. Because the system is overdamped, the friction coefficients for the microtubules are approximately proportional to the lengths of the microtubules. Therefore,$\zeta \cong \zeta_0 l_s$, where ζ_0 is the friction per unit length and l_s is the length of a microtubule segment. The diffusion coefficient for a microtubule segment $D = (1/\beta\zeta) \cong (1/\beta\zeta_0)(1/l_s)$ then varies inversely with the segment length l_s. An unconstrained segment will diffuse a distance of approximately $\sqrt{2Dh}$ in a time interval h. An order h^2 difference calculation scheme, described earlier, will begin to show substantial errors when $\sqrt{2Dh} \cong d_m$, where d_m is the distance over which a molecular crosslinking motor can be stretched without making large changes in its applied force. Then $h \cong (d_m^2/2D) \propto l_s$. Thus, doubling the number of segments not only increases the number of Langevin equations and increases the amount of geometrical calculations needed, but it also requires that the simulation time step be decreased. This decrease is required because the individual segments used to model each microtubule are smaller and therefore move more rapidly through the viscous medium.

The strength of coupling in the Langevin equations can be greatly decreased by converting to another coordinate system. The difference equations are all of the form (see Appendix B)

$$x_i(t_0+h) - x_i(t_0) = \sqrt{2D_i}\,Y_{1i}h^{\frac{1}{2}} + F_i h + \frac{1}{2}\sqrt{2D_i}\left\{\sum_{j\in I}(\partial_j F_i)\left(Y_{1j} + \frac{1}{\sqrt{3}}\,Y_{2j}\right)\right\} h^{\frac{3}{2}} + \mathfrak{O}(h^2)$$

The definition of Y_{1j} and Y_{2j} are given in Appendix B. These equations will be less-strongly coupled if coordinates are chosen such that the matrix $[\partial_j F_i]$ is diagonal. Unfortunately, the coordinate transformation to diagonalize this matrix must be recalculated at each time step.

One difficulty with this approach is that there are singular points where the diagonalizing transformation changes greatly for small changes to the state. This is particularly true where two adjacent segments have almost the same angular orientation. Such a segment pair could be replaced by a single segment of twice the length. This argues for using an adaptive, dynamic segmentation algorithm, where different microtubules will be divided into different numbers of different-length segments. One approach that appears to be promising is to require that adjacent segments have orientations that differ by at least θ_0 and at most θ_1 radians, where θ_0 and $\theta_1$are parameters whose values will be determined by the desired tradeoff between accuracy and calculation speed. Two segments where the difference is too small must be combined. Two segments that meet at too great an angle must be replaced by at least three smaller segments. This will not only decrease the number of Langevin equations that must be solved for each time step, but it will prevent the system from moving through a geometrical singularity during any one time step.

There are other possible approximations to decrease the computational load imposed by bent microtubules. For the centrosome-directed pathway, the spindle microtubules form substructures with distinct geometrical properties. The microtubules attached to a particular kinetochore and a particular pole is all close to each other and parallel, forming a K-bundle. This entire bundle can be replaced by a single, very stiff cylinder. The kinetochores control microtubule plus-end dynamic instability such that K-bundles are usually under tension. This tension is resisted by other microtubules under compression (Mitchison and Salmon, 2001). Each such compressional microtubule is paired with a compressional microtubule in the other direction, such that their plus ends overlap. These overlapping regions near the plus end are kept parallel by crosslinking plus-directed motors, usually Eg5. This introduces a bending torque in each microtubule. A problem involving a large number of individual microtubules can then potentially be changed into a problem involving a small number of tensile K-bundles and compressive bent pairs.

G. Soft Microtubule Contacts

In a 2D spindle model, microtubules are confined to a thin planar layer and can pass over each other without interacting. In a 3D model, microtubules can intersect at general angles and cannot pass through each other. In practice, this means that some regions of state space are inaccessible to a trajectory path, as an excluded volume. These constraints are very important to the system dynamics in 3D. Microtubules are on the order of 10 μm long, while crosslinking motors are on the order of 100 nm long. In order for a motor to crosslink, it must first be connected to one of the two microtubules that are candidates for crosslinking. The microtubules must approach each other to within about 1% of their sizes, and the singly connected motor must happen to be close to the point of closest approach. If microtubules were free to pass through each other, this confluence of events would happen rarely. However, a microtubule that contacts another microtubule will remain close to that microtubule for a longer time, greatly increasing the odds of motor connection.

Consider the states $\vec{x}(t)$ and $\vec{y}(t)$ of two microtubules, A and B. Suppose that there is some time t_0 at which the microtubules are almost in contact. We want to examine the system dynamics for a time interval h after t_0. As before, define local coordinate patches centered on $\vec{x}(t_0)$ and $\vec{y}(t_0)$. Make these patches small enough that they are almost flat. Choose an h small enough that any likely motion of the two microtubules over the interval will be confined to the patches. The Cartesian product of the two patches defines the state space for the two-microtubule subsystem over the time interval. This space is divided into three regions. First, since the microtubules have a positive thickness, there is a region that is excluded because the microtubules would overlap. This excluded region divides the rest of the space into two other regions, corresponding to microtubule A being on one side or the other of microtubule B. The trajectory over the time interval must be confined to one of these two regions.

There are two general approaches to solving a constrained problem of this kind. First, we can simply disallow any motion that violates the constraint. For the Langevin equation, this means that the probabilities for future positions will not be symmetrical Gaussian distributions but they will be one sided. This has two disadvantages. First, it is not easy to calculate constrained Brownian motion and the extra calculations will increase computer running time. Second, this abrupt transition between a free and an excluded region will stiffen the differential equations by introducing events with very short characteristic times. This has the effect of needing to reduce the time step h, further slowing computation. Both of these disadvantages stem from the fact that the geometrical constraints assume that microtubules are infinitely stiff and have infinitely hard outer walls. Neither of these assumptions is true in the actual biological system being modeled.

Another approach is to introduce contact forces sufficient to enforce the constraints. If the microtubules are infinitely rigid, this approach suffers from the same disadvantages as the first approach. However, we can introduce contact forces that are zero at the boundary of the allowed region and increase linearly as the

trajectory goes further into the excluded region. This does not mean that the microtubules actually interpenetrate. Rather, it means that the two microtubules bend or that the microtubule walls deform due to the contact. Not only are these "soft" contacts more biophysically accurate, but also they do not stiffen the differential equations. Figure 3 is a schematic diagram of such a soft contact.

Soft contacts introduce one geometrical complexity, even though the actual deformed microtubules will not. Consider $(\vec{p}_1, \hat{a_1}, l_1)$, a line segment with endpoints $\vec{p}_1$ and $\vec{p}_1 + l_1\hat{a_1}$. Let $(\vec{p}_2, \hat{a_2}, l_2)$ be another line segment. If the lines are almost parallel, $\hat{a} \cong \hat{a_2}$, then the contact must be treated as a special case. Otherwise, there will be a point $\vec{c}_1$ on the first line segment and a point $\vec{c}_2$ on the second segment such that these are the closest such points. If one of these points is at the end of the segment then the contact must again be treated as a special case, that of the end of one microtubule contacting the side (or even the end) of the other microtubule. By far the most common case is where the side of one microtubule contacts the side of another microtubule. In this case, two important geometrical conditions will remain invariant over the time interval from t_0 to $t_0 + h$. First, the cross-product $\hat{a_1}(t) \times \hat{a_2}(t)$ will be nonzero and will not change direction greatly. Second, the line segment $\vec{c}_2(t) - \vec{c}_1(t)$ will be perpendicular to the cross-product. Assume that the *sense* of the contact is defined by

$$s(t_0) = \text{sign}(\hat{a_1}(t_0) \times \hat{a_2}(t_0) \cdot (\vec{c}_2(t_0) - \vec{c}_1(t_0))).$$

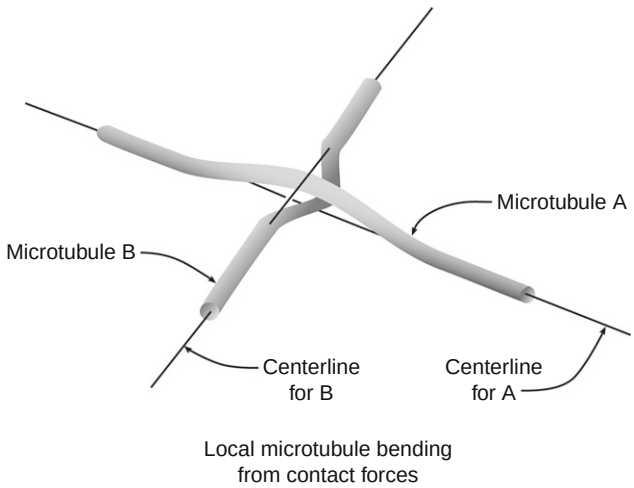

Fig. 3 Local microtubule bending from contact forces. When the sides of two microtubules come into contact, the microtubules bend locally, generating a smoothly varying repulsive force. Our biophysical model uses a centerline approximation to each microtubule, and it also remembers the sense of each contact. Here, when the contact first occurred, microtubule A was above microtubule B. However, the bending is sufficient to cause the centerline of microtubule A to be below the centerline of microtubule B. Read the body of the text for further explanations.

This is +1 if the contact is initially on one side and −1 if it is on the other. Define the *signed distance* of the contact be

$$\mathrm{d}(t) = s(t_0)(\hat{a_1}(t) \times \hat{a_2}(t) \cdot (\vec{c}_2(t) - \vec{c}_1(t))).$$

This will always be positive while the first microtubule remains on the same side of the other microtubule. As the first microtubule crosses to the other side this distance will move smoothly through zero.

H. Microtubule Dynamic Instability

One of the most important characteristics of microtubules is the degree to which they can change length quickly in response to changes in the chemical balance in the surrounding medium. This is called *dynamic instability*. These length changes are important to spindle formation. In later phases of mitosis, further changes in microtubule length are thought to be responsible for chromosome alignment and separation.

Early models of dynamic instability (Dogterom and Yurke, 1998; Martin *et al.*, 1993) emphasized length changes on single microtubules whose plus ends were free. The wall of a microtubule is formed by 11–15 protofilaments of $\alpha\beta$-tubulin dimers (Chretien *et al.*, 1992). Each $\alpha\beta$-tubulin contains a unit of either GTP or GDP (in the β part of the dimer). Most of the $\alpha\beta$-tubulin in the cytoplasm is GTP-$\alpha\beta$-tubulin. These dimers in the cytoplasm can attach to the plus ends of the proto-filaments, making them longer. It appears that the dimers have an enhanced probability of attaching to the shorter proto-filaments. Over time, this ensures that the plus ends of the proto-filaments are aligned to within one or two dimer units. There is then a region near the plus end of a microtubule in which all or most of the dimers are GTP-$\alpha\beta$-tubulin. This region is called the *growth cap*. Once incorporated in the microtubule walls, the GTP-$\alpha\beta$-tubulin is subject to hydrolysis, becoming GDP-$\alpha\beta$-tubulin. This is accompanied by a conformational change that introduces stress into the microtubule walls. This process of slow growth at the plus end, protected by the growth cap, is called *rescue*. However, it is not the only possible state of a microtubule. If the growth cap is disrupted for some reason, the stresses induced in the microtubule wall by the GDP-$\alpha\beta$-tubulin will cause the plus ends of the proto-filaments to dissociate from each other. Without the protective environment of adjacent proto-filaments, the plus ends rapidly depolymerize. The microtubule has entered another state, in which the plus end rapidly shortens. This state is called *catastrophe*. The microtubule remains in this state until it reaches some dimers that do not happen to have been hydrolyzed. When the depolymerization stops, the growth cap forms anew, and the microtubule enters the rescue state. A time plot of the length of a single microtubule describes a saw-tooth pattern, with long periods of slow increase interrupted by short periods of rapid decrease. Over longer periods of time, the microtubule will lengthen or shorten depending on the difference between the mean increase in length during the rescue states and the mean decrease in length during the catastrophe states.

The simplest model for spindle microtubule growth would be for the minus end to be inactive and for the plus end to display the catastrophe-rescue cycle described above. For example, the microtubules are assumed to form initially on some nucleating agent. The model could assume that this agent remained bound to the minus end, keeping it stable—while also allowing a flux that is known to occur at the minus end.

As mentioned before there are two complementary approaches to studying this model mathematically, corresponding to the Monte-Carlo and the Fokker–Planck approaches. In either case, the model has four parameters. A growing microtubule elongates at a rate v_+ and a shrinking microtubule shortens at a rate v_-. Growing microtubules become shrinking microtubules at a rate f_{+-} and shrinking microtubules become growing microtubules at a rate f_{-+}. The state of a microtubule can be described by the pair $\Big(s(t), l(t)\Big)$, where $s(t)$ is a Boolean variable having the value *true* if the microtubule is growing at time t and *false* if it is shrinking at time t. $l(t)$ is the microtubule length at time t.

In the Monte-Carlo approach, a numerical simulator would keep track of the state of each microtubule. If the microtubule is growing then one can use a Poisson random event generator with rate f_{+-} to determine how much longer it will grow. If it is shrinking, one can use the same generator with rate f_{-+} to see how much longer it will shrink (Schilstra *et al.*, 2008).

In the Fokker–Planck approach, consider an ensemble of N_T noninteracting microtubules, all of which are growing and shrinking according to the above model. At any time t, there will be a probability distribution $p(t; l)$ of microtubule of lengths l at time t. The total ensemble can be partitioned into N_- shrinking and N_+ growing microtubules. Since the size of the ensemble is fixed, $N_T = N_- + N_+$. The probability distribution can also be partitioned into $p_-(l)$ and $p_+(l)$, where

$$p(l) = p_-(l) + p_+(l), \tag{12}$$

$$N_s = \int_0^\infty p_-(\tau)\mathrm{d}\tau, \tag{13}$$

and

$$N_g = \int_0^\infty p_+(\tau)\mathrm{d}\tau. \tag{14}$$

The probability conservation law gives,

$$\partial_t p_- = v_-\partial_l p_- - f_{-+}p_- + f_{+-}p_+, \tag{15}$$

and

$$\partial_t p_+ = -v_+\partial_l p_+ - f_{+-}p_+ + f_{-+}p_-. \tag{16}$$

The solutions $p_-(l,t)$ and $p_+(l,t)$ must satisfy the boundary conditions that the lengths are bounded, i.e. $\lim_{l\to\infty} p_-(l,t) \to 0$, and $\lim_{l\to\infty} p_+(l,t) \to 0$. When a shrinking microtubule reaches zero length without a rescue, it disappears. A growing microtubule of infinitesimal length had to have come from somewhere. It came either from rescue of a shrinking microtubule or by spontaneous nucleation. Suppose that nucleation happens at a $v_N(t)$time rate. Consider a small time interval h. During that time a new region of width $\alpha = v_+ h$ appears at the $l = 0$ end of the interval. The total number of microtubules in this region is then

$$\alpha p_+ = \int_t^{t+h} \mathrm{d}\tau v(\tau) + f_{-+}\alpha p_- h, \tag{17}$$

and

$$p_+(0,t) = \lim_{h\to 0}[\frac{1}{hv_+}\int_t^{t+h} \mathrm{d}\tau v(\tau) + f_{-+}ph] = \frac{v(t)}{v_+}. \tag{18}$$

These equations were first proposed by Dogterom and Leibler (1993), although with a constant value for $v_N(t)$.

This simple model in which the minus end is inactive and the plus end is unconstrained has proven to be quite useful. However, it is unlikely that either assumption is true for mitotic spindle microtubules in either assembly pathway. In particular, in the centrosome-directed pathway all of the minus ends are bound by the centrosomes and most of the plus ends are bound by kinetochores. The rest of the microtubules are under compression. Their minus ends are bound to the centrosomes and their plus ends overlap with the plus ends of other compressional microtubules. Although this process is poorly understood, such an alignment will result in Eg5 crosslinking motors being bound to the plus ends of the microtubules, perhaps influencing their growth caps.

In the chromosome-directed pathway, microtubule minus ends are not bound by centrosomes and plus ends are not bound by kinetochores. However, the plus ends should be affected by the same plus-directed motors as in the other pathway. Since microtubules still nucleate even without the centrosomes, there can still be some nucleating agent bound to the minus ends.

It is, therefore, not hard to model dynamic instability numerically, but it is difficult to model it correctly. The dynamic effects at both plus and minus ends are modified by poorly understood processes, some of which change during the course of spindle assembly. For example, it has been proposed that growth and shrinkage rates can be affected by chemical gradients, such as for RanGTP (Kalab *et al.*, 2006). Although rates of microtubule growth and shrinkage can be measured experimentally in some systems (VanBuren *et al.*, 2005), they would have to be measured very carefully for the precise experimental conditions present around

chromatin-covered beads in *Xenopus* meiotic extracts. For these reasons, we have not yet included dynamic instability in our models.

Still, the simple model described above can be combined with the results of our numerical simulations of spindle assembly to place limits on such a model. Our simulations showed clearly that spindle formation in the chromosome-directed pathway is badly disrupted if there is a substantial distribution of microtubule lengths. This distribution makes it impossible for microtubule minus ends to meet in two compact poles. It also masks the spherical asymmetries of the chromosome (or chromatin-covered bead) distribution, making it difficult to keep poles opposite each other.

At the same time, analysis of the Dogterom–Leibler equations shows that wide spreads of microtubule lengths are almost inevitable unless there is some feedback mechanism to adjust the parameters of the catastrophe/rescue system. Much recent biological research has focused on the effect of a possible Ran gradient around the chromatin (Bastiaens *et al*., 2006; Kalab *et al*., 2006). However, such models must explain how such a gradient can regulate growth, since the steep part of the gradient affects the minus ends of the microtubules, not the supposedly more-active plus ends.

IV. Materials

Our numerical simulators have been written in FORTRAN 9X or in ANSI-standard C++. The basic architecture consists of two separate computer programs. The first program reads initialization data from files, computes simulation results, and writes them into data files. This program does not interact directly with a user.

This first program is almost entirely platform independent. It has been run successfully on MS Windows and on Unix operating systems. It is dependent on the open-source Boost library, version 1.33.1 (www.boost.org).

The second program reads the data files generated by the first, analyzes the results, and generates data for reports. This data includes tabular information to be converted into charts and graphs by *Mathematica*®. It also includes graphical visualizations, in the form of sequences of JPEG images. This program, because it has a complex user interface, is not entirely platform independent. It requires MS Windows XP or Vista. It is also dependent on the open-source Visualization Toolkit, version VTK4.2 (www.vtk.org).

Although the user interface for this second program is platform dependent, almost all of the code in the program is platform independent. Great care has been taken to share code wherever possible between the two computer programs. Also, the VTK library is available for many different platforms and programming languages.

All of our data files are human-readable text files with flexible formatting. We support this by using a simple recursive-descent parser that we developed. As a

result, it is easy for a researcher to make a quick assessment of the progress of a simulation run, or use a text editor to alter the input parameters for a subsequent run. Although the use of binary data files would speed up the writing and reading of data files, the overall speedup of the system would be negligible.

It is the intention of the authors to make this software available to others doing similar research, provided any changes made to the software also be made available. Maintenance of a full open-software public-domain project is currently beyond our resources. Anyone desiring access to this software is encouraged to contact the authors.

V. Discussion and Summary

Using experimental data and hypotheses from biologists, we have developed a biophysical model of the self-assembly of the mitotic spindle in *Xenopus* extracts. We have shown that the prevailing biological model for this self-assembly is biophysically plausible. We have also shown that a number of interesting phenomena, such as interactions between the plus-directed and minus-directed motors, are important in the formation of spindle patterns. These phenomena usually place constraints on the ranges of initial parameter values that will produce a spindle pattern. These constraints show the need for more finely nuanced biological hypotheses, and for further biological experimental testing to confirm or deny these hypotheses.

Mitotic spindle self-assembly is a biological process that is difficult to model numerically. It involves discrete events, continuous motion, and random (Brownian) motion. Here we have shown that it is possible to build such a model and to get results in agreement with biological data. In addition, our model calculations have allowed us to consider regions of parameter space not yet considered experimentally where the stability of formation of the spindle is compromised, e.g. changing the processivity and dynein nucleation rate. In this chapter, we have attempted to provide the foundation and details for those wishing to either repeat this work or to build models for similar cell biological systems.

Acknowledgments

We thank CIRCS, NSF, and the University at Buffalo for their support.

VI. Appendix A: Geometry of Dynamic Degrees of Freedom

The state space for particular values of M and N is a connected differentiable manifold $\mathfrak{M}(M, N)$. This is a continuous $3M + N$dimensional space with no preferred coordinate system. The complete state space is then a set of these

manifolds, one for each possible combination of M and N. This set of disjoint subspaces is then the manifold

$$\mathfrak{M} = \bigotimes_{M,N} \mathfrak{M}(M,N)$$

where $\otimes_{M,N}$ is the Cartesian product of the subspaces.

At each point in time, the system state is represented by a point in the manifold $\mathfrak{M}$. The evolution of the system over time is a path through the manifold, with time as the path parameter. When there are discrete events, such as motor head connections and disconnections, the path jumps from one sub-manifold to another. Between events, the trajectory is a smooth path through one particular sub-manifold. The Brownian motion due to thermal effects requires a special definition of "smooth," but this level of mathematical rigor is not required here.

VII. Appendix B: Langevin Calculation Algorithm

In this Appendix we provide the computational details of our numerical scheme for solving the Langevin stochastic differential equations. As a first step, consider a one-dimensional (1D) one-degree of freedom problem with a single Langevin equation. A formal integral solution is

$$x(t_0+h) - x(t_o) = \int_0^h \mathrm{d}\tau f\Big(x(t_0+\tau)\Big) + a\int_0^h \mathrm{d}\tau \eta(t_0+\tau). \tag{A1}$$

This is an implicit solution, as it requires the solution of x at points $(t_0+\tau)$ to calculate its value at (t_0+h). Note that the second term on the right-hand side is not dependent on x, and can be solved in general. Because of Eq. (11) $\gamma_h = \int_0^h \mathrm{d}\tau\eta(\tau)$ is a random variable. Breaking the integration range into n equal subintervals and taking the limit $n \to \infty$, γ_h has a Gaussian probability distribution

$$p(y) = \frac{1}{\sigma\sqrt{2\pi}} e^{-\frac{y^2}{2\sigma^2}}.$$

The σ value determines all of the properties of the stochastic term for any particular h and t. After comparing the second moments, one gets

$$\sigma = a\sqrt{h}.$$

Let Γ_h be a Gaussian random variable with $\sigma = 1$. Then $\sigma\Gamma_h$ is a random variable with the correct value of σ and

$$x(t_0+h)-x(t_0)=\int_0^h \mathrm{d}\tau f\Big(x(t_0+\tau)\Big)+a\sqrt{h\Gamma_h} \tag{A2}$$

The subscript on Γ_h is a reminder that $\sqrt{h\Gamma_h}=\int_0^h d\tau\eta(t_0+\tau)$. Similar variables for different values of h may not be correlated. Note that Eq. (A2) is still implicit because of the term $x(t_0+\tau)$ on the right hand side. However, it does show that the lowest power in h in an expansion will be 1/2.

To calculate x at finite time intervals, we assume that both x and f can be expanded in series about t_0. The expansion of f is a Taylor series in x:

$$f(x_0+\xi)=\sum\frac{\xi^n}{n!}f^{[n]}(x_0)=\sum\frac{\xi^n}{n!}f_n.$$

With the Taylor series definition of f_n. We expand x in half-integral powers of h:

$$x(t_0+h)=\sum_{n=0}^{\infty}p_n(h)h^{\frac{n}{2}},$$

where $p_0(h)=x_0$. We show the explicit dependence on h to keep track of the statistical properties of the random variable that will become part of some of the expansion coefficients. Equating the expansions we have,

$$\sum_{n=1}^{\infty}p_n(h)h^{\frac{n}{2}}=\int_0^h \mathrm{d}\tau\sum_{m=0}^{\infty}\frac{f_m}{m!}\left(\sum_{n=1}^{\infty}p_n(\tau)\tau^{\frac{n}{2}}\right)^m+\alpha\sqrt{h}\Gamma_h$$

Next approximate the expansion up to order h^2. To simplify further, the expansion inside the integrand needs be only up to τ because of the integration. Expanding to the same order in the two sides of the equation, we get

$$p_1(h)h^{\frac{1}{2}}+p_2(h)h+p_3(h)h^{\frac{3}{2}}+p_4(h)h^2=\int_0^h \mathrm{d}\tau\Big(f_0+f_1\Big(p_1(\tau)\tau^{\frac{1}{2}}+p_2(\tau)\tau\Big)+\frac{1}{2}f_2\Big(p_1(\tau)\tau^{\frac{1}{2}}\Big)^2\Big)+ah^{\frac{1}{2}}\Gamma_h+o\Big(h^{\frac{5}{2}}\Big)$$

By a process of identifying coefficients and comparing statistical moments, we get

$$x(t_0+h)\cong x(t_0)+\sqrt{2D}Y_1h^{\frac{1}{2}}+f\Big(x(t_0)\Big)h+(\partial_x f)\sqrt{2D}\frac{1}{2}\left(y_1+\frac{1}{\sqrt{3}}y_2\right)h^{\frac{3}{2}}$$

where Y_1 and Y_2 are independent Gaussian random variables with unit standard deviation. The size of the error in the expansion is

$$\text{error} \cong \left(\frac{1}{2}(\partial_x f)f + (\partial_x \partial_x f)D\right)h^2.$$

This result is valid for one variable. Consider now the N independent variables $x_i, i \in I, I = \{1, 2, \ldots, N\}$ that satisfy the Langevin equations

$$x_i(t) = f_i(x_1, x_2, \ldots, x_N) + \alpha_i \eta_{0i}(t),$$

where $\eta_{0i}(t)$ a Gaussian random variable as before and the subscript 0i denotes the context. We follow the 1D scheme given above, except that now each x_i and f_i must be expanded in a power series. The result is

$$x_i(t_0 + h) = x_i(t_0) + \sqrt{2D}\, Y_{1i} h^{\frac{1}{2}} + f_i h + \frac{1}{2}\sqrt{2D} \left\{ \sum_{j \in I} (\partial_j f_i)\left(Y_{1j} + \frac{1}{\sqrt{3}} Y_{2j} \right) \right\} h^{\frac{3}{2}} + Y_{1j} + \frac{1}{\sqrt{3}} Y_{2j} \mathfrak{D}(h^2).$$

This result involves first derivatives of the force functions, which are costly to calculate in a computer. Given these equations, one can set up then a Runge–Kutta scheme to eliminate the need to calculate the derivatives. Let

$$\begin{aligned} x_{i0} &= x_i(t_0), \\ x_{i1} &= x_{i0} + f_i(\vec{x_0})h + a_i, \\ x_{i2} &= x_{i0} + \frac{1}{2}h\{f_i(\vec{x_0}) + f_i(\vec{x_1})\} + h^{\frac{1}{2}}\sqrt{2D}\, Y_{1i}. \end{aligned}$$

The α_i and β_i are expressions to be determined. They will contain random variables and powers of $h^{\frac{1}{2}}$. Next we need to find α_i and β_i such that

$$x_{i2} = x_i(t_0 + h) + \mathfrak{D}(h^2).$$

To do this, we Taylor-expand $f_i(\vec{x_1})$, giving

$$\begin{aligned} x_{i2} &= x_{i0} + \frac{1}{2}hf_i(\vec{x_0}) + \frac{1}{2}h\left\{ f_i(\vec{x_0}) + \sum_{j \in i} \partial_j f_i(\vec{x_0})(x_{j1} - x_{j0}) + \mathfrak{D} + \left(h^{\frac{3}{2}}\right) \right\} \\ &+ \beta_i = x_{i0} + hf_i(\vec{x_0}) + \frac{1}{2}h \sum_{j \in I} \partial_j f_i(\vec{x_0}) \left\{ f_j(x_0)h + \alpha_j + \mathfrak{D}\left(h^{\frac{3}{2}}\right) \right\} \\ &+ \beta_i = x_{i0} + hf_i(\vec{x_0}) + \beta_i + \frac{1}{2}h \sum_{j \in I} \partial_j f_i(\vec{x_0}) + \alpha_j + \mathfrak{D}(h^2). \end{aligned}$$

Define $\alpha_j = h^{\frac{1}{2}}\sqrt{2D}\left(Y_{1j} + \frac{1}{\sqrt{3}}Y_{2j}\right)$ and $\beta_j = h^{\frac{1}{2}}\sqrt{2D}\,Y_{1j}$, so that

$$x_{i2} = x_{i0} + hf_i(\vec{x}_0) + h^{\frac{1}{2}}\sqrt{2D}\,Y_{1i} + \frac{1}{2}h^{\frac{3}{2}}\sqrt{2D}\times \sum_{j\in I}\partial_j f_i(\vec{x}_0)\left(Y_{1j} + \frac{1}{\sqrt{3}}Y_{2j}\right) + \mathfrak{D}(h^2),$$

and therefore $x_{i2} + x_i(t_0 + h) + \mathfrak{D}(h^2)$. Substituting for the α and β,

$$\begin{aligned} x_{i0} &= x_i(t_0), \\ x_{i1} &= x_{i0} + f_i(\vec{x}_0)h + h^{\frac{1}{2}}\sqrt{2D}\left(Y_{1i} + \frac{1}{\sqrt{3}}Y_{2i}\right), \\ x_{i2} &= x_{i0} + \frac{1}{2}h\{f_i(\vec{x}_0) + f_i(\vec{x}_1)\} + h^{\frac{1}{2}}\sqrt{2D}\,Y_{1i}. \end{aligned} \tag{A3}$$

We used Eq. (A3) in our computer calculations.

One could envision replacing the coordinate system in a coordinate patch with a transformed system in which the diffusions are uncorrelated. We have not done this in our model, but this approach promises in theory to substantially increase the maximum time step h, thereby shortening computation times.

References

Bastiaens, P., Caudron, M., Niethammer, P., and Karsenti, E. (2006). Gradients in the self-organization of the mitotic spindle. *Trends Cell Biol.* **16,** 125–134.

Boyce, W. E., and DiPrima, R. C. (2004). "Elementary Differential Equations and Boundary Value Problems, with ODE Architect CD." Wiley, New York.

Bras, W., Diakun, G. P., Diaz, J. F., Maret, G., Kramer, H., Bordas, J., and Medrano, F. J. (1998). The susceptibility of pure tubulin to high magnetic fields: A magnetic birefringence and X-ray fiber diffraction study. *Biophys. J.* **74,** 1509–1521.

Budde, P. P., Kumagai, A., Dunphy, W. G., and Heald, R. (2001). Regulation of Op18 during spindle assembly in *Xenopus* egg extracts. *J. Cell Biol.* **153,** 149–158.

Carazo-Salas, R. E., Guarguaglini, G., Gruss, O. J., Segref, A., Karsenti, E., and Mattaj, I. W. (1999). Generation of GTP-bound Ran by RCC1 is required for chromatin-induced mitotic spindle formation. *Nature* **400,** 178–181.

Chretien, D., Metoz, F., Verde, F., Karsenti, E., and Wade, R. H. (1992). Lattice defects in microtubules: Protofilament numbers vary within individual microtubules. *J. Cell Biol.* **117,** 1031–1040.

Dogterom, M., and Leibler, S. (1993). Physical aspects of the growth and regulation of microtubule structures. *Phys. Rev. Lett.* **70,** 1347–1350.

Dogterom, M., and Yurke, B. (1998). Microtubule dynamics and the positioning of microtubule organizing centers. *Phys. Rev. Lett.* **81,** 485–488.

Doi, M., and Edwards, S. F. (1986). "The Theory of Polymer Dynamics." Oxford University Press, New York.

Gadde, S., and Heald, R. (2004). Mechanisms and molecules of the mitotic spindle. *Curr. Biol.* **14,** R797–R805.

Goshima, G., Nedelec, F., and Vale, R. D. (2005). Mechanisms for focusing mitotic spindle poles by minus end-directed motor proteins. *J. Cell Biol.* **171,** 229–240.

Heald, R. (2000a). A dynamic duo of microtubule modulators. *Nat. Cell Biol.* **2,** E11–E12.

Heald, R. (2000b). Motor function in the mitotic spindle. *Cell* **102,** 399–402.

Heald, R. W. (2004). Cell division: Burning the spindle at both ends. *Nature* **427,** 300–301.

Heald, R., Tournebize, R., Blank, T., Sandaltzopoulos, R., Becker, P., Hyman, A., and Karsenti, E. (1996). Self-organization of microtubules into bipolar spindles around artificial chromosomes in *Xenopus* egg extracts. *Nature* **382,** 420–425.

Heald, R., Tournebize, R., Habermann, A., Karsenti, E., and Hyman, A. (1997). Spindle assembly in *Xenopus* egg extracts: Respective roles of centrosomes and microtubule self-organization. *J. Cell Biol.* **138,** 615–628.

Hinchcliffe, E. H., Miller, F. J., Cham, M., Khodjakov, A., and Sluder, G. (2001). Requirement of a centrosomal activity for cell cycle progression through G1 into S phase. *Science* **291,** 1547–1550.

Howard, J. (2001). ''Mechanics of Motor Proteins and the Cytoskeleton.'' Sinauer Associates, Sunderland, MA.

Kalab, P., Pralle, A., Isacoff, E. Y., Heald, R., and Weis, K. (2006). Analysis of a RanGTP-regulated gradient in mitotic somatic cells. *Nature* **440,** 697–701.

Kapoor, T. M., Lampson, M. A., Hergert, P., Cameron, L., Cimini, D., Salmon, E. D., McEwen, B. F., and Khodjakov, A. (2006). Chromosomes can congress to the metaphase plate before biorientation. *Science* **311,** 388–391.

Karsenti, E., Nedelec, F., and Surrey, T. (2006). Modelling microtubule patterns. *Nat. Cell Biol.* **8,** 1204–1211.

Karsenti, E., and Vernos, I. (2001). The mitotic spindle: A self-made machine. *Science* **294,** 543–547.

Kloeden, P. E., and Platen, E. (1999). ''Numerical Solution of Stochastic Differential Equations.'' Springer-Verlag, Berlin.

Martin, S. R., Schilstra, M. J., and Bayley, P. M. (1993). Dynamic instability of microtubules: Monte Carlo simulation and application to different types of microtubule lattice. *Biophys. J.* **65,** 578–596.

Mitchison, T. J., and Salmon, E. D. (2001). Mitosis: A history of division. *Nat. Cell Biol.* **3,** E17–E21.

Nedelec, F. (2002). Computer simulations reveal motor properties generating stable antiparallel microtubule interactions. *J. Cell Biol.* **158,** 1005–1015.

Nedelec, F., and Surrey, T. (2001). Dynamics of microtubule aster formation by motor complexes. *C. R. Acad. Sci.* **2,** 841–847.

Nedelec, F., Surrey, T., and Karsenti, E. (2003). Self-organisation and forces in the microtubule cytoskeleton. *Curr. Opin. Cell Biol.* **15,** 118–124.

Nedelec, F., Surrey, T., and Maggs, A. C. (2001). Dynamic concentration of motors in microtubule arrays. *Phys. Rev. Lett.* **86,** 3192–3195.

Pathria, R. K. (1996). ''Statistical Mechanics,'' 2nd ed. Butterworth-Heinemann, Oxford.

Phair, R. D., and Misteli, T. (2000). High mobility of proteins in the mammalian cell nucleus. *Nature* **404,** 604–609.

Press, W., Teukolsky, S., Vetterling, W., and Flannery, B. (1992). ''Numerical Recipes in C: The Art of Scientific Computing.'' Cambridge University Press, Cambridge, MA.

Rieder, C. L., Faruki, S., and Khodjakov, A. (2001). The centrosome in vertebrates: More than a microtubule-organizing center. *Trends Cell Biol.* **11,** 413–419.

Schilstra, M. J., Martin, S. R., and Keating, S. M. (2008). Methods for simulating the dynamics of complex biological processes. *Methods Cell Biol.* **84,** 807–842.

Surrey, T., Nedelec, F., Leibler, S., and Karsenti, E. (2001). Physical properties determining self-organization of motors and microtubules. *Science* **292,** 1167–1171.

VanBuren, V., Cassimeris, L., and Odde, D. J. (2005). Mechanochemical model of microtubule structure and self-assembly kinetics. *Biophys. J.* **89,** 2911–2926.

INDEX

N

VOLUMES IN SERIES

Founding Series Editor
DAVID M. PRESCOTT

Volume 1 (1964)
Methods in Cell Physiology
Edited by David M. Prescott

Volume 2 (1966)
Methods in Cell Physiology
Edited by David M. Prescott

Volume 3 (1968)
Methods in Cell Physiology
Edited by David M. Prescott

Volume 4 (1970)
Methods in Cell Physiology
Edited by David M. Prescott

Volume 5 (1972)
Methods in Cell Physiology
Edited by David M. Prescott

Volume 6 (1973)
Methods in Cell Physiology
Edited by David M. Prescott

Volume 7 (1973)
Methods in Cell Biology
Edited by David M. Prescott

Volume 8 (1974)
Methods in Cell Biology
Edited by David M. Prescott

Volume 9 (1975)
Methods in Cell Biology
Edited by David M. Prescott

Volume 10 (1975)
Methods in Cell Biology
Edited by David M. Prescott

Volume 11 (1975)
Yeast Cells
Edited by David M. Prescott

Volume 12 (1975)
Yeast Cells
Edited by David M. Prescott

Volume 13 (1976)
Methods in Cell Biology
Edited by David M. Prescott

Volume 14 (1976)
Methods in Cell Biology
Edited by David M. Prescott

Volume 15 (1977)
Methods in Cell Biology
Edited by David M. Prescott

Volume 16 (1977)
Chromatin and Chromosomal Protein Research I
Edited by Gary Stein, Janet Stein, and Lewis J. Kleinsmith

Volume 17 (1978)
Chromatin and Chromosomal Protein Research II
Edited by Gary Stein, Janet Stein, and Lewis J. Kleinsmith

Volume 18 (1978)
Chromatin and Chromosomal Protein Research III
Edited by Gary Stein, Janet Stein, and Lewis J. Kleinsmith

Volume 19 (1978)
Chromatin and Chromosomal Protein Research IV
Edited by Gary Stein, Janet Stein, and Lewis J. Kleinsmith

Volume 20 (1978)
Methods in Cell Biology
Edited by David M. Prescott

Advisory Board Chairman
KEITH R. PORTER

Volume 21A (1980)
Normal Human Tissue and Cell Culture, Part A: Respiratory, Cardiovascular, and Integumentary Systems
Edited by Curtis C. Harris, Benjamin F. Trump, and Gary D. Stoner

Volume 21B (1980)
Normal Human Tissue and Cell Culture, Part B: Endocrine, Urogenital, and Gastrointestinal Systems
Edited by Curtis C. Harris, Benjamin F. Trump, and Gray D. Stoner

Volume 22 (1981)
Three-Dimensional Ultrastructure in Biology
Edited by James N. Turner

Volume 23 (1981)
Basic Mechanisms of Cellular Secretion
Edited by Arthur R. Hand and Constance Oliver

Volume 24 (1982)
The Cytoskeleton, Part A: Cytoskeletal Proteins, Isolation and Characterization
Edited by Leslie Wilson

Volume 25 (1982)
The Cytoskeleton, Part B: Biological Systems and *In Vitro* Models
Edited by Leslie Wilson

Volume 26 (1982)
Prenatal Diagnosis: Cell Biological Approaches
Edited by Samuel A. Latt and Gretchen J. Darlington

Series Editor
LESLIE WILSON

Volume 27 (1986)
Echinoderm Gametes and Embryos
Edited by Thomas E. Schroeder

Volume 28 (1987)
***Dictyostelium discoideum:* Molecular Approaches to Cell Biology**
Edited by James A. Spudich

Volume 29 (1989)
Fluorescence Microscopy of Living Cells in Culture, Part A: Fluorescent Analogs, Labeling Cells, and Basic Microscopy
Edited by Yu-Li Wang and D. Lansing Taylor

Volume 30 (1989)
Fluorescence Microscopy of Living Cells in Culture, Part B: Quantitative Fluorescence Microscopy—Imaging and Spectroscopy
Edited by D. Lansing Taylor and Yu-Li Wang

Volume 31 (1989)
Vesicular Transport, Part A
Edited by Alan M. Tartakoff

Volume 32 (1989)
Vesicular Transport, Part B
Edited by Alan M. Tartakoff

Volume 33 (1990)
Flow Cytometry
Edited by Zbigniew Darzynkiewicz and Harry A. Crissman

Volume 34 (1991)
Vectorial Transport of Proteins into and across Membranes
Edited by Alan M. Tartakoff

Selected from Volumes 31, 32, and 34 (1991)
Laboratory Methods for Vesicular and Vectorial Transport
Edited by Alan M. Tartakoff

Volume 35 (1991)
Functional Organization of the Nucleus: A Laboratory Guide
Edited by Barbara A. Hamkalo and Sarah C. R. Elgin

Volume 36 (1991)
***Xenopus laevis:* Practical Uses in Cell and Molecular Biology**
Edited by Brian K. Kay and H. Benjamin Peng

Series Editors
LESLIE WILSON AND PAUL MATSUDAIRA

Volume 37 (1993)
Antibodies in Cell Biology
Edited by David J. Asai

Volume 38 (1993)
Cell Biological Applications of Confocal Microscopy
Edited by Brian Matsumoto

Volume 39 (1993)
Motility Assays for Motor Proteins
Edited by Jonathan M. Scholey

Volume 40 (1994)
A Practical Guide to the Study of Calcium in Living Cells
Edited by Richard Nuccitelli

Volume 41 (1994)
Flow Cytometry, Second Edition, Part A
Edited by Zbigniew Darzynkiewicz, J. Paul Robinson, and Harry A. Crissman

Volume 42 (1994)
Flow Cytometry, Second Edition, Part B
Edited by Zbigniew Darzynkiewicz, J. Paul Robinson, and Harry A. Crissman

Volume 43 (1994)
Protein Expression in Animal Cells
Edited by Michael G. Roth

Volume 44 (1994)
***Drosophila melanogaster:* Practical Uses in Cell and Molecular Biology**
Edited by Lawrence S. B. Goldstein and Eric A. Fyrberg

Volume 45 (1994)
Microbes as Tools for Cell Biology
Edited by David G. Russell

Volume 46 (1995)
Cell Death
Edited by Lawrence M. Schwartz and Barbara A. Osborne

Volume 47 (1995)
Cilia and Flagella
Edited by William Dentler and George Witman

Volume 48 (1995)
***Caenorhabditis elegans:* Modern Biological Analysis of an Organism**
Edited by Henry F. Epstein and Diane C. Shakes

Volume 49 (1995)
Methods in Plant Cell Biology, Part A
Edited by David W. Galbraith, Hans J. Bohnert, and Don P. Bourque

Volume 50 (1995)
Methods in Plant Cell Biology, Part B
Edited by David W. Galbraith, Don P. Bourque, and Hans J. Bohnert

Volume 51 (1996)
Methods in Avian Embryology
Edited by Marianne Bronner-Fraser

Volume 52 (1997)
Methods in Muscle Biology
Edited by Charles P. Emerson, Jr. and H. Lee Sweeney

Volume 53 (1997)
Nuclear Structure and Function
Edited by Miguel Berrios

Volume 54 (1997)
Cumulative Index

Volume 55 (1997)
Laser Tweezers in Cell Biology
Edited by Michael P. Sheetz

Volume 56 (1998)
Video Microscopy
Edited by Greenfield Sluder and David E. Wolf

Volume 57 (1998)
Animal Cell Culture Methods
Edited by Jennie P. Mather and David Barnes

Volume 58 (1998)
Green Fluorescent Protein
Edited by Kevin F. Sullivan and Steve A. Kay

Volume 59 (1998)
The Zebrafish: Biology
Edited by H. William Detrich III, Monte Westerfield, and Leonard I. Zon

Volume 60 (1998)
The Zebrafish: Genetics and Genomics
Edited by H. William Detrich III, Monte Westerfield, and Leonard I. Zon

Volume 61 (1998)
Mitosis and Meiosis
Edited by Conly L. Rieder

Volume 62 (1999)
Tetrahymena thermophila
Edited by David J. Asai and James D. Forney

Volume 63 (2000)
Cytometry, Third Edition, Part A
Edited by Zbigniew Darzynkiewicz, J. Paul Robinson, and Harry Crissman

Volume 64 (2000)
Cytometry, Third Edition, Part B
Edited by Zbigniew Darzynkiewicz, J. Paul Robinson, and Harry Crissman

Volume 65 (2001)
Mitochondria
Edited by Liza A. Pon and Eric A. Schon

Volume 66 (2001)
Apoptosis
Edited by Lawrence M. Schwartz and Jonathan D. Ashwell

Volume 67 (2001)
Centrosomes and Spindle Pole Bodies
Edited by Robert E. Palazzo and Trisha N. Davis

Volume 68 (2002)
Atomic Force Microscopy in Cell Biology
Edited by Bhanu P. Jena and J. K. Heinrich Hörber

Volume 69 (2002)
Methods in Cell–Matrix Adhesion
Edited by Josephine C. Adams

Volume 70 (2002)
Cell Biological Applications of Confocal Microscopy
Edited by Brian Matsumoto

Volume 71 (2003)
Neurons: Methods and Applications for Cell Biologist
Edited by Peter J. Hollenbeck and James R. Bamburg

Volume 72 (2003)
Digital Microscopy: A Second Edition of Video Microscopy
Edited by Greenfield Sluder and David E. Wolf

Volume 73 (2003)
Cumulative Index

Volume 74 (2004)
Development of Sea Urchins, Ascidians, and Other Invertebrate Deuterostomes: Experimental Approaches
Edited by Charles A. Ettensohn, Gary M. Wessel, and Gregory A. Wray

Volume 75 (2004)
Cytometry, 4th Edition: New Developments
Edited by Zbigniew Darzynkiewicz, Mario Roederer, and Hans Tanke

Volume 76 (2004)
The Zebrafish: Cellular and Developmental Biology
Edited by H. William Detrich, III, Monte Westerfield, and Leonard I. Zon

Volume 77 (2004)
The Zebrafish: Genetics, Genomics, and Informatics
Edited by William H. Detrich, III, Monte Westerfield, and Leonard I. Zon

Volume 78 (2004)
Intermediate Filament Cytoskeleton
Edited by M. Bishr Omary and Pierre A. Coulombe

Volume 79 (2007)
Cellular Electron Microscopy
Edited by J. Richard McIntosh

Volume 80 (2007)
Mitochondria, 2nd Edition
Edited by Liza A. Pon and Eric A. Schon

Volume 81 (2007)
Digital Microscopy, 3rd Edition
Edited by Greenfield Sluder and David E. Wolf

Volume 82 (2007)
Laser Manipulation of Cells and Tissues
Edited by Michael W. Berns and Karl Otto Greulich

Volume 83 (2007)
Cell Mechanics
Edited by Yu-Li Wang and Dennis E. Discher

Volume 84 (2007)
Biophysical Tools for Biologists, Volume One: *In Vitro* Techniques
Edited by John J. Correia and H. William Detrich, III

Volume 85 (2008)
Fluorescent Proteins
Edited by Kevin F. Sullivan

Volume 86 (2008)
Stem Cell Culture
Edited by Dr. Jennie P. Mather

Volume 87 (2008)
Avian Embryology, 2nd Edition
Edited by Dr. Marianne Bronner-Fraser

Volume 88 (2008)
Introduction to Electron Microscopy for Biologists
Edited by Prof. Terence D. Allen